

WOODHEAD PUBLISHING SERIES IN ENERGY



ADVANCES IN NUCLEAR FUEL CHEMISTRY



Edited by
MARKUS H.A. PIRO

Advances in Nuclear Fuel Chemistry

This page intentionally left blank

Woodhead Publishing Series in Energy

Advances in Nuclear Fuel Chemistry

Edited by

Markus H.A. Piro



ELSEVIER

WP

WOODHEAD
PUBLISHING

An imprint of Elsevier

Woodhead Publishing is an imprint of Elsevier
The Officers' Mess Business Centre, Royston Road, Duxford, CB22 4QH, United Kingdom
50 Hampshire Street, 5th Floor, Cambridge, MA 02139, United States
The Boulevard, Langford Lane, Kidlington, OX5 1GB, United Kingdom

Copyright © 2020 Elsevier Ltd. All rights reserved.

No part of this publication may be reproduced or transmitted in any form or by any means, electronic or mechanical, including photocopying, recording, or any information storage and retrieval system, without permission in writing from the publisher. Details on how to seek permission, further information about the Publisher's permissions policies and our arrangements with organizations such as the Copyright Clearance Center and the Copyright Licensing Agency, can be found at our website: www.elsevier.com/permissions.

This book and the individual contributions contained in it are protected under copyright by the Publisher (other than as may be noted herein).

Notices

Knowledge and best practice in this field are constantly changing. As new research and experience broaden our understanding, changes in research methods, professional practices, or medical treatment may become necessary.

Practitioners and researchers must always rely on their own experience and knowledge in evaluating and using any information, methods, compounds, or experiments described herein. In using such information or methods they should be mindful of their own safety and the safety of others, including parties for whom they have a professional responsibility.

To the fullest extent of the law, neither the Publisher nor the authors, contributors, or editors, assume any liability for any injury and/or damage to persons or property as a matter of products liability, negligence or otherwise, or from any use or operation of any methods, products, instructions, or ideas contained in the material herein.

British Library Cataloguing-in-Publication Data

A catalogue record for this book is available from the British Library

Library of Congress Cataloging-in-Publication Data

A catalog record for this book is available from the Library of Congress

ISBN: 978-0-08-102571-0 (print)

ISBN: 978-0-08-102651-9 (online)

For information on all Woodhead Publishing publications
visit our website at <https://www.elsevier.com/books-and-journals>

Publisher: Katie Hammon
Acquisitions Editor: Maria Convey
Editorial Project Manager: Lindsay Lawrence
Production Project Manager: Joy Christel Neumarin
Honest Thangiah
Cover Designer: Greg Harris

Typeset by MPS Limited, Chennai, India



Working together
to grow libraries in
developing countries

www.elsevier.com • www.bookaid.org

Contents

List of contributors	xiii
About the editor	xvii
Preface	xix

Part A Fundamentals 1

1 Reaction kinetics and chemical thermodynamics of nuclear materials	3
<i>Anna L. Smith and Rudy J.M. Konings</i>	
1.1 Introduction	3
1.2 Basic concepts of chemical kinetics	4
1.2.1 Reaction rates	4
1.2.2 Temperature dependence of rate constants	7
1.3 Fundamentals of chemical thermodynamics	9
1.3.1 Thermodynamic system and state functions	9
1.3.2 The laws of thermodynamics	10
1.3.3 Enthalpy, Helmholtz, and Gibbs energies	11
1.3.4 Heat capacity	13
1.3.5 Thermodynamic relations between state functions	15
1.4 Thermodynamics of condensed phases	15
1.4.1 Molar thermodynamic properties	15
1.4.2 Definition of the chemical potential	25
1.4.3 Mixing properties for gas, solid, and liquid solutions	29
1.4.4 Chemical reaction equilibria	34
1.5 Statistical thermodynamics applied to gases	35
1.5.1 Statistical thermodynamic basis	35
1.5.2 Molecular thermodynamic calculations (ideal gas)	41
1.5.3 The vibrational partition function	42
1.6 Thermodynamics of nuclear fuel and fission products	49
1.6.1 Phase diagrams	49
1.6.2 Melting transition	55
1.6.3 Effect of nonstoichiometry on thermodynamic properties	56
1.6.4 Sublimation and vaporization behavior	60
1.6.5 Chemical state of fission products: Ellingham diagrams	66
1.7 Solution thermodynamics applied to the storage of spent fuel and geological disposal	69
1.7.1 Hydrolysis and complexation	69

1.7.2 Solubility and precipitation	71
1.8 Basics of redox equilibria	72
1.8.1 Redox equilibria and Galvanic cell	73
1.8.2 Pourbaix diagrams	77
1.8.3 Speciation diagrams	82
1.9 Conclusion	84
Acknowledgment	84
References	85
Further reading	88
2 Experimental methods	89
<i>Dario Manara, Alice Seibert, Thomas Gouder, Ondřej Beneš, Laura Martel, Jean-Yves Colle, Jean-Christophe Griveau, Olaf Walter, Andrea Cambriani, Oliver Dieste Blanco, Dragos Staicu, Thierry Wiss and Jean-François Vigier</i>	
2.1 Introduction	89
2.2 Thermal analysis methods	90
2.2.1 Differential scanning and drop calorimetry	90
2.2.2 Thermogravimetric analysis	97
2.2.3 Laser heating	101
2.3 Spectroscopy techniques	106
2.3.1 Vibrational spectroscopy methods	107
2.3.2 X-ray absorption spectroscopy (EXAFS, XANES)	111
2.3.3 Photoelectron spectroscopy (XPS, UPS)	116
2.3.4 Electron microscopy and spectroscopy (SEM, TEM, EDS, EELS, EPMA)	121
2.3.5 Positron annihilation spectroscopy	126
2.4 Nuclear magnetic resonance	131
2.4.1 Liquid state nuclear magnetic resonance	131
2.4.2 Low-temperature nuclear magnetic resonance	131
2.4.3 High-resolution solid-state nuclear magnetic resonance	133
2.4.4 Some examples of nuclear magnetic resonance spectra acquired at JRC-Karlsruhe	134
2.5 Mass spectrometry techniques	135
2.5.1 Knudsen effusion mass spectrometry	136
2.6 Secondary ions mass spectrometry	137
2.7 Diffraction techniques	139
2.7.1 X-ray diffraction	139
2.7.2 Electron diffraction	141
2.8 Electrochemical techniques	143
2.8.1 Electromotive force and coulometry	143
2.9 Conclusion	146
References	146
Further reading	158

3 Computational thermochemistry of nuclear fuel	159
<i>Markus H.A. Piro</i>	
3.1 Introduction	159
3.2 Fundamentals	161
3.2.1 Thermodynamic laws	161
3.2.2 Derivation of fundamental thermodynamic properties	162
3.2.3 Conditions for equilibrium in a closed isothermal–isobaric system	166
3.2.4 Gibbs energy minimization	169
3.3 The CALPHAD method	169
3.4 Applications and limitations of computational thermodynamics	173
3.4.1 Phase diagram construction	173
3.4.2 Integral analyses	175
3.4.3 Limitations of thermodynamic calculations	177
3.5 Summary	180
References	180
Part B Fuel Designs	183
4 Oxide power reactor fuels	185
<i>Lian C. Wang and Matthew H. Kaye</i>	
4.1 Introduction	185
4.1.1 Crystal structures of various oxide nuclear fuels	185
4.1.2 Nuclear reactions	185
4.1.3 Thermal conductivity profiles for the U–Pu–Th–O system	188
4.2 Phase diagrams involving UO_2 , PuO_2 , and ThO_2	189
4.2.1 The uranium–oxygen system and UO_2	189
4.2.2 The plutonium–oxygen system and PuO_2	191
4.2.3 The thorium–oxygen system and ThO_2	192
4.3 Binary and higher order oxide phase diagrams	193
4.3.1 UO_2 – PuO_2 binary system	195
4.3.2 ThO_2 – UO_2 binary system	195
4.3.3 ThO_2 – PuO_2 binary system	197
4.3.4 Higher order system—diagrams of UO_2 – ThO_2 – PuO_2	203
4.4 Doped fuels	203
4.5 Summary	207
References	208
5 Other power reactor fuels	215
<i>Andrew T. Nelson and Paul Demkowicz</i>	
5.1 Introduction	215
5.2 Metallic fuels	216
5.2.1 Zirconium-based metallic fuels	216
5.2.2 Molybdenum-based metallic fuels	220

5.3	Nontraditional ceramic fuels	220
5.3.1	Carbide fuels	222
5.3.2	Nitride fuels	226
5.3.3	Other nontraditional ceramic fuel forms	229
5.4	Coated particle fuels	231
5.4.1	CO formation and the effect on particle integrity	232
5.4.2	Fission product chemistry and transport in tristructural isotropic fuel particles	237
5.4.3	Oxygen potential and fission products	241
5.5	Summary and outlook	242
	References	243
	Further reading	247
6	Molten salt reactor fuels	249
	<i>Ondřej Beneš and Pavel Souček</i>	
6.1	Introduction	249
6.1.1	Key advantages of the molten salt reactor	249
6.1.2	Challenges for molten salt reactor deployment	251
6.2	History of molten salt reactor research	252
6.3	Molten salt reactor renaissance	253
6.4	Molten salt reactor fuel concepts	254
6.5	Fuel salt properties	254
6.5.1	Melting point	255
6.5.2	Vapor pressure—boiling point	257
6.5.3	Heat capacity	258
6.5.4	Solubility of actinoids	259
6.5.5	Fission product retention	260
6.5.6	Stability to radiation	260
6.6	Measurements and experimental procedures	261
6.6.1	Handling	261
6.6.2	Sample synthesis and purification	261
6.6.3	High-temperature measurements—encapsulation	263
6.7	Redox potential of the fuel	265
6.7.1	Corrosion inhibition	266
6.7.2	Fission product speciation	267
6.7.3	Monitoring of redox potential during reactor operation	268
6.8	Effect of oxygen impurities	268
6.9	Effect of soluble fission product impurities	269
6.10	Conclusion	269
	References	270
7	Research reactor fuels	273
	<i>Mitchell K. Meyer, Dennis D. Keiser Jr., Jan-Fong Jue and Eric Shaber</i>	
7.1	Introduction	273
7.2	Fuel geometry	274

7.2.1	Plate-type fuels	274
7.2.2	Tubular fuels	275
7.2.3	Rod- and pin-type fuels	275
7.3	Fuel materials	276
7.4	Evolution of research reactor fuel during operation	278
7.5	Fabrication processes	281
7.6	Fuel behavior under irradiation	284
7.6.1	Uranium aluminides	284
7.6.2	Uranium silicides	286
7.6.3	Uranium oxides	290
7.6.4	Uranium–molybdenum alloys	293
7.6.5	Uranium–zirconium hydride fuel	301
7.7	Corrosion of aluminum research reactor fuel cladding	303
7.8	Conclusion	304
	References	305
Part C	Stages of the Fuel Cycle and Other Applications	313
8	Mining and milling	315
	<i>Markus H.A. Piro and Ksenia Lipkina</i>	
8.1	Introduction	315
8.2	Mining	315
8.2.1	Uranium resources	316
8.2.2	Uranium bearing minerals	316
8.2.3	Mining methods	318
8.3	Milling	324
8.3.1	Ion exchange	324
8.3.2	Solvent extraction	325
8.3.3	Precipitation	325
8.4	Tailings	326
8.5	Summary	328
	References	328
9	Uranium conversion and enrichment	331
	<i>Michael P. Murchie and Simon J. Reid</i>	
9.1	Introduction	331
9.2	Natural uranium conversion processes	331
9.2.1	What is uranium conversion?	331
9.2.2	The special role of UF ₆ in the nuclear fuel cycle	332
9.2.3	Wet conversion processes for production of UF ₆	334
9.2.4	Dry fluoride volatility process for production of UF ₆	340
9.2.5	Production of ceramic-grade UO ₂ for pressurized heavy-water reactors	342
9.2.6	Production of uranium metal for Magnox reactors	343

9.3	Uranium enrichment	343
9.3.1	Uranium enrichment processes	345
9.3.2	Quality and transportation of enriched UF ₆	361
9.4	Conversion of enriched UF ₆ to UO ₂	361
9.4.1	Wet conversion processes	362
9.4.2	Dry conversion processes	364
9.5	Conclusion and future trends	366
	References	367
10	Advances in fuel fabrication	371
	<i>Elizabeth Sooby Wood, Joshua T. White, Brian Jaques, Douglas Burkes and Paul Demkowicz</i>	
10.1	Introduction	371
10.2	Ceramic fuel fabrication	372
10.2.1	Oxide fuel fabrication	372
10.2.2	Nitride fuel fabrication	379
10.2.3	Other ceramic fuel fabrication	385
10.3	Metallic fuel fabrication	386
10.3.1	Introduction to metallic fuels	386
10.3.2	Fabrication methods for metallic fuels	387
10.4	Advanced reactor fuel fabrication	399
10.4.1	High-density light-water reactor fuels	399
10.4.2	Coated particle fuel fabrication	403
10.4.3	Molten-salt reactor fuel fabrication	405
10.5	Conclusion	407
	Acknowledgments	408
	References	408
11	In-reactor behavior	419
	<i>Christine Guéneau, Jean-Christophe Dumas and Markus H.A. Piro</i>	
11.1	Introduction	419
11.2	General description of fuel behavior	420
11.2.1	Thermal and fast reactor fuels	420
11.2.2	Radiation damage—irradiation effects	422
11.2.3	Microstructural evolution	428
11.2.4	Fuel swelling	429
11.3	Oxide fuel chemistry	432
11.3.1	UO ₂ and (U,Pu)O ₂ oxides	433
11.3.2	Irradiated oxide fuel	438
11.4	Other fuels chemistry	462
11.4.1	Irradiated fuel chemistry	462
11.4.2	Fuel—cladding chemical interaction	463
11.5	Conclusion—outlooks	464
	References	465

12 Reprocessing and recycling	469
<i>Guillermo D. DelCul and Barry B. Spencer</i>	
12.1 Introduction	469
12.1.1 Characteristics of used nuclear fuel	470
12.1.2 Reuse of uranium from used light-water reactor fuel	473
12.1.3 Zirconium recycle and disposition options	476
12.1.4 Hardware component recycle	477
12.1.5 Additional component recycle	478
12.2 Headend processing of Zircaloy-clad fuels for hydrometallurgical separations	478
12.2.1 Disassembly and decladding	480
12.2.2 Voloxidation	482
12.2.3 Nitric acid dissolution	485
12.2.4 Clarification and accounting	487
12.2.5 Disposition of cladding	487
12.3 Headend processing for alternative or advanced fuels	489
12.3.1 TRISO fuels	489
12.3.2 The process of direct use of pressurized water reactor fuel in CANDU	493
12.3.3 Thorium-enhanced fuels	494
12.4 Off-gas treatment and emission controls	497
12.4.1 Iodine	498
12.4.2 Tritium	499
12.4.3 Carbon-14	500
12.4.4 Krypton	500
12.4.5 Noble metals and other semivolatiles	501
12.5 Separations	501
12.5.1 Hydrometallurgical separations—solvent extraction	502
12.5.2 Hybrid aqueous processing	506
12.5.3 Pyrochemical processes	506
12.5.4 Fluoride volatility	508
12.5.5 Chloride volatility	511
References	516
13 Spent nuclear fuel and disposal	527
<i>Jordi Bruno, Lara Duro and François Diaz-Maurin</i>	
13.1 Introduction—generalities on spent nuclear fuel	527
13.2 Spent nuclear fuel management strategies, closed versus open nuclear cycles	530
13.3 Spent nuclear fuel and high-level waste storage—international practices	532
13.3.1 Wet storage	532
13.3.2 Dry storage	533
13.4 Spent nuclear fuel and high-level waste geological disposal—international practices	536

13.5	Key processes from operation to disposal through storage that impact the long-term stability of spent nuclear fuel	539
13.6	Dissolution and alteration of spent nuclear fuel under deep geological repository conditions	543
13.7	Outlook	546
13.8	Conclusion	547
	Appendix	548
	References	549
	Further reading	553
14	Advances in fuel chemistry during a severe accident	555
	<i>M. Kurata, M. Osaka, D. Jacquemain, M. Barrachin and T. Haste</i>	
14.1	Introduction	555
14.2	Chemistry on fuel/core degradation	557
14.2.1	Chemistry in early phase fuel degradation	557
14.2.2	Chemistry in transition from early phase to late phase	576
14.2.3	Chemistry in late phase degradation	576
14.2.4	Chemistry on fuel degradation ex-vessel conditions	582
14.3	Fission product chemistry at severe accident of light water reactors	593
14.3.1	Chemistry of fission product release from irradiated fuel during severe accident	595
14.3.2	Fission product chemistry in reactor coolant system, gas phase, and interactions with structure surface	599
14.3.3	Fission product chemistry in containment, gas phase, and interactions with containment surfaces	605
14.3.4	Chemistry in containment pools and in liquid scrubber containment venting systems	615
14.4	Conclusion	618
	References	619
Index		627

List of contributors

M. Barrachin Institute for Radiological Protection and Nuclear Safety (IRSN), PSN-RES/SAG, B.P. 3, St. Paul Lez Durance, France

Ondřej Beneš European Commission, Joint Research Centre, Nuclear Safety and Security Directorate, Karlsruhe, Germany

Jordi Bruno Amphos 21 Group, Barcelona, Spain

Douglas Burkes Nuclear Engineering and Analysis, Pacific Northwest National Laboratory, Richland, WA, United States

Andrea Cambriani European Commission, Joint Research Centre, Nuclear Safety and Security Directorate, Karlsruhe, Germany

Jean-Yves Colle European Commission, Joint Research Centre, Nuclear Safety and Security Directorate, Karlsruhe, Germany

Guillermo D. DelCul Isotope and Fuel Cycle Technology Division, Oak Ridge National Laboratory, Oak Ridge, TN, United States

Paul Demkowicz Idaho National Laboratory, Idaho Falls, ID, United States

François Diaz-Maurin Amphos 21 Group, Barcelona, Spain; Center for International Security and Cooperation (CISAC), Stanford University, Stanford, CA, United States

Oliver Dieste Blanco European Commission, Joint Research Centre, Nuclear Safety and Security Directorate, Karlsruhe, Germany

Jean-Christophe Dumas Commissariat à l'Energie Atomique et aux Energies Alternatives, CEA Cadarache, Saint-Paul-lez-Durance Cedex, France

Lara Duro Amphos 21 Group, Barcelona, Spain

Thomas Gouder European Commission, Joint Research Centre, Nuclear Safety and Security Directorate, Karlsruhe, Germany

Jean-Christophe Griveau European Commission, Joint Research Centre, Nuclear Safety and Security Directorate, Karlsruhe, Germany

Christine Guéneau Commissariat à l'Energie Atomique et aux Energies Alternatives, Université Paris-Saclay, Gif-sur-Yvette Cedex, France

T. Haste Institute for Radiological Protection and Nuclear Safety (IRSN), PSN-RES/SAG, B.P. 3, St. Paul Lez Durance, France

D. Jacquemain Institute for Radiological Protection and Nuclear Safety (IRSN), PSN-RES/SAG, B.P. 3, St. Paul Lez Durance, France

Brian Jaques Micron School of Materials Science and Engineering, Boise State University, Boise, ID, United States

Jan-Fong Jue Idaho National Laboratory, Idaho Falls, ID, United States

Matthew H. Kaye Ontario Tech University, Oshawa, ON, Canada

Dennis D. Keiser Jr. Idaho National Laboratory, Idaho Falls, ID, United States

Rudy J.M. Konings European Commission, Joint Research Centre, Karlsruhe, Germany

M. Kurata Japan Atomic Energy Agency (JAEA), Tokai, Japan

Ksenia Lipkina Faculty of Energy Systems and Nuclear Sciences, Ontario Tech University, Oshawa, ON, Canada

Dario Manara European Commission, Joint Research Centre, Nuclear Safety and Security Directorate, Karlsruhe, Germany

Laura Martel European Commission, Joint Research Centre, Nuclear Safety and Security Directorate, Karlsruhe, Germany

Mitchell K. Meyer Idaho National Laboratory, Idaho Falls, ID, United States

Michael P. Murchie Cameco Corporation, Port Hope, ON, Canada

Andrew T. Nelson Oak Ridge National Laboratory, Oak Ridge, TN, United States

M. Osaka Japan Atomic Energy Agency (JAEA), Tokai, Japan

Markus H.A. Piro Faculty of Energy Systems and Nuclear Sciences, Ontario Tech University, Oshawa, ON, Canada

Simon J. Reid Cameco Corporation, Port Hope, ON, Canada

Alice Seibert European Commission, Joint Research Centre, Nuclear Safety and Security Directorate, Karlsruhe, Germany

Eric Shaber Idaho National Laboratory, Idaho Falls, ID, United States

Anna L. Smith Department of Radiation Science & Technology, Faculty of Applied Sciences, Delft University of Technology, Delft, The Netherlands

Pavel Souček European Commission, Joint Research Centre, Karlsruhe, Germany

Barry B. Spencer Isotope and Fuel Cycle Technology Division, Oak Ridge National Laboratory, Oak Ridge, TN, United States

Dragos Staicu European Commission, Joint Research Centre, Nuclear Safety and Security Directorate, Karlsruhe, Germany

Jean-François Vigier European Commission, Joint Research Centre, Nuclear Safety and Security Directorate, Karlsruhe, Germany

Olaf Walter European Commission, Joint Research Centre, Nuclear Safety and Security Directorate, Karlsruhe, Germany

Lian C. Wang Ontario Tech University, Oshawa, ON, Canada

Joshua T. White Materials Science and Technology Division, Los Alamos National Laboratory, Los Alamos, NM, United States

Thierry Wiss European Commission, Joint Research Centre, Nuclear Safety and Security Directorate, Karlsruhe, Germany

Elizabeth Sooby Wood Department of Physics and Astronomy, The University of Texas at San Antonio, San Antonio, TX, United States

This page intentionally left blank

About the editor

Dr. Markus Piro earned a PhD in Nuclear Engineering from the Royal Military College of Canada, Canada with Profs W.T. Thompson and B.J. Lewis and held a postdoctoral fellowship (PDF) at the Oak Ridge National Laboratory, United States under the supervision of Dr. T.M. Besmann. Both PhD and PDF projects focused on computational thermochemistry of irradiated nuclear fuel. After the PDF, he worked at the Canadian Nuclear Laboratories (CNL) as a research scientist and then Head of the Fuel Modeling and Fission Product Transport section, where he led a multidisciplinary group that supported both basic and applied research for government and industry. While his research at CNL broadly involved various aspects of fuel behavior, the focus was on nuclear fuel chemistry of various fuel types, including conventional power reactor fuel, research reactor fuel, Generation IV concepts, and some exotic (proprietary) fuel designs for industry. In 2017 he was awarded a Canada Research Chair of Nuclear Fuels and Materials at the University of Ontario Institute of Technology, Canada (now “Ontario Tech University”). His group contributes to a number of research projects in collaboration with partners in industry and government with the ultimate goal of enhancing performance, safety, and environmental stewardship of nuclear fuels and related materials.

This page intentionally left blank

Preface

Nuclear science and technology have many positive effects on the daily lives of millions of people, ranging from reliable, safe, and clean electricity generation to the production of medical isotopes for the diagnosis and treatment of cancer patients. The foregoing objectives are supported by nuclear power reactors and research reactors. At the center of these nuclear reactors, there is the fuel, which, simply put, generates heat, and provides a neutron source. Critical to the performance of these fuels is having a thorough understanding of its chemical behavior across the entire fuel cycle—from mining uranium out of the ground to irradiation in-reactor to the disposition of waste. Throughout the course of irradiation, nearly every chemical element on the period table is produced in the fuel, which poses some pertinent challenges to scientists and engineers.

This book presents a high-level description of nuclear fuel chemistry based on the most recent research and development activities, and current practices in industry. It is intended to fill an important knowledge gap in the literature that consolidates the latest research on nuclear fuel chemistry into one comprehensive reference, covering all aspects of conventional and nonconventional nuclear fuel cycles. Each chapter includes contributions from world-renowned experts from many countries representing government, industry, and academia. It is aimed at graduate students, researchers, academics, and practicing engineers. This book will provide the reader with a single reference from which to learn the fundamentals of classical thermodynamics and radiochemistry.

The text is partitioned into three parts: (1) fundamentals, (2) fuel designs, and (3) stages of the fuel cycle and other applications. In part (1), fundamental concepts are established that are used throughout the book. This includes the fundamentals of thermodynamics and kinetics, experimental methods, and modeling and simulation. In part (2), various classes of fuel designs are reviewed for both power reactors and research reactors. The four broad classes include oxide fuels (i.e., which are predominantly used in current power reactors), other power reactor fuels (e.g., nonoxides), molten salt fuels (i.e., chlorides and fluorides), and research reactor fuels (i.e., not intended to generate heat but principally to provide a neutron source). Finally, part (3) covers all stages of the fuel cycle and other applications. Chapters include mining and milling, conversion and enrichment, fuel fabrication, in-reactor behavior, reprocessing and recycling, spent fuel storage and disposal, and severe accident behavior.

The collective hard work of the authors of all chapters is greatly appreciated. Without their efforts, this would not have been possible. Their extensive knowledgebase and experience in a wide range of disciplines have contributed to the

quality and breadth of the work. I am quite grateful to my colleagues who have kindly provided thorough and professional reviews of the chapters of this book. Thanks are in order to Tyler Gerczak, Charles Baldwin, and Kurt Terrani from the Oak Ridge National Laboratory for providing permission to use the image on the front cover. Assistance from Parikshit Bajpai in formatting, figures, and preparing permission logs is greatly appreciated.

Markus H.A. Piro
Ontario Tech University, Oshawa, ON, Canada

PART A

Fundamentals

This page intentionally left blank

Reaction kinetics and chemical thermodynamics of nuclear materials

1

Anna L. Smith¹ and Rudy J.M. Konings²

¹Department of Radiation Science & Technology, Faculty of Applied Sciences, Delft

University of Technology, Delft, The Netherlands, ²European Commission, Joint Research Centre, Karlsruhe, Germany

1.1 Introduction

Chemical kinetics and thermodynamics dictate the behavior of nuclear fuel at each stage of the nuclear fuel cycle, from mining to fuel fabrication, in-reactor behavior, storage of spent fuel, and geological disposal, and this chapter provides some of the background knowledge and key concepts needed to apprehend its chemistry.

Nuclear fuel is a particularly complex system to investigate. The chemistry of the actinoid elements, including uranium (U) and plutonium (Pu), which have fissionable isotopes, and the minor actinoids, neptunium (Np), americium (Am), and curium (Cm), is first very peculiar due to their $[Rn]5f^n$ electronic configuration. The 5f electrons of the actinoids have a large spatial extension, by contrast with the 4f electrons of the lanthanoids, which allows both a wide range of oxidation states (from +3 to +7) and the occurrence of magnetic ordering. In particular, the 5f electrons from thorium to neptunium in the actinoid series show an *itinerant* or *delocalized* character, meaning they are available for covalent bonding [1]. By contrast, the 5f electrons from americium to lawrencium are more *localized*. Plutonium and americium stand at the limit between the two behaviors and show localized or delocalized characteristics, depending on conditions of pressure, temperature, and magnetic field [1]. This ability to adopt various oxidation states makes the thermodynamics and kinetics of actinoid materials particularly rich, where oxidation and reduction reactions play a key role. In addition, the chemical composition of the nuclear fuel changes continuously during irradiation due to the fission reaction, and the fuel becomes a multi-component system, including fission products, as well as transuranium elements. The fission products can adopt various chemical forms depending on their specific physico-chemical properties, which again affects their behavior whether in the reactor or in the environment.

The present chapter introduces first the chemical kinetics aspects of fuel chemistry, focusing on reaction rates and their dependence on temperature. Then, the basic concepts of chemical thermodynamics are presented: the first, second, and third laws, state functions, enthalpy, Helmholtz and Gibbs energies, and chemical

potential. The molar thermodynamic functions of condensed and gaseous phases are furthermore defined (i.e., enthalpy of formation, entropy, and heat capacity), and the methods used for their theoretical and experimental determination are presented. Some of the key knowledge in solid state and solution thermodynamics of nuclear materials are finally treated, including the construction and interpretation of phase diagrams, Ellingham, Pourbaix, and speciation diagrams. Throughout this chapter, a number of examples are used to illustrate the complex chemistry of nuclear fuel materials at various stages of the fuel cycle.

1.2 Basic concepts of chemical kinetics

Chemical kinetics describe the rate of chemical processes. Let us consider a general reaction:



where the reactants A and B , and product C can be in the solid, liquid, or gaseous state, respectively, and v_A , v_B , and v_C are the corresponding stoichiometric coefficients.

In this chapter, various designators are used to indicate the physical state of reactants and products: these can be solids (s), crystalline solids (cr), amorphous solids (am), gases (g), pure liquid substances (l), or aqueous species (aq). Substances in solution are marked with (sln).

Chemical kinetics indicate how quickly this reaction will proceed, while a chemical thermodynamics computation reveals if this chemical reaction is favorable and can actually take place under the specified set of conditions (temperature, pressure, composition, etc.).

1.2.1 Reaction rates

The rate of the aforementioned reaction depends on the change of the concentrations with time, that is, $-dc_A/dt$, $-dc_B/dt$, and dc_C/dt , with a negative variation (decrease) for the reactants A and B and positive variation (increase) for the product C . In the simplest approximation the rate depends on the concentration of A and changes linearly with time, leading to the following rate equation:

$$-\frac{dc_A}{dt} = k_1 c_A \quad (1.2)$$

where k_1 is the reaction rate constant corresponding to A . Rewriting this equation $-(1/c_A)(dc_A/dt) = k_1$ and integrating leads to

$$\ln c_A = -k_1 t + \text{constant} \quad (1.3)$$

Since at $t = 0$ the concentration of A is $c_A = c_0$, one can write

$$\ln c_A = \ln c_0 - k_1 t \quad (1.4)$$

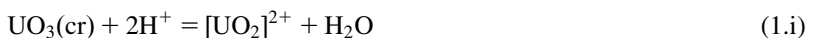
Rearranging gives

$$c_A = c_0 e^{-k_1 t} \quad (1.5)$$

The previous example refers to a *first-order* kinetic reaction (Box 1.1).

Box 1.1 Dissolution of UO₃.

The dissolution of UO₃ in acidic solutions proceeds according to the reaction:



Scott et al. [2] studied this reaction (using β -UO₃) by measuring the $[\text{UO}_2]^{2+}$ concentration with an electrochemical method and the evolved heat by a calorimetric method. The authors observed that the dissolution kinetics are first-order in time under all circumstances but can depend on a range of variables, such as specific surface of the powder, pH of the solution, or presence of other cations and anions. For easy comparison, they defined the “half-life constant” $k_{1/2}$, at which half of the material has dissolved. This constant can be derived by rewriting Eq. (1.3) as

$$\ln \frac{c_A}{c_{1/2}} = -k_{1/2} t + \text{constant} \quad (1.\text{ii})$$

Scott et al. [2] observed that $k_{1/2}$ decreases with the $[\text{H}^+]$ concentration in all solutions, in a linear relation with a slope of ~ 0.5 with deviation at very low pH. The dissolution rate is reduced by the presence of other cations in the solution, $\text{Mg}^{2+} \gg \text{Li}^+ > \text{Na}^+ > \text{NH}_4^+ > \text{K}^+ > \text{Cs}^+$.

The dissolution reaction of UO₃ in carbonate solutions is substantially different:



Again, the authors found that the reaction is first-order in time and that $k_{1/2}$ linearly decreases with the total CO₃²⁻ concentration in Na[HCO₃]-Na[CO₃] solutions of constant carbonate-to-bicarbonate ratio, with a slope of ~ 1 .

(Continued)

Box 1.1 (cont'd)

Scott et al. [2] argued that the UO_3 dissolution is a sequence of four possible rate-controlling processes: crystallization (conversion of bulk lattice to the interface surface with adsorbed species), reaction, charge transfer, and diffusion. The absence of an influence on process variables, such as stirring, and the strong dependence on the solution parameters, led them to conclude that the process of transfer of the lattice cations and anions of the solid across the electrochemical potential is determining the dissolution rate. Using charge transfer theory, they suggested that the charge transfer rates can be described as

$$r_U = \vec{k}_+ [\text{U}_{\text{ad}}][\text{CO}_3]_T^{n-m} e^{(\alpha_+ z_+ FE/RT)} - \overset{\leftarrow}{k}_+ [\text{UO}_2(\text{CO}_3)_n][\text{CO}_3]_T^{-m} e^{(-(1-\alpha_+)z_+ FE/RT)} \quad (1.\text{iv})$$

$$r_O = \vec{k}_- [\text{O}_{\text{ad}}][\text{H}^+]^{s-t} e^{(\alpha_- z_- FE/RT)} - \overset{\leftarrow}{k}_- [\text{OH}_s][\text{H}^+]^{-t} e^{(-(1-\alpha_-)z_- FE/RT)} \quad (1.\text{v})$$

In these equations, r_U and r_O are the rates of charge transfer of the uranyl and oxide species; $[\text{U}_{\text{ad}}]$ and $[\text{O}_{\text{ad}}]$ the concentrations of the uranyl and oxide ad-ions; $[\text{U}(\text{CO}_3)_n]$ ($n = 1-3$), $[\text{OH}]$, $[\text{H}^+]$, and $[\text{CO}_3]_T$ the concentrations of the carbonatouranate, hydroxide, hydrogen, and total carbonate ions $[\text{CO}_3]^{2-} + [\text{HCO}_3]^-$ in solution; \vec{k}_+ , $\overset{\leftarrow}{k}_+$, \vec{k}_- , and $\overset{\leftarrow}{k}_-$ forward and reverse rate constants for the lattice cation and anion charge transfer reactions; α_+ and α_- the transfer coefficients for the lattice cations and anions; z_+ and z_- the charges on the lattice cations and anions; and E the electrical potential difference between the UO_3 surface and the outer Helmholtz plane. Because the potential across the solid–solution interface was not controlled, the deposition rates can be neglected, and assuming r_U and r_O to be equal, the previous equations can be simplified to

$$r = \vec{k}_+ [\text{U}_{\text{ad}}][\text{CO}_3]_T^{n-m} \left(\frac{\vec{k}_- [\text{O}_{\text{ad}}][\text{H}^+]^{s-t}}{\vec{k}_+ [\text{U}_{\text{ad}}][\text{CO}_3]_T^{n-m}} \right)^x \quad (1.\text{vi})$$

with $x = \alpha_+ z_+ / (\alpha_+ z_+ - \alpha_- z_-)$. With a proper choice of the transfer coefficients, this equation can explain the 0.5 dependence on the $[\text{H}^+]$ concentration of ion carbonate-free acid solutions. It cannot explain the relation between dissolution rate and the carbonate dissolution assuming the uranyl monocarbonate species. However, with the dicarbonatouranyl ion as charge transfer species, the linear dependence of dissolution rate on total carbonate concentration can be predicted.

In a *second-order* kinetic reaction the rate depends on the concentration of two reactants or does not depend linearly but quadratically on the concentration of one reactant. For example, when $v_A = v_B$ in Eq. (1.1) and $c_{A,0} \neq c_{B,0}$, Eq. (1.2) becomes

$$-\frac{dc_A}{dt} = -\frac{dc_B}{dt} = k_1 c_A c_B \quad (1.6)$$

1.2.2 Temperature dependence of rate constants

It is obvious that temperature has an effect on both the thermodynamic chemical equilibrium and reaction rate. The Arrhenius equation given below relates the reaction rate constant k_r to temperature T :

$$\frac{d \ln k_r}{dT} = -\frac{E_a}{RT^2} \quad (1.7)$$

where E_a is the activation energy of the reaction and R the universal gas constant. This activation energy can be seen as the energetic barrier that must be overcome for the reaction to proceed. In cases where E_a is not a function of temperature itself, which is often a good approximation, integration of Eq. (1.7) leads to

$$k_r = \alpha e^{E_a/RT} \quad (1.8)$$

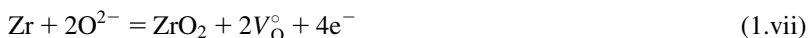
where α is a constant (Box 1.2).

The rate constants at different temperatures T_1 and T_2 can then be related by

$$\ln \frac{k_2}{k_1} = -\frac{E_a}{R} \left(\frac{1}{T_1} - \frac{1}{T_2} \right) \quad (1.9)$$

Box 1.2 Oxidation of the Zr-based cladding.

Zirconium alloys used as cladding for nuclear fuel are subjected to oxidation by the water of the surrounding coolant. This is a simple oxidation process by which a thin and dense layer of ZrO_2 is formed on the metal. The oxidation process is essentially an electrochemical reaction in which the zirconium is anodically oxidized [3]:



(Continued)

Box 1.2 (cont'd)

where V_O° represents an oxygen vacancy in the ZrO_2 layer and e^- the electron. The oxygen ions diffuse preferentially via the oxide crystallite boundaries to the oxide/metal interface, whereas the vacancies diffuse in the opposite direction.

The corresponding cathodic reaction at the oxide–coolant interface reflects the reduction of oxygen dissolved in the coolant:



The oxygen content is about 200 ppb in BWRs (boiling water reactors) and <0.05 ppb in PWRs (pressurized water reactors), but principally it is formed by the radiolytic decomposition of H_2O . The OH^\bullet radicals can combine with electrons to form molecular hydrogen and oxygen ions. The simplified overall reaction is



The formed hydrogen dissolves in the coolant water or diffuses to the metal, where it can precipitate.

This process has been extensively studied by autoclave experiments in which Zircaloy or $\text{Zr}-\text{Nb}$ alloys are exposed to typical reactor coolant conditions ($300-330^\circ\text{C}$, 15 MPa). The progress of the oxidation is then generally measured by the weight gain (ΔW) of the metallic sample, assuming that it follows the overall corrosion kinetics. It has been found that initially the kinetics progressively decrease with the growth of the oxide layer, and that they can be described by a cubic (i.e., a *third-order*) relation:

$$(\Delta W)^3 = k_1 t \quad (1.\text{x})$$

where k_1 is the preexponential factor. It is generally accepted that the oxygen transport in the dense layer determines the reaction rate. The temperature dependence of k_1 follows an Arrhenius equation, Eq. (1.8), with $\alpha_1 = 6.36 \times 10^{11}$ (mg dm²)³/day and $E_{a1}/R = 13640$ K, as found by Kass [4] for Zircaloy-2 and Zircaloy-4 cladding tubes. After some time the oxide layer cracks due to the accumulation of compressive stresses, and after this transition, the weight gain (kinetics) follows an approximately linear relation in time:

$$\Delta W = k_2 t + C \quad (1.\text{xi})$$

In this case the reaction rate is no longer determined by (faster) oxygen transport through the dense layer, but by transport through cracks. Detailed
(Continued)

Box 1.2 (cont'd)

studies have shown that the post-transition phase is essentially an accumulation of a series of successive cubic curves, yielding an apparent linear relation resulting from the superposition of various regions of the oxide layer following pre-transition growth rate but slightly out of phase with each other. Again, the rate constant k_2 can be described by an Arrhenius Eq. (1.8). Hillner et al. [5] described the post-transition kinetics in two stages with $\alpha_1 = 2.47 \times 10^8 \text{ (mg dm}^2\text{)}^3/\text{day}$ and $E_{a1/R} = 12880 \text{ K}$ for stage 1, and $\alpha_2 = 3.47 \times 10^7 \text{ (mg dm}^2\text{)}^3/\text{day}$ and $E_{a2/R} = 11452 \text{ K}$ for stage 2.

1.3 Fundamentals of chemical thermodynamics

While chemical kinetics describe the rate of a chemical reaction and its reaction mechanism, chemical thermodynamics is the study of the spontaneity of this transformation, and the associated exchanges of energy and matter. Thermodynamics is concerned with the attainment of a so-called equilibrium state, where the macroscopic physical and chemical properties of the system (e.g., temperature, pressure, chemical potential, and electrochemical potential) do not evolve anymore.

1.3.1 Thermodynamic system and state functions

A thermodynamic system, delimited from the surroundings by real or hypothetical boundaries, can either be (1) isolated, (2) adiabatic, (3) closed, or (4) open, depending on the type of exchange between the system under consideration and the surroundings. A system is defined as isolated in the absence of any exchange of energy or matter with the surroundings, adiabatic if only work is exchanged, closed if only energy is exchanged, and open if both energy and matter can be exchanged.

The state of a thermodynamic system is defined by its internal energy, U , and entropy, S , as well as a set of *state variables*, including temperature T , hydrostatic pressure p , volume V , and number of moles of components n . The former two thermodynamic quantities are functions of the state variables. Among these, temperature and pressure constitute intensive variables, which define properties independent of the size of the system, whereas volume, internal energy, and entropy constitute extensive variables, values of which vary with the size of the system. Intensive molar properties are obtained by dividing extensive properties by the number of moles n . The molar volume V_m is defined, for instance, by $V_m = V/n$. It is important to point out that the aforementioned state functions depend on the conditions, or in other words, the state of the system, but not on the path, process, or history that was followed to reach it.

The composition of a thermodynamic system is defined using components of fixed compositions that can be chemical elements, binary, ternary, or higher order

compounds depending on the situation. In the U–Pu–O ternary system, particularly relevant for the nuclear community, the components of the system can be defined by the elements U, Pu, and O. When treating the solid solution $\text{U}_{1-y}\text{Pu}_y\text{O}_{2 \pm x}$, it might be more convenient to use the $\text{UO}_{2 \pm x}$ and PuO_{2-x} components, however. This should not be confused with the components of a phase (for instance, the various species found in a gas phase).

1.3.2 The laws of thermodynamics

1.3.2.1 First law of thermodynamics

The first law of thermodynamics, which expresses the conservation of energy, can be formulated as follows:

Energy cannot be produced or destroyed, and the energy increase of a body or a system (dU) equals the sum of the heat absorbed from the environment (δQ) and the work (δW) done by the environment on the system.

The corresponding mathematical expression is

$$dU = \delta Q + \delta W \quad (1.10)$$

where δQ and δW are the heat transfer and work, respectively.

The δ notation is used here for the differentials to stress that both δQ and δW are path dependent. Hence, Q and W do not qualify as state functions by contrast with the internal energy. This equation shows that changes in internal energy can be measured, but not its absolute value. In the convention adopted generally, heat or work provided by the environment to the system lead to an increase of its internal energy.

Various types of work can be encountered: *mechanical*, which is of prime interest here and also known as “ pV work,” *electromagnetic* and *chemical*. The latter two forms of work are usually denoted as “external” and written as δW_{ext} . Mechanical work leads to a change in volume and is given by the product of a force f and the displacement of the system boundary dX resulting from the application of this force: $\delta W = fdX$. The latter equation can also be written as $\delta W = (f/A)(AdX)$, A being the surface area over which the force acts upon. The first term (f/A) is equivalent to the pressure p , while the second term corresponds to the volume change dV of the system. Hence, the mechanical work can also be expressed as

$$\delta W = -pdV \quad (1.11)$$

In this case, work is done by the system, and the negative sign expresses the fact that the internal energy of the system decreases when performing this work.

While energy is a property of a system that quantifies the capacity to perform work (e.g., kinetic and chemical), heat is the transfer of energy between systems as a result of their thermal interaction and is thus a property of a process. The unit of

energy and heat is Joule (J), $(\text{kg m}^2)/\text{s}^2$ in the International System of Units, normally expressed per unit of mass (g) or molar quantity (mol).

1.3.2.2 Second law of thermodynamics

The second law of thermodynamics accounts for the fact that heat “flows” from higher to lower temperatures in a spontaneous process, in a way that maximizes disorder. Rudolf Clausius formulated in 1850 a criterion for the direction in which this process occurs and called it entropy S .

In the course of a spontaneous process, the entropy change of the system dS and its surroundings dS_{surr} increases:

$$dS_{tot} = dS + dS_{surr} \geq 0 \quad (1.12)$$

In the course of a reversible process, the sum defined above is 0, and the entropy change is equal to

$$dS = \frac{\delta Q_{rev}}{T} \quad (1.13)$$

where δQ_{rev} is the heat provided by the surroundings to the system.

The Clausius inequality can subsequently be derived from the aforementioned equations for any process:

$$dS \geq \frac{\delta Q}{T} \quad (1.14)$$

Finally, in the case of an isolated system, $dS_{surr} = 0$ and $dS \geq 0$, hence, the entropy increases during the spontaneous process.

1.3.2.3 Third law of thermodynamics

The third law of thermodynamics assigns an entropy equal to zero at 0 K for any pure compound in stable and perfectly crystalline state. This definition allows one to express the absolute value of the entropy in contrast to the internal energy.

1.3.2.4 Zeroth law of thermodynamics

Finally, according to the zeroth law of thermodynamics, two systems in thermal equilibrium with a third system are in thermal equilibrium with each other.

1.3.3 Enthalpy, Helmholtz, and Gibbs energies

Three other state functions are of great practical importance in thermodynamics: the enthalpy H , Helmholtz energy A , and Gibbs energy G . Enthalpy changes are derived using calorimetry, while Helmholtz and Gibbs energies allow one to define chemical equilibrium conditions.

1.3.3.1 Enthalpy

The enthalpy is defined by the sum of the internal energy U and the product of the pressure p and volume V of the thermodynamic system:

$$H = U + pV \quad (1.15)$$

It is especially useful for experimental measurements carried out at constant pressure. It is a measure of the capacity of the thermodynamic system to release (for an exothermic process) or absorb heat (for an endothermic process).

The differentiation of this equation combined with the first law [see Eq. (1.10)] yields

$$dH = \delta Q + \delta W + pdV + Vdp \quad (1.16)$$

Considering expansion (mechanical) work only [see Eq. (1.11)], this equation reduces to

$$dH = \delta Q + Vdp \quad (1.17)$$

which further simplifies at constant pressure ($dp = 0$) to

$$dH = \delta Q_p \quad (1.18)$$

or for a finite change to

$$\Delta H = Q_p \quad (1.19)$$

Calorimetric measurements that monitor changes in heat flow during a process at constant pressure, thus allow one to derive enthalpy changes in the system.

1.3.3.2 Helmholtz energy

Next, the Helmholtz free energy is given by the relation

$$A = U - TS \quad (1.20)$$

The change in Helmholtz energy is a measure of the maximum work a system can do. When considering again expansion work only, the differentiation of the corresponding equation leads to

$$dA = \delta Q - pdV - TdS - SdT \quad (1.21)$$

For conditions of constant temperature ($dT = 0$) and volume ($dV = 0$) in a closed system in thermal equilibrium with its surroundings, one obtains $dA_{T,V} = \delta Q_V - TdS$,

which reduces to zero at equilibrium according to the second law of thermodynamics [see Eq. (1.13)]. Hence, at equilibrium, $dA_{T,V} = 0$ or $\Delta A_{T,V} = 0$, meaning that the value of the Helmholtz energy A reaches a minimum.

1.3.3.3 Gibbs energy

Finally, the Gibbs energy, which is the most practical quantity to describe experimental conditions (since the pressure is easier to control experimentally than the volume), is defined as

$$G = H - TS \quad (1.22)$$

The change in Gibbs energy is used to express the maximum non-expansion work that can be performed by a thermodynamic system at constant pressure and volume.

Using Eq. (1.15), the Gibbs energy is expressed as

$$G = U + pV - TS \quad (1.23)$$

Differentiation gives

$$dG = dU + Vdp + pdV - TdS - SdT \quad (1.24)$$

which further reduces at constant pressure ($dp = 0$) and temperature ($dT = 0$), considering expansion work only, to $dG_{T,p} = \delta Q_p - TdS$. This equality is zero at equilibrium; hence, $dG_{T,p} = 0$ or $\Delta G_{T,p} = 0$, meaning the value of the Gibbs energy G reaches a minimum.

Conditions of constant temperature and volume are usually fulfilled in numerical simulations, while conditions of constant temperature and pressure are achieved experimentally; hence, the criteria on the Helmholtz and Gibbs energies are used in each case, respectively. Those state functions decrease in a spontaneous process until they reach their minimum values, corresponding to the attainment of the equilibrium state.

1.3.4 Heat capacity

The heat capacity at constant volume, C_V , and heat capacity at constant pressure, C_p , are extensive properties of the system, defined as the partial derivatives of the internal energy and enthalpy, respectively, with respect to temperature.

$$C_V = \left(\frac{\partial U}{\partial T} \right)_V \quad (1.25)$$

$$C_p = \left(\frac{\partial H}{\partial T} \right)_p \quad (1.26)$$

Applying the first law of thermodynamics to a system at constant volume ($dV = 0$) that does not perform any external work ($\delta W_{ext} = 0$) yields

$$dU = \delta Q_V - pdV = \delta Q_V \quad (1.27)$$

where δQ_V is the change in heat flow at constant volume. For a finite change, this becomes

$$\Delta U = Q_V \quad (1.28)$$

The heat capacity at constant volume hence corresponds to the change in heat of the system following a change in temperature.

$$dU = \delta Q_V = C_V dT \quad (1.29)$$

Similarly, considering expansion work only, an infinitesimal change in enthalpy at constant pressure ($dp = 0$) is given by

$$dH = \delta Q_p + Vdp = \delta Q_p \quad (1.30)$$

where δQ_p is the change in heat flow at constant pressure, or for a finite change:

$$\Delta H = Q_p \quad (1.31)$$

The heat capacity at constant pressure, which is the quantity normally measured experimentally, corresponds to the enthalpy increase or heat of the system following a change in temperature.

$$dH = \delta Q_p = C_p dT \quad (1.32)$$

The relationship between heat capacity at constant pressure and constant volume is given by

$$C_p - C_V = \frac{\alpha^2 VT}{\kappa_T} \quad (1.33)$$

where α the isobaric expansivity, and κ_T the isothermal compressibility, themselves defined as

$$\alpha = \frac{1}{V} \left(\frac{\partial V}{\partial T} \right)_p \quad (1.34)$$

$$\kappa_T = - \frac{1}{V} \left(\frac{\partial V}{\partial p} \right)_T \quad (1.35)$$

Because the isobaric thermal expansivity is generally negligible at low temperatures for solid compounds, it is reasonable to assume that the heat capacity at constant pressure can be approximated with the heat capacity at constant volume, hence $C_p \sim C_V$. This approximation is very useful as detailed in [Section 1.4.1.4](#) when fitting the experimentally measured heat capacity at constant pressure to physical models.

1.3.5 Thermodynamic relations between state functions

The Gibbs energy, which is a function of temperature and pressure, that is, $G(T,p)$, is used to assess the stability of a component or phase in a system and is therefore the basic function used for modeling purposes, especially in the CALPHAD method [\[6\]](#) (see [Chapter 4](#)). All other thermodynamic quantities that are important in chemical thermodynamics can be simply derived from G , using the following relationships known as the Maxwell relations:

$$\begin{aligned} S &= - \left(\frac{\partial G}{\partial T} \right)_p \\ H &= G + TS = G - T \left(\frac{\partial G}{\partial T} \right)_p \\ V &= \left(\frac{\partial G}{\partial p} \right)_T \\ C_p &= - T \left(\frac{\partial^2 G}{\partial T^2} \right)_p \end{aligned} \tag{1.36}$$

A crystalline condensed phase might show different crystallographic structures depending on the temperature and pressure conditions. These stable phases are called polymorphs. The transition from one polymorph to another can be of first- or second-order. First-order transitions correspond to a discontinuous change in the first derivative of the Gibbs energy with respect to temperature and pressure, hence to a discontinuity in the enthalpy, entropy, and volume. Second-order transitions correspond to a discontinuous change in the second derivative, hence in the heat capacity, isobaric expansivity, and isothermal compressibility.

1.4 Thermodynamics of condensed phases

1.4.1 Molar thermodynamic properties

1.4.1.1 Definition of the reference and standard states

Since thermodynamics addresses energy changes and cannot quantify the absolute values of the internal energy and enthalpy, it is necessary to define a reference state

set as an arbitrary zero value. It is obvious in chemical thermodynamics to use the elements for this, as they form the basic blocks of chemical systems and processes. As most experimental work is carried out at atmospheric pressure, the most common reference state in use is the standard state, which is denoted with the symbol “ \circ ” and corresponds to a pressure p° equal to 1 bar.

Two definitions of the reference states are commonly used:

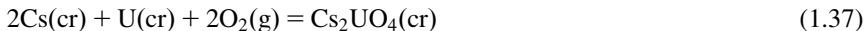
- The standard substance reference state, which defines the enthalpy of formation and Gibbs energy of formation of the elements in their most stable form at 1 bar as zero at any temperature. It is widely used in thermodynamic tables, such as those by the *National Institute of Standards and Technology* [7] and the *US Bureau of Mines*.
- The standard element reference (SER) state, which defines the enthalpy of formation of the elements in their most stable form at 1 bar and 298.15 K as zero. This definition is widely used for computer databases and CALPHAD assessments and is the one adopted in this chapter.

The thermodynamic properties of a compound are fully defined with the choice of the reference state and three thermodynamic quantities: the standard enthalpy of formation, the standard entropy, and the molar heat capacity, which are described in more detail hereafter.

1.4.1.2 Enthalpy of formation

The standard molar enthalpy of formation, $\Delta_f H_m^\circ$, corresponds to the enthalpy of reaction for the formation of one mole of a compound from its constitutive elements in their standard states. It is generally given for the common reference temperature 298.15 K (or 25 °C).

Taking the example of cesium uranate, Cs_2UO_4 , a phase that can be formed during irradiation in fast neutron reactors in the space between fuel pellet and cladding according to post-irradiation examinations of the Phénix fuel pins [8–10], the reaction corresponding to the standard enthalpy of formation is

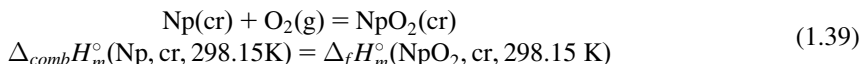


The standard molar enthalpy of formation at 298.15 K is subsequently given by the relation:

$$\begin{aligned} \Delta_f H_m^\circ(\text{Cs}_2\text{UO}_4, \text{cr}, 298.15\text{K}) &= H_m^\circ(\text{Cs}_2\text{UO}_4, \text{cr}, 298.15\text{K}) - 2H_m^\circ(\text{Cs, cr}, 298.15\text{K}) \\ &\quad - H_m^\circ(\text{U, cr}, 298.15\text{K}) - 2H_m^\circ(\text{O}_2, \text{g}, 298.15\text{K}) \\ &= H_m^\circ(\text{Cs}_2\text{UO}_4, \text{cr}, 298.15\text{K}) \text{ (in the SER)} \end{aligned} \quad (1.38)$$

Two common calorimetric methods for the determination of the standard enthalpy of formation at 298.15K are combustion calorimetry [11,12] and solution calorimetry [13,14], most often performed using a semi-adiabatic (or isoperibolic) calorimeter.

In a combustion calorimetry experiment, the energy released by the combustion in a closed reaction vessel (called the bomb) of a substance in a gas (typically oxygen or a halogen) under moderate pressure (~ 3 bar) is monitored. Oxygen bomb calorimetry has been used in the literature to measure the standard enthalpy of formation of a number of actinide compounds, for instance, $\text{NpO}_2(\text{cr})$ [15]. The energy of the combustion reaction $\Delta_{\text{comb}}H_m^\circ(\text{Np}, 298.15 \text{ K}, \text{cr})$ of $\text{Np}(\text{cr})$ in $\text{O}_2(\text{g})$ is directly equal to the standard molar enthalpy of formation of $\text{NpO}_2(\text{cr})$:



A solution calorimetry experiment consists of dissolving a sample that can be either solid or liquid into a solution, and measuring the temperature rise (for an exothermic reaction where heat is released) or decrease (for an endothermic reaction where heat is absorbed) following contact between the sample and solution. The reaction taking place can be one of dissolution or precipitation depending on the particular situation, although precipitation can lead to poorly defined crystalline states and therefore should be considered with caution. To relate the measured temperature effect to the value of the enthalpy of the reaction of dissolution or precipitation, electrical calibrations are moreover performed so as to determine the energy equivalent of the system. For a more detailed description of the technique, the reader is referred to more comprehensive and dedicated references [13,14,16].

Hess's law, which follows from the first law of thermodynamics, is commonly used for the determination of enthalpies of formation. Hess's law states that the standard enthalpy of a reaction is equal to the stoichiometric sum of the standard enthalpies of sub-reactions constituting a closed thermochemical cycle (Box 1.3).

Box 1.3 Enthalpy of formation of Cs_2UO_4 : derivation by solution calorimetry.

To illustrate the use of Hess's law along with the determination of the standard enthalpy of formation, the example of Cs_2UO_4 studied by solution calorimetry is considered, an experiment performed in 1986 by Cordfunke et al. [17]. The authors dissolved $\text{Cs}_2\text{UO}_4(\text{cr})$ as well as a mixture of $\{\gamma\text{-UO}_3(\text{cr}) + 2\text{CsF}(\text{cr})\}$ in 0.5 mol/L hydrofluoric acid HF solution and measured the thermal effects associated with the dissolution reactions: $\Delta_{\text{diss}}H_m^\circ(\text{Cs}_2\text{UO}_4(\text{cr})) = -(219.55 \pm 0.97) \text{ kJ/mol}$ and $\Delta_{\text{diss}}H_m^\circ(\gamma\text{-UO}_3(\text{cr}) + 2\text{CsF}(\text{cr})) = -(167.88 \pm 0.26) \text{ kJ/mol}$. The thermochemical cycle employed is detailed in Table 1.1. The dissolution experiments were carefully designed such that the quantities of materials dissolved were in stoichiometric molar proportions. Combining these results with the enthalpies

(Continued)

Box 1.3 (cont'd)

Table 1.1 Thermochemical cycle used for the determination of the enthalpy of formation of Cs_2UO_4 in 0.5 mol/L HF solution.

	Reaction	$\Delta_r H_m^\circ(298.15 \text{ K}) \text{ kJ/mol}$	Refs.
(a)	$\text{Cs}_2\text{UO}_4(\text{cr}) + 4\text{HF}(\text{sln}) = 2\text{CsF}(\text{sln}) + \text{UO}_2\text{F}_2(\text{sln}) + 2\text{H}_2\text{O}(\text{sln})$	-219.55 ± 0.97	[17]
(b)	$\text{UO}_3(\text{cr}) + 2\text{CsF}(\text{cr}) + 2\text{HF}(\text{sln}) = 2\text{CsF}(\text{sln}) + \text{UO}_2\text{F}_2(\text{sln}) + \text{H}_2\text{O}(\text{sln})$	-167.88 ± 0.26	[17]
(c)	$\text{U}(\text{cr}) + 3/2\text{O}_2(\text{g}) = \gamma\text{-UO}_3(\text{cr})$	-1223.8 ± 1.2	[18]
(d)	$2\text{Cs}(\text{cr}) + \text{F}_2(\text{g}) = 2\text{CsF}(\text{cr})$	-1114.58 ± 1.34	[17]
(e)	$\text{H}_2(\text{g}) + \text{F}_2(\text{g}) + (\text{sln}) = 2\text{HF}(\text{sln})$	-644.08 ± 0.08	[19,20]
(f)	$\text{H}_2(\text{g}) + 1/2\text{O}_2(\text{g}) = \text{H}_2\text{O}(\text{sln})$	-285.831 ± 0.040	[19,20]
(g)	$2\text{Cs}(\text{cr}) + \text{U}(\text{cr}) + 2\text{O}_2(\text{g}) = \text{Cs}_2\text{UO}_4(\text{cr})$	-1928.46 ± 2.06	

of formation of $\gamma\text{-UO}_3$ [18], $\text{CsF}(\text{cr})$ [17], $\text{HF}(\text{sln})$, and the partial enthalpies of formation of $\text{H}_2\text{O}(\text{sln})$ [19,20] and applying Hess's law,

$$\begin{aligned}\Delta_f H_m^\circ(\text{Cs}_2\text{UO}_4, \text{cr}, 298.15 \text{ K}) &= \Delta_r H(g) \\ &= \Delta_r H(b) - \Delta_r H(a) + \Delta_r H(c) + \Delta_r H(d) \\ &\quad - \Delta_r H(e) + \Delta_r H(f)\end{aligned}\tag{1.xii}$$

the standard enthalpy of formation of Cs_2UO_4 is derived as $-(1928.46 \pm 2.06) \text{ kJ/mol}$.

The standard enthalpy of formation of a substance at any temperature is then determined from the value at 298.15 K, plus its heat capacity, and heat capacity of the constitutive elements. The application of Eq. (1.32) yields for any substance the enthalpy change between 298.15 K and T :

$$H_m^\circ(T) = H_m^\circ(298.15 \text{ K}) + \int_{298.15}^T C_{p,m}^\circ dT\tag{1.40}$$

In the particular case of a compound showing a reversible phase transition at the transition temperature T_{tr} between a low-temperature α polymorph and a high temperature β polymorph, the enthalpy change is given by

$$H_m^\circ(T) = H_m^\circ(298.15 \text{ K}) + \int_{298.15}^{T_{tr}} C_{p,m}^\circ(\alpha) dT + \Delta_{tr} H_m^\circ(T_{tr}) + \int_{T_{tr}}^T C_{p,m}^\circ(\beta) dT\tag{1.41}$$

where $\Delta_{tr} H_m^\circ(T_{tr})$ is the associated transition enthalpy.

For the reaction of formation of a compound from its elements in their standard states, the enthalpy of formation at any temperature T is given by

$$\Delta_f H_m^\circ(T) = \Delta_f H_m^\circ(298.15 \text{ K}) + \int_{298.15}^T \Delta_r C_{p,m}^\circ dT \quad (1.42)$$

where $\Delta_r C_{p,m}^\circ$ is the stoichiometric difference between the heat capacities of the substance and the constitutive elements.

1.4.1.3 Standard entropy

The combination of Eqs. (1.13) and (1.32) for a reversible process at constant pressure, involving expansion work (pV work) only yields

$$\delta S = \frac{\delta Q_{rev}}{T} = \frac{C_p}{T} dT \quad (1.43)$$

Hence, the evolution with temperature of the standard molar entropy is given by the relation:

$$S_m^\circ(T) = S_m^\circ(0 \text{ K}) + \int_0^T \frac{C_{p,m}^\circ(T)}{T} dT \quad (1.44)$$

The application of the third law, assigning an entropy of zero at 0 K for any pure compound in stable and crystalline state allows one to express the absolute value of the standard entropy at any temperature, and in particular at 298.15 K, the common reference temperature in chemical thermodynamics.

$$S_m^\circ(298.15 \text{ K}) = \int_0^{298.15 \text{ K}} \frac{C_{p,m}^\circ(T)}{T} dT \quad (1.45)$$

The latter thermodynamic property is thus obtained by integration of the low-temperature heat capacity data ($C_{p,m}^\circ(T)/T = f(T)$) of a substance between 0 and 298.15 K.

The standard entropy has a substantial effect on the thermodynamic stability of materials at high temperatures via the $T\Delta S$ term in the Gibbs energy definition (1.28) ($\Delta G = \Delta H - T\Delta S$). For any temperature above 298.15 K, and in the absence of a phase transition, the standard entropy is given by the relation:

$$S_m^\circ(T) = S_m^\circ(298.15 \text{ K}) + \int_{298.15}^T \frac{C_{p,m}^\circ(T)}{T} dT \quad (1.46)$$

In cases where the material shows a reversible phase transition between α and β at the transition temperature T_{tr} , with an associated transition entropy $\Delta_{tr} S_m^\circ(T_{tr}) = \Delta_{tr} H_m^\circ(T_{tr})/T_{tr}$, the standard entropy equation becomes

$$S_m^\circ(T) = S_m^\circ(298.15 \text{ K}) + \int_{298.15}^{T_{tr}} \frac{C_{p,m}^\circ(\alpha)}{T} dT + \frac{\Delta_{tr} H_m^\circ(T_{tr})}{T_{tr}} + \int_{T_{tr}}^T \frac{C_{p,m}^\circ(\beta)}{T} dT \quad (1.47)$$

1.4.1.4 Heat capacity at low temperatures ($T < \sim 300 \text{ K}$)

The heat capacity at low temperatures can be measured using adiabatic ($7 < T < 350 \text{ K}$) or thermal-relaxation calorimetry ($1 < T < 300 \text{ K}$ using liquid helium, and for temperatures below 5 K ${}^3\text{He}$). The accuracy of the former method ($\sim 0.2\%$) is higher than the latter ($\sim 3\%$), but adiabatic calorimetry requires much larger samples (a few grams in comparison to 10–30 mg for the thermal-relaxation technique).

The evolution of the heat capacity between 0 and $\sim 300 \text{ K}$ is rather complex, and a number of models have been proposed, notably those of Dulong and Petit in 1819, Einstein in 1907, and Debye in 1912. The full detail of these models is not given in this chapter, but the reader is referred to a number of references for a more comprehensive description [21–24].

The heat capacity at constant volume $C_{V,m}$ of a solid at very low temperatures is given by the sum of lattice vibrations, electronic, and magnetic contributions. The relation between the heat capacity at constant pressure measured experimentally, $C_{p,m}$, and the heat capacity at constant volume, $C_{V,m}$, involves the isobaric thermal expansivity and isothermal compressibility of the material [see Eq. (1.34) and Eq. (1.35)]. Because the thermal expansivity is negligible near 0 K, the heat capacity at constant pressure can be approximated with the heat capacity at constant volume (i.e., $C_{p,m} \approx C_{V,m}$). Hence, the aforementioned models, applicable to $C_{V,m}$, can be applied with good approximation to the measured experimental heat capacity data at constant pressure.

In the first and very simple rule of Dulong and Petit, the molar heat capacities of all substances adopt a constant value equal to $\sim 3NR$, where N is the number of atoms in the formula unit. The Dulong and Petit limit is usually reached at high temperatures for most crystalline solids, but this crude approximation does not work well at low temperatures, where the heat capacity decreases smoothly with temperature to reach zero at 0 K.

The subsequent models by Einstein and Debye were developed to describe the lattice contribution to the heat capacity, and notably the decrease of the heat capacity at low temperatures. The model of Einstein, derived from quantum theory, supposes that all N atoms in a crystal vibrate independently from each other with the same angular frequency ω_E , and can be represented by a set of $3N$ independent harmonic oscillators. The evolution of the heat capacity at constant volume is given in this model by the following equation:

$$C_{V,m}^E(\theta_E) = 3NRx^2 \frac{e^x}{[e^x - 1]^2}, \quad x = \frac{\theta_E}{T} = \frac{\hbar\omega_E}{k_B T} \quad (1.48)$$

where θ_E is the Einstein temperature, \hbar is Planck's constant, and k_B is Boltzmann's constant. The heat capacity in the model of Einstein decreases at low temperatures and reaches the value of zero at 0 K (as predicted by the *third law of thermodynamics*), while it tends to the limit of Dulong and Petit, that is, $3NR$, at high temperatures. The weakness of this model is in the form of the evolution at low temperatures, which follows an exponential function (e^x), while experimental data show an evolution proportional to T^3 . This arises from the fact that the vibrations of the N atoms in a crystal are actually correlated, and not independent of each other.

The model of Debye accounts for the collective lattice vibrations. It introduces a continuous distribution of vibrational frequencies up to the maximum angular frequency ω_D of the form $g(\omega) = (3\omega^2/\omega_D^3)$ for $\omega \leq \omega_D$, and $g(\omega) = 0$ for $\omega > \omega_D$. The evolution of the heat capacity at constant volume follows the equation:

$$C_{V,m}^D(\theta_D) = 9NR \left(\frac{T}{\theta_D} \right)^3 \int_0^{\theta_D/T} \frac{e^x x^4}{[e^x - 1]^2} dx, \quad x = \frac{\hbar\omega}{k_B T} \quad (1.49)$$

where θ_D is the Debye temperature. In this model the heat capacity equals $3NR$ at high temperatures. This equation moreover simplifies to $C_{V,m}^D(T) = ((12\pi^4 R)/5)(T/\theta_D)^3$ at very low temperatures; hence, the heat capacity tends as T^3 to zero at 0 K. This model also has its limitations. In particular, the experimental data cannot be reproduced accurately over large temperature ranges with a constant Debye temperature, meaning the Debye temperature varies with temperature too, hence $\theta_D(T) = f(T)$.

It should be pointed out that both the values of the Einstein and Debye temperatures are related to the type and strength of the bonding in a crystal (van der Waals, covalent, ionic bonding): the stronger the bonding, the higher is this temperature. The Einstein and Debye models alone are usually not appropriate to satisfactorily model the low-temperature heat capacity data of materials.

One common approach used in the literature for temperatures above $T \sim 10$ K consists of modeling the experimental heat capacity with a combination of one Debye function, and one or more Einstein functions:

$$C_{p,m}^\circ = n_D D(\theta_D) + n_{E1} E(\theta_{E1}) + n_{E2} E(\theta_{E2}) \quad (1.50)$$

where $D(\theta_D)$, $E(\theta_{E1})$, and $E(\theta_{E2})$ are the Debye and two Einstein functions, respectively, as follows from Eqs. (1.49) and (1.48). θ_D , θ_{E1} , and θ_{E2} are the characteristic Debye and Einstein temperatures. n_D , n_{E1} , and n_{E2} are adjustable parameters, the sum of which ($n_D + n_{E1} + n_{E2}$) should be approximately equal to the number of atoms in the formula unit. The Debye function accounts for the vibrations of the unit cell as a whole entity, while the Einstein functions adjust for internal vibrations of specific chemical groups and bonds. This method has been applied successfully in the literature to different classes of inorganic compounds, including iron phosphate [25–27], zirconolite [28], calcium titanate [29], dicesium molybdate [30], sodium uranate [31], and sodium neptunate [31].

At very low temperatures ($T < 10$ K), the phonon contribution is usually represented in the literature using a harmonic lattice model [32], as expressed by Eq. (1.51), where the number of required terms augments with the high-temperature limit of the regression analysis:

$$C_{latt} = \sum B_n T^n, \quad \text{where } n = 3, 5, 7, 9, \dots \quad (1.51)$$

In addition to the lattice vibrations, other contributions to the heat capacity can be found at low temperatures, which may be of electronic or magnetic nature. The electronic heat capacity originates from the quantization and excitation of the electrons near the Fermi level and takes the form of a linear function of temperature:

$$C_{el} = \gamma T \quad (1.52)$$

where γ is the Sommerfeld coefficient, with values ranging from 1 to 30×10^{-4} J/K²/mol. Hence, the heat capacity for $T < 10$ K can be represented by the equation:

$$C_{V,m}^{\circ} = \gamma T + \sum B_n T^n, \quad \text{where } n = 3, 5, 7, 9, \dots \quad (1.53)$$

Finally, structural and configurational order-disorder transformations, magnetic transitions (ferromagnetic, antiferromagnetic, and ferrimagnetic), as well as Schottky-type transitions give rise to additional anomalies in the heat capacity curve (which may take the form of a sharp λ peak, broad smooth peak, etc.) (Box 1.4). The entropy contribution due to the transition from an ordered state to a paramagnetic state is of configurational nature and equals to $\Delta S = R \ln(2s + 1)$ where s is the spin quantum number. In practice, many materials show lower magnetic entropy contributions than this theoretical value. Schottky anomalies

Box 1.4 Low-temperature heat capacity of NaUO₃.

The example of NaUO₃, measured by Lyon et al. using adiabatic calorimetry in the temperature range 5K–350 K [35], is shown in Fig. 1.1A. The heat capacity of NaUO₃ increases with temperature and reaches values that are about 15.8 (J/(K mol)) below the classical Dulong–Petit limit ($C_{lat} = 15R \approx 124.7$ (J/(K mol)) for the five atoms in the formula unit) as the temperature approaches 298.15 K.

The heat capacity data for NaUO₃ moreover shows a λ anomaly at (31 ± 1) K related to antiferromagnetic ordering of the U⁵⁺ ions, as later confirmed by magnetic susceptibility, electron spin resonance, and neutron diffraction measurements [36–38]. The excess heat capacity corresponding to the electronic and magnetic contributions only, shown in Fig. 1.1B, can be derived by subtracting the lattice contribution. The resulting curve shows clearly the (Continued)

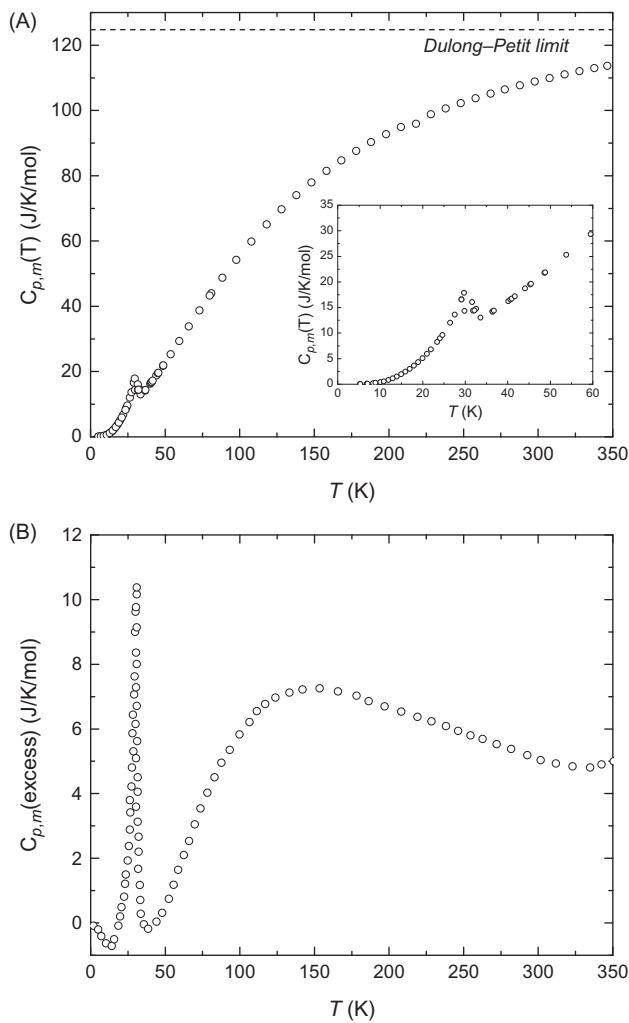
Box 1.4 (cont'd)

Figure 1.1 (A) Heat capacity data of NaUO_3 as measured by Lyon et al. [35], and (B) excess heat capacity obtained after subtracting the lattice contribution. The latter was approximated with the relation $C_{p,m}^{\circ}(\text{lattice}) = C_{p,m}^{\circ}(\text{Na}_3\text{UO}_4) - C_{p,m}^{\circ}(\text{Na}_2\text{O})$ [35].

magnetic contribution due to the antiferromagnetic transition, but also a very broad anomaly above ~ 50 K, which was related to a Schottky excess contribution [35].

arise in degenerate *d* transition element and *f*-element systems from the splitting of the ground-state electronic level by the crystalline electric field. The total number of energy levels and their respective degeneracies are predicted from

crystal field theory. For a simple two-level system with degeneracies g_0 for the ground-state level and g_1 for the excited level, the Schottky contribution to the heat capacity is given according to Boltzmann statistics by the equation [33]:

$$C_{\text{Schottky}} = Rx^2 \frac{g_0}{g_1} \frac{e^x}{(1 + (g_0/g_1)e^x)^2}, \quad x = \frac{\theta_S}{T} = \frac{\varepsilon_1}{k_B T} \quad (1.54)$$

where θ_S is the spacing between the two low-lying electronic levels expressed in K, g_0 and g_1 their respective degeneracy. θ_S is related to the energy separation ε_1 expressed in cm^{-1} between the two levels via the formula $\theta_S = \varepsilon_1/k_B$, where k_B is Boltzmann's constant. The measurement of the heat capacity in such cases hence allows one to derive information on the splitting of the energy levels by the crystalline electric field [34] and can be directly compared to the results of spectroscopy measurements.

1.4.1.5 Heat capacity at high temperatures ($T > 298.15 \text{ K}$)

Although the evolution of the heat capacity below 298.15K is rather complex, as detailed in the previous section, the variation at higher temperatures is more straightforward when no structural or magnetic transitions are involved. The heat capacity is most often described with a simple polynomial expression of the form:

$$C_{p,m}^\circ(T) = A + BT + CT^2 + DT^3 + ET^{-2} \quad (1.55)$$

Heat capacities at high temperatures can be measured directly using adiabatic calorimetry, differential scanning calorimetry, or indirectly using drop calorimetry. These techniques are described in detail in [Chapter 2, Experimental Methods](#). The reader is referred to that chapter for a more detailed description of the instruments and their capabilities.

Drop calorimetry measurements yield the enthalpy increment of a sample at temperature T_1 dropped in a calorimeter at T_2 . In traditional drop calorimetry, the sample is heated to a high temperature and then dropped into a cold calorimeter (e.g., ice, copper, and diphenyl ether), but in modern commercial instruments the sample is dropped from room temperature into a detector maintained at a set constant (higher) temperature. Thus the heat released to the detector (or the heat that is needed to maintain the detector at its set temperature when the “cold” sample reaches it) is recorded and is proportional to the enthalpy increment of the material between the two temperatures. The experiment is performed at several temperatures, and the experimental enthalpy increment data (see example on [Fig. 1.2A](#)) are subsequently fitted with a polynomial function of the form:

$$\begin{aligned} H_m^\circ(T) - H_m^\circ(298.15 \text{ K}) &= A(T - 298.15) + \frac{B}{2}(T^2 - 298.15^2) + \frac{C}{3}(T^3 - 298.15^3) \\ &\quad + \frac{D}{4}(T^4 - 298.15^4) - E(T^{-1} - 298.15^{-1}) \end{aligned} \quad (1.56)$$

The latter fitting is constrained by the value of the standard heat capacity at 298.15 K, that is, $C_{p,m}^\circ(298.15\text{ K})$, and the equality $H_m^\circ(T) - H_m^\circ(298.15\text{ K}) = 0$ at 298.15 K. The coefficients of the heat capacity function at constant pressure [Eq. (1.55)] are finally obtained by derivation of the enthalpy increment function according to Eq. (1.32) (Box 1.5).

1.4.1.6 Gibbs energy of formation

Finally, the Gibbs energy of formation can be calculated from the enthalpy of formation and the entropy of formation according to the following equation:

$$\Delta_f G_m^\circ(T) = \Delta_f H_m^\circ(T) - T \Delta_f S_m^\circ(T) \quad (1.57)$$

The Gibbs energy of formation is defined as the change in the Gibbs energy associated with the reaction of formation of 1 mol of a compound from its constituting elements in their standard states.

1.4.2 Definition of the chemical potential

1.4.2.1 General definition

The chemical potential is a very important thermodynamic quantity that is used to define the equilibrium state of a system. For open systems, or closed systems where the composition changes due to, for instance, a chemical reaction, the thermodynamic functions are determined by the (1) size of the system and its composition in addition to the (2) temperature and (3) pressure [22]. The Gibbs energy subsequently depends on all three variables, that is, $G = f(T, p, n_1, n_2, \dots, n_i)$, where n_i is the number of moles of the chemical component i . A more general expression for the differential dG is then given by

$$dG = \left(\frac{\partial G}{\partial T}\right)_{p,n_j} dT + \left(\frac{\partial G}{\partial p}\right)_{T,n_j} dp + \sum_i \left(\frac{\partial G}{\partial n_i}\right)_{T,p,n_{j \neq i}} dn_i \quad (1.58)$$

$$dG = -SdT + Vdp + \sum_i \left(\frac{\partial G}{\partial n_i}\right)_{T,p,n_{j \neq i}} dn_i \quad (1.59)$$

The chemical potential, μ_i , is defined by the partial derivative of the Gibbs energy with respect to n_i in the expression abovementioned.

$$\mu_i = \left(\frac{\partial G}{\partial n_i}\right)_{T,p,n_{j \neq i}} \quad (1.60)$$

Box 1.5 High-temperature heat capacity of NpO_2 .

The example of neptunium dioxide is displayed in Fig. 1.2A and B, enthalpy increments of which have been measured by Arkhipov et al. (350 K–1100 K) [39], Nishi et al. (334 K–1071 K) [40], and Beneš et al. (376 K–1770 K) [41]. The fitting equations at high temperatures by Beneš et al. are shown as red solid lines and match very well the low-temperature heat capacity data of Westrum et al. [42].

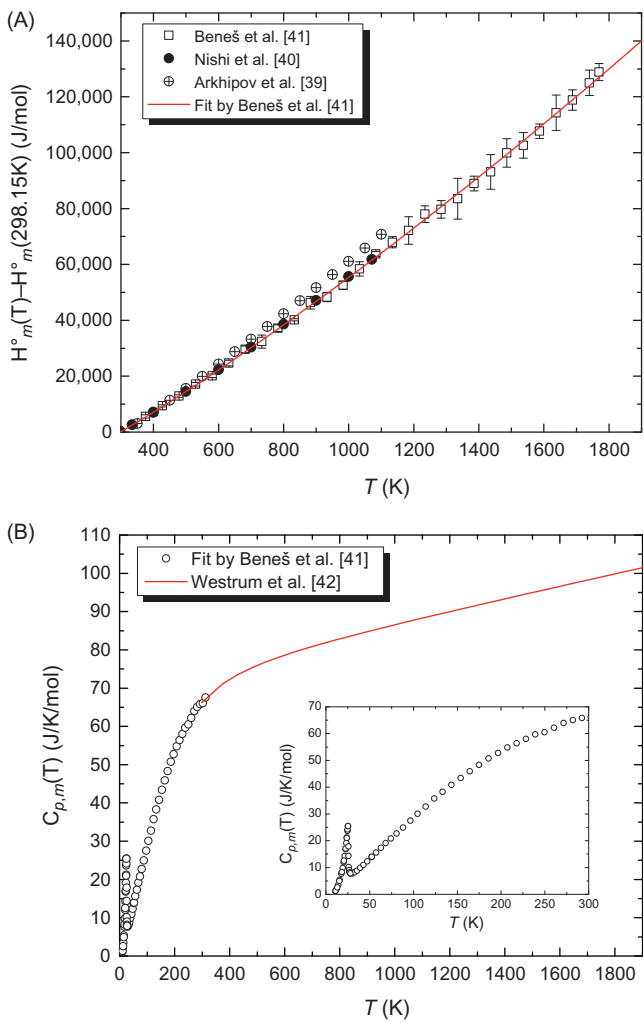


Figure 1.2 (A) Enthalpy increment and (B) heat capacity data for NpO_2 , and fit at high temperatures (red line).

Eq. (1.59) subsequently becomes

$$dG = -SdT + Vdp + \sum_i \mu_i dn_i \quad (1.61)$$

Under equilibrium conditions, the differential of the Gibbs energy equals zero as detailed in Section 1.3.3, which for an open system is written as

$$dG_{T,p,n_i} = 0 \quad (1.62)$$

At constant temperature T and pressure p , the combination of Eqs. (1.59) and (1.62) implies that the chemical potential of a given component is the same in all phases in equilibrium in the system:

$$\mu_i^{\phi 1} = \mu_i^{\phi 2} \quad (1.63)$$

where $\phi 1$ and $\phi 2$ denote the different phases in equilibrium, and i the given component in the system.

1.4.2.2 Chemical potential of an ideal single-component gas

In the case of a single-component gas at constant temperature, the application of Eq. (1.59) yields the following expression for the Gibbs energy of the gas at pressure p :

$$G(p) = G(p^\circ) + \int_{p^\circ}^p Vdp \quad (1.64)$$

where p° is the reference pressure.

Considering an ideal gas, for which the equation of state $pV = nRT$ applies, Eq. (1.64) simplifies to

$$\frac{G(p)}{n} = \frac{G(p^\circ)}{n} + RT \ln\left(\frac{p}{p^\circ}\right) \quad (1.65)$$

$$G_m(p) = G_m(p^\circ) + RT \ln\left(\frac{p}{p^\circ}\right) \quad (1.66)$$

The chemical potential of a pure single-component system is equal to its molar Gibbs energy, hence the previous equation becomes

$$\mu(p) = \mu^\circ(p^\circ) + RT \ln\left(\frac{p}{p^\circ}\right) \quad (1.67)$$

$$\mu = \mu^\circ + RT \ln p \quad (1.68)$$

where p° is the standard pressure set to 1 bar. μ° is called the standard chemical potential (typically available in a database) and corresponds to the molar Gibbs energy of the pure ideal gas at the standard pressure.

1.4.2.3 Chemical potential of a single-component condensed phase

The chemical potential, or molar Gibbs energy, of a single-component condensed phase (solid or liquid) varies with temperature, while the effect of pressure is usually very limited, by contrast with gases. This results from the fact that the molar volume of a condensed phase is much less affected by pressure variations than in the case of a gas [22]. Most experimental studies and modeling work in which condensed phases are involved are performed at 1 bar pressure (i.e., at the standard pressure), and the effect of pressure is often negligible. The standard chemical potential $\mu^\circ(T) = G_m^\circ(T)$ is a function of temperature only and is expressed as a temperature dependent power series, a form especially useful in the CALPHAD approach (see Chapter 4) [6]:

$$G_m^\circ(T) - \sum_i v_i H_{m,i}^{SER} = \alpha_0 + \alpha_1 T + \alpha_2 T \ln(T) + \alpha_3 T^2 + \alpha_4 T^{-1} + \alpha_5 T^3 + \alpha_6 T^4 \quad (1.69)$$

where $\sum_i v_i H_{m,i}^{SER}$ is the stoichiometric sum of the enthalpies of the constitutive elements of the substance in their reference states (noted SER), usually at 298.15 K and the standard state pressure of 1 bar. v_i is the stoichiometric coefficient of element i in the condensed phase. The expression of the Gibbs energy relative to this reference term results from the fact that only changes in enthalpies can be measured, and not the absolute values.

The aforementioned coefficients are calculated from the values of the standard enthalpy of formation at 298.15 K, standard entropy at 298.15 K, as well as the heat capacity temperature dependent function. In particular, the polynomial expression for the heat capacity function can be written equivalently:

$$C_{p,m}^\circ(T) = A + BT + CT^2 + DT^3 + ET^{-2} \quad (1.70)$$

$$= -\alpha_2 - 2\alpha_3 T - 6\alpha_5 T^2 - 12\alpha_6 T^3 - 2\alpha_4 T^{-2} \quad (1.71)$$

Moreover, from the relations defined in Eq. (1.36), one can easily derive the entropy and heat capacity of the substance in the system:

$$S_m^\circ(T) = -\alpha_1 - \alpha_2(1 + \ln T) - 2\alpha_3 T + \alpha_4 T^2 - 3\alpha_5 T^2 - 4\alpha_6 T^3 \quad (1.72)$$

$$H_m^\circ(T) - \sum_i v_i H_{m,i}^{SER} = \alpha_0 - \alpha_2 T - \alpha_3 T^2 + 2\alpha_4 T^{-1} - 2\alpha_5 T^3 - 3\alpha_6 T^4 \quad (1.73)$$

1.4.3 Mixing properties for gas, solid, and liquid solutions

1.4.3.1 Definition of a chemical solution

Solutions are defined as mixtures with two or more components. The composition of a solution of N components is defined by the molar fractions of the different components, expressed as

$$x_i = \frac{n_i}{\sum_{j=1}^N n_j}$$

$$\sum_{i=1}^N x_i = 1 \quad x_i > 0 \quad (1.74)$$

where n_i is the number of moles of component i in the solution.

1.4.3.2 Chemical potential of a gas in solution

As for a single-component gas, the application of Eq. (1.59) for a component i in an ideal gas solution at constant temperature yields

$$G_i(p_i) = G_i(p_i^\circ) + \int_{p_i^\circ}^{p_i} V_i dp_i$$

$$G_{i,m}(p_i) = G_{i,m}(p_i^\circ) + RT \ln\left(\frac{p_i}{p_i^\circ}\right)$$

$$\mu_i(p_i) = \mu_i^\circ(p_i^\circ) + RT \ln\left(\frac{p_i}{p_i^\circ}\right) \quad (1.75)$$

where $\mu_i^\circ(p_i^\circ)$ is the standard chemical potential of the pure ideal gas i at pressure $p_i^\circ = 1$ bar.

The application of the equation of state to component i , that is, $p_i V = n_i RT$, allows one to derive the following relationship between the pressure of component i and the total pressure $p = \sum_i p_i$:

$$p_i = x_i p \quad (1.76)$$

For an ideal gas at constant pressure ($p = p_i^\circ$), the chemical potential of component i in solution is given by

$$\mu_i = \mu_i^\circ + RT \ln x_i \quad (1.77)$$

1.4.3.3 Chemical potential of species in solid and liquid solutions

A new thermodynamic quantity, the chemical activity a_i of component i , is used to define the chemical potential of a solid or liquid in solution:

$$\mu_i = \mu_i^\circ + RT \ln a_i \quad (1.78)$$

where μ_i° is the standard chemical potential of pure component i at the standard pressure $p_i^\circ = 1$ bar.

Solutions are ideal when the chemical interactions between the components in solution are the same as those in the pure (non-mixed) end-members.

Most solutions in real systems do not follow an ideal behavior, and the activity coefficient γ_i is thus introduced to quantify the deviation from ideality. γ_i is given by the ratio of the chemical activity a_i and the mole fraction of component i in solution:

$$\gamma_i = \frac{a_i}{x_i} \quad (1.79)$$

In the case of an ideal solution, γ_i is equal to 1, and the chemical activity of a solution species equals its molar fraction. A positive deviation from ideality (the solution is destabilized compared to the ideal case) corresponds to $\gamma_i > 1$ ($\ln \gamma_i > 0$), and a negative deviation (the solution is stabilized compared to the ideal case) to $\gamma_i < 1$ ($\ln \gamma_i < 0$).

1.4.3.4 Raoult's law and Henry's law, and standard states for a solution

Like for single-component systems, solutions require the definition of a standard state. In this case, either the Raoultian or Henrian standard states are used.

Henry's law, demonstrated empirically in 1803, expresses that for dilute solutions, the partial pressure of a solute B above a solvent A containing the solute, is directly proportional to the concentration (mole or mass fraction) of the solute. The constant of proportionality k_H is called Henry's constant:

$$p_B = k_H x_B \quad (1.80)$$

where p_B is the partial pressure and x_B is the mole fraction of solute B .

Likewise, Raoult's law, formulated in 1887, states that for dilute solutions, the vapor pressure of the solvent p_A is given by the product of the vapor pressure of the pure solvent p_A^* and the mole fraction of the solvent x_A , hence,

$$p_A = x_A p_A^* \quad (1.81)$$

Real solutions follow the aforementioned laws at infinite dilution only. In the Raoultian and Henrian standard states, respectively, the activity coefficients γ_A^R and γ_B^H are given by

$$\gamma_A^R = \frac{a_A^R}{x_A} \quad (1.82)$$

$$\gamma_B^H = \frac{a_H^H}{x_H} \quad (1.83)$$

In the Raoultian standard state (the most widely used), $\gamma_A^R \rightarrow 1$ when x_A approaches unity. This means that the real solution tends to an ideal behavior when the solvent concentration is close to unity. The reference state for the solution is therefore simply the pure end-member. As for the Henrian standard state, $\gamma_B^H \rightarrow 1$ when $x_B \rightarrow 0$. This reference state is hypothetical, by contrast with the Raoultian standard state, which is effectively fulfilled at infinite dilution.

Nevertheless, the chemical potential can be expressed using both reference states and is independent of the choice of one or the other:

$$\mu_i = \mu_i^{\circ,R} + RT \ln a_i^R = \mu_i^{\circ,H} + RT \ln a_i^H \quad (1.84)$$

When expressing mixing properties (see next section), it is important, however, to state which convention is used for the standard state, as this will affect the result.

1.4.3.5 Mixing and excess thermodynamic properties in solution

It is often useful when studying the thermodynamics of solutions to look at the mixing properties, in particular the enthalpy $\Delta_{mix}H_m$, entropy $\Delta_{mix}S_m$ and Gibbs energy of mixing $\Delta_{mix}G_m$. A detailed description of the derivation of the Gibbs energy of mixing is given hereafter, but the other mixing properties also follow the same definition.

The Gibbs energy of mixing corresponds to the difference between the Gibbs energy of the solution before and after mixing takes place. The initial Gibbs energy is simply given by the stoichiometric sum of the Gibbs energies of the pure end-members (i.e., $\sum_i x_i G_{m,i}$). The final Gibbs energy after mixing is equal to the sum of the partial molar Gibbs energy of component i (i.e., $\sum_i x_i \bar{G}_{m,i}$). Hence, the Gibbs energy of mixing is defined as

$$\Delta_{mix}G_m = \sum_i x_i (\bar{G}_{m,i} - G_{m,i}) \quad (1.85)$$

Similarly, the enthalpy and entropy of mixing are defined as

$$\begin{aligned} \Delta_{mix}H_m &= \sum_i x_i (\bar{H}_{m,i} - H_{m,i}) \\ \Delta_{mix}S_m &= \sum_i x_i (\bar{S}_{m,i} - S_{m,i}) \end{aligned} \quad (1.86)$$

Because the molar Gibbs energy of a component is equivalent to its chemical potential, Eq. (1.85) can also be written as

$$\Delta_{\text{mix}}G_m = \sum_i x_i(\mu_i - \mu_i^\circ) \quad (1.87)$$

where μ_i and μ_i° are the chemical potentials of component i in the solution and as pure end-member, respectively.

Combining the latter equation with Eq. (1.78) yields the Gibbs energy of mixing as function of the chemical activity:

$$\Delta_{\text{mix}}G_m = RT \sum_i x_i \ln a_i \quad (1.88)$$

In the case of an ideal solution, activities and molar fractions are equal $a_i = x_i$; hence, the Gibbs energy of mixing becomes

$$\Delta_{\text{mix}}G_m^{\text{ideal}} = RT \sum_i x_i \ln x_i \quad (1.89)$$

Applying the thermodynamic relations Eq. (1.36), one derives the following results for the ideal entropy and enthalpy of mixing:

$$\begin{aligned} \Delta_{\text{mix}}S_m^{\text{ideal}} &= - \left(\frac{\partial \Delta_{\text{mix}}G_m^{\text{ideal}}}{\partial T} \right)_{p,n_i} \\ &= -R \sum_i x_i \ln x_i \end{aligned} \quad (1.90)$$

$$\begin{aligned} \Delta_{\text{mix}}H_m^{\text{ideal}} &= \Delta_{\text{mix}}G_m^{\text{ideal}} + T\Delta_{\text{mix}}S_m^{\text{ideal}} \\ &= 0 \end{aligned} \quad (1.91)$$

Hence, for an ideal solution, the enthalpy of mixing equals zero, and the solution is stabilized only by an entropy term. The latter term is called the configurational entropy. For a system with two components, as illustrated in Fig. 1.3 for the mixing of LiF and ThF₄ in liquid solution, the minimum of the ideal Gibbs energy of mixing curve is found at equimolar composition and equals $-RT \ln 2$.

Most real systems deviate from ideal behavior, however, and this deviation can be quantified by the excess molar Gibbs energy of mixing defined as follows:

$$\begin{aligned} \Delta_{\text{mix}}G_m^{\text{excess}} &= \Delta_{\text{mix}}G_m - \Delta_{\text{mix}}G_m^{\text{ideal}} \\ &= RT \sum_i x_i (\ln a_i - \ln x_i) \\ &= RT \sum_i x_i \ln \gamma_i \end{aligned} \quad (1.92)$$

Similarly, the excess enthalpy and entropy of mixing are defined as follows (Box 1.6):

Box 1.6 Mixing properties in the LiF–ThF₄ liquid solution.

The example of the liquid solution in the LiF–ThF₄ system is illustrated in Fig. 1.3, showing a negative deviation from the ideal behavior. This system is key for the design of next-generation molten salt reactors (see Chapter 6: Molten salt reactor fuels). In this case the Raoultian standard state was used to express the mixing properties.

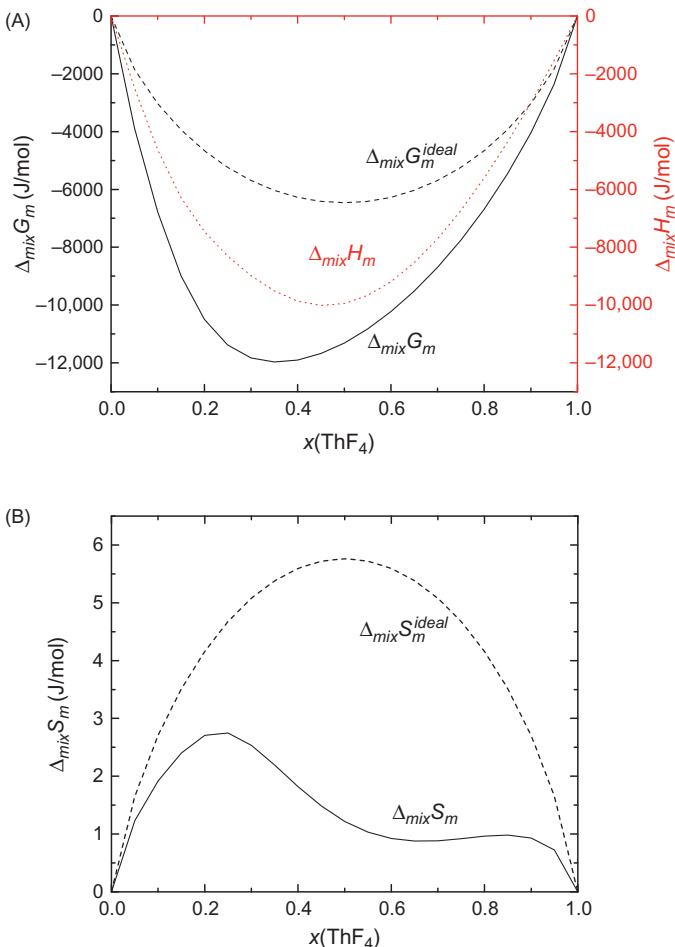


Figure 1.3 (A) Enthalpy, Gibbs energy of mixing and (B) entropy of mixing in the LiF–ThF₄ liquid solution as optimized in the thermodynamic model of Capelli et al. [43], and comparison with the ideal excess molar properties.

$$\begin{aligned}\Delta_{mix}S_m^{excess} &= \Delta_{mix}S_m - \Delta_{mix}S_m^{ideal} \\ &= \Delta_{mix}S_m + R \sum_i x_i \ln x_i\end{aligned}\quad (1.93)$$

$$\begin{aligned}\Delta_{mix}H_m^{excess} &= \Delta_{mix}H_m - \Delta_{mix}H_m^{ideal} \\ &= \Delta_{mix}H_m\end{aligned}\quad (1.94)$$

1.4.4 Chemical reaction equilibria

1.4.4.1 Equilibrium constant

An important quantity used in thermodynamics to define the equilibrium state of chemical reactions is the equilibrium constant K_{eq} . Considering again the general equation



the equilibrium constant of reaction (1.95) is defined by the ratio:

$$K_{eq} = \frac{(a_C^{eq})^{v_C}}{(a_A^{eq})^{v_A} (a_B^{eq})^{v_B}} \quad (1.96)$$

where a_A^{eq} , a_B^{eq} , and a_C^{eq} are the chemical activities of the reactants and products under equilibrium conditions.

When the chemical reaction is not yet at equilibrium, the ratio as defined above is denoted Q_R and named reaction quotient:

$$Q_R = \frac{(a_C)^{v_C}}{(a_A)^{v_A} (a_B)^{v_B}} \quad (1.97)$$

The standard equilibrium constant is directly related to the standard Gibbs energy of reaction as will be demonstrated hereafter. The Gibbs energy of Eq. (1.95) is equal to

$$\begin{aligned}\Delta_r G &= v_C \mu_C - v_A \mu_A - v_B \mu_B \\ &= v_C \mu_C^\circ - v_A \mu_A^\circ - v_B \mu_B^\circ + RT \ln \left(\frac{(a_C)^{v_C}}{(a_A)^{v_A} (a_B)^{v_B}} \right) \\ \Delta_r G &= \Delta_r G^\circ + RT \ln Q_R\end{aligned}\quad (1.98)$$

At equilibrium under standard conditions, $\Delta_r G = 0$, hence,

$$\Delta_r G^\circ = -RT \ln K_{eq} \quad (1.99)$$

1.4.4.2 Van't Hoff equation

Temperature has an effect on both chemical equilibrium and reaction rate as mentioned earlier. Similar to the Arrhenius equation that relates the reaction constant to temperature, the well-known Van't Hoff equation expresses the change in the equilibrium constant with respect to temperature. From the previous equation, we will get

$$\begin{aligned}\frac{\Delta_r G^\circ}{T} &= -R \ln K_{\text{eq}} \\ \frac{d(\Delta_r G^\circ / T)}{dT} &= -R \frac{d \ln K_{\text{eq}}}{dT} \\ \frac{\Delta_r H^\circ}{RT^2} &= \frac{d \ln K_{\text{eq}}}{dT}\end{aligned}\tag{1.100}$$

1.5 Statistical thermodynamics applied to gases

Classical thermodynamics and its experimental methods deal principally with macroscopic scale properties (bulk) and are therefore well suited for condensed matter, with strong and long-range interaction between the constituents. The situation is different for gases, which are composed of individual atomic or molecular species. Their macroscopic properties (heat capacity, entropy) can be obtained from statistical thermodynamic calculations that describe the internal energy at the atomic/molecular scale. The basis of statistical thermodynamics was formulated by Maxwell, Boltzmann, and Gibbs, among others, at the end of the 19th century. The discovery by Max Planck of the quantized (discontinuous) structure of nature on an atomic/molecular scale in 1900, and the subsequent work of Einstein (photon theory), Bohr (orbits model of the atom), de Broglie (wave-matter paradox), Schrödinger (electron waves), and others led to the development of a modern quantum mechanical formulation. However, for the derivation of the thermal functions above room temperature, many quantum mechanical formulations can be approximated by their classical counterparts. The following section gives a description of the derivation of the relevant equations.

1.5.1 Statistical thermodynamic basis

1.5.1.1 The Boltzmann distribution law

From a statistical point of view, the total energy of a system E composed of N distinguishable particles is the sum of the energies of the individual particles (ϵ):

$$E = \epsilon_1 + \epsilon_2 + \dots + \epsilon_n = \sum_{i=1}^n N_i \epsilon_i \quad (1.101)$$

If N_i is the number of particles in energy state ϵ_i , which has a statistical weight (degeneracy) g_i , and N_j the number of particles with energy ϵ_j and a degeneracy g_j , the ratio N_i/N_j is

$$\frac{N_i}{N_j} = \frac{g_i}{g_j} e^{-(\epsilon_i - \epsilon_j)/k_B T} \quad (1.102)$$

This equation is known as the Boltzmann distribution law and was derived in 1868. The fraction of particles N_i with energy ϵ_i out of the total of $N (= \sum N_i)$ is then given by the equation:

$$\frac{N_i}{N} = \frac{g_i e^{\epsilon_i/k_B T}}{\sum_i g_i e^{\epsilon_i/k_B T}} \quad (1.103)$$

The sum in the denominator is called the *molecular partitioning function* z :

$$z = \sum_i g_i e^{-\epsilon_i/k_B T} \quad (1.104)$$

and Eq. (1.103) can be rewritten as

$$\frac{N_i}{N} = \frac{g_i e^{\epsilon_i/k_B T}}{z} \quad (1.105)$$

1.5.1.2 Ensembles and probabilities

To describe a system consisting of a large number of particles, Gibbs introduced the term *ensemble*. An ensemble is a theoretical description of a number of identical subsystems that are subjected to the same thermodynamic constraints as the overall system. Gibbs made a distinction between microcanonical, canonical, and grand canonical ensembles. A microcanonical ensemble consists of subsystems of N particles in a volume V . The subsystems are completely isolated by fixed insulating walls, and therefore the ensemble is completely described by the variables N , V , and E . A canonical ensemble is in thermal contact with a large heat reservoir and will have an equilibrium temperature according to the zeroth law. This ensemble is therefore described by the variables N , V , and T . A grand canonical ensemble is an open system in which the number of molecules is not fixed. Its equilibrium state is described by V , T , and the chemical potential μ .

A macroscopic property \bar{M} of the system is the average of the n members of the ensemble:

$$\overline{M} = \frac{1}{n} \sum M_{member} \quad (1.106)$$

where the sum is taken over all members of the ensemble. Taking into account that some members of the ensemble have the same value of M_i , and introducing n_i as the statistical weight of state i , Eq. (1.106) becomes

$$\overline{M} = \frac{1}{n} \sum n_i M_i \quad (1.107)$$

The probability P of finding a member in state i with property M_i is

$$P_i = \frac{N_i}{N} \quad (1.108)$$

Eq. (1.106) can then be written as

$$\overline{M} = \sum P_i M_i \quad (1.109)$$

1.5.1.3 The canonical partition function

Focusing now on the energy as macroscopic property in a canonical ensemble, the probability P_i of a state depends on the energy of that state only:

$$P_i = P_i(E_i) \quad (1.110)$$

In the quantized structure of nature on the atomic/molecular scale, E_i is the sum of the (small) energy contributions of the quantum states:

$$E_i = \epsilon_1 + \epsilon_2 + \epsilon_3 + \dots = \sum_j \epsilon_j \quad (1.111)$$

Combining Eqs. (1.110) and (1.111) gives

$$P_i = P_i(\epsilon_1 + \epsilon_2 + \epsilon_3 + \dots) \quad (1.112)$$

The probability P_i of state i becomes the joint probability of j parts of the state i :

$$P_i(\epsilon_1 + \epsilon_2 + \epsilon_3 + \dots) = p_1(\epsilon_1)p_2(\epsilon_2)p_3(\epsilon_3)\dots \quad (1.113)$$

Taking the logarithm of both sides gives

$$\ln P_i(\epsilon_1 + \epsilon_2 + \epsilon_3 + \dots) = \ln p_1(\epsilon_1) + \ln p_2(\epsilon_2) + \ln p_3(\epsilon_3) + \dots \quad (1.114)$$

The left-hand side of this equation can be expanded in a power series of the type $f(x) = a_0 + a_1x + a_2x^2 + a_3x^3 + \dots$ with $x = \epsilon_1 + \epsilon_2 + \epsilon_3 + \dots$, the a_i being arbitrary quantities:

$$\ln P_i(\epsilon_1 + \epsilon_2 + \epsilon_3 + \dots) = a_0 + a_1(\epsilon_1 + \epsilon_2 + \epsilon_3 + \dots) + a_2(\epsilon_1 + \epsilon_2 + \epsilon_3 + \dots)^2 + \dots \quad (1.115)$$

It can be shown that a_2 and higher a must be zero, since no cross terms between the ϵ_i are allowed as Eq. (1.113) must be fulfilled. Thus

$$\ln P_i(\epsilon_1 + \epsilon_2 + \epsilon_3 + \dots) = a_0 + a_1(\epsilon_1 + \epsilon_2 + \epsilon_3 + \dots) \quad (1.116)$$

or

$$P_i(\epsilon_1 + \epsilon_2 + \epsilon_3 + \dots) = e^{a_0 + a_1(\epsilon_1 + \epsilon_2 + \epsilon_3 + \dots)} = e^{a_0} e^{a_1 E_i} \quad (1.117)$$

and in simplified form:

$$P_i(\epsilon_1 + \epsilon_2 + \epsilon_3 + \dots) = \alpha e^{-\beta E_i} \quad (1.118)$$

Because the sum of P_i over all members of the ensemble is unity, it follows that

$$\sum_i P_i = 1 = \alpha \sum_i e^{-\beta E_i} \quad (1.119)$$

$$\frac{1}{\alpha} = \sum_i e^{-\beta E_i} = Z \quad (1.120)$$

where Z is the canonical partition function, which is a function of V and T .

It can be shown that the factor β is inversely proportional to the temperature, whereby the proportionality constant is k_B (see, e.g., Andrews [44]), which follows from the comparison of the classical and statistical definitions of the average heat in an equilibrium state:

$$d\bar{Q}_{rev} = T d\bar{S} \quad (1.121)$$

and

$$d\bar{Q}_{rev} = -\frac{1}{\beta} \left(\sum_i P_i \ln P_i \right) \quad (1.122)$$

Eq. (1.122) can thus be written as

$$Z = \sum_i e^{-E_i/k_B T} \quad (1.123)$$

1.5.1.4 The relation between Z and z

The calculation of Z for a system consisting of interacting particles (a real gas or an imperfect crystal) is not (yet) possible with current techniques, but for systems consisting of isolated particles, for example, in an ideal gas or a perfect crystal, it is straightforward. For that case the total energy is the sum of the energies of the N individual particles (1.101):

$$E = \epsilon_a + \epsilon_b + \epsilon_c + \dots + \epsilon_n \quad (1.124)$$

The partitioning function Z then becomes

$$Z = \sum_i e^{-E_i/k_B T} = \sum_i e^{-\epsilon_{ai}/k_B T} \sum_i e^{-\epsilon_{bi}/k_B T} \dots = z_a z_b \dots \quad (1.125)$$

In an ideal gas, all molecules have the same allowable energy states, which implies that $z_a = z_b = z_c = z$, and Z would become z^N . However, because the atoms or molecules are indistinguishable, Z must be corrected by dividing by $N!$:

$$Z = \frac{1}{N!} z^N \quad (1.126)$$

1.5.1.5 The thermodynamic functions

The total energy of an assembly of N molecules is represented by

$$E^\circ = E_0^\circ + \sum_{i=1}^{\infty} N_i \epsilon_i \quad (1.127)$$

which is identical to (1.101), with N_i the number of molecules having energy ϵ_i , but taking also into account E_0° , the zero-point energy. According to the Boltzmann distribution law, N_i is proportional to the partition function Z :

$$N_i = N_A \frac{g_i e^{-\epsilon_i/k_B T}}{Z} \quad (1.128)$$

where N_A is the number of Avogadro and g_i is the statistical weight. Eq. (1.127) can now be rewritten as

$$E^\circ = E_0^\circ + \frac{\sum_i \epsilon_i g_i e^{-\epsilon_i/k_B T}}{Z} \quad (1.129)$$

Resolving this equation leads to

$$E^\circ = E_0^\circ + RT^2 \frac{d(\ln Z)}{dT} \quad (1.130)$$

The molar enthalpy is the sum of E and the external energy, which is simply $pV = RT$ in the case of an ideal gas. Thus

$$H = E_0^\circ + RT + RT^2 \frac{d(\ln Z)}{dT} \quad (1.131)$$

from which the molar heat capacity at constant pressure follows as

$$C_p^\circ(T) = \frac{dH^\circ(T)}{dT} = R + R \frac{d}{dT} \left(T^2 \frac{d(\ln Z)}{dT} \right) \quad (1.132)$$

The standard entropy is given by Boltzmann's equation as

$$S = k_B \ln \Omega \quad (1.133)$$

where Ω is the number of the arrangements of N molecules among the energy levels ϵ_i , with occupation N_i :

$$\Omega = \frac{N!}{(N_1! N_2! N_3! \dots)} \quad (1.134)$$

Substituting Eq. (1.134) into Eq. (1.133), applying Stirling's approximation (i.e., $\ln N! \sim N \ln N - N$), and realizing that $\sum N_i = N$, gives

$$S = -Nk_B \sum_i \left(\frac{N_i}{N} \right) \ln \left(\frac{N_i}{N} \right) \quad (1.135)$$

The ratio N_i/N is given by Eq. (1.128), and substitution yields

$$S = \frac{E^\circ}{T} + Nk_B \ln Z \quad (1.136)$$

It is thus clear that all the thermal functions of ideal gases can be derived from Z , because

$$Z = \frac{N!}{\prod N_i!} \quad (1.137)$$

and thus

$$Z = \frac{z_{trs} \cdot z_{vib} \cdot z_{rot} \cdot z_{elec}}{N!} \quad (1.138)$$

To calculate thermodynamic functions, a detailed knowledge of the translational, rotational, vibrational, and electronic partition functions is thus required. It should be realized that the total energy of a molecule is composed of an external and an internal component. The external component is equal to the translational energy, the internal energy is the sum of electronic, rotational, and vibrational components, which can be separated (e.g., Born–Oppenheimer approximation).

1.5.2 Molecular thermodynamic calculations (ideal gas)

1.5.2.1 The translational partition function

The translational energy levels are very closely spaced, about 10^{-42} J at room temperature. For this reason, it is a common approximation to treat the translational motion as non-quantized. The summation sign in the partition function can then be replaced by an integral, leading to

$$Z_{tr} = \frac{(2\pi k_B T)^{5/2} V}{h^3 M^{3/2}} \quad (1.139)$$

where M is the molar mass, V is the molar gas volume, and h is Planck's constant. This equation with its variations is derived from the work of Sackur and Tetrode around 1910 and is therefore called the Sackur–Tetrode equation.

Combining Eq. (1.139) with the general equations derived in Section 1.5.1.5 for H and S yields

$$\{H^\circ(T) - H^\circ(298.15 \text{ K})\}_{trans} = \frac{5}{2} R \quad (1.140)$$

and

$$S_{trans}(T) = \frac{3}{2} R \ln M + \frac{5}{2} R \ln T - R \ln p^\circ + R \ln \frac{2\pi^{3/2} k_B^{5/2}}{N_A h^3} \quad (1.141)$$

1.5.2.2 The electronic partition function

At room temperature, most molecules are in their lowest electronic state, the ground state, where the energy levels are about 10^{-42} J apart. At higher temperatures, the electrons can also occupy excited electronic levels by acquiring specific quanta of energy. The electronic partition function is given by

$$Z = \sum_{i=0}^{\infty} g_i e^{-\epsilon_i/k_B T} \quad (1.142)$$

where ϵ_i is the electronic energy, and g_i is the statistical weight of level i . When the excited states occur at energies that do not contribute to the sum, this equation reduces to

$$Z = z_0 \quad (1.143)$$

The thermal functions are then derived by combining Eq. (1.142) with Eqs. (1.131) and (1.136) in a direct numerical summation:

$$S_{el}(T) = \frac{Rc_2}{T} \frac{\sum_i \epsilon_i^2 g_i e^{-c_2 \epsilon_i/T}}{\sum_i g_i e^{-c_2 \epsilon_i/T}} R \ln \left(\sum_i g_i e^{-c_2 \epsilon_i/T} \right) \quad (1.144)$$

$$\{H^\circ(T) - H^\circ(0K)\}_{el} = Rc_2 \frac{\sum_i \epsilon_i g_i e^{-c_2 \epsilon_i/T}}{\sum_i g_i e^{-c_2 \epsilon_i/T}} \quad (1.145)$$

where c_2 is the second radiation constant, which is equal to hc/k_B .

1.5.3 The vibrational partition function

The vibrational energy levels are about 10^{-20} J apart at room temperature, and most molecules are in their lowest vibrational states. The simplest description of the vibrational motion in a molecule is the harmonic oscillator approximation. The quantum mechanical expression for the vibrational energy of a harmonic oscillator is

$$\epsilon_{vib} = h\nu \left(v + \frac{1}{2} \right) \quad (1.146)$$

where ν is the vibrational frequency and v is the vibrational quantum number, $v = 0, 1, 2, \dots, \infty$, and $\Delta v = \pm 1$. The number of vibrational frequencies of a molecule consisting of N atoms is $3N - 5$ in the case of a linear configuration and $3N - 6$ in the case of a nonlinear configuration.

The vibrational partition function can now be written as

$$Z_{vib} = \sum_{v=0}^{\infty} e^{-hv(v+(1/2))/k_B T} \quad (1.147)$$

From Eq. (1.146), it follows that the energy of the lowest vibrational state is not zero but $(1/2)h\nu$, which is called the zero-point energy. Since energy is always measured with respect to the lowest state, the exponent can be written as

$u = h\nu/k_B T$. Eq. (1.147) can now be expressed as $1 + e^{-u} + (e^{-u})^2 + (e^{-u})^3 + \dots$, and since e^{-u} is generally much smaller than unity, the vibrational partition function equals

$$Z_{vib} = (1 - e^{-u})^{-1} \quad (1.148)$$

Substituting this equation into the general equations derived in Section 1.5.1.5 for S and H gives

$$S_{vib}(T) = R \sum \left[\frac{ue^{-u}}{(1 - e^{-u}) - \ln(1 - e^{-u})} \right] \quad (1.149)$$

and

$$\{H^\circ(T) - H^\circ(0K)\}_{vib} = R \sum \frac{ue^{-u}}{(1 - e^{-u})} \quad (1.150)$$

A real molecule is of course not a harmonic but an anharmonic oscillator. The simplified quantum mechanical expression for the vibrational energy of an anharmonic oscillator is the Morse potential:

$$\epsilon_{vib} = h\nu \left[\left(v + \frac{1}{2} \right) - x_e \left(v + \frac{1}{2} \right)^2 \right] \quad (1.151)$$

where x_e is the anharmonicity constant. More extended expressions for the vibrational energy of an anharmonic oscillator are possible, including cubic and quartic terms in $(v + (1/2))$, with anharmonicity constants y_e, z_e , etc.

1.5.3.1 The rotational partition function

The rotational energy levels are about 10^{-23} J apart, and at room temperature, already a large number is occupied. Assuming a molecule to be a rigid rotor, the rotational partition function is given by

$$\epsilon_{rot} = J(J + 1) \frac{\hbar}{8\pi^2 I} = J(J + 1)B \quad (1.152)$$

where J is the rotational quantum number, and I is the moment of inertia. For linear molecules that are asymmetric around their center of mass, the rotational quantum number may have any value of J ; for symmetric molecules, only odd or only even values of J are allowed, depending on the nuclear spin.

Substitution of Eq. (1.152) into Eq. (1.128) and realizing that each rotational level has a statistical weight of $(2J + 1)$ gives

$$Z_{rot} = \sum_J (2J + 1) e^{-J(J+1)B/k_B T} \quad (1.153)$$

which simplifies to

$$Z_{rot} = \sum_J (2J + 1) e^{-J(J+1)\beta} \quad (1.154)$$

where $\beta = B/k_B T$. Since the term βT , which is the characteristic temperature of rotation Θ_{rot} , is small for most linear molecules, it is common to replace the summation sign by an integral for temperatures $T \gg \Theta_{rot}$, leading in the simplest approximation to the classic result:

$$Z_{rot} = \frac{8\pi I k_B T}{h^2 \sigma} \quad (1.155)$$

where σ is the symmetry number, which is 1 for asymmetric and 2 for symmetric diatomic molecules. The inclusion of the symmetry number arises from the fact that only odd or only even values of J are allowed in symmetric molecules.

A better approximation of the rotational partition function is obtained by an asymptotic expansion of the integral, leading to

$$Z_{rot} = \beta^{-1} \left[1 + \frac{\beta}{3} + \frac{\beta^2}{15} + \frac{4\beta^3}{315} + \dots \right] \quad (1.156)$$

which results from a direct application of the Euler–Maclaurin summation formula. The symmetry number σ for polyatomic molecules is the number of orientations of the molecule resulting from “rotation in itself” and is thus dependent on the point group for the molecular structure. I_A , I_B , and I_C are the moments of inertia along the principal axis and the general definition is

$$\begin{aligned} I_x &= \sum_i m_i (y_i^2 + z_i^2) & I_{xy} &= \sum_i m_i x_i y_i \\ I_y &= \sum_i m_i (x_i^2 + z_i^2) & I_{xz} &= \sum_i m_i x_i z_i \\ I_z &= \sum_i m_i (x_i^2 + y_i^2) & I_{yz} &= \sum_i m_i y_i z_i \end{aligned} \quad (1.157)$$

where m_i is the mass of the i th atom with coordinates x_i , y_i , and z_i . The product of the moments of inertia $I_A I_B I_C$ is then obtained by the determinant:

$$D = \begin{vmatrix} -I_x & -I_{xy} & -I_{xz} \\ -I_{xy} & -I_y & -I_{yz} \\ -I_{xz} & -I_{yz} & -I_z \end{vmatrix} \quad (1.158)$$

In the case of molecules with a high degree of symmetry, this formula can be reduced to more simple equations, as listed in [Table 1.2](#).

Table 1.2 The moment of inertia of some molecular structures. R denotes the interatomic distance.

	Formula	I
Linear triatomic spherical top	$A-B-C$	$m_A m_c (R_{AB} + R_{BC})^2$
Tetrahedron	AB_4	$(8/3)m_B R^2$
Octahedron	AB_6	$4m_B R^2$

Substituting this equation into the general equations derived in [Section 1.5.1.5](#) for S and H yields

$$S_{rot}(T) = \frac{3}{2}R + R \left(\frac{1}{2} \ln(I_A I_B I_C) + \frac{3}{2} \ln T + \frac{\pi^{1/2}}{\sigma} \frac{(8\pi^2 k_B)^{3/2}}{h^3} \right) \quad (1.159)$$

and

$$\{H^\circ(T) - H^\circ(0K)\}_{rot} = \frac{3}{2}RT \quad (1.160)$$

For nonrigid molecules, correction terms for centrifugal stretching should be included in the rotational energy. In its extended form the energy levels can include the quartic, sextic, and octic distortion constants D , H , and L :

$$\epsilon_{rot} = J(J+1)B - J^2(J+1)^2D + J^3(J+1)^3H - J^4(J+1)^4 \quad (1.161)$$

For linear molecules, inclusion of these terms leads to the following correction term to partition function of the rigid rotor [\[45\]](#):

$$f_c = 1 + 2d(3-b)/3b + 6(2d^2-h)/b^2 + 24(5d^3-5dh+1)/b^3 \quad (1.162)$$

where $d = D/B$, $h = H/B$, and $l = L/B$.

1.5.3.2 Coupling of internal motion

Up to now, the fact that some coupling occurs between the three forms of internal motion was neglected. For example, during the course of one rotation, a molecule vibrates about 1000 times, and thus the bond length will change continuously. Consequently, the moments of inertia and the rotational constant B will not be equal to the values derived from the equilibrium bond length: the bond length will increase with vibrational energy, and thus the rotational constant B in the upper vibrational states will be smaller than that in the lower vibrational states. This dependence can be formulated as follows:

$$B_v = B_e - \alpha \left(v + \frac{1}{2} \right) \quad (1.163)$$

where B_v is the rotational constant in level v , B_e is the equilibrium value, and α the rotation–vibration interaction constant. A similar dependence can be formulated for the centrifugal distortion constant:

$$D_v = D_e - \beta \left(v + \frac{1}{2} \right) \quad (1.164)$$

Mayer and Mayer [46] have derived an additive correction term $\ln Z_c$ to $\ln Z_{int}$ by a long but moderately straightforward perturbation procedure:

$$\ln Z_c = u^{-1} \left\{ 8 \frac{B_e}{\omega_e} + \frac{\alpha_e}{B_e} \frac{u}{e^u - 1} + 2x_e \frac{u^2}{e^u - 1} \right\} \quad (1.165)$$

This correction term accounts for the difference between the approximations for the two unseparated (uncoupled) rotation and vibration partition functions and the true coupled rotation–vibration partition function:

$$\ln Z_c = \ln Z_{rovib} - \ln Z_{rot} - \ln Z_{vib} \quad (1.166)$$

Coupling will also occur between the electronic energy, rotation, and vibration: the rotation and vibration parameters in the excited states will not always be the same as in the ground state. In such a case the partition function should be written as

$$Z_{int} = Z_{int(1)} + Z_{int(2)} + Z_{int(3)} + \dots = \sum Z_{int(i)} \quad (1.167)$$

where the individual terms $Z_{int(i)}$ are obtained in the usual manner.

1.5.3.3 Hindered rotation

In some molecules, especially larger organometallic ones, the internal rotation of groups may be hindered, leading to a change in the internal energy. Pitzer and Gwinn [47] have developed methods to correct the standard calculation for this effect. They assumed that the rotation is described by a potential V of the form:

$$V = \frac{1}{2} V_0 (1 - \cos n\phi) \quad (1.168)$$

where V_0 is the internal rotation barrier, n the number of maxima (or minima) on the potential curve, and ϕ is the angle of rotation of the top relative to the axis of rotation. By solving this equation and evaluating the rotational partition function, Pitzer and Gwinn derived correction terms that give the difference between free and hindered rotation as it applies to entropy:

$$S_{h,rot}(T) = S_{f,rot}(T) - \{S_{f,rot}(T) - S_{h,rot}(T)\} + \ln\left(\frac{n}{\sigma_m}\right) \quad (1.169)$$

and enthalpy:

$$\begin{aligned} \{H^\circ(T) - H^\circ(0K)\}_{h,rot} &= \{H^\circ(T) - H^\circ(0K)\}_{f,rot} \\ &- [\{H^\circ(T) - H^\circ(0K)\}_{f,rot} - \{H^\circ(T) - H^\circ(0K)\}_{h,rot}] \end{aligned} \quad (1.170)$$

Pitzer and Gwinn [47] compiled these differences as functions of the arguments V_0/RT and $1/Q_{f,rot}$, the latter being the statistical sum over the states of free internal rotation:

$$Z_{f,rot} = \frac{2\pi(2\pi I_{red} k_B T)^{1/2}}{nh} \quad (1.171)$$

where I_{red} is the reduced moment of inertia of the top. The last term in this equation accounts for the case when the number of maxima on the potential curve does not coincide with the symmetry number σ_m of the top. Pitzer and Gwinn give the general formulas to calculate I_{red} for the asymmetric top. In the case of a symmetric potential function, which generally implies a symmetric top molecule, these formulas reduce to

$$I_{red} = A \left(1 - \sum_{i=1}^3 A \lambda_i^2 / I_i \right) \quad (1.172)$$

which is exact for a single top and is a satisfactory approximation for molecules with several tops. In this equation, A is the moment of inertia of the top itself, λ_i is the direction cosine between the axis of the top and the i th principle axis of the whole molecule, and I_i is the moment of inertia of the whole molecule about this axis. In the case of several tops, this method is applied to each top separately, and the components of the thermodynamic functions are summed over the tops. The number of vibrations taken into account for the calculation of Z_{vib} in the harmonic oscillator approach is reduced by the number of internal rotations per molecule.

1.5.3.4 Limitations of the rigid rotor/harmonic oscillator model

In the harmonic oscillator approach, it is assumed that the number of vibrational levels could be infinite, and hence ϵ_{vib} can become very large. In practice, this is not true as the energy of the vibrational states cannot exceed the dissociation energy or bond energy. This becomes very important at high temperatures at which the number of populated rotational states is large, and a direct summation method therefore gives a much better description of the thermal function at high temperatures.

As mentioned earlier, the total internal energy of a molecule is

$$\epsilon_{int} = \epsilon_{elec} + \epsilon_{vib} + \epsilon_{rot} \quad (1.173)$$

or

$$E_{int} = T_e(i) + G(i, v) + F(i, v, j) \quad (1.174)$$

For a diatomic molecule, Z_{int} has the form:

$$Z_{int} = \sum_{i=x}^{i_{max}} \sum_{v=0}^{v_{max}} \sum_{J_{min}}^{J_{max}} g(i, J) e^{-c_2/T[T_e(i) + G(i, v) + F(i, v, j) - G(X, 0) - F(X, 0, J_{min})]} \quad (1.175)$$

where $G(X, 0)$ is the zero-point vibrational energy of the ground state, and $F(x, 0, J_{min})$ is the rotational energy of the ground state for $v = 0$. X refers to the electronic ground state of the molecule.

In order to employ these equations, it is important to know the maximum values of v . This is normally obtained from the dissociation energy D_0 (see Fig. 1.4):

$$G_0(v_{max}) = D_0 \quad (1.176)$$

and

$$\frac{dG_0(v_{max})}{dv} = 0 \quad (1.177)$$

It is outside the scope of this book to explain this procedure in detail and the interested reader is referred to Gurvich et al. [48] for an extensive treatise on this subject.

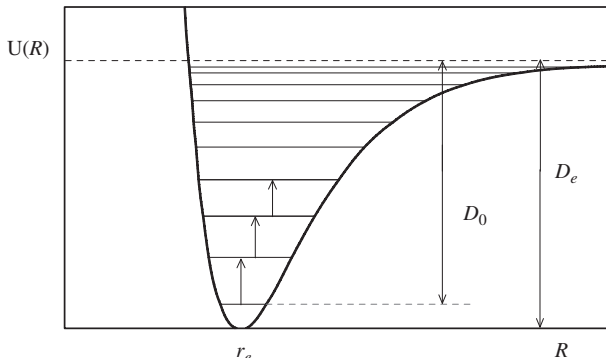


Figure 1.4 The vibrational energy spacing in an anharmonic oscillator.

1.5.3.5 Case studies

Examples are given hereafter, treating the cases of a monoatomic gas (Box 1.7), of a diatomic gas (Box 1.8), and of a poly-atomic gas (Box 1.9).

Box 1.7 Case study of a monatomic gas.

The internal energy of a monatomic gas is restricted to the electronic component, and as a result the thermal functions can be derived using Eqs. (1.140) and (1.141) plus the translational contribution using Eqs. (1.144) and (1.145). The electronic energy levels of most elements have been obtained from atomic spectroscopy, and numerical values can be found in compilations of the National Bureau of Standards (now National Institute of Standards and Technology). Table 1.3 shows the calculation of the thermal functions of Xe(g) and Cs(g) in the 298.15 K–3000 K range as examples. Xe is a noble gas with a nondegenerate ground state (1S_0) and has no low-lying electronic levels that contribute to the thermal functions in this temperature range. The electronic entropy is thus zero, and the total entropy is identical to S_{trans} . Cs(g), the next element in the periodic system, has a doubly degenerate ground state (${}^2S_{1/2}$) and also possesses low-lying levels that should be taken into account for temperatures above 1000 K.

Table 1.3 The entropy of Xe(g) and Cs(g).

T (K)	Xe(g)			Cs(g)		
	S_{trans}	S_{elec}	S_{tot}	S_{trans}	S_{elec}	S_{tot}
298.15	169.577	0.000	169.577	169.729	5.763	175.492
500	180.323	0.000	180.323	180.476	5.763	186.239
1000	194.731	0.000	194.731	194.884	5.763	200.647
2000	209.139	0.000	209.139	209.292	5.835	215.127
3000	217.567	0.000	217.567	217.720	6.764	224.484

1.6 Thermodynamics of nuclear fuel and fission products

After having presented the fundamentals of classical and statistical chemical thermodynamics, the basics of phase diagrams and Ellingham diagrams are explained hereafter, which are key tools used to predict chemical behavior. Moreover, some of the key parameters to consider when assessing the chemistry of nuclear fuel and fission products, namely, the melting temperature, the fuel oxygen-to-metal ratio, the evolution of the oxygen chemical potential, and the sublimation/vaporization behavior are described.

1.6.1 Phase diagrams

Phase diagrams are very useful representations of phases in chemical equilibrium under a given set of conditions of temperature, pressure, composition, chemical potential, etc.

Box 1.8 Case study of a diatomic gas.

Diatomeric molecules are characterized by one bond resulting in one value for the moment of inertia (they are linear) and a single vibrational frequency. The values for these quantities are usually derived from spectroscopic measurements, which normally yield the fundamental frequency ν , the anharmonicity constants x_e , y_e , etc., the rotational and centrifugal constants B , and the rotation–vibration interaction constant α . These constants can be used to calculate the thermal functions with [Eqs. \(1.159\) and \(1.160\)](#) for the rotational component and [Eqs. \(1.149\) and \(1.150\)](#) for the vibrational component, in combination with the equations for translation and electronic contribution.

However, spectroscopy is a very powerful tool and generally gives extensive information about the coupling of internal motion. As shown in [Table 1.4](#) for TeO(g), the parameters are different in the various electronic states of the molecules, and the use of [Eq. \(1.167\)](#) is necessary.

Table 1.4 The spectroscopic parameters for TeO(g) in units of cm^{-1} .

State	$T_{e(i)}$	g_i	ω_e	$x_e \omega_e$	B_e	D_e	α_e
X0 ⁺	0.0	1	797.11	4.00	0.3554	$2.7 \cdot 10^{-7}$	0.00237
X1	697.0	2	798.06	4.00	0.3564	$3.0 \cdot 10^{-7}$	0.00236

This chapter does not go into the detail of the construction of phase diagrams. The reader is referred to comprehensive references on this matter [\[22,24\]](#) and [Chapter 3](#), Computational Thermochemistry of Nuclear Fuel. But some of the key knowledge necessary to understand and interpret correctly phase diagrams are stressed.

1.6.1.1 Gibbs phase rule

Before introducing further these diagrams, the Gibbs phase rule needs to be mentioned, which determines the number of phases that can be in equilibrium in a stability field in relation to the number of state variables (temperature, pressure, and composition) that can be varied independently without modifying the stable phases, the so-called degree of freedom f or variance. According to Gibbs phase rule:

$$f = c + 2 - \phi \quad (1.178)$$

where c is the number of components, and ϕ the number of stable phases. The number 2 refers to the state variables temperature T and pressure p . In some cases, one also needs to take into account a constraint on electroneutrality, which is discussed in [Chapter 3](#). Commonly, phase diagrams are calculated for a pressure fixed to 1 bar, in which case the Gibbs phase rule reduces to

$$f = c + 1 - \phi. \quad (1.179)$$

Box 1.9 Case study of a polyatomic gas.

Generally, the information derived from spectroscopic measurements of polyatomic molecules is not so detailed as for diatomic molecules, except for simple ones such as H_2O , CO_2 , or NH_3 . This is due to the fact that the coupling of the internal energy results in extremely complex spectra, especially when elevated temperatures are required to bring the molecules in the gas phase. In practice, information from spectroscopy of most polyatomic molecules is restricted to the vibrational frequencies and sometimes the electronic states and no information about the rotational constants can be deduced. Therefore the rotational partition function is normally calculated from Eq. (1.105) in which the product of the moments of inertia is the main variable.

Considering the example of UF_6 :

- Uranium has a 6+ valence state in this molecule with a $5f^0$ electronic configuration and its spectroscopic ground state is 1S_0 , with multiplicity $J=0$. This means that in Eq. (1.142), $\epsilon_0 = 0$ and $g_0 = (2J+1) = 1$ and thus reduces to Eq. (1.143). The first excited electronic state is too high to contribute to the thermodynamic functions and excited states beyond the ground state can thus be excluded.
- UF_6 has a perfect octahedral O_h symmetry, and the symmetry number σ is thus 24. Its moment of inertia can be calculated from the U–F distance, 199.962 ± 0.07 pm, obtained from the analysis of the rotational spectrum of the v_3 stretching frequency [45], yielding $1.2712 \times 10^{-112} \text{ g}^3 \text{ cm}^6$.
- The UF_6 has $(3N - 6) = 15$ vibrational modes, which according to the symmetry rules for a perfect octahedral configuration $\Gamma = A_1 + E + 2F_1 + 2F_2$ reduce to six fundamentals. The A_1 is nondegenerate, the E mode is double degenerate, whereas the four F modes are triple degenerate. The values for the vibrational modes have been obtained in vibrational spectroscopy measurements: the two F_1 are infrared active (asymmetric), the A_1 and E modes as well as one of the F_2 modes can be observed by Raman spectroscopy, and the remaining F_2 mode is inactive in both infrared and Raman.

For a binary phase diagram plotted at 1 bar, where composition is displayed on the abscissa and temperature on the ordinate, the number of components c equals two, and the Gibbs phase rule is then $f = 3 - \phi$. In a single-phase region, the number of degree of freedom equals 2, meaning that the two state variables temperature and composition may be varied independently. In a two-phase region, $f = 1$, hence only one state variable can be defined, the other one being fixed a fortiori. The corresponding equilibrium is said to be univariant. Finally, three phases can only coexist in a binary isobaric system under the condition $f = 0$, that is, with a unique combination of temperature and composition, which corresponds to an invariant equilibrium. For a ternary system at constant pressure, $f = 4 - \phi$, the maximum number of stable phases in equilibrium is 4 but becomes three when computing an isothermal section (i.e., at fixed temperature).

1.6.1.2 Terminology and lever rule

Specific terminology exists to define the chemical equilibria represented in phase diagrams, as listed in Table 1.5 and illustrated in Fig. 1.5. In particular, the solidus line defines the temperature below which the phases in the diagram are solid, while the liquidus line defines the temperature above which the phases are completely liquid. The Zr–Sn phase diagram depicted in Fig. 1.5 is a very relevant system in the context of light water reactors (LWRs), as one of the chosen cladding material used to contain the fuel pellets is made of Zircaloy. Zircaloy is an alloy, major constituents of which are zirconium and tin, which shows good corrosion resistance, low neutron capture cross section, good mechanical and radiation stability, low permeability for fission gases and helium, relatively low hydrogen pickup, and high melting temperature. In the alloys used in LWRs, the Sn content remains below $\sim 1.2\text{--}1.7$ wt.%, which corresponds to the single-phase regions of the α -Zr and

Table 1.5 Invariant equilibria and associated reactions upon cooling in binary phase diagrams.

Equilibrium type	Reaction	Example in the Zr–Sn system
Eutectic	Liquid \rightarrow solid1 + solid2	Liq. \rightarrow β -Zr + η
Eutectoid	solid1 \rightarrow solid2 + solid3	
Peritectic	Liquid + solid2 \rightarrow solid1	η + Liq. \rightarrow Sn_2Zr
Peritectoid	solid2 + solid3 \rightarrow solid1	β -Zr + A15 \rightarrow α -Zr
Monotectic	Liquid1 \rightarrow Liquid2 + solid	
Monotectoid	solid1 \rightarrow solid2 + solid3	$\eta \rightarrow \eta_1 + \eta_2$

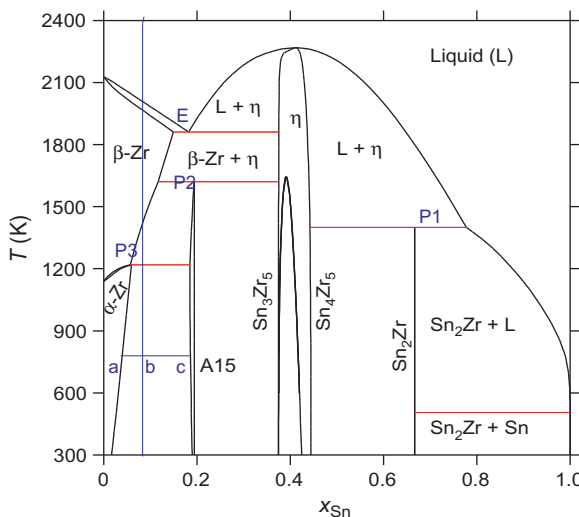


Figure 1.5 Zr–Sn phase diagram calculated at 1 bar pressure using the model by Lafaye et al. [49]. E, Eutectic, P1, peritectic, P2, peritectoid.

β -Zr solid solutions. The lines delimiting the stability region of those solid solutions are called solubility curves. In addition, three intermetallic compounds form in this binary system at specific compositions [i.e., Sn_2Zr , the A15 phase (SnZr_4)], and the η phase between Sn_3Zr_5 and Sn_4Zr_5 compositions. Such intermediate phases can be stoichiometric (as for Sn_2Zr), in which case they correspond exactly to the stoichiometric sum of the end-members, or they can show a homogeneity range meaning that they are stable within a certain temperature–composition region. This is the case for the A15 phase, for example. The situation for the η phase is rather complex. A homogeneity range is found between Sn_3Zr_5 and Sn_4Zr_5 compositions at high temperatures, while a miscibility gap is formed at low temperatures.

Several types of invariant equilibria are found in the Zr–Sn system. A eutectic equilibrium, which corresponds to a liquid phase transforming to two solid phases upon cooling, is found at $x(\text{Sn}) = 0.19$. Moreover, a peritectic transformation, where a liquid and solid phase react together to form a single solid phase, appears at $x(\text{Sn}) = 0.667$.

Two peritectoids, corresponding to the reaction of two solid phases to yield upon cooling a new third solid phase, are present at $x(\text{Sn}) = 0.06$ and $x(\text{Sn}) = 0.2$. Finally a monotectoid equilibrium is found, where a solid phase (η) transforms to two different solid phases upon cooling. Other types of possible three-phase equilibria in a binary phase diagram are eutectoid reactions, where in analogy with the eutectic equilibrium, one solid phase transforms upon cooling into two new solid phases; and monotectic reactions in the presence of a miscibility gap, where a liquid phase transforms to a second liquid phase and a solid upon cooling.

In a two-phase region, the relative amounts of the two phases in equilibrium at a given temperature on a tie-line can be determined using the lever rule. The tie-line or conode is the terminology used to designate the isothermal line connecting the compositions of the two phases in a two-phase field. Taking the example of the $\{\alpha\text{-Zr} + \text{A15}\}$ biphasic region, the tie-line corresponds to ac , and the fraction of A15 at the point b in Fig. 1.5 of composition $x(\text{Sn}) = x_e$ and temperature T_e is given by the ratio:

$$\frac{ab}{ac} = \frac{x_{\text{Sn}} - x_{\text{Sn}}^{\alpha\text{-Zr}}}{x_{\text{Sn}}^{\text{A15}} - x_{\text{Sn}}^{\alpha\text{-Zr}}} = x_{\text{A15}} \quad (1.180)$$

where x_{A15} is the relative fraction of A15 in the binary phase field, x_{Sn} is the overall composition, $x_{\text{Sn}}^{\alpha\text{-Zr}}$ the mole fraction of Sn in the $\alpha\text{-Zr}$ phase, and $x_{\text{Sn}}^{\text{A15}}$ the mole fraction of Sn in the A15 phase. This methodology works well for binary systems, and can also be applied to ternary phase diagrams.

Two common representations are used for ternary phase diagrams: the isothermal projection at a fixed temperature and polythermal liquidus projection as illustrated in Figs. 1.6 and 1.7, respectively. This is because plotting temperature versus composition in a ternary system requires a three-dimensional representation where temperature is on the vertical axis if composition would form the base.

Here we take the example of the $\text{LiF}-\text{ThF}_4-\text{UF}_4$ system, which can serve as molten salt fuel in certain types of molten salt reactor (MSR) designs (see Chapter 6:

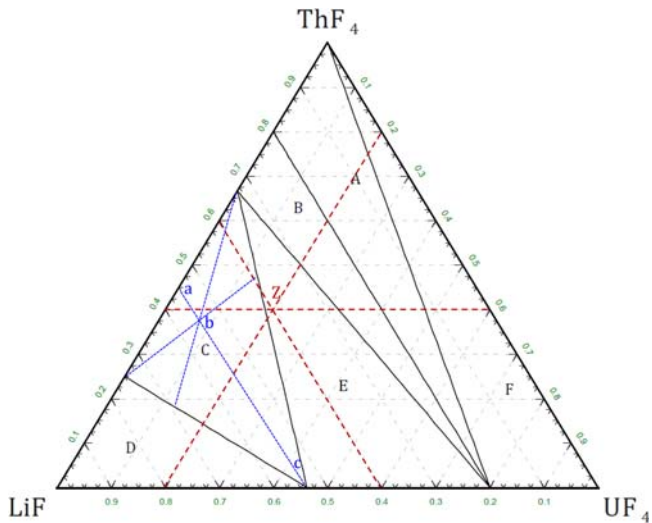


Figure 1.6 Isothermal projection of the LiF–ThF₄–UF₄ system at $T = 300\text{ K}$ as assessed by Ref. [50]. Ternary phase fields: (A) ThF₄ + LiTh₄F₁₇; (B) LiTh₂F₉ + LiTh₄F₁₇ + LiU₄F₁₇; (C) Li₃ThF₇ + LiTh₂F₉ + Li₇U₆F₃₁; (D) LiF + Li₃ThF₇ + Li₇U₆F₃₁; (E) LiTh₂F₉ + LiU₄F₁₇ + Li₇U₆F₃₁; (F) ThF₄ + UF₄ + LiU₄F₁₇.

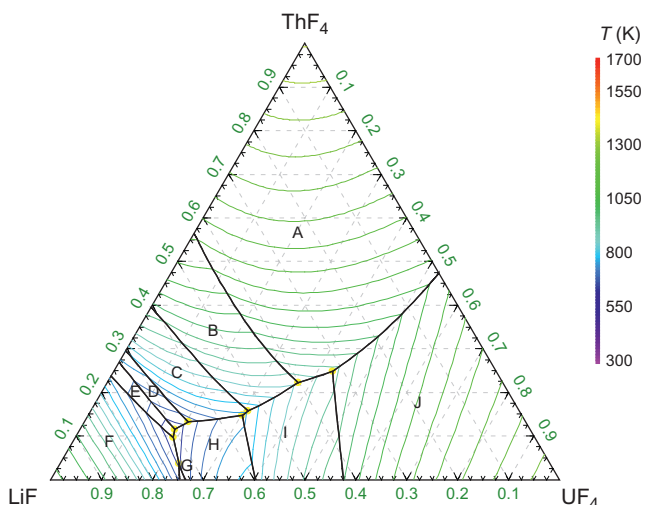


Figure 1.7 Liquidus projection of the LiF–ThF₄–UF₄ system as assessed by Ref. [50]. Primary crystallization phase fields: (A) ThF₄; (B) LiTh₄F₁₇; (C) LiTh₂F₉; (D) LiThF₅; (E) Li₃ThF₇; (F) LiF; (G) Li₄UF₈; (H) Li₇U₄F₃₁; (I) LiU₄F₁₇; and (J) UF₄.

Molten salt reactor fuels). In this case, the three components are not chemical elements, but the LiF, ThF₄, and UF₄ fluorides. The isothermal section at $T = 300$ K is shown in Fig. 1.6. The three corners correspond to the pure end-members, and the three edges to the LiF–ThF₄, LiF–UF₄, and ThF₄–UF₄ binary systems, while the three phases in equilibrium in each phase field are detailed in the caption. The overall composition of any ternary mixture in the phase diagram can be read easily as illustrated with point Z in Fig. 1.6. A line parallel to an edge (LiF–ThF₄ for instance) of the ternary phase diagram corresponds to a constant mole fraction of the third component (UF₄). Hence, point Z is obtained when mixing the end-members such that $x_{\text{LiF}} = 0.4$, $x_{\text{ThF}_4} = 0.4$, and $x_{\text{UF}_4} = 0.2$. Note that the thermodynamic equilibrium state at this composition is a mixture of {LiTh₂F₉ + LiU₄F₁₇ + Li₇U₆F₃₁}. To calculate the relative proportions of the three phases in equilibrium in a ternary phase field, the lever rule is applied as in a binary system. At point b in Fig. 1.6, the relative proportion of Li₇U₆F₃₁ compared to Li₃ThF₇ and LiTh₂F₉ is given by the ratio

$$\frac{ab}{ac} = \frac{n_{\text{Li}_7\text{U}_6\text{F}_{31}}}{n_{\text{tot}}} = x_{\text{Li}_7\text{U}_6\text{F}_{31}} \quad (1.181)$$

where $x_{\text{Li}_7\text{U}_6\text{F}_{31}}$ is the relative fraction of Li₇U₆F₃₁ in the ternary phase field, $n_{\text{Li}_7\text{U}_6\text{F}_{31}}$ the number of moles of Li₇U₆F₃₁, and n_{tot} the total number of moles.

The second type of representation, the polythermal liquidus projection is also very useful to visualize in a two-dimensional representation the liquidus surface of a ternary system. The thick lines in Fig. 1.7 represent the univariant lines at the intersection of two liquidus surfaces. Arrows are sometimes used to show the direction of decreasing temperature along those univariant lines. They intersect at invariant equilibria points, for instance, a ternary eutectic. The colored lines are the isotherms of the liquidus surface. The caption details finally the composition of the different primary crystallization fields, that is, of the first solid that would precipitate upon cooling below the liquidus temperature.

1.6.2 Melting transition

One key piece of information for the safety assessment of a nuclear reactor facility is the melting temperature of the materials inside the reactor core, in particular the fuel and cladding materials. Together with the thermal conductivity, this parameter defines the margin to melting (i.e., the difference between the operating temperature and the melting temperature of the reactor core materials). A melting event is a *first-order transition*, hence with a discontinuous change in enthalpy, entropy, and volume.

The melting (or fusion) enthalpy that accompanies the melting transition corresponds to the difference between the enthalpy of formation of the liquid and the solid at the transition temperature. Taking the example of thorium dioxide, which remains quasi-stoichiometric up to the melting temperature [51], the melting transition

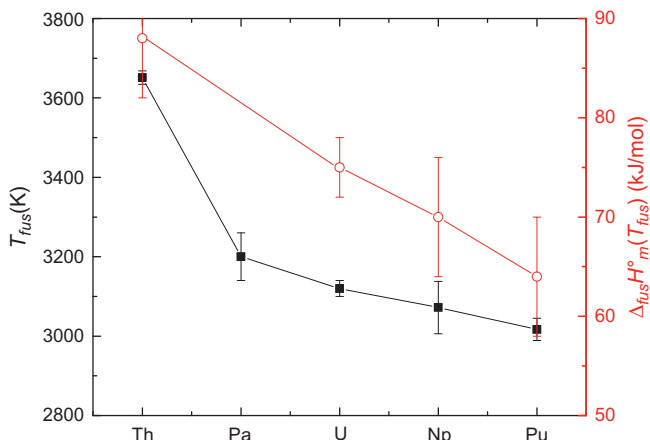


Figure 1.8 Evolution of the melting temperature and enthalpy of fusion along the series of the actinide oxides.



has an associated fusion enthalpy given by

$$\Delta_{fus}H_m^\circ(T_{fus}) = \Delta_fH_m^\circ(\text{ThO}_2, l, T_{fus}) - \Delta_fH_m^\circ(\text{ThO}_2, \text{cr}, T_{fus}) \quad (1.183)$$

It is interesting to point out that a decrease in both the melting temperatures and fusion enthalpies occurs along the series of the actinoid dioxides from ThO_2 to PuO_2 [52] (Fig. 1.8), which are all isostructural phases with a cubic fluorite structure. This trend expresses a decrease in stability along the series, especially since the fusion enthalpy is a good measure of the cohesion energy in the crystalline lattice. This result can be related to the particular $[\text{Rn}]5\text{f}^n$ electronic configuration of the actinoids, and to the influence of the 5f electrons on bonding. The 5f electrons become more localized toward plutonium and americium, meaning they are not available for covalent bonding, leading to less cohesion in the crystal lattice. As a consequence, the energy required for fusion is also reduced.

1.6.3 Effect of nonstoichiometry on thermodynamic properties

Certain classes of nuclear materials, uranium dioxide for instance used as nuclear fuel in current LWRs, are stable over a certain composition–temperature homogeneity range. This has a direct effect on their thermodynamic properties, in particular melting temperature and chemical oxygen potential, which are discussed here.

Uranium dioxide exhibits both hyperstoichiometric (i.e., UO_{2+x}) and hypostoichiometric (i.e., UO_{2-x}) compositions, as seen from the U–O phase diagram (Fig. 1.9A). The compound shows a wide homogeneity range, with compositions between $\text{UO}_{1.66}$ at ~ 2710 K and $\text{UO}_{2.25}$ at ~ 2006 K. The hypostoichiometric

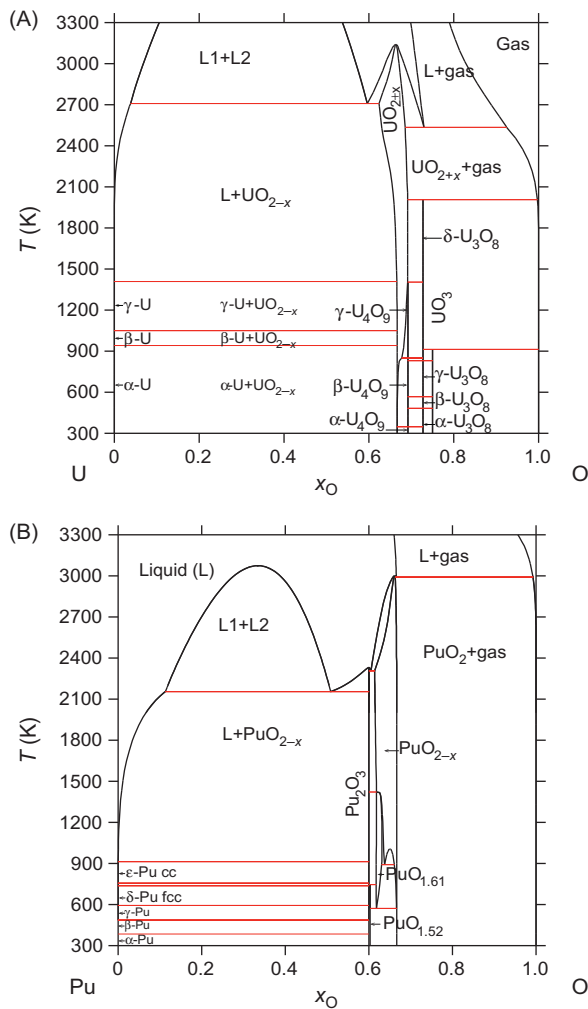


Figure 1.9 (A) U–O and (B) Pu–O phase diagrams calculated using the thermodynamic model by Guéneau et al. [53].

domain starts above about 1200 K, and the hyperstoichiometric domain above about 600 K. Its properties, in particular the melting temperature, are strongly dependent of the oxygen-to-uranium O/U ratio. The melting point has been measured experimentally at (3130 ± 20) K [52], although the exact congruent composition is still controversial. The calculated stoichiometry for the congruent melting point in the thermodynamic model of Guéneau et al. (based on the CALPHAD methodology [6], see Chapter 3) is $\text{UO}_{1.97}$. The melting temperature decreases on both sides on the congruently melting composition, which is an important feature for the assessment of the margin to melting for the nuclear fuel in the reactor core.

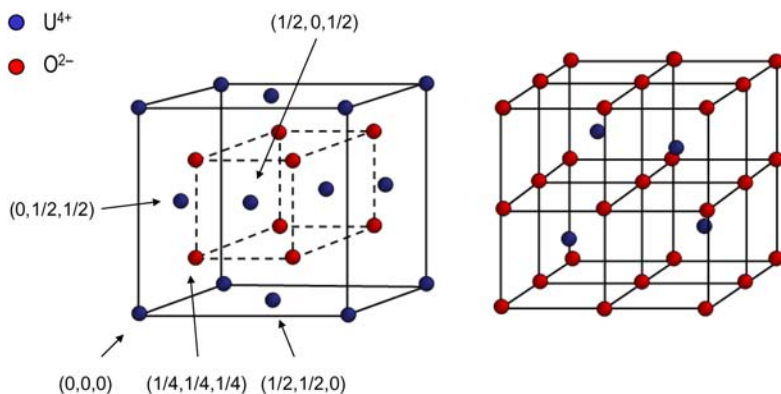


Figure 1.10 Fluorite structure of uranium dioxide; left the uranium sublattice and right the oxygen sublattice. Oxygen ions are represented in red, and uranium ions in blue.

The ability to accommodate departure from stoichiometry can be understood when looking at the crystal structure of uranium dioxide, that is face-centered cubic (fcc), isostructural with fluorite CaF_2 , in space group $Fm\bar{3}m$ (Fig. 1.10). The uranium cations occupy the octahedral positions $(0,0,0)$, $(1/2,1/2,0)$, $(1/2,0,1/2)$, and $(0,1/2,1/2)$, while the oxygen anions occupy the tetrahedral positions, that is, $(1/4,1/4,1/4)$ and equivalent positions. This structure is particularly well-adapted to accommodate interstitial atoms, such as fission products, and deviations from stoichiometry. Considering the oxygen sublattice, one sees that interstitial ions can be incorporated at the octahedral vacant sites since only half of the eight cubes of oxygen per unit cell are occupied by an U^{4+} ion.

In the hyperstoichiometric region, the excess oxygen is accommodated in the interstitial hole positions, which is compensated by a partial oxidation of the uranium from U^{4+} to U^{5+} to maintain electroneutrality. In the hypostoichiometric region, oxygen vacancies are formed in the lattice, which is then compensated by a partial reduction of the uranium from U^{4+} to U^{3+} .

Next, the oxygen chemical potential $\Delta\mu(\text{O}_2)$, defined as

$$\Delta\mu(\text{O}_2) = \mu(\text{O}_2) - \mu^\circ(\text{O}_2) = RT \ln\left(\frac{p(\text{O}_2)}{p^\circ}\right) \quad (1.184)$$

where $p(\text{O}_2)$ is the partial pressure of oxygen, and p° the standard pressure equal to 1 bar, is also directly related to the extent of the nonstoichiometric stability domain. It reflects the equilibrium between oxygen in the crystal lattice and the gas phase:



and shows a very distinct evolution with respect to the O/U ratio (Fig. 1.11), which is related to the evolution of the defect concentration in the crystal.

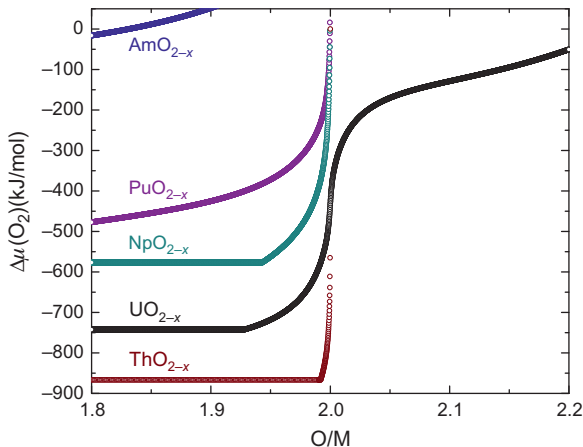


Figure 1.11 Evolution of the oxygen potentials of the actinide dioxides as a function of oxygen-to-metal ratio calculated at $T = 2000$ K using the thermodynamic models by Refs. [51,53–55].

In the hypostoichiometric region the oxygen potential is relatively low (around -800 kJ/mol), meaning that the oxygen is strongly bonded in the lattice. The equilibrium reaction involved is



This can be understood from the fact that it is difficult to extract oxygen ions from the lattice sites, and form oxygen vacancies.

By contrast, the oxygen potential is much higher in the hyperstoichiometric region (around -300 to -100 kJ/mol) as the bonding of the excess oxygen ions in the interstitial sites is much weaker. The corresponding equilibrium reaction is



Finally, a very rapid change of the oxygen potential is observed between the two regions, implying that even small deviations from the stoichiometric composition lead to significant differences in the oxygen potential and thermochemical properties.

The oxygen potentials of the other actinoid oxides (ThO_{2-x} , NpO_{2-x} , PuO_{2-x} , and AmO_{2-x}) are only described below $\text{O}/\text{M} = 2.0$ in Fig. 1.11 since these compounds cannot compensate for excess oxygen and become hyperstoichiometric. Plutonium dioxide PuO_{2-x} for instance, which is a key phase for nuclear fuel in LWRs and next-generation sodium-cooled fast reactors and lead-cooled fast reactors, shows the same fcc structure as uranium dioxide. In contrast to uranium dioxide, however, it shows a hypostoichiometric homogeneity range from 61.3 to

66.67 at.% O ($\sim 1.6 < \text{O/Pu} < 2.0$) in the temperature range $\sim 1400 \text{ K} - 2380 \text{ K}$, but no hyperstoichiometric region (Fig. 1.9B).

In the hypostoichiometric region, the oxygen potential increases along the actinoid series from thorium to americium, which is directly related to the ease of reduction of the oxide compounds. The americium oxide has the most extended region of its hypostoichiometric domain, reaching the $\text{AmO}_{1.58}$ composition at $\sim 2210 \text{ K}$ [55]. Conversely, thorium oxide is the most stable compound in the series with a very small deviation from stoichiometry. For all of them, the oxygen potential increases with temperature since the formation of oxygen vacancies is favored by higher temperatures.

1.6.4 Sublimation and vaporization behavior

The vapor pressure is the equilibrium pressure of the gaseous species over a condensed phase, a solid (sublimation) or liquid (vaporization). In the simplest case, the vapor consists of a single species and the reaction is described by

$$A(s, l) = A(g) \quad (1.188)$$

A number of techniques exist for vapor pressure measurements, including mass spectrometry, transpiration, and torsion methods. Mass spectrometry, in particular, is a very powerful technique for the determination of the thermodynamic properties of condensed and gaseous phases at high temperatures. Ionov [56], Honig [57], and Chupka and Inghram [58,59] were pioneers in this field with their studies on the vaporization behavior of alkali metal halides and carbon at high temperatures [60]. This technique is based on the conversion of mass spectral ion intensity to the corresponding partial pressures of the species detected in the gaseous phase [61]. It is used to identify the composition of the gas and to monitor the evolution of the partial pressures as a function of temperature [62]. The experimental conditions of the measurements are adjusted to ensure thermodynamic equilibrium between the condensed and gaseous phases. The method can hence be used to derive a number of thermodynamic properties, such as reaction enthalpies, sublimation, vaporization, and formation enthalpies, but also ionization and dissociation energies of vapor species. The Knudsen effusion method, which was developed by Knudsen in the 1900s [63], is the most popular variant of the high-temperature mass spectrometry techniques. It is characterized by a molecular flow regime, and the fact that the molecular beam analyzed has the same composition as the gaseous phase under investigation in the Knudsen cell [61]. The two parameters monitored during the Knudsen effusion mass spectrometry measurements are the temperature and the intensities of ion currents originating from ionization and fragmentation of the species in the gas. For more detail on this technique, the reader is referred to the comprehensive reviews by Refs. [60,61].

The equilibrium in Eq. (1.188) corresponds to the particular case of the azeotropic or congruent vaporization of a pure single species. The notions of azeotropic and congruent vaporization are explained in more detail in Box 1.10. The equilibrium constant of reaction (1.188) is equal to

Box 1.10 Azeotropic and congruent vaporization.

Azeotropic vaporization refers for a closed system to the state where gas and condensed phases reach, by loss of matter (effusion), the same composition [65]. Let us consider the effusion of a binary phase at fixed temperature, for example, uranium dioxide. The variance f of the system is equal to 1:

$$f = c + 1 - \phi = 2 + 1 - 2 = 1 \quad (1.\text{xiii})$$

where c is the number of components and ϕ the number of phases (in this case solid and gas).

To reach equilibrium conditions between the gas and the solid phases, the system needs an additional constraint. This can be, for example, an externally imposed gas pressure. In the absence of such a constraint, the system tends toward its azeotropic or congruent composition, which reduces its variance to zero [65]. For a binary oxide species such as UO_2 , this leads to reduction of the solid phase to $\text{UO}_{2-x}(\text{cr})$.

The vapor phase above condensed uranium dioxide is rather complex and constituted of several species, namely, O(g) , $\text{O}_2(\text{g})$, U(g) , UO(g) , $\text{UO}_2(\text{g})$, and $\text{UO}_3(\text{g})$. The predominant species depends on the uranium dioxide stoichiometry, that is, UO(g) for an hypostoichiometric sample ($\text{O/U} < \sim 1.95$), $\text{UO}_2(\text{g})$ for a sample close to stoichiometry, and $\text{UO}_3(\text{g})$ for a hyperstoichiometric composition. Regardless of the starting composition, the uranium dioxide sample will tend to its azeotropic composition at equilibrium.

The composition of the solid UO_{2-x} and gas phases are equal at azeotropic vaporization, meaning that

$$\left[\frac{n_{\text{O}}}{n_{\text{U}}} \right]^{\text{solid}} = \left[\frac{n_{\text{O}}}{n_{\text{U}}} \right]^{\text{gas}} = 2 - x \quad (1.\text{xiv})$$

The value of x can be determined directly from the partial pressures using the following equations derived from the ideal gas law:

$$n_{\text{O}} = \frac{(p_{\text{O}} + 2p_{\text{O}_2} + p_{\text{UO}} + 2p_{\text{UO}_2} + 3p_{\text{UO}_3})V}{RT} \quad (1.\text{xv})$$

$$n_{\text{U}} = \frac{(p_{\text{U}} + p_{\text{UO}} + p_{\text{UO}_2} + p_{\text{UO}_3})V}{RT} \quad (1.\text{xvi})$$

where V is the volume of the closed system, R the universal gas constant, and T the temperature.

(Continued)

Box 1.10 (cont'd)

Knudsen effusion cell measurements under vacuum correspond to open systems, however, as opposed to closed ones, where the azeotropic definition is substituted for a congruent flow relation. In this case, the value of x is estimated using the ratio of the atomic flows F_O and F_U :

$$\left[\frac{n_O}{n_U} \right]^{\text{solid}} = \left[\frac{F_O}{F_U} \right]^{\text{gas}} = 2 - x \quad (1.\text{xvii})$$

which are defined as

$$F_O = \frac{sC}{(2\pi RT)^{1/2}} \cdot \left[\frac{p_O}{(M_O)^{1/2}} + \frac{p_{UO}}{(M_{UO})^{1/2}} + \frac{2p_{UO_2}}{(M_{UO_2})^{1/2}} + \frac{2p_{O_2}}{(M_{O_2})^{1/2}} + \frac{3p_{UO_3}}{(M_{UO_3})^{1/2}} \right] \quad (1.\text{xviii})$$

$$F_U = \frac{sC}{(2\pi RT)^{1/2}} \cdot \left[\frac{p_U}{(M_U)^{1/2}} + \frac{p_{UO}}{(M_{UO})^{1/2}} + \frac{p_{UO_2}}{(M_{UO_2})^{1/2}} + \frac{p_{UO_3}}{(M_{UO_3})^{1/2}} \right] \quad (1.\text{xix})$$

where s is the area of the effusion orifice, C the Clausing factor (a factor accounting for the shape of the effusion orifice), M_i the molar mass, p_i the partial pressure, T the temperature, and R the universal gas constant.

The measurements of Pattoret [64] have in particular shown that the congruent composition of UO_{2-x} is equal to $\text{O}/\text{U} = (1.987 \pm 0.010)$ at 2250 K and $\text{O}/\text{U} = (1.981 \pm 0.010)$ at 2450 K.

$$K_{\text{eq}} = \frac{p_A}{p^\circ \cdot a_A} \quad (1.189)$$

where p_A is the partial pressure of gaseous species A , p° the standard pressure (typically equal to 1 bar), and a_A the activity of the condensed phase, which is equal to unity.

In the more general case where several species are encountered in the gas phase, the equilibrium constant is given by

$$K_{\text{eq}} = \prod \left(\frac{p_i}{p^\circ \cdot a_i} \right)^{v_i} \quad (1.190)$$

where p_i is the partial pressure of species i , p° the standard pressure equal to 1 bar, a_i the activity of the condensed phases equal to unity, and v_i is the stoichiometric coefficients of the reaction.

By measuring the evolution of the partial pressures with temperature, one can derive the evolution of the Gibbs energy of reaction, $\Delta_r G_m^\circ(T)$, as a function of temperature:

$$\Delta_r G_m^\circ(T) = \Delta_r H_m^\circ(T) - T \Delta_r S_m^\circ(T) = -RT \ln K_{\text{eq}} \quad (1.191)$$

where $\Delta_r H_m^\circ(T)$ and $\Delta_r S_m^\circ(T)$ are the enthalpy and entropy of reaction, respectively.

The enthalpy of reaction can be determined using a second law or third law method. The second law, or Clausius–Clapeyron equation, allows the determination of the enthalpy and entropy of reaction at a median temperature, T_{ave} , in a temperature interval:

$$\frac{d(\ln K_{\text{eq}})}{d(1/T)} = -\frac{\Delta_r H_m^\circ(T)}{R} \quad (1.192)$$

This method is based on the approximation that $\Delta_r H_m^\circ(T)$ is quasi-constant over the temperature interval. The curve $\ln K_{\text{eq}} = f(1/T)$ is fitted by linear regression, and the coefficients α and β are used to estimate $\Delta_r H_m^\circ(T_{\text{ave}})$ and $\Delta_r S_m^\circ(T_{\text{ave}})$:

$$\ln K_{\text{eq}} = \alpha/T + \beta \quad (1.193)$$

$$\alpha = \frac{-\Delta_r H_m^\circ(T_{\text{ave}})}{R} \quad (1.194)$$

$$\beta = \frac{\Delta_r S_m^\circ(T_{\text{ave}})}{R} \quad (1.195)$$

The reaction entropy and enthalpy values at 298.15 K are subsequently estimated from their experimental values at T_{ave} , and enthalpy (respectively entropy) increment, $\Delta_r H_m^\circ(T_{\text{ave}}) - \Delta_r H_m^\circ(298.15 \text{ K})$, calculated with the heat capacity data of the reactants tabulated in the literature ([Box 1.11](#)).

The enthalpy of reaction at 298.15 K can also be calculated using the third law, which involves the use of the absolute entropy via the free energy function, FEF_T° :

$$FEF_T^\circ = - (G_m^\circ(T) - H_m^\circ(298.15 \text{ K})) / T = S_m^\circ(T) - (H_m^\circ(T) - H_m^\circ(298.15 \text{ K})) / T \quad (1.196)$$

The standard enthalpy of reaction at 298.15 K is then derived for each measurement temperature using the equation:

$$\Delta_r H_m^\circ(298.15 \text{ K}) = -RT \ln K_{\text{eq}} + T \Delta_r FEF_T^\circ \quad (1.197)$$

Box 1.11 Determination of the sublimation and vaporization enthalpies of Cs_2MoO_4 using the second law method.

Cesium orthomolybdate Cs_2MoO_4 , together with Cs_2UO_4 mentioned already, is one of the main components of the joint oxide gain, the multicomponent phase that forms in fast neutrons reactors in the space between fuel and cladding [8–10]. Cs_2MoO_4 shows a phase transition at $T_{tr} = (841.3 \pm 1.0)$ K and melts at $T_{fus} = (1229.5 \pm 0.2)$ K [66]. Several authors have measured the vapor pressure above solid and liquid Cs_2MoO_4 using Knudsen effusion mass spectrometry [67,68] and the transpiration technique [69]. Their results are shown in Fig. 1.12. The sublimation and vaporization are both congruent in the measured temperature ranges, corresponding to the equilibrium reactions:

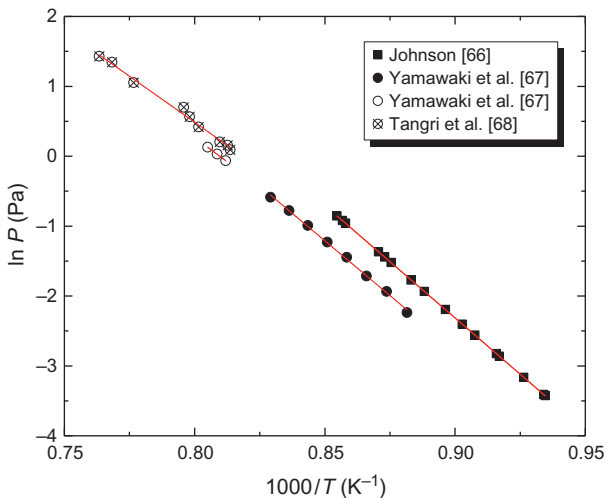
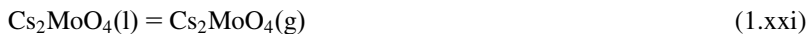


Figure 1.12 Total pressure above solid and liquid Cs_2MoO_4 as measured by Johnson [67], Yamawaki et al. [68], and Tangri et al. [69].

The least-squares fitting equations of the partial pressures data for $\text{Cs}_2\text{MoO}_4(\text{g})$ are reported in Table 1.6, together with the sublimation and vaporization enthalpies determined using the second law method. Let us explain in more detail one of these derivations.

The enthalpy of sublimation of $\text{Cs}_2\text{MoO}_4(\text{g})$, that is, $\Delta_{sub}H_m^\circ(\text{Cs}_2\text{MoO}_4)$ is equal to the enthalpy of reaction (1.xx), and the equilibrium constant

(Continued)

Box 1.11 (cont'd)

Table 1.6 Vapor pressure data of $\text{Cs}_2\text{MoO}_4(\text{g})$ over solid and liquid cesium molybdate, and derivation of the sublimation and vaporization enthalpies from the second law method.

Equilibrium type	$\ln p$ (Pa)	T (K)	$\Delta_{\text{sub}}H_m^\circ$ (298.15 K) (kJ/mol)	$\Delta_{\text{vap}}H_m^\circ$ (298.15 K) (kJ/mol)	Refs.
Sublimation	$-32200/T + 26.67$	1070.6–1167.2	(308.4 ± 11.3)		[67]
Sublimation	$-31348/T + 25.44$	1134.4–1206.0	(304.1 ± 7.1)		[68]
Vaporization	$-27872/T + 22.57$	1231.6–1242.2		(311.4 ± 2.5)	[68]
Vaporization	$-26345/T + 21.56$	1229–1310		(300.5 ± 7.1)	[69]

is directly related to the $\text{Cs}_2\text{MoO}_4(\text{g})$ partial pressure, that is, $K_{\text{eq}} = (p_{\text{Cs}_2\text{MoO}_4}/p^\circ)$.

From the data of Yamawaki et al. the enthalpy of sublimation is thereafter derived at the average temperature of the measured interval $T_{\text{ave}} = 1170$ K as $\Delta_{\text{sub}}H_m^\circ(\text{Cs}_2\text{MoO}_4, T_{\text{ave}}) = 31,348R = (260.6 \pm 7.1)$ kJ/mol. The enthalpy increment, $\Delta_rH_m^\circ(T_{\text{ave}}) - \Delta_rH_m^\circ(298.15 \text{ K}) = 43.5$ kJ/mol is obtained from the heat capacity data reported in the literature, and the enthalpy of sublimation at 298.15 K is thereafter derived as $\Delta_{\text{sub}}H_m^\circ(\text{Cs}_2\text{MoO}_4, 298.15 \text{ K}) = (304.1 \pm 7.1)$ kJ/mol.

Finally, combining this result with the enthalpy of formation of $\text{Cs}_2\text{MoO}_4(\text{cr})$ determined by solution calorimetry [70], that is, $\Delta_fH_m^\circ(\text{Cs}_2\text{MoO}_4, \text{cr}, 298.15 \text{ K}) = -(1514.7 \pm 1.5)$ kJ/mol, the enthalpy of formation of $\text{Cs}_2\text{MoO}_4(\text{g})$ is calculated as

$$\begin{aligned}\Delta_fH_m^\circ(\text{Cs}_2\text{MoO}_4, \text{g}, 298.15 \text{ K}) &= \Delta_{\text{sub}}H_m^\circ(\text{Cs}_2\text{MoO}_4, 298.15 \text{ K}) \\ &\quad - \Delta_fH_m^\circ(\text{Cs}_2\text{MoO}_4, \text{cr}, 298.15 \text{ K}) \\ &= -(1210.6 \pm 7.3) \text{ kJ/mol}\end{aligned}\tag{1.xxii}$$

The data treatment using the second- and third-law methods should give similar results, and the uncertainty associated with the third law should be within the uncertainty interval of the second law [61]. The second law yields an enthalpy value at 298.15 K derived from the median temperature of the temperature interval investigated, whereas the third law gives an enthalpy value for each measured temperature point. Third-law results are in general more reliable. Indeed, systematic errors can normally be detected with this method as they cause a

deviation of the result with temperature, but they are difficult to identify by the second law [61]. Third law treatment of the data requires one to know the entropy functions of all species involved in the reaction; however, this is not always the case.

1.6.5 Chemical state of fission products: Ellingham diagrams

Fission products are generated during irradiation of nuclear fuel, which thereafter becomes a very complex multi-component system, and accumulate up to several atomic percent. Their specific properties and effect on fuel chemistry and micro-structure will be treated in detail in [Chapter 11](#). Fission products are often classified in five distinct classes with distinct chemical and physical properties [71,72]:

- *Elements soluble in the fuel matrix* that can be accommodated on interstitial sites. These include the rare earths elements (La, Ce, Pr, Nd, Pm, Sm, and Eu), zirconium (Zr), yttrium (Y), tellurium (Te), and a few alkaline-earth elements, in particular strontium (Sr) and minor amounts of barium (Ba).
- *Oxide precipitates* formed at grain boundaries, such as the grey phase, which has the general formula $(\text{Ba}_{1-x-y}\text{Sr}_x\text{Cs}_y)(\text{Zr}, \text{U}, \text{Pu}, \text{Mo})\text{O}_3$.
- *Metallic precipitates*, including the noble metals (Ru, Rh, Tc, and Pd) as well as molybdenum Mo. They form the ε -phase, which appears as white inclusions on microscopic pictures.
- *Volatile species*, including cesium (Cs), iodine (I), tellurium (Te), and selenium (Se) in the form of cesium iodine CsI, cesium tellurate Cs_2Te , etc.
- *Inert gases*, such as xenon (Xe) and krypton (Kr), which show a very low solubility in the fuel matrix and accumulate in gas bubbles.

The chemical form of the fission products in the fuel depends on many factors including ionic size, stable valence states, oxygen affinity, thermodynamic stability, and kinetics of diffusion along the radial temperature gradient. Hereafter, Ellingham diagrams are introduced, which are very useful thermodynamic representations to predict the chemical state (e.g., oxide or metal), of some of the main fission products in the fuel (knowing the value of the oxygen potential). But Ellingham diagrams are also used to compare the relative stabilities of metal fluoride or chlorides systems of relevance for the MSR designs for instance, which are discussed in [Chapter 6](#), Molten salt reactor fuels.

Ellingham diagrams depict the evolution of the standard Gibbs energies of formation of an anion system such as oxides M_aO_z from pure metals M and oxygen gas at 1 bar pressure, and they allow a direct comparison of the relative stabilities of the different oxides. It is important to point out that the Gibbs energies are expressed per mole of O_2 (respectively F_2 or Cl_2). The corresponding equilibrium reaction is



and the corresponding Gibbs energy of reaction plotted in the diagram is

$$\begin{aligned}\Delta_r G_m^\circ(T) &= \frac{2}{z} \Delta_f G_m^\circ(M_a O_z T) - \frac{2a}{z} \Delta_f G_m^\circ(M, T) - \Delta_f G_m^\circ(O_2, T) \\ &= -RT \ln K_{eq} \\ &= RT \ln \frac{p(O_2)}{p^\circ} = \mu_{eq}(O_2) - \mu_{eq}^\circ(O_2)\end{aligned}\quad (1.199)$$

where K_{eq} is the equilibrium constant of the reaction. The activities of the condensed phases M and $M_a O_z$ are approximated to unity.

The more negative the Gibbs energy of reaction (or oxygen potential) of a metal/oxide couple is, the easier it is to form the oxide phase. Looking at Fig. 1.13, one can predict the chemical state of various fission products in the UO_2 fuel. All metal/oxide couples whose Gibbs energy of formation are found below the fuel oxygen potential will form oxides, while those whose Gibbs energy of formation is above will remain in the metallic state. For instance, lanthanum is predicted to be present as La_2O_3 , while palladium remains metallic Pd (Box 1.12).

In the case of fluoride or chloride systems, the principle of the construction of Ellingham diagrams remains the same, but in this case the fluorine and chlorine chemical potentials defined as $\Delta\mu(F_2) = RT \ln p(F_2)/p^\circ$ and $\Delta\mu(Cl_2) = RT \ln p(Cl_2)/p^\circ$, respectively, are derived as a function of temperature. Such diagrams allow to predict if a chemical element is stable in its metallic form or as a fluoride (respectively chloride) species in a molten salt reactor fuel.

Although Ellingham diagrams allow one to make predictions for the formation of binary oxides, they do not permit one to assess the formation of more complex ternary and higher order phases, such as the compounds of the grey phase. To this

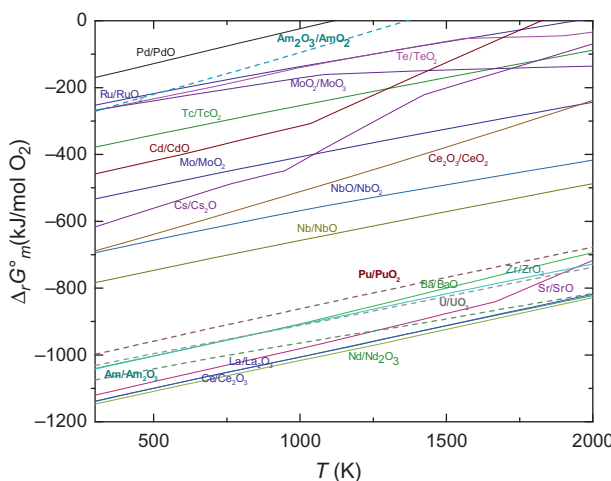


Figure 1.13 Ellingham diagram for various metal/metal oxide couples.

Box 1.12 Ellingham diagrams: example calculation.

To illustrate the information found in Ellingham diagrams, let us calculate the oxygen pressure necessary to form PdO(cr) and La₂O₃(cr) at 1500 K, knowing that the Gibbs energies of formation at this temperature are $\Delta_f G_m^\circ(\text{PdO, cr, 1500 K}) = 38.6 \text{ kJ/mol}$ and $\Delta_f G_m^\circ(\text{La}_2\text{O}_3, \text{cr, 1500 K}) = -1368.2 \text{ kJ/mol}$.

The reaction associated with the Gibbs energy of formation of PdO(cr) at 1500 K is



The equilibrium reaction depicted in the Ellingham diagram refers to 1 mol of O₂(g), however, that is,



The corresponding Gibbs energy of reaction is $\Delta_r G_m^\circ(1500 \text{ K}) = 2\Delta_f G_m^\circ(\text{PdO, cr, 1500 K}) = 77.2 \text{ kJ/mol}$. Hence,

$$\frac{p(\text{O}_2)}{p^\circ} = \exp\left(\frac{\Delta_r G_m^\circ(1500 \text{ K})}{RT}\right) \sim 488 \text{ bar} \quad (1.\text{xxv})$$

The reaction associated with the Gibbs energy of formation of La₂O₃(cr) at 1500 K is



The equilibrium reaction depicted in the Ellingham diagram refers to 1 mol of O₂(g); hence,



The corresponding Gibbs energy of reaction is $\Delta_r G_m^\circ(1500 \text{ K}) = \frac{2}{3}\Delta_f G_m^\circ(\text{La}_2\text{O}_3, \text{cr, 1500 K}) = -912.1 \text{ kJ/mol}$. The equilibrium constant for this reaction is $K_{\text{eq}} = 1/(p(\text{O}_2)/p^\circ)$ where $p^\circ = 1 \text{ bar}$. Since $\Delta_r G_m^\circ = -RT \ln K_{\text{eq}}$, it follows that

$$\frac{p(\text{O}_2)}{p^\circ} = \exp\left(\frac{\Delta_r G_m^\circ(1500 \text{ K})}{RT}\right) \sim 1.7 \cdot 10^{-32} \text{ bar} \quad (1.\text{xxviii})$$

end, a more sophisticated approach involving CALPHAD thermodynamic assessments is necessary.

1.7 Solution thermodynamics applied to the storage of spent fuel and geological disposal

Highly radioactive spent nuclear fuel (SNF) produced during reactor operation are destined either directly (in an open fuel cycle) or after reprocessing (in a closed fuel cycle) to long-term storage and final disposal in a geological repository [73]. Understanding the chemistry of the radionuclides in the environment and in particular in contact with groundwater is essential to reduce the potential risks of contamination. Among the radionuclides the long-lived fission products (^{99}Tc , ^{129}I , ^{79}Se), those with a high activity (^{90}Sr , ^{90}Y , ^{137}Cs , ^{137m}Ba), and the heavy uranium and transuranium elements (U, Np, Pu, Am, and Cm) are of major concern [74]. Various factors affect their migration and retention in the environment: (1) complexation/hydrolysis, (2) solubility/precipitation, (3) oxidation/reduction, (4) sorption on mineral surfaces, and (5) formation of colloids. In this chapter the fundamentals of (1)–(3) are discussed, and some basic concepts such as the construction of speciation and Pourbaix diagrams are introduced. These are needed to understand the detailed chemistry of the storage of SNF and disposal treated in Chapter 13, Spent nuclear fuel and disposal.

1.7.1 Hydrolysis and complexation

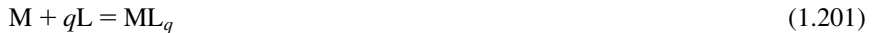
Hydrolysis and complexation are dependent on conditions of pH and ligand concentration in solution and affect the speciation of radionuclides, and thereafter their transport into the environment. Hydroxide, carbonate, sulfite, sulfate, oxalate, phosphate, fluoride, chloride, nitrate, and silicate are common inorganic ligands found in groundwater, hydroxide and carbonate being the most abundant ones [75–77].

The stability of a particular complex is expressed by the equilibrium constant of its formation from the metal ions and ligands and is named the stability or formation constant. The notations adopted in this chapter are the same as those of the *Stability Constants of Metal Ion Complexes* by Sillén and Martell [78,79] and retained in the Nuclear Energy Agency-Organization for Economic Cooperation and Development (NEA-OECD) Thermochemical Database (TDB) Project [18].

The reaction of formation of the complex ML_q by successive complexation of the metal ion M by the ligand L is written as follows in consecutive steps:



The overall reaction corresponds to



The stepwise formation constant for each consecutive reaction is defined as

$$K_q = \frac{[ML_q]}{[ML_{q-1}][L]} \quad (1.202)$$

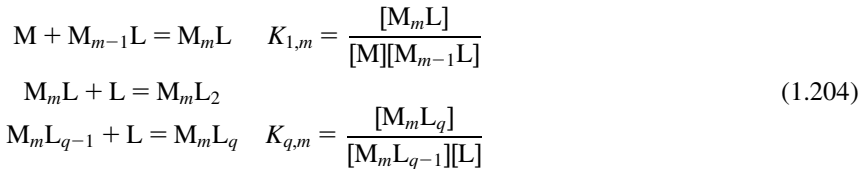
while the overall (or cumulative) formation constant for reaction (1.201)

$$\beta_q = \frac{[ML_q]}{[M][L]^q} = \prod_{i=1}^q K_i \quad (1.203)$$

is equal to the product of the successive stepwise formation constants.

$[M]$, $[L]$, $[ML_{q-1}]$, and $[ML_q]$ are the equilibrium concentrations of M , L , ML_{q-1} , and ML_q , respectively, in the involved reactions. The activities of the species in solution are approximated by their concentrations, which is a good approximation for dilute solutions. q refers to the number of ligands.

In the case of a polynuclear complex, the previous reactions become

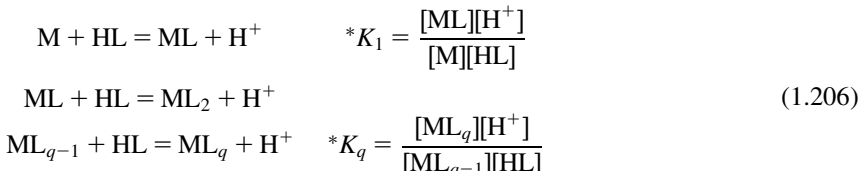


and the overall reaction and formation constant:

$$mM + qL = M_mL_q \quad \beta_{q,m} = \frac{[M_mL_q]}{[M]^m[L]^q} \quad (1.205)$$

Here again q refers to the number of ligands and m to the number of metal ions.

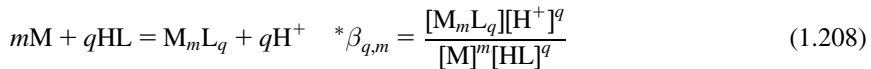
Hydrolysis corresponds to the specific case of the formation of hydroxide complexes by reaction of a metal ion M with the protonated ligand $HL = H_2O$, and subsequent deprotonation of the ligand. The corresponding equilibrium constants are marked with an asterisk.



and the overall reaction and formation constant are written:



For polynuclear complexes, the overall reaction is written:



In thermodynamic databases the logarithm of the equilibrium constant is generally listed (Box 1.13). The equilibrium constant is related to the Gibbs energy of formation of the complex via the relation:

$$\Delta_r G_m(M_mL_q) = \Delta_r G_m^\circ(M_mL_q) + RT \ln \beta_{q,m} \quad (1.209)$$

where $\Delta_r G_m^\circ(M_mL_q)$ is the Gibbs energy of formation at the standard pressure.

At equilibrium, $\Delta_r G_m(M_mL_q)$ is equal to zero; hence,

$$\Delta_r G_m^\circ(M_mL_q) = -RT \ln \beta_{q,m} \quad (1.210)$$

This relation shows that the higher the value of the stability constant is, the more stable the complex will be. In general, complexation and hydrolysis increase the total concentration of actinides or fission products in solution.

1.7.2 Solubility and precipitation

A precipitation reaction corresponds to the process where a cationic $M(aq)$ and anionic species $L(aq)$ in solution combine to form an insoluble solid phase $M_aL_b(s)$ named precipitate:



Solubility and precipitation determine the upper concentration of a given radionuclide in solution. The precipitation process will take place as long as the concentrations of cations and anions in solution are high enough, and until an equilibrium or steady state is reached at which the solution is said saturated. The corresponding equilibrium concentrations define the solubility constant:

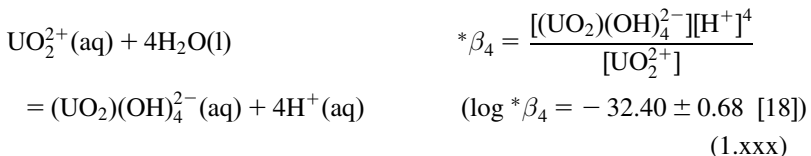
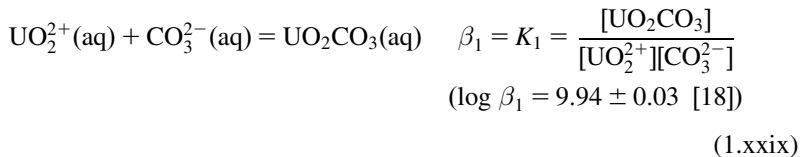
$$K_{s,0} = [M]^a[L]^b \quad (1.212)$$

where the subscript s refers to solubility, and “0” means that the formed ionic aqueous species are not complexed. Solubility is a function of temperature.

For aqueous complexed species, the following notation is adopted:

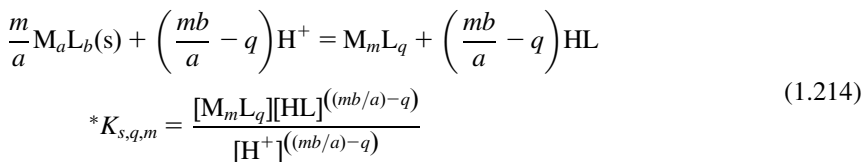
Box 1.13 Stability constants.

To illustrate the use of equilibrium constants, let us look at the formation of uranyl carbonate and uranium tetrahydroxide in solution:



$$\frac{m}{a} \text{M}_a\text{L}_b(\text{s}) = \text{M}_m\text{L}_q + \left(\frac{mb}{a} - q \right) \text{L} \quad K_{s,q,m} = [\text{M}_m\text{L}_q][\text{L}]^{((mb/a)-q)} \quad (1.213)$$

while an asterisk is added in cases where a protonation equilibrium is also involved:



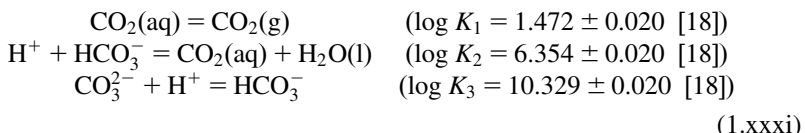
Here again the adopted notation is that of the NEA-OECD TDB Project [18] (Box 1.15).

1.8 Basics of redox equilibria

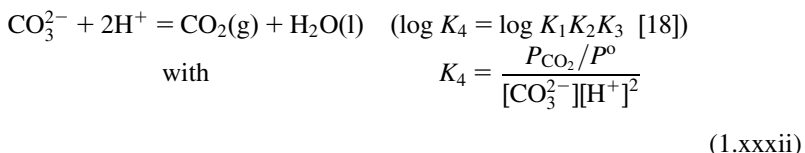
Understanding the migration of radionuclides into the geosphere involves (aqueous) electrochemistry and redox equilibria, and some of the basic concepts are introduced hereafter.

Box 1.14 Carbonate concentration in natural waters.

CO_3^{2-} is together with OH^- the most abundant ligand found in the environment. Its concentration is higher in underground waters compared to surface waters due to the increased $\text{CO}_2(\text{g})$ partial pressure (typically around 3×10^{-4} bar at the surface and 10^{-2} bar in groundwater). The relationship between carbonate concentration $[\text{CO}_3^{2-}]$ and $\text{CO}_2(\text{g})$ partial pressure is derived using Hess's law as follows:



The combination of the equations above yields



Hence,

$$\begin{aligned}\log [\text{CO}_3^{2-}] &= 2\text{pH} - \log K_4 + \log P_{\text{CO}_2} \\ &= 2\text{pH} - \log K_1 K_2 K_3 + \log P_{\text{CO}_2} \\ \log [\text{CO}_3^{2-}] &= 2\text{pH} - 18.155 + \log P_{\text{CO}_2}\end{aligned}\quad (1.\text{xxxiii})$$

1.8.1 Redox equilibria and Galvanic cell

An electrochemical reaction involves the transfer of z electrons, most often between a metal M and the cation M^{z+} dissolved in solution, hence a change in the oxidation state (also called valence state) of the chemical element considered, and a potential difference between the metal and the solution. An oxidation reaction corresponds to a loss of electrons for the element, while a reduction corresponds to the gain of electrons. The equilibrium reaction between M and M^{z+} is called redox reaction and is written:

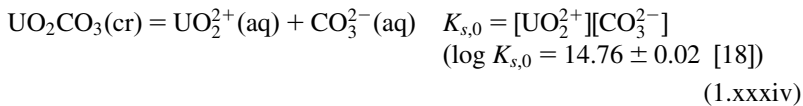


where e^- denotes the electron.

The transfer of electrons can be observed and measured using an electrochemical cell called Galvanic cell after the Italian physicist Luigi Galvani. The Galvanic cell (Fig. 1.14) is made of two half-cells consisting of a metal (the electrode) in contact

Box 1.15 Solubility constants.

Taking again the example of the uranyl carbonate, this time in the form of a precipitate, the solubility product is expressed as



Similarly, the solubility product of hydrated $\text{PuO}_2\text{OH}(\text{am})$ is

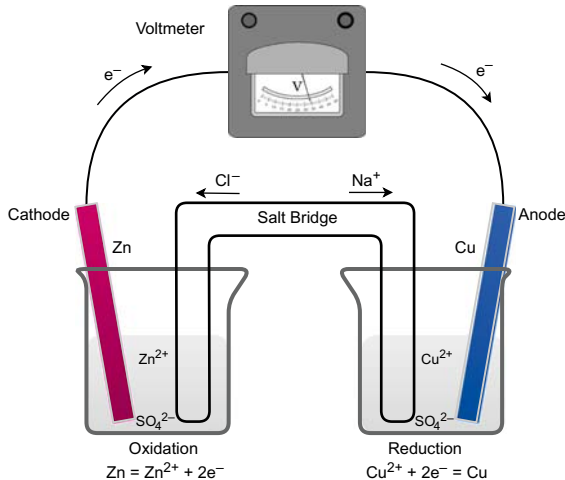
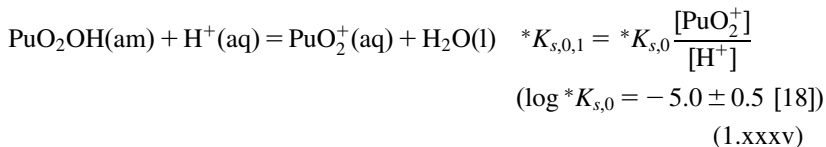


Figure 1.14 Sketch of a galvanic cell with copper and zinc electrodes immersed in copper sulfate and zinc sulfate solutions, respectively.

with a solution (the electrolyte) of the metal cations. The solution also contains anions such as SO_4^{2-} , NO_3^- , and Cl^- to maintain electroneutrality of the solution. An external electrical conductor connects the electrodes and allows the transfer of electrons from one half-cell to the other. The transfer of electric charge leads to an electric current, which can be measured using an ammeter in the external circuit. The movement of charged particles (the electrons) also leads to a potential difference between the electrode and electrolyte, which cannot be measured directly.

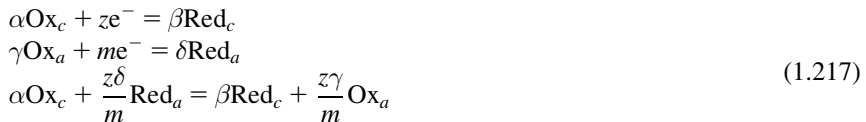
However, the potential difference between the two half-cells can be measured using a voltmeter placed in the external circuit. In addition, a salt bridge ensures contact between the two solutions, and allows cations and anions to move from one cell to the other to maintain the electroneutrality and avoid the buildup of excess net positive or negative charges.

The half-cell where the oxidation reaction takes place is named the anode, whereas the half-cell where the reduction reaction takes place is called the cathode. The half-cell reactions are written in a general form:



where Ox denotes the oxidant and Red the reductant of the redox couple Ox/Red. By convention the reactions are written with the reducing species on the right and electrons on the left.

The overall cell reaction corresponds to the transfer of z electrons between the anode and cathode, that is,



where the index c denotes the cathode and a the anode.

The voltage or electromotive force (emf) E measured with the voltmeter corresponds to the difference between the half-cell potentials of the reduction and oxidation reactions; hence,

$$E = E_{\text{cell}} = E_{\text{cathode}} - E_{\text{anode}} \quad (1.218)$$

It is not possible to measure directly the emf of a single electrode. The standard hydrogen electrode SHE, which corresponds to an inert metal electrode (Pt) immersed in a solution of $[\text{H}^+]$ cations (typically HCl electrolyte) and through which pure hydrogen gas is bubbled, has therefore been assigned arbitrarily a half-cell potential of zero. $\text{H}_2(\text{g})$ is at unit fugacity ($p_{\text{H}_2} = 1$ bar), and H^+ at unit activity ($[\text{H}^+] = 1$ mol/L) in the SHE. The half-cell potential of a redox couple is thereafter given by the emf of a Galvanic cell in which the cathode corresponds to the Ox/Red couple and the anode is the SHE. This half-cell potential is named standard electrode potential and noted E° .

In this particular case the half-cell reactions and overall reaction become ($m = 1$, $\gamma = 1$, $\delta = 1/2$):



1.8.1.1 Gibbs energy of the redox reaction and Nernst equation

Chemical energy is converted into electrical energy in the Galvanic cell since the movement of an electrical charge through an electrical potential difference results in electrical work.

The differentiation of the Gibbs energy equation [see Eq. (1.24)] at constant pressure ($dp = 0$) and temperature ($dT = 0$), and the application of the first law of thermodynamics yields

$$\begin{aligned} dG &= dU + pdV - TdS \\ &= \delta Q + \delta W_{exp} + \delta W_{elec} + pdV - TdS \\ dG &= \delta W_{elec} \end{aligned} \quad (1.220)$$

where δW_{exp} represents expansion work and δW_{elec} electrical work.

The electrical work is the product of the electrical charge by the potential difference E_{cell} . Hence, the Gibbs energy change of the overall reaction (1.217) is expressed as follows:

$$\Delta_r G_m = -z\mathcal{F} E \quad (1.221)$$

where z is the number of moles of electrons transferred per mole of reaction, and \mathcal{F} is the *Faraday constant*, which is the product of the electronic charge ($q = 1.602 \times 10^{-19} \text{ C}$) and Avogadro constant ($N_a = 6.02214076 \times 10^{23} \text{ mol}^{-1}$), that is, $\mathcal{F} = qN_a \sim 96,500 \text{ C/mol}$.

A positive number for the potential difference (emf) corresponds to a negative value for the Gibbs energy of reaction, and hence a spontaneous process. In such a case the system quickly reaches equilibrium and no current will flow in the external circuit. Using a battery, it is possible to force the reaction in the opposite direction by applying a current.

The Gibbs energy change of the overall reaction (1.217) can also be expressed in terms of the chemical potentials:

$$\Delta_r G_m = \beta\mu(\text{Red}_c) + \frac{z\gamma}{m}\mu(\text{Ox}_a) - \alpha\mu(\text{Ox}_c) - \frac{z\delta}{m}\mu(\text{Red}_a) \quad (1.222)$$

$$\begin{aligned} &= \beta\mu^\circ(\text{Red}_c) - \alpha\mu^\circ(\text{Ox}_c) + \frac{z\gamma}{m}\mu^\circ(\text{Ox}_a) - \frac{z\delta}{m}\mu^\circ(\text{Red}_a) \\ &\quad + RT \ln \left(\frac{a_{\text{Red}_c}^{\beta} a_{\text{Ox}_a}^{(z/m)\gamma}}{a_{\text{Ox}_c}^{\alpha} a_{\text{Red}_a}^{(z/m)\delta}} \right) \end{aligned} \quad (1.223)$$

where $\mu^\circ(\text{Ox}_i)$ and $\mu^\circ(\text{Red}_i)$ are the standard chemical potentials of the oxidant and reductant, respectively, and a_{Ox_i} and a_{Red_i} their activities.

The Gibbs energies of the half-cell reactions are similarly related to the standard electrode potentials of the half-cells $E^\circ(\text{Ox}_c/\text{Red}_c)$ and $E^\circ(\text{Ox}_a/\text{Red}_a)$ via the relations:

$$\Delta_r G_m^\circ(\text{cathode}) = \beta\mu^\circ(\text{Red}_c) - \alpha\mu^\circ(\text{Ox}_c) = -zFE^\circ(\text{Ox}_c/\text{Red}_c) \quad (1.224)$$

$$\Delta_r G_m^\circ(\text{anode}) = \delta\mu^\circ(\text{Red}_a) - \gamma\mu^\circ(\text{Ox}_a) = -mFE^\circ(\text{Ox}_a/\text{Red}_a) \quad (1.225)$$

The combination of Eqs. (1.221) and (1.223)–(1.225) yields

$$-z\mathcal{F}E = -z\mathcal{F}(E^\circ(\text{Ox}_c/\text{Red}_c) - E^\circ(\text{Ox}_a/\text{Red}_a)) + RT \ln \left(\frac{a_{\text{Red}_c}^\beta a_{\text{Ox}_a}^{(z/m)\gamma}}{a_{\text{Ox}_c}^\alpha a_{\text{Red}_a}^{(z/m)\delta}} \right) \quad (1.226)$$

which can be simplified as

$$E = E^\circ + \frac{RT}{z\mathcal{F}} \ln \left(\frac{a_{\text{Ox}_c}^\alpha a_{\text{Red}_a}^{(z/m)\delta}}{a_{\text{Red}_c}^\beta a_{\text{Ox}_a}^{(z/m)\gamma}} \right) \quad (1.227)$$

When applied to a Galvanic cell where the anode is the SHE [see Eq. (1.219)], the abovementioned equation becomes

$$E = E^\circ(\text{Ox}_c/\text{Red}_c) + \frac{RT}{z\mathcal{F}} \ln \left(\frac{a_{\text{Ox}_c}^\alpha p_{\text{H}_2}^{(z/2)}}{a_{\text{Red}_c}^\beta a_{\text{H}^+}^z} \right) \quad (1.228)$$

where by definition the fugacity of H_2 and activity of H^+ are equal to 1; hence,

$$E = E^\circ(\text{Ox}_c/\text{Red}_c) + \frac{RT}{z\mathcal{F}} \ln \frac{a_{\text{Ox}_c}^\alpha}{a_{\text{Red}_c}^\beta} \quad (1.229)$$

This relation corresponds to the well-known Nernst equation, often expressed in terms of base-10 logarithm, that is,

$$E = E^\circ(\text{Ox}_c/\text{Red}_c) + \frac{0.059}{z} \log \frac{a_{\text{Ox}_c}^\alpha}{a_{\text{Red}_c}^\beta} \quad (1.230)$$

1.8.2 Pourbaix diagrams

The stability of a chemical species in solution, its form and oxidation state, depends mainly on four parameters: the pH of the solution, the temperature, the redox potentials of the chemical species, and the concentration of ligands in solution. Pourbaix diagrams, which are diagrams with pH on the abscissa and electrode

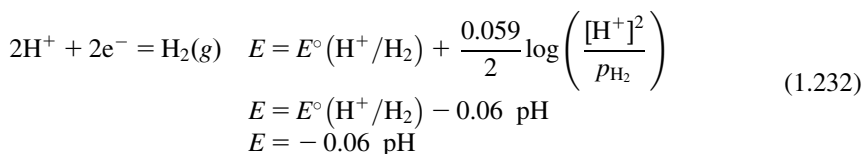
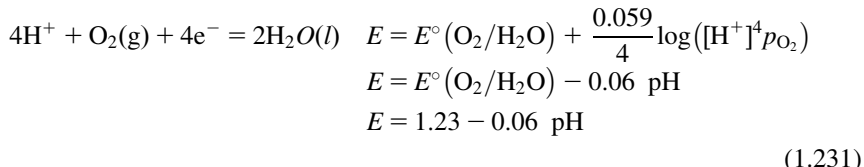
potentials E_{SHE} (vs the SHE) on the ordinate, are very useful representations to map out the possible equilibrium (stable) phases as a function of the pH and electric potential conditions in the aqueous solution/system considered. Pourbaix diagrams are constructed at a fixed temperature using the Nernst equation, and using a set of specific rules:

- The pressure of gases (H_2 , O_2) are fixed to 1 bar at the borders of water oxidation and reduction, respectively.
- The total initial concentration of all species in solution (except H^+) are fixed to a certain value¹ (for instance, 10^{-6} mol/L).
- The activities of H_2O and pure solids are equal to unity.
- The electrode potentials are expressed with respect to the SHE.

The chemical species encountered in Pourbaix diagrams are metals, metal oxides, hydroxides, oxy-hydroxides, and complexes when ligands (i.e., CO_3^{2-} , OH^-) are also considered. They can be in the form of undissociated and uncharged aqueous species, dissolved ions, or solids. The stability domains indicate the conditions under which a specific species or phases is predominant. Two chemical species in neighboring domains are in equilibrium at the phase boundaries between two domains and have equal activities at the boundary.

The example of the Np–O–H Pourbaix diagram, plotted at 298.15K and a fixed concentration of 10^{-6} mol/L for all Np ions in solution, is shown in Fig. 1.15. The equilibria for all phase boundaries are moreover listed in Table 1.7 (see Box 1.16 for the derivation of the phase boundary equilibria).

The Pourbaix diagram is superimposed with the equilibrium lines for the $O_2(g)/H_2O(l)$ [see Eq. (1.231)] and $H^+/H_2(g)$ [see Eq. (1.232)] couples, which define the stability region of water.



¹ It should be noted that in cases where the precipitation of solid phases is allowed in the calculation (as in Fig. 1.15), the total concentration in solution of the element evaluated decreases below the total initial concentration in the region where the solid phase is predominant. As a consequence, the equilibrium lines between aqueous species and solid precipitates depend upon the total initial concentration of the element evaluated (Np in Fig. 1.15).

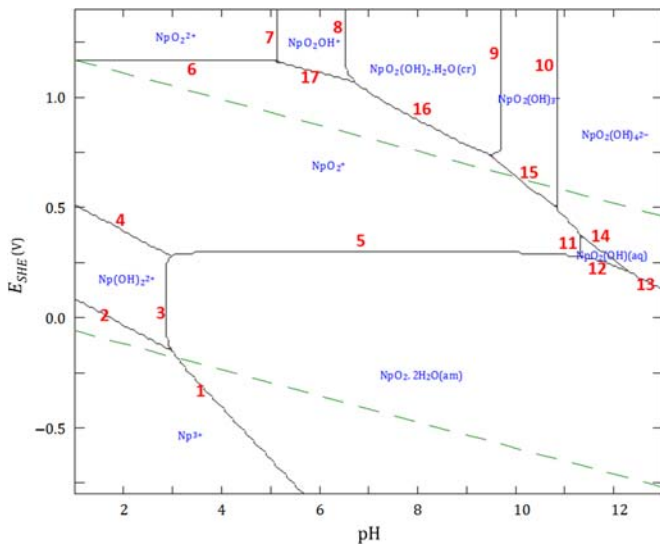


Figure 1.15 Pourbaix diagram for the Np–O–H system, plotted at 298.15K, 1 bar and $\Sigma\text{Np} = 10^{-6}$ mol/L using the thermodynamic data critically assessed by Ref. [80]. The dotted green lines denote the stability region of water.

Water is thermodynamically unstable above the upper line and will oxidize to oxygen gas $\text{O}_2(\text{g})$, while it will reduce to hydrogen gas $\text{H}_2(\text{g})$ below the lower line. Chemical species found outside of the stability domain of water will react with $\text{H}_2\text{O}(\text{l})$ to form species compatible with water. As can be seen in Fig. 1.15, Np(IV) [i.e., hydrated amorphous $\text{NpO}_2 \cdot 2\text{H}_2\text{O}(\text{am})$ and Np(OH)_2^{2+}] and Np(V) [i.e., NpO_2^+ and $\text{NpO}_2(\text{OH})(\text{aq})$] species are stable in aqueous systems, while Np(III) (i.e., Np^{3+}) and Np(VI) [i.e., NpO_2^{2+} , $\text{NpO}_2(\text{OH})_2 \cdot \text{H}_2\text{O}(\text{cr})$, and hydroxo complexes NpO_2OH^+ , $\text{NpO}_2(\text{OH})_3^-$, and $\text{NpO}_2(\text{OH})_4^{2-}$] species found close to the border of the water stability domain can only form under very reducing or oxidizing conditions, respectively.

Redox potentials and pH conditions in natural waters are in the range of −300 to +500 mV, and 5–9, respectively [76]; hence, NpO_2^+ will be the dominant species in solution in the Np–O–H system.

Pourbaix diagrams are very useful to predict the form and oxidation state of chemical species in natural waters (geological fluids, groundwater, soils, streams, and ocean) in the environment. Taking into account complexing ligands present in these waters, complex E – pH diagrams are obtained and can be used to make predictions for the mobility of the chemical species considered. However, it should be pointed out that these calculations are based on thermodynamic equilibrium conditions only and do not account for the kinetics. Moreover, these diagram suppose an ideal behavior (activities are approximated with concentrations) and do not consider deviations from ideality.

Table 1.7 Phase boundary equilibria in the Np–O–H Pourbaix diagram.

Phase boundary	Equilibrium reaction	Equilibrium type	Redox couples
1	$\text{NpO}_2 \cdot 2\text{H}_2\text{O}(\text{am}) + 4\text{H}^+ + \text{e}^- = \text{Np}^{3+} + 4\text{H}_2\text{O}(\text{l})$	Redox	$\text{NpO}_2 \cdot 2\text{H}_2\text{O}(\text{am})/\text{Np}^{3+}$
2	$\text{Np(OH)}_2^{2+} + 2\text{H}^+ + \text{e}^- = \text{Np}^{3+} + 2\text{H}_2\text{O}(\text{l})$	Redox	$\text{Np(OH)}_2^{2+}/\text{Np}^{3+}$
3	$\text{NpO}_2 \cdot 2\text{H}_2\text{O}(\text{am}) + 2\text{H}^+ = \text{Np(OH)}_2^{2+} + 2\text{H}_2\text{O}(\text{l})$	Dissolution	
4	$\text{NpO}_2^+ + 2\text{H}^+ + \text{e}^- = \text{Np(OH)}_2^{2+}$	Redox	$\text{NpO}_2^+/\text{Np(OH)}_2^{2+}$
5	$\text{NpO}_2^+ + 2\text{H}_2\text{O}(\text{l}) + \text{e}^- = \text{NpO}_2 \cdot 2\text{H}_2\text{O}(\text{am})$	Redox	$\text{NpO}_2^+/\text{NpO}_2 \cdot 2\text{H}_2\text{O}(\text{am})$
6	$\text{NpO}_2^{2+} + \text{e}^- = \text{NpO}_2^+$	Redox	$\text{NpO}_2^{2+}/\text{NpO}_2^+$
7	$\text{NpO}_2^{2+} + \text{H}_2\text{O}(\text{l}) = \text{NpO}_2\text{OH}^+ + \text{H}^+$	Hydrolysis	
8	$\text{NpO}_2\text{OH}^+ + 2\text{H}_2\text{O}(\text{l}) = \text{NpO}_2(\text{OH})_2 \cdot \text{H}_2\text{O}(\text{cr}) + \text{H}^+$	Precipitation	
9	$\text{NpO}_2(\text{OH})_2 \cdot \text{H}_2\text{O}(\text{cr}) = \text{NpO}_2(\text{OH})_3^- + \text{H}^+$	Dissolution	
10	$\text{NpO}_2(\text{OH})_3^- + \text{H}_2\text{O}(\text{l}) = \text{NpO}_2(\text{OH})_4^{2-} + \text{H}^+$	Hydrolysis	
11	$\text{NpO}_2^+ + \text{H}_2\text{O}(\text{l}) = \text{NpO}_2(\text{OH})(\text{aq}) + \text{H}^+$	Hydrolysis	
12	$\text{NpO}_2(\text{OH})(\text{aq}) + \text{H}_2\text{O}(\text{l}) + \text{H}^+ + \text{e}^- = \text{NpO}_2 \cdot 2\text{H}_2\text{O}(\text{am})$	Redox	$\text{NpO}_2(\text{OH})(\text{aq})/\text{NpO}_2 \cdot 2\text{H}_2\text{O}(\text{am})$
13	$\text{NpO}_2(\text{OH})_4^{2-} + 4\text{H}^+ + 2\text{e}^- = \text{NpO}_2 \cdot 2\text{H}_2\text{O}(\text{am}) + 2\text{H}_2\text{O}(\text{l})$	Redox	$\text{NpO}_2(\text{OH})_4^{2-}/\text{NpO}_2 \cdot 2\text{H}_2\text{O}(\text{am})$
14	$\text{NpO}_2(\text{OH})_4^{2-} + 3\text{H}^+ + \text{e}^- = \text{NpO}_2(\text{OH})(\text{aq}) + 3\text{H}_2\text{O}(\text{l})$	Redox	$\text{NpO}_2(\text{OH})_4^{2-}/\text{NpO}_2(\text{OH})(\text{aq})$
15	$\text{NpO}_2(\text{OH})_3^- + 3\text{H}^+ + \text{e}^- = \text{NpO}_2^+ + 3\text{H}_2\text{O}(\text{l})$	Redox	$\text{NpO}_2(\text{OH})_3^-/\text{NpO}_2^+$
16	$\text{NpO}_2(\text{OH})_2 \cdot \text{H}_2\text{O}(\text{cr}) + 2\text{H}^+ + \text{e}^- = \text{NpO}_2^+ + 3\text{H}_2\text{O}(\text{l})$	Redox	$\text{NpO}_2(\text{OH})_2 \cdot \text{H}_2\text{O}(\text{cr})/\text{NpO}_2^+$
17	$\text{NpO}_2\text{OH}^+ + \text{H}^+ + \text{e}^- = \text{NpO}_2^+ + \text{H}_2\text{O}(\text{l})$	Redox	$\text{NpO}_2\text{OH}^+/\text{NpO}_2^+$

Box 1.16 The Np–O–H Pourbaix diagram: determination of phase boundary equilibria.

Let us illustrate the determination of a few selected phase boundary equilibria in the Np–O–H Pourbaix diagram.

NpO₂²⁺/NpO₂⁺ redox equilibria—phase boundary 6

The redox equilibrium reaction is



The corresponding Nernst equation is

$$E = E^\circ (\text{NpO}_2^{2+}/\text{NpO}_2^+) + \frac{0.059}{1} \log_{10} \left(\frac{[\text{NpO}_2^{2+}]}{[\text{NpO}_2^+]} \right) \quad (1.\text{xxxvii})$$

Because the activities (concentrations) of NpO₂²⁺ and NpO₂⁺ are equal on the phase boundary equilibrium line, the abovementioned equation reduces to

$$E = E^\circ (\text{NpO}_2^{2+}/\text{NpO}_2^+) = (1.159 \pm 0.004) \quad [80] \quad (1.\text{xxxviii})$$

NpO₂²⁺/NpO₂OH⁺ hydrolysis equilibria—phase boundary 7

The Gibbs energy of reaction for the hydrolysis reaction:



is given by

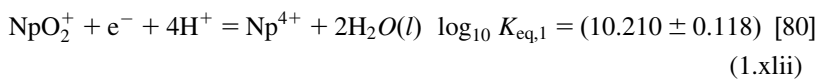
$$\begin{aligned} \Delta_r G_m^\circ &= -RT \ln \left(\frac{[\text{H}^+][\text{NpO}_2\text{OH}^+]}{[\text{NpO}_2^{2+}]} \right) \\ &= -RT \ln [\text{H}^+] \\ &= -2.3RT \log_{10} [\text{H}^+] \end{aligned} \quad (1.\text{xl})$$

$$\Delta_r G_m^\circ = 5.708 \text{ pH} \quad (1.\text{xli})$$

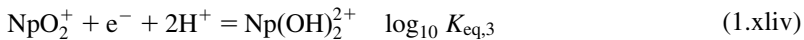
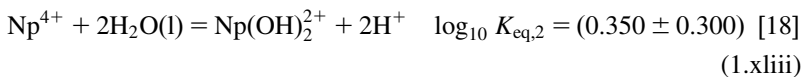
The combination of this equation with the data of [18]: $\Delta_r G_m^\circ (1.272) = (29.111 \pm 2.283) \text{ kJ/mol}$ or $\log_{10} K_{\text{eq}} = -(5.1 \pm 0.4)$ yields $\text{pH} = (5.1 \pm 0.4)$. Hence, the corresponding equilibrium is shown by a vertical line in Fig. 1.15 at $\text{pH} = 5.1$.

NpO₂⁺/Np(OH)₂²⁺ redox equilibria—phase boundary 4

The redox equilibria between NpO₂⁺ and Np(OH)₂²⁺ can be calculated using the combination of the two following redox and hydrolysis reactions:



(Continued)

Box 1.16 (cont'd)

Applying Hess's law, one derives $\log_{10} K_{\text{eq},3} = \log_{10} K_{\text{eq},1} + \log_{10} K_{\text{eq},2} = (10.560 \pm 0.322)$. The corresponding Nernst equation is defined by

$$\begin{aligned} E &= E^\circ(\text{NpO}_2^+ / \text{Np(OH)}_2^{2+}) + \frac{0.059}{1} \log_{10} \left(\frac{[\text{NpO}_2^+][\text{H}^+]^2}{[\text{Np(OH)}_2^{2+}]} \right) \quad (1.\text{xlv}) \\ &= E^\circ(\text{NpO}_2^+ / \text{Np(OH)}_2^{2+}) + 0.059 \log_{10} [\text{H}^+]^2 \\ &= E^\circ(\text{NpO}_2^+ / \text{Np(OH)}_2^{2+}) - 0.118 \text{ pH} \end{aligned} \quad (1.\text{xlvi})$$

The value of the standard electrode potential is obtained by combining Eqs. (1.99) and (1.221):

$$-RT \ln K_{\text{eq},3} = -z \mathcal{F} E^\circ(\text{NpO}_2^+ / \text{Np(OH)}_2^{2+}) \quad (1.\text{xlvii})$$

$$-2.3RT \log_{10} K_{\text{eq},3} = \mathcal{F} E^\circ(\text{NpO}_2^+ / \text{Np(OH)}_2^{2+}) \quad (1.\text{xlviii})$$

yielding $E^\circ(\text{NpO}_2^+ / \text{Np(OH)}_2^{2+}) = (0.625 \pm 0.019)$.

Finally, the equilibrium line for the $\text{NpO}_2^+ / \text{Np(OH)}_2^{2+}$ couple is given by the equation $E = 0.625 - 0.118 \text{ pH}$.

1.8.3 Speciation diagrams

Speciation diagrams showing the distribution of complexes in solution as function of ligand concentration or pH are finally another useful representation to understand the influence of complexation, hydrolysis, and precipitation on the nuclides migration in the environment. They are calculated combining the laws of mass balance with the expressions for the formation constants. According to the laws of mass balance, the total concentration of a species, denoted $[\text{M}]_{\text{tot}}$, is equal to the sum of the different forms of aqueous ions and complexes:

$$[\text{M}]_{\text{tot}} = [\text{M}] + [\text{ML}] + [\text{ML}_2] + \dots + [\text{ML}_q] \quad (1.233)$$

where L is a ligand such as OH^- and CO_3^{2-} .

Dividing by the concentration of the metal ion $[M]$ in the form of an aqueous cation, and combining with Eq. (1.205) gives

$$\begin{aligned}\frac{[M]_{tot}}{[M]} &= 1 + \frac{[ML]}{[M]} + \frac{[ML_2]}{[M]} + \cdots + \frac{[ML_q]}{[M]} \\ &= 1 + \beta_1[L] + \beta_2[L]^2 + \cdots + \beta_q[L]^q\end{aligned}\quad (1.234)$$

The fraction of a particular complex ML_q is thereafter defined as

$$X_n = \beta_q [L]^q \frac{[M]}{[M]_{tot}} \quad (1.235)$$

and can be calculated as a function of pH and ligand concentration (Box 1.17).

Box 1.17 The Np–C–O–H speciation diagram.

To illustrate the use of speciation diagrams, let us calculate the speciation diagram of neptunium, the most soluble of the actinides in the environment, considering hydrolysis and complexation by carbonate ligands in groundwater. Neptunium is found under numerous forms in solution depending on conditions of redox potential, pH, and carbonate concentrations: Np^{3+} , Np^{4+} , NpO_2^+ , NpO_2^{2+} , $NpO_2(OH)_4^{2-}$, $Np(OH)_3^{3+}$, $Np(OH)_2^{2+}$, $Np(OH)_4(aq)$, $NpO_2OH(aq)$, $NpO_2(OH)_2^-$, NpO_2OH^+ , $(NpO_2)_2(OH)_2^{2+}$, $(NpO_2)_3(OH)_5^+$, $NpOH^{2+}$, $NpO_2(OH)_3^-$, $NpO_2CO_3(aq)$, $NpO_2CO_3^-$, $NpO_2(CO_3)_2^{3-}$, $NpO_2(CO_3)_3^{4-}$, $Np(CO_3)_4^{4-}$, $NpO_2(CO_3)_3^{5-}$, $Np(CO_3)_5^{6-}$, $Np(CO_3)_3^{3-}$, $(NpO_2)_3(CO_3)_6^-$, $NpO_2(CO_3)_2OH^{4-}$, $(NpO_2)_2CO_3(OH)_3^-$. It can also precipitate in the form of $NpO_2OH(am)$, $NpO_2(am, hyd)$, $NpO_2(OH)_2 \cdot H_2O(cr)$, $NpO_2CO_3(cr)$. The formation constants of the hydroxo, carbonate, and hydroxocarbonate complexes have recently been reviewed by the Thermochemical Database team [80] and used herein for the speciation calculations.

The concentration of the actinides in natural waters are typically of the order of $10^{-6} M$ or lower, pH conditions are in the range $pH = 5-9$, and carbonate concentrations are expected to be in the range $10^{-5}-10^{-3} M$ in surface waters, but $10^{-2} M$ or higher in groundwater [due to the increased $CO_2(g)$ partial pressure]. The relationship between carbonate concentration, pH and $CO_2(g)$ partial pressure is given by the following equation as explained in detail in Box 1.14:

$$\log [CO_3^{2-}] = 2pH - 18.155 + \log P_{CO_2} \quad (1.xlix)$$

The speciation diagram in Fig. 1.16 was calculated as a function of pH for a total neptunium concentration of $10^{-6} M$, a $CO_2(g)$ partial pressure of 3×10^{-4} bar, and a redox potential of 500 mV, which are conditions that could be expected in surface waters (rain, streams, lakes, and oceans). The precipitation of solid phases was discarded for the calculation. As reported in the literature [77], $Np(V)O_2^+$ is the dominant species in natural waters.

(Continued)

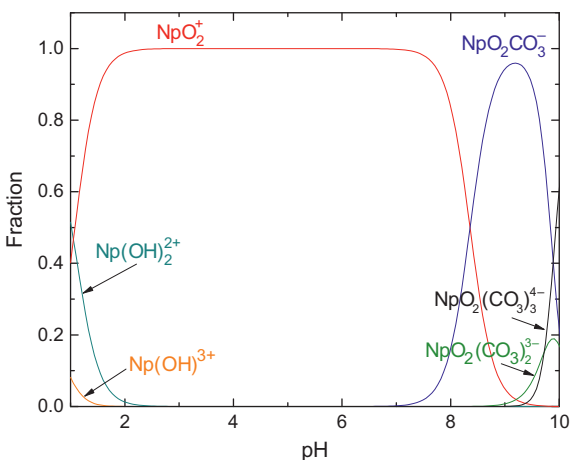
Box 1.17 (cont'd)

Figure 1.16 Distribution of neptunium species as a function of pH in natural water, for a total neptunium concentration of 10^{-6} M, a redox potential of 500 mV, and a $\text{CO}_2(\text{g})$ partial pressure of 3×10^{-4} bar, representative of surface conditions. The speciation diagram was calculated using the thermodynamic data critically assessed by Ref. [80].

1.9 Conclusion

The behavior of nuclear fuel at each stage of the fuel cycle depends on four key parameters: temperature, composition, chemical potential, and reaction rates as illustrated in this chapter. Chemical kinetics and thermodynamics are able to predict how the system evolves given a specific set of those conditions. The measurement of key nuclear materials properties (i.e., enthalpy of formation, entropy, heat capacity, complex formation constants and solubility products, phase diagram equilibria, and chemical rate constants) can be challenging due to (1) the complexity of the investigated systems adopting multiple oxidation states, (2) the radioactive nature of the materials, (3) the high temperatures involved, etc. (Chapter 2). Those are, nevertheless, essential to serve as input for the development of CALPHAD-based thermodynamic models and kinetic models, and to benchmark the results of modeling and simulation tools (Chapter 3). The key concepts presented herein form the base of our understanding of the nuclear fuel chemistry and will be encountered at several occasions in the subsequent chapters of this book treating specifics aspects of the fuel cycle.

Acknowledgment

The authors would like to acknowledge Dr. Xavi Gaona (Karlsruhe Institute of Technology KIT, Institute for Nuclear Waste Disposal INE, Karlsruhe, Germany) for the fruitful discussions on the thermodynamics of the $\text{Np}-\text{C}-\text{O}-\text{H}$ system. They are also very grateful to Dr. Caroline Toffolon-Masclet, and Dr. Emily Corcoran and Dr. Andrew Bergeron for sharing their CALPHAD assessments of the Zr-Sn and Th-O systems, respectively.

References

- [1] R.J.M. Konings, O. Beneš, J.-C. Griveau, Chapter 2.01: The actinide elements: properties and characteristics, *Comprehensive Nuclear Materials*, vol. 2, Elsevier, 2012, pp. 1–20.
- [2] P.D. Scott, D. Glasser, M.J. Nicol, Kinetics of dissolution of β -uranium trioxide in acid and carbonate solutions, *J. Chem. Soc., Dalton Trans.* 20 (1977) 1939–1946.
- [3] T.R. Allen, R.J.M. Konings, A.T. Motta, Chapter 5.03: Corrosion and hydriding of zirconium alloys, *Comprehensive Nuclear Materials*, vol. 5, Elsevier, 2012, pp. 49–68.
- [4] S. Kass, Aqueous corrosion of the zircaloys at low temperatures, *J. Nucl. Mater.* 28 (1969) 315–321.
- [5] E. Hillner, D.G. Franklin, J.D. Smee, Long-term corrosion of Zircaloy before and after irradiation, *J. Nucl. Mater.* 278 (2000) 334–345.
- [6] H.L. Lukas, S.G. Fries, B. Sundman, *Computational Thermodynamics: The Calphad Method*, Cambridge University Press, New York, 2007.
- [7] M.W. Chase, *NIST-JANAF Thermochemical Tables*, fourth ed., American Chemical Society, American Institute of Physics, National Bureau of Standards, 1998.
- [8] M. Tourasse, M. Boidron, B. Pasquet, Fission product behaviour in Phenix fuel pins at high burnup, *J. Nucl. Mater.* 188 (1992) 49–57.
- [9] J.-C. Dumas, Etude des conditions de formation du Joint-Oxyde-Gaine dans les combustibles oxydes mixtes des réacteurs à neutrons rapides, observations et proposition d'un modèle de comportement des produits de fission volatils (Ph.D. thesis), Institut National Polytechnique de Grenoble, Grenoble, France, 1995.
- [10] T.N. Pham Thi, Caractérisation et modélisation du comportement thermodynamique du combustible RNR-Na sous irradiation (Ph.D. thesis), Ecole Doctorale Physique et Sciences de la Matière, Aix-Marseille University, France, 2014.
- [11] W. Hemminger, G. Höhne (Eds.), *Calorimetry. Fundamentals and Practice*, Verlag Chemie, 1984.
- [12] P.A.G. O'Hare, *Combustion calorimetry, Characterization of Materials*, vols. 1 and 2, John Wiley & Sons, Inc., Hoboken, NJ, 2003.
- [13] J.K. Grime (Ed.), *Analytical Solution Calorimetry*, John Wiley & Sons, 1985.
- [14] K.N. Marsh, P.A.G. O'Hare, *Solution Calorimetry. Experimental Thermodynamics*, vol. IV, International Union of Pure and Applied Chemistry, Cambridge, 1994.
- [15] E.J. Huber Jr., C.E. Holley Jr., Enthalpy of formation of neptunium dioxide, *J. Chem. Eng. Data* 13 (4) (1968) 545–546.
- [16] I. Wadso, Appendix 4. Article describing calorimetric calculation methods, in: Reprint from Science Tools, vol. 13, LKB-Produkter AB, 1966, pp. 33–39.
- [17] E.H.P. Cordfunke, W. Ouweltjes, G. Prins, Standard enthalpies of formation of uranium compounds. XIII. Cs_2UO_4 , *J. Chem. Thermodyn.* 18 (1986) 503–509.
- [18] R. Guillaumont, T. Fanghanel, J. Fugér, I. Grenthe, V. Neck, D.A. Palmer, et al., Update on the Chemical Thermodynamics of Uranium, Neptunium, Plutonium, Americium & Technetium, Organisation for Economic Cooperation and Development (OECD) Nuclear Energy Agency (NEA), Data Bank, 2003.
- [19] D.D. Wagman, W.H. Evans, V.B. Parker, R.H. Schumm, I. Halow, S.M. Balley, et al., The NBS Tables of Chemical Thermodynamic Properties: Selected Values for Inorganic and C1 and C2 Organic Substances in SI Units, American Chemical Society and the American Institute of Physics for the National Bureau of Standards, 1982.
- [20] J.D. Cox, D.D. Wagman, V.A. Medvedev, *CODATA Key Values for Thermodynamics*, Hemisphere Publishing Corp, 1998.

- [21] R.A. Swalin, Thermodynamics of Solids, second ed., John Wiley & Sons, Inc, 1972.
- [22] S. Stølen, T. Grande, N.L. Allan, Chemical Thermodynamics of Materials, John Wiley & Sons, Ltd, 2004.
- [23] C. Kittel, Introduction to Solid State Physics, 8th ed., John Wiley & Sons, Inc, 2005.
- [24] Y.A. Chang, W.A. Oates, Materials Thermodynamics, John Wiley & Sons, Inc, 2010.
- [25] Q. Shi, L. Zhang, M.E. Schlesinger, J. Boerio-Goates, B.F. Woodfield, Low temperature heat capacity study of $\text{Fe}(\text{PO}_3)_3$ and $\text{Fe}_2\text{P}_2\text{O}_7$, *J. Chem. Thermodyn.* 61 (2013) 51–57.
- [26] Q. Shi, L. Zhang, M.E. Schlesinger, J. Boerio-Goates, B.F. Woodfield, Low temperature heat capacity study of FePO_4 and $\text{Fe}_3(\text{P}_2\text{O}_7)_2$, *J. Chem. Thermodyn.* 62 (2013) 35–42.
- [27] Q. Shi, L. Zhang, M.E. Schlesinger, J. Boerio-Goates, B.F. Woodfield, Low temperature heat capacity study of Fe_3PO_7 and $\text{Fe}_4(\text{P}_2\text{O}_7)_3$, *J. Chem. Thermodyn.* 62 (2013) 86–91.
- [28] B.F. Woodfield, J. Boerio-Goates, J.L. Shapiro, R.L. Putnam, A. Navrotsky, Molar heat capacity and thermodynamic functions of zirconolite $\text{CaZrTi}_2\text{O}_7$, *J. Chem. Thermodyn.* 31 (1999) 245–253.
- [29] B.F. Woodfield, J.L. Shapiro, R. Stevens, J. Boerio-Goates, R.L. Putnam, K.B. Helean, et al., Molar heat capacity and thermodynamic functions for CaTiO_3 , *J. Chem. Thermodyn.* 31 (1999) 1573–1583.
- [30] A.L. Smith, G. Kauric, L. van Eijck, K. Goubitz, G. Wallez, J.-C. Griveau, et al., Structural and thermodynamic study of dicesium molybdate $\text{Cs}_2\text{Mo}_2\text{O}_7$: implications for fast neutron reactors, *J. Solid State Chem.* 253 (2017) 89–102.
- [31] A.L. Smith, J.-C. Griveau, E. Colineau, P.E. Raison, G. Wallez, R.J.M. Konings, Low temperature heat capacity of Na_4UO_5 and Na_4NpO_5 , *J. Chem. Thermodyn.* 91 (2015) 245–255.
- [32] J. Majzlan, A. Navrotsky, B.F. Woodfield, B.E. Lang, J. Boerio-Goates, R.A. Fisher, Phonon, spin-wave, and defect contributions to the low temperature specific heat of $\alpha\text{-FeOOH}$, *J. Low Temp. Phys.* 130 (1–2) (2003) 69–76.
- [33] E.S. Gopal, Specific Heats at Low Temperatures, Plenum Press, New York, 1966.
- [34] E.F. Westrum, Lattice and Schottky contributions to the morphology of lanthanide heat capacities, *J. Chem. Thermodyn.* 15 (1983) 305–325.
- [35] W.G. Lyon, D.W. Osborne, H.E. Flotow, H.R. Hoekstra, Sodium uranium(V) trioxide, NaUO_3 : heat capacity and thermodynamic properties from 5 to 350 K, *J. Chem. Thermodyn.* 9 (1977) 201.
- [36] S. Van den Berghe, A. Leenaers, C. Ritter, Antiferromagnetism in MUO_3 ($\text{M} = \text{Na, K, Rb}$) studied by neutron diffraction, *J. Solid State Chem.* 177 (2004) 2231.
- [37] C. Miyake, K. Fuji, S. Imoto, An anomaly in the magnetic susceptibility of NaUO_3 , *Chem. Phys. Lett.* 46 (1977) 349.
- [38] C. Miyake, M. Kanamaru, H. Anada, S. Imoto, Neutron diffraction studies of NaUO_3 , *J. Nucl. Sci. Technol.* 22 (1985) 653.
- [39] V.A. Arkhipov, E.A. Gutina, V.N. Dobretsov, V.A. Ustinov, Enthalpy of heat capacity of neptunium dioxide at 350–1100 K, *Sov. Radiochem.* 16 (1974) 123.
- [40] T. Nishi, A. Itoh, M. Takano, M. Numata, M. Akabori, Y. Arai, et al., Thermal conductivity of neptunium dioxide, *J. Nucl. Mater.* 376 (2008) 78–82.
- [41] O. Beneš, P. Gotcu, F. Schwörer, R.J.M. Konings, T. Fanghänel, The high temperature heat capacity of NpO_2 , *J. Chem. Thermodyn.* 43 (2011) 651.
- [42] E.F. Westrum Jr., J.B. Hatcher, D.W. Osborne, The entropy and low temperature heat capacity of neptunium dioxide, *J. Chem. Phys.* 21 (1953) 419.

- [43] E. Capelli, O. Beneš, R.J.M. Konings, Thermodynamic assessment of the LiF-NaF-BeF₂-ThF₄-UF₄ system, *J. Nucl. Mater.* 449 (2014) 111.
- [44] F. C. Andrews, Equilibrium Statistical Mechanics. Second Edition. John Wiley & Sons, 1975.
- [45] J.P. Aldridge, E.G. Brock, H. Filip, H. Flicker, K. Fox, H.W. Galbraith, et al., Measurement and analysis of the infrared-active stretching fundamental (ν_3) of UF₆, *J. Chem. Phys.* 83 (1985) 34.
- [46] J.E. Mayer, M.G. Mayer, Statistical Mechanics, John Wiley & Sons, New York, 1940.
- [47] K.S. Pitzer, W.D. Gwinn, *J. Chem. Phys.* 10 (1942) 428.
- [48] L.V. Gurvich, I.V. Veyts, C.B. Alcock (Eds.), Thermodynamic Properties of Individual Substances, vol. I, Hemisphere, New York, 1991.
- [49] P. Lafaye, C. Toffolon-Masclet, J.-C. Crivello, J.-M. Joubert, Experimental investigations and thermodynamic modelling of the Cr-Nb-Sn-Zr system, *Calphad* 64 (2019) 43–54.
- [50] E. Capelli, O. Beneš, R.J.M. Konings, Thermodynamic assessment of the LiF-ThF₄-PuF₃-UF₄ system, *J. Nucl. Mater.* 462 (2015) 43–53.
- [51] A. Bergeron, D. Manara, O. Beneš, R. Eloirdi, M.H.A. Piro, E.C. Corcoran, Thermodynamic modelling of thoria-urania and thorium-plutonia fuels: description of the Th-U-Pu-O quaternary system, *J. Nucl. Mater.* 512 (2018) 324–348.
- [52] R.J.M. Konings, O. Beneš, A. Kovács, D. Manara, D. Sedmidubský, L. Gorokhov, et al., The thermodynamic properties of the f-elements and their compounds. Part 2. The lanthanide and actinide oxides, *J. Phys. Chem. Ref. Data* 43 (2014) 013101.
- [53] C. Guéneau, N. Dupin, B. Sundman, C. Martial, J.-C. Dumas, S. Gosse, et al., Thermodynamic modelling of advanced oxide and carbide nuclear fuels: description of the U-Pu-O-C systems, *J. Nucl. Mater.* 419 (2011) 145–167.
- [54] A.L. Smith, J.-Y. Colle, O. Beneš, R.J.M. Konings, B. Sundman, C. Guéneau, Thermodynamic assessment of the neptunium–oxygen system: mass spectrometric studies and thermodynamic modelling, *J. Chem. Thermodyn.* 103 (2016) 257–275.
- [55] E. Epifano, C. Guéneau, R.C. Belin, R. Vauchy, F. Lebreton, J.-C. Richaud, et al., Insight into the Am-O phase equilibria: a thermodynamic study coupling high-temperature XRD and CALPHAD modeling, *Inorg. Chem.* 56 (13) (2017) 7416–7432.
- [56] N.I. Ionov, Ionisation of KI, NaI and CsCl molecules by electrons, *Dokl. Akad. Nauk SSSR* 59 (1948) 467–469.
- [57] R.E. Honig, Sublimation studies of silicon in the mass spectrometer, *J. Chem. Phys.* 22 (1954) 126.
- [58] W.A. Chupka, M.G. Inghram, Investigation of the heat of vaporization of carbon, *J. Chem. Phys.* 21 (1953) 371–372.
- [59] W.A. Chupka, M.G. Inghram, Direct determination of the heat of sublimation of carbon with the mass spectrometer, *J. Chem. Phys.* 59 (2) (1955) 100–104.
- [60] M. Miller, K. Armatys, Twenty years of Knudsen effusion mass spectrometry: studies performed in the period 1990–2010, *Open Thermodyn. J.* 7 (2013) 2–9.
- [61] J. Drowart, C. Chatillon, J. Hastie, D. Bonnell, High-temperature mass spectrometry: instrumental techniques, ionization cross-sections, pressure measurements and thermodynamic data (IUPAC technical report), *Pure Appl. Chem.* 77 (4) (2005) 683–737.
- [62] C. Younès, Contribution à l'étude thermodynamique par spectrométrie de masse à haute température des oxydes MO_{2-x} [M = U, (U, La), (La, Ce), (La, Ce, Y), (U, Ce)], (Ph.D. thesis), Université de Paris-Sud, Centre d'Orsay, France, 1986.
- [63] M. Knudsen, Die Gesetze der Molekularströmung und der inneren Reibungsströmung der Gase durch Röhren, *Ann. Phys.* 29 (1909) 75–130.

- [64] A. Pattoret, Etudes thermodynamiques par spectrométrie de masse sur les systèmes uranium-oxygène et uranium-carbone (Ph.D. thesis), Université Libre de Bruxelles, Bruxelles, Belgique, 1969.
- [65] M. Heyrman, C. Chatillon, A. Pisch, Congruent vaporization properties as a tool for critical assessment of thermodynamic data. The case of gaseous molecules in the La-O and Y-O systems, *Calphad* 28 (2004) 49–63.
- [66] E.H.P. Cordfunke, R.J.M. Konings, *Thermochemical Data for Reactor Materials and Fission Products*, North Holland, 1990.
- [67] I. Johnson, Mass spectrometric study of the vaporization of cesium and sodium molybdates, *J. Phys. Chem.* 79 (7) (1975) 722–726.
- [68] M. Yamawaki, T. Oka, M. Yasumoto, H. Sakurai, Thermodynamics of vaporization of cesium molybdate by means of mass spectrometry, *J. Phys. Chem.* 201 (1993) 257–260.
- [69] R.P. Tangri, V. Venugopal, D.K. Bose, M. Sundaresan, Thermodynamics of vaporisation of caesium molybdate, *J. Nucl. Mater.* 167 (1989) 127–131.
- [70] A.L. Smith, M.-C. Pignie, L. van Eijck, J.-C. Griveau, E. Colineau, R.J.M. Konings, Thermodynamic study of $\text{Cs}_3\text{Na}(\text{MoO}_4)_2$: determination of the standard enthalpy of formation and standard entropy at 298.15 K, *J. Chem. Thermodyn.* 120 (2018) 205–216.
- [71] H. Kleykamp, The chemical state of the fission products in oxide fuels, *J. Nucl. Mater.* 131 (1985) 221–246.
- [72] Y. Guerin, Chapter 2.21: Fuel performance of fast spectrum oxide fuel, *Comprehensive Nuclear Materials*, vol. 2, Elsevier, 2012, pp. 548–578.
- [73] R.C. Ewing, Long-term storage of spent nuclear fuel, *Nat. Mater.* 14 (2015) 252–257.
- [74] J. Rydberg, C. Ekberg, G. Choppin, J.-O. Liljenzin, *Radiochemistry and Nuclear Chemistry*, fourth ed., Elsevier, 2013.
- [75] K. Maher, J.R. Bargar, G.E. Brown Jr., Environmental speciation of actinides, *Inorg. Chem.* 52 (2014) 3510–3532.
- [76] W. Runde, The chemical interactions of actinides in the environment, *Los Alamos Sci.* 26 (2000) 392–411.
- [77] G.R. Choppin, Actinide speciation in the environment, *J. Radioanal. Nucl. Chem.* 273 (3) (2007) 695–703.
- [78] L.G. Sillén, A.E. Martell, Special Publication, No. 17 Stability Constants of Metal Ion Complexes, Chemical Society, London, 1964p. 754.
- [79] L.G. Sillén, A.E. Martell, Stability constants of metal ion complexes. Suppl. No. 1, Special Publication, No. 25 Chemical Society, London, 1971, p. 865.
- [80] I. Grenthe, X. Gaona, A. Plyasunov, L. Rao, W. Runde, B. Grambow, R.J.M. Konings, A.L. Smith, E. Moor, Second Update on the Chemical Thermodynamics of Uranium, Neptunium, Plutonium, Americium and Technetium. Chemical Thermodynamics, Volume 14. OECD Nuclear Energy Agency. OECD Publications, Paris, France (in press).

Further reading

R.J. Lemire, J. Fuger, H. Nitsche, P. Potter, M.H. Rand, J. Rydberg, et al., Chemical thermodynamics of neptunium and plutonium, in: Organisation for Economic Cooperation and Development (OECD) Nuclear Energy Agency (NEA), Data Bank, 2001.

Experimental methods

2

Dario Manara, Alice Seibert, Thomas Gouder, Ondřej Beneš,
Laura Martel, Jean-Yves Colle, Jean-Christophe Griveau, Olaf Walter,
Andrea Cambriani, Oliver Dieste Blanco, Dragos Staicu, Thierry Wiss
and Jean-François Vigier

European Commission, Joint Research Centre, Nuclear Safety and Security Directorate,
Karlsruhe, Germany

2.1 Introduction

A broad spectrum of experimental techniques has been applied to the investigation of nuclear fuel chemical properties in the last 70 years. It is a difficult, if ever possible, task to summarize them all in a single publication. The present chapter has the ambition to provide a nonexhaustive, but still comprehensive, overview of the experimental methods most commonly used for the investigation of various nuclear fuel chemical properties. Every technique is briefly explained, including its physical background and, when possible, its main uncertainty sources. Some example results of its application to nuclear fuel analyses are reported.

Since 2000, the nuclear technical and scientific community has expressed renewed interest in various kinds of nuclear fuels, different than the uranium/plutonium dioxides prevalently used in industry. Minor actinoid-containing oxides, molten fluoride salts, metallic, carbide, and nitride fuels have been the object of studies as fuels for “Generation 4” [1] nuclear energy–production systems. The investigation of these kinds of fuels has led to the development or further upgrade of analytical techniques, which are nowadays more and more commonly used for the study of various types of nuclear fuels.

Experimental methods are classified in this chapter according to their physical nature: thermal analysis, mass spectrometry (MS), spectroscopy, and diffraction. Examples of existing facilities usable for radioactive materials and some of their applications to nuclear fuels are reported for each technique whenever possible.

Table 2.1 summarizes the various modern analytical techniques available for the investigation of various types of nuclear fuels. The list is obviously not exhaustive and is being continuously updated; therefore the current version might appear outdated to some readers. Nonetheless, it can be used as a useful starting point for the experimental researcher.

Hopefully, the present chapter will serve the reader as a sort of an early approach reference for the choice of the most suitable experimental techniques for the

Table 2.1 Current availability of analytical techniques for the chemical characterization of nuclear fuel.

Method/type of fuel	Oxide	Metal	Molten salt	Nitride	Carbide
Thermal analysis	I	I	MAP	I	I
Spectroscopy	I	I	NUT	I	I
Diffraction	I	I	I	I	I
Magnetic resonance	MAP	MAP	MAP	MAP	MAP
Mass spectrometry	I	I	I	I	I
Microscopy	I	I	I	I	I
Electrochemistry	I	I	I	I	I

I, Analysis possible on irradiated fuel; *MAP*, analysis possible only on unirradiated minor actinoids and plutonium; *NUT*, analysis available only on unirradiated natural uranium and thorium.

analysis of different kinds of materials or chemical properties. The numerous literature references reported at the end of this chapter will help the interested reader to better understand the individual techniques and their potential applications beyond the present concise description.

2.2 Thermal analysis methods

The fundamental premise of thermal analysis methods is the observation of the evolution of thermal properties of a sample as its temperature changes. The following subsections review several thermal analysis techniques, including differential scanning calorimetry (DSC), drop calorimetry, thermogravimetric analysis (TGA), and laser heating.

2.2.1 Differential scanning and drop calorimetry

2.2.1.1 Differential scanning calorimetry

DSC is a method to determine phase equilibrium data, melting points, enthalpies of transitions, enthalpies of mixing or heat capacity. The method is based on measuring a heat flow between the reference crucible and the sample crucible, which is filled with a sample while heating or cooling the whole detector at a given constant rate. The sample is typically constituted by a few tens of mg of powder or small fragments of a solid sample. A DSC sensor includes two crucible compartments surrounded by a series of thermocouples.

Melting point determination

Melting point determination using DSC is explained in Fig. 2.1 on a DSC output of NaF sample measurement performed at a constant heating rate of 5 K/min. The graph can be divided into three parts (A, B, and C), as indicated in the figure. Within section A the sample is constantly heated and since no phase transition occurs in the sample, the temperature in both crucibles (i.e., reference and sample compartment) constantly increases (*black curve*) and the monitored heat flux

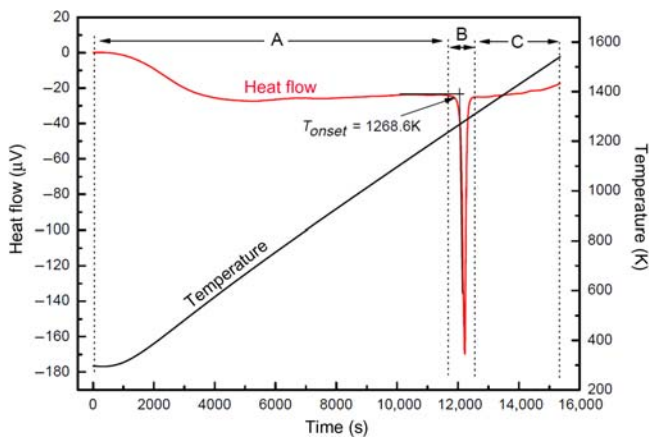


Figure 2.1 A DSC output of the melting temperature determination of the NaF compound. The red line is the heat flow between the reference and the measuring crucibles, whereas the black line corresponds to the temperature. *DSC*, Differential scanning calorimetry.

(red curve) between the crucibles is nearly constant. Slight curving appears at the beginning of the heat flux signal, which is a consequence of a nonstabilized heating rate occurring typically at the beginning of the sequence.

Once the melting temperature of NaF is reached, an additional amount of heat is consumed in order to melt the sample (i.e., the heat of fusion). Since the calorimeter is constantly increasing in temperature, the reference crucible follows this trend while the temperature of the crucible containing the sample is delayed leading to a thermal differential between two crucible compartments. At this stage, the heat is being delivered from the hotter (i.e., reference) crucible to the colder (i.e., sample) one and consequently the heat flow signal changes its slope resulting in a peak, as shown in section B of Fig. 2.1. From this peak the melting temperature is identified as the intersection of the linear extrapolation of the background before the peak and the first inflection tangent, as shown in Fig. 2.1.

After the phase transition is complete the heat flow signal is stabilized and is again characterized by a smooth line, as shown in section C of Fig. 2.1. It is important to note that the slope of the heat flow signal after the phase transition does not have to be the same as the slope prior to the transition. Its actual trend is highly dependent on the heat capacity of the measured material, which is usually different for different phases.

Phase equilibria in binary mixtures

In the previous section, it has been demonstrated that normally a sharp single peak is observed on a DSC heat flow curve upon melting of a pure component. When it comes to studies of binary (or higher order) phase diagrams, the DSC output becomes more complex, as the studied mixture may undergo several different equilibria. An example of such DSC output is demonstrated on the study of the LiF-PuF₃ pseudo-binary system [2] and particularly on two selected compositions: (1) a eutectic

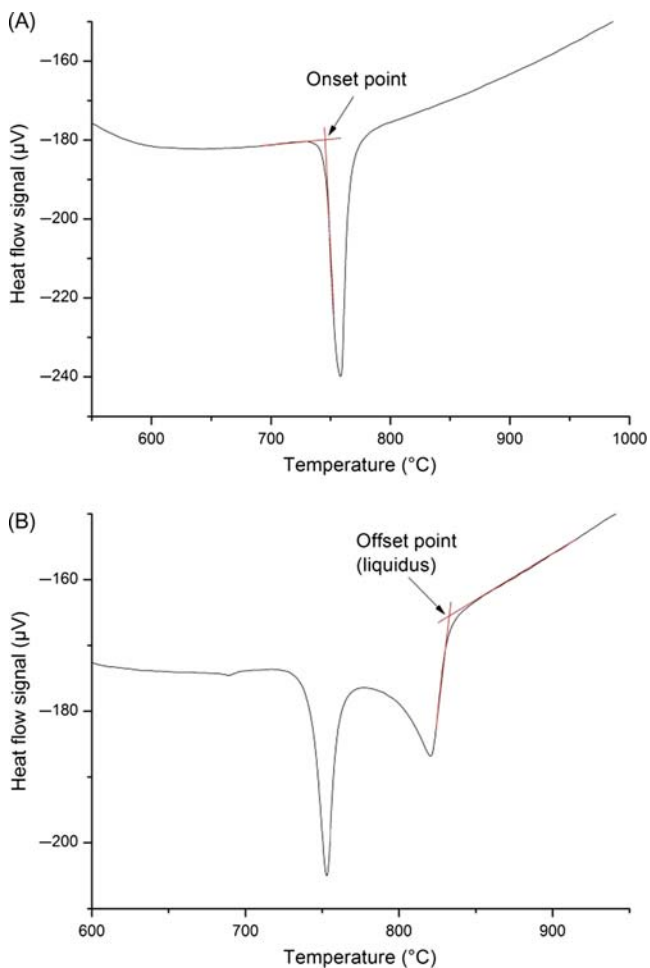


Figure 2.2 (A) Determination of the melting temperature of the eutectic composition LiF-PuF₃ (79–21 mol.%) and (B) determination of solidus and liquidus phase equilibria for LiF-PuF₃ (92.5–7.5 mol.%) mixture.

composition corresponding to LiF-PuF₃ (79–21 mol.%), and (2) a mixture of LiF-PuF₃ (92.5–7.5 mol.%) that is characterized by solidus and liquidus phase equilibria. Both outputs are shown in Fig. 2.2.

Since eutectic melting occurs at one single temperature, the DSC output has the same character as the one of melting of a pure component previously discussed and reveals one single peak, as shown in Fig. 2.2A. Similarly, the onset point determines the eutectic temperature, which is also indicated in Fig. 2.2A. A different DSC output, which is shown in Fig. 2.2B, is observed for the LiF-PuF₃ (92.5–7.5 mol.%) mixture, which reveals two peaks on the heat flow curve corresponding to noncongruent melting. The first sharp peak corresponds to a solidus

point, which in this case corresponds to the eutectic temperature. Since this is the point where the salt first melts upon heating, the solidus is identified from the onset point of the peak (the same way as indicated in Fig. 2.2A).

Enthalpy of transition

Enthalpy of transition is determined from the DSC heat flow curve by integrating the associated peak. Taking the example of the melting point measurement of pure NaF in Fig. 2.1, the area of the peak corresponds to the enthalpy of fusion of NaF. To quantify the area (i.e., to convert the value into energy units), calibration of the device must be made. This can be done either in a separate measurement using a reference material and melting of well-known metals of high purity is used or putting an internal standard into a reference crucible [3]. In both cases a correction for the temperature measurement must be made as the instrument can be quite sensitive (i.e., the ratio between the Joule's effect and the heat flow area changes with temperature, as discussed in Section 2.2.1.2).

Enthalpy of mixing

The principle of the experimental method to measure mixing enthalpies of liquid solutions using dynamic DSC runs is described by Capelli et al. [3] and is schematically shown in Fig. 2.3. Before the experiment, the end-members (in this case LiF and KF) were compressed into pellets and placed in the crucible. The compound with the lower melting point is placed on the bottom and the two salts are separated by a thin inert liner (in this case Ni plate) to avoid eutectic melting upon heating. The mixing occurs during the first heating cycle when the melting temperature of the lower melting temperature compound is reached. At this stage, the nickel separator sinks to the bottom of the crucible and the two salts come in contact with one another. The total enthalpy of this thermal event consists of three contributions: the fusion enthalpies of the two end-members and the enthalpy of mixing.

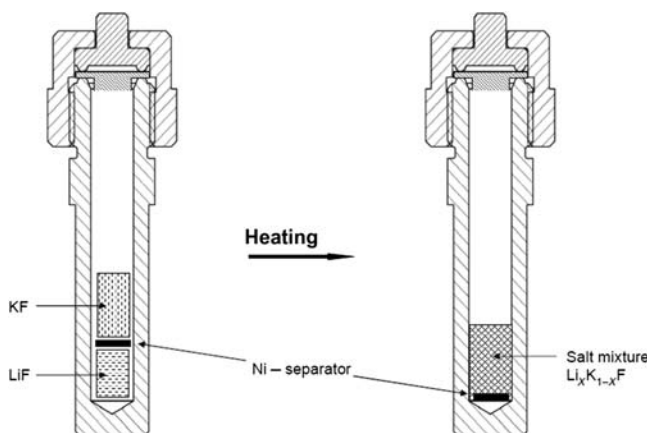


Figure 2.3 Schematic representation of the technique to measure the enthalpy of mixing [3].

It is therefore important to subtract the fusion contributions of both end-members from the total heat effect.

Heat capacity

DSC is widely used to measure the heat capacity and, as in the previous cases, is based on different heat flow between the reference and sample crucibles, which depends on heat capacity of the sample. Two methods are used: a continuous method and step method. Independent of the method employed, it is always necessary to perform three different measurements: (1) a run with an empty crucible to determine the background signal, (2) a run with a reference material to determine the relationship between the measured signal and heat capacity, and (3) the actual sample to be measured. From the latter two, it is always important to subtract the blank signal, and in all three cases, it is necessary to keep exactly the same experimental conditions (i.e., geometry, settings, gas flow, and temperature program).

Continuous method The continuous method is a faster way to identify heat capacity of measured material compared to the step method, but it is not necessarily more precise. This method consists of three measurements each of which contains three stages: (1) initial temperature stabilization, (2) heating sequence at constant rate, and (3) final temperature stabilization. From the three measurements the heat capacity is determined for every point measured as

$$C_p(\text{sample}) = C_p(\text{ref.}) \cdot \frac{m_{\text{ref.}} \cdot (\phi_{\text{sample}} - \phi_{\text{blank}})}{m_{\text{sample}} \cdot (\phi_{\text{ref.}} - \phi_{\text{blank}})} \quad (2.1)$$

where m refers to the mass of the reference or sample (indexed accordingly) and ϕ is the heat flow value for the respective experimental run (blank, reference, and sample).

Step method The step method is more time extensive compared to the continuous method but may result in higher precision measurements as it is based on an integral heat flow signal and not on direct comparison between the heat flow values. Each run consists of successive temperature increments (ΔT) performed at given heating rates. After each increment a stabilization period follows. The resulting heat capacity is determined for each of the increment as:

$$\bar{C}_p(\text{sample}) = C_p(\text{ref.}) \cdot \frac{m_{\text{ref.}} \cdot (A_{\text{sample}} - A_{\text{blank}})}{m_{\text{sample}} \cdot (A_{\text{ref.}} - A_{\text{blank}})} \quad (2.2)$$

in which A is the heat flow area value for the respective temperature increment done for respective experimental run (i.e., blank, reference, or sample). Note that the heat capacity value is thus determined by an average heat capacity assigned to the mean temperature of the incremental step.

2.2.1.2 Drop calorimetry

Drop calorimetry is a method to determine enthalpy increments of a sample that corresponds to an enthalpy change needed to heat a sample from an initial temperature (typically at room temperature) to a higher temperature determined by the experiment. Drop calorimetry can be as well applied to study enthalpies of formation by dropping a sample into an appropriate solvent while measuring the dissolution heat. During the experiment, the samples are dropped from the holder into the detector that is maintained at a given temperature keeping a constant heat flow signal between the measuring and the reference crucibles.

Prior to each drop, the ambient temperature is exactly measured. When the sample reaches the sensor, an additional amount of heat is brought into the system in order to maintain the predefined temperature. Consequently, the heat flow signal that is monitored in μV by a thermocouple(s) and is a function of time, resulting in a peak whose area is proportional to the total enthalpy increment of the material. Several individual drops are made during a measuring sequence, which are separated by an adequate time interval, which is needed to restabilize the temperature and heat flow signals. A typical time for signal restabilization using a Setaram device (MDHTC-96 type) shown in Fig. 2.4 is about 20 minutes. Since the drop method is

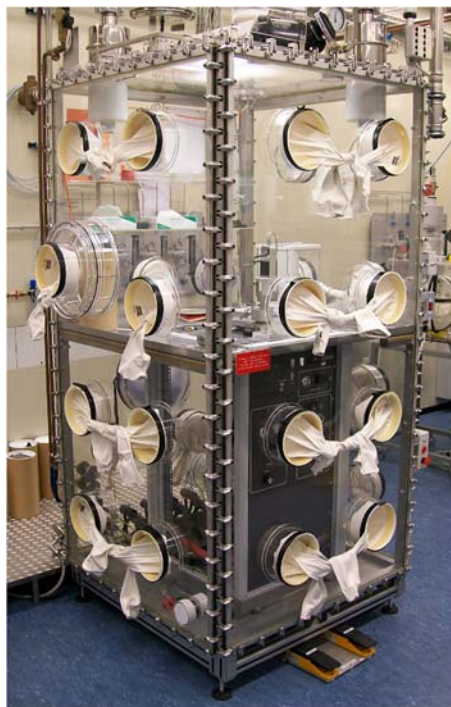


Figure 2.4 Setaram multi-detector high-temperature calorimeter (MDHTC-96 type) installed within a glove box for handling actinoid-containing materials.

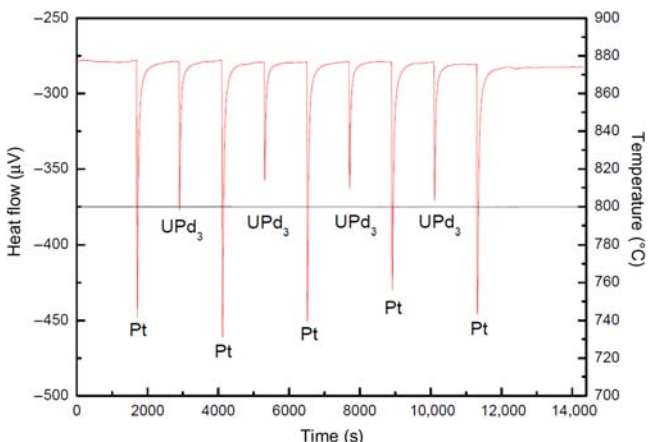


Figure 2.5 An example of a drop measurement. Red curve represents heat flow signal (read on left axis) and black line is the temperature (reads on the right axis).

Source: Taken from O. Beneš, R. Jardin, R.J.M. Konings, E. Colineau, F. Wastin, N. Magnani, The high-temperature heat capacity of ThPd₃ and UPd₃, *J. Chem. Thermodyn.* 41 (2009) 560–563 [4].

relative, it is necessary during each experiment to simultaneously measure a standard material with a known heat capacity. Therefore, each measurement consists of several consecutive drops of the unknown sample and the reference material.

An example of a typical measuring sequence is shown in Fig. 2.5, which represents the enthalpy increment measurement of a UPd₃ sample at 1073 K [4] with pure platinum metal as a reference material. The reference material drops the sensitivity, S , of the calorimeter, which is a measure between the heat flow peak area, $\int_{t_1}^{t_2} \phi_R dt$, and the respective enthalpy increment, and is determined as:

$$S = \frac{\int_{t_1}^{t_2} \phi_R dt}{\int_{T_a}^{T_m} C_{p,R}(T) dT} \cdot \frac{MW_R}{mw_R} \quad (2.3)$$

with MW_R and mw_R as molar weight and mass of reference material, respectively, and $C_{p,R}(T)$ is the molar heat capacity. T_a and T_m represent the ambient and measuring detector temperatures, respectively, the latter being evaluated as an average from the stable values before and after the drop. The sensitivity of a calorimeter is temperature dependent and is related to the type of thermocouple(s) used for measuring the heat flow signal.

For commonly used platinum-based thermocouples (e.g., S- or B-types), the sensitivity has low values at ambient or close to ambient temperatures but sharply increases with temperature. An example of such sensitivity with a type-S thermocouple is shown in Fig. 2.6, which shows a peak value around 1000°C. Each value is obtained from individual drop experiment performed at given temperature.

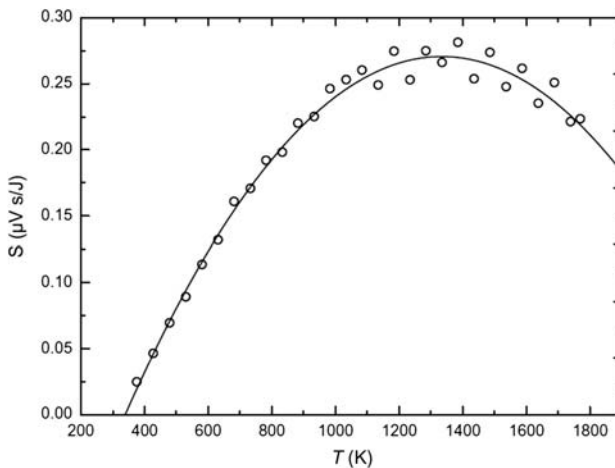


Figure 2.6 Sensitivity of a drop calorimeter with S-type thermocouple-based detector.

The enthalpy increment of the measured sample corresponding to heating from T_a to T_m is defined as:

$$\Delta_{T_a}^{T_m} H_m = \frac{\int_{t_1}^{t_2} \phi_R dt}{S} \cdot \frac{M_S}{m_S} \quad (2.4)$$

This is taken as an average value from the precedent and consecutive drops of the reference material. The area $\int_{t_1}^{t_2} \phi_R dt$ term is the heat flow corresponding to the sample drop, while M_S and m_S are molar weight, resp. mass of the sample.

2.2.2 Thermogravimetric analysis

Thermo-gravimetric analysis (TGA) consists of heat-treating a sample under a chemically reactive atmosphere and simultaneously measure its weight as precisely as possible. Weight changes entailed by the chemical reaction between the experimental atmosphere and the condensed sample are detected and related to the reaction process as a function of temperature [5]. If the sample chemical composition resulting from the thermogravimetric procedure is well determined, the initial sample composition, which is generally unknown, can be directly obtained from the total weight difference produced during the Thermogravimetric (TG) heat treatment. The chemical reactions occurring in the experimental chamber must therefore be well known in parallel to the thermogravimetric measurement. The final sample composition is generally easy to determine, as a stable compound is mostly produced during the TG heat treatment. It is therefore convenient to obtain the initial sample composition from the final one and the weight variation.

TG is the reference method for the determination of oxygen-to-metal (O/M) ratios for oxide nuclear fuels and for the oxygen potential determination in nuclear

fuels [6–8]. Typically, a powder sample of approximately 0.5 g, is placed in an inert crucible. The crucible is contained in a furnace where the powder is heat treated under an approximately $50 \text{ cm}^3/\text{s}$ air flow with temperature increasing by a few K/min up to approximately 1000 K. The crucible is fixed to a high-sensitivity analytical mass balance that allows *in situ* weighing of the powder during the reactive heating process. In most cases, a further reference crucible containing the same amount of an inert material is heated in parallel to the sample crucible, in order to define the buoyancy effect on the apparent thermogravimetric (i.e., weight vs time or temperature) curves.

Thermogravimetric measurements performed in an oxidizing atmosphere on stoichiometric and hyperstoichiometric uranium dioxide samples are shown, as an example, in Fig. 2.7 [9]. Similar measurements have been performed on mixed uranium–plutonium oxides, and on other types of fuels [6–8]. Of course, other stable oxides should be taken as final weight reference in different systems. Observing the thermogravimetric curves in this example, one can notice the occurrence of an intermediate weight arrest before definitive stabilization at a level corresponding to the final product. The nature of both the intermediate and the final oxidation products can be determined by X-ray diffraction (XRD)-analyzing small amounts (a few tens of mg) of the sample at the various stages of the heating process. In this particular example, the final stable oxide is U_3O_8 . The intermediate one corresponds to coexisting U_4O_9 and U_3O_7 phases. Therefore, the UO_2 air oxidation reaction proceeds in two steps: $\text{UO}_2 \rightarrow \text{U}_4\text{O}_9/\text{U}_3\text{O}_7 \rightarrow \text{U}_3\text{O}_8$. One can relate these phase changes with respect to the U–O phase diagram given in Chapter 5, Other power reactor fuels.

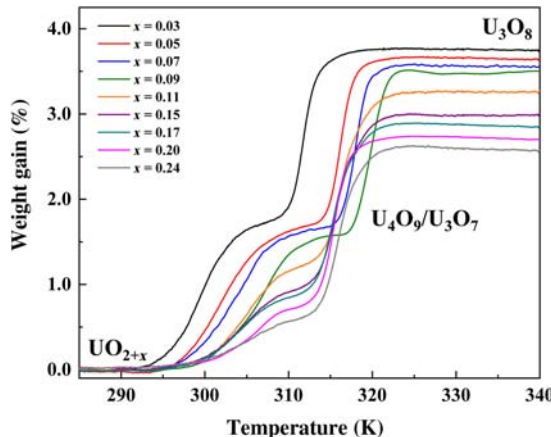


Figure 2.7 Thermogravimetric curves of UO_{2+x} samples oxidized in an air flow. The final material is U_3O_8 . The intermediate arrest in the weight versus time curve corresponds to the formation of intermediate oxides U_4O_9 and U_3O_7 .

Source: After J.M. Elorrieta, L.J. Bonales, N. Rodríguez-Villagra, V.G. Baonza, J. Cobos, A detailed Raman and X-ray study of UO_{2+x} oxides and related structure transitions, Phys. Chem. Chem. Phys. 18 (2016) 28209–28216 [9].

In order to obtain the initial sample composition, the total reaction occurring during the heating procedure can be written as follows:



From the weight difference measured between the initial and final powder, one can determine the initial composition through the following formula (assuming that all the weight change is due to oxidation only, as per reaction 2.5):

$$\frac{\Delta W}{W_i} = \frac{W_f - W_i}{W_i} = \frac{MW_{\text{UO}_{2.666}} - MW_{\text{UO}_{2+x}}}{MW_{\text{UO}_{2+x}}} \quad (2.6)$$

where W_i and W_f are the initial and final weights, and MW stands for “molar weight.”

From Eq. (2.6), one can get the formula that leads to x in UO_{2+x} from the measured $\Delta W/W$:

$$x = \frac{10.6556 - 270.0277(\Delta W/W)}{15.9994(\Delta W/W) + 15.9994}. \quad (2.7)$$

In Eq. (2.7), the molar mass of natural uranium has been used. An example procedure for uncertainty calculation based on the propagation of independent error sources is reported here for thermogravimetry. A similar procedure can be used for the other experimental techniques reported in this chapter. Although the TG procedure is rather straightforward, calculation of the uncertainty affecting the measured value of the initial sample composition can be tricky, depending on the complexity of the chemical reactions occurring during the TG heat treatment.

The instrumental uncertainty affecting the TG-measured value of the initial UO_{2+x} composition from its oxidation to U_3O_8 (i.e., reaction 2.5) is reported here. Uncertainty in the weight measured by the balance (δw) and uncertainty due to imprecision in the buoyancy correction (δb) constitute the main instrumental error sources affecting the measurement of $\Delta W/W_i$.

The error δw can be measured as by checking the stability and the reproducibility of the balance reading on the weight of standard samples. The buoyancy error consists of the apparent variation of weight of an empty-crucible heated from ambient temperature to 1000 K. Such an apparent weight difference is basically caused by fluctuating uncertainties in the equilibration of the gas fluxes in the balance and in the crucible chamber when the temperature of the crucible changes. By repeating several heating cycles on both empty crucibles and standard samples, the residual error in the measured weight difference can be established as δb .

To obtain the error in the composition x , one should use the relation between x and $\Delta W/W_i$ given by Eq. (2.7) and consider that $\delta x = (dx/dY)\delta Y$, with $Y = \Delta W/W_i$ in our case.

To obtain the uncertainty $\delta(\Delta W/W_i)$, one has to combine the reciprocally independent effects of δw and δb according to the error propagation law. In order to do that, one can consider the relative weight variation $\Delta W/W_i$ as a function of the independent variables W_f and W_i , as in Eq. (2.7). The uncertainty affecting W_i is δw . However, in determining the uncertainty affecting W_f , the buoyancy error should also be taken into account, whereby $\delta W_f = \sqrt{\delta w^2 + \delta b^2}$.

Similarly, for the uncertainty affecting $\Delta W/W_i$, one has

$$\delta\left(\frac{\Delta W}{W_i}\right) = \sqrt{A^2\delta W_i^2 + B^2\delta W_f^2} \quad (2.8)$$

The factors A and B are the partial derivatives of $\Delta W/W_i$ with respect to W_i and W_f , respectively,

$$A = \frac{\partial}{\partial W_i} \left(\frac{W_f - W_i}{W_i} \right) = -\frac{1}{W_i} - \frac{\Delta W}{W_i^2} \quad (2.9)$$

$$B = \frac{\partial}{\partial W_f} \left(\frac{W_f - W_i}{W_i} \right) = \frac{1}{W_i} \quad (2.10)$$

Substituting Eqs. (2.9) and (2.10) in Eq. (2.8) yields:

$$\delta\left(\frac{\Delta W}{W_i}\right) = \frac{1}{W_i} \sqrt{\left(2 + 2\frac{\Delta W}{W_i} + \left(\frac{\Delta W}{W_i}\right)^2\right)\delta w^2 + \delta b^2} \quad (2.11)$$

Once δw and δb are experimentally determined, Eq. (2.11) expresses the uncertainty connected to each TG measurement in terms of $\Delta W/W_i$ and W_i , which are the direct observables. Finally, substituting in Eq. (2.7) the expression obtained for $\delta(\Delta W/W_i)$ and differentiating x with respect to $\Delta W/W_i$, one obtains for the $\text{UO}_{2+x}/\text{U}_3\text{O}_8$ example:

$$\delta x = \frac{17.5433}{\left((\Delta W/W_i) + 1\right)^2} \frac{1}{W_i} \sqrt{\left(2 + 2\frac{\Delta W}{W_i} + \left(\frac{\Delta W}{W_i}\right)^2\right)\delta w^2 + \delta b^2} \quad (2.12)$$

As expected, Eq. (2.12) indicates that the error affecting the value of x obtained through TG measurements is reduced if the initial weight of the sample is increased. The effect of the weight change ΔW on the total uncertainty is, with good approximation, negligible. Substituting realistic values for δw and δb (order of 10^{-2} mg), and considering that in most of the measurements performed for the $\text{UO}_{2+x}/\text{U}_3\text{O}_8$ system the value of $\Delta W/W_i$ is around 3%, one obtains typical values of δx for TG-determined x in UO_{2+x} as $\delta x \approx \pm 0.005$ if $W \approx 100$ mg, whilst $\delta x \approx \pm 0.07$ if $W \approx 10$ mg.

2.2.3 Laser heating

Laser heating techniques employ a laser source to heat high-melting temperature materials. Very high temperatures (well beyond 2000 K, sometimes even exceeding 5000 K) are commonly attained in laser heating techniques, which are used for the study of physico-chemical properties (e.g., to measure noncongruent melting temperatures) under extreme conditions. Typical applications involving nuclear fuels are therefore related to the analysis of severe accidents in nuclear power plants, including core meltdown and corium formation [10]. Due to the extreme conditions produced in this kind of experiment (i.e., high temperature, massive vaporization, and melting), a typical problem of laser heating techniques is the nature of the sample holder, the atmosphere and pressure in the experimental chamber, and the duration of the heat treatments. In order to avoid high-temperature interaction between the hot sample and its containment, contacts between the investigated material and the holder are minimized.

Completely containerless conditions are ensured in levitation techniques. In other cases the laser-heated sample is held in place by small screws or pins made of a highly refractory material (e.g., graphite, tungsten, and molybdenum). If the sample is melted, the heat treatment duration is limited to a few seconds, although the melt can be held for a longer duration in levitation setups. Despite their short duration, thermodynamic equilibrium conditions are mostly guaranteed in the laser heat treatments by the very fast kinetics at such high temperatures. However, due to the surface heating nature of these techniques, sometimes homogeneous heating of the samples is not ensured, and further analysis, both experimental and theoretical, is needed in order to fully characterize and interpret laser-heated samples.

Two example laser heating facilities for the investigation of fresh nuclear fuels are reported here. In the laser heating and spectrometric analysis (LHASA - also known as Flash laser facility or "FLF") technique developed at JRC-Karlsruhe (see Fig. 2.8), a sample mounted in a controlled-atmosphere autoclave contained in an α -shielded glove box is heated by a 4.5 kW Nd:YAG continuous wave (CW) Laser (HLD4506, TRUMPF, Schramberg, Germany). Such a laser power is much larger than the typical power density needed to heat beyond melting oxide-based nuclear fuels. However, it permits the investigation of other kinds of materials such as ultra-refractory metals, carbides and nitrides (cf. [12–15]). Typically, this kind of laser heating test can be performed on a disk (or also fragment) of 3–15 mm in diameter and at least 2 mm thick. For nuclear fuels, such a sample usually weighs around 100 mg. These data should be taken into account when calculating the actual dose rate of a sample. Since the equipment available at JRC-Karlsruhe is only shielded for alpha-radiation, but not for gamma activity, the mass needed to perform a laser heating experiment limits the materials that can be analyzed by LHASA to actinoid-containing fresh fuels. The technique cannot be used for the investigation of irradiated fuels at JRC-Karlsruhe at the time of this publication.

Thermal radiation pyrometers measure the sample radiance, L_{ex} . This is the electromagnetic radiation power density per unit surface area, wavelength and solid

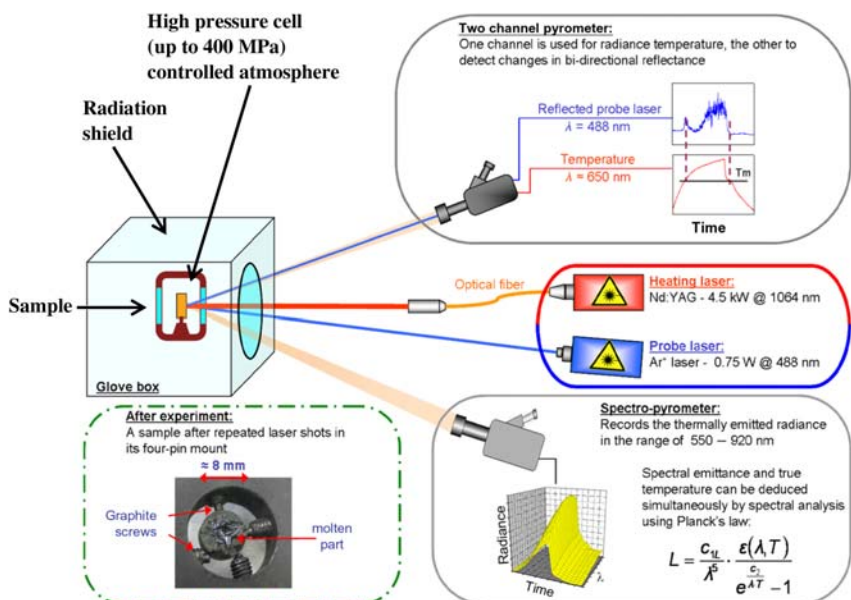


Figure 2.8 Schematic representation of the LHASA laser heating facility. *LHASA*, Laser heating and spectrometric analysis.

Source: After F. De Bruycker, K. Boboridis, P. Poeml, R. Eloirdi, J. Somers, R.J.M. Konings, et al., The melting behaviour of plutonium dioxide: a laser heating study, *J. Nucl. Mater.* 416 (2011) 166–172 [11].

angle emitted by the sample at a given temperature [16]. It is related to the sample surface temperature T through the modified Planck function:

$$L_\lambda = \frac{L_\lambda}{c_1} = \frac{1}{\lambda^5} \cdot \frac{\varepsilon_\lambda(T)}{e^{\frac{c_2}{\lambda T}} - 1} \quad (2.13)$$

where L_λ is the thermal radiative power; ε_λ is the temperature dependent spectral emissivity; c_1 is the $2 \cdot h \cdot c_0^2$ is the first radiation constant and c_2 is the $h \cdot c_0 \cdot k_B = 14,388 \mu\text{m K}$ is the second radiation constant; c_0 is the speed of light in vacuum; h is Planck's constant; and k_B is Boltzmann's constant. The spectral emissivity takes into account the fact that a real body will thermally radiate, at a given wavelength and temperature, only a fraction equal to ε_λ of the power emitted by an ideal blackbody at the same temperature. Therefore, ε_λ takes values between 0 and 1, whereby 1 corresponding to the ideal blackbody case for which Planck's law was derived. Since pyrometers in the present work were always set up near normal with respect to the sample surface, the angle dependence of ε_λ was not considered, and “emissivity” will always refer to normal spectral emissivity (NSE). The NSE must be determined in order to convert, through Eq. (2.13) and a pyrometer calibration procedure, L_λ into absolute temperature T .

The specimen temperature is detected using a fast pyrometer calibrated against standard lamps up to 2500 K at $\lambda = 655$ nm. An additional, 256-channel radiance spectro-pyrometer operating between 515 and 980 nm was employed for the study of the sample's thermal radiation emission, which yields essential information on some high-temperature optical properties of the material, and in particular on the NSE and its temperature dependence. Determination of the NSE (ε_λ) is possible by doing a nonlinear fit of the thermal emission spectrum with Eq. (2.13), T and ε_λ being the only two dependent variables. This approach has been demonstrated to be acceptably accurate in insulating refractory materials [17], like those usually present in a nuclear power plant, for which the NSE can be assumed to be wavelength-independent (gray body hypothesis) on a broad spectral range.

Once the temperature of the laser-heated sample is correctly measured as a function of time, thermal analysis can be performed on the resulting temperature–time curve, which is commonly referred to as a “thermogram.” Inflections or thermal arrests in the thermograms give information related to phase transitions (e.g., solidus, liquidus, and isothermal phase transformations). Moreover, besides being necessary to the NSE determination, direct spectral analysis of the radiance L_{ex} emitted by the hot sample also permits an *in situ* study of some optical properties of the studied surface. This constitutes a further supporting tool for the identification of high-temperature phenomena, such as phase transitions, chemical reactions between condensed material and gas phase, or segregation effects.

An additional technique called reflected light signal (RLS) analysis [18] is used to confirm phase transitions. It is conducted by using the second channel of the pyrometer tuned to a low-power (e.g., 1 W) Ar^+ laser (e.g., $\lambda = 488$ nm). This channel detects the laser beam originating from the Ar^+ cavity and reflected by the sample surface. A constant RLS signal indicates a solid surface while random oscillations appear after melting due to surface tension-induced vibrations on the sample liquid surface. This approach has been used for the investigation of several different kinds of unirradiated nuclear fuels, also containing large amounts of plutonium and minor actinides (e.g., neptunium and americium). Fig. 2.9 shows an example of laser heating analysis performed at JRC-Karlsruhe on PuO_2 [11].

Inflections or thermal arrests in the measured thermogram correspond to phase transformations. In the example of Fig. 2.9, a clear thermal arrest on the thermogram cooling flank reveals freezing of PuO_2 . Planck radiance spectra are also measured with the spectro-pyrometer at each full open circle in Fig. 2.9, whereby the sample NSE and temperature are obtained by fitting such spectra. In some cases, care should be taken to avoid confusing phase-transformation related thermal arrests with similar thermogram features rather due to a sample cracking or to other surface morphology changes. The difference can be easily revealed by checking the repeatability of thermogram features over successive laser heating cycles on the same sample, or on different specimens. Typically, four successive cycles of laser pulses separated by a short enough relaxation time to avoid the sample to cool to room temperature, but to remain at an intermediate temperature close to the lower pyrometer detection limit (1500 K approximately), creates ideal conditions to optimize the

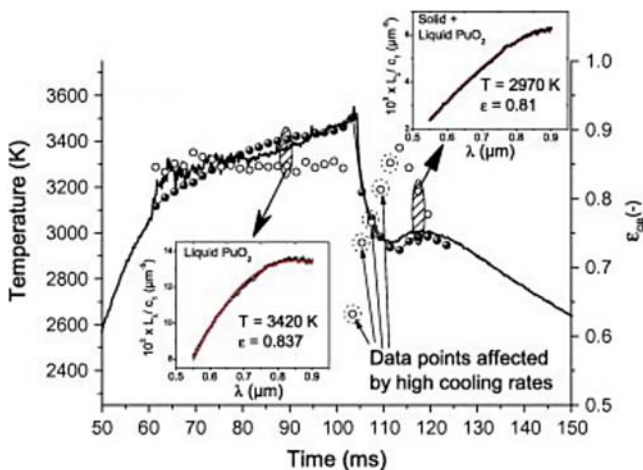


Figure 2.9 An example laser heating measurement performed at JRC-Karlsruhe on a PuO_2 sample [11].

sample mechanical stability by avoiding excessive thermal shocks. Moreover, such cycles permit a study of the thermogram feature repeatability. This is particularly useful in order to determine whether the phase transitions occur at thermodynamic equilibrium or if chemical reactions are occurring during the heating and cooling cycles (e.g., between the condensed phases and the autoclave atmosphere), which may result in a systematic evolution of the observed thermal inflections of arrests. Such an approach has been used in many cases, like, for example, in the study of high-temperature air oxidation of uranium-containing mixed oxides [17,19]. This kind of investigation shed important light on the phenomena that may occur in a nuclear power plant core overheating accident.

Another laser heating facility for the study of unirradiated nuclear fuels, which is limited to natural uranium and thorium compounds, is available at the Commissariat à l’Energie Atomique et aux Energies Alternatives CEA research center of Saclay (France). The advanced temperature and thermodynamic investigation by laser heating approach (ATTILHA) facility is based on a laser heating technique coupled with contactless or containerless temperature monitoring, obtained by aerodynamically levitating the sample [20,21]. A schematic of the ATTILHA setup is shown in Fig. 2.10. The sample is heated by means of a 250 W Coherent CO_2 laser emitting at $10.6 \mu\text{m}$ (*red line* in Fig. 2.10). The temperature is monitored by a bichromatic pyrometer (*blue dotted line*) and by a HgCdTe infrared (IR) detector (*yellow line*). Furthermore, a rapid IR camera (*green line*) is employed for temperature monitoring and to get useful spatial data on the melting and solidification of the investigated samples. Temperature gradients and emissivity variation during the experiments can be also observed.

Levitating the sample close to the output of the aluminum nozzle leads to a more stable sample position. In principle, any gas can be used for the levitation.

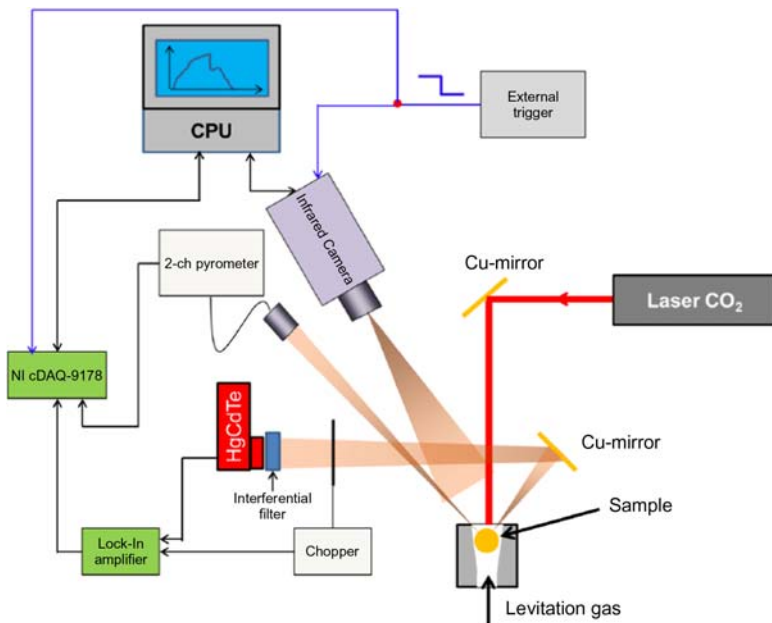


Figure 2.10 Schematic view of the ATTILHA setup in aerodynamic levitation configuration. ATTILHA, Advanced temperature and thermodynamic investigation by laser heating approach.

Source: After A. Quaini, Étude thermodynamique du corium en cuve – Application à l’interaction corium/béton (Ph.D. thesis), Université Grenoble-Alpes, 2014 [20].

Compressed air, Ar and Ar + 20% O₂ are typically used depending on the nature of the investigated sample. The pressure and the gas flow can be tuned.

During an experiment the sample’s thermophysical properties (e.g., density, surface tension, and viscosity) change as soon as the sample becomes liquid. The adjustable parameters allow reestablishing a stable levitation. ATTILHA presents all the advantages of a laser heating technique on an aerodynamically levitated sample: no contact between the sample and any containment, possibility to reach very high temperatures (> 2000 K) with a rather homogeneous distribution, broad variety of materials that can be studied, capability to study liquid samples. On the other hand, the technique can only be used for small spherical specimens (usually a couple of mm in diameter) displaying low radioactivity (no plutonium or minor actinides, no irradiated materials, a few mg of natural uranium or thorium). Developed in the last 5 years, ATTILHA has been used for the study of phase boundaries in prototypic corium subsystems, including miscibility gaps in the liquid phases [20,21].

The uncertainty affecting laser heating measurements can be calculated according to the error propagation law [18], taking into account the uncertainty associated with pyrometer calibration, emissivity determination, transmittance of the optical system, and sample composition/position stability. The estimated cumulative

uncertainty is mostly of the order of $\pm 1\%$ of the reported absolute temperatures in the worst cases, with a $1 - k$ coverage factor (corresponding to one standard deviation around the average value). The pyrometer calibration itself, defining the measurement temperature scale, is often affected by a nonnegligible uncertainty due to the lack of established primary temperature reference points beyond 2500 K, which implies the extrapolation of calibration curves over a broad temperature range.

Another important application of laser heating for the physicochemical characterization of nuclear fuels is the so-called LAser-Flash (LAF) technique. As an example, a shielded “laser-flash” device was designed and constructed at JRC-Karlsruhe for the measurement of thermal diffusivity, α , of highly γ -active samples [22], including nuclear fuels irradiated to high burn-up. These, in the form of a small disk or part of a disk weighing a few mg, are heated up to the measurement temperature in a high frequency furnace (Fig. 2.11). Thermal diffusivity is an essential heat transport parameter, which, combined with the sample’s heat capacity and density, yields the thermal conductivity. The latter is the fundamental material property governing heat transfer in a nuclear fuel element, hence the importance of the present LAF measurements.

A laser pulse is then applied to the front surface of the sample; the emerging temperature perturbation on the opposite surface is recorded by a photodiode-based pyrometer (0.05 K sensitivity) provided with a fast log-amplifier, and 24-bit A/D converter with a response time of the order of $10\ \mu\text{s}$. The recorded thermograms, consisting of several thousands of points, are analyzed by a realistic and accurate mathematical expression of the pulse propagation in the sample: α and various heat losses are calculated by a numerical fitting procedure followed by a self-consistency check of the fitting results. The precision of the α measurements is thus better than 5%.

The experiments are carried out for irradiated fuel samples with the aim of measuring α at increasing temperatures and of examining recovery effects after laboratory thermal annealing above the irradiation temperature. Thermal cycles are, therefore, applied corresponding to prefixed sequences of annealing temperatures up to $T_{ann} = 1550\ \text{K}$, a temperature at which radiation damage recovery processes are effectively completed, and gas and volatile fission product release takes place in concomitance with marked fuel swelling.

2.3 Spectroscopy techniques

A great variety of spectroscopic techniques are used for the chemical characterization of nuclear materials. Their common point is the observation of peculiar interaction features between the analyte and probe particles (generally photons or electrons, but not exclusively) in a given energy spectrum. The energy spectrum is defined by the nature of the probe particles and the interaction features define particular fingerprints by which the analyte can be chemically, and sometimes also physically, characterized.

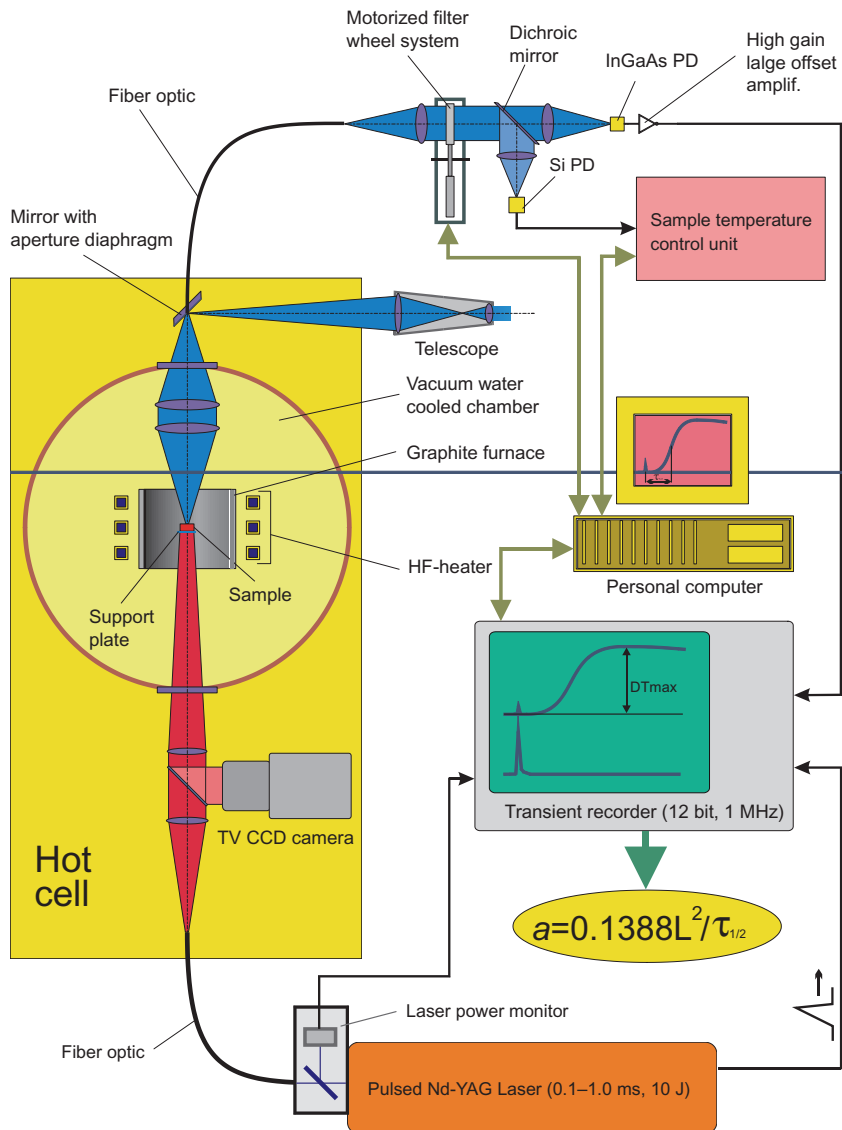


Figure 2.11 The laser-flash setup developed at JRC-Karlsruhe for the measurement of thermal diffusivity and conductivity in fresh and irradiated nuclear fuels.

2.3.1 Vibrational spectroscopy methods

Vibrational spectroscopy methods investigate nuclear fuels by detecting peculiar atomic-scale vibrations (i.e., phonons in crystalline samples) of the analyte. Such vibrations typically occur at energies in the IR range of the electromagnetic spectrum (i.e., wavelengths between 2.5 and 1000 μm). The energy units commonly used in

vibrational spectroscopy are the wavenumbers, expressed in reciprocal centimeters. Thus typical vibrational spectra occur between 10 and a few 1000 cm^{-1} .

The most common approaches to this type of analysis are Raman or IR spectroscopy, both based on electromagnetic radiation (photon) probes. They have been improved in the last few decades by the availability of high-quality monochromatic photon beams, such as lasers. Brillouin spectroscopy also belongs to the same category of methods. It is less frequently employed, yet very useful for the study of low-energy vibrational modes. Neutron scattering employs neutrons with various kinetic energies ($0\text{--}10000\text{ cm}^{-1}$) and momenta as probe particles. Neutron scattering experiments yield the most complete description of a material's vibrational and thermodynamic properties. However, it remains a complicated technique to be applied to nuclear materials because of the large and expensive infrastructures, not to mention the large amount of sample material needed (e.g., hundreds of milligrams). Nonetheless, some important neutron scattering data of unirradiated uranium and thorium dioxides were measured by Willis [23] and Dolling et al. [24]. Other techniques employing electron probes, such as low-energy electron spectroscopy (LEES), have not yet been employed for the investigation of nuclear fuels.

Raman and IR spectroscopy are both based on the interaction between a photon beam and a material sample. However, the physical effects on which these techniques are based radically differ in nature, which makes them complementary in many cases.

In IR spectroscopy, phonons impinging on the sample are absorbed, whereby they activate vibrational modes implying a net electric dipole variation. Therefore the main factor determining the IR-activity of a vibrational mode is that the vibration should imply a dipole moment variation. IR measurements are performed by irradiating a sample with an IR radiation beam the energy (or spatial frequency expressed in wavenumber) of which is varied by scanning a broad spectral range. The resulting spectra are obtained as a sequence of absorption peaks observed in the signal recorded by an IR detector analyzing the IR beam after its interaction with the sample. With respect to the IR beam source the detector can be mounted on the other side of the sample (i.e., 180 degrees geometry) for transmission measurements, or on the same side (i.e., 90 degrees geometry) for reflection measurements.

The first option generally yields more intense absorption peaks. However, it also requires a more complex sample preparation process, as the sample should be made thin enough (typically less than $1\text{ }\mu\text{m}$) to permit the IR beam to be transmitted. For this reason the second option (90 degrees geometry) is usually preferred to investigate nuclear fuel samples, which are particularly hard to prepare due to their radioactivity. IR detectors commonly work in a spectral range between 400 and 10000 cm^{-1} . Detectors for the analysis of lower energy IR absorption peaks are considerably more expensive and rarer. Unfortunately, precisely these types of IR detectors are needed for the study of dioxide-based nuclear fuels. In fact, the only IR-active vibrational mode foreseen by the Factor Group Theory [25] for fcc fluorite-like crystals is the T_{1u} band, which occurs approximately between 275 and 305 cm^{-1} [26]. Its exact position depends on the material composition. IR spectra

of various actinide dioxides were first measured by Begun et al. at the Oak Ridge National Laboratory [27].

Raman spectroscopy is based on nonelastic scattering of the probe photons due to their interaction with the analyte atomic vibrations. As opposed to IR, in Raman spectroscopy, atomic vibrations are studied by the modulation that they induce in the probe electromagnetic radiation. In this case, there is no need for the probe photons' frequency to sweep a given spectral range during a measurement. On the contrary, Raman scattering is best observed by the modulation that it induces on a monochromatic photon beam. For this reason, the rapid diffusion of lasers in the last four decades has broadly improved the quality and the applicability of Raman spectroscopy to the most diverse types of solid, liquid, and gaseous materials, including various kinds of nuclear fuels. The main factor determining the Raman activity of a vibrational mode is that the vibration should imply a net variation of the polarizability tensor of the analyte. The Raman effect is actually based on the fact that the electric field $\bar{E} = \bar{E}_0 \exp(i\omega t)$ of the incident (excitation) electromagnetic field generates an electrical polarization vector \bar{P} in the analyte, depending on the material's polarizability tensor α_p (not to be confused with the scalar thermal diffusivity term α):

$$\bar{P} = \alpha_p \bar{E} \quad (2.14)$$

The electric dipoles move following the superposition of the incident electromagnetic field vibration and the thermal vibrations (phonons in a crystal) intrinsically present in the material at any finite temperature. The superposition of the two types of vibrations causes a modulation of the excitation electromagnetic field frequency as it is scattered by the material. The function of a Raman spectroscope consists of detecting the scattered electromagnetic field and demodulating the frequencies in order to obtain those typical of the analyte's own vibrational modes. This mechanism can be understood with the help of Eq. (2.15), which describes Raman scattering in a one-dimensional and classical approach, expressing the material vibrations (of frequency ω_v) as Fourier series truncated at the first order, giving an expression for the polarizability of the type $\alpha_p = \alpha_{p0} + \alpha'_p \exp(i\omega_v t) + \dots$, α'_p being the first derivative of the polarizability with respect to the vibration coordinate.

$$\begin{aligned} P &= \alpha_p E = \alpha_{p0} E_0 \exp(i\omega t) + \alpha'_p E_0 \exp(i\omega t) \exp(i\omega_v t) \\ &= \alpha_{p0} E_0 \exp(i\omega t) + \alpha'_p E_0 \exp(i(\omega + \omega_v)t) + \alpha'_p E_0 \exp(i(\omega - \omega_v)t) \end{aligned} \quad (2.15)$$

Eq. (2.15) signifies that, in the scattered electromagnetic radiation regime, the fundamental scattered electromagnetic wave [e.g., Rayleigh or elastic term $\alpha_{p0} E_0 \exp(i\omega t)$] is modulated by two possible terms: one with higher frequency ($\alpha'_p E_0 \exp(i(\omega + \omega_v)t)$), resulting from the addition of the original frequency of the impinging radiation and the characteristic vibration frequency, and one with a lower frequency, given by the difference of the two ($\alpha'_p E_0 \exp(i(\omega - \omega_v)t)$). In the first case, one talks of Raman anti-Stokes lines, in the second of Stokes lines.

Eq. (2.15) also expresses the aforementioned necessary condition for Raman scattering: only vibrations implying net polarizability variations (i.e., $\alpha'_P \neq 0$) can be observed by Raman spectroscopy. The physical conditions that determine the IR- and Raman activity of atomic vibrations are often referred to as “selection rules.” It can be shown, with the help of Group Theory, that IR-activity excludes Raman activity in center-symmetric systems. In such systems, which include most of the common fcc-structured nuclear fuels, the two techniques are therefore complementary. It is worth noticing that the appearance of IR peaks in Raman spectra of nominally center-symmetric systems can be advantageously used for assessing the formation of defects which break the center-symmetry in the material.

It is also important to add that an additional “selection rule” applies to both IR and Raman spectroscopy, which is essentially linked to the momentum conservation in the matter-radiation interaction. This latter rule ensures that only crystal vibrations with vanishing momentum (i.e., in the close vicinity of the Γ -point in the Brillouin zone) can be directly observed by IR or Raman spectroscopy. This rule is however broken whenever second-order effects occur, which are beyond the scope of the present description.

Because of the momentum conservation selection rule, it is in principle impossible to observe acoustic phonons in crystals by IR or Raman spectroscopy. Only optical phonons having a finite energy at the Γ -point in the Brillouin zone can be observed. Brillouin spectroscopy, a particular evolution of Raman spectroscopy, can be used for the study of low-momentum and low-energy ($0.1\text{--}6\text{ cm}^{-1}$) vibrations in crystals (i.e., for the investigation of acoustic phonons). A complete description of phonon bands in crystals can be achieved with the help of neutron scattering. LEES also permits the determination of large portions of phonon dispersion curves in solids. Although this technique has not been applied to nuclear fuel studies, it looks promising for future investigations. Existing models of phonon spectra in nuclear fuel materials [28,29] can also be used as a starting point to be compared with experimental results obtained by vibrational spectroscopy.

Despite their fundamental limitations, Raman and IR spectroscopy are certainly well suited for the study of both fresh and irradiated nuclear fuels. Raman spectroscopy is an especially well adapted method for the investigation of nuclear materials, thanks to its flexibility permitting remote and *in situ* analyses and its relative ease of use, which requires very little sample preparation. It has been used particularly for the identification of different uranium oxides [9,30,31], oxygen defects [32,33], for the study of spent nuclear fuels [34,35] and mixed actinoid and lanthanoid–actinoid systems [17,36–40].

Raman facilities for the investigation of nuclear fuels are nowadays available in several laboratories worldwide. The use of different laser wavelengths permits one to study resonance phenomena, to vary the probe depth and to distinguish pure Raman peaks from the fluorescence background which can often be induced by interaction between the sample’s radioactivity and the containment. Some spectra are measured on highly radioactive samples confined in movable capsules, so that the entire Raman facility remains contamination-free [36]. Others are directly built inside hot cells or are connected to the fiber optics, enabling the analysis of

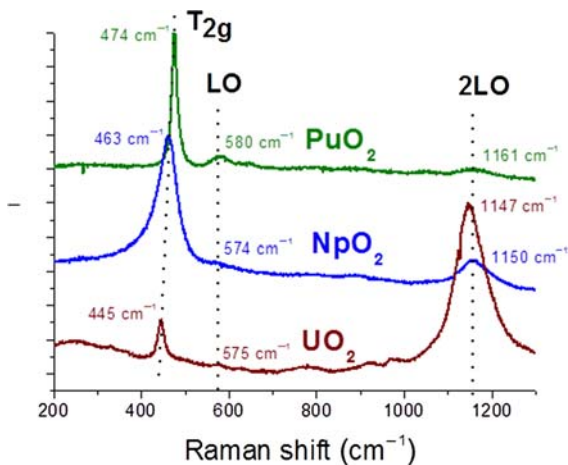


Figure 2.12 The Raman spectra of uranium, neptunium, and plutonium dioxides, where resonant and defect-induced lines are indicated in addition to the T_{2g} fundamental mode. Excitation source: 514 nm Ar^+ laser.

irradiated fuels [34,35,41–43]. This kind of approach has also been used for the study of fuel-cladding interaction in high burn-up nuclear fuel [44]. The use of a confocal microscope varies the associated surface/volume probed and the possibility to perform Raman imaging [45]. In all cases, the amount of analyte material can be quite small, a few mg or less, so that the activity can be reasonably reduced.

Figs. 2.12 and 2.13 show some example Raman spectroscopy measurements of relevant nuclear fuel components, including UO_2 and PuO_2 . The T_{2g} line observed in all the reported spectra is a clear fingerprint of the fcc fluorite-like structure of actinides. Its position changes with the cationic composition of the material, which is an important indication for the study (both *in situ* and *ex situ*) of mixed oxide fuels. Additional higher energy Raman lines of an electronic origin have recently been assessed for plutonium dioxide. They can conveniently be used for the identification of PuO_2 agglomerates in mixed oxide nuclear fuels under various conditions. This is a good example of how Raman spectroscopy many potential applications in nuclear fuel analysis, going from the nuclear safeguards to the analysis of nuclear waste and corium produced in nuclear plant meltdown accidents.

2.3.2 X-ray absorption spectroscopy (EXAFS, XANES)

A full description of the physical phenomena involved in X-ray absorption spectroscopy (XAS) lies beyond the scope of the present chapter and can be found in more dedicated literature (see, e.g., Ref. [47]). For a general introduction, it is sufficient to consider a phenomenological description of this technique.

At the X-ray radiation energy regime (approximately 500 eV–500 keV, or wavelengths from approximately 2.5–0.025 nm), light is absorbed by all matter through

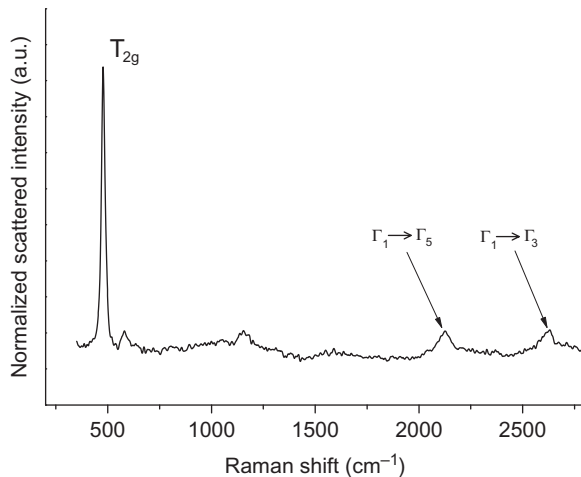


Figure 2.13 The extended Raman spectrum of plutonium dioxide, where electric field transition modes are indicated in addition to the fundamental T_{2g} vibrational one. Excitation source: 647 nm Kr⁺ laser.

Source: After D. Manara, M. Naji, S. Mastromarino, J.M. Elorrieta, N. Magnani, L. Martel, et al., The Raman fingerprint of plutonium dioxide: some example applications for the detection of PuO₂ in host matrices, *J. Nucl. Mater.* 499 (2018) 268–271 [46].

the well-known photo-electric effect. An X-ray photon is absorbed by an electron in a tightly bound quantum core level of an atom. In order for a particular electronic core level to participate in the absorption process, the binding energy (BE) of this core level must be less than the energy of the incident X-ray. If the BE is greater than the energy of the X-ray, the bound electron will not be perturbed from the well-defined quantum state and will not absorb the X-ray. If the BE of the electron is less than that of the X-ray, the electron may be removed from its quantum level. In this case the X-ray is absorbed and any energy in excess of the electronic BE is given to a photoelectron that is ejected from the atom into the continuum.

An XAS analysis is based on the measurement of the energy dependence of the absorption coefficient μ at and above the BE of a known core level of a known atomic species. The absorption coefficient is defined by the detected X-ray beam intensity I_d absorption as the beam of initial intensity I_0 passes across a sample having a thickness d (Beer's law):

$$I_d = I_0 \exp(-\mu d) \quad (2.16)$$

Following an absorption event, the atom is in an excited state with one of the core electron levels left empty (core hole) and a photoelectron ejected into the energy continuum. The excited state will eventually decay, typically within a few femtoseconds of the absorption event. There are two main mechanisms for the decay of the excited atomic state following an X-ray absorption event: (1) X-ray

fluorescence, in which a higher energy electron core level electron fills the deeper core hole, ejecting an X-ray of well-defined energy. The fluorescence energies emitted in this way are characteristic of the atom and can be used to identify the atoms in a system and to quantify their concentrations. For example, an L shell electron dropping into the K level gives the K_{α} fluorescence line. (2) The second process for deexcitation of the core hole is the Auger Effect, in which an electron drops from a higher electron level and a second electron is emitted into the continuum (and possibly even out of the sample). In the hard X-ray regime (i.e., >2 keV), X-ray fluorescence is more likely to occur than Auger emission, but for lower energy X-ray absorption, Auger processes dominate. Either of these processes can be used to measure the absorption coefficient, though the use of fluorescence is somewhat more common. Thus the energy dependence of the absorption coefficient $\mu(E)$ can be measured either in transmission as

$$\mu(E) = \log\left(\frac{I_0}{I_a}\right) \quad (2.17)$$

or in X-ray fluorescence (or Auger emission) as

$$\mu(E) \propto \frac{I_f}{I_0} \quad (2.18)$$

where I_f is the monitored intensity of a fluorescence line (or, again, electron emission) associated with the absorption process.

XAS is a widely used technique for determining the local geometric and electronic structure of matter with particular attention to valence states in which the various elements are present in a given material. A typical XAS spectrum (measured in the transmission geometry for a ZrO_2 sample) is shown in Fig. 2.14.

The X-ray absorption spectrum is typically divided into two parts (Fig. 2.14): X-ray absorption near-edge spectroscopy (XANES, also called NEXAFS) and extended X-ray absorption fine-structure spectroscopy (EXAFS). XANES is strongly sensitive to formal oxidation state and coordination chemistry (e.g., octahedral and tetrahedral coordination) of the absorbing atom, while EXAFS is used to determine the distances, coordination numbers, and species of the neighbors of the absorbing atom. XANES is dominated by absorption related to electronic excitations. It is valid for photoelectrons with kinetic energy (KE) in the range from -20 to $+30$ eV around the electron BE (chemical potential or absorption edge). In the high KE range of the photoelectron, the absorption spectra are dominated by EXAFS that presents the resonance of photoelectrons with neighboring atoms, resulting in resonant X-rays that can be observed as postedge oscillations in the experimental absorption curve up to a few hundreds of eV after the absorption edge.

For XANES analysis, experimental data are typically fitted within -20 and $+30$ eV around the absorption edge energy [often called “white line” (WL)] E_0 position. XAS data are obtained by tuning the photon energy using a crystalline monochromator to a range where core electrons can be excited. The corresponding

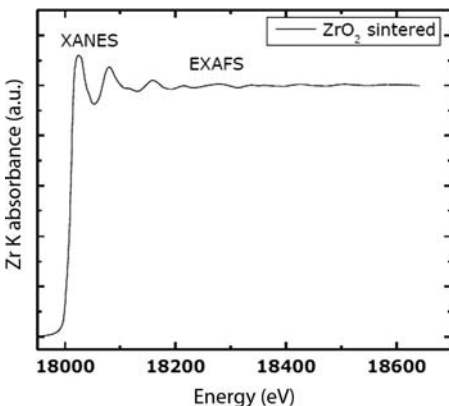


Figure 2.14 A typical XAS spectrum at the K-edge of zirconium in ZrO_2 , measured at the INE beamline of the KARA synchrotron of Karlsruhe, Germany. *XAS*, X-ray absorption spectroscopy, *INE*, Institut fuer Nukleare Entsorgung (Institute of Nuclear Waste Disposal), *KARA*, Karlsruhe Research Accelerator.

absorption edge depends upon the core electron which is excited: the principal three quantum numbers correspond to the K-, L-, and M-edges, respectively. For instance, excitation of a 1s electron occurs at the K-edge, while excitation of a 2s or 2p electron occurs at an L-edge and so on. In general, the energy calibration is performed prior to each measurement campaign using a standard reference material with an edge as close as possible to the edge of the element studied. In UO_2 , for example, tetravalent U L_{III} is commonly detected based on the K-edge XANES spectra of Y (17,038 eV) and tetravalent Pu L_{III} is referred to a Zr (17,998 eV) foil [48,49].

X-ray absorption measurements are usually performed at synchrotron radiation sources, which provide intense and tuneable X-ray beams, although in very recent times laser-based table-top XAS setups have also been developed [50]. Since the characteristics of synchrotron sources and experimental stations dictate what energy ranges, beam sizes and intensities are available; this often puts practical experimental limits on the XAS measurements.

Transmission XAS measurements are usually performed on approximately 3 mg of powdered sample mixed with 55 mg of Boron Nitride (BN), polyethylene, or another matrix transparent to X-rays. Fluorescence measurements can be performed also on specimens in the shape of disks or fragments.

In the case of radioactive materials, and in particular alpha-emitters, the sample shall be encapsulated within a double confinement, that is, at least two independent layers of alpha-shielding material shall separate the sample from the external world. In order to optimize the XAS measurement efficiency, one or both confinement layers can consist of thin Kapton foils.

Currently, few synchrotron facilities are available worldwide where radioactive and fissile materials can be investigated. A comprehensive list of synchrotron

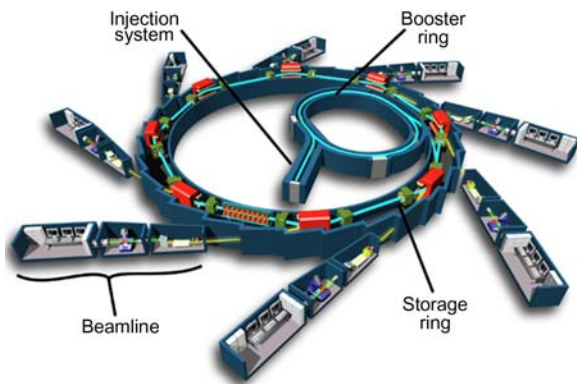


Figure 2.15 Schematic of a typical synchrotron facility, based on the European Synchrotron Radiation Facility of Grenoble (France). Booster ring, storage ring, and injection system refer to the accelerated electron beam. X-rays spanning various spectral ranges and with different characteristics are generated in the various beamlines, where they are used for XAS and other types of analyses (<https://www.esrf.eu/>). XAS, X-ray absorption spectroscopy.

facilities where radioactive materials and, in particular, nuclear fuels can be analyzed by XAS is provided by Denecke [51]. As an example, Fig. 2.15 shows a schematic view of the European Synchrotron Radiation Facility (ESRF) situated in Grenoble (France), where radioactive and fissile materials can be studied at the “RÖBL” (Rösendorf) Beamline [52].

The interpretation and analysis of XAFS is not always straightforward.

$\text{UO}_{2\pm x}$ XANES spectra are usually compared with standard spectra of U(IV) $\text{O}_{2.00}$, U(IV/V) $_{4}\text{O}_9$, U(V/VI) $_{3}\text{O}_8$, reference compounds in order to derive, by deconvolution of the experimental signal, the relative concentration of the various uranium valence states in the studied material. The absorption edge (E_0) values are defined as the first inflection point of the XANES spectra. The energy position of the most intense absorption resonance (WL) maximum is found by determining the energy position of the first node of the absorption curve's first derivative. The definition of the WL spectral position is one of the main uncertainty sources of this method and should be accurately discussed whenever analysis results are presented.

EXAFS analysis brings about a comprehensive description of the investigated material. This is obtained by deriving the spatial Fourier Transform of the experimental curve extended several hundreds of eV beyond the WL position. An EXAFS analysis implies the development of a full crystal model as an essential basis needed for accurate data fitting, especially for the correct determination of the phase terms in the Fourier Transform. For this reason, a sound EXAFS analysis should be accompanied by an accurate XRD study of the material. Uncertainty sources affecting an EXAFS analysis are generally instrumental and numerical, and both terms should be taken into account when reporting results.

Several XANES and EXAFS studies have been performed on nuclear fuels or nuclear fuel subsystems, mostly aimed at determining the chemical speciation and

local environment of fuel components [17,53–58]. Bès et al. recently published the results of a first XAS analysis successfully performed on UO₂ with a table-top setup [59].

High-energy resolution fluorescence detected or high-resolution-XANES can also be mentioned here as advanced XAS—fluorescence techniques, yielding highly accurate data that can be used for a detailed description of the chemical and structural speciation of various nuclear fuel components. They have been applied, for example, to an unprecedentedly accurate study of uranium speciation in complex oxides [60]. These techniques are now available on beamlines dedicated to radioactive materials, such as RÖBL [60] at ESRF, ACT at KARA [61], and MARS at SOLEIL [62,63].

2.3.3 Photoelectron spectroscopy (XPS, UPS)

Photoelectron spectroscopy (PES), also known as electron spectroscopy for chemical analysis, is a quantitative electron spectroscopic technique that allows the determination of the elemental composition and chemical state of a sample surface. It also provides information on the electronic structure of the elements. PES is based on the photoelectric effect and was developed as an analytical tool by Siegbahn and coworkers since the late 1950s [64]. PES can be divided into X-ray PES (XPS) and ultraviolet PES (UPS).

XPS spectra are obtained by irradiating a material with X-ray photons while measuring the KE and intensity of (mainly core level) electrons that escape from the top 1 to 10 nm of the material. In parallel with Siegbahn's work, David W. Turner developed in the 1960s a method to study the photoelectron spectra of free molecules in the gas phase [65] by using a helium discharge lamp as a photon source. This method, commonly referred to as UPS, is limited to the investigation of molecular energy levels in the valence band region. Beside the following relatively short description of PES, the reader is referred to the literature [66–69].

Fig. 2.16 shows schematically a typical PES setup. For XPS experiments, usually Mg K_{α} (1253.6 eV) or (mono-energetic) Al K_{α} (1486.6 eV) excitation radiation is used. UPS spectra can be taken with He I (21.22 eV) and He II (40.81 eV) UV light produced, for example, by a discharge lamp. Taking advantage of the different mean free paths for He I, He II, and Mg K_{α} (or Al K_{α}) excited photoelectrons, different information depths can be accessed [70]. The techniques therewith allow investigation of the uppermost surface layer with He II excitation and provide information also on “bulk properties” from regions down to some tens of monolayers when using Al K_{α} /Mg K_{α} X-ray sources. Excitation by synchrotron radiation is widely used nowadays allowing for advanced applications (see later).

Sample preparation—if the sample is not produced *in situ* as, for example, via thin film deposition—often comprises of a cleaning procedure such as scraping, breaking under vacuum conditions to create a fresh surface or sputter cleaning with energetic Argon ions to remove the ubiquitous surface contamination layer of carbonaceous material. Care has to be taken not to induce changes on the surface to be investigated by such procedures.

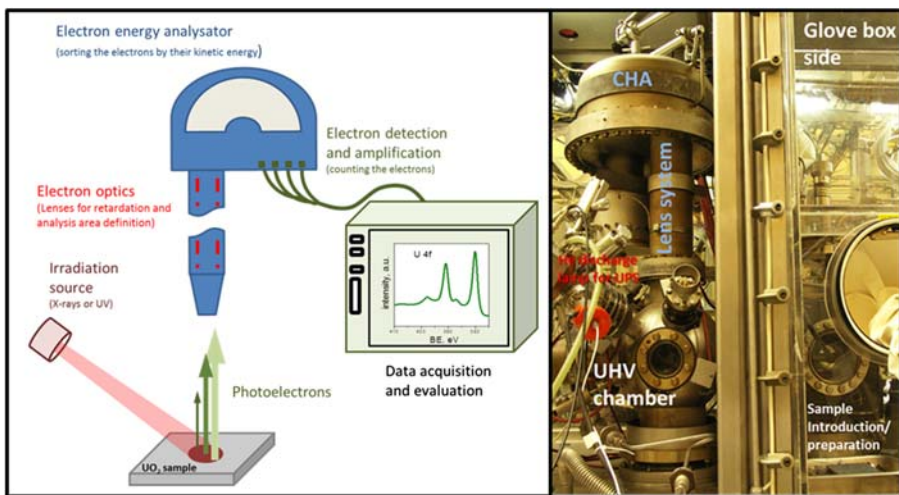


Figure 2.16 PES instrumentation, left: schematic representation of PES (the different elements indicated do not scale to real sizes); right: Photograph of PES instrumentation adapted to glove box for handling radioactive material (formerly installed at JRC-Karlsruhe). *PES*, Photoelectron spectroscopy.

The investigated sample area depends strongly on instrument design. Nonmonochromatic irradiation sources can have beams with 10–50 mm in diameter, while the largest size for a monochromatic beam of X-rays is in the range of 1–5 mm. The minimum analysis areas range from 10 to 200 μm obtained from (μ -focused) X-ray beams. Improved image resolution levels of 200 nm or below can be achieved with imaging XPS instrumentations using synchrotron radiation as X-ray source, see for example, Ref. [71].

Electron spectroscopy methods require ultra-high vacuum conditions. The background pressures in the analysis chamber are usually better than 2×10^{-9} mbar. Recently, “environmental” or “ambient pressure” XPS instrumentation (through the use of differential pumping stages) allowed for measurements in the mbar pressure range [72].

The electron KE spectra can be recorded with different types of electron energy analyzers such as the most common concentric hemispherical electron energy analyzers or the older design of a cylindrical mirror analyzer in combination with electron detectors such as channeltrons. The measured KE of the electrons can be easily transferred into BE values using the following equation:

$$BE = h\nu - KE - W \quad (2.19)$$

with $h\nu$, the energy of exciting radiation from its frequency, ν , and the Boltzmann constant, h , and W the work function (which is essentially the energy needed to remove an electron from the solid’s Fermi level into the vacuum immediately

outside the solid surface). As no two elements show the same set of electronic energy levels, the method enables elemental analysis. Changes in the chemical environment of an atom are reflected in a change of the respective BE and thereby provide for chemical information.

The elemental composition of a material can be determined by the identification of the specific photo emission peaks of the elements (see Fig. 2.17). From the evaluation of the intensity (area) ratios of these peaks, relative and absolute quantification can be obtained [73–75]. Relative quantification in a series of samples is more common than absolute quantification efforts. The accuracy of the method mainly depends on peak intensity (including background subtraction), signal to noise ratio, accuracy of the relative sensitivity factors for the photo emission peaks of the elements, corrections applied for the electron transmission function of the instrument, homogeneity of the investigated surface volume, correction for energy dependence of electron mean free path, and sample stability under analysis condition (ultra-high vacuum conditions and X-ray irradiation) [69,76–79]. For optimum conditions, the accuracy of atomic percent (at%) values calculated from major peaks can be approximately 90%. Detection limits are usually in the range of 0.1%–1.0%, with hydrogen not being detectable.

Induced by a different chemical environment, a “chemical shift” of the photoemission peaks for a certain element is observed which allows for a further characterization of an element in a compound. For uranium, the evaluation of the chemical shift of the photoemission peaks was investigated extensively [71,80–85] and is shown in Fig. 2.18 for the U4f peaks. These peaks show a spin-orbit splitting of approximately 11 eV and shifts depending on the uranium oxidation state from

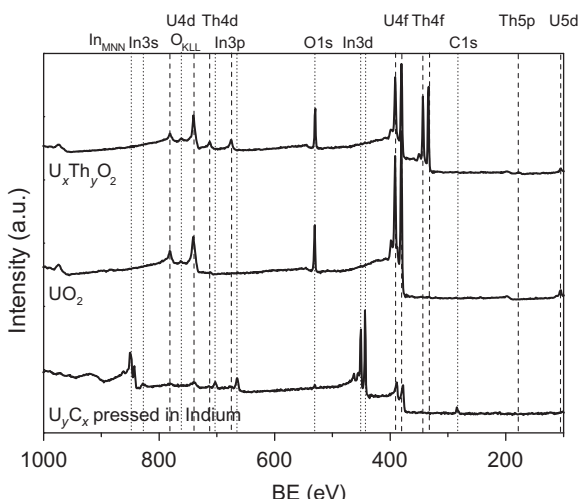


Figure 2.17 Overview spectra “ $U_y C_x$ ” embedded in Indium substrate, UO_2 and $(U, Th)O_2$ as example for the evaluation of elemental composition. Corresponding photoemission peaks for the marked peaks are given on the top of the plot (dashed lines: actinide elements, dotted lines: other elements).

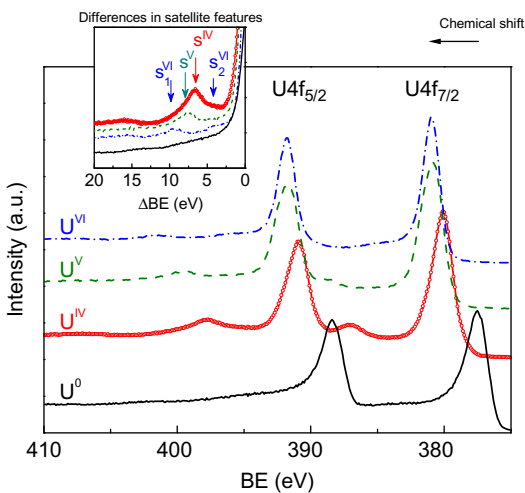


Figure 2.18 Example of speciation from chemical shift and peak shape for Uranium samples. U4f detail spectra of U metal, UO_2 , U_2O_5 , UO_3 . With increasing oxidation state the main lines shift to higher BE (chemical shift). Inset: satellite positions (main lines are superimposed at $\text{U } 4\text{f}_{5/2}$ maximum). The BE difference between satellite and main line (ΔE_{sat}) also increases with the oxidation state.

Source: Picture adapted from T. Gouder, R. Eloirdi, R. Caciuffo, Direct observation of pure pentavalent uranium in U_2O_5 thin films by high resolution photoemission spectroscopy, Sci. Rep. 8 (1) (2018) 8306 [86].

approximately 377 eV (for the $\text{U-4f}_{7/2}$ peak) in the metal to approximately 381 eV in UO_3 . In addition, a certain satellite structure (induced by charge transfer reactions or shake-up processes during the photoemission process) [84,86,87] is observed in this photoemission peak and can be used for identification of the surface oxidation state of uranium in these materials (see Fig. 2.18) [86,88].

Surfaces, especially interfaces, are of particular interest in fuel chemistry as they constitute an important part of condensed matter systems. Chemical reactions between different systems typically operate at their respective interfaces. For example, surface processes play a central role in nuclear fuel interaction with surrounding materials during processing, reactor operation, and back-end storage, which can involve photoemission studies.

Assessments of equipment allowing the investigation of radioactive material, fuel or even highly active samples such as irradiated fuel or material from reactor accidents, are seen through the decades [89–96]. Whereupon early studies on actinide surfaces mainly comprised oxidation and reaction studies of the actinoid metal and oxide surfaces with gaseous species, as example beside the already mentioned investigations, there are many investigations on uranium and thorium in the literature [97–102]. More recent studies from 2000 onwards are found investigating still the basic redox behavior of actinoids (An), An-oxides and mixed An-oxides

(An = Th, U, Pu, Np, and Am) [71,89,103–111] but with increasingly advanced equipment and often in combination with complementary techniques or theoretical calculation efforts.

There is also some interest in the characterization and behavior of other fuel or waste matrices, like uranium carbides [112–114], nitrides [115–117], and An-containing ceramic or glassy materials considered for waste storage [118–122].

Extensive studies were done on spent fuel model systems to investigate and understand the corrosion behavior of this system. As the actinoid dioxides, AnO₂, that are commonly used as reactor fuel (An = Th, U, Pu) or accumulated during in-reactor irradiation via neutron activation (An = Np, Pu, Am, etc.), their behavior under final waste repository conditions is of major interest for performance assessments of these future repositories (see Chapter 14: Advances in fuel chemistry during a severe accident for more information on spent fuel repositories). An important scenario in particular is the dissolution of spent fuel once in contact with intruded groundwater. For the fuel matrix, UO₂ and the higher actinoids Np and Pu, the solubility increases for the higher oxidation states (U(VI)/Pu(VI), V/V(Np(V)), which can lead to an enhanced risk for the release into the biosphere. The spent fuel itself is very complex, with a great variety of chemical elements intermixed or occurring in different phases. Describing surface reactions in such systems is difficult, and it is instead common to simplify the representation of the real system down into simpler model systems and reactions, which are easier to investigate. Thus, simplified model surfaces (pure UO₂, unirradiated fuel, SIMFUEL, other models like in situ produced thin films) exposed to well-defined experimental conditions in situ (molecular or atomic gases) or ex situ (various aqueous media) are investigated with XPS mainly to characterize the oxidation state of the constituents [123–133]. Also, the effect of irradiation is of some interest and was investigated recently in model experiments with PES [134].

Only very few XPS studies on real spent fuel [95,135] or nuclear accident materials (e.g., from Chernobyl [92,136,137]) were performed to the authors' knowledge with a focus on elemental characterization and speciation.

Numerous studies are using XPS for analytical purpose identifying elemental composition and chemical speciation as well in geological matrices that can be found in the far-field of a nuclear waste repository. Spent fuel constituents such as uranium, neptunium, plutonium, selenium, technetium, as well as matrix elements such as iron and other (nonredox sensitive) elements are investigated, in addition to the interaction with bacteria can be considered its own field all using XPS often in combination with XAS (especially XANES or EXAFS).

Fuel rod materials (e.g., Zircaloy or other Zr-alloy) or reactor structural materials (e.g., steel) interaction with the fuel can also be investigated [93]; however, the main focus of these studies is the behavior of the Zircaloy or Zr simulant itself under various conditions expected under in-reactor, disposal or accidental conditions (hydrogen uptake, irradiation, oxidative, sea water corrosion) not needing a special setup for radioactive samples. A detailed description of these topics, which are usually not involving high radioactive samples, would go far beyond the scope of this paper.

To extricate the various properties of a given surface in parallel to XPS complementary techniques are often applied, which are sometimes even combined in the same experimental facility. Namely, some of them are:

- methods sensitive to atomic geometry at surfaces [LEED (low-energy electron diffraction), TEM (transmission electron microscopy, see [Section 2.3.4.1](#)), SEM (scanning electron microscopy, see [Section 2.3.4.1](#)), LEIS (low-energy ion scattering spectroscopy), atomic scattering or diffraction, STM (scanning tunneling microscopy), AFM (atomic force microscopy)], for example, in Refs. [[89,95,116,121,134,138,139](#)];
- methods sensitive to electron distribution at surfaces (work function measurements like Kelvin probe);
- methods sensitive to chemical composition at surfaces [AES (auger electron spectroscopy), TDS (thermal desorption spectroscopy), SIMS (secondary-ion MS)], for example, in Refs. [[80,89,99,102,116](#)], see also [Section 5.2](#); and
- methods sensitive to the vibrational structure of surfaces or bulk {IR spectroscopy, Raman spectroscopy, HREELS [high-resolution electron energy loss spectroscopy (EELS)]} [[80,93,108](#)], see also [Section 2.3.1](#).

Also, for some specific purposes, bulk methods are combined with the foregoing surface sensitive techniques, such as methods sensitive to the bulk speciation (XANES, see [Section 2.3.2](#)) or structural investigations (especially XRD [[90,91,93,108,116,121](#)], see also [Section 2.7.1](#)) but also EXAFS (see [Section 2.3.2](#)) nuclear magnetic resonance (NMR) (see [Section 2.4](#)) as well as other electron spectroscopies (see Ref. [[140](#)]).

Advanced PES techniques using synchrotron light are for example described by Reinert and Hüfner [[141](#)]. The main advantages of this setup are that the photon energy can be selected by the use of a monochromator from a continuous spectrum over a wide energy range (e.g., allowing for high resolution, the use of high-energy photons yielding high KE photoelectrons with an increased probing depth or of soft X-rays probing the valence band). The high intensity and brightness of the synchrotron light facilitates measurements of surfaces at near-ambient pressures, as well as small probing area even enabling microscopy applications. Also, time-resolved and angle-resolved photo-electron spectroscopy (ARPES) measurements are possible (see Ref. [[142](#)] for ARPES on 4f and 5f compounds). There are several facilities (listed examples are not thought to be comprehensive) in the world that allowed at least for the use uranium-containing materials [[71,143](#)] but also transuramics [[144](#)].

In addition, a combination of PES with theoretical modeling, especially when also compared with other techniques, enhances the understanding of the special physical behaviors of actinoid elements due to their 5f states occupation [[142,145–147](#)].

2.3.4 Electron microscopy and spectroscopy (SEM, TEM, EDS, EELS, EPMA)

Electron microscopy and spectroscopy techniques are analytical tools used to non-destructively determine the chemical composition of small volumes of solid materials. As a general description of the approach, the sample is bombarded with an

electron beam. Electrons back-scattered or emitted by the bombarded sample are then detected together with X-rays emitted at wavelengths characteristic to the elements being analyzed. The procedure yields various types of electron images and the emitted X-ray spectroscopy gives an indication of the abundances of elements present within small sample volumes (typically 10–30 μm^3 or less) to be determined. The advantage of electron images as opposed to optical images lies in the fact that the electrons can be accelerated to have a much shorter wavelength (up to nanometers) than visible light (380–710 nm), following the De Broglie relation:

$$\lambda_e = \frac{h}{m_e v_e} \quad (2.20)$$

where m_e and v_e are the mass and the velocity of one electron, respectively. From the above formula, it is evident that the wavelength of the electrons can be reduced with a consequent greater resolving power of the image by increasing their momentum, which is the acceleration potential V through the formula

$$v_e = (2Ve m_e)^{1/2} \quad (2.21)$$

In Eq. (2.21), e is the electron charge. Typical acceleration voltages in the current applications range from tens to hundreds of keV. The actual limit of resolution can be calculated with the Rayleigh equation:

$$R = 0.61 \lambda_e \eta \sin \alpha \quad (2.22)$$

where η is the refractive index, α is the angle corresponding to the half of the maximum solid angle captured by the electron lens, and λ_e is the wavelength of the electron.

Different kinds of analytical techniques exploit the interaction of accelerated electrons with the analyte, depending on the experimental approach (reflection, emission, and transmission), and on the way characteristic X-rays emitted by the electron-hit sample are analyzed.

2.3.4.1 Scanning electron microscopy and transmission electron microscopy

Electron microscopy being SEM or TEM and all associated analytical techniques are powerful and versatile tools for the microstructure characterization but also for elemental and chemical analyses of solid samples. In the particular case of the investigation of radioactive materials, the instrumentation derives from standard equipment but must be adapted into glove boxes or shielded cells [148]. Different solutions have been used to deal with radioactive materials (e.g., installing either the main microscope components or only the parts hosting the radioactive sample in a confined environment).

As for the microscopes, the tools for the sample preparation of radioactive materials are conventional. However, they must be adapted to be used inside glove



Figure 2.19 Examples of adapted electron microscopes (A) SEM Phillips XL40 where high voltage unit, column, chamber, and turbo-molecular pump are mounted inside a glove box and the primary vacuum system, water cooling circuit and acquisition electronics are placed outside. (B) FEI Tecnai G20 TEM adapted with a flange that has been inserted in the octagon hosting the objective lenses, and a glove box mounted on this flange around the computer stage and equipped with a glove box attached to the column. (C) SEM JEOL 6300 mounted inside a Hot Cell for the study of highly radioactive samples and inserted in a lead shielded cell (not visible in this image). *SEM*, Scanning electron microscopy.

boxes (and possibly shielded; see examples in Fig. 2.19). For extremely radioactive specimens (i.e., irradiated nuclear fuel), standard methods can still be used, provided the amount of material handled is kept very small.

In the SEM conceived by Ardenne in 1938 [149] and mainly developed in the early 1960s, a sample surface is scanned with a high-energy beam of electrons (typically 30 keV). Different types of electrons resulting from the interaction of the primary beam can be used for imaging purposes: secondary electrons (SE) providing a topological contrast of surfaces or back-scattered electrons (BSE), which gives an elemental contrast providing information of about 15 nm depths in the sample. Images produced with SEM produce a characteristic 3D appearance due to its larger depth of field in comparison to optical microscopes.

As a side consequence of the interactions of the primary electron beam with the sample when the electron beam removes an inner shell electron from the sample, it forces a higher shell electron to fill the created hole emitting a characteristic X-ray. Different techniques such as energy dispersive X-ray spectroscopy (EDS) or wavelength dispersive spectroscopy (WDS) can be used for sample elemental composition determination taking advantage of these X-rays [150]. Examples of these techniques can be seen in Fig. 2.20.

Bulk samples can be directly studied by SEM with no further preparation if they are small and/or electron conductive. When the sample is not electron conductive, it may require an extremely thin coating (typically comprised of carbon or gold) to avoid charging effects that would reduce the quality of the images.

In the case of TEM, developed by Max Knoll and Ernst Ruska [151] in the early 1930s, the interaction of the electrons from the primary beam with the material atoms is different in the sense that they must be transmitted through the sample and

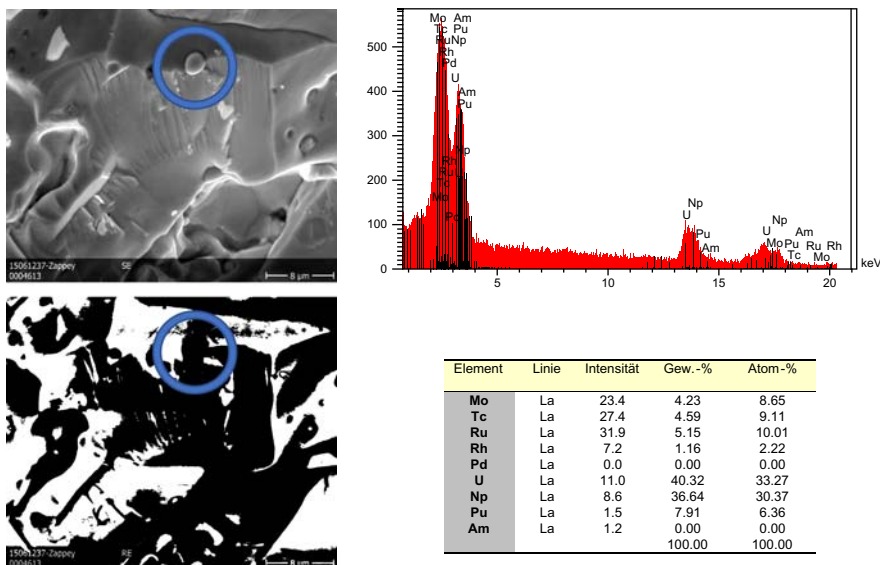


Figure 2.20 Examples of the different techniques explained on this chapter related to SEM: (A) SEM SE showing a round-shaped particle embedded on the bulk material (signaled with a blue ring), (B) SEM BSE proving that the average atomic number of the particle seen on the previous image (signaled with a blue ring) is well below that of the bulk material, (C) EDS spectrum performed on the particle shown in the previous images presenting peaks for the actinides present on the bulk material along with those of the metallic fission products (Mo–Tc–Ru–Rh–Pd), (D) elemental quantification proving the composition of the particle to be a metallic precipitate. Actinoids are present due to the signal coming not only from the particle, but also from the bulk material. *BSE*, Back-scattered electrons; *EDS*, energy dispersive X-ray spectroscopy; *SE*, secondary electrons; *SEM*, scanning electron microscopy.

collected afterwards. When studying crystalline materials, the electrons of the primary beam are diffracted through the matrix of the material providing information on its structure (by means of either imaging or electron diffraction), presence of extended defects (such as dislocations, precipitates or presence of bubbles), grain boundaries, multiple crystalline phases, and orientation of the crystal planes [152]. In amorphous materials, the thickness or composition contrast can be studied together with possible crystalline inclusions.

For TEM samples of highly radioactive materials, the crushing method is usually preferred. Focused ion beam (FIB) systems are being implemented, producing suitable/ideal specimens for TEM observations. Other methods include electro-polishing (e.g., for the preparation of metallic plutonium [153]), twin jet polishing or ion milling of dimpled disks; these methods are used in samples with very specific needs and it is not always possible to apply them.

Associated to TEM analyses, there are usually several techniques that provide a broad range of information of the sample (see examples in Fig. 2.21), such as bright field (TEM-BF, bringing elemental-related contrast, mixed with morphology

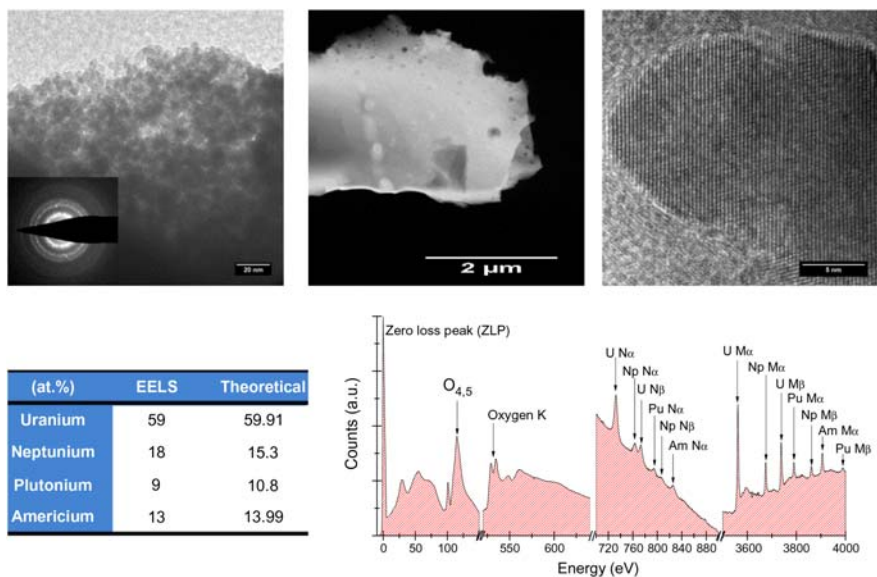


Figure 2.21 Examples of the different techniques described in this chapter related to TEM: (A) TEM bright field image; inset, electron diffraction on the same spot proving the polycrystalline structure of the studied region; (B) STEM of a particle with a high amount of bubbles, some containing metallic precipitate particles as that seen on the SEM example in Fig. 2.20; (C) high resolution image showing a defect-free particle; and (D) EELS spectrum showing the ZLP, the overlap of the O_{4,5} edges of all the actinides present on the sample and the N_{4,5} and M_{4,5} clearly resolved and the quantification obtained by means of the second derivative method applied to the M₅ lines of the elements present on the sample. *EELS*, Electron energy loss spectroscopy; *SEM*, scanning electron microscopy; *TEM*, transmission electron microscopy; *ZLP*, zero loss peak.

contrast that can also provide high resolution images up to atomic scale), dark field (TEM-DF, which helps to understand the variety of crystalline phases present on the sample), Scanning Electron Transmission Microscopy (STEM) (which brings inverted elemental-related contrast compared to that of the bright field images), electron diffraction (which shows the nature of crystals present on the material), EDS (in the same manner as for SEM, it provides information on the elemental composition of the sample) and EELS.

EELS is a powerful technique associated with TEM that can be used for elemental analyses [152] but can also be used to obtain information on the oxidation state of the sample, its thickness and the type of chemical bonding [154]. The physics underlying the technique is the interaction of the very energetic beam electrons with those from the atoms of the sample. By means of a prism and a camera, it is possible to determine the energy lost by the beam of electrons after their interaction with the sample constituents, which is characteristic of the atomic species, oxidation state, and atomic environment, together with the thickness of the sample. EELS can, therefore, be seen as the electron-absorption analogue to the XANES technique

presented in [Section 2.3.2](#). One of the advantages of this technique over the more widespread EDS technique is the fact that EELS is not affected by internal conversion—a common problem that affects active samples producing large peaks at different energies, that complicate the quantitative (and sometimes even qualitative) elemental analysis of the sample.

2.3.4.2 Electron probe microanalysis

An electron probe micro-analyzer (EPMA) works similarly to an SEM: the sample is bombarded with an electron beam and X-rays are emitted at wavelengths characteristic to the elements being analyzed. Typically, EPMA employs WDS to resolve the emitted characteristic X-rays, which ensures better resolution than most common electron microscopes. The concentrations of elements from beryllium to plutonium can be measured at levels as low as 100 ppm. Recent models of EPMA can accurately measure elemental concentrations of approximately 10 ppm.

Given its high sensitivity and flexibility, EPMA is broadly used for the elemental analysis of both fresh and irradiated nuclear fuel samples [\[155\]](#), nuclear severe accident debris, etc.

From the perspective of investigating irradiated nuclear fuel, however, this technique presents a number of limitations. For example, the fission gas krypton cannot be measured because the second-order Mo_{α_1} U X-ray line coincides with the Kr L_{α_1} line and the Kr K X-ray lines have a high critical excitation energy of 14.3 keV. Moreover, due to the shallow electron penetration depth in nuclear fuel, the fission gases trapped in pores and bubbles larger than about 0.1 μm cannot be detected. These deficiencies have been overcome by combining EPMA with other techniques, such as Knudsen Cell MS and SIMS (see further in this chapter).

[Fig. 2.22](#) shows an example of EMPA mapping on a metallic nuclear fuel sample irradiated to 7 at.% burn-up.

2.3.5 Positron annihilation spectroscopy

Positron annihilation spectroscopy is a powerful nondestructive characterization technique that can provide information about the defect structures of crystalline solids. The interaction of implanted positrons with matter is used to probe the electronic densities of vacancy defects, voids and dislocations sites in metals, semiconductors, ceramics, and polymers [\[157,158\]](#).

Positrons interact with the solid material under investigation by losing energy through inelastic scattering, ionization, and electron excitations. The slowing down to thermal energies takes a few picoseconds. The thermalized positron diffuses in a delocalized state for few hundreds of picoseconds until it eventually annihilates with an electron. In an insulator a positron can bind to an electron and form a hydrogen-like atom called positronium (Ps).

At vacancy defect sites, the electronic density and the electrostatic repulsion of the missing positive ions is lower than in the defect-free regions of the lattice. This results in a higher possibility for the positron to be trapped at the defect location

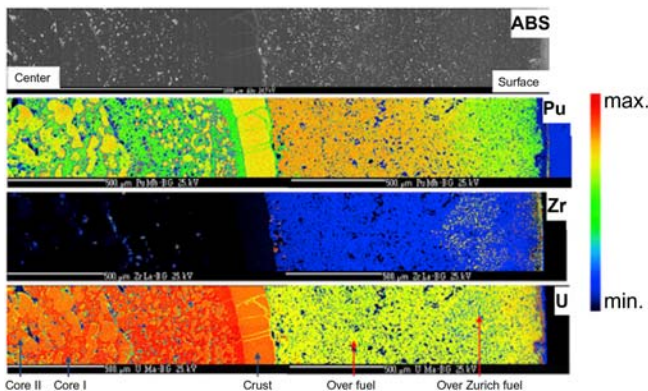


Figure 2.22 Radial absorbed electron image and elemental X-ray mapping for Pu, Zr, and U revealing the microstructure and the distribution of the fuel constituents after irradiation. The maps were built as a collage of four smaller maps obtained with an E_0 of 25 kV and a primary current of 100 nA. The AE large area image has a total resolution of 1024×768 pixels. The X-ray maps total resolution is 2905×410 pixels and covers an area of $2.9 \times 0.4 \text{ mm}^2$. The total dwell time was 52 h [156].

and in a longer lifetime compared to that of a positron in the defect-free lattice. The measurement of the positron lifetime thus provides an indication of the concentration and type of the vacancy defects. This measurement is the basis of the positron annihilation lifetime spectroscopy (PALS) method.

Positron/electron annihilation results in the emission of two 511 keV photons traveling in opposite directions. As energy and momentum are conserved in the annihilation process, the two photons carry information on the state of the annihilated electron/positron pair. The conservation of momentum law imposes a Doppler energy shift of the 511 keV energy line as well as an angular deviation with respect to the collinear direction of the gamma photons. These two phenomena are measured respectively in the Doppler broadening spectroscopy (DBS) method and in the angular correlation of annihilation radiation (ACAR) method. DBS and ACAR can also provide information on the chemical environment of the detected vacancy defect.

The implementation of both DB and ACAR methods requires more expensive (HPGe detectors and position sensitive detectors respectively) and more complicated setups with respect to the PALS technique. For this reason, PALS is more widespread at small scale facilities.

The most common positron source for PALS experiments is the radioisotope Na^{22} (half-life 2.6 years). Source activities in the MBq range are commonly used. Na^{22} decays through a β^+ process emitting positrons with a continuous energy distribution up to 545 keV. At this energy, positrons are implanted over a depth of approximately 100 μm in most solid materials. A 1274 keV gamma ray is emitted in prompt coincidence with the positron. In a number of applications, positrons emitted by the source are slowed down within a moderator and pass through an electromagnetic

energy filter before entering the material of interest. This generates monochromatic positron beams used to probe different layers of the material allowing the monitoring of defects as a function of depth. Higher intensity positron beams can be obtained through nuclear reactions with particle accelerators or at nuclear reactor sites.

The conventional measuring system for PALS is based on two fast scintillation-photomultiplier detectors and associated electronics. The detection of the 1274 keV gamma rays by the first detector is used as a start signal for the positron lifetime measurement (i.e., the positron birth). The stop signal is given by the detection of one of the 511 keV annihilation photons (the positron annihilation) by the other detector. Both analogue and digital arrangements can be implemented for the analysis of the detector signals. In the analogue implementation, both the start and stop detector signals are gated through an energy discriminator module (single channel analyzer) that accepts only signals within the specific energy range of the relevant gamma. The time delay between the start and stop signal is converted in a voltage signal through a time-to-amplitude converter module. The signal is then fed to a multichannel analyzer that generates a histogram of time intervals (the PALS spectrum). The time resolution of PALS systems is usually in the range of 200–250 ps [159].

The typical source–sample configuration consists of a deposit from a salt solution of $^{22}\text{NaCl}$ encapsulated in a foil material (Kapton, Al, or Ti) that is then “sandwiched” between two sample disks. The two collinear detectors are positioned in close proximity to the source/sample setup. This arrangement guarantees that all positrons emitted from the source are penetrating the sample material. The sample must be thick enough to completely stop the positron but not too thick to attenuate the 1.274 and 511 keV photons. Fig. 2.23 shows a schematic of the experimental setup (see Ref. [160]).

The PALS spectrum can be represented by $k + 1$ different exponential decay components, each related to a different lifetime, according to the equation

$$y(t) = B + \sum_{i=1}^{k+1} \frac{I_i}{\tau_i} \exp\left(-\frac{t}{\tau_i}\right) \quad (2.23)$$

where $y(t)$ is the counting rate as a function of the time t , τ_i is the mean lifetime of the i th component, I_i is the intensity of the i th component and B is the random background. Usually, $\tau_1 = \tau_b$, where τ_b is the mean lifetime for the bulk material without defects. Positron trapping in vacancy defects leads to long-lived decay components [159].

Fig. 2.24 shows a typical PALS spectrum obtained from Teflon (Trade Mark) where one can see the contribution of multiple lifetime components typical of insulators.

The trapping rate in a particular type of defect, K_d , can be related to the defect concentration, C_d , and the mean lifetimes by

$$K_d = \mu_d C_d = \frac{I_d}{I_b} \left(\frac{1}{\tau_b} - \frac{1}{\tau_d} \right) \quad (2.24)$$

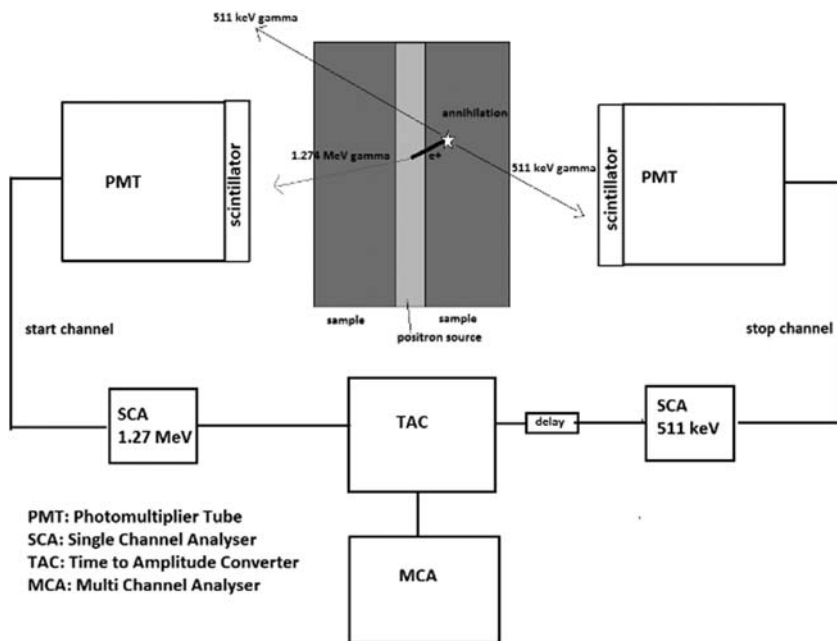


Figure 2.23 A typical PALS setup schematic. *PALS*, Positron annihilation lifetime spectroscopy.

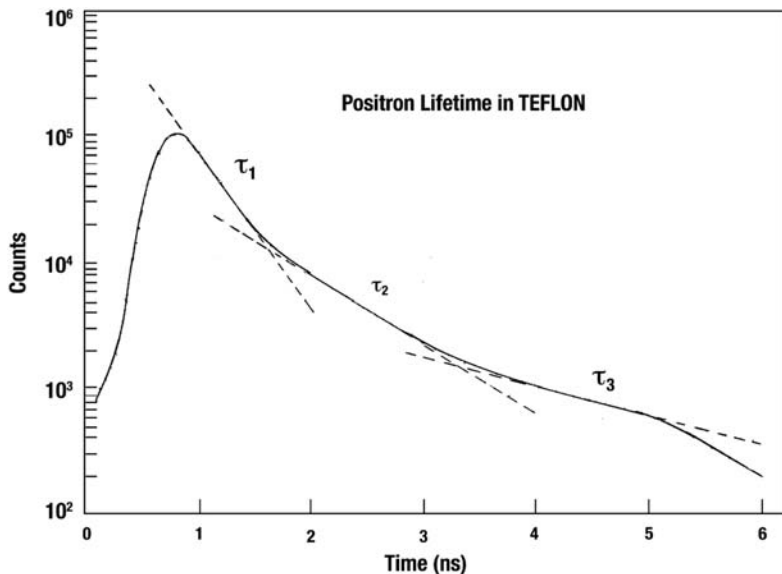


Figure 2.24 A typical PALS spectrum obtained from TEFLON where one can see the contribution of multiple lifetime components typical of insulators. *PALS*, Positron annihilation lifetime spectroscopy.

where μ_d is the trapping coefficient, I_b and τ_b are the intensity and the mean lifetime, respectively, for the bulk material component in Eq. (2.23), and I_d and τ_d are the intensity and mean lifetime, respectively, for the trapping defect component in Eq. (2.23). Obviously, the bulk component will have the highest intensity and the shortest mean lifetime.

The components caused by trapping will have lower intensities and longer mean lifetimes. Through Eq. (2.24), the prevalence of the various types of positron traps can be calculated from the measurement [159].

Eq. (2.23) does not take into account the finite time resolution of the detectors and electronics that affect the left side of the curve in Fig. 2.24. The measured spectrum is a convolution of the theoretical spectrum and the time resolution of the system. PALS spectrum analysis therefore requires a mathematical fitting and deconvolution process to extract the different lifetimes. Further corrections are required to consider the positrons annihilating in the source material (source correction).

PALS has been consistently applied to the characterization of defects induced by radiation damage on nuclear materials such as fuel, cladding, and structural material [161–166].

As an example, Table 2.2 shows the positron lifetime spectra decomposition for UO₂ disks before and after electron and alpha irradiations under different conditions [164]. It appears evident how the average lifetime increases with defect concentrations associated with the different degrees of radiation damage. A new lifetime component τ_2 appears in the spectrum of the irradiated samples and its intensity I_2 increases with the radiation fluence. Irradiation with 1 MeV electrons appears to have no effect (i.e., no new lifetimes components). This suggests that no vacancy defects are generated or that they are not detected due to their positive charge state or to their low concentration, whereas 2.5 MeV electrons and 45 MeV alpha particles appear to generate defects capable of trapping positrons. The researchers identified such defects as U monovacancy, U-O divacancy or Schottky defect.

Table 2.2 The positron lifetime spectra decomposition for UO₂ disks before and after electron and alpha irradiations under different conditions.

UO ₂ , 1700°C/24 h/ ArH ₂ (set G, L)	Fluence (cm ⁻²)	τ_{av} (ps)	Lifetime components		
			τ_1 (ps)	τ_2 (ps)	I_2 (%)
Virgin			168.7 ± 1.1	168.7 ± 1.1	
Irradiated e ⁻ , 1 MeV	5×10^{18}		165.9 ± 1.1	165.9 ± 1.1	
Irradiated e ⁻ , 2.5 MeV	5×10^{17}		195.5 ± 4.7	165.9 ± 4.5	301 ± 7
Irradiated e ⁻ , 2.5 MeV	5×10^{18}		252.8 ± 2.5	160.3 ± 4.3	307 ± 3
Irradiated α , 45 MeV	2×10^{16}		227.1 ± 2.5	161.6 ± 3.2	305 ± 4
Irradiated α , 45 MeV	3×10^{16}		252 ± 3.1	161.7 ± 4.3	307 ± 3
					61.9 ± 2

2.4 Nuclear magnetic resonance

NMR is a powerful analytical technique that allows one to investigate matter via the manipulations of nuclear spins [167]. At JRC-Karlsruhe, the focus has been on the development of liquid- and solid-state NMR for the characterization of actinoid-bearing compounds. High resolution liquid state NMR offers the opportunity not only to get structural information on actinoid complexes but as well to study the differences between lanthanoids and actinoids in their isostructural compounds. A profound knowledge contributes to the understanding and further developments of NMR, such as in the field of waste management and plant decommissioning [168].

Low-temperature solid-state NMR experiments allow one to have a better understanding of the ground state properties of the actinoid-bearing materials in order to support ab initio models to predict long-term behavior or extreme conditions of accident scenarios. It is also possible to directly detect the actinoid nuclei (e.g., ^{239}Pu , ^{235}U) at very low temperatures (approximately 2K) [169,170]. Finally, the local structure characterization of a variety of nuclear materials, with NMR active spins, is possible by using the magic angle spinning (MAS) technique. This MAS-NMR technique is quantitative and sensitive to local order and disorder making it a quiet unique tool in the nuclear field.

To perform these NMR experiments, JRC-Karlsruhe acquired a 9.4 T Bruker magnet coupled with a Bruker Avance III spectrometer. For the specificity of nuclear compounds, either the NMR container or the whole interface between the magnet and the spectrometer called the NMR probe had to be adapted. The following examples report on the procedures developed to ensure the safe confinement of radioactive samples during NMR measurements.

2.4.1 Liquid state nuclear magnetic resonance

As shown in Fig. 2.25, a doubly enclosed NMR sample is obtained by packing the liquid sample solution in a sealed polytetrafluoroethylene tube (without contamination on the outside) in a double-capped glass commercial NMR tube (contamination-free on the outside and inside). Should the glass NMR tube fail for any reason, the active sample is still trapped in the polytetrafluoroethylene tube, which is contaminant-free on the outside.

In this way, the properties of the packages are complemented by hard but brittle glass with that of the soft but flexible PTFE, a common break or joint damage is virtually eliminated during the measurement.

The sample is then introduced into the NMR liquid probe like any other liquid NMR tube.

2.4.2 Low-temperature nuclear magnetic resonance

The main requirement for this type of experiment is that the sample holder must sustain very low temperatures with no leakage of nuclear materials. A plexiglas double container sample carrier is therefore implemented with an inner container

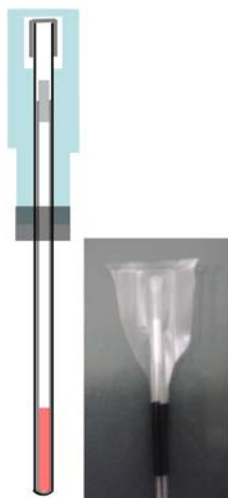


Figure 2.25 Liquid state NMR tube encapsulated for the study of radioactive materials. *NMR*, Nuclear magnetic resonance.

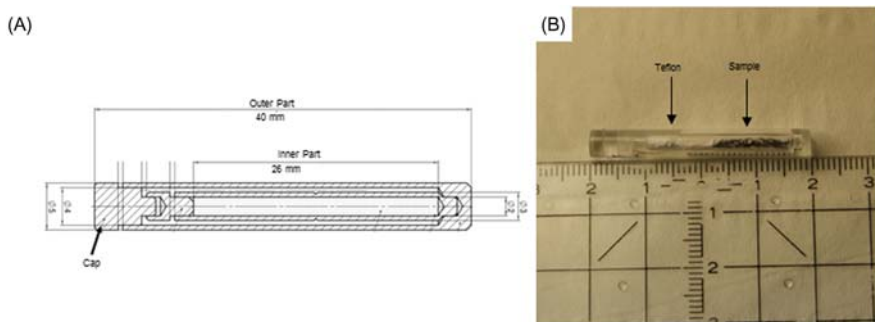


Figure 2.26 (A) Scheme of the double containers device (inner and outer part) and (B) sample holder with a radioactive sample NpAl_2 .

that confines the radioactive sample and an outer container acting as a second barrier (Fig. 2.26). In the case of a sample in powder form, the material is mixed with glue or inserted in a third small plexiglas container. In the case of a bulk or a single crystal, the piece is cleaned from dusts contamination by a neutral solvent and inserted in the inner container.

These operations are all performed in an active glove box (first decontamination or contamination fixing). Then, the inner container with the sample is introduced in a new container, which is clean, with external surfaces protected from the active environment of the glove box. The container is sealed with double component low-temperature araldite glue, removed from the glove box, and then transferred to a clean glove box for decontamination (second decontamination). This second

container is sealed and decontaminated (third decontamination) and removed from the glove box for a “contamination test” of external surface activity performed by the radio protection service. Finally, the container is wrapped up into Teflon band for manipulations (two turns).

A low-temperature NMR probe is used to allow the sample to reach temperatures down to 30 K in stable conditions. This probe is equipped with safety valves in the case of overpressure. Additional filters had to be added to the three valves in the case of a leaking of radioactive material in the closed NMR probe. Caution has also to be taken when opening the cryoprobe after the low-temperature experiment. Therefore, the probe is removed from the NMR spectrometer, and a manual “contamination test” is performed at each steps of the opening. The container and the Teflon band surrounding it are also both checked. In the case that contamination is detected the cryoprobe must be closed back and secured. It will be sealed in a double bag and disposed of as a contaminated device.

2.4.3 High-resolution solid-state nuclear magnetic resonance

Contrary to liquid and low-temperature NMR, for which the sample holder is the main barrier against radioactive contamination, high resolution solid-state NMR requires a different approach. In fact, the spectra of static powder samples is usually characterized by an important broadening due to various interaction (for more details about the typical interactions causing these broadening, the reader is referred to more NMR specific literature [171]), which is not favorable for the structural study of materials. Such effects are not present on the liquid state NMR spectra as they are averaged out by Brownian motion and a high spectral resolution is not necessary at low temperatures as the main focus is the understanding of magnetic behavior. To improve the spectral resolution, the sample in powder form has to be spun at an angle of about 54.74 degrees relative to the external magnetic field [172,173]. To do so, the powders are encapsulated in a sample carrier called a “rotor” (see Fig. 2.27A). This specific technique is called MAS. In order to perform

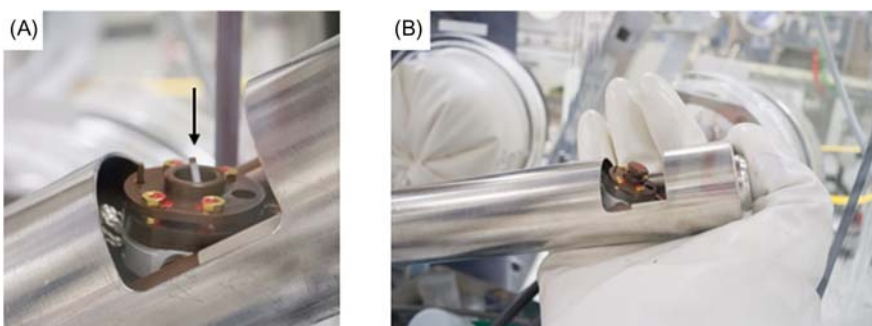


Figure 2.27 (A) The sample carrier called rotor is indicated by the black arrow and (B) the NMR probe is encapsulated in a radioactive glove box. *NMR*, Nuclear magnetic resonance.

MAS-NMR on radioactive powders, the complete NMR probe at JRC-Karlsruhe was integrated in a radioactive glove box (see Fig. 2.27B). With such an approach, MAS-NMR spectra can be acquired on a routine basis using the latest commercially available equipment. A full description of this specific equipment is given by Martel et al. [174].

2.4.4 Some examples of nuclear magnetic resonance spectra acquired at JRC-Karlsruhe

In Fig. 2.28, four spectra are presented of actinoid-based samples as a highlight of some experiments performed at JRC-Karlsruhe. The analysis of most of organometallics in the NMR facility is done using liquid state NMR. Here, in Fig. 2.28A, as an example of liquid spectrum, the ^{13}C - ^1H heteronuclear multiple-quantum correlation spectrum of $[(\text{Cp}_3)\text{U}(\text{OPh})]$ is shown. In combination with ^1H - ^1H correlation spectra, it is possible to perform a complete assignment of all resonances. Thus, ^1H NMR signals at -8.81 ppm are assigned to the protons of the cyclopentadienyl

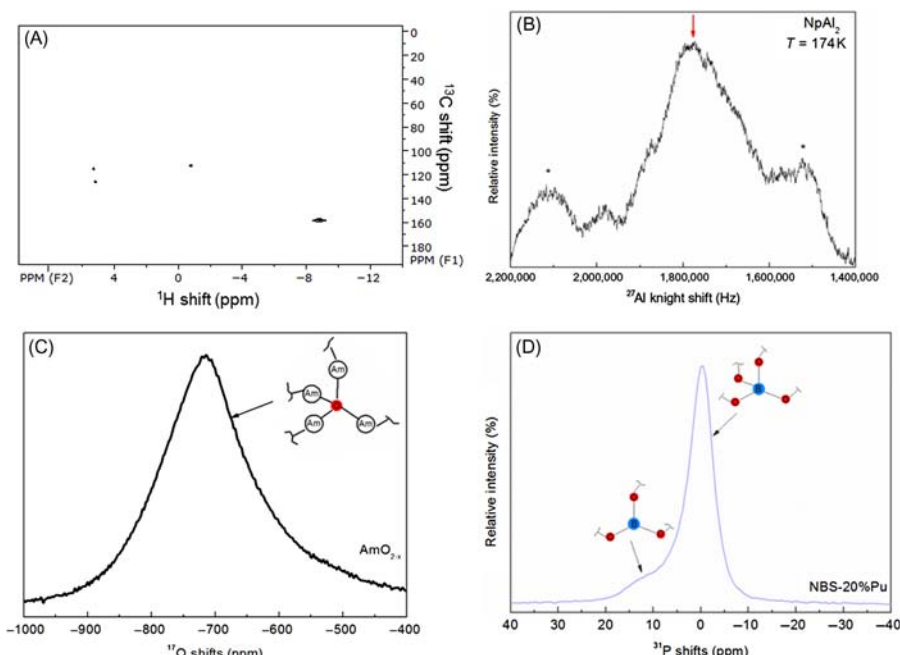


Figure 2.28 (A) ^{13}C - ^1H Liquid correlation spectrum, (B) ^{27}Al static NMR spectrum acquired at $T = 174\text{ K}$ (the red arrow represents the central transition ($-1/2 \leftrightarrow 1/2$) while the stars correspond to the ($-3/2 \leftrightarrow 3/2$) transition), (C) ^{17}O MAS-NMR spectrum of AmO_{2-x} recorded at 55 kHz , and (D) ^{23}Na MAS-NMR spectrum of a sodium borosilicate doped with 20% of plutonium recorded at 40 kHz . *MAS*, Magic angle spinning; *NMR*, nuclear magnetic resonance.

rings, whereas the protons corresponding to the phenyl (Ph) ring give rise to signals at -0.77 , 5.18 , and 5.32 ppm for the protons in ortho-, meta-, and para-position of the Ph ring. Other examples of recently studied transuranic compounds are given in the literature [175–177].

As an example of low-temperature experimental capabilities, the spectrum of NpAl_2 has been shown recorded at 174 K (Fig. 2.28B). While the temperature is not close to the ferromagnetic transition expected at 56 K, the ^{27}Al NMR peak already presents a strong broadening effect. This observation has been attributed to the sensing of the ferromagnetic fluctuations [178]. Similar studies have been done on $\text{U}_{0.15}\text{Np}_{0.85}\text{O}_2$ nuclear fuel [179] in order to have a better understanding of its magnetic properties and the possible use of these data for ab initio calculations.

Two selected materials were presented to illustrate the efficiency of high-resolution solid-state NMR in transuranic-based materials. First, the ^{17}O MAS-NMR spectrum of a crystalline AmO_{2-x} (Fig. 2.28C) shows the local environment of the O atoms surrounded by Am cations [180]. A main peak (68%) was detected at -754 ppm and attributed to the AmO_2 crystalline phase. Due to the nonstoichiometry of the sample, a second peak was detected at -613 ppm as the contribution of the substoichiometric phase in addition to two small additional peaks (in total 10% of the signal) attributed to oxygen in disordered phases, possibly because of self-irradiation damage. This study can easily be applied to mixed oxides as shown in the literature [57,181]. Second, the ^{11}B MAS-NMR spectrum of a sodium borosilicate doped with 20% of plutonium show the known efficiency (see Refs. [182,183]) of this technique to probe disordered materials. Two peaks were detected at -0.2 and 18 ppm and, respectively, attributed to BO_4 and BO_3 species (similarly to Ref. [184]). Such types of NMR characterization of the local environment in glasses can be extended to a better understanding of the effect of incorporation of actinide cations in glasses [185] and/or of their ageing influence under self-irradiation [186].

2.5 Mass spectrometry techniques

MS is an analytical technique in which chemical species are ionized and sorted based on their mass-to-charge ratio. In simpler terms, a mass spectrum measures the masses of the different chemical species contained within a sample. In a typical MS procedure, a sample (e.g., solid, liquid, or gas) is ionized, for example, by bombarding it with electrons. This may cause some of the sample's molecules to break into charged fragments. These ions are then separated according to their mass-to-charge ratio, typically by accelerating them and subjecting them to an electric or magnetic field: ions of the same mass-to-charge ratio will undergo the same amount of deflection [187]. The ions are detected by a mechanism capable of detecting charged particles, such as an electron multiplier. Results are displayed as spectra of the relative abundance of detected ions as a function of the mass-to-charge ratio. The atoms or molecules in the sample can be identified by correlating known masses (e.g., an entire molecule) to the identified masses or through a characteristic fragmentation pattern.

Various MS techniques that are currently used for the study of nuclear fuels also take advantage of their ability to distinguish between different isotopes. In particular, MS techniques are useful to analyze the broad inventory of fission products contained in spent nuclear fuels, the dispersion of radioactive species in the environment, the isotopic abundance of nuclides, etc.

The present summary reports only a couple of example applications of MS techniques to nuclear fuels. Specific works exist for more comprehensive descriptions of MS applications, in particular the so-called inductively coupled MS techniques [188]. The latter are broadly used for the investigation of nuclear materials, thanks to the very high sensitivity obtained (up to concentrations of 10^{-15} g).

2.5.1 Knudsen effusion mass spectrometry

Knudsen effusion MS (KEMS) is a powerful tool for the determination of the thermodynamic properties of nuclear fuels at high temperatures based on the equilibrium between condensed and gaseous phases. It can be used for the identification of the gas composition and its vaporizing behavior as a function of temperature by means of the conversion of the detected spectral ion intensity data into the corresponding vapor pressures of the species in the gaseous phase. This method can further be used for determination of other fundamental thermodynamic properties, such as sublimation enthalpies, ionization energies of gaseous species, enthalpies of formation or activity coefficients.

An example of a KEMS system, installed at JRC-Karlsruhe [189], with a scheme shown in Fig. 2.29, consists of a single Knudsen effusion cell of tungsten (or any other material that is compatible with a sample measured), which is placed in a vacuum chamber and coupled to a quadrupole mass spectrometer. The cell temperature is externally controlled and measured by a pyrometer (the uncertainty of the temperature measurement determined is ± 10 K). Equilibrium is achieved between the gas and condensed phases within the cell, which contains both the sample and the reference material.

To obtain quantitative data, it is very important to avoid calibration material from reacting with the sample during heating. The most common calibration material is silver metal, but experiments with other materials, such as platinum or copper, have been carried out too. Prior to every measurement, the cell and the whole experimental vessel is exposed to vacuum (10^{-6} – 10^{-7} mbar) to get accurate results via background reduction and by avoiding interferences between the atmosphere and the evaporated gaseous species. The cell is then heated by a tungsten coil under a constant heat rate, while appropriate thermal insulation is achieved by surrounding tungsten thermal shields. The beam of gaseous species then exits the cell through the small effusion orifice at the top and is further ionized with a cross beam electron bombardment ion source. The formed ions are then extracted toward a quadrupole where they are separated and measured by a secondary electron multiplier detector attached to the mass spectrometer. This allows ion current measurements and analysis of the mass spectrum of the beam and provides the intensities of ion currents of the evaporated species.

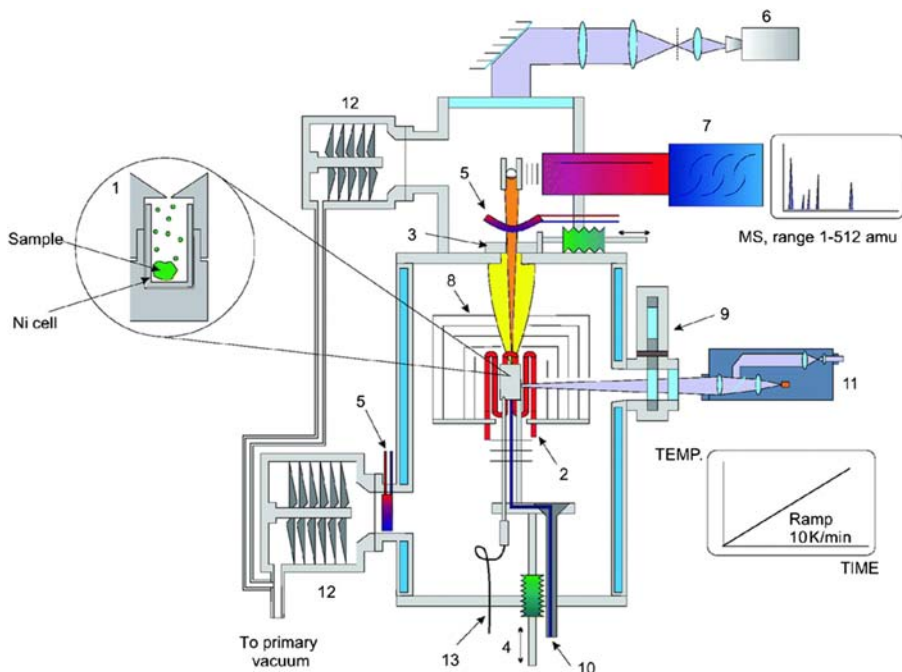


Figure 2.29 [190] A scheme of a Knudsen effusion mass spectrometer; (1) Knudsen cell with sample, in W liner, (2) tungsten heating coil, (3) molecular beam chopper, (4) cell lift facilities for fast heating or cooling, (5) liquid nitrogen trap to reduce background signal, (6) camera to align the cell holder and chopper diaphragm, (7) quadrupole mass spectrometer, (8) thermal shield, (9) revolving protection windows, (10) inlet gas capillary, (11) linear pyrometer, (12) turbo-molecular pump, (13) removable W/Re thermocouple.

The KEMS system installed at JRC-Karlsruhe is not only dedicated to the measurement of basic thermodynamic data, which are mainly done on nuclear materials, but due to the extra gamma radiation shielding it allows the handling of small samples (typically 5–10 mg) of irradiated fuel materials to study kinetics of fission product release. This makes the facility a truly unique technique.

2.6 Secondary ions mass spectrometry

The SIMS technique permits elemental and isotopic analyses on small volumes close to the surface of a specimen bombarded by a beam of “primary” ions. Under the impact of primary ions, several particles are emitted from the sample surface. SIMS instruments are also known as ion microprobes. They use an internally generated beam of either positive (e.g., Cs^+) or negative (e.g., O^{2-}) ions focused on a sample surface, generating an ionic current typically around 5–10 nA, and an impact energy of a few dozens of keV. These constitute a primary ion beam, which

in turn excite and eject ions from the analyte. The latter is referred to as secondary ions. These ionized atoms or molecules coming from the near-surface layers of the specimen are then transferred under vacuum into a mass spectrometer across a high electrostatic potential. Thus, every point of the analyzed sample surface behaves as a source of “secondary” ions characteristic of the elements present in it. Emitted secondary ions are then detected by the mass spectrometer, which provides a local distribution profile of the different species contained in the vicinity of the sample surface. The analysis can be extended to a depth of approximately 50 μm if the primary ions beam, with increased sputtering time, produces a suitable crater on the sample surface. The image field-of-view of a SIMS is of the order of 0.01 mm^2 , with a spatial resolution that can be better than 1 μm .

Samples are typically slices or disks with a well-polished flat surface, where the analysis is performed. Disks are a few mm thick and the amount of material is typically around 100 mg or more.

The local character of SIMS analyses permits a variety of studies on nuclear fuels [191], including the presence and distribution of various chemical species (e.g., fission products, plutonium and minor actinoids, and leaching products in spent fuel) and their diffusion into the fuel matrix [192–196]. SIMS is also employed in nuclear forensics for the identification of uranium particles, and the determination of their isotopic composition [197]. An example of SIMS mapping identifying uranium dioxide and fission products in an irradiated fuel sample is reported in Fig. 2.30.

Top row: Ion maps 3 at%; bottom: 8 at%

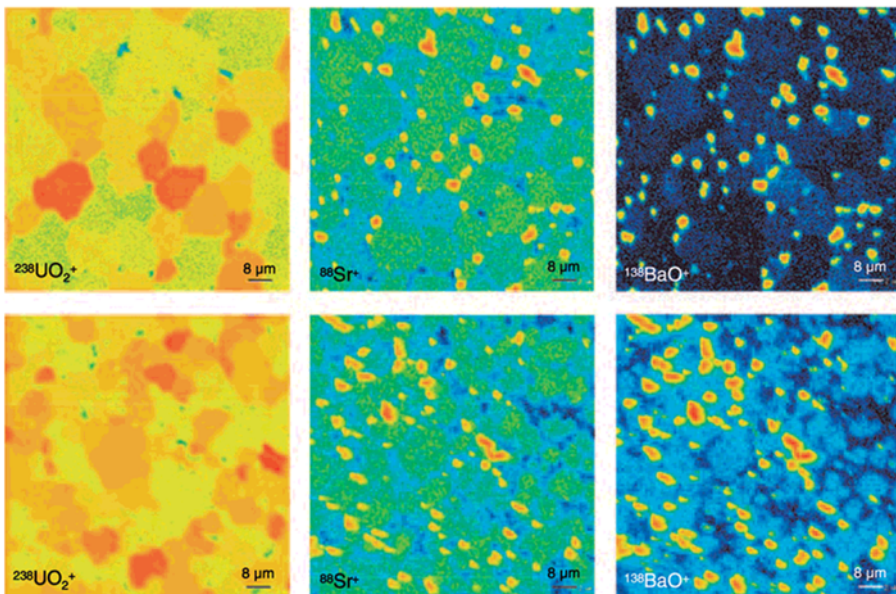


Figure 2.30 Example of SIMS mapping identifying uranium oxide and fission products in an irradiated fuel sample, obtained with a CAMECA IMS 6f shielded instrument installed at JRC-Karlsruhe (Germany) [198].

A common issue of SIMS, especially when analyzing large masses, is isobaric interferences between molecular species having the same mass. This problem can be tackled by resolving isotopic mass ratios, which is possible with most of the current SIMS facilities [199].

Recently, large geometry (LG) SIMS machines have been developed [200]. Basically, LG-SIMS instruments were developed in response to a demand for high mass resolution—high transmission instruments in geosciences and cosmochemistry. These instruments are, like the small geometry SIMS, based on a double focusing mass spectrometer, but with the implementation of a large-radius magnetic sector and improved secondary-ion optics. This allows measurements to be performed at high mass resolution while maintaining high transmission. The implementation of the LG-SIMS for safeguards purposes was made, for example, at JRC-Karlsruhe in close collaboration with CAMECA (Paris, France), NORDSIM laboratory (Stockholm, Sweden), and the University of Western Australia (Perth, Australia). In short, the LG-SIMS technique provides isotopic data for particle analysis that is truly state-of-the-art, combining the highest quality with high throughput. The latter is important for the analysis of small nuclear fuel samples for safeguards application, where timely analysis can be critical, especially in facilities with a high throughput.

2.7 Diffraction techniques

2.7.1 X-ray diffraction

XRD is a widely used and well-known technique based on the interaction of an X-ray electromagnetic beam with the atoms in a crystal lattice. X-rays are scattered in all the directions by atomic electrons in a coherent way. XRD occurs as a result of the constructive interference of photons scattered by the periodic configuration of atoms within crystalline materials. As illustrated in Fig. 2.31, such a constructive interference happens for specific angles following Bragg's law, which is given in Eq. (2.25). It shows how for a given spacing d between crystal planes, and

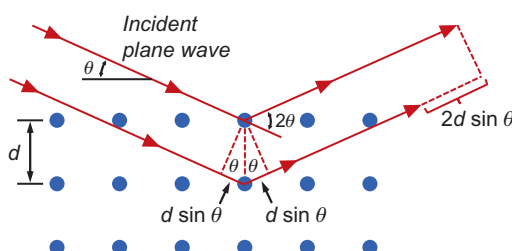


Figure 2.31 Schematic of X-ray diffraction from a two-dimensional atom lattice.

wavelength λ of the incident beam, the orders of constructive interference n result only for specific values of the angle θ :

$$n\lambda = 2d\sin\theta \quad (2.25)$$

The diffractograms obtained are then mathematically correlated to the structural arrangement of the atoms that cause scattering. The positions of the reflections are correlated to the size and the symmetry of the crystallographic lattice, whereas the relative intensity between the different reflections gives information about the atomic positions within the lattice. XRD gives a long-range ordering description of the atomic configuration in a material. However, materials can sometimes present local disorder despite a good crystallinity. In this case, XRD will provide an “average view” of the atomic configuration in the lattice, which can be significantly different from the actual local structure. This is, for example, well-illustrated by Belin et al. [201] where local disorder induced by self-irradiation is responsible for a phase transition in an americium pyrochlore with important differences between crystallographic structure and local structure.

Several variations of XRD techniques exist, but the two main laboratory scale devices that can be easily implemented in a nuclear fuel research facility are single crystal XRD and powder XRD. Single crystal XRD is the method of choice for coordination chemistry studies. It is generally used for ab initio structural determination of unknown structures and gives the information on atomic configuration with a high level of accuracy, including bond distances, bond angles, and shapes of polyhedral coordination. It is therefore an important tool in the field of nuclear fuel reprocessing development, since it describes the coordination configuration between extracting molecules and actinoids [202]. It has also been used for the description of homogeneous precursors used for the synthesis of mixed oxide nuclear fuel [203]. This technique requires the possibility to grow single crystals of the studied material. Recent developments of this technology have increased its spatial resolution and made possible the analysis of single crystals of only a few tens of micrometers in size.

In powder XRD techniques, a polycrystalline sample is irradiated by a monochromatic X-ray beam. The diffractometer varies the incidence angle θ , typically between 10 and 120 degrees, which yields a diffraction pattern. Fig. 2.32 gives an example of a powder XRD pattern of unirradiated PuO_2 . This technique is used in a routine way in the field of nuclear fuel research to confirm the phase purity of synthesized material, or for simple phase identification where the experimental pattern can be compared to libraries containing thousands of crystallographic data. However, more extensive use of the obtained diffractogram can be done since useful information can be extracted through the refinement of experimental pattern.

Detailed analyses of XRD are typically performed with the help of the so-called Rietveld refinement approach [204]. This technique is based on the theoretical calculation of an X-ray diffractogram profile by using library data for the known crystal structures. The calculated pattern is then used to fit the experimental ones by least square optimization. Lattice parameters extracted from powder XRD refinement have

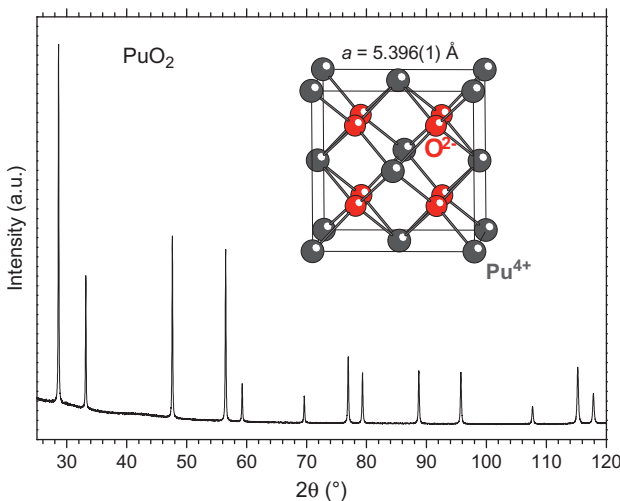


Figure 2.32 Powder XRD pattern measured on unirradiated PuO_2 . *XRD*, X-ray diffraction.

generally a high level of accuracy, of about 0.1 pm. This is of prior interest for nuclear fuel studies since many factors can have an influence on the lattice parameter, such as chemical composition, thermal expansion, radiation damage accumulation, or O/M ratio in the case of oxide fuel. Therefore, numerous studies have been performed based on lattice parameters variation measurement: thermal expansion coefficient can be obtained if the XRD device is equipped with a heating chamber [205,206]. Since noncubic materials generally show anisotropic thermal dilatation, the technique can be used to determine independently the thermal expansion coefficient in each crystallographic direction [207]. Accumulation of irradiation defects can be followed through the monitoring of lattice parameter variations with time [208], and the annealing of this defect structure can be studied using high-temperature powder XRD [209]. Lattice parameter measurement was also performed for the O/M ratio determination of actinide oxides in reductive conditions for a broad range of oxygen partial pressures, temperatures and cooling rates [210–213], which produced precious data for a better understanding of nuclear material behaviors in sintering condition. Still using correlation between lattice parameter and O/M ratio, oxidation of uranium oxide [214] and mixed oxides (MOX) [215] fuel were studied through this technique. Rietveld refinement can be used to obtain the phase proportions in multiphasic materials from powder diffraction pattern [216]. Finally, since the peak broadening is correlated to the material crystal size, powder XRD was used to monitor the crystallite growth as a function of temperature [217,218].

2.7.2 Electron diffraction

Electron diffraction provides similar information as XRD, but the probe particle is an electron instead of a photon. In order to obtain a diffraction pattern, the probe

electron beam must be accelerated to a sufficient KE for its de Broglie wavelength to be comparable with the lattice parameter of the analyzed crystal (order of magnitude of 0.1 nm). The electron beam will be diffracted across the sample only if the latter is sufficiently thin (tens of nm at most). The configuration is typical of a TEM. Therefore, electron diffraction is usually performed in a TEM. The main drawback of this technique is that due to the limitations on the sample size and thickness, it only provides very local information. In turn, this technique provides a two-dimensional diffraction pattern (see Fig. 2.33 [219]), which is a direct image of the reciprocal lattice of the investigated crystal. The spatial Fourier transform of the diffraction figure yields therefore a two-dimensional image of the atomic planes in the crystal (Fig. 2.33). This technique is broadly used for the study of nanocrystalline materials and radiation damage in nuclear fuels.

Associated to the SEM, there is a novel technique called electron back-scattered diffraction (EBSD), which involves the use of a charge coupled device (CCD) setup near the sample on a high angle of configuration to the electron beam [220]. Such a technique generates a diffraction that forms Kikuchi bands produced by each spot on the sample. These single spot diffractions (equivalent to the convergent beam electron diffraction associated to TEM) can be compared with a crystallographic database to obtain an indexation of the Kikuchi lines observed on the diffraction producing a map of the orientations of each observed grain. Such maps are of high relevance when using a FIB to cut out TEM lamellas or when producing micro-pillars for compression tests because it allows cutting them on a known orientation. They are also of interest to study possible strain effects, to characterize grain boundaries, grain size distribution, or even to compare relative orientation between adjacent grains. An example of an EBSD map is shown in Fig. 2.34.

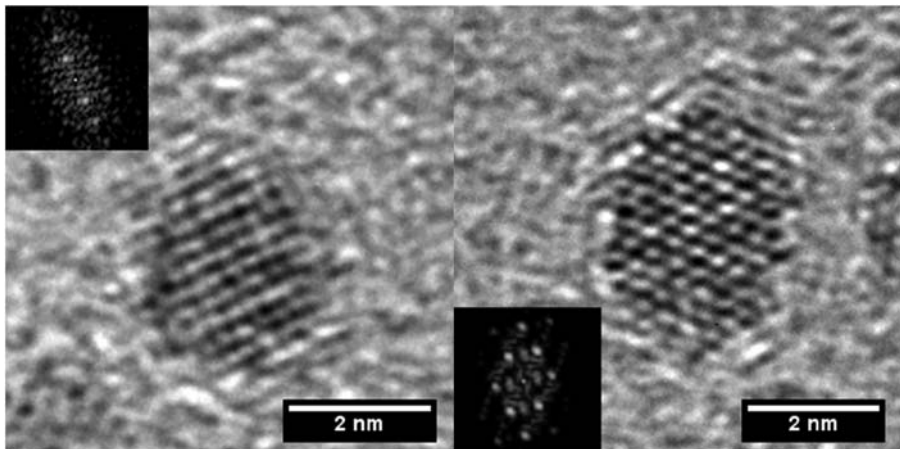


Figure 2.33 Electron diffraction images of a nano-crystalline PuO_2 sample. The main figures show the corresponding two-dimensional image of the atomic planes in the crystal. Insets on both images show the corresponding Fast Fourier Transforms of each particle, which is equivalent of the electron diffraction.

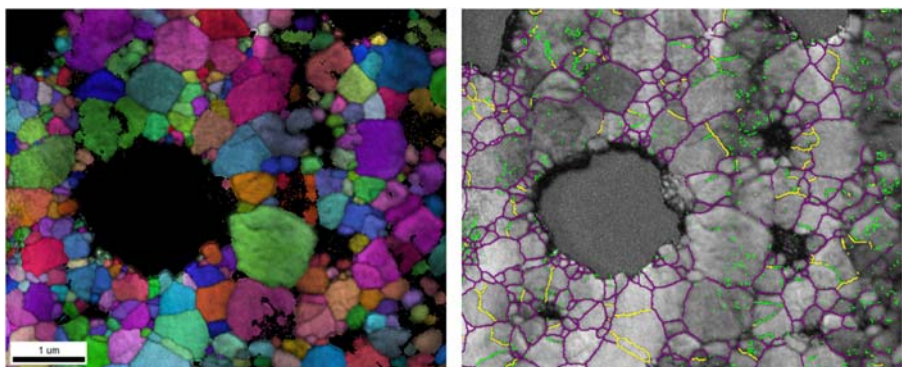


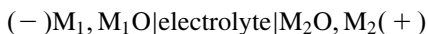
Figure 2.34 Example of EBSD mapping, showing colors for different oriented grains (left) and the identification of grain boundary misorientation (right), where green lines represent GBs with a difference of 2–5 degrees, yellow shown GBs misoriented by 5–15 degrees, and purple shows GBs with >15 degrees [221]. *EBSD*, Electron back-scattered diffraction, *GB*, Grain Boundaries.

2.8 Electrochemical techniques

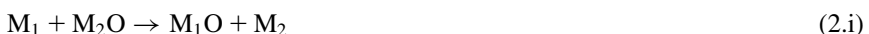
2.8.1 Electromotive force and coulometry

Electromotive force (EMF) measurements are mostly performed on UO₂-based fuel samples by means of solid-state galvanic cells. The use of high-temperature cells of this kind has been demonstrated to be a very useful method for the determination of the oxygen potential in a sample [222,223]. The method is based on the determination of the EMF generated across an electrochemical chain at high temperature. The electrochemical chain consists of two half-cells: the reference electrode, whose oxygen potential is known, and the measuring (sample) electrode. The two half-cells are connected through a solid-state electrolyte in which electrical conductivity is exclusively due to the migration of oxygen ions. Externally platinum jumpers complete the circuit. The process occurring in an EMF cell is well described by Charette and Flengas [224].

The electrochemical chain produced is



where M₁O and M₂O are the metal saturated phases of the two oxides, of which one constitutes the reference electrode and the other, the sample. The overall redox reaction in a cationic model, where the cell is seen as a galvanic chain, is



In this case, the cell potential is given by the Nernst equation

$$\Delta E_{(f)} = -\frac{\Delta G_{f,M_1O}^0 - \Delta G_{f,M_2O}^0}{2F} \quad (2.26)$$

where ΔG_f^0 indicates the standard Gibbs energy of formation of the oxides, and F is the Faraday constant, 96,490 C if ΔE is expressed in V.

In an anionic model, the system can be regarded as an oxygen concentration cell, with oxygen migrating from the anode to the cathode.

In this case, the overall reaction is



where p'_{O_2} and p''_{O_2} are the oxygen partial pressures over the oxide M_1O and M_2O , respectively. The cell potential for reaction (2.27) is given by

$$\Delta E_{(g)} = -\frac{RT}{2F} \ln \left(\frac{p'_{\text{O}_2}}{p''_{\text{O}_2}} \right)^{1/2}, \quad (2.28)$$

where R is the gas constant, 8.314 J/(K mol), and T is the absolute temperature.

In the case in which the oxygen pressures over the oxide phases correspond to the true equilibrium pressures, $\Delta E_{(e)}$ and $\Delta E_{(f)}$ represent the same cell potential

$$\Delta E = \Delta E_{(f)} = \Delta E_{(g)}. \quad (2.29)$$

Eq. (5.18) can be obtained also by considering that, at thermal and chemical equilibrium, the following relation holds

$$\Delta G_{f,\text{MO}}^0 = -RT \ln(p_{\text{O}_2})^{1/2} \quad (2.30)$$

Thus, the standard Gibbs energy of formation of the sample oxide can be measured in the EMF cell if the Gibbs energy of formation is known for the reference electrode.

Systems used for the investigation of nuclear fuels offer the possibility to perform measurements on very small specimens, as the sample half-cell was realized in a cylindrical hole 2 mm in diameter and 5 mm in height. The specimen was either a small amount of powder or a small splinter extracted from a pellet. This feature allowed measurement of the *local* oxygen potential, extracting small pieces from a selected zone of a larger sample. In this case the galvanic cell was placed in an alumina furnace maintained under high vacuum (10^{-9} bar) during the measurements. Temperatures up to 1400 K could be reached. A Fe/FeO reference electrode was employed, with a $\text{Y}_2\text{O}_3/\text{ThO}_2$ solid electrolyte. At thermal and chemical equilibrium, the reversible EMF is given by the following equation:

$$\Delta E_{(g)} = -\frac{RT}{2F} \ln \left(\frac{p_{\text{O}_2}^{\text{sample}}}{p_{\text{O}_2}^{\text{Fe/FeO}}} \right)^{1/2}. \quad (2.31)$$

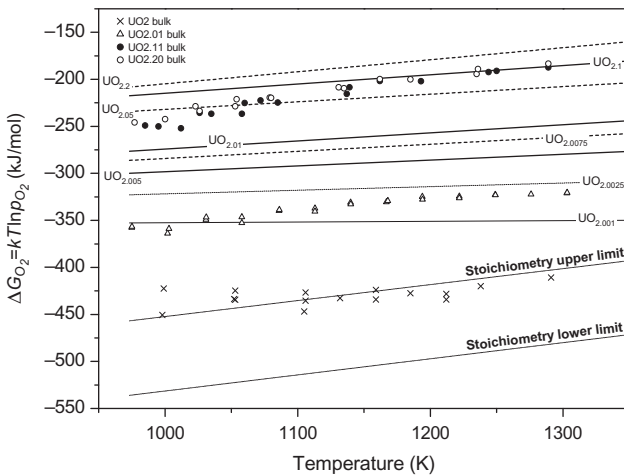


Figure 2.35 EMF measurements on UO_{2+x} samples compared to oxygen potential curves recommended in Ref. [225].

In Eq. (2.31) the following expression was taken for the oxygen potential of the reference electrode:

$$\Delta G_{\text{O}_2\text{Fe}/\text{FeO}} = RT \ln p_{\text{O}_2} \text{ Fe/FeO} = -529,778 + 130.583 T (\text{J/mol}). \quad (2.32)$$

The sample oxygen potential $\Delta G_{\text{O}_2\text{sample}} = RT \ln p_{\text{O}_2\text{sample}}$ was thus measured as a function of T . The use of EMF measurements consisted of the determination (at least qualitative) of the oxygen content in the samples. In principle, the oxygen potential may be translated into O/M ratio using empirical data relating these two properties.

Fig. 2.35 displays some measurements performed on stoichiometric and hyperstoichiometric urania samples along with the Ellingham diagram of UO_{2+x} according to Lindemer [225]. The “stoichiometry zone” was established on the basis of several measurements carried out at JRC-Karlsruhe. Its imprecision is due to the extreme sensitivity of the oxygen partial pressure to x in the very vicinity of the stoichiometry (see, for instance, [226]). In fact, over this range p_{O_2} can vary by several orders of magnitude for variations of x much smaller than the detection limits of any instrument available to measure it.¹

Therefore this method is more sensitive, the closer is the compositions to the exact stoichiometry.

The method complementary to EMF is based on the measurement of electrolytical currents, as opposed to the voltage, flowing in the electrochemical cell. Such a technique is called Coulometry and is advantageous, compared to EMF, in cases where EMF is less sensitive to large variations of analyte compositions, like, for example, in UO_{2+x} with large x values.

¹ By weight difference and TG, x could be measured with an uncertainty not better than 0.005 units O/U.

2.9 Conclusion

The present chapter summarizes some recent advances in the most common experimental techniques used for the chemical characterization of nuclear fuels. Progress in materials science and related techniques, including remote control of testing facilities, has permitted very accurate chemical and structural analyses of highly radioactive materials, which were hardly foreseeable in the end of the 1900s. However, it should be kept in mind that an exhaustive characterization of nuclear fuels, like any other material, should be based on the consistent combination of advanced structural analysis techniques and more “traditional methods,” which still provide the most fundamental materials engineering properties.

Further development of sampling and analysis methods for extremely radioactive materials is still ongoing, particularly in the aftermath of large-scale nuclear power plant core meltdown accidents. The management of sites affected by such accidents, such as Chernobyl in Ukraine and Fukushima-Daiichi in Japan, has been requiring important advances in robotized sampling and analysis techniques. They will lead to even further progress in the analysis of spent nuclear fuels and other sometimes still unknown material species that are synthesized under the extreme conditions of a core meltdown accident. They will hopefully permit a full cleaning and recovery of the accidented areas, in addition to relevant advances in the nuclear fuel chemistry understanding and, hence, safety.

References

- [1] Generation IV International Forum. <https://www.gen-4.org/gif/jcms/c_9260/public>, 2019.
- [2] A. Tosolin, P. Souček, O. Beneš, J.-F. Vigier, L. Luzzi, R.J.M. Konings, Synthesis of plutonium trifluoride by hydro-fluorination and novel thermodynamic data for the $\text{PuF}_3\text{-LiF}$ system, *J. Nucl. Mater.* 503 (2018) 171–177.
- [3] E. Capelli, O. Beneš, M. Beilmann, R.J.M. Konings, Thermodynamic investigation of the LiF-ThF_4 system, *J. Chem. Thermodyn.* 58 (2013) 110–116.
- [4] O. Beneš, R. Jardin, R.J.M. Konings, E. Colineau, F. Wastin, N. Magnani, The high-temperature heat capacity of ThPd_3 and UPd_3 , *J. Chem. Thermodyn.* 41 (2009) 560–563.
- [5] A.W. Coats, J.P. Redfern, Thermogravimetric analysis: a review, *Analyst* 88 (1053) (1963) 906–924.
- [6] M. Kato, T. Tamura, K. Konashi, S. Aono, Oxygen potentials of plutonium and uranium mixed oxide, *J. Nucl. Mater.* 344 (2005) 235–239.
- [7] M. Kato, K. Konashi, N. Nakae, Analysis of oxygen potential of $(\text{U}_{0.7}\text{Pu}_{0.3})\text{O}_{2\pm x}$ and $(\text{U}_{0.8}\text{Pu}_{0.2})\text{O}_{2\pm x}$ based on point defect chemistry, *J. Nucl. Mater.* 389 (2009) 164–169.
- [8] M. Kato, K. Takeuchi, T. Uchida, T. Sunaoshi, K. Konashi, Oxygen potential of $(\text{U}_{0.88}\text{Pu}_{0.12})\text{O}_{2\pm x}$ and $(\text{U}_{0.7}\text{Pu}_{0.3})\text{O}_{2\pm x}$ at high temperatures of 1673–1873K, *J. Nucl. Mater.* 414 (2011) 120–125.
- [9] J.M. Elorrieta, L.J. Bonales, N. Rodríguez-Villagra, V.G. Baonza, J. Cobos, A detailed Raman and X-ray study of UO_{2+x} oxides and related structure transitions, *Phys. Chem. Chem. Phys.* 18 (2016) 28209–28216.

- [10] D. Manara, L. Soldi, S. Mastromarino, K. Boboridis, D. Robba, L. Vlahovic, et al., Laser-heating and radiance spectrometry for the study of nuclear materials in conditions simulating a nuclear power plant accident, *J. Visual. Exp.* 130 (2017) 54807.
- [11] F. De Bruycker, K. Boboridis, P. Poeml, R. Eloirdi, J. Somers, R.J.M. Konings, et al., The melting behaviour of plutonium dioxide: a laser heating study, *J. Nucl. Mater.* 416 (2011) 166–172.
- [12] D. Manara, F. De Bruycker, K. Boboridis, O. Tougait, R. Eloirdi, M. Malki, High temperature radiance spectroscopy measurements of solid and liquid uranium and plutonium carbides, *J. Nucl. Mater.* 426 (2012) 126–138.
- [13] U. Carvajal Nunez, D. Prieur, R. Bohler, D. Manara, Melting point determination of uranium nitride and uranium plutonium nitride: a laser heating study, *J. Nucl. Mater.* 449 (2014) 1–8.
- [14] O. Cedillos-Barraza, D. Manara, K. Boboridis, T. Watkins, S. Grasso, D.D. Jayaseelan, et al., Investigating the highest melting temperature materials: a laser melting study of the TaC-HfC system, *Sci. Rep.* 6 (2016) 37962.
- [15] H.F. Jackson, D.D. Jayaseelan, D. Manara, C.P. Casoni, W.E. Lee, Laser melting of zirconium carbide: determination of phase transitions in refractory ceramic systems, *J. Am. Ceram. Soc.* 94 (2011) 3561–3569.
- [16] D.P. DeWitt, J.C. Richmond, Thermal radiative properties of materials, in: D.P. DeWitt, G.D. Nutter (Eds.), *Theory and Practice of Radiation Thermometry*, Wiley, New York, 1988.
- [17] R. Böhler, M.J. Welland, D. Prieur, P. Cakir, T. Vitova, T. Pruessmann, et al., Recent advances in the study of the $\text{UO}_2\text{--PuO}_2$ phase diagram, *J. Nucl. Mater.* 448 (2014) 330–349.
- [18] D. Manara, M. Sheindlin, W. Heinz, C. Ronchi, High-temperature phase transition measurements in highly volatile refractory materials via laser surface heating techniques, *Rev. Sci. Instrum.* 79 (2008) 113901.
- [19] S. Mastromarino, A. Seibert, E. Hashem, A. Ciccioli, D. Prieur, A. Scheinost, S. Stohr, P. Lajarge, J. Boshoven, D. Robba, M. Ernstberger, D. Bottomley, D. Manara, Assessment of solid/liquid equilibria in the $(\text{U}, \text{Zr})\text{O}_{2+y}$ system, *J. Nucl. Mater.* 494 (2017) 368–379.
- [20] A. Quaini, Étude thermodynamique du corium en cuve – Application à l’interaction corium/béton (Ph.D. thesis), Université Grenoble-Alpes, 2014.
- [21] A. Quaini, C. Guéneau, S. Gossé, T. Alpettaz, E. Brackx, R. Domenger, et al., Experimental contribution to the corium thermodynamic modelling – the $\text{U}\text{--Zr}\text{--Al}\text{--Ca}\text{--Si}\text{--O}$ system, *Ann. Nucl. Energy* 93 (2016) 43–49.
- [22] M. Sheindlin, D. Halton, M. Musella, C. Ronchi, Advances in the use of laser-flash techniques for thermal diffusivity measurement, *Rev. Sci. Instrum.* 69 (1998) 1426–1436.
- [23] B.T.M. Willis, Neutron diffraction studies of the actinide oxides. I. Uranium dioxide and thorium dioxide at room temperature, *Proc. R. Soc. London, A* 274 (1963) 122–133.
- [24] G. Dolling, R.A. Cowley, A.D.B. Woods, The crystal dynamics of uranium dioxide, *Can. J. Phys.* 43 (1965) 1397–1413.
- [25] T. Shimanouchi, M. Tsuboi, T. Miyazawa, Optically active lattice vibrations as treated by the GF-matrix method, *J. Chem. Phys.* 35 (1961) 1597.
- [26] V.G. Keramidas, W.B. White, Raman spectra of oxides with the fluorite structure, *J. Chem. Phys.* 59 (1973) 1561.
- [27] G.M. Begun, R.G. Haire, W.R. Wilmarth, J.R. Peterson, Raman spectra of some actinide dioxides and of EuF_2 , *J. Less-Common Met.* 162 (1990) 129.

- [28] Q. Yin, Y. Savrasov, Origin of low thermal conductivity in nuclear fuels, *Phys. Rev. Lett.* 100 (2008) 2255041–2255044.
- [29] Y. Yun, D. Legut, P.M. Oppeneer, Phonon spectrum, thermal expansion and heat capacity of UO_2 from first-principles, *J. Nucl. Mater.* 426 (2012) 109–114.
- [30] D. Manara, B. Renker, Raman spectra of stoichiometric and hyperstoichiometric uranium dioxide, *J. Nucl. Mater.* 321 (2003) 233–237.
- [31] T. Livneh, E. Sterer, Effect of pressure on the resonant multiphonon Raman scattering in UO_2 , *Phys. Rev. B* 73 (2006) 085118.
- [32] G. Guimbretière, L. Desgranges, A. Canizarès, G. Carlot, R. Caraballo, C. Jégou, et al., Determination of in-depth damaged profile by Raman line scan in a pre-cut He^{2+} irradiated UO_2 *Appl. Phys. Lett.* 100 (2012) 251914.
- [33] G. Guimbretière, L. Desgranges, A. Canizarès, R. Caraballo, F. Duval, N. Raimboux, et al., In situ Raman monitoring of He^{2+} irradiation induced damage in a UO_2 ceramic *Appl. Phys. Lett.* 103 (2013) 041904.
- [34] C. Jégou, R. Caraballo, S. Peuget, D. Roudil, L. Desgranges, M. Magnin, Raman spectroscopy characterization of actinide oxides $(\text{U}_{1-y}\text{Pu}_y)\text{O}_2$: resistance to oxidation by the laser beam and examination of defects, *J. Nucl. Mater.* 405 (2010) 235–243.
- [35] C. Jegou, M. Gennisson, S. Peuget, L. Desgranges, G. Guimbretière, M. Magnin, et al., Raman micro-spectroscopy of UOX and MOX spent nuclear fuel characterization and oxidation resistance of the high burn-up structure, *J. Nucl. Mater.* 458 (2015) 343–349.
- [36] M. Naji, J.-Y. Colle, O. Beneš, M. Sierig, J. Rautio, P. Lajarge, et al., An original approach for Raman spectroscopy analysis of radioactive materials and its application to americium-containing samples, *J. Raman Spectrosc.* 46 (2015) 750–756.
- [37] M.J. Sarsfield, R.J. Taylor, C. Puxley, H.M. Steele, Raman spectroscopy of plutonium dioxide and related materials, *J. Nucl. Mater.* 427 (2012) 333–342.
- [38] Z. Talip, T. Wiss, P. Raison, J. Paillier, D. Manara, J. Somers, et al., Raman and X-ray studies of uranium-lanthanum-mixed oxides before and after air oxidation, *J. Am. Ceram. Soc.* 98 (2015) 2278–2285.
- [39] M. Chollet, D. Prieur, R. Böhler, R. Belin, D. Manara, The melting behaviour of uranium/neptunium mixed oxides, *J. Chem. Thermodyn.* 89 (2015) 27–34.
- [40] J.M. Elorrieta, D. Manara, L.J. Bonales, J.-F. Vigier, O.B. Dieste, M. Naji, et al., Raman study of the oxidation in $(\text{U}, \text{Pu})\text{O}_2$ as a function of Pu content, *J. Nucl. Mater.* 495 (2017) 484–491.
- [41] K. Rickert, T.A. Prusnick, M.M. Kimani, E.A. Moore, C.A. Merriman, J.M. Mann, Assessing UO_2 sample quality with μ -Raman spectroscopy, *J. Nucl. Mater.* 514 (2019) 1–11.
- [42] Z. Talip, S. Peuget, M. Magnin, M. Tribet, C. Valot, R. Vauchy, et al., Characterization of un-irradiated MIMAS MOX fuel by Raman spectroscopy and EPMA, *J. Nucl. Mater.* 499 (2018) 88–97.
- [43] E. Villa-Aleman, N.J. Bridges, T.C. Shehee, A.L. Houk, Raman microspectroscopy of PuO_2 particulate aggregates, *J. Nucl. Mater.* 515 (2019) 140–149.
- [44] C. Ciszak, M. Mermoux, S. Miro, G. Gutierrez, F. Lepretre, I. Popa, et al., Micro-Raman analysis of the fuel-cladding interface in a high burnup PWR fuel rod, *J. Nucl. Mater.* 495 (2017) 392–404.
- [45] O.A. Maslova, G. Guimbretière, M.R. Ammar, L. Desgranges, C. Jégou, A. Canizarès, et al., Raman imaging and principal component analysis-based data processing on uranium oxide ceramics, *Mater. Charact.* 129 (2017) 260–269.

- [46] D. Manara, M. Naji, S. Mastromarino, J.M. Elorrieta, N. Magnani, L. Martel, et al., The Raman fingerprint of plutonium dioxide: some example applications for the detection of PuO_2 in host matrices, *J. Nucl. Mater.* 499 (2018) 268–271.
- [47] M. Newville, Fundamentals of XAFS, *Spectroscopic Methods in Mineralogy and Material Sciences*, De Gruyter, Berlin, Boston, MA, 2014.
- [48] J. Rothe, S. Butorin, K. Dardenne, M.A. Denecke, B. Kienzler, M. Löble, et al., The INE-Beamline for actinide science at ANKA, *Rev. Sci. Instrum.* 83 (2012) 043105.
- [49] T. Vitova, K.O. Kvashnina, G. Nocton, G. Sukharina, M.A. Denecke, S.M. Butorin, et al., High energy resolution X-ray absorption spectroscopy study of uranium in varying valence states, *Phys. Rev. B* 82 (2010) 235118.
- [50] D. Popmintchev, B.R. Galloway, M.-C. Chen, et al., Near- and extended-edge X-ray-absorption fine-structure spectroscopy using ultrafast coherent high-order harmonic supercontinua, *Phys. Rev. Lett.* 120 (2018) 093002.
- [51] M.A. Denecke, X-ray spectroscopy in studies of the nuclear fuel cycle, in: J.A.V. Bokhoven, C. Lamberti (Eds.), *X-Ray Absorption and X-Ray Emission Spectroscopy*, John Wiley & Sons, Ltd, 2016, pp. 523–559.
- [52] W. Matz, N. Schell, G. Bernhard, F. Prokert, T. Reich, J. Claussner, et al., ROBL – a CRG beamline for radiochemistry and materials research at the ESRF, *J. Synchrotron Radiat.* 6 (1999) 1076–1085.
- [53] D. Prieur, P.M. Baldo, A. Jankowiak, E. Gavilan, A.C. Scheinost, N. Herlet, et al., Local structure and charge distribution in mixed uranium–americium oxides: effects of oxygen potential and Am content, *Inorg. Chem.* 50 (2011) 12437–12445.
- [54] D. Prieur, P. Martin, F. Lebreton, T. Delahaye, D. Banerjee, A.C. Scheinost, et al., Accommodation of multivalent cations in fluorite-type solid solutions: case of Am-bearing UO_2 , *J. Nucl. Mater.* 434 (2013) 7–16.
- [55] D. Prieur, U. Carvajal-Nunez, J. Somers, O/M ratio determination and oxidation behaviour of $\text{Th}_{0.80}\text{Am}_{0.20}\text{O}_{2-x}$, *J. Nucl. Mater.* 435 (2013) 49–51.
- [56] R. Vauchy, R.C. Belin, A.-C. Robisson, F. Lebreton, L. Aufore, A.C. Scheinost, et al., Actinide oxidation state and O/M ratio in hypostoichiometric uranium–plutonium–americium $\text{U}_{0.750}\text{Pu}_{0.246}\text{Am}_{0.004}\text{O}_{2-x}$ mixed oxides, *Inorg. Chem.* 55 (2016) 2123–2132.
- [57] J.-F. Vigier, P.M. Martin, L. Martel, D. Prieur, A.C. Scheinost, J. Somers, Structural investigation of $(\text{U}_{0.7}\text{Pu}_{0.3})\text{O}_{2-x}$ mixed oxides, *Inorg. Chem.* 54 (2015) 5358–5365.
- [58] C. Degueldre, M. Martin, G. Kuri, D. Grolimund, C. Borca, Plutonium–uranium mixed oxide characterization by coupling micro-X-ray diffraction and absorption investigations, *J. Nucl. Mater.* 416 (2011) 142–150.
- [59] R. Bès, T. Ahopelto, A.-P. Honkanen, S. Huotari, G. Leinders, J. Pakarinen, et al., Laboratory-scale X-ray absorption spectroscopy approach for actinide research: experiment at the uranium L3-edge, *J. Nucl. Mater.* 507 (2018) 50–53.
- [60] K.O. Kvashnina, S.M. Butorin, P. Martin, P. Glatzel, Chemical state of complex uranium oxides, *Phys. Rev. Lett.* 111 (2013) 2530021–2530025.
- [61] A. Zimina, K. Dardenne, M.A. Denecke, J.D. Grunwaldt, E. Huttel, H. Lichtenberg, et al., The CAT-ACT Beamline at ANKA: a new high energy X-ray spectroscopy facility for CATalysis and ACTinide research, *J. Phys.: Conf. Ser.* 712 (2016) 0120191–0120194.
- [62] I. Llorens, P.L. Solari, B. Sitaud, R. Bes, S. Cammelli, H. Hermange, et al., X-ray absorption spectroscopy investigations on radioactive matter using MARS beamline at SOLEIL synchrotron, *Radiochim. Acta* 102 (2014) 957–972.

- [63] P.L. Solari, S. Schlutig, S. Hermange, B. Sitaud, MARS, a new beamline for radioactive matter studies at SOLEIL, *J. Phys.: Conf. Ser.* 190 (2009) 0120421–0120424.
- [64] E.B. Karlsson, H. Siegbahn, Introduction to Kai Siegbahn's memorial issue, *Nucl. Instrum. Methods Phys. Res., Sect. A* 601 (1) (2009) 1–7.
- [65] D.W. Turner, Limits to resolving power in photoelectron spectroscopy, *Nature* 213 (1967) 795–796.
- [66] D. Briggs, M.P. Seah, Practical surface analysis, second ed., *Auger and X-Ray Photoelectron Spectroscopy*, vol. 1, John Wiley and Sons, Chichester, 1990.
- [67] H. Bubert, J.C. Rivière, W.S. Werner, X-ray photoelectron spectroscopy (XPS), in: G. Friedbacher, H. Bubert (Eds.), *Surface and Thin Film Analysis*, Wiley, 2011.
- [68] S. Hüfner, *Photoelectron Spectroscopy, Principles and Applications*, Springer, 2003.
- [69] N.H. Turner, J.A. Schreibels, Surface analysis: X-ray photoelectron spectroscopy and auger electron spectroscopy, *Anal. Chem.* 72 (12) (2000) 99–110.
- [70] M.P. Seah, W.A. Dench, Quantitative electron spectroscopy of surfaces: a standard data base for electron inelastic mean free paths in solids, *Surf. Interface Anal.* 1 (1) (1979) 2–11.
- [71] S.D. Senanayake, G.I.N. Waterhouse, A.S.Y. Chan, T.E. Madey, D.R. Mullins, H. Idriss, Probing surface oxidation of reduced uranium dioxide thin film using synchrotron radiation, *J. Phys. Chem. C* 111 (22) (2007) 7963–7970.
- [72] D. Frank Ogletree, H. Bluhm, E.D. Hebenstreit, M. Salmeron, Photoelectron spectroscopy under ambient pressure and temperature conditions, *Nucl. Instrum. Methods Phys. Res., Sect. A* 601 (1–2) (2009) 151–160.
- [73] P.J. Cumpson, M.P. Seah, Random uncertainties in AES and XPS: I: Uncertainties in peak energies, intensities and areas derived from peak synthesis, *Surf. Interface Anal.* 18 (5) (1992) 345–360.
- [74] P.J. Cumpson, M.P. Seah, Random uncertainties in AES and XPS: II: Quantification using either relative or absolute measurements, *Surf. Interface Anal.* 18 (5) (1992) 361–367.
- [75] M.P. Seah, Quantitative analysis of surfaces by XPS: a review, *Surf. Interface Anal.* 2 (1980) 222–239.
- [76] M.P. Seah, M.T. Anthony, Quantitative XPS: the calibration of spectrometer intensity – energy response functions. Part 1 – The establishment of reference procedures and instrument behaviour, *Surf. Interface Anal.* 6 (1984) 230–241.
- [77] M.P. Seah, Quantitative AES and XPS: convergence between theory and experimental databases, *J. Electron Spectrosc. Relat. Phenom.* 100 (1999) 55–73.
- [78] M.P. Seah, Reference data for Auger electron spectroscopy and X-ray photoelectron spectroscopy combined, *Appl. Surf. Sci.* 144–145 (1999) 161–167.
- [79] M.P. Seah, M.E. Jones, M.T. Anthony, Quantitative XPS: the calibration of spectrometer intensity-energy response functions. Part 2 – Results of interlaboratory measurements for commercial instruments, *Surf. Interface Anal.* 6 (1984) 242–254.
- [80] S.D. Senanayake, R. Rousseau, D. Colegrave, H. Idriss, The reaction of water on polycrystalline UO₂: pathways to surface and bulk oxidation, *J. Nucl. Mater.* 342 (1–3) (2005) 179–187.
- [81] Y.A. Teterin, V.M. Kulakov, A.S. Baev, N.B. Nevzorov, I.V. Melnikov, V.A. Streltsov, et al., A study of synthetic and natural uranium oxides by X-ray photoelectron spectroscopy, *Phys. Chem. Miner.* 7 (4) (1981) 151–158.
- [82] G.C. Allen, J.A. Crofts, M.T. Curtis, P.M. Tucker, D. Chadwick, P.J. Hampson, X-ray photoelectron-spectroscopy of some uranium oxide phases, *J. Chem. Soc., Dalton Trans.* 12 (1974) 1296–1301.

- [83] G.C. Allen, I.R. Trickle, P.M. Tucker, Surface characterization of uranium metal and uranium-dioxide using X-ray photoelectron-spectroscopy, *Philos. Mag. B* 43 (4) (1981) 689–703.
- [84] G.C. Allen, P.M. Tucker, J.W. Tyler, Satellite structure in the U-4f X-ray photoelectron-spectrum of uranium-dioxide, *J. Chem. Soc., Chem. Commun.* 14 (1981) 691–692.
- [85] T. Gouder, C. Colmenares, J.R. Naegle, J. Verbist, Study of the surface oxidation of uranium by UV photoemission spectroscopy, *Surf. Sci.* 235 (2–3) (1990) 280–286.
- [86] T. Gouder, R. Eloirdi, R. Caciuffo, Direct observation of pure pentavalent uranium in U_2O_5 thin films by high resolution photoemission spectroscopy, *Sci. Rep.* 8 (1) (2018) 8306.
- [87] P.S. Bagus, C.J. Nelin, E.S. Ilton, Theoretical modeling of the uranium 4f XPS for U(VI) and U(IV) oxides, *J. Chem. Phys.* 139 (24) (2013) 244704.
- [88] E.S. Ilton, P.S. Bagus, XPS determination of uranium oxidation states, *Surf. Interface Anal.* 43 (13) (2011) 1549–1560.
- [89] S.D. Senanayake, H. Idriss, Water reactions over stoichiometric and reduced $\text{UO}_2(1\ 1\ 1)$ single crystal surfaces, *Surf. Sci.* 563 (1–3) (2004) 135–144.
- [90] S. Sunder, N.H. Miller, A.M. Duclos, In XPS and XRD studies of samples from the natural fission reactors in the OKLO uranium deposits, *Sci. Basis Nucl. Waste Manage.* XVII (1994) 631–638.
- [91] P.A. Tempest, P.M. Tucker, J.W. Tyler, Oxidation of UO_2 pellets in air at 503 and 543 K studied using X-Ray photo-electron spectroscopy and X-ray diffraction, *J. Nucl. Mater.* 151 (1988) 251–268.
- [92] Y.A. Teterin, A.S. Baev, S.A. Bogatov, X-ray photoelectron study of samples containing reactor fuel from “lava” and products growing on it which formed at Chernobyl NPP due to the accident, *J. Electron Spectrosc. Relat. Phenom.* 68 (C) (1994) 685–694.
- [93] Y.S. Youn, J. Lee, J. Kim, J.Y. Kim, Compositional changes at the interface between thorium-doped uranium dioxide and zirconium due to high-temperature annealing, *J. Nucl. Mater.* 504 (2018) 50–54.
- [94] G.C. Allen, P.M. Tucker, R.K. Wild, Surface analysis of HTR fuel particles by X-ray photoelectron spectroscopy, *J. Nucl. Mater.* 71 (2) (1978) 345–348.
- [95] T. Do, K.G. Irving, W.H. Hocking, Microchemical study of high-burnup CANDU® fuel by imaging-XPS, *J. Nucl. Mater.* 383 (1–2) (2008) 34–40.
- [96] A.F. Gerwing, F.E. Doern, W.H. Hocking, X-ray photoelectron spectroscopy on radioactive materials using a McPherson ESCA-36 equipped with an SSL position-sensitive detector, *Surf. Interface Anal.* 14 (9) (1989) 559–566.
- [97] G.C. Allen, P.M. Tucker, Surface oxidation of uranium metal as studied by X-ray photoelectron spectroscopy, *J. Chem. Soc., Dalton Trans.* 5 (1973) 470–474.
- [98] J. Bloch, U. Atzmony, M.P. Dariel, M.H. Mintz, N. Shamir, Surface spectroscopy studies of the oxidation behavior of uranium, *J. Nucl. Mater.* 105 (2–3) (1982) 196–200.
- [99] W. McLean, C.A. Colmenares, R.L. Smith, G.A. Somorjai, Electron-spectroscopy studies of clean thorium and uranium surfaces. Chemisorption and initial stages of reaction with O_2 , CO, and CO_2 , *Phys. Rev. B* 25 (1982) 8–24.
- [100] G.C. Allen, P.M. Tucker, R.A. Lewis, X-ray photoelectron-spectroscopy study of the initial oxidation of uranium metal in oxygen + water-vapor mixtures, *J. Chem. Soc., Faraday Trans.* 80 (1984) 991–1000.
- [101] G.C. Allen, P.M. Tucker, J.W. Tyler, The behavior of uranium-oxides in low partial pressures of O_2 studied using X-ray photoelectron-spectroscopy, *Vacuum* 32 (8) (1982) 481–486.

- [102] K. Winer, C.A. Colmenares, R.L. Smith, F. Wooten, Interaction of water vapor with clean and oxygen-covered uranium surfaces, *Surf. Sci.* 183 (1–2) (1987) 67–99.
- [103] A. Seibert, T. Gouder, F. Huber, Formation and stability of actinide oxides: a valence band photoemission study, *Radiochim. Acta* 97 (4–5) (2009) 247–250.
- [104] A. Seibert, T. Gouder, F. Huber, Interaction of PuO_2 thin films with water, *Radiochim. Acta* 98 (2010) 647–654.
- [105] J.E. Stubbs, C.A. Biwer, A.M. Chaka, E.S. Ilton, Y. Du, J.R. Bargar, et al., Oxidative corrosion of the UO_2 (001) surface by nonclassical diffusion, *Langmuir* 33 (46) (2017) 13189–13196.
- [106] P. Cakir, R. Eloirdi, F. Huber, R.J.M. Konings, T. Gouder, An XPS and UPS study on the electronic structure of ThO_x ($x \leq 2$) thin films, *J. Phys. Chem. C* 118 (42) (2014) 24497–24503.
- [107] P. Cakir, R. Eloirdi, F. Huber, R.J.M. Konings, T. Gouder, Thorium effect on the oxidation of uranium: photoelectron spectroscopy (XPS/UPS) and cyclic voltammetry (CV) investigation on $(\text{U}_{1-x}\text{Th}_x)\text{O}_2$ ($x = 0$ to 1) thin films, *Appl. Surf. Sci.* 393 (2017) 204–211.
- [108] S.B. Donald, M.L. Davisson, Z. Dai, S.K. Roberts, A.J. Nelson, Relative impact of H_2O and O_2 in the oxidation of UO_2 powders from 50 to 300°C, *J. Nucl. Mater.* 496 (2017) 353–361.
- [109] J.D. Farr, R.K. Schulze, M.P. Neu, Surface chemistry of Pu oxides, *J. Nucl. Mater.* 328 (2–3) (2004) 124–136.
- [110] T. Gouder, A. Seibert, L. Havela, J. Rebizant, Search for higher oxides of Pu: a photo-emission study, *Surf. Sci.* 601 (14) (2007) L77–L80.
- [111] T. Gouder, A.B. Shick, F. Huber, Surface interaction of PuO_2 , UO_{2+x} and UO_3 with water ice, *Top. Catal.* 56 (12) (2013) 1112–1120.
- [112] B.L. Scott, J.J. Joyce, T.D. Durakiewicz, R.L. Martin, T.M. McCleskey, E. Bauer, et al., High quality epitaxial thin films of actinide oxides, carbides, and nitrides: advancing understanding of electronic structure of f-element materials, *Coord. Chem. Rev.* 266–267 (2014) 137–154.
- [113] R. Sekine, H. Nakamatsu, T. Mukoyama, J. Onoe, M. Hirata, M. Kurihara, et al., Electronic structures of metal carbides TiC and UC : similarity and dissimilarity, *Adv. Quantum Chem.* 29 (1998) 123–136.
- [114] M. Eckle, R. Eloirdi, T. Gouder, M.C. Tosti, F. Wastin, J. Rebizant, Electronic structure of UC_x films prepared by sputter co-deposition, *J. Nucl. Mater.* 334 (1) (2004) 1–8.
- [115] L. Luo, Y. Hu, Q. Pan, Z. Long, L. Lu, K. Liu, et al., Extended study on oxidation behaviors of $\text{UN}_{0.68}$ and $\text{UN}_{1.66}$ by XPS, *J. Nucl. Mater.* 501 (2018) 371–380.
- [116] X. Wang, Z. Long, R. Bin, R. Yang, Q. Pan, F. Li, et al., Study of the decomposition and phase transition of uranium nitride under UHV conditions via TDS, XRD, SEM, and XPS, *Inorg. Chem.* 55 (21) (2016) 10835–10838.
- [117] L. Black, F. Miserque, T. Gouder, L. Havela, J. Rebizant, F. Wastin, Preparation and photoelectron spectroscopy study of UN_x thin films, *J. Alloys Compd.* 315 (1–2) (2001) 36–41.
- [118] K.I. Maslakov, Y.A. Teteri, S.V. Stefanovsky, S.N. Kalmykov, A.Y. Teterin, K.E. Ivanov, et al., XPS study of neptunium and plutonium doped iron-bearing and iron-free sodium-aluminium-phosphate glasses, *J. Non-Cryst. Solids* 482 (2018) 23–29.
- [119] N. Ollier, M.J. Guittet, M. Gautier-Soyer, G. Panczer, B. Champagnon, P. Jollivet, U environment in leached SON68 type glass: a coupled XPS and time-resolved photoluminescence spectroscopy study, *Opt. Mater.* 24 (1–2) (2003) 63–68.

- [120] J. Szajman, R.S. Smart, S. Myhra, X-ray photoelectron-spectroscopy studies of valence states of cerium and uranium in Synroc-C, *Surf. Coat. Technol.* 30 (1987) 333–342.
- [121] A.Y. Teterin, K.I. Maslakov, Y.A. Teterin, K.E. Ivanov, T.S. Livshits, S.V. Yudintsev, et al., The XPS study of the structure of uranium-containing ceramics, *Nucl. Technol. Radiat. Prot.* 25 (2) (2010) 107–113.
- [122] M. Karabulut, G.K. Marasinghe, C.S. Ray, D.E. Day, O. Ozturk, G.D. Waddill, X-ray photoelectron and Mossbauer spectroscopic studies of iron phosphate glasses containing U, Cs and Bi, *J. Non-Cryst. Solids* 249 (2–3) (1999) 106–116.
- [123] M.P. Lahalle, R. Guillaumont, G.C. Allen, Surface behavior of uranium-dioxide after immersion in mineral water studies by X-ray photoelectron-spectroscopy, *J. Chem. Soc., Faraday Trans.* 86 (14) (1990) 2641–2644.
- [124] M. Razdan, M. Trummer, D. Zagidulin, M. Jonsson, D.W. Shoesmith, Electrochemical and surface characterization of uranium dioxide containing rare-earth oxide (Y_2O_3) and metal (Pd) particles, *Electrochim. Acta* 130 (2014) 29–39.
- [125] B.G. Santos, H.W. Nesbitt, J.J. Noel, D.W. Shoesmith, X-ray photoelectron spectroscopy study of anodically oxidized SIMFUEL surfaces, *Electrochim. Acta* 49 (11) (2004) 1863–1873.
- [126] B.G. Santos, J.J. Noël, D.W. Shoesmith, The influence of calcium ions on the development of acidity in corrosion product deposits on SIMFUEL, UO_2 , *J. Nucl. Mater.* 350 (2006) 320–331.
- [127] B.G. Santos, J.J. Noel, D.W. Shoesmith, The influence of silicate on the development of acidity in corrosion product deposits on SIMFUEL (UO_2), *Corros. Sci.* 48 (11) (2006) 3852–3868.
- [128] S. Stumpf, A. Seibert, T. Gouder, F. Huber, T. Wiss, J. Römer, et al., Development of fuel-model interfaces: characterization of Pd containing UO_2 thin films, *J. Nucl. Mater.* 397 (1–3) (2010) 19–26.
- [129] S. Sunder, N.H. Miller, W.H. Hocking, P.G. Lucuta, X-ray photoelectron spectra of SIMFUEL, *J. Alloys Compd.* 213–214 (1994) 503–505.
- [130] M.E. Broczkowski, J.J. Noel, D.W. Shoesmith, The influence of temperature on the anodic oxidation/dissolution of uranium dioxide, *Electrochim. Acta* 52 (25) (2007) 7386–7395.
- [131] M.E. Broczkowski, J.J. Noel, D.W. Shoesmith, The influence of dissolved hydrogen on the surface composition of doped uranium dioxide under aqueous corrosion conditions, *J. Electroanal. Chem.* 602 (1) (2007) 8–16.
- [132] A. Espriu-Gascon, J. Llorca, M. Dominguez, J. Gimenez, I. Casas, J. de Pablo, UO_2 surface oxidation by mixtures of water vapor and hydrogen as a function of temperature, *J. Nucl. Mater.* 467 (2015) 240–243.
- [133] J. Giménez, F. Clarens, I. Casas, M. Rovira, J. de Pablo, J. Bruno, Oxidation and dissolution of UO_2 in bicarbonate media: Implications for the spent nuclear fuel oxidative dissolution mechanism, *J. Nucl. Mater.* 345 (2–3) (2005) 232–238.
- [134] A.J. Popel, T.W. Wietsma, M.H. Engelhard, A.S. Lea, O. Qafoku, C. Grygiel, et al., The effect of ion irradiation on the dissolution of UO_2 and UO_2 -based simulant fuel, *J. Alloys Compd.* 735 (2018) 1350–1356.
- [135] W.H. Hocking, A.M. Duclos, L.H. Johnson, Study of fission-product segregation in used CANDU fuel by X-ray photoelectron spectroscopy (XPS) II, *J. Nucl. Mater.* 209 (1) (1994) 1–26.
- [136] A.S. Baev, Y.A. Teterin, K.E. Ivanov, A.Y. Teterin, S.A. Bogatov, X-ray photoelectron study of the samples of fuel-containing masses (FCM) formed as a result of the Chernobyl accident, *Radiochemistry* 39 (2) (1997) 169–174.

- [137] Y.A. Teterin, A.S. Baev, A.Y. Teterin, K.E. Ivanov, L.G. Mashirov, D.N. Suglobov, X-ray photoelectron study of crystalline “new formations” over melted fuel-containing masses from the fourth block of the Chernobyl Nuclear Power Plant, *Radiochemistry* 39 (2) (1997) 175–179.
- [138] S. Stumpf, A. Seibert, T. Gouder, F. Huber, T. Wiss, J. Römer, Development of fuel-model interfaces: investigations by XPS, TEM, SEM and AFM, *J. Nucl. Mater.* 385 (1) (2009) 208–211.
- [139] M.N. Hedhili, B.V. Yakshinskiy, T.E. Madey, Interaction of water vapor with UO₂(001), *Surf. Sci.* 445 (2) (2000) 512–525.
- [140] J.G. Tobin, D.K. Shuh, Electron spectroscopy of the oxidation and aging of U and Pu, *J. Electron Spectrosc. Relat. Phenom.* 205 (2015) 83–91.
- [141] F. Reinert, S. Hüfner, Photoemission spectroscopy—from early days to recent applications, *New J. Phys.* 7 (2005) 97.
- [142] S.-I. Fujimori, Band structures of 4f and 5f materials studied by angle-resolved photo-electron spectroscopy, *J. Phys.: Condens. Matter* 28 (2016) 153002.
- [143] S.-I. Fujimori, T. Ohkochi, T. Okane, Y. Saitoh, A. Fujimori, H. Yamagami, et al., Itinerant nature of U5f states in uranium mononitride revealed by angle-resolved photoelectron spectroscopy, *Phys. Rev. B* 86 (2012) 235108.
- [144] J.G. Tobin, D.A. Arena, B. Chung, P. Roussel, J. Terry, R.K. Schulze, et al., Photoelectron spectroscopy of plutonium at the advanced light source, *J. Nucl. Sci. Technol.* 39 (2002) 98–101.
- [145] K.T. Moore, G. Van Der Laan, Nature of the 5f states in actinide metals, *Rev. Mod. Phys.* 81 (2009) 235–298.
- [146] J.G. Tobin, P. Söderlind, A. Landa, K.T. Moore, A.J. Schwartz, B.W. Chung, et al., On the electronic configuration in Pu: spectroscopy and theory, *J. Phys.: Condens. Matter* 20 (2008) 125204.
- [147] J. Kolorenč, A.B. Shick, A.I. Lichtenstein, Electronic structure and core-level spectra of light actinide dioxides in the dynamical mean-field theory, *Phys. Rev. B: Condens. Matter Mater. Phys.* 92 (2015) 085125.
- [148] T. Wiss, H. Thiele, A. Janssen, D. Papaioannou, V.V. Rondinella, R.J.M. Konings, Recent results of microstructural characterization of irradiated light water reactor fuels using scanning and transmission electron microscopy, *JOM* 64 (2013) 1390–1395.
- [149] M.V. Ardenne, Das Elektronen-Rastermikroskop, *Z. Phys.* 108 (1938) 553.
- [150] T. Wiss, H. Thiele, B. Cremer, I. Ray, Internal conversion in energy dispersive X-ray analysis of actinide-containing materials, *Microsc. Microanal.* 13 (2007) 196.
- [151] E. Ruska, M. Knoll, Die magnetische Sammelspule für schnelle Elektronenstrahlen, *Z. Techn. Phys.* 12 (1931) 389–400.
- [152] R. Egerton, *Electron Energy-Loss Spectroscopy in the Electron Microscope*, Springer, Boston, MA, 2011, ISBN: 978-1-4419-9583-4, .
- [153] A.J. Schwartz, M.A. Wall, T. Zocco, A.J. Schaldach, W.G. Wolfer, Characterization and modelling of helium bubbles in self-irradiated plutonium alloys, *Philos. Mag.* 85 (2005) 479–488.
- [154] J.M. Martin, B. Vacher, L. Ponsonnet, V. Dupuis, Chemical bond mapping of carbon by image-spectrum EELS in the second derivative model, *Ultramicroscopy* 65 (1996) 229–238.
- [155] S. Bremier, P. Poeml, R. Hasnaoui, Microbeam analysis techniques for the characterisation of irradiated nuclear fuel, *Microsc. Microanal.* 20 (2014) 1800–1801.
- [156] S. Brémier, K. Inagaki, L. Capriotti, P. Poeml, T. Ogata, H. Ohta, et al., Electron probe microanalysis of a METAPHIX UPuZr metallic alloy fuel irradiated to 7.0 at.% burn-up, *J. Nucl. Mater.* 480 (2016) 109–119.

- [157] F. Tuomisto, I. Makkonen, Defect identification in semiconductors with positron annihilation: Experiment and theory, *Rev. Mod. Phys.* 85 (2013) 1583–1627.
- [158] P. Hautojärvi, *Positrons in Solids*, Springer-Verlag, Berlin Heidelberg, 1979.
- [159] Ortec Technical Library, Positron Annihilation Lifetime Spectrometry, Ortec Technical Library, Experiment n° 27. Available from: <<https://www.ortec-online.com/>>, 2018.
- [160] Bondarenko V., Krause-Rehberg R., Study of semiconductors with positrons, Proceedings of international workshop on positronium physics, ETH Zurich, May 30–31, 2003, *Int. J. Mod. Phys. A* 19 (2004).
- [161] T. Onitsuka, H. Ohkubo, M. Takenaka, N. Tsukuda, E. Kuramoto, Positron lifetime calculation for defects and defect clusters in graphite, *J. Nucl. Mater.* 283–287 (2000) 922–926.
- [162] N. Baclet, B. Oudot, R. Grynszpan, L. Jolly, B. Ravat, P. Faure, et al., Self-irradiation effects in plutonium alloys, *J. Alloys Compd.* 444–445 (2007) 305–309.
- [163] D. Roudil, M.F. Barthe, C. Jégou, A. Gavazzi, F. Vella, Investigation of defects in actinide-doped UO₂ by positron annihilation spectroscopy, *J. Nucl. Mater.* 420 (2012) 63–68.
- [164] M.F. Barthe, H. Labrimm, A. Gentils, P. Desgardin, C. Corbel, S. Esnouf, et al., Positron annihilation characteristics in UO₂: for lattice and vacancy defects induced by electron irradiation, *Phys. Status Solidi C* 4 (10) (2007) 3627–3632.
- [165] N. Djourelov, B. Marchand, H. Marinov, N. Moncoffre, Y. Pipon, P. Nédélec, et al., Variable energy positron beam study of Xe-implanted uranium oxide, *J. Nucl. Mater.* 432 (2013) 287–293.
- [166] V. Slugeň, H. Hein, S. Sojak, J. Simeg Veterníková, M. Petříška, V. Šabelová, et al., Evaluation of the reactor pressure vessel steels by positron annihilation, *J. Nucl. Mater.* 442 (2013) 499–506.
- [167] H.L. Malcolm, *Spin Dynamics, Basics of Nuclear Magnetic Resonance*, Wiley and Sons, 2001.
- [168] C. Adam, B.B. Beele, A. Geist, U. Müllich, P. Kaden, P.J. Panak, NMR and TRLFS studies of Ln(III) and An(III) C5-BPP complexes, *Chem. Sci.* 6 (2015) 1548–1561.
- [169] H. Yasuoka, G. Koutroulakis, H. Chudo, S. Richmond, D.K. Veirs, A.I. Smith, et al., Observation of ²³⁹Pu nuclear magnetic resonance, *Science* 336 (2012) 901–904.
- [170] S. Ikushima, S. Tsutsui, Y. Haga, H. Yasuoka, R.E. Walstedt, N.M. Masaki, et al., First-order phase transition in UO₂-235U and ¹⁷O NMR study, *Phys. Rev. B* 63 (2001) 104404.
- [171] K.J.D. Mackenzie, M.E. Smith, In multinuclear solid-state NMR of inorganic materials, in: R. Cahn (Ed.), *Pergamon Materials Science*, vol. 6, Elsevier, Amsterdam, 2002, pp. 3–727.
- [172] E.R. Andrew, A. Bradbury, R.G. Eades, Removal of dipolar broadening of nuclear magnetic resonance spectra of solids by specimen rotation, *Nature* 183 (1959) 1802–1803.
- [173] E.R. Andrew, A. Bradbury, R.G. Eades, Nuclear magnetic resonance spectra from a crystal rotated at high speed, *Nature* 182 (1958) 1659.
- [174] L. Martel, J. Somers, C. Berkmann, F. Koepp, A. Rothermel, O. Pauvert, et al., A nuclear magnetic resonance spectrometer concept for hermetically sealed magic angle spinning investigations on highly toxic, radiotoxic, or air sensitive materials, *Rev. Sci. Instrum.* 84 (2013) 055112.
- [175] C. Apostolidis, M.S. Dutkiewicz, A. Kovács, O. Walter, Solid-state structure of tricyclopentadienide uranium(III) and plutonium(III), *Chem. – A Eur. J.* 24 (2018) 2841–2844.
- [176] C. Apostolidis, O. Walter, J. Vogt, P. Liebing, L. Maron, F.T. Edelmann, A structurally characterized organometallic plutonium(IV) complex, *Angew. Chem. Int. Ed.* 56 (2017) 5066–5070.

- [177] M.S. Dutkiewicz, C. Apostolidis, O. Walter, P.L. Arnold, Reduction chemistry of neptunium cyclopentadienide complexes: from structure to understanding, *Chem. Sci.* 8 (2017) 2553–2561.
- [178] L. Martel, J.-C. Griveau, R. Eloirdi, C. Selfslag, E. Colineau, R. Caciuffo, Ferromagnetic ordering in NpAl_2 : magnetic susceptibility and ^{27}Al nuclear magnetic resonance, *J. Magn. Magn. Mater.* 387 (2015) 72–76.
- [179] L. Martel, A. Hen, Y. Tokunaga, F. Kinnart, N. Magnani, E. Colineau, et al., Magnetization, specific heat, ^{17}O NMR, and ^{237}Np Mössbauer study of $\text{U}_{0.15}\text{Np}_{0.85}\text{O}_2$, *Phys. Rev. B* 98 (2018) 014410.
- [180] L. Martel, N. Magnani, J.-F. Vigier, J. Boshoven, C. Selfslag, I. Farnan, et al., High-resolution solid-state oxygen-17 NMR of actinide-bearing compounds: an insight into the 5f chemistry, *Inorg. Chem.* 53 (2014) 6928–6933.
- [181] L. Martel, J.-F. Vigier, D. Prieur, S. Nourry, A. Guiot, K. Dardenne, et al., Structural investigation of uranium – neptunium mixed oxides using XRD, XANES, and ^{17}O MAS NMR, *J. Phys. Chem. C* 118 (2014) 27640–27647.
- [182] H. Eckert, Spying with spins on messy materials: 60 years of glass structure elucidation by NMR spectroscopy, *Int. J. Appl. Glass Sci.* 9 (2018) 167–187.
- [183] D. Massiot, R.J. Messinger, S. Cadars, M. Deschamps, V. Montouillout, N. Pellerin, et al., Topological, geometric, and chemical order in materials: insights from solid-state NMR, *Acc. Chem. Res.* 46 (2013) 1975–1984.
- [184] F. Angeli, T. Charpentier, D. de Ligny, C. Cailleteauz, Boron speciation in soda-lime borosilicate glasses containing zirconium, *J. Am. Ceram. Soc.* 93 (2010) 2693–2704.
- [185] X. Deschanels, S. Peuget, J.N. Cachia, T. Charpentier, Plutonium solubility and self-irradiation effects in borosilicate glass, *Prog. Nucl. Energy* 49 (2007) 623–634.
- [186] T. Charpentier, L. Martel, A.H. Mir, J. Somers, C. Jégou, S. Peuget, Self-healing capacity of nuclear glass observed by NMR spectroscopy, *Sci. Rep.* 6 (2016) 25499.
- [187] O.D. Sparkman, *Mass Spectrometry Desk Reference*, Global View Pub, Pittsburgh, PA, 2000, ISBN: 978-0-9660813-2-9, .
- [188] R. Thomas, *A Beginner's Guide to ICP-MS*, *Spectroscopy* 16 (2001) 22–27.
- [189] J.-Y. Colle, D. Freis, O. Beneš, R.J.M. Konings, Knudsen effusion mass spectrometry of nuclear materials: applications and developments, *ECS Trans.* 46 (1) (2013) 23–38.
- [190] E. Capelli, O. Beneš, J.-Y. Colle, R.J.M. Konings, Determination of the thermodynamic activities of LiF and ThF_4 in the $\text{Li}_x\text{Th}_{1-x}\text{F}_{4-3x}$ liquid solution by Knudsen effusion mass spectrometry, *Phys. Chem. Chem. Phys.* 17 (2015) 30110–30118.
- [191] P. Peres, S.-Y. Choi, F. Desse, F. Bienvenu, I. Roure, Y. Pipon, et al., Dynamic SIMS for materials analysis in nuclear science, *J. Vac. Sci. Technol., B* 36 (2018) 03F117.
- [192] B. Marchand, N. Moncoffre, Y. Pipon, C. Garnier, N. Bérard, C. Delafoy, et al., Xenon migration in UO_2 : a SIMS study, *Prog. Nucl. Energy* 57 (2012) 145–149.
- [193] I. Marchetti, P. Carbol, J. Himbert, F. Belloni, T. Fanghänel, Room-temperature diffusion coefficients for oxygen and water in UO_2 matrices: a SIMS study, *Surf. Interface Anal.* 45 (2013) 360–363.
- [194] R. Vauchy, A.-C. Robisson, P. Bienvenu, I. Roure, F. Hodaj, P. Garcia, Oxygen self-diffusion in polycrystalline uranium–plutonium mixed oxide $\text{U}0.55\text{Pu}0.45\text{O}_2$, *J. Nucl. Mater.* 467 (2015) 886–893.
- [195] D. Willingham, B.E. Naes, J.G. Tarolli, A. Schemer-Kohrn, M. Rhodes, M. Dahl, et al., Image fusion of Secondary Ion Mass Spectrometry and Energy dispersive X-Ray Spectroscopy data for the characterization of uranium molybdenum fuel foils, *J. Nucl. Mater.* 498 (2018) 348–354.
- [196] C. Cagna, I. Zacharie-Aubrun, P. Bienvenu, L. Barrallier, B. Michel, J. Noirot, A complementary approach to estimate the internal pressure of fission gas bubbles by

- SEM-SIMS-EPMA in irradiated nuclear fuels, IOP Conf. Ser.: Mater. Sci. Eng. 109 (2016) 012002.
- [197] G. Tamborini, M. Betti, V. Forcina, T. Hiernaut, B. Giovannone, L. Koch, Application of secondary ion mass spectrometry to the identification of single particles of uranium and their isotopic measurement, Spectrochim. Acta, B: At. Spectrosc. 53 (1998) 1289–1302.
- [198] S. Portier, S. Brémier, R. Hasnaoui, O. Bildstein, C.T. Walker, Investigation of the relative sensitivity factor for the quantification of ion microprobe results for Nd isotopes in simulated nuclear fuel, Microchim. Acta 161 (2008) 479–483.
- [199] S. Portier, C. Degueldre, N. Kivel, Solving isobaric interferences in Secondary Ion Mass Spectrometry: the case of Am and Pu in irradiated thorium-based fuel, Spectrochim. Acta, B: At. Spectrosc. 73 (2012) 35–38.
- [200] P.M.L. Hedberg, P. Peres, F. Fernandes, N. Albert, C. Vincent, Latest improvements in isotopic uranium particle analysis by large geometry-secondary ion mass spectrometry for nuclear safeguards purposes, J. Vac. Sci. Technol., B: Nanotechnol. Microelectron. 36 (2018). 9 03F1081-5.
- [201] R.C. Belin, P.M. Martin, P.J. Valenza, A.C. Scheinost, Experimental insight into the radiation resistance of zirconia-based americium ceramics, Inorg. Chem. 48 (2009) 5376–5381.
- [202] S. Wahu, J.-C. Berthet, P. Thuéry, D. Guillaumont, M. Ephritikhine, R. Guillot, et al., Structural versatility of uranyl(VI) nitrate complexes that involve the diamide ligand $\text{Et}_2\text{N}(\text{C}=\text{O})(\text{CH}_2)_n(\text{C}=\text{O})\text{NEt}_2$ ($0 \leq n \leq 6$), Eur. J. Inorg. Chem. 2012 (2012) 3747–3763.
- [203] C. Tamain, B. Arab Chapelet, M. Rivenet, F. Abraham, R. Caraballo, S. Grandjean, Crystal growth and first crystallographic characterization of mixed uranium(IV)-plutonium(III) oxalates, Inorg. Chem. 52 (2013) 4941–4949.
- [204] H.M. Rietveld, A profile refinement method for nuclear and magnetic structures, J. Appl. Crystallogr. 2 (1969) 65–71.
- [205] D. Prieur, R.C. Belin, D. Manara, D. Staicu, J.C. Richaud, J.F. Vigier, et al., Linear thermal expansion, thermal diffusivity and melting temperature of Am-MOX and Np-MOX, J. Alloys Compd. 637 (2015) 326–331.
- [206] A.K. Tyagi, M.D. Mathews, Thermal expansion of ThO_2 –2 wt% UO_2 by HT-XRD, J. Nucl. Mater. 278 (2000) 123–125.
- [207] F. Lebreton, R.C. Belin, T. Delahaye, P. Blanchart, In-situ X-ray diffraction study of phase transformations in the Am–O system, J. Solid. State Chem. 196 (2012) 217–224.
- [208] D. Horlait, F. Lebreton, P. Roussel, T. Delahaye, XRD monitoring of α self-irradiation in uranium–americium mixed oxides, Inorg. Chem. 52 (2013) 14196–14204.
- [209] D. Prieur, G. Pagliosa, J. Spino, R. Caciuffo, J. Somers, R. Eloirdi, Thermal recovery and lattice expansion of self-irradiated $\text{U}_{0.80}\text{Am}_{0.20}\text{O}_{2-x}$, an in situ high temperature x-ray diffraction study, J. Solid. State Chem. 199 (2013) 334–337.
- [210] M. Strach, R.C. Belin, J.-C. Richaud, J. Rogez, Influence of phase separation on the oxidation of $(\text{U}, \text{Pu})\text{O}_{2-x}$, J. Phys. Chem. C 119 (2015) 23159–23167.
- [211] R. Vauchy, R.C. Belin, A.-C. Robisson, F. Hodaj, High temperature X-ray diffraction study of the kinetics of phase separation in hypostoichiometric uranium–plutonium mixed oxides, J. Eur. Ceram. Soc. 34 (2014) 2543–2551.
- [212] R. Vauchy, R.C. Belin, A.-C. Robisson, F. Hodaj, Effect of cooling rate on achieving thermodynamic equilibrium in uranium–plutonium mixed oxides, J. Nucl. Mater. 469 (2016) 125–132.

- [213] E. Epifano, C. Guéneau, R.C. Belin, R. Vauchy, F. Lebreton, J.-C. Richaud, et al., Insight into the Am–O phase equilibria: a thermodynamic study coupling high-temperature XRD and CALPHAD modeling, *Inorg. Chem.* 56 (2017) 7416–7432.
- [214] L.E. Thomas, R.E. Einziger, H.C. Buchanan, Effect of fission products on air-oxidation of LWR spent fuel, *J. Nucl. Mater.* 201 (1993) 310–319.
- [215] M. Strach, R.C. Belin, J.-C. Richaud, J. Rogez, High temperature X-ray diffraction study of the oxidation products and kinetics of uranium–plutonium mixed oxides, *Inorg. Chem.* 53 (2014) 12757–12766.
- [216] A.M. Olsen, I.J. Schwerdt, B. Richards, L.W. McDonald, Quantification of high temperature oxidation of U_3O_8 and UO_2 , *J. Nucl. Mater.* 508 (2018) 574–582.
- [217] K. Popa, O. Walter, O.D. Blanco, A. Guiot, D. Bouëxière, J.-Y. Colle, et al., A low-temperature synthesis method for AnO_2 nanocrystals ($\text{An} = \text{Th}$, U, Np, and Pu) and associate solid solutions, *CrystEngComm* 20 (2018) 4614–4622.
- [218] V. Tyrpekl, J.-F. Vigier, D. Manara, T. Wiss, O. Dieste Blanco, J. Somers, Low temperature decomposition of U(IV) and Th(IV) oxalates to nanograined oxide powders, *J. Nucl. Mater.* 460 (2015) 200–208.
- [219] D. Hudry, C. Apostolidis, O. Walter, A. Janßen, D. Manara, J.-C. Griveau, et al., Ultra-small plutonium oxide nanocrystals: an innovative material in plutonium science, *Chem. Eur. J.* 20 (2014) 1–9.
- [220] A.J. Wilkinson, T.B. Britton, Strains, planes, and EBSD in materials science, *Materials Today* 15 (2012) 366–376.
- [221] T.J. Gerczak, C.M. Parish, P.D. Edmondson, C.A. Baldwin, K.A. Terrani, Restructuring in high burnup UO_2 studied using modern electron microscopy, *J. Nucl. Mater.* 509 (2018) 245–259.
- [222] C.M. Mari, S. Pizzini, L. Manes, F. Toci, A novel approach to the oxygen activity microdetermination of oxides by EMF measurements, *J. Electrochem. Soc.* 124 (1977) 1831–1836.
- [223] F.T. Ewart, L. Manes, H.J. Matzke, C.M. Mari, F. Toci, R. Schreiber, Oxygen potential measurements on irradiated oxide nuclear fuel, *J. Nucl. Mater.* 81 (1979) 185–190.
- [224] G.G. Charette, S.N. Flengas, Thermodynamic properties of the oxides of Fe, Ni, Pb, Cu, and Mn, by EMF measurements, *J. Electrochem. Soc.: Electrochem. Sci.* 115 (1968) 796.
- [225] B. Lindemer, T. Besman, Chemical thermodynamic representation of $(\text{UO}_2)_{\pm x}$, *J. Nucl. Mater.* 130 (1985) 473–488.
- [226] P.E. Blackburn, Oxygen pressures over fast breeder reactor fuel (I) A model for $\text{UO}_2)_{\pm x}$, *J. Nucl. Mater.* 46 (1973) 244–252.

Further reading

- T. Malis, S.C. Cheng, R.F. Egerton, EELS log-ratio technique for specimen-thickness measurement in the TEM, *J. Electron. Microsc. Tech.* 8 (1988) 193–200.
- Y.A. Teterin, V.I. Nefedov, A.S. Nikitin, C. Ronneau, J. Vanbegin, J. Cara, et al., XPS study of U, Cs and Sr ionic forms in the “hot” particles formed due to the nuclear power plant accident simulation, *J. Nucl. Sci. Technol.* 39 (2002) 477–480.
- D.B. Williams, C.B. Carter, *Transmission Electron Microscopy*, Springer, Berlin, 2009, ISBN: 978-0-387-76501-3, .

Computational thermochemistry of nuclear fuel

3

Markus H.A. Piro

Faculty of Energy Systems and Nuclear Sciences, Ontario Tech University, Oshawa, ON,
Canada

3.1 Introduction

Thermochemical behaviors of nuclear fuel have implications at all stages of the nuclear fuel cycle, which are discussed throughout this book. Having the ability to predict the chemical behavior of the fuel provides a mechanism to inform decision-making processes at the engineering design stage, operations, and also safety analyses. Thermochemical predictions can potentially be used to explore chemical extraction processes involving various minerals at the mining and milling stage (see Chapter 8: Mining and milling), fluorination processes during conversion (see Chapter 9: Conversion and enrichment), controlling oxidizing/reducing environments during fuel fabrication (see Chapter 10: Fuel fabrication), understanding the evolution of fuel chemistry with respect to irradiation in-reactor (see Chapter 11: In-reactor behavior), uranium and plutonium extraction processes during reprocessing (see Chapter 12: Reprocessing and recycling), and finally the behavior of spent nuclear fuel in a repository, which may include possible groundwater contamination (see Chapter 13: Spent fuel behavior and disposal). Furthermore, predicting the behavior of irradiated nuclear fuel in the event of a severe accident (see Chapter 14: Advances in fuel chemistry during a severe accident) provides an important capability in prevention, informing decision-makers in response initiatives, and decommissioning.

There are a multitude of approaches to modeling and simulation of various aspects of nuclear fuels that apply to different length and time scales, which are graphically depicted in Fig. 3.1. Traditional approaches have focused primarily on the modeling of nuclear fuel behavior on a continuum scale using finite element simulations with a particular focus on fuel performance and safety [2]. These types of simulations typically solve heat transfer and Newtonian mechanics equations to predict temperature, stress and strain, fission gas release, etc. On the other extreme, electronic structure simulations based on density functional theory can be used to predict interatomic potentials and lattice parameters. Similarly, one can employ molecular dynamics simulations to predict the interaction of atoms and molecules to predict the behaviors of clusters of atoms. Even higher in length and time scales, one can employ the theory of irreversible processes in the form of phase field simulations to investigate microstructural evolution of materials with time. Finally,

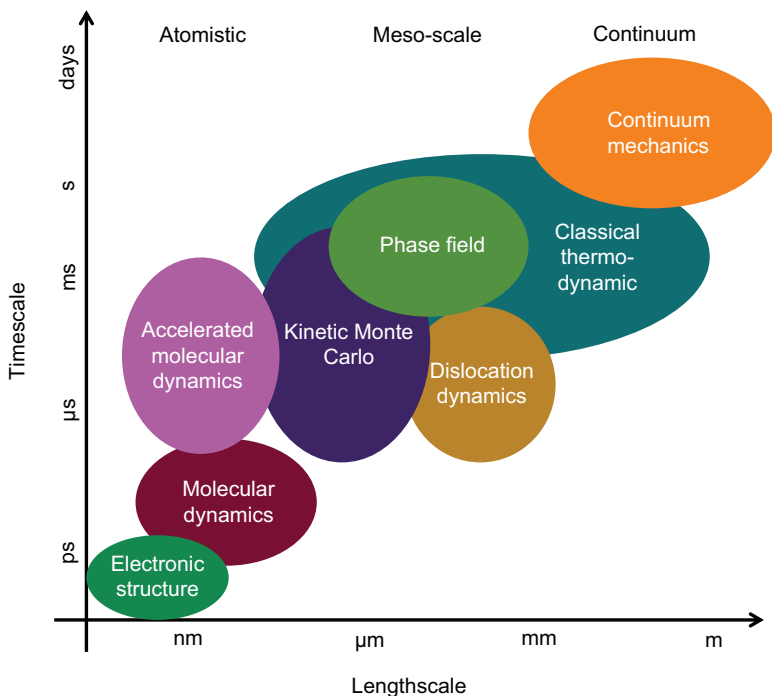


Figure 3.1 Various theoretical and modeling frameworks to predict material behavior are plotted on a multi-scale diagram.

Source: Adapted from M. Stan, Multi-scale models and simulations of nuclear fuels, Nucl. Eng. Technol. 41 (1) (2009) 39–52 [1].

thermochemical modeling provides a framework to predict phase equilibria, phase diagrams, and various thermodynamic properties.¹

This chapter will focus specifically on thermochemical modeling as it relates to many other chapters throughout this book. First, fundamentals of thermodynamic equilibria will be briefly reviewed in [Section 3.2](#). Second, the fundamental thermodynamic equations will then be applied to Gibbs energy minimization (GEM) in [Section 3.2.4](#), which is a numerical method to compute thermodynamic equilibria. Next, the CALPHAD method is reviewed in [Section 3.3](#), which is a methodical approach to developing thermodynamic models of various materials. Finally, applications of these models to predict various aspects of nuclear fuel chemistry are discussed in [Section 3.4](#).

¹ Note that the timescale applied to thermochemical modeling in [Fig. 3.1](#) is a bit misleading as thermochemical calculations necessarily apply to equilibrium conditions (i.e., a theoretically infinite time scale).

3.2 Fundamentals

3.2.1 Thermodynamic laws

The first law of thermodynamics effectively states that the energy of the universe is conserved² while the second law states that the entropy of the universe tends to a maximum. Through any irreversible process, the overall entropy of the universe increases. Suppose the change of entropy of a closed system and its surroundings are represented by dS_{sys} and dS_{surr} , respectively. Therefore, any irreversible process follows:

$$dS_{sys} + dS_{surr} > 0 \quad (3.1)$$

Suppose a closed system is in thermal and mechanical equilibrium, but not chemical equilibrium. An infinitesimal quantity of heat absorbed by the system from the surroundings is denoted by dQ_{sys} , which is related to the change in entropy to the surroundings and temperature, T , by

$$dS_{surr} = -\frac{dQ_{sys}}{T} \quad (3.2)$$

Substitution of Eq. (3.1) for dS_{surr} in Eq. (3.2) yields

$$dQ_{sys} - TdS_{sys} < 0 \quad (3.3)$$

The irreversible exchange of heat disturbs the internal energy of the system by dU_{sys} . In accordance with the first law of thermodynamics, the change in internal energy is conserved, which involves contributions from the change in internal heat and the change in internal work, dW_{sys} , by

$$dU_{sys} = dQ_{sys} + dW_{sys} \quad (3.4)$$

Substitution of dQ_{sys} from Eq. (3.4) into Eq. (3.3) gives the following

$$dU_{sys} + PdV_{sys} - TdS_{sys} < 0 \quad (3.5)$$

where P represents the hydrostatic pressure of the system and V_{sys} is the volume of the system. Under isothermal and isobaric conditions, Eq. (3.5) becomes

$$d(U_{sys} + PV_{sys} - TS_{sys}) < 0 \quad (3.6)$$

²One can more precisely define the first law of thermodynamics with Einstein's mass-energy equivalency, whereby mass and energy are together conserved.

The term represented in parentheses in Eq. (3.6) is more commonly known as the “Gibbs energy,” which yields the following condition for a thermodynamically favorable change in a system:

$$dG_{\text{sys}} < 0 \quad (3.7)$$

Therefore, a closed isothermal–isobaric system is at thermodynamic equilibrium when the Gibbs energy of the system is at a minimum. Equivalently, a system is in thermodynamic equilibrium when it is simultaneously in thermal, mechanical, and chemical equilibrium. A system is considered to be in equilibrium when there are no unbalanced thermodynamic potentials. Alternatively, one could have constrained temperature and volume to Eq. (3.5), which would ultimately yield a relationship involving the Helmholtz energy. Typically, the Gibbs energy function is more commonly used because pressure is more easily controlled during an experiment than volume. A more thorough discussion on the fundamentals of these equations is given in Chapter 1, Thermodynamics and kinetics.

3.2.2 Derivation of fundamental thermodynamic properties

The Gibbs energy can be written in compact form as a linear function of enthalpy, H , temperature, and entropy, S , as

$$G = H - TS \quad (3.8)$$

It should be noted that entropy is an absolute quantity, while enthalpy is a relative quantity, which therefore necessitates the Gibbs energy to be a relative quantity. A consistent reference frame to these quantities must, therefore, be established, which will be revisited shortly.

The integral Gibbs energy of the system is a summation of the individual phases, given by

$$G = \sum_{\lambda=1}^{\Lambda} n_{\lambda} g_{\lambda} + \sum_{\omega=1}^{\Omega} n_{\omega} g_{\omega} \quad (3.9)$$

where g_{λ} and g_{ω} represent the molar Gibbs energy of solution phase λ and stoichiometric phase ω , respectively. The number of moles of solution phase λ and stoichiometric phase ω is represented by n_{λ} and n_{ω} , respectively. Finally, the total number of stable solution phases is Λ and the total number of stable stoichiometric phases is Ω . By definition, g_{ω} is fixed; however, g_{λ} by definition varies with composition and is generally given as

$$g_{\lambda} = g_{\lambda}^{\text{ref}} + g_{\lambda}^{\text{id,mix}} + g_{\lambda}^{\text{ex,mix}} + g_{\lambda}^{\text{mag}} \quad (3.10)$$

where g_{λ}^{ref} represents the reference molar Gibbs energy of the pure species, $g_{\lambda}^{id,mix}$ represents the molar ideal Gibbs energy of mixing term, $g_{\lambda}^{ex,mix}$ represents non-ideal molar Gibbs energy of excess mixing terms, and finally g_{λ}^{mag} represents magnetic contributions to the molar Gibbs energy. Magnetic terms typically only apply to ferromagnetic materials. Expanding the reference molar Gibbs energy term gives

$$g_{\lambda}^{ref} = \sum_{i=1}^{N_{\lambda}} x_{i(\lambda)} g_{i(\lambda)}^{\circ} \quad (3.11)$$

where $x_{i(\lambda)}$ and $g_{i(\lambda)}^{\circ}$ represent the mole fraction and reference molar Gibbs energy of species i in solution phase λ , respectively, and N_{λ} represents the total number of species in solution phase λ . The reference molar Gibbs energy can be expanded using Eq. (3.8) and then integrated to yield the following equation:

$$g_i^{\circ} = \left(h_i^{\circ} + \int_{T_0}^T c_{p,i} dT \right) - T \left(s_i^{\circ} + \int_{T_0}^T \frac{c_{p,i}}{T} dT \right) + \int_{P_0}^P V_i dP \quad (3.12)$$

where Δh_i° and s_i° are the reference molar enthalpy and entropy terms at standard state (i.e., $T_0 = 25^{\circ}\text{C}$ and $P_0 = 1$ bar), respectively. The temperature dependent molar heat capacity of species i at constant pressure is $c_{p,i}$. Note that the last term in Eq. (3.12) does not correspond to a change in pressure, which would contradict the isobaric assumption of the system, but rather the difference between the volume of the material at the hydrostatic pressure of the system and the reference hydrostatic pressure. Practically, this does not vary significantly for solids and is typically neglected; the same often applies to liquids. Volumetric changes due to pressure are more meaningful to gases, which can be captured by the ideal gas approximation or an equation of state (e.g., van der Waals). For an ideal gas, Eq. (3.12) becomes

$$g_i^{\circ} = \left(h_i^{\circ} + \int_{T_0}^T c_{p,i} dT \right) - T \left(s_i^{\circ} + \int_{T_0}^T \frac{c_{p,i}}{T} dT - R \ln \left(\frac{P}{P_0} \right) \right) \quad (3.13)$$

Equations (3.12) and (3.13) are typically used in practice to constitute a thermodynamic database as the individual terms can be reliably measured experimentally (see Chapter 2: Experimental methods). Recall that both enthalpy and Gibbs energy terms are relative quantities, which require a consistent frame of reference to represent a thermodynamic system. This is typically applied by a consistent assignment of values for h_i° . For example, one convention is to establish a frame of reference corresponding to $h_i^{\circ} = 0$ for the dominant pure elemental species at standard state (e.g., $h_{\text{O}_{2(g)}}^{\circ} = 0$ J/mol at 25°C and 1 bar).

The mathematical form that ideal and non-ideal mixing terms in Eq. (3.10) take is specific to the class of thermodynamic model that is used to capture solution phase λ . Examples of common classes of thermodynamic solution models include (not exhaustive)

- ideal mixing,
- regular solution model,
- compound energy formalism (CEF),
- ionic liquid model, and
- modified quasichemical model.

The ideal mixing model assumes ideal mixing between species whereby the contribution to the overall Gibbs energy of the phase is entirely entropic (i.e., no non-ideal excess term). The regular solution model also considers the mechanical mixing of species; however, an excess term is added, which is typically a polynomial function involving the mole fractions of species and empirically derived interaction parameters [3]. The CEF is premised on the representation of a phase by multiple sublattices whereby constituents are able to mix on each sublattice [4]. Constituents may be represented by neutral species, cations, anions, and vacancies. In this case, the compound end members that are derived from the various extrema of combinations of constituents are used to derive g_{λ}^{ref} . The ionic liquid model is a derivation of CEF, but with only two sublattices and the stoichiometry ratios of each sublattice can vary (mainly to satisfy charge neutrality constraints). Another commonly employed model is the modified quasichemical model, which focuses on the mixing of pairs or quadruplets of species—rather than the species themselves—to capture short-range ordering [5]. In this case, both the ideal and excess mixing terms involve the mole fractions of the species and quadruplet fractions.

Typically, interaction parameters used in $g_{\lambda}^{ex,mix}$ correspond to the mixing between a pair of species that form a binary subsystem; however, a mechanism is required to relate binary subsystems to higher order solution phases. Multiple interpolation schemes are available and the selection of a particular scheme should be carefully considered, as discussed by Chartrand and Pelton [6]. The most commonly employed interpolation schemes include Kohler (Fig. 3.2), Kohler/Toop (Fig. 3.3), and Muggianu (Fig. 3.4) [6]. These figures show a generic ternary phase, involving species 1, 2, and 3.³ One should interpret these figures as point p representing the overall composition of the phase and the projections to the binary subsystems are represented by points a, b, and c. Note that point p remains stationary for all three interpolation schemes, but the positions of points a, b, and c are markedly different.

Both Kohler and Muggianu schemes are considered symmetric, whereas Kohler/Toop is asymmetric. That is to say that in an asymmetric interpolation scheme, one of the species is singled out. This can be advantageous if the chemical behavior between two species is fairly similar but that of the third is quite dissimilar, thereby making an asymmetric scheme favorable [6]. The interpolation schemes affect the calculation of $g_{\lambda}^{ex,mix}$, which is then used to calculate G.

³One should not misinterpret the extrema of these ternary plots as the system components—they are the species within a fictive solution phase.

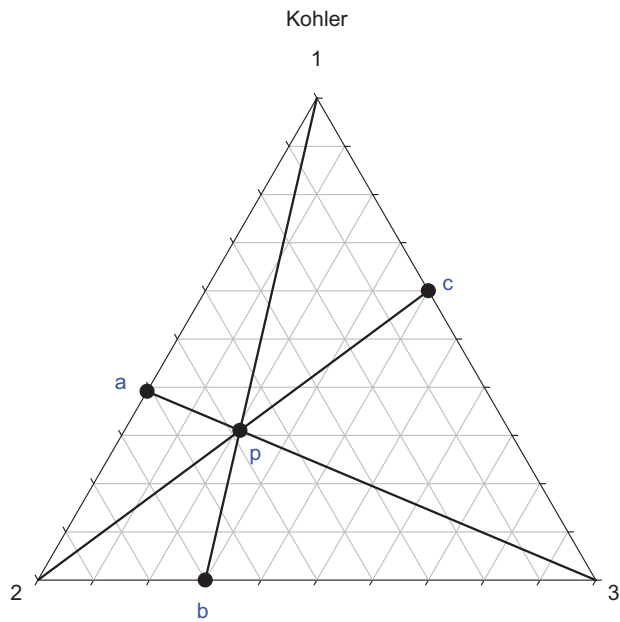


Figure 3.2 An illustration of Kohler interpolation.

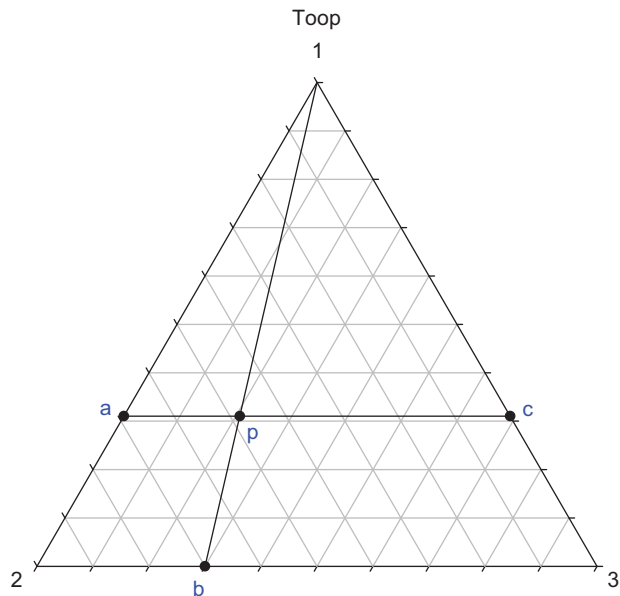


Figure 3.3 An illustration of Kohler/Toop interpolation.

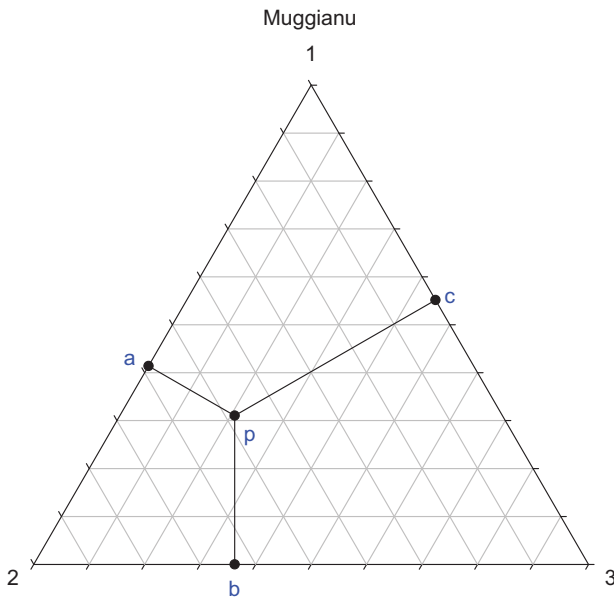


Figure 3.4 An illustration of Muggianu interpolation.

3.2.3 Conditions for equilibrium in a closed isothermal–isobaric system

The necessary and sufficient conditions for thermodynamic equilibrium in a closed isothermal–isobaric system must be respected by a computational thermodynamics calculation. These conditions are rooted in the fundamentals of thermodynamics, which are described in [Section 3.2](#). The necessary conditions for equilibrium must respect conservation of mass, Gibbs' phase rule, and a *local* minimum in the Gibbs energy function. The sufficient condition requires that G is at a *global* minimum.

3.2.3.1 Necessary conditions

Mass balance constraints are applied to each component of the system, which may be either a pure element or a constant combination of elements. The total number of moles of component j is b_j , which is defined as

$$b_j = \sum_{\lambda=1}^{\Lambda} \sum_{i=1}^{N_{\lambda}} n_{i(\lambda)} \nu_{i,j} + \sum_{\omega=1}^{\Omega} n_{\omega} \nu_{\omega,j} \quad (3.14)$$

where $\nu_{i,j}$ is the stoichiometry coefficient of component j in species i , and $n_{i(\lambda)}$ and n_{ω} are the independent variables in a calculation. The equilibrium condition must also adhere to Gibbs' phase rule, which requires the number of thermodynamic degrees of freedom, F , be non-negative. The number of degrees of freedom is

defined by the difference of the number of system components (C), the number of stable solution phases, number of stable stoichiometric phases, the number of ionic phases (Ξ), plus two (to account for temperature and pressure as independent variables). In the event that a phase is ionic, Ξ is non-zero and an electron associated with the charge of that ionic phase becomes a system component.

$$F = C - \Lambda - \Omega + \Xi + 2 \quad (3.15)$$

The final necessary condition requires that the Gibbs energy of the system is at a local minimum. A graphical interpretation of this requirement is that the chemical potentials of all stable species and phases lie on a line in two-dimensional space or as a plane/hyperplane in higher dimensional space. The chemical potential of species i is by definition:

$$\mu_i = \left. \frac{\partial G}{\partial n_i} \right|_{T,P,n_j \neq i} \quad (3.16)$$

Similarly, one can define the chemical potential of system component j as

$$\Gamma_j = \left. \frac{\partial G}{\partial b_j} \right|_{T,P,b_k \neq j} \quad (3.17)$$

At thermodynamic equilibrium, the chemical potentials of all species and phases are the same, thereby abiding by the fundamental conditions of equilibrium, which requires no unbalanced potentials. This is represented by the following linear equality [7]:

$$\mu_i = \sum_{j=1}^C \nu_{ij} \Gamma_j \quad (3.18)$$

One can visualize Eq. (3.18) as being a plane in a ternary system representing U–O–H in Fig. 3.5, whereby each corner of the base ternary plot corresponds to composition space and the vertical dimension corresponds to chemical potential. The corners of this three-dimensional triangular prism correspond to the chemical potentials of the system components, and the individual points on this plane correspond to the chemical potentials of individual species. In this particular example, $\text{UO}_{2\pm x}$ is modeled as a mixture of UO , UO_2 , and UO_3 . Suppose that $\text{UO}_{2\pm x}$ is stable and the system is homogenous. Therefore, the chemical potential of $\text{UO}_{2(f)}$ in the fluorite phase lies on this Gibbs Plane, in addition to the fictive species $\text{UO}_{(f)}$ and $\text{UO}_{3(f)}$. While the gas is not predicted to be stable, the chemical potential of gaseous species is defined by this plane, which can then be used to calculate the thermochemical activity of individual species. Similarly, note that the chemical potential of any composition of $\text{UO}_{2\pm x}$ can be defined by linear combinations of the chemical potentials of pure oxygen (i.e., Γ_O) and pure uranium (i.e., Γ_U).

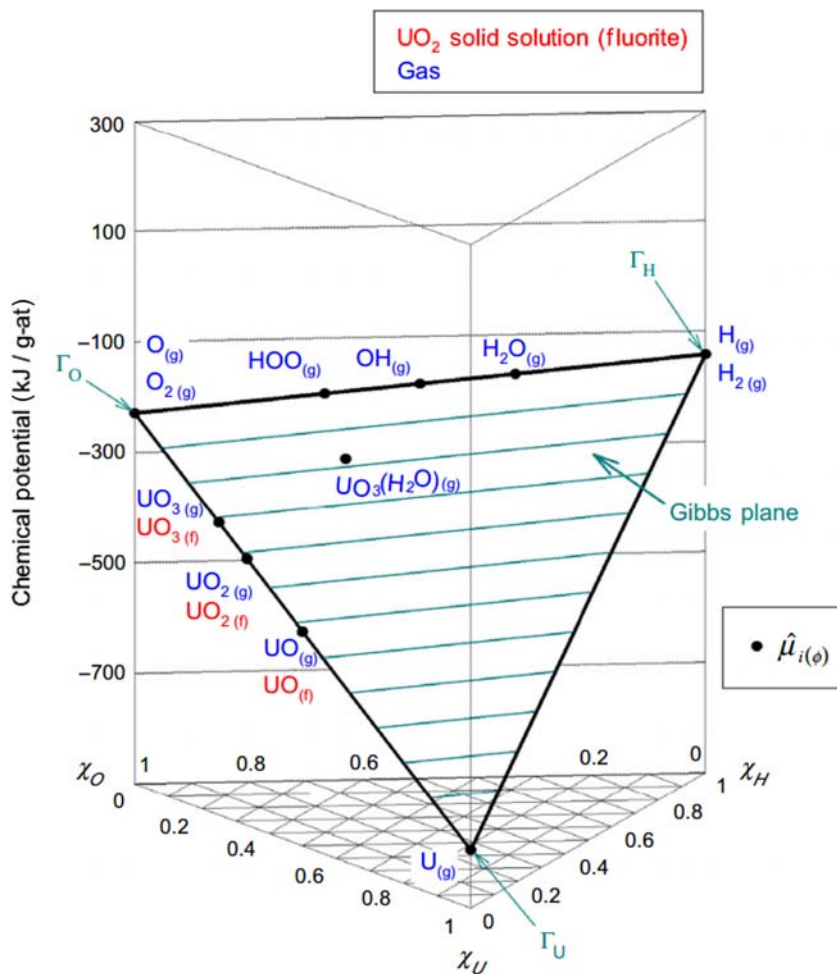


Figure 3.5 An illustration of the Gibbs Criteria for the U–O–H system.

Source: Copied from M. Piro, T. Besmann, S. Simunovic, B. Lewis, W. Thompson, Numerical verification of equilibrium thermodynamic computations in nuclear fuel performance codes, J. Nucl. Mater. 414 (3), (2011) 399–407.

3.2.3.2 Sufficient conditions

A system of phases believed to be stable that satisfies Eq. (3.18) corresponds to either a local minima or global minimum of G . However, satisfying this linear equation is insufficient to conclude that the system is at a *global* minimum since g_λ^{ex} can be non-convex [8]. The driving force of a phase, π_λ , is used to determine whether a system involving that phase is more stable than the previous system, which is defined as

$$\pi_\lambda = \min_x \sum_{i=1}^{N_\lambda} x_{i(\lambda)} \left(\mu_{i(\lambda)} - \sum_{j=1}^C \nu_{i,j} \Gamma_j \right) \quad (3.19)$$

which is subject to the following linear equality and inequality constraints:

$$\sum_{i=1}^{N_\lambda} x_{i(\lambda)} = 1, \quad x_{i(\lambda)} > 0, \quad \forall i \quad (3.20)$$

It is straightforward to ensure that Eq. (3.18) is satisfied for all stable phases; however, it is not straightforward to ensure that the system is at a global minimum via Eq. (3.19). Computational thermodynamic tools must ensure that both the necessary and sufficient conditions have been satisfied.

3.2.4 Gibbs energy minimization

The standard technique to solve for thermodynamic equilibria is based on GEM, which was originally developed by White et al. [9]. The premise of GEM is to exploit the fundamental laws of classical thermodynamics to predict the state of a closed isothermal–isobaric system at thermodynamic equilibrium. A Gibbs energy function is expressed as a second-order Taylor series expansion, and a system of undetermined Lagrangian multipliers are used to progressively minimize the system. This system is represented in matrix form below, which includes a Hessian matrix, \mathbf{H} , undetermined vector of Lagrangian multipliers, $\boldsymbol{\pi}$, and the constraint vector, $\boldsymbol{\varsigma}$.

$$\mathbf{H} \cdot \boldsymbol{\pi} = \boldsymbol{\varsigma} \quad (3.21)$$

The method begins with an initial estimate of an assemblage of stable phases with a particular composition of species; the mass balance constraints do not even need to be initially satisfied as they are corrected through the Lagrangian multipliers. The number of moles of individual species and phases are adjusted through Eq. (3.21) to progressively minimize the Lagrangian of the system. A full derivation of the equations can be found in the literature [9–12]. A critical input parameter to a GEM calculation is a thermodynamic database, which is described in the next section.

3.3 The CALPHAD method

Thermodynamic databases store Gibbs energy equations that collectively represent binary, ternary, and higher order systems. Specifically, the reference Gibbs energies of individual species (i.e., Eq. 3.12), the model type together with the conception of a model (e.g., the number of sublattices and constituents on each sublattice), and

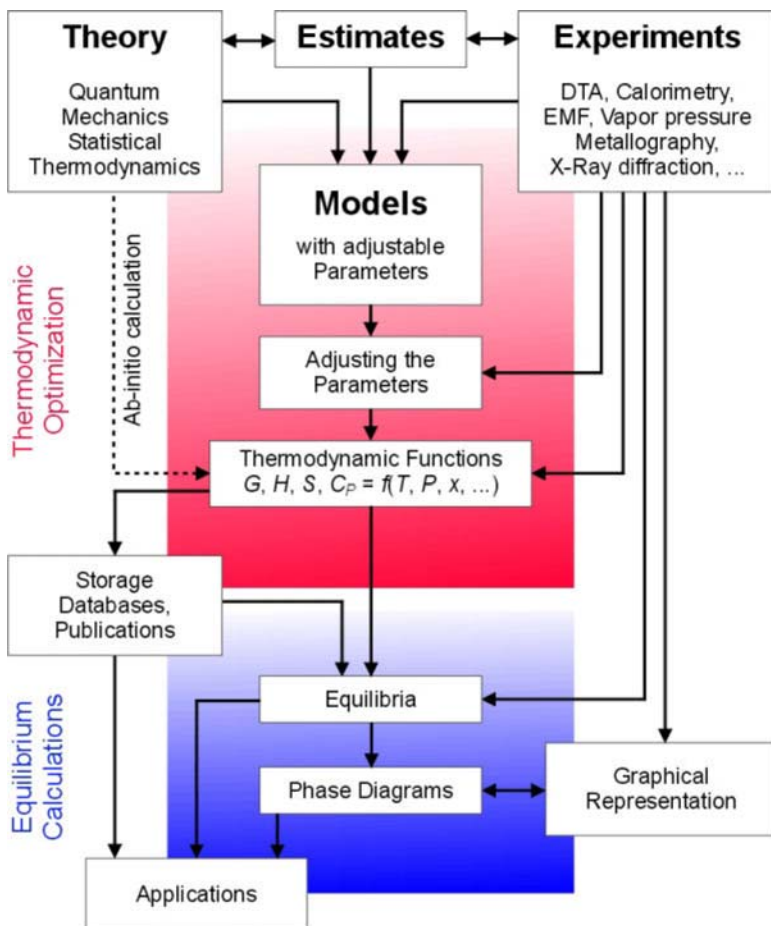


Figure 3.6 An illustration of the CALPHAD method [14].

the interaction parameters that constitute the excess Gibbs energy of mixing (i.e., $g_{\lambda}^{ex,mix}$ in Eq. 3.10) are typically stored in a database.

The development of a database and the equations therein typically follows a well-established technique called the Calculation of Phase Diagrams Method, or “CALPHAD” for short [13]. In essence, the CALPHAD method is a methodical linear/non-linear regression process, as depicted in Fig. 3.6, typically made closely with experimental values as input. For example, measurements made with a differential scanning calorimeter (see Chapter 2: Experimental methods) may be used to derive a polynomial expression for the heat capacity of a pure substance. Together with enthalpic and entropic data at standard state, this would be used to derive g_i° of a pure species. Similarly, thermal analyses with a thermogravimetric analyzer of an oxide can provide a relationship between oxygen potential, composition, and temperature, which can be used as input to a regression analysis to derive interaction

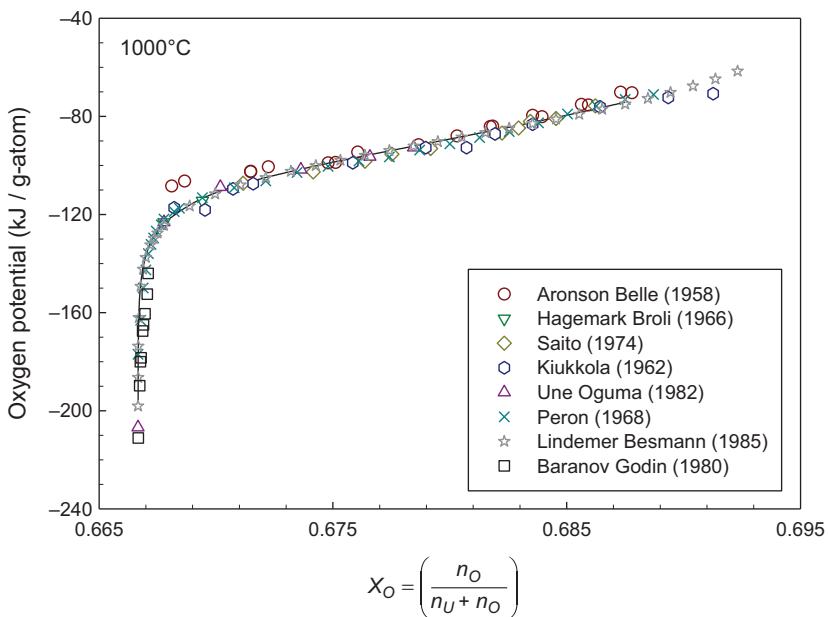


Figure 3.7 Various oxidation measurements involving UO_{2+x} are shown at 1000°C [12].

parameters for the excess mixing terms of a solution oxide phase. One can generally use the CALPHAD method to reliably perform interpolative calculations, while extrapolative predictions must of course be performed with deliberation.

An example is provided to give a brief introduction to the process. Suppose $\text{UO}_{2\pm x}$ is represented as a regular solution model consisting of UO , UO_2 , and UO_3 species.⁴ One can derive a reference molar Gibbs energy expression for UO_2 directly from experimental measurements as it is stable as a pure species; however, that cannot be done for UO or UO_3 .⁵ Similarly, one requires interaction parameters for the mixing of species. Therefore, a function can be derived of the Gibbs energy of $\text{UO}_{2\pm x}$ that involves unknown (tunable) parameters that apply to the reference Gibbs energies (i.e., lattice parameters) and excess Gibbs energy of mixing (i.e., interaction parameters).

One can make use of oxidation measurements of UO_{2+x} , as shown in Fig. 3.7, to develop a model. Recall the necessary condition for equilibrium defined by Eq. (3.18), which was also illustrated by Fig. 3.5 as a lowest common tangent between stable phases. Applying this principle, a line can be drawn tangent to the

⁴Indeed, there are multiple approaches to modeling the $\text{UO}_{2\pm x}$ phase. Alternatively, Guéneau et al. used a three sublattice model based on the CEF [15]. The type of model that is used is irrelevant to the current discussion as the regression process is the same.

⁵Recall that in this example, ‘ UO_3 ’ is also a species in a solution phase representing $\text{UO}_{2\pm x}$, which is different than ‘ UO_3 ’ that may be also represented as a separate stoichiometric phase.

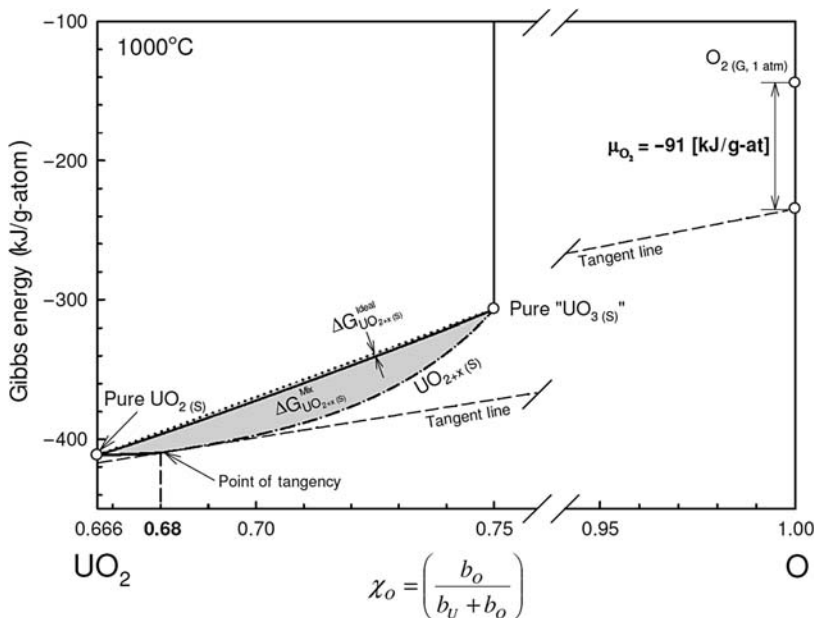


Figure 3.8 The molar Gibbs energy of $\text{UO}_{2\pm x}$ is plotted with respect to composition, which demonstrates how the oxygen potential is related to point of tangency [12].

Gibbs energy curve of $\text{UO}_{2\pm x}$ with a particular composition, which will have an equivalent oxygen chemical potential when extrapolating this line to pure oxygen. This is illustrated in Fig. 3.8 for this example, where the tangent line for a system with an overall oxygen fraction of 0.68 can be extended to pure oxygen, yielding a value of $1/2RT\ln(a_{\text{O}_2}) = -91 \text{ kJ/g-at}$. Note that this value was derived from experimental oxidation measurements shown in Fig. 3.7. One can exploit this relationship to derive tunable lattice parameters and interaction parameters.

Model development can be further expanded upon to include phase boundaries as well as chemical potential data. Fig. 3.9 illustrates the solidus and liquidus regions of hyperstoichiometric UO_2 with experimental laser flash measurements from Manara et al. [16] (see Chapter 2: Experimental methods for more information on this technique). Following the previous example, where oxidation data was used to derive a thermodynamic model for solid $\text{UO}_{2\pm x}$, a model for liquid $\text{UO}_{2\pm x}$ can also be developed. In this case, the Gibbs energy equation for the solid phase is fixed and the unknown parameters in the liquid phase are determined via regression involving phase boundaries shown in Fig. 3.9. In the case of a two-phase region, a line must be tangent to the two molar Gibbs energy curves corresponding to solid and liquid phases, whereby the points of tangency correspond directly to the composition points on the U–O phase diagram.

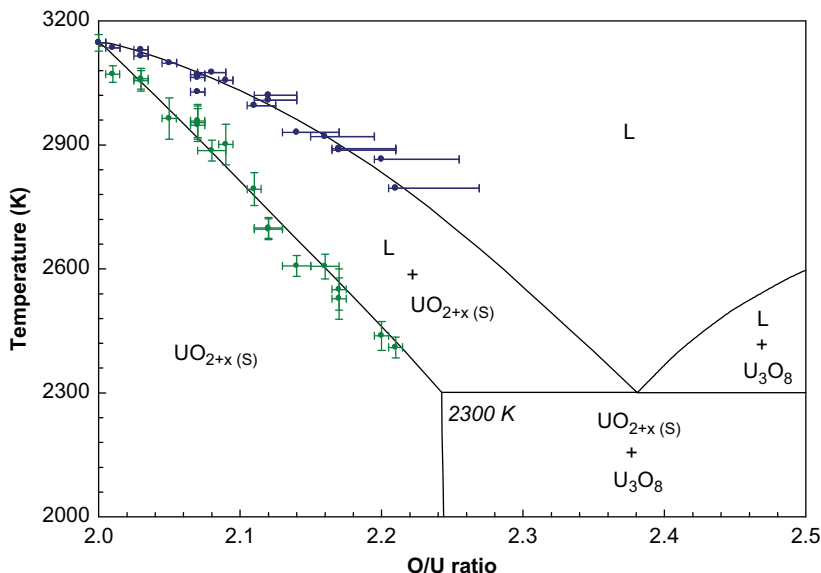


Figure 3.9 The modeled solidus and liquidus regions of hyperstoichiometric UO_2 [12] with experimental data points from Manara et al. [16].

3.4 Applications and limitations of computational thermodynamics

Once a thermodynamic database has been developed, one can apply it to a number of practical problems of engineering interest. Some examples include the construction of phase diagrams based on thermodynamic models and integral analyses to interrogate physical experiments. This section gives some examples of applications of computational thermodynamics to practical nuclear materials problems.

3.4.1 Phase diagram construction

Phase diagrams can be easily constructed from a thermodynamic database using a capable software tool, such as FACTSAGE [17] or THERMOCALC [18]. A significant advantage of being able to construct a phase diagram with such a tool in comparison to using a phase diagram directly from the literature is that one can customize the diagram to their own specifications. For example, typical phase diagrams are constructed in composition–temperature space with a specific composition and temperature range. Using a capable software tool, one is able to traverse different temperature and composition regimes, apply different system pressures. Of course, one must be competent in thermodynamic modeling; otherwise, the results may be misleading or incorrect. The following sections give some examples of such types of diagrams, which also appear in many chapters throughout the book.

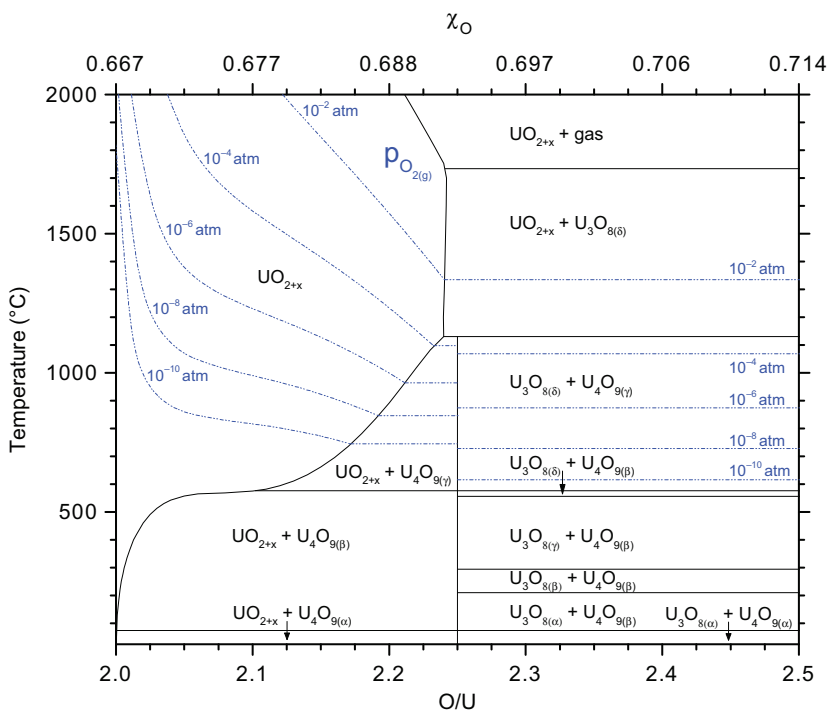


Figure 3.10 The calculated uranium–oxygen phase diagram from Guéneau et al. [19] is shown with oxygen partial pressure isobars superimposed [20].

3.4.1.1 Binary phase diagrams

Fig. 3.10 shows a section of the uranium–oxygen binary phase diagram from the thermodynamic treatment developed by Guéneau et al. [19] with oxygen partial pressure isobars superimposed [20]. Under some conditions, it is helpful to know the relationship between the oxygen partial pressure (or equivalently, the oxygen chemical potential) and $UO_{2\pm x}$ at a particular temperature and composition. For example, this may be helpful if one wanted to control the gaseous environment of a thermal analysis measurement in the presence of $UO_{2\pm x}$ at a particular temperature to prevent further oxidation.

3.4.1.2 Ternary phase diagrams

Fig. 3.11 shows the computed ternary phase diagram for the uranium–carbon–nitrogen system at 1973 K from Besmann et al. [21]. This particular system may be of interest in investigating TRISO fuel performance (see Chapter 5: Other power reactor fuels), where one candidate design uses UCN as a fuel kernel material. Through computational thermodynamics, one is able to explore different temperatures of the fuel material to investigate accident sequences.

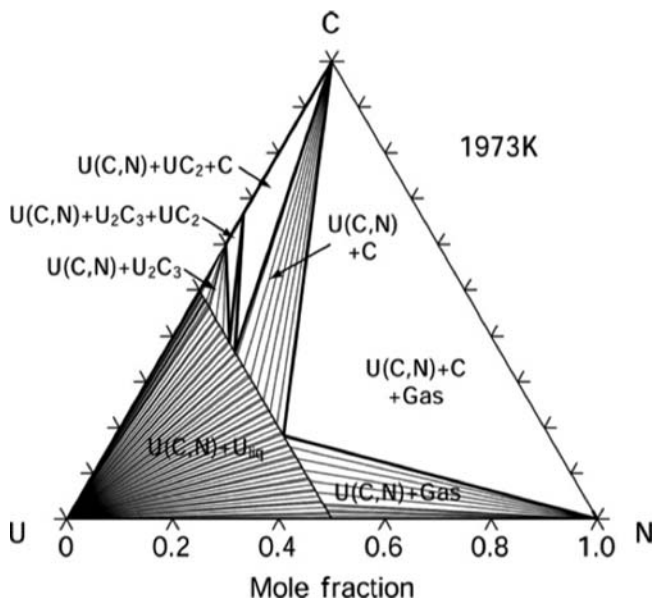


Figure 3.11 The calculated uranium–carbon–nitrogen ternary phase diagram at 1973 K by Besmann et al. [21].

3.4.1.3 Pourbaix diagrams

Another type of phase diagram relevant to aqueous chemistry is the Pourbaix diagram. As described in Chapter 1, Thermodynamics and kinetics, this type of diagram is useful in exploring aqueous chemistry of materials, whereby the temperature, hydrostatic pressure, and molality of one of the components is held constant, while pH and the redox potential are varied on the abscissa and ordinate, respectively. Fig. 3.12 gives an example of a computed Pourbaix diagram of uranium in the presence of water at 550 K [22]. Given the relatively high temperature in this diagram, it should be understood that the hydrostatic pressure of the system is sufficiently high to prevent boiling. This type of diagram may be helpful in various aqueous chemistry processes, including milling (see Chapter 8: Mining and milling), reprocessing (see Chapter 12: Reprocessing and recycling), or in the disposition of spent nuclear fuel (see Chapter 13: Spent nuclear fuel and disposal).

3.4.2 Integral analyses

In addition to investigating specific phase diagrams of binary and ternary systems, one can further interrogate real engineering problems that involve integral analyses using thermodynamic descriptions of material systems. As an example, Geiger et al. [23,24] have used the Thermodynamics of Advanced Fuels—International Database (TAF-ID) [15] to interpret the VERDON-1 integral severe accident experiment. The TAF-ID is a comprehensive thermodynamic database capable of

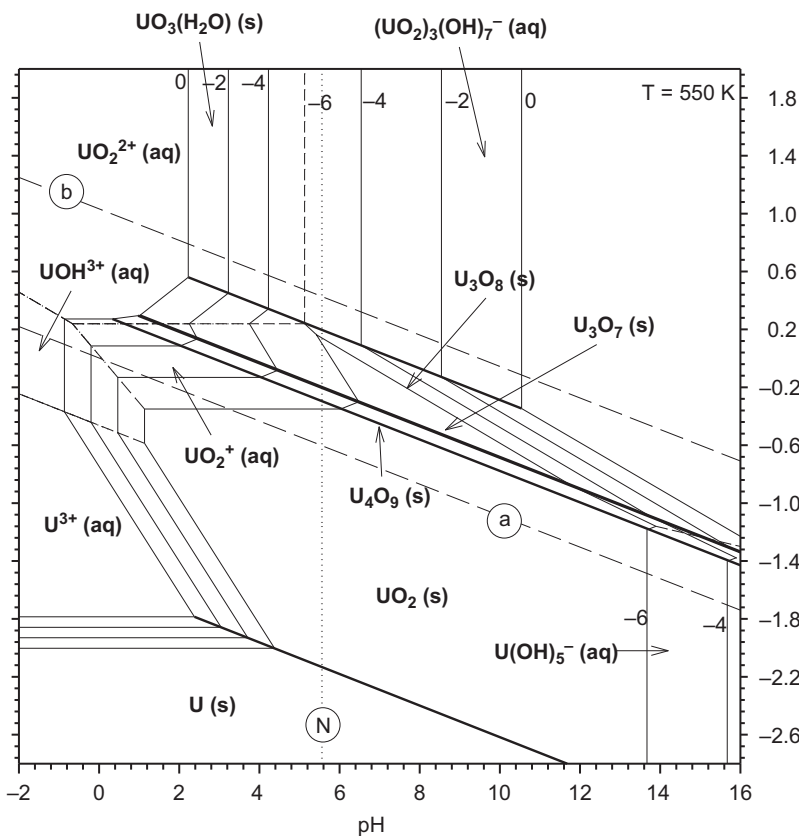


Figure 3.12 The calculated uranium Pourbaix diagram at 550K at $1, 10^{-2}, 10^{-4}$, and 10^{-6} molal [22].

capturing multiple nuclear fuels (e.g., oxide, metallic, carbide, nitride, and dispersion), transuranics and fission products, and structural materials (e.g., Zr-alloy cladding, steels, SiC, and concrete). The VERDON-1 test was aimed at measuring the release of various fission products from irradiated UO_2 fuel with 72 GWd/t(U) burn up under different atmospheres (i.e., inert, oxidizing, and reducing).

Geiger et al. [23] performed a number of thermodynamic analyses of the VERDON-1 test using the TAF-ID, including temperature ramps under a gaseous environment that changed with time. Thermodynamic calculations are able to predict the assemblage of phases that are stable at equilibrium, including their speciation. Fig. 3.13 gives an example calculation of the speciation of cesium during the experiment. The temperature of the system progressively increases, which is initially in an inert atmosphere and later switches to an oxidizing atmosphere. According to these predictions, the majority of cesium is retained in Cs_2MoO_4 at low temperatures, which implies that relatively little is released due the mobility of a solid. However, between approximately 750°C and 950°C, cesium becomes much

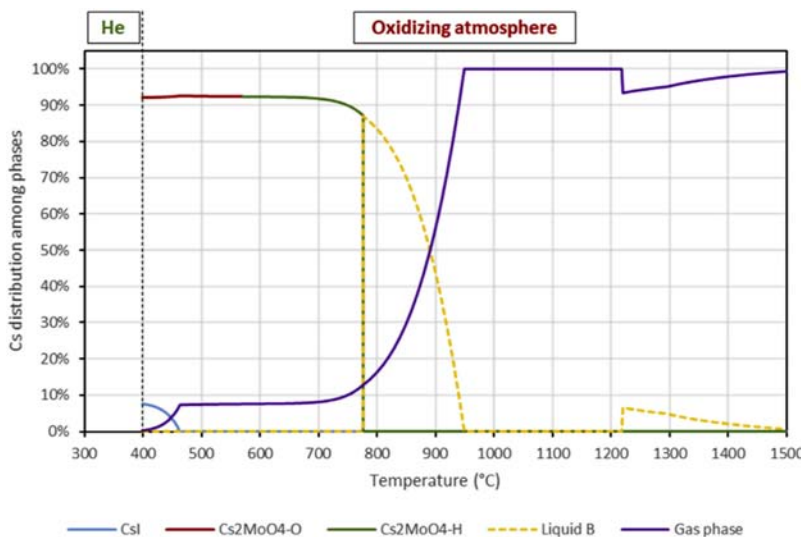


Figure 3.13 The calculated speciation of cesium for the VERDON-1 severe accident experiment by Geiger et al. [23].

more volatile and is largely stable in gaseous form. Therefore, the mobility of cesium changes markedly throughout the experiment, which has important safety implications.

3.4.3 Limitations of thermodynamic calculations

Indeed, GEM calculations rely on the underlying assumption that the system is at thermodynamic equilibrium; therefore, one must be cognizant of this assumption and its applicability to any particular problem being investigated. Generally, the validity of this assumption becomes more appropriate under the following three conditions: (1) elevated temperatures, (2) long periods of time, and (3) the more uniformly distributed atoms of different chemical elements are throughout the system. In many cases, irradiated nuclear fuel satisfies all three of the foregoing conditions; however, this is not always the case.

One example where assuming thermodynamic equilibrium may not be appropriate is with investigating mixed oxide (MOX) fuel. The fabrication technique employed for MOX fuel has a strong influence on how evenly UO_2 and PuO_2 particles are distributed throughout the matrix. MOX fuel fabrication typically involves vibratory milling of UO_2 and PuO_2 powder and the manner in which this is executed has a strong influence on homogeneity [25]. Fig. 3.14 shows a micrograph of MOX fuel irradiated in the NRU reactor in Chalk River, Canada, which was fabricated using the mastermix process [26]. Postirradiation examination has revealed an island rich in PuO_2 [26]. Since Pu has a higher fissile content (mainly ^{239}Pu) than U, it experiences a higher local area of fission, which is sometimes called the

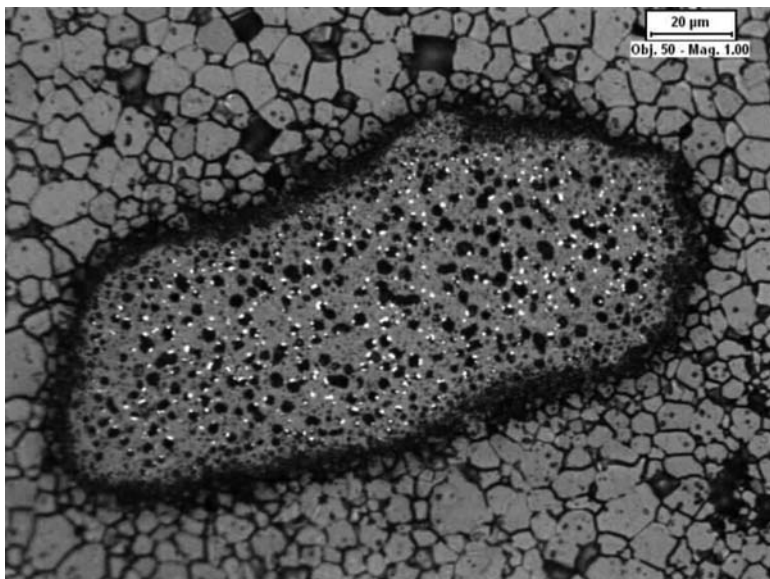


Figure 3.14 A HFA may form in MOX fuel due to high degrees of heterogeneity of UO_2 and PuO_2 [26]. *HFA*, High fission area.

“High Fission Area.” According to the $\text{U}-\text{Pu}-\text{O}$ phase diagram, one would be led to believe that this would be a homogeneous system; however, this is clearly not the case. In this situation, the assumption of thermodynamic equilibrium being appropriate would be limited by the aforementioned condition C, where UO_2 and PuO_2 particles were *not* evenly distributed. Also worth noting is that progress can be made in capturing time-dependent kinetic phenomena through the coupling of equilibrium calculations with irreversible processes, such as through phase field simulations [27–29].

In addition to assumptions made on the applicability of thermodynamic equilibrium, an important factor that can limit the fidelity of such calculations is the database that is utilized. Multiple databases have been developed for various systems, which intuitively have varying level of capabilities. For example, one database may treat a specific phase in a particular system in a different manner than another database. It is also possible that certain subsystems may be completely vacant in a database. Another consideration that must be taken is that experimental data needed to derive a thermodynamic treatment may be sparse or perhaps multiple experimental results may be in conflict with one another, thereby affecting the quality and uncertainty quantification of a particular system.

One example where the sparseness of experimental data impacts the quality of a thermodynamic assessment is the thorium–oxygen system, which is captured by two different phase diagrams shown in Fig. 3.15. In the work of McMurray et al. [30] (Fig. 3.15A), there is a miscibility gap, which follows earlier recommendations by Benz [32]. In contrast, the work of Bergeron et al. [31] (Fig. 3.15B) does not

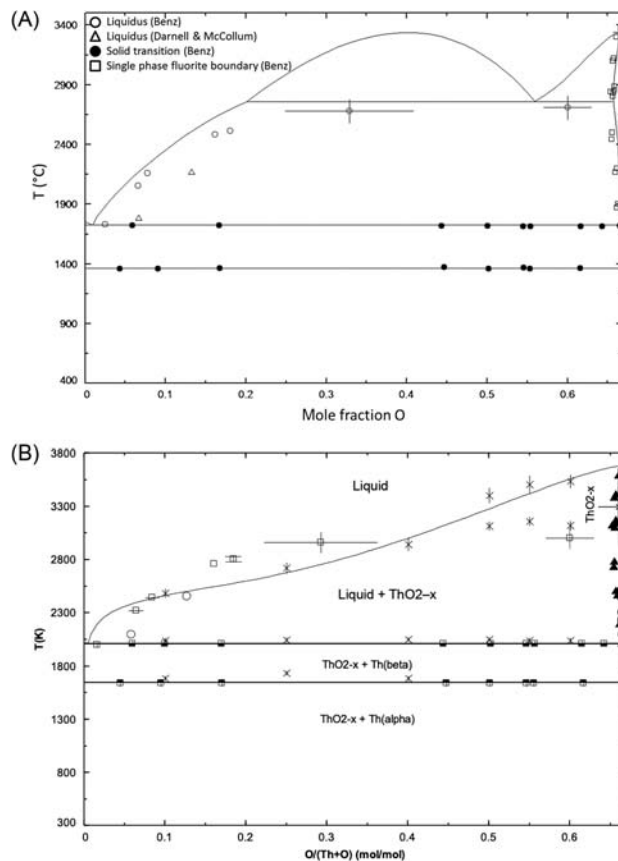


Figure 3.15 Two different phase diagrams of the Th–O system are shown as an example of how sparse experimental data may yield varied interpretations: (A) the Th–O phase diagram from McMurray et al. [30] and (B) the Th–O phase diagram, according to Bergeron et al. [31].

consider a miscibility gap in the same system. While the latter did include two additional more recent experimental data points, there is still much room for interpretation of the Th–O system due to the sparseness of experimental data. Both assessments are reasonable given the experimental data available. Ultimately, one must be cognizant of limitations in a database based on the experimental data used to derive it.

The foregoing example that identified uncertainties in the Th–O system gives evidence of the value of modeling as a form of knowledge gap identification. In this particular example, one must assess in great detail various aspects of the system through the CALPHAD model development process. As a result, one can make informed and objective recommendations of additional experimental measurements to fill knowledge gaps to yield a more complete understanding of the physical system—experimental, computational, and theoretical investigations being complementary pillars of scientific inquiry.

3.5 Summary

A high-level description of computational thermochemical modeling has been provided to preface subsequent chapters pertaining to various aspects of the nuclear fuel cycle. First, a brief summary of fundamental thermodynamics has been provided, which established that in order for a change in a system to proceed, the integral Gibbs energy change of the system must be negative. Various useful thermodynamic parameters were defined, which are typically derived through experimental measurements and empirical models derived thereupon stored in a thermodynamic database. Such a database is typically used by a thermodynamic solver based on the GEM technique, which must ensure that the necessary and sufficient conditions for thermodynamic equilibrium have been satisfied. The CALPHAD method has been introduced, which is a methodical method to develop a thermodynamic treatment of a material system. Finally, applications and limitations of thermodynamic calculations have been outlined as they may be applied to investigate nuclear fuel behavior at various stages of the nuclear fuel cycle.

References

- [1] M. Stan, Multi-scale models and simulations of nuclear fuels, *Nucl. Eng. Technol.* 41 (1) (2009) 39–52.
- [2] P.V. Uffelen, J. Hales, W. Li, G. Rossiter, R. Williamson, A review of fuel performance modelling, *J. Nucl. Mater.* 516 (2019) 373–412.
- [3] A. Pelton, C. Bale, Computational techniques for the treatment of thermodynamic data in multicomponent systems and the calculation of phase equilibria, *Calphad* 1 (3) (1977) 253–273.
- [4] M. Hillert, The compound energy formalism, *J. Alloy. Compd.* 320 (2) (2001) 161–176.
- [5] A. Pelton, S. Degterov, G. Eriksson, C. Robelin, Y. Dessureault, The modified quasi-chemical model I – binary solutions, *Metall. Mater. Trans. B* 31B (2000) 651–659.
- [6] P. Chartrand, A. Pelton, On the choice of geometric thermodynamic models, *J. Phase Equilibria* 21 (2) (2000) 141–147.
- [7] M. Piro, T. Besmann, S. Simunovic, B. Lewis, W. Thompson, Numerical verification of equilibrium thermodynamic computations in nuclear fuel performance codes, *J. Nucl. Mater.* 414 (3) (2011) 399–407.
- [8] M. Piro, S. Simunovic, Global optimization algorithms to compute thermodynamic equilibria in large complex systems with performance considerations, *Comput. Mater. Sci.* 118 (2016) 87–96.
- [9] W. White, S. Johnson, G. Dantzig, Chemical equilibrium in complex mixtures, *J. Chem. Phys.* 28 (5) (1958) 751–755.
- [10] G. Eriksson, E. Rosen, General equations for the calculation of equilibria in multiphase systems, *Chemica Scr.* 4 (1973) 193–194.
- [11] B. Jansson, Computer Operated Methods for Equilibrium Calculations and Evaluation of Thermochemical Model Parameters (Ph.D. thesis), Royal Institute of Technology, Stockholm, Sweden, 1984.

- [12] M. Piro, Computation of Thermodynamic Equilibria Pertinent to Nuclear Materials in Multi-Physics Codes (Ph.D. thesis), Royal Military College of Canada, Kingston, Canada, 2011.
- [13] L. Kaufman, H. Bernstein, Computer Calculation of Phase Diagrams With Special Reference to Refractory Metals, Academic Press, 1970.
- [14] R. Schmid-Fetzer, J. Grobner, Focused development of magnesium alloys using the Calphad approach, *Adv. Eng. Mater.* 3 (12) (2001) 947–961.
- [15] C. Guéneau, S. Gossé, A. Quaini, N. Dupin, B. Sundman, M. Kurata, et al., FUELBASE, TAF-ID databases and OC software: Advanced computational tools to perform thermodynamic calculations on nuclear fuel materials, in: The Seventh European Review Meeting on Severe Accident Research, 2015, Marseille, France.
- [16] D. Manara, C. Ronchi, M. Sheindlin, R. Konings, On the present state of investigation of thermodynamic properties of solid and liquid $\text{UO}_{2+\alpha}$, *J. Nucl. Mater.* 362 (2007) 14–18.
- [17] C. Bale, E. Bélisle, P. Chartrand, S. Decterov, G. Eriksson, A. Gheribi, et al., FactSage thermochemical software and databases, 2010–2016, *Calphad* 54 (2016) 35–53.
- [18] B. Sundman, B. Jansson, J.-O. Andersson, The Thermo-Calc databank system, *Calphad* 9 (2) (1985) 153–190.
- [19] C. Guéneau, N. Dupin, B. Sundman, C. Martial, J.-C. Dumas, S. Gossé, et al., Thermodynamic modelling of advanced oxide and carbide nuclear fuels: description of the U-Pu-O-C systems, *J. Nucl. Mater.* 419 (1–3) (2011) 145–167.
- [20] M. Piro, M. Welland, M. Stan, On the interpretation of chemical potentials computed from equilibrium thermodynamic codes, *J. Nucl. Mater.* 464 (2015) 48–52.
- [21] T. Besmann, D. Shin, T. Lindemer, Uranium nitride as LWR TRISO fuel: thermodynamic modeling of U-C-N, *J. Nucl. Mater.* 427 (2012) 162–168.
- [22] M. Piro, G. Bruni, B. Lewis, W. Thompson, F. Iglesias, M. Guoping, et al., Computation of actinide pourbaix diagrams at 298 k and 550 k (U,Np,Pu,Am,Cm – H_2O), in: 11th International Conference on CANDU Fuel (Niagara Falls, ON, Canada), Canadian Nuclear Society, Niagara Falls, 2010.
- [23] E. Geiger, C. Guéneau, Y. Pontillon, E. Corcoran, Modelling nuclear fuel behaviour with TAF-ID: Calculations on the VERDON-1 experiment, representative of a nuclear severe accident, *J. Nucl. Mater.* 522 (2019) 294–310.
- [24] Y. Pontillon, E. Geiger, C.L. Gall, S. Bernard, A. Gallais-During, P. Malgouyres, et al., Fission products and nuclear fuel behaviour under severe accident conditions part 1: main lessons learnt from the first VERDON test, *J. Nucl. Mater.* 495 (2017) 363–384.
- [25] M. Piro, A. Prudil, M. Welland, W. Richmond, A. Bergeron, E. Torres, et al., Nuclear fuel modelling and perspectives on Canadian efforts in fuel development, in: 12th Pacific Rim Conference on Ceramic and Glass Technology (Waikoloa, Hawaii), 2017.
- [26] N. Harrison, T. Janathasing, F. Dimayuga, Post-irradiation examination of MOX fuel with varying Pu homogeneity, in: 11th International Conference on CANDU Fuel, (Niagara Falls, ON, Canada), Canadian Nuclear Society, 2010.
- [27] M. Welland, M. Piro, S. Hibbins, N. Wang, A method of integrating CALPHAD data into phase-field models using an approximated minimiser applied to intermetallic layer growth in the al-mg system, *J. Nucl. Mater.* 59 (2017) 76–83.
- [28] M. Welland, S. Hanlon, Prediction of the zirconium hydride precipitation barrier with an anisotropic 3d phase-field model incorporating bulk thermodynamics and elasticity, *Comput. Mater. Sci.* 171 (109266) (2020).
- [29] X.-M. Bai, M. Tonks, Y. Zhang, J. Hales, Multiscale modeling of thermal conductivity of high burnup structures in UO_2 fuels, *J. Nucl. Mater.* 470 (2016) 208–215.

- [30] J. McMurray, S. Voit, T. Besmann, A combined experimental and computational thermodynamic investigation of the Th-U-O system, *J. Am. Ceram. Soc.* 99 (2016) 2197–2209.
- [31] A. Bergeron, D. Manara, O. Beneš, R. Eloirdi, M. Piro, E. Corcoran, Thermodynamic modelling of thoria-urania and thoria-plutonia fuels: description of the Th-U-Pu-O quaternary system, *J. Nucl. Mater.* 512 (2018) 324–348.
- [32] R. Benz, Thorium-thorium dioxide phase equilibria, *J. Nucl. Mater.* 29 (1969) 43–49.

PART B

Fuel Designs

This page intentionally left blank

Oxide power reactor fuels

4

Lian C. Wang and Matthew H. Kaye
Ontario Tech University, Oshawa, ON, Canada

4.1 Introduction

The most successful power reactor fuels have been oxide fuels. As of 2019, there are 452 commercial nuclear power reactors operating worldwide, and all of them use oxide fuels [1]. This chapter will focus on the fundamental thermochemistry of various oxide fuel types that are currently in service or are being considered for the next generation of power reactors. As will be seen, one advantage of oxide fuels is their chemical stability, as they are stable as a single phase over a relatively broad composition range and large temperature regime. Oxide fuels are also effective at retaining fission products [2,3], a subject that will be explored in depth in Chapter 11, In-reactor behavior. This chapter will begin with an examination of some properties of the metals U, Pu, and Th and the oxides UO_2 , PuO_2 , and ThO_2 . Calculated phase diagrams will be presented for the systems $\text{U}-\text{O}$, $\text{Pu}-\text{O}$, and $\text{Th}-\text{O}$. The pseudo-binary systems involving the three dioxides will then be discussed, and pseudo-ternary $\text{UO}_2-\text{PuO}_2-\text{ThO}_2$ diagrams will be shown. The chapter will conclude with a discussion of the use of oxide dopants in oxide fuels.

4.1.1 Crystal structures of various oxide nuclear fuels

One of the distinguishing characteristics of any material is its crystal structure. The three primary oxides that will be discussed in this chapter (i.e., UO_2 , ThO_2 , and PuO_2), all having a calcium fluorite structure, shown in Fig. 4.1. In essence this is a face-centered cubic structure (sites for the metal cations), with the tetrahedral sites occupied by the oxygen anions.

In the lattice shown in Fig. 4.1, the valences of all the metallic cations are 4^+ , while the oxygen anions are their usual 2^- . However, the metallic elements U, Th, and Pu have multiple valence possibilities (i.e., oxidation states) as shown in Table 4.1. It should be noted that the 7^+ oxidation state for plutonium is rare [4].

4.1.2 Nuclear reactions

The primary fission reaction of ^{235}U can be generally represented by Eq. (4.1), where it is recognized that when unstable ^{236}U splits, there are various pairs of

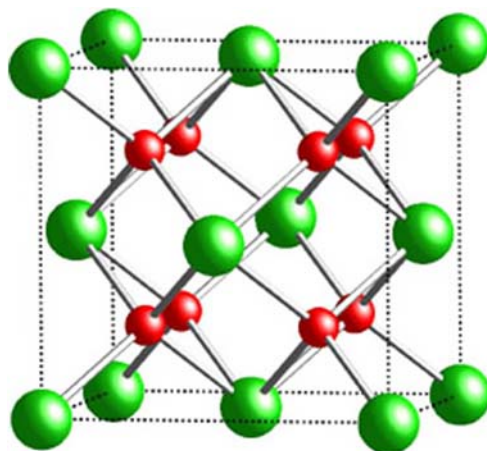


Figure 4.1 Calcium fluorite structure. Metal cations are green and oxygen anions are red.

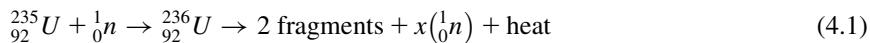
Table 4.1 Oxidation states and other properties of U, Th, and Pu [4].

Property	Th	U	Pu
Atomic number	90	92	94
Abundance in Earth's crust (ppm) [4]	8.1	2.3	Trace
Oxidation states [4]	3^+ , 4^+	3^+ , 4^+ , 5^+ , 6^+	3^+ , 4^+ , 5^+ , 6^+ , 7^+
Isotopes (abundance %)	^{232}Th (100%) ^a	^{233}U (trace) ^b ^{235}U (0.72%) ^b ^{238}U (99.28%) ^a	^{239}Pu (trace) ^b

^aFissile isotopes.

^bFertile isotopes.

fission fragments (e.g., fission product pairs, such as Ba, Kr and Sr, Xe) that form as well as two or three neutrons and heat.



For the fertile isotopes shown in Table 4.1, the relevant reactions to produce fissionable material are given here:

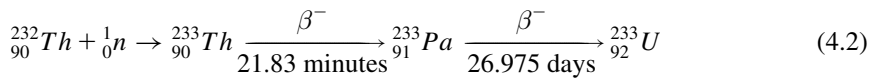
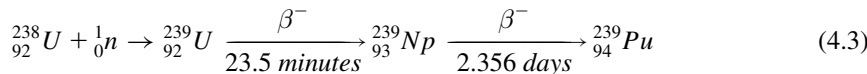


Table 4.2 Approximate mass proportions of plutonium isotopes [5,6].

Isotope	Mass %	Half-life (year)
$^{238}\text{Pu}^{\text{a}}$	1	87.7
$^{239}\text{Pu}^{\text{b}}$	60	24,390
$^{240}\text{Pu}^{\text{a}}$	25	6500
$^{241}\text{Pu}^{\text{b}}$	9	14.4
$^{242}\text{Pu}^{\text{c}}$	5	380,000

^aFertile isotopes.^bFissile isotopes.^cNeutron absorber [5].

Plutonium forms from ^{238}U via transmutation in a nuclear reactor. The approximate mass proportions of the five most prominent¹ plutonium isotopes are shown in **Table 4.2** [6].

As can be seen from **Table 4.2**, only ^{239}Pu and ^{241}Pu are potentially useful as fissile fuel in a reactor. However, via neutron capture reactions, ^{238}Pu and ^{240}Pu can yield ^{239}Pu and ^{241}Pu , respectively [5].

A comparison of selected material and thermochemical properties of ThO_2 , UO_2 , and PuO_2 [7–12] is given in **Table 4.3**. The elements Th, U, and Pu are all actinides separated by protactinium (Pa) to the left of uranium and neptunium (Np) to the right of uranium. Given the relative positions on the periodic table of the metal component of the three oxides, trends in the values can be observed, which can be useful when estimating other unknown properties from limited available data. Finally, in **Table 4.3**, it is important to note that positive deviations (i.e., $+x$) from stoichiometry for ThO_2 and PuO_2 have not been observed, which is in stark contrast to the significant positive deviation observed at elevated temperatures for UO_2 .

In the short history of nuclear fuel development, thoria-based nuclear fuel research has a relatively long history. For example, for more than 55 years, Canadian Nuclear Laboratories (formerly Atomic Energy of Canada Limited) has been conducting research on thoria-based fuels, including $(\text{Th}, \text{Pu})\text{O}_2$ [13]. And there are significant summaries of the advantages and challenges of thorium fuel cycles, such as the International Atomic Energy Agency report—*Thorium Fuel Cycle—Potential Benefits and Challenges* [14].

As mentioned in the introduction, thorium is not a fissile material. However, it is fertile (see Eq. 4.2), and as such there is some interest, especially in countries with abundant thorium resources, to harness thorium as fuel. One of the advantages of

¹ It should be noted that several other isotopes of plutonium exist, for example, ^{236}Pu , ^{237}Pu , ^{243}Pu , and ^{244}Pu . Of these, ^{244}Pu is the most stable with a half-life of 80 million years. But these isotopes, including ^{244}Pu do not form in irradiated fuel to any appreciable amount [5].

Table 4.3 A comparison of properties of ThO₂, UO₂, and PuO₂ [7–12].

Property	ThO ₂	UO ₂	PuO ₂
Crystal structure	Fluorite (cF12)	Fluorite (cF12)	Fluorite (cF12)
Theoretical density (g/cm ³)	10.00	10.97	11.50
Lattice constant (pm)	$a = 559.74$	$a = 547.1$	$a = 539.60$
Departure from stoichiometry	$-0.4 \leq x \leq \approx 0$	$-0.33 \leq x \leq +0.24$	$-0.29 \leq x \leq \approx 0$
Melting point (K)	3663 ± 20	3147 ± 20	3017 ± 20
ΔH_{298}° (kJ/mol)	-1226 ± 2	-1085 ± 2.5	-1056 ± 2
S_{298}° (J/mol/K)	65.2 ± 2	78.0	66.1
ΔH_{Fusion} (kJ/mol) ^a	90	78	67

Note that x represents the departure from stoichiometry for each oxide.

^aThe data were adopted from [9] (Table 1 on page 83).

thoria-based fuels includes the higher abundance of natural thorium compared to uranium. Coupling this with potential difficulties to make nuclear weapons with Th and the possibility of fuel recycling (which will be discussed in [Chapter 10: Advances in fuel fabrication](#)) make thorium fuels attractive. Of the three basic forms of thorium-based fuels (i.e., oxide, alloy, and carbide), only the oxide will be discussed in this chapter.

While it is beyond the scope of this chapter to explain how to utilize oxide material in a reactor, because it is naturally fissionable, UO₂ is “easy” to harness for nuclear power. That being said, plutonium and its oxides are important, especially when using natural uranium as fuel, because it is bred from ²³⁸U. In a similar manner the breeding of fertile thorium shows promise to extend fuel life. However, because they are fertile materials, pure PuO₂ or pure ThO₂ are not practical as fuels, they are only practical as mixed oxides (MOX) with UO₂.

4.1.3 Thermal conductivity profiles for the U–Pu–Th–O system

One of the disadvantages of using UO₂ as fuel in a nuclear reactor is that the thermal conductivity decreases as the temperature of the fuel increases, as illustrated in [Figs. 4.2](#) and [4.3](#). In these figures, the variation of thermal conductivity is a function of temperature and compositions of the system, shown by the points [15–17], and the fitted surface [17]. While less than desirable thermal conductivity values are not an insurmountable problem, it does provide an incentive to investigate other fuel chemistries, both oxide or otherwise, to achieve fuel compositions that have better thermal conductivity properties while maintaining other functionality.

Somayajulu et al. [18] investigated the thermal expansion and thermal conductivity of (Th, Pu)O₂ fuels both theoretically [using the molecular dynamic (MD) method] and experimentally. As thermal conductivity and diffusivity are closely

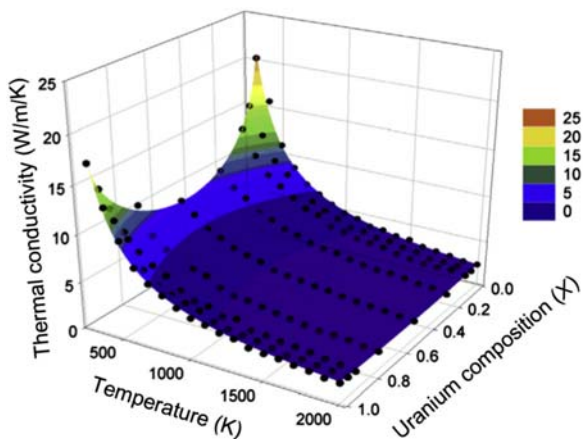


Figure 4.2 The variation of thermal conductivity as a function of uranium composition and temperature for the $(U_xTh_{1-x})O_2$ solid solution. Molecular dynamic data [15] are shown with black spheres, while the result of fitting equation to this data is indicated by the surface [17].

related to the performance of nuclear fuel, these types of measurements give an indication of the efficiency of conducting heat from the core of a nuclear reactor. Several methods have been used in determining the thermal conductivity or the thermal diffusivity of UO_2 and a new laser flash method was adopted recently [19].

Cooper et al. [17] investigated the degradation of the thermal conductivity due to the non-uniform cation lattice of $(U_xTh_{1-x})O_2$ and $(U_xPu_{1-x})O_2$ solid solutions by means of nonequilibrium method, which is an important characteristic factor of MOX and thorium-based nuclear fuels. MD simulations [20,21] calculate thermal conductivity by determining the temperature gradient in a rectangular cuboid with heat added and removed at a hot and cold plate, respectively. Fig. 4.2 and its complimentary diagram, Fig. 4.3, illustrate the suitability of using the MD method for the $(U_xPu_yTh_{1-x-y})O_2$ quaternary system.

As mentioned in the introduction, this chapter focuses on the thermochemistry of oxide fuels, so the discussion of thermal conductivity is limited and mostly beyond the scope of this chapter. However, it would be remiss to not comment on the importance this material property is to the performance and safety of nuclear fuel, and because it is one of the contributing factors driving research into other fuel types.

4.2 Phase diagrams involving UO_2 , PuO_2 , and ThO_2

4.2.1 The uranium-oxygen system and UO_2

Considering that uranium dioxide (urania) is the most commonly used oxide fuel in nuclear power reactors, it is not surprising that the uranium-oxygen system has

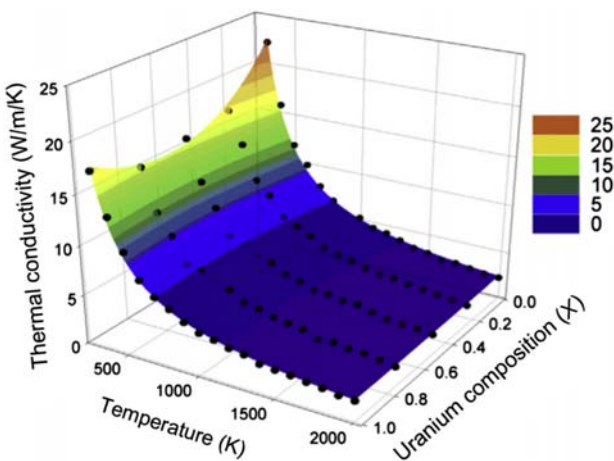


Figure 4.3 The variation of thermal conductivity as a function of uranium composition and temperature for the $(U_xPu_{1-x})O_2$ solid solution. Molecular dynamic data are shown with black spheres, while the result of fitting equation to this data is indicated by the surface [16,17].

been very well studied. A computed phase diagram [22–25], modeled using the CALPHAD method [26,27], showing the important $UO_2 \pm x$ region, representing the fuel, is shown in Fig. 4.4 with experimental data-points superimposed [28]. It should be noted that in Fig. 4.4 the range of values for x is $-0.33 \leq x \leq 0.24$. Often, this is written as $UO_2 \pm x$.

The partial U–O diagram shown in Fig. 4.4 can be compared to the evaluated U–O diagram from Guéneau et al. [29] presented in Chapter 1, Reaction kinetics and chemical thermodynamics of nuclear materials, Figure 1.9. While both diagrams capture the features determined by the experimental data, Fig. 4.4 captures the boundary between UO_{2+x} and the two-phase region of $UO_{2+x} + U_4O_9$ much better. It is left to the reader to choose their preferred evaluation.

It can be inferred from Fig. 4.4 that, at temperatures above about 400°C, the fluorite lattice of UO_2 can accommodate oxygen into the lattice resulting in a hyperstoichiometric regime. Furthermore, above about 1100°C, it is possible for the fluorite lattice to be deficient in oxygen resulting in hypostoichiometric regime. Further, although not readily apparent from the partial U–O phase diagram shown in Fig. 4.4, close examination of the U-rich side shows three solid (allotropic) forms of uranium metal (labeled as S1, S2, and S3, which correspond to α -U stable to 942 K; β -U, stable from 942 K to 1049 K; and γ -U, stable from 1049 K to 1405 K, the melting point for U metal). Because uranium metal undergoes these crystal transitions (and as a consequence volume changes) as temperature increases, it is not suitable for a power reactor. Further the melting temperature of pure uranium is relatively low.

One of the advantages of oxide fuels is their relatively high melting temperatures. An early study by Latta and Fryxell examined the solidus and liquidus temperatures of $UO_{2 \pm x}$ [30]. In the comprehensive review of the thermophysical

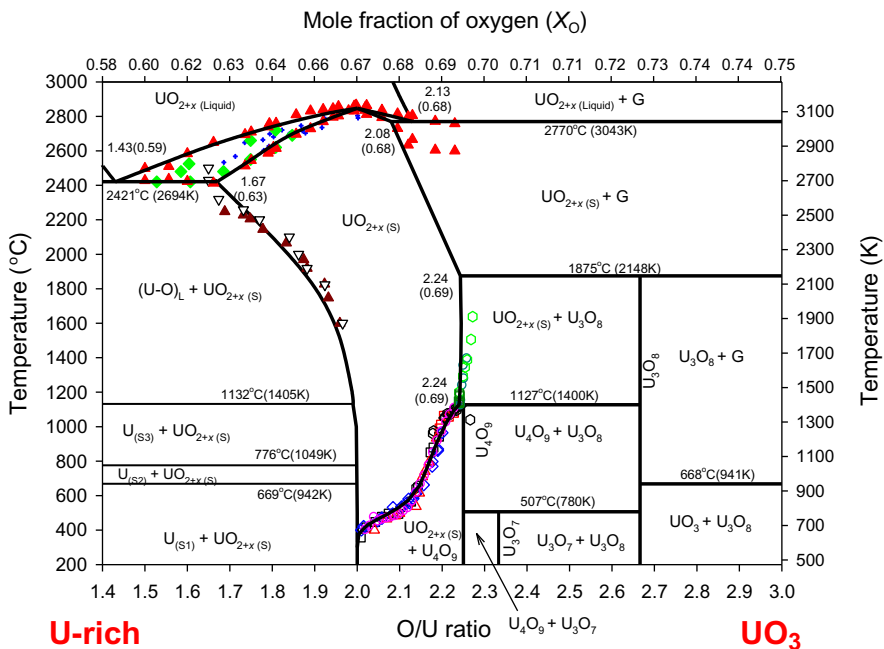


Figure 4.4 A partial U–O diagram concentrating on the $\text{UO}_{2\pm x}$ region, compared to experimental data.

Source: Diagram from W.T. Thompson, B.J. Lewis, E.C. Corcoran, M.H. Kaye, S.J. White, F. Akbari, et al. Thermodynamic treatment of uranium dioxide based nuclear fuel, Int. J. Mater. Res. 98 (10) (2007) 1004–1011. doi:10.3139/146.101556.

properties of uranium dioxide, Fink [31,32] uses the melting temperature of 3120 ± 30 K, which was based on the value reported by Fink and Petri [33], and is consistent with much earlier work by Fink et al. [34]. In 2000 this was the internationally accepted value. However, in recent studies by Böhler et al. [35,36], the melting temperature of UO_2 was reinvestigated using laser heating techniques [37], which reports a measured melting temperature of 3126 ± 55 K, which is in good agreement with the originally proposed value. Previously, Manara et al. at the same laboratory reported a value of 3147 ± 20 K [37]. Thus it can be seen that the results from these difficult and costly experiments are producing values well within the experimental error, making the selection of a “correct value” somewhat arbitrary and, to a certain degree, a matter of personal preference, which is a less than ideal situation.

4.2.2 The plutonium–oxygen system and PuO_2

The plutonium–oxygen system was modeled by Guéneau et al. [38]. A complete diagram of the system is shown in Fig. 4.5. It should be noted that the experimental

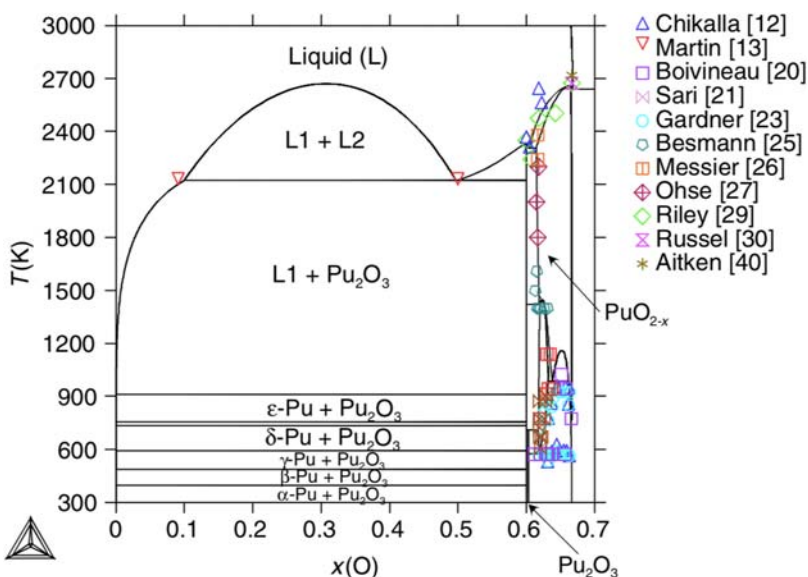


Figure 4.5 The Pu–O phase diagram as modeled by Guéneau et al. [38]. Note that the experimental data points shown correspond to the references listed on the right. The reference numbers are from the original paper by Guéneau et al. [38].

data used in the thermodynamic evaluation is included on this diagram, but the reference numbers listed are from the original paper by Guéneau et al. [38] and are not included as references in this chapter.

From Fig. 4.5, it can be seen that Pu has six stable solid phases and a lower melting point than uranium metal. Thus using fertile Pu as a fuel has greater challenges than U metal.

An enlarge view of the PuO_{2-x} region is shown in Fig. 4.6 [29], which represents an updated assessment of the Pu–O system. In contrast to the UO_{2±x} region of Fig. 4.4, the PuO_{2-x} region (shown in Fig. 4.6) has lower solidus and liquidus temperatures, which represents a challenge if pure PuO_{2-x} were considered as a fuel. Also, it can be seen that there is a relatively large hypostoichiometric region (i.e., PuO_{2-x}), but a negligible, if any, hyperstoichiometric region. Also of interest, and differing from the U–O system, is the suggestion that an intermediary oxide, Pu₂O₃, is stable, and other oxides have possibilities as well.

4.2.3 The thorium–oxygen system and ThO₂

Ackermann and Tetenbaum [39,40] studied the Th–O system in the composition range of pure thorium to ThO₂. In 2013 Das and Bharadwaj [41] evaluated the system. But more recently, McMurray et al. [42] evaluated the thorium side of the diagram, using experimental work not only primarily by Benz [43] and Darnell and

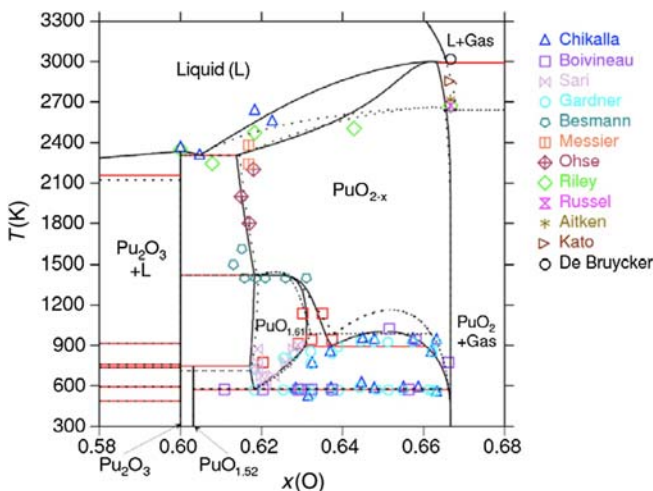


Figure 4.6 Pu–O phase diagram emphasizing the PuO_{2-x} region as modeled by Guéneau et al. [29]. The dotted line represents the phase boundaries as calculated by Guéneau et al. [38]. Experimental data points shown correspond to the references listed on the right.

McCollum [44] but also others [45–51]. From their experimental measurements, the diagram shown in Fig. 4.7 bears some similarity to the accepted U–O diagram shown in Fig. 4.4. McMurray et al. [42] found a sharp decrease of the oxygen potential while ThO_2 was reduced and homogeneity is slight. Their analyses, suggested that the stability of ThO_{2-x} is more stable than that of UO_{2-x} and PuO_{2-x} .

Bergeron et al. [52] established a thermodynamic model of Th–U–Pu–O quaternary system by means of the CALPHAD method. As part of that larger work, they recalculated the Th–O binary phase diagram as shown in Fig. 4.8. Also on this diagram is the experimental data of Benz ($\square, \blacktriangle, \blacksquare, \blacksquare$) [43], Ronchi and Hiernaut (\blacksquare) [53], Darnell and McCollum (\circ) [44], and Ackermann and Tetenbaum (\bullet) [39,40], and recent data (x) from JRC-Karlsruhe.

For the Th–O phase diagram, the main difference between Fig. 4.8 and the previously shown diagram of Fig. 4.7 is the profile of the liquidus. This may be caused by the selection of melting points of the oxides and some other thermodynamic properties (e.g., heat capacities).

4.3 Binary and higher order oxide phase diagrams

MOX fuel refers to a mixture of UO_2 and PuO_2 [54–58]. The concept of MOX fuel has been expanded to include other oxides, specifically thoria–urania MOX fuel (sometimes called TOX). Fabrication of MOX fuels will be discussed in Chapter 10, Advances in fuel fabrication, and the characteristic of irradiated MOX fuels will be presented in Chapter 11, In-reactor behavior.

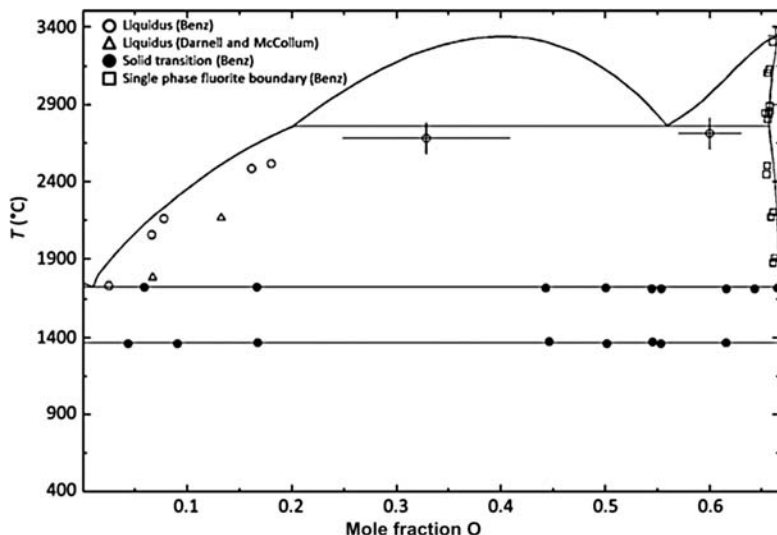


Figure 4.7 Calculated Th–O phase diagram from McMurray et al. [42–44].

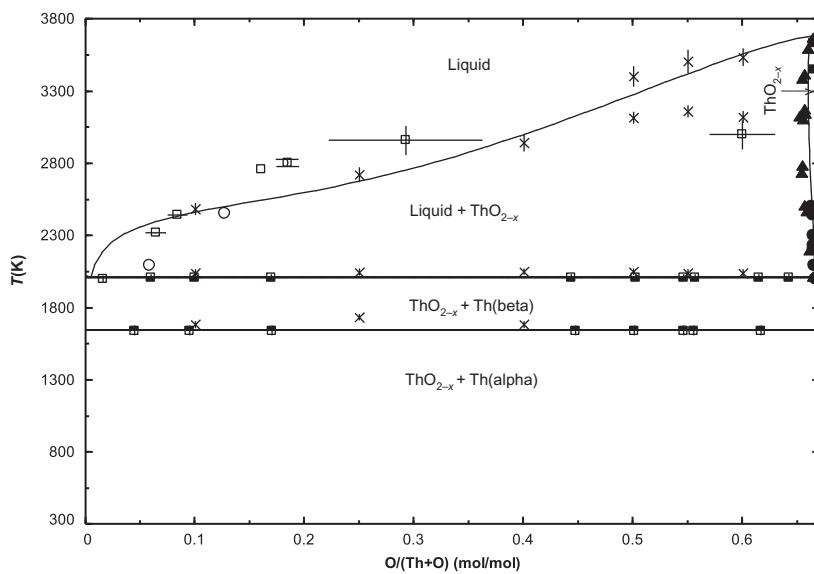


Figure 4.8 Calculated Th–O phase diagram [0 ≤ O/(Th + O) ≤ 0.67] by Bergeron et al. [52] with experimental points from Benz (□, ▲, ■) [43], Ronchi and Hiernaut (■) [53], Darnell and McCollum (○) [44], and Ackermann and Tetenbaum (●) [39,40] overlaid and new data from JRC-Karlsruhe (x).

This section examines the various phase diagrams involving the oxides, beginning with the binary systems that have UO_2 , PuO_2 , and ThO_2 as components. The discussion will then shift to focus on higher order systems and how models of these systems assist in the study of oxide fuels, be they MOX or otherwise.

4.3.1 $\text{UO}_2\text{--PuO}_2$ binary system

The first reported phase diagram for the $\text{UO}_2\text{--PuO}_2$ binary system is that of Lyon and Baily [59]. This diagram, shown in Fig. 4.9, is seen to be a rather simple lens (name taken from optics, as it looks like a double concave lens), which is fairly typical of diagrams of materials with the same basic crystal structure² (i.e., fluorite, in this case). Note that the estimated error on the data points reported by Lyon and Baily is ± 20 K. A second ideal lens is shown with the dashed red lines on Fig. 4.9 to illustrate where the lens would be placed using the more contemporary melting temperature for UO_2 (i.e., $T_{\text{Fusion UO}_2} = 3147$ K).

4.3.2 $\text{ThO}_2\text{--UO}_2$ binary system

A recent evaluation of the $\text{UO}_2\text{--ThO}_2$ phase diagram at the high temperatures bracketing the solidus and liquidus was made by Böhler et al. [36], and is presented in Fig. 4.10. This evaluation incorporates earlier work by Belle et al. [60], Lambertson et al. [61], and Latta et al. [62], which showed that the ideal behavior, originally proposed for the $\text{ThO}_2\text{--UO}_2$ system, deviated from ideal behavior on the U-rich side. Note that in Fig. 4.10 the work referenced in the legend as numbers 11 and 12 refers to Lambertson et al. [61] and Latta et al. [62].

In 2016 Kim and Kim [63] also thermodynamically assessed the $\text{UO}_2\text{--ThO}_2$ binary phase diagram. Based on work by Shuller et al. [64], Kim and Kim modeled a miscibility gap at relatively low temperatures. This work is shown in Fig. 4.11.

In 2018 the $\text{UO}_2\text{--ThO}_2$ system was reevaluated by Bergeron et al. [52] as part of the Th–U–Pu–O quaternary system. Diagrams from this work showing ternary diagrams will be presented later in this chapter.

Böhler et al. [35,36] carried out a broad thermodynamic study on the U–Pu–O ternary system and comparisons between calculated data with experimental data are shown in Fig. 4.12. The measurements by Böhler et al. are shown in black squares and red circles and other literature experimental data points for the solidus are shown as squares and liquidus as triangles [35,59,65] compared with CALPHAD optimized phase boundaries (black dashed curves after [29]).

Konings et al. [66] examined the liquidus data at PuO_2 -rich section by laser heating samples (their aptly named self-crucible method), vapor pressure measurements, and calorimetry. Their experimental results and the modeling results of Guéneau et al. [29] are presented in Fig. 4.13, together with experimental results from De Bruycker et al. [67]. The results of these studies highlighted an apparent uncertainty of the melting point of these oxides in the U–Pu–Th–O quaternary system.

²Other prominent examples are: Cu–Ni (both fcc), Pd–Rh (both fcc), and Ag–Pd (both f.c.c.)

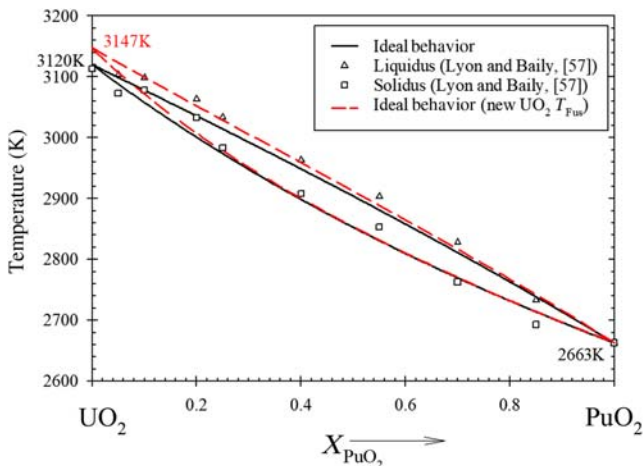


Figure 4.9 The $\text{UO}_2\text{--PuO}_2$ diagram comparing the data of Lyon and Baily [59] with an ideal solution model [28].

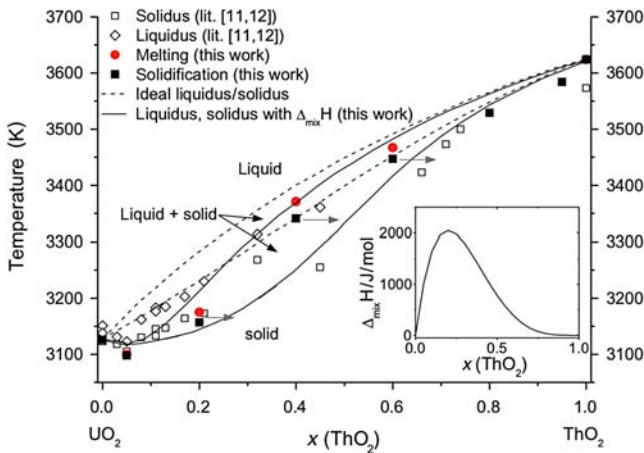


Figure 4.10 $\text{UO}_2\text{--ThO}_2$ phase diagram reevaluated by Böhler et al. [36].

For this reason, De Bruycker et al. [68] reassessed the melting point of PuO_2 , proposing a new value of 3017 ± 28 K.

Strach et al. [69] examined the oxygen potential effects under different compositions of Pu by laser melting experiments. The thermal arrests in Ar correspond to those found in the literature. A significant decrease can be observed for melting in air. They concluded that the gaseous phase impacts the measurements of surface temperatures, and the melting temperatures of the MOX compounds decreases as the O/M ratio increased. Their results are presented in Fig. 4.14.

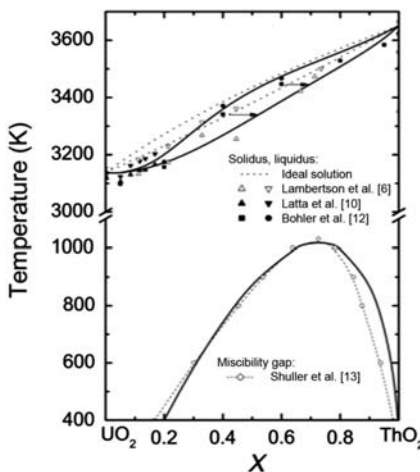


Figure 4.11 Thermodynamic model of the ThO₂–UO₂ system, with miscibility gap [63,64].

4.3.3 ThO₂–PuO₂ binary system

Fig. 4.15 shows the ThO₂–PuO₂ phase diagram proposed by Bakker et al. [70], where they adopted the value of 2663 K for the melting temperature of PuO₂ from Cordfunke and Konings [12]. Bakker et al. noted that this value was 130 K above the previously accepted value proposed by Freshley and Mattys in 1962 [71]. In the Freshley and Mattys work [71] the solidus temperature (reported as “melting”) was measured for four alloys in this oxide system, shown in Fig. 4.15. On the diagram, the melting temperature for ThO₂ was taken from Ronchi and Hiernaut [53].

The study by Bergeron et al. [52] showed that the calculated results match the experimental data from Böhler et al. [36] and Latta et al. [62]. Fig. 4.16 shows that the (Th,U)O₂ phase is stable below about 3100 K and in a wide composition range.

However, Fig. 4.16 is obviously different from Figs. 4.10 and 4.11. It seems like a pseudo-binary isopleth from a UO₂–ThO₂–O system at a constant O composition. Some limited experimental work (not as extensively studied as U and Pu) has been conducted on this ternary system since the 1960s [72–75]. McMurray et al. [42] systematically studied the ternary system and some of their thermodynamic calculation results are summarized here.

McMurray et al. [42] also calculated the UO₂–ThO₂ isopleths in the UO₂–ThO₂–O system as shown in Fig. 4.17. It can be seen that the calculated diagram is in good agreement with the experimental data of Böhler et al. [36] and Latta et al. [62].

This phase diagram is similar to Fig. 4.16, but the computed liquidus and solidus at the UO₂-rich side are higher than the experimental data. The oxygen concentration is specified as 0.667. In comparing Fig. 4.17 with Figs. 4.10 and 4.11,

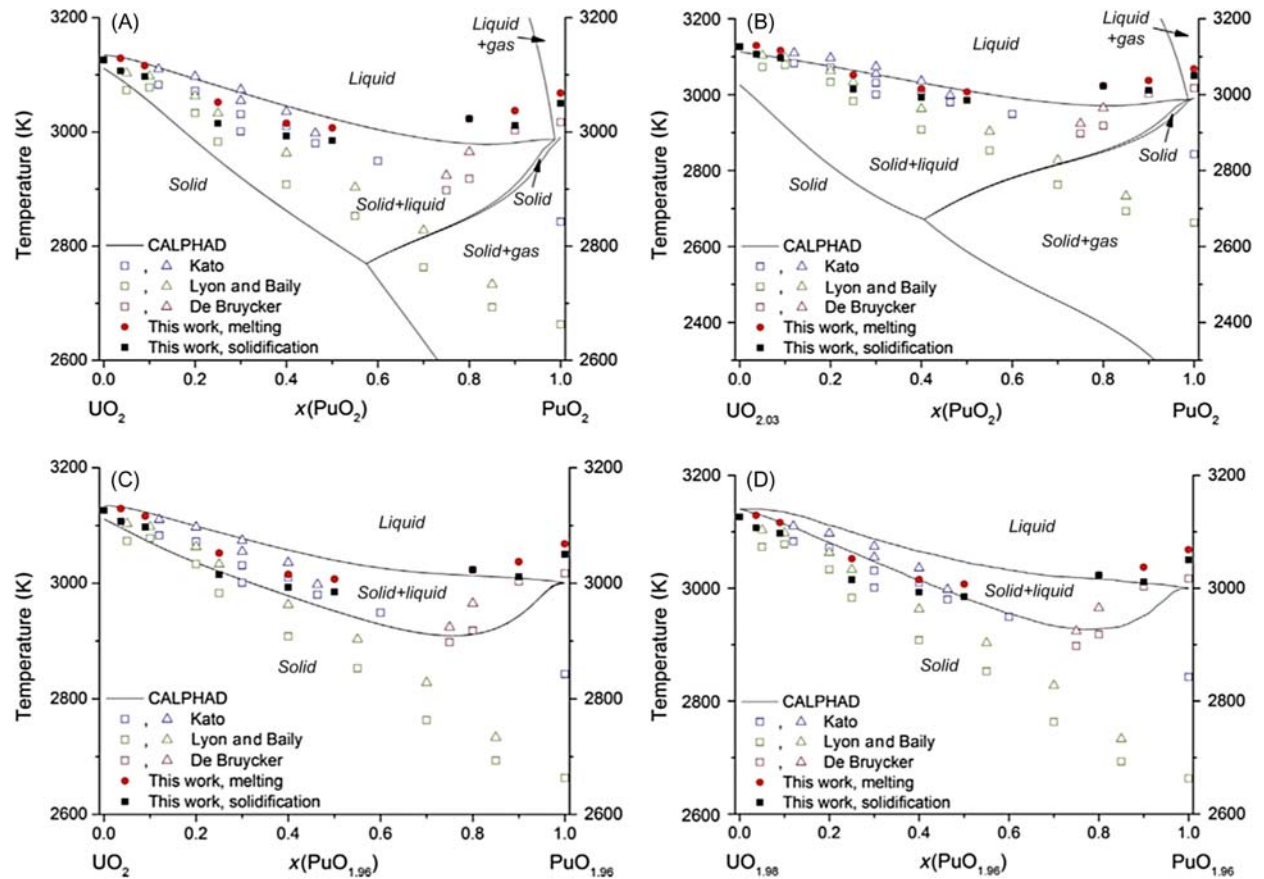


Figure 4.12 UO_2 – PuO_2 -related phase diagrams [35]. (A) In the pseudo-binary UO_2 – PuO_2 phase diagram, (B) in the “skew” $\text{UO}_{2.03}$ – PuO_2 section of the U – Pu – O ternary system, (C) in the “skew” UO_2 – $\text{PuO}_{1.96}$ section, and (D) in the “skew” $\text{UO}_{1.98}$ – $\text{PuO}_{1.96}$ section.

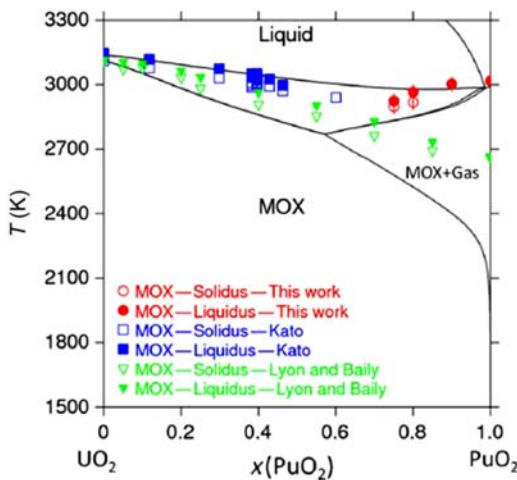


Figure 4.13 The $\text{UO}_2\text{--PuO}_2$ phase diagram model by the CALPHAD method [29]. Experimental results from Konings et al. [66] and De Bruycker et al. [67] are shown in red.

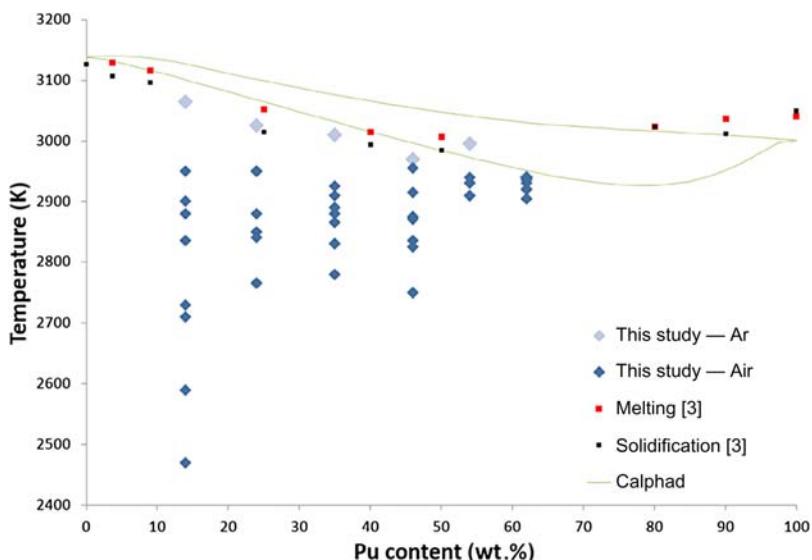


Figure 4.14 The thermal arrests for the six MOX samples and two series (air and Ar) compared to results of solidus and liquidus temperatures reported by Strach et al. [69]. *MOX*, Mixed oxide.

the difference in the system oxygen pressure could explain why both UO_2 and ThO_2 do not have definitive melting points. It should also be noted that the error bars associated with measurements shown in Fig. 4.17 make selecting one model over the other a debatable point.

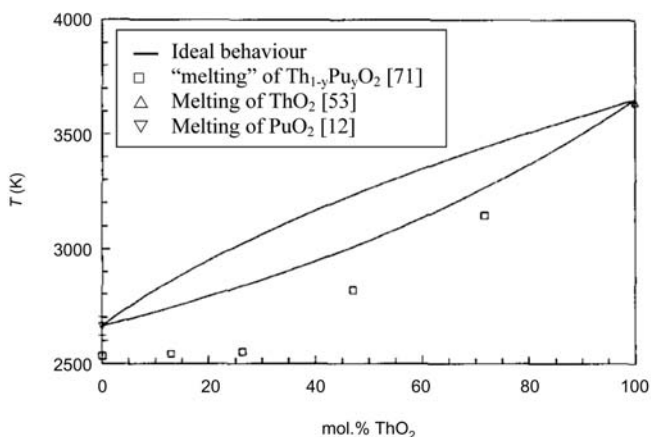


Figure 4.15 Phase diagram of PuO₂–ThO₂ [12,53,70,71].

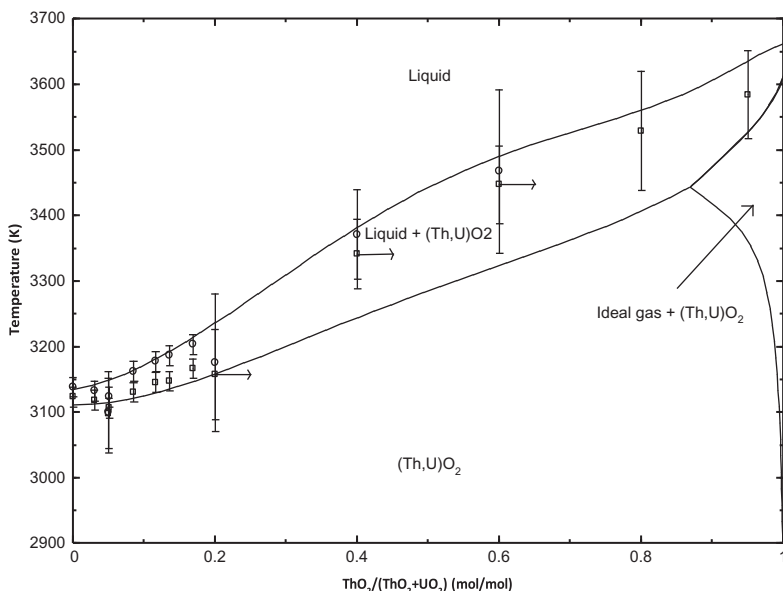


Figure 4.16 Calculated pseudo-binary phase diagram for ThO₂–UO₂ [52]. The experimental points are from Böhler et al. [36] and Latta et al. [62].

McMurray et al. [42] obtained ternary isothermal sections at different temperatures. In Fig. 4.18 a miscibility gap of F₁ and F₂ [two fluorite (F) structures] is shown at 750°C, but at 1400°C the miscibility gap disappears.

A more detailed ThO₂–PuO₂ pseudo-binary phase diagram was obtained by Bergeron et al. [52] from the model, as shown in Fig. 4.19. In comparison to Fig. 4.15, the gaseous phase is described and the calculated liquidus and solidus

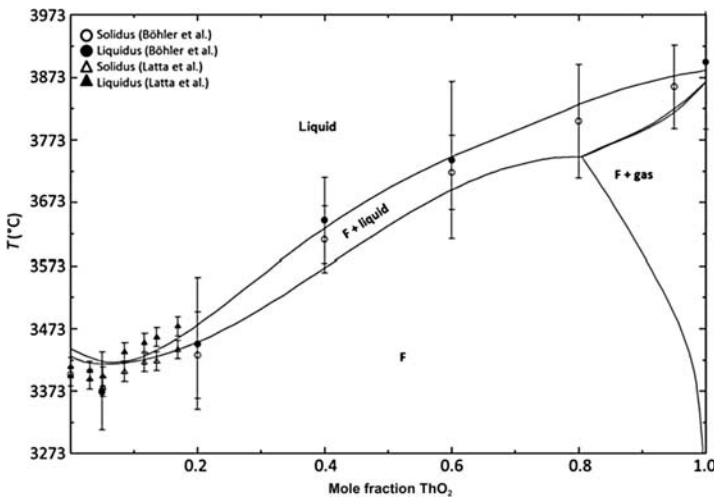


Figure 4.17 Calculated diagram for the UO_2 - ThO_2 system [36,42,62]. F , Fluorite.

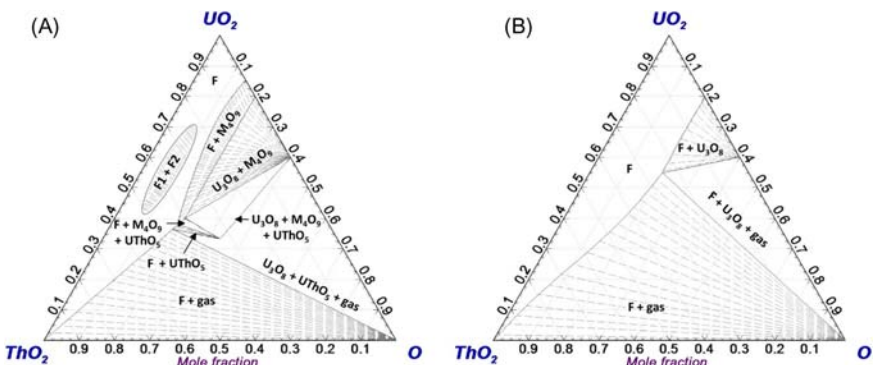


Figure 4.18 Computed phase relations using the models developed in McMurray et al. [42] for the UO_2 - ThO_2 - O pseudo-ternary system at (A) 750°C and (B) 1400°C. F , Fluorite.

(Note: In this case, “solidus” is not quite accurate because an ideal gas phase is stable at relatively low temperatures) are more consistent with the experimental phase boundary data from Böhler et al. [76]. It should be noted that the ThO_2 - PuO_2 binary system is probably the least well understood of the three oxide binary systems examined.

Fig. 4.20 is a calculated UO_2 - ThO_2 - UO_3 pseudo-ternary phase diagram at 1473 K [52]. Experimental points superimposed on it are from Cohen and Berman [77] at the same temperature. Bergeron et al. [52] believe that the better part of the experimental points are in agreement with the calculated phase diagram, though the boundaries of the calculated $(\text{Th},\text{U})\text{O}_{2+x} + \text{U}_3\text{O}_8$ two-phase field do not capture all the experimental points. The experimental points indicating the presence of two

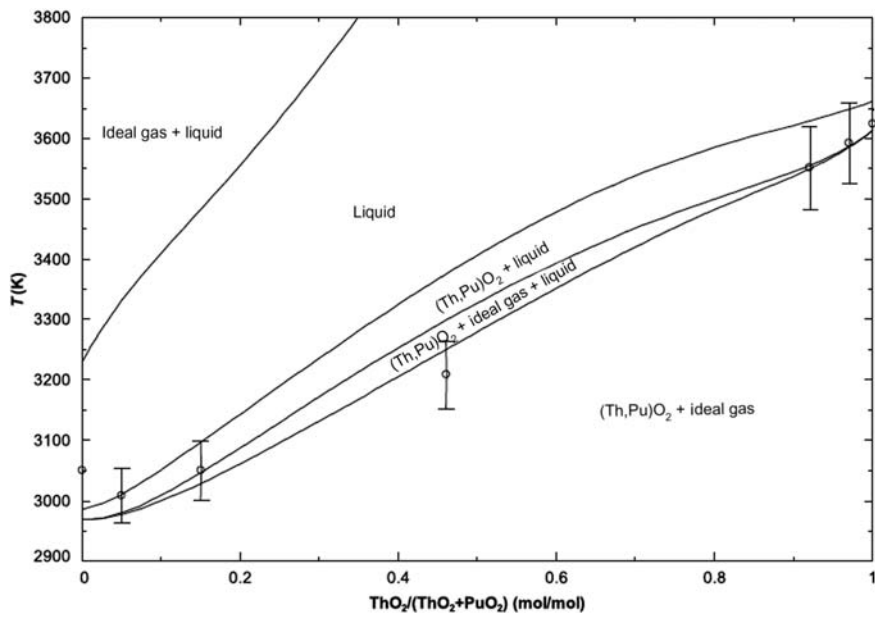


Figure 4.19 Calculated pseudo-binary $\text{ThO}_2\text{--PuO}_2$ phase diagram calculated by Bergeron et al. [52] compared to experimental data from Böhler et al. [76].

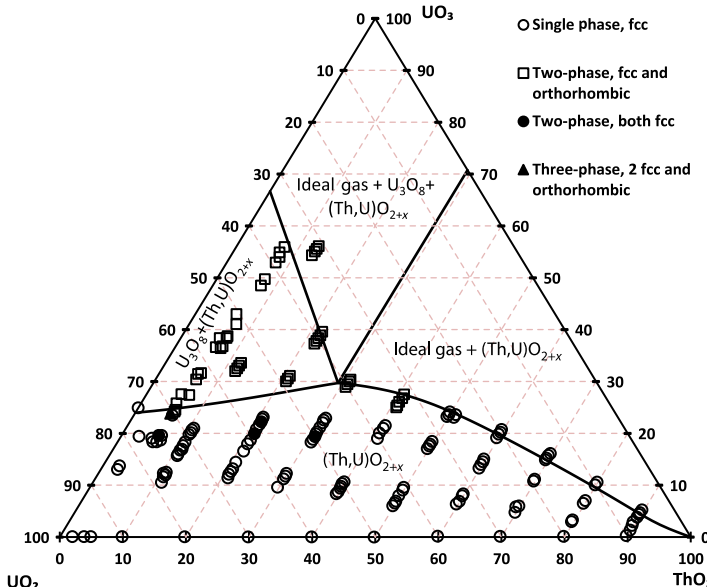


Figure 4.20 Calculated $\text{UO}_2\text{--ThO}_2\text{--UO}_3$ pseudo-ternary phase diagram at 1473 K [52] with experimental points from Cohen and Berman [77] superimposed.

face-centered cubic phases and those indicating three phases (two face-centered cubic phases and one orthorhombic phase) do not appear to be in agreement with the calculated phase diagram.

By means of this model, the phase behavior of the $\text{UO}_2\text{--ThO}_2\text{--O}$ ternary system can be analyzed. Fig. 4.21 compares calculated pseudo-ternary phase diagrams at various temperatures with experimentally derived diagrams reported by Paul and Keller [75]. The calculated diagram in Fig. 4.21A represents the same trend observed in Paul and Keller [75] under similar conditions (Fig. 4.21B) whereby the two-phase $(\text{Th},\text{U})\text{O}_{2+x} + \text{U}_3\text{O}_8$ region diminishes with increasing temperature. In Fig. 4.21C, the calculated pseudo-ternary phase diagram at 873 K is illustrated. The calculated diagram agrees well with the experimental work of Paul and Keller [75] (Fig. 4.21D). Additional computed pseudo-ternary phase diagrams are provided as Supplementary Information by Bergeron et al. [52], which provide comparisons to the computed phase diagrams of McMurray et al. [42]. However, these diagrams do not correspond to any published experimental phase data and are therefore not included in this section assessing the validity of the model.

4.3.4 Higher order system—diagrams of $\text{UO}_2\text{--ThO}_2\text{--PuO}_2$

The models from Bergeron et al. [52] provide a valuable predictive tool for determination of the stable phases at various temperature and pressure conditions for fuel compositions that have not yet been studied experimentally. As an example, the phase evolution in the $\text{UO}_2\text{--ThO}_2\text{--PuO}_2$ pseudo-ternary with increasing temperature (2500–3300 K) is presented in Fig. 4.22. At 2500 K, only two stable phase regions exist: the fluorite solid solution phase as well as a two-phase region, toward compositions rich in ThO_2 and PuO_2 , including the ideal gas phase and the fluorite phase as was observed in the $\text{ThO}_2\text{--PuO}_2$ pseudo-binary in Fig. 4.19. As the temperature increases past the melting points of both PuO_2 and UO_2 , the liquid phase region begins to form and grow. Toward the PuO_2 corner in Fig. 4.22C, a miscibility gap in the liquid phase is predicted to exist at 3100 K and persists in Fig. 4.22D at 3300 K. At 3300 K, above the melting points of PuO_2 and UO_2 as one would expect, the solid phase only exists toward the ThO_2 corner.

4.4 Doped fuels

The oxide fuels (UO_2 , ThO_2 , and PuO_2) can be doped with some other specific oxides to alter the microstructure of the calcium fluoride crystal structure, and therefore, improve the operational characteristics of the fuel pellets.

The objective in developing doped fuels is to increase the average grain size. Without the dopants, the gaseous release of the fission products tends to occupy the free space within the pellet and thereby these gases increase the inner pressure, which, in turn, compromises the integrity of the pellet [78–82]. With proper concentrations of the appropriate dopants, the average grain size of the fuel matrix

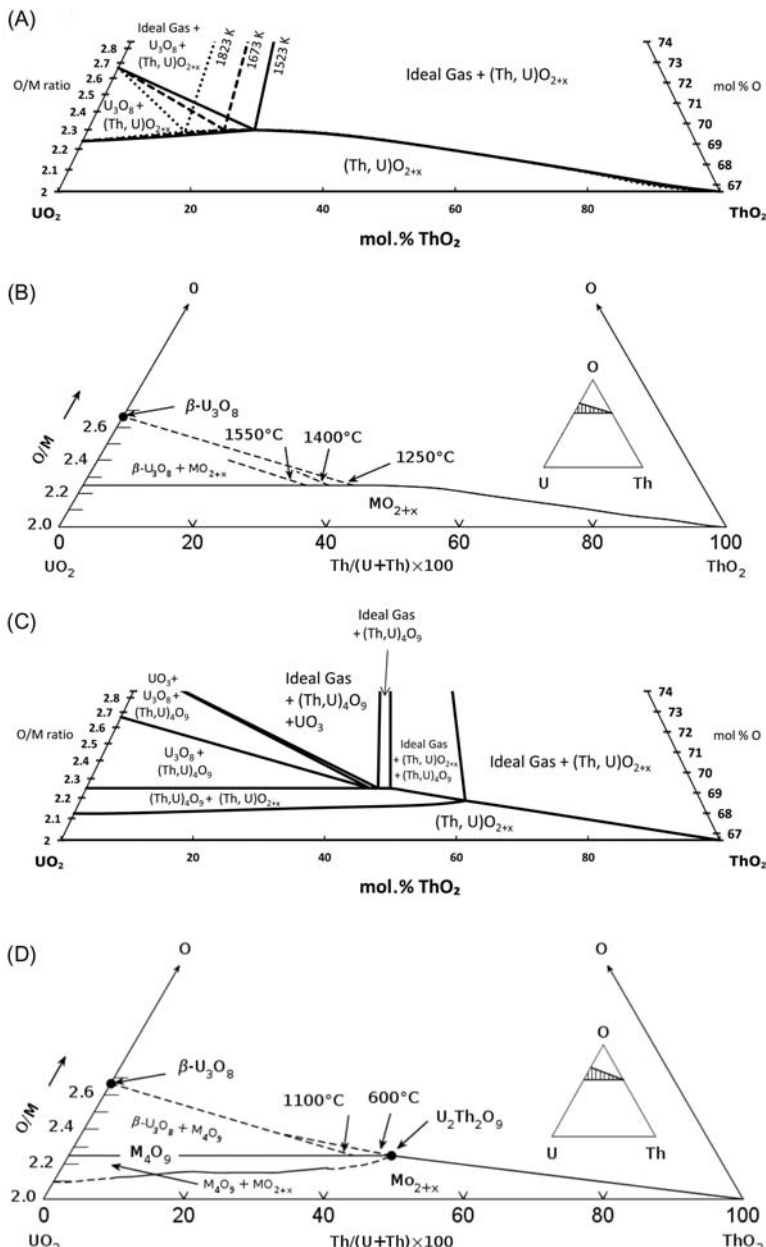


Figure 4.21 Calculated UO₂-ThO₂-O pseudo-ternary diagrams from Bergeron et al. [52] compared with data reported by Paul and Keller [75]. (A) The calculated phases at 1523 K, 1673 K, and 1823 K. (C) The calculated phases at 873 K. (B) and (D) The data from Paul and Keller [75].

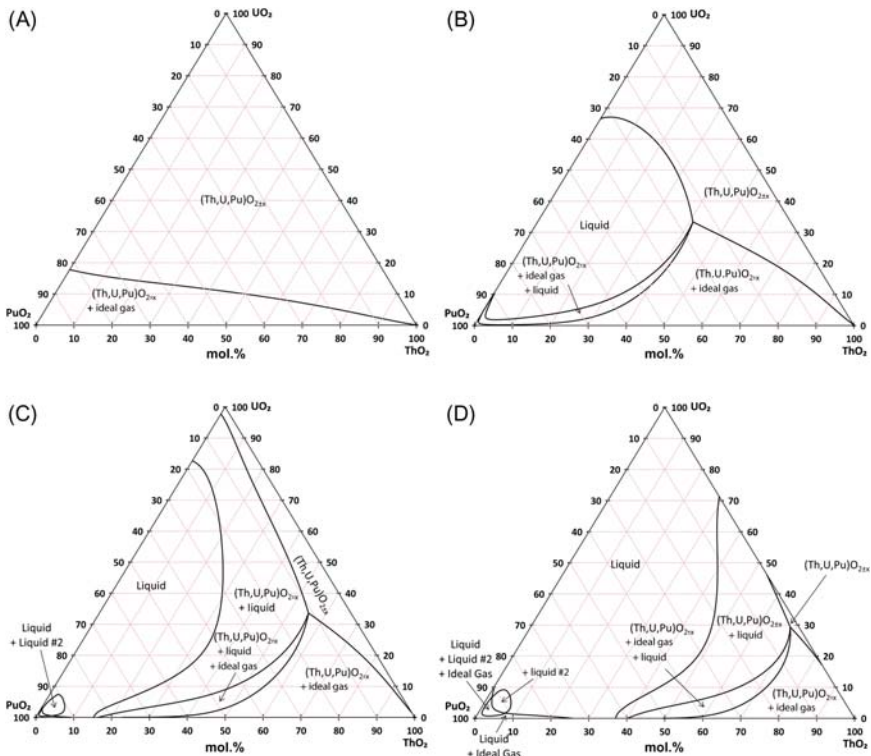


Figure 4.22 Calculated isothermal ThO_2 – UO_2 – PuO_2 pseudo-ternary phase diagrams at (A) 2500 K; (B) 2900 K; (C) 3100 K; and (D) 3300 K [52].

increases and the gas phase that develops is contained within the fuel. This trapping of the gases in the fuel enhances the mechanical properties of the fuel, in particular creep resistance. In this way, the nuclear fuel can tolerate a longer burnup while at the same time more fission products will be retained in the fuel than for dopant free fuels.

Doping techniques have been developed for other materials for optimizing the structure of traditional materials to improve their physical or chemical properties. For instance, dopants can modify optical or electrical properties, as seen in multiple purposed optical instruments or semiconductive devices. In 2008 the US Department of Energy set up the Advanced Fuel Cycle Initiative program [83,84], which promoted the studies of doped nuclear fuels, among other initiatives. It is hoped that by doping fuels it will be possible to optimize the structure and thereby enhance the accident tolerance of fuel and prolong fuel burnup, two concerns that have been identified as issues.

Typical oxide dopants used in recent studies include chromia (Cr_2O_3), alumina (Al_2O_3), titania (TiO_2), niobia (Nb_2O_5), and vanadia (V_2O_5). The concentration of the dopants varies, but is usually up to 0.5 wt.% [85].

For unirradiated doped UO_2 fuels, a fabrication process may include the mixing of the UO_2 powder with that of the dopant, cold pressing of the mixture, and then sintering. A summary of results from previous studies taken from Dooies [85] for different dopant concentrations and sintering conditions is presented in Table 4.4. In the work of Dooies, TiO_2 and Nb_2O_5 were found to give most effective grain size changes, that is, 279% and 117%, respectively.

Since fuel pellets in a nuclear reactor are sensitive to many physical, chemical, and mechanical factors, parameters other than the grain sizes should also be considered. In their experiments, Jernkvist and Massih [86,87] showed that additives (dopants) such as Nb_2O_5 and Cr_2O_3 , affect the creep rate of the pellets. Fig. 4.23 shows the effect of Nb_2O_5 concentration on the measured grain sizes and creep rates of Nb_2O_5 doped UO_2 samples in the stress range of 0.5–90 MPa at temperatures from 1422 K to 1773 K [86,88].

Table 4.4 Summary of grain size analysis by Dooies [85].

Sample	Dopant	Mean grain size (μm)	Std. dev (μm)	Percentage of error	Percentage of change
1	Undoped	2.73	0.35	12.6	—
2	Nb_2O_5	5.94	0.58	9.7	117
3	Al_2O_3	5.14	0.50	9.8	88
4	Cr_2O_3	4.77	0.58	12.1	74
5	Sc_2O_3	2.63	0.35	13.4	—4
6	V_2O_5	3.41	0.13	3.7	25
7	TiO_2	10.37	1.19	11.4	279

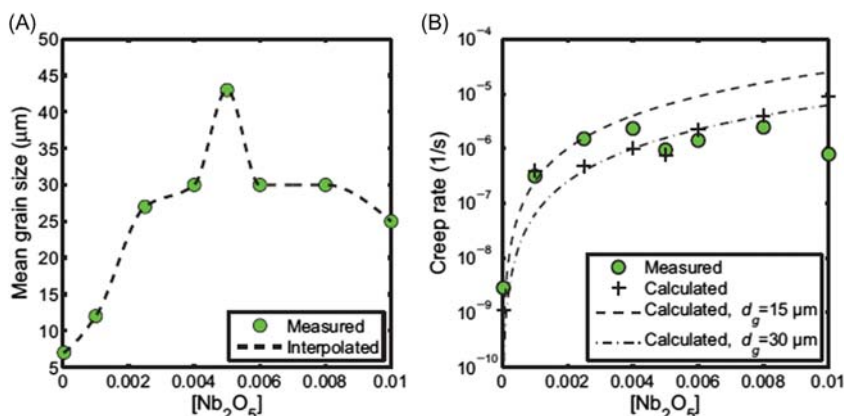


Figure 4.23 (A) Measured grain size versus mole fraction of Cr_2O_3 in doped UO_2 from Sawbridge et al. [88]. (B) Measured creep rates [88] versus calculated values by Jernkvist and Massih [86].

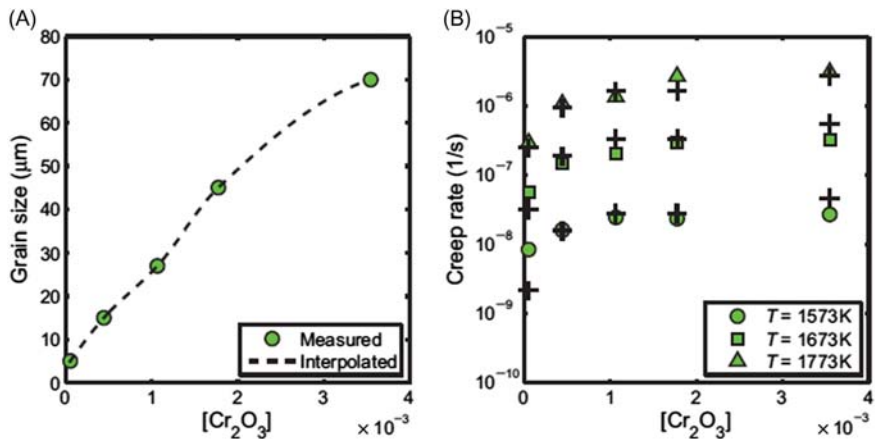


Figure 4.24 (A) Measured grain size versus mole fraction of Cr_2O_3 in doped UO_2 from Dugay et al. [89]. (B) Measured creep rates versus calculated values (+) as a function of mole fraction Cr_2O_3 in doped UO_2 at an applied stress of 45 MPa at three elevated temperatures [86].

Fig. 4.24 shows the changes of grain sizes and creep rates as functions of concentration of dopants and temperature, as measured by Dugay et al. [89].

Recently, the scope of the studies on unirradiated doped nuclear fuels has grown. Using the small polaron theory, Massih [90] studied the electronic transport phenomenon in Cr_2O_3 , Gd_2O_3 , Y_2O_3 , and Nb_2O_5 . Research by Xiao et al. [91], with dopant concentrations far beyond 0.5 wt.%, was published. The concentration range is 0–20 wt.%, but the concentration interval within this range is 5 wt.%, which is broader than the trace doping range of 0.3–0.5 wt.% from earlier studies. As a result, they did not see the effect of doping in improving fuel properties. In addition, such large amounts of additives of oxides (e.g., 20 wt.% ZrO_2) goes beyond the usual definition of doping. Nevertheless, the authors concluded that the grain sizes decreased from 20–30 to 10 μm as ZrO_2 concentration reaches 20 wt.% [91].

Dehaudt et al. [92] explored a composite fuel concept to measure mean grain size of the matrix of UO_2 . Fig. 4.25 shows curves of grain sizes of dopant concentration in at.% of Cr_2O_3 , TiO_2 , V_2O_3 , and Al_2O_3 in a matrix of UO_2 . Note that the curve for Cr_2O_3 has two peaks, but despite that a maximum mean grain size seems to be achieved for all dopants by a concentration of 0.5 at.%.

4.5 Summary

Thermodynamic properties of nuclear materials determine the phase transformation behavior of fuel in a nuclear reactor. Applications include investigating the margin to fuel melting, fuel oxidation, severe accident behavior, and the reprocessing of

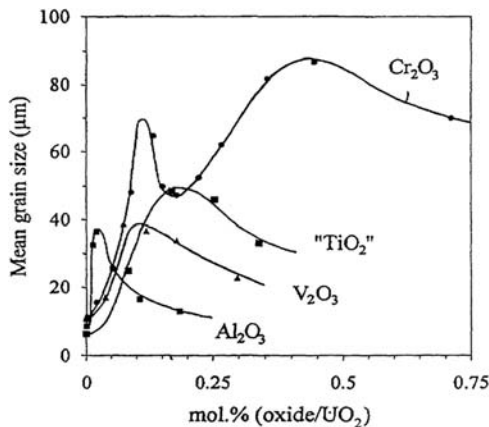


Figure 4.25 Influence of a corundum type oxide addition on grain size [92].

the waste. The U–O, Pu–O, and Th–O binary phase diagrams have been examined experimentally and have been evaluated thermodynamically by the CALPHAD method. The $\text{UO}_2 \pm x$ phase region in the phase diagram shows the wide stability range of the fluorite UO_2 , and this is important when discussing the dissolution of fission products in nuclear fuel (see Chapter 12, Irradiated fuel chemistry). For MOX fuels the development of $\text{UO}_2\text{–PuO}_2$, $\text{UO}_2\text{–ThO}_2$, and $\text{PuO}_2\text{–ThO}_2$ phase diagrams have been reviewed in detail, and a model for a pseudo-ternary $\text{UO}_2\text{–PuO}_2\text{–ThO}_2$ has been presented. U–Pu–O phase relations have been studied widely, which provide bench marks for the fabrication of MOX fuels and some of recent developments (e.g., dopants) are included in this chapter.

References

- [1] International Atomic Energy Agency – IAEA, PRIS – Reactor Status Reports – Operational & Long-Term Shutdown – By Type. [online] Pris.iaea.org, 2019. Available from: <<https://pris.iaea.org/PRIS/WorldStatistics/OperationalReactorsByType.aspx>> (accessed 01.01.19).
- [2] E.C. Corcoran, M.H. Kaye, M.H.A. Piro, An overview of thermochemical modelling of CANDU fuel and applications to the nuclear industry, *Calphad* 55 (2016) 52–62.
- [3] B. Lewis, W.T. Thompson, F.C. Iglesias, Fission product chemistry in oxide fuels, *Compr. Nucl. Mater.* 2 (2012) 515–546.
- [4] N.N. Greenwood, A. Earnshaw, *Chemistry of the Elements*, second ed., Butterworth Heinemann, GB, 1997.
- [5] OECD Nuclear Energy Agency, Working Group on Strategies for Plutonium Utilisation, Plutonium Fuel: An Assessment/Report by an Expert Group, 1989.
- [6] A.R. Massih, Statens kärnkraftinspektion, *Models for MOX Fuel Behaviour: A Selective Review*, Statens kärnkraftinspektion, Stockholm, 2006. SKI Report 2006:10, ISSN 1104-1374.

- [7] T. Yamashita, N. Nitani, T. Tsuji, H. Inagaki, Thermal expansions of NpO_2 and some other actinide dioxides, *J. Nucl. Mater.* 245 (1) (1997) 72–78.
- [8] G. Leinders, T. Cardinaels, K. Binnemans, M. Verwerft, Accurate lattice parameter measurements of stoichiometric uranium dioxide, *J. Nucl. Mater.* 459 (2015) 135–142.
- [9] S.R. Bharadwaj, D. Das, Thoria-based nuclear fuels: thermophysical and thermodynamic properties, fabrication, reprocessing, and waste management, Springer, London, 2013.
- [10] G.K. Johnson, W.V. Steele, The standard enthalpy of formation of uranium dioxide by fluorine *bomb* calorimetry, *J. Chem. Thermodyn.* 13 (8) (1981) 717–723.
- [11] I. Barin, *Thermochemical Data of Pure Substances*, Springer-Verlag, Germany, 1995.
- [12] E.H.P. Cordfunke, R.J.M. Konings, *Thermochemical Data for Reactor Materials and Fission Products*, Elsevier Science Pub. Co., Inc, New York, 1990.
- [13] K. Leeder, S. Yatabe, M.R. Floyd, G. Cota-Sanchez, R. Beier, C. Mayhew, Fabrication and characterization of $(\text{Th}, \text{Pu})\text{O}_2$ fuel at Canadian Nuclear Laboratories, *J. Nucl. Mater.* 508 (2018) 599–608.
- [14] IAEA, *IAEA-TECDOC-1450: Thorium Fuel Cycle—Potential Benefits and Challenges*, IAEA, Austria, 2005.
- [15] J. Ma, J. Du, M. Wan, G. Jiang, Molecular dynamics study on thermal properties of ThO_2 doped with U and Pu in high temperature range, *Journal of Alloys and Compounds* 627 (2015) 476–482.
- [16] T. Arima, S. Yamasaki, Y. Inagaki, K. Idemitsu, Evaluation of thermal conductivity of hypostoichiometric $(\text{U}, \text{Pu})\text{O}_{2-x}$ solid solution by molecular dynamics simulation at temperatures up to 2000 K, *Journal of Alloys and Compounds* 415 (12) (2006) 43–50.
- [17] M.W.D. Cooper, S.C. Middleburgh, R.W. Grimes, Modelling the thermal conductivity of $(\text{U}_x\text{Th}_{1-x})\text{O}_2$ and $(\text{U}_x\text{Pu}_{1-x})\text{O}_2$, *J. Nucl. Mater.* 466 (2015) 29–35.
- [18] P.S. Somayajulu, P.S. Ghosh, A. Arya, K.V.V. Devi, D.B. Sathe, J. Banerjee, et al., Thermal expansion and thermal conductivity of $(\text{Th}, \text{Pu})\text{O}_2$ mixed oxides: a molecular dynamics and experimental study, *J. Alloys Compd.* 664 (2016) 291–303.
- [19] L. Vlahovic, D. Staicu, A. Küst, R.J.M. Konings, Thermal diffusivity of UO_2 up to the melting point, *J. Nucl. Mater.* 499 (2018) 504–511.
- [20] P. Jund, R. Jullien, Molecular-dynamics calculation of the thermal conductivity of vitreous silica, *Phys. Rev., B* 59 (21) (1999) 13707–13711.
- [21] P. Schelling, S. Phillpot, P. Kebinski, Comparison of atomic-level simulation methods for computing thermal conductivity, *Phys. Rev. B* 65 (14) (2002) 1–12.
- [22] B.J. Lewis, D.M. Thompson, W.T. Thompson, F. Akbari, C. Thurgood, J. Higgs, Thermodynamic and kinetic modelling of fuel oxidation behaviour in operating defective fuel, *J. Nucl. Mater.* 328 (2) (2004) 180–196.
- [23] J.D. Higgs, B.J. Lewis, W.T. Thompson, Z. He, A conceptual model for the fuel oxidation of defective fuel, *J. Nucl. Mater.* 366 (1–2) (2007) 99–128.
- [24] J.D. Higgs, B.J. Lewis, W.T. Thompson, Modelling of fuel oxidation behaviour for defected fuel, in: Ninth International Conference on CANDU Fuel, ‘Fuelling a Clean Future’, Canadian Nuclear Society, Canada, 2005. 0-919784-84-4.
- [25] F. Akbari, M.J. Welland, B.J. Lewis, W.T. Thompson, Considerations in modelling the melting of fuel containing fission products and solute oxides, in: Ninth International Conference on CANDU Fuel, ‘Fuelling a Clean Future’, Canadian Nuclear Society, Canada, 2005. 0-919784-84-4.
- [26] L. Kaufman, M. Cohen, *J. Met.* 8 (10) (1956) 1393–1401.
- [27] H. Bernstein, L. Kaufman, *Computer Calculation of Phase Diagrams: With Special Reference to Refractory Metals*, Academic Press, 1970.

- [28] W.T. Thompson, B.J. Lewis, E.C. Corcoran, M.H. Kaye, S.J. White, F. Akbari, et al., Thermodynamic treatment of uranium dioxide based nuclear fuel, *Int. J. Mater. Res.* 98 (10) (2007) 1004–1011.
- [29] C. Guéneau, N. Dupin, B. Sundman, C. Martial, J.C. Dumas, S. Gossé, et al., Thermodynamic modelling of advanced oxide and carbide nuclear fuels: description of the U–Pu–O–C systems, *J. Nucl. Mater.* 419 (2011) 145–167.
- [30] R.E. Latta, R.E. Fryxell, Determination of solidus-liquidus temperatures in the $\text{UO}_{2+\chi}$ system ($-0.50 < \chi < 0.20$), *J. Nucl. Mater.* 35 (2) (1970) 195–210.
- [31] J.K. Fink, Enthalpy and heat capacity of the actinide oxides, *Int. J. Thermophys.* 3 (2) (1982) 165–200.
- [32] J.K. Fink, Thermophysical properties of uranium dioxide, *J. Nucl. Mater.* 279 (1) (2000) 1–18.
- [33] J.K. Fink, M.C. Petri, Thermophysical Properties of Uranium Dioxide – Version 0 for Peer Review, USDOE Assistant Secretary for Nuclear Energy, Washington, DC, 1997.
- [34] J.K. Fink, M.G. Chasanov, L. Leibowitz, Thermophysical properties of uranium dioxide, *J. Nucl. Mater.* 102 (1) (1981) 17–25.
- [35] R. Böhler, M.J. Welland, D. Prieur, P. Cakir, T. Vitova, T. Pruessmann, et al., Recent advances in the study of the UO_2 – PuO_2 phase diagram at high temperatures, *J. Nucl. Mater.* 448 (1–3) (2014) 330–339.
- [36] R. Böhler, A. Quaini, L. Capriotti, P. Çakır, O. Beneš, K. Boboridis, et al., The solidification behaviour of the UO_2 – ThO_2 system in a laser heating study, *J. Alloys Compd.* 616 (2014) 5–13.
- [37] D. Manara, C. Ronchi, M. Sheindlin, M. Lewis, M. Brykin, Melting of stoichiometric and hyperstoichiometric uranium dioxide, *J. Nucl. Mater.* 342 (1–3) (2005) 148–163.
- [38] C. Guéneau, C. Chatillon, B. Sundman, Thermodynamic modelling of the plutonium–oxygen system, *J. Nucl. Mater.* 378 (3) (2008) 257–272.
- [39] R.J. Ackermann, M. Tetenbaum, High-temperature thermodynamic properties of the thorium-oxygen system, in: International Colloquium on Materials for High-Temperature Energy, Toronto, Canada, 1978.
- [40] R.J. Ackermann, M. Tetenbaum, High-temperature thermodynamic properties of the thorium-oxygen system, *High Temp. Sci. (United States)* 13 (1) (1980) 91–95.
- [41] D. Das, S.R. Bharadwaj, Thoria-Based Nuclear Fuels: *Thermophysical and Thermodynamic Properties, Fabrication, Reprocessing, and Waste Management*, 2013th ed., Springer, London, 2013.
- [42] J.W. McMurray, S.L. Voit, T.M. Besmann, C. Jantzen, A combined experimental and computational thermodynamic investigation of the U–Th–O system, *J. Am. Ceram. Soc.* 99 (6) (2016) 2197–2209.
- [43] R. Benz, Thorium-thorium dioxide phase equilibria, *J. Nucl. Mater.* 29 (1) (1969) 43–49.
- [44] A.J. Darnell, W.A. McCollum, North American Aviation – Atomics International Division, & U.S. Atomic Energy Commission, High Temperature Reactions of Thorium and Thoria and the Vapor Pressure of Thoria, 1961.
- [45] W.H. Zachariasen, Crystal chemical studies of the 5f-series of elements. XVI. Identification and crystal structure of protactinium metal and of protactinium monoxide, *Acta Crystallogr.* 5 (1) (1952) 19–21.
- [46] R.E. Rundle, A new interpretation of interstitial compounds—metallic carbides, nitrides and oxides of composition MX, *Acta Crystallogr.* 1 (4) (1948) 180–187.
- [47] R.J. Ackermann, E.G. Rauh, R.J. Thorn, M.C. Cannon, A thermodynamic study of the thorium-oxygen system at high temperatures, *J. Phys. Chem.* 67 (4) (1963) 762–769.

- [48] H.E. Swanson, E. Tatge, United States National Bureau of Standards, Standard X-Ray Diffraction Powder Patterns, 1953.
- [49] L. Brewer, The thermodynamic properties of the oxides and their vaporization processes, *Chem. Rev.* 52 (1) (1953) 1–75.
- [50] L. Eyring, Lanthanide and actinide oxides: a case study in solid state chemistry, in: *Solid State Chemistry*, Marcell Dekker, New York, 1974, pp. 565–634.
- [51] A.J. Darnell, W.A. McCollum, North American Aviation Report NAA-SR-6498, Office of Technical Services, Department of Commerce, Washington, DC, 1960.
- [52] A. Bergeron, D. Manara, O. Beneš, R. Eloirdi, M.H.A. Piro, E.C. Corcoran, Thermodynamic modelling of thoria-urania and thoria-plutonia fuels: description of the Th-U-Pu-O quaternary system, *J. Nucl. Mater.* 512 (2018) 324–348.
- [53] C. Ronchi, J.P. Hiernaut, Experimental measurement of pre-melting and melting of thorium dioxide, *J. Alloys Compd.* 240 (1–2) (1996) 179–185.
- [54] R.G. Cochran, N. Tsoulfanidis, *The Nuclear Fuel Cycle: Analysis and Management*, second ed., American Nuclear Society, La Grange Park, IL, 1999.
- [55] R. Parrish, A. Aitkaliyeva, A review of microstructural features in fast reactor mixed oxide fuels, *J. Nucl. Mater.* 510 (2018) 644–660.
- [56] T.M. Besmann, J.W. McMurray, S. Simunovic, Application of thermochemical modeling to assessment/evaluation of nuclear fuel behavior, *Calphad* 55 (2016) 47–51.
- [57] G. Brillant, F. Gupta, A. Pasturel, Fission products stability in uranium dioxide, *J. Nucl. Mater.* 412 (1) (2011) 170–176.
- [58] J. Noirot, Y. Pontillon, J. Lamontagne, I. Zacharie-Aubrun, K. Hanifi, P. Bienvenu, et al., High burn-up structure in nuclear fuel: impact on fuel behavior, in: Paper Presented at the Second Int. Workshop, *EPJ Web of Conference*, 115 4005, 2016.
- [59] W.L. Lyon, W.E. Baily, The solid-liquid phase diagram for the $\text{UO}_2\text{-PuO}_2$ system, *J. Nucl. Mater.* 22 (3) (1967) 332–339.
- [60] J. Belle, R.M. Berman, Thorium Dioxide: Properties and Nuclear Applications, USDOE Assistant Secretary for Nuclear Energy; Office of Naval Reactors, Washington, DC, 1984.
- [61] W.A. Lambertson, M.H. Mueller, F.H. Gunzel, Uranium oxide phase equilibrium systems: IV, $\text{UO}_2\text{-ThO}_2$, *J. Am. Ceram. Soc.* 36 (12) (1953) 397–399.
- [62] R.E. Latta, E.C. Duderstadt, R.E. Fryxell, Solidus and liquidus temperatures in the $\text{UO}_2\text{-ThO}_2$ system, *J. Nucl. Mater.* 35 (3) (1970) 347–349.
- [63] J. Kim, S.S. Kim, Thermodynamic modeling of the $\text{UO}_2\text{-ThO}_2$ phase diagram, *Modell. Simul. Mater. Sci. Eng.* 24 (2) (2016) 1–9.
- [64] L.C. Shuller, R.C. Ewing, U. Becker, Thermodynamic properties of $\text{Th}_x\text{U}_{1-x}\text{O}_2$ ($0 < x < 1$) based on quantum-mechanical calculations and Monte-Carlo simulations, *J. Nucl. Mater.* 412 (1) (2011) 13–21.
- [65] M. Kato, K. Morimoto, H. Sugata, K. Konashi, M. Kashimura, T. Abe, Solidus and liquidus temperatures in the $\text{UO}_2\text{-PuO}_2$ system, *J. Nucl. Mater.* 373 (1–3) (2008) 237–245.
- [66] R.J.M. Konings, D. Manara, O. Beneš, C. Guéneau, Nuclear reactor fuels: materials with highly complex behaviour, *EPJ Web Conf.* 51 (2013) 3001.
- [67] F. De Bruycker, K. Boboridis, R.J.M. Konings, M. Rini, R. Eloirdi, C. Guéneau, et al., On the melting behaviour of uranium/plutonium mixed dioxides with high-Pu content: a laser heating study, *J. Nucl. Mater.* 419 (1) (2011) 186–193.
- [68] F. De Bruycker, K. Boboridis, D. Manara, P. Pöml, M. Rini, R.J.M. Konings, Reassessing the melting temperature of PuO_2 , *Mater. Today* 13 (11) (2010) 52–55.

- [69] M. Strach, D. Manara, R.C. Belin, J. Rogez, Melting behavior of mixed U-Pu oxides under oxidizing conditions, *Nucl. Instrum. Methods Phys. Res., Sect. B* 374 (2016) 125–128.
- [70] K. Bakker, E.H.P. Cordfunke, R.J.M. Konings, R.P.C. Schram, Critical evaluation of the thermal properties of ThO_2 and $\text{Th}_{1-y}\text{U}_y\text{O}_2$ and a survey of the literature data on $\text{Th}_{1-y}\text{Pu}_y\text{O}_2$, *J. Nucl. Mater.* 250 (1) (1997) 1–12.
- [71] M.D. Freshley, H.M. Mattys, Properties of sintered ThO_2 - PuO_2 , in: General Electric Report HW-76300, 1962, Richland, WA, 1962.
- [72] F.A. Mumpton, R. Roy, Low-temperature equilibria among ZrO_2 , ThO_2 , and UO_2 , *J. Am. Ceram. Soc.* 43 (5) (1960) 234–240.
- [73] S. Dash, S.C. Parida, Z. Singh, B.K. Sen, V. Venugopal, Thermodynamic investigations of ThO_2 - UO_2 solid solutions, *J. Nucl. Mater.* 393 (2) (2009) 267–281.
- [74] H.J.C. Boekschoten, N.V. Kema, The formation of compounds in the UO_3 - ThO_2 system, *J. Inorg. Nucl. Chem.* 30 (1) (1968) 119–126.
- [75] R. Paul, C. Keller, Phasengleichgewichte in den systemen UO_2 - $\text{UO}_{2,67}$ - ThO_2 und UO_{2+x} - NpO_2 , *J. Nucl. Mater.* 41 (2) (1971) 133–142.
- [76] R. Böhler, P. Çakir, O. Benes̄, H. Hein, R.J.M. Konings, D. Manara, High temperature phase transition of mixed ($\text{PuO}_2 + \text{ThO}_2$) investigated by laser melting, *J. Chem. Thermodyn.* 81 (2015) 245–252.
- [77] I. Cohen, R.M. Berman, A metallographic and X-ray study of the limits of oxygen solubility in the UO_2 - ThO_2 system, *J. Nucl. Mater.* 18 (1966) 77–107.
- [78] J.A. Turnbull, R.M. Cornell, The re-solution of fission-gas atoms from bubbles during the irradiation of UO_2 at an elevated temperature, *J. Nucl. Mater.* 41 (2) (1971) 156–160.
- [79] Y. Kim, Theoretical analysis of two-stage fission gas release processes: grain lattice and grain boundary diffusion, *J. Nucl. Mater.* 326 (2) (2004) 97–105.
- [80] Y. Che, G. Pastore, J. Hales, K. Shirvan, Modeling of Cr_2O_3 -doped UO_2 as a near-term accident tolerant fuel for LWRs using the BISON code, *Nucl. Eng. Des.* 337 (2018) 271–278.
- [81] M.W.D. Cooper, C.R. Stanek, A.D.R. Andersson, Milestone Report: Calculate Parameters Controlling Grain Growth in Doped UO_2 [M3MS-18LA0201035], Los Alamos National Lab. (LANL), Los Alamos, NM, 2018.
- [82] A. Massih, Faculty of Technology and Society, Malmö University, Effects of additives on uranium dioxide fuel behavior, in: Report Number: 2014:21, 2014. ISSN:2000-0456.
- [83] National Research Council, Review of DOE's Nuclear Energy Research and Development Program, The National Academies Press, Washington, DC, 2008.
- [84] DOE, Advanced Fuel Cycle Initiative, U.S. Department of Energy, (2008). Retrieved from: <<http://www.ne.doe.gov/afci/neAFCI.html>>.
- [85] B.J. Dooies, Enhancement of Uranium Dioxide Thermal and Mechanical Properties by Oxide Dopants (thesis M.S.), University of Florida, 2008.
- [86] L. Jernkvist, A. Massih, Effect of Additives Nb_2O_5 and Cr_2O_3 on Creep of UO_2 , SMiRT Organization, 2015.
- [87] A.R. Massih, L.O. Jernkvist, Effect of additives on self-diffusion and creep of UO_2 , *Comput. Mater. Sci.* 110 (2015) 152–162.
- [88] P.T. Sawbridge, G.L. Reynolds, B. Burton, The creep of UO_2 fuel doped with Nb_2O_5 , *J. Nucl. Mater.* 97 (3) (1981) 300–308.
- [89] C. Dugay, A. Mocellin, P. Dehaut, M. Sladkoff, High Temperature Mechanical Tests Performed on Doped Fuels (IAEA-TECDOC-1036), International Atomic Energy Agency (IAEA), 1998.

- [90] A.R. Massih, Electronic transport in pure and doped UO₂, *J. Nucl. Mater.* 497 (2017) 166–182.
- [91] H. Xiao, X. Wang, C. Long, Y. Liu, A. Yin, Y. Zhang, Investigation of the mechanical properties of ZrO₂-doped UO₂ ceramic pellets by indentation technique, *J. Nucl. Mater.* 509 (2018) 482–487.
- [92] P. Dehadt, C. Lemaignan, L. Caillot, A. Mocellin, G. Eminet, New UO₂ Fuel Studies (IAEA-TECDOC-1036), International Atomic Energy Agency (IAEA), 1998.

This page intentionally left blank

Other power reactor fuels

5

Andrew T. Nelson¹ and Paul Demkowicz²

¹Oak Ridge National Laboratory, Oak Ridge, TN, United States, ²Idaho National Laboratory, Idaho Falls, ID, United States

5.1 Introduction

Actinoid oxide compounds have seen broad use as nuclear fuels for nearly all reactor types. As detailed in [Chapter 4](#), Oxide power reactor fuels, the thermochemistry of uranium and plutonium dioxide provides many advantages for service as a nuclear fuel. Foremost of these are satisfactory accommodation of both transuranic and fission products and acceptable chemical compatibility with many cladding types and coolant forms. However, oxide fuels possess some less desirable material properties. The thermal conductivity of UO₂ is poor even in the unirradiated state and degrades further during irradiation. More generally, monolithic oxide fuels are subject to the same performance challenges of all monolithic fuel forms. Retention of fission products during transients is a consistent difficulty. Service under high-temperature gradients, chemical and microstructural evolution, and the mechanical integrity of the fuel pellet further challenge fission product retention and performance. Views on the strengths and weaknesses of UO₂ have been long understood and have minimally changed since the early decades of the nuclear era [\[1\]](#).

While the many favorable aspects of UO₂ have resulted in it being the primary fuel choice for many different reactor types, alternative fuels offer different sets of advantages as well as challenges. Many different fuel forms have been proposed and developed to varying extents to address the limitations of UO₂. In some cases, a specific reactor type or fuel cycle objective has motivated the advancement of a nonoxide fuel. Metallic fuels are well suited to transmutation and breeding given their high actinoid densities, ease of separation processes, and remote fabrication. Coated particle fuels employ a more advanced composite architecture through the use of an inert matrix material and multiple engineered layers to encapsulate the fuel itself in pursuit of greater fission product retention under even the most extreme conditions. Other ceramics have also been explored. Carbide and nitride forms have been the historic reference fuels in this category, but recent years have seen exploration of uranium silicide fuels. Modern fuel development efforts have also examined composite fuels that comprised multiple fissile phases using the aforementioned components and even more exotic uranium compounds.

The chemistry of these fuel forms and concepts governs many important aspects, including initial development and property assessment, irradiation performance, and

eventual commercial deployment. Fabrication of metallic, nonoxide ceramic, and particle fuels presents specific challenges and is detailed in [Chapter 10](#), Advances in fuel fabrication. The chemistry themes introduced in [Chapter 11](#), **In-reactor behavior**, with regard to fission product behavior remain critical to the performance of these fuel forms. [Chapter 6](#), Molten salt reactor fuels, is dedicated to molten salt fuel forms. This chapter will provide an overview of relevant topics for three fuel types of interest for power production: metallic fuels, nontraditional ceramics, and coated particle fuels.

5.2 Metallic fuels

Alloys of uranium and other transuranic elements with secondary and ternary metallic constituents have been long viewed as an attractive nuclear fuel concept. From a fabrication standpoint, metal alloys are economical to produce—casting, drawing, rolling, and other forming processes are readily scalable and can be performed with a high degree of control and repeatability. Adaptation of these processes for uranium alloys has some challenges but in general is easily achieved. These same aspects make metallic fuel formats attractive for remote fabrication where the activity of minor actinides and fission products forces operations into shielded hot cells. In addition to fabrication, the other general advantages of metallic fuels are high heavy metal (i.e., fissile) density and good thermal conductivity.

A limited number of elements can be alloyed with uranium without yielding intermetallic phases. While some uranium intermetallics with higher melting points and other favorable properties are of interest as nuclear fuels and will be discussed in [Section 5.3](#), intermetallic phases in general make poor nuclear fuels due to their low melting points, poor mechanical properties, challenges in fabrication processes, and susceptibility to amorphization and swelling once their structure is perturbed by irradiation.

Two metallic fuels have seen broad exploration and assessment for power reactor applications. Zirconium metallic fuels received interest dating back to the 1960s. In parallel, molybdenum–uranium compositions were developed at a slower rate (see [Chapter 7](#): Research reactor fuels). While both fuel forms are perhaps best known for other reactor platforms (i.e., U–Zr fuels as transmutation concepts and U–Mo as dispersion fuels for low power research reactors), both concepts have been considered power reactor fuels.

5.2.1 Zirconium-based metallic fuels

Uranium–zirconium (U–Zr) alloys have been explored as reactor fuels since the earliest years in the field. Zirconium was a natural choice as an alloying compound due to its low neutron absorption cross section and comparatively high melting point. The bulk of work on U–Zr fuels has been in the area of fast reactor and transmutation applications for the rationale introduced earlier. However, U–Zr

alloys are often discussed as candidates for fast or mixed spectrum power reactors. Reactor designs that aim to produce economical electricity but operate in higher neutron energy spectrums generally do so to take advantage of plutonium production. It is possible to minimize the requirements for enriched uranium if fissions primarily occur from the plutonium bred from ^{238}U . Reactor designs of this nature are highly sensitive to neutron economy; a fuel form such as U–Zr that maximizes heavy metal density and minimizes the neutronic penalty incurred by nonfissile isotopes is ideal.

The greatest challenges relating to the chemistry of U–Zr fuels stem from the high homologous operating temperatures that result from the comparatively low melting point of metallic fuels despite their higher thermal conductivities relative to other options. The solidus temperature of U–Zr fuels is highest in the vicinity of 1800 K (U–50Zr) [2] and decreases with both increasing uranium content and/or the addition of plutonium, as shown in Fig. 5.1. The centerline temperature of U–Zr (and derivative composition) fueled reactors can reach above 1000 K. For example, U–19Pu–10Zr fuel used in the Fast Flux Test Facility reached a maximum centerline temperature of roughly 980 K [3]; this fuel composition possesses a solidus temperature of 1250 K. The fuel centerline would therefore be operating at a homologous temperature of nearly 0.8.

There are many effects of this high homologous temperature in terms of fuel performance. There are two primary outcomes specific to the area of fuel thermochemistry, both of which stem from the increased solid-state diffusion of elemental species at relatively high temperatures. First, the transport of fission products is accelerated in metallic fuels relative to ceramic fuels [4]. The outcomes of this have been studied most extensively in U–Zr. Second, rapid diffusion coupled with the complexity of the U–Zr and U–Pu–Zr systems causes the formation of multiple phases of primary fuel components across the pellet radius. Readers interested

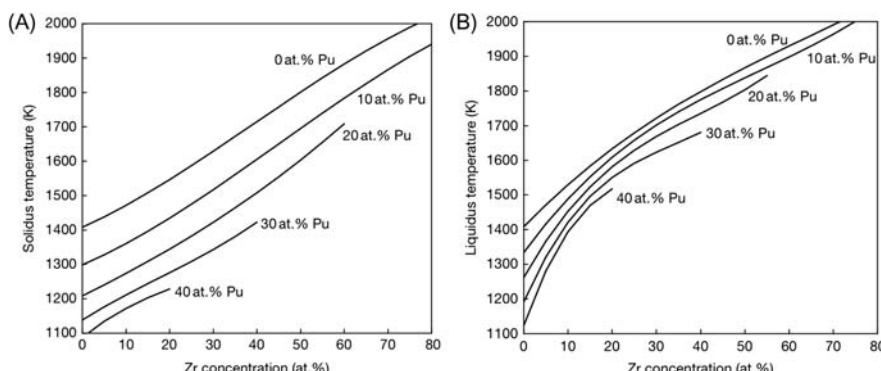


Figure 5.1 Solidus (A) and liquidus (B) of U–Zr alloy compositions. The effect of plutonium content is also shown on each figure.

Source: Reproduced from T. Ogawa, Metal fuel, in: R. Konings (Ed.), Comprehensive Nuclear Materials, vol. 3. Elsevier Ltd., 2012, pp. 1–40.

in the development of metallic fuels are referred to the overview provided by Hofman et al. [5]. The performance of U–Pu–Zr fuels with an emphasis on fast reactor and transmutation applications is summarized by Ogawa [2].

5.2.1.1 Restructuring in U–Zr fuels

Casting and extrusion of U–Zr is an established production process, yielding uniform chemical composition and microstructure. The challenge inherent to all metallic fuels is the multiple phases of uranium as a function of temperature, and how these in turn affect the binary alloy (and higher order systems if transuranic elements are also present). Fig. 5.2 plots a partial binary phase diagram of the U–Zr system. Three solid phases are present for pure uranium: orthorhombic (α), tetragonal (β), and body-centered cubic (γ). The most important behavior of the low-temperature alpha phase is its propensity to swell at a rate that is difficult to accommodate [5]. The realization by nuclear engineers of this fact prompted even further exploration of secondary elements that could be alloyed with uranium to extend the stability field of the more desirable gamma phase. Zirconium achieves this objective, as shown in Fig. 5.2 [6]. Fabrication of U–Zr and U–Pu–Zr alloys retains this structure through rapid quenching to room temperature.

However, the complexity of the phase diagrams and high homologous operating temperature yield a situation where constituent migration can lead not only to chemical gradients but also to phase partitioning. This occurs through zirconium redistribution. Zirconium migration is a highly complex process due to the many competing factors, including diffusion along the temperature gradient (thermomigration), local chemical potential gradients, and restructuring of initial porosity. The general behaviors have been understood for many years, but it has only been

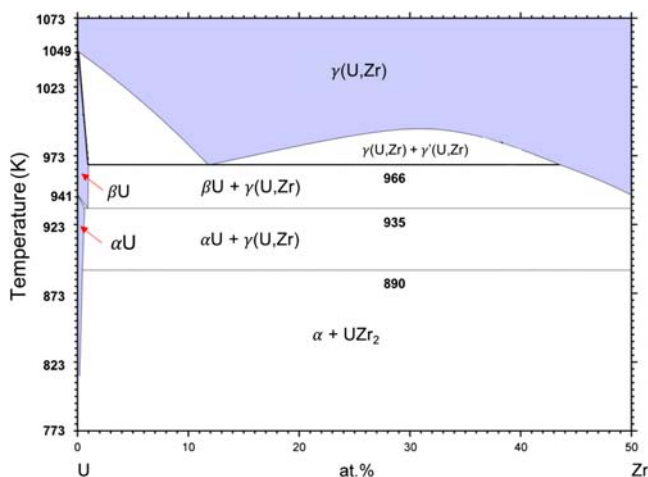


Figure 5.2 Partial binary phase diagram of uranium–zirconium extending shown to 1073K.
Source: Reproduced from H. Okamoto, J. Phase Equilib. 13 (1992) 109.

the recent advancements in fuel performance codes that mechanistic models began to better capture the effects of these competing mechanisms [7].

The expected behavior of zirconium in U–Zr will be to concentrate near the pin centerline and outer radius. These variations can be extreme; zirconium contents from 5% to 50% are observed across a span of only a few millimeters for a representative fast reactor fuel [5]. This is illustrated in Fig. 5.3, where the results of a redistribution model are compared to experimental data. Despite a temperature difference of less than 200 K from the centerline to outer radius, gross partitioning of zirconium has occurred. This will result in the appearance of at least four distinct phases, each with differing thermophysical, mechanical, and irradiation behaviors.

Restructuring as described earlier due to Zr mobility is unavoidable in this family of fuels. Models to predict fuel performance behavior (e.g., temperature, dimensional change, and fission gas release) will be highly dependent upon the phase composition. It is therefore important to develop an improved understanding of these behaviors. It may be possible to devise more advanced alloying schemes that could further extend the regions of phase stability under operating conditions, but this would come at the expense of reduced heavy metal density.

5.2.1.2 Fission product migration

Another consequence of the high relative homologous operating temperature of U–Zr is fission product mobility. Lanthanoid fission products, primarily Nd, Ce, and Pr, have limited solubility in the U–Pu–Zr matrix; it is postulated that their

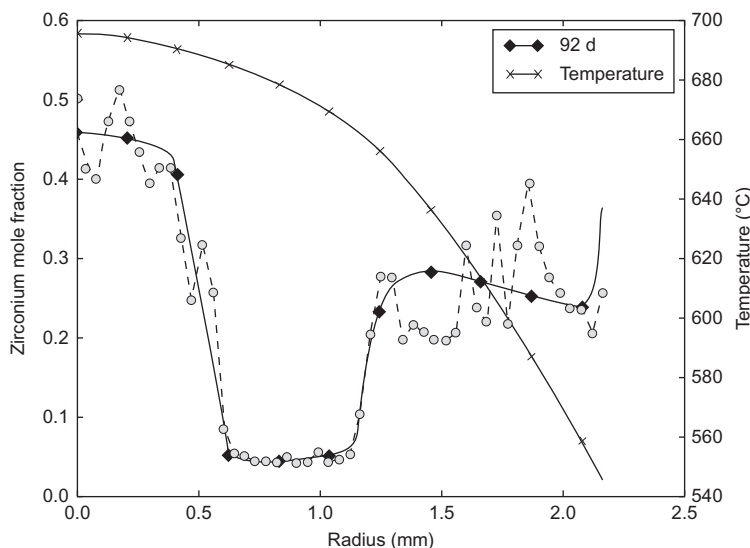


Figure 5.3 Comparison of zirconium content as calculated using the model developed by Galloway et al. [7] (solid line) to experimental data (dashed line). Calculated pin temperature is indicated by the gray curve.

existence as metallic precipitates accelerates diffusion toward cooler portions of the fuel, where they ultimately reach either the sodium bond or the cladding [3]. Advanced reactor fuels have historically used stainless steel cladding alloys (e.g., 316 L). The presence of these lanthanoid fission products embrittles the cladding material, reducing its strength and increasing the chances of a breach.

Multiple mitigation methods have been proposed to address this vulnerability, including alternative cladding alloys and cladding liner materials. Recent years have seen exploration of additive elements to metallic fuel compositions as a means to slow the diffusion of problematic elements. Palladium is the foremost example [8], but indium, tin, and others have been suggested based upon their ability to form intermetallic compounds with the lanthanoids of concern. Both indium [9] and tin [10] have shown promise in this regard, but these studies have been largely based on simulated fission product behavior. More expansive irradiation testing and postirradiation examination are necessary to draw broader conclusions on their effectiveness.

5.2.2 Molybdenum-based metallic fuels

Uranium–molybdenum fuel development for power reactors has seen limited historic attention, but it warrants brief mention in the present context due to consideration as a possible light-water reactor (LWR) fuel [11]. Interest in the system grew from early exploratory efforts at extension of the favored body-centric cubic gamma phase for fuel applications. A partial binary phase diagram of U–Mo is given in Fig. 5.4. Comparison of the U–Mo system to the U–Zr system shown in Figs. 5.1 and 5.2 highlights two important features. First, the eutectoid temperature in the U–Mo system is 838 K rather than 966 K, as is found in U–Zr. This extends the region of stability for the gamma phase relevant to operating conditions. Exploration of U–Mo dispersion (e.g., U–Mo/Al or U–Mo/Mg) [13] and monolithic fuels (e.g., U–10Mo) [14] for research reactor applications has found that phase partitioning as encountered in U–Zr fuels does not occur in the U–Mo system. In addition, studies have found that retention of the lanthanoid fission products is improved compared to U–Zr [15]. However, the general maturity of U–Mo fuels is far below that of U–Zr and very limited data exists on the effect of transuranic elements on these behaviors.

5.3 Nontraditional ceramic fuels

The design objectives for nuclear fuels that originally drove early nuclear engineers to select, study, and optimize oxides identified ceramics other than UO_2 that would satisfy the foregoing criteria. Uranium carbides, mainly uranium monocarbide (UC), were noted as plausible nuclear fuels for many of the same reasons that oxide fuels are successful: high melting point, high actinoid density, and reasonable stability under irradiation. Uranium mononitride (UN) was investigated for the same

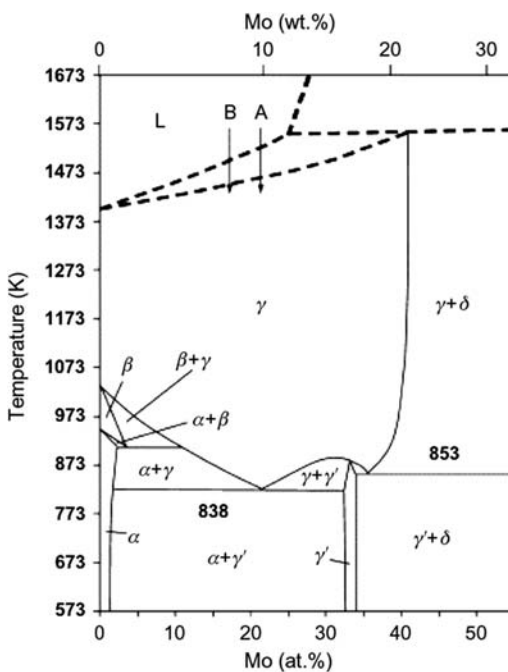


Figure 5.4 Uranium–molybdenum partial binary phase diagram based upon the compilation of Kim [12]. Points A and B as indicated by Kim identify 7 and 10 wt.% Mo, two typical fuel compositions.

reasons. However, the field of nitride ceramics was less mature than carbides during this initial phase of the nuclear era. It would not be until the 1970s that the broad study of UN as a nuclear fuel would commence when methods for synthesis and fabrication of UN would mature to the point that property assessment and irradiation studies could begin. A comprehensive overview of carbide, nitride, and other fuels for fast reactor applications is provided by Matzke [16].

A challenge common to all nonoxide ceramic fuels is susceptibility to oxidation. The stability of the uranium–oxygen bond, and specifically UO_2 compared to other uranium compounds, is formidable. The practical consequence of this behavior is that most nonoxide compounds of uranium, such as those that will be discussed in this chapter, will rapidly oxidize and subsequently pulverize following exposure to an oxidant (e.g., oxygen, water/steam, and carbon monoxide). Even when the selected reactor coolant is not oxidizing itself, for example, salt or liquid metal, oxidation of feedstock powders can challenge processing and storage requirements if air exposure is not possible. This concern has been understood since early in the development of nonoxide compounds [17].

The kinetics of oxidation are dependent upon a number of factors. Dense pellets of most fuel forms are reasonably stable at ambient temperature, but powders may oxidize even when stored under an inert atmosphere. This has significant

implications to fabrication of these fuel forms, as discussed in [Chapter 10](#), Advances in fuel fabrication. Beyond synthesis and storage of powders, use of these fuels in reactors that rely upon water coolants will pose a similar challenge. One beneficial aspect of this behavior is that reprocessing routes developed for oxide fuels can be readily deployed for nonoxide fuels following their conversion to an oxide as a lead step (see [Chapter 12](#): Reprocessing and recycling). However, oxidation of used fuels will introduce pulverization and release of retained fission gasses and volatile fission product species.

Despite the challenge presented by oxidation, common advantages of the fuel forms introduced here relative to oxide forms are high heavy metal density and thermal conductivity. Both attributes are benefits to any reactor fuel, but of particular importance to fast reactors used for transmutation. Development activities in this area peaked during the 1960s and 1970s stemming from interest in reactors for plutonium breeding and disposal of long-lived transuranic isotopes. These designs were best positioned to take advantage of the attributes provided by carbide and nitride fuels. The refractory nature of carbide and nitride systems offered the opportunity to overcome the main liability of metallic fuels, where a low melting point promotes restructuring and rapid fission product mobility. Both carbide and nitride plutonium-bearing fuels have been studied through experimentation to varying degrees. Incorporation of minor actinoids (i.e., Np and Am) has received even less attention, but nonoxide fuels remain attractive candidates for these reactor applications.

Recent interest in high-density fuel candidates for LWRs has promoted evaluation of nonoxide fuels for the same reasons. High-density compounds are valued due to their ability to offer an increased uranium density relative to UO_2 . The increased uranium density would allow for more fissile material within the fuel volume at a fixed enrichment; this would be particularly valuable in the case of cladding materials such as FeCrAl that suffer neutronic penalties compared to zirconium alloys [\[18\]](#). This section will conclude with a brief introduction to other fuel forms that may provide advantages in this area, assuming known vulnerabilities can be surmounted.

5.3.1 Carbide fuels

UC first rose to prominence as nuclear engineers sought fuel concepts that improved upon the breeding characteristics of oxide fuels. UC possesses a much higher heavy metal density than UO_2 or $(\text{U}, \text{Pu})\text{O}_2$, a higher thermal conductivity, and only a small reduction in melting point. Early interest in uranium and plutonium carbides was driven by these factors as well as the potential carbide fuels present for dispersion in a graphite matrix. Their present use in such an architecture is limited, with the important exception of uranium oxycarbide kernels employed in tristructural isotropic (TRISO) fuels detailed later in this chapter.

The greatest challenge to broader study and deployment of carbide fuels is the difficulty in synthesis and fabrication, as discussed in [Chapter 10](#), Advances in fuel fabrication. Researchers seeking to perform fundamental investigations or execute

test irradiations of UC are first tasked with the challenge of synthesizing high-purity feedstock, which must then be sintered into pellets. Unlike UO₂, which can be stored, handled, and fabricated into high-density pellets using fairly simple methods and infrastructure, inert atmosphere gloveboxes and high-temperature (> 2100 K) controlled furnaces are required for processing of UC.

The key operational issues that challenge broader consideration of monolithic UC and (U, Pu)C fuel forms are swelling and carburization of cladding at high burnup. Limited international interest in both breeding and fast reactor technologies has blunted research programs aimed at better understanding and mitigating these challenges. However, modern reactor designers remain interested in UC fuel concepts. Uranium carbide exhibits good chemical compatibility with SiC cladding and structural components, thereby making it a candidate for high-temperature reactor concepts [19].

5.3.1.1 *Binary phase diagram of U–C*

The most recent assessments of the uranium–carbon binary system have been performed by Chevalier and Fischer [20] and Guéneau et al. [21]. UC is the most important of the three known solid phases in the C–U binary system for nuclear fuel applications. Uranium sesquicarbide (U₂C₃) is stable at intermediate temperatures, decomposing to UC and graphite below approximately 1123 K, and uranium dicarbide (UC₂) plus UC above 2100 K. Uranium dicarbide is stable at elevated temperatures, existing as a tetragonal, substoichiometric structure below approximately 1123 K (α -UC₂) before undergoing what is generally accepted to be a diffusionless transformation to a face-centered cubic structure (β -UC₂) at high temperatures.

Fig. 5.5 shows a partial binary phase diagram from Okamoto [22]; this representation is in general agreement with the more recent assessments referenced earlier. Early exploration of the uranium–carbon system observed that UC₂ would commonly persist to lower temperatures at carbon contents that would be anticipated to be comprised of UC and graphite or U₂C₃ based upon Fig. 5.5 [23]. This led to debate regarding the true character of the uranium–carbon system, but subsequent investigations have reinforced the practical stability of UC₂ to room temperatures despite its thermodynamic instability. Uranium dicarbide is an important component of “UCO” particle fuels, as will be detailed in Section 5.4.

5.3.1.2 *Clad carburization*

Deployment of carbide fuel forms inherently introduces carbon activity that may impact cladding performance. Early in life, the pellet-clad gap will limit the potential for direct interaction, but fuel swelling will rapidly bring the fuel into contact with the cladding. The carbon activity and availability of carbon monoxide will then induce thermodynamic conditions that may favor carburization of stainless steel cladding alloys. Experimental and theoretical assessments have found a strong correlation of carbon stoichiometry, secondary carbide content, and plutonium

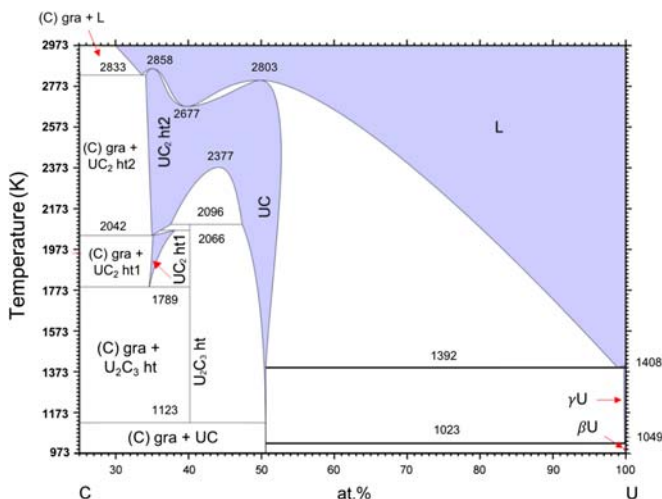


Figure 5.5 Carbon–uranium partial binary phase diagram.

Source: Reproduced from H. Okamoto, in: T.B. Massalski (Ed.), *Binary Alloy Phase Diagrams*, second ed., vol. 1, 1990, pp. 892–893.

content to degradation of steel cladding alloys [24–26]. Minimal data is available on the impact of cladding carburization to fuel safety or transient performance. Carburization and embrittlement of the cladding would be expected to increase cladding failure rates and significantly degrade burst strength as relevant to transient performance.

5.3.1.3 Incorporation of actinoids and fission products in uranium monocarbide

The majority of monolithic carbide fuel experience gained in recent decades has been in the area of fast breeder reactors, and specifically through the Indian development programs. Use of mixed carbide fuels rather than mixed oxides provides benefits to many important transport properties, most notably thermal conductivity, but this comes at the expense of broad thermodynamic stability offered by oxide systems. The uranium–plutonium monocarbide ($(U, Pu)C$) fuel form can accommodate minimal off-stoichiometry; this contrasts with the uranium–plutonium dioxide ($(U, Pu)O_2$), where significant deviation from stoichiometry is possible without either reduction of actinoids to their metal form or oxidation of uranium to U_3O_8 . Hypostoichiometry in a mixed carbide fuel therefore could result in the formation of metallic uranium and plutonium, a highly undesirable outcome due to the low melting point and potential for direct attack of the cladding. Mixed carbide fuels are therefore designed with excess carbon to avoid this outcome. However, this results in the formation of uranium and plutonium sesquicarbide. Increasing carbon activity of the fuel also enhances the potential for carburization of the cladding as detailed earlier.

The behavior of fission products in carbide fuels is slightly more complex but generally comparable to that observed in oxide fuels. Many of the transition metal and lanthanoid fission products form carbides and are similarly retained in solution or as solid phases during burnup. The behavior of volatile fission products is largely unchanged from that found in oxide fuels. Iodine is observed to bind with cesium as CsI [27]. More intermetallic phases are formed in monolithic carbide fuels when used under fast reactor service conditions, specifically UPd₃ and CeRu₂-type structures that have been observed to bind lanthanoids and noble metals for monolithic carbide fuels [28]. Ternary carbide formation appears to occupy Mo through various phases [27,29]. The inventory of the (U, Pu)C (shown as "MC") phases and several fission product phases as a function of burnup are shown in Fig. 5.6 for a single mixed carbide fuel composition.

An additional difference observed in mixed carbide compared to mixed oxide fuels is an overall decrease in stoichiometry of the (U, Pu)C phase with burnup. The lack of carbon available to the primary actinoid matrix is caused by the preferred thermodynamic state of fission products and comparative stability of the sesquicarbide phase, as shown in Fig. 5.6. Decreasing stoichiometry with burnup is the opposite of the trend observed in oxide fuels, where oxygen potential increases with burnup [30]. Reduced carbon activity will decrease the potential for carburization of the cladding but simultaneously increase the possibility of metallic uranium or plutonium formation. The design of carbon content in mixed carbide fuel form must therefore balance these two operational aspects.

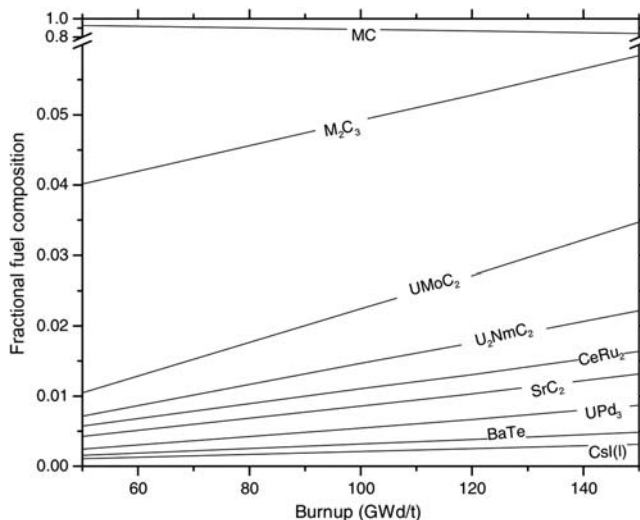


Figure 5.6 The relative mole fraction of solid phases present in a fast reactor fuel with initial composition U_{0.7}Pu_{0.3}C_{1.03} as a function of burnup calculated for 1273K.

Source: Reproduced from R. Agarwal, V. Venugopal, J. Nucl. Mater. 359 (2006) 122–131.

5.3.2 Nitride fuels

UN is often cited as a high-performance nuclear fuel in reactor designs due to its combination of high uranium density, melt point, and thermal conductivity. When compared to UC, UN offers modest improvements in these areas that are achieved at the expense of more complex synthesis and fabrication, a probable need for Nitrogen-15 enrichment, and a less-developed irradiation database [31,32]. However, as detailed in Chapter 10, Advances in fuel fabrication, synthesis and processing of UN powder into dense samples is a significant challenge. This challenge has been relaxed in recent years by the demonstration of spark plasma sintering methods for fabrication of high-density UN [33]. These challenges have limited the amount of data for UN regarding both its fundamental properties and performance under irradiation.

5.3.2.1 Binary phase diagram and relevant derivatives

The uranium–nitrogen binary system contains four reported solid phases: UN, $\text{UN}_{1.6}$, $\text{UN}_{1.5}$, and UN_2 , as shown in Fig. 5.7. Of these, UN is the only compound of practical relevance to nuclear fuel applications. The other phases exist only in temperature ranges too limiting for the conditions needed for a nuclear fuel. Data on the extent of off-stoichiometry that can be accommodated by the mononitride phase is limited, and the reported phase diagrams present significant differences in this regard. Early phase diagrams presented UN as a stoichiometric compound at low temperatures, but a limited capacity for off-stoichiometry is reported at

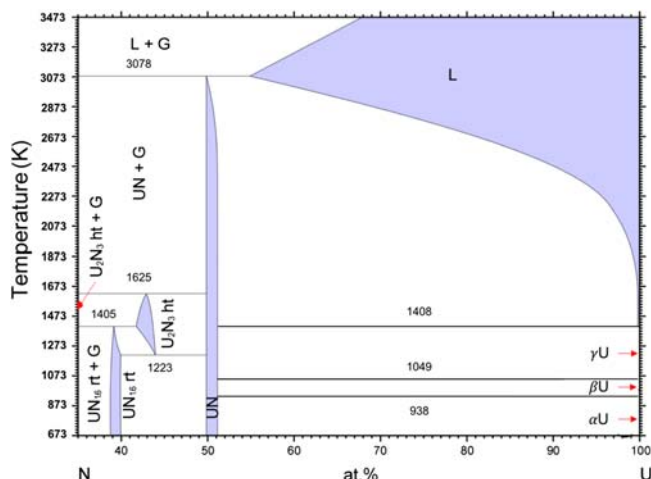


Figure 5.7 Nitrogen–uranium partial binary phase diagram.

Source: Reproduced from H. Okamoto, J. Phase Equilib. 18, 1997, 107.

elevated temperatures [35]. More recent years have seen depictions of off-stoichiometry restricted to hypostoichiometry (UN_{1-x}) and extended from ambient temperatures to near the disassociation temperatures [34]. The most recent thermodynamic assessment of the N–U binary was performed by Chevalier et al. [36]. The authors reviewed the available data and describe UN using a nonideal two-sublattice model. This presents a narrow degree of hypostoichiometry ($x < 0.05$) beginning at approximately 1300 K and extending through melting.

The relation between nitrogen activity and phase stability as typically driven by the partial pressure of nitrogen (P_{N_2}) provided during an experiment or to a fuel rod prior to sealing is far less established in the U–N system rather than in the U–O system. Although the presently accepted description of the binary system incorporates UN_{1-x} , very limited data exists linking equilibrium P_{N_2} versus UN_{1-x} as a function of temperature. Russian researchers provide data collected at 1800 K and 2000 K in the UN_{1-x} region, but data is limited to P_{N_2} values of 10^{-3} and 10^{-7} atm [37]. All data falls between $\text{UN}_{1.995}$ and $\text{UN}_{1.985}$, which agrees with the region provided by Chevalier et al. [36].

The role of nitrogen partial pressure on decomposition and melting point has been studied more broadly. Unlike most other fuel forms, UN will either decompose to $\text{U}_{(\text{s,l,g})} + 1/2 \text{N}_{2(\text{g})}$ or melt congruently as a function of the available nitrogen partial pressure. It has been reported that a partial pressure of N_2 greater than 2.5 atm is needed to retain congruent melting at the melting point of UN, reported to fall between 3080 K and 3120 K [34,36,38]. Oxides of uranium, plutonium, and thorium exhibit a similar dependence of melting point on stoichiometry [21,39], but this behavior in the U–N system is significant. Hayes et al. provide the following power law correlation that links melting/decomposition point (K) to nitrogen partial pressure (atm) [40]:

$$T_m = 3035.0(P_{\text{N}_2})^{0.02832}$$

Examination of the relation shows that comparatively small variations in P_{N_2} will have a significant effect on fuel stability and therefore reactor safety margins. The correlation provided by Hayes et al. is plotted in Fig. 5.8 for the temperature range where decomposition to $\text{U} + \text{N}_2$ occurs; congruent melting is assumed to occur at 3120 K for nitrogen partial pressures above approximately 2.5 atm in the model to match experimental observations.

The figure highlights two important chemical aspects of UN. First, a reduction in P_{N_2} from 1 to 0.1 atm will correspond to a 200 K reduction in melt point. An accurate representation of P_{N_2} as a function of fuel burnup is therefore necessary to determine the maximum fuel temperature that is allowable during a transient. Second, examination of the region where UN fuel is typically processed (1800 – 2200 K) highlights that decomposition will become a concern when P_{N_2} levels fall to part per million levels. This aspect has been reported to enhance sintering of UN by accessing the UN_{1-x} region, provided care is taken to avoid formation of metallic U [41].

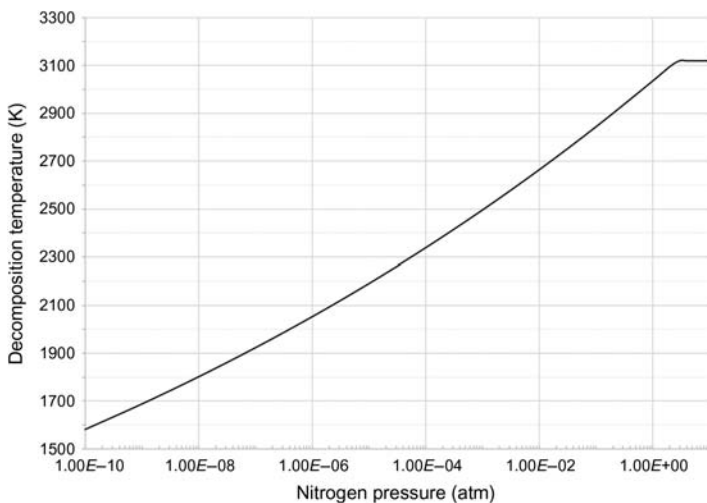


Figure 5.8 Melting/decomposition temperature of UN as a function of nitrogen partial pressure.

5.3.2.2 Relevance of carbon and oxygen impurities to in-pile performance

As detailed in [Chapter 10](#), Advances in fuel fabrication, the reference synthesis process for UN is carbothermic reduction-nitridation where UO_2 is reacted with a carbon source (typically graphite) in the presence of nitrogen at high temperature. A challenge of this process, particularly when used for large batch production, is purity of the resulting UN. In-pile performance of UN and mixed nitrides will inherently require an understanding of the controls utilized in preparation of UN. The importance of variations in carbon and oxygen content in UN on irradiation performance is not presently understood. A number of researchers have investigated the extent of oxygen solubility in UN and $(\text{U}, \text{Pu})\text{N}$ [42], and other studies have identified effects that carbon, nitrogen, and oxygen impurity and stoichiometry have on baseline fuel properties of both carbide and nitride systems [43,44]. However, the limited amount of irradiation data challenges translation of impurity levels to in-pile evolutions. Studies that investigate the irradiation behavior of UN samples of multiple impurity contents, either by design or coincidence, are generally inconclusive with respect to its role [45] or include other parameters that prevent true independence of impurities on irradiation behavior [46]. Investigations of the swelling behavior of UN are presented with wide disparities in reported response [47], and historically this is attributed to an incomplete understanding of impurity phases. For example, irradiations of UN executed at nominally similar temperatures and burnup conditions have been reported to yield swelling of 2%–30% [48]. It is possible that carbide or oxygen content has influenced this response, but it is more likely that metallic uranium or U_2N_3 is responsible.

Further analysis is needed in this area to advance understanding and improve fuel performance models for nitride fuels.

5.3.2.3 Incorporation of actinoids and fission products in uranium mononitride

A major advantage of nitride fuels is their ability to readily incorporate transuranic elements in a solid solution. Thorium, plutonium, neptunium, and americium are all stable as mononitrides. This feature has made mixed nitrides an attractive format for transmutation designs, both for conventional fast reactor irradiations and accelerator-driven systems [49]. Although the effect of carbon and oxygen impurities on swelling and fission gas behavior is not yet understood with certainty, postirradiation examination of irradiated nitride and mixed nitride fuels have observed a strong linkage between carbon and oxygen content on fission product behavior. This is because of the differing stability of carbide, nitride, and oxide phases of the major fission products.

Fission product behavior in nitrides mirrors that of oxides; many high inventory transition metals and lanthanoids will substitute on U sites. As with oxides, it is plausible that noble metals, such as Pd, Rh, and Ru, will form metallic precipitates. The evolution of P_{N_2} as a function of burnup will be an important parameter to understand better if nitride fuels are more widely used. Nitrogen backpressure in fuel rods is impractical due to poor thermal conductivity compared to He or Na. Fissions will liberate nitrogen but create more fission products that in turn tie up nitrogen atoms. The limited literature [50] has shown that (U, Pu)N appears to retain excess nitrogen following approximately 10% burnup, but further study is needed. As found in carbide fuels, intermetallic phases of the UMe_3 type ($Me = Ru, Rh, Pd$) as well as Ba–Te and Cs–Te are prevalent [51]. Many transition metal and lanthanide fission products similarly form mononitride phases and are therefore generally soluble in the matrix. However, the availability of carbon or oxygen can perturb this behavior. Carbon activity will promote the formation of barium, strontium, and molybdenum carbides as well as more complex ternary carbides of uranium and other fission products [52]. Oxygen has been found to drive the formation of Nd_2O_3 , Pu_2O_3 , and $BaUO_3$ [52]. As discussed earlier, it is not known how these evolutions affect the irradiation behavior of nitride fuels.

5.3.3 Other nontraditional ceramic fuel forms

While carbide and nitride fuels have seen the largest amount of historic assessment, other nontraditional fuel forms are of increasing interest today and may play a larger role in future nuclear fuels. The basic thermochemistry and thermochemical performance challenges of these systems are far less developed than for more common nuclear fuels such as oxides and those discussed elsewhere in this chapter. However, certain favorable attributes may drive expanded evaluation of these concepts in the future.

5.3.3.1 Exploration of uranium silicide compounds for light-water reactor applications

Beyond pure ceramics, intermetallic uranium compounds have also been studied to varying degrees. Most modern interest is focused on uranium silicide behavior for LWR applications. Assessment of uranium silicide fuels, primarily U_3Si_2 , is motivated by their high thermal conductivity, high uranium density, and generally acceptable other behaviors [53]. Active research efforts are underway to establish their viability for LWR application. Like most intermetallic systems, the Si-U binary phase diagram contains a number of stoichiometric compounds. Experimental investigations have found that the thermochemistry of the system is likely more complicated than presently understood [54–56], and modeling efforts have suggested that off-stoichiometry of U_3Si_2 may be relevant to system behavior at elevated temperature [57].

As is expected of all nonoxide compounds of uranium, compatibility of U_3Si_2 with water coolant is understood as a major liability. Recent investigations have demonstrated that pulverization of fuel pellets will result following exposure to steam or pressurized water [58,59]. These investigations have identified both oxidation as well as hydriding as mechanisms by which pulverization will occur. At present, it is not understood how directly the reactions as observed for samples of U_3Si_2 tested independently of cladding will translate to gross failures in the event of a clad breach during reactor operation. Further study is needed in this area to elucidate the specific challenges and liabilities posed by the use of nonoxide fuel forms in LWRs.

Limited data exists to facilitate discussion of the thermochemical challenges of U_3Si_2 applications beyond preliminary assessments of its stability of following exposure to LWR coolants. Explorations of interactions between U_3Si_2 and LWR cladding materials have been performed to provide a baseline indication of potential issues [60,61]. More complex interactions and phase evolution are observed compared to the reference UO_2 –zirconium system, particularly at temperatures above 1000 K. However, to date no data exists regarding the fuel–clad interactions for U_3Si_2 fuels and likely companion cladding alloys at temperatures and times representative of those expected during normal operating conditions.

Analysis of the behavior of solid fission products in U_3Si_2 is also cursory. Fission product speciation and mobility has been analyzed for U_3Si_2 when deployed as a dispersion fuel in low power reactors [62], but extrapolation of this data to LWR-relevant burnup and temperature regimes is speculative. Initial PIE data for U_3Si_2 pellets irradiated under LWR-representative conditions revealed no unexpected results, but further data and analysis is needed [63].

5.3.3.2 Other fuel systems

Uranium borides, specifically UB_2 and UB_4 , have received limited study due to their refractory nature. Interest in borides stems principally from neutronic rationale; they have the potential to incorporate a burnable poison by the use of specific

B-10/B-11 isotopic ratios, while in parallel providing high fissile density [64]. However, this approach would increase helium generation within the fuel yielding either swelling or an increase in gas pressure within the fuel rod.

Uranium hydride fuels have also received analysis and investigation. Use of uranium hydride fuels is generally achieved through alloying with zirconium, most typically U-ZrH_{1.6}. The main motivation for the evaluation of hydride fuels in LWRs is the flexibility in core design afforded by the availability of hydrogen in the fuel material coupled with favorable thermophysical properties. The presence of a moderating isotope inside the fuel itself reduces the volume of water needed inside the core [65]. A large program executed in the 2000s assessed the behavior of hydride fuels and greatly augmented the literature for this fuel form. The primary thermochemical challenges and limitations of hydride fuel are its operating temperatures, above which disassociation of the hydrogen will yield metallic uranium, hydriding of the cladding material, and reaction with water coolants [66].

5.4 Coated particle fuels

The TRISO-coated particle is a fuel form that has been developed primarily for use in high-temperature gas-cooled reactors (HTGRs). It consists of a small spherical fuel kernel (typically $\leq 500 \mu\text{m}$ diameter) coated by several layers of pyrolytic carbon and silicon carbide (Fig. 5.9). The first layer is a porous (approximately 50% of theoretical density) carbon buffer layer designed to provide a plenum for fission gases released from the kernel and to accommodate fission recoils. Next is a dense inner pyrolytic carbon (IPyC) layer that provides a surface for depositing the SiC layer, a seal to protect the kernel from corrosion by the chlorine by-products of SiC deposition, and contributes to retention of gaseous fission products during irradiation. The SiC layer provides the main structural integrity of the particle and constitutes a main barrier to the release of certain fission products. Finally, the dense outer pyrolytic carbon layer presents an additional barrier to the release of fission products (especially fission gases), protects the SiC layer during handling, and

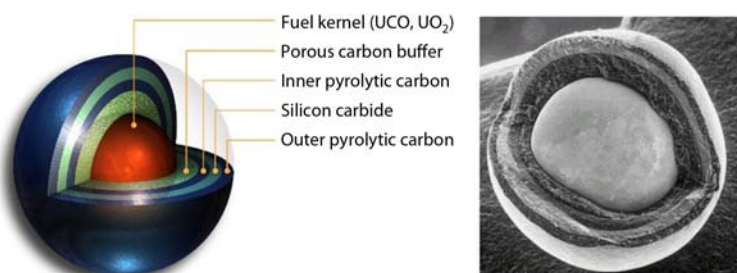


Figure 5.9 Drawing of a TRISO-coated particle (left) and micrograph of a particle with partial coating removal and exposed kernel (right). *TRISO*, Tristructural isotropic.

provides a surface for bonding with the fuel matrix once the particles are compacted into the final fuel form [67]. The total coated particle diameter ranges from about 800 to 1000 μm depending on the particle design.

The coated particles are embedded in a graphitic matrix in one of two common fuel forms (spherical pebbles or cylindrical compacts) containing several thousand particles, depending on the type of reactor. The TRISO particle is a robust fuel form designed to retain fission products within the particle under normal and accident conditions, which can include peak fuel temperatures as high as 1873 K.

Many different types of fuel kernels have been explored in the course of TRISO fuel development over the last five decades to support a variety of fuel cycles, including oxides and carbides, fissile and fertile fuels, uranium and plutonium fuels, and high and low uranium enrichments. By the early 1980s, most fuel development programs had settled on low-enriched uranium (LEU) with uranium dioxide (UO_2) being the most common, while uranium oxycarbide fuel (referred to as UCO) was pursued primarily in the United States [68].

More recently, the basic TRISO architecture has been modified for non-HTGRs. Zirconium has been proposed as a matrix material to enable use of a coated kernel in LWRs [69]. Silicon carbide has also been considered a matrix material. The excellent performance of SiC at high temperatures and under oxidizing environments is well known, and its use as a matrix for coated particle LWR fuels could provide enhanced stability of the fuel following a cladding breach or accident. Investigators first developed methods of fabricating compacts of TRISO UCO kernels in a SiC matrix [70,71], but subsequently advanced concepts to incorporate uranium carbonitride [72] and eventually high-density UN [73]. This was necessary to match the power and cycle length of existing commercial reactors. Attempts to engineer a “drop-in” replacement using high-density UN is challenged by the volume of SiC required by the concept. The corresponding loss of fissile inventory would require kernel sizes greater than used in HTGR TRISO (800 vs 400–500 μm) and enrichment levels approaching 20% ^{235}U [74].

Although the previously mentioned approaches highlight the appeal and adaptable nature for particle fuels, discussion here will focus on UO_2 and UCO-based particle fuels given their maturity. An overview of the chemistry of TRISO particle fuel fabrication is provided in Chapter 10, Advances in fuel fabrication, as well as in several published summaries in the open literature [68,75–77].

Fuel chemistry plays an important role in determining fuel irradiation performance. With TRISO fuel, important considerations include the chemical state and mobility of fission products, the formation of carbon monoxide in UO_2 fuel by reaction of the kernel with the surrounding carbon, and various phenomena related to CO formation, including kernel migration and degradation of the structurally important SiC layer.

5.4.1 CO formation and the effect on particle integrity

As covered in detail elsewhere in this book (see Chapter 1: Reaction kinetics and chemical thermodynamics of nuclear materials; and Chapter 11, In-reactor behavior),

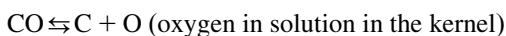
the irradiation of oxide fuel (e.g., UO₂) results in a gradual increase in the oxygen potential (μ_{O_2}). In TRISO fuel, this increasing oxygen potential may result in reaction with the carbon in the surrounding buffer layer to generate CO_(g) [66,78]. The formation of CO inside the particle has a number of implications for fuel performance, discussed briefly in the following sections.

5.4.1.1 Pressure vessel failure

In UO₂ fuel, CO contributes—along with the fraction of fission gases Kr and Xe that are released from the kernel—to the overall gas pressure inside the particle.¹ As burnup and temperature increase, the relative contribution of CO to total pressure inside UO₂ particles increases [68,79]. This internal gas pressure influences the stresses experienced by the coating layers. The buffer layer is specifically designed to provide adequate volume for fission gas to keep total particle pressure below acceptable limits and avoid coating failure under normal UO₂ operating temperatures and burnup as well as higher temperature accident conditions; observation of this particle failure mechanism in normal particles is accordingly extremely rare [80]. However, in particles with a missing or undersized buffer, insufficient void volume is available, and overpressurization of the particle can result in pressure vessel failure [76,80]. Therefore, strict quality control is imposed on coated particles in order to reduce the likelihood of particles with missing buffers.

5.4.1.2 Kernel migration

When CO gas exists in the buffer layer of the TRISO particle, a sufficiently large temperature gradient in the fuel can induce appreciable carbon transport from one side of the particle to the other. This is due to the difference in thermochemical equilibrium between CO, CO₂, C, and UO₂ at different temperatures. The basic mechanism is diffusion of CO_(g) from the hot side of the particle, down the temperature gradient to the cold side, where it can decompose to form carbon, freeing oxygen in the process by one of the following two reactions [68,81]:



Oxygen can then diffuse back to the hot side of the particle, either via solid-state diffusion of O²⁻ through the kernel, or via gas-phase transport of CO_{2(g)}. On the hot side, oxygen or CO₂ can react with carbon to form CO, and the process can repeat [82]. Thus, there is a net transfer of carbon to the cold side of the particle, and consequentially the kernel is seen to migrate toward the hot side of the particle

¹ CO_{2(g)} can also be generated, and the ratio of CO/CO₂ will depend on the total oxygen potential in the system. At normal HTGR fuel operating conditions, however, CO_(g) pressure is much higher than CO_{2(g)} in UO₂ TRISO fuel [78].

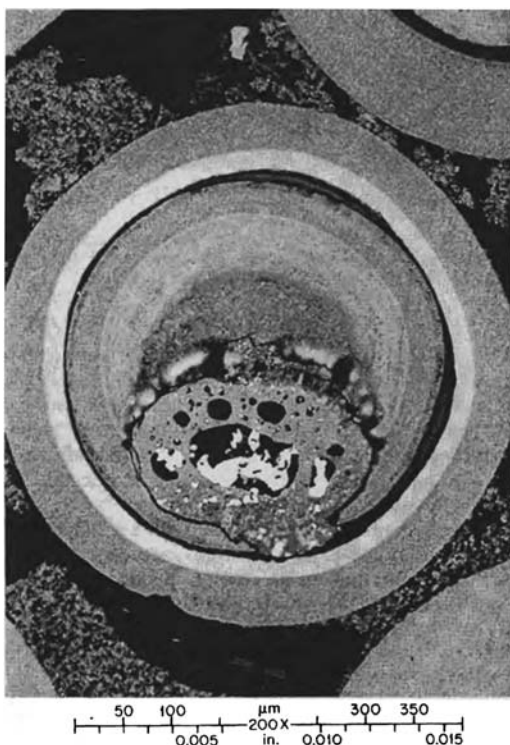


Figure 5.10 Kernel migration in UO_2 particle irradiated to 80% FIMA at 1573K in a 500K/cm temperature gradient.

Source: From F.J. Homan, T.B. Lindemer, E.L. Long, Jr., T.N. Tiegs, R.L. Beatty, Nucl. Technol. 35 (1977) 428–441 [83].

(up the temperature gradient) (Fig. 5.10). If the process proceeds for sufficient duration that the kernel penetrates the IPyC layer on the hot side of the particle and comes into contact with the SiC layer (as in Fig. 5.10), it can result in rapid degradation and ultimately failure [68,82]. Carbide kernels (e.g., UC_2) can also exhibit kernel migration, although the mass transport mechanism differs from that of oxide fuel [68,84].

The migration of the kernel can be represented by a kernel migration coefficient [KMC ; ($\text{K cm}^2/\text{s}$)], which corresponds to the following equation (after Refs. [68,85]):

$$KMC = T^2 \left(\frac{dy}{dt} \right) \left(\frac{dT}{dx} \right)^{-1}$$

where T is the irradiation temperature (in K), dy/dt is the observed kernel migration rate (cm/s), and dT/dx is the thermal gradient (K/cm). KMC for a particular fuel type is

usually determined empirically from postirradiation observations of kernel migration. The migration coefficient can be represented as an Arrhenius-type correlation:

$$KMC = KMC_o \exp\left(-\frac{\Delta H}{RT}\right)$$

where KMC_o is the preexponential term ($\text{K cm}^2/\text{s}$), ΔH is the apparent activation energy for migration (kJ/mol), and R is the gas constant (kJ/mol/K). By plotting empirically determined KMC versus T^{-1} , one can determine KMC_o and the apparent activation energy [85]. Different kernel materials will tend to have unique migration coefficients.

As this phenomenon is strongly driven by temperature gradient and temperature, prismatic reactor fuel is more susceptible to this particle failure mechanism due to the higher power densities in the fuel and larger temperature gradients compared to pebble bed reactor fuel. Nonetheless, modern UO_2 fuel is typically operated under conditions that limit kernel migration, such that this failure mechanism is not commonly observed. For example, it was not observed in the extensive German TRISO fuel development program under normal operating conditions (including irradiation in the AVR pebble bed reactor) because of the relatively low thermal gradients in the fuel elements [68,76]. For fuel to be operated at higher power densities, temperatures, and burnups (e.g., in a very high-temperature prismatic reactor design), a viable remedy is to minimize the formation of CO altogether by altering the kernel chemistry (as discussed in section 5.4.1.4).

5.4.1.3 CO corrosion of SiC

The generation of CO in the particle can also result in chemical attack of the SiC layer [67,77,86], and CO attack of the SiC layer has been observed experimentally in several instances [83,87]. The mechanism proposed is the reaction of SiC with CO to form SiO_2 , with a significant vapor pressure of $\text{SiO}_{(g)}$, which can then relocate away from the corrosion site and deposit as SiO_2 in other regions within the particle [87]. A key requirement in this process is either a gas-permeable IPyC layer or a breached layer, such that CO can readily reach the SiC surface. If reaction with SiC is sufficiently severe, it can result in failure of the layer and loss of fission product retention.

Recent 1873 K postirradiation heating tests with LEU UO_2 fuel irradiated to 10%–11% FIMA at average temperatures of approximately 1280–1330 K reveal a SiC corrosion mechanism very similar in appearance to that observed previously by Minato et al. [87] (Fig. 5.11), exhibiting several key hallmarks observed in the earlier work, including preferential attack along SiC grain boundaries and relocation of silicon elsewhere in the particle [88]. A major advantage of the recent work was the ability to perform detailed microstructural analysis on the small number of particles (generally less than approximately 1% of the total particles in the compact) from the heated compacts that exhibited elevated Cs release, characteristic of a compromised SiC layer.

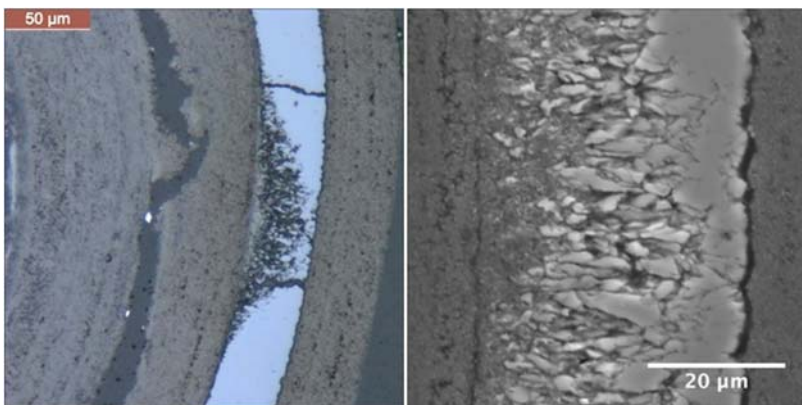


Figure 5.11 Optical (left) and electron (right) micrographs of a region of the SiC layer corroded by CO in an irradiated UO₂ particle heated to 1873 K.

Source: From R.N. Morris, J.D. Hunn, C.A. Baldwin, F.C. Montgomery, T.J. Gerczak, P.A. Demkowicz, Nucl. Eng. Des. 329 (2018) 124–133.

Quantitative data on this particle failure mechanism is scarcer than for the other CO-driven mechanisms cited here, but it is likely dependent on temperature and burnup, as these will impact the CO pressure on the particle and affect the thermochemical equilibria governing reaction with the SiC layer [87].

5.4.1.4 *Alternate tristructural isotropic fuels to address CO formation*

The addition of carbide phases to oxide fuel kernels has been employed to address potential problems related to the formation of CO in pure UO₂ fuel. This has been pursued most notably in the US HTGR fuel programs because of the focus on prismatic reactor designs with higher particle packing fractions and power densities, whereas programs relying on pebble bed designs have traditionally utilized UO₂ fuel [68]. The thermochemical basis for this approach is the fact that UC₂ in UCO fuel will be oxidized in response to the increasing oxygen potential in the UO₂ phase, avoiding the reaction with the carbon layers to create CO or CO₂ [66,83]. The result is substantially lower CO pressures in UCO fuels compared to particles with standard UO₂ kernels [89], eliminating the potential for the abovementioned particle failure mechanisms driven by CO formation. Recent irradiation testing with UCO fuels fabricated with high-quality coatings has demonstrated very promising fuel performance both during irradiation and during postirradiation heating tests at temperatures as high as 2073 K [90].

Additional approaches to limit the oxygen potential in the kernel and reduce CO pressure include the addition of nonfissile carbide phases (e.g., ZrC, SiC) to the kernel to act as an oxygen getter in a similar manner as UC₂ [89,91,92]. One such

variation involves ZrC applied as a thin coating directly to the fuel kernel and has exhibited good performance during irradiation and postirradiation annealing [93].

5.4.2 Fission product chemistry and transport in tristructural isotropic fuel particles

The chemical state of fission products in UO₂ has been studied extensively in the context of LWR fuel (for reviews, see Refs. [30,94]) and is discussed elsewhere in this volume (see Chapter 11, In-reactor behavior). Fission product chemistry within UO₂ TRISO kernels generally exhibits similar trends to that of LWR UO₂ fuel. In addition, TRISO fuel often has higher enrichment and achieves higher burnup than LWR fuel, which can also affect chemical speciation in the kernel [76]. The behavior of fission products in the fuel kernel has important implications for fuel performance, since it dictates the level of fission product release from the kernel to the coating layers. Once released from the kernel, fission gases can contribute to overall pressurization of the particle and are available to be released from the particle in the case of complete coating failure. Condensable fission products released from the kernel can migrate to the dense coating layers and either diffuse through intact coatings or contribute to chemical attack on the SiC layer. Dedicated studies of fission product behavior in TRISO fuel kernels have included computational studies from a thermochemical basis [79] or empirical studies in combination with thermodynamic calculations for UO₂ [95] or UCO fuels [83,96].

5.4.2.1 Palladium

Behavior of certain period 5 transition metal fission products is of particular interest in coated particle fuels. These can form metallic inclusions within the fuel kernel with various combinations of Mo, Ru, Rh, Tc, and Pd. Pd has been observed in these inclusions in the UO₂ kernels of irradiated TRISO particles, as well as in separate phases consisting of Pd and Te [76,95]. In contrast, a study of UO₂ TRISO fuel irradiated to 10% FIMA at 1250°C indicated that Pd was not present in the metallic kernel inclusions [97]. Pd has a significantly higher vapor pressure than the other metals listed such that it tends to migrate from the kernel to a significantly greater extent and can transport to the coating layers [68]. If it accumulates at the SiC layer, it can react to form silicides (e.g., x Pd + SiC \rightleftharpoons Pd_xSi + C), which chemically degrade the function of the SiC layer [76,98–100]. This effect is observed in both UO₂ and UCO TRISO fuel and is more pronounced at higher temperatures [68]. Fig. 5.12 shows several examples of Pd corrosion of SiC. It has also been observed that localized Pd attack on the SiC layer is more prominent in regions where the IPyC layer fails [99].

5.4.2.2 Silver

Silver, although a relatively low-yield fission product, has importance in TRISO fuel performance analysis because it is released in significant fractions from the

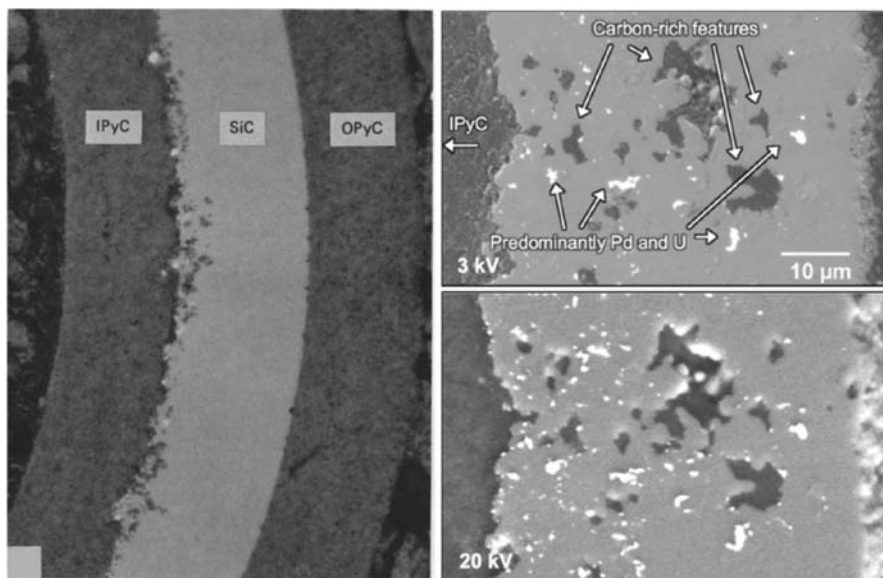


Figure 5.12 Examples of Pd corrosion of the SiC layer. (Left) UCO TRISO particle irradiated at 1698 K [98]. (Right) Secondary electron (top) and backscattered electron (bottom) micrographs of the severely corroded SiC layer of a UCO TRISO particle irradiated to 19.1% FIMA at 1324 K heated to 1973 K for 300 hours after irradiation [99]. *TRISO*, Tristructural isotropic.

kernel and can transport through intact TRISO coatings at sufficiently high temperature [68,101–103] and subsequently be released to the reactor coolant circuit. While not representing a safety concern for off-site dose, the activation product ^{110m}Ag can represent a plant maintenance concern as it is deposited on cooler portions of the coolant circuit [68]. The transport mechanism for silver in SiC is not well understood, despite the nearly ubiquitous experimental observation of silver release through intact SiC in irradiation experiments and in postirradiation heating tests. In the last decade, however, a number of studies motivated by TRISO fuel performance implications have focused on understanding this behavior through detailed microanalysis of irradiated TRISO microstructures [104,105], dedicated diffusion experiments using surrogate materials [106–112] and computational modeling [113–117].

5.4.2.3 Fission gas

Fission gas behavior in UO_2 fuel is discussed in Chapter 11, *In-reactor behavior*, although in TRISO kernels the fission rate and temperature tend to be higher compared to LWR fuel, and this may influence fission gas behavior [79]. Once released from the TRISO fuel kernel, fission gas is retained within the particle by any intact pyrocarbon or SiC layer and will only be released in the event that all three dense

coating layers fail. Fission gas release from TRISO fuel is therefore the key indicator of TRISO coating layer failure, both during in-pile experiments and postirradiation accident simulations. The dominant sources of fission gas release to the main coolant circuit are uranium contamination in the fuel spheres or compacts (i.e., uranium located outside of intact TRISO coatings) and defective or failed particles (i.e., particles where the coating layers are no longer retentive and fission gas released from the kernels is released from the particle). A number of computational models have been developed to predict fission gas release from HTGR fuel. These typically utilize simplified “effective” diffusion coefficients for fission gas in the kernels, which are based on empirical measurements. A review of some of these models is provided in a compilation by the IAEA [75].

5.4.2.4 Cesium and iodine

Cesium and iodine are two of the most important fission products in terms of off-site radiological dose during an HTGR accident [76,118], and their behavior in TRISO fuel is of great significance. Cesium is considered a volatile fission product and has a low solubility in UO₂ [79,119,120]. Thermochemical calculations indicate that Cs may exist in ternary oxide phases in UO₂ fuel (e.g., Cs₂UO₄, Cs₂MoO₄), but this is dependent on the oxygen potential; higher μ_{O_2} in the fuel generally favors retention in ternary phases, while as UO₂ decreases, the Cs partial pressure increases [30]. Nonetheless, cesium release from UO₂ is relatively high and can be similar in magnitude to that of fission gas xenon [97,119,121].

Experimental observations of irradiated UO₂ particles indicate the absence of the ternary Cs oxide phases in the kernel, with Cs primarily located in the buffer layer instead [95,97]. It is known that Cs can react with carbon in the buffer layer of TRISO particles to form stable carbide compounds (C_nCs) [79], and significant Cs concentrations have been observed outside of the kernel in elemental maps of irradiated UO₂ and UCO TRISO particles [95,97,122,123]. Once outside the kernel, cesium can transport through intact pyrocarbon but is retained well by intact SiC. It is therefore considered a key indicator of SiC layer failure in TRISO particles, since it is released from the particle in significant fractions only when the SiC layer is compromised [90,101,124]. Fig. 5.13 shows the fraction of ¹³⁴Cs released from UCO TRISO fuel during isothermal postirradiation heating tests [90]. The releases $>10^{-4}$ were demonstrated through extensive posttest destructive examination to be from a small fraction of particles with a failed SiC layer, while releases $<5 \times 10^{-6}$ indicated no particles in the fuel specimens suffered SiC failure.

Iodine is among the most volatile of fission products and is noted to have a very high mobility in UO₂ [30,121]. Iodine has a higher diffusivity in UO₂ compared to either Cs or Xe and is reported to exhibit higher release fractions from UO₂ than either of these elements [30,121], although it has also been observed that ¹³¹I has a somewhat lower release from (U, Th)O₂ TRISO kernels compared to ¹³⁷Cs [125]. While thermochemical models have predicted the formation of CsI in UO₂ fuel, empirical evidence for the existence of this compound is scarce [30]. Iodine has been observed along with Cs in the buffer layer of irradiated TRISO particles,

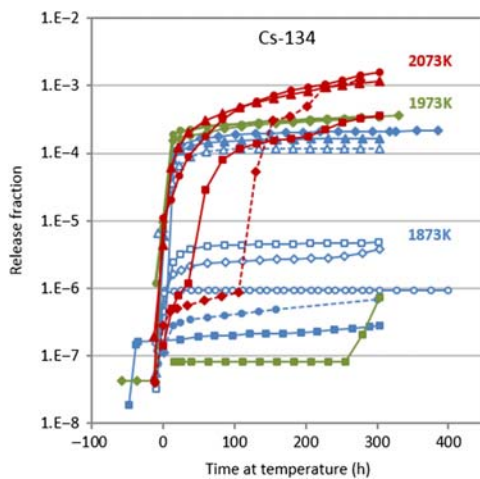


Figure 5.13 Release fractions of ^{134}Cs from UCO TRISO fuel compacts irradiated to burnup of 11%–20% FIMA. *TRISO*, Tristructural isotropic.

Source: From P.A. Demkowicz, J.D. Hunn, D.A. Petti, R.N. Morris, Nucl. Eng. Des. 329 (2018) 102–109.

leading to the speculation that it may exist as CsI [126]. However, their dissimilar transport behavior in other oxide fuels tends to contradict the formation of CsI [30].

Once outside the TRISO fuel kernel, iodine behaves in a similar manner to fission gases: it will be retained by any intact pyrocarbon or SiC layer and released from a particle only once all layers have failed. Empirical data on iodine release from TRISO particles both in-pile and during postirradiation heating tests is much more limited compared to some other important fission products, largely because the key gamma-emitting iodine isotope, ^{131}I , has a short half-life (8.02 days) and radioactive decay eliminates the inventory before measurements can readily be performed. However, available iodine release data from UO_2 TRISO fuel supports the notion that iodine behaves similar to Xe [126–128]. Thus, as with the fission gases, the main sources of ^{131}I release from the HTGR core are uranium contamination in the fuel, initially defective TRISO coatings, and in-service TRISO coating failure. As a consequence, manufacture of TRISO fuel seeks to minimize the first two sources through stringent quality control techniques and the occurrence of in-service failures through a robust fuel particle design operated within an appropriate performance envelope.

5.4.2.5 Fission product transport in the reactor

When fission products are released from TRISO particles, they may migrate through the fuel matrix, through graphite support structures, and finally enter the helium coolant. This transport behavior involves processes such as solid-state diffusion, sorption/desorption, vapor-phase transport, and chemical reactions with the

surrounding materials (e.g., the fuel matrix) and is important for determining total radionuclide source terms during reactor accidents. Discussion of these phenomena is not presented here, but the reader is directed to several sources for additional information [68,76].

5.4.3 Oxygen potential and fission products

As described earlier, UCO fuel was developed to address CO formation in the particle, and it substantially lowers the oxygen activity compared to UO₂-coated particle fuel. This has some important implications for fission product chemistry. In pure UC₂ fuel, lanthanide fission products (e.g., La, Ce, Pr, and Nd) are present in the form of carbides, and the mobility of these elements is much greater in carbide fuel compared to the oxide form [76,83]. These elements can then be released from the carbide kernels and migrate to the coating layers [96], where they can react with SiC and degrade the integrity of the layer [83,122,129]. UCO fuel is therefore designed to limit CO formation, while also allowing certain fission products to form oxides to increase retention in the kernel.

Fig. 5.14 presents the oxygen potential as a function of temperature calculated by Homan et al. [83] for the oxide–carbide equilibria for selected elements (carbide + O₂ ⇌ oxide + C). Elements for which the equilibrium oxygen potential is lower than for UC₂ at a given temperature (notably the carbides of certain rare-earth elements including La, Ce, Pr, and Nd) will preferentially react with the excess oxygen generated by fission of UO₂ to form oxides. On the other hand, elements for which the equilibrium oxygen potential is greater than UC₂ will remain as carbides as long as UC₂ is present in the kernel to form UO₂. Therefore, the

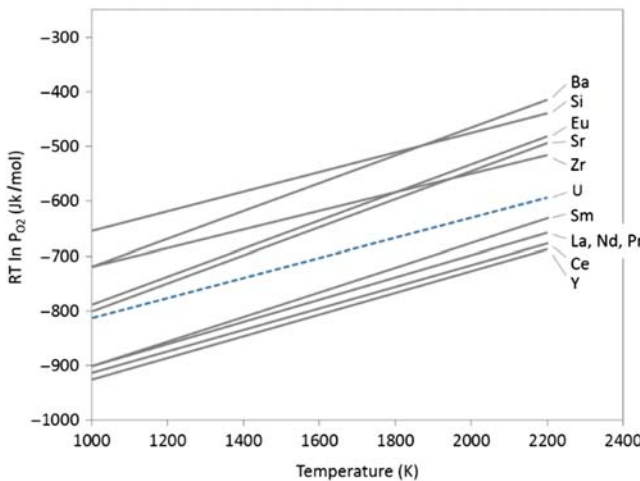


Figure 5.14 Equilibrium oxygen potential for the formation of oxides from carbides.
Source: Reproduced from F.J. Homan, T.B. Lindemer, E.L. Long, Jr., T.N. Tiegs, R.L. Beatty, Nucl. Technol. 35 (1977) 428–441.

chemical state of various elements (oxide or carbide) will depend on such factors as the starting kernel chemistry (UO_2/UC_2 ratio) and the burnup [83]. The tendency of the lanthanoid elements Ce, La, Pr, and Nd to form oxides in UCO kernels significantly limits their release from the kernel [83,96,122,129].

One important implication is that the elements Sr and Eu are predicted to remain as carbides, while UC_2 is present to react with oxygen. In this form, they have higher mobility relative to the oxides, can be released from the kernel, and have been observed to transport in small fractions through intact TRISO coatings in UCO fuel [93,130,131]. Recent thermochemical calculations have been performed to optimize the UCO kernel chemistry to suppress CO formation while at the same time enabling Eu to oxidize at relatively low burnups to reduce mobility in the kernel [132]. The results suggest that UC_x fractions as low as 5–6 mol.% may be acceptable for LEU fuel irradiated to a peak burnup of 16% FIMA.

5.5 Summary and outlook

A wide variety of fuel forms have been briefly presented in this section. Compared to monolithic oxide fuel, it is clear that the dominant challenges with respect to chemistry generally stem from a lack of concept maturity. Both U–Zr and TRISO particle fuels have historically seen more focused attention than U–Mo, UC, UN, or other variants for power reactor applications. However, commercial nuclear fuel vendors and power utilities are currently assessing the viability of high uranium density fuel forms such as those outlined in this chapter. The greatest strength of U–Zr comes in the experience acquired when it is used as an actinide-bearing fuel. For applications where power production alone is the major interest, advancements in lanthanide immobilization may not overcome the challenge presented by zirconium migration. Uranium carbide and nitride fuels offer many favorable attributes when irradiation performance is considered, but they require more sophisticated fabrication and processing methods compared to oxide fuel. Other systems, such as U_3Si_2 , have received recent interest. U_3Si_2 suffers similar vulnerabilities to oxidation as UC or UN, presents the same challenges with respect to fabrication, and also suffers a greatly reduced melt point. TRISO particle fuel is a relatively mature fuel form, having seen six decades of development and use in demonstration and prototype reactors [133]. Current qualification efforts in the United States have demonstrated the performance of UCO TRISO fuel. Large-scale fabrication of UO_2 TRISO fuel is currently taking place in China, with deployment in a modular HTGR expected to begin within a few years.

This theme of potential at the cost of uncertainty is common for all fuels introduced in this chapter. The dominance of UO_2 as a fuel for power production speaks to its strengths, but it should not be interpreted as evidence that alternative fuels do not offer an advantage that successfully outweighs any detrimental aspects of performance or uncertainties. Instead, UO_2 is particularly well matched to the LWR that has dominated electricity generation in recent decades. A more optimistic view

of the outlook for alternative fuel systems is that exploration of new reactor concepts and platforms may prove the impetus to address the challenges and uncertainties summarized earlier and advance these systems.

References

- [1] M. Lyons, R. Boyle, J. Davies, V. Hazel, T. Rowland, Nucl. Eng. Des. 21 (1972) 167–199.
- [2] T. Ogawa, Metal fuel, in: R. Konings (Ed.), Comprehensive Nuclear Materials, vol. 3, Elsevier Ltd., 2012, pp. 1–40.
- [3] C. Matthews, C. Unal, J. Galloway, D. Keiser, S. Hayes, Nucl. Technol. 198 (2017) 231–259.
- [4] G.L. Hofman, R. Pahl, C. Lahm, D. Porter, Metall. Trans. A 21 (1990) 517–528.
- [5] G.L. Hofman, L.C. Walters, T.H. Bauer, Prog. Nucl. Energy 31 (1997) 83–110.
- [6] H. Okamoto, J. Phase Equilib. 13 (1992) 109.
- [7] J. Galloway, C. Unal, N. Carlson, D. Porter, S. Hayes, Nucl. Eng. Des. 286 (2015) 1–17.
- [8] R.D. Mariani, D.L. Porter, T.P. O'Holleran, S.L. Hayes, J.R. Kennedy, J. Nucl. Mater. 419 (2011) 263–271.
- [9] Y.-S. Kim, T. Wiencek, E. O'Hare, J. Fortner, A. Wright, J. Cheon, et al., J. Nucl. Mater. 484 (2017) 297–306.
- [10] M. Benson, J. King, R. Mariani, M. Marshall, J. Nucl. Mater. 494 (2017) 334–341.
- [11] R. Montgomery, W. Bennett, C. Henager, C. Lavender, M. Smith, R. Omberg, An innovative accident tolerant LWR fuel rod design based on uranium-molybdenum metal alloy, in: Proceedings of Top Fuel 2016: LWR Fuels With Enhanced Safety and Performance, 2016, pp. 1375–1387.
- [12] Y.-S. Kim, Uranium intermetallic fuels (U-Al, U-Si, U-Mo), in: R. Konings (Ed.), Comprehensive Nuclear Materials, vol. 3, Elsevier Ltd., 2012, pp. 391–422.
- [13] M. Kulakov, M. Saoudi, M. Piro, R. Donaberger, J. Nucl. Mater. 484 (2017) 288.
- [14] J.-F. Fue, B. Park, C. Clark, G. Moore, D. Keiser, Nucl. Technol. 172 (2010) 204.
- [15] Y.-S. Kim, G.L. Hofman, A.M. Yacout, J. Nucl. Mater. 392 (2009) 164–170.
- [16] H. Matzke, Science and Technology of Advanced LMFBR Fuels, Elsevier Scientific Publishing Company, New York, 1986.
- [17] R. Dell, V. Wheeler, E. McIver, Trans. Faraday Soc. 62 (1966) 3591–3606.
- [18] N. George, K. Terrani, J. Powers, A. Worrall, I. Maldonado, Ann. Nucl. Energy 75 (2015) 703.
- [19] H. Choi, R. Schleicher, Nucl. Technol. 200 (2017) 106–124.
- [20] P. Chevalier, E. Fischer, J. Nucl. Mater. 288 (2001) 100–129.
- [21] C. Guéneau, N. Dupin, B. Sundman, C. Martial, J.-C. Dumas, S. Gossé, et al., J. Nucl. Mater. 419 (2011) 145–167.
- [22] H. Okamoto, in: T.B. Massalski (Ed.), Binary Alloy Phase Diagrams, second ed., vol. 1, 1990, pp. 892–893.
- [23] W. Chubb, R.F. Dickerson, Am. Ceram. Soc. Bull. 41 (1962) 564–569.
- [24] M. Saibaba, S. Vana Varamban, C.K. Mathews, J. Nucl. Mater. 144 (1987) 56–64.
- [25] C. Ganguly, A.K. Sengupta, J. Nucl. Mater. 158 (1988) 159–165.
- [26] S. Pillai, S. Rajendran, S. Anthony, P. Prakashan, R. Ranganathan, P. Rao, et al., J. Nucl. Mater. 167 (1989) 105–109.

- [27] R. Agarwal, V. Venugopal, J. Nucl. Mater. 359 (2006) 122–131.
- [28] H. Kleykamp, J. Nucl. Mater. 47 (1973) 271–277.
- [29] U. Benedict, G. Giacchetti, H. Matzke, K. Richter, C. Sari, H. Schmidt, Nucl. Technol. 35 (1977) 154–161.
- [30] H. Kleykamp, J. Nucl. Mater. 131 (1985) 221–246.
- [31] A.K. Sengupta, R. Agarwal, H.S. Kamath, Compr. Nucl. Mater. (2012) 55. 3.03.
- [32] Y. Arai, Compr. Nucl. Mater. (2012) 41. 3.02.
- [33] K. Johnson, J. Wallenius, M. Jolkkonen, A. Claisse, J. Nucl. Mater. 473 (2016) 13–17.
- [34] H. Okamoto, J. Phase Equilib. 18 (1997) 107.
- [35] R. Benz, W. Hutchinson, J. Nucl. Mater. 36 (1970) 135–146.
- [36] P. Chevalier, E. Fischer, B. Cheynet, J. Nucl. Mater. 280 (2000) 136–150.
- [37] I. Kromov, R. Liutikov, At. Energy 49 (1980).
- [38] W. Olson, R. Mulford, J. Phys. Chem. 67 (1963) 952–954.
- [39] A. Bergeron, D. Manara, O. Beneš, R. Eloirdi, M.H.A. Piro, E.C. Corcoran, J. Nucl. Mater. 512 (2018) 324–348.
- [40] S. Hayes, J. Thomas, K. Peddicord, J. Nucl. Mater. 171 (1990) 300–318.
- [41] V. Tennery, T. Godfrey, R. Porter, J. Am. Ceram. Soc. 54 (1971) 327–331.
- [42] G. Jain, C. Ganguly, J. Nucl. Mater. 202 (1993) 245–251.
- [43] J. Routbort, R. Singh, J. Nucl. Mater. 58 (1975) 78–114.
- [44] V. Vybyvanets, M. Taubin, E. Solntseva, I. Galev, V. Baranov, A. Tenishev, At. Energy 117 (2015) 257–264.
- [45] K. Tanaka, K. Maeda, K. Katsuyama, M. Inoue, T. Iwai, Y. Arai, J. Nucl. Mater. 327 (2004) 77–87.
- [46] K. Richter, C. Sari, J. Nucl. Mater. 184 (3) (1991) 167–176.
- [47] R. Matthews, LA-UR 93-2392, 1993.
- [48] S. Ross, M. El-genk, R. Matthews, J. Nucl. Mater. 170 (1990) 169–177.
- [49] K. Minato, M. Akabori, M. Takano, Y. Arai, K. Nakajima, A. Itoh, et al., J. Nucl. Mater. 320 (2003) 18–24.
- [50] M. Bradbury, H. Matzke, J. Nucl. Mater. 91 (1980) 13–22.
- [51] Y. Arai, A. Maeda, K. Shiozawa, T. Ohmichi, J. Nucl. Mater. 210 (1994) 161–166.
- [52] I. Deryabin, V. Kharitonov, D. Lyubimov, At. Energy 121 (2016) 96–105.
- [53] A. Nelson, J. White, D. Byler, J. Dunwoody, J. Valdez, K. McClellan, Trans. Am. Nucl. Soc. 110 (2014) 987–989.
- [54] A. Berche, C. Rado, O. Rapaud, C. Guenéau, J. Rogez, J. Nucl. Mater. 389 (1) (2009) 101–107.
- [55] J. White, A. Nelson, D. Byler, D. Safarik, J. Dunwoody, K. McClellan, J. Nucl. Mater. 456 (2015) 442–448.
- [56] C.-K. Chung, X. Guo, G. Wang, T.L. Wilson, J.T. White, A.T. Nelson, et al., J. Nucl. Mater. 523 (2019) 101–110.
- [57] S. Middleburgh, R. Grimes, E. Lahoda, C. Stanek, D. Andersson, J. Nucl. Mater. 482 (2016) 300–305.
- [58] E. Wood, J. White, C. Grote, A. Nelson, J. Nucl. Mater. 501 (2018) 404–412.
- [59] A. Nelson, A. Migdisov, E. Wood, C. Grote, J. Nucl. Mater. 500 (2018) 81–91.
- [60] L. He, J. Harp, R. Hoggan, A. Wagner, J. Nucl. Mater. 486 (2017) 274–282.
- [61] R. Hoggan, L. He, J. Harp, J. Nucl. Mater. 502 (2018) 356.
- [62] M. Ugajin, A. Itoh, J. Alloy and Comp. 213–214 (1994) 369–371.
- [63] F. Cappia, J.M. Harp, J. Nucl. Mater. 518 (2019) 62–79.
- [64] N. Brown, A. Aronson, M. Todosow, R. Brito, K. McClellan, Nucl. Eng. Des. 275 (2014) 393–407.

- [65] E. Greenspan, M. Fratoni, F. Ganda, F. Ginex, D. Olander, N. Todreas, et al., Nucl. Eng. Des. 239 (2009) 1374–1405.
- [66] D. Olander, J. Nucl. Mater. 389 (2009) 1–22.
- [67] K. Verfondern, H. Nabielek, J.M. Kendall, Nucl. Eng. Technol. 39 (2007) 603–616.
- [68] M.J. Kania, H. Nabielek, H. Nickel, Coated particle fuels for high-temperature reactors, Materials Science and Technology, Wiley, 2015, pp. 1–183.
- [69] K. Terrani, J. Kiggans, L. Snead, J. Nucl. Mater. 427 (2012) 79–86.
- [70] K. Terrani, J.O. Kiggans, Y. Katoh, K. Shimoda, F.C. Montgomery, B.L. Armstrong, et al., J. Nucl. Mater. 426 (2012) 268–276.
- [71] K. Terrani, L. Snead, J. Gehin, J. Nucl. Mater. 427 (2012) 209–224.
- [72] C. Silva, T. Lindemer, S. Voit, R. Hunt, T. Besmann, K. Terrani, et al., J. Nucl. Mater. 454 (2014) 405–412.
- [73] J. McMurray, J. Kiggans, G. Helmreich, K. Terrani, J. Am. Ceram. Soc. 101 (2018) 4492–4497.
- [74] R. Shapiro, M. Fratoni, Nucl. Technol. 194 (2016) 15–27.
- [75] International Atomic Energy Agency, Fuel Performance and Fission Product Behavior in Gas Cooled Reactors, TECDOC-978, 1997.
- [76] International Atomic Energy Agency, High Temperature Gas Cooled Reactor Fuels and Materials, TECDOC-1645, 2010.
- [77] International Atomic Energy Agency, Advances in High Temperature Gas Cooled Reactor Fuel Technology, TECDOC-1645, 2012.
- [78] E. Proksch, A. Strigl, H. Nabielek, J. Nucl. Mater. 107 (1982) 280–285.
- [79] M. Barrachin, R. Dubourg, M.P. Kissane, V. Ozrin, J. Nucl. Mater. 385 (2009) 372–386.
- [80] D.A. Petti, J. Buongiorno, J.T. Maki, R.R. Hobbins, G.K. Miller, Nucl. Eng. Des. 222 (2003) 281–297.
- [81] T.B. Lindemer, H.J. de Nordwall, An Analysis of Chemical Failure of Coated UO₂ and Other Oxide Fuels in the High-Temperature Gas-Cooled Reactor, Oak Ridge National Laboratory, Oak Ridge, TN, ORNL-4926, 1974.
- [82] M. Wagner-Löffler, Amoeba behavior of UO₂ coated particle fuel, Nucl. Technol. 35 (1977) 392–402.
- [83] F.J. Homan, T.B. Lindemer, E.L. Long Jr., T.N. Tiegs, R.L. Beatty, Nucl. Technol. 35 (1977) 428–441.
- [84] O.M. Stansfield, C.B. Scott, J. Chin, Nucl. Technol. 25 (1975) 517–530.
- [85] T.B. Lindemer, R.L. Pearson, J. Am. Ceram. Soc. 60 (1977) 5–14.
- [86] John T. Maki, David A. Petti, Darrell L. Knudson, Gregory K. Miller, J. Nucl. Mater. 371 (2007) 270–280.
- [87] K. Minato, T. Ogawa, S. Kashimura, K. Fukuda, I. Takahashi, M. Shimizu, et al., J. Mater. Sci. 26 (1991) 2379–2388.
- [88] R.N. Morris, J.D. Hunn, C.A. Baldwin, F.C. Montgomery, T.J. Gerczak, P.A. Demkowicz, Nucl. Eng. Des. 329 (2018) 124–133.
- [89] E. Proksch, A. Strigl, H. Nabielek, J. Nucl. Mater. 139 (1986) 83–90.
- [90] P.A. Demkowicz, J.D. Hunn, D.A. Petti, R.N. Morris, Nucl. Eng. Des. 329 (2018) 102–109.
- [91] R.E. Bullock, J.L. Kaae, J. Nucl. Mater. 115 (1983) 69–83.
- [92] R.D. Hunt, J.D. Hunn, J.F. Birdwell, T.B. Lindemer, J.L. Collins, J. Nucl. Mater. 401 (2010) 55–59.
- [93] R.E. Bullock, J. Nucl. Mater. 125 (1984) 304–319.

- [94] D. Olander, Fundamental Aspects of Nuclear Reactor Fuel Elements, United States, 1976.
- [95] K. Minato, T. Ogawa, K. Fukuda, M. Shimizu, Y. Tayama, I. Takahashi, *J. Nucl. Mater.* 208 (1994) 266–281.
- [96] T.N. Tiegs, T.B. Lindemer, T.J. Henson, *J. Nucl. Mater.* 99 (1981) 222–234.
- [97] M. Barrachin, R. Dubourg, S. de Groot, M.P. Kissane, K. Bakker, *J. Nucl. Mater.* 415 (2011) 104–116.
- [98] T.N. Tiegs, *Nucl. Technol.* 57 (1982) 389–398.
- [99] J.D. Hunn, C.A. Baldwin, T.J. Gerczak, F.C. Montgomery, R.N. Morris, C.M. Silva, et al., *Nucl. Eng. Des.* 306 (2016) 36–46.
- [100] K. Minato, T. Ogawa, S. Kashimura, K. Fukuda, M. Shimizu, Y. Tayama, et al., *J. Nucl. Mater.* 172 (1990) 184–196.
- [101] W. Schenk, G. Pott, H. Nabielek, *J. Nucl. Mater.* 171 (1990) 19–30.
- [102] J.J. van der Merwe, *J. Nucl. Mater.* 395 (2009) 99–111.
- [103] H. Nabielek, P.E. Brown, P. Offerman, *Nucl. Technol.* 35 (1977) 483–493.
- [104] I.J. van Rooyen, E.J. Olivier, J.H. Neethling, *J. Nucl. Mater.* 476 (2016) 93–101.
- [105] T.M. Lillo, I.J. van Rooyen, *J. Nucl. Mater.* 460 (2015) 97–106.
- [106] R.A. Coward, C.R. Winkler, W.A. Hanson, M.L. Jablonski, M.L. Taheri, *J. Nucl. Mater.* 457 (2015) 298–303.
- [107] E. Friedland, N.G. van der Berg, J.B. Malherbe, J.J. Hancke, J. Barry, E. Wendler, et al., *J. Nucl. Mater.* 410 (2011) 24–31.
- [108] T.J. Gerczak, G. Zheng, K.G. Field, T.R. Allen, *J. Nucl. Mater.* 456 (2015) 281–286.
- [109] E. López-Honorato, D. Yan, J. Tan, P.J. Meadows, P. Xiao, *J. Am. Ceram. Soc.* 93 (2010) 3076–3079.
- [110] J.H. Neethling, J.H. O'Connell, E.J. Olivier, *Nucl. Eng. Des.* 251 (2012) 230–234.
- [111] J.H. O'Connell, J.H. Neethling, *J. Nucl. Mater.* 445 (2014) 20–25.
- [112] E.J. Olivier, J.H. Neethling, *J. Nucl. Mater.* 432 (2013) 252–260.
- [113] J. Rabone, E. López-Honorato, *J. Nucl. Mater.* 458 (2015) 56–63.
- [114] D. Shrader, S.M. Khalil, T. Gerczak, T.R. Allen, A.J. Heim, I. Szlufarska, et al., *J. Nucl. Mater.* 408 (2011) 257–271.
- [115] J. Deng, H. Ko, P. Demkowicz, D. Morgan, I. Szlufarska, *J. Nucl. Mater.* 467 (2015) 332–340.
- [116] H. Ko, J. Deng, I. Szlufarska, D. Morgan, *Comput. Mater. Sci.* 121 (2016) 248–257.
- [117] A. Londono-Hurtado, A.J. Heim, S. Kim, I. Szlufarska, D. Morgan, *J. Nucl. Mater.* 439 (2013) 65–71.
- [118] D.A. Petti, R.R. Hobbins, P. Lowry, H. Gougar, *Nucl. Technol.* 184 (2013) 181–197.
- [119] C.T. Walker, C. Bagger, M. Mogensen, *J. Nucl. Mater.* 240 (1996) 32–42.
- [120] H. Kleykamp, *J. Nucl. Mater.* 206 (1993) 82–86.
- [121] S.G. Prussin, D.R. Olander, W.K. Lau, L. Hansson, *J. Nucl. Mater.* 154 (1988) 25–37.
- [122] C.L. Smith, *J. Am. Ceram. Soc.* 62 (1979) 600–606.
- [123] K.E. Wright, I. van Rooyen, Paper 18570, in: Proceedings of the Eighth International Topical Meeting on High Temperature Reactor Technology (HTR-2016), Las Vegas, NV, 6–10 Nov. 2016.
- [124] H. Nickel, H. Nabielek, G. Pott, A.W. Mehner, *Nucl. Eng. Des.* 217 (2002) 141–151.
- [125] M. Akabori, K. Fukuda, *J. Nucl. Mater.* 183 (1991) 70–75.
- [126] W. Schenk, H. Nabielek, *Nucl. Technol.* 96 (1991) 323–336.
- [127] K. Sawa, S. Shiozawa, K. Fukuda, Y. Ichihashi, *J. Nucl. Sci. Tech.* 29 (1992) 842–850.

- [128] W. Schenk, D. Pitzer, H. Nabielek, Fission Product Release Profiles from Spherical HTR Fuel Elements at Accident Temperatures, JüI-2234, Kernforschungsanlage Jülich, 1988.
- [129] C.L. Smith, *J. Am. Ceram. Soc.* 62 (1979) 607–613.
- [130] P.A. Demkowicz, J.D. Hunn, R.N. Morris, C.A. Baldwin, J.M. Harp, P.L. Winston, et al., *Nucl. Eng. Des.* 306 (2016) 2–13.
- [131] R.N. Morris, P.A. Demkowicz, J.D. Hunn, C.A. Baldwin, E.L. Reber, *Nucl. Eng. Des.* 306 (2016) 24–35.
- [132] J.W. McMurray, T.B. Lindemer, N.R. Brown, T.J. Reif, R.N. Morris, J.D. Hunn, *Ann. Nucl. Energy* 104 (2017) 237–242.
- [133] P.A. Demkowicz, B. Liu, J.D. Hunn, *J. Nucl. Mater.* 515 (2019) 434–450.

Further reading

D. Olander, E. Greenspan, H. Garkisch, B. Petrovic, *Nucl. Eng. Des.* 239 (2009) 1406–1424.

This page intentionally left blank

Molten salt reactor fuels

6

Ondřej Beneš and Pavel Souček

European Commission, Joint Research Centre, Karlsruhe, Germany

6.1 Introduction

Although the technology of molten salt reactors (MSR) was first studied in the 1960s, it is currently one of the six advanced reactor concepts selected by the Generation IV forum as a potential candidate to fulfill future energy needs. It is quite a unique concept compared to current reactor types, such as light water reactors (LWRs), or other Generation IV reactors as the fuel is not of solid nature but is a homogeneous liquid [except, e.g., fluoride-cooled high-temperature reactor (FHR) design which is nowadays considered part of the MSR group as well and which is briefly discussed in [Section 6.3](#)]. In the MSR, the fissile material is dissolved in an inorganic liquid (most likely a mixture of fluorides or chlorides) that is pumped at low pressure through the reactor vessel and the primary circuit and thus also serves as the primary coolant. The heat generated by the fission process is transferred to a secondary coolant in a heat exchanger, which is generally comprised of a molten salt as well, to avoid direct contact of the fuel salt with water, which is used to run the turbine for electricity production in a third cycle. This remains the main design approach to keep the water circuit in a safe distance from the fuel salt and thus to limit water contamination in case of leakage in the heat exchangers. Besides having a three circuit approach alternative solutions, for example, secondary circuit based on gas coolant, are being explored. A schematic of a general MSR, as presented on Generation IV international forum [\[1\]](#), is given in [Fig. 6.1](#).

6.1.1 Key advantages of the molten salt reactor

Many advantages arise from the liquid nature of the fuel. The most important advantage of the MSR in comparison to other reactor designs is its inherent safety features. Since the fuel is in a liquid state during normal operation and it serves as a primary coolant with low vapor pressures and high boiling temperatures (i.e., $>1400^{\circ}\text{C}$), the hydrostatic pressure of the primary circuit is kept very low (~ 1 bar) compared to current LWRs. It thus inherently avoids the major driving force of the radioactivity release during an accident—the high pressure. Another aspect that contributes to the safety of the MSR is that the fuel has a strong negative temperature coefficient invoked by thermal expansion of the fuel salt, which decreases the fuel density and causes a subcritical state. In addition, some of the MSR concepts are equipped with emergency

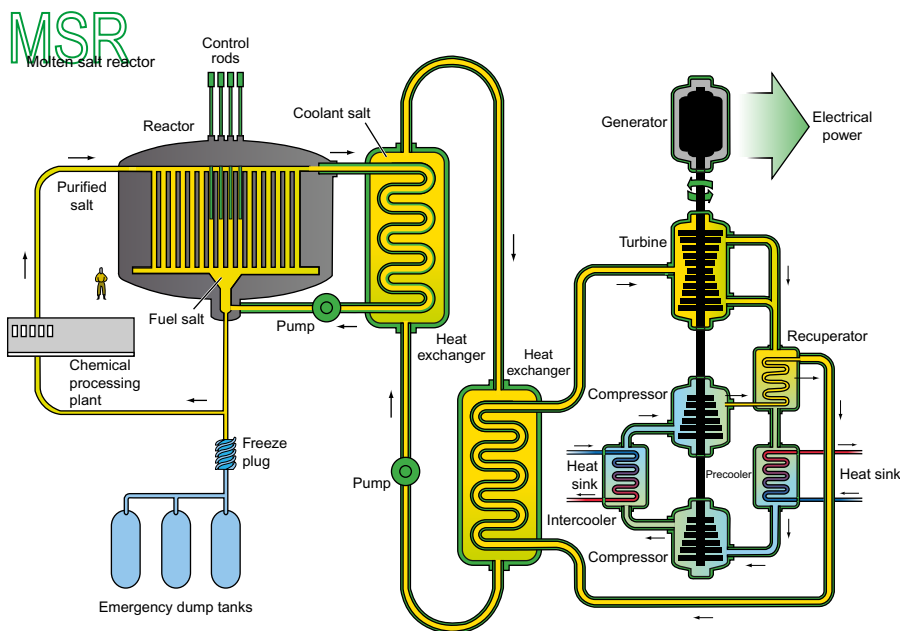


Figure 6.1 A schematic representation of a general molten salt reactor [1].

dump tanks into which the fuel can be drained in case of overheating. The emergency tanks are installed under the reactor and are designed in such a way that once dumped, the fuel becomes subcritical and the remaining decay heat is removed naturally with no need for an external power supply. The opening of the valves to let the fuel flow into these emergency tanks is designed as a passive system based on freeze plugs that melt once the fuel overheats [2].

The operating temperature of an MSR depends on the reactor concept and the fuel used (e.g., chlorides vs fluorides, specific mixtures), but generally range from 500°C to 750°C; thus the operating temperature is high enough to increase the energy conversion efficiency of the reactor compared to conventional LWRs. It is foreseen by the scientific community that the efficiency of an MSR can be as high as 40%–45%, which provides economic incentives for their consideration. The upper temperature limit of the operating temperature of the reactor is mostly limited by the corrosion resistance of the used structural materials, which generally decreases with increasing temperature.

A big advantage of some MSR designs, which increases the efficiency of the fuel burnup, is the possibility of performing a continuous fuel salt cleanup. This can be achieved by coupling online cleanup by helium bubbling with batch processing that utilizes pyrochemistry. The concept is proposed in such a way that the cleanup chemical plant is installed adjacent to the nuclear reactor to eliminate risks associated with fuel transportation over large distances. The goal of the fuel cleanup process is to separate fission products from the fuel and disposition them as nuclear waste.

Alternatively, MSRs can be used for isotope production, whereby some key isotopes are extracted during the chemical cleanup process. Successively, the cleaned fuel is returned to the primary circuit. Although there are nowadays commercial MSR designs that for simplicity do not utilize the cleanup scheme, the separation of fission products from the primary salt still remains a very attractive option as many fission products have high parasitic neutron-capture cross sections and thus negatively influence the neutron economy. Due to this onsite cleanup, a relatively small initial inventory of fissile material is possible. Moreover, it is also possible to profit from the neutron economy coupled with online cleanup and design the MSRs as a breeder reactor to breed plutonium-239 from uranium-238 or uranium-233 from thorium-232, as was demonstrated by the molten salt breeder reactor (MSBR) project discussed in the next section [3].

The MSR can be designed as an actinoid burner reactor. It is possible to inject minor actinoids contained in nuclear waste from conventional power reactors into the MSR fuel cycle and transmute these long-lived isotopes into short-lived fission products. The transmutation process is very challenging, but it would help to address nuclear waste disposal, which is generally considered a major disadvantage of nuclear power due to the presence of the long-lived actinides that need millions of years before they decay to natural levels.

Yet another advantage of the MSR, which is linked to the homogeneous state of the fuel, is the absence of significant radiation damage mechanisms, which is an important challenge in other reactor designs that use various structural materials to contain the fuel and fuel assemblies. Radiolytic decomposition of the fluoride or chloride salts does indeed take place under irradiation resulting in the formation of free fluorine or chlorine radicals, but studies from the Oak Ridge National Laboratory (ORNL) [4] showed that at operating temperatures of the reactor, the recombination process is so fast that no fluorine or chlorine gases are practically produced.

6.1.2 Challenges for molten salt reactor deployment

As briefly summarized in the previous section, MSR technology provides many safety-related and/or potential economic benefits, but there are still many challenges that need to be addressed before final commercialization of the technology.

Among the first one is the compatibility of the fuel salt with structural materials at high (operating) temperature and related development of alloys that are resistant enough under these conditions. Dedicated text on corrosion and related redox control of the salt is given in [Section 6.7](#), indicating options how to inhibit the corrosion rate, but further research must be still done in this domain to go toward licensing and qualification of novel and compatible alloys.

Another challenge is the establishment of a full procedure of the fuel cleanup scheme, in the case an MSR will be coupled with a chemical plant. Although several methods and sequence of physicochemical steps are proposed at the moment, significant research and validations must be done to properly design an effective scheme with properly installed safeguards and utilizing safe handling of separated fission products.

In case the MSR fuel salt is based on lithium fluoride-containing matrix, an issue with tritium production must be taken into account and very likely only coolant salts with high tritium retention must be used as a secondary coolant medium.

The last, but not the least identified challenge is the need for reliable data on relevant physicochemical properties that can be used by authorities for licensing of the reactors. A list of properties of concern is discussed throughout this chapter. It is not only important to address properties of the fuel composition but also to assess how the fuel properties will be affected by a small composition shift caused by factors such as long-lasting fission.

6.2 History of molten salt reactor research

The first proposal for an MSR dates back to the 1940s when Bettis and Briant proposed it for aircraft propulsion [5]. A substantial research program was initiated at ORNL in the United States to develop this concept, culminating in the aircraft reactor experiment (ARE), which became critical in 1954. The ARE was operated successfully over a period of 221 hours at steady state with outlet temperatures up to 860°C and at powers up to 2.5 MWth. The ARE used molten fluoride salt with NaF–ZrF₄–UF₄ (53–41–6 mol.%) as an initial fuel mixture; it was moderated by beryllium oxide (BeO), and it used liquid sodium as a secondary coolant material [5]. This experiment used Inconel 600 alloy (a nickel-based alloy) for the metal structure and piping. The ARE showed that the fissile compound UF₄ was chemically stable in the solvent and that gaseous fission products were removed essentially automatically by the pumping action of the salt circulation pump, which accumulated in the pump bowl above the reactor. The fluid fuel had a very strong negative temperature coefficient, which made the reactor inherently safe.

By the end of the 1950s, molten salt technology was transferred to the civilian nuclear program in the United States. At that time, many nuclear reactor concepts were being explored and the interest in breeder reactors was palpable. It was recognized that the MSR would be ideal for thermal breeding of uranium from thorium [6], and the MSR experiment (MSRE) was initiated at ORNL to demonstrate the operability of MSRs and to advance the technology toward industry. Because of the breeding aspect of this design, the neutron economy in the reactor was considered to be of key importance and ⁷LiF–BeF₂ (commonly referred to as “FLiBe”), with 5% ZrF₄ as an oxygen getter, was selected as a fuel carrier because of the very low neutron-capture cross sections of ⁷Li and Be. To achieve net positive breeding, it required enrichment of ⁷Li to 99.99% to avoid high concentrations of another naturally occurring lithium isotope, ⁶Li with high parasitic neutron capture.

The MSRE was a graphite-moderated reactor of 8 MWth that operated from 1965 to 1969 and the top perspective of the reactor is depicted in Fig. 6.2. Three different fissile sources were used: ²³⁵UF₄, ²³³UF₄, and ²³⁹PuF₃. FLiBe was used as a coolant in the secondary circuit. The results of MSRE, which have been reported in great detail by Haubenreich and Engel [7], revealed that all the selected materials (e.g., fuel mixture and structural materials) performed well and that the equipment

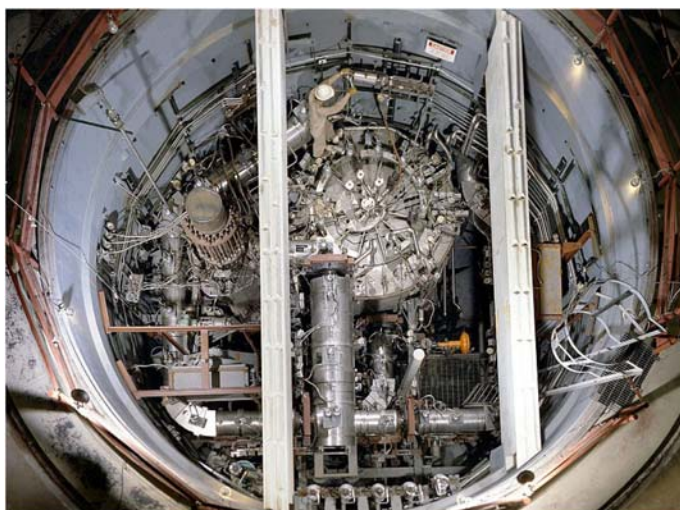


Figure 6.2 Top perspective of MSRE as taken at ORNL. *MSRE*, Molten salt reactor experiment; *ORNL*, Oak Ridge National Laboratory.

was considered a reliable technology. In that respect, the MSRE project was concluded as a great success.

After the completion of the MSRE project, a design for a prototype MSBR was made by ORNL in the early 1970s [3], in which a continuous cleanup of the fuel was foreseen to reduce the neutron loss by capture in fission products. The program was terminated in 1976 in favor of the liquid metal–cooled fast reactor (LMFR) [6]; although the MSR technology was considered promising, LMFR was perceived to be more promising at the time. The MSBR design was a 2250 MW_{th} reactor, optimized to breed ^{233}U from ^{232}Th in a single-fluid system. Online pyrochemical reprocessing was planned to clean the fuel solvent from the neutron-absorbing fission products. Nevertheless, interruption of reactor operation was planned every 4 years to replace the graphite moderator, as experiments had revealed significant swelling of graphite due to radiation damage. As a result of the online cleanup capability of the fuel, the addition of zirconium to the fuel (as an oxygen getter) was not necessary, and FLiBe could be used as a carrier of fertile (e.g., ThF_4) and fissile components (e.g., UF_4). As a secondary coolant, a $\text{NaF}-\text{NaBF}_4$ mixture (0.08–0.92 mol %) was foreseen because the retention of tritium, which is formed by neutron interaction with lithium and beryllium, is much better than FLiBe.

6.3 Molten salt reactor renaissance

The MSR is among six Generation IV advanced reactor concepts selected to meet future energy needs and to make major contributions to decarbonization. The current Generation IV signatories are Australia, Canada, the European Union (EU),

France, Russia, Switzerland, and the United States. It is worth noting that there is a significant MSR project currently established in China as well independent of the Generation IV initiative. Four major national concepts are studied worldwide:

1. The molten salt fast reactor (MSFR) is the reference concept studied in the EU with the lead in France. It is a non-moderated reactor using a ^7LiF fuel salt, which serves as a solvent to utilize fertile ThF_4 and fissile uranium and plutonium in the form of tetra- and trifluorides. The reactor is designed for an epithermal spectrum.
2. The molten salt recycle and transmuter concept is a Russian MSR design developed for use as an efficient burner of transuranic (TRU) waste from spent UO_2 and mixed oxide LWR fuel without any uranium and thorium support but also including this option [8].
3. The thorium MSR is a Chinese MSR concept utilizing thorium, taking the parameters and models of MSRE and MSBR designs studied at ORNL in the 1960s as a reference.
4. The Indian MSBR (IMSR) has been extensively studied in India, which is also based on the reference MSBR concept, whereby thorium is utilized as a fertile material to breed fissile uranium.

In recent years, interest of utilizing this liquid-fueled technology increased not only on a national level, but several start-up companies in Canada, the EU, and the United States selected this technology with short(er) term deployment. This includes both large-scale power plants (e.g., 1000 MWe) and small modular reactors (e.g., <300 MWe).

In the United States, alternative concepts called the advanced high-temperature reactor (AHTR) and the FHR are also being explored. The AHTR uses liquid salts (in FHR, it is specifically fluoride salt) as a coolant but has the graphite core structures and coated tristructural-isotropic (TRISO) fuel particles (see [Chapter 5: Other power reactor fuels](#)) of the very high-temperature reactor. The superior heat transport characteristics of salts compared to helium could enable power densities four to six times higher and power levels up to 4000 MWth with passive safety characteristics inherent in the design [9].

6.4 Molten salt reactor fuel concepts

MSR fuel concepts are mostly based on fluoride salts, but chloride salts are considered as potential candidates as well. As listed in the preceding text, several substantially supported national programs exist on the development of MSR technologies with increased interest by many start-ups in recent years. [Table 6.1](#) gives an overview of a variety of fuels selected for different reactor concepts with the main characteristics described.

6.5 Fuel salt properties

To make MSR safe, viable, and economically viable, the knowledge of fuel properties must be established. This section summarizes and explains the most relevant

Table 6.1 List of main MSR systems studied in France (EU), China, Russia, and India.

MSR concept	Country	Fuel system	Neutron spectrum
MSFR	France—EU	LiF–ThF ₄ –UF ₄ –PuF ₃	Nonmoderated
TMSR	China	LiF–BeF ₂ –ThF ₄ –UF ₄	Moderated
MOSART	Russia	LiF–NaF–BeF ₂ –PuF ₃	Nonmoderated
IMSR	India	LiF–BeF ₂ –ThF ₄ –UF ₄	Moderated

EU, European Union; *IMSR*, Indian molten salt breeder reactor; *MOSART*, molten salt recycle and transmuter; *MSFR*, molten salt fast reactor; *MSR*, molten salt reactor; *TMSR*, thorium molten salt reactor.

topics that must be taken into account to ensure the success of an MSR design and highlights the key reasons why they are important. There are databases on many properties of predominantly fluoride fuel mixtures; however, as the fuel concepts currently considered differ from the past experience of MSRs, logically these gaps must be filled. Moreover, even the data that have been measured in the past may need to be re-evaluated as they might not meet the current requirements by licensing authorities that maintain stringent quality-assurance standards.

6.5.1 Melting point

Although chloride salts melt at somewhat lower temperatures compared to fluorides, metal halides of both groups melt well above room temperature. In general, lower melting points are better for the following two reasons: (1) less heat is needed to put the reactor into operation during start-up and (2) the lower the melting point, the lower the operating temperature of the reactor, which can significantly mitigate potential corrosion of structural materials. The melting point of the fuel mixture depends on the exact composition and can significantly depend on the amount of dissolved actinoid fluoride or chloride content due to limited solubility in the fuel salt. It also depends on the form (i.e., valence) of the actinoid halide as trihalides have generally much higher melting points compared to actinoid tetrahalides. Using fluoride salts as a fuel, the operating temperature of the reactor (i.e., at the outlet) should not exceed 750°C, which is mainly limited by structural strength and corrosion resistance of the Ni-based alloys developed as structural materials for MSR.

Melting point behavior of the MSR fuel, which is a multicomponent salt system, is very well described by thermodynamic models. Figs. 6.3 and 6.4 show calculated liquidus surfaces of the respective LiF–ThF₄–PuF₃ and LiF–UF₄–ThF₄ systems, based on the thermodynamic data published by Capelli et al. [10] and Beneš et al. [11]. From such a description, the melting point of any composition from the described system can be computed as well as the information on the chemical form of the first precipitate. The LiF–ThF₄–PuF₃ system has a computed eutectic temperature of 820 K (547°C) corresponding to the (75.3–21.6–3.1 mol.%) composition and in total of eight primary crystallization fields are found in the system. The chemical forms of these precipitates are given in the caption of Fig. 6.3. The LiF–UF₄–ThF₄ system shown in Fig. 6.4 is characterized by the lowest melting

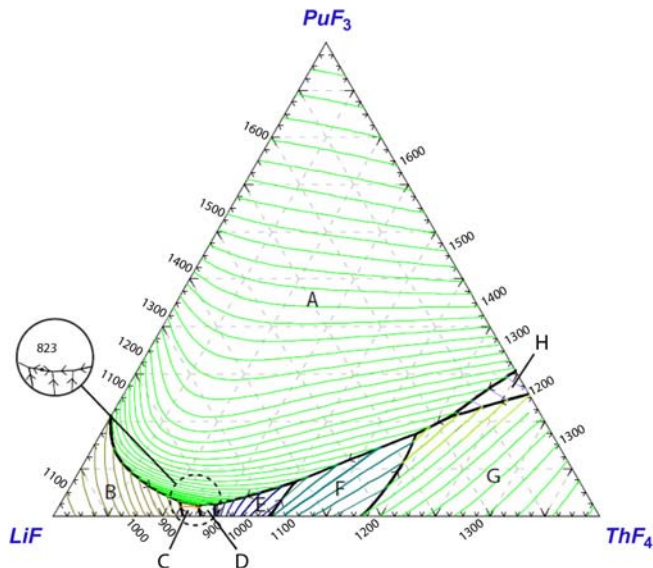


Figure 6.3 The liquidus projection of the $\text{LiF}-\text{ThF}_4-\text{PuF}_3$ system assessed by Capelli et al. [10], temperatures are in K scale. Primary crystallization phase fields: (A) $(\text{Pu}, \text{Th})\text{F}_x$ (s.s.); (B) LiF ; (C) Li_3ThF_7 ; (D) LiThF_5 ; (E) LiTh_2F_9 ; (F) $\text{LiTh}_4\text{F}_{17}$; (G) ThF_4 ; (H) $\text{PuTh}_2\text{F}_{11}$. s.s., Solid solution.

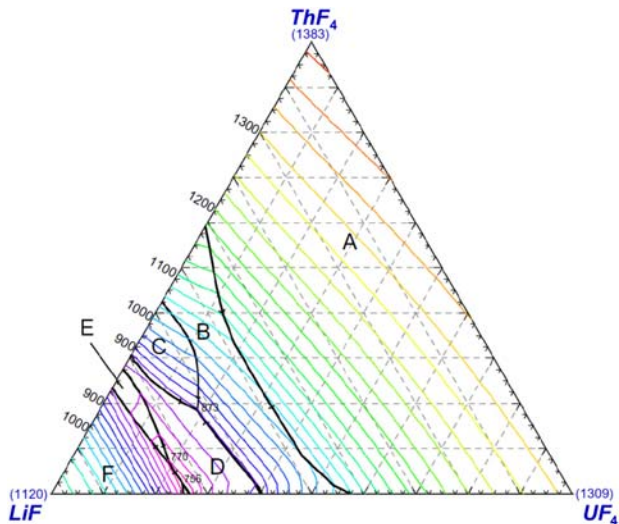


Figure 6.4 The calculated liquidus projection of the $\text{LiF}-\text{ThF}_4-\text{UF}_4$ system published by Beneš et al. [11]. Isotherms and the invariant equilibria are labeled in K with the interval of 25K. Primary phase fields: (A) $(\text{Th}, \text{U})\text{F}_4$ (s.s.); (B) $\text{Li}(\text{Th}, \text{U})_4\text{F}_{17}$ (s.s.); (C) $\text{Li}(\text{Th}, \text{U})_2\text{F}_9$ (s.s.); (D) $\text{Li}_7(\text{Th}, \text{U})_6\text{F}_{31}$ (s.s.); (E) $\text{Li}_3(\text{Th}, \text{U})\text{F}_7$; (F) LiF . s.s., Solid solution.

point corresponding to the ternary eutectic point found at 756 K and LiF–UF₄–ThF₄ (73.8–24.0–2.2 mol.%) composition, but this point is of no design considered as a fuel option.

6.5.2 Vapor pressure—boiling point

An inherent safety feature of the MSR is the ability of the reactor to operate at high temperature while maintaining nearly atmospheric pressure. However, the volatility of the fuel salt is an important parameter as it determines the equilibrium pressure of the fuel during operation. The boiling point determines the critical temperature that should not be exceeded, but since boiling points of considered MSR fuels are fairly high—around 1700°C–1800°C for fluorides and somewhat lower for chlorides—the temperature margin between fuel melting and boiling is very large. Lastly, the partial vapor pressures of individual fuel components in the gas are likely very different from one component to another, leading to a fuel composition shift in case of continuous vaporization. As an example, if LiF_(g) is the most volatile component in the LiF–ThF₄–UF₄ MSFR fuel, as experimentally observed in the work of Tosolin et al. [12] and indicated in Fig. 6.5, the long-term vaporization into an open space would continuously increase in concentration of actinoid fluorides originating from the fuel melt. Furthermore, this would result in modification

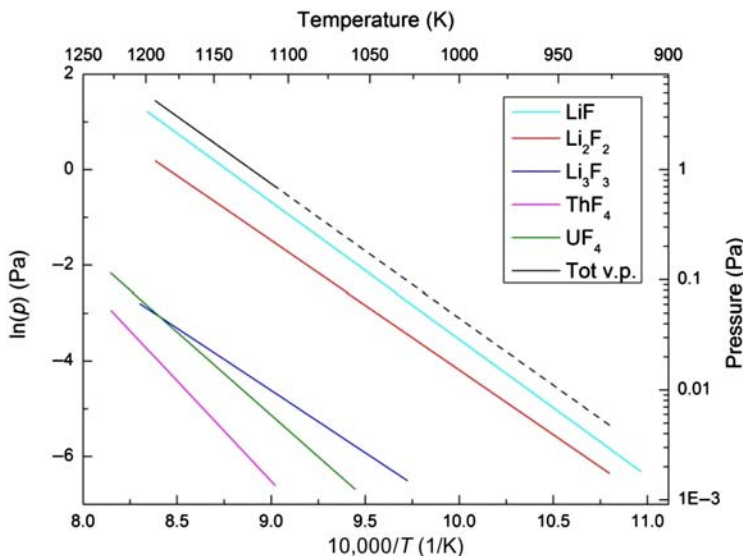


Figure 6.5 Partial (colored) and total (black) vapor pressures for the mixture LiF–ThF₄–UF₄ (77.5–20.0–2.5 mol.%) measured by Tosolin et al. [12]. The dashed line is the total vapor pressure considering only LiF and Li₂F₂ (their partial vapor pressures are several orders of magnitude higher than other species and could be detected in the lower temperature range).

of fuel characteristics, not only on fuel properties (e.g., the melting point would likely rise), but as well on neutronics, thermal hydraulics, etc.

6.5.3 Heat capacity

The heat capacity of the fuel determines how much heat is needed to increase the temperature of the fuel by a unit amount. From a safety point of view, it is especially important to know how much heat can be stored (buffered) in the fuel before it reaches a critical temperature (e.g., during cooling failure).

The heat capacity of a salt mixture is based on the heat capacity contributions of individual end-members that form the mixture. An easy approximation to estimate the value for the exact fuel composition applies the Neumann–Kopp rule, which takes the proportional weight of each end-member based on its mole fraction. Recent studies by Beilmann et al. [13] showed that this approximation may lead to high departures from real behavior. In this study a significant excess heat capacity was revealed by performing systematic experimental investigation of LiF-AlkF (Alk = alkaline) binary systems using drop calorimetry with obtained results shown in Fig. 6.6. This phenomenon must be taken into account for the assessment of fuel performance in the reactor and gives credence that experimental confirmation of the molten salt fuel heat capacity is needed.

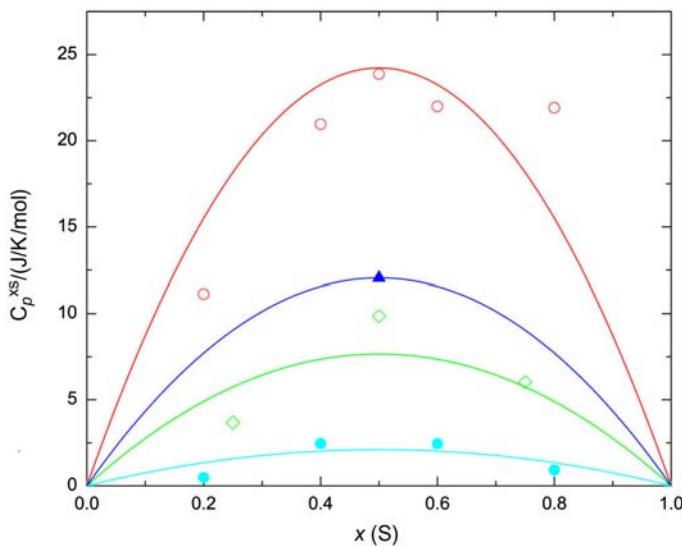


Figure 6.6 Excess heat capacity of LiF-AlkF binary liquid mixtures [9].

Red open circles: LiF-CsF system; blue triangle: LiF-RbF system; green diamonds: LiF-KF system; and light blue solid circles: LiF–NaF system.

6.5.4 Solubility of actinoids

To operate an MSR efficiently, perhaps as a breeder reactor, enough actinoid halides must be dissolved in the fuel salt. In other words, the solubility of these actinoid halides must be high enough to fulfill these goals. The solubility depends on two main factors: the solvent used and the temperature. Generally, the solubility of a given actinoid halide increases with temperature, but it must be taken into account that operating temperature must be kept at suitable value, which is limited by several factors (e.g., corrosion rate of the structural materials). Therefore it is very important to select such a fuel mixture that allows dissolution of a high enough quantity of actinoid halides while keeping the temperature at reasonably low values. Solubility of actinoids significantly varies depending on whether the actinoids are stabilized in the fuel salt as either tetra- or trifluorides. The latter have generally much higher melting points, and thus the related solubility is far lower compared to tetravalent actinoids [14,15].

It is important for reactor designers to look carefully at the fuel solvent salt, as some variants may suppress solubility of actinoids far more compared to others. Take for example the use of BeF_2 -containing salt, which significantly suppresses the solubility of PuF_3 , as demonstrated in Fig. 6.7 [16]. The figure illustrates a large liquidus surface in the mid- to high-concentration range of BeF_2 , which is responsible for very low solubility of PuF_3 in the salt.

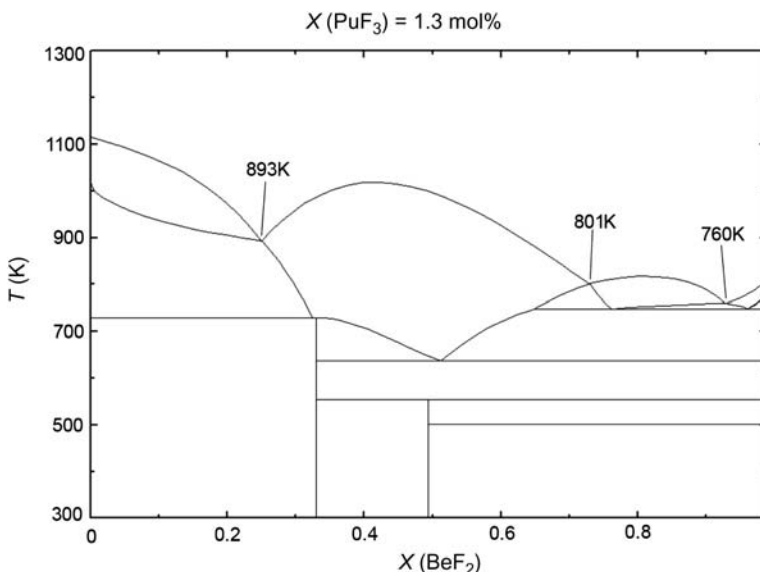


Figure 6.7 A calculated pseudo-binary phase diagram of the LiF-BeF₂ system (with 1.3 mol% PuF_3 constrained) is shown based on a thermodynamic assessment by Beneš et al. [16].

6.5.5 Fission product retention

The fission products that are formed during the MSR operation can be divided into three main groups based on their solubility in the carrier salt: noble gases, stable salt-soluble fluorides, and solid precipitates in the form of noble metals or other chemical forms that are insoluble in the fluoride matrix. Whether a fission product will or will not be dissolved in the salt is determined by the redox potential of the salt, which is usually proportional or controlled by the $\text{U}^{4+}/\text{U}^{3+}$ ratio.

The nature of the liquid form of the MSR fuel is related to the key advantage that significantly lowers the source term of potential radionuclide release during a severe accident. This so-called retention capacity of the fuel for various volatile fission products, or more specifically volatile fission products categorized by Kleykamp [17] for conventional oxide fuels, makes the MSR design a very promising and inherently safe concept. The main concern involves the fission products cesium and iodine that were responsible for the environmental and health safety burdens from the severe accidents in Chernobyl in 1986 and Fukushima in 2011. Upon heating, these two fission products are released from grain boundaries of solid oxide fuel between 800 K and 1500 K, as experimentally confirmed by several studies on irradiated fuel samples [18,19], depending on the burnup and/or oxidation state of the fuel.

In the MSR, cesium and iodine may be sufficiently soluble in the fuel salt and thus significantly reduce the source term. One main factor for compound formation of fission product in the liquid fuel is the mobility, which is heavily suppressed in solid fuels. This allows stabilization of thermodynamically favorable compounds, which in the case of cesium and iodine are likely CsI and CsF (or CsCl in case of chloride melt utilization). Since the fission yield of Cs and I has a 10:1 ratio, there will be an excess of Cs, which will likely take the form of CsF. It still needs to be proven experimentally whether these two fission products are fully dissolved in most fuel mixtures; however, the work from Capelli et al. indicates that CsF (or CsCl) would completely mix in the fuel matrix, and thus the cesium volatility with respect to the total concentrations in the fuel will be negligible [20]. On the other hand, CsI may have very limited solubility and may still result in a volatile form (although not as volatile as elemental cesium) [20]. Nevertheless, even if CsF would be soluble and CsI not, considering that most of the iodine stabilizes as CsI and the remaining cesium (which will still remain in substantial quantities) takes the form of CsF, the source term of these two fission products during a reactor accident could be significantly less compared to pressurized water reactor (PWR) fuels.

6.5.6 Stability to radiation

As in ceramic fuels, the fuel carrier in a MSR will be subjected to various types of radiation that can cause damage, such as α - and β -decay, γ -radiation, and neutron and fission fragments. But unlike ceramic fuels, a liquid fuel does not have a lattice structure with long-range order and thus cannot be distorted. As reported by Blankenship [21], radiolytic formation of F_2 occurs in the fluoride salts at low

temperatures ($T < 100^\circ\text{C}$); however, since all salts considered as MSR fuels are in the solid state at these temperatures, the evolution rate is somehow limited by a slow fluorine diffusion within the crystal. At higher temperatures, a reverse reaction counteracts primary radiolysis events, which happens for most of the salts far below their melting points. It has been demonstrated that during this recombination process, F_2 reacts more rapidly with salts that have primarily lost their fluorine atoms, and hence, the F_2 build-up effect in-reactor is eliminated [21]. Since the MSR operates at high temperatures, the recovery process is rapid, and radiation damage to the salt is very small. This has been confirmed in separate experiments, using gamma sources, and in in-pile tests for the ARE and MSRE projects. None of these experiments have revealed indications that the fluoride salts are unstable in radiation fields [21]. It is believed that this radiation stability is responsible for the demand that only very stable salts must be considered in the reactor in order to keep the construction alloys thermodynamically stable with respect to the salt.

6.6 Measurements and experimental procedures

Measurement techniques to investigate physicochemical properties, such as those listed above, have been discussed in Chapter 2, Experimental methods. This section will not describe all techniques for high temperature investigation of molten fluoride or chloride salts as the principles are very similar. It will only highlight the need of special handling that is vital to obtain reliable data on actinoid-containing halides.

6.6.1 Handling

Besides the fact that handling fuel salts (and especially when containing TRU elements) must be performed in alpha tight glove boxes for the radioprotection reasons, the atmosphere must be low in oxygen and moisture content. Experience has shown that inert atmosphere glove boxes used to handle fluoride and chloride salts are best done when using argon (inert) atmosphere and connected to online purifiers with permanent monitoring of oxygen and moisture concentrations. Experience further shows that long-term concentrations of O_2 and H_2O should be maintained lower than 5 ppm. Under such conditions, even long-term storage of solid fluoride samples did not indicate any impurities arising from parasitic reactions with oxygen or water vapor.

6.6.2 Sample synthesis and purification

Before every measurement, it is important to ensure that the starting material is free of any significant impurities that could lead to false or misleading results. Alkali and alkali earth halides, which are the main candidates used as solvents for actinoid halide fuel, can be purchased from several commercial providers with certified

levels of purity. This does not, however, necessarily mean that they will be free of contaminants arising from interaction with air, which usually takes place during packaging and delivery processes. It is therefore very important to account for this issue by purifying these starting materials from mainly absorbed water due to the hygroscopic nature of alkali and alkali earth halides. The suggested purification process that is based on long-term experience is a treatment of the salt in the form of very fine powder (mortar milling of the as-received material is sufficient) at elevated temperature for several hours under inert atmosphere (e.g., in a glovebox). A vacuum can be applied to increase the kinetics of water desorption, but experience has shown that performing the process in an argon atmosphere works just as well. Details about this procedure have been published in the literature [22–24].

A more complicated process is applied if the material contains oxides or oxyfluoride/oxychloride contaminants that cannot be converted to halides or separated with simple heating but require fluorinating/chlorinating agents to purify the base fluoride. For the case of fluorination, several fluorination media exist with the most commonly applied being fluorine (F_2) and hydrogen fluoride (HF) gases. There is no doubt that fluorine gas is a stronger fluorinating agent compared to HF as the fluorine activity of the former gas is higher, but there are also drawbacks that must be considered when using F_2 gas. This is described in [Chapter 9](#), Conversion and enrichment. Besides the fact that F_2 gas is highly toxic, which increases safety requirements, it is an oxidizing agent, so temperature must be carefully maintained to achieve a desired valency of the product. For instance, if UF_4 is to be formed, one has to account for possible formation of UF_5 or UF_6 higher fluorides and adjust the conditions of fluorination processes accordingly. In addition, the reaction of fluorine gas with oxides is highly exothermic, so gas dilution with inert argon gas is necessary to suppress the heat generation during fluorination. On the other hand, HF gas is not an oxidizing agent; it fluorinates the material while keeping the same valency of the cation. Considering this fact, UF_4 synthesis is achieved if the starting material is stoichiometric UO_2 and keeping the reaction at elevated temperature, as described by Souček et al. [25]. To handle both corrosive gases, the whole fluorination line must be constructed with appropriate materials with applications of nickel-based alloys. It is important to work in an absolutely dry environment to suppress corrosion of formed HF acid at high temperature. The experimental setup developed to synthesize and purify actinoid fluoride samples at JRC Karlsruhe is shown in [Fig. 6.8](#). It consists of tubular horizontal gas tight reactor (two pictures on the right side) connected to a gas bottle filled with pure liquid HF with a heated sleeve (picture second from left). Upon heating of the sleeve, the pressure of HF increases, and the formed HF gas is delivered through Inconel tubes into the reactor. The sample to be fluorinated is placed in a dedicated boat made of compatible material; the most commonly used is pure nickel (> 99.9 wt.% purity).

It is also important to verify the purity of starting materials before the measurement. Two independent methods are suggested, as described in our earlier studies [25,26]: X-ray diffraction (XRD) technique (for phase analysis) and melting point determination. The second method is a very sensitive technique for impurity check as already very little concentrations, which might not be detected by XRD, can be



Figure 6.8 HF line installed at JRC Karlsruhe to synthesize and purify actinoid fluorides [25]. HF, Hydrogen fluoride.

revealed by melting point analysis. Beside these, a chemical analysis of the formed product is made using, for example, inductively coupled plasma mass spectrometry (ICP–MS) to quantify impurities of other elements that may be present in the sample, either from initial material or by cross-contamination during handling.

6.6.3 High-temperature measurements—encapsulation

To obtain reliable data on physicochemical properties of salt mixtures that are subject to high-temperature measurements, typically several hundreds of degrees above the melting temperature, several factors must be taken into account. Besides the need to handle all fluoride and chloride salts under an inert atmosphere for the reasons described above, the halides must be encapsulated to avoid their evaporation during high-temperature measurements. This is done for two main reasons: (1) to protect the instrument from corrosive behavior of halide vapors and (2) to ensure

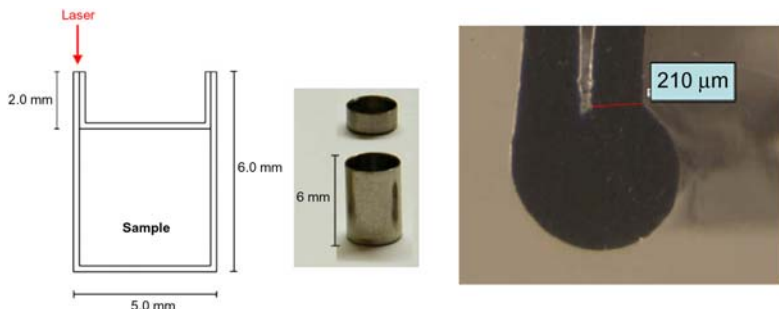


Figure 6.9 (Left) A schematic representation and a picture of the nickel crucible designed for the encapsulation of fluoride and chloride salt samples. The wall thickness is ~ 0.2 mm. (Right) Metallography of the welded edge of the crucible.

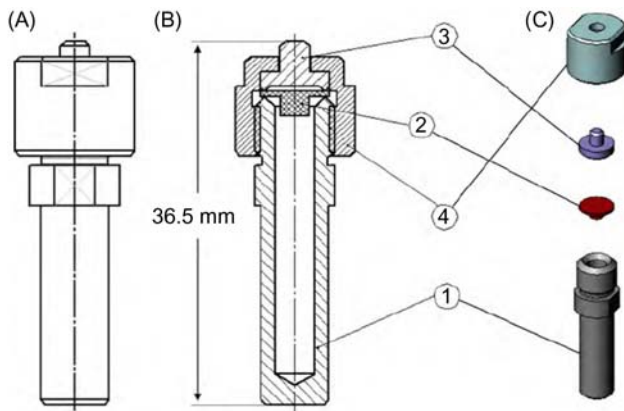


Figure 6.10 Schematic representation of the DSC crucible developed for fluoride samples measurements. (A) A scheme of the side of the developed DSC crucible; (B) a scheme of a cut of the crucible; (C) various parts of a crucible: (1) stainless steel crucible, (2) nickel sealing, (3) stainless steel stopper, and (4) stainless steel closing bolt. An insert made of BN, Ni, or graphite is typically inserted in the crucible (1). *DSC*, Differential Scanning Calorimetry.

that the salt mixture that is subjected to the measurement will not change composition due to incongruent vaporization and that the weight of the sample remains unchanged for the whole measurement, which is especially important when performing quantitative analysis. The encapsulation technique must be selected for the purpose of the measurement and must be compatible with the specific instrument. It is also very important to select such an encapsulation material that will withstand high temperature and will remain chemically intact by the halide molten salt.

In the past, the JRC research group (as example used in this chapter, but other similar techniques exist elsewhere) proposed two different encapsulation techniques

for the measurements of high-temperature properties of molten fluoride and chloride salts: one rather compact in size and based on laser welding of nickel capsules and the other one using a rigid stainless steel crucible with an inert liner, which can be from nickel metal, boron nitride (oxygen free), graphite, all chemically compatible with most of the fluoride salts of MSR interest or any other inert material with respect to the sample. Inner coatings are possible as well. Both techniques have been described in detail in earlier studies [11,27,28], and their schematic drawings are shown in Figs. 6.9 and 6.10. Different techniques are used for different purposes, that is, if there is a need for size minimization of the sample (e.g., for drop calorimetry), the welded crucible represented in Fig. 6.9 is ideal as it has a very simple design, which allows high ratio of sample versus encapsulated material and thus increases the precision of the measurement. On the other hand, if the measuring device allows bigger crucibles, the latter encapsulation may become more appropriate, due to easier handling and no need for high power laser facility, which may not be available in every laboratory.

6.7 Redox potential of the fuel

The redox potential of the MSR fuel salt is constituted by the electrode potential corresponding to the electrochemical redox reaction (Eq. 6.1) between the ions in oxidized (M_{ox}) and reduced (M_{red}) forms of the element M_i dissolved in the carrier salt according to:



where n is the valence number of oxidized cation and z the number of electrons are involved in the pair reaction.

The value of the redox potential depends on the activity of the corresponding ions in the particular carrier melt, as defined by the Nernst equation (Eq. 6.2):

$$E = E_{M_{\text{ox}}/M_{\text{red}}}^0 + \frac{RT}{nF} \ln \left(\frac{a_{M_{\text{ox}}}}{a_{M_{\text{red}}}} \right) = E_{M_{\text{ox}}/M_{\text{red}}}^0 + \frac{RT}{nF} \ln \left(\frac{\gamma_{M_{\text{ox}}}}{\gamma_{M_{\text{red}}}} \right) + \frac{RT}{nF} \ln \left(\frac{c_{M_{\text{ox}}}}{c_{M_{\text{red}}}} \right) \quad (6.2)$$

in which E^0 is the standard potential of the $M_{\text{ox}}/M_{\text{red}}$ couple (V), R the ideal gas constant (J/K/mol), F the Faraday constant (C/mol), a is the thermochemical activity, γ is the activity coefficient, and c the concentration (mol/L).

This implies that for the same element dissolved in different melts, the redox potential will be different since the activities of the dissolved species depend on the chemical nature of the carrier melt. This is especially true for the activity of fluorine in the melt, the so-called fluoroacidity, which influences the speciation of the ions in the melt. The redox potential value would thus change as well with different concentrations of the ions dissolved in the melt.

The redox potential of the fuel salt is determined by the dissolved element, whose ions in the oxidized form M_{ox} are at the given conditions the least stable in the melt. For example, in a LiF–BeF₂ eutectic melt (67–33 mol.%) containing nickel(II) and uranium(IV) ions at similar concentrations, the redox potential would correspond to the potential value of the redox pair Ni(II+) / Ni(0) in the melt. Since the standard electrode potentials¹ E^0 of Ni(II)/Ni(0) and U(IV)/U(III) are app. +0.47 and −1.41 V versus HF/F[−] in LiF–BeF₂ (67–33 mol.%) at 1000 K [29], respectively, the less stable ion would be nickel(II), as the electrode potential of the Ni(II)/Ni(0) redox couple in the melt would be more positive than the electrode potential of U(IV)/U(III).

The redox potential of the fuel salt can be expressed in other terms as activity of fluorine [$a(F_2)$] in the melt, which is proportional to the partial vapor pressure of the fluorine gas in equilibrium with the melt. The higher its activity (pressure) is, the more fluorine is available for chemical reactions with the species in contact with the melt, and thus, the melt is more oxidative. It corresponds to the abovementioned fluoroacidity of the melt. The elements dissolved in the melt are influencing the activity of fluorine by different jointly formed chemical bonds and thus changing the value of the redox potential.

6.7.1 Corrosion inhibition

The redox potential is therefore a measure of chemical reactivity of the fuel salt. The more negative it is, the lower the activity of fluorine is, and the more reductive is the salt leading to a less corrosive environment. On the contrary, the more positive the redox potential, the more oxidative and corrosive the salt will be. Since most of the MSR concepts consider UF₄ as one of the major actinoid-bearing constituents of the salt, the most suitable way to control the redox potential is to regulate the concentrations, respectively, activities, of the dissolved uranium(IV) and (III) ions, the so-called U(IV)/U(III) redox buffer. The higher concentration, resp. activity of U³⁺ ions, the more negative the redox potential of the fuel salt E_{redox} will be, as can be shown by modifying the equation (Eq. 6.2) to this particular example (Eq. 6.3):

$$\begin{aligned} E_{\text{redox}} &= E_{\text{U}(4+)/\text{U}(3+)}^0 + \frac{RT}{nF} \ln \left(\frac{a_{\text{U}(4+)}}{a_{\text{U}(3+)}} \right) \\ &= E_{\text{U}(4+)/\text{U}(3+)}^0 + \frac{RT}{nF} \ln \left(\frac{\gamma_{\text{U}(4+)}}{\gamma_{\text{U}(3+)}} \right) + \frac{RT}{nF} \ln \left(\frac{c_{\text{U}(4+)}}{c_{\text{U}(3+)}} \right) \end{aligned} \quad (6.3)$$

At the same time, the salt will be less corrosive against construction materials with higher U(III) ion content.

During the MSR reactor operation, fluorine gas is produced by the fission reaction of UF₄, during which fission products with the average of the total valence less than four are formed according to the simplified equation (Eq. 6.4). Depending on

¹ The standard state of the ions used for the standard electrode potentials calculation is the hypothetical mole fraction solution in 0.67LiF–0.33BeF₂ (mol.%).

the value, the fluorine potential (or partial pressure of fluorine gas in equilibrium with the salt) can oxidize UF_3 to UF_4 , according to Eq. (6.5), which leads to an increase of the U(IV)/U(III) concentration ratio, increase of the redox potential of the fuel salt and to the reactor vessel corrosion [30,31].



As the most reactive element of the considered structural materials based on Ni-based alloys is chromium, the main corrosion reaction would be oxidation of chromium by uranium(IV) ions (Eq. 6.6):



Therefore, control of the U(IV)/U(III) concentration ratio is needed, and if the ratio increases over 100, part of the UF_4 content must be reduced back to UF_3 . It can be done chemically by introducing a suitable metal as a reductant. The metal must be chemically reducing enough to reduce U^{4+} ions to U^{3+} , and in the same time, it should not form a product introducing new chemical species to the fuel salt. In practice, suitable metals include Be (if BeF_2 is part of the fuel matrix) or U, which cations are already present in the fuel salt. The reduction is described by the chemical equilibrium using the example of Be metal as the reductant (Eq. 6.7):



6.7.2 Fission product speciation

The value of the redox potential at the same time determines the oxidation state of the formed fission products. For example, if the redox potential is higher than the electrode potential of the fission product tellurium, it would be formed as metal Te (0), in the opposite case tellurium would be dissolved forming $\text{Te}(\text{II}-)$ ions (tellurides) in the melt [30]. This example is very important for the specific corrosion of the Ni-based alloys considered as construction materials for the MSR core. Metallic Te can react with both nickel and chromium content of the Ni-alloys according to the following equations, forming brittle telluride compounds, which would cause specific intergranular cracking at the grain boundaries of the construction material [32] causing embrittlement:



This effect can be suppressed by controlling the redox potential of the melt to stay below the tellurium electrode potential, which was achieved by keeping the U(IV)/U(III) concentration ratio lower than 60 in case of the MSBR concept [33]. The ratio will be different for various reactor concepts utilizing different fuel mixtures, but it gives range of magnitude.

6.7.3 Monitoring of redox potential during reactor operation

The monitoring of the redox potential is a rather difficult and complex problem. The majority of attention has been focused on development of electrochemical methods by applying voltammetric analysis to characterize the U(IV)/U(III) redox couple directly in the fuel salt and to evaluate the concentration ratio from the obtained potential values. However, this method requires reversibility of the electrochemical reduction of U(IV) ions to U(III), which is not always fulfilled [34]. An additional difficulty is poor availability of thermodynamic reference electrodes for high-temperature fluoride melts, which would enable direct measurement of the potential values against a defined reference value.

Another method is spectrophotometric measurements of the samples taken from the fuel salt, but this method provides delayed results [35]. A robust method for monitoring of the redox potential of the fuel salt providing real-time results is very important for control of the corrosion and chemistry of the MSR fuel salt, and it requires further development.

6.8 Effect of oxygen impurities

Several of the physicochemical properties discussed in [Section 6.5](#) may be to some extent affected by the presence of oxide ions or oxygen that might originate from contamination of the salt system. For example, the presence of reactive oxides, in the moisture, can result in precipitation of the UO_2 phase [36] or oxyfluoride phases which may lead to instabilities in the reactor core.

Following the actinide series UO_2 , ThO_2 , PuO_2 , or eventually PaO_2 can be formed under the redox conditions of the MSR, and due to the very low solubilities of these species in the fluoride salt, they can easily precipitate in a solid form. Therefore it is important to keep the fuel salt free from oxide contamination to avoid this inadvertent event. This will certainly require strict salt control, but as mentioned in Rosenthal et al. [36], the results of the MSRE project have shown that the oxide content can be maintained at an adequately low level in order to achieve successful long-term operation of the MSR. It is still uncertain as to how well this can be practically managed and if an oxygen getter needs to be added to the fuel salt, as was done in the MSRE project using ZrF_4 .

6.9 Effect of soluble fission product impurities

As briefly discussed in the preceding section, not only can oxygen interaction result in a change in molten salt fuel properties and thus negatively influence the reactor performance, but the same is true for fission products that are formed throughout the course of irradiation. It is therefore very important to assess the concentrations of fission products, its chemical form that will be thermodynamically favorable, and whether they will or will not be separated from the fuel cycle by performing either online or batch process salt cleanup. It is important to mention that unlike solid oxide fuels, in which the formation of thermodynamically stable secondary phases containing fission products is greatly impeded by relatively slow diffusion processes through the fuel matrix, the formation of secondary phases will more rapidly reach thermodynamic equilibrium due to the fast mobility and reaction times in a molten medium at relatively high temperatures.

To understand the effects of soluble fission products on MSR fuel properties, experimental validation of simulated fuel samples containing selected fission products (and the appropriate chemical forms) will be necessary to perform. Nevertheless, for most material properties, large departures from the values obtained for fresh fuel samples are not expected, mainly due to low concentrations of most of the fission products. Even the amounts of CsF and LaF₃ (as stable chemical forms of major fission products cesium and lanthanum) accumulated in the fuel cycle after 30 years of operation [37] to 0.06 mol.% of CsF and 0.37 mol.% of LaF₃ are relatively low. This was confirmed by calculations performed by Beneš and Konings [38], which demonstrated a negligible effect on the melting and vaporization behavior of the fuel.

6.10 Conclusion

This chapter highlighted some of the key material properties that must be known to perform design studies of MSRs and to perform integral safety analyses. It showed that experiments are of key importance as some properties may be very difficult to estimate. Dealing with fluoride and chloride salts require some special handling in an inert atmosphere as these materials are hygroscopic, and some of the halides tend to oxidize in an air environment, in addition to the fact that many of these salts become volatile at high temperatures.

Since MSR fuel is a multicomponent system, it is nearly impossible to measure every composition of the system of interest. Notwithstanding, previous studies demonstrated that a systematic experimental approach may lead to the development of robust models and simulation tools that can help to optimize the fuel composition with respect to key properties (e.g., thermodynamic modeling is very useful to optimize the fuel composition with respect to melting behavior), but it is important to keep in mind that finding such optimal compositions must be subjected to further experimental validation of its properties.

References

- [1] The Generation IV International Forum, <www.gen-4.org>, 2018.
- [2] M. Richardson, Development of freeze valve for use in the MSRE, in: Oak Ridge National Laboratory, ORNL-TM-128, Oak Ridge, TN, 1962.
- [3] R.C. Robertson, Conceptual design study of a single-fluid molten-salt breeder reactor, in: Technical Report ORNL-4541, Oak Ridge, TN, 1971.
- [4] F.F. Blankenship, Effects of radiation on the compatibility of MSRE materials, in: Oak Ridge National Laboratory, ORNL-3708, Oak Ridge, TN, 1964.
- [5] E.S. Bettis, R.W. Schroeder, G.A. Cristy, H.W. Savage, R.G. Affel, L.F. Hemphill, The aircraft reactor experiment-design and construction, *Nucl. Sci. Eng.* 2 (1957) 804–825.
- [6] H.G. MacPherson, *Nucl. Sci. Eng.* 90 (1985) 374–380.
- [7] P.N. Haubenreich, J.R. Engel, *Nucl. Appl. Technol.* 8 (1970) 118–133.
- [8] V. Ignatiev, O. Feynberg, I. Gnidoi, A. Merzlyakov, V. Smirnov, A. Surenkov, et al., Progress in development of Li, Be, Na/F molten salt actinide recycler and transmuter concept, in: Proceedings of the ICAPP, Nice, France, 2007.
- [9] GIF R&D, Outlook for Generation IV nuclear energy systems, in: GIF Report, 2009.
- [10] E. Capelli, O. Beneš, R.J.M. Konings, *J. Nucl. Mater.* 501 (2018) 238–252.
- [11] O. Beneš, M. Beilmann, R.J.M. Konings, *J. Nucl. Mater.* 405 (2010) 186–198.
- [12] A. Tosolin, O. Beneš, J.-Y. Colle, P. Souček, L. Luzzi, R.J.M. Konings, *J. Nucl. Mater.* 508 (2018) 319–328.
- [13] M. Beilmann, O. Beneš, E. Capelli, V. Reuscher, R.J.M. Konings, Th Fanghänel, *Inorg. Chem.* 52 (2013) 2404–2411.
- [14] C.J. Barton, *J. Phys. Chem.* 64 (1960) 306–309.
- [15] J.C. Mailen, F.J. Smith, L.M. Ferris, *J. Chem. Eng. Data* 16 (1971) 68–69.
- [16] O. Beneš, R.J.M. Konings, *J. Chem. Thermodyn.* 41 (2009) 1086–1095.
- [17] H. Kleykamp, *J. Nucl. Mater.* 131 (1985) 221–246.
- [18] J.-P. Hiernaut, T. Wiss, D. Papaioannou, R.J.M. Konings, V.V. Rondinella, *J. Nucl. Mater.* 372 (2008) 215–225.
- [19] R.J.M. Konings, T. Wiss, O. Beneš, *Nat. Mater.* 14 (2015) 247–252.
- [20] E. Capelli, O. Beneš, R.J.M. Konings, *J. Nucl. Mater.* 462 (2015) 43–53.
- [21] F.F. Blankenship, Oak Ridge National Laboratory, ORNL-3708, Oak Ridge, TN, 1964.
- [22] O. Beneš, R.J.M. Konings, D. Sedmidubský, M. Beilmann, O.S. Valu, E. Capelli, et al., *J. Chem. Thermodyn.* 57 (2013) 92–100.
- [23] E. Capelli, O. Beneš, M. Beilmann, R.J.M. Konings, *J. Chem. Thermodyn.* 58 (2013) 110–116.
- [24] O. Beneš, R.J.M. Konings, *J. Nucl. Mater.* 435 (2013) 164–171.
- [25] P. Souček, O. Beneš, B. Claux, E. Capelli, M. Ougier, V. Tyrpekl, et al., *J. Fluor. Chem.* 200 (2017) 33–40.
- [26] A. Tosolin, P. Souček, O. Beneš, J.-F. Vigier, L. Luzzi, R.J.M. Konings, *J. Nucl. Mater.* 503 (2018) 171–177.
- [27] O. Beneš, R.J.M. Konings, C. Kuenzel, M. Sierig, A. Dockendorf, L. Vlahovic, *J. Chem. Thermodyn.* 41 (2009) 899–903.
- [28] O. Beneš, R.J.M. Konings, S. Wurzer, M. Sierig, A. Dockendorf, *Thermochim. Acta* 509 (2010) 62–66.
- [29] C.F. Baes, Jr., The chemistry and thermodynamics of molten-salt-reactor fluoride solutions, in: Proceedings of Symposium on Thermodynamics With Emphasis on Nuclear Materials and Atomic Transport in Solids, Vienna (Austria), 22–27 July 1965, IAEA-

- SM--66/60; ISSN 0074-1884, International Atomic Energy Agency (IAEA), 1966, pp. 409–433.
- [30] S. Delpech, C. Cabet, C. Slim, G.S. Picard, *Mater. Today* 13 (12) (2010) 34–41.
 - [31] M. Gibilaro, L. Massot, P. Chamelot, *Electrochim. Acta* 160 (2015) 209–213.
 - [32] V. Ignatiev, A. Surenkov, I. Gnidoj, A. Kulakov, V. Uglov, A. Vasiliev, et al., *J. Nucl. Mater.* 440 (2013) 243–249.
 - [33] H.E. McCoy Jr., Status of materials development for molten salt reactors, in: Oak Ridge National Laboratory, ORNL-TM-5920, Oak Ridge, TN, 1978.
 - [34] V. Afonichkin, A. Bovet, V. Shishkin, *J. Nucl. Mater.* 419 (1) (2011) 347–352.
 - [35] J.M. Dale, Theoretical considerations of the voltammetric in-line determination of U (III), in: MSR Program, Prog. Rep. ORNL-4782, 1972, pp. 80–81.
 - [36] M.W. Rosenthal, P.N. Haubenreich, R.B. Briggs, The development of molten-salt reactors, in: Oak Ridge National Laboratory, ORNL-4812, Oak Ridge, TN, 1972.
 - [37] International Atomic Energy Agency, Status of small reactor designs without on-site refuelling, in: TECDOC-1536, Vienna, Austria, 2007.
 - [38] O. Beneš, R.J.M. Konings, *J. Nucl. Mater.* 377 (2008) 449–457.

This page intentionally left blank

Research reactor fuels

7

Mitchell K. Meyer, Dennis D. Keiser Jr., Jan-Fong Jue and Eric Shaber
Idaho National Laboratory, Idaho Falls, ID, United States

7.1 Introduction

Approximately 250 research and test reactors are used for materials research, education and training, neutron scattering, isotope production, and materials research in 55 countries. This class of nuclear reactors operate over an enormous range of core power densities, ranging from near zero to more than 30 times higher than conventional pressurized water reactors [1]. Because research and test reactors are designed to meet a wide range of needs, a broad spectrum of fuel system designs and material chemistries are used to meet reactor performance objectives; this is most apparent in the class of high-performance research reactors. High-performance research reactors are designed with the overarching goal of producing a sustained high neutron flux focused toward a specific purpose; for example, neutron scattering, material testing, or isotope production. To achieve this goal requires fuel systems designed to operate at power levels and fission densities that exceed the requirements of commercial power reactors. The complex irradiation-enhanced chemical evolution of the fuel with respect to the cladding, noble fission gases, and solid fission products determines the performance and lifetime of these fuels.

A much broader and more numerous class of general-purpose research reactors operate at lower core power density, often at much lower duty factors. These reactors perform a number of tasks such as training, neutron radiography, production of specialty isotopes, and neutron activation analyses. General-purpose reactors often share the same types of fuels with high-performance reactors, although operation at lower power density results in lower fuel operating temperature and much slower chemical kinetics. Many of these reactors can be pulsed at higher power levels for durations of a few tens of milliseconds.

A third class of research reactors focuses on safety testing at very high power. Numbering only a few worldwide, these reactors produce tailored short pulses of tens of gigawatts for a total of a few seconds per year. The fuels required for these reactors are highly specialized, and typically life-limited by mechanical fatigue, chemical evolution being a relatively minor concern.

This chapter provides a brief description of the major categories of research reactor fuel systems. Chemical evolution of the fuel system is most apparent under conditions where the fuel is operating at a high fission rate, and a significant focus is placed on fuels designed for use in higher performance reactors. Chemical

changes brought about by thermomechanical processing determine the initial as-fabricated state, followed by irradiation-enhanced and nonequilibrium processes that reshape the fuel during fission. Since these fuels are most often designed with aluminum cladding, in-reactor corrosion of aluminum is also discussed.

7.2 Fuel geometry

Although there are dozens of reactor configurations, many use similar fuels based on aluminum plates or tubes that contain a dispersion of fuel particles, so-called dispersion fuels. Multipurpose TRIGA (Training, Isotope, General Atomics) reactors were developed around a distinctly different uranium–zirconium hydride (U–Zr–H) fuel system configured into rod-shaped elements that offers safety characteristics inherent to the fuel. Other less numerous reactors were designed around either pin-type dispersion fuel elements or fuel rods containing oxide pellet-type fuel similar in concept to commercial water reactor fuel.

7.2.1 Plate-type fuels

Many reactors fall into the broad class of Materials Test Reactors (MTRs), or similarly configured reactors, and are designed to use fuel elements built around thin aluminum fuel plates. Fuel plates can be fabricated over a wide range of sizes and fuel loadings and assembled in element configurations suitable for operation in a range of applications from 100 kW training reactors to 250 MW test reactors.

Plate-type fuels are thin (typically 1.3 mm thick) sandwich structures consisting of a fueled region (commonly called “fuel meat”) bonded between two layers of aluminum alloy cladding. These fuels are designed with high thermal conductivity materials and a large cladding surface to fuel volume ratio to optimize heat transfer to the coolant. Although plate-type fuels are optimized for use in high-flux (high power density) neutron source reactors and test reactors, many lower flux research reactors also use this fuel because it is robust and commercially available. The fuel meat is composed of a dispersion of fuel particles in an aluminum matrix (Fig. 7.1A). Fuel particle chemistry of current commercial fuels includes uranium oxide ceramics (UO_2 and U_3O_8) and uranium intermetallic compounds (UAl_x , U_3Si , U_3Si_2). Recent development of new high-density uranium fuels has focused on uranium alloy dispersion fuels and a solid metal alloy fuel meat to further increase uranium density (Fig. 7.1B), often called “monolithic” fuel.

Aluminum alloy structural components are used to configure the fuel plates into an array (fuel element) designed to meet specific reactor needs for cooling of the fuel and the geometry of the core. The geometry of a typical plate-type fuel element is shown in Fig. 7.2A, where thin plates are fixed into side plates by mechanical swaging or welding. Fig. 7.2B shows a schematic diagram of curved plates assembled in such a way as to form a cylindrical element [3,5].

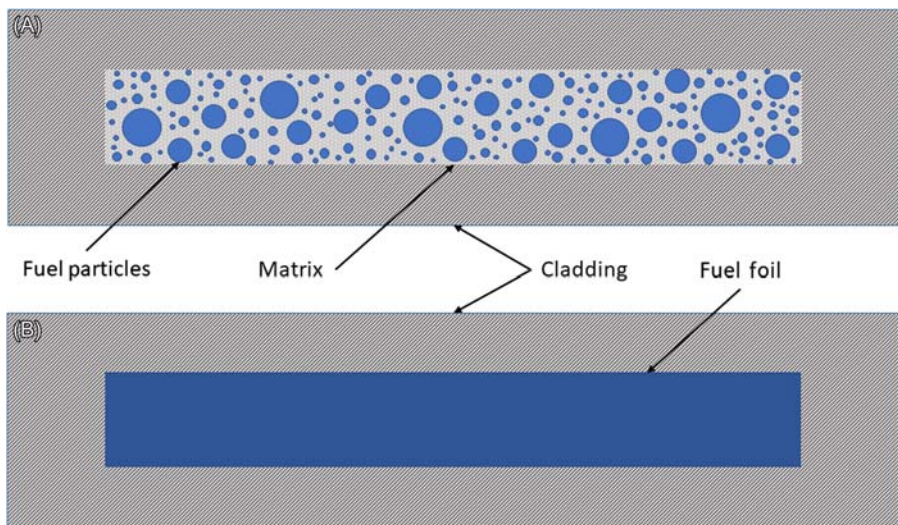


Figure 7.1 Representation of a lateral cross section of (A) plate-type dispersion fuel and (B) plate-type monolithic fuel.

7.2.2 **Tubular fuels**

Tubular fuels are based on concentrically arranging a series of thin-walled aluminum-clad dispersion fuel tubes fabricated by extrusion ([Fig. 7.2C](#)). Very similar to plate-type dispersion fuels, except for the fabrication process, these fuels are often based on dispersions of uranium dioxide (UO_2) in an aluminum matrix and used mostly in Russian-designed research reactors.

7.2.3 **Rod- and pin-type fuels**

Rod- and pin-type fuels are typically sealed metal tubes that encapsulate fuel pellets, slugs, or dispersions. TRIGA reactors represent the most prevalent use of rod-type fuel for research reactors; in this case the cladding tube is stainless steel and the fuel slugs are $\text{UZrH}_{1.6}$ ([Fig. 7.3A](#)).

A few research reactors use uranium dioxide pellets clad in a zirconium alloy, which are based on the design and fabrication processes for commercial power reactor UO_2 fuel.

The NRU (National Research Universal) reactor previously operated in Canada and the HANARO (High-Flux Advanced Neutron Application Reactor) reactor operating in the Republic of Korea use an extruded pin-type fuel consisting of an aluminum-clad, aluminum matrix dispersion of uranium silicide. A picture of the components a fuel pin are shown in [Fig. 7.3A](#), and a cross section is shown in [Fig. 7.3B](#). This fuel design incorporates fins in the extrusion to increase the surface area to enhance convective heat transfer.

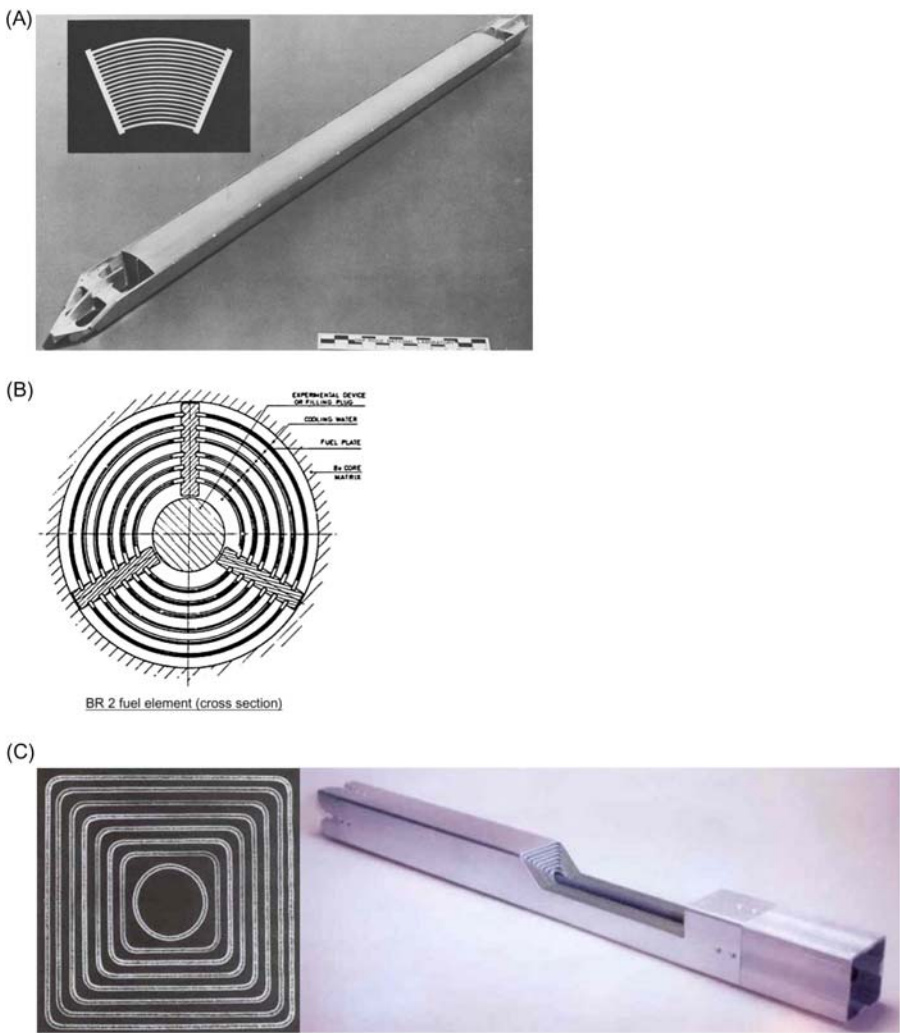


Figure 7.2 Examples of (A) a curved plate-type Advanced Test Reactor [2] fuel element and (B) a cylindrical plate-type BR2 [3] fuel element constructed from formed plates, and (C) extruded IRT-3M element [4] constructed from square tube shapes nested together.

7.3 Fuel materials

Research and test reactors are often optimized around a specific function, such as isotope production, neutron scattering, material testing, or training. The first three functions require high flux, which is proportional to core power density. Beginning in the 1950s, the design of special purpose high-performance reactors evolved continuously to meet the specific needs of individual research institutions. Few, if any,

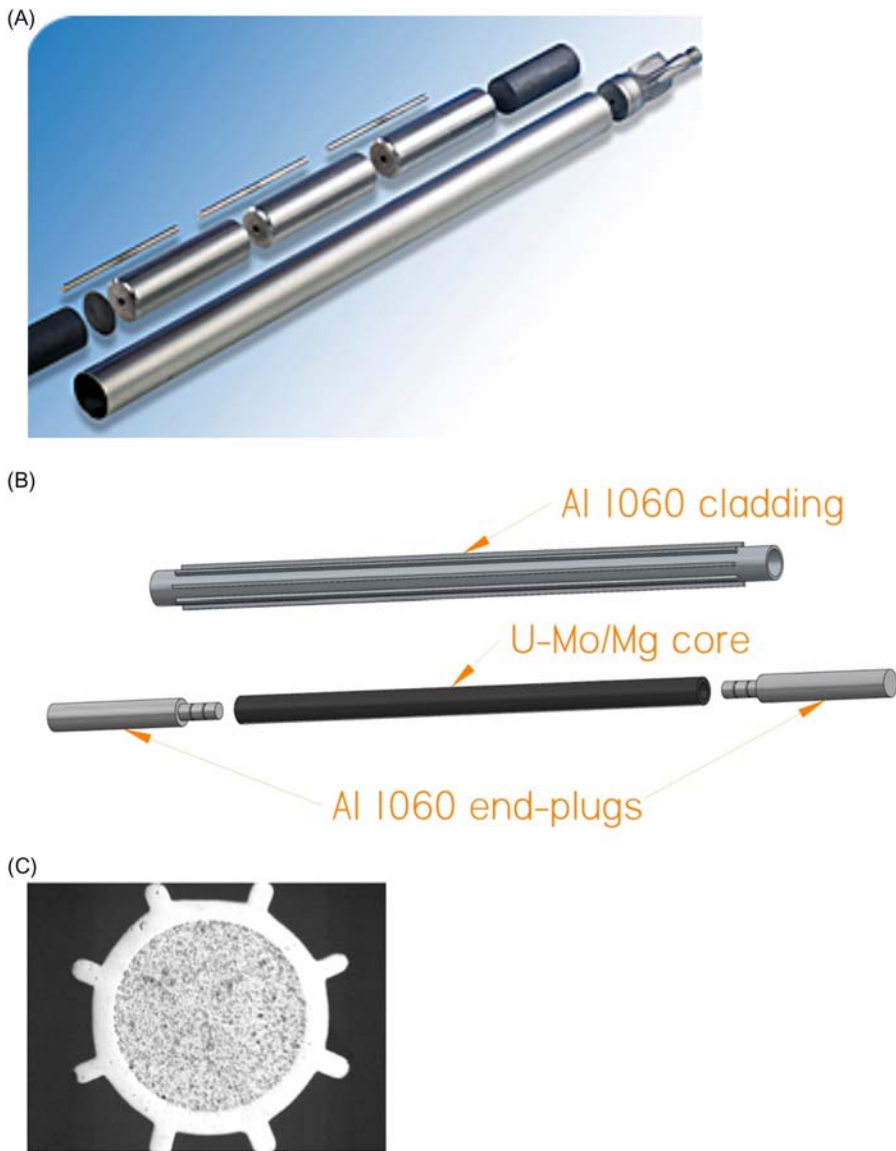


Figure 7.3 Rod-type fuels used in research reactors. (A) Components of U–Zr–H fuel used in TRIGA reactors [6]. The fuel slugs are ~4 cm in diameter. (B) Photograph of extruded pin-type experimental U–Mo/Mg dispersion fuel used to fuel the NRU (National Research Universal) and HANARO reactors. (C) Cross section of extruded U₃Si dispersion fuel rod for the HANARO and NRU reactors [7]. *HANARO*, High-Flux Advanced Neutron Application Reactor.

Source: Copied from M. Kulakov, M. Saoudi, M.H.A. Piro, R.L. Donaberger, J. Nucl. Mater., 484 (2017) 288–296.

Table 7.1 Fuel materials used in research and test reactor dispersion fuels.

Material	Theoretical density (g/cm ³)	Uranium density (g/cm ³)	Maximum possible fission density (f/cm ³) for 19.75 wt. % ²³⁵ U
UAI _x	6.4 ^a	4.5	2.3×10^{21}
U ₃ O ₈	8.4	7.1	3.6×10^{21}
UO ₂	10.9	9.7	4.9×10^{21}
U ₃ Si ₂	12.2	11.3	5.7×10^{21}
U ₃ Si	15.6	15	7.5×10^{21}

^aUAI_x is a mixture of UAl₂, UAl₃, and UAl₄ and varies in density based on composition.

reactors share the same design. Because the desired reactor performance characteristics are closely tied to the design of the fuel system, many different fuel configurations and fuel materials were developed to meet reactor design requirements. Table 7.1 lists fuel materials that have been qualified and are currently used as materials in dispersion fuels.

The density of ²³⁵U atoms in the fuel limits, for a given reactor design, the core power density and peak flux [8]. The ²³⁵U density can be increased by selection of an appropriate high-density fuel material, increasing the volume fraction of the dispersed fuel particles, or by increasing ²³⁵U enrichment. The ²³⁵U enrichment is limited by nonproliferation policies in many countries to less than 20% [9]. Recent developments of new research reactor fuels for conversion of existing reactors to low enrichment and for fueling of new reactors [10] have therefore focused on the development of high-density fuel materials for use in dispersion and monolithic fuels, in particular uranium–molybdenum alloys.

In contrast, multipurpose reactors and training reactors with lower power density often share design characteristics and use similar fuels. Examples of these reactors include the class of mid– to low power density reactors based on the design of the original MTR [11], TRIGA [12] reactors, and the Argonaut [13] training reactors.

7.4 Evolution of research reactor fuel during operation

During its operational lifetime, research reactor fuel must maintain mechanical integrity to prevent release of fission products to the coolant, maintain geometric stability to ensure that the dimensions of coolant channels are within specifications and exhibit stable and predictable behavior over the entire design operating range so that fuel and reactor behavior can be quantitatively predicted. These requirements must be met during the extreme changes in fuel properties brought about by chemical evolution during operation to high burnup, including large changes in solid-state chemistry due to fission, production of large amounts of noble gases, fission-enhanced diffusion, and formation of nonequilibrium phases.

Because the objective of high-performance research reactors is to operate at a high neutron flux and thus high power density, fission rate densities on the order of

$10^{14} \text{ cm}^{-3} \text{ s}^{-1}$ are often required. Operation at these high power densities results in rapid depletion of ^{235}U (months vs. years) relative to commercial power reactors. Research reactor fuels can reach peak volumetric powers in the fuel meat that may exceed 70 kW/cm^3 and fission densities that approach $7.8 \times 10^{21} \text{ f/cm}^3$. Dispersion fuels are ideal for this application, because the fuel design isolates individual fuel particles from each other within a high thermal conductivity matrix. Isolation of particles from one another promotes local retention of fission products, most importantly noble gases, and provides local mechanical restraint to particle swelling.

Fission fragments deposit an immense amount of energy, on the order of 20 keV/nm , into the electronic structure of nuclear fuel material and into the matrix phase over a range of $5\text{--}10 \mu\text{m}$ [14]. Material response to these swift, heavy fission ions depends heavily on the thermal conductivity of the fuel and the coupling between the electronic and lattice structures of the fuel material [15]. In some cases, such as during room temperature irradiation of UO_2 with high energy heavy ions, there are indications of the immediate effects of swift heavy ion damage (ion tracks) that only occur at energies higher than those possible with fission fragments. Other materials respond through the formation of persistent ion tracks with structures and properties different than the base material, in some cases destroying the crystalline structure of the fuel [16]. Electronic energy deposition from fission fragments greatly increases the population of defects (predominantly Frenkel pairs) around the fission fragment trajectory.

Fission-enhanced diffusion results from the increased population of point defects. The effects of fission-driven (athermal) processes compete with thermally driven processes to shape the microstructure and phase array of the fuel. Material undergoing fission is not well described by equilibrium thermodynamics, and phases and solubilities predicted by equilibrium phase diagrams are often modified by the nonequilibrium conditions present during fission. Material systems that are thermodynamically unstable but kinetically limited out-of-pile (such as the reaction of aluminum with U_3O_8) can undergo rapid changes in the presence of high non-equilibrium defect concentrations. New phases that form under these conditions may be benign, detrimental, or even beneficial to irradiation behavior. For example, phase reversion is an important process that ensures predictable swelling behavior of uranium–molybdenum alloy fuel [17] through the low-temperature fission-induced stabilization of the isotropic γ -(U, Mo) phase that only exists in *thermal equilibrium* at temperatures above 565°C (see Section 7.6.4). As another example, at the relatively low fuel operating temperature of U_3Si_2 and U_3Si in dispersion fuel, the thermodynamic driving force for thermally induced crystallization is smaller than the fission-induced driving force for amorphization. This results in the amorphization of these normally crystalline materials at low fission density, and maintenance of the amorphous state during irradiation to high burnup (see Section 7.6.2). There is also strong experimental evidence for amorphization of UAl_x and U_3O_8 at low fission densities during irradiation of research reactor fuel. Amorphization occurs in all four materials mentioned here without significant degradation in fuel swelling behavior under research reactor operating conditions. Other

fuel materials (e.g., U₆Mn and U₆Fe) tested in aluminum-based systems exhibit rapid and unpredictable increases in swelling rate, often referred to as breakaway swelling.

Most research reactors are water-cooled. In order to maintain a sufficient margin to melting for the fuel meat and fuel cladding materials, coolant systems are often operated at temperatures of less than 100°C and slightly elevated coolant pressures (<4 MPa). Peak normal fuel meat operating temperatures are generally less than 250°C for plate-type fuels and 350°C for pin-type dispersion fuels but are highly dependent on the fuel volume fraction in the dispersion. High power densities result in high surface heat flux, which, along with reactor coolant parameters, determines the fuel surface temperature and oxidation rate [18]. Upper and lower bounds of thermal conductivity are often calculated using variations on the method used to calculate the effective magnetic permeability of multiphase materials developed by Hashin and Shtrikman [19]. An auto-coherent model developed by Marelle et al. [20], which allows a smooth transition between the upper and lower bounds, has been shown to be in good agreement with measured values for aluminum matrix dispersion fuels. The thermal conductivity and the resulting fuel temperature of dispersion fuels are largely determined by the volumetric loading of fuel particles in the fuel meat and decrease during irradiation as the volume of fuel/matrix reaction phases increases. Intermetallic phases that form as a result of irradiation-enhanced reaction between fuel particles and the matrix have thermal conductivity values lower than the matrix aluminum that was consumed by the reaction. As these fission-enhanced reactions between the fuel particles and the aluminum matrix proceed, decreases in fuel meat thermal conductivity result in temperature increases that further drive increased rates of solid-state reactions and gas diffusion.

Fission of uranium results in large changes in fuel chemistry. Because every uranium fission event results in the production of two fission product atoms, fission of 80% of the ²³⁵U in 20% enriched material results in a 16 at.% reduction in the uranium content and creation of 32 at.% of new elements. These fission product elements in turn decay to form long-lived fission products including Cs, Sr, Tc, Zr, Mo, I, Pd, Ru, lanthanide elements, and the noble gases Xe and Kr. A U₃Si fuel that began with a composition of 75 at.% U and 25 at.% Si becomes 53 at.% U, 21 at.% Si, and 27% fission products at 80% ²³⁵U depletion. Because the net density of the two fission products is less than that of the fissile atom, solid fission products cause the fuel density to decrease at a constant rate as a function of burnup. There have been few detailed studies on the chemical state and transport of solid fission products in research reactor fuels, perhaps because the behavior of the noble gas fission products dominates the overall fuel behavior and is life limiting.

The behavior of fission gas is critical to the performance of research reactor fuel. Approximately 25% of the fission products are in the form of the noble gases krypton and xenon. High fission density in high-performance reactor fuels results in a larger gas inventory than is typical for commercial oxide fuels. Xenon and krypton are insoluble in solid fuel matrices, and there is a strong driving force for precipitation as gas bubbles. Dispersion fuels have no gas plenum available to collect fission gas, as is the case in commercial power reactor fuels, and the gas therefore remains in solution or in bubbles in the fuel particles. The equilibrium pressure (P)

in a gas bubble is classically defined by the bubble size (r), the intrinsic surface energy of the host matrix (γ_s), and the externally applied hydrostatic stress (σ_h), according to [21]:

$$P = \frac{2\gamma_s}{r} + \sigma_h \quad (7.1)$$

Note that the material parameter γ_s is not well known for most materials of interest to nuclear fuel technologies, and that aluminum-based plate-type fuels offer limited external constraint (σ_h) from the cladding and matrix relative to rod-type dispersion fuels.

As irradiation continues, persistent point defects created by fission events form two-dimensional defect structures (dislocations) that accumulate to form subgrains within the original grain structure, a process referred to as polygonization (because of microstructural similarities to processes in common industrial materials). The subgrain boundaries in turn provide additional nucleation sites for fission gas, linked to a change in the swelling rate as the rate of gas-driven swelling becomes relatively more important than the constant swelling rate from solid fission products. This process is often discussed in the research reactor fuel literature as a “knee” in the swelling curve [22]. The large fission gas inventory produced at high burnup in research reactor fuels is somewhat compensated for by lower operating temperatures that reduce the thermal transport rate of the gas. The precipitation of gas occurs in competition with fission fragment-induced athermal dissolution, termed resolution. Gas resolution has been experimentally observed during irradiation at temperatures relevant to research reactor fuel [23,24]; however, this process not mechanistically understood [25,26] in relation to its effect on fuel swelling rate. As the fission gas inventory continues to increase, gas bubbles grow in size and exceed the equilibrium hydrostatic pressure provided by the surface tension of the fuel phase and other restraining forces (such as coolant pressure or mechanical restraint) and expand at an accelerated rate. This can occur either in the fuel particles or in new phases that form by solid-state reaction between the fuel and the matrix or cladding material through fission-enhanced processes. The increased fuel swelling rate eventually leads to an unacceptable volume increase that decreases the width of the fuel coolant channel or leads to rupture of the cladding, limiting the useful life of the fuel.

7.5 Fabrication processes

Early plate-type fuels were fabricated by casting of multiphase uranium–aluminum metal “alloys,” which were clad in aluminum and hot rolled into plates. Limitations in uranium loading using this fabrication method lead to the development of a powder metallurgy process [27] that resulted in improvements in fuel homogeneity, higher uranium density, and the flexibility in accommodating uranium density gradients

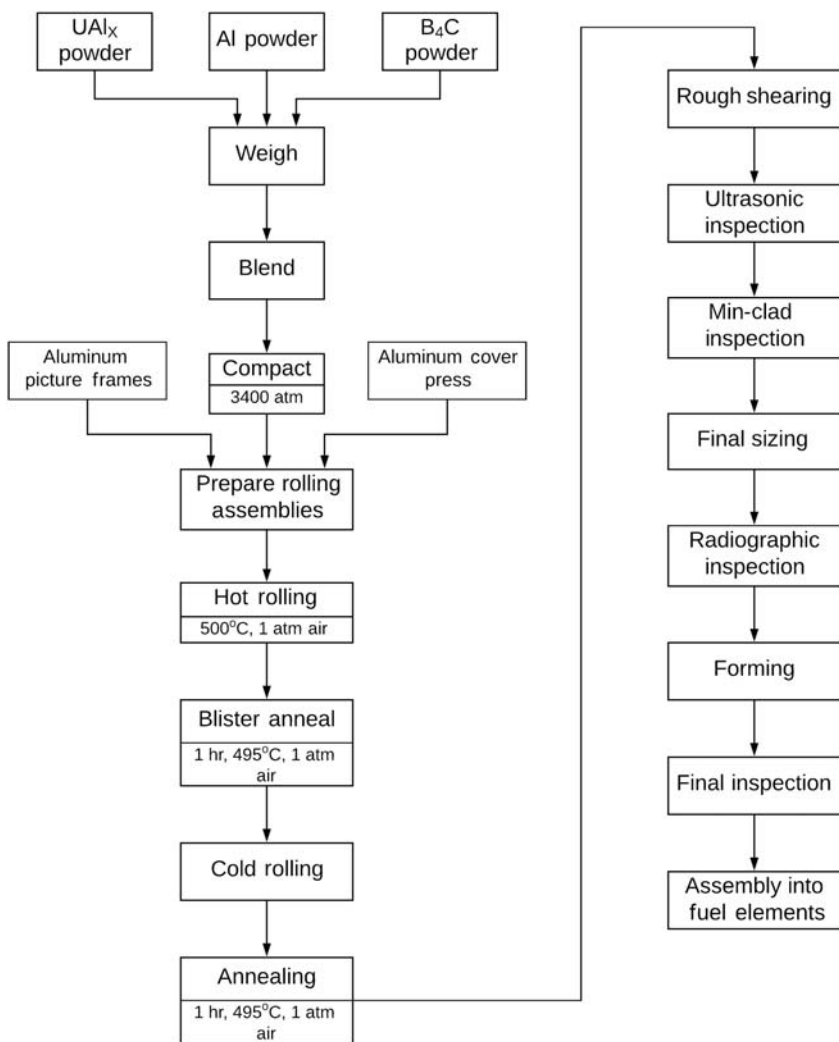


Figure 7.4 Typical process flow for fabrication of aluminum-based, plate-type dispersion fuels.

within fuel plates. The process is illustrated in Fig. 7.4. The fuel material is reduced to powder by comminution of brittle solids or by atomization of ductile materials from the melt, or in the case of oxides, through precipitation reactions. The fuel powder is weighed and mixed with aluminum or aluminum alloy powder, and compacted into a rectangular billet that forms the fuel meat composite. The fuel meat is then placed in a “picture frame” assembly comprised of Al alloy cladding, and the cover plates are attached by perimeter welding to form a rolling assembly. The cleanliness of the aluminum alloy components is critical to successful bonding of the aluminum components; these components are cleaned using mechanical

processes followed by etching in a solution of hot sodium hydroxide and then rinsing in dilute nitric acid. Assembly occurs as quickly as possible after cleaning. A hot rolling process at $\sim 500^\circ\text{C}$ ($\pm 50^\circ\text{C}$) is used to bond the components of the rolling assembly and reduce the thickness of the assembly by a ratio of $\sim 8:1$. Additional cold rolling follows to improve uniformity in thickness, resulting in a finished fuel plate ~ 1.3 mm thick [28]. A similar process is used to fabricate aluminum-based pin-type dispersion fuel [29]. In this case, hot extrusion is used to bond the aluminum cladding to the fuel meat. A unique feature of rod-type dispersion fuels is the use of fins to enhance heat transfer between the fuel and the cladding.

U-Zr-H alloys [30] used in TRIGA reactors are fabricated by alloying and casting uranium-zirconium alloy slugs of the required composition, varying from 8.5 to 45 wt.% uranium [31]. This is shown in Fig. 7.5. Erbium may also be added

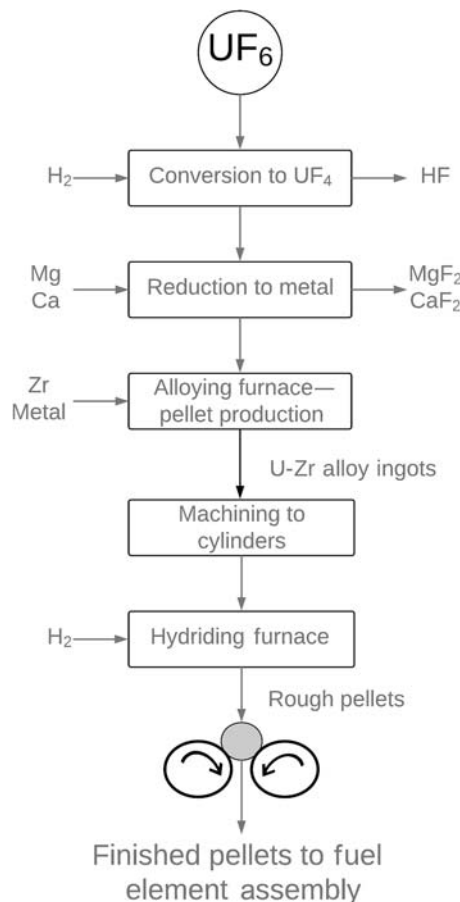


Figure 7.5 Overview of the fabrication process for TRIGA fuels.

as a burnable absorber. The fuel slugs are machined to the correct diameter and exposed to high temperature in a hydrogen atmosphere to form zirconium hydrides within the fuel.

7.6 Fuel behavior under irradiation

The choice of fuel material for use in dispersion fuels has historically depended on the preference of individual reactor design organizations, based on reactor performance, material availability, fabrication infrastructure and expertise, and compatibility with existing fuel cycles. Each fuel material has trade-offs in terms of uranium density, ease of fabrication, and irradiation performance. As reactors convert from high- to low-enriched uranium, the necessity for higher uranium density has driven convergence toward high-density intermetallic fuel phases, such as U_3Si_2 [32], and sparked the development of very high-density concepts based around metallic alloys [33]. In the case of dispersion fuels the irradiation-enhanced chemical interaction between the fuel phase and the matrix, usually aluminum, is unavoidable, and it is essential to consider the in-reactor behavior of the fuel in the context of higher order systems.

In the absence of a gas plenum in dispersion fuel, the interaction of insoluble noble gas fission products with the crystalline lattice (or radiation amorphized material) is critical to the behavior of these materials under irradiation. Fission gas behavior has been studied in terms of the empirical behavior of gas bubbles under neutron [34] and ion [35] irradiation and through simulations but is generally not well understood. Of similar complexity, but lesser importance, is the chemical behavior of solid fission products in the fuel, which has not been extensively treated experimentally or by simulation for most of the fuel systems relevant to research reactors; the majority of work in this area has concerned the fractional release of fission products during postulated reactor events that may result in fuel overheating [36–38].

7.6.1 Uranium aluminides

Uranium aluminide dispersion fuel evolved from the need for higher density fuels than those possible from the use of low uranium content “uranium–aluminum alloys” [39,40] used to fuel early reactors. Uranium–aluminum alloy fuels are not true alloys, but multiphase mixtures of aluminum with low-volume concentrations of intermetallic-phase uranium aluminide formed by casting from the melt. Uranium and aluminum form three stoichiometric compounds, with Al/U ratios of 2, 3, and 4. Because phase-pure stoichiometric aluminides are difficult to produce and readily react with aluminum in the fuel matrix to form a nonequilibrium conglomeration of UAl_2 , UAl_3 , and UAl_4 , the resulting phase array is referred to as UAl_x , and fuel based on this system is specified by the overall uranium mass fraction rather than a specific phase or mixture of phases.

Early work on the development of uranium aluminide dispersion fuel focused on dispersions of UAl_3 in aluminum [41–43]. Significant later work was focused on increasing the fuel meat density utilizing single-phase UAl_2 as the dispersed component [44]. Similar work in this system has focused on the development of high-density uranium aluminide targets for the production of the ^{99}Mo fission product precursor to the widely used medical isotope $^{99\text{m}}\text{Tc}$ [45]. Higher uranium density in low-enriched uranium targets is necessary to obtain isotope production rates comparable to high-enriched targets. The alkaline process commonly used for target dissolution requires the presence of intermetallic-phase aluminide instead of metallic uranium, so these investigations focus on the use of UAl_2 [46]. The use of in-situ intermetallic formation through the reaction of uranium metal with the aluminum matrix has also been investigated [47].

Investigations by Nazare et al. [40] indicate that the in-laboratory reaction between UAl_3 and Al to form UAl_4 is sluggish below 400°C , and that the reaction between UAl_2 and Al also proceeds slowly. These phases are thus thermally stable with respect to the Al matrix at temperatures representative of in-reactor conditions, typically less than 200°C . During irradiation, however, enhanced diffusion moves the fuel material composition toward equilibrium with the aluminum matrix while the uranium concentration is also depleted by fission, and the fuel particles become enriched in aluminum [48]. Postirradiation examination indicates reaction of uranium aluminide fuel particles with the aluminum matrix and the presence of phases with stoichiometry representative of UAl_2 , UAl_3 , and UAl_4 [49].

The activation energies for these reactions were measured to be 220 kJ/mol (UAl_3) and 178.2 kJ/mol (UAl_2). X-ray diffraction and Rietveld analyses indicate that after 7 hours at 540°C , all of the original UAl_2 phase in a target fabricated with (nominally) UAl_2 has been consumed by reaction to form UAl_3 and UAl_4 and that after 10 hours the fuel meat was 90 wt.% UAl_4 [50]. Work by Boucher [51] indicates that the addition of 0.6 wt.% silicon to the aluminum matrix stabilizes the UAl_3 phase for 1000 hours during laboratory heating tests at 600°C , but it is not clear if this stabilization mechanism is operative in-reactor. Similarly, Thurber and Beaver [52] found that 3 wt.% Si, Ge, Zr, Sn, and Ti resulted in nearly complete suppression of the formation of UAl_4 during fabrication of U-Al alloy fuel prior to the development of powder metallurgy dispersion fuels. Extensive analysis of the U-Al-Si system by Dwight [53] indicates complete solubility between isostructural USi_3 and UAl_3 at 900°C ; although it is uncertain whether a miscibility gap occurs at lower temperatures. Later chemical and microstructural analyses indicated that when Si is present above a 1:1 atom ratio with U, it did not have a beneficial effect in suppressing the formation of UAl_4 [54].

During irradiation, UAl_x becomes amorphous at fission densities of less than $2.2 \times 10^{21} \text{ f/cm}^3$, although the fuel particles retain distinct compositional zones characteristic of uranium aluminide crystalline phases. Fission gas is distributed homogeneously within the fuel particles (composition of UAl_x) with a lower concentration in the interaction region ($\text{U}_{0.9}\text{Al}_4$ composition) and an increased concentration at the fuel/aluminum interface [55,56]. No evidence of fission gas bubbles in these phases has been observed using scanning electron microscopy (SEM) [48,49].

or higher resolution transmission electron microscopy (TEM) [56]. The behavior of aluminide fuel during an in-reactor heating event was reported by Leenaers [55]. The lack of detectable fission gas bubbles is hypothesized to be related to trapping of gas in solid solution by the structure of the amorphous material, which has a relatively large free volume. At temperatures above typical UAl_x fuel operating temperatures (i.e., 200°C), fission gas bubbles were observed in the fuel/aluminum interaction layer. The presence of visible clusters of gas bubbles in oxygen rich impurity phases was also noted by Hofman [48].

7.6.2 Uranium silicides

Uranium silicide intermetallics have a higher uranium density than uranium aluminide intermetallics (Table 7.1) and have been important in enabling the conversion of research reactors from the use of high- to low-enriched uranium. Two compounds in this system are used as fuel materials. The higher density compound U_3Si has been used as a dispersed phase in aluminum-based rod-type fuel in several reactors [57]. Although it has a lower uranium density, U_3Si_2 fuel exhibits higher resistance to gas-driven swelling. The SEM micrographs in Fig. 7.6 provide a comparison of the size distribution of gas bubbles in U_3Si_2 and U_3Si ; the smaller gas bubble size distribution at similar fission densities is an indicator of a lower swelling rate. U_3Si_2 has been qualified and is commercially manufactured for reactors that require low-enrichment plate-type fuels [32]. U_3Si has been qualified for use as a rod-type fuel in Canada and Korea.

During fabrication of aluminum-based dispersion fuels, U_3Si_2 exhibits some reaction with the matrix to form a $\text{U}(\text{Si},\text{Al})_3$ phase [58,59]. The rate of reaction is limited by the surface area and mesoscopic defects, such as cracking, present in fuel particles [60]. Recent experimental work reports the formation of a nonstoichiometric U_3Si_2 phase by X-ray diffraction and energy dispersive spectroscopy, slightly enriched in silicon [61] but free of aluminum. Density functional theory and thermochemical calculations [62], however, predict a negligible equilibrium nonstoichiometry range for U_3Si_2 at the peak fabrication temperature of 500°C.

The fundamental irradiation behavior of intermetallic compounds in the $\text{U}_3\text{Si}-\text{U}_3\text{Si}_2$ system is complex with respect to reaction of the silicide intermetallics with the aluminum matrix, the crystalline to amorphous transformation of the fuel, and the behavior of noble fission gases. During irradiation, radiation-enhanced diffusion allows the low-temperature growth of the fuel/matrix reaction layer. The layer increases in thickness, becomes amorphous [63], and deviates in stoichiometry from $\text{U}(\text{Al},\text{Si})_3$. Different $(\text{Si} + \text{Al})/\text{U}$ ratios measured for the interaction layer in U_3Si_2 are observed as ~ 4.6 at a fuel particle fission density of $4.8 \times 10^{21} \text{ f/cm}^3$ using electron microprobe [64], 5.3 over a range of fission density from 1.7 to $14.3 \times 10^{21} \text{ f/cm}^3$ estimated from the interaction layer thickness and density [65], and 6.5–9.3 for a fission density of $5.4 \times 10^{21} \text{ f/cm}^3$ using TEM [66]. The reduction in stoichiometry is consistent with the reduction in uranium concentration as it is depleted by fission.

During irradiation at temperatures typical for research reactor fuel (<200°C), U_3Si [67] rapidly undergoes a crystalline to amorphous transformation at a fission

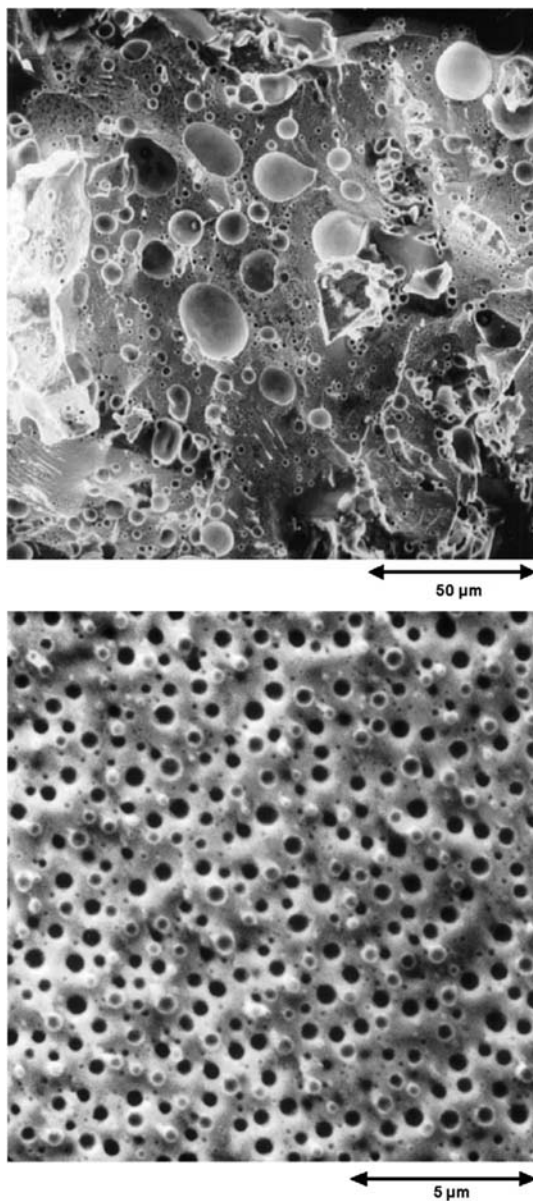


Figure 7.6 Comparison of the microscopic swelling behavior of U₃Si (top, 4.3×10^{21} f/cm³) and U₃Si₂ fuel (bottom, 5.2×10^{21} f/cm³) irradiated in aluminum plate-type dispersion fuel. The smaller size distribution of gas bubbles in U₃Si₂ relative to U₃Si is an indicator of improved resistance to gas-driven swelling.

Source: M.R. Finlay, G.L. Hofman, J.L. Snelgrove, Irradiation behaviour of uranium silicide compounds, J. Nucl. Mater. 325 (2004) 118–128.

density between 0.85 and 1.1×10^{23} f/m³. Amorphization is preceded by significant *a*-axis expansion and a slight *c*-axis contraction of the tetragonal (I4/mcm) unit cell, resulting in a maximum volume expansion of the lattice of $\sim 1.6\%$, indicated by neutron diffraction measurements of the lattice parameters [68]. The measured bulk volume change is 2.0% [66]. The anisotropic volume change results in plastic deformation and mechanical strain, driving a simultaneous strain-induced transformation of the remaining crystalline phase from the tetragonal equilibrium structure to the closely related high-temperature cubic (Cu_3Au) structure, which is complete at a fission density of 0.35×10^{23} f/m³, a damage level where $\sim 10\%$ of the crystalline phase remains in an amorphous matrix. The same amorphization behavior occurs under heavy ion irradiation (1.5 MeV Kr), at a roughly equivalent atomic displacement parameter (displacements per atom ~ 0.5) as fission. The critical temperature above which ion-induced amorphization will not occur is 290°C, congruent with results of in-pile irradiation at temperatures above 375°C [69].

Similarly, U_3Si_2 also undergoes a complete fission-induced crystalline to amorphous transformation at approximately the same fission density (1.1×10^{23} f/m³) as U_3Si [70]. The critical temperature above which ion-induced amorphization will not occur is $\sim 250^\circ\text{C}$, slightly lower than that of U_3Si . In the case of U_3Si_2 the *a*-axis of the tetragonal (P4/mbm) unit cell exhibits a large contraction and the *c*-axis contracts slightly, resulting in a net unit cell density increase of 2.2%, in contrast to the 2.3% density decrease exhibited by U_3Si under the same conditions. TEM examination indicates occasional nanocrystalline grains of less than 10 nm at 5.4×10^{21} f/cm³.

Although both U_3Si and U_3Si_2 become amorphous at low fission density, the differing fission gas behavior of these fuels is dominated by other factors not well identified. U_3Si exhibits a high unconstrained swelling rate caused by the coalescence and growth of noble gas bubbles (Fig. 7.6), although it behaves acceptably when constrained in pin-type form at higher temperature. Several other compounds exhibit similar high swelling behavior, including U_6Fe , U_6Mn , and U_3SiAl (Fig. 7.7). Attempts to link this behavior to a physical or thermodynamic parameter [71] have not been successful. It is possible that the propensity for this behavior is related to a high degree of plasticity in the fuel during irradiation, as indicated by postirradiation micrographs that indicate extreme plastic flow associated with gas bubble coalescence in failed fuel specimens [72]. Note that the fuel exhibits brittle behavior when not under irradiation.

In contrast, U_3Si_2 exhibits stable and predictable swelling behavior to high fission density at lower powers and temperatures (~ 140 W/cm² and $\sim 130^\circ\text{C}$) [73] when unconstrained. Analysis of bubble populations in U_3Si_2 indicated that the number density of bubbles is high and occurs in a narrow distribution as they first become observable in an SEM image, potentially indicating a widespread nucleation event. As fission density increases from 2.8 to 4.6×10^{21} f/cm³, the number density of bubbles decreases by a factor of four while the size distribution broadens and moves to larger diameter, indicating the possibility of bubble growth by gas transport through the matrix, bubble coalescence, or radiation-induced changes in surface energy. At a slightly higher fission density (5.1×10^{21} f/cm³), a new population of small bubbles forms with high number density, indicating a second

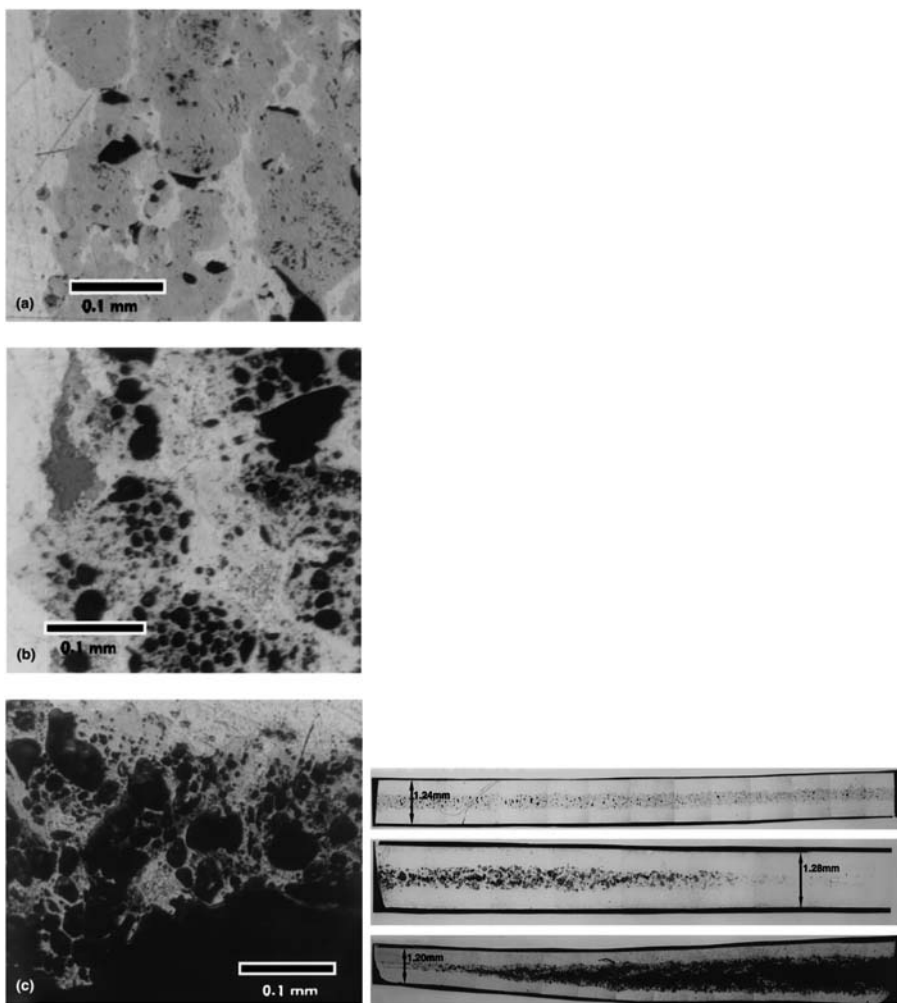


Figure 7.7 Example of breakaway swelling behavior, here observed in U_6Mn fuel. Microscopic behavior (left), macroscopic behavior (right). Transition from incipient behavior (top), growth and coalescence of fission gas bubbles (center), and delamination (bottom).
Source: M.K. Meyer, T.C. Wienczek, S.L. Hayes, G.L. Hofman, Irradiation behavior of $\text{U}_6\text{Mn}-\text{Al}$ dispersion fuel elements, *J. Nucl. Mater.* 278 (2000) 358–363.

widespread nucleation event, while the original population of (now) larger bubbles continues to grow in size and decrease in number. Analysis of the gas stored in the bubbles using a classical force balance (Eq. 7.1) estimates that a relatively small fraction (10–30 mol.%) of the gas is present in bubbles, indicating that a substantial amount must be stored in the lattice structure or smaller gas bubbles, since no gas release to a plenum occurs in this fuel configuration. TEM examination at a

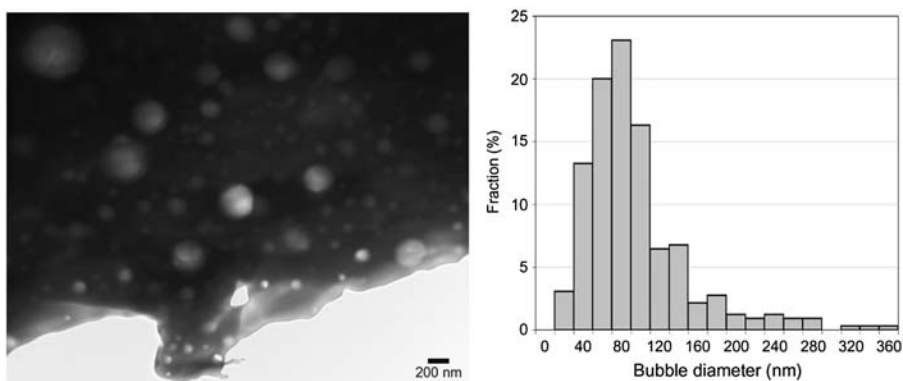


Figure 7.8 Distribution of nanoscale fission gas bubbles in U_3Si_2 at a fission density of $5.4 \times 10^{21} \text{ f/cm}^3$.

Source: J. Gan, D.D. Keiser Jr., B.D. Miller, J.-F. Jue, A.B. Robinson, J.W. Madden, P.G. Medvedev, D.M. Wachs, Microstructure of the irradiated $\text{U}_3\text{Si}_2/\text{Al}$ silicide dispersion fuel, *J. Nucl. Mater.* 419 (2011) 97–104.

slightly higher fission density ($5.4 \times 10^{21} \text{ f/cm}^3$) reveals a distribution of nanoscale bubbles that is not visible in SEM, as shown in Fig. 7.8, with an average size of 94 nm and number density of $\sim 1.1 \times 10^{20} \text{ m}^{-3}$ [63]. An additional identified population of bubbles of $\sim 2 \text{ nm}$ in size may indicate that a periodic sequence of bubble precipitation and growth occurs. Irradiation of materials at different fission rates results in an inverse relationship between the calculated volume of fission gas present in bubbles and the fission rate, pointing to the substantial role that fission-induced gas resolution may play in the behavior of U_3Si_2 .

Out-of-pile studies on the behavior of the primary solid fission products in U_3Si_2 show that there is little solubility for these elements in the U_3Si_2 matrix, with the exception of 1.2 wt.% Zr [74]. Molybdenum exhibits ~ 0.1 wt.% solubility in the Al matrix, the remainder precipitating in U_3MoSi_2 phases. Ruthenium partitions between U_3MoSi_2 and URuSi precipitates, while palladium and rare earth elements (RE = Nd, Ce, La, Pr, Y) form (RE, Pd)Si precipitates. Information on the behavior of fission products generated during irradiation is mostly anecdotal, for example, observation of clusters of variable composition Ru–Al–Si–Mo precipitates associated with aluminum-filled cracks in U_3Si_2 particles that formed during fuel plate fabrication [63].

7.6.3 Uranium oxides

U_3O_8 was investigated along with UO_2 and UAl_x [27] in the late 1950s to fuel isotope and test reactors being designed to operate at very high flux. U_3O_8 was selected as the fuel for the High-Flux Isotope Reactor [1,75] based on higher uranium density relative to uranium alloy fuel and the lack of reaction between the aluminum matrix and fuel particles during fabrication that occurs in UO_2 [76,77].

Used as the fuel for the majority of commercial nuclear power reactors, uranium dioxide (UO_2) is also used as the fuel phase in aluminum-based dispersion fuels used in Russian-designed reactors, and to a lesser extent as a rod-type fuel based on commercial fuel design used in a few low power density research reactors. The fuel fabrication process developed in Russia uses coextrusion instead of rolling to avoid the fuel/matrix reaction issue. Although little information is available in the open literature about the behavior of the UO_2 fuel phase at temperatures less than 200°C, Chapter 11, In-reactor behaviour, provides a comprehensive treatment of UO_2 used in commercial power reactors at higher temperatures.

Unlike the intermetallic and metal alloy fuels discussed here, which are produced by processes based on reactions between molten metals, U_3O_8 has been produced by a variety of chemical and solid state processes, including the oxidation of UO_2 [78] and precipitation from uranyl nitrate [79]. The morphology and mechanical integrity of the fuel particle is important in preventing fracturing during fabrication that leads to an excessive level of fuel meat porosity [80]. A typical process for the production of U_3O_8 consists of oxidation of uranium metal in air and oxygen to U_3O_8 , dissolution of the oxide in nitric acid, precipitation of uranium peroxide from the uranyl nitrate solution at a pH of 2, and calcination in nitrogen at 800°C to produce U_3O_8 powder [81,82]. The calcined U_3O_8 is then sized by sieving, sintered (hard-fired) at a peak temperature of 1400°C, and resized.

During fabrication, little reaction of this U_3O_8 powder with the matrix occurs at temperatures up to 590°C for ~1 hour [83]. At longer times above ~500°C, U_3O_8 reacts with Al to first form UO_2 and aluminum oxide; the UO_2 is then reduced successively to UAl_2 , UAl_3 , and UAl_4 [84–88]. The extent of the reaction depends on the stoichiometry of the reactants, the temperature of the reaction, particle surface area, and the time at temperature. The reaction products have a higher density than the reactants, resulting in a net volume decrease that may partially offset fission-induced swelling.

Of past concern in the U_3O_8 –Al system during fabrication and operation was the potential for a self-propagating high-temperature aluminothermic reaction during fabrication or high-temperature off-normal events during irradiation [89–92], which peak in reaction enthalpy in the uranium density range of interest for research reactor fuels. Measurements of the reaction enthalpies by differential scanning calorimetry indicate a temperature for initiation of the self-propagating reaction above 900°C [87] and energy of 74 J/g for 79 wt.% U_3O_8 in Al, 243 J/g for a clad sample containing 45 wt.% U_3O_8 , and 71 J/g for a clad sample containing 35 wt.% U_3O_8 . For reference, the enthalpy of melting of pure aluminum is 397 J/g. Heating of miniature fuel plates above 900°C showed that although the cladding melted, the fuel meat remained intact. Testing using nuclear heating in the Transient Reactor Test facility indicated similar behavior [93], and the conclusion is that this reaction is not detrimental during fabrication and normal operation and does not significantly change the behavior of the fuel during a high-power operational transient.

During irradiation at low temperature, reaction of U_3O_8 fuel particles with the aluminum matrix increases primarily as a function of temperature [94,95]. As U_3O_8

reacts with aluminum, the apparent particle size (original particle + reaction products) increases by a factor of three or more as the matrix is consumed and reaction products form [42]. Similar to U_3Si_2 , U_3O_8 becomes amorphous at very low fission densities, as does Al_2O_3 [96], so that the evolution of phases under irradiation is not quantifiable using diffraction methods. Investigations using SEM and Auger electron spectroscopy tentatively identified the presence of UAl_4 , Al_2O_3 , UO_2 (or possibly U_4O_9), and a U_3O_8 phase containing aluminum [97]. Analysis of the volume change on reaction provides the same result [43]. At irradiation temperatures less than 65°C , the reaction of U_3O_8 with aluminum does not reach completion; complete reaction occurs relatively rapidly at temperatures in excess of 170°C . The net mass density of the reaction products is higher than that of the reactants, and in the case of a complete reaction, the fuel particles shrink ~ 7 vol.% and separate from the aluminum matrix (Fig. 7.9).

At low particle loadings, low temperature, and low burnup, sufficient aluminum matrix remains so the reacted fuel particles remain dispersed and separated by a relatively thick layer of aluminum. At higher fuel particle loading and under irradiation conditions where reaction of the particles with the matrix is complete, fissures can form through interconnection of regions where aluminum is completely depleted. When filled with fission gas, these fissures offer little mechanical resistance to expansion of the gas volume, which may propagate to join with other fissures, and form large areas of separation. The inherently high swelling of amorphous Al_2O_3 under irradiation may also contribute to this behavior. Fission gas bubbles in the reaction product were found to be in the size range of

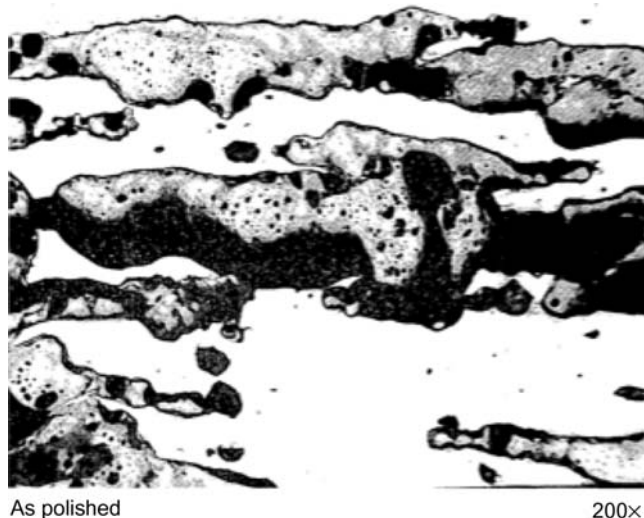


Figure 7.9 Microstructure of U_3O_8 showing separation of fuel particles from matrix at a fission density of $1 \times 10^{21} \text{ f/cm}^3$ and peak irradiation temperature of 206°C .

Source: M.J. Gruber, G.W. Gibson, V.A. Walker, W.C. Francis, Report IDO—16958, 1964.

0.5–0.7 μm , with indications of coalescence into larger bubbles at fission densities near the failure threshold ($5.7\text{--}7.3 \times 10^{20} \text{ f/cm}^3$), which indicates a transition to a higher swelling rate.

7.6.4 Uranium–molybdenum alloys

Although not a qualified fuel system for research reactors, much research and testing has been conducted on the U–Mo/Al system to understand the behavior of this fuel under the challenging conditions required for operation of high-performance research reactors. To transition to the use of low-enrichment fuel, high-performance research reactors require fuel material with uranium densities on the order of 16 g U/cm³ that exhibit stable swelling, maintain geometric stability and mechanical integrity at high-power density (surface heat flux $>450 \text{ W/cm}^2$) to fission densities of $7.8 \times 10^{21} \text{ f/cm}^3$. Only a few candidate materials meet the aforementioned uranium density requirements. Of those materials, most can be ruled out on the basis of unsuitable irradiation behavior, for example, breakaway swelling behavior in U₆Mn [98] and U₆Fe [71] and incipient breakaway swelling behavior in U–Nb–Zr alloys [99]. In contrast, uranium–molybdenum alloys containing more than 7 wt.% molybdenum have sufficient uranium density and have exhibited stable irradiation behavior to fission density in excess of 10^{22} f/cm^3 [33,100].

According to the U–Mo phase diagram shown in Fig. 7.10, U–Mo alloys with less than 33 at.% Mo (~16 wt.% Mo) exist in thermodynamic equilibrium as a two-phase mixture of orthorhombic α -U and the U₂Mo intermetallic phase [101,102] at typical research reactor fuel operating temperatures. α -U exhibits dramatic anisotropic growth during fission [103] and is not suitable for use as a research reactor fuel material. On cooling through the high-temperature body-centered-cubic γ -phase, however, transformation to the equilibrium phases is sluggish, and the γ -(U,Mo) solid solution phase can be maintained as a metastable phase at room temperature. The thermal decomposition rate of the γ -phase is a function of the Mo concentration in the alloy, with alloys containing 10 wt.% Mo requiring an incubation period of ~8 hours at 500°C (Fig. 7.11) before equilibrium phases are detected [106–109]. Reducing the Mo content to 8 wt.% results in a substantial decrease in time to start of detectable decomposition, to less than 1 hour.

Metastability of the γ -(U,Mo) phase allows fabrication of aluminum-based fuel plates to proceed with minimal reaction of the fuel with the matrix material, in contrast to the more rapid reaction of α -U with Al [110]. This metastability also enables fission-induced phase reversion, whereby fission fragment interactions within the U–Mo alloy drive material in the equilibrium α -U + U₂Mo phase field to the nonequilibrium γ -(U, Mo) solid solution. Phase reversion is fission rate, composition, and temperature dependent but occurs in the parameter space required for operation of most research reactors, and the alloy remains in the γ -(U,Mo) phase during irradiation. Fission spikes have the effect of remixing and locally quenching the lamellar structure of the equilibrium alloy composition, forcing reversion of the two-phase as-fabricated microstructure back to the single γ -(U, Mo) phase as shown

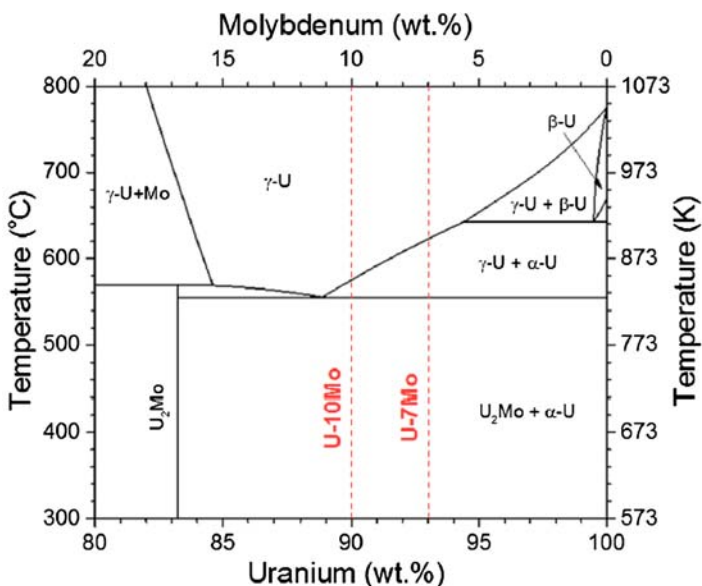


Figure 7.10 Uranium-rich region of the binary U–Mo phase diagram. Typical compositions considered for research reactor fuels are U-7 and U-10 wt.% molybdenum. Aluminum-based research reactor fuel operates at temperatures <250°C.

Source: M. Kulakov, M. Saoudi, M.H.A. Piro, R.L. Donaberger, J. Nucl. Mater., 484 (2017) 288–296.

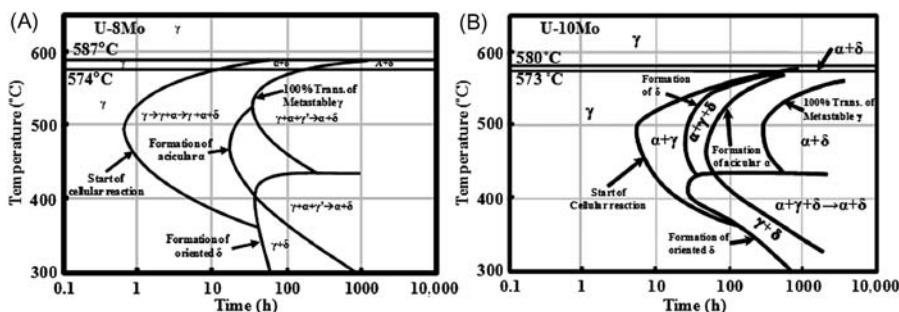


Figure 7.11 Time–temperature–transformation diagrams for (A) U–8 wt.%Mo [104] and (B) U–10 wt.%Mo [105].

by X-ray diffraction (Fig. 7.12) [111], metallography [26], and electrical resistivity measurements [112].

During irradiation testing, the γ -(U,Mo) phase has been found to be stable against breakaway swelling under irradiation to high fission density. This fuel exhibits the formation of a fission gas bubble superlattice (GBS) [113,114] whereby the insoluble fission gas precipitates in an ordered superlattice of nano-size bubbles. This phenomenon has been experimentally observed in alloys with

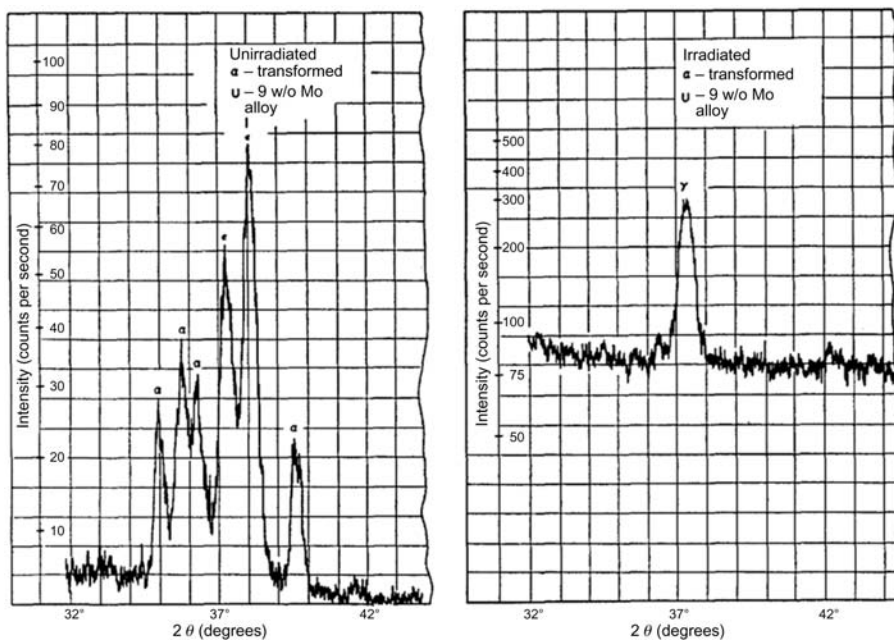


Figure 7.12 X-ray diffraction data for a U–9Mo alloy before and after irradiation demonstrating phase reversion ($\alpha + \gamma' \rightarrow \gamma$).

Source: M.L. Bleiberg, L.J. Jones, and B. Lustman, Phase changes in pile-irradiated uranium base alloys, J. App. Phys. 27 (1956) 1270–1283.

>7 wt.% Mo content but may also occur in γ -(U,Mo) alloys with slightly lower Mo content. The face-centered-cubic nanobubble superlattice develops on the underlying γ -(U,Mo) body-centered-cubic structure. Analysis of U–7Mo, using TEM, shows that the GBS has developed at a fission density of 1.4×10^{21} f/cm³. Fig. 7.13 shows the superlattice observed in U–10Mo at a fission density of $\sim 4.5 \times 10^{21}$ f/cm³ with an average bubble size of ~ 3.5 nm and superlattice constant ~ 11.1 nm. In situ heating of irradiated U–10Mo fuel in the TEM suggests that the fission GBS is thermally stable [115] after exposure to high temperatures (500°C–846°C) for an accumulated time of 80 minutes.

At low fission density the formation of the fission GBS proceeds in parallel with the precipitation of larger gas bubbles on grain boundaries and low-molybdenum cell boundaries that result from solidification from the melt. Fig. 7.14 shows images of the fuel microstructure as a function of increasing fission density that illustrates the progression of gas bubble growth from grain boundaries into the interior of the grains [116] as recrystallization proceeds along the same path. At fission densities greater than $\sim 3 \times 10^{21}$ f/cm³, subgrains of 100–300 nm in size begin to form by polygonization [117,118], as shown in Fig. 7.15 [119]. The formation of a higher density of grain boundaries is associated with an increase in fuel swelling rate caused by an increase in the number of grain boundary nucleation sites available

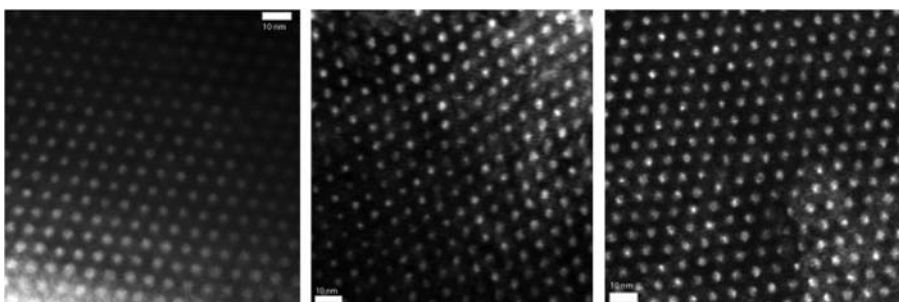


Figure 7.13 TEM micrograph of the fission gas bubble superlattice present in the intragranular regions of U–Mo alloy fuel at progressively higher fission densities. (A) $3.0 \times 10^{21} \text{ cm}^{-3}$, (B) $3.3 \times 10^{21} \text{ cm}^{-3}$, and (C) $4.5 \times 10^{21} \text{ f/cm}^3$. The average gas bubble size for these three fission densities is $3.4 \pm 0.5 \text{ nm}$, and the average gas bubble superlattice constant is 11.7 nm . *TEM*, Transmission electron microscopy.

Source: B.D. Miller, J. Gan, D.D. Keiser Jr., A.B. Robinson, J.F. Jue, J.W. Madden, P.G. Medvedev, Transmission electron microscopy characterization of the fission gas bubble superlattice in irradiated U–7 wt%Mo dispersion fuels, *J. Nucl. Mater.* 458 (2015) 115–121.

for precipitation of fission gas and decreased distances for gas diffusion to bubbles [120]. At very high fission density ($9 \times 10^{21} \text{ f/cm}^3$), the GBS is replaced by population of larger gas bubbles, presumably through coalescence of the nanoscale GBS bubbles [118].

During operation of a U–Mo dispersion fuel with Al matrix at the high–power density required for high-performance research reactors and the high particle loading in the matrix (> 50 vol.%), the majority of the matrix aluminum is consumed by reaction with the γ -(U,Mo) particles to form a continuous (or nearly so) (U,Mo) Al_x amorphous phase of variable composition [114,121]. This continuous amorphous phase is mechanically weak, exhibits plasticity under irradiation, and provides a potential path for long-range transport of fission gas. The growth of the interaction layer sweeps fission gas to the (U, Mo) Al_x /Al interface, where it accumulates in crescent-shaped cavities [122]. The combination of a weakened matrix phase and fission gas accumulation results in loss of mechanical integrity of the fuel meat, resulting in delamination-type failures referred to as “pillowing” in plate-type fuels at a fission density of $\sim 2.5 \times 10^{21} \text{ f/cm}^3$. This behavior also occurs at higher temperature in pin-type fuels, as shown in Fig. 7.16. Pillowing behavior has been demonstrated not to occur in fuel operating at a lower surface heat flux of less than 188 W/cm^2 to very high burnup ($> 6.5 \times 10^{21} \text{ f/cm}^3$) during large-scale testing [124].

A decrease in the formation rate of the unstable (U,Mo) Al_x phases under high-power irradiation can be achieved by altering the aluminum matrix chemistry (e.g., by adding Si to the Al) [111]. By altering the Al matrix composition, energetically and kinetically favorable alternative reaction phases can form that have improved stability under irradiation. Extensive work has been focused on modifications to the chemistry of the aluminum matrix. Silicon is experimentally known

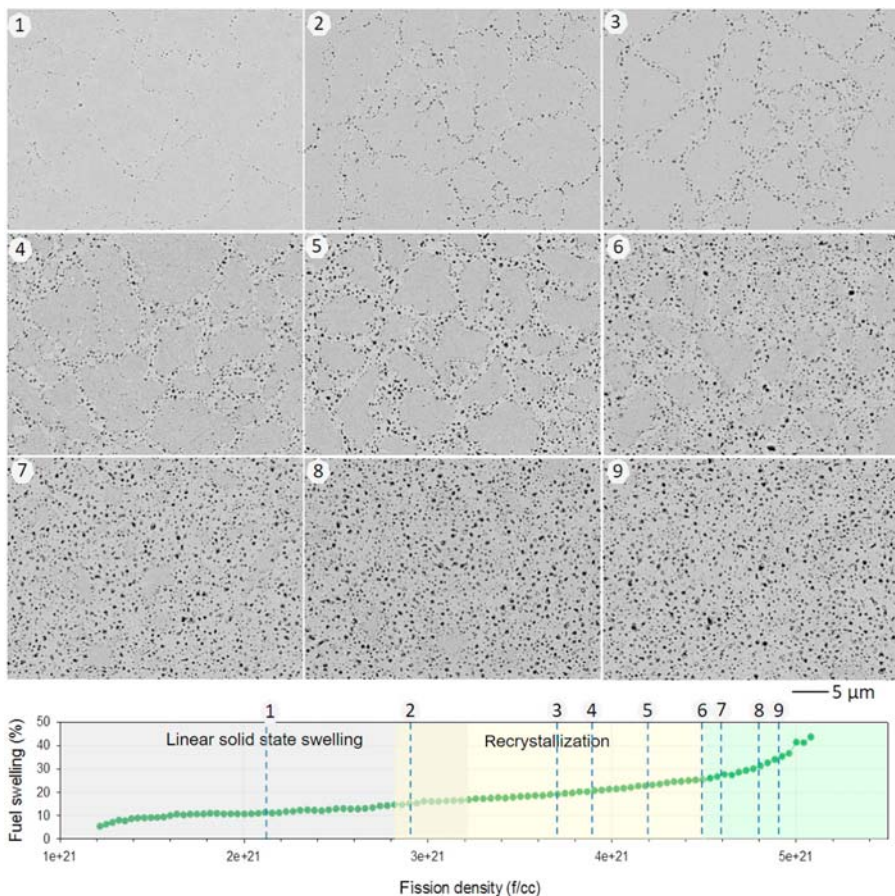


Figure 7.14 BSE images (1-9) showing the microstructural evolution for a U-7Mo fuel plate irradiated in the SELENIUM experiment. The bottom graph shows the location of each image on a plot of swelling for this fuel plate.

Source: A. Leenaers, W. Van Renterghem, S. Van den Berghe, High burnup structure of U(Mo) dispersion fuel, J. Nucl. Mater. 476 (2016) 218–230.

to slow the interdiffusion of α -U and Al [125,126], and this is also true of γ -(U,Mo) and Al.

Experimental measurements of the heat of the formation of USi_x/Al indicate a more negative enthalpy of the formation of $(\text{U},\text{Al})\text{Si}_3$ as the ratio of Si/Al is increased [127]. Measurements of the kinetics of the formation of silicide and aluminide intermetallic phases using thin films have been performed [128] to measure the order of formation and apparent activation energies for diffusion-limited formation of aluminide and silicide intermetallic phases on a U-Mo substrate. Thermal testing verifies that a silicon-rich reaction layer forms that impedes the formation of aluminum-rich phases [129,130]. Irradiation testing has confirmed that additions of

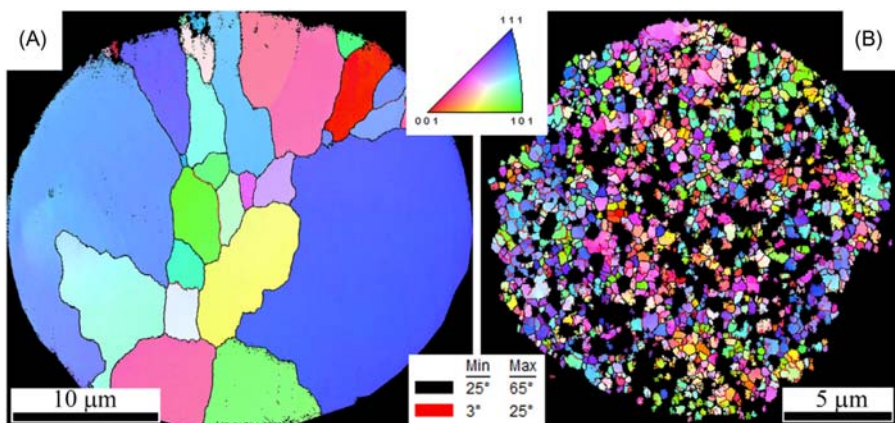


Figure 7.15 (A) EBSD of an as-fabricated U–Mo fuel particle showing grain size from 2 to 10 μm. (B) EBSD pattern of U–Mo fuel irradiated to a fission density of $5.3 \times 10^{21} \text{ cm}^{-3}$ showing a grain size of $\sim 0.3 \mu\text{m}$. *EBSD*, Electron backscatter diffraction pattern.
Source: D. Jadernas, J. Gan, D.D. Keiser, J. Madden, M. Bachhav, J.-F. Jue, A.B. Robinson, Microstructural characterization of as-fabricated and irradiated U-Mo fuel using SEM/EBSD, *J. Nucl. Mater.* 509 (2018) 1–8.

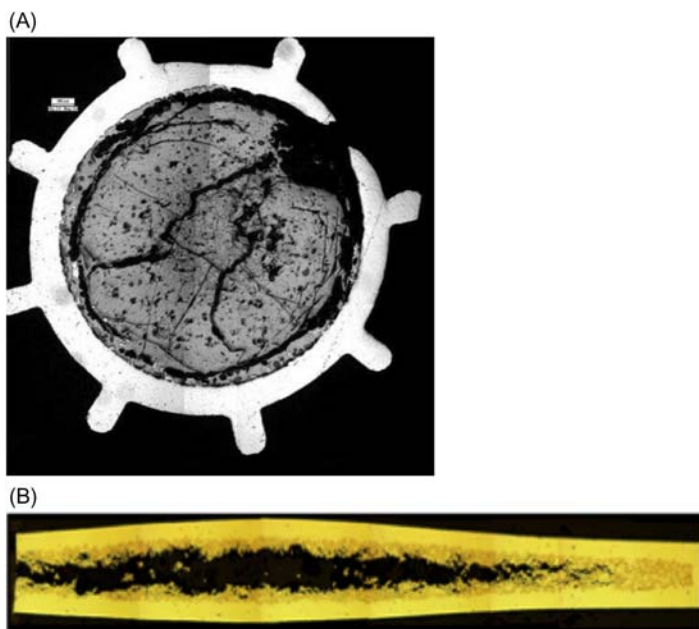


Figure 7.16 Failures in (A) U–Mo pin-type [123] and (B) plate-type [122] aluminum matrix dispersion fuel.

silicon to the matrix of 6 wt.% extended fuel lifetime to beyond 4.5×10^{21} f/cm³ [131,132] at a maximum heat flux of 465 W/cm² before pillowing-type failure occurred at the location of peak power on the fuel plate.

Surface engineering of fuel particles through application of thin coatings of Si (0.6 μm) resulted in further improvements in behavior through the localization of Si at the U–Mo/Al interface, resulting in retarded development of interaction phase formation at fission density below 4.5×10^{21} f/cm³ [133], although similar interface behavior manifested at higher fission density. Surface engineering by sputter coating with a thin layer of ZrN (1 μm) that acts as a diffusion barrier eliminated the majority of U–Mo/Al reaction to a fission density of 4.5×10^{21} f/cm³. In the absence of a deformable interdiffusion layer, swelling of the U–Mo alloy results in rupture of the Al matrix. Both types of surface engineered plates undergo accelerated macroscopic thickness increases in the fission density range of $5.0\text{--}5.5 \times 10^{21}$ f/cm³, although no delamination-type failure occurs. The consistent macroscopic swelling behavior for fuel plates and the rapid change in microstructural evolution at fission densities of 4.5×10^{21} f/cm³ for different approaches to control (U,Mo)Al_x phase formation indicate that secondary processes related to the intrinsic behavior of U–Mo and its interaction with the aluminum matrix may limit the achievable peak fission density [134].

An alternative approach to eliminating deleterious (U,Mo)Al_x phases in U–Mo dispersion fuels is through a complete change in the elemental chemistry of the matrix phase (e.g., substituting Al with Mg or Zr). U and Mo have low mutual solubility with Mg in the solid and liquid state. No evidence of reaction or chemical interaction of U–Mo with Mg is detectable using TEM to a fission density of 5.5×10^{21} f/cm³, although intermixing of U and Mg occurs in the zone outside of the particle affected by fission fragment recoil [135]. No fission gas bubbles were detected in the Mg matrix phases [136]. Interconnected fission gas bubbles that were observed resulted in some transport of solid fission products to the U–Mo/Mg interface. The presence of these fission products did not result in the presence of large porosity at the U–Mo/Mg interface. Complex but stable interaction layers develop at the interface of the Mg matrix with the aluminum alloy fuel cladding consisting of Al₃Mg₂ and Al₁₂Mg₁₇ along with precipitates of MgO, Mg₂Si, and FeAl_{5.3} that form from elements present in the cladding alloy [136,137].

Complete elimination of the matrix provides another alternative to managing detrimental fuel/matrix chemical and mechanical interactions [138], resulting in a “monolithic” fuel meat composed of a solid foil of U–Mo alloy. This configuration has the advantage of the highest possible fuel density but relies on the structural properties of the U–Mo fuel phase to maintain fuel integrity at high burnup. The formation of the (U,Mo)Al_x phase is limited to the interface of the fuel with the cladding material, where they exhibit behavior similar to that described earlier [139], resulting in the need for modification of the fuel/cladding interface (Fig. 7.17). Zirconium was thus selected as a diffusion barrier because of chemical compatibility with U–Mo, the ability to achieve a robust thermomechanical bond between U–Mo and Zr, and the stability of the Zr/Al

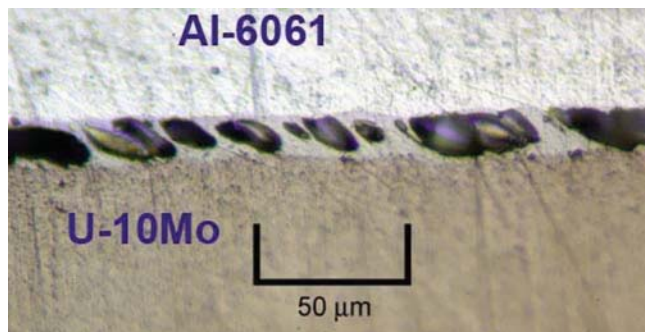


Figure 7.17 Bubble formation in the interaction layer between a U–10Mo Foil and Al–6061 cladding in U–Mo monolithic fuel without a fuel/cladding diffusion barrier at a fission density of 7×10^{21} f/cm³.

Source: A.B. Robinson, D.M. Perez, D.L. Porter, et al., Irradiation performance of U–Mo alloy based ‘monolithic’ plate-type—design selection update, in: Report INL/EXT-09–16807, 2013.

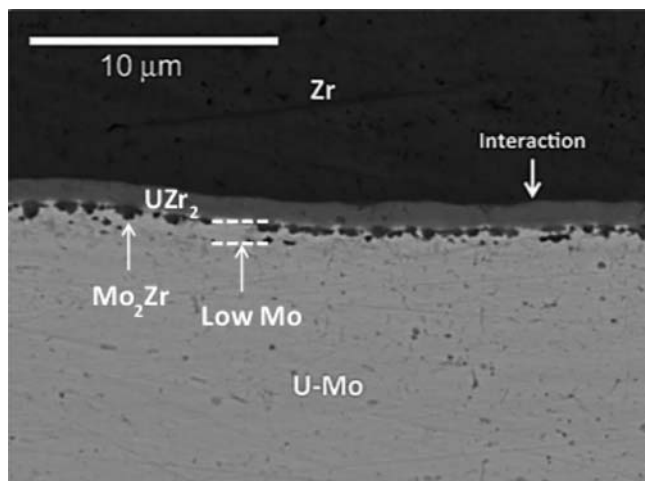


Figure 7.18 Microstructure of the interaction layer that forms between U–Mo alloy and zirconium during fabrication.

Source: J.F. Jue, D.D. Keiser, B.D. Miller, et al., Effects of irradiation on the interface between U–Mo and zirconium diffusion barrier, J. Nucl. Mater. 499 (2018) 567–581.

interface during fabrication and irradiation [140–144]. The microstructure at the U–Mo/Zr interface that is created during thermomechanical bonding of Zr to U–Mo consists of UZr₂, a body-centered-cubic γ-UZr phase, Mo₂Zr, Zr solid solutions, and small amounts of Mo-depleted α-U phases [145] within a 2–3 μm thick region, as shown in Fig. 7.18. These phases are retained during irradiation.

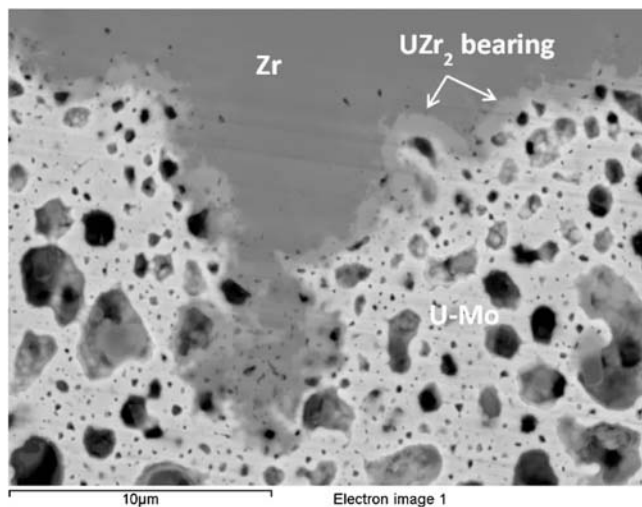


Figure 7.19 SEM micrograph showing the interfacial region between zirconium and U–Mo in a miniature fuel plate irradiated to a fission density of $9.8 \times 10^{21} \text{ cm}^{-3}$. SEM, Scanning electron microscopy.

Source: J.F. Jue, D.D. Keiser, B.D. Miller, et al., Effects of irradiation on the interface between U–Mo and zirconium diffusion barrier, *J. Nucl. Mater.* 499 (2018) 567–581.

The primary effect of the chemical interdiffusion that occurs during fabrication on fuel behavior is through the depletion of Mo from the (U–Mo) phase to form Mo₂Zr. As the fission gas inventory increases as a function of fission density, fission bubbles grow and coalesce more readily in the Mo-depleted region of the fuel, leading to a population of larger diameter fission gas bubbles near the interface with Zr [146], as shown in Fig. 7.19 for a miniature fuel plate irradiated to a fission density of $9.8 \times 10^{21} \text{ f/cm}^3$. At this very high fission density the UZr₂ phase becomes discontinuous, which does not appear to have an effect on fuel performance.

7.6.5 Uranium–zirconium hydride fuel

The most common rod-type fuel in use in research reactors today is the U–Zr–H system used in TRIGA reactors that operate in steady state at low power densities, although many are configured to operate in pulsing mode, producing a single short burst at high power. U–ZrH_{1.6} fuel consists of a continuous matrix of δ-ZrH_{1.6} phase surrounding up to 21 vol.% uranium (45 wt.%) in low-enrichment fuel, as shown in Fig. 7.20A. Fig. 7.20B shows that the fuel microstructure does not dramatically change after irradiation for a sample taken from a fuel element irradiated to 21.8% average ²³⁵U depletion.

Of most interest in this system is the behavior of hydrogen in terms of the equilibrium pressure and release kinetics. Hydrogen pressure in the rod-type fuel defines

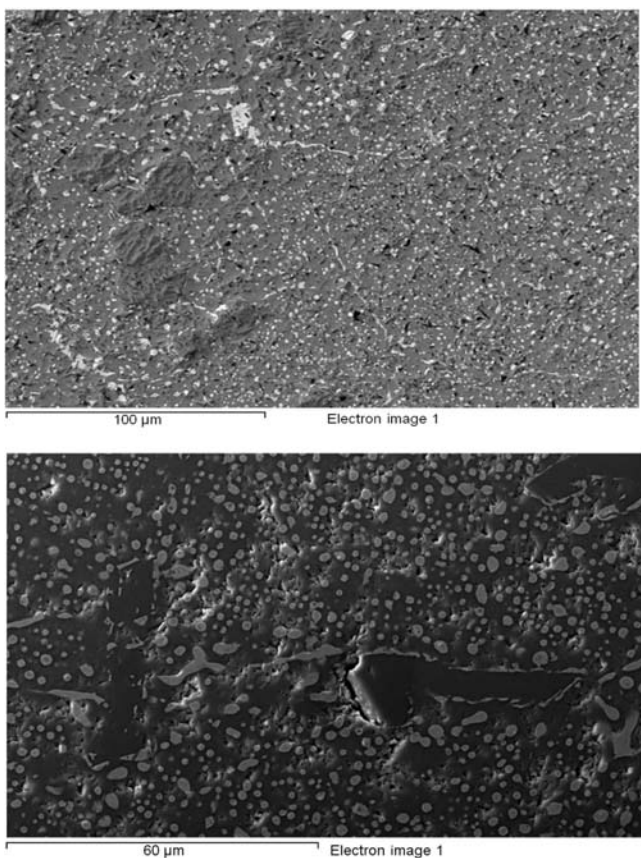


Figure 7.20 SEM micrographs of (A) as-fabricated and (B) TRIGA fuel microstructure for a sample taken from a fuel element irradiated to an average of 21.8% ^{235}U depletion. The U-rich phase is bright contrast and the ZrH matrix is dark contrast. *SEM*, Scanning electron microscopy.

the operating limits of the fuel. The equilibrium pressure (MPa) of hydrogen above the hydride phase [147] is provided by Eq. (7.2):

$$P_{\text{H}_2} = \left(\frac{C}{2-C} \right)^2 \exp \left(5.72 + 5.21C - \frac{172\text{kJ}}{RT} \right) \quad (7.2)$$

where C is the ratio of H/Zr, T is in K, and R is 8.314 J/mol K. The equilibrium hydrogen pressure above $\sim 800^\circ\text{C}$ is sufficient to allow accumulation of hydrogen in the plenum. Hydrogen pressure-build experiments [148] using $\text{ZrH}_{1.6}$ indicate that the equilibrium is reached within a few minutes above 880°C . Desorption kinetics calculated using both thermogravimetry and the pressure-build data

indicate unusual zeroth order kinetics according to Eq. (7.3), where k is in units of mol H/m² s:

$$k_{\text{des}} = \exp \left(27.0 + \frac{-205 \text{ kJ}}{RT} \right) \quad (7.3)$$

It was postulated that the high concentration and high mobility of hydrogen in this material at high temperature result in a system that is not diffusion limited; instead the rate-limiting process is surface recombination of H to form H₂, which only holds away from equilibrium.

7.7 Corrosion of aluminum research reactor fuel cladding

The successful application of aluminum cladding is well established for research reactors [149]. Since aluminum in water is protected by a hydroxide “corrosion” product, the term corrosion as used here indicates an uncontrolled or unexpected increase or change in the rate of hydroxide growth. Corrosion rates may be altered significantly (either positively or negatively) as a result of combinations of dissimilar metals that result in galvanic currents. Corrosion can generally be minimized by maintaining high-purity water and preventing interactions with dissimilar materials in the reactor.

At temperatures below 400°C in water, aluminum forms one of several hydroxide phases on exposed surfaces. When the temperature of formation is below ~77°C, the end product will be a trihydroxide with the structure of gibbsite (hydrargillite) [γ -Al(OH)₃], if the pH is lower than ~5.8 or higher than ~9; bayerite [α -Al(OH)₃], if the pH is between ~5.8 and ~9; or nordstrandite [Al(OH)₃], often considered a mixture of the other forms. When the temperature is above ~77°C and below ~102°C, a pseudoboehmite structure is formed, which may age to other hydroxide forms or retain its pseudoboehmite structure. Between ~102°C and ~400°C and at pressures below ~20 MPa (2900 psi), crystalline boehmite [γ -AlOOH] will form. These hydroxides form from precipitation and aging of gelatinous compounds with low crystalline order. The primary ionic species formed is [Al(H₂O)₆]³⁺, which provides the building block for octahedral chain molecules or hexagonal ring polynuclear complexes. Deprotonation and condensation reactions form a gelatinous boehmite that is the chemical precursor to both the trihydroxide and monohydroxide crystalline structure. Octahedral chain molecules, polynuclear complexes, and the gelatinous boehmite structures should be avoided on fuel plates because these low-density structures can reduce the channel gap between fuel plates [150]. The growth of these chemical complexes in reactor service can be avoided by preparing the fuel with a boehmite surface layer prior to usage and preventing the dissolution of that hydroxide during operation.

Aluminum hydroxides are amphoteric (can act either as an acid or base) but relatively stable over a specific range of pH, primarily because of passivation due to

the positive charge on the hydroxide surface provided by the Al^{3+} ion. The trihydroxide forms have a wider range of chemical stability (pH of $\sim 4.0\text{--}8.5$) but do not provide exceptional corrosion resistance within the region of passivation. Crystalline boehmite (monohydroxide) has a narrower passivation range (pH of $\sim 4.7\text{--}6.2$) but better water corrosion resistance within its range of stability. As a best practice for research reactor fuel, maintenance of core water at the center of the passivation region (a pH of 5.4–6.0) is recommended as it provides the most margin for abnormal water conditions without any significant effect on the fuel. ASTM D1193 – 99 Type II or Type III water should be acceptable, although tighter control over organic carbon than allowed in Type III water is preferred when aluminum fuel is involved.

Based on experience with avoiding catastrophic corrosion events, some high-performance reactors operate at a pH of 5.0. In this case, to obtain a thin, protective, oxide with minimal impact on thermal transport and minimize upsets caused by abnormal water conditions, fuel surfaces should be pretreated to achieve a consistent, fully aged fuel hydroxide surface to achieve a minimum hydroxide layer thickness of $0.3\text{--}0.5\ \mu\text{m}$.

Recently analyzed oxide thickness data from irradiated fuel plate experiments using five different published oxide growth rate correlations for aluminum fuel plates and four surface heat transfer correlations [151] found that the oxide growth rate was found to be relatively insensitive to the choice of surface heat transfer correlation in comparison to other variables over a range of surface heat flux. The Petukhov-Popov heat transfer correlation was recommended for use on the basis that it envelopes the fuel plate operating conditions and yields a smaller correlation error than other commonly used correlations. The Kim [152] correlation for oxide growth was found to provide a slight over prediction of oxide growth rate, while the Pawel [153] correlation was found to slightly under predict oxide growth rate.

7.8 Conclusion

There are ~ 250 research reactors operating worldwide. The majority of these reactors use as fuel some combination of uranium aluminide (UAl_x), uranium oxide (UO_2 or U_3O_8), or uranium silicide (U_3Si or U_3Si_2) in contact with aluminum, or $\text{UZrH}_{1.6}$ clad in stainless steel. Fuels used in the highest flux reactors operate at very high fission rates, and the high rate of electronic energy deposition by fission fragments into the fuel and fuel/cladding interface has a profound effect on the irradiation behavior of the fuel system. This energy deposition accelerates chemical diffusion and pushes these systems far from equilibrium in terms of phase array, crystalline state, and solubility. The viability of these fuels is, in fact, largely determined by the nonequilibrium interactions of noble fission gases with the fuel matrix.

New developments in research reactor fuel over the last 40 years have been in response to national policies to convert the remaining research reactors from high- to

low-enriched uranium. Conversion of these reactors has required stepwise development of higher density fuels that maintain reactor operating performance, starting with increasing the fuel loading in UZrH_{1.6} and oxide fuels and continuing with the development of high-density silicide fuels. Conversion of the remaining high-performance research reactors requires increasing the uranium density from the currently licensed 4.8 to 8 g U/cm³, with uranium–molybdenum alloys being the leading candidate fuel. This fuel is quite robust but does exhibit an incompatibility with the matrix for current aluminum-based dispersion fuel systems.

References

- [1] C.E. Winters, *The High Flux Isotope Reactor*, Nucl. Sci. Eng. 17 (3) (1963) 443–447.
- [2] R.W. Knight, C.F. Leitten, Jr., Development of the Assembly Method for Fuel Elements for the Advanced Test Reactor, Oak Ridge National Laboratory Report ORNL-3643 (1964).
- [3] J.M. Baugnet, A. Beeckmans de West-Meerbeeck, H. Lenders and F. Leonard, The BR2 Materials Testing Reactor and the RERTR Program – Present Status and Future Trends (ANL/RERTR/TM-6). International Atomic Energy Agency (IAEA), 1985.
- [4] J. Roglans, NNSA’s Russian Reactor Conversion Program: Historical Overview, Major Accomplishments, Current Status, 2015 Presentation to National Academy of Sciences. <http://nassites.org/dels/files/2015/05/Day2_02_ROGLANS_NASRussiaConvertApr2015.pdf>, 2015.
- [5] I. Cailliere, et al., LTA’s manufacturing for JHR fuel qualification in BR2 reactor, in: Trans. Res. Reactor Fuel Management. Available from: <www.euronuclear.org/meetings/rrfm2009/transactions>, 2009.
- [6] <<http://www.ga.com/triga-fuels>>
- [7] D.F. Sears, K.T. Conlon, Development of LEU fuel to convert research reactors: NRU, MAPLE, and SLOWPOKE, in: International Symposium on Minimization of HEU in the Civilian Nuclear Sector, Oslo Norway, 2006.
- [8] R. Brown, R. Harrington, J. Hayter, et al., *The Advanced Neutron Source: Designing for Science*, Prog. Nucl. Energy 30 (1) (1996) 67–118.
- [9] National Academies Press, Reducing the Use of Highly Enriched Uranium in Civilian Research Reactors, National Academies Press, 2016.
- [10] C.G. Seo, H.T. Chae, B.C. Lee, et al., Conceptual nuclear design of the Kijang Research Reactor, in: Trans. Research Reactor Fuel Management. Available from: <www.euronuclear.org/meetings/rrfm2013/transactions/RRFM2013-projects.pdf>, 2013.
- [11] S. Stacey, *Proving the Principle*, United States Department of Energy, 2000.
- [12] International Atomic Energy Agency, History, Development, and Future of TRIGA Research Reactors, IAEA Technical Report Series No. 482, International Atomic Energy Agency, 2016.
- [13] Argonaut <www.ne.anl.gov/About/reactors/training.shtml> (accessed August 2019).
- [14] T. Wiss, Hj. Matzke, C. Trautmann, M. Toulemonde, S. Klaumiinzer, *Radiation damage in UO₂ by swift heavy ions*, Nucl. Instr. Meth. Phys. Res. B 122 (1997) 583–588.
- [15] D.M. Duffy, et al., *Making tracks in metals*, J. Phys.: Condens. Matter 20 (2008) 082201.

- [16] M. Lang, R. Devanathan, M. Toulemonde, C. Trautmann, Advances in understanding of swift heavy-ion tracks in complex ceramics, *Curr. Opin. Solid State Mater. Sci.* 19 (2015) 39–48.
- [17] R.M. Willard, A.R. Schmitt, Irradiation swelling, phase reversion and intergranular cracking of U–10wt%Mo fuel alloy, in: Report NAA SR 8956, Atomics International, 1964.
- [18] J.C. Griess, H.C. Savage, J.L. English, Effect of heat flux on the corrosion of aluminum by water, in: Part IV: Tests Relative to the Advanced Test Reactor and Correlation With Previous Results, ORNL-3531, 1964.
- [19] Z. Hashin, S. Shtrikman, A variational approach to the theory of the effective magnetic permeability of multiphase materials, *J. Appl. Phys.* 33 (10) (1962).
- [20] V. Marelle, F. Huet, P. Lemoine, Thermo-mechanical modeling of U–Mo fuels with MAIA, in: Proceedings of the Eighth International Topical Meeting on Research Reactor Fuel Management, 2004.
- [21] D.R. Olander, Fundamental aspects of nuclear fuel elements, in: Technical Information Center, Office of Public Affairs Energy Research and Development Administration, TID-26711-P1, 1976, ISBN 0-87079-031-5.
- [22] J. Rest, G.L. Hofman, Kinetics of recrystallization and fission-gas-induced swelling in high burnup UO_2 and U_3Si_2 nuclear fuels, in: S.E. Donnelly, J.H. Evans (Eds.), *Fundamental Aspects of Inert Gases in Solids*. NATO ASI Series (Series B: Physics), vol. 279, Springer, Boston, MA, 1991.
- [23] A.D. Whapham, Electron microscope observation of the fission-gas bubble distribution in UO_2 , *Nucl. Appl.* 2 (2) (1966) 123–130.
- [24] J.A. Turnbull, R.M. Cornell, The resolution of gas atoms from bubbles, during the irradiation of UO_2 , *J. Nucl. Mater.* 36 (1970) 161–168.
- [25] D.R. Olander, D. Wongsawaeng, Re-solution of fission gas – a review: Part I. Intragranular bubbles, *J. Nucl. Mater.* 354 (2006) 94–109.
- [26] M. Tonks, et al., Unit mechanisms of fission gas release: current understanding and future needs, *J. Nucl. Mater.* 504 (2018) 300–317.
- [27] J.E. Cunningham, R.J. Beaver, W.C. Thurber, R.C. Waugh, Fuel dispersions in aluminum-base elements for research reactors, in: Proceedings of the Fuel Elements Conference, TID-7456 Book 1, 1957, pp. 269–297.
- [28] T.C. Wiencek, ANL/RERTR/TM-15 Summary Report on Fuel Development and Miniplate Fabrication for the RERTR Program 1978 to 1990, Argonne National Laboratory, Argonne, IL, 1995.
- [29] J.M. Park, J.Y. Eom, J.Y. Jung, Y.M. Ko, G.S. Joo, C.T. Lee, et al., Development of the Fabrication Technology for a HANARO Fuel Rod by the Indirect Extrusion Method, in: Proceedings of the International Meeting on Reduced Enrichment for Research and Test Reactors. Available from: <www.rertr.anl.gov/RERTR25>.
- [30] M.T. Simnad, The U-ZrH_x alloy: properties and use in TRIGA fuel, *Nucl. Eng. Des.* 64 (1981) 403–422.
- [31] D. Olander, E. Greenspan, H.D. Garkisch, B. Petrovic, Uranium–zirconium hydride fuel properties, *Nucl. Eng. Des.* 239 (2009) 1406–1424.
- [32] NUREG-1313, Safety Evaluation Report Related to the Evaluation of Low-Enriched Uranium Silicide-Aluminum Dispersion Fuel for Use in Non-Power Reactors, U.S. Nuclear Regulatory Commission, Office of Nuclear Reactor Regulation, 1988.
- [33] M.K. Meyer, G.L. Hofman, S.L. Hayes, C.R. Clark, T.C. Wiencek, J.L. Snelgrove, et al., Low-temperature irradiation behavior of uranium–molybdenum alloy dispersion fuel, *J. Nucl. Mater.* 304 (2002) 221–236.

- [34] R.H. Cornell, An electron microscope examination of matrix fission-gas bubbles in irradiated uranium dioxide, *J. Nucl. Mater.* 38 (1971) 319–328.
- [35] B. Ye, S. Bhattacharya, K. Mo, D. Yun, W. Mohamed, M. Pellin, et al., Irradiation behavior study of U–Mo/Al dispersion fuel with high energy Xe, *J. Nucl. Mater.* 464 (2015) 236–244.
- [36] G.W. Parker, C.J. Barton, G.E. Creek, W.J. Martin, R.A. Lorenz, Out-of-pile studies of fission-product release from overheated reactor fuels at ORNL, in: ORNL-3981, 1967.
- [37] M.B. Reynolds, Fission gas behavior in the uranium-aluminum system, *Nucl. Sci. Eng.* 3 (1958) 428.
- [38] M.J. Gruber, M. Zukor, G.W. Gibson, Fission gas release from fuel plate meltdown, in: Annual Progress Report on Reactor Fuels and Materials Development, for FY 1966, IDO-17218, 1966.
- [39] G.W. Cunningham, S.J. Paprocki, A new concept for aluminum base fuel elements, in: Research Reactor Fuel Element Conference, TID-7642 vol. 2, 1962, pp. 369–375.
- [40] S. Nazare, G. Ondracek, F. Thummel, Investigations on UAl_x -Al dispersion fuels for high flux reactors, *J. Nucl. Mater.* 56 (1975) 251–259.
- [41] F. Thummel, S. Nazare, G. Ondracek, The technology of UAl_3 -Al irradiation test plates, *Powder Metall.* 10 (20) (1967) 264–287.
- [42] M.J. Gruber, G.W. Gibson, V.A. Walker, W.C. Francis, Results of ATR sample fuel plate irradiation experiment, in: IDO-16958, 1964.
- [43] M.J. Gruber, W.F. Zelezny, G.W. Gibson, Annual progress report on reactor fuels and materials development for FY 1964, in: IDO-17037, 1964.
- [44] F. Thummel, H.E. Lilienthal, S. Nazare, UAl_2 -Al instead of UA_3 -Al in fuel element plates for advanced test reactors, *Powder Metall.* 12 (23) (1969) 1–22.
- [45] The National Academies Press, Molybdenum-99 for Medical Imaging, The National Academies Press. Available from: <<http://www.nap.edu/23563>>, 2016.
- [46] K.L. Ali, et al., Development of low enriched uranium target plates by thermo-mechanical processing of UAl_2 -Al matrix for production of ^{99}Mo in Pakistan, *Nucl. Eng. Des.* 255 (2013) 77–85.
- [47] H.J. Ryu, et al., Development of high-density U/Al dispersion plates for Mo-99 production using atomized uranium powder, *Nucl. Eng. Technol.* 45 (7) (2013) 979–986.
- [48] G.L. Hofman, Fission gas bubbles in uranium-aluminide fuels, *Nucl. Technol.* 77 (1) (1987) 110–115.
- [49] W. Dienst, S. Nazarre, F. Thummel, Irradiation behaviour of UAl_x -Al dispersion fuels for use in high flux reactors, *J. Nucl. Mater.* 64 (1977) 1–13.
- [50] G.L.C.R. Conturbia, M. Durazzo, E.F. Urano de Carvalho, H.G. Riella, Phase quantification in UAl_x -Al dispersion targets for Mo-99 production, *J. Nucl. Mater.* 509 (2018) 405–477.
- [51] R. Boucher, Etude des alliages aluminium-uranium application à la transformation à l'état solide $UAl_2 + UAl_4$, *J. Nucl. Mater.* 1 (1) (1959) 13–27.
- [52] W. Thurber, R. Beaver, Development of silicon modified 48 wt.% U-Al alloys for aluminum plate-type fuel elements, in: ORNL-2602, Oak Ridge National Laboratory, 1959.
- [53] A.E. Dwight, A study of the uranium–aluminum–silicon system, in: ANL-82-14 Argonne National Laboratory, 1982.
- [54] B. Paige, G. Gibson, K. Rohde, The effect of silicon on fabrication and reprocessing of aluminum alloy reactor fuels, in: Report IN-1194, Idaho National Laboratory, 1968.
- [55] A. Leenaers, F. Joppen, S. Van den Berghe, Microstructural analysis of MTR fuel plates damaged by a coolant flow blockage, *J. Nucl. Mater.* 394 (2009) 87–94.

- [56] W. Van Renterghem, A. Leenaers, S. Van den Berghe, Transmission electron microscopy investigations of UAl_x based MTR fuel, Proceedings of the 2010 Conference on Research Reactor Fuel Management, European Nuclear Society, 2010.
- [57] D.F. Sears, K.D. Vaillaincourt, D.A. Leach, E.L. Plaice, E.J. McKee, R.R. Meadowcroft, W.S. Simmons, Status of LEU fuel development and irradiation testing at Chalk River Laboratories, in: Proceedings of the 18th International Meeting on Reduced Enrichment for Research and Test Reactors, Argonne National Laboratory Report ANL/RERTR/TM-18, 1990.
- [58] T.C. Wienczek, R.F. Domagala, H.R. Thresh, Thermal compatibility studies of unirradiated uranium silicide dispersed in aluminum, *Nucl. Technol.* 71 (3) (1985) 608–616.
- [59] J. Marín, J. Lisboa, J. Ureta, L. Olivares, H. Contreras, J.C. Chávez, Synthesis and clad interaction study of U_3Si_2 powders dispersed in an aluminum matrix, *J. Nucl. Mater.* 228 (1) (1996) 61–67.
- [60] K.H. Kim, J.M. Park, C.K. Kim, G.L. Hofman, K.W. Paik, Thermal compatibility studies of U_3Si_2 dispersion fuels prepared with centrifugally atomized powder, *J. Nucl. Mater.* 270 (1999) 315–321.
- [61] M. Mirandou, S. Aricó, R. Sanabria, S. Balart, D. Podestá, J. Fabro, Study of the interaction between $\text{U}_3\text{Si}_2/\text{Al}$ in dispersion plates at the end of the fabrication process, *Nucl. Technol.* 199 (1) (2017) 96–102.
- [62] S.C. Middleburgh, R.W. Grimes, E.J. Lahoda, C.R. Stanek, D.A. Andersson, Non-stoichiometry in U_3Si_2 , *J. Nucl. Mater.* 482 (2016) 300–305.
- [63] J. Gan, D.D. Keiser Jr., B.D. Miller, J.-F. Jue, A.B. Robinson, J.W. Madden, et al., Microstructure of the irradiated $\text{U}_3\text{Si}_2/\text{Al}$ silicide dispersion fuel, *J. Nucl. Mater.* 419 (2011) 97–104.
- [64] A. Leenaers, E. Koonen, Y. Parthoens, P. Lemoinne, S. Van den Berghe, Post-irradiation examination of AlFeNi cladded U_3Si_2 fuel plates irradiated under severe conditions, *J. Nucl. Mater.* 375 (2008) 243–251.
- [65] Y.S. Kim, G.L. Hofman, Interdiffusion in $\text{U}_3\text{Si}-\text{Al}$, $\text{U}_3\text{Si}_2-\text{Al}$, and $\text{USi}-\text{Al}$ dispersion fuels during irradiation, *J. Nucl. Mater.* 410 (2011) 1–9.
- [66] M.L. Bleiberg, L.J. Jones, *Trans. Metall. Soc. AIME* 212 (1958) 758.
- [67] B. Bethune, Structural transformations in U_3Si , *J. Nucl. Mater.* 31 (1969) 197–202.
- [68] R.C. Birtcher, J.W. Richardson Jr., M.H. Mueller, Amorphization of U_3Si by ion or neutron irradiation, *J. Nucl. Mater.* 244 (1997) 251–257.
- [69] C.R. Hann, R.D. Leggett, X-ray diffraction studies of irradiated U_3Si , *J. Nucl. Mater.* 13 (1969) 114–116.
- [70] R.C. Birtcher, J.W. Richardson, M.H. Mueller, Amorphization of U_3Si_2 by ion or neutron irradiation, *J. Nucl. Mater.* 230 (1996) 158–163.
- [71] G.L. Hofman, Crystal structure stability and fission gas swelling in intermetallic uranium compounds, *J. Nucl. Mater.* 140 (1986) 256–263.
- [72] M. Ugajin, M. Akabori, A. Itoh, N. Ooka, Y. Nakakura, Behavior of neutron-irradiated U_3Si , *J. Nucl. Mater.* 248 (1997) 204–208.
- [73] M.R. Finlay, G.L. Hofman, J.L. Snelgrove, Irradiation behaviour of uranium silicide compounds, *J. Nucl. Mater.* 325 (2004) 118–128.
- [74] M. Ugajin, A. Itoh, Experimental investigations on the chemical state of solid fission-product elements in U_3Si_2 , *J. Alloy. Compd.* 213/214 (1994) 369–371.
- [75] W.J. Werner, T.D. Watts, J.P. Hammond, Metals and ceramics Div. Ann. Progr. Rept., in: ORNL-3470, 1963, pp. 173–174.
- [76] R.C. Waugh, The reaction and growth of uranium dioxide-aluminum fuel plates and compacts, in: ORNL-2701, 1959.

- [77] M.L. Picklesimer, The reaction of UO_2 with aluminum, in: Oak Ridge National Laboratory Report CF-56-80135, 1956.
- [78] D. Stahl, Fuels for research and test reactors, status review: July 1982, in: ANL-83-5, 1982.
- [79] M.F. Hrovat, H. Huschka, K.H. Koch, S. Nazare, G. Ondracek, Status of fuel element technology for plate type dispersion fuels with high uranium density, in: Proceedings of the International Meeting on Development, Fabrication and Application of Reduced Enrichment Fuels for Research and Test Reactors, ANL/RERTR/TM-3, 1980.
- [80] D.O. Hobson, C.F. Leitten, Jr., Characterization of U_3O_8 dispersions in aluminum, in: ORNL-TM-1692, 1967.
- [81] W.J. Werner, J.E. Barkman, Characterization and production of U_3O_8 for the High Flux Isotope Reactor, in: ORNL-4052, 1967.
- [82] R.W. Knight, J. Binns, G.M. Adamson, Jr., Fabrication procedures for manufacturing High Flux Isotope Reactor fuel elements, in: ORNL-4242, 1968.
- [83] M.M. Martin, W.J. Werner, C.F. Leitten, Jr., Fabrication of aluminum-base irradiation test plates, in: ORNL-TM-1377, 1966.
- [84] C.F. Reinke, Irradiation and postirradiation annealing of some aluminum-base fuels, in: ANL-6665, 1963.
- [85] **J.D. Fleming, J.W. Johnson, Aluminum- U_3O_8 exothermic reactions, Nucleonics 21 (5) (1963) 84–85.**
- [86] L. Baker, J.D. Bingle, Aluminum- U_3O_8 thermite reactions, in: Chemical Engineering Division Semiannual Report, ANL-6900, 1964, pp. 298–303.
- [87] A.E. Pasto, G.L. Copeland, M.M. Martin, Quantitative differential thermal analysis study of the U_3O_8 -Al thermite reaction, in: ORNL-5659, 1980.
- [88] **H.E. Rollig, The compatibility of uranium dioxide and aluminum, Part I: Investigations into the kinetics of the UO_2 -Al reaction in mixed powder compacts, Kemzenergie 6 (12) (1963) 685–691.**
- [89] J.D. Fleming, J.W. Johnson, Exothermic reactions in Al- U_3O_8 composites, in: Proceedings of the Research Reactor Fuel Element Conference, TID-7642, 1963, pp. 649–666.
- [90] L. Gray, W.J. Kerrigan, Exothermic reactions leading to unexpected meltdown of scrap uranium-aluminum cermet cores during outgassing, in: Savannah River National Laboratory Report DP-1485, 1978.
- [91] L. Gray, H. Peacock, A differential thermal analysis study of the effect of tramp impurities on the exothermic U_3O_8 -Al reactions, in: Savannah River National Laboratory Report DP-1770, 1989.
- [92] **G. Ondracek, E. Patrassi, The unstable cermet combination U_3O_8 and aluminum II: reactivity and properties of U_3O_8 -Al cermets, Ber. Deutsch. Keram. Ges. 45 (12) (1968) 617–621.**
- [93] R.O. Ivins, F.J. Testa, Studies with aluminum- U_3O_8 cermet fuel (HFIR fuel) in TREAT, in: Chemical Engineering Division Semiannual Report, July–December 1965, ANL-7125, 1966, pp. 163–170.
- [94] M.M. Martin, A.E. Richt, W.R. Martin, Irradiation behavior of aluminum-base dispersion fuels, in: ORNL-4856, 1973.
- [95] A.E. Richt, R.W. Knight, G.W. Adamson, Postirradiation examination and evaluation of the performance of HFIR fuel elements, in: ORNL 4714, 1971.
- [96] **R.M. Berman, M.L. Bleiberg, W. Yeniscavich, Fission fragment damage to crystal structures, J. Nucl. Mater. 2 (1960) 129–140.**
- [97] **G.L. Hofman, G.L. Copeland, J.E. Sanecki, Microscopic investigation into the irradiation behavior of U_3O_8 -Al dispersion fuel, Nucl. Technol. 72 (3) (1986) 338–344.**

- [98] M.K. Meyer, T.C. Wiencek, S.L. Hayes, G.L. Hofman, Irradiation behavior of U₆Mn-Al dispersion fuel elements, *J. Nucl. Mater.* 278 (2000) 358–363.
- [99] M.K. Meyer, G.L. Hofman, T.C. Wiencek, S.L. Hayes, J.L. Snelgrove, Irradiation behavior of U-Nb-Zr alloy dispersed in aluminum, *J. Nucl. Mater.* 299 (2001) 175–179.
- [100] D.D. Keiser Jr., J.F. Jue, B.D. Miller, J. Gan, A.B. Robinson, J. Madden, Observed changes in as-fabricated U-10Mo monolithic fuel microstructures after irradiation in the advanced test reactor, *JOM* 69 (12) (2017) 2538–2545.
- [101] A.E. Dwight, The uranium-molybdenum equilibrium diagram below 900°C, *J. Nucl. Mater.* 2 (1960) 81–87.
- [102] M. Kulakov, M. Saoudi, M.H.A. Piro, R.L. Donaberger, Structure and thermal properties of as-fabricated U-7Mo/Mg and U-10Mo/Mg low-enriched uranium research reactor fuels, *J. Nucl. Mater.* 484 (2017) 288–296.
- [103] R.D. Leggett, B. Mastel, T.K. Beirlin, Irradiation behavior of high purity uranium, in: HW-79559, 1963.
- [104] P.E. Repas, R.H. Goodenow, R.F. Hehemann, Transformation Characteristics of Three Uranium-Base Alloys, Technical Report AMRA CR 63-02/1(F), U.S. Army Materials Research Agency, 1963.
- [105] C.A.W. Peterson, W.J. Steele, S.L. DiGiallardo, Isothermal Transformation Study of Some Uranium-Base Alloys, Report UCRL-7824, Univ. of California Lawrence Radiation Lab., Livermore, CA, 1964.
- [106] G. Cabane, G. Donzé, Stabilisation de la phase dans les alliages ternaires à base d'uranium-molybdène, *J. Nucl. Mater.* 4 (1959) 364–3373.
- [107] Y. Goldstein, A. Bar-Or, Decomposition kinetics of gamma phase uranium alloys containing 8, 10.8, and 14.3 wt% molybdenum, *J. Inst. Met.* 95 (1967) 17–21.
- [108] P.E. Repas, R.H. Goodenow, R.F. Hehemann, Transformation characteristics of U-Mo and U-Mo-Ti alloys, *Trans. Am. Soc. Met.* 13 (1964) 150–163.
- [109] R.J. Van Thyne, D.J. McPherson, Transformation kinetics of uranium-molybdenum alloys, *Trans. ASM* 49 (1957) 598–621.
- [110] E. Perez, Y. Sohn, D.D. Keiser Jr., Role of Si on the diffusional interactions between U-Mo and Al-Si alloys at 823K (550°C), *Met. Mater. Trans. A* 44A (2013) 584–595.
- [111] M.L. Bleiberg, L.J. Jones, B. Lustman, Phase changes in pile-irradiated uranium base alloys, *J. Appl. Phys.* 27 (1956) 1270–1283.
- [112] M. Bleiberg, Effect of fission rate and lamella spacing upon the irradiation-induced phase transformation of U-9Mo alloy, *J. Nucl. Mater.* 2 (1959) 182–190.
- [113] S. Van den Berghe, W. Van Renterghem, A. Leenaers, Transmission electron microscopy investigation of irradiated U-7 wt%Mo dispersion fuel, *J. Nucl. Mater.* 375 (2008) 340–346.
- [114] B.D. Miller, J. Gan, D.D. Keiser Jr., A.B. Robinson, J.F. Jue, J.W. Madden, et al., Transmission electron microscopy characterization of the fission gas bubble superlattice in irradiated U-7 wt%Mo dispersion fuels, *J. Nucl. Mater.* 458 (2015) 115–121.
- [115] J. Gan, D.D. Keiser Jr., B.D. Miller, A.B. Robinson, D.M. Wachs, M.K. Meyer, Thermal stability of fission gas bubble superlattice in irradiated U-10Mo fuel, *J. Nucl. Mater.* 464 (2015) 1–5.
- [116] A. Leenaers, W. Van Renterghem, S. Vann den Berghe, High burnup structure of U(Mo) dispersion fuel, *J. Nucl. Mater.* 476 (2016) 218–230.
- [117] J. Gan, B.D. Miller, D.D. Keiser Jr., J.F. Jue, J.W. Madden, A.B. Robinson, et al., Irradiated microstructure of U-10Mo monolithic fuel plate at very high fission density, *J. Nucl. Mater.* 492 (2017) 195–203.

- [118] J. Gan, D.D. Keiser Jr., B.D. Miller, A.B. Robinson, J.F. Jue, P. Medeved, et al., TEM characterization of U–7Mo/Al–2Si dispersion fuel irradiated to intermediate and high fission densities, *J. Nucl. Mater.* 424 (2012) 43–50.
- [119] D. Jadernas, J. Gan, D.D. Keiser, J. Madden, M. Bachhav, J.-F. Jue, et al., Microstructural characterization of as-fabricated and irradiated U-Mo fuel using SEM/EBSD, *J. Nucl. Mater.* 509 (2018) 1–8.
- [120] L. Liang, Z.-G. Mei, A.M. Yacout, Fission-induced recrystallization effect on inter-granular bubble-driven swelling in U-Mo fuel, *Comput. Mater. Sci.* 138 (2017) 16–26.
- [121] J. Gan, D.D. Keiser Jr., B.D. Miller, D.M. Wachs, T.R. Allen, M. Kirk, et al., Microstructure of RERTR DU-alloys irradiated with krypton ions up to 100 dpa, *J. Nucl. Mater.* 411 (2011) 174–180.
- [122] A. Leenaers, S. Van den Berghe, J. Van Eyken, E. Koonen, F. Charollais, P. Lemoine, et al., Microstructural evolution of U(Mo)–Al(Si) dispersion fuel under irradiation – destructive analyses of the LEONIDAS E-FUTURE plates, *J. Nucl. Mater.* 441 (2013) 439–448.
- [123] M. Kulakov, M. Piro, A. Williams, L. Xiao, M.J. Welland, N. Wang, *Proc. Mater. Mod. Sim. Nucl. Fuel Conf.*, Karlsruhe, Germany, 2015.
- [124] J.S. Yim, Y.W. Tahk, J.Y. Oh, H.J. Kim, E.H. Kong, B.H. Lee, et al., Ongoing status of KJRR fuel (U-7Mo) qualification, in: *Proceedings of the Research Reactor Fuel Management Conference*, INL/CON-17-41243, 2017.
- [125] J.E. Cunningham, R.E. Adams, Techniques for canning and bonding metallic uranium with aluminum, in: *Proceedings of the Fuel Elements Conference*, TID-7456 book 1, 1957.
- [126] A. Leenaers, C. Detavernier, S. Van den Berghe, The effect of silicon on the interaction between metallic uranium and aluminum: a 50-year long diffusion experiment, *J. Nucl. Mater.* 381 (2008) 242–248.
- [127] H.J. Ryu, Y.S. Kim, G.L. Hofman, J.M. Park, C.K. Kim, Heats of formation of (U, Mo)Al₃ and U(Al, Si)₃, *J. Nucl. Mater.* 358 (2006) 52–56.
- [128] A. Leenaers, S. Van den Berghe, C. Detavernier, Determination of activation energies of the U(Mo)/Si and U(Mo)/Al solid state reaction using in-situ x-ray diffraction and Kissinger analysis, *Solid State Sci.* 14 (2012) 1133–1140.
- [129] A. Leenaers, S. Van den Berghe, C. Detavernier, AlSi matrices for U(Mo) dispersion fuel plates, *J. Nucl. Mater.* 439 (2013) 7–18.
- [130] M. Mirandou, S. Arico, M. Rosenbusch, M. Ortiz, S. Balart, L. Gribaudo, Characterization of the interaction layer grown by interdiffusion between U–7wt.% Mo and Al A356 alloy at 550 and 340°C, *J. Nucl. Mater.* 384 (3) (2009) 268–273.
- [131] A. Leenaers, S. Van den Berghe, W. Van Renterghem, F. Charollais, P. Lemoine, C. Jarousse, et al., Irradiation behaviour of ground U(Mo) fuel with and without Si added to the matrix, *J. Nucl. Mater.* 412 (2011) 41–52.
- [132] S. Van den Berghe, Y. Parthoens, F. Charollais, Y.S. Kim, A. Leenaers, E. Koonen, et al., Swelling of U(Mo)-Al(Si) dispersion fuel under irradiation - Non-destructive analyses of the LEONIDAS E-FUTURE plates, *J. Nucl. Mater.* 430 (1-3) (2012) 246–258.
- [133] A. Leenaers, S. Van den Berghe, E. Koonen, V. Kuzminov, C. Detavernier, Fuel swelling and interaction layer formation in the SELENIUM Si and ZrN coated U(Mo) dispersion fuel plates irradiated at high power in BR2, *J. Nucl. Mater.* 458 (2015) 380–393.
- [134] S. Van Berghe, P. Lemoine, Review of 15 years of high-density low-enriched UMo dispersion fuel development for research reactors in Europe, *Nucl. Eng. Technol.* 46 (2) (2014) 125–146.

- [135] J. Gan, D.D. Keiser Jr., B.D. Miller, J.F. Jue, A.B. Robinson, J. Madden, TEM characterization of irradiated U-7Mo/Mg dispersion fuel, *J. Nucl. Mater.* 494 (2017) 380–397.
- [136] D.D. Keiser Jr., J.F. Jue, B.D. Miller, J. Gan, A.B. Robinson, P.G. Medvedev, et al., Microstructural characterization of a Mg matrix U-Mo dispersion fuel plate irradiated in the advanced test reactor to high fission density: SEM results, *Met. Mat. Trans. 3E* (2016) 71–89.
- [137] L. Xiao, N. Wang, Growth behavior of intermetallic compounds during reactive diffusion between aluminum alloy 1060 and magnesium at 573–673K, *J. Nucl. Mater.* 456 (2015) 389–397.
- [138] M.K. Meyer, J. Gan, J.F. Jue, D.D. Keiser, E. Perez, A. Robinson, et al., Irradiation performance of U-Mo monolithic fuel, *Nucl. Eng. Technol.* 46 (2) (2014) 169–182.
- [139] A.B. Robinson, M.R. Finlay, RERTR-7 post irradiation examination (PIE) letter report, in: Idaho National Laboratory Report INL/EXT-07-13271, 2007.
- [140] E.E. Pasqualini, A.B. Robinson, D.L. Porter, D.M. Wachs, M.R. Finlay, Fabrication and testing of U-7Mo monolithic plate fuel with Zircaloy cladding, *J. Nucl. Mater.* 479 (2016) 402–410.
- [141] J.F. Jue, et al., Fabrication of monolithic RERTR fuels by hot isostatic pressing, *Nucl. Technol.* 72 (2) (2010) 204–210.
- [142] G.A. Moore, M.C. Marshall, Co-rolled U-10Mo/zirconium barrier-layer monolithic fuel foil fabrication process, in: Idaho National Laboratory report INL/EXT-10-17774, 2010.
- [143] K. Huang, C.C. Kammerer, D.D. Keiser Jr., Y.H. Sohn, Diffusion barrier selection from refractory metals (Zr, Mo, and Nb) via interdiffusion investigation of U-Mo RERTR fuel alloy, *J. Phase Equilib. Diffus.* 35 (2014) 146–156.
- [144] J.F. Jue, D.D. Keiser, C.R. Breckenridge, G.A. Moore, M.K. Meyer, Microstructural characteristics of HIP-bonded monolithic nuclear fuels with a diffusion barrier, *J. Nucl. Mater.* 448 (2014) 250–258.
- [145] E. Perez, B. Yao, D.D. Keiser Jr., Y.H. Sohn, Microstructural analysis of as processed U-10 wt.% Mo monolithic fuel plate in AA6061 matrix with Zr diffusion barrier, *J. Nucl. Mater.* 402 (2010) 8–14.
- [146] J.F. Jue, D.D. Keiser Jr., B.D. Miller, J.W. Madden, A.B. Robinson, B.H. Rabin, Effects of irradiation on the interface between U-Mo and zirconium diffusion barrier, *J. Nucl. Mater.* 499 (2018) 567–581.
- [147] W. Wang, D. Olander, Thermodynamics of the Zr-H system, *J. Am. Ceram. Soc.* 78 (1995) 3323.
- [148] K.A. Terrani, M. Balooch, D. Wongsawaeng, S. Jaiyen, D.R. Olander, The kinetics of hydrogen desorption from and adsorption on zirconium hydride, *J. Nucl. Mater.* 397 (2010) 61–68.
- [149] E. Shaber, G. Hofman, Corrosion minimization for research reactor fuel, in: INL/EXT-05-00256, Idaho National Laboratory, 2005.
- [150] M.L. Griebenow, et al., TRA oxide film control and surveillance, in: EG&G Idaho Report RE-A-77-059, 1977.
- [151] W.R. Marcum, D.M. Wachs, A.B. Robinson, M.A. Lillo, Aluminum cladding oxidation of prefilmed in-pile fueled experiments, *J. Nucl. Mater.* 471 (2016) 136–148.
- [152] Y.S. Kim, et al., Oxidation of aluminum alloy cladding for research and test reactor fuel, *J. Nucl. Mater.* 278 (2008) 220–228.
- [153] R.E. Pawel, G.L. Yoder, C.D. West, B.H. Montgomery, The development of a preliminary correlation of data on oxide growth on 6061 aluminum under ANS thermal-hydraulic conditions, in: ORNL-TM-11517, Oak Ridge National Laboratory.

PART C

Stages of the Fuel Cycle and Other Applications

This page intentionally left blank

Mining and milling

8

Markus H.A. Piro and Ksenia Lipkina

Faculty of Energy Systems and Nuclear Sciences, Ontario Tech University, Oshawa,
ON, Canada

8.1 Introduction

The nuclear fuel cycle is a multistage industrial process revolving around the utilization of uranium to produce electricity and is depicted in Fig. 8.1. The front-end of the fuel cycle begins with mining uranium out of the ground, milling it into a more concentrated form (e.g., U_3O_8), converting it either into a useable form for enrichment for light water reactors (LWR; i.e., UF_6) or into a reactor-grade form for CANDUs (i.e., UO_2), enrichment of uranium to increase fissile content in LWR fuel, fabrication of the fuel into assemblies, and the service period in-reactor. The back end of the fuel cycle may take two different paths: (1) an open fuel cycle, whereby irradiated fuel discharged from the reactor is put into temporary wet storage and then dry-storage with the ultimate hope of permanent disposal or (2) a closed fuel cycle, whereby irradiated fuel discharged from the reactor undergoes a reprocessing stage to extract useable components from the used fuel (i.e., uranium and/or plutonium), recycling usable components from the reprocessing stage to fabricate new fuel (e.g., MOX), whereby nonrecyclable components are disposed of as waste. This chapter describes the mining (Section 8.2) and milling (Section 8.3) stages of the uranium fuel cycle with a focus on fuel chemistry.

8.2 Mining

The mining process involves the extraction of raw uranium bearing minerals out of the ground, which is accomplished with various techniques. First, this section will give a global perspective of reasonably assured resources (RAR) of uranium in Section 8.2.1. Next, commonly mined uranium bearing minerals will be reviewed in Section 8.2.2. Finally, mining practices used in industry will be reviewed in Section 8.2.3.

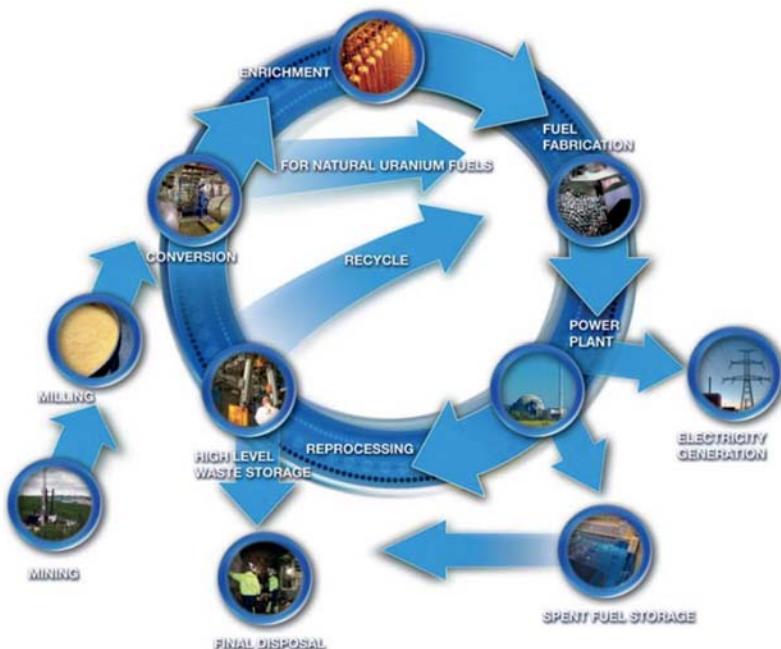


Figure 8.1 An overview of the uranium fuel cycle.

Source: Used with permission from the International Atomic Energy Agency.

8.2.1 Uranium resources

Uranium is found throughout the Earth's crust in various concentrations with an average abundance of approximately 2.8 g/t [1]. To put this value into perspective, uranium is more abundant than gold but less than copper [1]. Australia, Canada, and Kazakhstan have the highest RAR of uranium, whereby Australia has 30% in total identified resources in the <130 USD/kgU price category [2]. A regularly updated report on uranium resources is jointly published by the Organization for Economic Co-operation and Development (OECD) Nuclear Energy Agency (NEA) and the International Atomic Energy Agency (IAEA) [2]. Fig. 8.2 highlights the global distribution of identified uranium resources in the <130 USD/kgU price category. The distribution of RAR and inferred resources varies not only by nation state but also by price category. The production cost of uranium depends on many factors, including the method used to mine the ore, geography, geology, the quality of grade of the ore, and the mineral type.

8.2.2 Uranium bearing minerals

There are approximately 200 known minerals that contain uranium [3]; however, only a small subset of those is commercially mined. Table 8.1 gives a summary of commonly mined uranium-bearing minerals. Many of these minerals have



Figure 8.2 The global distribution of identified uranium resources (<130 USD/kgU) [2].

Table 8.1 Commercially mined uranium-bearing minerals are summarized [1,3–5].

Mineral type	Mineral name	Chemical formula	U content
Oxides	Brannerite	(U,Ca,Fe,Th,Y)(Ti,Fe) ₂ O ₆	26–44
	Davidite	(Fe,Co,U,Ca,Zr,Th) ₆ (Ti,Fe,V,Cr) ₁₅ (O,OH) ₃₆	
	Pyrochlore	(Na,Ca,Fe,U,Sb,Pb,Th,Zr,Ce,Y) ₂ (Nb,Ta,Ti,Sn,Fe) ₂ O ₆ (OH,F)	
Silicates	Uraninite (aka pitchblende)	UO _{2 ± x}	46–88
	Coffinite	U(SiO ₄) _{1-x} (OH) _{4x}	40–60
Phosphates	Uranophane (aka uranotile)	Ca(UO ₂) ₂ (SiO ₃) ₂ (OH) ₂ H ₂ O	55
	Autunite	Ca(UO ₂) ₂ (PO ₄) ₂ xH ₂ O, where 10 < x < 12	48–50
	Torbernite	Cu(UO ₂) ₂ (PO ₄) ₂ xH ₂ O, where 10 < x < 12	47
Vanadates	Carnotite	K ₂ (UO ₂) ₂ (VO ₄) ₂ 3H ₂ O	53–55
	Tyuyamunite	Ca(UO ₂) ₂ (VO ₄) ₂ xH ₂ O, where 5 < x < 8	49–54

characteristic colors. For example, uranophane is bright yellow, torbernite is bright green, autunite is yellow/green, and uraninite is black. The most common form of uranium deposit across most price categories is sandstone, which primarily consists of uraninite and coffinite [2]. Polymetallic iron-oxide deposits are also prevalent, but only at the higher price categories [2]. These minerals often contain daughter products of uranium—principally, radium-226 and radon-222 [4]. These components are of concern from a radiation protection perspective, particularly the latter, which is often stable in gaseous form. Radiation protection is, therefore, an important concern in mining and milling operations to protect operating staff, surrounding communities, and the environment.

8.2.3 Mining methods

There are three principal methods to mine uranium ore: (1) open-pit, (2) underground, and (3) in-situ leaching (ISL). Some other methods are also used, such as co-/by-product methods, but to a far lesser degree. The decision to use one method or another depends on the specific site, which includes the size and location of the ore. Historically speaking, the majority of mining operations involved open-pits and underground mines, which are now considered “conventional” mining techniques. In recent decades, ISL has become the prevalent method of mining uranium. In 2017, the global distribution of mining methods in OECD countries is as follows: 14% open-pit, 32% underground, 48% ISL, and 6% co-/by-product mining [2]. **Table 8.2** summarizes the top 10 uranium producing mines in 2018 by mine site, country, principal owner, mine type, and the percentage of world production.

Table 8.2 A summary of the top 10 uranium mines in 2018 and the methods that they use.

Mine site	Country	Principal owner	Mine type	% of world
Cigar Lake	Canada	Cameco/Orano	Underground	13
Olympic Dam	Australia	BHP Billiton	By-product/ underground	6
Husab	Namibia	Swakop Uranium (CGN)	Open pit	6
Inkai (1–3)	Kazakhstan	Kazatomprom/ Cameco	ISL	5
Rössing	Namibia	Rio Tinto	Open pit	4
Budenovskoye 2	Kazakhstan	Uranium One/ Kazatomprom	ISL	4
Tortkuduk	Kazakhstan	Orano/ Kazatomprom	ISL	4
Société des Mines de l'Air	Niger	Orano (formerly Areva)	Open pit	3
Ranger	Australia	Rio Tinto/ERA	Open pit	3
Kharasan 2	Kazakhstan	Kazatomprom	ISL	3
Sum of top 10				51

ISL, In-situ leaching.

Source: Reproduced from the World Nuclear Association, Uranium mining overview.

While the three main recovery methods differ in their general approaches, they all share some general health, safety, and environmental concerns—albeit to varying degrees. Of particular concern in uranium mining is the radioactivity of materials, which may be transported through multiple pathways (i.e., airborne, surface water, and groundwater). It is important to monitor the aforementioned pathways to minimize the risk to workers, the surrounding community, and the environment. Underground mining operations pose the greatest challenge due to the confined spaces and airborne particulates that may contain radioactive materials. Alpha emitting isotopes are the greatest concern if inhaled as they can cause significant internal radiological damage. These risks are largely mitigated by robust radiation protection procedures, ventilation, remote handling, etc.

8.2.3.1 Open pit mining

Open pit mining refers to mining directly on the ground surface, thereby producing an open pit. This method is practical and cost-effective when the uranium ore is located near the surface (e.g., within 100 m). Underground mining and ISL methods may be considered for sites that have uranium ores at deeper depths. An open pit mine is typically excavated with a series of benches to reach greater depths. Open pit mining initially involves the removal of soil and rock on top of the ore via drilling or blasting, which is put aside for future reclamation purposes after the useful

content of the mine has been extracted. The resulting broken up rock materials are removed with front-end loaders and loaded onto dump trucks, which then transport the ore to a milling facility.

8.2.3.2 *Underground mining*

Underground mining is applied when the uranium ore is at depths that render open pit mining impractical and not economical. There are three main access methods: shafts, adits, and declines. Shafts are vertical in orientation, which are typically a few meters in diameter and upwards of a few hundred meters in depth. Adits are horizontal and typically normal to a shaft, which may include an entrance, ventilation, drain pathway, or tunnel for ore extraction. An elevator would typically be used to navigate between adits. Declines are effectively ramps, which can be used to move up and down, and are often spiral in shape. An advantage of underground mining in comparison to open pit mining is that relatively little of the surface is disturbed by the overall operation. A significant challenge with underground mining is the increased risk to health and safety due to operators working underground in confined spaces. Specifically, there is a greater risk of radioactive dust inhalation, tunnels collapsing, etc.

8.2.3.3 *In situ leaching*

ISL (also often referred to as “in-situ recovery”) is becoming the more prevalent approach to mine uranium in comparison to open-pit and underground mining techniques. The premise of ISL is to exploit the local geology of some orebodies that may be in somewhat porous material by dissolving the ore in solution, which can then be relatively easily recovered. These uranium-bearing species are typically insoluble in groundwater. The general extraction process involves injecting a leaching agent called “lixiviant” into the ore body (below the water table), dissolving uranium bearing species in solution, recovering the uranium bearing solution (sometimes referred to as “pregnant solution”) to the surface by pumping the material through production wells.

There are three principle advantages of ISL in comparison to conventional methods: (1) reduced risk to operators by avoiding underground mining; (2) stripping, mining, and milling of the ore on the surface is unnecessary, which is a great advantage as it minimizes the burden of dealing with tailings; (3) as a concomitant effect to the last point, there is a reduced amount of radioactivity reaching the surface; (4) one is able to extract lower grade ore than is possible with other techniques; and (5) there is minimal surface disturbance with the least environmental impact [6]. The greatest disadvantage of ISL is that there is a lower recovery rate in comparison to other methods. Also, there is a risk of potentially contaminating ground water. Clearly, this operation must be far removed from any source of water that may become potable.

Uranium deposits suitable for ISL are in permeable sand or sandstone that are confined by adjacent impermeable structures, which facilitates the chemical solution injection and recovery. A lixiviant is pumped into the orebody (below the water table) via a borehole for the purpose of dissolving the uranium in solution,

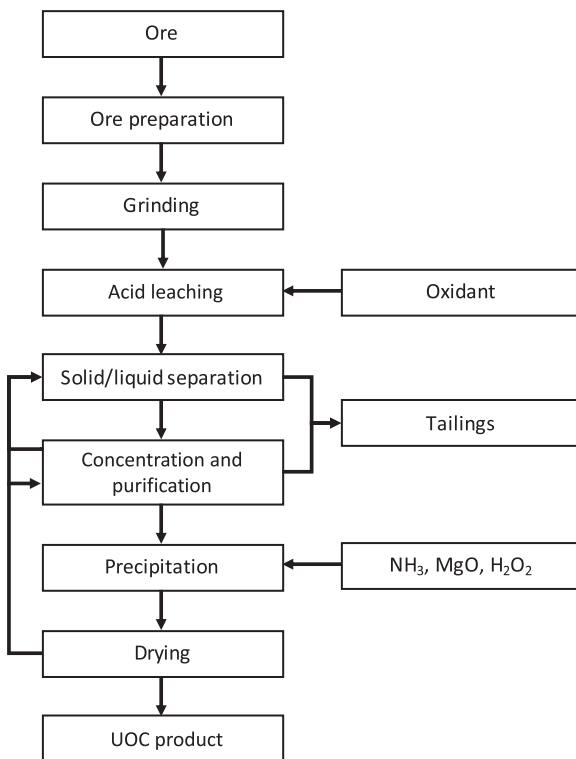


Figure 8.3 A generic schematic of the acid-leaching process.

Source: Adapted from C. Edwards, A. Oliver, Uranium processing: a review of current methods and technology, JOM (2000) 12–20 [4].

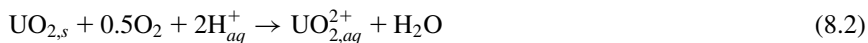
thereby mobilizing it. A large number of lixiviant materials are used that broadly fall under two categories: acids and carbonate reactants. Commonly used reactants include sulfuric acid, nitric acid, hydrochloric acid, sodium bicarbonate, and hydrogen peroxide [7]. Sulfuric acid offers high leach performance at a relatively low cost but produces residues (e.g., gypsum), which degrades performance [7].

The choice of lixiviant often depends on the amount of calcium in the ore. If calcium content is significant, alkaline leaching is typically used; otherwise, acid leaching is used, which typically yields higher recovery rates at a lower cost [7]. One advantage of alkaline leaching is that undesired impurities are less likely to be dissolved in solution; however, this can also be a disadvantage as uranium minerals must be directly exposed to the solution in order to permit extraction [4].

The general process used in acid leaching is illustrated in Fig. 8.3. After the ore is received in the mill, it may go through a grinding process, as described in the previous section. Then, the chemical process involving sulfuric acid in ISL is described in the following partial reactions, beginning with dissolution [7]:



then oxidation,



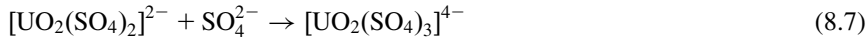
a ferrous oxidation reaction,



with sodium chlorate oxidation,



Dissolution of uranium by sulfuric acid involves the following three partial reactions:



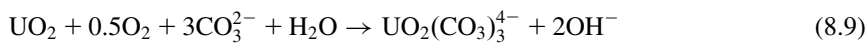
The composition of the solution obviously depends on a number of factors, such as the pH and redox potential, which is affected by the local geochemistry and lixiviant added to the system. Uranium bearing species in solution may include $\text{UO}_{2,qaq}^{2+}$, UO_2SO_4 , $\text{UO}_2(\text{SO}_4)_{2,qaq}^{2-}$, and $\text{UO}_2(\text{SO}_4)_{3,qaq}^{4-}$.

Alkaline leaching with a carbonate lixiviant, such as bicarbonate (HCO_3^-), carbon dioxide gas (CO_2), or sodium carbonate (Na_4CO_3), involves a neutral or slightly alkaline solution. Fig. 8.4 gives an overview of the general alkaline leaching process. This process is generally preferred when sulfuric acid is largely consumed by the host rock, rendering acid leaching less desirable from an economic perspective. The predominant species in carbonate leaching is $\text{UO}_2(\text{CO}_3)_3$.

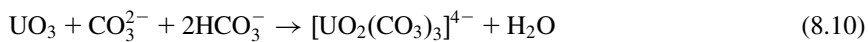
Chemical reactions pertinent to the fortification of lixiviants in alkaline leaching begins with oxidation [7,8]:



followed by



or with bicarbonate,



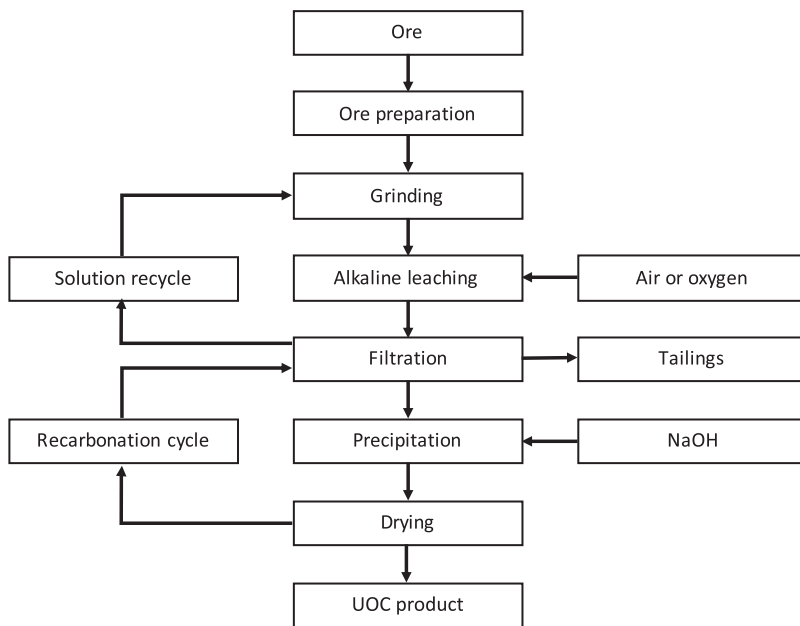


Figure 8.4 A generic schematic of the alkaline leaching process.

Source: Adapted from C. Edwards, A. Oliver, Uranium processing: a review of current methods and technology, JOM (2000) 12–20 [4].

or with sodium carbonate,



Once uranium in the ore has been dissolved in solution and is now mobile, it can be more easily transported by submersible pumps in the production well. Uranium is removed from solution at a surface processing facility using an ion exchange resin or polymer [9]. Ion exchange involves the following two stages: (1) loading/absorption and (2) elution. During stage (1) the solution is in contact with the ion exchange resin permitting selective adsorption of uranium. During stage (2), uranium is stripped from the resin yielding a uranium-rich solution called “eluate.” Then, hydrogen peroxide may be added to assist with uranium precipitation, which, after drying, produces yellow cake. Different ISL plants may execute this process slightly differently, which may yield ammonium diuranate ($(\text{NH}_4)_2\text{U}_2\text{O}_7$) or uranyl peroxide ($\text{UO}_4n\text{H}_2\text{O}$) [9]. Residual material is typically combined with fresh leaching chemicals and then recycled into the injection wells to continue the ISL cycle. The interested reader is referred to several IAEA technical reports that have thoroughly covered a number of details pertaining to ISL processes related to uranium [7,9].

8.3 Milling

The fundamental purpose of milling is to receive ore materials from the mining operation and extract uranium from it, yielding a higher uranium density and more useable form called “yellowcake.” Uranium mills are typically located near its associated mine to reduce transportation costs, since there can be a large weight reduction during the milling process. The milling process is quite similar when preceded by open-pit (Section 8.2.3.1) or underground mining (Section 8.2.3.2) operations; however, the process is reduced if preceded by ISL (Section 8.2.3.3) since the end product of ISL yields a chemical solution rather than solid ore materials.

During milling the uranium bearing ore is initially crushed (if preceded by conventional mining), which is typically a dry process, and then ground into a slurry, which is a wet process. The intent of crushing and grinding is to effectively increase the surface area to volume ratio of the material, which facilitates chemical leaching. Two stages of crushing may be used: primary (yields ≈ 15 cm material) and fine crushing (yields ≈ 1 cm material) [3]. Crushing is typically accomplished by semiautogenous grinding or autogenous grinding [4].

The material is typically roasted to remove a large portion of organic matter, such as sulfides and carbon-bearing compounds. Note that UO_3 is stable in air up to about 668°C , which then decomposes to U_3O_8 at higher temperatures [10]. Next, the slurry is leached in solution, whereby the solution is selected depending on the ore materials. Sulfuric acid is the most commonly used solution, in addition to various carbonates. Much of this process is akin to ISL, which was described in Section 8.2.3.3. One advantage of using ISL is that crushing is avoided, which reduces dust production and thereby reduces radon gas release, which is a radioactivity concern.

The next stage in the process requires separation of liquids and solids, which is typically a relatively expensive process. A number of methods have been used to achieve this objective, including counter-current decant, drum filters, high-rate thickeners, cyclones, and horizontal belt filters [3]. After solids have been separated from solution, the remaining liquid solution must be purified. The precise process that is taken depends on the composition of the solution, which depends principally on the original ore material and the desired purity of the end product. This is typically accomplished through ion exchange or solvent extraction. The end product of milling is typically yellowcake, which principally contains U_3O_8 in addition to some impurities.

8.3.1 Ion exchange

The primary role of ion exchange is to purify and concentrate the uranium bearing material, which is typically based on absorption or elution processes. Uranyl bisulfate ($\text{UO}_2(\text{SO}_4)_2^{2-}$) and uranyl trisulfate ($\text{UO}_2(\text{SO}_4)_3^{4-}$) are the most common liquors used in acid processes (typical pH of around 1.5–2.5 [11]), while uranyl bicarbonate ($\text{UO}_2(\text{CO}_3)_2^{2-}$) and uranyl tricarbonate ($\text{UO}_2(\text{CO}_3)_3^{4-}$) are common in alkaline liquors (typical pH of around 6–11) [12]. Most ion exchange processes employ a

gel type resin, which occupy a large portion of the sorption and elution columns. Some commercial gel resins used in uranium milling include Amberlite IRA-400, Dowex 21-K, and Permutit SK [12]. Preferred resin properties include selective, rapid, and reversible absorption of uranyl complexes [3].

Ion exchange systems typically come in two varieties: batch and continuous systems. Batch systems may take the form of conventional fixed bed systems or moving bed systems. Fixed bed systems comprise three columns where two of those columns are in series on sorption and the third for eluted purposes [12]. The moving bed system differs from the fixed bed system in that three columns are used in series sorption with an additional three columns in series for elution. Also, an additional column is available for recirculating resin. The net effect is higher performance and lower waste than the fixed bed system.

Continuous ion exchange systems perform multiple steps in a single unit, including adsorption, regeneration, and rinsing. A major advantage of the continuous ion exchange method compared to batch methods is that it can tolerate appreciable quantities of solids—up to 15% in some instances [3]. Therefore the requirement for solid/liquid separation is lessened, which is a relatively expensive stage in the process. There are multiple types of continuous ion exchange systems, including fluidized bed, multiple tank fluidized bed, and pulsed bed down flow [12].

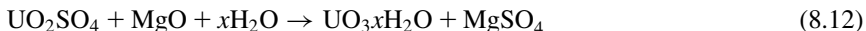
8.3.2 Solvent extraction

An alternate method to ion exchange in purifying the solution is solvent extraction. This method is often preferred when the uranium concentration in solution is high (e.g., >800 mg/L [13]); however, there is no practical solvent extraction process developed for carbonate solutions [14]. The basic premise of solvent extraction is to have the leach solution mix with an organic solvent in a large tank. Uranium that is initially soluble in aqueous solution is transferred to the organic phase. The depleted lixiviant (often called “raffinate”) is typically recycled for subsequent processes or disposed of as waste. Next, the organic solution is purified to remove impurities (e.g., iron and silica), which may otherwise precipitate unwanted materials and contaminating the product. This step can be accomplished with a number of agents, such as nitrates, chlorides, sulfates, and acids. The solution then undergoes an additional step, whereby uranium bearing compounds are precipitated, such as the addition of NH₃ yielding (NH₄)₂U₂O₇ [12].

8.3.3 Precipitation

At the end of either ion exchange or solvent extraction methods, one has an enhanced concentration of uranium in solution. The pregnant liquor then undergoes a precipitation stage whereby uranium bearing compounds are precipitated out of solution, producing yellowcake. This can be accomplished by the introduction of a neutralizing agent such as magnesia, ammonia, sodium hydroxide, or hydrogen peroxide. The particular agent that is used depends on several factors, mainly the composition of the solution, cost, and environmental factors.

Magnesia is often added to solution, which yields the following reaction [3]

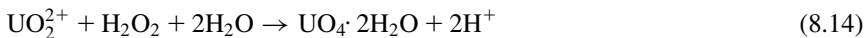


where $1 < x < 2$ and the resulting solution typically has a pH between 7.0 and 7.5 [12]. Alternatively, ammonia may be used with modest heating to 30°C–50°C [3]

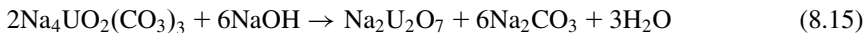


While the use of ammonia was favored at one point due to its ability to produce a high purity product, it is less often used now due to environmental issues associated with this process.

Hydrogen peroxide may also be used at near room temperature (i.e., 25°C) [3]



For alkaline solutions, sodium hydroxide is added at about 25°C, yielding the following precipitation reaction [12]:



The final stage of precipitation involves moisture removal and drying, which generally varies depending on the preceding processes but often involves rinsing with high grade water. Specific techniques include horizontal belt filters, batch filters, and centrifuges, which may involve spray-drying, calcinating, or roasting as intermediary processes at temperatures ranging from 150°C to 700°C [11]. The end product of milling is often called “uranium ore concentration” (UOC) or colloquially as “yellowcake.” This material will be predominantly U₃O₈ with some impurities. The final product will be shipped in 200 L drums, which weigh around 300 kg [11].

The UOC that is produced at the end of the milling process can take on different forms depending on the chemical processes employed. This includes an impure uranium-bearing compound triuranium octaoxide (U₃O₈), or ammonium, sodium or magnesium diuranate (e.g., (NH₄)₂U₂O₇). Yellowcake typically contains 65%–75% uranium and 20%–25% combined oxygen and anionic compounds ranging from a few ppm to a few percent. Refining is performed to further purify the uranium bearing material prior to conversion, which will be discussed in the next chapter.

8.4 Tailings

After the useful uranium bearing material has been extracted from the ore, the leftover material, which is often referred to as “tailings,” must be appropriately dispositioned. This material constitutes the lion’s share of the original ore material volume,

which is often disposed of in the near vicinity of a mining/milling site. The principle concern of tailings is that it is radioactive and contains toxic constituents; therefore, there are concerns from both environmental and human health and safety perspectives. In addition to the responsible stewardship of a mining/milling operator, there are typically legal requirements that must be respected in regards to the handling of tailings.

While the total radioactivity of this material is less than the original ore extracted from the ground, appropriate precautions must be taken to handle tailings, which are in a different form than their natural state. For instance, much of the returned ore has been crushed and ground, which may cause concerns with respect to dust dispersion. Moreover, there is an increased risk to leaching of contaminants (e.g., heavy metals and arsenic) into the groundwater and/or surface water systems. Also, the large surface area of the land renders it unusable for other applications. Engineered remediation measures can be taken to mitigate the aforementioned hazards to the environment and human health. Precautions taken in the handling of tailings (e.g., engineered barriers and legislation) varies from one site to another.

The volume, specific activity, and chemistry of the tailings are all unique to the specific site, which depends on the geochemistry of the ore site, engineering operations that were used, and the extent of operation. The specific activity of the tailings can range from 1 to over 100 Bq/g [15]. Specific components of the tailings may potentially have a large impact from radiological and chemical perspectives.

Radium, which is produced as a daughter product of uranium, is radioactive and remains as residue in the tailings. Radium further decays to radon, which is also radioactive and is stable as a gas. The concern with radon is due to the mobility and transport of radioactive gases to the environment. Tailings must be carefully controlled and monitored for alpha, beta, and gamma radiation. One can quantitatively characterize the tailings in terms of volume and surface areas of impacted zones, concentrations of radioactive elements, and radioactivity.

The primary risk to human health from uranium tailings is due to radioactivity [15]. It is difficult and impractical to quantify specific contributions to overall dose, which may include mining, milling, transportation, distribution of dust, and water contamination. One of the more immediate impacts of radiation dose from tailings to human health has been in the historical reuse of tailings for other applications. There have been some instances where mill tailings were reused as building materials, mainly in the form of concrete with applications ranging from sidewalks to private homes [15]. This practice is now considered inappropriate and is often controlled by legislation, which varies by nation state.

Concerns regarding the chemical nature of the tailings include the chemical toxicity of radionuclides, heavy metals, and nonmetallic compounds (e.g., kerosene). The pH levels depends strongly on whether acid or alkaline leaching was used. Examples of the negative chemical impact of tailings include destruction of vegetation and contamination of groundwater systems, which affects surrounding ecosystems [15].

Historically, a number of practices were followed for the disposition of tailings, including returning the tailings to a mined pit or underground mine, placement in a

valley, or discharging to a deep lake or river [15]. While some of these methods are still used in-practice, some are now considered unacceptable due to the high probability of containment failure (or lack thereof).

Present practices of handling tailings have evolved considerably, which are based on a significant body of information and experience on the impact of tailings on the environment, human health, and economics. The development of regulations by nation states and best practice guidelines—most notably from the IAEA [16,17]—on the design and management of tailing systems tremendously improve the performance and stewardship of these sites.

8.5 Summary

An overview of mining and milling operations employed in industry has been provided. Mining operations typically take on one of three forms: open-pit mining, underground mining, or ISL. The specific type of mining that is employed is typically determined by the location and geochemistry of the uranium bearing ore; however, ISL has become more prevalent for economic reasons. The overall objective of mining is to remove the raw uranium-bearing material from the earth. Milling follows the mining process, which is intended to extract the uranium from the ore. Milling is largely a chemical process, which yields a product much higher in uranium content than mining, but not yet pure enough for the fabrication of nuclear fuel. Several chemical processes used in milling were summarized. The next stage of the nuclear fuel cycle further refines the milled product and converts it into a useable form for subsequent stages of the nuclear fuel cycle involving conversion.

References

- [1] N. Tsoulfanidis, *The Nuclear Fuel Cycle*, American Nuclear Society, La Grange Park, IL, 2013.
- [2] Nuclear Energy Agency & International Atomic Energy Agency, Uranium resources, production and demand, in: Tech. Rep. NEA No. 7413, Nuclear Energy Agency & International Atomic Energy Agency, 2018.
- [3] P. Wilson (Ed.), *The Nuclear Fuel Cycle – From Ore to Waste.*, Oxford University Press, New York, 2001.
- [4] C.R. Edwards, A.J. Oliver, *Uranium processing: a review of current methods and technology*, *JOM* 52 (9) (2000) 12–20.
- [5] J.W. Frondel, M. Fleischer, Glossary of uranium- and thorium-bearing minerals, in: Tech. Rep. 3, US Atomic Energy Commission, 1954.
- [6] World Nuclear Association, Uranium mining overview. <<https://www.world-nuclear.org/information-library/nuclear-fuel-cycle/mining-of-uranium/uranium-mining-overview.aspx>>, Last visited Feb. 28, 2020.
- [7] International Atomic Energy Agency, Manual of acid in situ leach uranium mining technology, in: Tech. Rep. IAEA-TECDOC-1239, Vienna, Austria, 2001.

- [8] R. Butler, Carbonate leaching of uranium ores: a review, in: Tech. Rep. AAEC/E-238, Robertson Research, Lucas Heights, Australia, 1972.
- [9] International Atomic Energy Agency, Uranium in situ leaching, in: Tech. Rep. IAEA-TECDOC-720, Vienna, Austria, 1993.
- [10] M. Piro, Computation of Thermodynamic Equilibria Pertinent to Nuclear Materials in Multi-Physics Codes (Ph.D. thesis), Royal Military College of Canada, 2011.
- [11] I. Hore-Lacy (Ed.), *Uranium for Nuclear Power – Resources, Mining and Transformation to Fuel*, Woodhead, 2016.
- [12] International Atomic Energy Agency, Uranium extraction technology, in: Tech. Rep. TECDOC 359, Vienna, Austria, 1993.
- [13] D. Tonder, M. Kotze, Uranium recovery from acid leach liquors: Ix or sx, in: ALTA Uranium Conference, Perth, Australia, 2007.
- [14] Z. Zhu, C.Y. Cheng, A review of uranium solvent extraction: it's present status and future trends, in: ALTA 2011 Uranium, Perth, Australia, 2011.
- [15] International Atomic Energy Agency, The long term stabilization of uranium mill tailings, in: Tech. Rep. IAEA-TECDOC-1403, Vienna, Austria, 2004.
- [16] International Atomic Energy Agency, Management of radioactive waste from the mining and milling of ores, in: Tech. Rep. WS-G-1.2, Vienna, Austria, 2002.
- [17] International Atomic Energy Agency, Monitoring and surveillance of residues from the mining and milling of uranium and thorium, in: Tech. Rep. Safety report series no. 27, 2002.

This page intentionally left blank

Uranium conversion and enrichment

9

Michael P. Murchie and Simon J. Reid
Cameco Corporation, Port Hope, ON, Canada

9.1 Introduction

Uranium conversion and enrichment follow mining and milling steps and are the precursor processes to fuel manufacturing and, subsequently, to nuclear power generation. The central role of these processes is highlighted in the simplified nuclear fuel cycle shown in Fig. 9.1.

This chapter acquaints the reader with the chemical and physical processes that are used to produce nuclear-grade materials that meet standard specifications for fuel manufacturing, specifically (1) refining/conversion of uranium in preparation of materials for natural nuclear fuel manufacturing or enrichment, (2) enrichment, and (3) conversion of enriched uranium in the preparation of materials for enriched nuclear fuel manufacturing.

The complexity of a nuclear fuel cycle increases with the elaboration of nuclear fuel reprocessing, uranium and plutonium recycling, mixed-oxide fuel (MOX) processes, conversion of depleted UF_6 tails to more stable or useful chemicals, and the thorium fuel cycle. These processes are outside of the scope of this present work.

9.2 Natural uranium conversion processes

9.2.1 What is uranium conversion?

Following the mining and milling of uranium ore, an impure uranium ore concentrate (UOC), which is often referred to as “yellowcake,” is produced. Depending on the ore type and the milling process used, the UOC chemical forms may be different and can include triuranium octaoxide (U_3O_8), uranyl peroxide (UO_4), or to a lesser degree ammonium, sodium, or magnesium diuranates. Uranium conversion, which also incorporates uranium refining, is a necessary processing step for the production of nuclear fuel. The primary purpose of refining is to remove impurities from the uranium that could lead to deleterious effects during fuel manufacturing, enrichment, and irradiation in a nuclear power reactor. The objective of conversion is to produce uranium in a chemical form suitable for enrichment (i.e., UF_6) or a form for direct fuel fabrication for heavy-water reactors (i.e., UO_2 , since heavy-water reactors do not require enrichment). Typically, the sequence of operations is

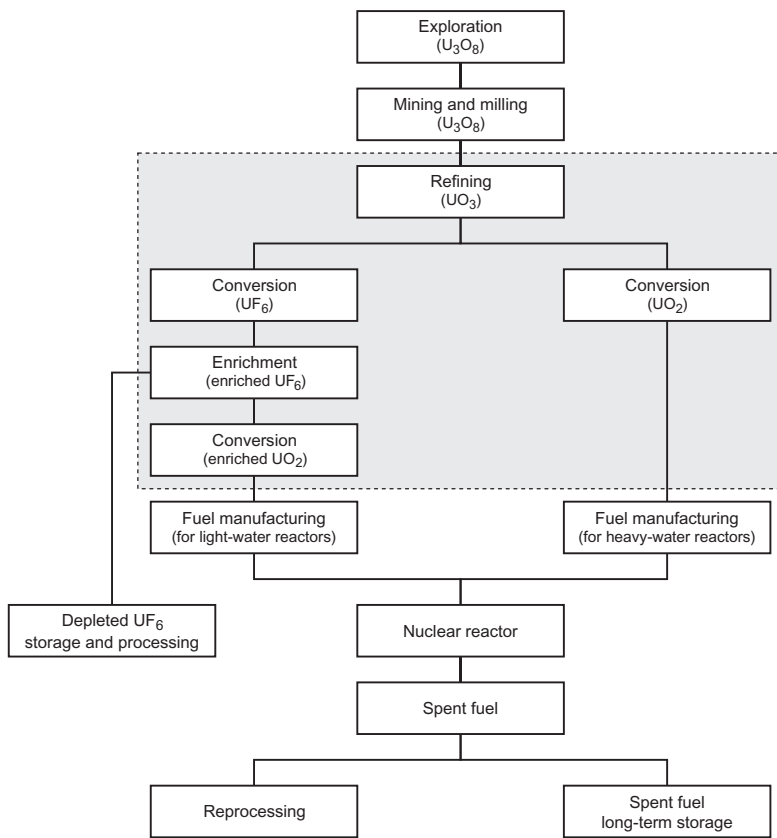


Figure 9.1 Nuclear fuel cycle.

refining first followed by conversion. However, at the Honeywell Metropolis Works facility in the United States, the sequence is reversed, with conversion followed by refining.

Since the majority of commercial nuclear power reactors in the world require enriched fuel, essentially all commercial fuel conversion facilities are dedicated to refining and production of UF₆. In general, there are two methods used for the production of UF₆—the “wet” conversion process and the “dry” fluoride volatility process. These two processes and the production of ceramic-grade UO₂ for pressurized heavy-water reactors (PHWR) are described. First, the special role of UF₆ in the nuclear fuel cycle is presented.

9.2.2 The special role of UF₆ in the nuclear fuel cycle

Uranium hexafluoride (UF₆) is the feed material used in all commercial enrichment processes around the world. It is an ideal chemical for enrichment processes due to

its physicochemical properties [1,2]. It has a convenient triple point at 64°C and 152 kPa, where manipulation of UF₆ as a gas, liquid, or solid is achieved by subtle manipulations of temperature and pressure [1]. A second advantage of UF₆ is that the fluorine atom only has one naturally occurring isotope, which makes uranium isotope separation processes based on mass difference feasible. Since all fluorine atoms in UF₆ are the same, any mass difference in UF₆ must be due to different uranium isotopes. Production of UF₆ is a well-established process; one that has not had any significant process advances in recent years. Uranium hexafluoride production has been summarized previously in the literature [3–7].

The world's demand for UF₆ is met by a relatively small number of producers with a combined, nameplate capacity of 60,000 metric tons of uranium per year as UF₆ (see Table 9.1). Recent changes in the UF₆ production state of affairs include the closure of the facility at Springfield Fuels Limited (United Kingdom) in 2014, the suspension of production at Honeywell (United States) in 2017, and the upgrading and modernization of conversion facilities at Orano in France.

Uranium hexafluoride conversion removes impurities that are capable of forming volatile fluorides that will impact the final UF₆ quality. Thus the goal is to produce a product that meets the chemical specifications of the enricher, enabling the ²³⁵U to be enriched to the desired level. The ASTM specification for UF₆ provides a representation of the UF₆ purity requirements [9].

The hazards associated with processes involving UF₆ are well-known. It is a radioactive and chemically reactive material that requires stringent safety and environmental controls at conversion and enrichment plants [10,11]. Some of the important safety aspects to be considered are related to storage and processing of hydrogen fluoride, fluorine, and UF₆ [6,10,11].

Uranium hexafluoride is transported from conversion facilities to uranium enrichment plants in standard 48Y cylinders, which can contain up to 12,500 kg of UF₆ [10,12–14]. Cylinders used for commercial transport are fabricated from

Table 9.1 Commercial uranium hexafluoride producers.

Company	Country	Refining/ conversion process	Nameplate capacity (tU/a as UF ₆) ^a
Orano (formerly Areva)	France	Wet	15,000
Honeywell	United States	Dry	15,000 ^b
Cameco (also natural UO ₂)	Canada	Wet	12,500
TVEL	Russia	Wet	12,500
CNNC	China	Wet	5000
Springfields Fuels (also natural U-metal)	United Kingdom	Wet	(Closed 2014)
World total			60,000

^aRef. [8].

^bUF₆ production at Honeywell suspended in 2017.

carbon steel in accordance with international standards organizations [International Organization for Standardization (ISO) and American National Standard Institute]. These standards apply to packaging used for transporting UF₆ as well as inspections and maintenance.

9.2.3 Wet conversion processes for production of UF₆

UOC from uranium mines and mills is impure, and it still contains elements other than uranium that are undesirable. These impurities in UOC vary due to differences in milling processes and the sources of the ores. The nuclei of impurity elements can absorb neutrons to different degrees than uranium and thus impact fuel performance in a nuclear reactor. Refining is necessary to achieve highly pure UO₃. UOCs are shipped in drums to the refinery/conversion facility, which typically refines it into uranium trioxide (UO₃) before conversion to UF₆.

Uranium refining/conversion is a multistep chemical process involving several unit process stages, as indicated in the basic flowsheet shown in Fig. 9.2. Where available, the enthalpies of reaction are included [4,15]. The refining/conversion process includes the following steps described next [16,17].

9.2.3.1 Dissolution

The first step of the refining process involves the dissolution of UOC in nitric acid, HNO₃. This step is commonly called digestion. The UOC is added as a powder from drums into a stirred tank reactor where it forms a solution of uranyl nitrate, according to the equations in Fig. 9.2. The uranium concentration, solution density, temperature, and free acid concentration are carefully controlled in this step. The off-gases, containing nitrogen oxides, are sent to a scrubber for recovery of nitric acid for reuse.

9.2.3.2 Solvent extraction

Uranium purification is achieved by solvent extraction. The solvent extraction process equipment varies among uranium refiners, but their basic process steps are similar. In a typical arrangement, the aqueous uranyl nitrate solution is fed to a series of three agitated columns: extraction, scrubbing, and stripping. The aqueous stream enters the extraction column at the top, and it is contacted with an organic solvent that is fed from the bottom. The organic solvent is a solution of tri-*n*-butyl phosphate (TBP) in an inert hydrocarbon diluent (e.g., kerosene or dodecane). The TBP is highly selective to uranium, and they form a uranyl nitrate–TBP complex in the organic solvent, thus separating the uranium from its impurities, which remain in the aqueous solution [18]. The extraction reaction is exothermic ($\Delta H = -18.8 \text{ kJ/mol}$ at 0.5 M HNO₃) [15]. The aqueous stream with impurities is called “raffinate,” and it is concentrated, so that the impurities may be recovered for packaging or further processing. In cases where the raffinate contains residual uranium, the dried raffinate may be recycled to a uranium mill.

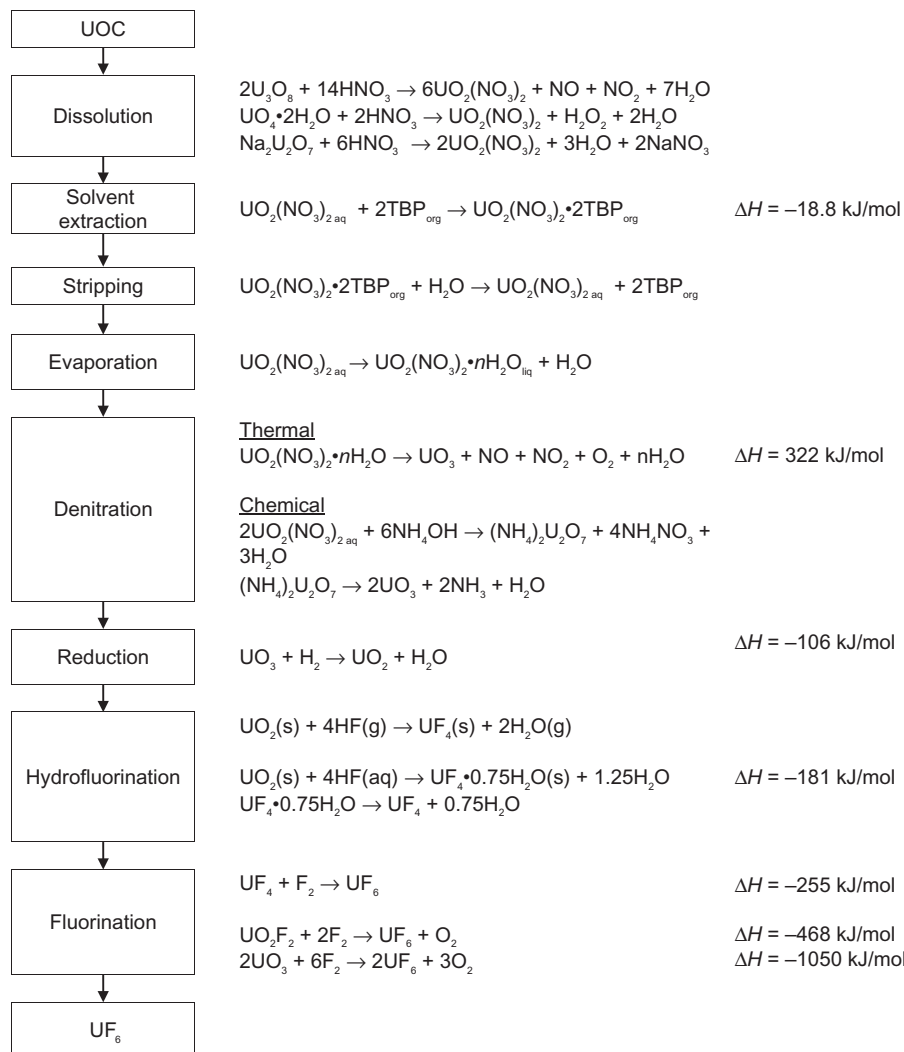


Figure 9.2 Conversion of UOC to uranium hexafluoride (UF_6) using the “wet process.”
UOC, Uranium ore concentrate.

The uranium-“loaded” organic solution is withdrawn from the top of the first column and fed to the bottom of the scrubbing column, where it is contacted with an aqueous scrubbing solution being fed from the top of the column. The purpose of the scrubbing stage is to remove residual impurities that loaded into the organic phase and reduce entrained nitric acid.

The scrubbed, loaded organic solution is fed to the bottom of the stripping column (also referred to as reextraction column), and it is contacted with an aqueous stream, which results in the transfer of uranyl nitrate back into the aqueous phase.

The now barren organic phase is regenerated before recycling back to the start of the continuous solvent extraction process.

9.2.3.3 Concentration

Depending on the facility, the aqueous uranyl nitrate solution is advanced to one or more evaporator units, where water and nitric acid are removed, producing a nuclear-grade uranyl nitrate hydrate molten salt. The molten salt leaving the concentration circuit is often referred to as uranyl nitrate hexahydrate (UNH), but likely the product will be a mixture of known hydrates of uranyl nitrate. UNH is a yellow solid at room temperature, but at elevated temperatures, it can be maintained in the molten state.

The product from the concentration step may be either a molten uranyl nitrate hydrate liquid or a concentrated aqueous solution of uranyl nitrate. The degree of concentration required will vary depending on the refining/conversion facility and the process that it uses for denitration of uranyl nitrate.

9.2.3.4 Denitration (thermal and chemical)

Thermal denitration for conversion of UNH to UO_3 is commonly used among commercial uranium refiners. Typical reaction equipment include heated stirred pots, fluidized beds, or covered trough reactors. In each case, the molten UNH is fed to the denitration reactor, which is heated to temperatures in the range of 250°C–400°C. The reaction is endothermic with a heat of reaction of 322 kJ/mol [19]. Thermal analysis studies have demonstrated that the denitration occurs through successive steps of dehydration and finally decomposition of uranyl nitrate [20,21]. The off-gases from the reaction include nitrogen oxides, oxygen, and water, which are withdrawn to a nitric acid recovery circuit. Control of the temperature and UNH addition rates are necessary to achieve the desired material flow within the reactor and product quality. Purified UO_3 powder can be transferred into approved packages (e.g., drums or tote bins) for transport or fed to the next step in the conversion process.

The refining/conversion facility in Malvesi, France, has implemented a variant of the thermal denitration process; one that produces UO_3 powder with a surface area that is significantly greater than that achieved with the traditional thermal denitration process described above. High surface area UO_3 is a requirement for their downstream reduction and hydrofluorination processes. The new process uses the “Isoflash effect,” where heat for the reaction is provided by the combustion of natural gas (e.g., propane) and air [22]. The denitration reaction takes place when a spray of UNH is efficiently contacted with the combustion flame. It is claimed that the surface area of the UO_3 produced by the Isoflash process is similar to that achieved by the chemical denitration process described next.

Prior to the introduction of the Isoflash process in France for denitration, the facility in Malvesi converted uranyl nitrate to UO_3 using a chemical process. In this process, ammonia is added to the concentrated aqueous uranyl nitrate solution

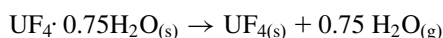
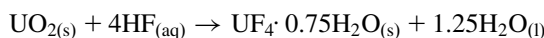
following the concentration stage. Ammonium diuranate $[(\text{NH}_4)_2\text{U}_2\text{O}_7]$, also referred to as ADU) is formed as a finely divided precipitate. The solution is filtered to remove ammonium nitrate, which is concentrated to give a useful by-product, fertilizer. The ADU filter cake is dried and calcined, at 200°C and 400°C , to give UO_3 with a high surface area, typically 11 g/m^2 [23].

9.2.3.5 Reduction

The first step in conversion to UF_6 is reduction of UO_3 to UO_2 , as shown in Fig. 9.2. Some processes may include an additional step to increase reactivity of UO_3 , such as pulverizing UO_3 or UO_3 hydration that was used in the British Nuclear Fuels Process [24]. Regardless of the method, if an activation step is used, uranium dioxide is produced by reduction of UO_3 with gaseous hydrogen, as shown in Fig. 9.2. Hydrogen gas may be supplied by vaporizing liquid hydrogen or produced from ammonia cracking. The reaction is carried out in various reactors, including kilns, fluid beds, or vertical reactors. Incomplete reaction leads to impurities of unreacted UO_3 or partially reduced species such as U_3O_8 or U_4O_9 . Pure UO_2 reacts with oxygen, with the reaction rate dependent on such factors as partial pressure of oxygen, surface area, particle size, and temperature of the powder [25]. This has the effect of increasing the oxygen to uranium ratio and rendering downstream steps less efficient.

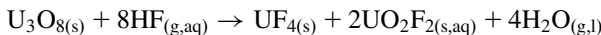
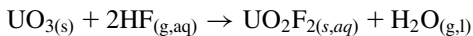
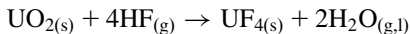
9.2.3.6 Hydrofluorination

The next step in conversion is the production of UF_4 , which is also known as green salt, as shown in Fig. 9.2. Uranium tetrafluoride is produced from the reaction of HF with UO_2 . Uranium tetrafluoride can be produced in a wet (aqueous) process or in a dry process. At the Cameco Port Hope Conversion Facility in Canada, UF_4 is produced in an aqueous process in which a slurry of UO_2 reacts with aqueous hydrofluoric acid to produce a uranium fluoride hydrate. The temperature and acid concentration are controlled to produce the desired hydrate and achieve a high level of reaction to $\text{UF}_4 \cdot 0.75\text{H}_2\text{O}$. As the hydrofluorination process is carried out as an aqueous reaction, drying of the $\text{UF}_4 \cdot 0.75\text{H}_2\text{O}$ is required to remove free water. Calcination is subsequently required to convert the hydrate to a dry UF_4 powder. The drying and calcination steps are important for the subsequent fluorination of UF_4 to UF_6 as residual water will react with fluorine to produce hydrogen fluoride and oxygen. While the aqueous process requires extra processing for drying and calcining, the advantage of the aqueous process is that it allows for use of aqueous HF recovered from the acid recovery systems. This allows the conversion facility to operate without producing an aqueous HF by-product.

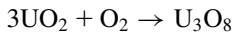


At other UF_6 producers, UF_4 is produced in a dry reaction of UO_2 powder with $\text{HF}_{(\text{g})}$. This is carried out in a reactor such as a kiln, as was previously the case at Springfields Fuels Limited, fluidized-bed reactors as used at Honeywell or in reactors, such as the moving bed reactor used at Orano. In the dry process the HF concentration must be maintained in excess of the stoichiometric requirement, and the temperature is maintained greater than 400°C to achieve the desired conversion. As water vapor forms during the dry hydrofluorination process, the gaseous atmosphere contains a mixture of hydrogen fluoride and water vapor. The ratio of hydrogen fluoride to water vapor must be controlled to ensure the reaction equilibrium is shifted to provide conversion to UF_4 . The off-gas from the reactor can be condensed to produce hydrofluoric acid.

Unreduced UO_3 or partially reduced UO_3 reacts in both the dry and wet hydrofluorination processes to produce a mixture of UF_4 and uranyl fluoride, UO_2F_2 , as shown next.



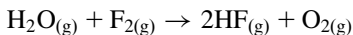
Oxygen is not desired in the dry hydrofluorination process as it reacts with UO_2 to form U_3O_8 , as shown in the following equation. The U_3O_8 then reacts with hydrogen fluoride to produce UO_2F_2 .



9.2.3.7 Fluorination

Direct fluorination of UF_4

Uranium hexafluoride is produced from the reaction of solid UF_4 with fluorine gas, $\text{F}_{2(\text{g})}$, as shown in Fig. 9.2. The reaction is highly exothermic and produces UF_6 in a gaseous form. The UO_2 and UO_2F_2 impurities present in UF_4 also react with fluorine to produce $\text{UF}_{6(\text{g})}$, although these reactions require three and two moles of fluorine, respectively. The fluorination of UO_2 and UO_2F_2 are more exothermic compared to the fluorination of UF_4 and the resulting higher temperatures may cause operating problems that are dependent upon the type of reactor employed. Residual water in UF_4 , or from leaks in the reactor system, also reacts with fluorine, producing hydrogen fluoride, oxygen, and additional heat, which contribute to the corrosion of reactor materials. The efficiency of fluorine use decreases due to the presence of small percentages of water in UF_4 .



The reaction of UF_4 with fluorine gas is carried out in vertical tube reactors, referred to as flame reactors. In these reactors, temperatures can be greater than 1000°C due to the high exothermicity of the reaction. The reaction is also carried out in fluid bed reactors where UF_4 is fed into a calcium fluoride bed and contacted with fluorine. These reactors can be maintained closer to 500°C due to better heat distribution. The UF_4 -to-fluorine ratio must be controlled in order to maintain the fluorination reaction and typically a 10% excess of fluorine is required. Poor control of the UF_4 -to-fluorine ratio with an excess of the required amount of fluorine can lead to inefficient use of fluorine and create stresses to plant scrubbing systems. Poor control of the UF_4 -to-fluorine ratio with a deficiency in the required amount of fluorine can lead to lack of reaction and formation of partially fluorinated UF_4 species, known as “intermediate fluorides.” These intermediate fluorides are UF_5 , U_2F_9 , and U_4F_{17} and are only stable under an atmosphere of UF_6 .

Fluorine production

Fluorine gas required for UF_6 production is not transported or stored in the large quantities required for conversion and must be produced on site. The main precursor to fluorine is anhydrous hydrogen fluoride, and it is transported and received in bulk quantities, for example, in railcars or ISO tank containers. Hydrogen fluoride is a common material for many industrial processes. Fluorine gas is produced in electrolytic cells by the electrolysis of hydrogen fluoride in a potassium fluoride–hydrogen fluoride molten salt, where the composition of the molten salt electrolyte is approximated by $\text{KF} \cdot 2\text{HF}$. In the electrolytic cell, fluorine gas is produced at the anode, while hydrogen gas is produced at the cathode.



The carbon anode is made of nongraphitized carbon while the cathode can be carbon steel. The fluorine and hydrogen gas produced must be physically separated in the cell as recombination of the gases can be explosive. While the thermodynamic voltage required for electrolysis of HF to fluorine and hydrogen is only approximately 2.7 V, the operating cell voltage is significantly higher, 8–12 V, due primarily to anode overvoltage and electrolyte voltage drop (also known as IR drop) from the anode–cathode distance. IR drop is a phenomenon related to the electrical resistance of the electrolyte, which contributes to excessive power consumption and overheating the cell. The fluorine gas produced in an electrolytic cell contains up to 7 vol.% of hydrogen fluoride due to the vapor pressure of HF above the $\text{KF} \cdot 2\text{HF}$ electrolyte. The HF can be removed prior to fluorination of UF_4 or removed during the purification of the resulting UF_6 .

UF_6 recovery

Due to the high reactivity of fluorine, essentially all organic and inorganic trace impurities in UF_4 undergo reaction with fluorine. Impurities that form nonvolatile fluorides, such as ferric fluoride, FeF_3 , and nickel fluoride, NiF_2 , are removed from the gaseous UF_6 through a gas–solid separation process, such as filtration. Special

practices must be employed in the management of the nonvolatile fluorides due to the presence of radioactive metal fluorides that accumulate over time during gas–solid filtration. Impurities that remain with UF₆ following fluorination of UF₄ are those that have formed volatile fluorides. These include inorganic fluorides, such as molybdenum hexafluoride, MoF₆, tungsten hexafluoride, WF₆, arsenic pentafluoride, AsF₅, and chromium pentafluoride, CrF₅.

After UF₆ is produced as a gas, it is typically collected as a solid by deposition in cold traps/condensers. Temperatures in condenser systems are controlled such that collection of HF with the UF₆ is minimized and oxygen and inert gases are not trapped. Volatile inorganic fluorides are also collected and remain as impurities in the UF₆. The solid UF₆ is then heated and liquified at temperatures greater than 64°C and pressures greater than 150 kPa. The liquid UF₆ is then transferred by gravity into shipping cylinders, typically 48Y cylinders, or to a distillation process. Once UF₆ is transferred to a shipping cylinder, it will cool and solidify. The transition of UF₆ from liquid to solid results in an approximate 40% decrease in volume, which reduces the gas pressure within the cylinder.

There are a number of processes that are peripheral but essential in supporting commercial conversion and enrichment operations. These are listed next and have been explained in detail in the literature [10,26,27].

- UF₆ feeding—preparing a cylinder containing solid, natural UF₆, heating the cylinder, and feeding the gaseous UF₆ to an enrichment plant
- UF₆ withdrawal—recovering gaseous natural, enriched and depleted UF₆ into cold traps, placing the cold traps into a heating cycle, and transferring the liquid UF₆ into product and tails cylinders
- UF₆ cylinder handling—transporting UF₆ to and from the site, on-site storage
- UF₆ cylinder weighing—UF₆ in feed, product, and tails cylinders are accurately weighed for material accountability and process control
- UF₆ cylinder inspection, testing, cleaning, and repairing
- UF₆ sampling—UF₆ cylinders are sampled to ensure chemical purity and verify the ²³⁵U concentration to meet feed and product specifications

9.2.4 Dry fluoride volatility process for production of UF₆

The dry fluoride volatility route is unique to Honeywell in the United States. The process does have similarities to the wet conversion process, however with one major difference; uranium purification is at the end of the process rather than the beginning, as indicated in Fig. 9.3.

A summary of the major process steps for the Honeywell process is provided as follows [3,7]. In cases where the feed to the plant contains sodium, for example, sodium diuranate, the feed is treated to remove the sodium, which can cause interferences in the downstream processes. The feed is dissolved in sulfuric acid, forming a uranyl sulfate solution, which is contacted with ammonia to form a precipitate of ADU. The ADU solid is separated from the soluble impurities by filtration.

The calcination step is designed to produce U₃O₈, and in this step, ADU is thermally decomposed to produce solid U₃O₈ and volatile products. When the calciner

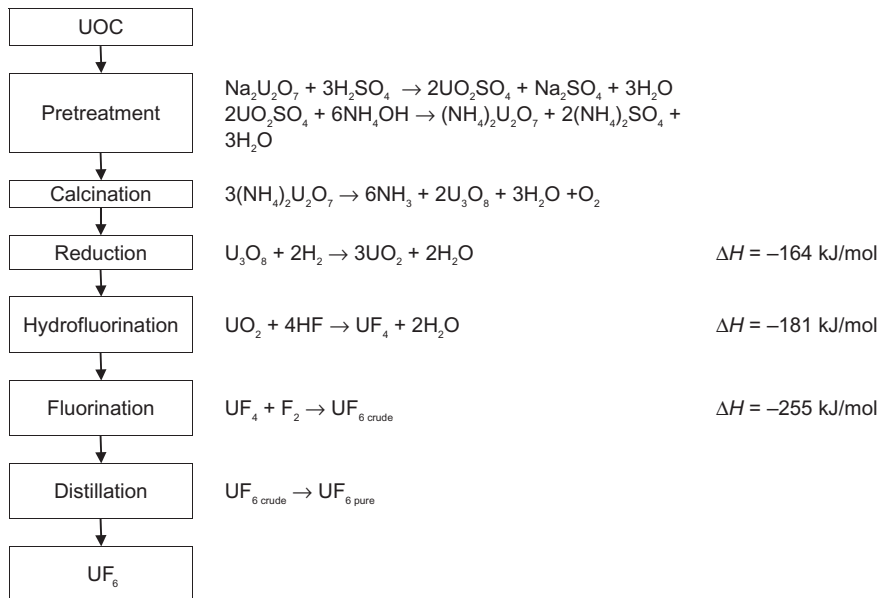


Figure 9.3 Conversion of UOC to UF_6 using the “Dry Process.” *UOC*, Uranium ore concentrate.

feed is UOC in the form of U_3O_8 , impurities such as carbonates, water, organics, and other volatiles are driven off during the process. The U_3O_8 after this stage has the chemical and physical characteristics that are required for the reduction stage.

The reduction, hydrofluorination, and fluorination stages are similar to those previously discussed, except that the UF_6 produced is impure and requires purification by fractional distillation. Each of these unit processes involve gas/solid reactions that take place in fluid bed reactors, each designed for the specific process.

The crude UF_6 is contaminated with the fluorides of elements that were present in the UOC, including vanadium, molybdenum, silicon, carbon, sulfur, thorium, and protactinium. These fluorides must be separated from the UF_6 before it can be advanced to an enrichment process. Fractional distillation using two columns is used to purify UF_6 from these contaminants. Liquid UF_6 is fed to the low-temperature distillation column, and low-boiling, volatile fluorides exit the top of the column leaving UF_6 and the high-boiling compounds behind. The material left behind is then fed to the high boiler distillation column, where the more volatile UF_6 will exit the top of the column leaving the high-boiling and nonvolatile fluorides behind. These solid remnants are disposed of as waste. The distillation system yields UF_6 with a purity of greater than 99.99%. The pure UF_6 is deposited into cold traps and then subsequently transferred into cylinders for transport to uranium enrichment plants.

9.2.5 Production of ceramic-grade UO_2 for pressurized heavy-water reactors

PHWRs, such as the CANDU reactor, require fuel fabricated from natural-uranium, ceramic-grade UO_2 . Smaller quantities of this material are also used as blanket fuel in pressurized water reactors and boiling water reactors, which use low-enriched uranium (LEU) fuel. Production of ceramic-grade UO_2 is accomplished by the ADU route, a chemical process involving several unit process stages, as illustrated in Fig. 9.4.

It is interesting to note that enriched uranium, ceramic-grade UO_2 powder, is also produced by similar ADU chemical processing route, which is discussed later in this chapter. Similarly, as mentioned before, the chemical denitration process in UOC refining also employs the ADU chemical processing route.

In Canada, UO_3 powder is shipped in specially designed tote bins from the refinery to the conversion facility [7,16,28]. Uranium trioxide is conveyed to a dissolution tank containing nitric acid, where it readily dissolves producing uranyl nitrate, which is then fed to a stirred precipitation tank. The aqueous uranyl nitrate is reacted with ammonium hydroxide to give a yellow, ADU precipitate, according to the equation in Fig. 9.4. ADU has an elemental analysis that closely approximates the recognized chemical formula, $(\text{NH}_4)_2\text{U}_2\text{O}_7$. However, studies have shown that the compound is a complex mixture that can vary with production conditions [25,29]. The physical characteristics of the precipitated ADU, such as morphology, porosity, particle size, and filterability, have an influence on the final product quality, and thus precipitation conditions must be carefully controlled to ensure that the final UO_2 powder is suitable for pellet fabrication.

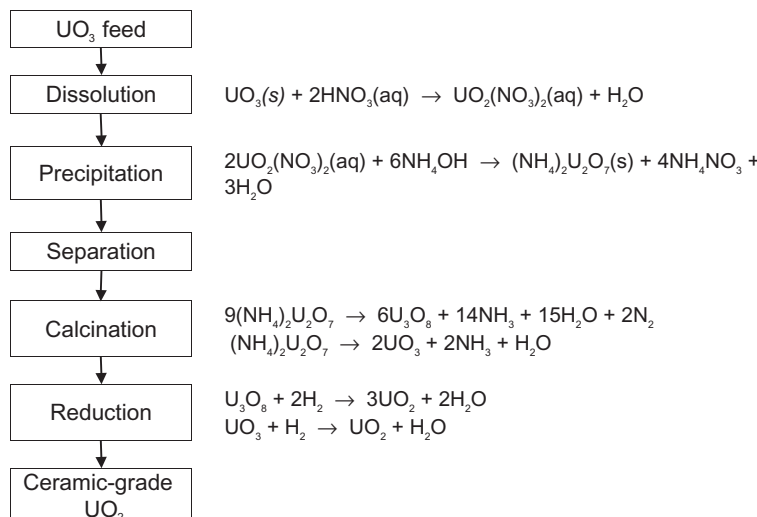


Figure 9.4 Conversion of UO_3 to ceramic-grade UO_2 for CANDU reactors.

The ADU slurry is fed to a centrifuge where the mother liquor is removed producing an ADU cake. The moist ADU solid is fed to a dryer to remove free water and then fed to a horizontal rotary kiln, where it is heated in a countercurrent flow of hydrogen. ADU is thermally decomposed, and its decomposition products are reduced during this step. Calcination at temperatures between 300°C and 400°C yields uranium trioxide (UO_3), whereas U_3O_8 is formed at temperatures greater than 500°C [29,30]. Both U_3O_8 and UO_3 are reduced in excess hydrogen between 500°C and 750°C to form fuel-grade UO_2 . The process is controlled to produce a highly pure, ceramic-grade UO_2 powder. While considered pure, the UO_2 stoichiometry can deviate from an O:U ratio of 2.0. The crystal lattice of UO_2 readily enables the inclusion of oxygen, such that there is a considerable region of nonstoichiometric, solid-phase composition for “ UO_2 ” [6,31]. The product is blended, packaged, and shipped to fuel manufacturers where the powder is reduced, pressed, and sintered into commercial-grade pellets [7,16,28].

Gaseous products from all process vessels are scrubbed before release to the atmosphere. The ammonium nitrate (NH_4NO_3) solution from the ADU precipitation step is further treated to produce fertilizer by-product.

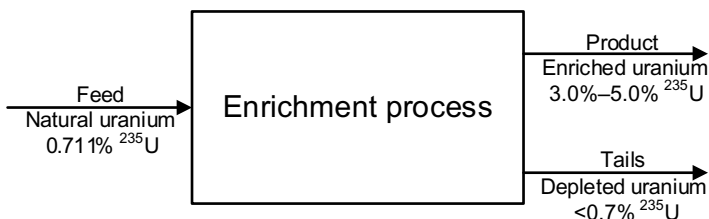
9.2.6 Production of uranium metal for Magnox reactors

The last of the Magnox reactors closed at the end of 2015, and the production of Magnox fuel had ceased several years earlier. These reactors had operated for nearly 50 years, using natural uranium metal as fuel. In the United Kingdom, refining and conversion services included the preparation of natural uranium metal for Magnox reactors. The conversion process in this case was similar to the wet conversion processes for production of UF_4 described earlier [7]. However, instead of reacting UF_4 with fluorine, the UF_4 was fed to a uranium metal production circuit. In this circuit, UF_4 powder was mixed with magnesium turnings, and the mixture was fed to a pelleting stage where 125 mm × 85 mm cylindrical pellets were produced. These pellets were loaded in a specific arrangement into a reactor with pellets of magnesium. The reactor was sealed and then preheated in an electric furnace. After a soaking period, the mixture fired releasing heat and pressure. This exothermic oxidation–reduction (redox) reaction resulted in the formation of a uranium metal billet and magnesium fluoride slag, as indicated in the next equation [25,32]. The uranium billet was advanced to a casting facility and then on to fuel fabrication [6,32].



9.3 Uranium enrichment

The large majority of nuclear reactors in commercial operation in the world today are light-water reactors, which require enriched uranium in the fuel [33].



		Example A ^a		Example B ^b	
		Total mass U (kg)	Mass ^{235}U (kg)	Total mass U (kg)	Mass ^{235}U (kg)
Feed	Natural uranium	1000	7.11	1000	7.11
Product	Enriched uranium	152	4.57	87	4.37
Tails	Depleted uranium	848	2.54	913	2.74

^a Example A—3.0% ^{235}U product assay and 0.3% ^{235}U tails assay; 521.39 SWU

^b Example B—5.0% ^{235}U product assay and 0.3% ^{235}U tails assay; 629.42 SWU

Figure 9.5 Block flow diagram for an enrichment process.

Only the Magnox and CANDU reactors are designed to use natural uranium. Uranium found in nature consists of three isotopes, ^{238}U , ^{235}U , and ^{234}U , with natural abundances of 99.28%, 0.71%, and less than 0.01%, respectively [3,25]. It is the ^{235}U isotope that undergoes fission by collision with thermal neutrons, which releases a large amount of energy as heat. Enrichment is the process whereby the ^{235}U concentration in the feed material is increased. Typically, in uranium enrichment for light-water reactors, the ^{235}U content in the feed is increased from 0.71% to 3.0%–5.0%. The basic enrichment process illustrated in Fig. 9.5 compares the mass balances for two enrichment levels: 3.0% and 5.0%.

Uranium enriched to less than 20% ^{235}U is considered LEU, whereas enrichment to ^{235}U concentrations of 20%–100% is highly enriched uranium (HEU). With the production of an enriched uranium stream, there is a concomitant generation of a depleted uranium stream.

In an enrichment facility, separation of the feed stream into enriched and depleted product streams occurs at a separation element. The throughput and separation factor are key characteristics of a separation element, and these can vary greatly, depending on the isotope separation technology. The throughput is the rate at which feed material is processed, while the separation factor is a ratio of the concentration of ^{235}U in the enriched stream to that in the depleted stream. Detailed descriptions of the separation factor have been published [11,34]. To achieve commercial-scale enrichment capacities, the combination of separation elements into stages and stages into cascades is necessary.

Two factors determine the overall performance of an enrichment plant, the separation capacity, and separative work. The rate at which a cascade performs separation is the separation capacity, and it is commonly measured in kilograms of

material per day. The work performed by an enrichment process to convert natural uranium to a quantity of enriched product and a corresponding quantity of depleted product is called separative work, and it is measured as kilogram separative work units (SWU) or simply SW, that is, 1 SWU equals 1 kg SW.

A particular uranium enrichment process may be characterized by the cost of SWU (\$/SWU), which is presented in [Table 9.2](#). An enrichment plant capacity is characterized by metric tons separative work per annum (tSW/a), and a plant with a capacity of 1000 tSW/a is capable of enriching sufficient uranium to fuel several large nuclear power stations. Two examples are given in [Fig. 9.5](#), where 1000 kg of natural uranium are enriched to 3% and 5% ^{235}U . In each case, the tails assay or depleted stream was 0.3% ^{235}U . The extra effort required to enrich uranium to 5% is readily apparent, as it requires 629 SWU versus the 521 SWU needed to enrich to only 3% ^{235}U . In ordinary practice, the following equation can be used for the calculation of separative work [3,26,34–36].

$$S = P(2x_p - 1)\ln\frac{x_p}{1-x_p} + T(2x_t - 1)\ln\frac{x_t}{1-x_t} - F(2x_f - 1)\ln\frac{x_f}{1-x_f}$$

where S is the effort in SWU; P is the mass of the product, the enriched uranium; T is the mass of the tails; F is the mass of the feedstock; x_p is the assay of the product; x_t is the assay of the tails; and x_f is the assay of the feedstock.

Uranium isotope separation processes must take advantage of very small differences in the physicochemical properties of the isotopes. The options can be grouped as physical and chemical processes.

Uranium enrichment is achieved predominantly by exploiting the mass difference between ^{235}U and ^{238}U , and all current and past commercial enrichment processes have relied on this difference.

Chemical and photochemical processes for isotope separation have been the subject of much research and development for uranium enrichment, but no commercial-scale process has been achieved to this date.

9.3.1 Uranium enrichment processes

Uranium enrichment technologies are well-known, and many have been developed since the Manhattan Project in the 1940s. The two commercial-scale enrichment processes that have been successfully demonstrated are gaseous diffusion and gas centrifuge enrichment. Since 2013, enrichment by gaseous diffusion has been discontinued and fully replaced by the gas centrifuge process [37]. The retirement of gaseous diffusion plants was largely due to their energy intensive nature. Currently, all commercial enrichment facilities utilize a gas centrifuge process, which require less electricity than gas diffusion plants and are generally far less expensive. However, developments in laser enrichment technologies suggest that it may be the next-generation enrichment technology [37]. A key feature for consideration of laser enrichment is its low energy intensity relative to that of the gas centrifuge (see [Table 9.2](#)).

Table 9.2 Uranium enrichment processes^a.

Enrichment process	Operating principle	Single-stage separation factor	Stages required 3% enriched and 0.3% tails	Energy intensity per SWU (kW h)	Operating cost (\$/kg SWU)	Scale of use
Gaseous diffusion	Nuclear mass difference, molecular diffusion through porous barrier	1.0040–1.0045	1000–1700	2300–3000	44	First-generation, commercial
Gas centrifuge	Nuclear mass difference, diffusion in a pressure gradient	1.3–1.6	10–13	40–100	8	Second-generation, commercial
Laser • Atomic • Molecular	Photoexcitation (quantum principle) Selective absorption of ultraviolet/visible light Selective absorption of infrared light	5–15 ^b	1	10–50	1	In development, potential Third-generation technology
Electromagnetic	Nuclear mass, electromagnetic principles, difference in charge to mass ratio in a magnetic field	20–40 ^b	N/A	3000–4000	N/A	Mature, not suitable for large-scale production

Aerodynamic	Nuclear mass, mass difference, diffusion in a pressure gradient principle	1.015 1.025–1.030	550–750 1800–1900 ^c	3000–3500 3000–3500	53 56	Demonstration Demonstration
Chemical ^d	Valence change behavior, chemical equilibrium principles, quantum theory of molecular bonds	1.0025–1.0030 1.0013	40	< 600 400–700	20	Pilot Pilot
Thermal diffusion	Heat transfer	N/A	N/A	N/A	N/A	Mature, not suitable for large-scale production

^aGeneral review of enrichment processes, as well as more detailed accounts and technology performance characteristics can be found in Refs. [3,11,34,37–45].

^bEnrichment factor—simple relationship between isotopic ratio at any stage and that of the previous and subsequent stages.

^cFor the Helikon process, 1848 stages are assembled in about 100 modules [45].

^dIX, Ion exchange process; SX, solvent extraction process.

The principles, characteristics, economics, and scale of use for uranium enrichment technologies that have reached an advanced technology readiness level are summarized in [Table 9.2](#). These technologies and their associated characteristics are briefly described next. Uranium enrichment for commercial purposes is carried out around the world, primarily in France, Germany, The Netherlands, United Kingdom, Japan, United States, Russia, and China. As previously described, UF_6 is the feed material to all commercial enrichment processes around the world.

The unique features of the two commercial enrichment processes and a number of enrichment technologies that have been developed to the near-commercial, pilot plant, or laboratory scales are described next.

9.3.1.1 Gas centrifuge enrichment process

Gas centrifuge enrichment technology was originally developed in the early 1940s, at the same time as other technologies were being developed. However, it was not advanced at the time due to technical disadvantages and the availability of the simpler gaseous diffusion process. After World War II, additional development and significant technical advances were made to this technology, such that gas centrifuge technology was reintroduced during the 1960s and took its place as the second-generation enrichment technology. Since that time, the implementation of this technology has grown to the point that it is now the sole technology used at commercial enrichment facilities.

A gas centrifuge is a long, narrow, vertical cylinder known as a rotor, which is rapidly rotated on its axis within an evacuated casing. A schematic of a centrifuge, based on the Zippe design from the early 1960s, is illustrated in [Fig. 9.6 \[3\]](#). The operating principle of the gas centrifuge is centrifugal force operating at thousands of times that of gravity, which creates a density gradient in a gas mixture. In uranium enrichment, UF_6 gas is fed to the rotor, and the heavier $^{238}\text{UF}_6$ molecules move toward the outer wall, while the lighter $^{235}\text{UF}_6$ molecules gather at the center of the cylinder. This partial separation is enhanced by an induced, axial, countercurrent flow of UF_6 , which causes enriched and depleted streams to migrate toward opposite ends of the cylinder. The depleted and enriched streams are withdrawn from the cylinder via stationary fixtures at each end.

The separative capacity of a gas centrifuge improves with increases in two key design features: the length and rotational speed. At rotational speeds of up to 700 m/s, proper selection of materials of construction for the rotor is essential in order for it to withstand the mechanical stresses and the corrosive nature of UF_6 . Increasing the length of the rotor requires precision fabrication capabilities, since the rotor must be finely balanced, straight, and of uniform wall thickness to prevent vibration and wobbling [\[26\]](#). Other factors that influence the separation factor include the axial location of the UF_6 feed point within the centrifuge, feed rate, and temperature [\[46,47\]](#).

The separation factor of a gas centrifuge is in the range of 1.3–1.6, and while small, it is greater than separation factors for gaseous diffusion or aerodynamic processes. The process has to be repeated many times to achieve the desired ^{235}U

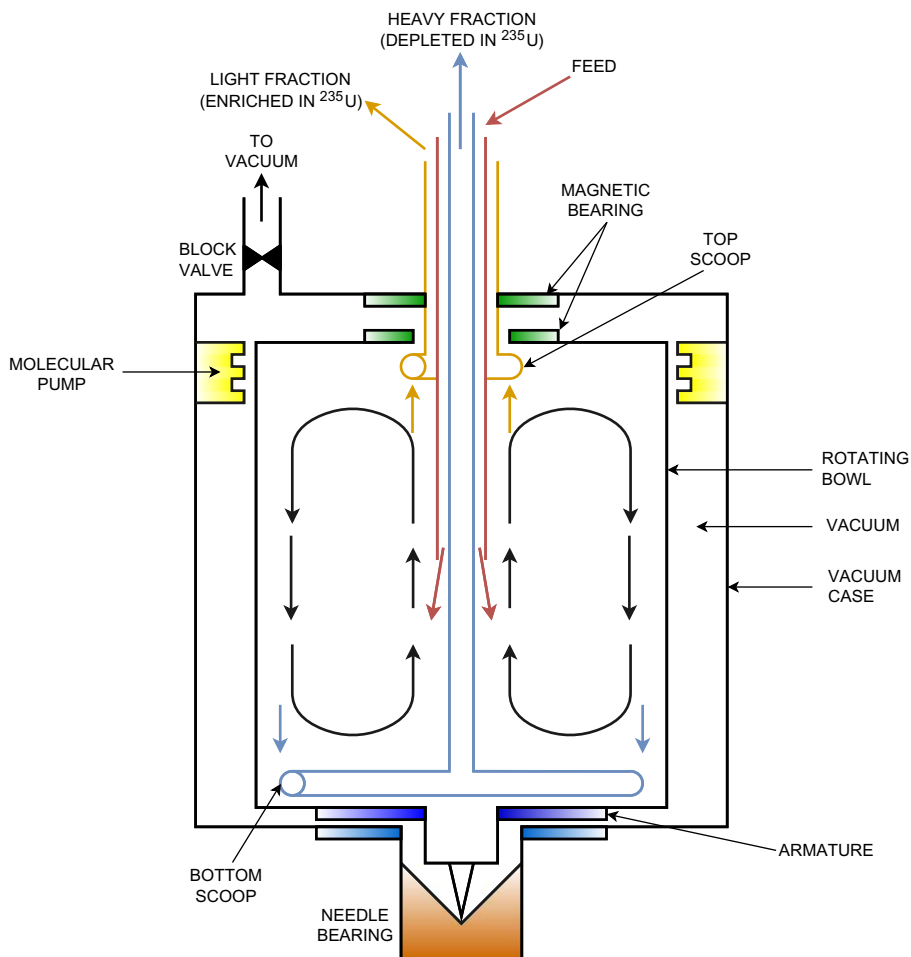


Figure 9.6 Gaseous UF_6 centrifuge enrichment schematic.

concentration that is required for nuclear power plants. Centrifuges are connected in series, and the concentration of ^{235}U in the enriched stream is incrementally increased until the desired enrichment level is attained. Similarly, the depleted stream is further successively “stripped” in a series of centrifuges to reach a final ^{235}U concentration. In a cascade arrangement, centrifuges are also connected in parallel to attain the designed material flow rate for the enrichment plant (see Fig. 9.7).

Key features of gas centrifuge enrichment, relative to gaseous diffusion, are as follows:

- Higher separation factor
- Smaller equipment
- Lower energy consumption/cost
- Modular—flexible for adjusting to required production rates



Figure 9.7 Cascade of gas centrifuges for the enrichment of uranium (Courtesy of the U.S. Department of Energy).

9.3.1.2 Gaseous diffusion process

The first commercial, large-scale process was the gaseous diffusion process. Developed in the early 1940s during World War II, it became the first-generation enrichment technology.

The general principle behind gaseous diffusion exploits the mass difference between the two uranium isotopes. At thermal equilibrium, the average kinetic energies of gases in a mixture are the same. Since the kinetic energy of a molecule is a function of its mass and velocity, molecules with the same average kinetic energy have different average velocities that are related to their mass difference. On average, lighter molecules travel faster than heavier molecules and thus contact the walls of a vessel more frequently. If one of the walls is a membrane with holes large enough to allow single molecules to pass, but small enough to prevent bulk flow of the gas, more of the lighter molecules will pass through the holes than the heavier molecules (see Fig. 9.8).

At an enrichment facility, each separation element consists of a converter, which is also known as a diffuser. The converter contains thousands of tubes of diffusion barriers [3]. Fig. 9.9 illustrates the size of a converter. The diffusion barrier or membrane is perforated with submicron holes. Gaseous UF_6 is pumped to higher pressure by primary and secondary compressors and then fed to a cooler where the heat created from gas compression is removed. The cooled gas then flows to the inside of the barrier tubes, and the faster moving $^{235}\text{UF}_6$ molecules more readily pass through the holes into the lower pressure area of the converter. Thus the gas diffusing through these tubes is partially enriched, having a slightly higher concentration of ^{235}U . The diffused gas is then fed to the next stage, and the process is repeated. The remaining, partially depleted, stream from the converter is fed to another stage where the material is treated further.

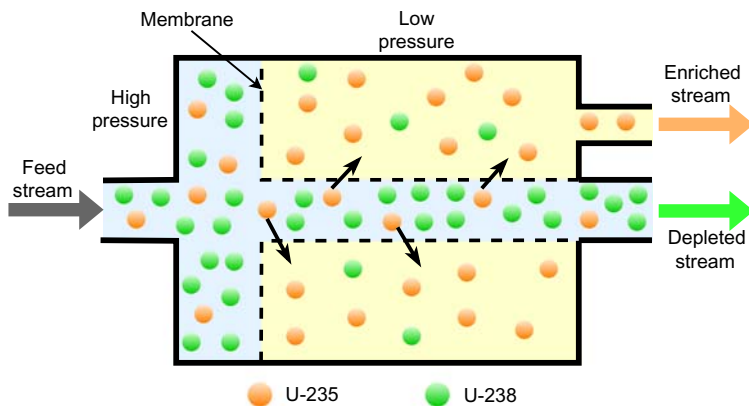


Figure 9.8 Gaseous UF_6 diffusion enrichment separator.



Figure 9.9 Compressors and converters at the Atomic Energy Commission's Oak Ridge Gaseous Diffusion Plant—c.1972.

The separation factor of a gaseous diffusion stage for UF_6 is very small and in the range of 1.0040–1.0045 due to the very small mass difference between the two uranium isotopes. Thus, gaseous diffusion cascades consist of many separation stages.

Key features of gaseous diffusion enrichment are as follows:

- Low separation efficiency—requires hundreds of stages
- High energy consumption
- Significant holdup of uranium in cascades
- Fixed capacity—not modular

9.3.1.3 Laser isotope enrichment process

Laser isotope separation differs from the commercial separation technologies since it does not rely solely on the small mass difference between the two uranium isotopes. It is based on quantum processes and takes advantage of the isotope shifts of discrete electronic excitation or infrared absorption energy levels for atomic or molecular processes, respectively. These phenomena can be used to discriminate ^{235}U from ^{238}U .

In the atomic vapor laser isotope separation (i.e., AVLIS in the United States and SILVA in France) process, uranium liquid is produced by bombarding an ingot of uranium metal with an electron beam. The molten uranium provides a source of uranium atoms that migrate to the irradiation zone. A laser beam strikes uranium atoms in the gas phase, and since the electron energy states for ^{235}U and ^{238}U are different, the ^{235}U can be selectively excited through absorption of light. A highly precise combination of lasers is used to selectively photoionize only ^{235}U . The positive $^{235}\text{U}^+$ ions can then be separated from the bulk atomic vapor by passing the mixture through an electrostatic field, which deflects the ions to collectors. The bulk vapor containing ^{238}U passes through the chamber, unaffected by the laser light and ion collector.

The molecular laser isotope separation (MLIS) process relies on a two-step interaction of laser light with cooled, gaseous UF_6 in the presence of a carrier gas, such as N_2 , Ar, He, or H_2 . First, an infrared laser is precisely tuned to selectively excite $^{235}\text{UF}_6$, which can then be separated from the bulk vapor through ionization, dissociation, or chemical reaction. Two MLIS techniques are described next.

- Molecular obliteration laser isotope separation—The excited $^{235}\text{UF}_6$ is photodissociated by an ultraviolet laser to yield $^{235}\text{UF}_5$ and fluorine gas. Solid UF_5 is collected on an impact plate, and the bulk UF_6 gas passes through the reactor unchanged. Some $^{238}\text{UF}_5$ will also be produced and collected due to overlap of the absorption bands of $^{235}\text{UF}_6$ and $^{238}\text{UF}_6$.
- Chemical reaction laser isotope separation—Excited $^{235}\text{UF}_6$ molecules react with a gaseous coreactant to become a new compound. The reaction rate of laser-excited $^{235}\text{UF}_6$ is much greater than the reaction rate of $^{238}\text{UF}_6$. The product of the reaction has a lower vapor pressure than UF_6 , and thus, it can be deposited on a collector and then removed by mechanical or chemical methods.

Advancement of the AVLIS method has ceased. In the United States, laser isotope separation is focused on the separation of isotopes by laser excitation (SILEX) process, which was developed in Australia in the 1990s. Similar to other MLIS processes, SILEX is based on highly selective laser excitation to facilitate separation of the isotopes. In the case of SILEX, gaseous UF_6 in a carrier gas is fed through a Laval nozzle to a lower pressure chamber forming a supersonic jet. As the gas expands, it is cooled adiabatically, and the cooling enhances the separation efficiency. The $^{235}\text{UF}_6$ molecules, excited by laser radiation, resist condensation due to the nearly instantaneous dissociation of dimers on their formation. The recoil energy acquired by the molecules allows for their separation from the bulk flow of the gas jet. The $^{235}\text{UF}_6$ -enriched periphery of the gas jet is collected by a skimmer,

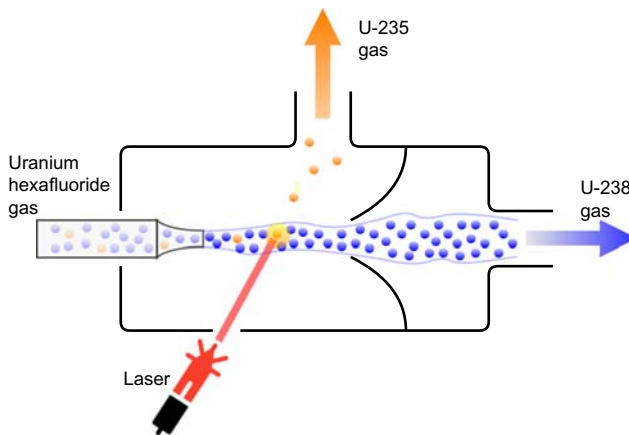


Figure 9.10 Laser enrichment schematic (SILEX). *SILEX*, Separation of isotopes by laser excitation.

which directs it to the product outlet of the chamber (see Fig. 9.10) [48]. The total energy consumption of a SILEX enrichment plant with 10-m long separation units could be as low as 9.8 kW h/SWU, approximately five times less than a gas centrifuge process [42].

Laser isotope separation processes show great promise with high separation efficiencies and high energy efficiencies. It is expected that the footprint of a laser enrichment facility would be small relative to current enrichment facilities.

Key features of laser enrichment processes relative to gaseous diffusion and gas centrifuge are as follows:

- High separation efficiency
- Attainment of very low-level tails assay
- Low energy consumption
- Lower capital costs
- Modular plant expansion
- Complexity and reliability of laser systems need to be established
- Concern over new proliferation risk
- Low technology readiness level

9.3.1.4 Electromagnetic enrichment process

The electromagnetic process was one of a number of technologies being advanced in the early 1940s, but due to its high costs, it was abandoned in favor of gaseous diffusion. The electromagnetic isotope separation process used devices called calutrons, a contraction of California University cyclotron, where the technology was developed. Calutrons operate similarly to a mass spectrometer. Uranium tetrachloride is heated electrically to produce a UCl_4 vapor, which is the source for uranium ions in the calutrons. As uranium ions containing ^{235}U and ^{238}U pass through a

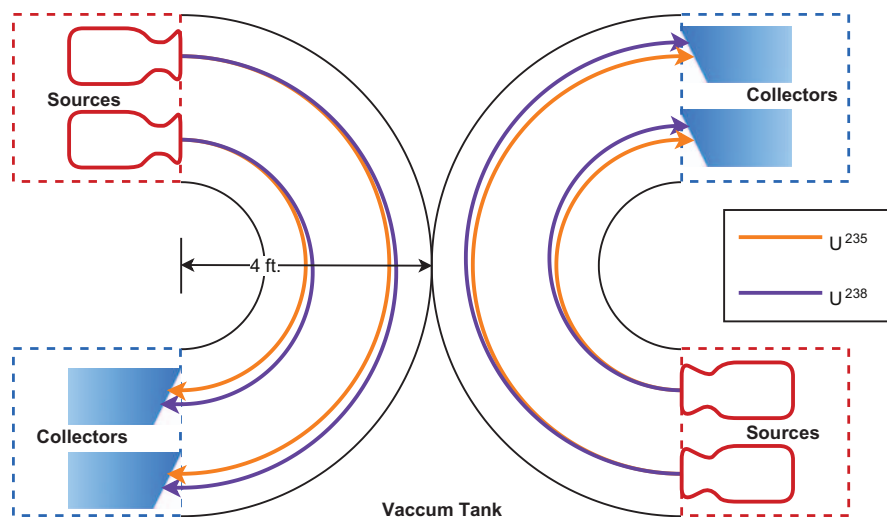


Figure 9.11 Electromagnetic isotope separation—alpha calutron.

magnetic field, the heavier ^{238}U -containing ions travel in orbits of larger radii than the lighter ions. Figs. 9.11 and 9.12 illustrate the general schematic and the practical arrangement of individual calutrons into a racetrack configuration [49,50]. At the Y-12 facility in the United States, 17 racetracks were constructed [49]. Each calutron could only collect very small quantities of enriched material; however, the process was effective, and enrichment levels of 90% ^{235}U were achieved at the Y-12 facility in Oak Ridge, TN.

9.3.1.5 Thermal diffusion process

Thermal diffusion enrichment technology was developed during World War II, and it was one of four technologies being advanced in the United States. The technology employed heat transfer to separate isotopes. A vertical layer of liquid UF_6 is heated on one side and cooled on the other, giving rise to an upward flow on the hot side and downward flow on the cold side due to natural circulation (see Fig. 9.13). The heavier $^{238}\text{UF}_6$ tends to migrate toward the cold wall, whereas the lighter $^{235}\text{UF}_6$ moves toward the hot surface. The diffusion and convection flows in the column allowed for the takeoff of partially enriched and depleted streams at opposite ends of the column. Each column comprised three tubes, an outer cooling water jacket, middle tube containing the UF_6 film, and inner tube for steam heating (Fig. 9.14). The one production facility in the United States consisted of more than 2000 15 m columns (see Fig. 9.15) [51,52]. While simple in operation and low capital cost, the operation of the S-50 plant in the United States was discontinued in 1945 after less than 1 year due to the availability of the more efficient gaseous diffusion process.

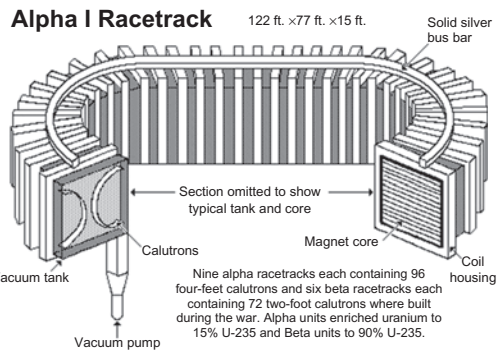
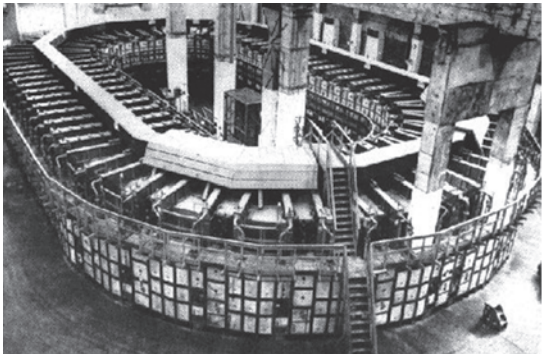


Figure 9.12 Arrangement of calutrons into “racetrack” configuration (Alpha I Racetrack schematic used with permission of Richard Rhodes).

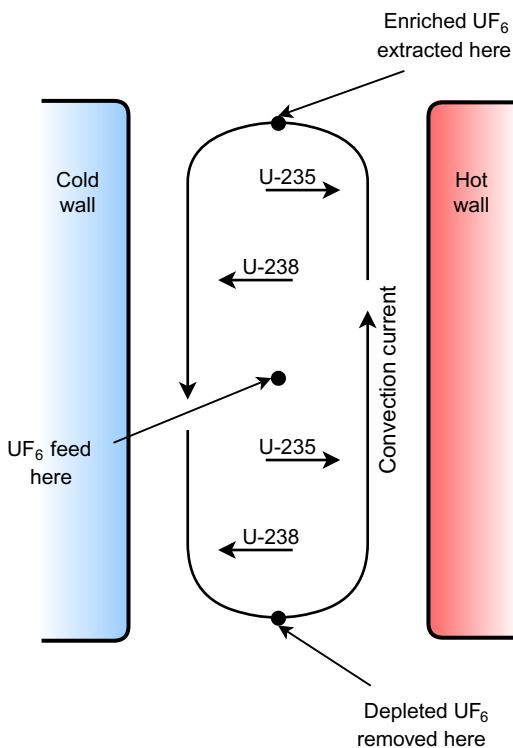


Figure 9.13 UF₆ thermal diffusion enrichment schematic.

9.3.1.6 Aerodynamic enrichment process

Two aerodynamic processes were developed and brought to the demonstration stage. The separation nozzle process was developed in Germany, and it relied on a high-speed gas stream, comprising UF₆ highly diluted by hydrogen or helium, which is forced to turn through a very small radius [53]. The separation of ²³⁵UF₆ from ²³⁸UF₆ occurs due to the resultant pressure gradient. Similar to the behavior in a gas centrifuge, the heavier molecules are forced to the outside of the curved wall, and the lighter ²³⁵UF₆ molecules migrate toward the center. The centrifugal force is enhanced by the presence of the carrier gas, which enables a higher flow velocity for the gas. A knife-edge skimmer at the exit of the curved wall cuts the gas stream into partially enriched and depleted streams (see Fig. 9.16) [53]. The position of the skimmer determines the “cut.” Decreasing the cut reduces the quantity of enriched material but increases the level of enrichment. Similar to the gaseous diffusion and gas centrifuge processes, many hundreds of stages are required to produce sufficient product on a commercial scale.

The Helikon vortex tube process was developed and used in South Africa to produce HEU in the early 1980s. It is based on the same principle as the jet nozzle,

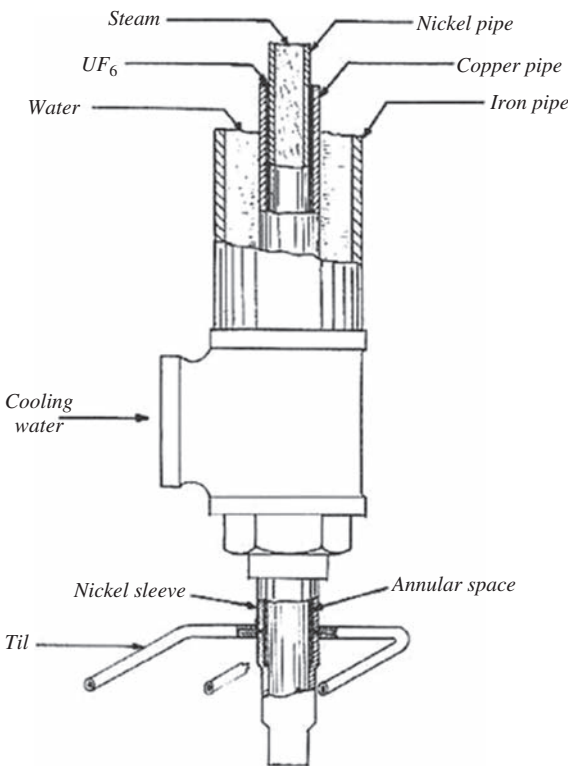


Figure 9.14 UF_6 thermal diffusion enrichment column design.

and it employs the Helikon cascade method, developed specifically for the process. The process has also been referred to as “a stationary-walled centrifuge.”

The aerodynamic processes are capable of producing HEU. However, they are energy intensive due to the large amount of electric power required to compress the gas mixture, which makes them uneconomical as a commercial process. The separation factor is small, and in the range of 1.015–1.030, between that of gaseous diffusion and gas centrifuge processes.

9.3.1.7 Chemical exchange process

Uranium isotope separation using chemical exchange processes relies on segregation of uranium compounds in separate, immiscible streams that are intimately contacted. Early attempts to develop and commercialize a chemical uranium enrichment process were not successful, being too slow and too expensive relative to the gaseous diffusion process. In the 1970s two chemical exchange processes that showed promise were developed and have been tested on a pilot plant scale. Neither of the two processes use UF_6 ; instead uranium is dissolved in aqueous or organic solutions.

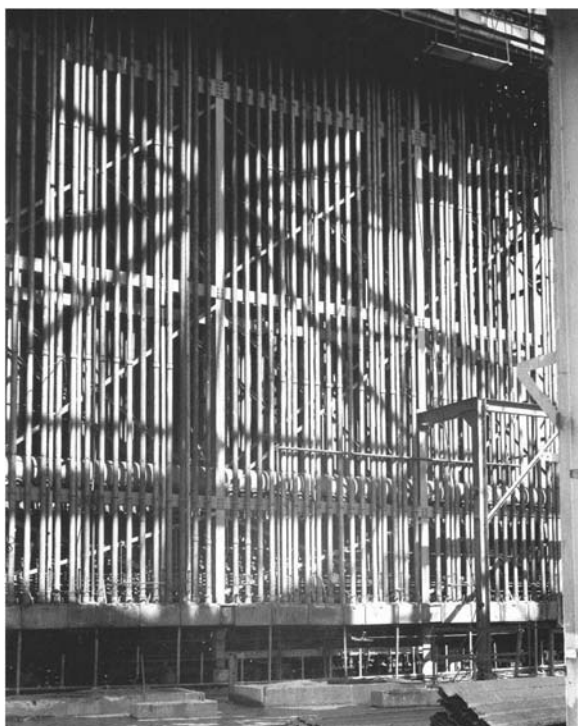


Figure 9.15 UF_6 diffusion columns, S-50 Liquid Thermal Diffusion Plant at Oak Ridge, Tennessee, 1945.

The French CHEMEX process is a solvent extraction process, where an oxidative–reductive reaction between uranium(III) and uranium(IV) ions occurs in aqueous and organic liquid phases. Isotope separation occurs due to the tendency of ^{238}U ions to concentrate in the compounds with a U(III) valence, with ^{235}U concentrating in the U(IV) compounds. In the process, an aqueous phase containing U(III) is fed at the top of a column, and an organic phase containing U(IV) is fed at the bottom. The two solutions flow through each other in a countercurrent manner, where the effectiveness of the solution-contact is increased through agitation, by means of a pulsed column (see Fig. 9.17) [26]. The partially enriched organic phase containing U(IV) and partially depleted aqueous phase containing U(III) are withdrawn from opposite ends and then treated, so that they can be recirculated through the column or advanced to another column.

A redox ion exchange (IX) process was developed in Japan to exploit the chemical isotope effect with uranium in the U(IV) and U(VI) oxidation states. A pilot plant was built in the late 1980s, and uranium enriched to 3% ^{235}U was produced. In 2011 the conceptual design of a commercial enrichment plant based on the redox IX process was reported [54].

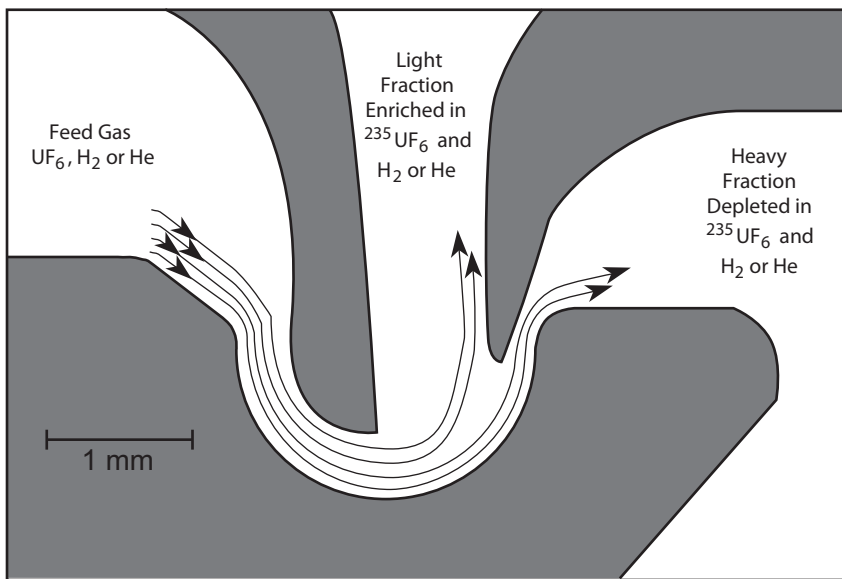


Figure 9.16 Aerodynamic isotope enrichment (jet nozzle) schematic.

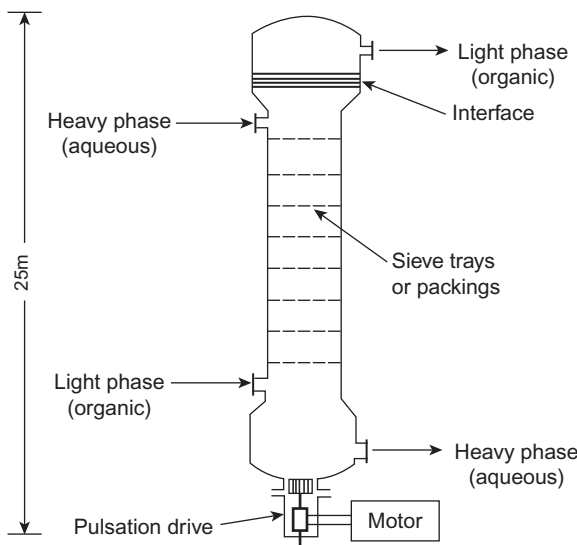


Figure 9.17 Column for solvent extraction isotope enrichment.

In the redox IX process, a column containing spherical beads of a proprietary anion exchange resin is first treated with an oxidizing solution (see Fig. 9.18) [26]. An aqueous solution containing U(IV) is then supplied at the top of the column, and the U(IV) is oxidized to the hexavalent UO_2^{2+} , which is then adsorbed onto the

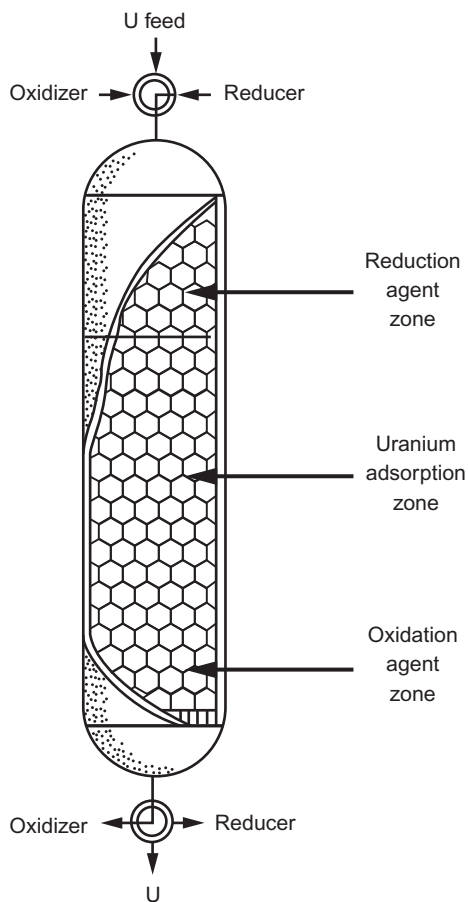


Figure 9.18 Ion exchange column for isotope enrichment.

resin. The adsorbed uranium forms a well-defined band on the column. The flow of U(IV) solution is halted once an appropriate length of resin has been saturated with U(VI). The exchange between the U(IV) flowing through the band and that adsorbed on the resin enhances the isotopic separation. The isotope discrimination is the result of ^{235}U accumulating at the top of the adsorption band and ^{238}U accumulating at the bottom of the band. A reducing reagent is then added to the top of the column, which reduces the U(VI) to U(IV). The eluted U(IV) progresses through the column until it encounters an oxidized region of the column, where it is again oxidized and adsorbed as UO_2^{2+} . The progression of the uranium adsorption band is controlled until the desired concentration of ^{235}U is achieved [54,55].

The separation factor for the chemical exchange processes is low, and thus thousands of stages may be required to achieve the ^{235}U enrichment levels required for reactor fuel for light-water reactors. However, each column can contain hundreds of

stages, which would significantly reduce the total equipment requirement in an enrichment plant.

The advantages of the chemical exchange methods are that they are modular, relatively low in power consumption, and free from the need for cascade control. In addition, these processes are not convenient for military applications, due to the length of time required to produce HEU, which is large compared to conventional methods. It has been stated that the time required to produce HEU is in the range of years, versus 1 year for gaseous diffusion and less than 1 year for gas centrifuge processes [54].

9.3.2 Quality and transportation of enriched UF_6

Enriched UF_6 must conform to a standard specification for impurity and isotope concentration limits [56]. This specification provides the nuclear industry with a standard for enriched UF_6 that is used in the production of sinterable UO_2 powder for fuel fabrication.

Enriched UF_6 is transported in standard 30B cylinders with overpacks, and each cylinder can contain up to 2275 kg of UF_6 . These cylinders are restricted to a maximum uranium enrichment of 5% ^{235}U [10]. The transportation of enriched UF_6 must also adhere to stringent standards similar to the transportation of natural UF_6 in 48Y cylinders [10,12–14]. Uranium hexafluoride cylinders have been reviewed from a nuclear safety perspective and have been found to have a transport index of zero for criticality safety purposes [57,58].

9.4 Conversion of enriched UF_6 to UO_2

Enriched UF_6 is converted to enriched UO_2 powder for the subsequent fabrication of fuel for nuclear power plants. This part of the nuclear fuel cycle has also been referred to as “deconversion” and “reconversion” [7,10]. The conversion of UF_6 to fuel-grade UO_2 is accomplished via aqueous or gas phase chemical processes, which can be categorized into wet and dry processes.

Uranium hexafluoride is received at fuel fabrication facilities in 30B transport cylinders. Vaporization of UF_6 is the common, first stage to all wet and dry conversion processes. Uranium hexafluoride is withdrawn from the cylinder as a gas by heating the cylinder with steam in an autoclave, electrically heated hot air chamber, or electrically heated blanket. When UF_6 is heated in the cylinder, it is liquefied, and sufficient UF_6 gas pressure is generated above the liquid to feed the downstream conversion process. Uranium hexafluoride can also be withdrawn under vacuum from the cylinder at ambient temperatures.

Many of the production processes and chemical reactions for the processing of enriched uranium are similar to those for processing of natural uranium. However, conversion facilities that process natural uranium, plants that process enriched uranium materials must incorporate criticality safety control in the plant design and

operation. Typically, controls consider upper limits of one or more of the following parameters: uranium mass, concentration of uranium in solution, geometrical dimensions of process equipment, moderator ratio, and the presence of neutron absorbers. The wet and dry conversion processes of enriched UF_6 that have been proven at commercial scales are briefly described next.

9.4.1 Wet conversion processes

9.4.1.1 Ammonium diuranate route

The ADU route is a multistep chemical process involving several unit process stages, as illustrated in Fig. 9.19.

After the initial vaporization step, gaseous UF_6 is contacted with water and hydrolyzed to produce a solution of uranyl fluoride (UO_2F_2) and hydrofluoric acid ($\text{HF}_{(\text{aq})}$). The reaction is exothermic and occurs instantaneously. Uranyl fluoride is readily soluble in pure water with solubilities of 65.6 wt.% (25.0°C) and 71.0 wt.% (60.0°C); however, the presence of HF in the product solution limits the solubility of UO_2F_2 [59]. In commercial operations a number of designs have been used for the gaseous UF_6 feed to the hydrolysis reactor and the reactor itself. Important features in the design of the hydrolysis reactor include nozzle designs that prevent clogging by hydrolysis products, materials of construction that provide corrosion resistance, sizing to achieve production requirements, ability to control the concentration of UO_2F_2 , and provide adequate mixing.

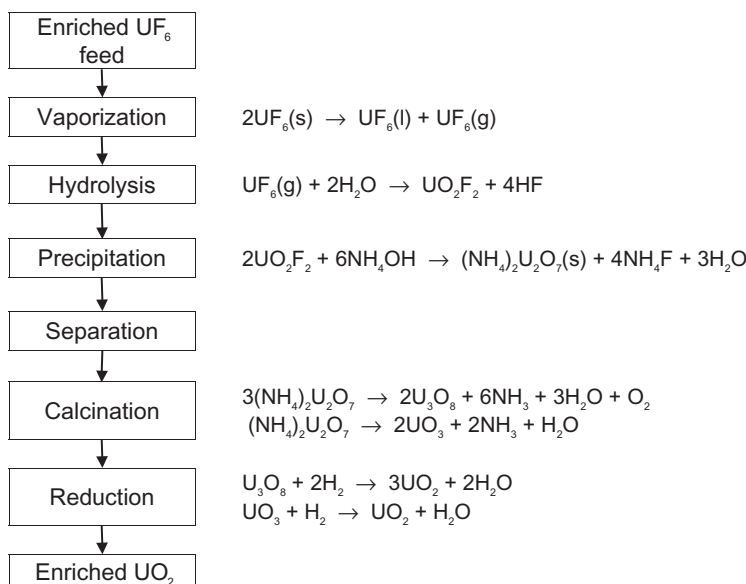


Figure 9.19 Conversion of enriched UF_6 by the ADU route. *ADU*, Ammonium diuranate.

The uranyl fluoride solution is contacted with ammonia or ammonium hydroxide in the next step to produce a yellow precipitate, ADU. The ADU process from this stage onward is similar to that previously described for the production of natural-uranium, ceramic-grade UO_2 powder.

Typical properties of the nuclear fuel-grade UO_2 powder, produced by the ADU route, are given next [37].

- Mean particle size—0.4–1.0 μm
- Specific surface area—2.5–6.0 m^2/g
- O/U ratio—2.03–2.17
- Bulk density—1.5 g/cm^3
- Tap density—2.4–2.8 g/cm^3

9.4.1.2 Ammonium uranyl carbonate route

In the ammonium uranyl carbonate (AUC) conversion process, UF_6 gas is fed into a stirred aqueous system at the same time as gaseous CO_2 and NH_3 , as illustrated in Fig. 9.20.

The reaction produces an AUC precipitate with NH_4F in solution. The AUC precipitate is separated from the mother liquor by filtration followed by washing to reduce the fluoride content in the UO_2 product. The filter cake is further washed with methanol to reduce the moisture content [60].

Solid AUC is converted to UO_2 by thermal decomposition and reduction in one or more fluidized-bed reactors between 520°C and 650°C [29]. Detailed thermal decomposition studies using differential thermal analysis and mass spectrometry have demonstrated that, in a reducing environment, ammonium uranyl carbonate decomposes to UO_3 solid with the evolution of NH_3 , CO_2 , and H_2O [25]. Uranium trioxide is then reduced by hydrogen in the fluidizing gas stream to UO_2 . The

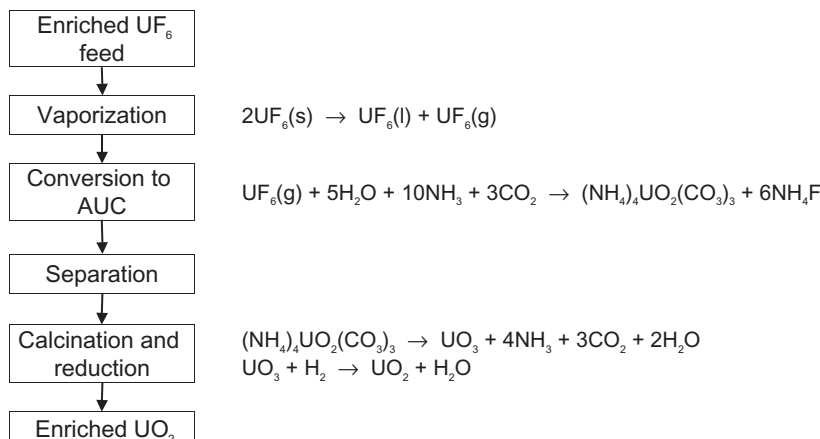


Figure 9.20 Conversion of enriched UF_6 by the AUC route. *AUC*, Ammonium uranyl carbonate.

fluoride content of the product is further reduced during the decomposition–reduction process and removed from the reactor as HF. Due to the surface activity and reactivity of the reduced UO_2 , the powder must be stabilized in order to maintain a relatively constant O/U ratio, when exposed to air [10,29].

The AUC route is considered to produce a free-flowing UO_2 powder that does not require precompaction and granulation prior to pressing. One commercial producer reported the following key powder characteristics [61].

- Mean particle size— $20\ \mu\text{m}$
- Specific surface area— $5.0\text{--}6.0\ \text{m}^2/\text{g}$
- O/U ratio— $2.08\text{--}2.12$
- Bulk density— $2.2\text{--}2.4\ \text{g}/\text{cm}^3$

9.4.2 Dry conversion processes

The term “dry conversion” refers to the fact that all steps involve either gas–gas or gas–solid reactions. In all dry conversion processes, hydrolysis of UF_6 to UO_2F_2 is followed by the pyrohydrolysis and reduction of UO_2F_2 to produce nuclear-grade UO_2 . Different reactor configurations and commercial processes have been developed, including the following:

- Integrated dry route (IDR): single rotary kiln reactor [40,62]
- Fluid bed conversion process: multiple fluidized-bed reactors in series [63]
- Hybrid process: fluidized bed—kiln process [40,64]

9.4.2.1 Integrated dry route

The IDR process was developed and implemented as a commercial process in the United Kingdom in 1969, and the technology has been employed by other producers. The key benefit of the IDR process is that UF_6 is converted to nuclear-grade UO_2 powder in one reaction vessel, as indicated in the reaction scheme in Fig. 9.21.

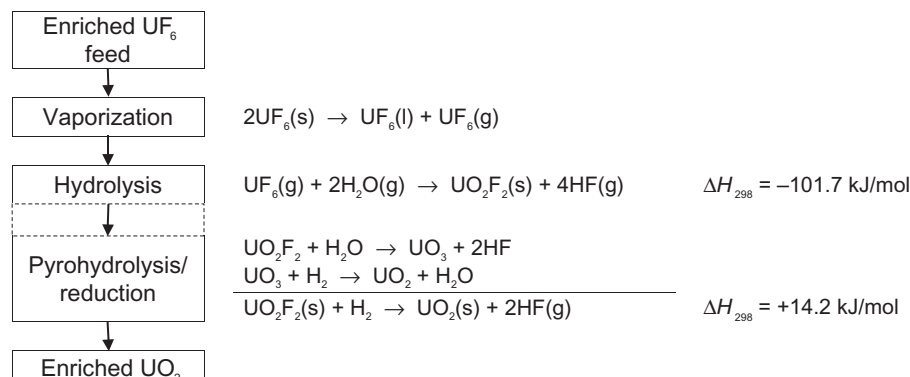


Figure 9.21 Conversion of enriched UF_6 by the IDR. *IDR*, Integrated dry route.

Vaporized UF₆ is injected into a reaction chamber at the front end of the reaction vessel at 150°C–250°C and contacted with a jet of superheated steam, forming a product plume of UO₂F₂ particulate and HF [61]. The reaction is instantaneous and exothermic [10,63,65]. The UO₂F₂ disengages from the HF in the reaction chamber and is subsequently fed into the rotary kiln by a screw feeder. In one variation of the IDR process the reaction chamber and horizontal kiln are two separate vessels separated by a screw feeder [40]. The HF is removed from the reaction chamber through sintered metal filters and directed to an HF recovery process.

Uranyl fluoride that is produced in the inlet reaction chamber is converted to nuclear-grade UO₂ powder by a countercurrent flow of steam and hydrogen at 500°C–800°C in a horizontal, rotary kiln. The mechanism of the reaction is considered to proceed through separate pyrohydrolysis and reduction steps; however, the mechanism may be more complex with a number of competing reactions. The overall process step is endothermic [63,65]. The temperature profile along the length of the kiln can be adjusted through zone control to meet the required powder characteristics.

The physical characteristics of the product such as morphology, porosity, particle size, flow, and density are dependent on the operating parameters of the kiln, which must be carefully controlled to ensure that the final UO₂ powder is suitable for pellet fabrication [66].

Typical properties of the nuclear fuel-grade UO₂ powder, produced by the IDR route, are given next [40].

- Mean particle size—2.4 μm
- Specific surface area—2.5–3.0 m²/g
- O/U ratio—2.05
- Bulk density—0.7 g/cm³

The advantages of the IDR process are considered to be its relative simplicity, low environmental impact, and product quality.

9.4.2.2 Fluidized-bed conversion process

In the fluid bed conversion process, UF₆ is converted to UO₂ in a multistep process that comprises three fluidized-bed reactors in series: a primary reactor, a fluoride stripper, and a cleanup reactor [63]. Gaseous UF₆ is contacted with steam and hydrolyzed to UO₂F₂ in the primary reactor at 550°C. The operating conditions of the primary reactor are controlled to ensure that the particle size of the UO₂F₂ is maintained within a specific range. The UO₂F₂ is fed into the fluoride stripper where it is converted to UO₂ by pyrohydrolysis and reduction in a gas stream of steam and hydrogen. The bed temperature in the fluoride stripper is 630°C. The conversion to UO₂ is completed in the cleanup reactor, where the conditions are essentially the same as the fluoride stripper. The gaseous effluent streams from both reactors are combined for recovery of hydrofluoric acid or neutralization.

The dry conversion fluidized-bed conversion process produces a free-flowing powder with bulk and tap densities that are greater than those for ADU powder [63].

9.4.2.3 Fluidized bed—kiln conversion process

Framatome has facilities in the United States and Germany that employ a two-step process, comprising a fluidized-bed reactor and a rotary kiln [40,64]. Gaseous UF_6 is contacted with superheated steam in the upper zone of a fluidized-bed reactor, instantly forming UO_2F_2 powder. The UO_2F_2 is then partially converted to UO_2 by pyrohydrolysis and reduction by contacting a preexisting bed of UO_2 -uranium oxide held at 600°C. The bed is fluidized by a stream of steam, hydrogen, and nitrogen. The product is withdrawn from the bottom of the fluidized-bed reactor and fed to a rotary kiln at 700°C, where the conversion is completed in a countercurrent flow of steam and hydrogen. The gaseous effluent streams from both reactors are combined for recovery of hydrofluoric acid. The characteristics of the UO_2 powder can be tightly controlled through adjustment of the operating parameters of both reactors.

It is well recognized that the physical characteristics of the UO_2 powders produced by different process routes can vary, despite having the same chemical composition. Physical characteristics such as particle size, morphology, and specific surface area can impact downstream processing. A fundamental understanding of the powder properties is necessary to achieve the desired UO_2 pellet quality after granulation, pressing, and sintering.

9.5 Conclusion and future trends

Refining and conversion processes are well-established and produce pure materials that are suited for the existing enrichment process or direct to fuel manufacture, in the case of natural UO_2 for PHWR. There has been little in the way of radical innovation, in terms of changes to refining and conversion processes. However, in general at all facilities, there have been numerous incremental changes to the traditional processes that have led to improved safety and environmental performances, as well as improved financial performance through reduced operating costs. These advancements are important as facilities maintain the trust of regulators and the communities in which they operate.

Many uranium enrichment techniques have been developed, but only two have been found suitable for commercial enrichment of ^{235}U . The fundamental principles behind each process determine the separation factor, throughput, energy requirements, equipment size, in-process inventory, and, ultimately, capital and operating costs. Currently, the gas centrifuge process has proven to have the right balance of these factors, and it is firmly placed as the sole commercial enrichment process.

While it is encouraging that newer methods of enrichment and alternative fuels such as thorium and MOX are still being investigated, providing opportunities for future technological advancements, factors such as nuclear non-proliferation, local and global politics, and energy diversity and supply will continue to shape the direction of nuclear fuel for the foreseeable future.

References

- [1] R. DeWitt, Uranium Hexafluoride: A Survey of the Physico-Chemical Properties, Goodyear Atomic Corporation Report No. GAT-280, 1960.
- [2] J.C. Anderson, C.P. Kerr, W.R. Williams, Correlation of the thermophysical properties of uranium hexafluoride over a wide range of temperature and pressure, in: Oak Ridge National Laboratory Report No. ORNL/ENG/TM-51, 1994.
- [3] M. Benedict, T.H. Pigford, H.W. Levi, Nuclear Chemical Engineering, second ed., McGraw-Hill Book Company, New York, 1981.
- [4] J.H. Pashley, Conversion of uranium trioxide to uranium hexafluoride, Radiochim. Acta 135 (1978) 138.
- [5] C.R. Edwards, A.J. Oliver, Uranium processing: a review of current methods and technology, JOM 52 (9) (2000) 12–20.
- [6] C.D. Harrington, A.E. Ruehle (Eds.), Uranium Production Technology, D. Van Nostrand Company, Inc., New York, 1969.
- [7] A.J. Oliver, E. Özberk, Conversion of natural uranium, in: I. Hore-Lacy (Ed.), Uranium for Nuclear Power – Resources, Mining and Transformation to Fuel, Woodhead Publishing Series in Energy, Number 93, 2016.
- [8] Conversion and deconversion, World Nuclear Association, 2017. <<http://www.world-nuclear.org/information-library/nuclear-fuel-cycle/conversion-enrichment-and-fabrication/conversion-and-deconversion.aspx>>.
- [9] ASTM C787-15, Standard Specification for Uranium Hexafluoride for Enrichment, 2015.
- [10] Manual on Safe Production, Transport, Handling and Storage of Uranium Hexafluoride, IAEA-TECDOC-771, 1994.
- [11] Uranium hexafluoride – safe handling, processing, and transporting, in: W.D. Strunk, S.G. Thornton (Eds.), Conference Proceedings Oak Ridge Tennessee, May 24–26, 1988.
- [12] American National Standard for Nuclear Materials – Uranium Hexafluoride – Packaging for Transport, American National Standards Institute, Inc. Report No. ANSI N14.1-2001, 2001.
- [13] UF₆ Cylinder Identification, World Nuclear Transport Institute Standard, Version 1, 2017.
- [14] Nuclear Energy – Packaging of Uranium Hexafluoride (UF₆) for Transport, International Organization for Standardization, ISO 7195:2005.
- [15] J. Stas, A. Dahdough, H. Shlewit, Extraction of uranium (VI) from nitric acid and nitrate solutions by tributylphosphate/kerosene, Period. Polytech. Ser. Chem. Eng. 49 (1) (2005) 3–18.
- [16] A.W. Ashbrook, The refining and conversion of uranium yellowcake to uranium dioxide and uranium hexafluoride fuels in Canada: current practices, Advances in Uranium Refining and Conversion, International Atomic Energy Agency, IAEA-TECDOC-420, 1986, pp. 9–21.
- [17] H. Page, Conversion of uranium ore concentrates and reprocessed uranium to nuclear fuel intermediates at BNFL Springfields, Advances in Uranium Refining and Conversion, International Atomic Energy Agency, IAEA-TECDOC-420, 1986, pp. 9–21.
- [18] A.H. Orabi, Determination of uranium after separation using solvent extraction from slightly nitric acid solution and spectrophotometric detection, J. Radiat. Res. Appl. Sci. 6 (2013) 1–10.

- [19] J.A. Rindfleisch, P.C. Durst, C.A. Dahl, C.E. Casterline, A.V. Petig, The Idaho Chemical Processing Plant Product Denitration Upgrade, Exxon Nuclear Idaho Company, Inc., ENICO-1114, 1982.
- [20] R.D. Kozlova, V.A. Matyukha, N.V. Dedov, Mechanism and kinetics of thermal decomposition of uranyl nitrate hexahydrate under the nonisothermal conditions, *Radiochemistry* 49 (2) (2007) 130–134.
- [21] H.D. Ringel, P.A. Haas, Partial Thermal Denitration of Uranyl Nitrate Solutions in a Screw Denitration, Oak Ridge National Laboratory, ORNL-TM6264, 1978.
- [22] G. Schaal, R. Faron, Method of Obtaining Uranium Trioxide by Directly Heat Denitrating Uranyl Nitrate, EP Patent No. 0713479 B1, COMURHEX Inventors, 1998.
- [23] C.K. Gupta, H. Singh, *Uranium Resource Processing, Secondary Sources*, Springer-Verlag, Berlin, 2003.
- [24] BNFL Production of Nuclear Powder, Information Services, British Nuclear Fuels Limited, Warrington, 1981.
- [25] J.J. Katz, G.T. Seaborg, L.R. Morss (Eds.), *Actinide Elements*, vol. 1, Chapman and Hall, New York, 1986.
- [26] J.M. Whitaker, Uranium Enrichment Plant Characteristics – A Training Manual for the IAEA, Oak Ridge National Laboratory Report ORNL/TM-2005/43, ISPO-310/R1, 2005.
- [27] Uranium Hexafluoride: A Manual of Good Handling Practices, United States Enrichment Corporation Report No. USEC-651 (Revision 7), 1995.
- [28] I.J. Itzkovitch, T.W. Zawidzki, Yellowcake to uranium dioxide, in: Presented at the 3rd International Conference Nuclear Technology, Madrid, Spain 14–16 October, 1985.
- [29] R.E. Lerch, R.E. Norman, Nuclear fuel conversion and fabrication chemistry, *Radiochim. Acta* 36 (1984) 75–88.
- [30] R. Eloirdi, D. Ho Mer Lin, K. Mayer, R. Caciuffo, T. Fanghänel, Investigation of ammonium diuranate calcination with high-temperature X-ray diffraction, *J. Mater. Sci.* 49 (2014) 8436–8443.
- [31] J.J. Katz, E. Rabinowitch, *Actinide elements, National Nuclear Energy Series, Division 8*, McGraw-Hill Book Company, New York, 1951.
- [32] The Nuclear Fuel Cycle, Radiochemistry Group of the Royal Society of Chemistry, Essays on Radiochemistry, No. 7, Royal Society of Chemistry, 2018. <<http://www.rsc.org/Membership/Networking/InterestGroups/Radiochemistry/Essays.asp>>.
- [33] Nuclear Power Reactors, World Nuclear Association. <<http://www.world-nuclear.org/information-library/nuclear-fuel-cycle/nuclear-power-reactors/nuclear-power-reactors.aspx>> (Last accessed Feb. 27, 2020).
- [34] A.S. Krass, P. Boskma, B. Elzen, W.A. Smit, *Uranium Enrichment and Nuclear Weapon Proliferation*, Stockholm International Peace Research Institute, Taylor & Francis Ltd., London, 1983.
- [35] K.T. Brown, Basic Information Relating to Uranium Enrichment Calculations and Fuel Requirements for Nuclear Power Reactors, Atomic Energy Board, Republic of South Africa Report PER-10, 1977.
- [36] Separation Theory, Federation of American Scientists. <<https://fas.org/issues/nonproliferation-counterproliferation/nuclear-fuel-cycle/uranium-enrichment-gas-centrifuge-technology/separation-theory/>> (Last accessed Feb. 27, 2020).
- [37] Uranium Enrichment, World Nuclear Association. <<http://www.world-nuclear.org/information-library/nuclear-fuel-cycle/conversion-enrichment-and-fabrication/uranium-enrichment.aspx>> (Last accessed Feb. 27, 2020).

- [38] J.R. Merriman, M. Benedict, Recent Developments in Uranium Enrichment, vol. 78, American Institute of Chemical Engineers Symposium Series, Number 221, 1982.
- [39] P. Harding, Uranium enrichment, in: I. Hore-Lacy (Ed.), *Uranium for Nuclear Power – Resources, Mining and Transformation to Fuel*, Woodhead Publishing Series in Energy, Number 93, 2016.
- [40] P.D. Wilson (Ed.), *The Nuclear Fuel Cycle, From Ore to Waste*, Oxford University Press, New York, 1996.
- [41] A. Makhljani, L. Chalmers, B. Smith, *Uranium Enrichment – Just Plain Facts to Fuel an Informed Debate on Nuclear Proliferation and Nuclear Power*, Institute for Energy and Environmental Research for the Nuclear Policy Research Institute, October 2004.
- [42] R. Snyder, A proliferation assessment of third generation laser uranium enrichment technology, *Sci. Global Secur.* 24 (2) (2016) 68–91.
- [43] S. Villani (Ed.), *Uranium Enrichment*, Springer-Verlag, New York, 1979.
- [44] A. Pouris, *The Future Cost of Uranium Enrichment, Technology and Economics*, Energy Policy, Butterworth and Company Ltd., 1986, pp. 558–567.
- [45] J.D.L. Moore, *South Africa and Nuclear Proliferation*, Palgrave Macmillan, New York, 1987, pp. 167–175.
- [46] C. Ying, S. Zeng, Y. Nie, X. Shang, H.G. Wood, Over all separation factors for stable isotopes by gas centrifuge, *Sep. Sci. Technol.* 36 (2) (2006) 159–175.
- [47] D.R. Olander, *The Theory of Uranium Enrichment by the Gas Centrifuge*, Lawrence Berkeley Laboratory, University of California Report No. LBL-10253, 1981.
- [48] S. Upson, Laser uranium enrichment makes a comeback, *IEEE Spect.* (2010). <<https://spectrum.ieee.org/energy/nuclear/laser-uranium-enrichment-makes-a-comeback>> (Last accessed Feb. 27, 2020).
- [49] B.C. Reed, From treasury vault to the Manhattan Project, *Am. Sci.* 99 (1) (2011) 40. Also <<https://www.americanscientist.org/article/from-treasury-vault-to-the-manhattan-project>>.
- [50] A.L. Yerger, A.K. Yerger, Preparative scale mass spectrometry: A brief history of the calutron, *J. Am. Soc. Mass Spectr.* 8 (9) (1997) 943–953.
- [51] B.C. Reed, B. Cameron, Liquid thermal diffusion during the Manhattan Project, *Phys. Persp.* 13 (2) (2011) 161–188.
- [52] The Manhattan Project, An Interactive History, U.S. Department of Energy. <https://www.osti.gov/opennet/manhattan-project-history/Events/1942-1944_ur/navy_ltd.htm>.
- [53] E.W. Becker, The separation nozzle process for enrichment of uranium-235, *Progr. Nucl. Energy* 1 (1977) 27–39.
- [54] F. Kawakami, M. Tokiaw, Y. Fujii, Plant designing of ion exchange chemical uranium enrichment and its non-proliferation aspects, *Progr. Nucl. Energy* 53 (2011) 974–979.
- [55] M. Seko, T. Miyake, K. Inada, K. Takeda, Uranium isotope enrichment by chemical method, *Nucl. Technol.* 50 (1980) 178–186.
- [56] ASTM C996-15, Standard Specification for Uranium Hexafluoride for Enrichment to Less Than 5% 235U, 2015.
- [57] H.Z. Mokhatri, M. Nematollahi, S. Kamyab, Criticality safety evaluation for 30B and 48X UF6 cylinders for transportation and storage, *IAEA Int. Nucl. Inf. Syst.* 44 (36) (2011).
- [58] B.L. Broadhead, Criticality Safety Review of 2½-, 10-, and 14-Ton UF6 Cylinders, Oak Ridge National Laboratory Report ORNL/TM-11947, 1991.
- [59] W.L. Myers, *Literature Review on the Chemical and Physical Properties of Uranyl Fluoride (UO₂F₂)*, National Technical Information Service, Technical Report 199023, 1990.

- [60] V.S. Keni, S.K. Ghosh, C. Ganguly, S. Majumdar, Development of AUC-Based Process at BARC for Production of Free-Flowing and Sinterable UO₂ Powder, Government of India Atomic Energy Commission, Bhabha Atomic Research Centre Report, 1994.
- [61] E. Thulin, J. Arborelius, Fuel manufacturing and its environmental effects, in: ATS YGN Meeting in Espoo, Finland, 2006.
- [62] Improvements in or Relating to Rotary Kilns, UK Patent Specification No. 1,341,379, 1973.
- [63] K.C. Radford, W.L. Lyon, J.E. Hart, Fluid-bed conversion of UF₆ to UO₂, Ceram. Bull. 58 (2) (1979) 219–232.
- [64] Conversion of Uranium Hexafluoride to Uranium Dioxide, Advanced Nuclear Fuels Corporation, US Patent No. 4,830,841, 1989.
- [65] I.E. Knudsen, H.E. Hootman, N.M. Levitz, A fluid-bed process for the direct conversion of uranium hexafluoride to uranium dioxide, Nucl. Sci. Eng. 20 (1964) 259–265.
- [66] A.P. Bromley, R. Logsdon, V.A. Roberts, Changes in UO₂ Powder Properties During Processing via BNFL's Binderless Route, pp. 99–106.

Advances in fuel fabrication

10

*Elizabeth Sooby Wood¹, Joshua T. White², Brian Jaques³,
Douglas Burkes⁴ and Paul Demkowicz⁵*

¹Department of Physics and Astronomy, The University of Texas at San Antonio, San Antonio, TX, United States, ²Materials Science and Technology Division, Los Alamos National Laboratory, Los Alamos, NM, United States, ³Micron School of Materials Science and Engineering, Boise State University, Boise, ID, United States, ⁴Nuclear Engineering and Analysis, Pacific Northwest National Laboratory, Richland, WA, United States, ⁵Idaho National Laboratory, Idaho Falls, ID, United States

10.1 Introduction

Advances in the nuclear fuel cycle and the introduction of novel fuel forms necessitate advances in fuel fabrication that encompass not only the development of commercially scalable fabrication techniques for novel fuel forms but also innovative synthesis and fabrication methods for conventional reactor fuels. Fuel fabrication can entail several pivotal processes that lead to the implementation of a specific nuclear fuel form. Whether uranium dioxide (UO_2) clad in a zirconium-based alloy, such as Zircaloy, or microencapsulated tristructural isotropic (TRISO) particles dispersed in a graphite matrix, the fabrication techniques employed in the manufacturing of each nuclear fuel form are multifaceted. Traditional powder metallurgical methods, spark plasma sintering (SPS), mechanical processing, alloying, casting, the application of coatings—each of these fuel fabrication or synthesis techniques requires specific process parameters to produce precision engineered and qualified fuel forms. Often times, specifically for light-water reactor (LWR) fuels, the fuel cladding is an integral, almost always neutronically optimized, part of the fuel form. Since the work presented here focuses specifically on the advances of nuclear fuel chemistry, this chapter narrows the scope of the broader term “fuel fabrication” and details specifically the synthesis techniques for a variety of actinoid-bearing nuclear fuels, with little discussion to the cladding and containment aspects specific to each fuel form, unless it proves essential to the synthesis of the fuel itself (e.g., TRISO fuel particles).

Earlier chapters of this book detail the importance of and techniques for the mining, milling, conversion, and enrichment of uranium. Therefore this chapter will cover the synthesis techniques for a variety of fuel forms starting from uranium metal or stable uranium precursor compounds that result from traditional conversion processes (e.g., UF_6 , UO_3 , and elemental uranium). Spanning the breadth of fuel

cycle research and development (R&D), this chapter begins with a detailed description of conventional UO_2 fuel fabrication. The authors then introduce some of the latest techniques for ceramic fuel fabrication including an extensive discussion of nitride fuel fabrication followed by a brief discussion of the capabilities utilized to fabricate carbide and boride fuels. The latter sections of this chapter will detail techniques used for nonceramic fuel forms, specifically metallic fuel fabrication, and advanced reactor fuels (e.g., accident tolerant, high-temperature reactor, and molten-salt reactor fuel). The authors stress that this work leans on the productive works produced over decades of research performed worldwide.

10.2 Ceramic fuel fabrication

10.2.1 Oxide fuel fabrication

10.2.1.1 Commercial oxide fuel production

Commercial production of UO_2 has been covered in detail by other sources [1] and will only be summarized in this portion of the chapter. Fabrication of UO_2 to be deployed in LWRs, which require enrichment as opposed to heavy water reactors, begins with UF_6 in LWRs, which require enrichment, as opposed to pressurized heavy water reactors that do not. For LWR fuels, UF_6 is converted through various processes to the final feedstock powder of UO_2 . The most common synthesis routes used to date employ either a wet or dry chemical technique. Wet chemistry UO_2 synthesis generally not only provides a more consistent end feedstock with high sinterability but also generates considerable amounts of radioactive liquid waste. A more direct conversion to UO_2 can be accomplished using solid-state reaction synthesis, where fewer processing steps are employed; however, the end result generates a poor flowing powder that requires additional processing prior to pelletization. A comparison of these two processes can be seen in Fig. 10.1, which portrays the conventional wet and dry chemical processing procedures.

Wet chemical processing to produce UO_2

The wet processing route is subdivided based on the intermediate uranium-bearing chemical used during the process: ammonium diuranate (ADU) or ammonium uranyl carbonate (AUC). Both the processes start with UF_6 that is vaporized and added to steam, which converts the hexafluoride to uranyl fluoride (UO_2F_2). The UO_2F_2 is then reacted with liquid NH_3 (for ADU) [6,7] or $\text{NH}_3 + \text{CO}_2(\text{g})$ (for AUC) [4] to form the intermediate compound $(\text{NH}_4)_2\text{U}_2\text{O}_7$ or $(\text{NH}_4)_4(\text{UO}_2(\text{CO}_3)_3)$, respectively. The precipitates are then filtered, rinsed, and dried prior to a calcination step under a reducing atmosphere to form the oxide precursor. Given that both processes are a wet chemical method, many of the steps provide room for process refinement to control the resulting particle morphology and distribution to aid in the flowability of the powder along with aiding in the sintering process.

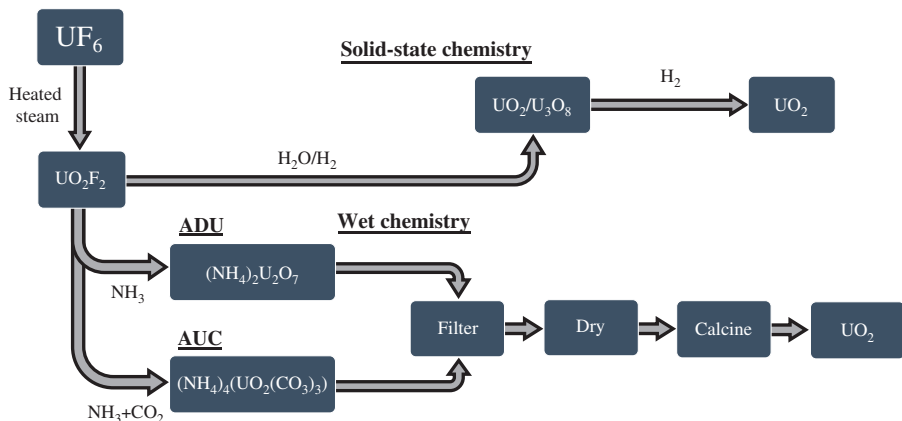


Figure 10.1 Diagram outlining the commercial UO₂ processing techniques as interpreted from several sources [2–5].

Solid-state synthesis of UO₂

Dry processing routes also begin with a conversion of UF₆ to UO₂F₂ using superheated steam in a rotating kiln [3]. The kiln allows for a counterflow of H₂/H₂O gas mixture that reacts with the UO₂F₂ compound resulting in a mixture of U₃O₈ and UO₂. This can be further reduced to UO₂ by heating under diluted hydrogen gas (Ar–H₂) at elevated temperatures. The limited number of steps during this fabrication route requires tight control of the processing parameters that lead to consistently low surface area powders with higher fluorine content than the wet chemical routes. The powder produced from this route has poor flowability that requires additional steps such as granulation and the addition of lubricants to aid in the automated production of pellets.

Commercial powder metallurgy of UO₂

Although wide variability exists between the starting powder feedstock from either the wet chemical or dry routes, the following processes to fabricate pellets utilize similar techniques. Initially, the powders are prepared for pressing by adding common powder metallurgical additives, such as organic binders and pore formers, to aid in control of the final sintered product. Pellets are pressed above 150 MPa using a dished and chamfered die. The resulting green pellets are sintered in a two-stage process. In the first stage, volatile organic binders/pore formers are removed. In the second stage the pellets are sintered at temperatures above 1600°C in a reducing atmosphere to densities between 95% and 97% of the theoretical density, which depend on the design requirements of the particular vendor. Sintered monoliths are then centerless ground to the designed diameter to account for the plenum gap between the fuel and the cladding.

10.2.1.2 Additives to UO_2

Uranium dioxide has been deployed in all commercial LWRs over the past 50 years and is therefore a likely uranium compound to consider for advanced reactor concepts, given its documented success in the nuclear industry. Incremental progress to this commercial fuel form has been in the form of minor alloying additions/dopants to improve the fission gas retention as well as creep behavior at operating temperatures to minimize detrimental pellet–cladding interactions (PCI) [8]. An exhaustive list of dopants has been examined in the literature, including niobium [9,10], titanium [11], silicon [12], aluminum [12,13], and chromium [14,15]. Each investigation studies the impact of these dopants on the microstructure as well on the operating parameters of the fuel, in particular grain size, thermal conductivity, ionic conductivity, mechanical properties, etc.

Industry teams have each put forth concepts for fuel additions that attempt to improve upon the aforementioned properties and, at a minimum, do not greatly degrade the performance of UO_2 in-pile with respect to other performance metrics (e.g., oxidation behavior and washout). To this end, Cr_2O_3 was first proposed, which enhances grain growth during sintering of the fuel pellets when added near the solubility limit of Cr_2O_3 in UO_2 of 0.16 wt.% [14,16]. Chromia additions above 0.16 wt.% rely on higher temperatures during sintering, which reduces Cr cations to a +2 valency state and is suspected to form liquid phases to increase grain growth [17,18].

Chromium additions increase the grain size of the native UO_2 from $\sim 10 \mu\text{m}$ to $50\text{--}60 \mu\text{m}$ with pellet densities in excess of 96% [17]. Enlarged grains increase the diffusion length of fission product gasses, thus improving the retention of these gases in the fuel as well as slight improvements to the sintered density, benefitting the core economics. However, irradiation tests on Cr_2O_3 -doped UO_2 have also shown increased diffusion of fission gases (e.g., ^{133}Xe) from the enhancement of defect sites of the UO_2 lattice leading to similar or even accelerated gas release [12,15]. It is noted that the referenced two studies were conducted at temperatures greater than standard reactor operating conditions, which is anticipated to give rise to higher defect concentrations and thus higher fission gas diffusion [18]. Current studies are evaluating if dopants provide a beneficial impact on fission gas retention at standard operating conditions. Given that Cr_2O_3 is a known neutron absorber, teams have also investigated other cations that can substitute Cr^{3+} cations while also contributing to grain growth and minimizing the Cr^{3+} neutronic penalty within the fuel. Al_2O_3 additions with <1000 ppm by weight Cr_2O_3 are added to UO_2 , which yields densities $>97\%$ with slightly smaller grain sizes of $40\text{--}55 \mu\text{m}$ [19]. Note that grain growth can be facilitated by the higher Cr_2O_3 -doped UO_2 as reported by [17] and is displayed in Fig. 10.2.

For boiling water reactors (BWRs) the mechanical behavior of the fuel is a key parameter since higher failure rates are attributed to PCI during burnup in comparison to pressurized water reactors. It should be noted that the primary design feature to mitigate PCI in BWR fuel is modified, liner cladding. Nonetheless, because of the known susceptibility to PCI, additives to UO_2 are designed to improve creep

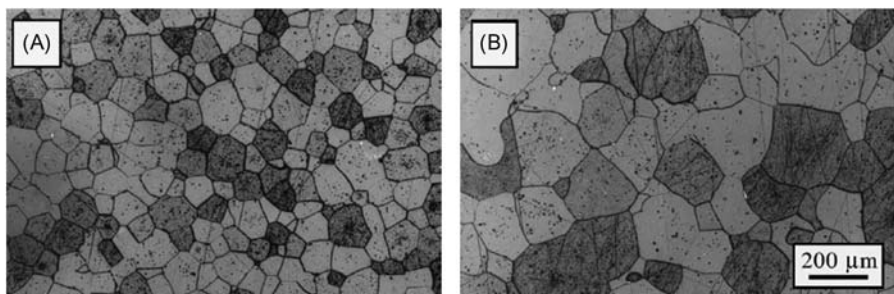


Figure 10.2 Optical micrographs of Cr_2O_3 -doped UO_2 sintered under the same conditions where the Cr_2O_3 concentration is (A) 0.1 wt.% and (B) 0.25 wt.% [17]. The provided scale bar is representative for both figures.

resistance of the fuel during operation. Promising additives generally include nonsoluble aluminosilicates that coat the UO_2 grain boundaries, allowing viscous flow between the grains at operating temperatures [13]. Grain growth and density is also improved with the viscous grain boundary phases, which promotes liquid-phase sintering, yielding densities $\sim 95\%-97\%$, and grain sizes $\sim 30\text{--}60 \mu\text{m}$ for additions of Al-Si-O of 2500 wppm [13,20,21].

Commercially, the additives are introduced to UO_2 by solid-state synthesis, whereby the as-fabricated feedstock UO_2 powder from the standard powder line is comixed with oxide additives to distribute the dopants. The combined powders are then pressed and sintered under a reducing atmosphere to yield sufficiently high density to meet fuel pellet design requirements.

Recent modeling efforts have suggested that other unexplored dopants to UO_2 could yield improved grain growth and densification [22]. In particular, elements such as Fe^{3+} and Mn^{3+} at low concentrations could increase the defect concentration yielding improved sintering kinetics similar to the aforementioned cations. However, these concepts will require considerable experimental effort for acceptance in commercial reactors, including but not limited to fresh fuel property characterization, irradiation testing, and postirradiation examinations to fully realize opportunities with these new dopants.

10.2.1.3 Advanced fabrication of UO_2

Recent research efforts on the fabrication of UO_2 have focused on (1) improving the economics of fuel fabrication by decreasing sintering temperatures and times, (2) mitigating the high burnup rim structure via grain boundary engineering, and (3) atomically mixing the cations on the crystalline lattice. These three areas of interest are addressed in a number of research efforts from fabricating nanocrystalline UO_2 to increasing the surface area of powders, applying pressure or electric fields, new furnace concepts, or as a combination of all of the above. Each new processing route generates a unique microstructure that provides a rich field of

investigation to explore how the processing parameters alter the resulting properties of the sintered compact.

Sol–gel and hydrothermal routes for nanocrystalline UO_2 synthesis

A number of studies have investigated routes to fabricate uranium oxides using aqueous solutions. Many actinoid oxides can be produced via an aqueous processing route, each employing similar methodologies. For uranium, typically a salt (i.e., nitrate or chloride) is dissolved into a strong acid to avoid hydrolysis [23]. Methods diverge after this point depending on the desired final uranium-bearing compound or microstructure.

Methods have been developed to form porous microbeads of UO_2 by stabilizing the U(IV) cations with surfactants and adding a thickening agent prior to atomization and gelation in an ammonia bath to form 40–150 μm beads [24–26]. The microbeads are then carefully calcined to remove the organic material from the beads and subsequently annealed above 600°C to control the crystallite size to <100 nm. However, standard sintering and compaction of the microbeads typically lead to poor densification given the low starting density of the porous microbeads [27]. It is noted that similar methods can be employed to yield dense microspheres of UO_2 yielding similar sized microbeads [28].

Nanocrystalline UO_2 has also been fabricated by stabilizing acidic solutions of $\text{UO}_2(\text{NO}_3)_2$ through an electroreduction of the uranium to the 4+ state followed by precipitation of the crystallites with NaOH [23]. With this methodology, crystallite sizes on the order of 38 nm can be produced. Methods have also used the uranyl nitrate solution to produce an oxalate precursor [29] that are decomposed above 600°C to yield 5–13 nm crystallites and further annealed to control the resulting UO_2 crystallite size.

Field-assisted sintering of UO_2

Conventional sintering of UO_2 requires high temperatures and long dwell times to facilitate diffusion, which densifies the green pellet into a high-density monolithic fuel pellet. This requires temperatures in excess of 1600°C and dwell times on the order of 4 hours to achieve pellets at ~95% of the theoretical density of UO_2 . Oxidative environments or the addition of U_3O_8 aids the sintering process by increasing the number of point defects on the lattice, thus enhancing sintering, which slightly reduces the sintering temperature while the dwell times are largely unaffected [30–32].

Recent efforts have employed the use of applied fields across the green pellet, commonly referred to as field assisted or SPS, to achieve dense pellets on the order of minutes [25,33,34]. This technique yields high-density compacts while also minimizing grain growth yielding grain sizes from 60 nm to 10 μm depending on parameters used to sinter the compact. Sintering has been demonstrated using commercial starting ADU [33] along with internal gelation microbeads [25]. Dopants, such as TiO_2 , have also been mechanically incorporated to commercial UO_2 powder with this technique yielding beneficial large grain sizes on the order of

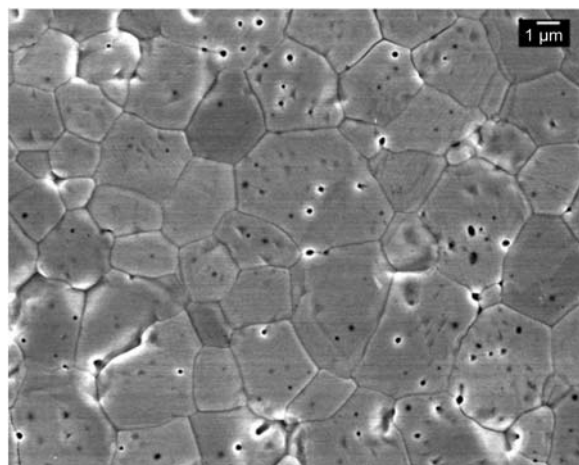


Figure 10.3 Polished microstructure of a UO_2 pellet produced using field-assisted sintering at 1150°C for 5 min using commercial powders [33].

$80\ \mu\text{m}$ in a fraction of the time, although secondary U-, Ti-bearing oxides were observed at the grain boundaries [35].

Powders sintered by SPS are commonly loaded into a graphite die. Process variables include pressure, current, temperature, and time, which are controlled to achieve the desired microstructure. Reported pressures for UO_2 range from 18 to 100 MPa in the literature, with heating rates predominantly controlled by heating through the pellets ranging anywhere from 50 to $200^\circ\text{C}/\text{min}$ and holds on the order of 5–20 minutes. It is noted that reactivity between the UO_2 and graphite die is observed at temperatures $>1450^\circ\text{C}$ yielding mechanically unstable pellets [25,33]. Note the grain sizes reported by Ge et al. [33] and displayed in Fig. 10.3 are approximately the same as a commercial sintering profile of undoped UO_2 in a fraction of the time.

Furthermore, cooling rates must be carefully controlled to prevent cracking in the sintered monolith. It is important to note that most of the SPS methods employ a pyrometer aimed at the surface of the graphite die, which makes temperature determination difficult for this method. Considerable technique development is required for actinide research in this field, particularly with dopant investigations and influence on microstructures. See characteristic microstructures reported by Cologna et al. [25] and displayed in Fig. 10.4.

Microwave sintering

The use of microwaves to sinter nuclear fuel has been known since the 1980s owing to the ability of UO_2 to absorb microwave radiation [36]. This has led to a number of patents including the development of microwave sintering furnaces for nuclear fuel production [37] as well as methods to recover scrap UO_2 that is lost during centerless grinding after conventional sintering [38]. A 2.45 GHz magnetron with up to 10 kW of power can be used, but power as low as 1000 W has been shown

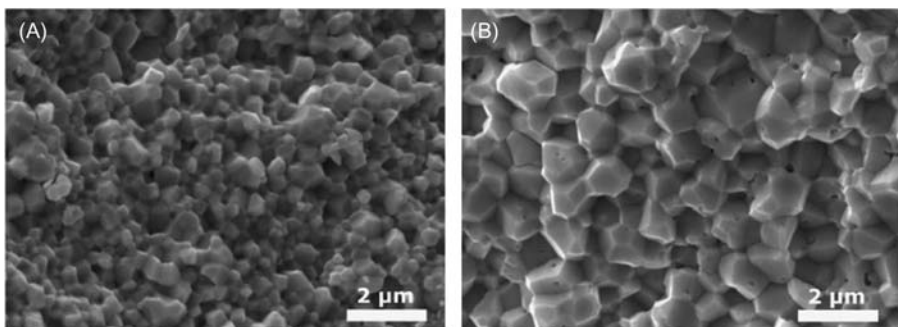


Figure 10.4 Fracture surface images collected on UO₂ pellets sintered with field-assisted sintering under approximately the same conditions using (A) nanocrystalline sol–gel prepared material and (B) commercial powders [25].

with appropriate refractory to achieve ~93%–96% of the theoretical density of UO₂ [39,40]. For UO₂, commercial microwave furnaces are adapted to control the atmosphere usually by employing a microwave transparent material, such as Al₂O₃ [37]. Microstructures are currently only available for undoped UO₂, which is similar in size to conventionally sintered UO₂; however, the sintering can be achieved in less than 1 hour [39]. Extremely high heating rates are also possible using microwave furnaces, but low thermally conductive materials, such as UO₂, tend to crack under the large thermal gradients [40].

Additive manufacturing

Application of additive manufacturing (AM) to nuclear fuel fabrication is a relatively new field of study, which has only been reported on ThO₂ at the time of preparation of this chapter [41]. In this example, stereolithography was applied to prepare hollow cubes that were built using 50 μm thick layers employing a commercial 3D printing system. Sintering was achieved after 16 hours to 89%–92% of the theoretical density of ThO₂. This field is expected to have considerable growth given the general interest in AM across multiple industries. Potential to make fuels with tailored microstructures to control the thermophysical properties or the neutronics are just some of the potential benefits that AM might afford fuel designers.

Powder injection molding UO₂

Powder injection molding (PIM) has well-known industrial applications in the fabrication of net shape parts for a variety of materials that require complex geometries or are air sensitive [42]. The general methodology of this approach requires a high-volume fraction loading of polymeric material to the powder feedstock of interest, which is subsequently melted to encase the powder, protecting it from oxidation and allowing either direct pressing or injection into a die-body enabling complex geometries. The green bodies with binder then require various steps to carefully debind the organic constituents from the matrix and subsequently sintered in a

vacuum or refractory furnace. Application of this methodology to nuclear fuels is limited in the literature and has been utilized in the fabrication of high-density UO₂ LWR-sized pellets [43]. It was proposed by Bricout et al. that PIM could enhance production rates and also aid in minimizing spread of powder contamination in industrial operations [43].

10.2.2 Nitride fuel fabrication

10.2.2.1 Introduction to nitride fuel forms

As discussed in [Chapter 5, Other power reactor fuels](#), nitride fuels are being investigated for space reactors, fast reactors, and commercial accident tolerant fuels (ATFs). The potential use of nitride fuel forms as high-performance nuclear fuels has been previously established. However, the lack of funding for fundamental research (when compared to the extent that has been invested in commercialized oxide fuels) results in inadequacies for deployment readiness due to inconsistencies in, and optimization of, fabrication methods, resulting in scattered thermophysical and irradiation behavior. Historical reviews provide a comprehensive overview of uranium mononitride (UN) and uranium–plutonium mononitride [(U, Pu)N] fuel synthesis, properties, and performance [42,44–50]. UN as well as (U, Pu)N solid solutions have been considered advanced nuclear fuels for space nuclear reactors identified within the SP-100 program, LWRs, and developmental fast-spectrum nuclear reactors since the 1960s [42,44–55]. UN fuel forms have been demonstrated in the sodium cooled BR-10 reactor in Russia for nearly 20 years as well as in the Fast Flux Test Facility, Experimental Breeder Reactor-2 (EBR-II), and the Advanced Test Reactor, each of which are test reactors [56–58].

UN has potential advantages as a reactor fuel due to its high melting temperature (2762°C), good thermal conductivity (20.5 W/m K at 500°C), high uranium density (13.5 g/cm³), lower heat capacity than UO₂ (230 vs 300 J/kg K at 500°C), and performance under irradiation (such as low fission gas release and low swelling rates) [47,48,54,56,59]. These desirable properties contribute to larger power uprates, increased fuel cycle time, and higher burnup [56,59,60]. It is important to note that the thermophysical and irradiation performance of nitride fuel forms is largely dependent on the minor impurities and additives that exist in the final fabricated fuel form [42,61–65]. Many of the light-element impurities (e.g., oxygen and carbon) are introduced during handling and processing of the fuels during fabrication, which can be difficult to remove and adversely affect its performance in-reactor. Accordingly, major drawbacks to UN fuels are their unvetted thermophysical performance, low oxidation resistance, and poor hydrothermal corrosion resistance [66–77]. However, additives, such as uranium silicide, uranium dioxide, uranium carbide (UC), and zirconium mononitride, are incorporated in attempts to increase its high-temperature water corrosion resistance. This subsequent section will briefly review traditional nitride synthesis strategies and advances in synthesis and fabrication strategies as well as recent nitride synthesis with additives.

10.2.2.2 UN synthesis and fabrication techniques

UN powders intended for the manufacture of fuel pellets can be synthesized via multiple processes, as demonstrated over the past 60 years of R&D [42,45,54,61,65,68,76,78–126]. The most studied UN powder synthesis methods are the carbothermic reduction (CTR) of the uranium oxide prior to nitridization (CTR–N) and hydriding prior to nitridization (H–D–N) of elemental uranium. However, multiple alternative methods have also been investigated, which include aqueous synthesis routes, arc melting elemental uranium in nitrogen, flash sintering, and a gas–solid reaction at room temperature. In any case, once the powders are synthesized, they must be consolidated into dense fuel forms (>90% theoretical density), which is completed via multiple routes: pressureless sintering, hot pressing, hot isostatic pressing (HIP), and SPS.

Another important consideration in the synthesis of nitride fuel forms is the necessity to fabricate fuel using isotopically separated nitrogen. The high neutron cross section of ^{14}N will negatively affect fuel performance as well as produce ^{14}C through neutron adsorption and proton emission. It is therefore required to enrich naturally occurring nitrogen (99.6% ^{14}N and 0.4% ^{15}N) to concentrate ^{15}N , which is expensive and not currently feasible for large-scale production. Therefore a flow through synthesis process, such as CTR–N, must be reconsidered, and the nitrogen must be efficiently used in order for nitride fuel fabrication to be industrialized.

Carbothermic reduction and nitridation

The CTR and nitridation (CTR–N) is the most scalable and commonly used synthesis route to produce UN. It has been used and optimized for many decades in the synthesis of mononitride fuel forms using N_2 , $\text{N}_2 + \text{H}_2$, or ammonia gas atmospheres [42,53,54,65,68,78,80,81,84–86,88–93,96,99,107,108,110–120,124]. Accordingly, advances in the CTR–N method over the past decade have been minimal, although the CTR–N method is also the only synthesis route that has been demonstrated in the synthesis of large quantities of UN.

The starting materials for the CTR–N reaction method, uranium dioxide, and carbon, are first blended/milled and compacted prior to an extended thermal profile (up to 2000°C) that can last several days. This step is often repeated (the compacts are pulverized prior to subsequent pressing and heating to optimize the oxygen removal, nitrogen adsorption, and carbon cleanup) as seen in Fig. 10.5, adapted from Choi et al. [107].

The general reaction proceeds as follows:



where M is for the metal oxide to be converted (i.e., uranium, plutonium, or an alloy of the two). In the case of UN synthesis the intermediate reactions are thought to proceed as follows:

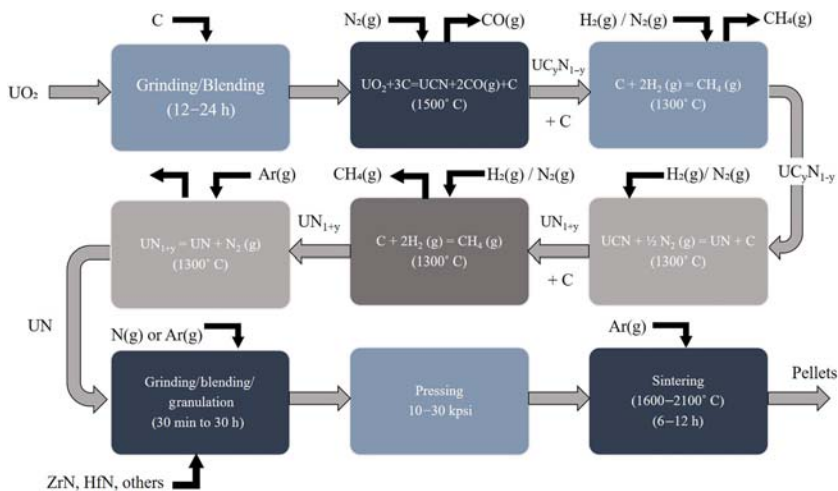
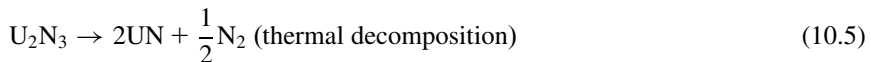


Figure 10.5 Diagram of process to produce UN pellets utilizing carbothermic reduction and nitridation as published by Choi et al. [107].



According to Braase et al., the CTR–N process is best thought of as a combination of three processes: (1) oxygen removal (reduction), (2) nitrogen introduction (nitridation), and (3) removal of excess carbon (carbon cleanup) [99]. The temperatures and duration of each of the steps must be optimized in order to optimize the mononitride powder. The process has been highly successful in consistently achieving low concentrations of residual oxygen and carbon, as low as 300 ppm, but usually at the expense of one another [42,46,68].

One advancement, which shortens the CTR–N synthesis time and describes a method for the continuous production of UN (rather than a batch process), has been filed with the US patent office [127]. Another recent advancement of the CTR–N method is the use of uranium trioxide microspheres and carbon synthesized from the sol–gel process as the starting material [86,108,111,112,115–117]. Although the process requires high-temperature furnaces and long dwell times, the starting materials (UO₂ and C) are significantly less expensive and pose less criticality concerns than those proposed by aqueous synthesis routes (e.g., elemental uranium,

UF_4 , HgI_2 , CCl_4 , and NH_4I) [82,100–103]. The CTR–N process also avoids the production of intermediate solutions and unnecessary creation of mixed waste streams, which have associated disposal costs. More importantly, the process can yield a final product that is significantly more pure than other synthesis routes, resulting in impurities less than 300 ppm depending on the starting molar ratio of $\text{C}:\text{UO}_2$ (ranging from 2 to 3), time, temperature, dwell time, and synthesis atmosphere [42,46,68]. The allowable oxygen and carbon impurity levels in UN for advanced fuel applications are an area that is currently under further investigation [99] for advanced fuel concepts. The disadvantages to the CTR–N method is the use of large volumes of nitrogen, high temperatures, and extended durations at which the reactions must take place all increase processing costs and created challenges for the process engineers that carry out the fabrication steps in inert atmosphere glove boxes.

Direct thermal (hydride–nitride)

As previously stated, another well-studied synthesis route to UN is a thermal treatment of elemental uranium. Although much less developed than the CTR–N synthesis route, the hydride–dehydride–nitride (H–D–N) synthesis route has been investigated for many years by multiple authors [45,46,61,76,77,82,83,87,94,95,98,121–123]. The H–D–N synthesis route uses a starting material of chemically cleaned, elemental uranium that is hydrided at temperatures ranging from 200°C to 300°C. The metal hydride is then dehydrated near 500°C in an inert atmosphere and then nitrided at elevated temperatures in a nitrogen gas stream to form a sesquinitride. The sesquinitride is reduced to a mononitride by exposure to temperatures above 1100°C in an inert environment or reduce nitrogen partial pressure. The reactions proceed as follows:



Although the H–D–N synthesis route results in reduced carbon impurities, the synthesized powder is very fine from the hydride–dehydride process. As a result, the powder has a high propensity for oxidation, which is highly exothermic. Handling must be completed in low oxygen and moisture partial pressure atmospheres to reduce oxygen pickup and oxide phase formation. Although high purity UN can be made from the H–D–N synthesis method in much less time than the CTR–N method, the required elemental metal feedstock makes it a less attractive synthesis solution. In addition, the highly controlled atmospheres required for the synthesis and handling of the powders make the H–D–N process difficult to scale to a production facility. A potential advantage of the H–D–N synthesis method

(when compared to the CTR–N synthesis method) is that it can be completed in a nearly closed reaction vessel, thereby significantly reducing the nitrogen consumption and, thus, reducing the synthesis cost when enriched nitrogen is used.

Alternative synthesis routes

As previously stated, multiple alternative synthesis routes have also been considered for the synthesis of UN powder, which include multiple solution routes using uranium halides [82,100–103], a molten cadmium precipitation [104,105], and a direct mechanochemical synthesis route [97]. However, the advancements in these areas are limited. Cleveland et al. [82] introduced a method where UN is synthesized by reacting a solution of the iodide with a solution of sodium, potassium, or calcium in anhydrous liquid ammonia. The method is relatively rapid, requires low temperatures, and yields a product that requires no grinding or ball milling prior to sintering. The process is described by reacting elemental uranium with hydrogen at room temperature to produce uranium hydride, which is then reacted with HgI_2 to form uranium tetraiodide (UI_4). Alternatively, one can synthesize UI_4 by reacting UO_2 with a stream of CCl_4 vapor at 800°C – 900°C to form uranium tetrachloride (UCl_4) prior to heating with NH_4I to form UI_4 and NH_4Cl . The precipitated UI_4 is dissolved in ammonia and mixed with a solution of sodium in ammonia whereby UN precipitates form. The primary drawback is in the purity of the product, which can have an impurity content of $\sim 10\%$. These impurities may escape during sintering, but the process has yet to be optimized or properly characterized. In another low temperature nitride synthesis process, Jaques et al. [97] proposed a gas–solid reaction between elemental uranium and gaseous nitrogen in a high energy planetary ball mill. Although the process has not been optimized or thoroughly characterized, it is an attractive technique due to the fact that it is completed in a sealed environment in a single processing step at room temperature and efficient nitrogen consumption. The novel synthesis routes present low temperature, relatively rapid, and potentially low-cost processes to uranium nitrides. However, inherent to milling operations and chemical synthesis routes, much optimization is required to reduce impurities to an acceptable level.

Nitride consolidation methods

Nitride powders are generally difficult to sinter relative to oxides and carbides [44]. However, many authors have reported the feasibility of sintering UN via methods such as cold pressing prior to sintering, arc melting and casting, hot pressing, HIP, SPS (also known as a field-assisted sintering technique or pulsed electric current sintering), and reaction sintering of mixtures of metal and higher nitrides (also known as combustion synthesis) [45,46,51,53,54,64,72,77,78,80,87,98,107,113,121,124–126,128–137]. Variables in these sintering studies include particle size (0.01–40 μm), compaction pressure (20–1100 MPa), organic binders (0–2 wt.%, PEG, PVA, PVB), sintering durations (0–48 hours), sintering atmospheres (vacuum, Ar, 0%–100% N_2 , Ar– H_2 , N_2 – H_2), and sintering temperatures (1300°C–2100°C). Regardless of the sintering technique or processing parameters, a stoichiometric mononitride (1.0 ± 0.02 U/N) is desired with minimal residual oxygen and carbon (<1000 ppm C and O). However,

the density and pore structure are dependent on the application. Choi et al. suggest that a desired final density of 90% TD with a closed pore structure and a relatively large grain structure ($> 40 \mu\text{m}$) is necessary [107]. However, during the SP-100 program, desired mononitride would have a final density of $87\% \pm 2\%$ TD with an open pore structure, no cracks, less than 500 ppm of each O and C, and a grain size of $\sim 20 \mu\text{m}$ [42]. Once sintered, the circumferential surfaces of the pellets are ground to meet the dimensional requirements of the fuel pin using a centerless grinder (Figs. 10.6–10.8).

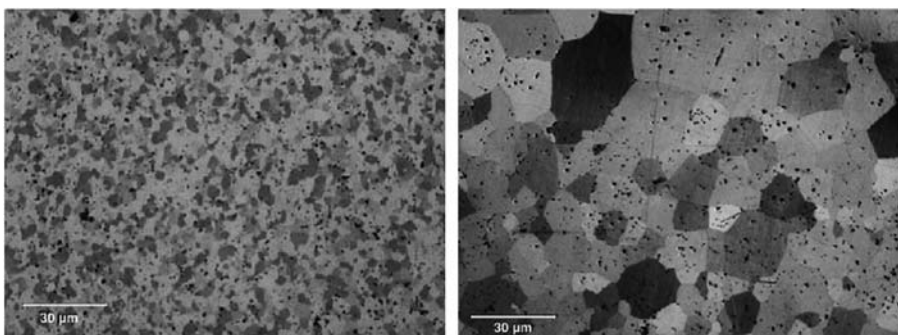


Figure 10.6 Micrographs of UN from SPS showing 6.7 and $23.8 \mu\text{m}$ grain sizes [128]. SPS, Spark plasma sintering.

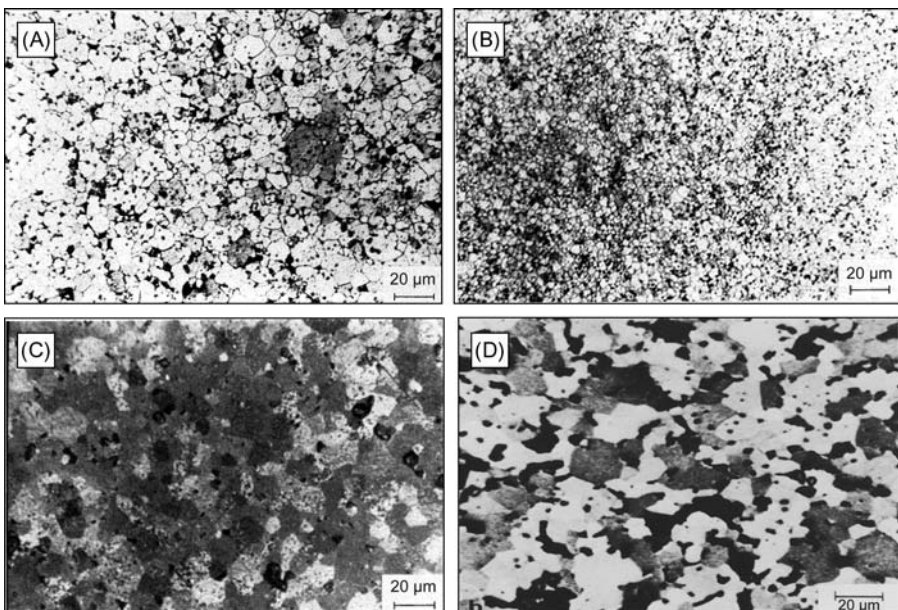


Figure 10.7 Micrographs of (U, Pu)N from cold pressing and sintering at 1750°C in (A) Ar, (B) N_2 —8% H_2 , (C) Ar—8% H_2 [78], and (D) pure UN sintered at 1800°C in Ar [42].

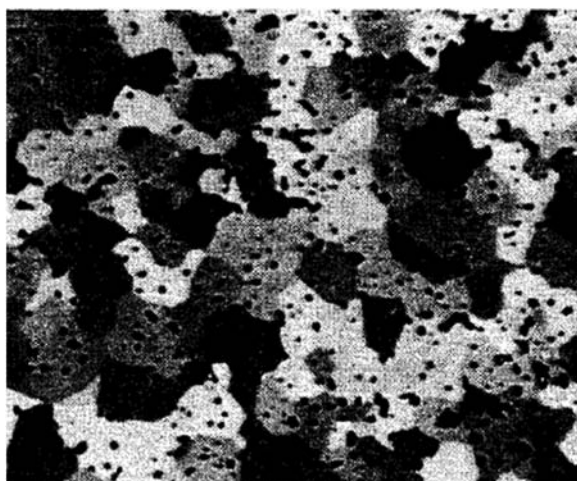


Figure 10.8 Micrograph of UN hot isostatically pressed at 1900°C [126].

10.2.3 Other ceramic fuel fabrication

10.2.3.1 Uranium borides

The uranium–boron binary system consists of three high-temperature melting point compounds: UB_2 , UB_4 , and UB_{12} along with the pure metallic phases [138]. The fabrication of the borides has not been demonstrated commercially but would be expected to follow a similar processing route as the U–Si binary alloys, discussed in Section 10.4.1. Three common methods are typically employed, which involve thermal mixing of the phase pure elements or hydrides in an inert atmosphere to exothermically react and form the desired compound [139,140], borothermic reduction of UO_2 and B_2O_3 with a reactive element (i.e., C, Al, and Mg) [140], or arc melting the metallic elements [141,142]. Electrolysis in molten fluoride or chloride salts has been demonstrated [143] along with reaction of UH_3 with diborane [144].

Processing the uranium boride compounds into geometries for a given experimental technique is nontrivial given that high temperatures in excess of 2100°C are necessary to sinter dense compacts. Tripler et al. were able to sinter UB_2 pellets to 60% of the theoretical density at 1953 K using a pressureless method in a vacuum furnace and opted to arc melt the low-density pellet to achieve a 99% dense sample [142]. Matterson and Jones utilized a hot press at 2273 K and 28 MPa to fabricate 98% dense UB_4 pellets, but noted UB_2 decomposed when in contact with the graphite dies used in the hot press [140]. The same study attempted pressureless sintering in a vacuum furnace using graphite dies at 2273 K, but both UB_2 and UB_4 decomposed to the metal or lesser boride.

10.2.3.2 Uranium carbides

UC and mixed uranium/plutonium carbides $[(\text{U}, \text{Pu})\text{C}]$ have been proposed for deployment as fast reactor fuels. Similar to UN, UC has a high uranium density and

therefore is capable of sustaining fast reactor and/or breeder reactor cycles. Typical UC and U(Pu)C synthesis has been limited to CTR [145–148]. The CTR process, though capable of high purity UC production from a UO₂ precursor, requires high sintering temperatures ($T > 1400^{\circ}\text{C}$) and long milling times. However, arc melting synthesis from uranium metal and graphite precursors has also been achieved [149]. See the subsection “Arc melting” in 10.3.2.1. for detailed discussion of arc melt synthesis. While arc melting can produce high purity, bulk feedstock material, additional efforts are necessary to produce uniform geometries. Furthermore, work has been done to evaluate alternative carbon sources for the preparation of precursor material [150] for traditional CTR or advanced techniques such as SPS [151].

10.3 Metallic fuel fabrication

10.3.1 Introduction to metallic fuels

Uranium metal is an ideal reactor fuel because of its superior neutronic properties, high density and thermal conductivity, low radiation level, and ease of handling (when compared to other fissionable materials such as ²³³U and ²³⁹Pu). However, unalloyed uranium is susceptible to surface corrosion, low hardness and yield strength, and lack of dimensional stability in the room temperature α -phase. Similar challenges exist with uranium–plutonium metal alloy systems. This challenge can be overcome by alloying uranium and uranium–plutonium with transition metals in Groups V through VIII, particularly 4d and 5d elements. Solubility of the alloying metal decreases as the size difference with U atoms becomes larger and increased bond strength promotes intermetallic compound formation. Thus selection of an alloying metal must be considered carefully, along with engineering of fuel fabrication technologies with the desired properties of the fuel in mind.

Detailed next are considerations specific to metallic fuel fabrication that can be addressed during the alloy synthesis process, although the list is not all inclusive.

1. The alloy must possess sufficient *phase stability* since the fuel will undergo various heat treatments to either homogenize or anneal the as-cast and thermomechanical processed structure. Microsegregation resulting from differences in the liquidus and solidus temperatures of alloying elements occurs during the casting process that creates a chemical gradient across dendrites growing within the melt. While this can be overcome by performing a homogenization treatment, consideration should be given to secondary precipitate formation that could consume a portion of the alloying metal leading to earlier phase destabilization. The metal fuel should exhibit a strong degree of isotropy and minimal growth or distortion during thermal cycling throughout its lifetime.
2. The metal fuel should have a *high resistance to corrosion* that, depending upon application, can be aqueous or gaseous.
3. The metal fuel should have sufficient *fatigue strength* and consideration given to potential stress corrosion cracking scenarios that it could be exposed to over its lifetime.
4. Alloying metals should not result in a significant neutronic penalty.

5. Finally, the metal fuel should possess mechanical properties compatible with the envisioned thermal–mechanical fabrication process, such that introduction of alloying elements does not significantly complicate the ability to fabricate the alloys on a production scale.

Furthermore, additions of other metals (e.g., Pu) require special handling and additional consideration, including but not limited to use of hot cells, equipment capable of being operated remotely, glove boxes, and safety concerns associated with handling of α -emitting powders. This section will discuss fabrication techniques applied to metal fuels and provide some specific material systems used in various reactor applications, that is, research reactors, fast reactors, and pulse reactors.

Some examples of alloying additions to U- and/or Pu-based alloys and the basis behind selection are given as follows. Additions of Nb typically result in decreased transformation rates, increased hot hardness (yield strength), and progressively lower corrosion rates. Similarly, additions of Ru have shown a strong gamma-stabilizing effect that increases corrosion behavior of any U–X (where X is most commonly Mo)-based alloy in high-temperature water. However, alloys containing Ru can be challenging to fabricate because of extremely brittle U₂Ru intermetallic formation along with an accompanying decrease in hot hardness. Additions of Zr raise the solidus temperature of the alloy, possess enhanced dimensional stability under irradiation, and have reduced fuel–cladding chemical interaction [152,153]. In addition, alloys containing Zr have shown significant corrosion resistance in high-temperature water ($> 260^\circ\text{C}$) because of reduced hydride formation rate. This is a noteworthy improvement as hydrides lead to accelerated stress corrosion cracking in the U alloy systems. However, Zr is a notorious γ -U phase destabilizer because of UZr₂ (and Mo₂Zr in the case of ternary additions) intermetallic formation. Like Ru, these intermetallics could be problematic during postcasting operations such as rolling. Minor additions of Cr minimally improve the phase stability but result in a hot hardness reduction. The corrosion effectiveness of these alloys has not been well characterized. Interestingly, minor additions of Ti result in significantly higher tensile strength, but the effects on phase stability, corrosion, and transformation (particularly stress corrosion cracking) need further investigation.

The overview by Burkes et al. [152] details the US perspective on fast reactor metal fuel fabrication technology, some examples of which are included and expanded upon here. The review by Kittel et al. [153] provides a detailed review of the properties, fabrication methods, and performance characteristics associated with plutonium as a nuclear fuel material, although basic methods are summarized here. The fuel fabrication process description by Hubbard et al. [154] provides a modern-day description of plate-type research reactor fuel fabrication, specifically U–Mo, but the fundamental characteristics provided here can be easily extended to other uranium binary and ternary alloy systems.

10.3.2 Fabrication methods for metallic fuels

10.3.2.1 Alloying and casting

Most successful alloying metals in metallic nuclear fuel possess a high melting point that requires methods to effectively dissolve and diffuse the alloying additions

with uranium and/or plutonium. This section describes a few of the most successful and demonstrated methods to produce a homogeneous alloy product capable of delivering desired stability and performance during irradiation as well as several modifications to those methods that may be required to minimize introduction of impurities and incorporate lower melt temperature or volatile compounds, that is, plutonium and americium.

Arc melting

Arc melting involves a water-cooled crucible or hearth typically made from copper and a nonconsumable electrode typically made from solid tungsten, referred to as the cathode. The electrode rod penetrates through the top of the unit providing tight control over the environment during melting. To produce and maintain an arc under vacuum or argon, a strong positive charge is applied to the cathode while a strong negative charge is applied to the crucible, or anode. Temperatures can reach over 3000°C during melting, well above the liquidus temperatures of typical alloying metals used for uranium and plutonium metal fuels. Arc melt furnaces can be used to produce ingots or “buttons” ranging from grams to kilograms in scale, although maintaining the arc within the pool becomes increasingly more challenging as the size of the button increases. The electrode is movable by an operator and promotes stirring of the molten materials and thus homogeneity of the melt. The use of this process also limits impurity pickup during melting, given the high temperatures that can be achieved and relatively rapid cooling times after the arc is extinguished. The buttons are used as feedstock for subsequent melting and shape casting operations, such as vacuum induction or microwave melting, but seldom as an individual product due to size limitations. Fig. 10.9 displays a R&D scale arc melt furnace in a glove box at Los Alamos National Laboratory. In addition, the melt furnace itself and characteristic buttons are displayed in Fig. 10.9B and C, respectively.

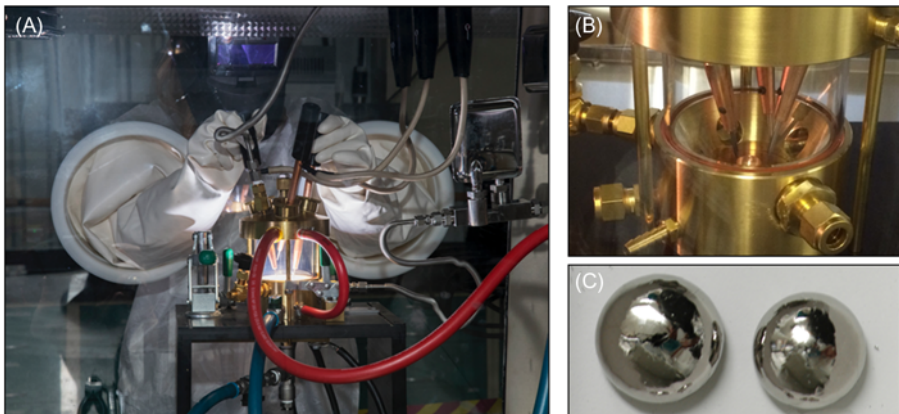


Figure 10.9 (A) R&D scale arc melt furnace in a glove box at Los Alamos National Laboratory, (B) picture of melt furnace with copper hearth, and (C) characteristic buttons produced by this method. *R&D*, Research and development.

Another type of arc melting, referred to as vacuum arc remelting (VAR), uses a consumable electrode containing the desired metal fuel constituents. The electrode can consist of consolidated rods of uranium/plutonium and alloying metal, prealloyed metal, metal turnings from scrap, or consolidated powder. The electrode is brought into close proximity with the crucible and the arc established. The electrode is withdrawn from the molten pool to maintain the arc that causes the metal to melt. VAR is desirable to produce high purity feed for subsequent melting and casting operations on a large scale. The process permits the control of solidification rates such that the microstructure can be tightly controlled, an important fabrication step for fuel systems such as U–Mo, U–Zr, ternary alloys containing Pu, and intermetallic fuel compounds such as UAl_x and U_3Si_2 (see [Chapter 7](#): Research reactor fuels).

Vacuum induction melting

Vacuum induction melting (VIM) methods have been used for well over a half-century to fabricate various metallic fuels for nuclear reactors. The first loading of U-5 wt.% fissium¹ driver fuel for EBR-II was fabricated by countergravity injection casting. The VIM process was used to dissolve and alloy the fissium (see footnote 1) elements, representing simulated fission products from recycled irradiated nuclear fuel, with the uranium. After melting and holding for a sufficient time to achieve homogeneity, the material was tilt-poured into graphite molds with a zirconia mold wash. Eventually, technology moved to an injection casting process that involved mechanically stirring the melt with a tantalum paddle contained within the VIM crucible to achieve homogeneity of the melt. Once sufficient homogeneity was achieved, injection casting molds made of quartz were introduced and the furnace was pressurized, forcing molten metal into the quartz molds to produce fuel “slugs.” Stirring within the melt reduced time associated with mixing feedstock components and distributed thin layers of oxide formation within the melt. The fabrication process was greatly simplified by combining alloying and injection casting steps into a single batch with a single heat-up/cool-down cycle, and the approach also reduced the concentration of impurities introduced into as-cast fuel slugs.

A basic introduction into the VIM technique is derived from an excellent review by Jackson [155]. VIM is based upon an induction coil coupled with a crucible that transmits heat to the metal charge by conduction and radiation, commonly referred to as coreless heating. Heat is generated by the induced flow of current and the material’s electric resistance to the current. Different frequencies are applied to the coil to overcome the “skin effect” that occurs when the induced current is concentrated into a thin section at the periphery of the material being heated. Heat travels from the outer skin to the inside of the charge via conduction, and the depth of current penetration varies inversely as the square root of current frequency. Thus the lower the frequency, the greater the depth of penetration. Furthermore, the size of

¹ Fissium (Fs) is nominally 2.4 wt.% Mo, 1.9 wt.% Ru, 0.3 wt.% Rh, 0.2 wt.% Pd, 0.1 wt.% Zr, and 0.01 wt.% Nb and designed to mimic the noble metal fission products remaining after a simple reprocessing technique based on melt refinement.

the piece to be heated is an important consideration in association with the skin effect. When the depth of penetration exceeds half the thickness of the piece to be heated, there is a resultant loss of efficiency therefore limiting the minimum size of a piece that can be heated at a given frequency.

The most common type of vacuum induction furnace is a pour-type design, which can either be bottom poured or top poured (also referred to as “tilt” pour). Bottom pouring claims simplicity and economics of furnace design, simplicity of operation, less probability of slag entrapment in ingots, and the crucible and mold can be heated with a single induction coil. However, bottom-pouring metal is initially at a high hydrostatic head that can lead to rapid mold erosion and formation of cold shuts and a larger facility footprint is required. Tilt pouring claims accurate control of the metal stream entering the mold, limiting mold erosion and metal splattering, and modern systems require significantly less facility footprint than bottom-pour designs. [Fig. 10.10](#) displays a pilot scale tilt-pour VIM within an enclosure at Pacific Northwest National Laboratory used to prepare U–Mo castings for research reactors (these fuels are discussed further in [Chapter 7](#): Research reactor fuels).

Several factors must be considered when utilizing VIM for metallic fuel fabrication. If parameters such as temperature, pressure, pressurizing rate, geometry, feeding distance, directional and progressive solidification ratios, and mold coating are not properly engineered and optimized, the formation of defects manifesting themselves as shrinkage pipes, microshrinkage, and hot tears is expected (see Ref. [156] as an example). For example, shrinkage pipes form from an imbalance between progressive shrinkage, created by radial solidification toward the center of the cast part, and directional shrinkage, created by axial solidification toward the heat



Figure 10.10 Pilot scale tilt-pour VIM within an enclosure at Pacific Northwest National Laboratory. *VIM*, Vacuum induction melting.

source or melt pool. Careful balance between progressive and directional solidification is essential to eliminating these defects in the cast fuel. Control can be provided by maintaining a small axial temperature gradient from top to bottom through slow removal of the casting from the melt pool (in the case of injection casting) or by delaying the radial cooling created with an argon gas purge along the mold walls until a strong directional solidification front is established. Impurities are typically buoyant within the fuel melt and concentrate at the top of the solidified ingot if directional solidification is properly established. The thin layer containing the impurities can be easily cropped from the cast part. A chill block under the mold can be used to induce heat flow from the bottom of the mold rather than through the sides, effectively improving directional solidification. The mold must be positioned properly within the induction coil to establish a steep temperature gradient that initiates progressive solidification from the bottom to top of the mold. An example detailing the effect and importance of maintaining proper thermal gradients within the mold can be found by Nyberg [157] for the U-10Mo system.

Microshrinkage is characteristic of alloys with a wide freezing temperature range, such as those of interest in metal nuclear fuel applications. For example, the U–19Pu–10Zr alloy liquidus is at 1300°C while the solidus is at 1080°C, a 220°C freezing range [158]. This is complicated further by maintaining a melt temperature with sufficient fluidity to effectively cast the alloy. Solidification begins at the mold wall and chilled end of the casting, either top or bottom depending upon geometry and design, and propagates toward the thermal center of the casting. Grain growth simultaneously occurs in the partially liquid portion of the casting, creating an increasingly resistive path for molten metal to flow as grains coarsen. Microshrinkage occurs when grain growth starves the shrinkage areas of molten metal, leaving behind undesirable voids. With metallic alloys containing Pu, managing the defect becomes more challenging as the Pu content is increased, on account of increased freezing range. With injection casting, microshrinkage is minimized by increasing pressure over the molten pool during solidification, effectively increasing the feeding distance and promoting an extended nucleation and growth process [159]. Feeding distance is a function of the casting diameter and the metal being cast. Therefore feeding distance is critical for a liquid reservoir of metal to continually feed a solidification front. Finally, hot tears occur when an area of a casting is not allowed to shrink properly, placing the area under tension from metal contraction near the solidus temperature of the alloy [160]. The axially propagating solidification fronts contract if cooling is initiated too quickly, causing the solidification front to effectively tear away from the solidified casting. Dimensional variations within the mold can also cause increased tension between solidification fronts, ultimately resulting in hot tears. Considerations to reduce shrinkage pipe formation are also effective at reducing hot tears.

Refractory coatings on graphite molds are essential when melting alloys containing carbide-forming elements. These coatings are also important to produce high-quality castings with acceptable dimensional tolerance. Many refractory coatings have been demonstrated, and selection depends ultimately upon the application and product specification, but at a minimum the coating should be mechanically stable,

resistant to thermal shock, inert to the molten metal (uranium, plutonium, and alloying constituents), and harmless as a contaminant (see Ref. [161] as an example). Coatings can also be useful on the external surface of molds to minimize heat loss, which helps with establishing proper thermal gradients and therefore improved directional solidification. The use of uncoated graphite molds results in the formation of a continuous carbide layer formed on the molten metal pool in contact with the crucible and protects the graphite from rapid erosion [162]. While undesirable, the continuous layer can be removed following solidification using other techniques, either chemical or mechanical, postprocess.

Microwave melting

Microwave melting is a recent technology used to fabricate uranium alloy nuclear fuels but has not been known to be applied to other metal nuclear fuel alloys, for example, those containing plutonium. The casting process is similar to that used for VIM, that is, bottom-pour designs or melting in place. Similar to VIM where the induction coil couples with the crucible, microwave melting also couples with the crucible since bulk metals do not readily couple with microwave energy. With this processing method a ceramic crucible that absorbs microwaves must be utilized. A metal charge placed within the crucible can be heated rapidly through radiation, conduction, and convection in a manner that could not be achieved otherwise. An important consideration when utilizing this method is to avoid arcing or plasma formation, which effectively absorbs all of the energy being delivered by the microwaves leaving little energy to be absorbed by the crucible and melt the metal charge.

Microwave melt pools are relatively quiescent compared to VIM pools due to the lack of electromagnetic stirring. This can be advantageous in instances where high temperatures must be achieved for melting (e.g., U–Zr alloys) to avoid breakdown of mold washes and interaction with the ceramic crucible materials. On the other hand, this can be a serious disadvantage when alloying is desired, since some homogeneity of the melt pool is promoted through active mixing. Therefore the method often requires the introduction of some additional mixing methods, such as filters placed between the crucible and mold (assuming a bottom pour design) to create a tortuous path during the molten metal pour to improve mixing, an argon lance inserted into the molten metal to stir the melt by bubbling argon, or methods to slowly introduce higher temperature alloying elements to a molten uranium metal pool. Mold coatings successful for VIM casting are also successful for microwave melting, although detailed studies have not been reported in the open literature. However, without the aid of mechanical mixing, extended hold times or multiple melt and cast cycles are required to achieve sufficient homogeneity using microwave melting. This leads to deterioration of even the best mold coating applications and the increased potential for impurity pickup, most commonly Si.

10.3.2.2 Thermomechanical processing

While some metal fuels can be direct cast to shape, such as slugs for fast reactors or pulse reactors, thermomechanical processing is often required to overcome

inherent casting defects, such as microshrinkage and dimensional variations discussed previously, or process the part into a different desired geometry, such as a foil for plate-type designs like those used in research reactors. Different thermomechanical processing steps lead to different microstructures (which lead to different in-reactor fuel performance), manufacturing process robustness, and manufacturing yields. This section describes a few of the most successful and demonstrated methods to produce a uniform microstructure foil, plate, slug, or tube. The importance of combining thermal conditions with mechanical conditions (e.g., strain, reduction ratios) and the ability to manage impurities (e.g., carbides, silicides) with this type of processing are discussed.

Rolling

Primary breakdown of uranium alloy castings produced from the casting methods described earlier typically occurs at temperatures that place the material in the γ -U phase, that is, 750°C–1000°C. As alloying content is increased, there is a concomitant increase in the resistance to deformation in the γ -U phase. Thus the higher the concentration of alloying metal, the higher the rolling temperature required to effectively deform the metal alloy being worked (see Ref. [163] as example for the U-10Mo system). Heating can be accomplished by inert atmosphere-purged electric furnaces, induction heating or infrared heating. If an inert atmosphere is not possible, the casting to be rolled is typically canned to minimize oxidation during the process. Molten-salt baths can also be utilized, although much more common for unalloyed or low alloy uranium. Rolled plate and sheets with acceptable surface finish can be produced using hot rolling only through use of clean, well-oiled rolls, using castings with minimal surface imperfections, rolling to finish thickness without reheats in between, minimizing the preheat temperature and time, using an inert atmosphere furnace, and water quench of the product immediately upon reaching the final thickness.

Hot rolling of as-cast metal fuels is one of the most common methods to eliminate microshrinkage introduced during casting while maintaining dimensional tolerance without significant machining. However, the method does not typically fracture second-phase particles, such as carbides or silicides. Hot rolling is most useful when conducted around the homologous melt temperature of the alloy, and loads introduced to the mill are significantly less than those introduced during cold rolling for the same reduction ratio and starting ingot thickness achieving the criteria described earlier. When significant reductions are introduced during hot rolling, dynamic recrystallization can be induced that leads to grain refinement and a more uniform microstructure, a desirable feature in most metal nuclear fuel applications. An example of a R&D scale instrumented rolling mill used to process uranium alloys at Pacific Northwest National Laboratory is shown in Fig. 10.11.

Cold rolling of an as-cast product is ineffective at improving homogeneity, and in some cases, exacerbates any as-cast defects that are present. Grains typically elongate in the rolling direction and form a pancake shape, while intergranular carbides fracture perpendicularly to the rolling direction creating porosity between the fractured carbides. In this sense the method is usually avoided to breakdown as-cast

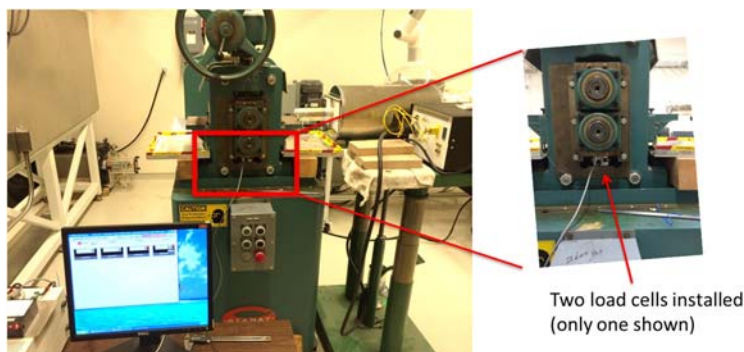


Figure 10.11 Side view of Stanat TA-215 Rolling Mill, with load cells shown in the inset, used to process uranium alloys at Pacific Northwest National Laboratory.

parts and typically used to improve dimensional control over the final product. Depending upon the degree of dimensional control required for the application, cold rolling is usually conducted in multiple, light reduction passes. However, given the limitations of cold rolling, it is important to ensure a homogeneous product is introduced that has taken impurity concentration and distribution into effect. Failure to do so can create additional challenges during subsequent processing and/or irradiation.

Understanding parameters such as effect of rolling an as-cast structure, homogenization, and rolling technique (hot/cold, reduction ratios, mill requirements, etc.) are critical to effective use of the rolling method. Optimization requires that undesirable microstructures are avoided and that desirable microstructure features are produced keeping in mind that alteration of processing parameters leads to certain advantages and disadvantages such as overall process robustness and yield. Rolling methods, particularly if conducted warm or cold, often lead to other product attributes that must be treated, often thermally, before introduction into service. This is true when combining multiple methods described in this section to create a metal fuel fabrication system. For example, casting of uranium alloys may lead to macrosegregation (discussed earlier) that requires a homogenization heat treatment (discussed below). Homogenization in turn leads to coarsening of grains that affect rolling behavior and ultimately thickness variation (and thus yield) of the rolled product. Furthermore, final grain size of a rolled product is highly dependent upon the final heat treatment temperature during annealing (discussed in [Section 10.3.2.3](#)) if conducted at all. Given that rolling is used to break down cast parts into plates, sheets, or foils, and the type of reactor designs that utilize these geometries (i.e., plate-type research reactors), most processing experience is limited to binary uranium alloys.

Coextrusion

Coextrusion is a high-pressure and high-strain bonding process typically used to bond metallic nuclear fuel cores to cladding or diffusion barriers in a single step. The process results in a very high-quality metallurgical bond that was used for

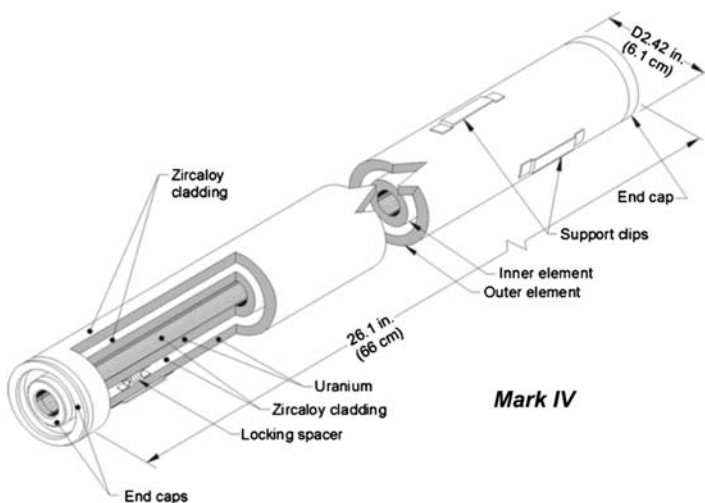


Figure 10.12 Schematic of the coextruded α -uranium zirconium–clad fuel used in N-reactor.

many years in the US Department of Energy (DOE) complex, particularly at the Hanford site, to produce metallic uranium fuels [164]. These unalloyed uranium fuels were typically processed at α -U temperatures and clad by coextrusion with zirconium, an example of which is shown in Fig. 10.12 [165]. As with rolling of uranium alloys the resistance to deformation increases with the concentration of alloying metal, meaning that higher concentration alloys, such as those for most modern-day reactor applications, require higher extrusion forces. Coextrusion has mostly been utilized to process unalloyed uranium and uranium alloys for various reactor applications, although there is also some experience with plutonium binary alloys, specifically Pu–Al, and there is little open literature experience published on ternary alloys containing both U and Pu.

There are many forms of coextrusion, but the most common metal fuel fabrication form uses a machined uranium billet sleeved with zirconium or zirconium alloys (e.g., Zry-2 and Zry-4) and encapsulated with an outer can [166]. The outer can is normally evacuated and sealed to serve as a hermetic barrier preventing oxidation during preheat and extrusion, required when working reactive, high-strength metals. The challenge with canned extrusion is selection of can materials, which protect the cladding (often Zircaloy, as indicated in Fig. 10.12), during extrusion, that are weldable, oxidation resistant and ideally possess a flow stress matching that of the material to be extruded. Alternatively, the outer can may provide a softer outer layer having lower flow stress and low reactivity with steel extrusion tooling. Copper canning of uranium extrusions was a standard practice for extruding fuels commonly used throughout the DOE complex [167] that resulted in lower extrusion forces and less oxidation of the uranium metal billet.

Uranium alloys, processed at the γ -U temperature, possess increased strength compared to α -U requiring extrusions at higher temperature and under higher forces, mentioned previously [168]. For direct extrusion, limiting stresses occur in the stem (which is the approximate diameter of the inside of the container liner), and the use of high-quality hot-working steels (such as H-13 and H-21) provides a safe working stress of ~ 190 ksi. This stress limit determines the size of the hydraulic ram and the design of the container. For the container a three-part shrink fit design provides for higher safe working pressures by introducing compressive stresses between each of the cylinders, which acts to keep stress levels for the heated container temperature (450°C) at safe working levels. Care must also be exercised during preheat of the extrusion billet to avoid thermal gradients that may exist from the surface of the billet to the core, owing to the relatively poor thermal properties associated with uranium alloys and the design of the extrusion can or container.

A very low friction viscous lube process, called Ugine Séjournet process [166], can produce low extrusion forces due to low redundant work and friction; however, the low heat capacity of a small billet size can lead to excessive thickening of the glass and bonding of the billet to the cooler tooling, ultimately limiting the usefulness of glass lubricants. Filled grease lubricants capable of use at higher temperatures (up to 800°C) are more useful in these processing scenarios. Application of the grease lubricant inside of the container and the face of the die, combined with coating of the billet with graphite, results in significant reduction in extrusion load and superior surface finish. Copper-based alloys are typically utilized as the can material, although any alloy possessing similar flow stress to the metal fuel being extruded can be used, depending upon factors such as availability, cost, and machinability. An example of a Cu-based alloy can, U-10Mo cast and machined ingot prior to extrusion, and an extruded U-10 fuel “slug” are shown in Fig. 10.13. An example of a R&D extrusion press at Pacific Northwest National Laboratory is provided in Fig. 10.14, used to process the billet as shown in Fig. 10.13.

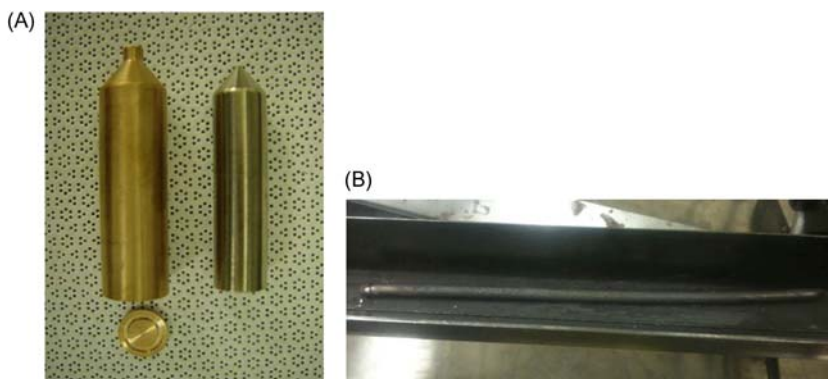


Figure 10.13 (A) Cu-based alloy can and U-10Mo cast and machined billet prior to assembly and extrusion and (B) extruded U-10Mo fuel slug.



Figure 10.14 Example of a R&D extrusion system at Pacific Northwest National Laboratory used to extrude uranium alloys. The control system is shown in the left foreground, and the press and snorkel are in the background. *R&D*, Research and development.

10.3.2.3 Heat treatment

Heat treatment of metallic fuel is required to enable processing to achieve desired material and mechanical properties that deliver expected performance during irradiation. As briefly mentioned earlier, as-cast uranium alloys typically have a dendritic microstructure and chemical inhomogeneity that must be addressed before subsequent thermal–mechanical processing and/or direct use as a nuclear fuel, since the inhomogeneity may lead to loss of dimensional control and predictable performance during irradiation. Homogenization treatments can range from 900°C to 1100°C with typical durations ranging from a few hours to a day (see Refs. [163,169,170] as examples). Lower homogenization temperatures typically require longer durations while higher homogenization temperatures typically require shorter durations. Homogenization is typically conducted under high vacuum to minimize any impurity pickup that may occur at such high temperatures and extended durations. Care must be exercised while addressing microsegregation, since extended durations at high temperatures can lead to a number of secondary and tertiary challenges during fabrication. For example, yield/flow stress is inversely proportional to the grain size, that is, the coarser the grain size, the lower the yield and flow stress and the finer the grain size, the higher the yield/flow stress [163,169]. This may have direct impact on subsequent thermomechanical processing methods such as rolling and extrusion discussed previously. An example of a typical vacuum annealing furnace used for homogenization of uranium alloy products at Pacific Northwest National Laboratory is shown in Fig. 10.15.



Figure 10.15 An example of a typical vacuum annealing furnace used to homogenize cast uranium alloy products at Pacific Northwest National Laboratory.

In addition, the impact of impurities that are present in the metal fuel alloy, which can have both positive and negative impacts, can be influenced during high-temperature postcasting homogenization or postthermomechanical processing heat treatments. For example, carbon impurities present in the melt feedstock or introduced during melting and casting operations, particularly with VIM, can have significant impact upon grain size and recrystallization during thermomechanical processing. Fine carbides are typically pushed to grain boundaries during solidification, where they coarsen and spheroidize during high-temperature homogenization treatments for extended durations (see Ref. [157] as an example). Coarser carbides, such as those introduced during melting and casting, are typically intragranular and fracture during subsequent thermomechanical processing, resulting in less distribution throughout the product. Silicon, which is commonly introduced with microwave melting, is considered an impurity in Zr- or Mo-alloyed fuel materials because it removes some of the Zr (or Mo) from solution by precipitating as a stable silicide. For example, soluble Zr increases fuel melting temperature, decreases fuel/cladding chemical interaction, and is therefore beneficial to fuel performance. Reduction of soluble Zr through precipitation of stable phases reduces these benefits. Mo, as a second example, is added to the alloy to stabilize the metastable $\gamma\text{-U}$ phase, discussed previously. Reduction of soluble Mo through precipitation of stable phases leads to decomposition of the desired $\gamma\text{-U}$ phase during thermomechanical processing and premature transformation, which can potentially be problematic during irradiation. Careful inoculation of melts with selective impurities can be useful to provide finer grain size that is useful for some metal nuclear fuel applications. The purity of a casting depends on the purity of the charge, and every melting and casting cycle increases carbon concentration by 20–40 ppm and

iron and silicon by 5–10 ppm [155]. Oxygen, carbon, and nitrogen were similarly tracked as impurities in the U–Zr and U–Pu–Zr alloys because they also reduce soluble Zr by forming stable oxide, carbide, and nitride, or Zr precipitates stabilized by these impurities. Typical impurity levels of depleted uranium alloys are 8–40 ppm aluminum, 10–50 ppm carbon, 5–50 ppm copper, 2–10 ppm hydrogen, 30–100 ppm iron, 1–10 ppm magnesium, 10–50 ppm nickel, 8–40 ppm nitrogen, and 10–80 ppm silicon [155]. These impurity levels do not hold true for every application but provide a general rule of thumb when processing uranium-bearing metal fuels.

Furthermore, thermomechanical processes such as rolling and coextrusion, discussed here, can result in high-residual strains that require relief prior to irradiation. These types of operations are typically carried out under vacuum at temperatures above the homologous melt temperature of the metal or alloy, although in some instances, inert gases have also been used. Similar to homogenization, annealing of uranium and uranium alloys in the γ -U phase can be conducted under inert atmospheres with little concern of hydrogen pickup, which otherwise might result in deleterious mechanical properties [171]. Annealing atmospheres and cooling rates used can have significant effect on the resultant properties of the product, depending upon the specific nuclear fuel alloy and desired performance. For example, solutionization heat treatment times are not critical to the product unless the final grain size is important. Since oxidation of the final product is typically undesirable (see Ref. [172] as an example), annealing furnaces with a rapid, internal quenching mechanism are desirable that also minimizes the amount of distortion introduced in the part, particularly for thin parts (i.e., foils). The amount of alloy metal also affects time–temperature–transformation relationships and the relative ability to quench. It is pointed out the main difference between homogenization and annealing, as discussed here, is in the time required for the two methods. With homogenization the treatment is carried out at γ -U temperatures for many hours to days, while for annealing, exposure at γ -U temperatures is conducted for tens of minutes to a few hours.

10.4 Advanced reactor fuel fabrication

10.4.1 High-density light-water reactor fuels

High-density fuels for LWR applications have seen a recent surge in interest. As discussed in Chapter 5, Other power reactor fuels, “drop-in replacements” or direct alternatives for UO_2 can provide enhancements in thermal conductivity, neutron economy, fission gas retention, and overall enhanced reactor performance under certain accident scenarios. The nonoxide-based fuel types receiving the most attention at the present for this application are uranium silicides. Two uranium silicide compounds, U_3Si and U_3Si_2 , contain uranium densities superior to UO_2 and have seen of the most extensive historic interest. The increased uranium density would allow these fuel forms to be operated for longer durations for higher power output

(higher burnups) in the core and/or more readily accommodate changes to the cladding material. However, the low melting point of U₃Si coupled with its understood limitations due to amorphization and swelling observed during research reactor irradiation ($T < 200^\circ\text{C}$) have limited its consideration as a nuclear fuel [173,174]. The majority of recent interest has been focused on U₃Si₂ due to the above properties coupled with demonstrated irradiation history. In addition, composite fuel forms are also under consideration with a high-density fuel form as constituent, including U₃Si₂ and UN. A challenge to the deployment of either U₃Si₂ or UN in water-cooled reactors is susceptibility to washout and pulverization [175–177] of these oxidation-prone compounds. This section will focus on the methods used to produce nonceramic high-density fuels intended for drop-in replacements to UO₂, address the challenges to industrial-scale fabrication and LWR deployment, and introduce considerations to mitigate these challenges.

10.4.1.1 *Uranium silicide pellet fabrication*

Compound synthesis

Uranium silicides, though often treated as ceramics, are intermetallic compounds, and therefore the fabrication of U–Si fuel forms merges two synthesis approaches already discussed in great detail: ceramic and metallic fuel fabrication. There are three approaches that have been considered for lab to industrial scale production of uranium silicide fuels: (1) mechanical, (2) melt synthesis, and (3) reactionary synthesis.

For both mechanical/powder metallurgical and melt synthesis, stoichiometric amounts of uranium and silicon are used as the precursor materials. Powder metallurgical approaches have been published recently by Sinha et al. [178] and Alanko and Butt [179]. The investigation by Sinha was directed for a dispersoid fuel fabrication application, and significant UO₂ contamination was observed. In addition, the work by Alanko required long milling times, and UO₂ contamination was also observed [179]. Melt synthesis for U₃Si₂ fuel fabrication via induction melting was investigated by Taylor et al. in 1961 [180]. In this effort the authors reported USi₂ formation during the melt synthesis. In addition, U₃O₈ contamination was reported. In each of the previously referenced efforts, uranium powder was used as a precursor. Uranium is susceptible to oxidation, and even in “inert” atmospheres with only ppm levels of O₂, U has been shown to rapidly oxidize. Thus the use of a large surface area precursor, such as a powder, often yields appreciable oxide contamination in the final fuel form.

The melt synthesis process, arc melting in particular, as described in the subsection “Arc melting,” in 10.3.2.1, is more commonly used for U–Si compound synthesis. There are two approaches used for R&D scale production to prepare the precursor materials prior to arc melting. Some investigators introduce bulk uranium and silicon directly to the melt furnace [181], while others utilize a hydride–dehydride process to start with a fine U metal powder then Si powder is added, and a compact is formed prior to arc melting [182,183]. For either the bulk uranium or powder/compact case the “charge” (stoichiometric uranium and silicon) is melted three to six times, and

the resulting ingot is flipped between each melt to encourage homogenization and subsequent formation of a single-phase U–Si product. An annealing, or thermal solutionization, step is often added after arc melt synthesis to further homogenize the product, but most recently has been shown to not be necessary to produce phase pure U_3Si_2 and U_3Si_5 .

The primary advancement in the last 50 years of uranium silicide fabrication has been the enhancement in product purity, though efforts are still underway to mitigate the formation of Si-rich phases [182]. The improvement is largely due to advanced gas purification, the use of getters, and O_2 monitoring of process gases. These engineering controls used during pellet synthesis are incorporated at each stage of the fabrication process, importantly during the powder metallurgy portions described in the next section. An advancement on the horizon is the synthesis of U_3Si_2 via a reaction synthesis method that begins with a nonmetal compound of uranium (e.g., UC, UC_2 , UF_4 , or UF_6). Precursor uranium metal presents both criticality and proliferation concerns, when the currently used fabrication process is increased to an industrial scale. Therefore a nonmetal precursor route is actively under investigation by multiple researchers; however, no published data on these efforts is yet available, likely due to the cutting-edge nature of this development and intellectual property precautions actively being pursued. The same statement is also true for current efforts for advanced manufacturing and AM efforts for uranium silicide fuels.

Pellet fabrication

Once the silicide is formed, whether via arc melting, mechanical, or reaction synthesis, it must be formed into pellet geometry to be a suitable drop-in replacement for current LWR fuel. In a typical pellet fabrication process the uranium silicide is milled with a binder to homogenize and produce a small particle size prior to compaction. The powder is then sieved and pressed (150–300 MPa) into a cylindrical geometry using a punch and die set. This entire process must occur in a controlled, inert atmosphere due to the reactivity of U_3Si_2 with oxygen [181,182]. The geometric green densities that result range from 50% to 65% theoretical density typically. These green bodies are then sintered under a high purity argon atmosphere to temperatures of 1200°C–1500°C [181,182,184]. Finally, centerless grinding is used to produce the final pellet geometry prior to fuel pin loading [182]. The conventional process outlined here is capable of producing pellets with final densities up to 97% theoretical density and is described in the diagram displayed in Fig. 10.16.

A major challenge for the implementation of U–Si fuels for commercial LWRs is the industrial scale-up of the fabrication process. The air sensitivity of these materials requires inert atmosphere glove box handling, close attention to gas purity, and furnace fixturing contamination. Advancements to the fabrication process that address these issues are ongoing.

Advances to pellet fabrication of U_3Si_2 include SPS efforts that are just now producing preliminary results [185]. SPS is a promising technique for fabrication of several fuel forms due to its high-temperature, quick sintering capability. Scale-up

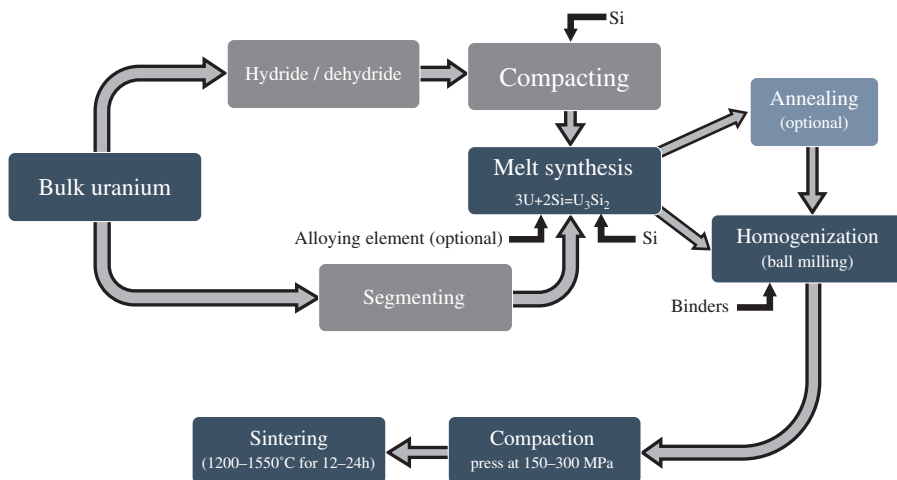


Figure 10.16 Process diagram for conventionally used U_3Si_2 fuel pellet fabrication.

of this technique is also of current interest as described in the previous section of this chapter.

Alloying additions to U–Si fuels

U_3Si_2 has shown susceptibility to pulverization and washout in LWR relevant atmospheres: high-temperature steam and pressurized water [175–177]. The pulverization of U_3Si_2 when exposed to steam at reactor-typical temperatures proves it highly vulnerable to washout (i.e., the fuel pulverizes and is swept out of the fuel pin when cladding is compromised), in the event of a cladding breach. While oxidation and washout behavior comparable to UO_2 would not necessarily eliminate U–Si fuel systems from consideration, it is strongly desired that any ATF concept provides some degree of enhanced performance under off-normal conditions. One approach to improving the oxidation resistance of U_3Si_2 is to incorporate alloying additives to the U–Si matrix. The addition of alloying elements shows promise in enhancing the accident tolerance and oxidation resistance of this fuel form. Recent works have preliminarily looked at the addition of Al [186] and B [187] to U_3Si_2 . In these efforts the alloying additions were added at the arc melting step. There could be advancements in this area by investigating various alloying element additions at either the milling step, during melt, or via advanced manufacturing and/or coating methods.

10.4.1.2 High-density composite fuels for light-water reactors

Composite fuel concepts have recently been proposed to address both the thermal conductivity limitations of UO_2 and the susceptibility of high-density fuel forms to washout, specifically U_3Si_2 and UN [188–190]. A recent, exhaustive review of

these concepts was recently performed by Zhou and Zhou [191]. Therefore no additional depth in this topic will be sought in this chapter.

10.4.2 Coated particle fuel fabrication

10.4.2.1 Introduction to coated particle fuel

TRISO-coated particles are the fuel form used in high-temperature gas-cooled reactors. The particle consists of a spherical fissile kernel surrounded by four coating layers. The first layer is a porous carbon “buffer” layer. The next layer is a dense, isotropic pyrolytic carbon (the inner pyrolytic carbon or IPyC layer). This is followed by a layer of silicon carbide (SiC), and finally an outer pyrolytic carbon (OPyC) layer with properties similar to the IPyC layer. The particles are designed so that fission products are effectively retained at their source in the fuel during normal reactor operation and during high-temperature accidents. TRISO particles are also considered for the fluoride salt-cooled high-temperature reactor concept and as an LWR fuel in the form of fully ceramic microencapsulated pellets. Summarized here is the fabrication process for this unique, advanced reactor fuel form.

10.4.2.2 Tristructural isotropic fabrication

A number of kernel compositions have been used for coated particle fuels, including oxides, carbides, and oxide/carbide mixtures (termed “UCO,” and consisting of a heterogeneous mixture of the two phases). The most common kernel types that have been developed are low-enriched UO₂ and UCO. Although a variety of kernel fabrication methods were employed in the early years of TRISO fuel R&D, the most common method is the aqueous sol–gel process [192,193]. While specifics can vary, the two main processes are internal and external gelation. Both involve preparation of an aqueous uranium-bearing precursor solution, for example, by dissolving U₃O₈ in nitric acid. Additional additives are included as process aids or to adjust kernel chemistry (e.g., carbon black particulate to introduce carbon when making UCO kernels). Droplets of the solution are formed by expelling the solution through vibrating nozzles, and the droplets fall via gravity through a liquid forming column. In the external gelation process the liquid column consists of ammonium hydroxide, which causes the precipitation of solid ADU from the solution, forming hydrated gel microspheres as the reaction progresses. In the internal gelation process the column consists of a hot liquid that is immiscible with water (e.g., trichloroethylene), and as the aqueous droplets fall into the column they form into a spherical geometry due to surface tension. The heat in the column initiates decomposition of an ammonia donor compound included as an additive in the solution (e.g., hexamethylenetetramine), with the ammonia causing gelation of the microspheres [193,194].

After formation the gelled microspheres are typically washed and dried. Dried microspheres undergo a multistep heat treatment for calcination, reduction of

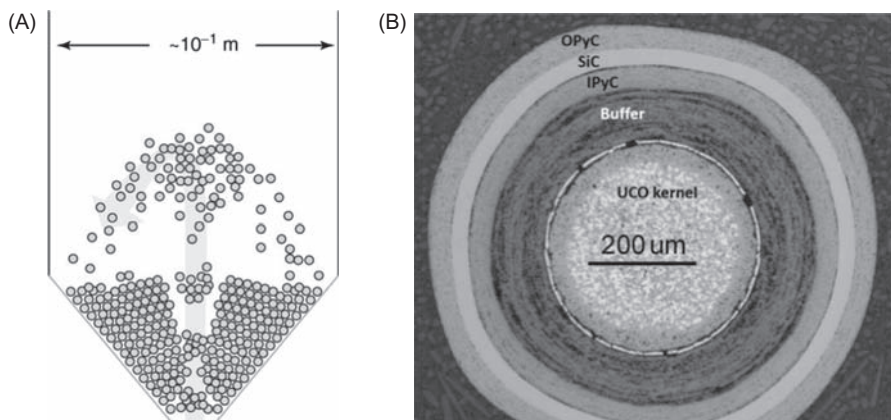


Figure 10.17 (A) Schematic diagram of a fluidize bed coater [192] and (B) cross section of a UCO TRISO particle (kernel diameter $\sim 425 \mu\text{m}$). *TRISO*, Tristructural isotropic.

hyperstoichiometric UO_{2+x} phases, and final sintering to form kernels with near theoretical density. Temperatures and heating schedules vary with the specific process and type of kernel fabricated, with reported temperatures ranging from $\sim 1500^\circ\text{C}$ to 1900°C [194–196]. UO_2 kernels are homogeneous, while UCO kernels at this stage consist of a fine heterogeneous mixture of UO_2 , UC_2 ,² and UC phases [196]. Upon subsequent heating in the presence of excess carbon in the buffer layer during the TRISO coating process and compact heat treatment (discussed further below), the UC phases in the kernel convert to UC_2 . The composition of the precursor solution can be varied to produce final sintered kernels with the desired UC_2/UO_2 ratio.

The TRISO coatings are applied to the sintered kernels using a fluidized bed chemical vapor deposition technique. The coating furnace consists of a cylindrical vessel with a conical base, where the reactive gases are injected (Fig. 10.17A). A number of parameters are important in determining the final properties of the deposited layers, including the specific reactive gases used and their concentrations in the inert carrier gas, coating temperature, flow rate, depth of the particle bed, and others. The charge of kernels (the optimum mass of which will depend on the diameter of the vessel) is inserted into the furnace, and the gas flowing from the bottom causes fluidization of the particle bed. The vessel is heated to the target temperature, and the various coatings are applied by injecting specific gas mixtures formulated to give the desired coating properties. The carbon layers are deposited from either acetylene (C_2H_2), propylene (C_3H_6) or mixtures of the two, and at temperatures in the range of $\sim 1100^\circ\text{C}–1450^\circ\text{C}$, depending on the layer and the specific process. The SiC layer is deposited at a relatively higher temperature

² The dicarbide of uranium (UC_2) does not exist with integer stoichiometry, but rather with a slightly sub-stoichiometric composition, varying with temperature and other variables [197]. It is referred to in this chapter in the generic form “ UC_2 .”

($\sim 1500^{\circ}\text{C}$ – 1600°C) from methyltrichlorosilane in a hydrogen carrier gas (and in some processes the H_2 carrier gas is diluted with argon to improve fluidization of the particles in the coater and to obtain the desired SiC microstructure). Fig. 10.17B shows a cross section of a UCO TRISO particle.

TRISO particles can be formed into either spherical pebbles (for use in a pebble bed reactor) or cylindrical compacts (for use in a prismatic block reactor). The process differs significantly for spheres and compacts but generally starts with overcoating the TRISO particles with the powdered fuel matrix material. This consists of graphite powder and a thermoplastic or thermosetting resin to help achieve the desired density and give the unfired compact or sphere structural integrity. Overcoated particles are then formed into the desired shape in a mold with application of pressure. Spherical fuel elements are typically machined at this stage to achieve the desired dimensions, while fuel compacts are pressed to the desired green dimensions. The fuel is then heat treated using an often complex heating schedule to carbonize (decompose organic compounds from the resin) and drive off impurities at temperatures in the range of 1800°C – 1950°C [192,194,195].

TRISO fuel is subjected to extensive quality control (QC) analysis to verify that the properties meet specifications for kernels, coated particles, and the compacts or spheres [192,193,195]. For fuel kernels, specifications may include the diameter, sphericity, ^{235}U enrichment, density, and stoichiometry. Coated particle specifications include individual layer thickness and density, anisotropy of the pyrocarbon layers, and microstructure of the SiC layer. For the fuel compact or spherical fuel element, specifications include dimensions, matrix density, uranium contamination level, and defective particle fraction. Fuel specifications will vary depending on reactor design and radionuclide control requirements. For example, kernel enrichment will depend on target burnup goals, and fuel diameter will vary depending on enrichment. Furthermore, the allowable fraction of defective particles (those with coating defects that will result in release of fission products during operation) is determined through reactor safety analyses that take into account all barriers to fission product release from the coated particle to the reactor building.

A variety of characterization methods are used for QC analysis. These include optical microscopy or X-radiography for coating layer thickness, density gradient columns for coating layer density, ellipsometry for pyrocarbon anisotropy, microscopy for coating layer microstructure, and “burn-leach” analysis to determine exposed uranium content in a compact or sphere. Sufficient particle populations must be sampled to quantify a particular property with the desired statistical confidence. Detailed discussion of TRISO fuel QC methods employed in various fuel manufacturing programs is discussed in Refs. [192,193,195].

10.4.3 Molten-salt reactor fuel fabrication

The molten-salt reactor experiment (MSRE) paved the way for molten-salt technology in the nuclear industry. A number of molten-salt reactor designs have been proposed since the operation of the MSRE at Oak Ridge National Laboratory in the 1960. These reactors have spanned both thermal and fast-spectrum designs and

have been configured as both breeder and burner cores [198–206]. In addition, several start-up and venture capitalist funded programs are currently developing molten-salt reactor designs. These designs range from fluoride-based molten salt–cooled concepts to actinoid-bearing fluoride/or chloride salt reactors. These developers, particularly those proposing salt fueled reactor concepts, face a number of challenges including but not limited to licensing, actinoid solubility, high-temperature corrosion, fuel salt preparation, in-line processing, and composition control throughout burnup. The chemistry of molten salts is further described in [Chapter 6](#), Molten-salt reactor fuels.

10.4.3.1 Pyrochemical fuel salt synthesis

This section provides a brief overview of the technologies proposed to synthesize salt fueled reactor compositions. The only viable processes to produce industrial scalability are electrolytic chemical processing, similar to that used to reprocess spent nuclear fuel (SNF), covered in the previous chapter. Depending on the reactor design, whether a breeder/burner design operating with a fast or thermal spectrum, the fuel salt synthesis process will vary significantly. For example, a thorium fueled salt core will require different processing steps than a core designed for the transmutation of actinides, as these elements have varied electronegativities and abundances in SNF (if SNF is to be the source of fissionable fuel). Similarly, a fluoride host salt will entail different separations and purification avenues than chlorides. Along these same lines, if spent fuel is to be used to fuel the proposed core, then steps to reduce the spent oxide fuel have to be incorporated into the processing. Independent of the core design and fuel salt composition, the primary challenges to handling actiniod molten salts are similar, and thus the processing systems engineering will likely be very similar.

Electrochemistry, specifically pyrochemistry, arguably offers the most industrial scalable heavy metal chloride salt synthesis route for these ionic liquids [207]. An inert environment is requisite as these materials are hydroscopic, and water can increase the corrosiveness of the fuel salt in core. Pyrochemistry readily permits the oxidation of a metal to its chloride in a host salt [208,209]. Oxide fuel that has been used and discarded from a conventional reactor can be made into a chloride or fluoride fuel in a host salt (typically a mixture of LiCl/F, KCl, BeF₂, and/or NaCl).

If U and/or Pu reprocessed from SNF is the source of fissionable material, then the first step in a salt synthesis procedure is decladding and oxide fuel recovery from the SNF rods [206]. Voloxidation of the chopped fuel pins is a headend step involving high-temperature oxidation of SNF. It has been investigated in recent years as a way to both to separate the SNF from the cladding hulls and to release then trap the volatile fission products [210–212]. In addition, voloxidation reduces the particle size of the material continuing to electrolytic reduction, increasing the efficiency of that reaction. More information on reprocessing and recycling is described in [Chapter 12](#), Reprocessing and recycling, and SNF in [Chapter 13](#), Spent nuclear fuel and disposal.

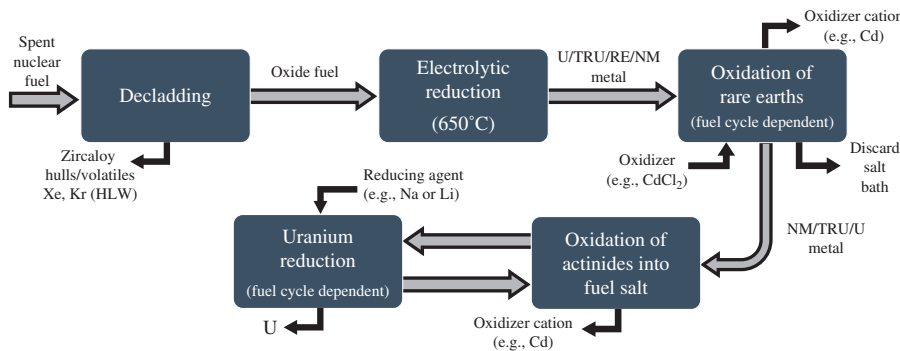


Figure 10.18 One proposed method for molten-salt reactor fuel production from spent nuclear fuel as simplified from [208].

The second step in a SNF conversion to molten-salt fuel would be to prepare the fissionable material to be converted to salt. One proposed step to initiate that process is electrolytic reduction, to produce metals from the oxides present in SNF, followed by rare earth oxidation. Certain elemental species would have to be carefully monitored during these subsequent processes as they will reduce/oxidize or dissolve (e.g., Cs, Ba, I, and Sr) at varied rates depending on the processing conditions [213] (Fig. 10.18).

If previously segregated actinoid precursor metal is used, then only oxidation into the host salt, up to the solubility limit or to a neutronically designed limit, is necessary. If synthesized from SNF, the actinoids and noble metals will be the last to oxidize pyrochemically in a host salt; however, depending on the reactor concept, steps in the process would need to be altered to result the desired fuel salt composition; for example, uranium may need to be extracted if a purely transuranic fuel salt is desired [198,206]. In the previously reported process that proposed fuel salt synthesis from SNF, the final step in fuel salt synthesis was aimed to replace UCl_3 with transuranic chlorides [198,206].

10.5 Conclusion

The advances to the nuclear fuel chemistry for synthesis and fabrication of reactor fuel are expansive, considering the development of new fabrication techniques and proposal of several advanced fuel forms for the next generation of reactor concepts. Fabrication and compaction advances such as sintering agents, SPS, and liquid-phase sintering, associated mostly with composite fuel forms, enable enhanced densification and or geometry control. However, for techniques such as advanced manufacturing, further development is necessary to ensure comparable throughput and scalability to the current industrial processes. In addition, for advanced fuel forms that are oxygen sensitive, such as carbides, nitrides, and silicides, atmosphere control must be addressed. As our reactor designs continue to advance, so too must

fuel fabrication and uranium compound synthesis. As advanced manufacturing techniques mature, it is anticipated that they will be employed for the fabrication and optimization of fuel cycle materials.

Acknowledgments

The authors of this chapter would like to acknowledge the support of their institutions, The University of Texas at San Antonio, Los Alamos National Laboratory, Boise State University, Pacific Northwest National Laboratory, and Idaho National Laboratory, for the time and effort dedicated to assembling the current chapter. Special acknowledgment is due to Mr. Cole Moczygemba, an undergraduate student at the University of Texas at San Antonio, for his help in creating the process diagram figures used throughout the chapter.

A portion of this work was conducted at Pacific Northwest National Laboratory operated by Battelle for the US DOE under contract DE-AC05-76RL01830. This chapter was prepared as an account of work sponsored by an agency of the US government. Neither the US government nor any agency thereof, nor Battelle Memorial Institute, nor any of their employees, makes any warranty, express or implied, or assumes any legal liability or responsibility for the accuracy, completeness, or usefulness of any information, apparatus, product, or process disclosed, or represents that its use would not infringe privately owned rights. Reference herein to any specific commercial product, process, or service by trade name, trademark, manufacturer, or otherwise does not necessarily constitute or imply its endorsement, recommendation, or favoring by the US government or any agency thereof, or Battelle Memorial Institute. The views and opinions of authors expressed herein do not necessarily state or reflect those of the US government or any agency thereof.

References

- [1] T. Abe, K. Asakura, 2.15 - Uranium oxide and MOX production, in: R.J.M. Konings (Ed.), *Comprehensive Nuclear Materials*, Elsevier, 2012, pp. 393–422.
- [2] W.R. Hollander, Method of Preparing Uranium Diuranate, 1965, U.S. Patent US3394997A.
- [3] J. Littlechild, G. Gillies, Production of Uranium Dioxide in a Rotary Kiln, United Kingdom Atomic Energy Authority, 1970.
- [4] H. Vietzke, et al., Method for the Preparation of Uranium Dioxide Powder (UO_2) With Good Pressing and Sintering Properties From Uranium Hexafluoride (UF_6) or Aqueous Solutions of Uranyl Nitrate ($\text{UO}_2(\text{NO}_3)_2$), Nukem GmbH United States of America, 1970.
- [5] G. Butler, et al., Conversion of Uranium Hexafluoride to Oxides of Uranium, 1979.
- [6] R.R. Fuller, Production of Ammonium Diuranate, Westinghouse Electric Company, 1976.
- [7] W.R. Hollander, Method of Preparing Uranium Diuranate, General Electric Co United States, 1968.
- [8] M.H.A. Piro, et al., A review of pellet-clad interaction behavior in zirconium alloy fuel cladding, in: S. Hashmi (Ed.), *Reference Module in Materials Science and Materials Engineering*, Elsevier, Oxford, 2017, pp. 1–68.

- [9] J.C. Killeen, The effect of additives on the irradiation behaviour of UO_2 , *J. Nucl. Mater.* 58 (1) (1975) 39–46.
- [10] J.B. Ainscough, F. Rigby, S.A. Morrow, Effect of oxygen potential on the thermal creep of niobia-doped UO_2 , *J. Am. Ceram. Soc.* 64 (5) (1980) 315–318.
- [11] J.B. Ainscough, F. Rigby, S.C. Osborn, The effect of titania on grain growth and densification of sintered UO_2 , *J. Nucl. Mater.* 52 (2) (1974) 191–203.
- [12] S. Kashibe, K. Une, Effect of additives (Cr_2O_3 , Al_2O_3 , SiO_2 , MgO) on diffusional release of ^{133}Xe from UO_2 fuels, *J. Nucl. Mater.* 254 (2-3) (1998) 234–242.
- [13] K. Une, et al., Rim structure formation and high burnup fuel behavior of large-grained UO_2 fuels, *J. Nucl. Mater.* 278 (1) (2000) 54–63.
- [14] A. Leenaers, et al., On the solubility of chromium sesquioxide in uranium dioxide fuel, *J. Nucl. Mater.* 317 (1) (2003) 62–68.
- [15] J.C. Killeen, Fission gas release and swelling in UO_2 doped with Cr_2O_3 , *J. Nucl. Mater.* 88 (2–3) (1980) 177–184.
- [16] T. Cardinaels, et al., Dopant solubility and lattice contraction in gadolinia and gadolinia–chromia doped UO_2 fuels, *J. Nucl. Mater.* 424 (1–3) (2012) 289–300.
- [17] L. Bourgeois, et al., Factors governing microstructure development of Cr_2O_3 -doped UO_2 during sintering, *J. Nucl. Mater.* 297 (3) (2001) 313–326.
- [18] M.W.D. Cooper, C.R. Stanek, D.A. Andersson, The role of dopant charge state on defect chemistry and grain growth of doped UO_2 , *Acta Mater.* 150 (2018) 403–413.
- [19] J. Arborelius, et al., Advanced doped UO_2 pellets in LWR applications, *J. Nucl. Sci. Technol.* 43 (9) (2006) 967–976.
- [20] T. Matsuda, et al., Characteristics of Fuel Pellet With Additive of Al and Si, 1998. Technical committee meeting on advances in fuel pellet technology for improved performance at high burnup, Tokyo, Japan, 1996.
- [21] K. Une, I. Tanabe, M. Oguma, Effects of additives and the oxygen potential on the fission gas diffusion in UO_2 fuel, *J. Nucl. Mater.* 150 (1) (1987) 93–99.
- [22] M.W.D. Cooper, S.T. Murphy, D.A. Andersson, The defect chemistry of $\text{UO}_{2 \pm x}$ from atomistic simulations, *J. Nucl. Mater.* 504 (2018) 251–260.
- [23] R. Jovani-Abril, et al., Synthesis of nc- UO_2 by controlled precipitation in aqueous phase, *J. Nucl. Mater.* 477 (2016) 298–304.
- [24] A. Fernández, et al., Transmutation of actinides, *J. Am. Ceram. Soc.* 85 (3) (2002) 694–696.
- [25] M. Cologna, et al., Sub-micrometre grained UO_2 pellets consolidated from sol gel beads using spark plasma sintering (SPS), *Ceram. Int.* 42 (6) (2016) 6619–6623.
- [26] V. Tyrpekl, et al., Synthesis of dense yttrium-stabilised hafnia pellets for nuclear applications by spark plasma sintering, *J. Nucl. Mater.* 454 (2014) 398–404.
- [27] J. Somers, A. Fernández, Fabrication routes for yttria-stabilized zirconia suitable for the production of minor actinide transmutation targets, *J. Am. Ceram. Soc.* 88 (4) (2005).
- [28] R.D. Hunt, et al., Production of small uranium dioxide microspheres for cermet nuclear fuel using the internal gelation, *Ann. Nucl. Energy* 69 (2014) 139–143.
- [29] V. Tyrpekl, et al., Low temperature decomposition of U(IV) and Th(IV) oxalates to nanograined oxide powders, *J. Nucl. Mater.* 460 (2015) 200–208.
- [30] K.W. Lay, R.E. Carter, Role of the O/U ratio on the sintering of UO_2 , *J. Nucl. Mater.* 30 (1969) 74–87.
- [31] P. Dehaudt, L. Bourgeois, H. Chevrel, Activation energy of UO_2 and UO_{2+x} sintering, *J. Nucl. Mater.* 299 (2001) 250–259.
- [32] I. Amato, R.L. Colombo, A.M. Protti, On the activation energy of sintering non-stoichiometric uranium oxide, *J. Nucl. Mater.* 11 (2) (1964) 229–235.

- [33] L. Ge, et al., Densification of uranium dioxide fuel pellets prepared by spark plasma sintering (SPS), *J. Nucl. Mater.* 435 (1–3) (2013) 1–9.
- [34] T. Yao, et al., Grain growth and pore coarsening in dense nano-crystalline UO_{2+x} fuel pellets, *J. Am. Ceram. Soc.* 100 (6) (2017) 2651–2658.
- [35] T. Yao, et al., TiO_2 doped UO_2 fuels sintered by spark plasma sintering, *J. Nucl. Mater.* 469 (2016) 251–261.
- [36] P.A. Haas, Heating of uranium oxides in a microwave oven, *Am. Ceram. Soc. Bull.* 58 (9) (1979).
- [37] W. Dörr, et al., Method and Furnace for Microwave Sintering of Nuclear Fuel, 2002.
- [38] T.A. Thornton, J. Veldon, D. Holaday, Sintering UO_2 and Oxidation of UO_2 With Microwave Radiation, 1981.
- [39] T. Subramanian, et al., A novel method of sintering UO_2 pellets by microwave heating, *Mater. Lett.* 46 (2–3) (2000) 120–124.
- [40] J.H. Yang, et al., Microwave process for sintering of uranium dioxide, *J. Nucl. Mater.* 325 (2–3) (2004) 210–216.
- [41] A. Bergeron, J.B. Crigger, Early progress on additive manufacturing of nuclear fuel materials, *J. Nucl. Mater.* 508 (2018) 344–347.
- [42] R.B. Matthews, et al., Fabrication and testing of uranium nitride fuel for space power reactors, *J. Nucl. Mater.* 151 (3) (1988) 334.
- [43] J. Bricout, et al., Evaluation of the feasibility of the powder injection moulding process for the fabrication of nuclear fuel and comparison of several formulations, *Powder Technol.* 297 (2015) 49–60.
- [44] Y. Arai, 3.02 – Nitride fuel A2, in: R.J.M. Konings (Ed.), *Comprehensive Nuclear Materials.*, Elsevier, Oxford, 2012, pp. 41–54.
- [45] A.A. Bauer, Nitride fuels: properties and potentials, *React. Technol.* 15 (2) (1972) 87–104.
- [46] H. Matzke, *Science of Advanced LMFBR Fuels.*, Elsevier Science Publishing Company, Inc, Amsterdam, The Netherlands, 1986, p. 740.
- [47] S.L. Hayes, J.K. Thomas, K.L. Peddicord, Material property correlations for uranium mononitride. 3. Transport-properties, *J. Nucl. Mater.* 171 (2–3) (1990) 289–299.
- [48] S.L. Hayes, J.K. Thomas, K.L. Peddicord, Material property correlations for uranium mononitride. 4. Thermodynamic properties, *J. Nucl. Mater.* 171 (2–3) (1990) 300–318.
- [49] S.L. Hayes, J.K. Thomas, K.L. Peddicord, Material property correlations for uranium mononitride. 1. Physical properties, *J. Nucl. Mater.* 171 (2–3) (1990) 262–270.
- [50] S.L. Hayes, J.K. Thomas, K.L. Peddicord, Material property correlations for uranium mononitride. 2. Mechanical properties, *J. Nucl. Mater.* 171 (2–3) (1990) 271–288.
- [51] R.B. Matthews, Overview of SP-100 fuel development activities, Proceedings of the Seventh Symposium on Space Nuclear Power Systems (CONF-900109), University of New Mexico, Albuquerque, NM, 1990, pp. 883–888.
- [52] R.B. Matthews, Overview of space reactor fuel development activities, *Trans. Am. Nucl. Soc.* 64 (1991) 266–267.
- [53] R.B. Matthews, Ceramic fuel development for space reactors, *Am. Ceram. Soc. Bull.* 51 (1) (1992) 96–101.
- [54] R.B. Matthews, et al., Fuels for space nuclear power and propulsion: 1983–1993, in: M. S. El-Genk (Ed.), *A Critical Review of Space Nuclear Power and Propulsion 1984–1993*, American Institute of Physics, New York, 1994, pp. 179–220.
- [55] K.S. Chaudri, et al., Coupled analysis for new fuel design using UN and UC for SCWR, *Prog. Nucl. Energy* 63 (2013) 57–65.

- [56] G.J. Youinou, R.S. Sen, Impact of accident-tolerant fuels and claddings on the overall fuels cycle: a preliminary systems analysis, *Nucl. Technol.* 188 (2) (2014) 123–138.
- [57] A.G. Kordyukov, et al., Tests of models of BREST-OD-300 reactor fuel elements in an autonomous lead-cooled channel of a BOR-60 reactor, *At. Energy* 97 (2) (2004) 564–570.
- [58] P.A. Lessing, Oxidation Protection of Uranium Nitride Fuel Using Liquid Phase Sintering, Idaho National Laboratories, 2012.
- [59] N.R. Brown, et al., Neutronic performance of uranium nitride composite fuels in a PWR, *Nucl. Eng. Des.* 275 (2014) 393–407.
- [60] J. Zakova, J. Wallenius, Fuel residence time in BWRs with nitride fuels, *Ann. Nucl. Energy* 47 (2012) 182–191.
- [61] B.D. Rogozkin, et al., Thermochemical stability, radiation testing, fabrication, and reprocessing of mononitride fuel, *At. Energy* 95 (6) (2003) 835–844.
- [62] D.A. Lopes, A. Claisse, P. Olsson, Ab-initio study of C and O impurities in uranium nitride, *J. Nucl. Mater.* 478 (2016) 112–118.
- [63] T. Schuler, et al., Transport properties of C and O in UN fuels, *Phys. Rev. B* 95 (9) (2017).
- [64] Y. Arai, M. Morihira, T. Ohmichi, The effect of oxygen impurity on the characteristics of uranium and uranium-plutonium mixed nitride fuels, *J. Nucl. Mater.* 202 (1–2) (1993) 70–78.
- [65] P. Bardelle, D. Warin, Mechanism and kinetics of the uranium-plutonium mononitride synthesis, *J. Nucl. Mater.* 188 (1992) 36–42.
- [66] S. Sugihara, S. Imoto, Hydrolysis of uranium nitrides, *J. Nucl. Sci. Technol.-Tokyo* 6 (5) (1969) 237.
- [67] S. Sunder, N.H. Miller, XPS and XRD studies of corrosion of uranium nitride by water, *J. Alloy. Compd.* 271 (1998) 568–572.
- [68] G.A.R. Rao, et al., Oxidation and hydrolysis kinetic studies on UN, *J. Nucl. Mater.* 185 (2) (1991) 231–241.
- [69] R.M. Dell, V.J. Wheeler, N.J. Bridger, Hydrolysis of uranium mononitride, *Trans. Faraday Soc.* 63 (533P) (1967) 1286–1294.
- [70] R.M. Dell, V.J. Wheeler, E.J. McIver, Oxidation of uranium mononitride and uranium monocarbide, *Trans. Faraday Soc.* 62 (528P) (1966) 3591.
- [71] J. Bugl, A.A. Bauer, Corrosion and oxidation characteristics of uranium mononitride, *International Symposium on Compounds of Interest in Nuclear Reactor Technology X* (13) (1964).
- [72] D.A. Lopes, S. Uygur, K. Johnson, Degradation of UN and UN-U₃Si₂ pellets in steam environment, *J. Nucl. Sci. Technol.* 54 (4) (2017) 405–413.
- [73] M. Jolkkonen, et al., Uranium nitride fuels in superheated steam, *J. Nucl. Sci. Technol.* 54 (5) (2017) 513–519.
- [74] J.V. Dehadraya, et al., The oxidation of uranium-cerium mononitride microspheres, *J. Alloys Compd.* 257 (1–2) (1997) 313–321.
- [75] J.E. Antill, B.L. Myatt, Kinetics of oxidation of UN and U(CO) in carbon dioxide steam and water at elevated temperatures, *Corros. Sci.* 6 (1) (1966) 17–23.
- [76] M. Paljevic, Z. Despotovic, Oxidation of uranium nitride, *J. Nucl. Mater.* 57 (3) (1975) 253–257.
- [77] K. Johnson, et al., Oxidation of accident tolerant fuel candidates, *J. Nucl. Sci. Technol.* 54 (3) (2017) 280–286.

- [78] Y. Arai, et al., Fabrication of (U, Pu)N fuel pellets, *J. Nucl. Mater.* 168 (3) (1989) 280–289.
- [79] F. Anselin, Etude des Nitrures D'Uranium, de Plutonium et de Leurs Solutions Solides, *J. Nucl. Mater.* 10 (4) (1963) 301–320.
- [80] Y. Arai, K. Minato, Fabrication and electrochemical behavior of nitride fuel for future applications, *J. Nucl. Mater.* 344 (1–3) (2005) 180–185.
- [81] H. Bernard, Advanced fuel fabrication, *J. Nucl. Mater.* 166 (1–2) (1989) 105–111.
- [82] J.M. Cleveland, et al., A new, low-temperature synthesis of plutonium and uranium nitrides, *Nucl. Technol.* 25 (3) (1975) 541–545.
- [83] F. Delvoye, J. Larroque, M. Beauvy, Synthesis of (U, Pu) nitrides from the elements, *J. Less-Common Met.* 121 (1985) 656–657.
- [84] J.T. Dunwoody, C.R. Stanek, K.J. McClellan, S.L. Voit, H.M. Volz, H.M. Hickman, Synthesis of uranium nitride and uranium carbide powder by carbothermic reduction, in: Global 2007, Boise, ID, 2007, pp. 586–590.
- [85] W.O. Greenhalgh, Kinetic measurements for the carbothermic synthesis of UN, PuN, and (U, Pu)N, *J. Am. Ceram. Soc.* 56 (11) (1973) 553–557.
- [86] G. Ledergerber, et al., Preparation of uranium nitride in the form of microspheres, *J. Nucl. Mater.* 188 (1992) 28–35.
- [87] J.R. McLaren, P.W.M. Atkinson, The sintering of uranium mononitride, *J. Nucl. Mater.* 17 (2) (1965) 142–148.
- [88] T. Muromura, H. Tagawa, Formation of uranium mononitride by the reaction of uranium dioxide with carbon in ammonia and a mixture of hydrogen and nitrogen—I synthesis of high purity UN, *J. Nucl. Mater.* 71 (1) (1977) 65.
- [89] T. Muromura, H. Tagawa, Mechanism and kinetics for the formation of uranium mononitride by the reaction of uranium dioxide with carbon and nitrogen, *J. Am. Ceram. Soc.* 61 (1–2) (1978) 30–35.
- [90] T. Muromura, H. Tagawa, Formation of uranium mononitride by the reaction of uranium dioxide with carbon in ammonia and a mixture of hydrogen and nitrogen. II. Reaction rates, *J. Nucl. Mater.* 80 (2) (1979) 330–338.
- [91] T. Muromura, H. Tagawa, Synthesis of high purity uranium mononitride from oxide through carbide, *J. Nucl. Sci. Technol.* 17 (1) (1980) 57–66.
- [92] T. Nakagawa, et al., Formation of uranium and cerium nitrides by the reaction of carbides with NH₃ and N₂/H₂ stream, *J. Nucl. Mater.* 247 (1997) 127.
- [93] T. Nakagawa, et al., Preparation of lanthanide nitrides by carbothermic reduction using ammonia, *J. Nucl. Mater.* 247 (1997) 147.
- [94] N. Oi, et al., Preparation of high density uranium nitride and uranium carbonitride fuel pellets, *J. Nucl. Sci. Technol.* 9 (9) (1972) 521–527.
- [95] N.H. Olschewski, et al., Fate of nitrogen upon reprocessing of nitride fuels, *J. Nucl. Mater.* 188 (1992) 244–248.
- [96] T. Muromura, H. Tagawa, Lattice parameter of uranium mononitride, *J. Nucl. Mater.* 79 (1) (1979) 264–266.
- [97] B.J. Jaques, et al., Synthesis of uranium nitride by a mechanically induced gas-solid reaction, *J. Nucl. Mater.* 381 (3) (2008) 309–311.
- [98] B.J. Jaques, et al., Synthesis and sintering of UN-UO₂ fuel composites, *J. Nucl. Mater.* 466 (2015) 745–754.
- [99] L. Braase, W.E. May, Fuel Cycle Research and Development: Advanced Fuels Campaign: FY2015 Accomplishments Reports., Idaho National Laboratory, 2015.

- [100] F. Poineau, et al., X-ray absorption fine structure spectroscopic study of uranium nitrides, *J. Radioanalytical Nucl. Chem.* 292 (3) (2012) 989–994.
- [101] C.M. Silva, R.D. Hunt, L.L. Snead, Synthesis of uranium mononitride microspheres via higher uranium nitrides, in: Abstracts of Papers of the American Chemical Society, 2014, p. 248.
- [102] G.W.C. Silva, et al., Microscopic characterization of uranium nitrides synthesized by oxidative ammonolysis of uranium tetrafluoride, *Chem. Mater.* 20 (9) (2008) 3076–3084.
- [103] C.B. Yeamans, et al., Oxidative ammonolysis of uranium(IV) fluorides to uranium (VI) nitride, *J. Nucl. Mater.* 374 (1–2) (2008) 75–78.
- [104] M. Akabori, A. Itoh, T. Ogawa, Nitridation of uranium and rare-earth metals in liquid Cd, *J. Nucl. Mater.* 248 (1997) 338–342.
- [105] Y. Arai, et al., Synthesis of actinide nitrides in molten cadmium, *Nucl. Technol.* 162 (2) (2008) 244–249.
- [106] M. Katsura, M. Miyake, H. Serizawa, Some problems in nonstoichiometry of alpha-uranium sesquinitride, *J. Alloys Compd.* 193 (1-2) (1993) 101–103.
- [107] J.S. Choi, et al., Laboratory Directed Research and Development (LDRD) on Mono-Uranium Nitride Fuel Development for SSTAR and Space Applications, Lawrence Livermore National Laboratory and University of California, Berkeley, CA, 2006.
- [108] R.D. Hunt, et al., Preparation of spherical, dense uranium fuel kernels with carbon, *Radiochim. Acta* 95 (4) (2007) 225–232.
- [109] T.B. Lindemer, Rate controlling factors in carbothermic synthesis of advanced fuels, *Nucl. Appl. Technol.* 9 (5) (1970). p. 711-&.
- [110] T.B. Lindemer, Kinetics of the $\text{UO}_2\text{-C-N}_2$ reaction at 1700°C, *J. Am. Ceram. Soc.* 55 (12) (1972) 601–605.
- [111] T.B. Lindemer, et al., Quantification of process variables for carbothermic synthesis of $\text{UC}_{1-x}\text{N}_x$ fuel microspheres, *J. Nucl. Mater.* 483 (2017) 176–191.
- [112] T.B. Lindemer, et al., Carbothermic synthesis of 820 μm uranium nitride kernels: literature review, thermodynamics, analysis, and related experiments, *J. Nucl. Mater.* 448 (1–3) (2014) 404–411.
- [113] H. Muta, et al., Thermophysical properties of several nitrides prepared by spark plasma sintering, *J. Nucl. Mater.* 389 (1) (2009) 186–190.
- [114] T. Ogawa, et al., Thermodynamics of carbothermic synthesis of actinide mononitrides, *J. Nucl. Mater.* 247 (1997) 151–157.
- [115] R.D. Shoup, Process variables in preparation of UN microspheres, *J. Am. Ceram. Soc.* 60 (7–8) (1977) 332–335.
- [116] C.M. Silva, et al., Characteristics of uranium carbonitride microparticles synthesized using different reaction conditions, *J. Nucl. Mater.* 454 (1–3) (2014) 405–412.
- [117] R.D. Hunt, et al., Preparation of $\text{UC}_{0.07\text{-}0.10}\text{N}_{0.90\text{-}0.93}$ spheres for TRISO coated fuel particles, *J. Nucl. Mater.* 448 (1–3) (2014) 399–403.
- [118] J.M. Leitnake, T.B. Lindemer, C.M. Fitzpatr, Reaction of UC with nitrogen from 1475°C to 1700°C, *J. Am. Ceram. Soc.* 53 (9) (1970) 479–&.
- [119] T.B. Lindemer, M.D. Allen, J.M. Leitnake, Kinetics of graphite-uranium dioxide reaction from 1400°C to 1756°C, *J. Am. Ceram. Soc.* 52 (5) (1969). p. 233–237.
- [120] T.B. Lindemer, J.M. Leitnake, M.D. Allen, Kinetics of reaction of UC_2 and nitrogen from 1500°C to 1700°C, *J. Am. Ceram. Soc.* 53 (8) (1970) 451–456.
- [121] P. Malkki, et al., Manufacture of fully dense uranium nitride pellets using hydride derived powders with spark plasma sintering, *J. Nucl. Mater.* 452 (1–3) (2014) 548–551.

- [122] Z.H. Qu, et al., Low temperature synthesis of uranium mononitride powder, *J. Nucl. Mater.* 496 (2017) 193–196.
- [123] W.D. Wilkinson, *Uranium Metallurgy: Uranium Process Metallurgy.*, vol. 1, Interscience Publishers, New York, 1962.
- [124] S.P. Willson, R. Margevicius, Fabrication of Transuranic Actinide Ceramic Fuels, *Trans. Am. Nucl. Soc.* 91 (2004) 451–452.
- [125] V.J. Tennery, E.S. Bomar, Sintering of (U, Pu)N as a function of temperature and nitrogen pressure, *Trans. Am. Nucl. Soc.* 19 (1974) 101–102.
- [126] V.J. Tennery, T.G. Godfrey, R.A. Potter, Sintering of UN as a function of temperature and N₂ pressure, *J. Am. Ceram. Soc.* 54 (7) (1971) 327–331.
- [127] A. Parkison, A.T. Nelson, Fabrication of uranium nitride, in: U.S. Provisional Application No. 62/455, 408, 2017.
- [128] K.D. Johnson, D.A. Lopes, Grain growth in uranium nitride prepared by spark plasma sintering, *J. Nucl. Mater.* 503 (2018) 75–80.
- [129] R.B. Matthews, et al., Fabrication and testing of uranium nitride fuel for space power reactors, *J. Nucl. Mater.* 151 (3) (1988) 345.
- [130] H.J. Ryu, et al., Sintering behaviour and microstructures of carbides and nitrides for the inert matrix fuel by spark plasma sintering, *J. Nucl. Mater.* 352 (1–3) (2006) 341–348.
- [131] K.D. Johnson, et al., Spark plasma sintering and porosity studies of uranium nitride, *J. Nucl. Mater.* 473 (2016) 13–17.
- [132] J.W. McMurray, et al., Thermodynamic assessment of the oxygen rich U-Ce-O system, *J. Nucl. Mater.* 467 (2015) 588–600.
- [133] J.H. Yang, et al., UO₂–UN composites with enhanced uranium density and thermal conductivity, *J. Nucl. Mater.* 465 (2015) 509–515.
- [134] S.T. Voit, et al., *The Design and Production of Actinide Nitride Fuels at the Los Alamos National Laboratory for the Advanced Fuel Cycle Initiative Program.*, Los Alamos National Laboratory, 2006.
- [135] Arai, Y., Fabrication of actinide mononitride fuel, in: Proceedings of the Workshop on Manufacturing Technology and Process for Reactor Fuels, Tokai, Japan, 1995.
- [136] Y. Arai, K. Nakajima, Y. Suzuki, Thermal conductivity of actinide mononitride solid solutions, *J. Alloy. Compd.* 271–273 (1998) 602–605.
- [137] T.J. Davies, P.E. Evans, The preparation and examination of mixtures of aluminum nitride (AlN) and uranium mononitride (UN), *J. Nucl. Mater.* 13 (2) (1964) 152–168.
- [138] H. Okamoto, B-U (boron-uranium), in: T.B. Massalski (Ed.), *Binary Alloy Phase Diagrams*, ASM International, 1990, pp. 551–552.
- [139] L. Brewer, et al., A study of the refractory borides, *J. Am. Ceram. Soc.* 34 (6) (1951).
- [140] H.K. Matterson, H. Jones, A study of the tetraborides of uranium and thorium, *Trans. Br. Ceram. Society* 60 (1961) 475–493.
- [141] E. Yamamoto, et al., Electrical and thermal properties of UB₂, *J. Phys. Soc. Jpn.* 68 (3) (1999) 972–975.
- [142] A.B. Tripler, M.J. Snyder, W.H. Duckworth, Further studies of sintered refractory uranium compounds, UC-25 Metallurgy and Ceramics, Battelle Memorial Institute, Columbus, OH, 1959.
- [143] J.L. Andrieux, P. Blum, *Comptes Rendus* 229 (1949) 210.
- [144] A.S. Newton, O. Johnson, Preparation of Compounds of Uranium and Nonmetals, Amos S Newton Johnson Oliver, 1945.

- [145] A.K. Sengupta, R. Agarwal, H.S. Kamath, Carbide fuel, in: R. Konings (Ed.), *Comprehensive Nuclear Materials*, Elsevier, Oxford, 2012, pp. 55–86.
- [146] Y. Suzuki, et al., Fabrication of uranium-plutonium mixed carbide pellets, *J. Nucl. Sci. Technol.* 18 (1981) 61–70.
- [147] C. Ganguly, P.V. Hegde, G.C. Jain, Fabrication of $(\text{Pu}_{0.55}\text{U}_{0.45})\text{C}$ fuel pellets for the second core of the fast breeder test reactor in India, *Nucl. Technol.* 105 (1994) 346–354.
- [148] C. Duguay, G. Pelloquin, Fabrication of mixed uranium–plutonium carbide fuel pellets with a low oxygen content and an open-pore microstructure, *J. Eur. Ceram. Soc.* 35 (2015) 3977–3984.
- [149] J. Crane, F.B. Litton, H.S. Kalish, ARC skull melting and casting of uranium carbide, *Am. Soc. Met. Trans.* 56 (1963).
- [150] D. Salvato, et al., Innovative Preparation route for uranium carbide using citric acid as a carbon source, *Ceram. Int.* 42 (15) (2016).
- [151] D. Salvato, et al., Spark plasma sintering of fine uranium carbide powder, *Ceram. Int.* 43 (1 Part A) (2017).
- [152] D.E. Burkes, et al., A US perspective on fast reactor fuel fabrication technology and experience part I: metal fuels and assembly design, *J. Nucl. Mater.* 389 (3) (2009) 458–469.
- [153] J.H. Kittel, et al., Plutonium and plutonium alloys as nuclear fuel materials, *Nucl. Eng. Des.* 15 (1971) 373–440.
- [154] L.R. Hubbard, et al., U-10Mo baseline fuel fabrication process description, PNNL-26880., Pacific Northwest National Laboratory, Richland, WA, 2017.
- [155] R.J. Jackson, *Vacuum-Induction Melting, Refining, and Casting of Uranium and Its Alloys*, Rockwell International, Golden, CO, 1989.
- [156] C.W. Wilkes, et al., EBR-II fuel slug casting experience, ANL-IFR-73., Argonne National Laboratory, 1987.
- [157] E.A. Nyberg, et al., The Influence of Casting Conditions on the Microstructure of As-Cast U-10Mo Alloys: Characterization of the Casting Process Baseline., Pacific Northwest National Laboratory, Richland, WA, 2013.
- [158] L. Leibowitz, et al., Solidus and liquidus temperatures in the uranium-plutonium-zirconium system, *J. Nucl. Mater.* 154 (1) (1988) 145–153.
- [159] J.J. Frawley, W.F. Moore, A.J. Kiesler, Solidification under the application of pressure greater than atmospheric, *AFS Int. Cast. Met. J.* 5 (31) (1980).
- [160] Analysis of Casting Defects. American Foundrymen's Society, Des Plaines, IL, 1966.
- [161] J.W. Koger, C.E. Holcombe, J.G. Bunker, Coatings on graphite crucibles used in melting uranium, *Thin Solid Films* 39 (1976) 297–303.
- [162] E.L. Swarts, The action of molten uranium on graphite, *Trans. Metall. Soc. AIME* 215 (1959) 553–554.
- [163] V.V. Joshi, et al., Thermomechanical process optimization of U-10 wt% Mo – Part I: High-temperature compressive properties and microstructure, *J. Nucl. Mater.* 465 (2015) 805–813.
- [164] M. Lewis, J.E. Minor, J.T. Stringer, Report to working committee from Hanford, in: RL-REA-1025, Richland, Washington, DC, 1965.
- [165] L.L. Taylor, *N Reactor (U-Metal) Fuel Characteristics for Disposal and Criticality Analysis.*, Idaho National Engineering and Environmental Laboratory, Idaho Falls, ID, 2000.
- [166] K. Laue, Stenger, Helmut, Extrusion., American Society for Metals, 1981.

- [167] M.S. Gerber, Characterization of mixed wastes resulting from fuel fabrication at the Hanford site: use of historical research, *Proc. Waste Manage. Symp.* 1 (1993) 549–554.
- [168] M.B. Waldron, R.C. Burnett, S.F. Pugh, The mechanical properties of U-Mo alloys, *Nucl. Eng. Sci. Congr.* (1955) 630.
- [169] V.V. Joshi, et al., Thermomechanical process optimization of U-10wt% Mo – Part 2: The effect of homogenization on the mechanical properties and microstructure, *J. Nucl. Mater.* 465 (2015) 710–718.
- [170] A.J. Clarke, et al., Microstructural evolution of a uranium-10 wt% molybdenum alloy for nuclear reactor fuels, *J. Nucl. Mater.* 465 (2015) 784–792.
- [171] P. Adamson, S. Orman, G. Picton, The effects of hydrogen on the tensile properties of uranium when tested in different environments, *J. Nucl. Mater.* 33 (1969) 215–224.
- [172] J.E. Antill, K.A. Peakall, Oxidation of uranium alloys in carbon dioxide and air, *J. Less Common Met.* 3 (1961) 239–246.
- [173] I.J. Hastings, Burnup and temperature dependence of swelling in U_3Si , *J. Nucl. Mater.* 41 (2) (1971) 195–202.
- [174] I.J. Hastings, R.L. Stoute, Temperature-dependent swelling in irradiated U_3Si , *J. Nucl. Mater.* 37 (3) (1970) 295–302.
- [175] A.T. Nelson, et al., U_3Si_2 behavior in H_2O environments: Part II, Pressurized water with controlled redox chemistry, *J. Nucl. Mater.* 500 (2018) 81–89.
- [176] E. Sooby Wood, et al., U_3Si_2 behavior in H_2O : Part I, Flowing steam and the effect of hydrogen, *J. Nucl. Mater.* 501 (2018) 404–412.
- [177] E. Sooby Wood, J.T. White, A.T. Nelson, Oxidation behavior of U-Si compounds in air from 25 to 1000 C, *J. Nucl. Mater.* 484 (2017) 245–257.
- [178] V.P. Sinha, et al., Development of powder metallurgy technique for synthesis of U_3Si_2 dispersoid, *J. Nucl. Mater.* 383 (2008) 196–200.
- [179] G.A. Alanko, D.P. Butt, Mechanochemical synthesis of uranium sesquisilicide, *J. Nucl. Mater.* 451 (2014) 243–248.
- [180] K.M. Taylor, C.H. McMurry, Synthesis and Fabrication of Refractory Uranium Compounds, Atomic Energy Commission Office of Technical Information, 1961.
- [181] A.T. Nelson, et al., Overview of properties and performance of uranium-silicide compounds for light water reactor applications, *Trans. Am. Nucl. Soc.* 110 (2014).
- [182] J.M. Harp, P.A. Lessing, R.E. Hoggan, Uranium silicide pellet fabrication by powder metallurgy for accident tolerant fuel evaluation and irradiation, *J. Nucl. Mater.* 466 (2015) 728–738.
- [183] R.E. Hoggan, J.M. Harp, Initial microstructure evaluation of a $U_3Si_2 + W$ fuel pin fabrication via arc melt gravity drop casting, *JOM* 70 (2) (2018).
- [184] J.T. White, et al., Thermophysical properties of U_3Si_2 to 1773K, *J. Nucl. Mater.* 464 (2015) 275–280.
- [185] D.A. Lopes, et al., Spark plasma sintering and microstructural analysis of pure and Mo doped U_3Si_2 pellets, *J. Nucl. Mater.* 496 (2017) 234–247.
- [186] E. Sooby Wood, J.T. White, A.T. Nelson, The effect of aluminum additions on the oxidation resistance of U_3Si_2 , *J. Nucl. Mater.* 489 (2017) 84–90.
- [187] E. Sooby Wood, J.T. White, A.T. Nelson, The Synthesis and Air Oxidation Behavior of U-Si-Al and U-Si-B Compositions, *Transactions of the American Nuclear Society*, 2016. TopFuel2016.
- [188] L.H. Ortega, et al., Development of an accident-tolerant fuel composite from uranium mononitride (UN) and uranium sesquisilicide (U_3Si_2) with increased uranium loading, *J. Nucl. Mater.* 471 (2016) 116–121.

- [189] J.T. White, et al., Fabrication and thermophysical property characterization of UN/U₃Si₂ composite fuel forms, *J. Nucl. Mater.* 495 (2017) 463–474.
- [190] K.D. Johnson, et al., Fabrication and microstructural analysis of UN-U₃Si₂ composites for accident tolerant fuel applications, *J. Nucl. Mater.* 477 (2016) 18–23.
- [191] W. Zhou, W. Zhou, Enhanced thermal conductivity accident tolerant fuels for improved reactor safety – a comprehensive review, *Ann. Nucl. Energy* 119 (2018) 66–86.
- [192] M.J. Kania, H. Nabielek, N. Nickel, Coated particle fuels for high-temperature reactors, *Mater. Sci. Technol.* (2015) 1–183.
- [193] J.S. Thomason, et al., High temperature gas cooled reactor fuels and materials IAEA, Vienna, 2010 IAEA-TECDOC-1645-CD ISBN 978-92-0-153110-2.
- [194] IAEA, Fuel Performance and Fission Product Behavior in Gas Cooled Reactors, IAEA, Vienna, Austria, 1997.
- [195] IAEA, Advances in High Temperature Gas Cooled Reactor Fuel Technology, IAEA, Vienna, Austria, 2012.
- [196] J.A. Phillips, S.G. Nagley, E.L. Shaber, Fabrication of uranium oxycarbide kernels and compacts for HTR fuel, *Nucl. Eng. Des.* 251 (2012).
- [197] E.K. Storms, The Refractory Carbides., Academic Press, 1967.
- [198] E. Sooby, et al., Candidate molten salt investigation for an accelerator driven subcritical core, *J. Nucl. Mater.* 440 (1–3) (2013) 298–303.
- [199] K. Furukawa, et al., in: P. Tsvetkov (Ed.), New Sustainable Secure Nuclear Industry Based on Thorium Molten-Salt Nuclear Energy Synergetics (THORiMS-NES), Nuclear Power-Deployment, Operation and Sustainability, 2011.
- [200] C.D. Bowman, Once-through thermal-spectrum accelerator-driven system for light water reactor waste destruction without reprocessing, *Nucl. Appl. Technol.* 132 (2000).
- [201] V. Berthou, I. Slessarev, M. Salvatores, Proposal of a molten-salt system for long-term energy production, in: Advanced Reactors with Innovative Fuels, Workshop on Advanced Reactors with Innovative Fuels, Chester, UK, 2001.
- [202] L. Mathieu, et al., *Nucl. Sci. Eng.* 161 (2009) 78–99.
- [203] Lecarpentier, D., et al., AMSTER: a molten-salt reactor concept generation its own 233U and incinerating transuranium elements, in: Workshop on Advanced Reactors With Innovative Fuels, Chester, UK, 2001.
- [204] M. Hron, Project SPHINX spent hot fuel incinerator by neutron flux (the development of a new reactor concept with liquid fuel based on molten fluorides), *Prog. Nucl. Energy* 47 (1–4) (2005) 347–353.
- [205] K. Furukawa, Y. Kato, S.E. Chingrinov, Plutonium (TRU) transmutation and 233U production by single-fluid type accelerator molten-salt breeder (AMSB), in: Conf. Accel.-Driven Transm. Tech. Appl., Las Vegas, NV, 1994.
- [206] P. McIntyre, et al., Accelerator-driven subcritical fission in molten salt core: closing the nuclear fuel cycle for green nuclear energy, *AIP Conf. Proc.* 1525 (1) (2013) 636–642.
- [207] F. Lantelme, H. Groult (Eds.), Molten Salts Chemistry From Lab to Applications, Elsevier, 2013.
- [208] E.S. Sooby, Experimental and computational investigations of candidate fuel salt melt properties and corrosion and irradiation damage in nickel for a molten chloride fission system, Physics and Astronomy, Texas A&M University, College Station, TX, 2014.

- [209] R.W. Benedict, H.F. McFarlane, *Radwaste Manage.* 5 (5) (1998) 23–28.
- [210] B.R. Westphal, K.J. Baeman, S.D. Herrmann, Top ten reasons for DEOX as a front end to pyroprocessing, Winter Meeting of the American Nuclear Society, American Nuclear Society, 2007.
- [211] Westphal, B.R., et al., Evaluation of analytical results following laboratory scale feasibility study of voloxidation, in: International Pyroprocessing Research Conference, Fontana, WI, 2012.
- [212] M.F. Simpson, R.W. Benedict, 2007. Strategic minimization of high level waste from pyroprocessing of spent nuclear fuel, in: Global 2007, Boise, ID.
- [213] S.D. Herrmann, et al., *Sep. Sci. Technol.* 41 (10) (2006) 1965–1983.

Christine Guéneau¹, Jean-Christophe Dumas² and Markus H.A. Piro³

¹Commissariat à l'Energie Atomique et aux Energies Alternatives, Université Paris-Saclay, Gif-sur-Yvette Cedex, France, ²Commissariat à l'Energie Atomique et aux Energies Alternatives, CEA Cadarache, Saint-Paul-lez-Durance Cedex, France, ³Ontario Tech University, Oshawa, ON, Canada

11.1 Introduction

Within the core of a nuclear reactor, fuel comprises of fissile materials contained in a matrix (oxide, metallic, carbide, or nitride) where fission reactions occur, involving heavy fissile atoms of uranium and plutonium. Fuel provides the heat source that ultimately will be transferred to the coolant to generate electricity.

In most cases, the “fuel element” takes the form of a stack of cylindrical fuel pellets encapsulated in a cladding tube, which constitutes the first containment barrier toward the release of radioactive species. Design and dimensioning studies of fuel elements have the objective of guaranteeing the resistance of that first barrier in the various operating situations. In the event of an accident situation, fuels are the main potential source term for radioactive release to the environment, and this aspect has to be taken into account.

During irradiation, the fuel element is subjected to extreme conditions of radiation, temperature and changes in its chemical composition due to the formation of fission products (FPs) and activation products.

Understanding and modeling all the phenomena occurring in the fuel involve many areas of physics and chemistry:

- *Neutronics* to specify the fission and transmutation nuclear reactions.
- *Physics of materials* to evaluate the damage caused to the crystal structure by neutrons and the dissipation of fission energy.
- *Heat transfer* to achieve an accurate evaluation of heat removal from the fissile material to the coolant fluid and to compute the evolution of temperatures at every point in the fuel.
- *Mechanics* allows strains and stresses to be computed in the pellet and in the cladding, along with the risks of cladding failure.
- *Thermodynamics* makes it possible to evaluate the changes in the chemical composition of the fuel matrix and of the phases to be formed from the FPs.
- *Solid-state chemistry* considers the kinetics according to which the system, as a rule out of equilibrium condition, evolves in nominal operating conditions, and during the various transients that may arise.

Fuel performance codes (FPCs) are computational tools that are developed to simulate the behavior of fuel pins under normal and off-normal conditions, in which all the abovementioned scientific domains are involved and coupled. These codes are used both for the design of advanced new fuel materials and for the understanding and prediction of the fuel behavior.

The aim of the present chapter is to give a short general introduction on the behavior of nuclear fuels under irradiation. A special emphasis will be put on the chemistry of oxide fuels and very briefly on other types of fuels.

This chapter is divided into three parts:

- a first section presenting the main phenomena occurring in the fuel during irradiation: heat transfer and temperature effects, irradiation effects, microstructure evolution, and behavior of fission gases;
- a second section detailing the chemistry of oxide fuels and the effect of FPs on fuel chemistry; and
- a third section describing shortly the chemistry of other types of fuels (metallic, carbide, and nitride fuels).

11.2 General description of fuel behavior

An exhaustive description of all the different kinds of fuels used in all reactor types cannot be addressed in the present chapter. Only the behavior of the most commonly used oxide fuels will be described. The chemistry of a few other types of fuels (metallic, carbide, and nitride) will be shortly presented.

11.2.1 Thermal and fast reactor fuels

Different kinds of materials are used for the fuel matrix depending on the type of reactor, which may be under a thermal or a fast neutron spectrum: oxide, metal, carbide, or nitride.

In the current generation of thermal spectrum nuclear reactors, that is to say pressurized water reactors (PWRs) and boiling water reactors, uranium dioxide (UO_2) is predominantly used. Also, mixed oxide of uranium and plutonium (U,Pu) O_2 , called MOX, is also used in PWRs.

In fast spectrum reactors, normally cooled by a liquid, various types of fuel materials have already been irradiated in fast breeder reactors (FBRs) (Table 11.1). The key properties for the choice of the fuel are as follows:

- Low neutron capture cross section of the nonfissile elements.
- High density of heavy atoms per unit volume.
- No chemical reaction with the environment (cladding and coolant).
- High thermal conductivity and high melting temperature that define the margin to melting.
- High mechanical stability to maintain the fuel assembly geometry; not only the intrinsic thermomechanical properties of the fuel and cladding materials have to be considered.

Table 11.1 Main properties of the current fuel materials considered for fast breeder reactor.

	Metal (U,Pu,Zr)	Oxide (U,Pu)O ₂	Carbide (U,Pu)C	Nitride (U,Pu)N
Density in fissile atoms (g/cm ³)	14.1	9.7	12.9	13.5
Melting temperature (solidus) (K)	1340	3000	2580	2990
Thermal conductivity (W/m K)	17.5	2.4	19.5	20
Thermal expansion (10^{-6}K^{-1})	17	10	11	9
Swelling under irradiation (%/10 GWj/t)	2	0.7	1.8	1.4
Countries	France, United States, Canada, Japan, United Kingdom, Russia, Germany	India, Russia	Russia (<i>only with enriched U</i>)	United States, United Kingdom

Source: From M. Pelletier, Quel Combustible Pour les RNR-Na?, Clefs du CEA, 2012, pp. 32–37 [1].

Under irradiation, fission gas bubbles are produced within the fuel matrix that leads to its swelling.

- High thermal stability (no phase transition).

As reported in **Table 11.1**, the fuels have quite different physical properties. Oxide fuels have a lower density in fissile atoms but the lowest swelling rate under irradiation. Metal fuels have the highest thermal expansion and swelling rate, which is not favorable from a thermomechanical perspective despite the metal fuel operates at low temperatures. The low melting point of metal fuels is compensated by its high thermal conductivity. On the contrary, the relatively low thermal conductivity of oxides is compensated by its high melting temperature. Both combinations are favorable and thus both types of fuels can be used in nuclear reactors. Carbide and nitride fuels have a quite high melting temperature, a high thermal conductivity, a lower thermal expansion but a higher swelling rate under irradiation compared to oxide fuels.

As an example, the standard geometry of a fuel pin in the Phénix FBR is shown in **Fig. 11.1**. It is a long cylinder (2–3 m long, 5–10 mm diameter) made of a steel cladding tube (~0.4–0.6 mm thick) closed at both ends by welded plugs, preventing direct contact between the radioactive material and the sodium coolant. The cladding serves as the first barrier and is designed to maintain its integrity and tightness in nominal and off-normal conditions.

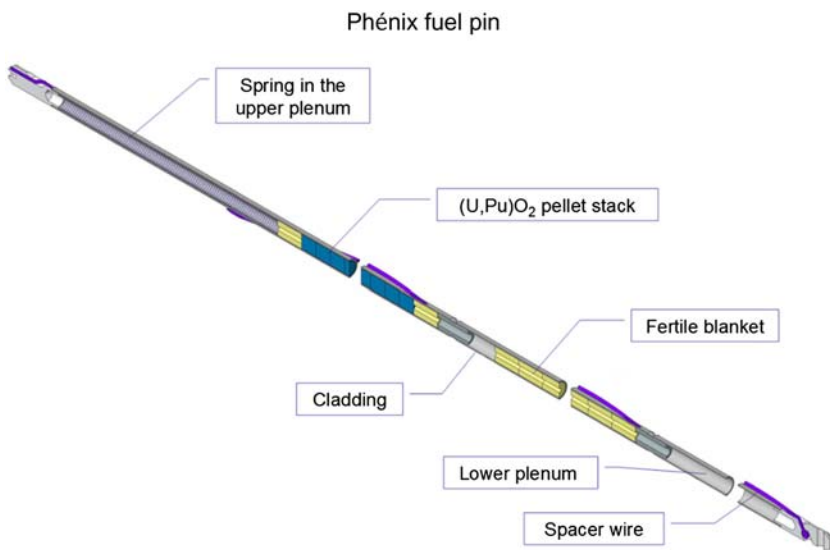


Figure 11.1 Standard Phénix fuel pin.

Source: From M. Pelletier, Quel Combustible Pour les RNR-Na?, Clefs du CEA, 2012, pp. 32–37.

11.2.2 Radiation damage—irradiation effects

Nuclear fuels are exposed to high levels of radiation fluxes and thus undergo radiation damages. The neutron flux is much higher in fast neutron reactors than in thermal neutron reactors: for example, the order of magnitude of the neutron flux in a light water reactor (LWR) is $10^{13}\text{--}10^{14}\text{ n}/(\text{cm}^2\text{ s})$ whereas it can reach up to $6.10^{15}\text{ n}/(\text{cm}^2\text{ s})$ in the core center of a fast reactor (FR) core.

During irradiation, the fuels are subjected to several types of energetic particles with different masses and energies (Table 11.2). In general, particles or ions passing through matter lose energy via two processes: direct collisions with the atoms (elastic collisions) or dissipating their energy to electrons (inelastic collisions).

In Table 11.2, representative values for the different particles involved during the irradiation process are reported: energy and distance, as well as the damage quantification (dpa = displacement per atom, giving how many times each atom has been displaced from its own site).

There are long-range radiation damage effects (as in structural materials) by neutrons and photons γ but also short-range energetic particles (specific to nuclear fuel), such as irradiation by α (=He nucleus) decay and also by fission fragments, which play a predominant role.

In thermal reactors, thermal neutrons (low energy) do not produce any direct displacements whereas fast neutrons will transmit part of their energy to displacement collisions (cascades) of atoms. Also, α decay of 100 keV produces displacement cascades.

Table 11.2 Different types of irradiation damages in nuclear fuels.

Particle	Energy	Distance	Damage
Neutrons	0.025 eV to ~ 2 MeV: • Fast: $E > 10$ keV • Epithermal: $1 \text{ eV} < E < 10 \text{ keV}$ • Thermal: $E < 1 \text{ eV}$	$\geq 1 \text{ cm}$	Elastic collision with nucleus of lattice atoms: • Conservation of energy and momentum on primary knock atom (pka) → may induce displacement cascades with other atoms
Photons γ	$\sim 10 \text{ keV}$ to $\sim 2 \text{ MeV}$	Several 10 cm	Low interaction cross section (ionization)
α Decay	$\sim 5 \text{ MeV}$	$\sim 15\text{--}20 \mu\text{m}$	200 dpa (electronic interaction)
α Decay	Recoil energy of new atom: $\sim 100 \text{ keV}$ $\rightarrow 200 \text{ MeV}$	$\sim 20 \text{ nm}$	1500 dpa (elastic collision cascade)
Fission fragments	• Light FP: 95 MeV • Heavy FP: 65 MeV	6–8 μm	pka → displacement cascades: several 10^4 atoms may be displaced: • Large part recombine • Remaining part → point defects

The slowing down of fission fragments will lead to the production of a large number of point defects in the material. Those defects (vacancies and interstitials atoms) migrate and then either annihilate or cluster together or disappear on sinks (grain boundaries, dislocations, etc.).

In service, nuclear fuels are submitted to intense irradiation fluxes, whose nature, spectra, and intensity can vary over large ranges. In addition to the creation of fission fragments (see Fig. 11.2), the interaction of these energetic particles with the atoms of the solid displaces those atoms from their stable positions in the crystal; thus, point defects and extended defects are created in the lattice. This damage process induces changes in the microstructure of the fuel and in its different physical properties, which have various effects on the in-reactor behavior of the fuel material.

An important consequence of irradiation and thus of the formation of FPs in the fuel matrix is that the chemical composition of the fuel changes with time.

The analysis of the irradiated fuel composition with time requires information on the quantities of FPs that are produced. Fission reactions produce two fission fragments (FPs) plus two to three neutrons. The probability per fission of directly forming

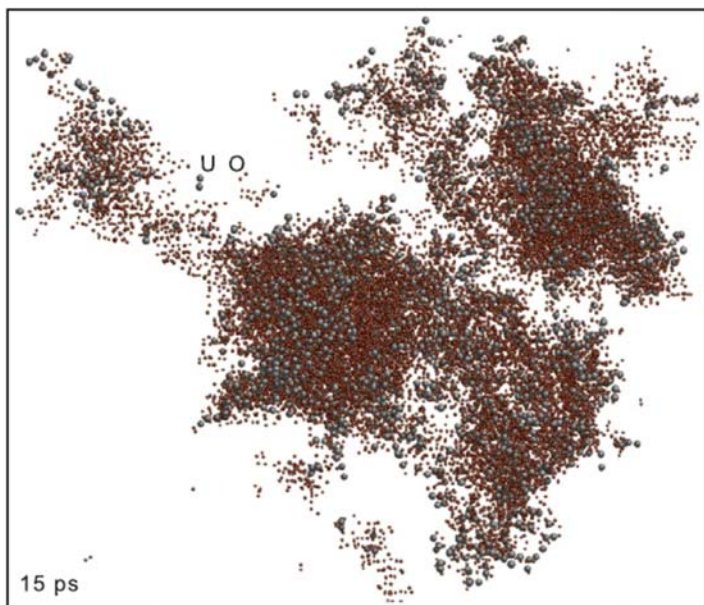


Figure 11.2 Atoms displaced in UO₂ resulting from a displacement cascades initiated at 100 keV at 700K.

Source: G. Martin, P. Garcia, L. Van Brutzel, B. Dorado and S. Maillard, Effect of the cascade energy on defect production in uranium dioxide, *Nucl. Instrum. Methods Phys. Res., B* **269**, 2011, 1727–1730 [2].

a particular nuclide is defined as the *independent fission yield* of the nuclide. Because the predominant mode of FP decay is β and γ emission, the decay process *does not change the mass number* of the species. Thus, fission can be considered to produce decay chains containing many nuclides of the same mass number [3]. Then, one can deduce from neutronic calculations the cumulative yield of the last member of a chain (i.e., the stable member) as the sum of the independent yields of all nuclides of the chain, assimilated as the whole quantity of a given element of the periodic table. It is thus possible to evaluate the chemical composition of the corresponding multi-component system versus temperature from those given contents.

Fig. 11.3 shows the relative yield rate for the FPs depending on the mass number. As it can be seen, two groups of FPs are produced: the light ones and the heavy ones. One can also point out that both figures give yield curves for both ²³⁵U and ²³⁹Pu under both thermal and fast spectra.

Otherwise, neutronic calculation modules directly coupled to FPCs allow to determine directly the quantity of a given isotope, and thus of an element versus time (or burnup) by taking into account all the decay processes [5]. It gives, at each irradiation step, the actinides, FP and oxygen/nitrogen/carbon or metal concentrations in the fuel [6,7]. As mentioned in Section 11.3.2.1, the FPs that can be grouped in different classes according to the phases they form in the fuel:

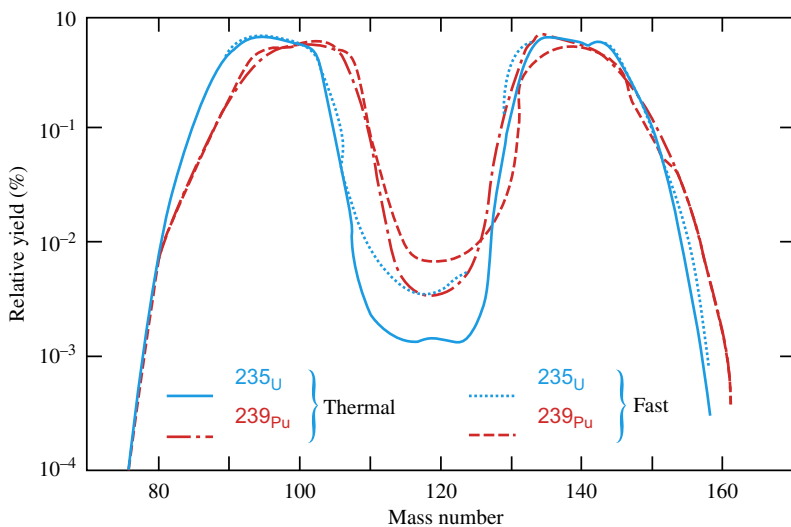


Figure 11.3 Relative yield of isotopes of FP, for ^{235}U and ^{239}Pu fissions, in thermal and fast flux. FP, Fission product.

Source: From J.H. Davies, F.T. Ewart, The chemical effects of composition changes in irradiated oxide fuel materials, *J. Nucl. Mater.* 41 (1971) 143–155 [4].

- He, Xe, and Kr for rare gases: insoluble elements resulting from fission events or α decay of actinides,
- Cs, Te, I, Rb, and Se: volatile FPs,
- Mo, Zr, Ba, Rb, etc. forming oxide secondary precipitates,
- Mo, Pd, Ru, Rh, Tc, etc. forming metallic secondary precipitates, and
- Nd, La, Gd, Ce, Eu, Sm, etc.: FPs dissolved into the fuel matrix.

The total amount of FP is often characterized by the burnup, which measures the part of the fuel that is consumed to produce energy. It is representative of the residence time of the fuel in the reactor. It can be expressed in two different ways:

- the percentage of atoms that have been subjected to fission reactions $\Rightarrow \%$ FIMA: % of fissions per initial metal atom and
- the released energy in GWD/t (GigaWatt day per ton of fuel or of heavy metal).

In the first case, based on the fact that two FPs are formed when one heavy atom is fissioned, we can quickly have an estimation of the quantity of FPs created since the beginning of the irradiation. In the second case, it gives an estimation of the thermal energy quantity obtained in reactor between the loading and the discharging of the fuel. A burnup of 1 at.% FIMA corresponds to approximately 10 GWD/t.

The formation of fission gas and especially gas bubbles induces also considerable changes in the microstructure and morphology of ceramic fuel, which are frequently observed during postirradiation examination (PIE) aiming at studying fission gas behavior (see Fig. 11.4). The formation of gas bubbles, as well as solid

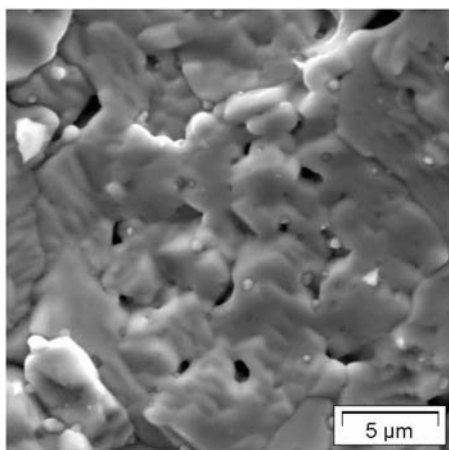


Figure 11.4 SEM fractograph of a 73 GWd/tU UO₂ sample in the center of the pellet.
Source: J. Noirot, I. Zacharie-Aubrun and T. Blay, Focused ion beam-scanning electron microscope examination of high burn-up UO₂ in the center of a pellet, *Nucl. Eng. Technol.* **50**, 2018, 259–267 [8].

second phases as the metallic precipitates, depends on irradiation conditions essentially temperature and burnup. Observation of these aggregates depends on the means of investigation being used. Some illustrations of those phenomena are proposed hereafter for the oxide fuels.

Irradiation damage (both the creation of defects and the change in the chemical composition) of the fuel has influence on the physicochemical properties of the fuel, which varies with time and/or burnup.

11.2.2.1 Temperature distribution

The main function of a fuel element is to produce heat by fission reactions and to transfer that heat to the coolant. The consequence is that there is a very large temperature gradient between the center of the fuel pellet and the periphery, close to the cladding that is in contact with the coolant. This induces a considerably large temperature range within the fuel element.

The temperature distribution in a fuel rod is of primary importance because most phenomena occurring in fuels are thermally activated and often exponentially dependent on temperature. In order to predict fuel behavior, it is necessary to have a very good knowledge of the temperature distribution in the fuel elements during the entire time in-reactor, which is a challenging task due to the numerous complex coupled phenomena occurring in the fuel.

The key quantity is the power density P_v of the fuel (i.e., the produced energy per unit volume). As most of the fuels are cylindrical, one often uses the linear power P_l (or linear rating or linear heat generating rate), which is the energy

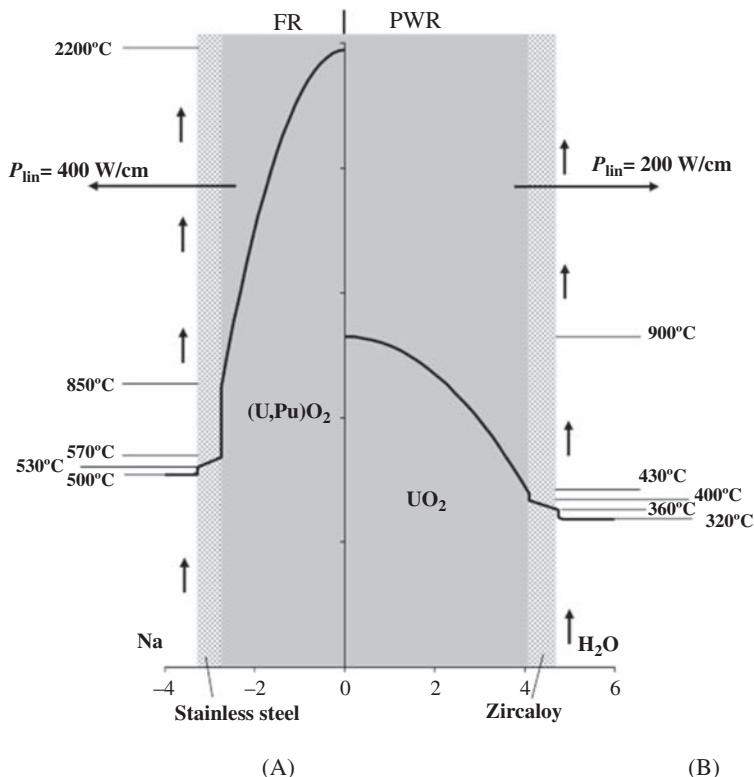


Figure 11.5 Example of radial temperature profiles in a fuel rod in fast reactor (A) and in pressurized water reactor (B).

Source: Courtesy CEA.

produced per unit length of fuel rod. This linear rating is a function of time and axial position in the rod.

The commercial oxide fuels have a poor thermal conductivity, inducing rather high temperature even at moderate power ratings as in LWRs where the temperature in the center of the fuel pellet reaches typically around 1100°C. In FRs, which use higher coolant temperatures and higher linear rating, fuel temperatures can reach much higher values (up to 2200°C). These high temperatures and steep temperature gradients induce in fuel pellets a lot of modifications of the microstructure and chemical composition of the fuel occurring during the initial irradiation period, commonly called “beginning of life.”

Fig. 11.5 shows typical radial temperature profiles in FBRs and in PWR, respectively. It has to be kept in mind that in PWRs, typical fuel surface temperatures T_s are about 500°C for a centerline temperature T_c of about 1000°C, while in FBRs, T_s is in the range 800°C–1000°C and T_c is about 2000°C, up to 2200°C at the beginning of life.

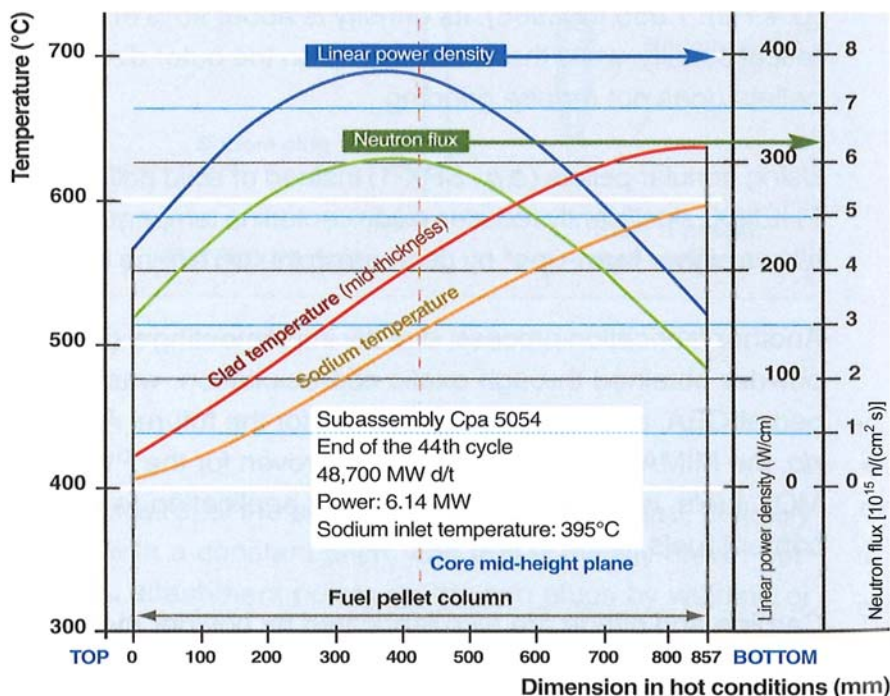


Figure 11.6 Schematic example of axial temperature profiles in fast reactor.

Source: M. Pelletier, SFR Fuel in Sodium Cooled Nuclear Reactors, DEN Monographs, CEA Saclay et Groupe Moniteur, Paris, 2016 [9].

Fig. 11.6 shows a schematic view of the axial evolution of the cladding and fuel temperatures in a FR rod. Coolant temperature continuously increases from the bottom to the top of the fuel column. A maximum temperature [or peak power node (PPN)] is found near the middle of the pin. At the top and bottom of the fuel column, the linear power is about 60% of its maximum value. The clad temperature is tightly linked to coolant temperature whereas the fuel temperature (not represented here for the clarity of the figure) is linked to linear power with a maximum located between the PPN—close to the core mid-height plane—and the top of the fuel.

11.2.3 Microstructural evolution

In FR fuel, the very high-temperature level and steep temperature gradients induce spectacular changes in the microstructure, which occurs in a short time, during the first hours and days at full power. Fig. 11.7 shows an example of this restructuring effect. In fact, the initial porosity resulting from the fuel pellet fabrication is homogeneously distributed in the fuel pellet volume as small pores. Due to the very high thermal level that takes place in FBR oxide fuels, these pores are redistributed

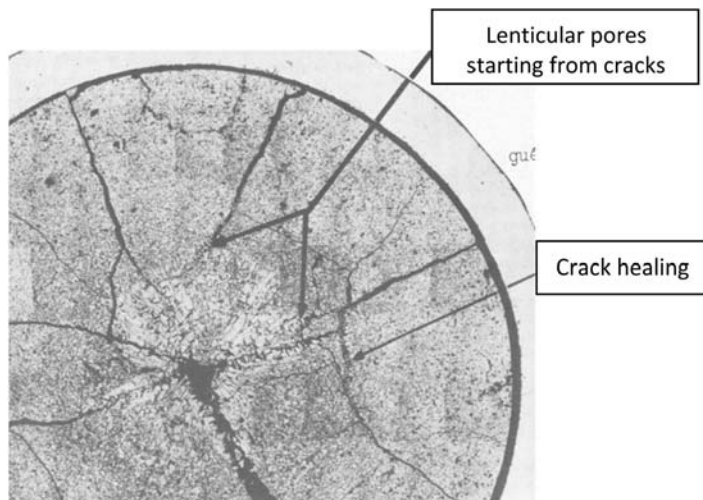


Figure 11.7 Micrograph of a fast reactor MOX pellet irradiated at start-up of RAPSODIE during 4 hours at 380 W/cm.

Source: Y. Guérin, Chapter 2.21 fuel performance of fast spectrum oxide fuel, In: R.J.M. Konings, (Ed), *Comprehensive Nuclear Materials*, 2012, Elsevier, 548–572 [10].

along the radius through an evaporation–condensation mechanism between the hot side and the cold side of each pore. This phenomenon is related to the fact that the vapor pressure of the fuel components in equilibrium with the oxide is higher on the hot side of the lenticular pore than on its cold side. This difference in vapor pressures induces an evaporation–condensation mechanism: matter evaporating from the hot face and condensing on the cold face travels down the thermal gradient, inducing an inverse displacement of the lenticular pores that climb the thermal gradient upwards the center of the pellet.

In PWR fuels, the thermal level is much lower, and microstructural changes are less drastic than in FBR fuels. Nevertheless, one can notice the formation of fission gas bubbles for high burnups and, in the specific case of MOX fuel (low Pu content compared to FBR fuels) for PWR. The initial heterogeneous distribution of plutonium in the fresh fuel pellet has special consequences on the in-reactor behavior as Pu-rich agglomerates locally reach burnup much higher than mean pellet burnup (dark spots on Fig. 11.8). Only in the central part of the pellet are the agglomerates no longer visible without strain-etching (see Fig. 11.9).

11.2.4 Fuel swelling

Another important effect of radiation damage is the swelling of the fuel material. This is due to the increase of the number of atoms inside the fuel with burnup, which leads to the increase of the fuel volume. Indeed, as two FP atoms are created

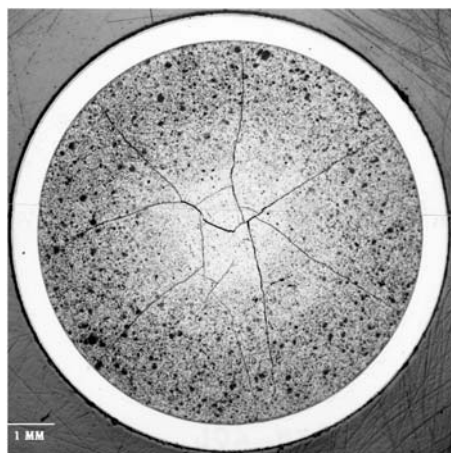


Figure 11.8 Metallograph on a cross section of PWR MOX pellet at 50 GWd/t.

Source: Y. Guérin, J. Noirot, D. Lespiaux, C. Struzik, P. Garcia, P. Blanpain, et al., Microstructure evolution and in-reactor behaviour of MOX fuel, in: ANS International Topical Meeting on LWR Fuel Performance, Park City, UT, 2000 [11]. PWR, Pressurized water reactor.

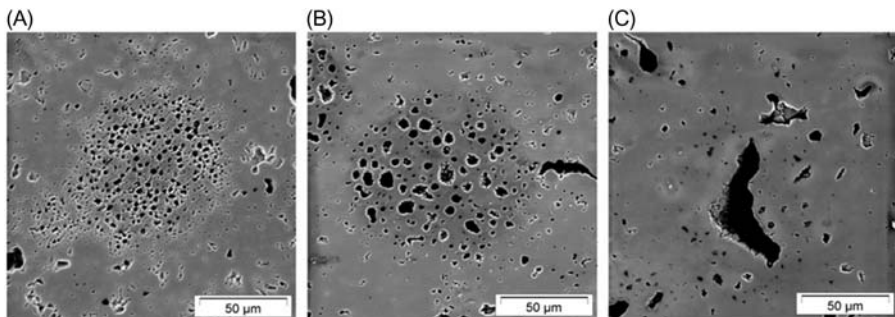


Figure 11.9 Radial evolution of bubbles in the Pu agglomerate HBS for a 45 GWd/t MOX (3) sample [(A) 0.9 R, (B) 0.5 R, and (C) 0 R] (SEM images).

Source: J. Noirot, L. Desgranges and J. Lamontagne, Detailed characterisations of high burn-up structures in oxide fuels, *J. Nucl. Mater.* **372**, 2008, 318–339 [12]. HBS, high burnup structure.

when one heavy atom is consumed, the total number of atoms is increased by one for one heavy atom fissioned. The two created atoms occupy a larger volume than the initial actinoid (U,Pu) atom. The total swelling has two contributions:

- the swelling due to solid FPs and
- the swelling due to rare gas species formation (e.g., Kr, Xe).

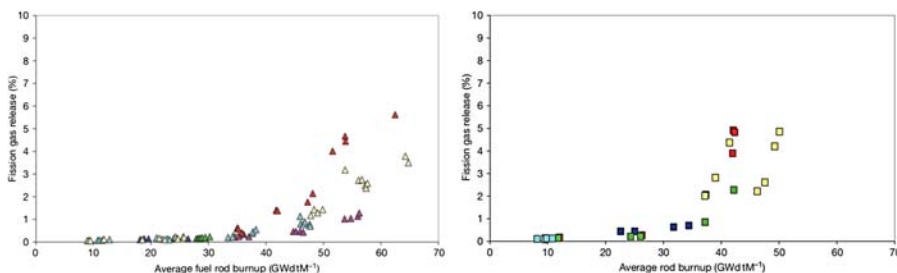


Figure 11.10 Gas release in irradiated UO₂ (left) and MOX (right) PWR fuel rods.

Source: D.D. Baron and L. Hallstadius, Chapter 2.19 fuel performance of light water reactors (uranium oxide and MOX), In: R.J.M. Konings, (Ed), *Comprehensive Nuclear Materials* 2012, Elsevier, 481–514 [13]. PWR, Pressurized water reactor.

In the first case, the total solid FP swelling is the contribution of three kinds of FPs that are as follows:

- The volatile FP created in hot zones that migrate and condensate in colder zones: ~3/4 of actinide volume (per atom).
- The metallic FP: ~1/3 of the volume of one actinoid atom.
- The oxide precipitates: ~1.7 of the volume of one actinoid atom (per atom).

Hydrostatic density measurements performed on specimens from irradiated fuels give access to the global change of volume, where a linear evolution is of 0.6%/at. % is deduced. Anyway, the contribution coming from the rare gas swelling is lower than the solid FP ones.

During operation the gaseous FPs are released with time and burnup. For illustration the evolution of the fission gas release versus burnup is shown for MOX fuel rods in PWRs in Fig. 11.10 and for mixed oxide FR Phénix fuel in Fig. 11.11.

In PWR fuels the gaseous FPs can accumulate at grain boundaries or in bubbles that have formed, grown, and moved both by thermal diffusion and nonthermal processes. In the case of oxide PWR fuel, the contribution of gaseous species to total swelling is significantly higher than in FBR oxide fuel.

Other kinds of ceramics, carbide, and nitride fuels having a higher thermal conductivity than oxide fuels and a high melting temperature have a lower nominal operating temperature as well as a much higher melting margin compared to oxide fuels. Nevertheless, those “cold” fuels have a swelling factor two to three times higher than oxides. The high swelling rate, combined with a quite lower viscoplasticity (by a factor of 10), leads to a strong mechanical interaction between the fuel and the clad, when the fuel/pellet gap is closed. In addition, comparatively to the past feedback on oxide fuels, there are still unanswered questions about the real potential of carbide and further nitride fuels, as future SFR fuels.

Metallic fuels (U,Pu,Zr) have also some disadvantages. The main one is the risk of the potential formation of a eutectic liquid phase from the chemical interaction between the fuel and the cladding steel material, which penalizes the maximum

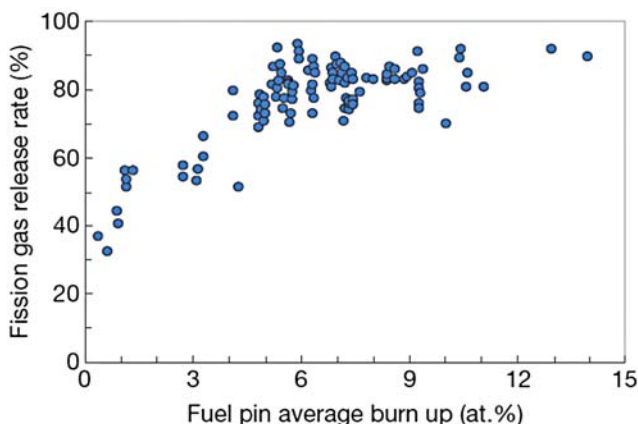


Figure 11.11 Evolution with burnup of global fission gas release in Phénix pins.

Source: Y. Guérin, Chapter 2.21 fuel performance of fast spectrum oxide fuel, In: R.J.M. Konings, (Ed), *Comprehensive Nuclear Materials*, 2012, Elsevier, 548–572 [10].

temperature that can reach the coolant in nominal operating conditions (of about -40°C compared to ceramic fuels).

The second one is linked to its quite high swelling behavior during irradiation. Indeed, in addition to the usual swelling mechanisms by solid FPs depending almost entirely on burnup and to the gaseous swelling due to fission gas bubbles precipitation and growth (thermally activated), a contribution to cavitation swelling takes place for temperatures between 400°C and 600°C . This phenomenon is characterized by the presence of cavities of different shapes with a very troubled microstructure (see Fig. 11.12). We observe a sharp increase of the axial length that can reach 2% to 6%–8% (for U–Zr alloys) before 2 at.% which becomes later much more moderated with the increase in burnup, mainly due to solid FPs swelling (see Fig. 11.13). This aspect led to recommend an initial porosity of 25% (of the theoretical density) for the as-fabricated metallic fuel pellets in conjunction with a high volume plenum, which provides accommodation for the fission gases and thus limits the clad constraint.

The final issue concerns the overall fuel cycle (plutonium recycling and minor actinides, wastes management), from which the industrial-scale demonstration is still to be done.

11.3 Oxide fuel chemistry

In thermal and FRs, actinide oxides are the most commonly used fuels in nuclear power reactors. To understand the fuel behavior at high temperatures, fundamental data have to be considered. First, the U–O and U–Pu–O phase diagrams and the related thermodynamic properties of UO_2 and $(\text{U},\text{Pu})\text{O}_2$ oxides will be presented. Then, the effect of the FPs in these fuels will be discussed.

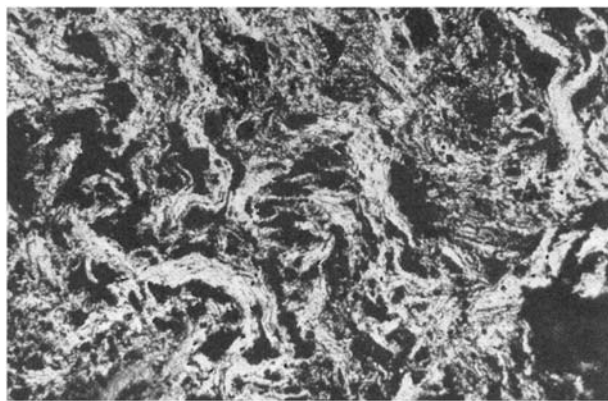


Figure 11.12 Cavitation in uranium metallic fuel at 1.25 GWj/t.

Source: G. Hofman and L.C. Walters, Metallic fast reactor fuels, In: R.W. Cahn, P. Haasen and E.J. Kramer, (Eds.), *Materials Science and Technology* vol. 10A, 1994, VCH Publishers Inc., New York, 1–43, 1994 [14].

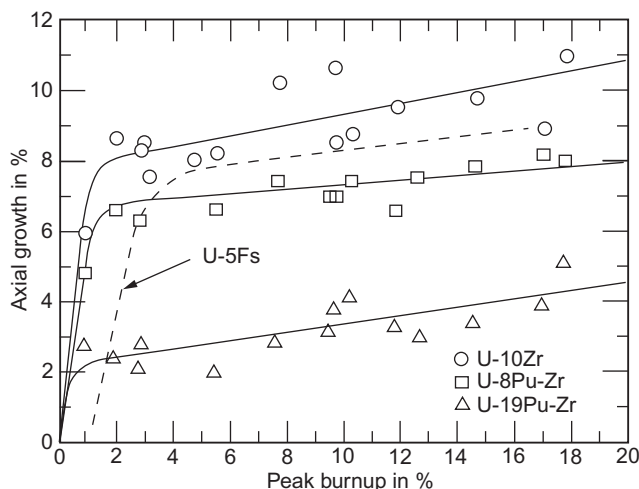


Figure 11.13 Axial swelling versus burnup for different fuel alloys irradiated in EBR II.

Source: R. Kennedy, (2019). *Nuclear reactors physics, fuels, and systems*. Frédéric Joliot/Otto Hahn Summer School, Karlsruhe [15].

11.3.1 UO_2 and $(U,Pu)O_2$ oxides

11.3.1.1 $U-O$ and $U-Pu-O$ phase diagrams

The oxide fuels are the most commonly used fuels in the world in the following forms:

- UO_2 fuel, uranium dioxide, in LWRs and CANDUs and

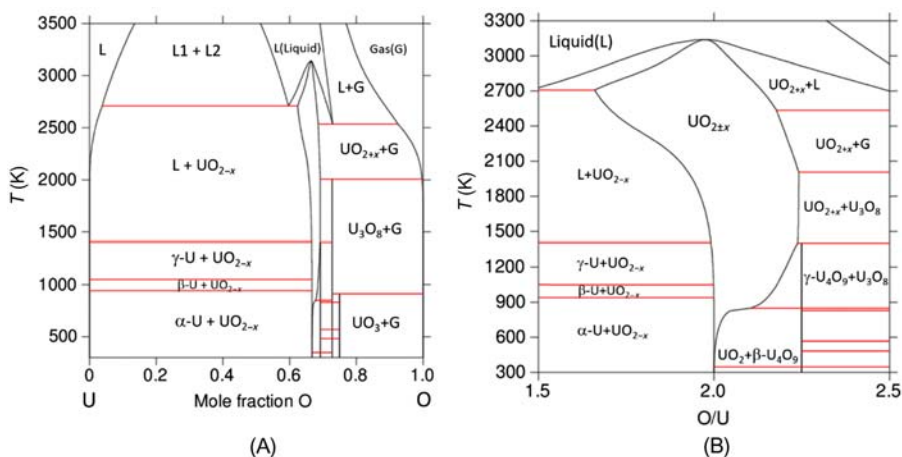


Figure 11.14 (A) uranium–oxygen phase diagram and (B) zoom in the range $1.5 < \text{U}/\text{O} < 2.5$.

Source: C. Guéneau, N. Dupin, B. Sundman, C. Martial, J.-C. Dumas, S. Gossé, et al., Thermodynamic modelling of advanced oxide and carbide nuclear fuels: description of the U–Pu–O–C systems, *J. Nucl. Mater.* **419** (1–3), 2011, 145–167 [16].

- (U,Pu)O₂ fuel, mixed oxide of uranium and plutonium (called MOX), containing 3–10 wt.% Pu in LWRs and 20–30 wt.% Pu in FBRs.

To understand the physical–chemical behavior of oxide fuels, the uranium–oxygen phase diagram has to be considered (Fig. 11.14A). Pure uranium exists in three different allotropic forms from low to high temperature: α -U (orthorhombic), β -U (tetragonal), and γ -U (bcc). Uranium can be oxidized in the form of various compounds ranging from UO₂ to U₄O₉, U₃O₈, and UO₃. The stability of these numerous oxides can be explained by the existence of many oxidation states for uranium: U³⁺, U⁴⁺, U⁵⁺, and U⁶⁺.

Uranium dioxide is an iono-covalent compound. It is the most stable oxide in the uranium–oxygen system. It has a very high melting point of 3123 K [17]. The compound has the peculiarity to exhibit a wide oxygen composition range in both hypostoichiometric (from $\sim \text{O}/\text{U} = 1.6$ at 2720 K) and hyperstoichiometric regions (to ~ 2.25 at 2050 K).

Uranium dioxide has a face-centered cubic (fcc) crystalline structure (also called fluorite) (Fig. 11.15). Different kinds of defects can exist in the crystal: oxygen vacancies for $\text{O}/\text{U} < 2$, oxygen interstitials and aggregates for $\text{O}/\text{U} > 2$ that can accommodate these changes in the oxygen stoichiometry. Simultaneously to this variation in the oxygen composition, a change in the oxidation state of uranium occurs: uranium reduction from U⁴⁺ to U³⁺ for $\text{O}/\text{U} < 2$ and uranium oxidation from U⁴⁺ to U⁵⁺ for $\text{O}/\text{U} > 2$.

This peculiarity of uranium dioxide has two important consequences:

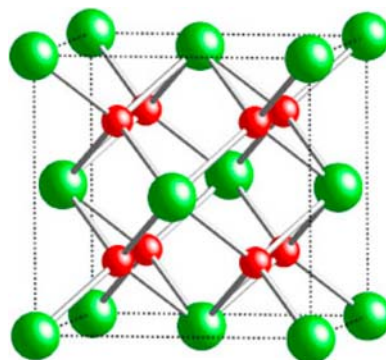


Figure 11.15 UO_2 fluorite crystalline structure.

- A large degree of freedom exists for the choice of the initial oxygen composition of nuclear fuel.
- The oxygen composition (or stoichiometry) of oxide fuel is affected by the environment (more or less reducing or oxidizing atmosphere, cladding materials, FPs formation, etc.) and temperature.
- All the physical–chemical properties of oxide fuels vary with the oxygen stoichiometry and temperature.

For UO_2 commercial fuel, the initial oxygen stoichiometry is typically very close to 2.

As an example, the equilibrium O_2 partial pressure of uranium dioxide is calculated in Fig. 11.16A as a function of oxygen to metal ratio at 750 K and 1273 K, the temperatures reached in the fuel at the periphery and the center of the pellet, respectively. This property is of upmost importance because it corresponds to the oxygen bonding energy in the crystal. It reflects the equilibrium between oxygen in the crystal and in the gas phase. The lowest values are found for O/U ratio smaller than 2. It steeply increases at the stoichiometry O/U = 2 and then increases smoothly with the oxygen content for O/U > 2. It means that oxygen is less and less bound in the crystal with an increasing oxygen content. The larger the O/U ratio, the easier uranium dioxide loses oxygen and so the easier it is reduced.

Uranium dioxide can be represented by a simple defect model $(\text{U}^{3+}, \text{U}^{4+}, \text{U}^{5+})_1(\text{O}^{2-}, \text{V})_2(\text{O}^{2-}, \text{V})_1$ as per Guéneau et al. [16]. In the cationic site, uranium can have different oxidation states 3+, 4+, and 5+. There are two sites for oxygen anions. The first site is the normal site for oxygen in the fluorite structure. “V” denotes vacancies. And the second oxygen site is the interstitial site. The crystal must be neutral in charge. From this simple model, the following points can be deduced:

- $(\text{U}^{4+})(\text{O}^{2-})_2(\text{V})_1$ corresponds to the perfect UO_2 crystal in which the normal site for oxygen is fully occupied and the interstitial site for oxygen is empty (with only vacancies).

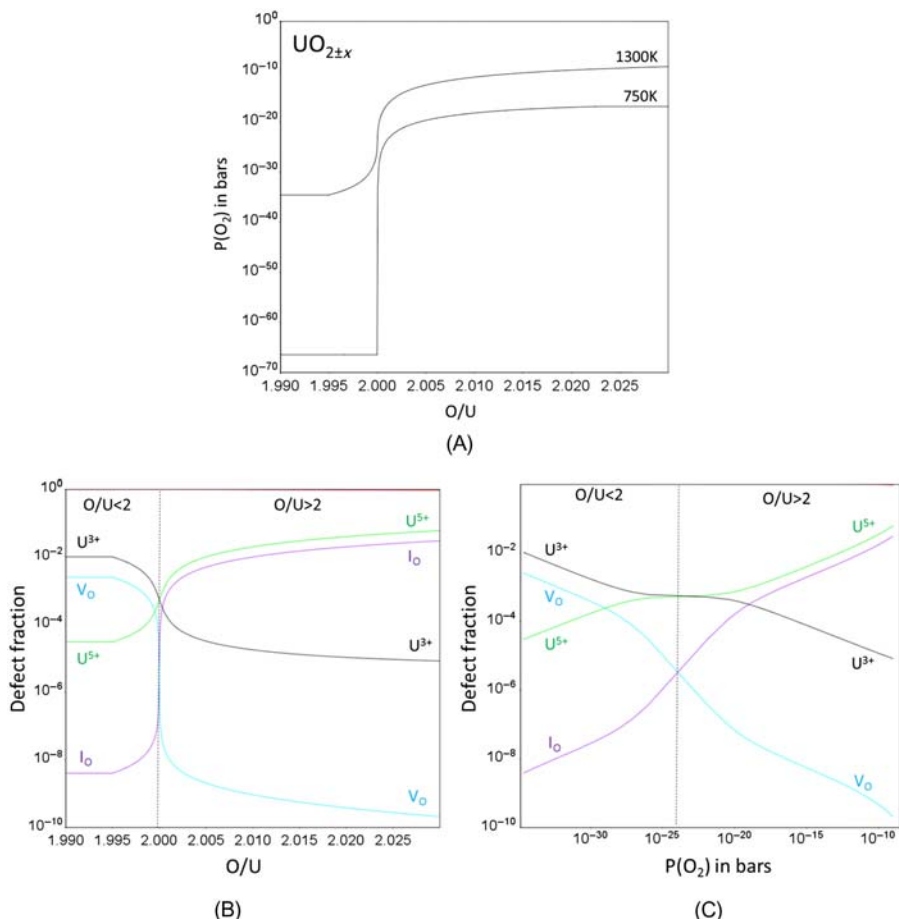


Figure 11.16 (A) Partial pressure of O_2 (in bars) above $UO_{2\pm x}$ as a function of O/U ratio at 750K and 1300K; defect fraction in $UO_{2\pm x}$ at 1300K (B) versus O/U ratio (C) versus $p(O_2)$ in bars.

- $(U^{3+}, U^{4+})(O^{2-}, V)_2(V)_1$ is the hypostoichiometric uranium dioxide UO_{2-x} ($O/U < 2$); the oxygen deficit is due to the presence of oxygen vacancies in the normal site for oxygen; as the oxide has to remain neutral, a fraction of uranium is reduced from 4+ to 3+.
- $(U^{4+}, U^{5+})(O^{2-}, V)_2(O^{2-}, V)_1$ is the hyperstoichiometric uranium dioxide UO_{2+x} ($O/U > 2$); the oxygen excess is due to the introduction of oxygen interstitials in the third site for oxygen; as the oxide has to remain neutral, a fraction of uranium is oxidized from 4+ to 5+.

In Fig. 11.16B and C, at 1300 K, the corresponding defect fractions in $UO_{2\pm x}$ are reported. V_O denotes the fraction of oxygen vacancies in the first site for oxygen whereas I_O designates the fraction of oxygen interstitials in the second site for oxygen. It shows the link between oxygen partial pressure curves and defect fractions.

In the hypostoichiometric region, the oxygen partial pressure is governed by oxygen vacancies and U^{3+} concentrations whereas oxygen interstitials and U^{5+} are the main defects in the hyperstoichiometric region. For large deviations from stoichiometry ($\text{O}/\text{U} > 2.001$), more complex defects exist. The oxygen interstitials interact and form aggregates with different kinds of structures, which are not taken into account in the present simple thermodynamic model [18].

Among the consequences, the oxidation of the cladding is important to consider. In LWRs, the cladding is made of a zirconium-based alloy. Zirconium is a metal that oxidizes very easily due to the fact that it can dissolve up to 30 at.% oxygen in the beta phase (hexagonal hcp) and can form zirconia, ZrO_2 , a very stable oxide phase. The largest the oxygen partial pressure is in $\text{UO}_{2 \pm x}$, the largest is the oxygen amount available for the cladding oxidation. Thus in a nuclear reactor, controlling the oxygen pressure of the fuel is of upmost importance.

Another property that depends on the oxygen stoichiometry is the melting temperature of the oxide fuel. As can be seen in Fig. 11.14B, the melting of pure UO_2 is congruent. But for any deviation from this ideal stoichiometry, the melting is no longer congruent. There is a (liquid + solid) interval and the liquidus temperature decreases with x for $\text{UO}_{2 \pm x}$, which means that the margin to fuel melting is reduced.

In the following sections, the effect of both the presence of plutonium and of FPs on the thermodynamic properties of the oxide fuels is addressed.

11.3.1.2 MOX fuel: effect of Pu

The MOX fuel used in FBRs contains about 20–25 wt.% Pu. The uranium–plutonium–oxygen phase diagram at 1500 K is presented in Fig. 11.17.

At 1500 K, the dioxides of uranium and plutonium form a continuous solid solution $(\text{U},\text{Pu})\text{O}_{2 \pm x}$ that extends from $\text{UO}_{2 \pm x}$ to PuO_{2-x} . Plutonium dioxide only exists as stoichiometric and hypostoichiometric in oxygen (with an O/Pu ratio ≤ 2). It explains the fact that for plutonium-rich compositions, the mixed oxide exists only for O/M ratio smaller than or equal to 2. On the contrary, at 1500 K, UO_2 extends toward O/M ratio ≥ 2 then the mixed oxide enriched in uranium extends in the hyperstoichiometric region of the phase diagram.

In Fig. 11.18A, the oxygen partial pressure for a typical MOX fuel composition, $(\text{U}_{0.8}\text{Pu}_{0.2})\text{O}_{2 \pm x}$ is calculated at 900 K and 2200 K, which are the temperatures at the periphery and center of the MOX fuel pellet in FBRs, respectively. As for $\text{UO}_{2 \pm x}$, the oxygen partial pressure steeply increases at $\text{O}/(\text{U} + \text{Pu}) = 2$. But compared to uranium dioxide (Fig. 11.16), for a given oxygen to metal ratio and temperature, the oxygen potential of $(\text{U},\text{Pu})\text{O}_{2 \pm x}$ is higher due to the higher oxygen potential of PuO_{2-x} compared to $\text{UO}_{2 \pm x}$. It is one of the reasons why the initial oxygen stoichiometry of the MOX fuels is chosen to be significantly lower than 2, around 1.96–1.97, to maintain the oxygen pressure low enough to avoid the oxidation of the steel cladding.

The defect fractions in $(\text{U}_{0.8}\text{Pu}_{0.2})\text{O}_{2 \pm x}$ are reported at 1300 K versus $\text{O}/(\text{U} + \text{Pu})$ ratio and oxygen partial pressure in Fig. 11.18B and C, respectively. When

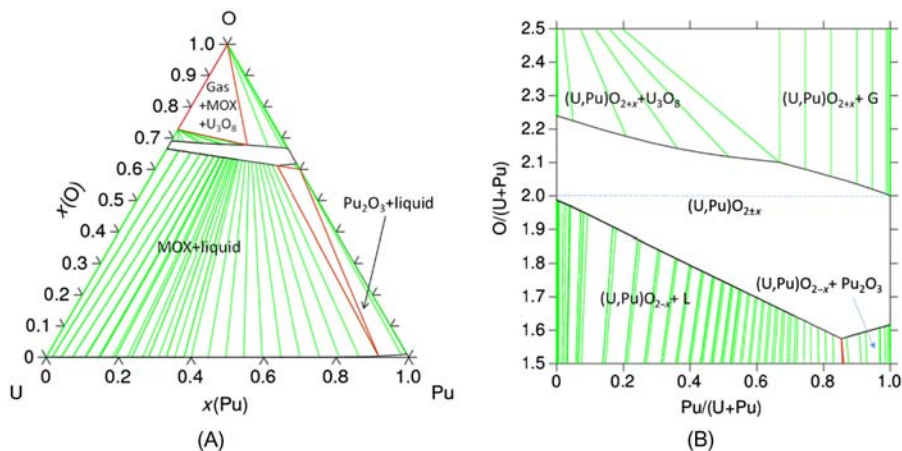


Figure 11.17 (A) Uranium–plutonium–oxygen phase diagram at 1500 K and (B) zoom with $0 < Pu/(U + Pu) < 1$ and $1.5 < O/(U + Pu) < 2.5$.

Source: C. Guéneau, N. Dupin, B. Sundman, C. Martial, J.-C. Dumas, S. Gossé, et al., Thermodynamic modelling of advanced oxide and carbide nuclear fuels: description of the U–Pu–O–C systems, *J. Nucl. Mater.* **419** (1–3), 2011, 145–167 [16]. The dashed line indicates the composition line for $O/(U + Pu) = 2$.

plutonium substitutes for uranium, the oxygen deficit (formation of oxygen vacancies V_O) is compensated by the reduction of Pu^{4+} into Pu^{3+} , whereas uranium remains U^{4+} . It can be explained by the fact that the oxygen potential of PuO_2 is higher than the one of UO_2 and thus plutonium is easier reduced compared to UO_2 . For hyperstoichiometric oxygen compositions, the excess of oxygen (oxygen interstitials I_O) is compensated by the oxidation of U^{4+} into U^{5+} . As plutonium dioxide does not exist as PuO_{2+x} , plutonium remains Pu^{4+} .

11.3.2 Irradiated oxide fuel

During irradiation, the fissile isotopes ^{235}U and ^{239}Pu are split into two fission fragments. This reaction leads to the release of mainly kinetic energy of these fragments. The quantity of FPs depends on the burnup, which measures the extent of fission of the U and Pu in the fuel. The FP when forming at an atomic scale causes damage to the lattice. The transfer of their kinetic energy occurs via collisions to surrounding atoms. But many of the displaced atoms by these damage cascades quickly relocate. Many elements (more than 30) are produced in the fuel during operation due to the fission reactions which make the chemistry of irradiated fuels quite complex.

It is very important to point out that the chemical behavior of nuclear fuels is driven by different coupled phenomena:

- The increasing formation of FPs with time within the fuel matrix. It means that the chemical composition of the fuel changes with time without reaching a steady state.

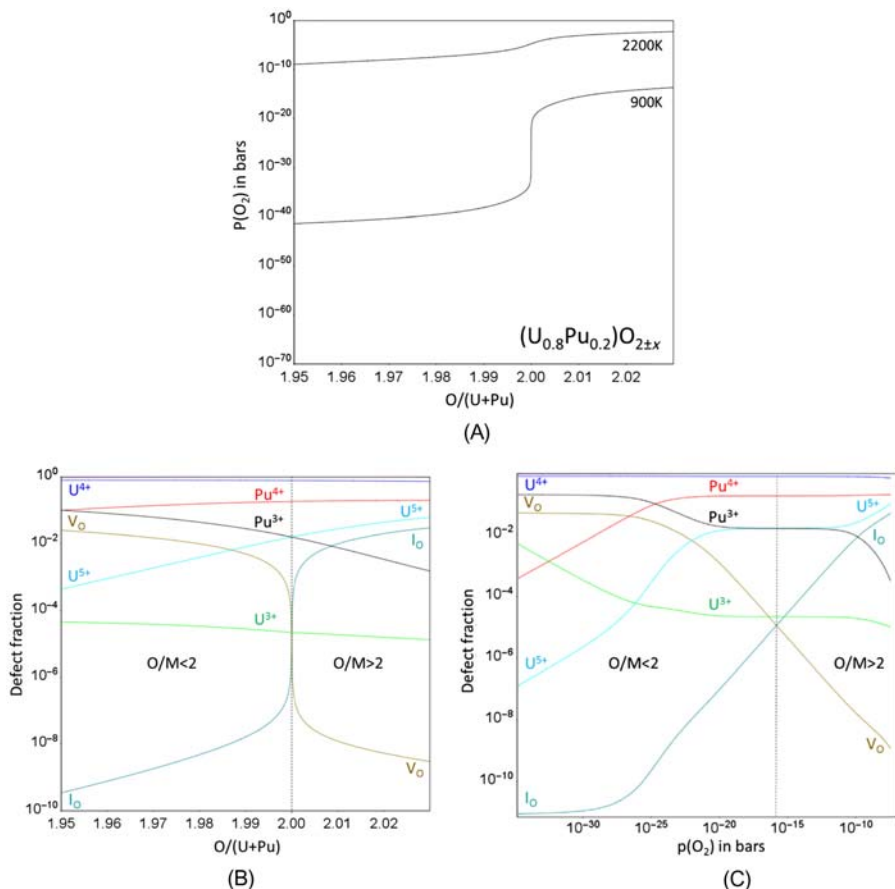


Figure 11.18 (A) Partial pressure of O_2 (in bars) above $(U_{0.8}Pu_{0.2})O_{2\pm x}$ as a function of O/U ratio at 900 K and 2200 K; defect fraction in $(U_{0.8}Pu_{0.2})O_{2\pm x}$ at 1300 K (B) versus O/U ratio (C) versus $p(O_2)$ in bars.

- Thermodynamics. The energy of formation provides the driving force for a phase to form.
- Thermal (or chemical) diffusion. A high enough temperature level has to be reached in the fuel for the atoms to have a high enough mobility to diffuse and to form the phases predicted by thermodynamics.
- A thermal radiation-enhanced diffusion. At low temperature, where the mobilities are low, radiations produce a high concentration of defects (point defects: vacancies, interstitials and extended defects: clusters, dislocations, etc.) that enhance the diffusion of the elements.
- Thermodiffusion; the large thermal gradient between the center and the periphery of the pellet leads to mass transport of the elements in both gas and solid state along the radius.

In a first part the overall picture of the FPs will be presented. Predictions from thermodynamics will be discussed and compared with experimental observations in the case of both LWR and FBR fuels.

11.3.2.1 Chemical form of the fission products

The amount of the FPs (typically up to several at.%) can be quantified using neutronic codes such as DARWIN [19] or ORIGEN [20]. The chemical composition of the fuel changes with time (and burnup) and consequently its physical–chemical properties too.

In Fig. 11.19 the main FPs that are formed in the fuel are reported in the periodic table.

The FPs can be grouped into four main categories as follows:

- The volatile FPs: He, Xe, Kr, Br, I, Rb, Cs present in gaseous state (in green).
- The FPs in solution in the oxide matrix: Y, La, Ce, Pr, Nd, Pm, Sm, Eu, Gd (in yellow).
- The elements forming metallic precipitates: Mo, Tc, Ru, Rh, Pd, Ag, Cd, In, Sn, Sb, Te (in red).
- The elements forming separated oxide precipitates: Ba, Nb, Zr, Sr, Cs, Mo (in blue).

A few elements such as Cs, Sr, Ba, Mo, Te, and Zr are marked with mixed colors because they can be distributed in several kinds of phases, as detailed in the following section.

Depending on their affinity for oxygen and their ionic radius, the FPs are either dissolved in the oxide fuel matrix or located in different separated secondary phases (metallic or oxide). A very useful way to give out an overall view of the affinity of the elements for oxygen is to calculate Ellingham diagrams (Fig. 11.20). The difficulty in case of oxide fuels is that the oxygen potential of the fuel varies very

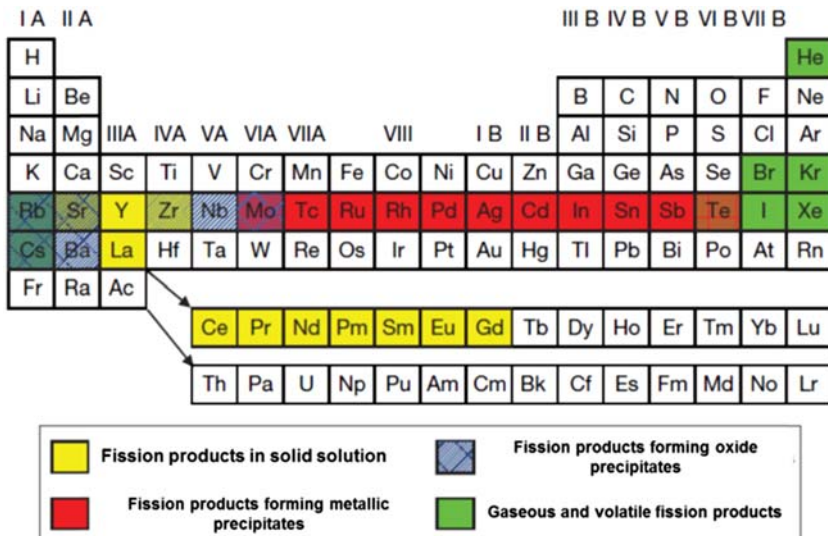


Figure 11.19 Mendeleev periodic table with the main fission products.

Source: Y. Guérin, Chapter 2.21 fuel performance of fast spectrum oxide fuel, In: R.J.M. Konings, (Ed), *Comprehensive Nuclear Materials*, 2012, Elsevier, 548–572 [10].

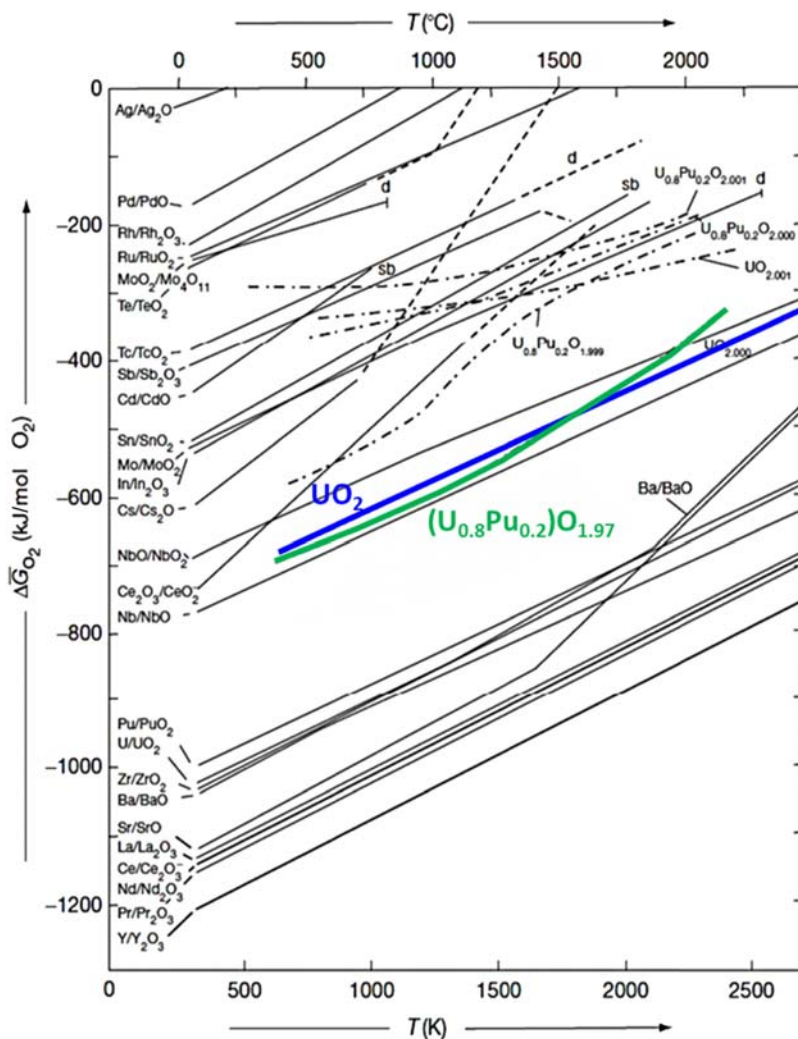


Figure 11.20 Ellingham diagram of main fission product oxides.

Source: From H. Kleykamp, The chemical state of the fission products in oxide fuels, J. Nucl. Mater. 131 (1985) 221–246.

steeply with the oxygen stoichiometry. So data are reported for several oxygen stoichiometries for both $\text{UO}_{2 \pm x}$ and $(\text{U}_{0.8}\text{Pu}_{0.2})\text{O}_{2 \pm x}$ fuels in the Ellingham diagram. The FPs with an oxygen potential lower than the one of UO_2 or $(\text{U},\text{Pu})\text{O}_2$ fuel (Nb, Zr, Ba, Sr, La, Ce, Nd, Pr, Y) are stable as oxide phases, whereas those whose oxygen potential is higher, exist in the form of metallic phases (Ag, Pd, Rh, Ru, Te, Tc, Sb, Cd). For FPs such as Sn, Mo, In, Cs, it is less easy to conclude as the oxygen potential for these elements is close to the one of MOX fuels.

From Fig. 11.20, it is obvious that the formation of the FPs affects the oxygen potential of the fuel.

The Ellingham diagram (Fig. 11.20) is useful but limited to understand the chemistry of irradiated oxide fuels as it does not take into account the possible formation of mixed oxide or metallic solution phases nor the phase transitions occurring with temperature (decomposition, melting...).

So to conclude, the lanthanoid elements (Ln) and Zr are dissolved in the (U,Zr, Ln) O_2 or (U,Pu,Zr,Ln) O_2 fuel matrix and the other FPs are either released because they are very volatile or form secondary phases (oxide or metallic phases). And some elements can be distributed into several phases.

One key factor to keep in mind is that the chemical state of these FPs within the fuel can change with the oxygen potential (or the related oxygen stoichiometry) which varies with time (and burnup) and thus leads to a quite complex chemical behavior of the oxide fuels under irradiation.

Furthermore, the PIE of irradiated fuels is quite complicated to carry out due to the high radiotoxicity level of irradiated fuels. In most of cases, only the overall composition of the elements is measured by X-ray microanalysis and/or electron microprobe but the local composition of the elements in the precipitates is generally not measured, and there is no deep analysis of the crystalline structure of these secondary phases. The small quantity of FPs and thus of the phases where these ones are located makes the analysis quite tricky. Very recently, characterization of MOX irradiated fuels was performed using transmission electron microscopy alloying to measure the composition of very small oxide and metallic precipitates of several hundred nanometers diameters [21]. The use of these techniques is very promising. Another difficulty is that the chemical composition of irradiated fuels continues to change with time by alpha decay after the fuel is discharged from the reactor.

Thus the irradiated fuel chemistry is still not very well known. To improve the knowledge on this topic, thermodynamic calculations by Gibbs energy minimization have been performed to predict the phases to be formed (see Chapter 3, Computational thermochemistry of nuclear fuel). These calculations assume that the fuel is at thermodynamic equilibrium, which is of course in most of the cases not true but it provides the driving force for the formation of these phases.

Depending on the temperature level in the fuel, these phenomena will more or less dominate the changes in the irradiated fuel chemistry and microstructure. Fuel chemistry will be discussed in both LWRs and FBRs cases for which the temperature levels are quite different.

In the following section, the phases that form from the different classes of FPs in oxide fuels are described, and phase diagrams containing these phases are presented.

The gaseous fission products: He, Xe, Kr, I, Br, Rb, Cs

The noble gas FPs He, Xe, and Kr are inert and therefore have no chemical interaction with the fuel. Because of their large atomic size compared with the lattice spacing, Xe and Kr are insoluble in UO_2 . Grain boundaries in the fuel form a network for fast diffusion of the elements. They are present as intragranular and

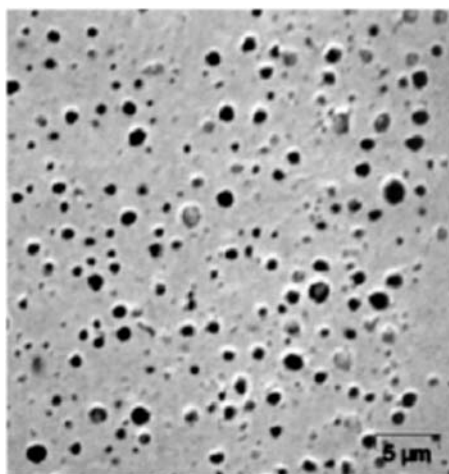


Figure 11.21 SEM image of the peripheral part of a fuel pellet revealing large micron size pores characteristic of the rim structure.

Source: P. Garcia, G. Carlot, B. Dorado, S. Maillard, G. Martin, J.Y. Oh, et al., Chapter 1. Mechanisms of microstructural changes of fuel under irradiation, in: NEA/NSC/R(2015)5 Report, 2015, 22–58 [22].

intergranular bubbles within the fuel (Fig. 11.21). A part of those elements is released to open porosity of the fuel and then to the plenum.

In comparison, the solubility of helium even small can be measured by forcing the gas to penetrate into the solid using high pressures (~ 100 atm).

The halogens bromine and iodine are very volatile FPs too, which leads to their high release.

The chemistry of Cs and I is of practical importance to reactor operation in the context of cladding susceptibility to iodine-induced stress corrosion cracking (SCC) [23].

The chemical state of iodine in the oxide fuels is still not clearly established. The formation of the CsI compound has been suggested from thermodynamic calculations, but the experimental evidence of this compound in irradiated fuels and/or in the gas phase has never been clearly shown. The Cs–I phase diagram is reported in Fig. 11.22.

The analysis of bromine distribution in irradiated fuels is very scarce. The chemical form of this element in the fuel is thus not known.

In LWRs, only a small fraction (less than 1 at.%) is released into the gap between the fuel pellet and the cladding and to the plenum. It is postulated that bubbles of rare gases (He, Xe, Kr) shall also contain the volatile elements I, Br, Cs, or Te.

In FBRs, due to the high fuel temperature, the release is much higher up to 40%–50% in the early irradiation stages and up to 80%–90% at high burnup.

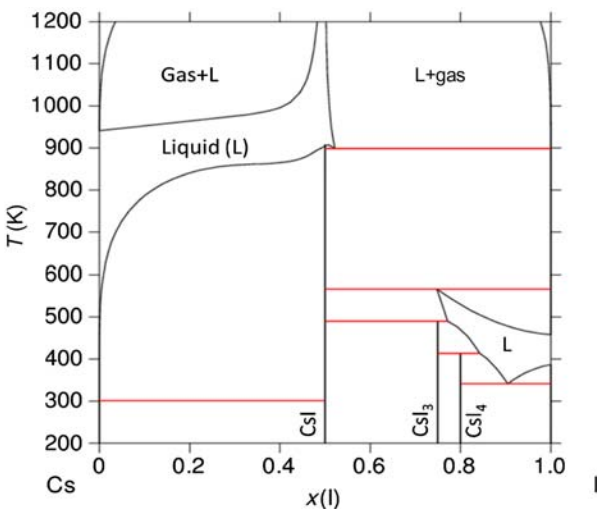


Figure 11.22 Cs–I phase diagram.

Source: P. Garcia, G. Carlot, B. Dorado, S. Maillard, G. Martin, J.Y. Oh, et al., Chapter 1. Mechanisms of microstructural changes of fuel under irradiation, in: NEA/NSC/R(2015)5 Report, 2015, 22–58 [24].

The Cs uranate and molybdate phases

Interaction between cesium and oxide fuel can lead to the formation of urano and/or uranoplutonate cesium compounds: $\text{Cs}_2\text{U}_4\text{O}_{12}$ in Cs–U–O and $\text{Cs}_2(\text{U},\text{Pu})_4\text{O}_{12}$ in Cs–U–Pu–O systems. It is not surprising considering the large number of ternary compounds that exist in the Cs–U–O phase diagram (Fig. 11.23A). $\text{Cs}_2\text{U}_4\text{O}_{12}$ is found in equilibrium with hyperstoichiometric UO_{2+x} , thus in oxidizing conditions ($\Delta G(\text{O}_2) > -280 \text{ kJ/mol}$ at 1000 K). The formation of these compounds was predicted by thermodynamic calculations but never observed experimentally in irradiated fuels.

As shown in Fig. 11.23B, numerous compounds exist in the Cs–Mo–O system. Cs_2MoO_4 is reported to form in the oxide fuel but in the area close to the cladding. The compound in equilibrium with Mo and MoO_2 , also exists in the gaseous state as $\text{Cs}_2\text{MoO}_4(\text{g})$. In FBR fuels, the molecule $\text{Cs}_2\text{MoO}_4(\text{g})$ is expected to dissociate into MoO_3 and Cs_2O at high temperatures and to be transported and condensed in the cold fuel zone (close to the cladding), as $\text{Cs}_2\text{MoO}_4(\text{s})$, at high oxygen potential.

Also, cesium is expected to exist as CsO_x gaseous molecules (Cs_2O , Cs_2O_2 , CsO) in bubbles and closed pores within the fuel. It is also reported to exist in the form of Cs_2Te compound.

The existence of these phases containing cesium has never been evidenced experimentally either in LWRs or FBRs fuels.

Fission products dissolved in the matrix: $(\text{U},\text{Pu},\text{Sr},\text{Y},\text{Zr},\text{Nb},\text{La},\text{Ce},\text{Pr},\text{Nd},\text{Pm},\text{Sm},\text{Eu}, \text{Gd})\text{O}_{2 \pm x}$

Many FPs are dissolved in the fluorite matrix. The existence of the numerous possible oxidation states of uranium in the fluorite phase and the related wide oxygen

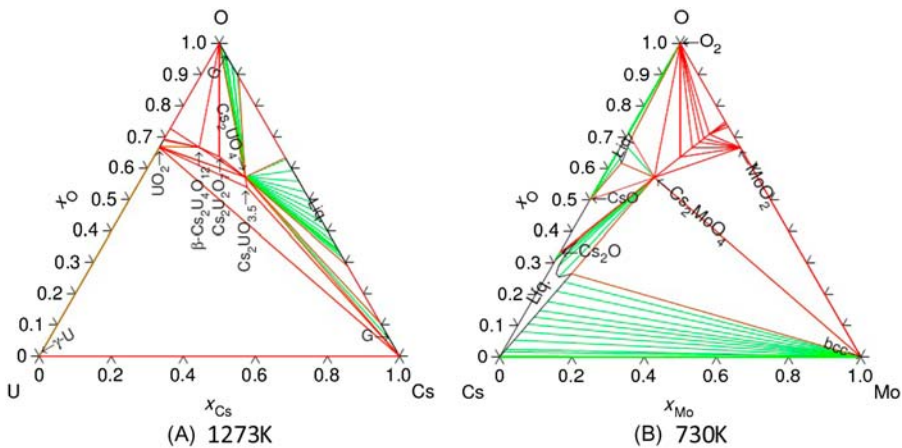


Figure 11.23 Phase diagrams of (A) Cs–U–O at 1273 K and (B) Cs–Mo–O at 730 K.
Source: P. Garcia, G. Carlot, B. Dorado, S. Maillard, G. Martin, J.Y. Oh, et al., Chapter 1. Mechanisms of microstructural changes of fuel under irradiation, in: NEA/NSC/R(2015)5 Report, 2015, 22–58 [24].

stoichiometry range make it possible for many elements with oxidation states from 2+ to 4+ to dissolve in solid solution in UO_2 .

All the lanthanides exist as sesquioxides Ln_2O_3 with oxidation states of 3+, except cerium oxides that exhibit both 3+ and 4+ oxidation states, like plutonium. The rare earth (RE) elements La, Gd, Nd (Fig. 11.24A–C) and also Pm, Sm, Eu (with 3+ oxidation state) and Ce, Pr (with 3+ and 4+ oxidation states such as plutonium) have a high solubility in UO_2 and $(\text{U}, \text{Pu})\text{O}_2$ fuels, as shown in the foregoing phase diagrams.

Also, strontium (with a 2+ oxidation state) has a large solubility in UO_2 but to a lesser extent than the RE elements (Fig. 11.25A). Zirconium, yttrium, and niobium can also be dissolved in the fuel matrix (Fig. 11.25B and C).

In case of zirconium the solubility depends much on temperature. It is negligible at temperatures below 1400 K. In this case, ZrO_2 with a tetragonal structure is expected to precipitate. The solubility in the fluorite matrix starts to be significant above 1500 K and increases up to 100 at.% above 2600 K. The analysis of irradiated fuels (both LWRs and FBRs) shows that these elements are present in the oxide fuel matrix, which is in agreement with the thermodynamic calculations.

Metallic precipitates: Mo, Tc, Ru, Rh, Pd

Molybdenum, technetium, and the noble metals ruthenium, rhodium, and palladium form metallic precipitates, also called “white inclusions” (Fig. 11.26A and B). These precipitates are easy to detect in irradiated fuels because of their metallic state. These phases are the only secondary phases that are detected in irradiated UO_2 fuels at high burnup in LWRs (Fig. 11.26A). In larger quantities in FBR fuels, they are easily observed (Fig. 11.26B).

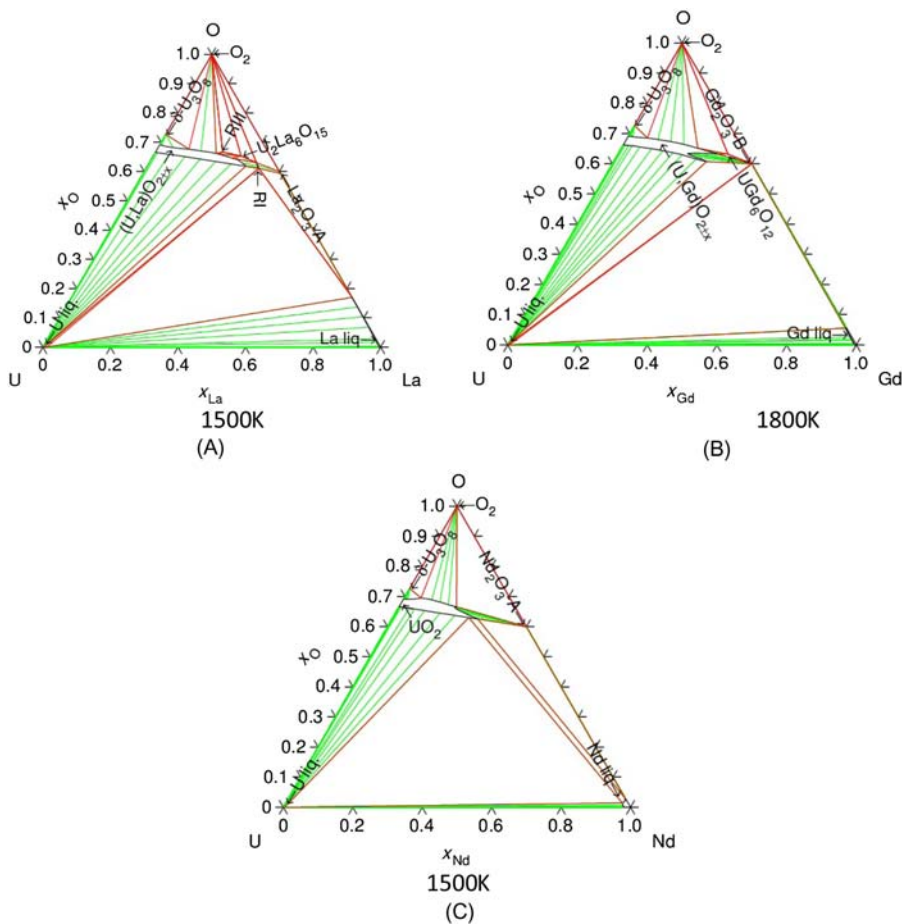


Figure 11.24 Phase diagrams of (A) U-La-O at 1500 K [24], (B) U-Gd-O at 1800 K [24], and (C) U-Nd-O at 1500 K [24,26].

Source: (A, B,C) P. Garcia, G. Carlot, B. Dorado, S. Maillard, G. Martin, J.Y. Oh, et al., Chapter 1. Mechanisms of microstructural changes of fuel under irradiation, in: NEA/NSC/R (2015)5 Report, 2015, 22–58. (C) A. Quaini, C. Guéneau, S. Gossé, N. Dupin, B. Sundman, E. Brackx, et al., Contribution to the thermodynamic description of the corium – the U-Zr-O system, *J. Nucl. Mater.* **501**, 2018, 104–131.

The metallic state of these elements in the oxide fuel is consistent when looking at the Ellingham diagram (Fig. 11.20). Molybdenum and ruthenium are the main components of the metallic precipitates (Fig. 11.27A). These elements form solid solutions with each other with hexagonal hcp and cubic bcc crystal structures (Fig. 11.27B–D). Depending on the oxygen potential, molybdenum concentration in these phases can vary as this element can also enter into other phases such as $BaMoO_4$.

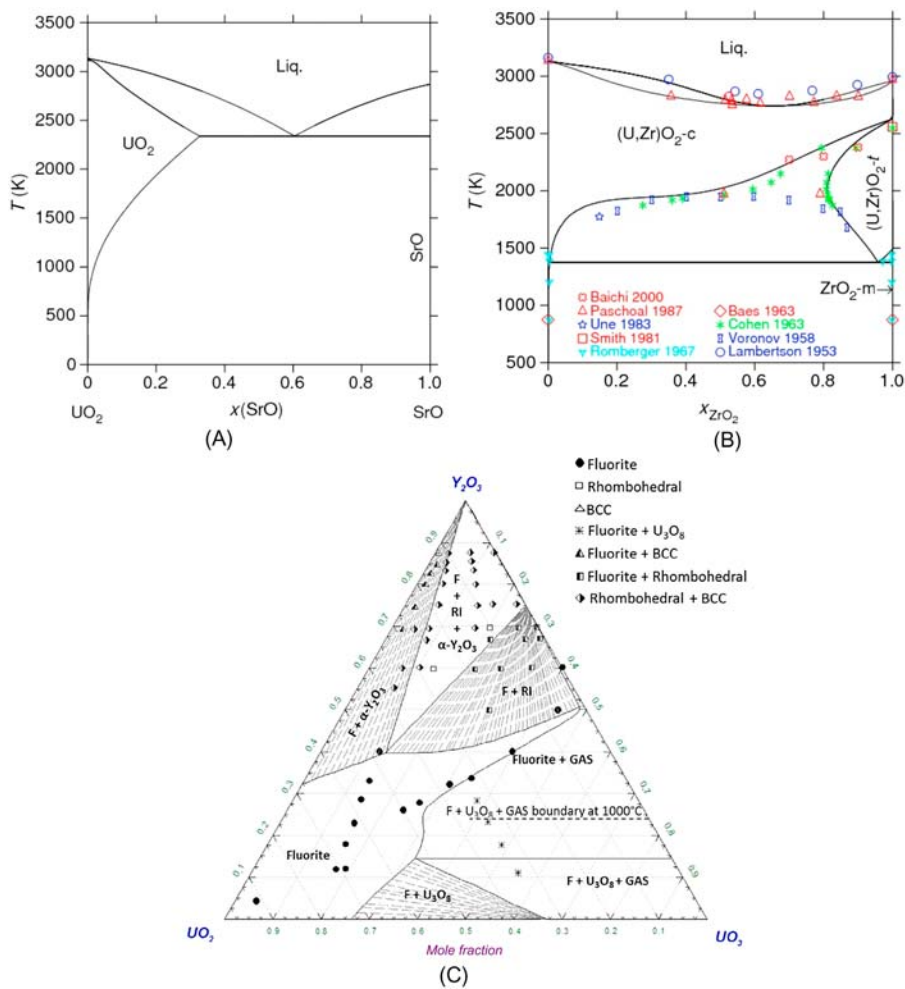


Figure 11.25 Phase diagrams (A) UO_2 -SrO [24], (B) UO_2 - ZrO_2 [24,26], and (C) UO_2 - U_3O_8 - Y_2O_3 at 1773 K [27].

Source: (A,B) P. Garcia, G. Carlot, B. Dorado, S. Maillard, G. Martin, J.Y. Oh, et al., Chapter 1. Mechanisms of microstructural changes of fuel under irradiation, in: NEA/NSC/R (2015)5 Report, 2015, 22–58. (B) J.A. Quaini, C. Guéneau, S. Gossé, N. Dupin, B. Sundman, E. Brackx, et al., Contribution to the thermodynamic description of the corium – the U-Zr-O system, *J. Nucl. Mater.* **501**, 2018, 104–131. (C) R.G. Brese, J.W. McMurray, D. Shin and T.M. Besmann, Thermodynamic assessment of the U-Y-O system, *J. Nucl. Mater.* **460**, 2015, 5–12.

The metallic solid solutions are mainly hexagonal (hcp structure), cubic fcc, and/or bcc structure solid solutions with variable compositions. At high temperature and low oxygen potential conditions, the interaction with the fuel can also lead to the

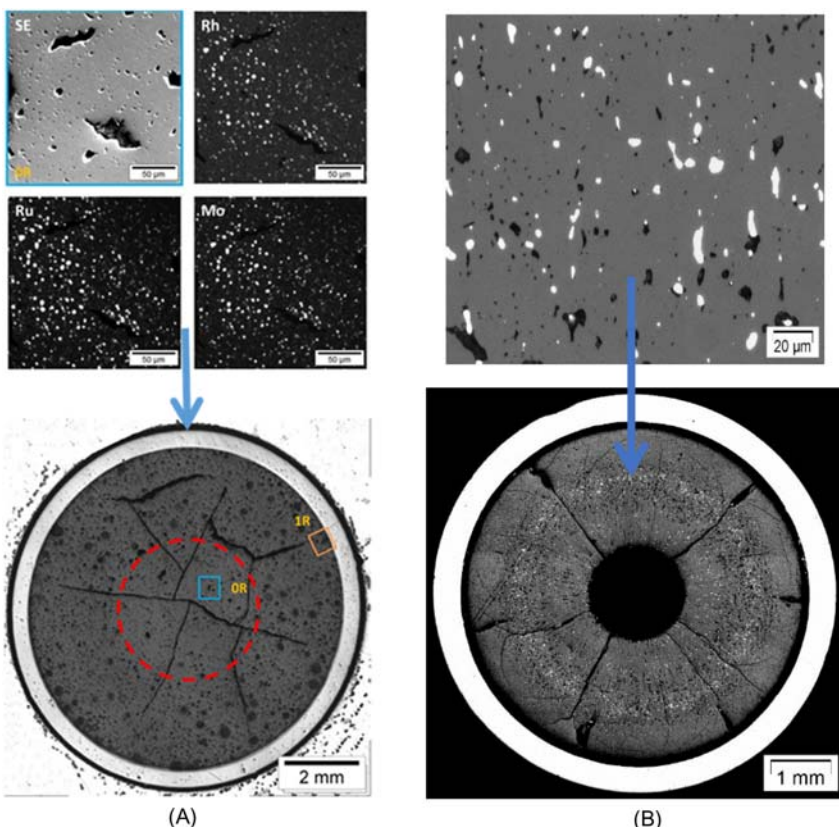


Figure 11.26 SEM photo of white precipitates (A) in a MOX fuel irradiated in a PWR [28] and (B) in an $(U_{1-y} Pu_y)O_{2-x}$ fuel irradiated into the Phénix reactor [29]. PWR, Pressurized water reactor.

Source: (A) C. Le Gall, Contribution to the Study of Fission Products Release From Nuclear Fuels in Severe Accident Conditions: Effect of the PO_2 on Cs, Mo and Ba Speciation (Ph.D. thesis), Université Grenoble Alpes, 2018. <<https://tel.archives-ouvertes.fr/tel-02052819>>. (B) J. Lamontagne, State-of-the art and challenges for post-irradiation examinations, in: Proceedings of the Nuclear Materials Conference (NUMAT 2014), 27–30 October 2014, Clearwater Beach, FL, 2014.

formation of quite stable intermetallic compounds $(U, Pu)(Rh, Pd)_3$ (with cubic $AuCu_3$ -type structure).

The compositions of the white precipitates measured in different types of fuels have been reported by Kleykamp [6] on the phase diagram in Fig. 11.28.

Radial transport of molybdenum and ruthenium is expected to occur via the transport of the gaseous species $MoO_3(g)$ and $RuO_3(g)$.

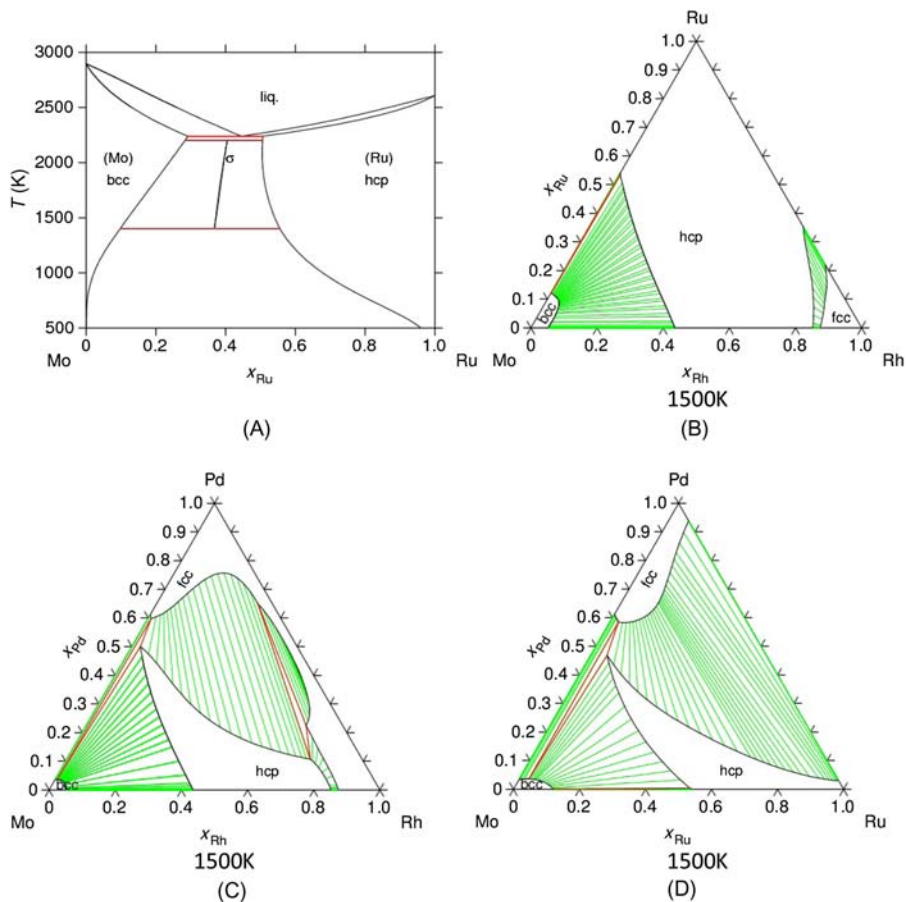


Figure 11.27 Phases diagrams of (A) Mo–Ru [24], (B) Mo–Rh–Ru [24], (C) Mo–Rh–Pd [24], and (D) Mo–Pd–Ru [24].

Source: (A,B,C,D) P. Garcia, G. Carlot, B. Dorado, S. Maillard, G. Martin, J.Y. Oh, et al., Chapter 1. Mechanisms of microstructural changes of fuel under irradiation, in: NEA/NSC/R (2015)5 Report, 2015, 22–58.

Other Pd rich phases: (Pd,Ag,Te) and (Pd, Ag, Cd, In, Sn, and Sb phases), Te rich phases

In FBRs, due to its high volatility, palladium is transported within the fuel via Pd(g) and can condense and interact with other volatile FPs in the fuel/cladding gap region. The exact nature of the formed metallic phases is not well known. Typical compositions were measured as follows: (Pd 81–Sn 9–Sb 2–Te 8) (wt.%) and (Pd 69–Sn 3–Sb 4–Te 24) [6]. In view of the low melting points of Ag (1235 K), Cd (594 K), In (430 K), Sn (505 K), and Sb (904 K) elements, the formation of liquid phases is expected to happen with palladium.

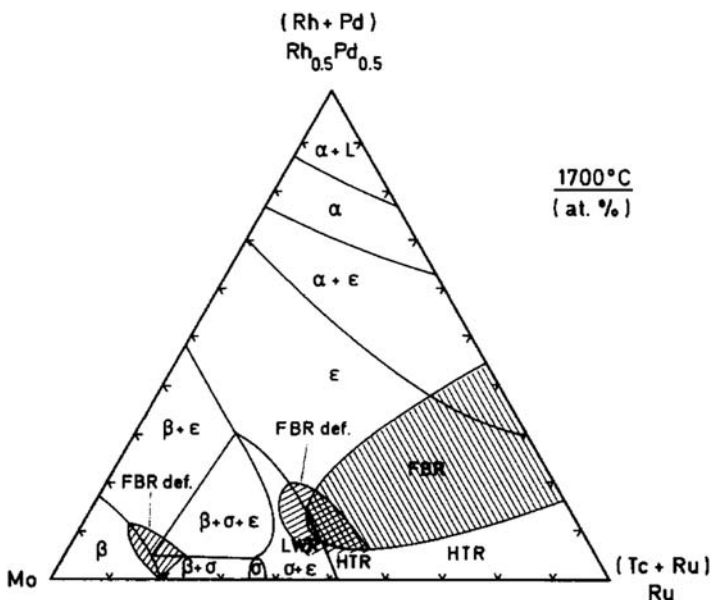


Figure 11.28 Compositions of the metallic precipitates measured in different types of FBR fuels [6]; α = Pd-based alloy with cubic fcc structure, β = Mo-based alloy with cubic bcc structure, ϵ = Ru-based alloy with hexagonal hcp structure, σ : Intermetallic compound Mo_5Ru_3 with tetragonal structure. *FBR*, Fast breeder reactor.

Source: H. Kleykamp, The chemical state of the fission products in oxide fuels, *J. Nucl. Mater.* 131, 1985, 221–246.

Also, metallic precipitates enriched in Pd, Te, and Ag were detected in FBR fuels. Because of the low eutectic reactions in the Pd–Te system (Fig. 11.29), it was probably a liquid phase in the fuel during operation.

The gray phases $(\text{Ba}, \text{Sr}, \text{Cs})(\text{U}, \text{Pu}, \text{Zr}, \text{Mo}, \text{RE})\text{O}_3$

The gray phase is an oxide phase with a perovskite structure type and the chemical formula $(\text{Ba}, \text{Sr}, \text{Cs})(\text{U}, \text{Pu}, \text{Zr}, \text{Mo}, \text{RE})\text{O}_3$ with RE. The composition of RE is generally very low except for highly irradiated fuels. These precipitates are observed in FBR fuels only (Fig. 11.30). In some cases, the presence of cerium has been detected in the gray precipitates.

The Ba–Zr–O system is the basic ternary system with the BaZrO_3 perovskite phase (Fig. 11.31). SrUO_3 , SrZrO_3 , BaUO_3 , and BaMoO_3 also exist which explains the formation of the mixed perovskite phase.

Computational thermodynamics to predict the fission product phases in irradiated fuels

To perform thermodynamic calculations on complex materials with a large number of chemical elements, computational thermodynamics has been developed since the 1980s. The principle (described in Chapter 3, Computational thermochemistry of nuclear fuel)

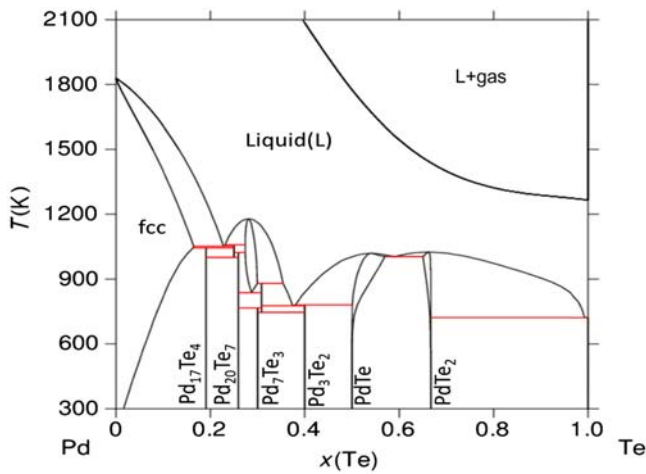


Figure 11.29 Phase diagram Pd–Te.

Source: P. Garcia, G. Carlot, B. Dorado, S. Maillard, G. Martin, J.Y. Oh, et al., Chapter 1. Mechanisms of microstructural changes of fuel under irradiation, in: NEA/NSC/R(2015)5 Report, 2015, 22–58; S. Gossé and C. Guéneau, Thermodynamic assessment of the palladium-tellurium (Pd-Te) system, *Intermetallics* **19**, 2011, 621–629 [24,31].

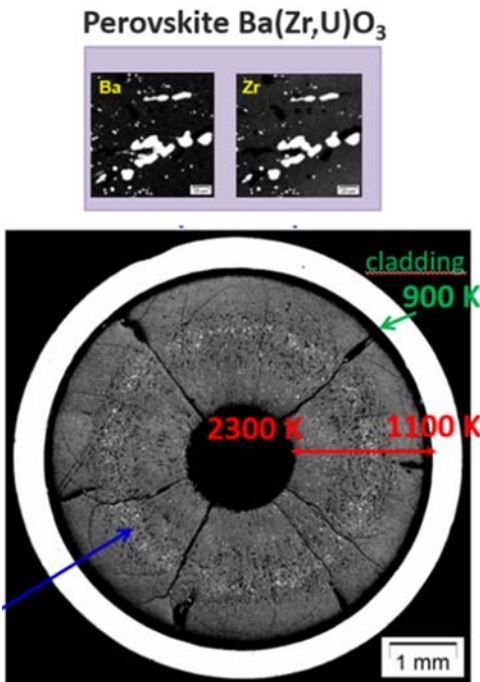


Figure 11.30 Gray phase precipitates observed in 13.3% FIMA irradiated fuel in Phénix [28].

Source: C. Le Gall, Contribution to the Study of Fission Products Release From Nuclear Fuels in Severe Accident Conditions: Effect of the PO_2 on Cs, Mo and Ba Speciation (Ph.D. thesis), Université Grenoble Alpes, 2018. <<https://tel.archives-ouvertes.fr/tel-02052819>>.

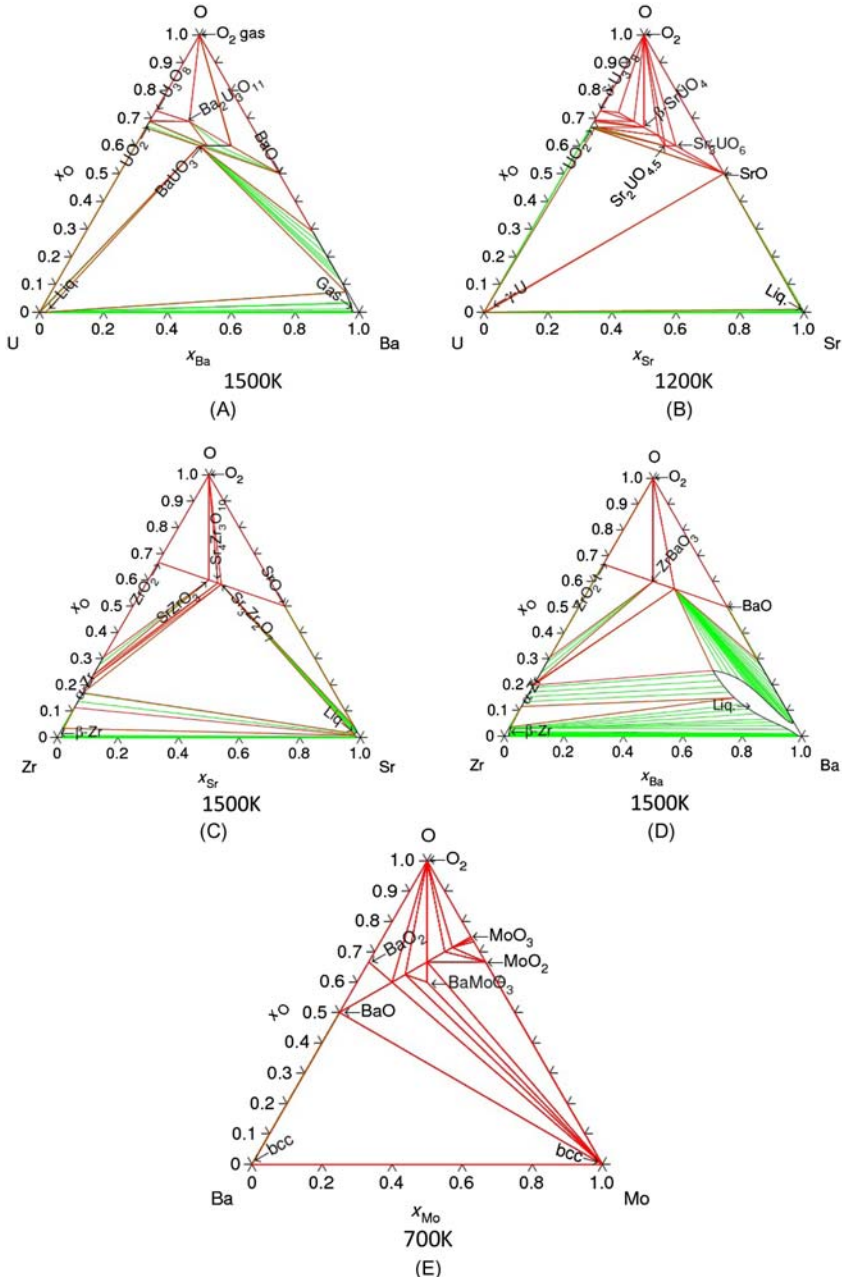


Figure 11.31 Phase diagrams (A) Ba–U–O [24], (B) Sr–U–O [24], (C) Sr–Zr–O [24], (D) Ba–Zr–O [24], and (E) Ba–Mo–O [24].

Source: P. Garcia, G. Carlot, B. Dorado, S. Maillard, G. Martin, J.Y. Oh, et al., Chapter 1. Mechanisms of microstructural changes of fuel under irradiation, in: NEA/NSC/R(2015)5 Report, 2015, 22–58.

is to calculate the thermodynamic equilibrium for given pressure, temperature, and composition conditions by minimizing the total Gibbs energy of the system. It requires the development of mathematical models to describe the Gibbs energy of each solid, liquid and gas phase as a function of temperature and composition (generally the pressure is fixed at $P = 1$ bar). With this approach, the Gibbs energy of a multicomponent system is described by extrapolation from the unary, binary, and ternary (in some cases quaternary) subsystems. When all the solutions are described, it is then possible to calculate phase diagrams. This is also called the Calphad method (Calculation of phase diagrams).

In the field of nuclear materials, several databases have been built that contain the elements of the fuel matrix: U–Pu–O as well as many FPs. In some of the databases (RMCC and TBASE databases), only a few solid solutions are described, the fuel matrix $(U,Pu,FP)O_{2 \pm x}$ (FPs that are soluble in the fuel matrix) and a few solid solutions. In the TAF-ID (Thermodynamic Advanced Fuels—International Database), developed in the frame of an OECD/NEA joint project [24], the solid and liquid solutions are fully modeled. Thus it is possible to calculate phase diagrams as it can be seen in the previous figures. The whole range of temperature is modeled. It makes it possible to perform calculations for severe accident studies.

Samuelsson et al. [32] performed thermodynamic calculations using the OpenCalphad software [33] with the TAF-ID [24] to predict the chemistry of an uranium and plutonium mixed oxide fuel irradiated up to 13.3% FIMA in the French Phénix reactor. In Fig. 11.32, the moles of the secondary phases formed in the fuel matrix are calculated as a function of temperature. It shows that during operation, many different kinds of phases can form in the fuel. And there is also small fraction of liquid phases. It is due to the existence of low-temperature eutectic reactions in systems such as Pd–Te and Cs–I.

11.3.2.2 Oxygen chemical potential

As mentioned in the introduction, the oxygen potential of the fuel is a key parameter to assess because it controls the fuel thermodynamic and thermal physical properties such as the thermal conductivity for instance and it can affect the corrosion of the cladding. In fact, the larger it is, the higher is the risk of cladding oxidation. As the oxide matrix of the fuel is the major phase, its oxygen potential is mainly controlled by this phase.

The thermodynamic studies on the ternaries containing lanthanides U–O–Ln ($Ln = Nd, Gd, La, Ce$, etc.) have shown that the oxygen potential increases with an increasing amount of REs dissolved in UO_2 , compared to pure UO_2 fuel. This can be clearly seen in Fig. 11.33 where experimental data were measured by Une and Oguma [34] on pure UO_{2+x} samples and on SIMFUEL samples (UO_2 doped with small quantities of Zr, Ce, Pr, Nd, Y to simulate the composition of irradiated fuels with burnups of 5 and 10 at.%). The increase in the oxygen potential of UO_2 caused by the soluble FPs can be explained as follows: the replacement of uranium by RE ions with lower valence ($3+$) requires an increase in the oxidation state of the remaining uranium ions (from $4+$ to $5+$), with a more positive oxygen potential.

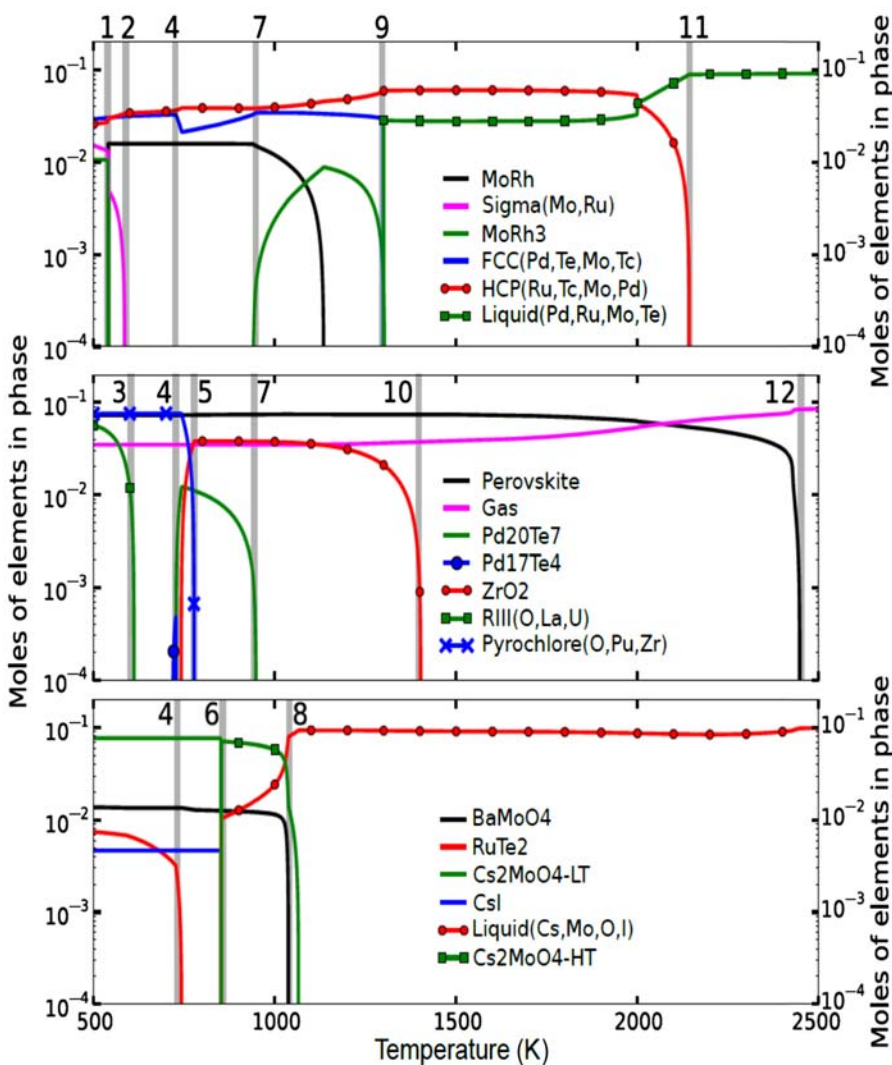


Figure 11.32 Calculated moles of the secondary phases forming in the 13.3% FIMA irradiated fuel in Phénix.

Source: K. Samuelsson, J.C. Dumas, B. Sundman, J. Lamontagne, C. Guéneau, Simulation of the chemical state of high burnup ($\text{U}, \text{Pu}\text{O}_2$) fuel in fast reactors based on thermodynamic calculations, *J. Nucl. Mater.* 532 (2020) 151969 [32].

As the initial oxygen stoichiometry of UO_2 LWR fuel is close to 2, the oxygen stoichiometry of irradiated fuel is expected to be slightly higher than 2.

The measurements of oxygen potential on unirradiated and irradiated fuels show the same tendency. The oxygen potential of irradiated fuels is higher than the one of fresh fuels, and it increases with burnup for both LWR [35] and FBR fuels.

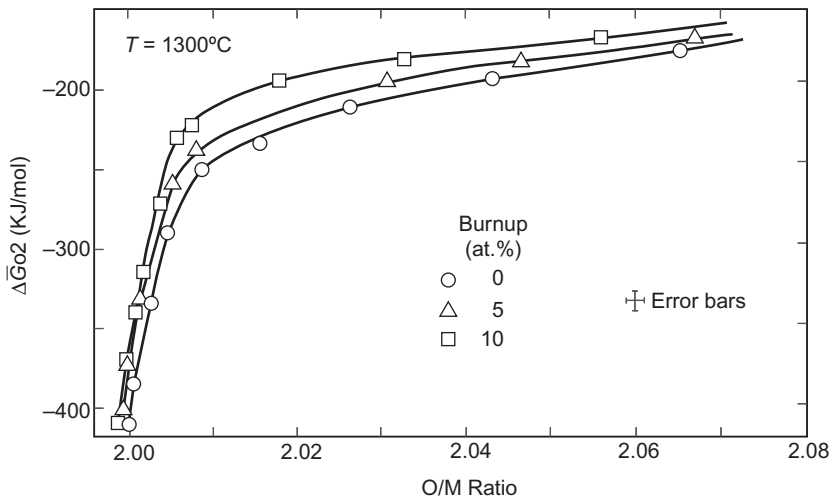


Figure 11.33 Oxygen potential for UO_{2+x} and SIMFUEL samples simulating irradiated fuels with 5 and 10 at.% compared to experimental data of Une and Oguma.

Source: K. Une and M. Oguma, Oxygen potential of UO_2 fuel simulating high burnup, *J. Nucl. Sci. Technol.* **20**, 1983, 844–851 [34].

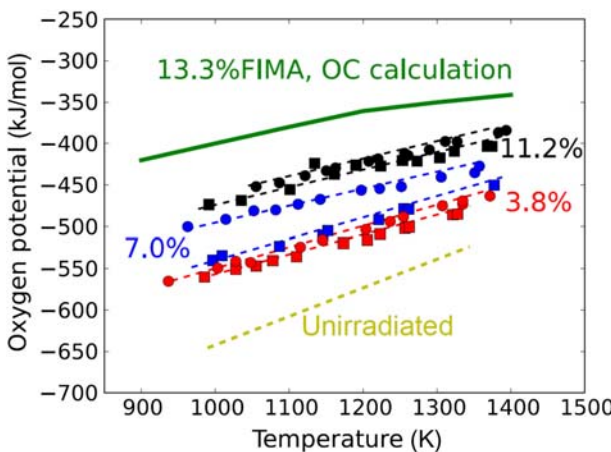


Figure 11.34 Oxygen potential for FBR MOX fuels (unirradiated and irradiated with burnups of 3.8, 7.0, 11.2, and 13.3 at.%).

Source: S. Gossé and C. Guéneau, Thermodynamic assessment of the palladium-tellurium (Pd-Te) system, *Intermetallics* **19**, 2011, 621–629 [31]. FBR, Fast breeder reactor.

To illustrate this tendency, oxygen potential data are presented in Fig. 11.34 for irradiated MOX fuels containing 20 mol.% of PuO_2 with different burnups (3.8, 7, 11.2, and 13.3 at.%). The results are compared to the reference oxygen potential for

Table 11.3 Fission product phases formed in UO_2 fuel at 1673 K as a function of oxygen potential.

Burnup	$\Delta G(\text{O}_2)$ (kJ/mol)	Phases at 1673 K
5	-540	Fluorite + ε + α
	-340	Fluorite + ε + α
	-270	Fluorite + ε + α
	-160	Fluorite + ε + α
10	-540	Fluorite + Pv + ε + α
	-340	Fluorite + Pv + S + ε + α + σ
	-270	Fluorite + Pv + S + ε + α + σ
	-160	Fluorite + S + ε + α
20	-540	Fluorite + Pv + ε + α
	-340	Fluorite + Pv + S + ε + α + σ
	-270	Fluorite + Pv + S + ε + α + σ
	-160	Fluorite + S + ε + α
30	-540	Fluorite + Pv + ε + α
	-340	Fluorite + Pv + S + ε + α + σ
	-270	Fluorite + S + ε + α + σ
	-160	Fluorite + S + ε + α

The phases are fluorite: $(\text{U},\text{FPs})\text{O}_2$, Pv or perovskite: $(\text{Ba},\text{Sr})(\text{U},\text{Mo},\text{Zr})\text{O}_3$, S or scheelite (tetragonal): $(\text{Ba},\text{Sr})\text{MoO}_4$, α : Pd-based FCC cubic phase, ε : Ru-based HCP hexagonal phase, S: intermetallic compound Mo_5Ru_3 with tetragonal structure.

Source: From E. Corcoran, B.J. Lewis, W.T. Thompson, J. Mouris, Z. He, Controlled oxidation experiments of simulated irradiated UO_2 fuel in relation to thermochemical modelling, *J. Nucl. Mater.* 414 (2011) 73–82.

the fresh fuel before irradiation. The measurements and the thermodynamic calculations clearly show the increase of the oxygen potential with an increasing burnup.

As experiments on irradiated fuels are very complex and expensive, some measurements have been conducted on unirradiated samples called SIMFUELS simulating the FP chemistry of irradiated fuels. These samples are prepared by sintering UO_2 powder together with small quantities of FP oxides that are adjusted to reach the chemical composition of an irradiated fuel with a given burnup.

As an example, Muromura et al. [36] and Adachi et al. [37] have investigated the FP chemistry of UO_2 fuels by performing heat treatments (1273 K–2273 K) followed by characterizations by X-ray diffraction of SIMFUEL samples with 5%–30% FIMA in a wide oxygen potential range ($-540 < \Delta G(\text{O}_2) < -160$ kJ/mol). Small amounts of FPs Ce, Nd, Cs, Rb, Ba, Sr, Zr, Mo, Ru, Rh, Pd, Ag, Cd, Sn, Te were incorporated in a UO_2 sample. The phases found in the different samples annealed at 1673 K as function of burnup and oxygen potential are reported in Table 11.3.

At low burnup (5%), only metallic precipitates are found in the fluorite matrix. From a burnup of 10%, oxide secondary phases are observed. The $(\text{Ba},\text{Sr})(\text{U},\text{Mo},\text{Zr})\text{O}_3$ perovskite phase is formed by oxidation of metallic precipitates containing molybdenum to perovskite phase where molybdenum is $\text{Mo}(4+)$ in the Zr site of the $(\text{Ba},\text{Zr})\text{O}_3$ phase. This is consistent with the oxygen potential for the oxidation

reaction of molybdenum: $[Mo]_{\text{metallic phase}} + [O_2]_{\text{fuel}} = [MoO_2]_{\text{Perovskite}}$ that occurs around -300 kJ/mol at 1673 K . For higher oxygen potential, the scheelite phase (BaMoO_4) is found and the perovskite phase tends to disappear. The formation of this phase may be due to the further oxidation of $\text{Mo}(4+)$ in the perovskite phase into $\text{Mo}(6+)$ in the BaMoO_4 phase occurring for an oxygen potential higher than -200 kJ/mol .

These results show that molybdenum, which can be distributed into several phases in the fuel, both metallic (white precipitates with HCP and/or FCC structures) and oxide phases ($(\text{Ba}, \text{Sr})(\text{U}, \text{Mo}, \text{Zr})\text{O}_3$ and BaMoO_4) can play the role of buffer. In fact, its oxidation state seems to fix the oxygen potential of the fuel.

Also several types of metallic phases form, mainly HCP and BCC phases.

11.3.2.3 Mass transport phenomena

As mentioned previously, a large temperature gradient exists between the center and the periphery of the fuel pellet:

- for LWR: $750 < T < 1300 \text{ K}$ and
- for FBR: $900 < T < 2300 \text{ K}$

In the oxide materials, oxygen diffuses much faster than the metals (uranium and plutonium) by several orders of magnitude.

As the average temperature of the fuel in LWRs is relatively low, thermal diffusion for metals does not occur. In normal conditions, once the FPs form, they stay in their position within the UO_2 matrix. Due to the higher number of thermal neutrons at the periphery of the fuel pellet, the fission rate is higher in this zone. It explains the higher concentration of plutonium and FPs in the rim of the fuel pellet. The plutonium content can be two to three times larger than in the center of the pellet (Fig. 11.35) [7].

In case of an incidental power ramp, due to the rapid rise of the temperature in the fuel (up to 2200 K at the center), the release of iodine, cesium, and tellurium occurs and consequently to the mass transport of these elements toward the inner colder side of the cladding. Depending on the oxygen potential of the fuel (and of its related oxygen stoichiometry), the gas species can be $\text{TeI}_2(\text{g})$, $\text{CsI}(\text{g})$ or $\text{Cs}(\text{g})$ and $\text{I}(\text{g})$, $\text{I}_2(\text{g})$ for more oxidized UO_{2+x} fuels [38]. Simultaneously oxygen is also transported to the cold part of the fuel.

In FBRs, as the temperature level of the fuel is very high, the large thermal gradient induces the mass transport of the elements from the hot zone to the colder region, at the periphery of the fuel, close to the cladding. This mass transport phenomenon leads to the redistribution of the elements (constituents of fuel matrix and the most volatile FPs) along the radius of the fuel pellet. It can lead to the corrosion of the steel cladding by the FPs such as Cs, Te, I, Mo, Pd, which is a limiting factor for the lifetime of the cladding.

Under isothermal conditions, the mass flux (flow) is driven by a chemical potential gradient. The large temperature gradient within the fuel pellet constitutes another driving force. Under these conditions the mass transport is called “solid-

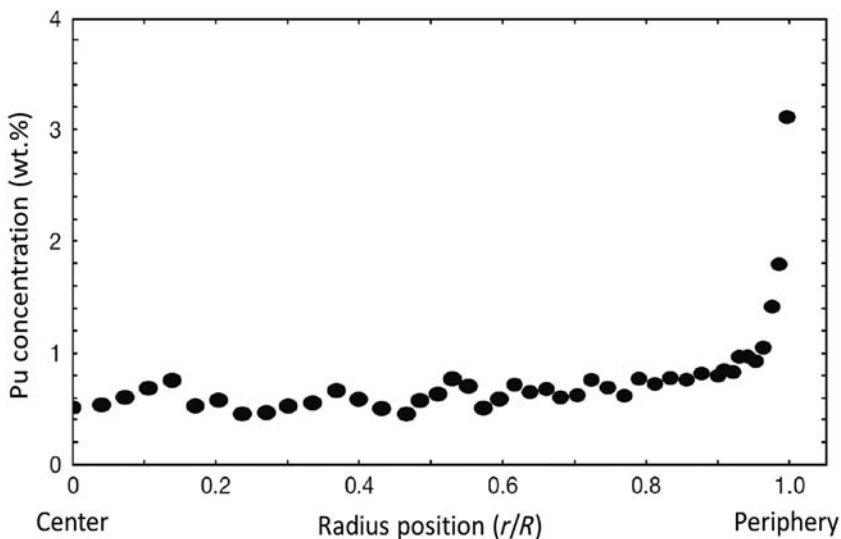


Figure 11.35 Plutonium distribution along the UO_2 pellet radius (LWR).

Source: T. Adachi, T. Muromura, H. Takeishi and T. Yamamoto, Metallic phases precipitated in UO_2 fuel: II. Onsoluble residue in simulated fuel, *J. Nucl. Mater.* **160**, 1988, 81–87 [37]. LWR, Light water reactor.

state oxygen thermal diffusion.” At high temperature, oxygen mass transport can also occur via the gas phase. Thus in FBR fuels, oxygen is transported via combined solid state and gas transport.

The oxygen diffusion under a temperature gradient through the fuel pellet radius is called thermal diffusion. The metal sublattice occupied by uranium and plutonium cations is assumed to be immobile. On the contrary, oxygen can move because of the existence of point defects (mainly oxygen vacancies and interstitials). As mentioned, oxygen vacancies and interstitials are the major defects in hypo- and hyperstoichiometric regions of MOX, respectively.

Thermal diffusion of oxygen vacancies and interstitials can be described using flux equations governed by thermodynamics of irreversible processes [39].

In $(\text{U},\text{Pu})\text{O}_{2+x}$ the flux of oxygen vacancies, J_v , is

$$J_v = -ND_v \left[\nabla x_v + \frac{(1-x_v)x_v}{1 + (\partial \ln \gamma_v / \partial \ln x_v)} \frac{Q_v^*}{RT^2} \nabla T \right]$$

whereas the flux of oxygen interstitials in hyperstoichiometric MOX is

$$J_i = -ND_i \left[\nabla x_i + \frac{x_i}{1 + (\partial \ln \gamma_i / \partial \ln x_i)} \frac{Q_i^*}{RT^2} \nabla T \right]$$

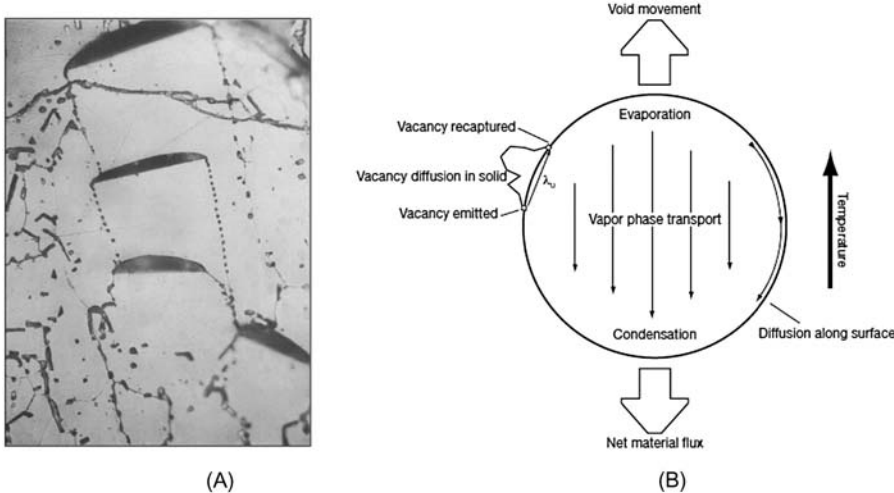


Figure 11.36 (A) Lenticular pores migrating up to the temperature gradient [38] and (B) schematic view of the mechanism of the pore migration [38].

Source: (A,B) B. Burens, Couplages thermo-chimie-mécaniques dans l'UO₂ – Application à l'interaction pastille-gaine, Thesis Aix-Marseille, 2014.

where N is the total number of oxygen atoms; D_v and D_i are the diffusion coefficients of vacancies and interstitial oxygen atoms; x_v and x_i are the atomic fraction of vacancies and interstitial oxygen atoms; γ_v and γ_i are the activity coefficients of vacancies and interstitial oxygen atoms; Q_v^* and Q_i^* are the molar heats of transport of vacancies and interstitial oxygen atoms; R is the gas constant; and T is the temperature.

In a MOX fuel pellet, mass is also transported via the so-called evaporation–condensation mechanism ([Fig. 11.36A and B](#)). When a solid fuel grain is adjacent to a void, it spontaneously vaporizes parts of its components as the solid solution $(\text{U}, \text{Pu})\text{O}_{2 \pm x}$ tends to establish an equilibrium with the gas phase constituted of a mixture of $\text{U}(\text{g})$, $\text{Pu}(\text{g})$, $\text{UO}_2(\text{g})$, $\text{PuO}_2(\text{g})$, and $\text{UO}_3(\text{g})$ gas species. The local equilibrium is defined by the equality of the chemical potential of the components in both phases (solid and gas). Once in the vapor phase, the gas species diffuse in the gas phase through the voids and cracks and condense in the colder region. As the vapor pressure of the U-bearing gas species is about 10 times greater than the Pu-bearing species, the transport of U-bearing species is dominant. Due to the large temperature gradient within the fuel pellet, there is a fast transport mechanism from the inner hot regions to the outer cooler regions.

Bober et al. [[40](#)] investigated the thermomigration of U–Pu by performing a series of out-of-pile experiments. A linear temperature gradient (1500 K/cm) was applied in MOX samples containing 15% PuO_2 with different oxygen stoichiometries. In [Fig. 11.37](#), the MOX sample with O/M = 2 was heated for 2 hours. Urania species $\text{UO}_3(\text{g})$ is expected to vaporize preferentially according to thermodynamics.

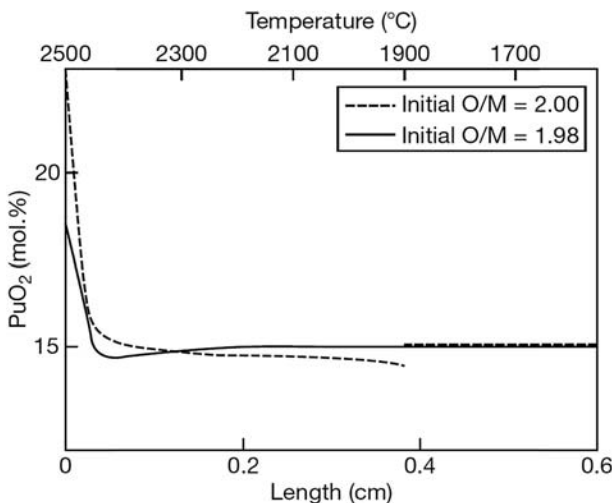


Figure 11.37 Plutonium radial redistribution along a $(\text{U},\text{Pu})\text{O}_2$ fuel pellet radius after heat treatment under a large linear thermal gradient in case of two different initial oxygen to metal ratios [38].

Source: B. Baurens, Couplages thermo-chimie-mécaniques dans l' UO_2 – Application à l’interaction pastille-gaine, Thesis Aix-Marseille, 2014.

Pore migration was postulated to move plutonium up to the temperature gradient but only in the region with $T > 2173$ K. At the outer surface, preferential evaporation occurred. It results in sharp plutonium enrichment in the outer part of the sample. For the second sample, heated for 48 hours, as the O/M ratio of 1.98 is close to the congruent vaporization composition, the preferential evaporation had a less large effect at the surface of the sample. But the longer heat treatment and lack of vaporization allowed thermodiffusion to occur, which induces plutonium migration from the hotter to the colder regions of the pellet. It leads to the existence of the minimum in the plutonium redistribution curve.

The flux of plutonium is given by the following expression [38]:

$$J_{\text{Pu}} = -N D_{\text{Pu}-\text{U}} \left[\nabla N_{\text{Pu}} + N_{\text{Pu}} N_{\text{U}} \frac{Q_{\text{Pu}-\text{U}}^*}{kT^2} \nabla T \right]$$

where N is the total number of metal atoms, $D_{\text{Pu}-\text{U}}$ is the interdiffusion coefficient of $\text{Pu}-\text{U}$ atoms, N_{Pu} is the number of plutonium atoms, N_{U} is the number of uranium atoms, $Q_{\text{Pu}-\text{U}}^*$ is the molar heat of transport of Pu and U atoms, R is the gas constant, and T is the temperature.

11.3.2.4 Fuel-cladding chemical interaction

Fuel-cladding chemical interaction (FCCI) is a general term designating all types of chemical interaction between the fuel and cladding inner surface. FCCI can be

one of the potential life-limiting factors for high burnup fuel elements, mainly in FRs.

In case of PWR or LWR, as the cladding material is often a Zr-based alloy and as the thermal level of the fuel element is not especially very high compared to those of FR, this phenomenon is not really problematic. Indeed, it consists mainly in a small oxidation of the inner part of the clad, leading to the formation of zirconia with a low kinetic.

If this phenomenon has not much impact in “standard operating conditions,” it can be really a source of problems in the case of power ramp. Indeed, after a long period of operation, the cladding material grows by creeping and comes in contact with the external fuel pellet. Then any significative change in power induces a consequent dilatation of the pellet, which will deform the cladding material.

In the case of a power ramp, where the temperature increases drastically in a short time, the release of Cs, Te, and I, designed as the “corrosive FP,” will be enhanced. Those volatile FPs, almost iodine, will be able to induce some cracks by SCC and thus to initiate clad failure. Some routes to limit these phenomena are underway:

- addition of a protective layer of zirconium, less sensitive to oxygen, to the cladding inner tube;
- addition of chromium, silicon, or titanium to the oxide ceramic, limiting the deformation due to creeping; and
- modification of the geometry of the cladding tube or of the fuel pellet in order to limit the FP release.

In case of FR $(U,Pu)O_2$ fuel, the cladding material is usually made of stainless steel, thus constituted of iron (major element), chromium, and nickel (15 at.% each one). In that case, FCCI can have drastic consequences, namely, a breach that can lead to failure of the clad.

Three types of phenomena can be observed [41] (see Fig. 11.38):

- The first type of cladding attack is a general oxidation and is confined mainly to the shallow inner surface of the clad, designed as matrix attack.
- The second one is an intergranular corrosion affecting only a shallow layer of the metal.
- The third one is a combined effect of matrix attack and the progression of intergranular corrosion which can progress into intragranular corrosion, and that is characteristically observed in local areas.

FCCI is the FP-accelerated oxidative attack of the cladding that is frequently observed in FR fuel pins involving volatile FPs such as Cs, Te, Pd, Mo, and I. Local breakdown of the protective layer and subsequent corrosion appear to depend on the local accumulation of observed major FPs, such as Cs and Te or I, which are considered important corrosive elements. Indeed, contrarily to PWR operating conditions, the thermal level encountered in FBR fuel during irradiation is very high with a temperature at the fuel center higher than 2000°C and a temperature gradient reaching $4000^{\circ}\text{C}/\text{cm}$. For the main reason, some particular phenomena that are not observed in standard PWR fuel occur with increasing burnup, the most specific one being the formation of a layer enriched in FPs located between the fuel periphery

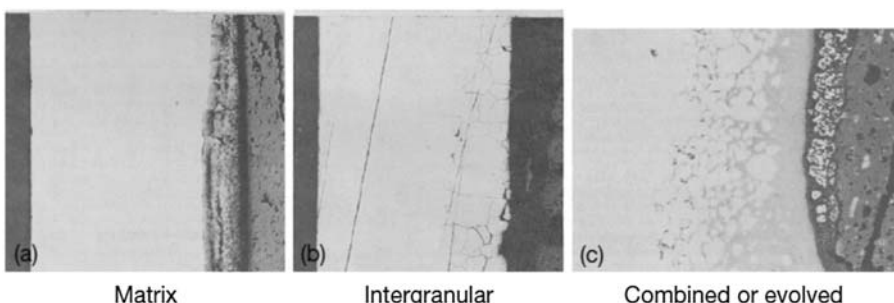


Figure 11.38 Three types of FCCI can be observed on stainless steel clad pins.

(A) Matrix attack, (B) intergranular, and (C) combined or evolved.

Source: K.J. Perry, G.F. Melde, W.H. McCarthy, R.N. Duncan, Fast reactor fuel element technology, in: R. Farmakes (Ed.), Proceedings of Conference, 13–15 April 1971, New Orleans, LA, American Nuclear Society, Hinsdale, IL, 1971, pp. 411–429 [42].

and the cladding material between 6 and 8 at.%. This layer, called JOG for *joint oxyde-gaine* [43] is due to the migration and association with oxygen and molybdenum of volatile FP created in the fuel pellet. The JOG formation may either degrade the heat transfer in case of good contact between fuel and cladding or improve it in case of gap reopened by clad deformation. Specifically, cesium and tellurium are thought to contribute to the most aggressive intergranular attack modes [44,45]. The FCCI phenomenon is generally recognized to be the result of the oxidation of chromium in the stainless steel cladding under the influence of FPs; cladding attack by Cs_2Te has not been considered as an oxidation mechanism of the cladding materials. Whether a chemical reaction between components of the irradiated fuel and constituents of the cladding can occur at all is determined by the thermodynamics of the reactions involved. When fuel surface oxygen potential exceeds the threshold necessary for oxygen transport to the cladding inner surface, excess oxygen and corrosive FPs can interact with the cladding inner surface leading to FCCI. Internal wastage of the stainless steel cladding is related to the complex phenomenon of corrosion established by the presence of FPs (Cs, I, and Te) and oxygen at the fuel–cladding interface. The threshold temperature for cladding attack is around 500°C.

11.4 Other fuels chemistry

11.4.1 Irradiated fuel chemistry

Like for oxide fuels, we find again the same main chemical families for carbide and nitride fuels: gaseous and volatile FP, noble metals precipitates, carbide or nitride precipitates, lanthanides in solution, and other secondary phases. A synthesis coming from [46] is presented in Fig. 11.39, including the fission creation inventory as well as the existence of information solubility data when available.

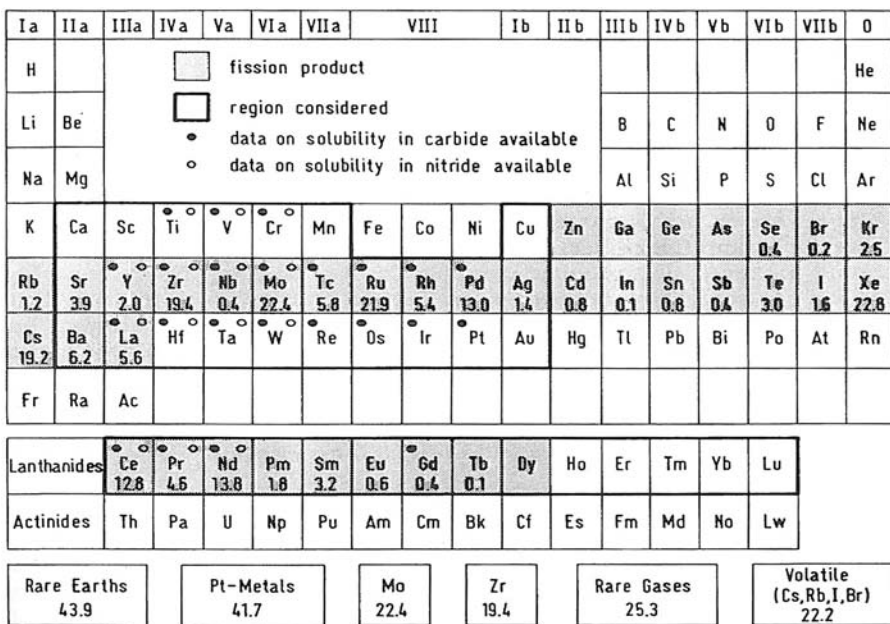


Figure 11.39 Stable or long-lived fission products created per 100 fissions of ^{239}Pu .

Source: M.G. Adamson, E.A. Aitken, R.W. Caputi, P.E. Potter, M.A. Mignanelli, Thermodynamics of nuclear materials, Proceedings of an International Symposium, vol. I, Jülich, January 29–February 2 1979, IAEA, Vienna, Austria, 1980, pp. 503–538 [45].

11.4.2 Fuel–cladding chemical interaction

Carbide and nitride fuels are generally irradiated at lower temperatures and lower radial temperature gradients than oxide fuels, although at high linear heat rating, which results in low FPs release rate. In addition, the volatile FPs (Br, I, Cs, and Rb) do not form carbides or nitrides and fuel pins are kept with low oxygen potential at the inner cladding surface. Thus oxidative FCCI of the FPs is not expected. Moreover, compatibility with cladding materials has been investigated in out-of-pile examinations and thermodynamic analyses. Indeed, the carburizing and nitriding of cladding and also the formation of intermetallic compounds of fuel and cladding are planned for those types of fuels [40].

In the case of hyperstoichiometric carbide (MC_{1+x}) fuels, the presence a sesquicarbide phase (M_2C_3) can lead to the carburization of the cladding material. The creep and swelling properties of stainless steels are sensitive to carburization and precipitation of M_{23}C_6 . On the other side, in the case of hypostoichiometric carbide (MC_{1-x}) that contains (U,Pu) metal as a second phase, low melting point eutectics with iron- or nickel-based cladding alloys may form and thus have an impact on the integrity of the whole fuel element.

In the case of hyperstoichiometric nitride (MN_{1+x}) fuel, the presence of sesquinitride phase (M_2N_3) can cause nitrogen penetration and form a reaction layer at the

cladding inner surface, which results in the clad nitriding and thus which decreases the ductility and increases the mechanical strength. For hypostoichiometric fuel (MN_{1-x}) that contains (U,Pu) metal, it can lead to the formation of an eutectic melting reaction between the free metal and the cladding, which results in the formation of (U,Pu)Fe₂- and (U,Pu)Ni₅-type intermetallic compounds.

However, regarding FCCI, MC or MN fuels are less impacted by fuel–cladding compatibility than oxide fuels, but that is not the same for metallic fuels. Indeed, these kinds of fuels are alloys containing U/Pu and metals such as Mo, Ru, Rh, Pd, Nb, or Zr. In fact, they are particularly concerned by lanthanide–cladding interactions, as lanthanides migrate into the fuel and diffuse into the cladding material rapidly [47,48]. Metallic fuels can also be affected by the formation of low-temperature eutectics (U,Pu)Zr-(Fe/Cr) and intermetallics of the type (U/Pu–Fe) [49].

11.5 Conclusion—outlooks

The chemistry of irradiated fuels is complex due to the large number of FPs that modify the fuel composition with the formation of secondary phases, the large thermal gradient, the radiation effects that change the physical properties of the fuel with time. In FRs the higher thermal and power level in the fuel leads to the restructuring of its microstructure.

Among the fuel properties the change in the thermal conductivity and melting point has a significant influence on the thermal performance of the fuel pin. Indeed, the formation and accumulation of xenon and krypton in the fuel–cladding gap reduce the thermal conductance of the gap. In high burnup conditions, the chemical activity of either oxygen, carbon or nitrogen depending on the type of fuel, depends on the chemical state of FPs. These activities partially govern the chemical interaction with the cladding material that can result in its corrosion and thus affect its mechanical resistance in normal operating conditions, and the chemical interaction with other materials in case of severe accident.

For safety reasons, it is thus essential to be able to describe and precisely predict the physicochemical behavior of the fuel during irradiation. For that purpose, not only thermodynamics but also kinetics of chemical reactions occurring in the fuel has to be taken into account into FPCs.

Even if experimental methods to characterize the materials have made a lot of progress, there is still a lack of experimental characterizations of irradiated fuel samples because of the expensive cost of these analyses. Furthermore, the small quantities of the FPs make it tricky the identification of the chemical state of these elements in the fuel matrix. Also due to the change in their amount with time in relation with neutronic (creation, absorption) that has to be taken into account when interpreting the characterizations. Today, oxide fuel and in a smaller extent metallic fuel behavior are quite well understood, but there is still a noticeable lack of information regarding the carbide or nitride fuel behavior.

Modeling in materials science is progressing very quickly. The aim is to develop multiscale modeling techniques to simulate the materials operating behavior. This

promising approach allows coupling atomic scale calculations (first principle, molecular dynamics ...) and mesoscopic modeling (such as computational thermodynamics) to improve the understanding of the complex phenomena occurring at different scales in the irradiated fuels and estimate basic data, in some cases, not reachable, up to now, by experimental characterizations. Computational thermodynamics applied to nuclear materials has already substantially contributed to the design of nuclear materials ranging from oxide to metal fuels processing and to the assessment of the cladding behavior. In the coming years the coupling of those reliable computational tools as well as the increase of power computing will certainly improve the modeling of the irradiated fuels chemistry in the FPC.

References

- [1] M. Pelletier, Quel Combustible Pour les RNR-Na?, Clefs du CEA, 2012, pp. 32–37.
- [2] G. Martin, P. Garcia, L. Van Brutzel, B. Dorado, S. Maillard, Effect of the cascade energy on defect production in uranium dioxide, *Nucl. Instrum. Methods Phys. Res., B* 269 (2011) 1727–1730.
- [3] D.R. Olander, Report No.TID-26711-P1 Fundamentals of Aspects of Nuclear Reactor Fuel Elements, Technical Information Center, Office of Public Affairs, Energy Research and Development Administration, 1976.
- [4] J.H. Davies, F.T. Ewart, The chemical effects of composition changes in irradiated oxide fuel materials, *J. Nucl. Mater.* 41 (1971) 143–155.
- [5] M.H.A. Piro, J. Banfield, K.T. Clarno, S. Simunovic, T.M. Besmann, B.J. Lewis, et al., Coupled thermochemical, isotopic evolution and heat transfer simulations in highly irradiated UO₂ nuclear fuel, *J. Nucl. Mater.* 441 (2013) 240–251.
- [6] H. Kleykamp, The chemical state of the fission products in oxide fuels, *J. Nucl. Mater.* 131 (1985) 221–246.
- [7] B. Lewis, W. Thompson, F. Iglesias, 2.20 – Fission product chemistry in oxide fuels, *Compr. Nucl. Mater.* 2 (2012) 515–546.
- [8] J. Noirot, I. Zacharie-Aubrun, T. Blay, Focused ion beam–scanning electron microscope examination of high burn-up UO₂ in the center of a pellet, *Nucl. Eng. Technol.* 50 (2018) 259–267.
- [9] M. Pelletier, SFR Fuel in Sodium Cooled Nuclear Reactors, DEN Monographs, CEA Saclay et Groupe Moniteur, Paris, 2016.
- [10] Y. Guérin, Chapter 2.21 Fuel performance of fast spectrum oxide fuel, in: R.J.M. Konings (Ed.), *Comprehensive Nuclear Materials*, Elsevier, 2012, pp. 548–572.
- [11] Y. Guérin, J. Noirot, D. Lespiaux, C. Struzik, P. Garcia, P. Blanpain, et al., Microstructure evolution and in-reactor behaviour of MOX fuel, in: ANS International Topical Meeting on LWR Fuel Performance, Park City, UT, 2000.
- [12] J. Noirot, L. Desranges, J. Lamontagne, Detailed characterisations of high burn-up structures in oxide fuels, *J. Nucl. Mater.* 372 (2008) 318–339.
- [13] D.D. Baron, L. Hallstadius, Chapter 2.19 fuel performance of light water reactors (uranium oxide and MOX), in: R.J.M. Konings (Ed.), *Comprehensive Nuclear Materials*, Elsevier, 2012, pp. 481–514.
- [14] G. Hofman, L.C. Walters, Metallic fast reactor fuels, in: R.W. Cahn, P. Haasen, E.J. Kramer (Eds.), *Materials Science and Technology*, vol. 10A, 1994 VCH Publishers Inc., New York, 1994, pp. 1–43.

- [15] R. Kennedy, (2019). *Nuclear reactors physics, fuels, and systems*. Frédéric Joliot/Otto Hahn Summer School, Karlsruhe.
- [16] C. Guéneau, N. Dupin, B. Sundman, C. Martial, J.-C. Dumas, S. Gossé, et al., Thermodynamic modelling of advanced oxide and carbide nuclear fuels: description of the U–Pu–O–C systems, *J. Nucl. Mater.* 419 (1–3) (2011) 145–167.
- [17] R.J.M. Konings, O. Benes, A. Kovács, D. Manara, D. Sedmidubský, L. Gorokhov, et al., The thermodynamic properties of the f-elements and their compounds. Part 2. The lanthanide and actinide oxides, *J. Phys. Chem. Ref. Data* 43 (1) (2014) 013101.
- [18] Y. Ma, P. Garcia, J. Léchelle, A. Miard, L. Desgranges, G. Baldinozzi, et al., Characterization of oxygen defect clusters in UO_{2+x} using neutron scattering and PDF analysis, *Inorg. Chem.* 57 (2018) 7064–7076.
- [19] L. San-Felice, R. Eschbach, P. Bourdot, Experimental validation of the DARWIN2.3 package for fuel cycle applications, *Nucl. Technol.* 184 (2013) 217–232.
- [20] I. Gauld, O. Hermann, R. Westfall, ORIGEN scale system module to calculate fuel depletion, actinide transmutation, fission product buildup and decay, and associated radiation terms, in: Tech. Rep. ORNL/TM-2005/39, Version 6, vol. II, Sect. F7, Oak Ridge National Laboratory, 2005.
- [21] R.J. Parrish, K.E. Wright, A.J. Winston, C. McKinney, J.M. Harp, A. Aitkaliyeva, Characterization of solid fission products in 13.7% FIMA MOX fuel using electron microscopy techniques, *J. Nucl. Mater.* 524 (2009) 67–69.
- [22] P. Garcia, G. Carlot, B. Dorado, S. Maillard, G. Martin, J.Y. Oh, et al., Chapter 1. Mechanisms of microstructural changes of fuel under irradiation, in: NEA/NSC/R (2015)5 Report, 2015, 22–58.
- [23] M.H.A. Piro, D. Sunderland, S. Livingstone, J. Sercombe, W. Revie, A. Quastel, et al., A review of pellet-clad interaction behaviour in zirconium alloy fuel cladding, *Ref. Module Mater. Sci. Mater. Eng.* (2017).
- [24] C. Guéneau, S. Gossé, A. Quaini, N. Dupin, B. Sundman, M. Kurata, et al., FUELBASE, TAF-ID databases and OC software: advanced computational tools to perform thermodynamic calculations on nuclear fuel materials, in: Proceedings of the Seventh European Review Meeting on Severe Accident Research (ERMSAR-2015), TAF-ID Database Version 8, 24–26 March 2015, Marseille, France, NEA/OECD, 2015. <<https://www.oecd-nea.org/science/taf-id/>>.
- [25] G. Dottavio, Y. Pontillon, L. Desgranges, C. Guéneau, R. Belin, Characterising the U–Nd–O miscibility gap by an experimental and a theoretical approach, *J. Nucl. Mater.* 458 (2015) 394–405.
- [26] A. Quaini, C. Guéneau, S. Gossé, N. Dupin, B. Sundman, E. Brackx, et al., Contribution to the thermodynamic description of the corium – the U–Zr–O system, *J. Nucl. Mater.* 501 (2018) 104–131.
- [27] R.G. Brese, J.W. McMurray, D. Shin, T.M. Besmann, Thermodynamic assessment of the U–Y–O system, *J. Nucl. Mater.* 460 (2015) 5–12.
- [28] C. Le Gall, Contribution to the Study of Fission Products Release From Nuclear Fuels in Severe Accident Conditions: Effect of the PO_2 on Cs, Mo and Ba Speciation (Ph.D. thesis), Université Grenoble Alpes, 2018. <<https://tel.archives-ouvertes.fr/tel-02052819>>.
- [29] J. Lamontagne, State-of-the art and challenges for post-irradiation examinations, in: Proceedings of the Nuclear Materials Conference (NUMAT 2014), 27–30 October 2014, Clearwater Beach, FL, 2014.

- [30] S. Gossé, N. Dupin, C. Guéneau, J.M. Joubert, Thermodynamic assessment of the Pd-Rh-Ru system using calphad and first-principle methods, *J. Nucl. Mater.* 474 (2016) 163–173.
- [31] S. Gossé, C. Guéneau, Thermodynamic assessment of the palladium-tellurium (Pd-Te) system, *Intermetallics* 19 (2011) 621–629.
- [32] K. Samuelsson, J.C. Dumas, B. Sundman, J. Lamontagne, C. Guéneau, Simulation of the chemical state of high burnup (U,Pu) O_2 fuel in fast reactors based on thermodynamic calculations, *J. Nucl. Mater.* 532 (2020) 151969.
- [33] B. Sundman, U.R. Kattner, M. Palumbo, S.G. Fries, OpenCalphad – a free thermodynamic software, *Integr. Mater. Manuf. Innov.* 4 (2015) 1–15.
- [34] K. Une, M. Oguma, Oxygen potential of UO_2 fuel simulating high burnup, *J. Nucl. Sci. Technol.* 20 (1983) 844–851.
- [35] E. Corcoran, B.J. Lewis, W.T. Thompson, J. Mouris, Z. He, Controlled oxidation experiments of simulated irradiated UO_2 fuel in relation to thermochemical modelling, *J. Nucl. Mater.* 414 (2011) 73–82.
- [36] T. Muromura, T. Adachi, H. Takeishi, Z. Yoshida, T. Yamamoto, K. Ueno, Metallic phases precipitated in UO_2 fuel: I. Phases in simulated fuel, *J. Nucl. Mater.* 151 (1988) 318–326.
- [37] T. Adachi, T. Muromura, H. Takeishi, T. Yamamoto, Metallic phases precipitated in UO_2 fuel: II. Onsoluble residue in simulated fuel, *J. Nucl. Mater.* 160 (1988) 81–87.
- [38] B. Baurens, Couplages thermo-chimie-mécaniques dans l' UO_2 – Application à l'interaction pastille-gaine, Thesis Aix-Marseille, 2014.
- [39] M.J. Welland, Chapter 3.21: Matter transport in fast reactors fuels, in: R.J.M. Konings (Ed.), *Comprehensive Nuclear Materials*, Elsevier, 2012.
- [40] M. Bober, C. Sari, G. Schumacher, Redistribution of plutonium and uranium in mixed (U,Pu) oxide fuel materials in a thermal gradient, *J. Nucl. Mater.* 39 (1971) 265–284.
- [41] K. Maeda, Chapter 3.16: Ceramic fuel-cladding interaction, in: R.J.M. Konings (Ed.), *Comprehensive Nuclear Materials*. 3 (16) (2012) 443–483.
- [42] K.J. Perry, G.F. Melde, W.H. McCarthy, R.N. Duncan, Fast reactor fuel element technology, in: R. Farmakes (Ed.), *Proceedings of Conference*, 13–15 April 1971, New Orleans, LA, American Nuclear Society, Hinsdale, IL, 1971, pp. 411–429.
- [43] M. Tourasse, M. Boidron, Fission products behaviour in Phénix fuel pins at high burn-up, *J. Nucl. Mater.* 188 (1992) 49–57.
- [44] M.G. Adamson, Technical committee, in: *Meeting on Fuel and Cladding Interaction, Proceedings of the International Working Group on Fast Reactors*, IWGFR/ 16, 21–25 February 1977, Tokyo, Japan, IAEA, Austria, 1977, pp. 170–189.
- [45] M.G. Adamson, E.A. Aitken, R.W. Caputi, P.E. Potter, M.A. Mignanelli, Thermodynamics of nuclear materials, *Proceedings of an International Symposium*, vol. I, Jülich, January 29–February 2 1979, IAEA, Vienna, Austria, 1980, pp. 503–538.
- [46] Hj. Matzke, *Science of Advanced LMFBR fuels*, Elsevier Publisher, North Holland, 1986.
- [47] C. Matthews, C. Unal, J. Galloway, D.D. Keiser Jr., S.L. Hayes, Fuel-cladding chemical interaction in U-Pu-Zr metallic fuels, *Nucl. Technol.* 198 (3) (2017) 231–259.
- [48] Y. Xiea, J. Zhangb, X. Lib, J.P. Islerb, M.T. Bensone, R.D. Marianic, et al., Lanthanide migration and immobilization in metallic fuels, *Prog. Nucl. Energy* 109 (2018) 233–238.
- [49] D.D. Keiser Jr., Recent progress in metal fuel-cladding interaction research, in: R. Murthy (Ed.), *Materials Science and Materials Engineering*, Elsevier, Amsterdam, 2015.

This page intentionally left blank

Reprocessing and recycling

12

Guillermo D. DelCul and Barry B. Spencer

Isotope and Fuel Cycle Technology Division, Oak Ridge National Laboratory, Oak Ridge, TN, United States

12.1 Introduction

The societal perception of nuclear technology is ambivalent. Many people recognize the great benefits of nuclear technology such as the ability of nuclear power plants to generate massive amounts of electricity with very low carbon emissions as well as the contributions of nuclear medicine as a powerful means of diagnostics and treatment of many illnesses. However, there are profound fears and reservations concerning the use of nuclear power, mostly due to the connection with nuclear weapons, severe nuclear accidents (e.g., Three Mile Island, Chernobyl, and Fukushima), and legacy of nuclear wastes. Addressing the public concerns related to nuclear waste can have a big impact on the public acceptability of nuclear technology.

Reprocessing is performed in some countries to permit the recovery and recycle of reusable components in used nuclear fuel and to minimize wastes requiring geologic disposal. In that regard, used nuclear fuel may be considered a resource. Separation of long-lived radioactive actinides for use as fuel materials greatly reduces the long-term radiotoxicity of the remaining waste. When properly practiced, reprocessing should address the public concerns related to “nuclear wastes.”

Early reprocessing was centered on the recovery of plutonium for military purposes, and the technology was later adapted to the processing of used light-water reactor (LWR) commercial fuel but still centered on the fissile value of the residual Pu (~1% of the mass) [1,2]. Because of this historical legacy, reprocessing attracts some negative connotation. Most recent developments prescribe reprocessing as a means to provide fissile material for “advanced reactors” several decades into the future.

Neither recovery of the fissile value of residual plutonium nor reprocessing to provide fuel materials for advanced reactors have encouraged expanding reprocessing, and this technology is not fully supported even in the nuclear community itself as many prefer the direct disposal of used nuclear fuel in geological repositories. Consequently, the public concerns regarding a legacy of nuclear wastes for future generations remain mostly unabated. However, when reprocessing is presented as a technology that permits the recovery, recycle, and reuse of most of the components in used nuclear fuel while minimizing the wastes requiring geologic disposal,

the perception becomes significantly more positive. Existing technologies allow the reuse of a very large fraction of the components of used fuel in existing reactors, and the same technologies can be adapted for new types of future reactors as they become a reality [3].

Beyond the association of reprocessing with production of nuclear weapons and nuclear waste, there are two major remaining challenges: (1) perceived risks of proliferation and (2) the cost of reprocessing. The proliferation concerns and the need for rigorous safeguards and physical protection are rather similar for storage, reprocessing, or geological disposal. An internationally recognized reprocessing facility, such as the Rokkasho Reprocessing Plant in Japan, is a fortified, safeguarded, highly scrutinized, heavily guarded, and protected facility, which addresses proliferation concerns [4].

Both geological disposal and reprocessing are expensive. The actual cost of either option is difficult to evaluate as they are mostly “one-of-a-kind facilities” that are very much dependent on the local, political, and regulatory environment. In the United States (c.2007), studies indicated that the estimated disposal costs were \$550/kg and estimated reprocessing costs ranged from \$585/kg to \$1300/kg [5]. However, at about the same cost, reprocessing has some very clear advantages: it recycles valuable energy and chemical resources, creates new long-term high-tech industries with high-paying jobs, and minimizes legacy nuclear waste requiring geologic disposal. In either case the overall cost of direct disposal and reprocessing is not a significant fraction of the overall nuclear fuel cycle, but a reprocessing plant represents a significant cost for a single installation. Geological disposal will always be needed, but for a greatly reduced volume when reprocessing and recycle are implemented to recover both the uranium and plutonium. Direct disposal of 1000 t of fuel (heavy metal) requires $\sim 2000 \text{ m}^3$ of repository space. Reprocessing, as presently done, reduces the volume to about 300 m^3 . Enhanced reprocessing can further reduce the volume to under 10 m^3 [3].

12.1.1 Characteristics of used nuclear fuel

The current fleet of nuclear-powered electricity-generating plants in the United States uses LWR technology. Fuel for these reactors is uranium, generally enriched to 3–5 wt.% ^{235}U with the remainder being ^{238}U . The chemical form of the uranium is uranium dioxide (UO_2), formed into ceramic pellets that are encased in zirconium alloy (e.g., Zircaloy) tubing to form fuel pins. A number of these fuel pins are combined into fuel assemblies, held together with stainless steel and Inconel spacer grids. Heavy stainless-steel nozzles are affixed to each end of the fuel assembly to facilitate handling, placement in the reactor, and insertion of control rods at the top of the assembly. For example, a Westinghouse pressurized water reactor (PWR) fuel assembly is shown in Fig. 12.1. It has a 17×17 pin array, of which 264 array positions are occupied by fuel pins and the remaining positions are used for control rods. A common PWR fuel assembly contains $\sim 525 \text{ kg}$ of UO_2 ($\sim 461 \text{ kg}$ U metal), $\sim 108 \text{ kg}$ of Zircaloy, and $\sim 26 \text{ kg}$ of other steel-based hardware [6]. Details on various types of fuel assemblies can be found elsewhere [7].



Figure 12.1 Westinghouse PWR fuel assembly (Oak Ridge National Laboratory Photo 3897-77). *PWR*, Pressurized water reactor.

Nuclear fission of the ^{235}U produces heat, neutrons, and other subatomic particles, and fission products. Some of the neutrons can transmute the uranium, especially the ^{238}U , to transuranium (TRU) elements, such as ^{239}Pu , that accumulate over time and also participate in the fission process. As the fissile content is consumed and the fission products build up, the fuel elements must eventually be removed from the reactor and replaced, usually after 3–5 years. Fig. 12.2 shows the calculated average weight composition of the used nuclear fuel produced in commercial reactors in the United States from 1968 to 2002 based on 40 years of postirradiation cooling [8].

Present reprocessing practices in France, United Kingdom, and Russia recover the uranium and plutonium from the used nuclear fuel. The recovery of fissile content in the Pu and U streams compared to the use of fuel made from fresh uranium ore is a borderline commercial proposition. However, the direct disposal of spent LWR fuel requires geological repositories that are very difficult to site and very expensive to build and operate [estimations range from \$255k to \$755k per metric ton of uranium (MTU)] after adjusting to calendar year (CY) 2018 dollars [9,10].

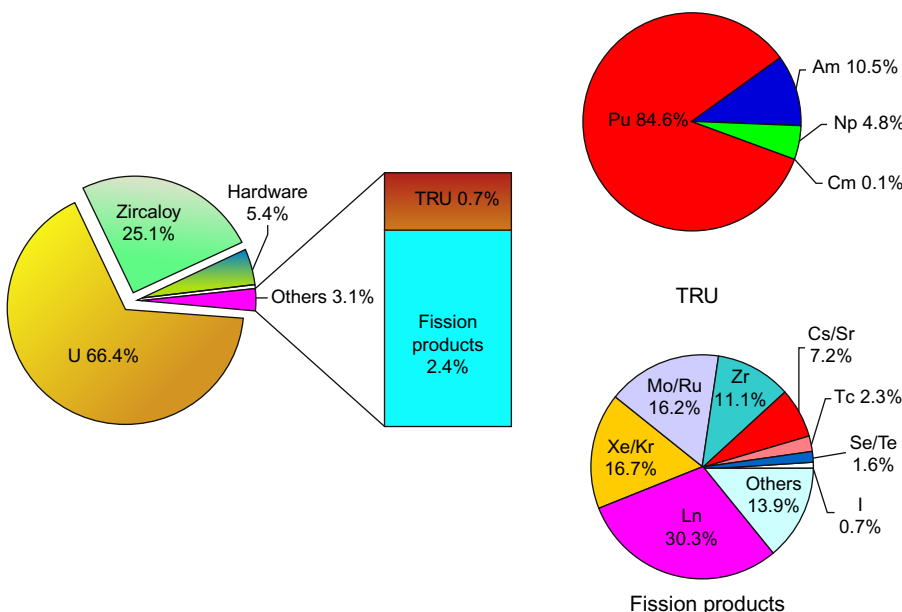


Figure 12.2 Average weight composition, PWR and BWR fuel, accumulated from 1968 to 2002. *BWR*, Boiling water reactor; *PWR*, pressurized water reactor.

The construction cost of the Yucca Mountain nuclear waste repository in the United States, a project that has experienced multiple delays and protracted opposition, implies a disposal cost of about \$790k/MTU (CY 2007 dollars), based on life-cycle costs and an expanded capacity [11], and approximately \$1500k/MTU (CY 2008) based on the most recent 2008 estimate at the original design capacity (63,000 t) [12]. The Onkalo facility under construction in Finland followed a long process to reach consensus. Based on the Onkalo facility's capacity and estimated cost [13], disposal cost is about \$600k/MTU (CY 2018 dollars). Most recent news updated the cost to about \$660k/MTU [14]. Chapter 13, Spent nuclear fuel and disposal, discusses spent fuel and disposal in greater detail.

When all the factors are considered, reducing geological disposal costs may be the most significant economic factor determining the viability of reprocessing. In addition to the actinides that can be used for new fuel, other components that currently require a geologic repository potentially could be recovered, further reducing the amount of waste.

Studies and recent developmental efforts have shown that the recovery of other components, such as the zirconium in cladding, is also possible and economically viable [15,16]. Table 12.1 lists the main groups of components that potentially can be recycled, totaling about 99 wt.% of the used nuclear fuel [3].

Advanced reactors that are under development use very different nuclear fuels (metallic fuel, particle fuel, molten salts, etc.) and may eventually be deployed in commercial power systems. These fuels will require the adaptation of the present

Table 12.1 Recoverable components in used nuclear fuel.

Component	Fraction (wt.%)
Uranium	66.4
Zirconium	24.6
Hardware (steel, Inconel, etc.)	5.4
Transuranics	0.7
Light lanthanides (La, Ce, Pr, Nd)	0.7
Xenon gas	0.4
Noble metals (Ru, Rh, Pd, Ag)	0.3

Source: Adapted from E.D. Collins, G.D. Del Cul, J.E. Rushton, K.A. Williams, A Practical Solution to Used Nuclear Fuel Treatment to Enable Sustained Nuclear Energy and Recovery of Vital Materials, ORNL/TM-2010/81, Oak Ridge National Laboratory, Oak Ridge, TN, 2010.

reprocessing technology, or the use of very different approaches, and will be described in some detail in the following sections.

12.1.2 Reuse of uranium from used light-water reactor fuel

Uranium is the largest component in used nuclear fuel. In LWR fuel, uranium comprises about 66 wt.% of the total mass and 95 wt.% of the oxide fuel (Fig. 12.2). Residual ^{235}U enrichment for all discharged LWR fuel in the United States as of 2002 is estimated to be 0.84 wt.% [0.77 wt.% for boiling water reactor (BWR) fuel and 0.88 wt.% for PWR fuel], and is increasing because of greater initial enrichment in newer fuels. As an example, in CY 2018, the average residual enrichment for BWR used fuel is estimated to be around 0.94 wt.%, and greater than 1 wt.% for used PWR fuels. Other significant uranium isotopes in used fuel include ^{232}U (<5 ng/g U), ^{234}U (0.02–0.04 wt.%), and ^{236}U (0.3–0.7 wt%) [17,18].

Uranium recovered from commercial LWR used fuels can be reused by either recycling it as fuel for heavy-water reactors, such as the Canada Deuterium Uranium (CANDU) reactor, or reenriching it as feedstock for LWR fuels.

12.1.2.1 Direct reuse in heavy-water reactors

Heavy-water reactors operating with natural uranium (NU) fuel, such as the CANDU, can utilize uranium recovered from LWR reactors that has been diluted with some depleted uranium to produce a fuel with an effective enrichment equivalent to NU, taking into account the presence of ^{234}U and ^{236}U [19]. The use of NU was demonstrated in the Qinshan CANDU reactors in China. Refueling with recycled uranium (RU) without dilution could increase the burnup by about 30% [20]. A typical CANDU reactor with NU oxide fuel will use approximately 5200 fuel bundles per year, or about 100 MT of NU per year. Depending on the specific CANDU nuclear power plants and their fuel cycles, the CANDU fleet in Canada could use approximately 2000–2800 MT of RU per year.

About twice as much energy can be extracted from the initial uranium without reenrichment when the RU is used in a CANDU nuclear power plant. Another important consideration is that the RU feed for CANDU fuel may not require the same stringent levels of purification that are required for reenrichment feed because of its intrinsically better neutron economy.

12.1.2.2 Reenrichment option

Currently, low-enriched uranium fuels are prepared commercially by downblending of excess higher enrichment uranium stockpiles and by reenrichment of NU using centrifuges.

Some 16,000 MT of RU from Magnox reactors in the United Kingdom has been used to make about 1650 MT of enriched advanced gas-cooled reactor fuel. In Belgium, France, Germany, and Switzerland, over 8000 MT of RU has been recycled in nuclear power plants. In France, Électricité de France reported in 2011 that 60% of the uranium recovered from its used nuclear fuel ($\sim 0.8\% \text{ }^{235}\text{U}$) was reenriched at Seversk and recycled to four reactors at Cruas (900 MWe PWRs). These reactors have operated with a 100% RU core since the mid-1980s. At present the recovered uranium at Cruas is being stored to produce a strategic stockpile. In Russia, more than 2500 MT of RU has been recycled in Reaktor Bolshoy Moshchnosty Kanalny fuel. In Japan, about 350 MT of RU from the Tokai reprocessing plant was used at the Ningyo-toge enrichment facility for reenrichment examination [21].

In the United States, there is no current source of RU because commercial reprocessing is not practiced. Historically, however, more than 100,000 MT of RU was fed into three gaseous diffusion enrichment plants in the United States [22]. This experience demonstrated at large scale the feasibility and economics of reenriching RU.

In the case of reenrichment the RU replaces a portion of the NU feedstock required to fuel the fleet of reactors: replacing $\sim 18\%$ for 3 wt.% assay fuel and $\sim 12\%$ for 4.5 wt.% assay fuel.

Two strategies are possible: (1) to reenrich the RU and use the product in a small number of reactors as practiced in the Cruas reactors in France [23] or (2) to use the uranium recovered from one reactor and blending it with sufficient natural-assay uranium hexafluoride (UF_6) to produce the required enrichment product for fueling the next reactor. In the latter scenario the uranium product can be made to meet the standard of the American Society for Testing and Materials [17].

The radioactivity of RU is significantly higher than that of NU because of the presence of ^{232}U , ^{233}U , and elevated ^{234}U as well as traces of fission products. During reenrichment, most of the lighter ^{232}U , ^{233}U , and ^{234}U , and 60%–70% of the ^{236}U , follow the enriched uranium stream. Consequently, the resulting uranium tails should follow the disposal route of standard uranium tails.

Without the benefit of blending the reenriched product, although entirely manageable, handling requires some additional shielding and some comprehensive radiation-management controls. A technology developed in Russia separates the

^{232}U from the enriched product by adding a Freon carrier gas, $\text{C}_8\text{H}_3\text{F}_{13}$, which is inert to UF_6 and whose molecular weight ($\text{MW} = 346$ amu) matches that of $^{232}\text{UF}_6$. This eliminates the need for special handling [24].

In a typical PWR neutron spectrum, only about 5% of the neutrons captured by ^{236}U result in fission. Since ^{236}U is a mostly nonfissioning neutron absorber, its presence imposes a reactivity penalty on fuel (the so-called ^{236}U penalty), generally expressed as the increase in ^{235}U enrichment required to compensate for the level of ^{236}U present. Without the benefit of blending the ^{236}U penalty is significant (e.g., 0.5% increase in ^{235}U). System studies have shown that blending allows for multiple-reactor recycling of recovered uranium [17]. Elevated ^{234}U is sometimes mentioned as a potential problem. However, because it is a fertile isotope with ^{235}U as an activation product, it does not introduce an actual net reactor penalty at the end of the fuel cycle [17].

12.1.2.3 Regenerated mixture

The REMIX (regenerated mixture) process was developed by the V. G. Khlopin Radium Institute for Tenex. It uses the entire $\text{U} + \text{Pu}$ fraction resulting from the reprocessing of LWR fuel and adds ~ 20 wt.% of high-assay low-enriched uranium (i.e., $\sim 19.75\%$ ^{235}U) to produce fuel with about 1% ^{239}Pu and 4% ^{235}U , which can sustain a burnup of 50 GWd/MT over 4 years [25]. The spent REMIX fuel can be subjected to about five cycles of U/Pu recovery when using a high-assay low-enriched uranium addition. Table 12.2 shows an approximate composition of the fuel during the first, third, and fifth REMIX cycle.

The REMIX process significantly reduces the amount of fuel requiring geological disposal but adds the reprocessing costs. Rosatom loaded three experimental REMIX fuel assemblies into the Balakovo unit 3 in June 2016. They will remain for two fuel cycles of about 3 years. Commercial application is planned for the mid-2020s [26].

Table 12.2 Uranium and plutonium content in regenerated mixture fuel^a.

	First cycle	Third cycle	Fifth cycle
^{232}U	2.4×10^{-6}	5.6×10^{-6}	7.3×10^{-6}
^{235}U	41.71	43.12	44.65
^{236}U	4.71	9.74	12.19
^{238}Pu	0.24	0.76	0.98
^{239}Pu	5.38	7.25	7.23
^{240}Pu	2.54	3.65	3.71
^{241}Pu	1.13	1.78	1.86
^{242}Pu	0.71	1.90	2.67
$^{239,241}\text{Pu} + ^{235}\text{U}$	48.2	52.1	53.7

^aValues are in g/MTHM.

Source: Adapted from D.V. Postovarova, N.V. Kovalev, M.S. Onegin, B.A. Bibichev, Radiation characteristics of REMIX fuel during multiple recycling in VVER-1000 reactors, Nucl. Energy Technol. 2 (2) (2016) 119.

12.1.3 Zirconium recycle and disposition options

Common types of Zircaloy cladding, Zircaloy-2 and Zircaloy-4, contain about 98% Zr, 1.2%–1.7% Sn, and fractional percentages of Fe, Cr, and Ni [27]. Trace amounts of other elements, including O, N, Hf, Mg, Mn, Mo, W, Ti, and U, are also present [28]. Advanced zirconium alloys, such as Zirlo and M5, contain about 1% niobium with or without tin; zirconium remains 98%–99% [29].

Zirconium represents about 25% of the mass of used nuclear fuel as shown in Fig. 12.2. Therefore there is significant interest to reduce the amount of Zircaloy requiring expensive geologic disposal.

As Zircaloy is nominally hafnium-free, the recovered zirconium is similarly low in hafnium and has a significant value. Moreover, recovery for reuse, or disposal as low-level waste, avoids the high cost of geologic disposal (\$20k/MT vs. ~\$1M/MT, respectively) [12,30,31]. Nonetheless, ^{93}Zr produced by neutron activation renders the recovered zirconium radioactive. Since the ^{93}Zr is long-lived (half-life 1.5×10^6 years) and the beta emission is weak, the zirconium may be suitable for reuse in nuclear applications. The zirconium can be separated from alloying components in the Zircaloy, and from associated fuel materials, by converting it to volatile zirconium tetrachloride, as discussed in Section 12.2.5. Fig. 12.3 shows how the

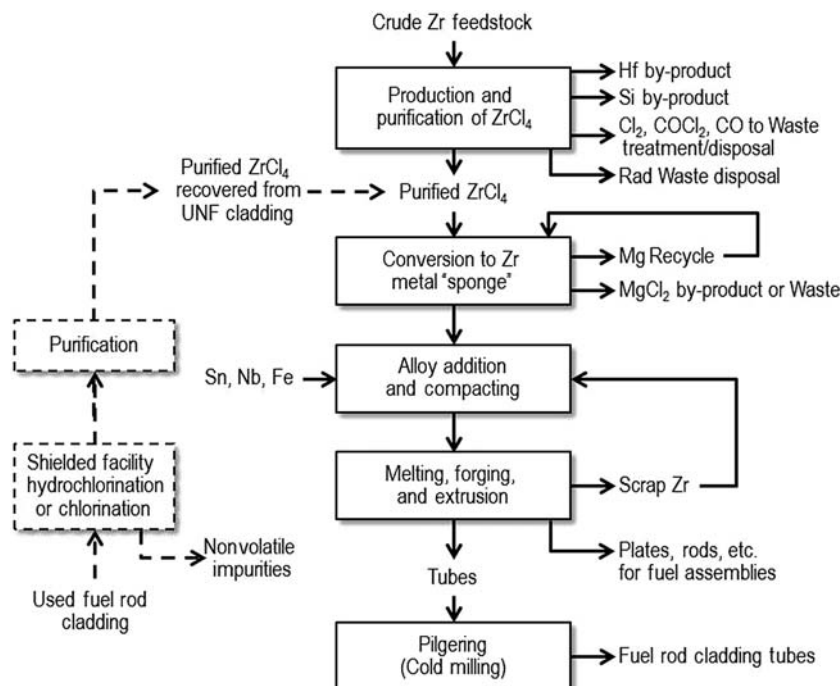


Figure 12.3 Potential interfaces of purified recycle zirconium in the process for zirconium alloy-cladding manufacture.

ZrCl_4 can be integrated with a traditional zirconium metal production operation to recycle it into metal. Should recycling be undesirable, the ZrCl_4 can be converted to ZrO_2 by steam pyrohydrolysis. The decontaminated ZrO_2 is a good form for disposal as low-level waste because of its high chemical stability and resistance to dissolution in groundwater.

12.1.4 Hardware component recycle

In addition to cladding, used nuclear fuel contains a significant amount of structural materials, such as end fittings, grid spacers, and guide tubes, that are generically termed “hardware.” The specific nature of the hardware varies significantly according to the different fuel designs in use and includes various alloys such as stainless steel, Inconel, and Zircaloy.

For aged fuel, most of the gamma-emitting activation products embedded in the hardware components will have significantly decayed (notably ^{60}Co , half-life, $t_{1/2} = 5.27$ years; ^{54}Mn , $t_{1/2} = 312.2$ days; and ^{125}Sb , $t_{1/2} = 2.77$ years) after prolonged storage. The remaining long-lived isotopes may include ^{14}C ($t_{1/2} = 5730$ years), ^{59}Ni ($t_{1/2} = 7.5 \times 10^4$ years), ^{63}Ni ($t_{1/2} = 100$ years), and ^{94}Nb ($t_{1/2} = 2 \times 10^4$ years). Although these isotopes may be considered a long-term concern for the environment, they are a limited exposure concern and may be allowed for surface disposal as low-level waste.

The present industrial practice where reprocessing is implemented is to remove the heavy end-piece nozzles and chop the remaining assembly of fuel pins into small pieces (1–3 in. long). The resulting segmented material is then leached with concentrated nitric acid to dissolve the oxide fuel. During this step the hardware that initially contained a small amount of activation products becomes further contaminated with fission products and actinides, either embedded mechanically or sorbed on the surface metal oxide film. The added alpha and gamma contamination significantly complicate the handling and final disposition of this material. As a result the current practice at the La Hague reprocessing plant in France is to compact the hardware and cladding in high integrity waste containers similar to the ones used for vitrified high-level wastes [32]. The practice at the Thermal Oxide Reprocessing Plant is to encase the hardware and cladding pieces in concrete [33].

A different approach for future recycling plant designs, to avoid contamination of the hardware materials with fission products and actinides from the fuel, is to mechanically remove the fuel rods from the used fuel assemblies (called “debundling”). Such a process was considered in previous studies and was shown to be cost-effective for the consolidation of the fuel rods and minimization of the storage volume [34,35]. The mechanically separated hardware would be clean enough to be handled without significant shielding; thus making a melt-recast operation economically feasible. Recasting of the hardware components for other nuclear components, such as containers for other wastes or making a cermet waste form that replaces glass, could compare favorably to geological disposal.

12.1.5 Additional component recycle

Other potentially recoverable components in used nuclear fuel include the xenon and ^{85}Kr gases, highly valuable noble metals (Ru, Rh, Pd, Ag) [36–38], and nonradioactive light lanthanide elements (La, Nd, Ce, Pr) [3]. For a fuel recycle capacity of 1000 MT/year, initial heavy metal fuel basis, the following approximate amounts of additional components that could be recycled is expected:

- xenon gas, 7 MT/year
- noble metals (Ru, Rh, Pd, Ag), 6 MT/year
- lanthanides (La, Nd, Ce, Pr), 11 MT/year

The noble metals have a very high commercial value. The potential commercial value of the light lanthanides is very limited, but their recovery for reuse or disposal as low-level waste (\$20k/MT) [30] should compare favorably to the cost of geological disposal ($\sim \$1 \text{ M}/\text{MT}$) [12,31].

12.2 Headend processing of Zircaloy-clad fuels for hydrometallurgical separations

Most often, the treatment of used nuclear fuel for recovering valuable components requires a headend process that exposes the components of interest and adjusts the chemical and physical form of those components to be compatible for the particular processing technology that will be used for the purification and recovery. At present, only Zircaloy-clad LWR fuels are being reprocessed at an industrial scale using hydrometallurgical separations. However, significant research and development efforts, both past and present, are geared not only to the development of hydrometallurgical variants for processing a variety of new fuels that will fuel advanced reactors but also to the development of “dry” treatments based on pyrochemical, electrochemical, and halide volatility processes [39]. Some of these treatment schemes use a combination of techniques and can be termed as “hybrid” processes.

Zircaloy-clad fuels are represented primarily by those designed for LWR, either PWR or BWR. In each case the fuel consists of ceramic UO_2 fuel pellets encased in zirconium-based alloy tubing (e.g., Zircaloy), called fuel pins. The PWR and BWR fuel elements differ primarily in the number of fuel pins, the dimensions of the fuel pins (i.e., diameter and length), and cladding alloy used (e.g., Zircaloy-4 and 1%Nb alloys for PWRs, Zircaloy-2 and 1%Nb alloys for BWRs). The CANDU and other pressurized heavy-water reactors also use UO_2 fuel pellets encased in Zircaloy-4 tubes, and although the fuel elements are much smaller in length with fewer fuel pins and use NU, they may be processed using similar methods.

The headend of present commercial LWR fuel reprocessing plants includes a mechanical disassembly and shearing step, followed by nitric acid dissolution to remove the fuel from the cladding segments (or hulls). Steps are added to remove solids that did not dissolve in the leaching step, which reduces problems in downstream-processing steps, and to adjust the heavy metal and free acid

concentrations in the dissolver liquor before the solvent-extraction separation. Measurements of the volume of the clarified dissolver solution and its assay of fissile materials are used for the accountability of nuclear material entering the separation portion of the plant. A generalized flow diagram is shown in Fig. 12.4.

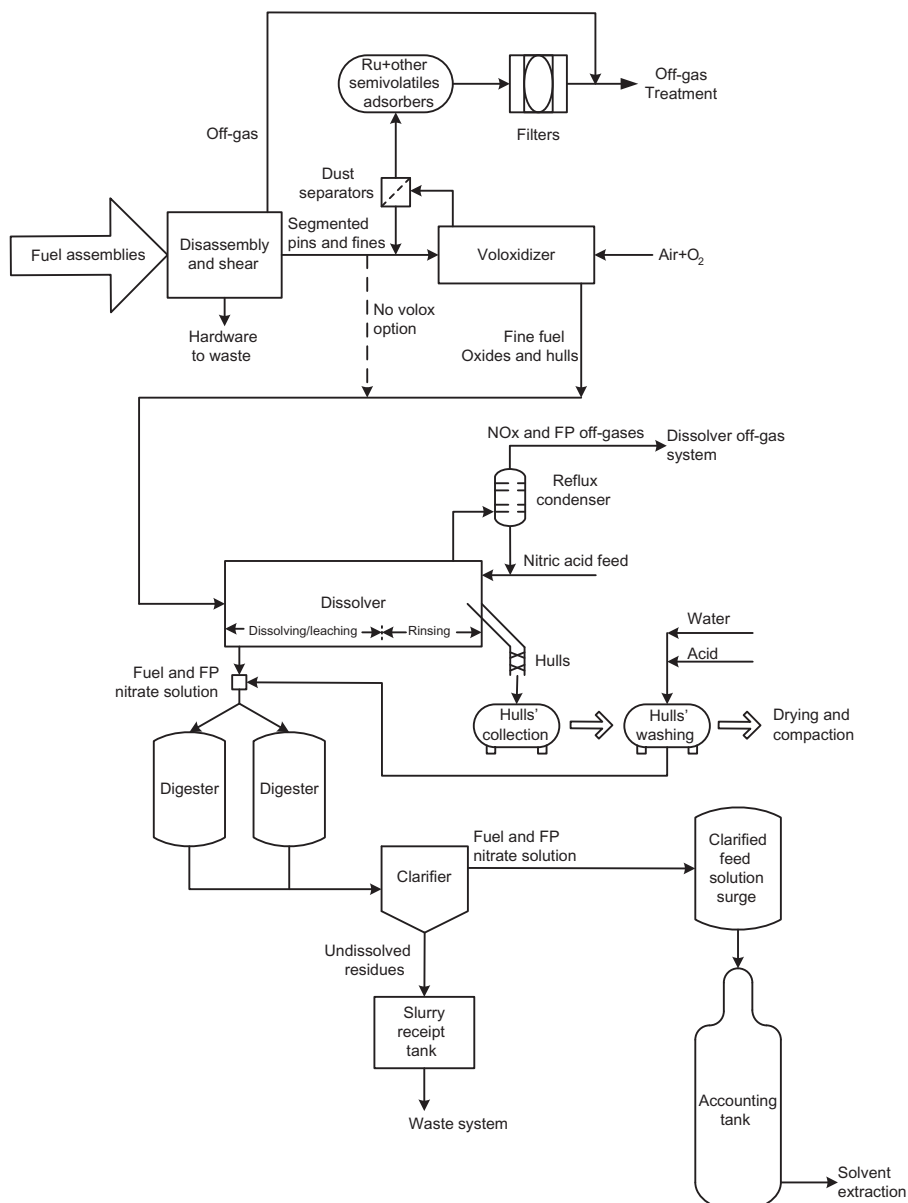


Figure 12.4 Typical headend processing steps for aqueous-based reprocessing.

12.2.1 Disassembly and decladding

Traditional disassembly involves cutting the end nozzles from the fuel assembly, followed by shearing the fuel assembly into short segments, usually 1–5 cm in length. The choppers used in present operating plants are based on the concept of progressive feeding, clamping, and cutting of fuel with a single shear blade [40]. More recent designs include cutting multiple pieces, termed “gang chopping” [41]. Some volatile fission products are released, requiring that the off-gas from the disassembly and shearing machine be routed to treatment before release to the environment.

Since whole-assembly chopping requires downstream processes, such as dissolution, to be able to handle metal pieces that are chemically inert within those processes, various alternatives have been developed for mechanically separating the fuel material from the cladding so that only the fuel material (or pellets) requires further processing.

12.2.1.1 Alternative mechanical-segmenting methods

Mechanical decladding alternatives require removal of the fuel pins and cutting the fuel pins into segments that are further processed by mechanical techniques. Debundling into individual pins that can be easily cut into shorter segments allows for a potentially significant downsizing of the headend, and the entire separation plant that would be more amenable for smaller throughputs to accommodate processing of used fuel from a small number of reactors and preparing feed for a few advanced reactors while maintaining economy of scale.

The following mechanical options may be used to separate fuel pins:

1. Roller straighteners that deform the segments of cladding, breaking the brittle fuel material within the cladding so that it may be dumped from the clad tube. Segment lengths range from 100 to 200 cm [42,43].
2. Agitation, which consists of hammer milling and tumbling, was tested on 7 cm fuel segments [43]. Hammering to deform the cladding allowed broken fuel to be dumped from the 20 cm long segment [44].
3. Axial slitting of segments, up to 25 cm in length, for releasing the fuel pellets [45].
4. Longitudinal rod laser cutting and stripping [46].

12.2.1.2 Chemical decladding methods

The volatility of the zirconium and resistance of the fuel material to common chlorination agents at moderate temperatures (i.e., <400°C) makes chemical decladding by chloride volatility an attractive decladding alternative. Zircaloy cladding is around 98% zirconium metal. Treatment of either segments of fuel pins or entire fuel assemblies with anhydrous HCl or Cl₂ converts the zirconium to volatile ZrCl₄ (see [Section 12.2.5](#) for details of the reaction). The oxide fuel and steel components are not significantly attacked [47]. The gaseous ZrCl₄ separates from the fuel and hardware. The remaining fuel pellets are suitable for voloxidation or dissolution processing. Because a fraction of the tritium in used fuel is bound in the cladding

as, presumably, zirconium hydride, vaporization of the cladding metal matrix releases this tritium in gaseous form.

Oxidation is another chemical decladding method. Oxidation is used in the voloxidation process to separate tritium from the fuel, but the accompanying comminution of the fuel releases it from the short cladding segments as a side benefit, enabling mechanical separation (e.g., sieving) of the clad from the powdered oxide fuel. See [Section 12.2.2](#) for details of the process.

12.2.1.3 Thionyl chloride-based chemical decladding

An alternative approach to chemical decladding of LWR fuel rods takes advantage of the fact that thionyl chloride reacts readily with both metals and metal oxides, such as UO_2 , but at very different rates that may allow the selective dissolution of the cladding under mild conditions without attacking the fuel [48,49]. Reactions of SOCl_2 with zirconium metal and zirconium oxide (ZrO_2) are discussed in [Section 12.2.5.2](#). The chlorination product from the cladding, ZrCl_4 , is very soluble in thionyl chloride and may, therefore, be removed from undissolved fuels by filtration. Pure ZrCl_4 can be obtained by mild heating under vacuum or in a stream of nitrogen, and the liquid thionyl chloride can be recycled. A schematic overview of this thionyl chloride decladding procedure is shown in [Fig. 12.5](#).

12.2.1.4 Hybrid decladding methods

Treatment of fuel cladding with nitrogen at high temperature (i.e., 1000°C – 1100°C) causes nitrogen to diffuse into the solid matrix and embrittle the Zircaloy [50,51]. Low mechanical stresses will then cause the cladding to break or shatter, exposing the fuel to subsequent chemical processing. It should be noted that at temperatures $>900^\circ\text{C}$, the cladding will burn in air [52], producing a powdery

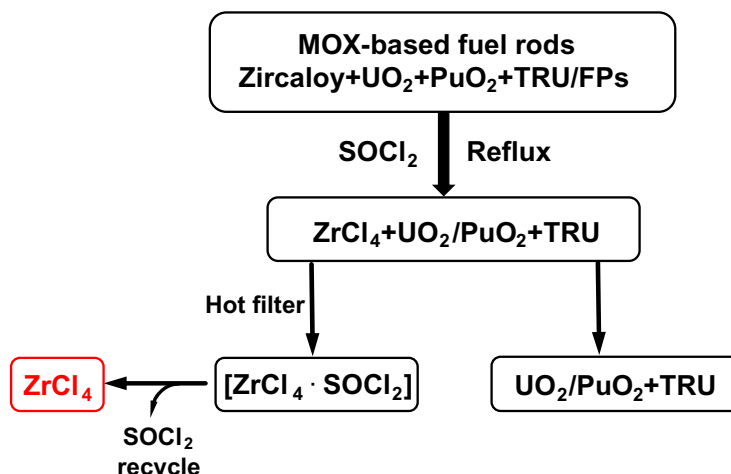


Figure 12.5 Schematic of the thionyl chloride chemical decladding.

ZrO₂ with a tan color due to oxides of the other metals in the alloy. Using oxidation to declad the fuel is avoided because of the very high heat of reaction that must be managed, and because of the introduction of large quantities of ZrO₂ to the dissolution and separation processes.

Cladding can also be embrittled by exposure to hydrogen at elevated temperature. The hydride reaction is complete in less than 4 hours in 5%H₂–95%Ar at temperatures between 480°C and 640°C [53]. Again, small mechanical stresses will readily break the cladding, or a grinding operation will pulverize it. When the cladding is breached, fission product gases will be released, as in shearing. In addition, the effect of residual hydrogen on off-gas treatment needs to be considered.

12.2.2 Voloxidation

12.2.2.1 Early development

Voloxidation was developed as a dry headend method for removing tritium from used nuclear reactor fuel after fuel chopping and before aqueous processing [54]. This avoids introducing the tritium through the dissolution process into the aqueous systems where it will accumulate until the evaporative losses of water to various off-gas effluents balance the input with the fuel [55].

The UO₂ reacts with oxygen to form U₃O₈, which results in a large (~30%) decrease in the fuel density, accompanied by particle spalling and crumbling. Powder size distribution depends on the temperature of the voloxidation process [56,57] and other factors related to the spent fuel characteristics, but nearly all the particles will be under 20 µm and a good fraction will be under 10 µm [58]. Tritium, which may be present in the fuel in elemental form, diffuses to the surface of the particle where it reacts with oxygen to form water, which enters the gas stream [54]. A fraction of the tritium (0% up to 60%) is associated with the cladding as zirconium hydride, ZrT_x, and is not readily released by standard voloxidation [59]. The fine powder will easily dislodge from short segmented fuel so that the hulls may be separated before feeding the dissolver for hydrometallurgical processing. The powder can also be interfaced with halide volatility or electrochemical separation methods, both discussed later in the chapter.

12.2.2.2 Coupled end-to-end demonstration at multikilogram scale with irradiated fuel

A laboratory-scale demonstration of a complete cycle for reprocessing of used fuel to prepare new fuel using a UREX process was completed at a multikilogram scale in 2008. The demonstration, termed coupled end-to-end, started with a high-burnup LWR fuel and included a voloxidation process [59]. The oxygen depletion in the process gas and the ⁸⁵Kr release was used as indicators of voloxidation reaction progress. Data were collected from semibatch experiments where a solid batch was charged to a rotary reactor and process gas was fed and withdrawn continuously from the reactor. These data indicate that the oxidation reaction reaches ~100%

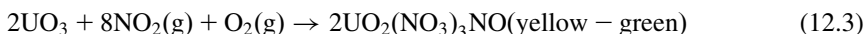
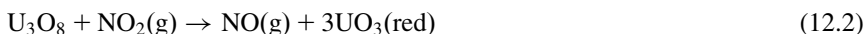


Figure 12.6 Voloxidation of irradiated fuel produced a fine powder that readily separated from the cladding (an empty cladding segment held in tongs is shown).

completion in ~ 10 hours at 500°C in air. The data also show that the reaction is essentially complete in $\sim 3\text{--}4$ hours at 600°C in oxygen-enriched ($\sim 50\%$ oxygen) atmospheres. The fuel became a fine powder that readily separated from the cladding, see Fig. 12.6. The data suggested that all the tritium associated with the oxide fuel was removed, whereas the tritium associated with the cladding was not fully released, resulting in about 24% of all fuel element tritium to remain in the cladding. About 50% of the krypton was removed from the fuel [60].

12.2.2.3 Recent advanced methods

Advanced voloxidation has been pursued using a stronger oxidant, a NO_2/O_2 mix [61]. Advantages of the process include rapid conversion of the UO_2 fuel to the higher oxides at lower temperatures ($<300^\circ\text{C}$), the option to recycle the by-product NO with O_2 feed to keep the gaseous effluent volume low, and the option to select U_3O_8 , UO_3 , or $\text{UO}_2(\text{NO}_3)_3\text{NO}$ products based on operating temperature.



Kilogram-scale tests with surrogate materials and gram-scale tests with commercial fuel indicate that this dry process releases iodine as well as all the tritium from the fuel. The increased fracturing of the fuel grain boundaries during conversion to

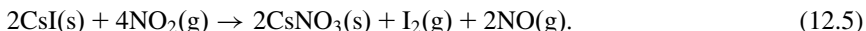
the higher oxides is also expected to release greater fractions of other fission gases such as Kr, Xe, and CO₂ [62–64]. Other advantages include reduced acid usage in the dissolution step, nearly fumeless dissolution of UO₃, and rapid dissolution in an acid of low concentration. Low acid dissolver product, ~0.8 M, is preferred for the UREX + separation processes [65].

Nitric oxide gas readily reacts with O₂ during cooling to regenerate NO₂ based on the reaction



A process system that recirculates NO_X in a closed loop with an O₂ addition can be implemented. Multikilogram-scale tests using high quality UO₂ pellets with an initial NO₂ charge and make up O₂ confirmed the viability of a closed-loop, very low-volume voloxidation system, as illustrated in Fig. 12.7.

Because most of the iodine and cesium in used fuel is coreleased at high temperature, iodine is believed to be found in used fuel primarily as CsI [66]. Cesium iodide has been observed to react with NO₂ to produce CsNO₃, liberating I₂ as shown by



As mentioned, tests using surrogate materials at the kilogram scale and gram quantities of used nuclear fuel confirmed the removal of iodine [61]. The release of iodine in a dry headend process is desired because it could eliminate the need for subsequent trapping of iodine from several humid off-gas streams present in a reprocessing facility.

Fine UO₃ powders can easily be selectively dissolved using tri-*n*-butyl phosphate (TBP) preequilibrated with HNO₃; the nitrated uranyl species will dissolve directly into TBP. Studies at the Savannah River National Laboratory are underway for

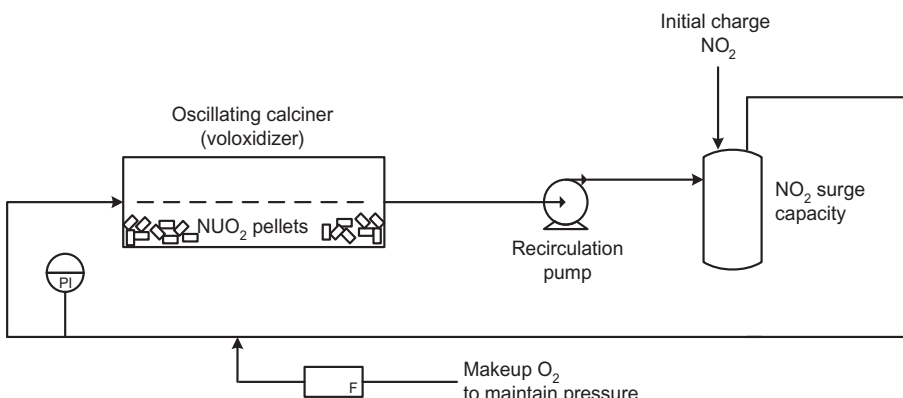


Figure 12.7 Schematic of closed-cycle voloxidation.

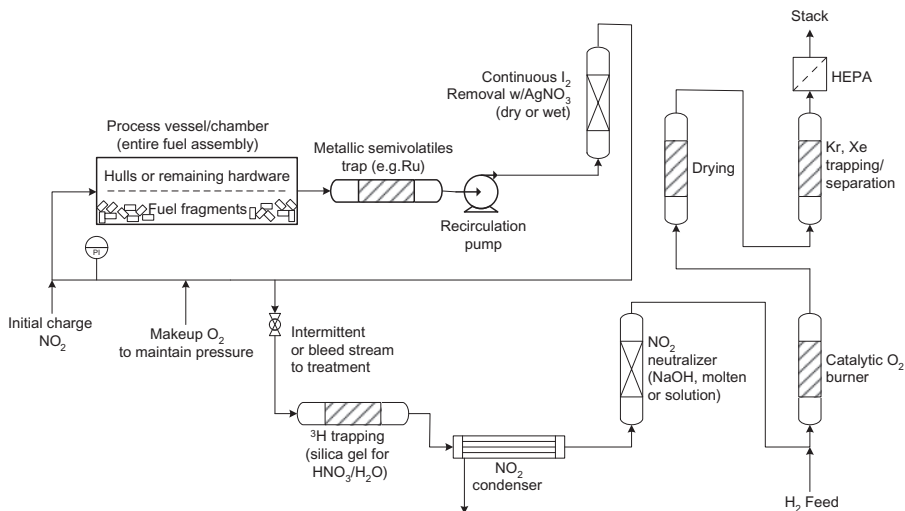


Figure 12.8 Flow sheet of voloxidation process using NO_2 , illustrating recovery of volatile fission products.

demonstrating the feasibility of a direct extraction method without the need for acid dissolution [67].

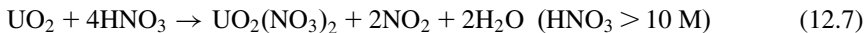
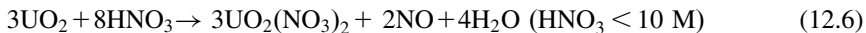
The closed-loop NO_2 advanced voloxidation and the advanced dissolution under development can result in a much more compact and economical system with an off-gas system tasked to handle much lower gas volumes, a few cubic meters, compared to $>1000 \text{ m}^3/\text{MT}$ of fuel as in a conventional system.

A schematic of such a system is shown in Fig. 12.8. A hot demonstration using commercial fuel was planned in conjunction with testing of the coextraction and decontamination (Co-D-Con) solvent-extraction process at the Pacific Northwest National Laboratory [68], but results were not available as of this writing.

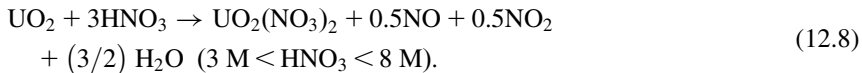
12.2.3 Nitric acid dissolution

12.2.3.1 Traditional process

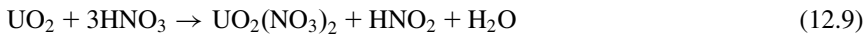
The segmented fuel pins, and any fuel rubble resulting from the shearing operation, are fed directly to the dissolver—the voloxidation step is not used in traditional flow sheets. Hot nitric acid, at temperatures around the boiling point (BP) ($\sim 105^\circ\text{C}$), dissolves the fuel into the aqueous solution. Nitrogen oxides are produced as by-products from the dissolution reactions shown in Eqs. (12.6) and (12.7), with nitric oxide favored at nitric acid concentrations less than 10 M, and nitrogen dioxide favored at nitric acid concentrations greater than 10 M [54]. The breakpoint is not sharp, with both NO and NO_2 by-products over a range of concentrations. The reaction is exothermic, and both nitric acid and water vapors are evolved.



A recent study on the mechanism of dissolution [69] includes a third reaction:



The mechanism also includes steps that form nitrous acid, and the nitrous acid attacks the UO_2 , which catalyzes the dissolution.

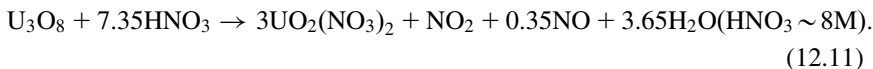


The dissolution destroys the solid matrix, releasing various volatile fission products. Because the exothermic dissolution reaction produces nitrogen oxides (NO_X) and evaporates a large fraction of the water from dissolver solution, condensers are used to condense water and acid vapors arising from the dissolution to return these materials to the dissolver vessel. The liquid film on the condenser surfaces also absorbs part of the NO_X , reforming some acid that is also returned to the dissolution vessel. Xenon and krypton are sparingly soluble in the dissolver solution and are released to the process off-gas.

As shown in Fig. 12.4, the dissolver product is collected in digestor tanks, where the additional holding time permits additional leaching of undissolved particles. The dissolver solution in these tanks is sparged with a mixture of air and NO_2 to keep the particles suspended and to provide an oxidant.

12.2.3.2 Dissolution following oxygen-based voloxidation

Conventional voloxidation converts the UO_2 , the predominant component of the fuel, to U_3O_8 . Triuranium octoxide can be loosely considered a 2:1 mixture of UO_2 and UO_3 , which requires a lesser amount of acid to produce the uranyl nitrate than does UO_2 . The approximate stoichiometry [39] is



12.2.3.3 Dissolution following advanced voloxidation

As discussed in Section 12.2.3, advanced voloxidation using NO_2 as an oxidant can convert all the uranium to UO_3 and dissolution is fumeless (as shown in Eq. 12.12), which requires less acid than does dissolution of the other oxides of

uranium previously discussed. (Because of nonidealities, some NO_x fumes result in practice.)



Tests have also shown that UO_3 readily dissolves in low HNO_3 concentrations of 0.3 M or above and in TBP solutions preequilibrated with HNO_3 [67,68]. This is advantageous to those separation processes that function better at lower nitric acid concentrations.

The uranium produced by advanced voloxidation can also be converted to the nitrosyl nitrate form, $\text{UO}_2(\text{NO}_3)_3\text{NO}$. This compound can be dissolved in very weak acid or in water. Since it is also soluble in TBP–dodecane mixtures, other separation processes are also possible [70].

12.2.4 Clarification and accounting

Chemical processing does not take place in the clarification or accounting steps, but both are included here for completeness. However, clarification does mechanically remove undissolved particulates from the dissolver solution, and the characteristics of the undissolved residue depend on prior chemical-conditioning steps.

The undissolved residue generally contains noble metals, zirconium, trivalent metals, and plutonium. Less than 0.1% of the fuel material is found in the undissolved residue. Analysis of the residue recovered from the dissolution of unvoloxidized irradiated UO_2 fuel reveals that Mo, Pu, and Zr account for ~46% of the mass, with the remainder being made up of a large number of other metals [71].

Volvoxidation of irradiated mixed oxide fuels has been shown to have no effect on the amount of Pu in the undissolved residue, although the rate of dissolution may be slightly slower [72]. The effect of advanced voloxidation on undissolved residue has not been characterized, and presents an opportunity for further study.

12.2.5 Disposition of cladding

12.2.5.1 Current industrial practice

Following the dissolution step, the Zircaloy cladding hulls retain trace amounts of fuel materials because of residual dissolver/wash solution contaminating the surface and microscopic particles of fuel embedded in the inner surface by fission recoil. The penetration depth of particles by fission recoil is around 8 μm for fuel having a burnup of 37 GWd/MTU [73]. The contamination is sufficient to render the cladding a TRU waste. The steel hardware removed in the disassembly step is also contaminated by activation products, primarily cobalt, and is generally not considered a TRU waste.

Two common methods of preparing the cladding hulls and hardware pieces for disposal are supercompaction and grouting. Supercompaction is used for a mixture of the cladding hulls, which have a large void fraction, and steel hardware pieces.

The steel pieces are surrounded by the more malleable Zircaloy cladding before compaction. The compacted material behaves as a monolith, has very little void, and is placed in a standard canister of compacted waste (CSD-C canister) for disposal [74]. In the grouting process the hulls may, or not, be compacted. The hulls and other structural metal pieces are placed in 500 L stainless-steel drums. Grout is mixed with the waste and allowed to cure, encasing the hulls [75]. These waste streams will require geological disposal and their volume exceeds the volume of high-level waste glass that encapsulates the unextracted fission products and minor actinides. As discussed in [Sections 12.1.3 and 12.1.4](#), the recovery of Zircaloy cladding and hardware for reuse or rendering the waste level low could reduce the waste volume, requiring geological disposal by more than half [3].

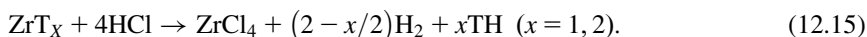
12.2.5.2 Zirconium recovery for alternative dispositions

The zirconium component of the alloy reacts readily either with anhydrous hydrogen chloride or chlorine at temperatures above 350°C, producing volatile zirconium tetrachloride, ZrCl_4 .

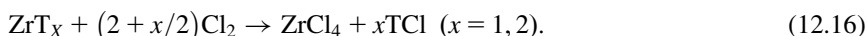


The primary alloying agents, such as Sn or Nb, and some of the minor components are also volatilized as chlorides. Zirconium dioxide on the inner, outer, or inner and outer surfaces, and other oxide particles embedded in the inner surfaces by fuel-cladding interaction or recoil do not react. The volatile zirconium tetrachloride separates from the residual ash with a high decontamination factor [76], rendering it a low-level radioactive material. ZrCl_4 salt is recovered by condensation, and additional sublimation steps may be used to separate it from the SnCl_4 or NbCl_5 [77].

Volatilezation of the cladding releases the tritium trapped in the cladding. Hydrochlorination with HCl is thought to release the tritium, T, as free hydrogen:



Chlorine releases the tritium as tritium chloride:



An alternative decontamination strategy [78] uses thionyl chloride (SOCl_2) as a low-temperature chlorination agent [48,49], oxygen sink, and ultimately as a recrystallization solvent for obtaining the tetrachloride product from Zircaloy cladding in one step (refer to [Fig. 12.9](#)). Chlorination and dissolution of several, different Zircaloy cladding types is slow (days) in refluxing thionyl chloride but accelerates significantly at temperatures slightly above its boiling temperature, thereby achieving practical rates. When the final solution is cooled to the room temperature, the thionyl chloride adduct of zirconium tetrachloride ($\text{ZrCl}_4 \cdot \text{SOCl}_2$) [79] is obtained as

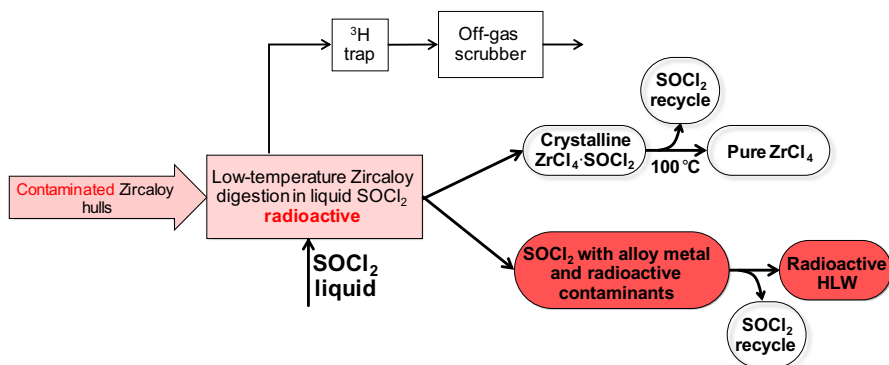


Figure 12.9 Schematic illustration of the process steps in the thionyl chloride Zircaloy purification scheme. Red coloring represents the location and the relative concentration of radioactive contaminants. Tritium trapping is not part of the main strategy but must also be addressed in the overall process.

a crystalline solid. After separating the mother liquor from the solid thionyl chloride adduct, pure ZrCl_4 can be obtained by mild heating under vacuum or in a stream of nitrogen [80]. Thionyl chloride freed by the decomposition process can be recycled.

Reaction with zirconium metal in Zircaloy cladding materials involves oxidation and chlorination, whereas reaction with the metal oxide (ZrO_2) only involves exchange of oxygen for chlorine. The possible reactions involved are summarized in the following equations:



In both cases, formation of sulfur dioxide is one of the main driving forces for these reactions.

12.3 Headend processing for alternative or advanced fuels

12.3.1 TRISO fuels

Particle fuel was initially developed for high-temperature gas-cooled reactors (HTGRs) but, more recently, also for high-temperature molten salt-cooled reactors. Each spherical particle of fuel, called a kernel, is encased in layers of amorphous carbon (buffer layer), pyrolytic carbon (hard structural layer for separating the buffer from the next layer), and a tough silicon carbide layer that acts as a pressure vessel to contain fission products. Another pyrolytic carbon layer is laid down on the SiC layer to bond with the graphite organic binder used to fabricate fuel sticks or spheres. This fuel design is discussed in greater detail in Chapter 5, Other power reactor fuels.

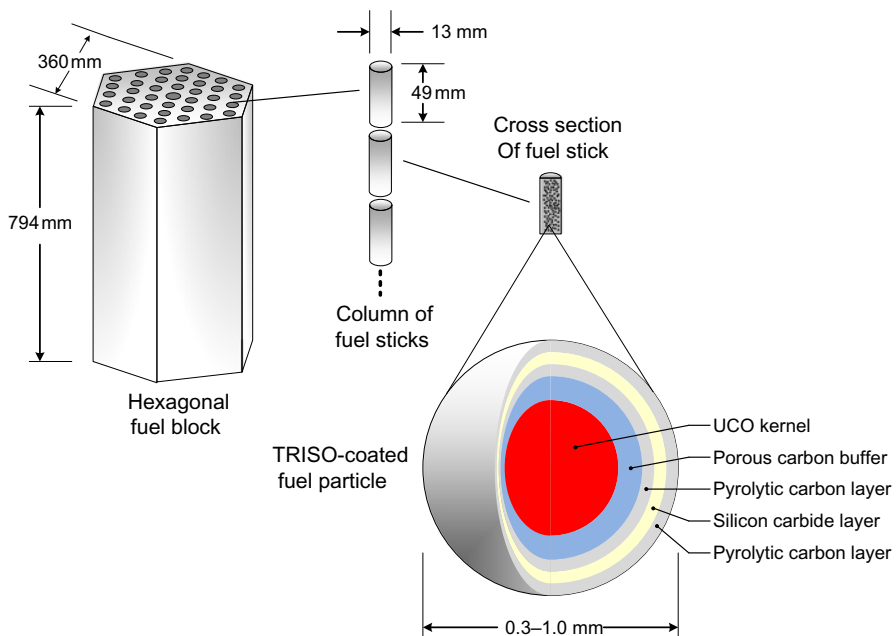


Figure 12.10 Configuration of HTGR fuel: individual particle, compacts (fuel sticks), and fuel assembly. HTGR, High-temperature gas-cooled reactor.

Fig. 12.10 shows the typical configuration of the prismatic fuel elements that were used to fuel the Fort Saint Vrain reactor designed by General Atomics [81]. The individual fuel particles (about 7160) are held together in a carbon matrix of cylindrical form (0.5 in. diameter and 1.94 in. long) that is called a fuel stick or “compact.” These compacts are inserted in a prismatic graphite block that has bored holes to hold a column of compacts and machined channels for the coolant flow. In total, there are about 3010 compacts per prismatic fuel assembly. The amount of fuel is a relatively very small fraction of the fuel assembly, about 0.8 kg out of 120 kg. The graphite block itself weighs about 90 kg [82].

The other type of TRISO-based fuel adopts the shape of a sphere (pebble) typically around 60 mm in diameter, such as the ones that fuel the Arbeitsgemeinschaft Versuchsreaktor (AVR) reactor at Jülich [83,84]. Pebble construction is shown in Fig. 12.11.

For the AVR fuel, each pebble contains about 195 g of carbon, 2.25 g of SiC, and about 10 g of heavy metal fuel [85]. A more complete description of HTGR fuels was compiled by the International Atomic Energy Agency [86].

The overall reprocessing of TRISO fuel involves a pretreatment for removing the protective layers of carbon and silicon carbide and expose the fuel kernels for further treatment. Several processing technologies have been developed to recover the fissile content of the fuel kernels, including a combination of chemical and mechanical means [82,87–90]. Fig. 12.12 shows the early processing methods for

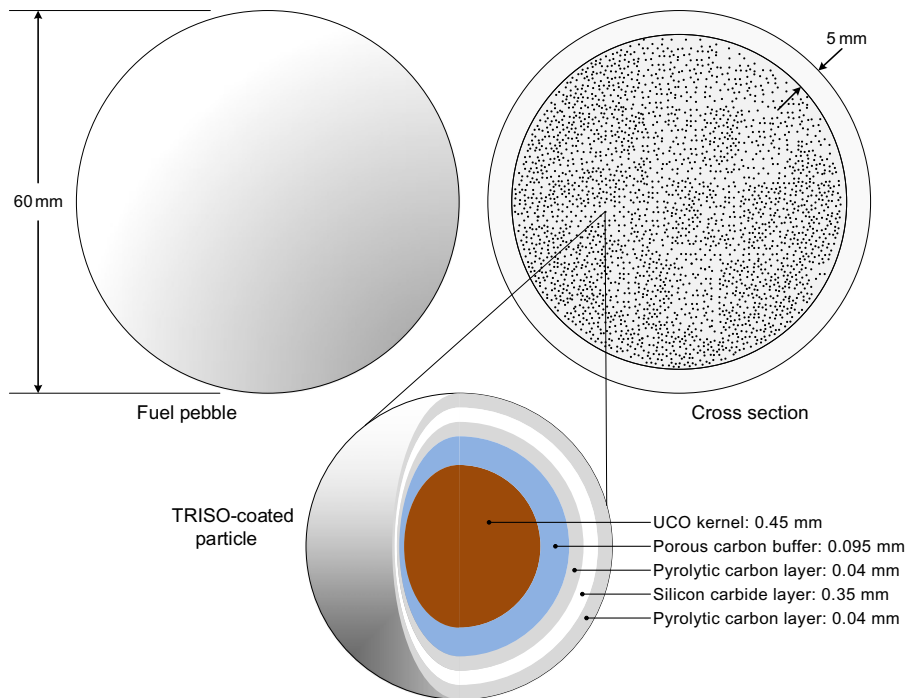


Figure 12.11 Configuration of pebble: individual particles and fuel pebble.

prismatic fuels that generally involved a crush-burn-crush-burn-leach approach. None of these approaches have been commercialized.

Burning of graphite fuels is very difficult and results in large quantities of carbon dioxide contaminated with ^{14}C , which is a beta emitter that is produced during irradiation. A recent patent indicates that HNO_3 or its decomposition products mixed with air or oxygen can be used to oxidize graphite to CO_2 at low temperature [91].

Current regulations would require that much of the ^{14}C -containing carbon dioxide be sequestered. Typically, this is accomplished by a reaction with calcium hydroxide or barium hydroxide, producing large quantities of CaCO_3 or BaCO_3 wastes that require disposal. Since the contaminated graphite blocks are made of high-purity graphite and constitute the largest volume fraction of the fuel, their recovery and reuse can result in significant waste minimization and cost reduction. Fig. 12.13 shows the schematic of a headend that recovers the graphite blocks and breaks down the fuel cores to expose the kernels for further processing (hydrometallurgical [82,90], electrochemical [82,90], fluoride volatility [92]).

A lab-scale process has demonstrated that the recovered graphite could be reused to produce nuclear-grade graphite [93]. The schematic of the recovery process is shown in Fig. 12.14.

Processing of the pebble-bed nuclear fuel from the AVR reactor is underway at Savannah River National Laboratory. The processing scheme involves the digestion

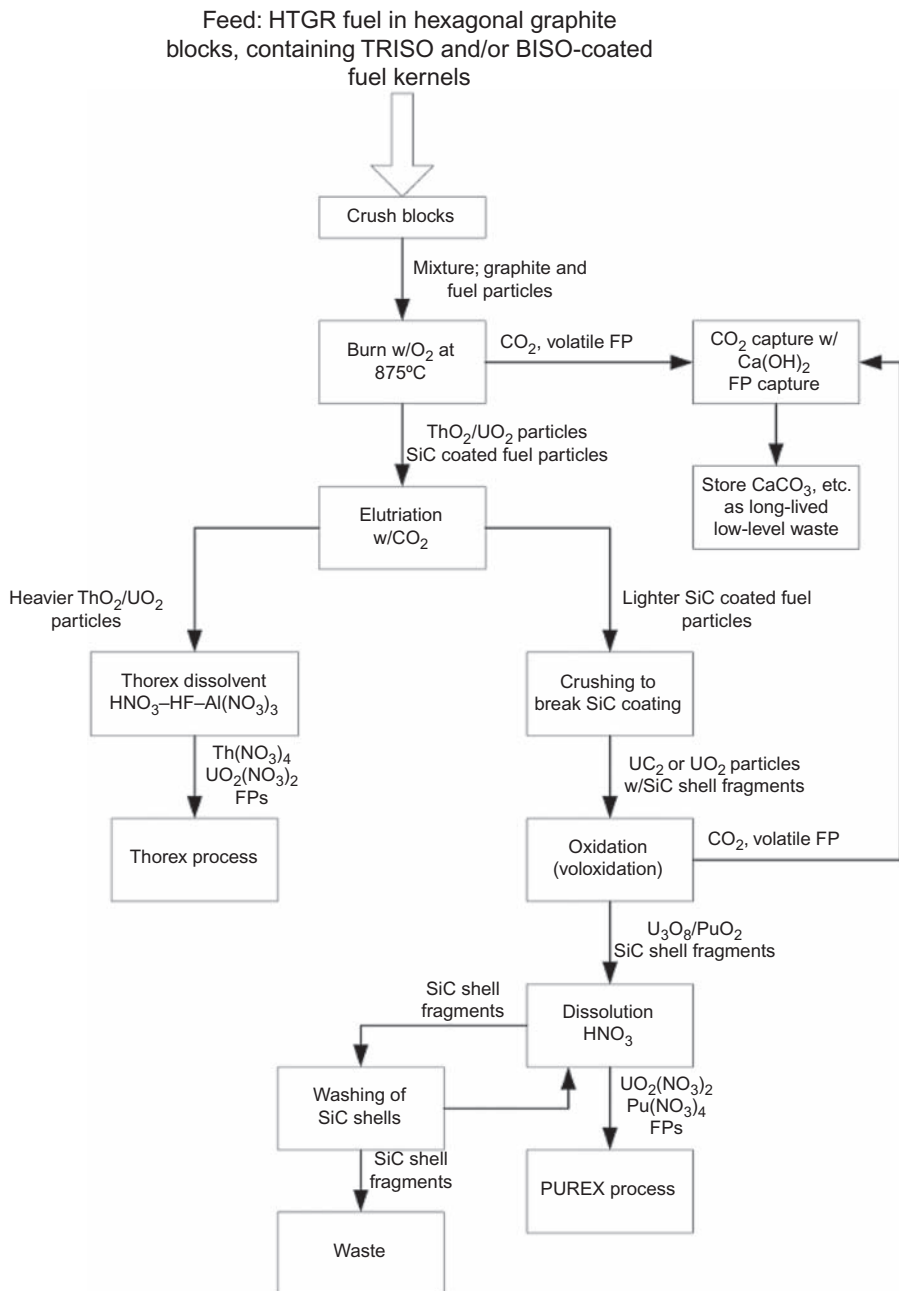


Figure 12.12 Early processing crush-burn-crush-burn-leach method for prismatic fuels.

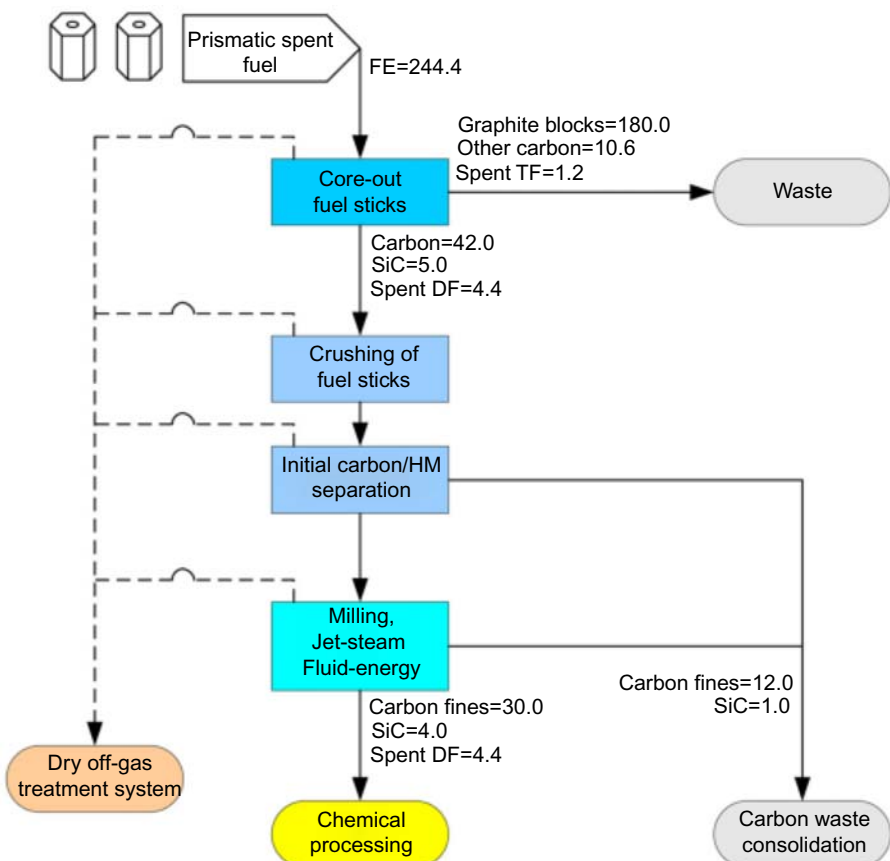


Figure 12.13 Mechanical headend for prismatic fuels (values represent relative masses).

of the graphite outer layer and carbon matrix for separating the fuel particles for further processing [94,95].

12.3.2 *The process of direct use of pressurized water reactor fuel in CANDU*

The direct use of PWR fuel in CANDU (DUPIC) process was codeveloped by AECL and KAERI [96,97]. Used LWR fuel is pulverized using a combination of high-temperature voloxidation and hydrogen-reduction cycles. During these cycles, UO_2 is transformed into U_3O_8 and reduced back to UO_2 . The large density changes from UO_2 ($d = 10.97 \text{ g/mL}$) to U_3O_8 (8.39 g/mL) cause the breakage of the used fuel into very fine particles. The process does not include any separation process; however, during the thermal treatment, a very large fraction of ${}^3\text{H}$, ${}^{14}\text{C}$, Cs, noble gases, and noble metals are volatilized and removed. Finally, the fine UO_2 powder,

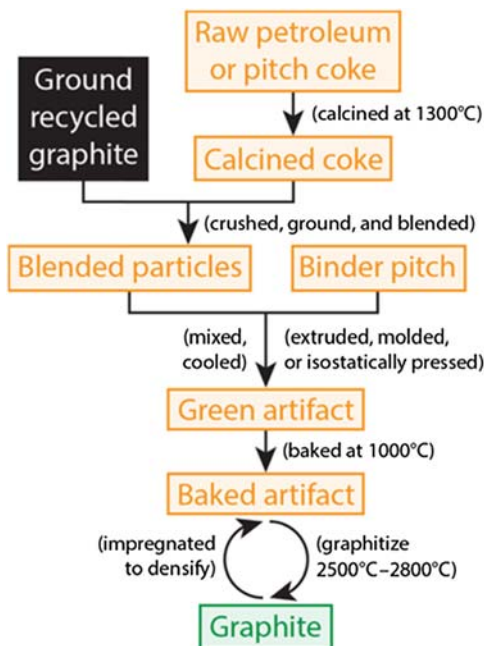


Figure 12.14 A method to recover nuclear-grade graphite for future use.

including impurities, is used to refabricate CANDU fuel pellets. Due to the high radiation levels of the DUPIC powder, remote refabrication in hot cells is required. Similarly, the refueling operation needs to be modified for allowing shielded loading of DUPIC fuel. Studies of South Korea's Wolsong CANDU units indicate that both the front- and rear-loading techniques could be used with some plant modification. The process was fully demonstrated but not implemented commercially [97].

12.3.3 Thorium-enhanced fuels

Thorium exists in nature as the mostly monoisotopic form, ^{232}Th . However, thorium ores are often commingled with uranium and, consequently, there is usually a small concentration of ^{230}Th that arises from the alpha decay of ^{234}U , a decay daughter of the more abundant ^{238}U . Thorium is not fissile, but it is fertile. Fissile ^{233}U can be produced by neutron adsorption on natural thorium. In practice, the fuel requires a fissile component, and a mixed oxide of ThO_2 and UO_2 and/or PuO_2 is prepared for in-reactor use [98].

Once sufficient ^{233}U is available to fuel a reactor, it is possible to achieve a breeding closed fuel cycle where more fissile ^{233}U is generated from cycle to cycle. This fact, and the relatively wide availability of thorium from ores, resulted in interest during the first decades of the nuclear era. However, as shown in Fig. 12.15,

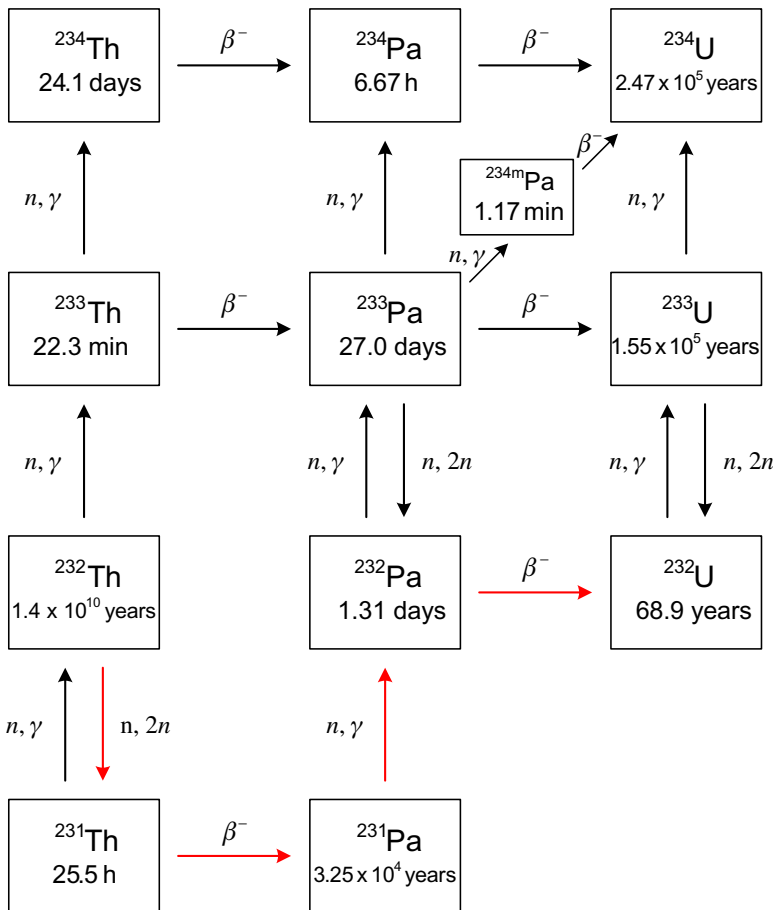


Figure 12.15 Pathways to produce ^{232}U from various activation and decay reactions (red arrows show primary pathway).

there are several routes that also generate ^{232}U . Double neutron capture by ^{230}Th , a common impurity in mined thorium, also generates ^{232}U .

The cogeneration of the relatively short-lived ($t_{1/2} = 68.9$ years) ^{232}U is problematic, and it is one of the main reasons why the thorium fuel cycle was never commercialized. The decay chain of ^{232}U shown in Fig. 12.16 includes a gaseous ^{220}Rn ($t_{1/2} = 55.6$ seconds), a species that can easily spread the decay daughters that include two very high energy gamma-emitting radioisotopes, ^{212}Bi and ^{208}Tl . The practical consequence is the requirement for remote handling the reprocessed uranium and remote fuel refabrication.

The other inconvenience is that thorium oxide fuels and targets are very difficult to dissolve in acid, requiring long times (10–18 hours) and harsh conditions: boiling temperatures and the use of the so-called Thorex dissolvent, a corrosive mixture of 13 M HNO_3 , 0.03–0.05 M HF, and 0.1 M $\text{Al}(\text{NO}_3)_3$ [99].

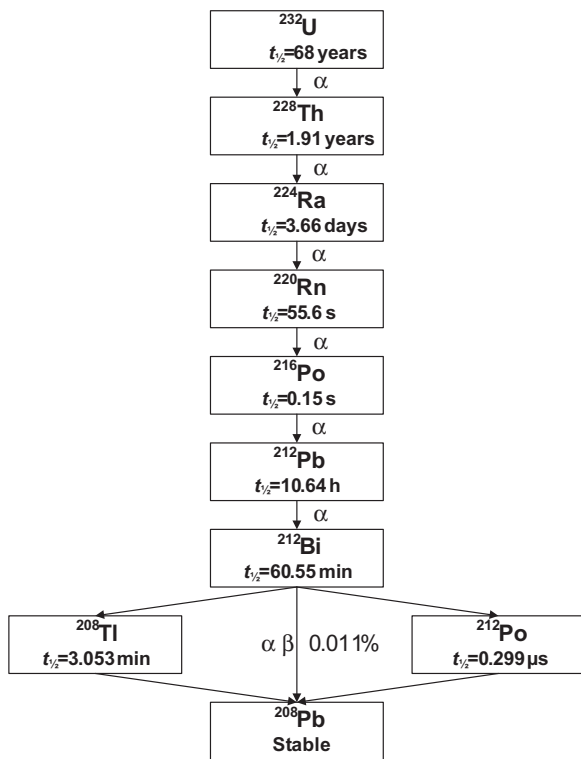


Figure 12.16 Decay chain for ^{232}U .

Several variations of PUREX-like processes were developed over the years, depending on the targeted separation: (1) only U, (2) Pa and U, or (3) Pa, U, and Th.

The Interim-23 process was designed for the extraction of only uranium using a dilute (1.5 v/v%) TBP extraction cycle, and it was used to separate kilogram quantities of ^{233}U from aluminum-clad thorium metal slugs. The extracted uranium was further purified by contact with silica gel to remove Pa. A Dowex 50 cation exchanger was used to concentrate the uranium product [100].

One variant of Thorex included three extraction cycles: (1) Pa extraction using diisobutyl carbinol, (2) uranium extraction using 5% TBP, and finally, (3) Th extraction using an organic extract made of 45 v/v% TBP, 15 v/v% benzene, and 40 v/v% Amsco solvent [100].

Another variant was developed to recover both thorium and uranium. Before solvent extraction the dissolver solution was evaporated at around 150°C to remove most of the free acid, creating an “acid-deficient” feed that was contacted with 42.5 v/v% TBP in Amsco to coextract thorium and uranium. Thorium and uranium were separated by selective stripping using two acid concentrations. First, thorium was stripped with dilute HNO_3 , followed by stripping of uranium using a very

dilute nitric acid. Next, protactinium was removed from the raffinate using a silica gel column [100].

12.3.3.1 Thorex

The first small pilot plant was started in the 1960s for aluminum-clad thorium metal/ThO₂ targets. The aluminum was dissolved in sodium hydroxide, and the exposed thorium target was dissolved in a thermosiphon dissolver using HNO₃, NaF, and Al(NO₃)₃. The uranium was extracted using 5 v/v% TBP in kerosene. The uranium was further purified using 8 M HCl and Dowex 1 anionic exchanger. More recent developments used 3 v/v% TBP in dodecane for the U extraction and Dowex 50 cationic exchanger for purification. Solvent extraction studies for the recovery of Th from the raffinate used an extraction cycle using 30–42 v/v% TBP in dodecane [101].

12.4 Off-gas treatment and emission controls

Several key regulations impact volatile gas emissions from a nuclear fuel recycle facility. The US Environmental Protection Agency has established annual individual dose limits for specific organs and for the whole body resulting from nuclear fuel cycle facilities in the commercial sector; the limits are defined in 40 CFR Part 190. Radionuclide-specific release limits in terms of curies released per unit of power produced are also defined in 40 CFR Part 190. Storage of used fuel allows the short-lived isotopes (e.g., ³H and ⁸⁵Kr) to decay significantly after 10–20 years.

The primary radioactive volatiles in the fuel include ³H, ¹⁴C, ⁸⁵Kr, and ¹²⁹I. Radioactive ³⁶Cl is of about the same quantity as the ¹²⁹I, but it is not as biologically active. Bromine and chlorine are chemically similar to iodine and are assumed to follow a similar fate during processing operations. Although there are no radioactive species of xenon remaining in fuel that has been cooled for 5 years or longer, it is useful to note the quantities—about 15 times as much xenon as krypton and about 300 times as much xenon and nonradioactive krypton as there is radioactive ⁸⁵Kr. This will have implications on the trapping systems.

Another group of radiological species that form gaseous compounds is the semi-volatiles. Typically, only a fraction of these species is converted to gaseous compounds in aqueous-based reprocessing plants. These include Ru, Te, Rh, Tc, Mo, and Cs, which are volatilized in oxidizing conditions at very high temperatures. Volatile oxides of ruthenium and technetium may be produced in oxidizing aqueous media (e.g., nitric acid dissolution).

Chemical and physical trapping methods have been, and are being, developed to sequester the gaseous radio-species to reduce the quantities emitted into the atmosphere below regulatory levels. Due to the differences in the chemical reactivity of the primary volatile radio-species, trapping of the I, ³H, ¹⁴C, and ⁸⁵Kr can be accomplished in a series of steps that target each specific compound. The

semivolatiles arise primarily in certain fuel-processing options, and additional steps can be used to trap them.

12.4.1 Iodine

Fission product ^{129}I is a long-lived ($t_{1/2} = 1.57 \times 10^7$ years) beta emitter, and it is biochemically active. It enters the gas phase primarily during nitric acid dissolution. Processing using voloxidation or enhanced voloxidation steps can release fractions of the iodine, ranging from traces to all the iodine contained in used nuclear fuel. In dry processes, iodine is released primarily in the elemental form, I_2 . In aqueous dissolver systems, iodine may be released in elemental form, as hydroiodic acid (HOI), or as an organic iodide species. Organic forms are produced because recycled nitric acid contains organic compounds that originated in the solvent-extraction system, and the iodine can react with these organic compounds [102].

Several methods to remove iodine from off-gas streams have been identified and tested [103,104]. Fluid scrubbing systems include, but are not limited to, alkaline scrubbing, the Iodox process, and scrubbing with molten hydroxide and fluorocarbon sorbents. Alkaline scrubbing is effective for inorganic iodine forms, but it fails to remove organic forms and will also neutralize and scrub associated acid gases (e.g., HNO_3 , NO_X , and CO_2). Molten hydroxide scrubbing will remove both organic and inorganic iodine forms and also scrub acidic gases, but little experimental data are available. The Iodox process scrubs the off-gas with hyperazeotropic nitric acid solution, converting both inorganic and organic iodine-containing forms to an iodate having very low vapor pressure. A significant disadvantage is that strong acid that contains iodine is extremely corrosive, requiring expensive alloys for fabrication, and the equipment requires a significant amount of space. Fluorocarbon sorbents (e.g., dichlorodifluoromethane or R-12) operate at low temperatures (-32°C to -12°C) and high pressure (300 psig) [103], which requires that the gas stream be dewatered. In addition, noble gases and carbon dioxide are coabsorbed.

Solid sorbent systems include activated carbon, macroreticular resins, and zeolites [104]. The activated carbon is negatively affected by oxidizing gases, such as NO_X , and the iodine retention is greatly retarded or reversed at elevated temperatures. The resins, such as Amberlite AMD, attract uncharged elemental or organic iodine species. However, little data are available on these sorbents, and the existing data indicate that removal of iodine is greatly reduced at temperatures above about 50°C . Zeolitic materials impregnated with silver nitrate or silver very effectively remove iodine from off-gas streams, converting the iodine to the highly insoluble silver iodide. In addition, the zeolites are resistant to acid gases. Silver nitrate solution is used to introduce the silver into the zeolite structure. After drying at an elevated temperature the supported silver nitrate reacts with either inorganic or organic iodine-bearing species to capture the iodine as silver iodide. The affinity for iodine can be increased by first treating the silver nitrate–impregnated zeolite (e.g., silver mordenite and AgZ) with hydrogen at elevated temperature to convert the silver to the elemental form [105].

Recent studies have focused on the AgZ and silver-impregnated aerogels for removing iodine from reprocessing plant off-gas streams [106]. The silver aerogel adsorbs a greater amount of iodine per unit weight than the AgZ; the aerogel has a greater silver content. When normalized to the silver content, the capacity of both AgZ and silver aerogel were the same. The AgZ was more structurally sound than the aerogel, which tended to degrade to a powder during the sorption tests.

Reduction of the silver in AgZ improves both the capacity and affinity for iodine. The reduction process used for the AgZ generally takes place at temperatures near 270°C in a hydrogen-containing atmosphere. In normal use the zeolite is heated to around 150°C, which improves the kinetics of sorption and reaction, but is not high enough to damage the mineral structure over extended time periods. Flow of iodine-free air through a freshly loaded AgZ bed was shown to remove up to 25% of the iodine, indicating that a portion of the iodine was physisorbed and not yet bound to the silver [107]. Other researchers have attributed the removal to the decomposition of the AgI [108]. Exposure of reduced AgZ to both dry and humid air degraded its capacity over time, indicating that in normal use, the last-to-be-used portion of a sorption bed will not adsorb as much iodine as the initial portion [109]. The reduction in capacity has been attributed to oxidation of the silver to Ag₂O [110]. It has been found that heating of the mordenite to the reduction temperature causes it to later adsorb water up to about 2 wt.% at operating temperatures around 150°C [111]. This has implications on how the iodine and tritium sorption beds should be sequenced in an engineering implementation.

12.4.2 Tritium

12.4.2.1 Tritium released by voloxidation of fuel

Tritium enters the off-gas streams in the form of tritiated water (HTO or ³H₂O). Because the voloxidation process is intended to remove tritium from used nuclear fuel, water removal from the voloxidation process off-gas is the key to curbing emissions. Various desiccants, such as calcium sulfate, can be used, but molecular sieves exhibit the highest loading of water per unit mass [103]. Type 3A molecular sieve (3AMS) can reduce the dew point of a gas stream to very low values, and it has a water capacity of around 20% by mass. Operating at room temperature, the dew point of air exiting a bed of 3AMS is under -70°C. It has also been found to absorb a small amount of iodine, which can result in adding a high-level waste component (¹²⁹I) to the low-level waste (³H), an undesirable effect on waste disposal costs [111]. The 3AMS can be regenerated at temperatures up to 270°C, releasing the water to a carrier gas stream of low volume, which can be cooled for condensing the water as a pure product.

Proper sequencing of the 3AMS and AgZ sorption beds has been shown to cleanly separate the tritiated water from the iodine [111]. An AgZ bed is first used to trap iodine. It will quickly saturate with water because there is more water in the stream than iodine. The 2% loading of water had little effect on the iodine retention

in short duration tests. As the AgZ bed continues to collect iodine, the water passes through the bed into a 3AMS bed for collection of the tritiated water. When the AgZ bed is approaching breakthrough of iodine, it is replaced with a fresh AgZ bed. The first AgZ bed is fed a low flow of clean air and is heated to drive the water from it, and the effluent joins the primary off-gas stream to flow into the second AgZ bed. Both the physisorbed iodine and water are removed from the first AgZ bed, and the iodine is trapped in the second bed. Iodine-free effluent flows to the 3AMS where the water is recovered. When the first AgZ bed is dried, it contains most of the iodine it originally trapped (as AgI) and only trace amounts of water, and it is then suitable for processing into a waste form. The tritiated water collected in the 3AMS bed(s) contains no iodine, qualifying it for low-level waste disposal.

12.4.2.2 Tritium released by cladding recycle

The zirconium recycling process is under development for recovering zirconium from the Zircaloy cladding component of used nuclear fuel. Small quantities of all isotopes of hydrogen are trapped in the Zircaloy as zirconium hydride. Processing releases and converts this hydrogen to hydrogen chloride, including tritium-substituted hydrogen chloride, ^3HCl (a.k.a., TCI). This compound of tritium must be removed from the zirconium recycle process off-gas and sequestered to satisfy regulations governing emissions of tritium. It is preferred that any method to remove the tritium be compatible with the recycle of the chlorine used to convert the zirconium to ZrCl_4 . Methods presently under testing include adsorption on 13 × or 5A molecular sieve, chemisorption on BiOF or NaF , and thermal pretreatment to remove the tritium before the cladding is contacted with chlorine [112].

12.4.3 Carbon-14

Molecular sieves can be used to collect carbon dioxide, the form in which ^{14}C enters the off-gas streams. Usually, the capacity is low and caustic scrubbing is preferred [103]. Sodium hydroxide and/or potassium hydroxide is/are customarily used at room temperature. For example, sodium hydroxide reacts with the CO_2 to produce sodium carbonate, which precipitates and can be recovered by filtering.

12.4.4 Krypton

Fluorocarbon sorbents have been used to capture ^{85}Kr . Cocapture of Xe , CO_2 , NO_2 also occur [113,114]. These processes require low-temperature operation, dewatering of the gas stream to be processed, and cryogenic distillation if separation is desired for the individual components.

In recent years, solid sorbents have been under investigation to adsorb krypton from effluent streams. Hydrogen form of mordenite (H-mordenite) has a high capacity for krypton, while the silver form of mordenite (Ag-mordenite) has a high capacity for xenon [115]. Appropriate temperatures of operation can be used to

prevent significant coadsorption of the noble gases, resulting in separation of Kr from Xe [116]. Commercially available activated charcoals can also be used [117,118]. However, there is a risk of a spontaneous combustion due to the potential presence of O₂, O₃, and NO_X in the off-gas stream.

Metal organic frameworks consisting of tridimensional porous structures made of metal centers cross-linked and coordinated with organic ligands that can be tailored to the separation of specific gases are also being considered and studied for the separation of Kr and Xe [119,120].

12.4.5 Noble metals and other semivolatiles

High-temperature oxidation of oxide nuclear fuels can be used to remove several semivolatile fission products such as Ru, Rh, Tc, Mo, Se, and Te [121,122].

The oxidizing nitric acid used for the dissolution of fuel has also been implicated in the production of RuO₄. Removal of RuO₄ from humidified gas streams using silica gel has been studied the most. A review of methods to capture volatile ruthenium tetroxide (RuO₄) was recently published [123]. The literature also contains information on the deposition of, presumably, RuO₂ on metal substrates where the RuO₄ decomposes to release oxygen. Recent studies that address speciation and sorption rate have shown that RuO₂ readily deposits on a steel substrate maintained at ~150°C from a gas stream containing RuO₄ [124]. Higher temperatures increase the deposition rate [125].

Pertechnetic acid (HTcO₄) may be released from the hot dissolver solution. Such species have been identified in off-gases, but they have not been well quantified. The fate of other semivolatile metals, or metal compounds, is less well-known [122].

12.5 Separations

Early reprocessing was centered on the recovery of Pu for military purposes, and the technology was later adapted to the processing of used LWR commercial fuel to separate the Pu (~1 wt.%) from the uranium, which is the major constituent (~95 wt.%), and a plethora of fission products (3–4 wt.%).

Present industrial-scale reprocessing is based solely on solvent extraction from aqueous solutions prepared by nitric acid dissolution of the LWR fuel, as described in Section 12.2.3. The recovered products are Pu and U as pure components. Separated plutonium is remixed with uranium to make mixed oxide fuel for LWRs and the uranium may be reenriched, also for use in LWRs. Hardware and cladding, fission products, and minor actinides are historically disposed as waste.

Most present developments are aimed at no separation of a pure Pu stream to address proliferation concerns. Instead, the Pu commingles with some U, U and Np, or U and the minor actinides (Np, Am, and Cm). The concentration of Pu in the mixed actinide product ranges from 30% to 50% in the different approaches under

development. This master mix product is then blended with uranium to meet the fuel requirements of the reactors that will use it.

There are two philosophies behind the present development efforts that are somewhat interrelated. One approach considers reprocessing as an integral tool for going from used nuclear fuel to a new fuel for either existing reactors or, more extensively, into yet to be deployed Gen IV reactors (e.g., solid-fueled fast reactors, thermal or fast neutron spectrum molten-salt reactors, gas-cooled particle-fuel high-temperature reactors). Other approaches include the concept of fuel recycling among similar reactors but also aim at minimizing the wastes that will require the very costly and difficult-to-site geological disposal by recovering other streams, such as zirconium cladding and hardware, sufficiently decontaminated to allow for disposal as low-level wastes or for reuse in the nuclear fuel cycle.

The existing developments include improvement in aqueous processing, such as advanced solvent-extraction processes and hybrid processes, that may include separation of actinides by crystallization or ion exchange; and nonaqueous processes that may include electrochemical, halide volatility, or a combination of both steps.

A report published by the OECD/NEA (Organisation for Economic Co-operation and Development/Nuclear Energy Agency) [39] describes in significant detail the present developments in reprocessing around the world. The following section provides some background information and highlights some of the newer processes, including some recent developments not included in the OECD/NEA report.

12.5.1 Hydrometallurgical separations—solvent extraction

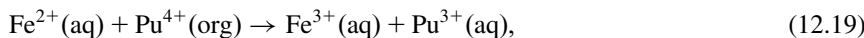
The chemistry of the PUREX process is based on different extraction equilibria of the actinides and fission products between an aqueous HNO_3 acid solution and organic phase containing TBP dissolved in an aliphatic solvent, such as kerosene or dodecane, at a typical concentration of 30 v/v%. TBP forms a neutrally charged nitrate complex generally with the formula $\text{M}(\text{NO}_3)_4 \cdot 2\text{TBP}$ or $\text{MO}_2(\text{NO}_3)_2 \cdot 2\text{TBP}$ that is soluble in the organic phase. Increasing the concentration of nitrate by, for example, adding a nitrate salt (e.g., Al or Ca) increases the fraction of the actinide metal extracted by the organic phase. This is usually not done at industrial scale as it increases the amount of waste; however, the mechanism is important for “the direct extraction” process introduced in [Section 12.2.2.3](#).

The extractability of actinides in 30 v/v% TPB from nitric acid solutions generally decreases in the following order $\text{U(VI)} > \text{Pu(IV)} > \text{Np(VI)} > \text{Np(IV)} > \text{Pu(VI)} > \text{U(IV)} > \text{Np(V)} > \text{Pu(III)}$ [126]. The distribution factor ($D_f = C_{\text{org}}/C_{\text{aq}}$), that is the ratio of the concentration in the organic phase to the concentration in the nitric acid solution, is less than 1 for Np(V) and Pu(III), meaning that in multistage solvent-extraction system, they stay in the aqueous solution (not extracted) or they deextract from the organic solution. The majority of the fission products and the minor actinides, Am and Cm (present as Am^{3+} and Cm^{3+}), have distribution factors < 1 ; thus they are not extracted. Technetium and zirconium are the main exceptions as technetium is extracted and zirconium is partially extracted.

The predominant actinide species in the dissolver solution are U(VI), Pu(IV), and Np(V). Without much need of redox adjustment, U and Pu can be extracted while Np will remain unextracted along with the vast majority of the fission products. Contacting the organic solution laden with U and Pu with a solution containing a reagent that reduces Pu(IV) to Pu(III) allows for a clean separation of a pure Pu stream. By careful adjustments of the extraction conditions, and, in particular, the concentration of nitrous acid, it is possible to convert the Np(V) into extractable Np(VI), resulting in an organic phase laden with U, Np, and Pu [127]. After the coextraction, Pu and Np can be stripped from the organic phase by complexation with reagents such as aceto-hydroxamic acid (AHA), $\text{CH}_3\text{CO}-\text{NHOH}$ [128].

The simplicity of the PUREX process along with its adaptability for the individual separation or group separations of the actinides, and great efficiency, make it hard to beat despite great efforts over many decades for developing superior processes.

Historically, ferrous sulfamate was the reagent of choice for reducing Pu(IV) to Pu(III), because Fe^{2+} rapidly reduces Pu^{4+} to Pu^{3+}



whereas the sulfamate acts as a “holding reductant” by rapidly destroying nitrite, which is radiolytically produced from the nitrate ions.



However, there were several disadvantages with this process, including plutonium losses, due to plutonium sulfate complexes, increased wastes, accelerated corrosion of stainless-steel equipment, and problems in the formulation of a glass waste form. The present reductants of choice are either hydroxylamine nitrate or U (IV) using hydrazine as the holding reductant. However, one of the significant disadvantages is the reaction of hydrazine and nitrous acid, resulting in the formation of hydrazoic acid, HN_3 , which can be extracted by TBP, and is potentially explosive; thus requiring process controls to eliminate this possibility [128].

As mentioned, AHA has also been studied as a possible alternative to back-extract Pu(IV) from the organic phases into the aqueous phase by forming a stable complex with Pu(IV) [and other (IV) species]. The Pu(IV) complexed in the aqueous phase is then reduced to Pu(III) due to the formation of hydroxylamine by hydrolysis of AHA. The potential disadvantages are twofold: the resulting hydroxylamine produced by hydrolysis could undergo an autocatalytic reaction with nitric acid, which may produce overpressurization and its decomposition to form acetic acid, which hampers nitric acid recycling [128].

Several variants of the PUREX processes were designed to produce a U + Pu or U + Pu + Np product in place of separated pure plutonium. They include the COEX process developed by Commissariat à l’Energie Atomique in France [129],

the Novel Uranium Extraction (NUEX) process developed by an industrial consortium led by Energy Solutions in the United States [130], the National Nuclear Laboratory advanced process developed in the United Kingdom [131], several UREX processes developed by the US Department of Energy, and the Russian simplified PUREX, and the REprocessing-PARTitioning (REPA) processes [39].

As an example of one of the many alternative processes, Fig. 12.17 shows the Co-D-Con process currently being developed by the US Department of Energy [132], where U(IV) is used to prepare a U–Pu costripped product separated from the bulk of the purified uranium. The minor actinides Am, Cm, and Np remain unextracted along with the fission products. The main goal of this project is to tightly control and measure the U–Pu ratio at around 30 wt.% Pu using online monitoring that includes Raman and ultraviolet–visible spectroscopy to quantify the concentrations of the actinide species in the different oxidation states, along with the concentrations of NO_3^- , HNO_3 , H^+ , etc. In addition, process temperatures, tank levels, and flow rates are also monitored online and used to provide process feedback. Independent instrumentation will be used to monitor fissile material inventory with the goal of implementing an integrated system that could provide a near real-time fissile inventory for process control and to provide near real-time information of fissile constituents, enabling a robust system for safeguards and non-proliferation purposes.

In addition to the solvent-extraction module a future integrated Co-D-Con demonstration is being planned, which will include all processing steps from receipt of used fuel to the fabrication of new fuel. The demonstration will include an

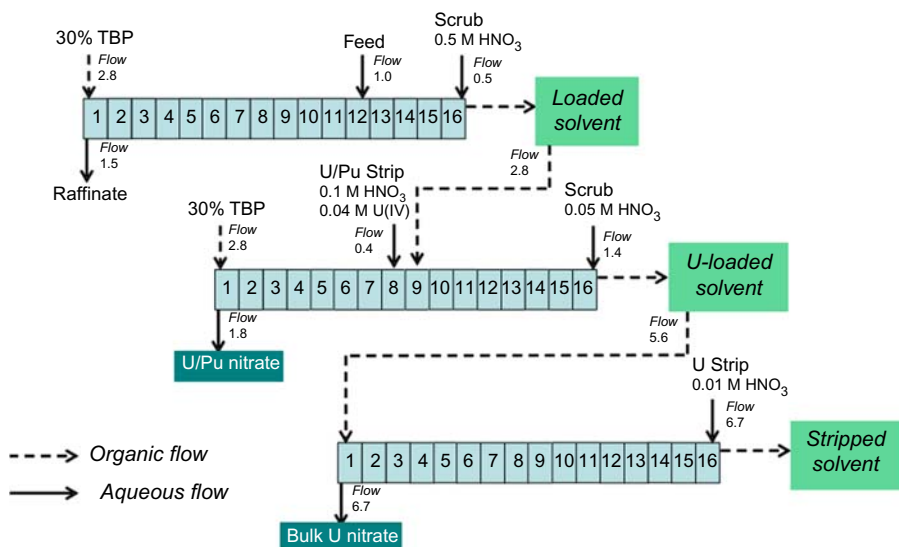


Figure 12.17 Co-D-Con solvent-extraction flow sheet exemplar.

advanced headend that separates and captures tritium, recovers, and purifies zirconium from cladding, and fabricates fuel [133]. Group Actinide Extraction (EURO-GANEX) [39] is a radically different solvent-extraction process that is under development in Europe with the goal of coseparating Pu, Am, and Cm to support the homogeneous recycling of the TRU actinides in fast reactors. Fig. 12.18 shows a schematic of the process.

N,N-di-2-ethylhexyl-isobutyramide is used upfront for the selective extraction of uranium (GANEX-1). The extractant for the TRU is a mixture of 0.2 M of *N,N,N'*, *N'*-tetraoctyl diglycolamide (TODGA) and 0.5 M of *N,N*'-dimethyl-*N,N*'-dioctyl-2-(2-hexyloxyethyl)malonamide (DMDOHEMA).

Numerous processes are being evaluated to separate the minor actinides, Am and Cm, from the lanthanides. Neutron poisoning is usually quoted as a rationale for this separation; however, the highly absorbing rare earths are transmuted during the irradiation of the fuel in the reactor so that the remaining rare earths at the end of life in the reactor have very limited effect. On the other hand, material burden for homogeneous recycle schemes is a real factor, because the rare earths in used fuel exist at a significantly larger concentration, compared to the minor actinides. In addition, rare earths are highly corrosive to the cladding in sodium-bonded metallic fuel. However, for oxide targets that need to be diluted to accommodate helium

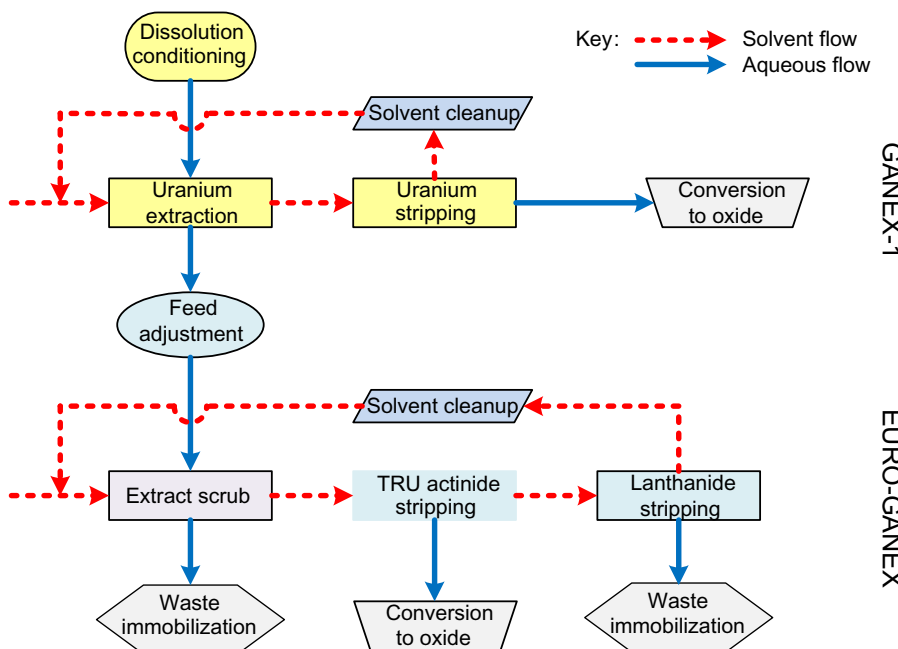


Figure 12.18 Flow sheet for EURO-GANEX.

generation, there is no need for separation, or at most a very limited separation, to raise the target concentration.

The difficult lanthanide–minor actinide separation usually requires one step to separate, as a group, the minor actinides and lanthanides from the rest of the fission products, followed by a second step that separates the minor actinides from the lanthanides. Examples of these dual processes include the TRU extraction–trivalent actinide lanthanide separation with phosphorus-reagent extraction from aqueous complexes (TRUEX–TALSPEAK), developed in the United States or the diamide extraction–selective actinide extraction (DIAMEX–SANEX) variants developed in Europe [39].

Efforts on a combined one-step process are also under development at the laboratory scale. One example is the actinide–lanthanide separation process being developed by the US Department of Energy [134], which uses an organic solvent consisting of a neutral diglycolamide extractant, either *N,N,N',N'*-tetra(2-ethylhexyl)diglycolamide (T2EHDGA) or TODGA, and an acidic extractant 2-ethylhexylphosphonic acid mono-2-ethylhexyl ester (HEH[EHP]), dissolved in an aliphatic diluent (e.g., *n*-dodecane). This extractant combination coextracts the minor actinides and lanthanides, separating them from the rest of the fission products. Selective stripping of the minor actinides from the lanthanides is carried out using a polyaminocarboxylic acid/citrate buffered solution at pH anywhere between 3 and 4.5.

12.5.2 Hybrid aqueous processing

In 1974 a reprocessing plant was built at Morris, Illinois, based on a hybrid technology named “Aquafluor” that included solvent extraction, ion exchange, and fluoride volatility [135]. The initial step was a high acid TBP extraction of U, Np, and Pu. Anionic exchange resins were used to separate purified aqueous streams of Pu, Np, and U. The uranium fraction was concentrated and then calcined to UO_3 . The uranium trioxide was then converted to UF_6 and purified using fluoride volatility. The plant encountered several operational problems that likely could have been resolved, but changes in the regulations and other economic factors caused the closure of the plant soon after the initial startup.

Another hybrid process currently under development, named FLUOREX, includes the separation of a large fraction of the uranium by crystallization (~70 wt.%) followed by the recovery of the remaining uranium along with Pu and Np by solvent extraction for generating a grouped U, Np, and Pu product [136,137]. A Russian (U and Pu) cocrystallization process is also used to achieve a homogeneous precursor to $(\text{U}, \text{Pu})\text{O}_2$ fuel [39].

12.5.3 Pyrochemical processes

Pyrochemical processes for producing uranium or plutonium metal by electrorefining have been used from the very beginning of the nuclear era. Molten-salt processes usually using low melting temperature chloride salt mixtures in contact with

molten active metals have long been used to separate and purify actinides. Electrochemical separations based on the selective reduction of species add flexibility to the same basic pyrochemical separations. Two main electrochemical processes have been used at pilot scale: the first was developed in the United States for sodium-bonded metallic fuel used in the integral fast reactor and must take place in a nearly pure argon gas inert atmosphere; the second was developed at the Research Institute of Atomic Reactors in Russia for the treatment and refabrication of oxide fuels, which operates in air [138].

In these pyroprocesses, the fuel is recycled using an electrochemical process based on molten chloride salts and liquid metals. The fuel is electrochemically dissolved using an appropriate potential between the basket, used as the anode, and a stainless-steel electrode in the salt phase, used as the cathode. As the fuel starts to dissolve, uranium and a small part of the TRU elements are collected at the cathode. Once the fuel is completely dissolved and most of the uranium is deposited on the solid steel, this cathode is replaced by a liquid cadmium cathode, and the remaining TRUs can be codeposited with the remaining uranium. A liquid cadmium cathode is a ceramic crucible containing molten cadmium that can be lowered into the salt bath. The cadmium in the crucible is put at cathodic potential. Due to the chemical activities of the TRU elements in cadmium, they can be more easily deposited in liquid cadmium cathodes than on solid cathodes. The cathode products from electrorefining operations are further processed for distilling adhering salt and cadmium and to consolidate the recovered actinides. Those are remotely fabricated into the new fuel for recycling.

The alkali, alkaline earth, rare earth, and halide fission products primarily remain dissolved in the salt phase. These elements can be separated from the salt phase (e.g., by extraction or precipitation processes) and are eventually conditioned in a ceramic high-level waste before being disposed. More than 90% of the noble-metal fission products and fuel alloy material are retained in the chopped fuel-cladding segments in the anode baskets. This residue can be stabilized into a metallic high-level waste to be prepared for disposal.

Adaptations of the integral fast reactor technology for the treatment of both oxide and nitride fuels are being developed in Japan. The flow sheet for the treatment of nitride fuels is similar to that of the metal fuel. Nitride fuels are also fed directly into the electrorefiner; the actinides are dissolved from the fuel cladding and collected all together electrochemically in liquid cadmium or liquid bismuth cathodes. A by-product of this process is an evolution of nitrogen gas. If the formation of ^{14}C from ^{14}N is to be avoided during the fuel irradiation, the initial nitride fuel should be enriched in ^{15}N . For obvious economic reasons the enriched nitrogen should be recycled, where it can be collected and fed back into the liquid cathodes where actinide nitrides are formed. This process and the fuel refabrication are challenging. After distillation of the cadmium the recovered nitrides are separated and then fabricated into a new fuel using a vibro-packing step [39].

12.5.4 Fluoride volatility

12.5.4.1 Introduction

Of the actinides, U, Np, and Pu can form volatile hexafluorides. UF_6 and NpF_6 are stable, but PuF_6 is thermally and radiolytically unstable. The thorium and the transplutonium elements form nonvolatile fluorides (e.g., ThF_4 , AmF_3 , AmF_4 , and CmF_3).

Of the fission products the rare earths and alkaline elements (e.g., La, Er, Cs, Sr) all form nonvolatile fluorides. The so-called noble-metal fission products—Mo, Tc, Ru, and Rh—and the fission products Sb, I, Br, Cl, S, Nb, Se, and Te form volatile fluorides and oxyfluorides. The krypton and xenon are permanent gases that escape the fuel when the solid is disintegrated.

Table 12.3 shows a list of the volatile actinide and fission-product fluorides, their BP, and a typical weight concentration in used LWR nuclear fuel. The concentrations expected for different reactor fuels will depend on the particular fuel cycle involved.

Relevant to structural materials is the fact that chromium forms two volatile oxyfluorides CrOF_4 (BP 30°C) and CrOF_4 (BP 95°C) [142].

Table 12.3 Boiling point of selected fluorides.

Volatile fluorides	BP (°C)	Typical elemental metal weight % in LWR used nuclear fuel	References
UF_6	56.5	94.7	[139]
NpF_6	76.8	0.06	[139]
PuF_6	61.8	0.94	[139]
Xe	– 108.4	0.68	[139]
MoF_6	33.8	0.40	[139]
MoOF_4	185.8		[139,140]
RuF_6	100	0.28	Unstable, [140]
RuF_5	226.8		[139,140]
RuOF_4	186		[135,141]
TcF_6	55.3	0.09	[22]
TcO_3F	100		
TcOF_4	165		
RhF_6	73.5	0.06	[141]
TeF_6	– 46.5	0.06	[139]
Kr	– 153.2	0.04	[139]
IF_7	4.8	0.03	[139]
IF_5	100.5		
SeF_6	– 46.5	0.006	[139]
BrF_5	40.8	0.002	[139]
BrF_3	125.8		
SbF_5	143	0.001	[139]

BP, Boiling point; LWR, light-water reactor.

FeF_3 becomes volatile above 450°C , ZrF_4 above 600°C , and CrF_3 above 650°C [139].

Typically, individual components of the volatile fluorides can be separated using fractional distillation and/or selective trapping. Fluoride volatility can offer a very high throughput in a very small footprint and can be used for a wide variety of fuels and targets.

12.5.4.2 Fluorinating agents

Several fluorinating agents can be used for fluoride volatility processes, including F_2 (the most common), interhalogens (ClF_3 , BrF_3 , BrF_5 , ClF , etc.), and fluorine-rich compounds (NF_3 , SF_6 , etc.). F_2 and ClF_3 can produce PuF_6 ; bromine fluorides, chlorine monofluoride, and nitrogen trifluoride will not [143]. The interhalogens can be used for low-temperature fluorination processes, even at room temperature [143].

Fluorine requires moderate to high temperatures. Low-temperature fluorination (e.g., 300°C – 350°C) can produce UF_6 with very little PuF_6 . Increasing the temperature above 600°C greatly increases the yield of PuF_6 [144,145].

Nitrogen trifluoride requires higher temperatures ($>550^\circ\text{C}$) to produce UF_6 but will not produce PuF_6 . Another good feature of this reagent is that it is relatively innocuous at room temperature [146].

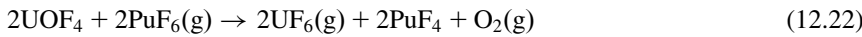
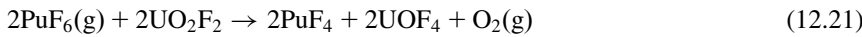
12.5.4.3 Separation methods

Depending on the particular type of reactor and its associated fuel cycle, it would be necessary to separate, concentrate, or separate and concentrate the volatile, fissile, and/or fertile species from the other fuel components. The two main options are fractional distillation and selective trapping.

Uranium recovered from ores is converted to uranium hexafluoride, and purification by distillation has been implemented at an industrial scale. However, distillation for separating UF_6 from PuF_6 , NpF_6 , or both has not yet been demonstrated.

12.5.4.4 Coseparation of Pu , Np , and U from the bulk of UF_6

PuF_6 and NpF_6 are very strong fluorinating agents, and they will fluorinate uranyl fluorides (UO_2F_2 , UOF_4) and lower uranium fluorides (UF_4 , UF_5).



PuF_6 is thermally and radiolytically unstable, and efficient plutonium recovery requires rapid cooling and trapping. An upfront trap made of uranyl or lower fluorides could allow the fast recovery of the plutonium produced during the volatilization process. Since it will always be comingled with uranium and neptunium, this trapping methodology will provide a degree of proliferation protection by never producing a pure stream of plutonium. This trapping technology has been demonstrated at laboratory scale using UO_2F_2 [147], and has been patented [148].

Such a trap will not retain any net amount of UF_6 ; however, there will be exchange between the UF_6 in the gas phase and uranium compounds in the solid phase [149]. Such a trap will need to be regenerated using the recovered uranium stream. For a 30% plutonium loading, it would require the recycling of about 3% of the uranium stream for preparing the trapping media.

The remainder of the volatile fluorides, except for ruthenium and niobium fluorides, will not react and should bypass the trap. Ruthenium and niobium fluorides can be condensed as solids at temperatures below 200°C, so they can be recovered upstream of the plutonium trap [147].

12.5.4.5 Selective trapping of impurities using metallic fluorides

Volatile fluorides and oxyfluorides sorb and chemisorb on other fluorides or oxyfluorides with bonding strengths ranging from weak adsorption to forming double salts with a degree of interaction that varies significantly with temperature. The appropriate sorbent at a given range of temperature can be used as a means for selective trapping. A large number of reagents were tried and tested at the laboratory scale, including BiF_3 , CoF_2 , CoF_3 , PbF_2 , MnF_2 , SnF_4 , KF , BiOF , K_3NiF_6 , and Na_3AlF_6 [150]. A few were used at pilot scale, such as LiF , and two were used at industrial scale, NaF and MgF_2 . Of these, BiOF shows promise for selectively trapping HF comingled with UF_6 [150].

Magnesium fluoride

Magnesium fluoride is highly insoluble in water (0.0076 g/100 mL) at 18°C [151]. It can be agglomerated with water, pressed into green pellets, dewatered, and sintered at high temperatures to produce porous pellets that can be used to selectively trap technetium. Trapped technetium cannot be easily desorbed from the MgF_2 , requiring temperatures above 1000°C. However, trapped technetium can be easily removed by washing with water or dilute nitric acid. The magnesium fluoride can be reused after a drying step [152]. Magnesium fluoride has been used at a large scale for the selective trapping of volatile technetium fluorides and oxyfluorides of technetium comingled with UF_6 [22,152,153].

Sodium fluoride

Early references to interactions between UF_6 on KF and NaF dates back to the early 1900s, but they erroneously reported a violent interaction [154,155]. The trapping of UF_6 by NaF was revisited by Grosse in 1941 [156]. Since then, numerous studies

have reported the reversible sorption of UF_6 on NaF [157,158], including large-scale industrial use [159].

NaF pellets can be made by mixing the powder with water to form agglomerates that are pelletized. The pellets are then dewatered and sintered [160]. Sodium fluoride will also sorb other species such as HF and MoF_6 . Fig. 12.19 shows the respective vapor pressures for UF_6 , MoF_6 , and HF over NaF . Operating somewhat below 200°C allows the selective trapping of UF_6 , whereas MoF_6 and HF will bypass the trap. UF_6 can later be desorbed at higher temperatures [161,162].

12.5.5 Chloride volatility

12.5.5.1 Introduction

As shown in Table 12.4, protactinium and uranium form chlorides that are volatile at relatively low temperatures (PaCl_5 , UCl_5 , UCl_6). Increasing the temperature will volatilize ThCl_4 , followed by NpCl_4 , and at even higher temperatures, AmCl_3 . The volatility of PuCl_3 by itself is very low, but it is increased by the formation of PuCl_4 in the gas phase [163] according to the reaction



Of the fission products the rare earths and alkaline earths form nonvolatile chlorides. The fission products Mo, Zr, Nb, In, I, Br, Cl, Se, and Te form volatile chlorides and enter the gas phase along with Kr and Xe, which are permanent gases. Technetium forms volatile oxychlorides and TcCl_4 , which are volatile but not well characterized [164,165].

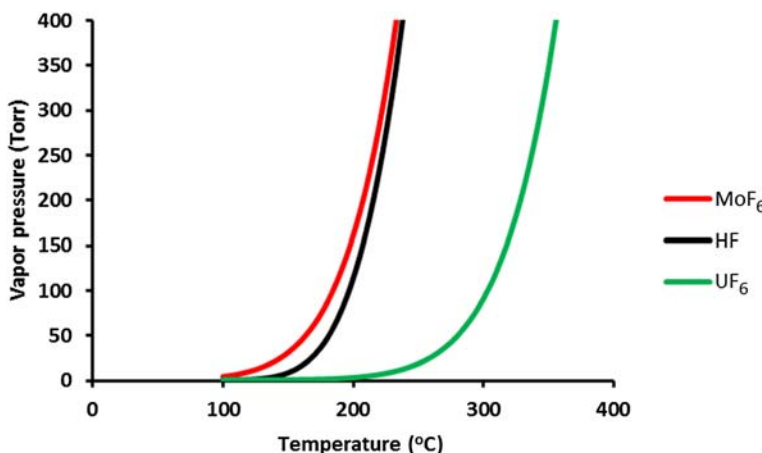


Figure 12.19 Comparison of equilibrium vapor pressure of MoF_6 , HF , and UF_6 over NaF as a function of temperature.

Table 12.4 Vapor pressure of select chlorides.

Species	Vapor pressure (Torr)			BP (°C)	Reference
	300°C	500°C	700°C		
ThCl ₄	5.9×10^{-9}	4.0×10^{-3}	10.8	922	[163]
PaCl ₅	4.6	520	> 760	420	[163]
UCl ₅	2.4	370	> 760	527	[163]
UCl ₆	> 760	> 760	> 760	277	[163]
NpCl ₄	3.3×10^{-7}	9.3×10^{-3}	0.60	847	[139]
PuCl ₃	7.9×10^{-15}	2.0×10^{-8}	1.1×10^{-3}	1790	[163]
AmCl ₃	9.6×10^{-12}	8.4×10^{-6}	2.63×10^{-2}	1180	[163]
ZrCl ₄	225	> 760	> 760	331	[163]
NbCl ₅	> 760	> 760	> 760	267	[163]
MoCl ₅	> 760	> 760	> 760	260	[163]
MoOCl ₄	> 760	> 760	> 760		[139]
TcCl ₅	> 760	> 760	> 760	232	[139]
InCl ₃	2.26×10^{-2}	82	> 760	582	[139]
TeCl ₄	266	> 760	> 760	387	[139]
CsCl	6.5×10^{-8}	2.0×10^{-3}	0.7	1300	[158]
RuCl ₃	3.4×10^{-12}	3.1×10^{-5}	0.3	Decomposes	[163]
RhCl ₃	2.5×10^{-17}	3.7×10^{-9}	2.0×10^{-4}	Decomposes	[163]
SrCl ₂	2.3×10^{-18}	2.5×10^{-11}	3.5×10^{-7}	2027	[163]
BaCl ₂	1.8×10^{-16}	1.6×10^{-9}	1.5×10^{-5}	2100	[163]
CeCl ₃	1.0×10^{-16}	6.8×10^{-9}	1.7×10^{-4}	1730	[163]
GdCl ₃	8.3×10^{-15}	3.5×10^{-7}	1.7×10^{-3}	1580	[163]

BP, Boiling point.

12.5.5.2 Processing of fuels

Early attempts to develop chloride volatility processing schemes for nuclear fuels were not very successful. Warren and Ferris studied the possibility of using a chloride volatility process on mixed oxide fuel and concluded it was impractical [166]. To speed the chlorination process the fuel was pretreated with air/oxygen oxidation in the 400°C–600°C range to form a very fine U₃O₈ powder. This pretreatment process was successful for fuels having concentrations of PuO₂ up to 20 wt.%. A mixture of 85% Cl₂ and 15% CCl₄ was used as the chlorination agent. The chlorination itself required 3–5 hours. However, a method could not be devised at that time to separate the uranium chlorides from other components, and the removal of Pu at temperatures of 550°C required a huge amount of excess chlorine gas (10,000 mol of chlorine per mole of Pu). Operating at higher temperatures was impractical because of corrosion and the formation of liquid oxychloride phases.

The laboratory investigations by Hariharan and his group appears somewhat more promising [163,167]. A 4:1:1 Cl₂–CCl₂–N₂ mixture was used as the chlorinating reagent on powdered Th–U and U–Pu oxide fuels. As trapping materials, two alumina filter beds were used, followed by a NaCl bed. For the Th–U fuels a

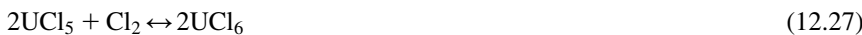
chlorination temperature of 750°C was used and over 99% of the Th was collected on the first alumina filter, and over 90% of the uranium was collected in the NaCl trap with decontamination factors in the order of 10². It was observed that both UCl₅ and UCl₆ are retained in the NaCl bed, forming a sharp orange-red band, possibly as the binary compound of U(V), NaUCl₆, that can be transformed into a green U(IV) compound, Na₂UCl₆, by reduction with hydrogen. Based on these results, a flow sheet was developed, which adds a second-stage purification for the U and Th products achieving an overall 10⁴ decontamination factor.

In contrast, powdered U–Pu fuel was chlorinated at 450°C. The uranium was trapped on the NaCl along with Mo, Nb, and Zr. The rest of the fission products remained with the plutonium in the chlorination chamber. No attempts were made for the recovery and purification of Pu because it was concluded that a fluoride volatility step would be more efficient.

12.5.5.3 Chloride volatility in molten salts

Very limited information is available on this topic. Olander and Camahort [168] describe the chlorination of UCl₄ dissolved in a eutectic salt of KCl and LiCl. Using Cl₂ at 400°C, about 30% of the uranium is volatilized in 1 hour. Operating at 600°C, about 50% of the uranium is volatilized in 1 hour. In addition to pure chlorine, mixtures of Cl₂/Ar (50–50 and 25–75 mol.%) and Cl₂/He (50–50 mol.%) were used.

Uranium forms four chlorides (i.e., UCl₆, UCl₅, UCl₄, and UCl₃) and numerous oxychlorides (e.g., UOCl, UOCl₂, UOCl₃, and UO₂Cl₂). During chlorination the products can be UCl₄, UCl₅, or both, and in some instances, UCl₆. All three chlorides are interrelated by the following reactions:



In addition, the presence of oxygen as an impurity can also cause the formation of oxychlorides. Typically, chlorination is done in open systems. However, just to exemplify the different equilibria, Figs. 12.20 and 12.21 show the preponderate phases as a function of temperature and Cl₂ partial pressure at two fixed oxygen levels, which were calculated using the thermochemical modeling program HSC Chemistry [139].

12.5.5.4 Interconversion of chlorides and fluorides

Fluorides (e.g., UF₄ or UF₆) can be transformed into UCl₄, using reagents such as BCl₃ or AlCl₃. For example,

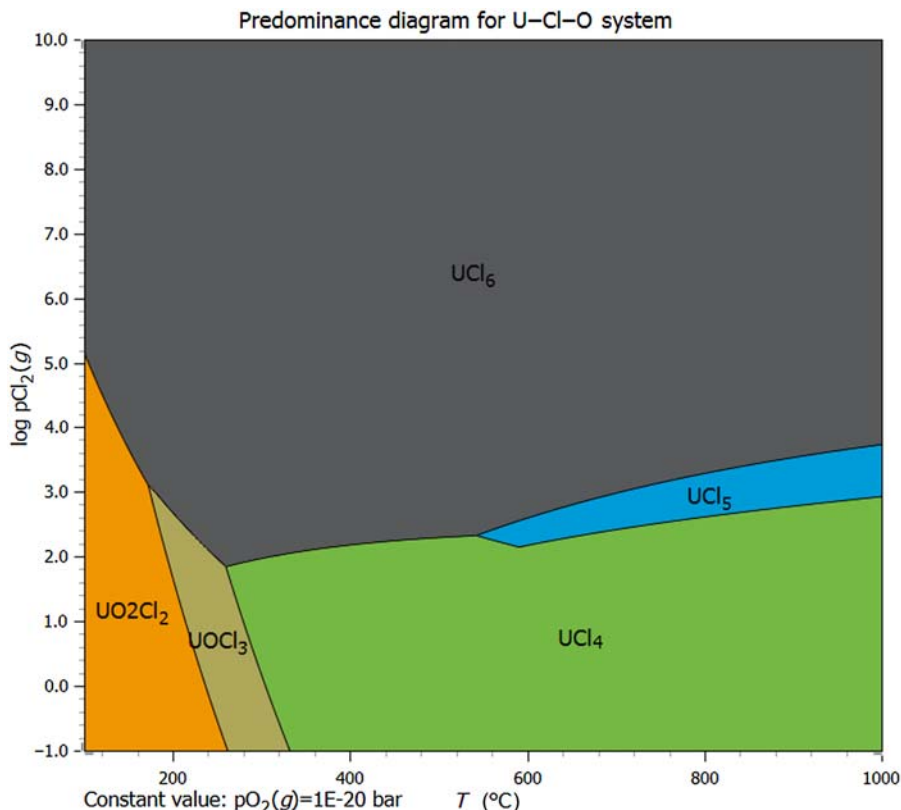
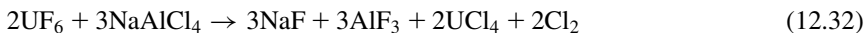


Figure 12.20 Predominance diagram for U–Cl–O system (O_2 partial pressure 1×10^{-20} bar).



Chlorides can be transformed into fluorides using anhydrous HF. These reactions take place at moderate temperatures of $250^\circ\text{C}–500^\circ\text{C}$ [169].

Similarly, UF_6 can be directly converted to UCl_4 using Al_2Cl_6 , BCl_3 , or NaAlCl_4 [170]:



With other reagents the reverse transformation can be made; specifically, chlorides can be transformed into fluorides. Fluorinating agents, such as F_2 , NF_3 , ClF_3 ,

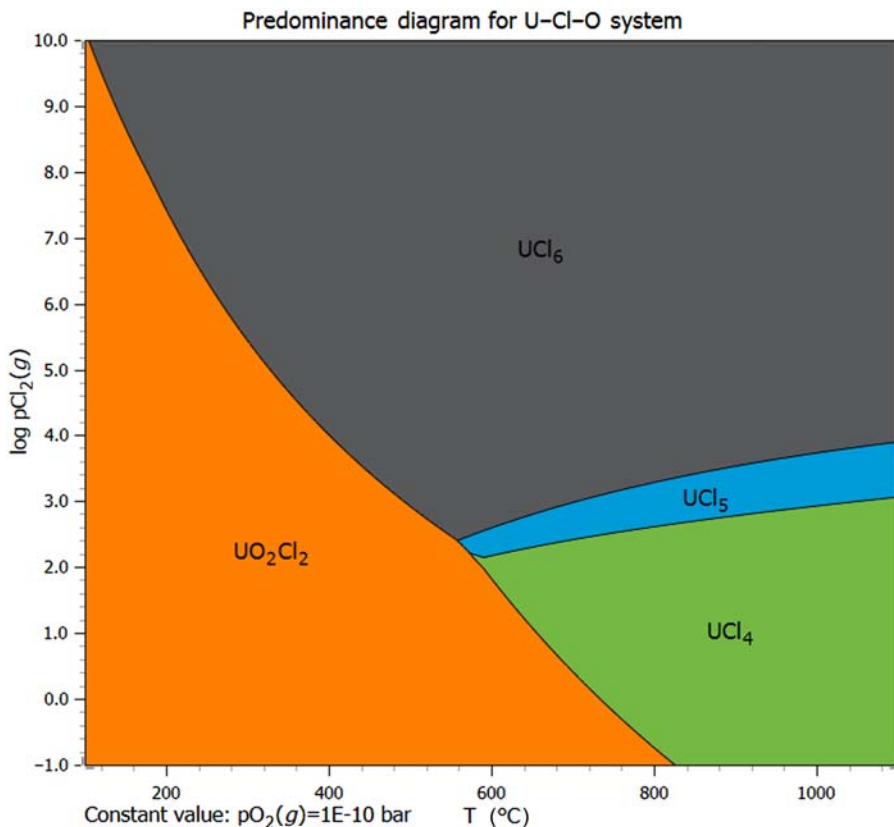


Figure 12.21 Predominance diagram for U–Cl–O system (O_2 partial pressure 1×10^{-10} bar).

and anhydrous HF, may be used, and recovery of actinides may be accomplished using fluoride volatility processes [171].

12.5.5.5 Overall assessment of chloride volatility

Chloride volatility processes are more complicated than and not as effective as fluoride-based processes. Thorium–uranium fuels appear more amenable to chloride volatility processes.

Recent developments in voloxidation using NO_2 can produce a UO_3 powder at a lower temperature. A low-temperature UO_3 can be chlorinated at a lower temperature and a faster rate using Cl_2 or $\text{Cl}_2\text{--CCl}_4$ mixtures, allowing for the distillation of a pure uranium stream. Other chlorinating agents can also be used, including liquid CCl_4 [172], SOCl_2 [173], Al_2Cl_6 [169,170,174–176], and hexachloropropene [177,178].

The effective trapping of volatile uranium chlorides in NaCl suggests a strong complexation. This, in turn, suggests a more difficult volatilization of uranium chlorides out of alkaline molten chloride salt.

References

- [1] A. Andrews, Nuclear fuel reprocessing: US policy development, in: CRS Report for Congress, Order Code RS22542, March 2008, <<https://fas.org/sgp/crs/nuke/RS22542.pdf>>.
- [2] A.G. Croff, R.G. Wymer, L.T. Tavlarides, J.H. Flack, H.J. Larson, Background, status, and issues related to the regulation of advanced spent nuclear fuel recycle facilities, in: A White Paper of the US Nuclear Regulatory Commission's Advisory Committee on Nuclear Waste and Materials, September 2007, <<https://www.nrc.gov/docs/ML0728/ML072850765.pdf>>.
- [3] E.D. Collins, G.D. Del Cul, J.E. Rushton, K.A. Williams, ORNL/TM-2010/81 A Practical Solution to Used Nuclear Fuel Treatment to Enable Sustained Nuclear Energy and Recovery of Vital Materials, Oak Ridge National Laboratory, Oak Ridge, TN, 2010.
- [4] Japan Nuclear Fuel Limited, The Rokkasho Reprocessing Plant, (last visited Feb. 27, 2020) <<https://www.jnfl.co.jp/en/business/reprocessing/>>.
- [5] P.R. Orszag, Costs of reprocessing versus directly disposing of spent nuclear fuel, in: Congressional Budget Office Testimony before the Committee on Energy and Natural Resources United States Senate, November 14, 2007.
- [6] A.G. Croff, C.W. Alexander, ORNL/TM-7431 Decay Characteristics of Once-Through LWR and LMFBR Spent Fuels, High-level Wastes, and Fuel-Assembly Structural Material Wastes, Oak Ridge National Laboratory, Oak Ridge, TN, 1980.
- [7] US Department of Energy, DOE/RW-184-R1-V1 Characteristics of Potential Repository Wastes, Office of Civilian Radioactive Waste Management, Washington, DC, 1992.
- [8] G.D. Del Cul, B.B. Spencer, E.D. Collins, A new paradigm: near-complete recycling of spent fuel—a path to sustainable nuclear energy, in: Proceedings of Global 2007 International Conference, Advanced Nuclear Fuel Cycles and Systems, Boise, ID, September 9–13, 2007.
- [9] E. Hardin, T. Hadgu, D. Clayton, R. Howard, H. Greenberg, J. Blink, et al., FCRD-UFD-2012-000219 rev. 2 Repository Reference Disposal Concepts and Thermal Load Management Analysis, Sandia National Laboratories, Albuquerque, NM, 2012.
- [10] Turner Construction Company, Turner Building Cost Index, 1st Quarter 2012 and 1st Quarter 2018, <<http://www.turnerconstruction.com/cost-index>>.
- [11] US Department of Energy Office of Civilian Radioactive Waste Management (OCRWM), DOE/RW-0591. Analysis of the Total System Life Cycle Cost of the Civilian Radioactive Waste Management Program, Fiscal Year 2007, July 2008.
- [12] World Nuclear News, Yucca Mountain Cost Estimate Rises to \$96 Billion, August 2008, <http://www.world-nuclear-news.org/WR-Yucca_Mountain_cost_estimate_rises_to_96_billion_dollars-0608085.html>.

- [13] T. Kukkola, T. Saanio, POSIVA-WR-05-10. Cost Estimate of Olkiluoto Disposal Facility for Spent Nuclear Fuel, Helsinki, Finland, March 2005.
- [14] H. Fountain, On Nuclear Waste, Finland Shows US How It Can Be Done, New York Times, June 9, 2017, <<https://www.nytimes.com/2017/06/09/science/nuclear-reactor-waste-finland.html>>.
- [15] E.D. Collins, G.D. Del Cul, J.A. Johnson, T.D. Hylton, R.D. Hunt, B.B. Spencer, et al., Engineering scale development/demonstration of zirconium recovery from used fuel cladding, *Trans. Am. Nucl. Soc.* 116 (2017) 59–62. ANS Annual Meeting, San Francisco, CA, June 11–15, 2017.
- [16] G.D. Del Cul, E.D. Collins, B.B. Spencer, R.D. Hunt, Recovery, purification, and recycle of zirconium from used nuclear fuel, in: Actinide Separations Conference, Albuquerque, NM, June 2014.
- [17] G.D. Del Cul, L.D. Trowbridge, J.P. Renier, R.J. Ellis, K.A. Williams, B.B. Spencer, et al., ORNL/TM-2007/207, also ORNL/GNEP/LTR-2008-002 and ORNL/TM-2009/023. Analysis of the reuse of uranium recovered from the reprocessing of commercial LWR spent fuel, UT-Battelle, Oak Ridge National Laboratory, Oak Ridge, TN, January 2009.
- [18] International Atomic Energy Agency, IAEA-TECDOC-1529. Management of Reprocessed Uranium Current Status and Future Prospects, Vienna, 2009.
- [19] R.J. Ellis, Prospects of using reprocessed uranium in CANDU reactors in the US GNEP program, *Trans. Am. Nucl. Soc.* 97 (1) (2007) 107.
- [20] F. Shen, M. Zhiliang, Q. Gang, C. Mingjun, Demonstration test of recycled uranium reprocessed from PWR spent fuel in CANDU reactors, *At. Energy Sci. Technol.* 47 (Suppl) (2013) 128–131.
- [21] World Nuclear Association, Processing of Used Nuclear Fuel, <<http://www.world-nuclear.org/information-library/nuclear-fuel-cycle/fuel-recycling/processing-of-used-nuclear-fuel.aspx>> (updated 2018).
- [22] D.W. Simmons, K/TSO-39. An introduction to technetium in the gaseous diffusion cascades, Oak Ridge K-25 Site, Oak Ridge, TN, 1996.
- [23] World Nuclear Association, Nuclear Power in France, <<http://www.world-nuclear.org/information-library/country-profiles/countries-a-f/france.aspx>> (updated 2018).
- [24] V.N. Prusakov, A.A. Sazykin, L. Yu Sosnin, D.V. Utrobin, A.N. Chel'tsov, Correcting the isotopic composition of regenerated uranium with respect to ^{232}U by a centrifuge method with introduction of a carrier gas, *At. Energy* 105 (3) (2008) 194–201.
- [25] D.V. Postovarova, N.V. Kovalev, M.S. Onegin, B.A. Bibichev, Radiation characteristics of REMIX fuel during multiple recycling in VVER-1000 reactors, *Nucl. Energy Technol.* 2 (2) (2016) 119.
- [26] World Nuclear Association, Russia's Nuclear Fuel Cycle, <<http://www.world-nuclear.org/information-library/country-profiles/countries-o-s/russia-nuclear-fuel-cycle.aspx>> (updated 2018).
- [27] M.H.A. Piro, D. Sunderland, S. Livingstone, J. Sercombe, W. Revie, A. Quastel, et al., A Review of Pellet–Clad interaction behavior in zirconium alloy fuel cladding, in: Saleen Hashmi (Ed.), Reference Module in Materials Science and Materials Engineering, Oxford Elsevier, 2017, pp. 1–68.
- [28] Sandvik Special Metals, Zirconium Alloy Fuel Clad Tubing: Engineering Guide, Sandvik Special Metals Corp., Kennewick, WA, 1989.
- [29] A.T. Motta, A. Couet, R.J. Comstock, Corrosion of zirconium alloy used for nuclear fuel cladding, *Annu. Rev. Mater. Res.* 45 (2015) 311.

- [30] Atlantic Compact Regional Waste (Barnwell, SC), Uniform Schedule of Maximum Disposal Rates for Atlantic Compact Regional Waste, 2017, <<http://www.energy.gov/files/MURS%202018.pdf>>.
- [31] Nuclear Engineering International, Estimating the Disposal Costs of Spent Fuel, 2011, <<http://www.neimagazine.com/features/featureestimating-the-disposal-costs-of-spent-fuel>>.
- [32] D. Greeneche, Reprocessing and recycling of used nuclear fuels: the French feedback experience and international aspects, in: IAEA-INPRO Meeting, Vienna, 2010.
- [33] C. Burrows, C. Phillips, A. Milliken, The thermal oxide reprocessing plant at Sellafield—lessons learned from 10 years of hot operations and their applicability to the DOE environmental management program, in: WM'06 Conference, February 26–March 2, 2006, Tucson, AZ, <<http://www.wmsym.org/archives/2006/pdfs/6482.pdf>>.
- [34] NUS Co, EPRI NP-6892. Fuel consolidation demonstration program: final report, 1990.
- [35] KAERI, KAERI/TR-1612/2000. Model development for quantitative evaluation of proliferation resistance of nuclear fuel cycles: DUPIC, 2000.
- [36] A. MacCragh, Extraction of Fission Product Noble Metals From Spent Nuclear Fuels, US Patent, 3,672,875, 1972.
- [37] G.A. Jensen, A.M. Platt, G.B. Mellinger, W.J. Bjorklund, Recovery of noble metals from fission products, Nucl. Technol. 65 (1984) 305.
- [38] J. Naito, Recovery of noble metals from insoluble residues of spent fuel, J. Nucl. Sci. Technol. 23 (1986) 540.
- [39] OECD-NEA Report, NEA No. 7267. State-of-the-art Report on the Progress of Nuclear Fuel Cycle Chemistry, Nuclear Energy Agency, 2018.
- [40] G. Duffy, M. Astill, The oxide fuel shearing system for THORP, in: Waste Management '88: Symposium on Radioactive Waste Management; Tucson, AZ, 1988 <<http://www.wmsym.org/archives/1988/V2/74.pdf>>.
- [41] S. Karunakaran, K.N.S. Nair, D.A.S. Rao, Development of a novel spent fuel chopper for PHWR fuel, Bhabha Atomic Research Centre (BARC), Technical Development Article, 317, 2010 <<http://www.barc.gov.in/publications/nl/2010/2010111209.pdf>>.
- [42] K. Okada, Separation Method for a Spent Fuel Rod, European Patent Application No. 19850302514, 1985.
- [43] W.D. Bond, J.C. Mailen, G.E. Michaels, ORNL/TM-12104 Evaluation of Methods for Decladding LWR Fuel for a Pyroprocessing-Based Reprocessing Plant, Oak Ridge National Laboratory, Oak Ridge, TN, 1992.
- [44] S.D. Hermann, S. Li, M. Simpson, Electrolytic reduction of spent light water reactor fuel—Bench-scale experimental results, J. Nucl. Sci. Technol. 44 (2007) 361–367.
- [45] K.C. Song, G.I. Park, J.W. Lee, J.J. Park, M.S. Yang, Fractional release behavior of volatile and semivolatile fission products during a voloxidation and OREOX treatment of spent PWR fuel, Nucl. Technol. 162 (2008) 158–168.
- [46] R.S. Frazier, D.C. Campbell, Production decladding of irradiated fuel assemblies using a YAG laser, Trans. Am. Nucl. Soc. 55 (1987) 645.
- [47] G.D. Del Cul, J.A. Johnson, B.B. Spencer, E.D. Collins, R.T. Jubin, J.C. Bresee, Dry pretreatment of used nuclear fuel to simplify storage or recycle—shearing or chemical decladding and voloxidation, Trans. Am. Nucl. Soc. 107 (2012) 246. 2012 ANS Winter Meeting, San Diego, CA.
- [48] H. Hecht, G. Jander, H. Schlapmann, Über die einwirkung von thionylchlorid auf oxyde (Action of thionyl chloride on oxides), Z. Anorg. Chem. 254 (1947) 255–264.
- [49] H.B. North, A.M. Hageman, The action of thionyl chloride on metals and metalloids, J. Am. Chem. Soc. 34 (1913) 890–894.

- [50] M.M. Metalidi, S.V. Shapovalov, R.V. Ismailov, M.I. Skriplev, V.I. Beznosuk, Yu. S. Fedorov, Thermochemical embrittlement of the zirconium cladding of a fuel rod and oxidative recrystallization of the fuel material in the course of spent nuclear fuel reprocessing, *Radiochemistry* 57 (1) (2015) 98–102.
- [51] Yu.S. Fedorov, V.F. Saprikin, V.I. Beznosuk, A.B. Koljadin, Thermo-chemical destruction of zirconium cladding of the spent fuel assembly and oxidation of the fuel composition using technology of spent nuclear fuel reprocessing at the experimental-demonstration, Paper No. 9055, Proceedings of Global 2009, Paris, France, September 6–11, 2009.
- [52] M. Steinbrück, M. Böttcher, Air oxidation of Zircaloy-4, M5 and ZIRLO™ cladding alloys at high temperatures, *J. Nucl. Mater.* 414 (2) (2011) 285.
- [53] A.J. Parkison, Hydride production in zircaloy-4 as a function of time and temperature (Masters' thesis), Texas A&M University, College Station, TX, 2008.
- [54] M. Benedict, T. Pigford, H. Levi, *Nuclear Chemical Engineering*, second ed., McGraw Hill, New York, 1981.
- [55] R.T. Jubin, B.B. Spencer, Tritium management approaches and their impacts on tritium distribution within a UNF reprocessing plant, in: 2017 AIChE Annual Meeting, Minneapolis, MN, October 26–November 3, 2017.
- [56] M. Iwasaki, T. Sakurai, N. Ishikawa, Y. Kobayashi, Oxidation of UO₂ pellets in air: effect of heat-treatment of pellet on particle size distribution of powders produced, *J. Nucl. Sci. Technol.* 5 (12) (1968) 652–653.
- [57] K.A. Peakall, J.E. Antill, Oxidation of uranium dioxide in air at 350–1000°C, *J. Nucl. Mater.* 2 (2) (1960) 194–195.
- [58] G. Uchiyama, et al., Study on voloxidation process for tritium control in reprocessing, *Radioactive Waste Manage. Nucl. Fuel Cycle* 17 (1) (1992) 63–79.
- [59] R.T. Jubin, G.D. Del Cul, B.D. Patton, R.S. Owens, D.W. Ramey, B.B. Spencer, Advanced fuel cycle initiative coupled end-to-end research, development, and demonstration initial performance, in: Waste Management 2009 Conference, Phoenix, AZ, March 1–5, 2009, <<http://www.wmsym.org/archives/2009/pdfs/9226.pdf>>.
- [60] B.B. Spencer, G.D. Del Cul, R.T. Jubin, D.W. Ramey, E.D. Collins, Voloxidation processing of kilogram quantities of used nuclear fuel, in: 16th Symposium on Separation Science and Technology for Energy Applications, Gatlinburg TN, October 18–22, 2009.
- [61] G.D. Del Cul, R.D. Hunt, J.A. Johnson, B.B. Spencer, R.T. Jubin, E.D. Collins, Advanced head end for the treatment of used LWR fuel, in: OECD Nuclear Energy Agency 11th Information Exchange Meeting on Actinide and Fission Product Partitioning and Transmutation, San Francisco, California, November 1–5, 2010, <https://www.oecd-nea.org/pt/iemt11/documents/IV-6_OECDNov2011FR.pdf>.
- [62] J.A. Johnson, C.J. Rawn, G.D. Del Cul, E.D. Collins, Kinetic studies of NO₂ oxidation of uranium oxides by *in situ* XRD and neutron diffraction, *Trans. Am. Nucl. Soc.* 107 (2012) 243.
- [63] E.D. Collins, G.D. Del Cul, R.D. Hunt, J.A. Johnson, B.B. Spencer, Advanced Dry Head-End Reprocessing of Light Water Reactor Spent Nuclear Fuel, Patent US 8,574,523, November 2013.
- [64] E.D. Collins, G.D. Del Cul, R.D. Hunt, J.A. Johnson, B.B. Spencer, Advanced Dry Head-End Reprocessing of Light Water Reactor Spent Nuclear Fuel, Patent US 8,747,790, June 2014.
- [65] T.A. Todd, R.A. Wigeland, Advanced separation technologies for processing spent nuclear fuel and the potential benefits to a geologic repository, in: *Separations for the*

- Nuclear Fuel Cycle in the 21st Century, Chapter 3, 41–55, ACS Symposium Series, vol. 933, 2006.
- [66] C.E.L. Hunt, F.C. Iglesias, D.S. Cox, N.A. Keller, R.D. Barrand, J.R. Mitchell, et al., Fission product release during UO₂ oxidation, in: Conference Proceedings: International Conference on CANDU Fuel, 508–526, October 1986.
 - [67] T.S. Rudisill, T.C. Shehee, D.H. Jones, G.D. DelCul, Dissolution of used nuclear fuel using a tributyl phosphate/n-paraffin solvent, *Sep. Sci. Technol.* (2019). Available from: <https://doi.org/10.1080/01496395.2019.1578805>. Published online: 22 Feb.
 - [68] J. Bressee, Exploring the accountability aspects of the CoDCon project, in: 42nd Annual Actinide Separation Conference, Charleston, SC, May 21–24, 2018.
 - [69] N. Desigan, N.P. Bhatt, N.K. Pandey, U.K. Mudali, R. Natarajan, J.B. Joshi, Mechanism of dissolution of nuclear fuel in nitric acid relevant to nuclear fuel reprocessing, *J. Radioanal. Nucl. Chem.* 312 (2017) 141–149.
 - [70] G.D. Del Cul, B.B. Spencer, R.D. Hunt, FCRD-MRWFD-2016-000001, also INL/EXT-15-37053. Tritium pretreatment, material recovery and waste form development FY-15 accomplishments report, November 2015, <<https://inldigitallibrary.inl.gov/sites/sti/sti/6748414.pdf>>.
 - [71] G.J. Lumetta, K.L. Nash, S.B. Clark, J.I. Friese, ACS Symposium Series 933 Separations for the Nuclear Fuel Cycle in the 21st Century, American Chemical Society, Washington, DC, 2006, pp. 71–88.
 - [72] J.H. Goode (Ed.), ORNL/TM-3723. Voloxidation-Removal of Volatile Fission Products from Spent LMFBR Fuels, Oak Ridge National Laboratory, Oak Ridge, TN, 1973.
 - [73] K.H. Kang, C.H. Lee, M.K. Jeon, S.Y. Han, G.I. Park, S.-M. Hwang, Characterization of cladding hull wastes from used nuclear fuels, *Arch. Metall. Mater.* 60 (2) (2015) 1199–1203.
 - [74] ANDRA, Synthesis Report: 2009 National Inventory of Radioactive Materials and Waste, French National Radioactive Waste Management Agency, June 2009.
 - [75] Office of Nuclear Regulation, The United Kingdom's Fourth National Report on Compliance with the Obligations of the Joint Convention on the Safety of Spent Fuel Management and on the Safety of Radioactive Waste Management, September 2011.
 - [76] E.D. Collins, G.D. Del Cul, A practical solution to used nuclear fuel recycling, in: Integrated Radioactive Waste Management in Future Fuel Cycles, Charleston, SC, November 2009.
 - [77] E.D. Collins, G.D. Del Cul, B.B. Spencer, R.R. Brunson, J.A. Johnson, Feasibility study to combine chemical decladding and zirconium recovery and recycle, in: ANS 2013 Winter Meeting, Washington, DC, November 2013.
 - [78] C. Barnes, J.R. Travis, B.K. Vestal, G.D. DelCul, D.F. McLaughlin, New reconditioning strategies of spent nuclear fuel rods, in: 2019 ANS Annual Meeting, Minneapolis, MN, June 9–13, 2019.
 - [79] R.K. Collins, M.G.B. Drew, Crystal and molecular structure of Di-p-chloro-bis[trichloro(thionyl chloride)zirconium(IV)], *J. Chem. Soc. A* (1971) 3610–3613.
 - [80] I. Buscaglione, C. Stables, H. Sutcliffe, The reaction of zirconium oxide chloride octahydrate with thionyl chloride, *Inorg. Chim. Acta* 128 (1) (1987) 7–9.
 - [81] D.A. Copinger, D.L. Moses, ORNL/TM-2003/2, also NUREG/CR-6839. Fort Saint Vrain gas cooled reactor operational experience, September 2003, <<https://www.nrc.gov/docs/ML0403/ML040340070.pdf>>.
 - [82] G.D. Del Cul, B.B. Spencer, C.W. Forsberg, E.D. Collins, W.S. Rickman, ORNL/TM-2002/156, UT-Battelle TRISO-Coated Fuel Processing to Support High-Temperature Gas-Cooled Reactors, Oak Ridge National Laboratory, Oak Ridge, TN, 2002.

- [83] R. Moormann, Safety Re-Evaluation of the AVR Pebble Bed Reactor Operation and its Consequences for Future HTR Concepts, Jü1-4275, Jülich, Germany, 2008, <http://www.iaea.org/inis/collection/NCLCollectionStore/_Public/39/099/39099096.pdf>.
- [84] H. Nabielek, G. Kaiser, Fuel for pebble-bed HTRs, Nucl. Eng. Des. 78 (1984) 155–166.
- [85] E.N. Moore, et al., SRNL-TR-2014-00209 Process Description for Processing of HTGR Pebble Fuel at SRS, Savannah River National Laboratory, Aiken, SC, 2014.
- [86] International Atomic Energy Agency, IAEA-TECDOC-1645. High temperature gas cooled reactor fuels and materials, Nuclear Fuel Cycle and Materials Section, Vienna, Austria, 2010, <https://www-pub.iaea.org/MTCD/Publications/PDF/TE_1645_CD/PDF/TECDOC_1645.pdf>.
- [87] B.B. Spencer, G.D. Del Cul, C.W. Forsberg, E.D. Collins, W.S. Rickman, Processing of TRISO-coated fuel in support of high-temperature gas-cooled reactors, Trans. Am. Nucl. Soc. 88 (2003) 376. ANS Annual Meeting, San Diego, CA, June 2003.
- [88] B.B. Spencer, C.H. Mattus, G.D. Del Cul, R.D. Hunt, E.D. Collins, Scoping experiments on processing of spent TRISO-coated GEN IV reactor fuels, Trans. Am. Nucl. Soc. 91 (2004) 525. ANS Winter Meeting, Washington, DC, November 2004.
- [89] G.D. Del Cul, B.B. Spencer, Processing of graphite based nuclear fuels: a review, Trans. Am. Nucl. Soc. 111 (2014) 394. ANS Winter Meeting, Anaheim, CA, November 2014.
- [90] A.G. Croff, E.D. Collins, G.D. Del Cul, R.G. Wymer, A.M. Krichinsky, B.B. Spencer, et al., ORNL experience and perspectives related to processing of thorium and ^{233}U for nuclear fuel, Nucl. Technol. 194 (2) (2016) 252.
- [91] R.A. Pierce, Low Temperature Vapor Phase Digestion of Graphite, US Patent 2017/0087511 A1, March 30, 2017.
- [92] J.J. Laidler, Reprocessing of gas-cooled reactor particulate graphite fuel in a multi-strata transmutation system, in: Global 2001 International Conference on Back-end of the Fuel Cycle: From Research to Solutions, Paris, France, September 9–13, 2001, <http://www.iaea.org/inis/collection/NCLCollectionStore/_Public/33/031/33031080.pdf>.
- [93] T. Burchell, P. Pappano, ORNL/TM-2010/00169 The Characterization of Grade PCEA Recycle Graphite Pilot Scale Billets, Oak Ridge National Laboratory, Oak Ridge, TN, 2010.
- [94] E.N. Moore, R.H. Jones, T.F. Severynse, SRNL-TR-2014-00209. Process description for processing of HTGR pebble fuels at SRS, Savannah River National Laboratory, Aiken, SC, 2014.
- [95] M. Maxted, Update on the German Graphite Fuel Project, US Department of Energy, 2018, <<http://www.admin.sc.gov/files/nac/German%20Project%20Update.pdf>>.
- [96] G.E. Schweitzer (Ed), An international spent nuclear fuel storage facility. in: Russian Academy of Sciences and National Research Council. National Academies Press, 2005.
- [97] M.S. Yang, H. Choi, C.J. Jeong, K.C. Song, J.W. Lee, G.I. Park, et al., The status and prospect of DUPIC fuel technology, Nucl. Eng. Technol. 38 (4) (2006) 359.
- [98] A. Bergeron, D. Manara, O. Beneš, R. Eloirdi, M.H.A. Piro, E.C. Corcoran, Thermodynamic modelling of thoria-urania and thoria-plutonia fuels: description of the Th-U-Pu-O quaternary system, J. Nucl. Mater. 512 (2018) 324–348.
- [99] R.H. Rainey, A.B. Meservey, R.G. Mansfield, ORNL-2591 Laboratory Development of the Thorex Process: Progress Report December 1, 1955 to January 1, 1958, Oak Ridge National Laboratory, Oak Ridge, TN, 1959.

- [100] R.E. Brooksbank, W.T. McDuffee, R.H. Raine, A review of thorium fuel reprocessing experience, in: CONF-780223-3, AIChE National Meeting, Atlanta, GA, February 24, 1978.
- [101] D. Dasarathi, S.R. Bharadway (Eds.), *Thoria-Based Nuclear Fuels: Thermophysical and Thermodynamic Properties, Fabrication, Reprocessing, and Waste Management*, Springer-Verlag, London, 2013.
- [102] S.H. Bruffey, B.B. Spencer, D.M. Strachan, R.T. Jubin, N. Soelberg, B.J. Riley, ORNL/SPR-2015/290 A Literature Survey to Identify Potentially Problematic Volatile Iodine-bearing Species Present in Off-Gas Streams, Oak Ridge National Laboratory, Oak Ridge TN, 2015.
- [103] D.R. Haefner, T.J. Tranter, INL/EXT-07-12299 Methods of Gas Phase Capture of Iodine From Fuel Reprocessing Off-Gas: A Literature Survey, Idaho National Laboratory, Idaho Falls, ID, 2007.
- [104] B. Clément, L. Cantrel, G. Ducros, F. Funke, L. Herranz, A. Rydl, et al., NEA/CSNI/R (2007) 1. State of the Art Report on Iodine Chemistry, Organisation for Economic Cooperation and Development, Paris, France, 2007.
- [105] R.T. Jubin, The Mass Transfer Dynamics of Gaseous Methyl-Iodide Adsorption by Silverexchanged Sodium Mordenite (Ph.D. dissertation), University of Tennessee (1994).
- [106] R.T. Jubin, J.A. Jordan, S.H. Bruffey, ORNL/SR-2017/477 Performance of Silver-Exchanged Mordenite and Silver-Functionalized Silica-Aerogel Under Vessel Off-Gas Conditions, Oak Ridge National Laboratory, Oak Ridge, TN, 2017.
- [107] R.T. Jubin, Advances in off-gas treatment for used nuclear fuel processing, in: 33rd Nuclear Air Cleaning Conference, St. Louis, MO, June 2014.
- [108] Y. Nan, L.L. Tavlarides, D.W. DePaoli, Adsorption of iodine on hydrogen-reduced silver-exchanged mordenite: experiments and modeling, *AIChE J.* 63 (3) (2017) 1024–1035.
- [109] R.T. Jubin, D.W. Ramey, B.B. Spencer, K.K. Anderson, S.M. Robinson, Impact of pretreatment and aging on the iodine capture performance of silver-exchanged mordenite, in: WM2012 Conference, Phoenix, AZ, February 26–March 1, 2012.
- [110] Y. Nan, S. Choi, A.P. Ladshaw, S. Yiakoumi, C. Tsouris, D.W. DePaoli, et al., Aging processes of silver mordenite and silver functionalized aerogel in dry air, humid air and NO/N₂, *Trans. Am. Nucl. Soc.* 116 (2017) 130–132. San Francisco, CA, June 11–15.
- [111] B.B. Spencer, S.H. Bruffey, J.F. Walker, R.T. Jubin, Adsorption of iodine and tritium from UNF reprocessing off-gas streams, *Trans. Am. Nucl. Soc.* 114 (2016) 89. ANS Annual Meeting, New Orleans, LA, June 12–16, 2016 (presented June 13, 2016).
- [112] B.B. Spencer, S.H. Bruffey, R.T. Jubin, ORNL/SPR-2018/984, also NTRD-MRWFD-2018-000208 Design of Laboratory System to Recover Tritium From Zirconium Recycle and Plan to Test System, Oak Ridge National Laboratory, Oak Ridge, TN, 2018.
- [113] M.J. Stephenson, R.S. Eby, Development of the FASTER process for removing Krypton-85, Carbon-14, and other contaminants from the off-gas of fuel reprocessing plants, in: Proceedings of the 14th ERDA Air Cleaning Conf., vol. 2, CONF-760822, Sun Valley, ID, 1976.
- [114] L.M. Toth, J.T. Bell, D.W. Fuller, ORNL/TM-6484 Chemical and Physical Behavior of Some Contaminants in the Fluorocarbon Off-Gas Process, Oak Ridge National Laboratory, Oak Ridge, TN, 1978.

- [115] K. Munakata, S. Kanjo, S. Yamatsuki, A. Koga, D. Ianovski, Adsorption of noble gases on silver-mordenite, *J. Nucl. Sci. Technol.* 40 (9) (2003) 695–697.
- [116] R.T. Jubin, G.D. Del Cul, B.D. Patton, R.S. Owens, D.W. Ramey, B.B. Spencer, Advanced fuel cycle initiative coupled end-to-end research, development, and demonstration project: integrated off-gas treatment system design and initial performance, in: Waste Management Conference 2009, Phoenix, AZ, March 2009.
- [117] R.E. Bazan, M. Bastos-Neto, A. Moeller, F. Dreisbach, R. Staudt, Adsorption equilibria of O₂, Ar, Kr and Xe on activated carbon and zeolites: single component and mixture data, *Adsorption* 17 (2011) 371–383.
- [118] A.M. Eshaya, W.L. Kaljnowski, BNL 724(T-258) Adsorption of Krypton and Xenon and of Mixed Krypton and Xenon on Activated Charcoal, Brookhaven National Laboratory, Upton, NY, 1961.
- [119] D. Banerjee, A.J. Cairns, J. Liu, R.K. Motkuri, S.K. Nune, C.A. Fernandez, et al., Potential of metal organic frameworks for the separation of xenon and krypton, *Acc. Chem. Res.* 48 (2015) 211.
- [120] L. Jian, C.A. Fernandez, P.F. Martin, P.K. Thallapally, D.M. Strachan, A two-column method for the separation of Kr and Xe from process off-gases, *Ind. Eng. Chem. Res.* 53 (2014) 12893.
- [121] B. Westphal, K.J. Bateman, R.P. Lind, K.L. Howden, G.D. Del Cul, Fission product removal from spent oxide fuel by head-end processing, in: Proceedings of Global 2005, paper 345, INL/CON-05-00687, Tsukuba, Japan, 2005.
- [122] L.A. Bray, L.L. Burger, L.G. Morgan, D.L. Baldwin, PNL-4488 Thermal Release of Volatile Fission Products from Irradiated Nuclear Fuel, Pacific Northwest Laboratory, Richland, WA, 1983.
- [123] R.T. Jubin, S.H. Bruffey, B.B. Spencer, D.M. Strachan, ORNL/TM-2017/330 Evaluation of Ruthenium Capture Methods for Tritium Pretreatment Off-gas Streams, Oak Ridge National Laboratory, Oak Ridge, TN, June 2017.
- [124] B.B. Spencer, M.L. Parks, S.H. Bruffey, ORNL/SPR-2017/576, also NTRD-MRWFD-2018-000200 Initial Assessment of Ruthenium Removal Systems for Tritium Pretreatment Off-Gas, Oak Ridge National Laboratory, Oak Ridge, TN, 2018.
- [125] B.B. Spencer, S.H. Bruffey, ORNL/SPR-2018/913, also NTRD-MRWFD-2018-000197 Initial Series of Ruthenium Adsorption Optimization Studies, Oak Ridge National Laboratory, Oak Ridge, TN, 2018.
- [126] L.R. Morss, N. Edelstein, J. Fuger, J.J. Katz, *The Chemistry of the Actinide and Transactinide Elements*, fourth ed., Springer, 2010.
- [127] J.P. Guillaume, C. Maurice, J.P. Moulin, Chemical properties of neptunium applied to neptunium management in extraction cycles of Purex process, in: Symposium of Liquid-Liquid Extraction, Dounreay, CEA-CONF-7772, 1984.
- [128] P. Paviet, INL/CON-12-28006 Overview of Reductants Utilized in Nuclear Fuel Reprocessing/Recycling, Idaho National Laboratory, Idaho Falls, ID, 2013.
- [129] F. Drain, J.L. Emin, R. Vinoche, P. Baron, COEX – process: cross-breeding between innovation and industrial experience, in: Waste Management Symposium 2008, Phoenix, AZ, 2008.
- [130] C. Phillips, I. Thomas, S. McNiven, Improving the estimates of waste from the recycling of used nuclear fuel, in: Waste Management Conference, Phoenix, AZ, 2013.
- [131] R. Taylor, B. Stéphane, J.-P. Glatz, G. Modolo, Development of actinide separation processes for future nuclear fuel cycles in Europe, *Nucl. Futures* 11 (2015) 38–43.
- [132] B. Cipiti, SAND2017-2253 CoDCon Dynamic Modeling, Sandia National Laboratories, Albuquerque, NM, 2017.

- [133] J.C. Bresee, P.D. Paviet, T.A. Todd, US Department of Energy's CoDCon project: an aqueous safeguards R&D program, 25th International Conference on Nuclear Engineering (ICONE-25) 2017, vol. 7, Shanghai, China, July 2–6, 2017.
- [134] A. Gelis, G. Lumetta, Actinide Lanthanide Separation Process—ALSEP, *Ind. Eng. Chem. Res.* 53 (4) (2014) 1624.
- [135] W.H. Reas, KR-126. Aquafluor Process, 1968.
- [136] A. Sasahira, Recent development of FLUOREX process for the next generation fuel cycle, *At. Energy Soc. Jpn.* (2008). Tokyo, 2022.
- [137] O. Amano, FLUOREX reprocessing technology with uranium removal from spent fuel by fluorination, *J. Nucl. Sci. Technol.* 39 (2002) 890.
- [138] S. Valilov, Principle and test experience of the RIAR's oxide pyro-process, *J. Nucl. Sci. Technol.* 41 (10) (2004) 1018.
- [139] HSC Chemistry Software, Version 9, Outotec, Finland, 2016.
- [140] U.J. Vyzkumu, UJV 4502-CH Physical and Chemical Properties of Volatile Ruthenium Fluorides, REZ Nuclear Research Institute, 1979.
- [141] L.H. Ngai, F.E. Stafford, Gaseous oxohalides, hydroxides, and complex oxides of group III and transition elements, in: L. Eyring (Ed.), *Advances in High Temperature Chemistry*, vol. 3, Academic Press, 1971.
- [142] B.M. Johnson, Chemistry of Chromium Oxyfluorides and Group VIB Perfluoroglutarates (Master's Thesis), Portland State University, Portland, OR, 1981.
- [143] J.J. Schmets, Report KR-126 Review of Halide Volatility Processes, Nuclear Research Center, Mol, Belgium, 1968.
- [144] C.L. Chernick, H.H. Claassen, B. Weinstock, Rhodium hexafluoride, *J. Am. Chem. Soc.* 83 (1961) 3165.
- [145] V.V. Shatalov, M.B. Seregin, V.F. Kharin, L.A. Ponomare, Gas-fluoride technology for processing spent oxide fuel, *At. Energy* 90 (3) (2001) 224.
- [146] R. Scheele, B. McNamara, A.M. Casella, A. Kozelisky, On the use of thermal NF₃ as the fluorination and oxidation agent in treatment of used nuclear fuels, *J. Nucl. Mater.* 424 (2012) 224–236.
- [147] A. Sasahira, Y. Kani, F. Kawamura, K. Hoshino, V.N. Prusakov, O. Amano, Adsorption of plutonium fluoride with uranyl fluoride trap, in: Proceedings of Global 2005, Paper 395, Tsukuba, Japan, 2005.
- [148] I. Amamoto, K. Sato, Reprocessing Method by Fluoride Volatility Process Using Solid–Gas Separation, US Patent 7208129 B2, 2007.
- [149] Y. Yato, Uranium isotope exchange between gaseous UF₆ and solid UF₅, *J. Nucl. Sci. Technol.* 33 (10) (1996) 758–766.
- [150] R.H. Capps, USAEC Report K-770 Reactions of Gaseous Uranium Hexafluoride and Hydrogen Fluoride with Metallic Fluorides, Oak Ridge Gaseous Diffusion Plant, Oak Ridge, TN, 1951.
- [151] R.C. Weast (Ed.), *CRC Handbook of Chemistry and Physics*, 70th edition, CRC-Press, 1990.
- [152] W.R. Golliher, R.A. LeDoux, S. Bernstein, V.A. Smith, TID-18290 Separation of Technetium-99 From Uranium Hexafluoride, Union Carbide Nuclear Co., Paducah, KY, 1960.
- [153] S. Katz, ORNL-3544 Reduction of Uranium Hexafluoride Retention on Beds of Magnesium Fluoride Used for Removal of Technetium Hexafluoride, Oak Ridge National Laboratory, Oak Ridge, TN, 1964.
- [154] O. Ruff, Über Einige Neue Fluoride, *Berichte der Deutschen Chemischen Gesellschaft* 42 (1) (1909) 492.

- [155] O. Ruff, A. Heinzelmann, Über lithiumamalgame, Zeitschrift anorganische Chemie 72 (1911) 63.
- [156] A.V. Grosse, Report A-83. Chemical Properties of UF₆, US Department of Energy, Washington, DC, 1941.
- [157] G.I. Cathers, et al., UF₆·3NaF complex formation and decomposition, Ind. Eng. Chem. 50 (11) (1958) 1709.
- [158] S. Katz, ORNL-3497 Apparatus for the Gasometric Study of Solid-gas Reactions: Sodium Fluoride with Hydrogen Fluoride and Uranium Hexafluoride, Oak Ridge National Laboratory, Oak Ridge, TN, 1963.
- [159] R.M. Schultz, K/ET-5025 Sorbent Selection and Design Considerations for Uranium Trapping, Oak Ridge Gaseous Diffusion Plant, Oak Ridge, TN, 1981.
- [160] E.W. Richardson, Process for Making Porous Sodium Fluoride Pellets, US Patent 3372004, 1968.
- [161] S. Katz, Use of high-surface-area sodium fluoride to prepare MF₆·2NaF complexes with uranium, tungsten, and molybdenum hexafluoride, Inorg. Chem. 3 (11) (1964) 1598–1600.
- [162] S. Afzal, Experimental study of hydrogen fluoride adsorption on sodium fluoride, J. Ind. Eng. Chem. 16 (2010) 147.
- [163] A.V. Hariharan, D.D. Sood, S.P. Sood, R. Prasad, R. Sampathkumar, CONF-690916-vol. 2 Laboratory Investigations in Non-Aqueous Process Chemistry, Bhaba Atomic Research Centre, Bombay, India, 1970. <<https://www.osti.gov/servlets/purl/4106332>>.
- [164] E.V. Johnstone, Technetium tetrachloride revisited, Inorg. Chem. 51 (2012) 8462.
- [165] K. Schwochau, Technetium: Chemistry and Radiopharmaceutical Applications, Wiley, 2000.
- [166] K.S. Warren, L.M. Ferris, ORNL-3977 *Oxidation and Chlorination of UO₂–PuO₂*, Oak Ridge National Laboratory, Oak Ridge, TN, 1966.
- [167] A.V. Hariharan, S.P. Sood, R. Prasad, M.V. Ramaniah, Direct chlorination volatility processing, in: P. Chiotti (Ed.), Nuclear Metallurgy, Symposium on Reprocessing of Nuclear Fuels, CONF-690801, Ames, IA, vol. 15, 1969.
- [168] D.R. Olander, J.L. Camahort, Reaction of chlorine and uranium tetrachloride in the fused lithium chloride-potassium chloride eutectic, AIChE J. 12 (4) (1966) 693.
- [169] S. Fried, USAEC N-2188. The Reaction of Uranium Compounds with Aluminum Chloride, Chicago University Metallurgical Laboratory, US Atomic Energy Agency, Washington, DC, 1945.
- [170] V.P. Calkins, Production of Uranium Tetrachloride, US Patent 2864666, 1958.
- [171] H. Matsuda, H. Habuka, Y. Ishida, T. Ohno, Metal fluorides produced using chlorine trifluoride gas, J. Surf. Eng. Mater. Adv. Technol. 5 (2015) 228.
- [172] C.H. Krauss, A-726. Summarizing Report of Investigations Relating to Uranium Covering the Period September 1, 1942 to April 15, 1943, Brown University, Providence, RI, June 1, 1943.
- [173] A.A. Alberts, W.S. Barnhart, R.E. Burns, L.R. Evans, E.S. Gantz, R.E. Hatton, et al., Report A-2706 Chlorination of Tuballoy Oxides with Thionyl Chloride, Department of Chemistry, Purdue University, 1946.
- [174] D.M. Gruen, R.L. McBeth, Uranium tetrachloride—aluminum trichloride vapor complex, Inorg. Nucl. Chem. Lett. 4 (1968) 299.
- [175] D.M. Gruen, R.L. McBeth, Vapor complexes of uranium pentachloride and uranium tetrachloride with aluminum chloride, Inorg. Chem. 8 (12) (1969) 2625–2633.

- [176] S.S. Rudel, F. Kraus, Facile syntheses of pure uranium halides UCl_4 , UBr_4 , and UI_4 , *Dalton Trans.* 46 (2017) 5835.
- [177] E.T. McBee, L.R. Evans, Report A-2704 The Identification of the By-Products From the Reaction of Tuballoy Trioxide with Hexachloropropene, Department of Chemistry, Purdue University, 1945.
- [178] D. Patel, A.J. Woole, E. Hashem, H. Omorodion, R.J. Baker, S.T. Liddle, Comments on reactions of oxide derivatives of uranium with hexachloropropene to give UCl_4 , *New J. Chem.* 39 (2015) 7559.

Spent nuclear fuel and disposal

13

Jordi Bruno¹, Lara Duro¹ and François Diaz-Maurin^{1,2}

¹Amphos 21 Group, Barcelona, Spain, ²Center for International Security and Cooperation (CISAC), Stanford University, Stanford, CA, United States

13.1 Introduction—generalities on spent nuclear fuel

Natural uranium (U) is formed by 99.3% of fertile ^{238}U and 0.7% of fissile ^{235}U . Before it is used as fuel in a commercial reactor, uranium is enriched up to 2%–5% of ^{235}U , so that the electricity yield of a light-water reactor (LWR) is maximized. The exception is Canada Deuterium Uranium (CANDU) reactor fuels, which account for 11% of the total commercial spent nuclear fuel (SNF), and they run, in principle, with unenriched uranium dioxide. After approximately 18 months of operation the LWR reactor is fed by a substitution of about one-third of the fuel assemblies with assemblies containing newly enriched fuel rods. The used rods constitute the SNF. Highly radioactive fission products (FPs) and transuranic elements are contained within the SNF, namely, plutonium, along with unused uranium. The ^{239}Pu contained in the spent fuel rods is produced by the absorption of 1 n by ^{238}U followed by subsequent beta decay, and this Pu produces about 25% of the energy generated in a nuclear power plant (NPP) [1,2]. There is between 7 and 8 kg of Pu available per ton of U in the spent fuel, which can be reused for energy production by reprocessing methods, as discussed in Chapter 12, Reprocessing and recycling.

After typical burnup in a nuclear reactor, the radioactivity of the nuclear fuel increases by a factor of around 1 million with respect to the fresh fuel, in the order of 10^{17} Bq/MT of fuel [3]. This is mainly due to the generation of FPs, transuranium elements, and the activation products formed from the materials in the metallic cladding. The residual activity in the SNF, dominated by beta and gamma decay, generates a decay heat of 1000 W/t 10 years after discharge, while after 10,000 years the activity will be predominantly caused by alpha decay, generating a decay heat of about 20 W/t [4]. Thus while the initial activity, immediately after discharge from the core, is in the order of 10^{17} Bq/m³, after 1 year, it decreases to 5% of this value (see Fig. 13.1).

A summary of the typical composition of fresh fuel versus SNF with 46 GWd/t burnup at its discharge from the reactor is shown in Table 13.1.

The various elements in the SNF are present in different chemical forms. Ewing and Weber [3] and Kleykamp [7] differentiate the following groups, which are also described in Chapter 1, Reaction kinetics and chemical thermodynamics of nuclear materials:

1. fission gases (e.g., Xe and Kr) in the form of bubbles in the fuel grains or in the gap between the cladding and the spent fuel pellet;
2. metallic FPs (e.g., Mo, Tc, Ru, Rh, and Pd) in the form of isolated metallic precipitates, known as ϵ -particles;
3. FPs in the form of oxide precipitates of Rb, Cs, Ba, and Zr;
4. FPs in the UO_2 matrix as solid solutions (e.g., Sr, Zr, Nb, and the rare-earth elements); and
5. transuranium elements substituting for U in a solid solution in the UO_2 matrix.

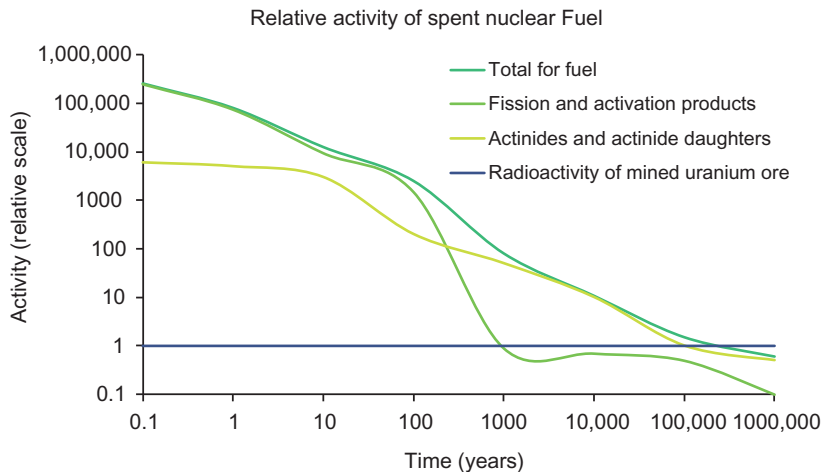


Figure 13.1 Relative radioactivity of a typical LWR spent nuclear fuel with a burnup of 38 GWd/tHM as compared with the total activity of the uranium ore required to manufacture the nuclear fuel. The activity is dominated by fission products during the first 100 years and by actinides thereafter. *LWR*, Light-water reactor.

Source: Adapted from A. Hedin, Spent nuclear fuel – how dangerous is it?, in: SKB Technical Report No. 97–13, Svensk Kärnbränslehantering AB, Stockholm, Sweden, 1997 [5].

Table 13.1 Average composition of a fresh and a 46 GWd/t burnup spent nuclear fuel in wt.% of metal atoms [6].

Element/isotope		wt.% in fresh fuel	wt.% in 46 GWd/t spent nuclear fuel
Uranium	^{235}U	4.00	0.67
	^{236}U		0.50
	^{238}U	96.00	93.06
Plutonium	Total		1.01
	Fissile		0.67
Minor actinides			0.10
Fission products			4.00

Note: wt.% refers to the weight percentage of the initial metal atoms, so that the weight percentage of the oxygen atoms in UO_2 is not shown.

In a rod containing stacked pellets of polycrystalline UO_2 fuel during reactor operation, concentration and thermal gradients drive diffusive redistribution of some of the FPs into the intergranular space and outside the pellet toward the inner-rod void space.

Because of a steep thermal gradient, elements are not homogenously distributed across each pellet [8]. Thermal excursions—events caused by uncontrolled nuclear chain reactions—during reactor operation can damage the fuel by coarsening the grain size as well as restructuring and microfracturing the pellets. Some FPs are rather volatile, such as Cs and I, and migrate to the grain boundaries, the fractures, and the gap between the fuel pellet and the metal cladding (Fig. 13.2). The burnup is also not uniform across the fuel pellet with higher burnups occurring at the edge of the pellet. This leads to a fuel edge enriched in ^{239}Pu , an increased porosity, and a polygonization of

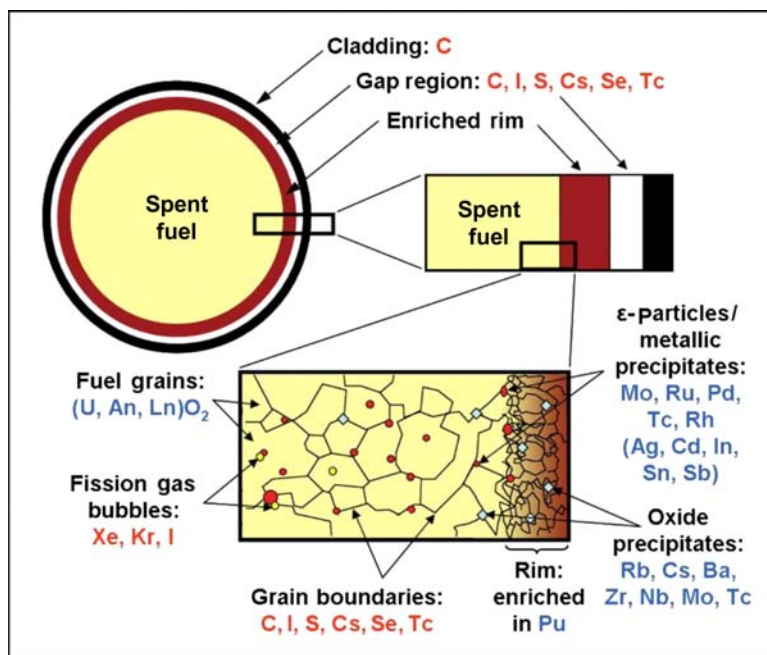


Figure 13.2 Schematic illustration of the microstructure of spent fuel and the distribution of actinides and fission products following burnup in a reactor. Elements in red are released rapidly on first contact with water, while elements in blue are released more slowly as the UO_2 matrix corrodes (An = actinides and Ln = lanthanides in solid solution in the UO_2 structure).

Source: J. Bruno, R.C. Ewing, Spent nuclear fuel, Elements 2 (2006) 343–349 [9]. Adapted from E.C. Buck, B.D. Hanson, B.K. McNamara, The geochemical behaviour of Tc, Np and Pu in spent nuclear fuel in an oxidizing environment, in: R. Gieré, P. Stille (Eds.), Energy, Waste and the Environment: A Geochemical Perspective, Geological Society, London, Special Publications, 2004, pp. 65–88 [10] and D.W. Shoesmith, Fuel corrosion processes under waste disposal conditions, J. Nucl. Mater. 282 (2000) 1–31 [11].

the UO_2 grains, called the “rim effect” [3]. The rim effect is the result of the resonance absorption of epithermal neutrons by ^{238}U , which produces enrichment of ^{239}Pu , increases local burnup, and as a result, larger porosity and grain subdivision. These factors increase the probability of cladding failure and subsequent FP release [12].

Although the SNF composition is dominated by U, radionuclides are heterogeneously distributed through the fuel and come in a variety of phases, from inert gases to relatively stable oxides [9]. The final composition will depend on the initial fuel type, initial chemical composition, level of enrichment of ^{235}U , neutron energy spectrum, and the burnup or amount of fission occurring in the fuel during reactor operation [3]. For instance, a burnup of 40 GWd/tHM will deplete 4% of the uranium and produce approximately 3% FPs and 1% transuranium elements [10]. Trends in industry indicate that discharge burnups are increasing, and new fuels are being developed, which include different metal additives, such as Al and/or Cr, in their composition in order to increase grain size, decrease release of fission gases, and improve mechanical compliance [13,14].

While the activity of the spent fuel will decrease with time, the distribution of the total activity among FPs and actinoids will also change (Fig. 13.1). In this example, the activity will be dominated by fission and activation products during the initial 100 years, whereas actinoids and actinoid daughter products will dominate after 500 years; FPs will eventually be less radioactive than natural U after 1000 years. This is a very important factor for spent fuel disposal because the actinoids that dominate long-term activity have extremely low accessibility in a deep geologic repository [5]. However, even in the long term, with surface storage spanning over several decades, FPs will still dominate the total activity of the spent fuel.

In summary, SNF is a very complex material in terms of both chemical composition and physical properties. It takes several thousands of years for the SNF to reach radioactivity levels close to the ones of natural uranium ore (see Fig. 13.1), which means a time longer than the known human history, dated 60,000 years BCE. Thus the management of SNF requires a robust and well-thought-out strategy to ensure present and future safety for very long time periods.

This section has briefly presented the nature of SNF (see Chapter 11: In-reactor Behavior for more details). In this chapter, the international strategies and practices followed for its management, including storage and final disposal, are presented. For further information, the reader is referred to the “References” section at the end of the chapter.

13.2 Spent nuclear fuel management strategies, closed versus open nuclear cycles

The remaining Pu in the SNF, once reprocessed (see Chapter 12: Reprocessing and recycling), is used for the fabrication of mixed oxide (MOX) fuel, which comprises $\text{PuO}_2 + \text{UO}_2$. Currently, 20%–25% of the unloaded SNF is reprocessed (see Fig. 13.3A) in France, United Kingdom, Russia, Japan, and India. The waste

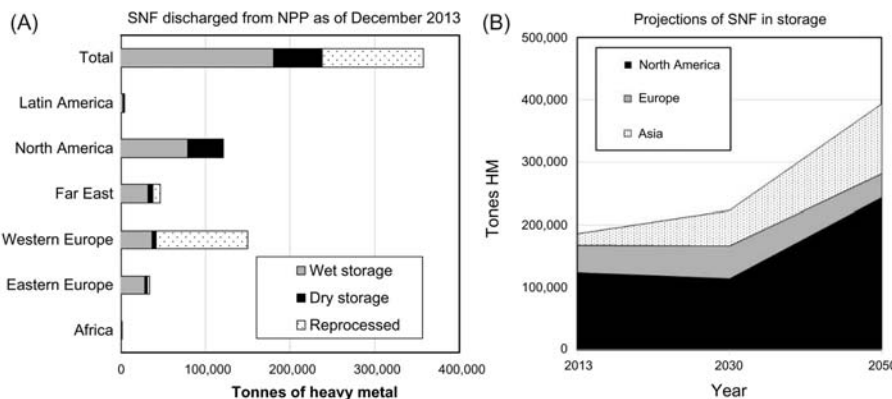


Figure 13.3 (A) Status of total SNF discharged from NPPs up to December 2013. No data is available for the Middle East, South Asia, and Pacific regions. (B) Data for 2013 and projections of the amounts of SNF in storage. *NPP*, Nuclear power plant; *SNF*, spent nuclear fuel.

Source: Data processed from International Atomic Energy Agency (IAEA), Status and trends in spent fuel and radioactive waste management, in: IAEA Nuclear Energy Series No. NW-T-1.14, Vienna, Austria, 2018 [15].

remaining after reprocessing is vitrified and encapsulated in steel containers. Therefore SNF discharged from a NPP constitutes either a waste or a resource to generate other type of fuels, depending on whether the national policy is to follow an open (i.e., no reprocessing) or a closed (i.e., reprocessing) fuel cycle, as described in Chapter 12, Reprocessing and recycling.

According to the Euratom Council directive 70 of 2011 [16], each member state remains free to define its fuel cycle policy. The decision between an open and closed fuel cycle is one of individual national sovereignty, and no unique rules are defined in this regard. Each member state shall have ultimate responsibility for the management of SNF and radioactive waste it has generated and must put actions in place to ensure safe management of the waste.

Whatever strategy is followed, a given storage period before disposal is needed. Storage options include wet storage in storage pools or dry storage in casks or vaults. Most NPPs have temporary on-site storage facilities, although due to the limited space at NPP facilities, several countries have larger centralized storage facilities to which SNF and vitrified high-level waste (HLW) from the various NPPs are transported and stored. Delays in the decision of final waste disposal strategies increase the period for temporary waste storage installations. Therefore new centralized storage facilities or extensions of existing facilities are needed in order to hold all the waste volumes produced. Increases in the discharge burnup of fuels will have the effect of increasing the storage times needed for the fuel to reach thermal charges that will not pose additional requirements to the engineered barriers of a final disposal facility. For some of the expected scenarios in temporary storage, fuel could be cooled in interim storage for 100 years or more [17].

Intermediate, low, and very low radioactive wastes require different strategies which are not dealt with in this chapter, as it is considered out of scope. The interested reader is referred to the various sources on the subject in the open literature.

Högselius [18] presented an overview of the different management policies followed in the world and concludes that approximately 13 out of the 32 nuclear countries follow a direct disposal policy (i.e., open cycle), six follow the reprocessing alternative (i.e., closed cycle), and six have opted for exporting their waste to other countries. The remaining countries have not yet made any clear decision.

The 70/2011 Euratom directive also states that the storage of radioactive waste, including long-term storage, is an interim solution but not an alternative to disposal [16]. The widely accepted option for long-term management of SNF and HLW after temporary storage is its disposal in deep geological repositories (~500 m depth) built in an adequate host rock. Host rock options discussed herein include clay formations, crystalline rock, and salt domes. To date, there is no deep geological deposition for civilian nuclear wastes in operation. Only the United States has a geological disposal for transuranics, the WIPP (Waste Isolation Pilot Plant) site. The WIPP repository is hosted in a salt formation and holds the transuranic wastes originated from the US defense program. No HLW (including SNF) coming from civilian electricity production is currently disposed of in a geological repository. All of it is stored in different nonpermanent facilities, which vary from country to country. Some countries not producing nuclear electricity store HLW originated from research or experimental reactors, isotope production, or military purposes.

The following sections present the international practices for SNF storage and disposal.

13.3 Spent nuclear fuel and high-level waste storage—international practices

The two main techniques for SNF and HLW storage are wet and dry storage.

13.3.1 Wet storage

Wet storage is usually accomplished in water pools at the NPP, what is known as at reactor (AR) storage, and it normally precedes any further management option. The SNF discharged from the reactor cools down in these pools typically for 3–10 years, although SNF can remain in pools for longer periods as long as there is sufficient spacing between the fuel assemblies. The objective of wet storage is to provide an environment for the radioactivity and heat generation rate to decrease from the SNF. The surrounding water provides both radioactive shielding and a thermal sink. After this initial cooling period, the SNF can be removed from a wet storage facility, encapsulated, and transported to other types of storage. In some cases, wet centralized storage is also pursued, as is the case in Sweden, in the CLAB

facility [19]. Initially, the spent fuel is stored at the NPP, but after about a year, it is moved to CLAB. During interim storage, it is kept in deep storage pools about 30 m below ground in the rock.

13.3.2 Dry storage

SNF and HLW can be stored dry either in facilities located in the vicinity of the reactor (AR), intended for the SNF discharged from that reactor, or in centralized facilities, what is known as away from the reactor (AFR), which receives waste from various NPPs. Dry storage is gaining in importance, especially since the need for centralized facilities to hold waste from different reactors is increasing, and considering the extended time periods needed, mostly due to political reasons associated with public acceptance but also due to technical issues encountered and the difficulty to decide on long-term disposal [20,21].

According to the last overview of the status of radioactive waste management in the world by the International Atomic Energy Agency [15], since the start of nuclear power production in 1954 until the end of 2013, about 370,000 tonnes of SNF have been discharged in the world, excluding India and Pakistan as data was not available for these two countries. Of that amount, 180,800 tonnes are currently in wet storage, 56,900 tonnes in dry storage, and around one-third, 120,300 tonnes, has been reprocessed (see Fig. 13.3A).

Out of the 28 member states of the European Union, 16 produce or have produced commercial SNF from nuclear power generation. Of the six non-member states, only Switzerland and Ukraine hold commercial SNF.

The projections indicate that by 2050, the amount of SNF in storage will be twice as much as the amount existing in 2013; hence, nuclear power-operating countries—especially Canada, the United States, and Asiatic countries—have to ensure sufficient storage capacity at their facilities (see Fig. 13.3B). A decrease in the projected inventories of stored SNF is foreseen in Europe, mainly due to the planned deep geological disposal facilities for SNF, especially in Finland, Sweden, and France. These projections have been viewed by some as too optimistic, given the delays in siting and licensing deep geological disposal facilities [20].

The three main dry storage techniques currently used in the world are casks, silos, and vaults. According to the IAEA [22], the technology options for SNF storage can be selected according to the following criteria: heat transfer method, type of shielding, transportability, location with respect to the geological surface, degree of independence of the individual storage units, etc. Storage in casks is increasingly gaining acceptance mainly due to its modular character, which makes it easier to adapt to whatever configuration is needed, and facilitating the transport of the SNF, contrary to vaults and silos.

13.3.2.1 Storage in casks/containers

Casks were initially intended for transporting SNF from NPP ponds to reprocessing facilities. Today, the main use of casks is for SNF storage beyond the initial cooling



Figure 13.4 Example of cask storage horizontally placed in open air (A) and vertically placed inside a building (B) [22].

time in ponds. SNF is placed inside cylindrical casks placed on concrete floors. In most cases, the casks are vertically emplaced, although some horizontal examples can be also found (see Fig. 13.4). These storage systems can be open or located inside a protected building [23].

Concrete casks, metallic casks (canister-like), and a combination of both can be used. Also, the combination between metal and concrete casks and vaults (i.e., a canister in a concrete overpack inside a vault) is used. Concrete casks contain an inside cavity coated with a metallic layer. These casks are cooled either through natural or forced convection to allow for SNF cooling [24,25].

Metallic casks are made of steel-, iron-, or lead-lined steel. In this case, the metal confers both confinement and radioactive shielding. To avoid criticality, the SNF is previously located inside metallic containers made with a neutron-absorbing material, such as boron-bearing stainless steel. Boron provides thermal neutron absorption and, after being activated by neutrons, emits alpha particles. Decay heat generated is conducted through the metallic materials [24,25].

All these types of casks are large, several meters height, and a variety of configurations exist, depending on the type of SNF (i.e., composition, size, burnup, thermal pulse) and storage system (i.e., casks, silos, vaults) being used. The requirements for casks and/or containers for storage are different for those for multipurpose, such as the ones engineered for storage and deposition. As explained by the IAEA [22], the USDOE has an initiative to develop an MPC (multipurpose canister) in order to compatibilize the interface between different stages of the spent fuel management, including containment and deposition. A complete description can be found in [22] and references therein.

Although containers and casks were initially engineered for temporary storage purposes, recent new developments permit configurations allowing for temporary storage and transport (i.e., these are dual purpose) or even for final disposal (i.e., multiple purpose containers) are being developed. This simplifies the amount of manipulation of SNF once discharged from the cooling pond at the NPP and decreases risks to safety associated with fuel handling.

13.3.2.2 Storage in silos

This is not a very common type of storage. The system is very similar to the one in casks/containers. Silos are made of reinforced concrete. Inside the silos, one or several metallic containers can be emplaced. One of the drawbacks is that silos cannot be transported but confer more effective shielding and isolation than simple purpose casks stored in outdoor facilities ([Fig. 13.5](#)).

13.3.2.3 Storage in vaults

Vaults are made of reinforced concrete with a series of cavities (rooms) where the SNF is stored. This structure has shielding purposes and can be built either on the surface or underground. In the different rooms or cavities, the SNF can be stored either in casks or containers. It is common practice to fill the cavities with an inert gas (normally He) once the vault has been filled with SNF containers in order to prevent oxidation. Once the cavities are full, they are sealed with a concrete plug. Different monitoring processes are put in place to follow possible He leaks that could be indicative of structural failures.

Ventilation procedures can be natural or forced convection and different heat dissipation measures are put in place [\[24\]](#). Most of these facilities are located outside of the NPP (AFR), and they are prepared to receive SNF from different reactors. Some examples are found in Belgium, France, the Netherlands, the United Kingdom, Japan, and Sweden.



Figure 13.5 Example of dry storage in standalone concrete silos at a nuclear power plant site.



Figure 13.6 Picture of the HABOG building for high-level radioactive waste treatment and storage in the Netherlands.

One example of central storage in dry conditions is HABOG, which is located in the Netherlands. The Dutch Government decided to follow a reprocessing strategy of SNF from their only commercial reactor in the Netherlands located in Borssele. A total of 100 year interim storage of the radioactive waste was decided upon. This led to the founding of the Dutch radioactive waste management agency (COVRA) and the construction of the high-level radioactive waste treatment and storage building, HABOG, as shown in Fig. 13.6. The HABOG building has different halls for the purposes of reception, preparation of the waste, unloading and packaging, transport, storage of heat producing waste, and for non-heat producing waste. The building is equipped with a control area and several rooms for auxiliary systems, among them the venting and energy supplies. The heat producing HLW is stored in one of the three available storage compartments for this purpose. Several steel cylindrical wells are located in each compartment. Within each well, five canisters can be stored on top of each other.

The situation of the status of temporary storage of SNF and vitrified HLW in the world is shown in Table 13.A.1 in the “Appendix” section.

13.4 Spent nuclear fuel and high-level waste geological disposal—international practices

In 2008 the Radioactive Waste Management Committee of the Organisation for Economic Co-Operation and Development, Nuclear Energy Agency issued a statement regarding the suitability and the feasibility of geological disposal for specified

categories of radioactive waste [26]. The deep geological disposal of spent fuel is the preferred route for the final disposal of the stored SNF and HLW. The disposal is based on a multibarrier system, where the host rock constitutes the ultimate barrier isolating the repository system from the biosphere. Different geological materials are proposed as host rocks for the repository: clay, salt, and crystalline rocks (see Ref. [26]). While many countries have specific plans for geological disposal of their SNF, only three European countries (Sweden, Finland, France) have been able to specify a specific site for the disposal (at the time of this publication), which constitutes the main obstacle for the progress toward a definitive solution.

Multibarrier, deep geological disposal systems are the preferred options when dealing with the high-energy contents of SNF. The main challenges in this respect are to ensure thermal and radioactive isolation of the fuel elements for a long period of time, mainly because of the FP and actinoid (mainly Pu) content of the fuel after discharge. The various concepts that will be discussed fulfill these requirements.

Finland is the country most advanced in the licensing process with Sweden slightly behind. Both countries share the so-called KBS-3 concept developed by the Swedish Nuclear Fuel and Waste Management Company (SKB) in the early 1980s. Fig. 13.7 shows a scheme of this multibarrier concept, which is primarily based on the long-term stability of the spent fuel matrix under reducing conditions in neutral to slightly alkaline media [9]. Although there are various barriers, container, buffer, and rock play important safety roles in the concept.

Maintaining reducing conditions in the repository is a prerequisite of the concept, which is driven by the lower solubility and thus mobility of U(IV) versus U(VI). While SNF contains uranium predominantly in its more immobile reduced redox state [i.e., U(IV)], the presence of oxidants in the media destabilizes uranium causing the alteration of the SNF matrix as well as that of the elements imbedded in the SNF material. Reducing conditions in the repository are secured by keeping the spent fuel in copper canisters with iron insets. The copper canister gives

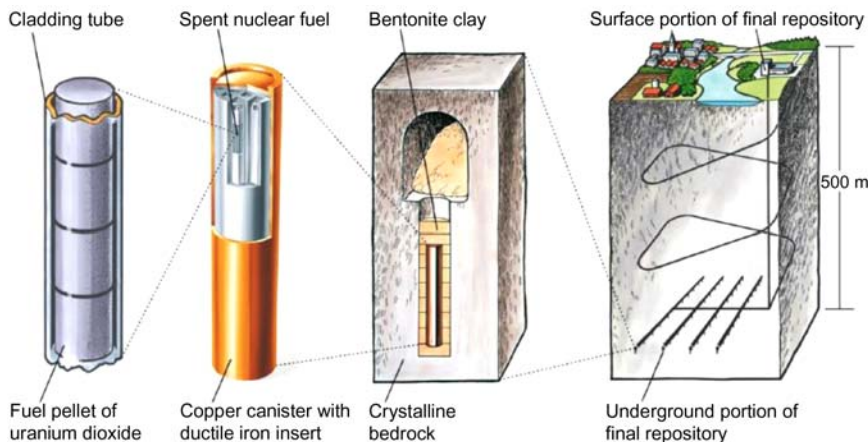


Figure 13.7 The KBS-3 method for spent nuclear fuel disposal [27].

chemical and mechanical stability to the fuel while the anoxic corrosion of the iron inlets produces highly reducing conditions and hydrogen gas generation in the case of anoxic corrosion of the iron-bearing materials [28]. The dissolved hydrogen content keeps the UO_2 surface reduced and counterbalance the radiolytic oxidation of the fuel surface [29,30]. The hydraulic and mechanical stability of the copper canisters is provided by the iron inlet and the surrounding bentonite buffer, which in addition minimizes the groundwater flow. A complete description of the engineered barrier system of the KBS-3 concept can be found in SKB [27].

The granitic groundwater at depths below 400 m is also reducing with Eh values under -300 mV [31]. These waters are slightly alkaline with an HCO_3^- concentration in the millimolar level and a pH around 8 [31]. The combination of these features are designed to render the spent fuel matrix to be very stable for hundreds of thousands of years and mimic the conditions for which uranium(IV) oxides have been preserved in natural uranium ore deposits.

The closed cycle alternative to SNF disposal is used in those countries that reprocess the fuel to extract the FPs generated by AR operation, particularly Pu, which is later used in MOX production. The HLW originated in this process is vitrified by using borosilicate glasses and geologically disposed. This is the preferred route for France that has developed a concept called Cigeo (acronym for the French name of Industrial Centre for Geological Storage: Centre Industriel de Stockage GEOlogique), proposed by the French National Radioactive Waste Management Agency (ANDRA). As it can be seen in Fig. 13.8, the Cigeo concept is also multi-barrier with stainless steel canisters emplaced in a Callovo-Oxfordian clay formation at a depth of 400–500 m.

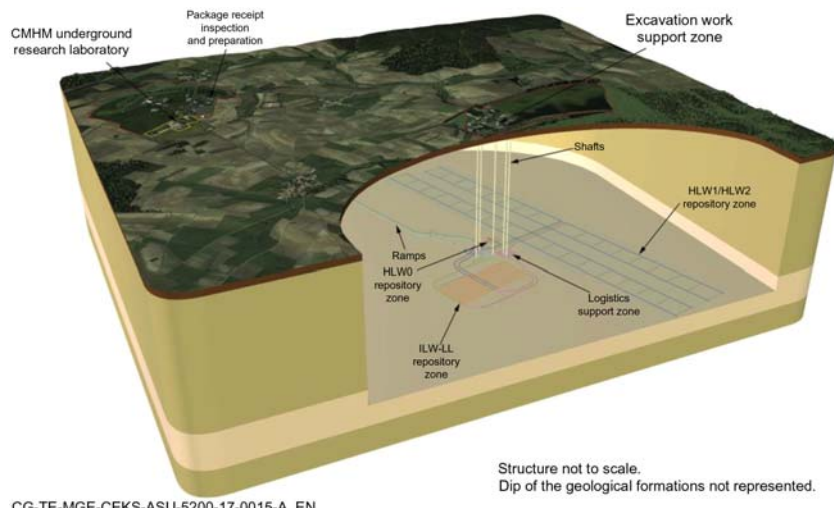


Figure 13.8 Overview of the Cigeo concept for high-level nuclear waste in France. *Cigeo*, Centre Industriel de Stockage GEOlogique.

Other countries have generic SNF disposal designs that are variations of the KBS-3 and the Cigeo concepts. The concepts being explored by the United Kingdom and Canada follow the KBS-3 design with stainless steel in the case of the United Kingdom replacing the copper in the containers and carbon steel (SA516) with a copper outer layer. Belgium and Switzerland are in line with the Cigeo concept. The reasons behind these choices are mainly a result of the different geological environments available.

A summary of the current status of spent fuel disposal options adopted internationally is summarized by the International Atomic Energy Agency [15].

13.5 Key processes from operation to disposal through storage that impact the long-term stability of spent nuclear fuel

Most of the vitrified HLW and SNF are currently kept in interim wet and dry storage facilities. This has a number of implications for the composition and structure of the SNF, which will eventually be disposed of. It is very important to consider these changes when defining the source term of the geological repositories to be designed and constructed and even more important to devise proper monitoring strategies of the potential changes to the integrity of the spent fuel, the cladding and the associated container. A brief summary of the changes incurred by SNF during dry storage is given in Duro et al. [32] and references therein.

The fate of the fuel within the reactor is reasonably well-known, although there is a substantial lack of knowledge regarding the variability of composition and structure with defected fuel elements, which are bound to be more fragile and could render higher dose contributions (i.e., since there is no longer a complete barrier between the fuel and its surroundings). Burns et al. [33] compiled information from several investigations performed in the United States, France, Canada, and Japan on the behavior of damaged fuel elements with temperature, whereby significant deformation and bursting of the cladding starting at temperatures around 750°C in reactor. However, most of the fuel failures are due to crud/corrosion-debris fretting, pellet cladding interaction, grid to rod fretting, and manufacturing defects. This is an area where more knowledge of the root cause of fuel failures from the operators would better inform the initial state situation of the waste in the safety assessment of storage and disposal facilities.

Alvarez et al. [34] discussed the potential consequences of long-term storage in the pools and the subsequent reracking of the fuel elements as is currently done in the United States and many other countries (e.g., Spain) that follow the recommendations of the US Nuclear Regulatory Commission. Although the probability of a pool dry-out is deemed to be very low, the consequences could be substantial, particularly as a result of increased temperatures and subsequent FP release to the

environment. Therefore it is recommended that a successive transition is implemented of the spent fuel elements from the pools to dry storage.

One of the key issues regarding the transition from wet to dry storage and eventual disposal concerns the potential for water content in the fuel elements. Once spent fuel is removed from the storage pools, it is typically dried before it can be placed into dry storage and before transportation and disposal [35]. The objective of the drying process is to remove as much water from the system as possible to limit fuel degradation caused by the association of water and elevated temperature. The combination of the initial high temperatures of the fuel together with the remaining water content could trigger spent fuel alteration reactions as a result of the local hydrolysis of uranium and associated nuclides.

Various drying methods exist for spent fuel. Typically, the vacuum drying method, with or without heat, consists of reducing the pressure inside the canister, so moisture can evaporate. The vacuum drying method has a high mass transfer efficiency but a low heat transfer efficiency. For this reason, it must be combined with a purge or cyclic backfill to improve the heat transfer between the fuel and any remaining water [35]. In this second process, the moisture is forced out of the canister by backfilling it with inert gas, typically He.

In the vacuum drying method, adequate moisture removal is generally assessed by monitoring the pressure increase in the canister isolated from the vacuum pump. This method is based on the principle that any liquid water remaining in the isolated volume of the canister would produce distinct pressure increases when subject to elevated temperature. Typically, the endpoint of the vacuum drying process occurs when the pressure is 3 Torr (approximately 400 Pa) or less during an isolation period of 30 minutes [36]. In the forced helium gas method, the level of dryness is based on the moisture content (water vapor pressure) measured in the outlet gas, and the endpoint can be estimated by the number of turnovers. Yet, characterizing the dryness of the fuel is difficult because of the uncertainty in estimating the amount of residual water in the fuel in dry storage [35]. For instance, in degraded fuel or fuel debris, the vapor pressure might take more than 30 minutes to increase because of the equilibrium water vapor pressure over hydrated corrosion products or the high surface area particle microstructure to which water physically adheres. Moreover, moisture removal by forced helium drying may be impeded if the occluded internal volume is not at equilibrium with the outlet gas.

Three forms of water can be retained in a sealed canister: free water, physically sorbed (physisorbed) water, and chemisorbed water [37]. Free water, either in vapor or liquid form, is the main driver of fuel degradation, because it can cause corrosion and hydrogen gas production, which increases pressure, even at ambient conditions. The free water can be removed by heating or reducing pressure as it is not physically or chemically bound to anything. Physisorbed water, which is physically adsorbed on the exposed fuel and canister surfaces, is in equilibrium with the free water and can recharge it even at ambient conditions. For most surfaces with physically bound water the external layer of water can be removed by heating the fuel to 50°C under vacuum [36].

Chemisorbed water, which is bound to various corroded fuel or fuel phases, can be present in quantities up to three orders of magnitude greater than the combined amounts of free and physisorbed water together in certain types of research and test reactor SNF, such as aluminum-based fuel managed by the US Department of Energy [36], see more on research and test reactor fuels in [Chapter 7](#), Research reactor fuels. Chemisorbed water does not participate in the fuel degradation mechanisms as much as free and physisorbed water. However, if it remains in the fuel, long-term fuel decomposition mechanisms will release the chemisorbed water, which will then recharge the free and physisorbed water. In order to remove this chemisorbed water from the corroded fuel and fuel components, it requires higher drying temperatures, which are generally not well-tolerated by aluminum-based fuel [37], thereby limiting the dryness achievable.

At any rate, under normal operating conditions, there are a series of changes that will affect the composition and structure of SNF under storage conditions. Wyss et al. [38] have performed the most extensive investigation of the effects of long-term storage of SNF. The radiation environment changes for the SNF discharged from the reactor and is dominated by alpha decay. According to Wyss et al. [38], radiogenic self-production of helium, a direct product of alpha particles, will prevail and a number of atomic level changes will occur in the fuel. In this respect, the SNF presently characterized and investigated is not representative of that which will be disposed of after hundreds to thousands' years of storage mainly because of the accumulation of He and microstructural defects [38].

Wyss et al. [38] performed a very thorough study of the long-term effects of He production on fluorite-type structures by using a range of spent fuel specimens, alpha-doped samples, and some natural uraninites. By and large, the outcome of their investigations indicates that for boiling water reactor (BWR) and pressurized water reactor (PWR) spent fuel, no major structural damage is predicted for storage times under 1000 years. However, given the rate at which current disposal decisions are being made in some countries, there is a risk and a temptation to make storage indefinite, which would increase the probability of structural damage of the stored SNF.

The effect of extended burnup on the spent fuel structure will have to be considered as well as burnup rates, which are gradually being increased. Rondinella and Wyss [39] have made an extensive investigation of the structural effects of high burnup fuels [50 MWd/kg(HM)], which could give rise to localized burnups of 75 MWd/Kg(HM). This results in a region known as high burnup structure (HBS) with grain subdivision, redistribution of fission gases and extended defects (see [Fig. 13.10](#)). The HBS is discussed in more detail in [Chapter 11](#).

Manzel and Walker [40] studied the width of the HBS with increased burnup resulting in [Fig. 13.9](#).

It is clear that for burnups over 50–60 MWd/kgHM in LWR fuel, the formation of the HBS has to be taken into consideration for the safety assessment of the subsequent storage and eventual disposal, as the distribution of the various FPs at the surface will increase, and the physical condition of the grains will change, becoming more porous. In addition, there will be an enhanced fission gas release.

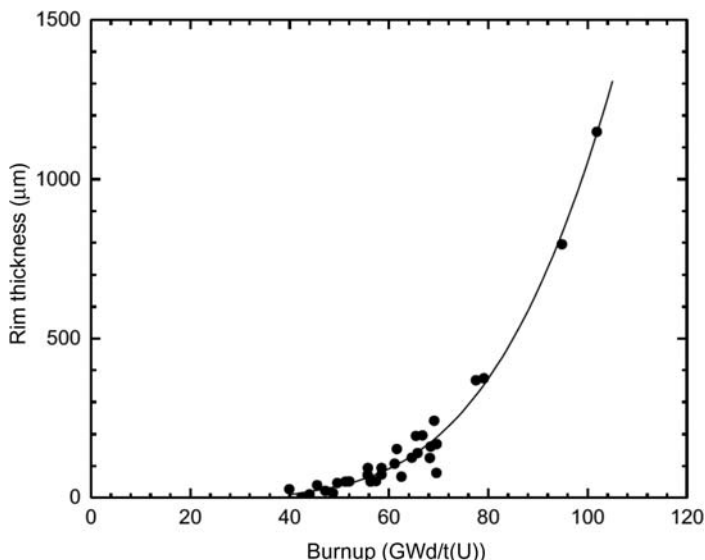


Figure 13.9 Radial thickness of the HBS as a function of burnup measured by optical microscopy on cross sections of LWR fuel. *HBS*, High burnup structure; *LWR*, light-water reactor.

Source: Copied from M.H.A. Piro, D. Sunderland, S. Livingstone, J. Sercombe, W. Revie, A. Quastel, et al., A review of pellet–clad interaction behavior in zirconium alloy fuel cladding, in: S. Hashmi (Editor-in-Chief), Reference Module in Materials Science and Materials Engineering, Elsevier, Oxford, 2017, pp. 1–68, which was reproduced from Manzel and Walker (2002) [40].

The alteration of the microstructure of SNF in long-term dry storage is also activated by other processes, mainly, temperature-driven diffusion and radiation-enhanced diffusion of radionuclides. The diffusion of radionuclides in spent fuel at high temperatures varies depending on the FPs. Thermal diffusion has been considered negligible over the time range of dry storage (i.e., less than 100 years) and at temperatures expected under storage conditions (i.e., less than 400°C) [41]. However, the conditions under which a material is irradiated can significantly modify its response. For instance, the high temperatures encountered in the center of the fuel pellets can alter the kinetics of radiation-enhanced damage mechanisms, making the tolerance to radiation of materials vary within specific temperature ranges [42]. Moreover, the process of thermal diffusion at the grain boundaries differs, particularly when the radionuclides are nonuniformly distributed through the fuel [43,44].

Generally, the effects of highly ionizing radiation are not as well understood as the elastic interactions from displacing radiation [42]. But FPs at the grains, which fall into the high-energy range, are known to cause significant degradation in nuclear fuels [45]. It is not clear, however, to what extent highly ionizing radiation will affect the physical integrity of spent fuel at the temperature levels and time scale involved in long-term, dry storage. This issue requires further research effort.

13.6 Dissolution and alteration of spent nuclear fuel under deep geological repository conditions

In-reactor irradiation of nuclear fuel yields a continuous production of FPs. The FPs include isotopes of noble gases (mainly Xe and Kr) and others, such as ^3H , ^{14}C , ^{79}Se , ^{99}Tc , ^{107}Pd , ^{125}Sn , ^{129}I , ^{135}Cs , and ^{137}Cs . As described in Chapter 11, FPs may be present in the fuel as volatiles (i.e., I, Br, Cs, Rb, Te), metallic precipitates (i.e., Mo, Tc, Ru, Rh, Pd, Ag, Cd, In, Sn, Sb, Te), secondary oxide precipitates (i.e., Rb, Cs, Sr, Ba, Zr, Nb, Mo, Te), or the soluble oxides in the in the UO_2 fluorite matrix (i.e., Cs, Nb, Te, Y, Zr, the earth alkaline elements Sr, Ba, Ra and the lanthanides La, Ce, Pr, Nd, Pm, Sm, Eu) [46]. Piro et al. [43] have predicted the evolution of the various FPs as a function of burnup.

In a rod containing stacked pellets of polycrystalline UO_2 fuel during reactor operation, concentration and thermal gradients drive redistribution of some of the FPs from intragranular to the intergranular space and outside the pellet toward the inner-rod void space. It is thought that under repository conditions, breaching of the cladding would rapidly release the inventory accumulated in the void space of the rod. Also, radionuclides that are segregated to the fuel grain boundaries would be released relatively quickly. The instant release fraction (IRF) is the fraction of the radioactive inventory that will be released from the waste “immediately” after the fuel rod cladding fails, and the waste containment is compromised. The IRF is the sum of the FPs in the void space plus the FPs in the grain boundaries divided by the total FP inventory. It constitutes the main portion of the dose at early disposal times as discussed in the previous sections of this chapter.

The IRF may have important implications for future assessments of the performance of a repository, as some of the preferentially released radionuclides are characterized by both relatively long half-lives and high degrees of mobility (e.g., ^{129}I and ^{36}Cl [47]). As a result a great deal of effort has been directed toward improving the understanding and quantifying the physicochemical processes involved in the IRF from SNF. These goals are being achieved through a combination of experimental and modeling work, and there is a complete body of literature on the subject [48].

After the instant release of radionuclides from the fuel, a much slower radionuclide release mechanism would occur over long periods of time due to dissolution of the UO_2 matrix [49,50]. The main alteration reactions that may occur at the spent fuel/iron canister/groundwater interface were described as a result of a Euratom collaborative project [49] and have been depicted in Fig. 13.10.

It is quite important to realize that the schematic shown in Fig. 13.10 is not drawn to scale. The oxidizing front extends some hundred microns from the surface at maximum, while the reducing front covers some decimeters in range. The near field rock, which is placed at meters length and separated from the canister by the backfill, ensures that the overall redox condition remains reducing. The net effect is that H_2 generation at the reducing front is able to offset the surface oxidation [29].

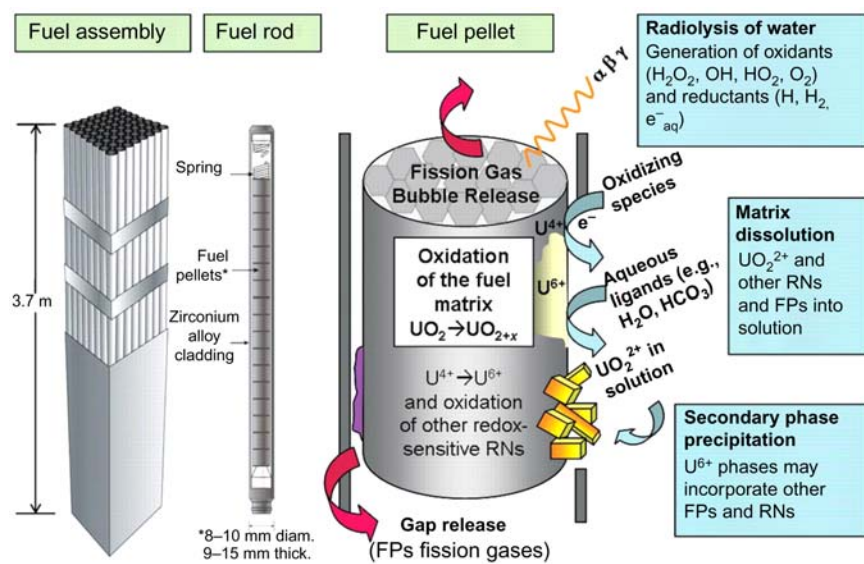


Figure 13.10 The main chemical processes that may occur when spent nuclear fuel comes in contact with groundwater within a failed container showing the influences of both radiolytic oxidation, the anoxic corrosion of the steel container, and processes occurring in the near field outside the container. The fuel assembly is representative of one used in a typical light-water reactor. *FPs*, Fission products; *RNs*, radionuclides.

Source: From J. Bruno, R.C. Ewing, Spent nuclear fuel, Elements 2 (2006) 343–349.

The rate of dissolution of the UO_2 matrix under oxidizing conditions is larger than under reducing conditions. Under reducing conditions, the overall dissolution will be controlled by the thermodynamic solubility of $\text{U}(\text{IV})$ dioxide, which is low ($10^{-8} - 10^{-9}$ mol/dm 3) [51,52] and depends on the crystallinity and degree of oxidation of the spent fuel surface. In this context, it is important to bear in mind the potential dislocation and crystallinity effects previously discussed as a result of higher burnup and extended storage times.

Furthermore, there is a potential destabilizing mechanism under reducing conditions, which is the potential transformation of the UO_2 matrix to USiO_4 (coffinite) by the presence of silicate in the contacting groundwaters. While recent thermodynamic studies indicate that coffinite is metastable with respect to $\text{UO}_2(\text{s})$, the fact is that coffinite coexists and forms in many natural environments [53,54,55].

As has been previously discussed (see Table 13.1), there are a number of minor components of SNF that are intimately bound within the UO_2 matrix. These are mainly the actinoids (Pu, Np) and the lanthanoids. Plutonium is one of the main contributors to the long-term dose from disposed SNF, which is illustrated in Fig. 13.1. These components are soluble in the fluorite matrix, and therefore their release is controlled by the rate of dissolution/alteration of the spent fuel matrix, which is a much slower process than the one governing the so-called IRF.

In the last few decades, SKB has performed a number of safety assessments of the KBS-3 concept and the SR-Site assessment in preparation for the continued underground site characterization at Forsmark, Sweden [56]. The outcome of these safety assessment exercises has been that the projected doses will never be over the regulatory limit if the KBS-3 concept is fully deployed. Likewise, Posiva has also performed similar safety assessments that have granted the permission to construct the repository [56]. The first and innermost barrier for radionuclide release in the KBS-3 concept is the fuel itself, and the cumulative studies throughout the scientific community have provided a robust base upon which to develop the overall disposal concept.

The alteration of SNF under repository conditions has been studied experimentally since the second half of the 20th century, and different types of models have been developed to ascertain SNF behavior. SNF will evolve under the conditions expected in a repository. Semiempirical models studying the influence of pH, oxygen, hydrogen peroxide, carbonate, and temperature on the dissolution of SNF have been developed and used in the long-term performance assessment of the repository. Some examples are the ones of Schortmann and DeSesa [57] and the ones from the Spanish investigations that led to the development of the matrix alteration model [58–61].

Models relevant to SNF can be classified as either chemical or electrochemical. The conceptualization is the same in both cases, in which the SNF can be dissolved in water nonoxidatively, in the form of U(IV), or oxidatively, after its oxidation to U(VI). The main difference among both types of models is that whereas the electrochemical models calculate the corrosion potential and corrosion rate at the SNF surface, the chemical models simulate the SNF oxidation through redox processes. Some experiences relevant to Canadian applications have been reported by Wu et al. [62,63] and He et al. [64], while results in the United States are reported by Jerden et al. [65]. These authors apply the conclusions drawn from previous Swedish investigations [66–70] to select and implement the most relevant processes and associated parameters. Developments from France include its last refinement of the matrix alteration model by considering the presence of the metallic container and how it interacts with the SNF.

Poinssot and Gin [71] assessed two different approaches for scaling mechanistic detailed models built to explain laboratory experiments of alteration of SNF to operational models useful for assessing the performance of a deep geological repository. The first approach is the development of numerical 2D/3D geometries of the complete repository system. These models use complex calculation software tools to solve the whole repository system. It is difficult to ensure consistency of these type of models, due to the large number of parameters involved and the lack of data available for specific interactions between processes and components of the repository system. The only path forward is to use less favorable data to ensure that the predictions are conservative, and the model does not reproduce a too optimistic behavior of the repository in the long term. The second approach is the progressive simplification of the phenomenology with the aim to developing specific purpose-oriented models. This second approach requires a deep understanding

of the system to ensure that the simplified models capture key trends of the actual system.

There is a general uniformity and consensus among the different models selected by the different agencies responsible for SNF management on spent fuel corrosion. This is a logical consequence of the close collaboration between agencies and the numerous research projects with participants from the different countries with advanced nuclear programs. Due to the long-term predictions needed to assess the performance of deep geological repositories for SNF disposal, predictive models are continuously being developed by the scientific community with the support of nuclear waste management organizations. Examples of joint projects dealing with the behavior of SNF under repository conditions can be found in the study of the SNF corrosion mechanisms [49,72]; the study of the uncertainties associated with the spent fuel corrosion models [73]; the study of the IRF for different types of spent fuel [48,41,74]. At the time of this publication, a joint effort aimed at investigating the behavior of new-generation fuels that contain different levels of dopant such as Cr, Al, and Gd to improve performance and decrease release of fission gases is under development. The aim of this initiative is to compare the behavior of doped with that of nondoped fuels and check whether the conclusions obtained from the study of traditional SNF are applicable to the new doped fuels [75].

13.7 Outlook

Current SNF stability models have been developed for the initial strategy in which moderate burnup fuels were intended to be stored a few decades in wet storage and later disposed of in geological repositories. In most concerned countries, this strategy has changed because of delays in taking the appropriated SNF management decisions.

Some of the current and future challenges to ensure the applicability of the models of SNF alteration are as follows:

- Spatial and temporal upscaling. Our current understanding of the SNF disposal behavior is mainly focused in quantifying processes that occur at the nano- to centimeter scale and for a limited amount of time (decades). There is a need to expand our models to the repository spatial and temporal scales. This has been done previously by looking at appropriated natural analogues, but this knowledge should be updated.
- Fate of the active nuclides: effect of the formation of new secondary solid phases that may act as a sink or as a future source of radionuclides released from the SNF.
- Upgrading the models to simulate the dissolution of minor elements, particularly the actinoids and lanthanoids, the epsilon phases, and the FPs, present in the SNF.
- Will hydrogen counteract the oxidation of the SNF in the long term? To what extent and under what conditions could the catalytic effect of the epsilon particles be inhibited and become incapable of activating hydrogen?

- Integration of the radiolytic and the geochemical models. This is a consequence of the need for spatial and temporal scaling, bridging the micrometer scale to the kilometer scale can only be done if these two sub-models are integrated.
- Integration of the different subsystems: SNF, container, engineering barriers, host rock. This should be accomplished by designing appropriated multicomponent experiments together with the development of integrated multicomponent process models.
- How will the higher burnups and the different dopants incorporated in modern fuels affect their long-term behavior?
- How is the transient dry storage before deposition considered in the initial state of the SNF?

Future SNF stability models will have to take into consideration higher burnups and longer dry storage periods with consequences for the definition of the source term, mainly due to the formation of highly altered rims and the structural changes due to longer alpha activity times in dry storage with potential oxidative processes occurring at the surface of the fuel.

New-generation fuels will have to be taken into consideration as well as the fact that some of the stored fuels will be defective and prone to give the higher doses on a safety assessment. These issues are further discussed in [Chapters 5–7](#) where other reactor fuels, molten salt reactor fuels, and research and test reactor fuels, respectively, are presented. There is a need to understand the behavior of these non-UO₂ fuels in the context of geological disposal.

13.8 Conclusion

The safety assessment of the geological disposal of SNFs requires a deep understanding of the process that may destabilize the UO₂ matrix as well as the various phases and FPs generated during reactor operation. SNF is the first and last barrier of the disposal system.

There is a fundamental understanding of the key processes and the master variables (pH and Eh) that control the stability of the SNF matrix. The design of many multibarrier disposal systems is geared toward ensuring neutral to alkaline pH media and reducing conditions.

Initial doses will be the result of the release of the so-called IRF that is mainly composed by the FPs contained at grain and grain boundaries.

At present, all the safety assessment exercises concerning the spent fuel disposal in deep reducing environments indicate that the calculated doses are always under the regulatory limits. This is a confirmation of the robustness of the multibarrier spent fuel disposal concept. This is particularly so for the KBS-3 concept whose licensing is quite advanced both in Finland and Sweden.

With increasing burnup and storage times, there is a need to assess the consequence of not taking the appropriated management decisions on time. This is particularly sensitive for the SNF specimens that are defective from operation.

Appendix

Table 13.A.1 International situation of temporary storage.

Country	Facility	Type of storage	Type of waste ^a
Germany	Ahaus	Metallic containers	SNF
	Gorleben	Metallic containers	SNF; VW
	ZNL	Metallic containers	SNF
	Jülich	Metallic containers	RF
	Obrigheim	Pond + metallic containers ^b	SNF
	Distintas centrales	Metallic containers	SNF
Belgium	Tihange	Pond	SNF
	Doel	Metallic containers	SNF
	Dessel	Vault	SNF; VW
France	La Hague	Ponds	SNF
	La Hague	Vault	VW
	CASCAD	Vault	SNF
	Marcoule	Vault	SNF
The Netherlands	Petten	Concrete casks	RF
	HABOG	Vault	RF; VW
Hungary	Paks	Vault	SNF
United Kingdom	Sellafield	Pond	SNF
	Sellafield	Vault	VW
	Wylfa	Vault	SNF
Sweden	CLAB	Pond	SNF
Finland	Loviisa	Pond	SNF
	Olkiluoto	Pond	SNF
Switzerland	ZWILAG	Metallic containers	SNF; VW
Czech Republic	Dukovany	Ponds + dry	SNF
	Temelin	Ponds + dry	SNF
	Rez NRI	Ponds + dry	RW
Bulgaria	KOZLODUY	Ponds	SNF
Slovakia	Bohunice	Ponds	SNF
Lithuania	Ingalina	Dry casks	SNF
Russia	Krasnoyarsk	Pond	SNF
	Leningrad	Concrete casks	SNF
	Kursk	Concrete casks	SNF
Japan	Fukushima-Daiichi	Metallic containers	SNF
	Tokai-Daini	Metallic containers	SNF
	Rokkasho	Vault	VW
	Mutsu ^b	Vault	SNF
China	Several NPPs	Ponds at NPP	SNF
	Qinshan	Dry	SNF

(Continued)

Table 13.A.1 (Continued)

Country	Facility	Type of storage	Type of waste ^a
Canada	Pickering	Concrete casks	SNF
	Bruce	Concrete casks	SNF
	Darlington	Concrete casks	SNF
	Gentilly	Concrete casks	SNF
	Point Lepreau	Concrete casks	SNF
	Chalk River	Concrete casks	RF
	Whiteshell	Concrete casks	RF
United States	Different NPPs	Concrete-metal containers, silos, vaults	SNF
	Hanford Site		SNF
	INL		SNF
	SRS		SNF
Brazil	ANGRA 1	Ponds	SNF
Argentina	Atucha I/II	Pond	SNF
	Embalse	Pond + silo dry	SNF
	Ezeiza	Pond	SNF, RW

INL, Idaho National Laboratory; *SRS*, Savannah River Site.

^aSNF: spent nuclear fuel. VW: vitrified HLW; RF: research fuel.

^bNot yet in operation.

Source: International Atomic Energy Agency (IAEA), Status and trends in spent fuel and radioactive waste management, in: IAEA Nuclear Energy Series No. NW-T-1.14, Vienna, Austria, 2018; International Atomic Energy Agency (IAEA), Operation and maintenance of spent fuel storage and transportation cask containers, in: IAEA-TECDOC-1532, Vienna, Austria, 2007, and information from different websites from the Radioactive Waste Management agencies and regulators.

References

- [1] A. Makijami, Plutonium as an energy source, energy and security, no. 1, in: Newsletter of the Institute for Energy and Environmental Research, IEER Publication, 1996.
- [2] F.N. Von Hippel, Plutonium and reprocessing of spent nuclear fuel, *Science* 293 (5539) (2001) 2397–2398.
- [3] R.C. Ewing, W.J. Weber, Ch. 35: Actinide waste forms and radiation effects, in: L.R. Morss, N.M. Edelstein, J. Fuger (Eds.), *The Chemistry of the Actinides and Transactinide Elements*, vol. 6, Springer, Dordrecht, The Netherlands, 2011, pp. 3813–3887.
- [4] P. Carbol, H.D. Wegen, T. Wiss, P. Fors, Spent fuel as a waste material, in: R.J.M. Konings (Ed.), *Comprehensive Nuclear Materials*, vol. 5, Elsevier, 2012, pp. 389–420.
- [5] A. Hedin, Spent Nuclear Fuel—How Dangerous is It? (SKB Technical Report No. 97–13), Svensk Kärnbränslehantering AB, Stockholm, Sweden, 1997.
- [6] International Atomic Energy Agency, Management and Storage of Research Reactor, Spent Nuclear Fuel Proceedings of a Technical Meeting held in, Thurso, United Kingdom, 2009.
- [7] H. Kleykamp, The chemical state of the fission products in oxide fuels, *J. Nucl. Mater.* 131 (1985) 221–246.
- [8] R.C. Ewing, Long-term storage of spent nuclear fuel, *Nat. Mater.* 14 (2015) 252–257.

- [9] J. Bruno, R.C. Ewing, Spent nuclear fuel, *Elements* 2 (2006) 343–349.
- [10] E.C. Buck, B.D. Hanson, B.K. McNamara, The geochemical behaviour of Tc, Np and Pu in spent nuclear fuel in an oxidizing environment, in: R. Gieré, P. Stille (Eds.), *Energy, Waste and the Environment: A Geochemical Perspective*, Geological Society, London, Special Publications, 2004, pp. 65–88.
- [11] D.W. Shoesmith, Fuel corrosion processes under waste disposal conditions, *J. Nucl. Mater.* 282 (2000) 1–31.
- [12] M.H.A. Piro, D. Sunderland, S. Livingstone, J. Sercombe, W. Revie, A. Quastel, et al., A review of pellet–clad interaction behavior in zirconium alloy fuel cladding, in: S. Hashmi (Ed.), *Reference Module in Materials Science and Materials Engineering*, Elsevier, Oxford, 2017, pp. 1–68.
- [13] J. Arborelius, K. Backman, L. Hallstadius, M. Limbäck, J. Nilsson, B. Rebensdorff, et al., Advanced doped UO₂ pellets in LWR applications, *J. Nucl. Sci. Technol.* 43 (2012) 967–976.
- [14] International Atomic Energy Agency (IAEA), Advanced fuel pellet materials and fuel rod design for water cooled reactors, in: IAEA TECDOC No. 1654, Vienna, Austria, 2010.
- [15] International Atomic Energy Agency (IAEA), Status and trends in spent fuel and radioactive waste management, in: IAEA Nuclear Energy Series No. NW-T-1.14, Vienna, Austria, 2018.
- [16] Council directive 2011/70/Euratom of 19 July 2011 establishing a Community framework for the responsible and safe management of spent fuel and radioactive waste, Official Journal of the European Union. L199/48, 2011.
- [17] International Atomic Energy Agency (IAEA), Potential interface issues in spent fuel management, in: IAEA TECDOC Series No. 1774, Vienna, Austria, 2015
- [18] P. Högselius, Spent nuclear fuel policies in historical perspective. An international comparison, *Energy Policy* 37 (2009) 254–263.
- [19] O. Olsson, T. Hedman, B. Sundman, C. Svemar, Geological disposal of radioactive waste—experience from operating facilities in Sweden, in: N.T. Rempe (Ed.), *Reviews in Engineering Geology Volume XIX: Deep Geologic Repositories*, vol. XIX, 2008, pp. 73–80. <[https://doi.org/10.1130/2008.4119\(08\)](https://doi.org/10.1130/2008.4119(08))>.
- [20] M.V. Ramana, Technical and social problems of nuclear waste, *Wiley Interdiscip. Rev. Energy Environ.* 7 (4) (2018) e289.
- [21] Reset Steering Committee, *Reset of America's Nuclear Waste Management Strategy and Policy*, Stanford University, Stanford, CA, 2018.
- [22] International Atomic Energy Agency (IAEA), Operation and maintenance of spent fuel storage and transportation cask containers, in: IAEA-TECDOC-1532, Vienna, Austria, 2007.
- [23] M. Bunn, J.P. Holdren, A. McFarlane, S.E. Picket, A. Suzuki, T. Suzuki, et al., *Interim Storage of Spent Fuel: A Safe, Flexible, and Cost-Effective Approach to Spent Fuel Management*, Managing the Atom Project, Harvard University, Cambridge, MA, 2001. 127 pp. <<https://dash.harvard.edu/handle/1/29914175>>.
- [24] International Atomic Energy Agency (IAEA), Survey of wet and dry storage, in: IAEA-TECDOC 1100, Vienna, Austria, 1999.
- [25] M.Y. Rao, D. Hardy, Technical methods. Status of centralized storage systems for used nuclear fuel, in: NWMO Background Papers, 2003.
- [26] Organisation for Economic Co-Operation and Development (OECD), Nuclear Energy Agency, *Geological disposal of radioactive waste: national commitment, local and regional involvement*, in: NEA No. 7082, Paris, France, 2012.

- [27] Svensk Kärnbränslehantering AB (SKB), Design and production of the KBS-3 repository, in: SKB TR-10-12, ID 1168741, Stockholm, Sweden, 2010, Updated 2013-10.
- [28] L. Duro, C. Domènec, M. Grivé, G. Roman-Ross, J. Bruno, K. Källström, Assessment of the evolution of the redox conditions in a low and intermediate level nuclear waste repository (SFR1, Sweden), *Applied Geochemistry* 49 (2014) 192–205.
- [29] P. Carbol, P. Fors, T. Gouder, K. Spahiu, Hydrogen suppresses UO₂ corrosion, *Geochim. Cosmochim. Acta* 73 (15) (2009) 4366–4375.
- [30] M.E. Broczkowski, J.J. Noël, D.W. Shoesmith, The inhibiting effects of hydrogen on the corrosion of uranium dioxide under nuclear waste disposal conditions, *J. Nucl. Mater.* 346 (1) (2005) 16–23.
- [31] I. Grenthe, W. Stumm, M. Laaksorharju, C. Nilsson, P. Wikberg, Redox potentials and redox reactions in deep groundwater systems, *Chem. Geol.* 98 (1992) 131–150.
- [32] L. Duro, O. Riba, A. Martínez-Esparza, J. Bruno, Changes in spent nuclear fuel due to dry interim storage, in: Materials Research Society Symposium Proceedings, vol. 1475, 2012, pp. 137–142.
- [33] P.C. Burns, R.C. Ewing, A. Navrotsky, Nuclear fuel in a reactor accident, *Science* 335 (2012) 1184. Available from: <https://doi.org/10.1126/science.1211285>.
- [34] R. Alvarez, J. Beyea, K. Janberg, J. Kang, E. Lyman, A. Macfarlane, G. Thompson, F. von Hippel, *Sci of Global Security* 11 (2003) 1–51.
- [35] R.E. Smith, Annotated Bibliography for Drying Nuclear Fuel (No. INL/EXT-11-23561). Idaho National Laboratory, Nuclear Materials Disposition and Engineering, Idaho Falls, ID, 2011.
- [36] W.L. Hurt, Material Interactions on Canister Integrity during storage and transport. In International Atomic Energy Agency (2009) Management and Storage of Research Reactor, Spent Nuclear Fuel Proceedings of a Technical Meeting held in, Thurso, United Kingdom, 2009.
- [37] U.S. Nuclear Waste Technical Review Board, Management and Disposal of U.S. Department of Energy Spent Nuclear Fuel, Report to the United States Congress and the Secretary of Energy, Arlington, VA, 2017, p. 213.
- [38] T. Wyss, J.-P. Hiernaut, D. Roudil, J.-Y. Colle, E. Maugeri, T. Zeynep, et al., Evolution of spent nuclear fuel in dry storage conditions for millennia and beyond, *J. Nucl. Mater.* 451 (2014) 198–206.
- [39] V. Rondinella, T. Wyss, The high burnup structure in nuclear fuel, *Mater. Today* 13 (12) (2010) 24–32.
- [40] R. Manzel, C.T. Walker, EPMA and SEM of fuel samples from PWR rods with an average burn-up of around 100 MWd/kgHM, *J. Nucl. Mater.* 301 (2–3) (2002) 170–182.
- [41] C. Ferry, J.P. Piron, A. Poulesquen, C. Poinsot, Radionuclides release from the spent fuel under disposal conditions: Re-Evaluation of the Instant Release Fraction, in: MRS Proceedings 1107 (2008) 447.
- [42] C.L. Tracy, M. Lang, J.M. Pray, F. Zhang, D. Popov, C. Park, et al., Redox response of actinide materials to highly ionizing radiation, *Nat. Commun.* 6 (2015) 6133.
- [43] M.H.A. Piro, J. Banfield, K.T. Clarno, S. Simunovic, T.S. Besmann, B.J. Lewis, et al., Coupled thermochemical, isotopic evolution and heat transfer simulations of irradiated UO₂ nuclear fuel, *J. Nucl. Mater.* 441 (1–3) (2013) 240–251.
- [44] M. Stan, Discovery and design of nuclear fuels, *Mater. Today* 12 (11) (2009) 20–28.
- [45] H. Matzke, P.G. Lucuta, T. Wiss, Swift heavy ion and fission damage effects in UO₂, *Nuclear Instruments and Methods in Physics Research Section B: Beam Interactions with Materials and Atoms* 166–167 (2000) 920–926.

- [46] V. Metz, E. González-Robles, A. Loida, C. Bube, B. Kienzler, Radionuclide behaviour in the near-field of a geological repository for spent nuclear fuel, *Radiochim. Acta* 100 (2012) 699–713.
- [47] L. Johnson, I. Günther-Leopold, J. Kobler Waldis, H.P. Linder, J. Low, D. Cui, et al., Rapid aqueous release of fission products from high burn-up LWR fuel: experimental results and correlations with fission gas release, *J. Nucl. Mater.* 420 (2012) 54–62.
- [48] K. Lemmens, E. González-Robles, B. Kienzler, E. Curti, D. Serrano-Purroy, R. Sureda, et al., Instant Release of fission products in leaching experiments with high-burnup nuclear fuels in the framework of the Euratom project FIRST-nuclides, *J. Nucl. Mater.* 484 (2017) 307–323.
- [49] C. Poinssot, C. Ferry, M. Kelm, B. Granbow, A. Martínez, L. Johnson, et al., Spent fuel stability under repository conditions – final report of the European (SFS) project, in: Commissariat à l'énergie atomique (CEA), Marcoule, France, 2005.
- [50] J. Bruno, I. Casas, B. Lagerman, M. Munoz, The determination of the solubility of amorphous UO₂ and the mononuclear hydrolysis constants of uranium(IV) at 25°C, *MRS Proc.* 84 (1986) 153. Available from: <https://doi.org/10.1557/PROC-84-153>.
- [51] V. Neck, J.I. Kim, Solubility and hydrolysis of tetravalent actinides, *Radiochim. Acta* 89 (1) (2009) 1–16.
- [52] J. Bruno, E. Cera, L. Duro, T.E. Eriksen, L.O. Werme, A kinetic model for the stability of the spent fuel matrix under oxic conditions, *J. Nucl. Mater.* 238 (1996) 110–120.
- [53] M. Amme, T. Wiss, H. Thiele, P. Boulet, H. Lang, Uranium secondary phase formation during anoxic hydrothermal leaching processes of UO₂ nuclear fuel, *J. Nucl. Mater.* 341 (2005) 209–223.
- [54] L. Duro, M. Grivé, J. Bruno, Potential long-term conversion mechanisms of spent fuel after repository closure, in: 13th International High-Level Radioactive Waste Management Conference 2011, IHLRWMC 2011, vol. 2, Las Vegas, NV, 2011, pp. 702–709.
- [55] S. Szenknect, A. Mesbah, T. Cordara, N. Clavier, H.P. Brau, X. Le Goff, et al., First experimental determination of the solubility constant of coffinite, *Geochimica et Cosmochimica Acta* 181 (2016) 36–53.
- [56] Svensk Kärnbränslehantering AB (SKB), Long-term safety for the final repository for spent nuclear fuel at Forsmark, in: Main Report of the SR-Site Project, Stockholm, Sweden, 2011, Updated 2015-05.
- [57] W.E. Schortmann, M.A. DeSesa, Kinetics of the dissolution of uranium dioxide in carbonate-bicarbonate solutions, in: Proceedings of the Second International Conference on the Peaceful Uses of Atomic Energy, vol. 3, United Nations, Geneva, Switzerland, 1958.
- [58] F. Clarens, E. Gonzales-Robles, F.J. Gimenez, I. Casas, J. de Pablo, D. Serrano, et al., Effect of Burn-Up and High Burnup Structure on Spent Nuclear Fuel Alteration, Enresa, Madrid (Spain), 2009. Enresa Report 04/2009.
- [59] J. de Pablo, I. Casas, J. Giménez, M. Molera, M. Rovira, L. Duro, et al., The oxidative dissolution mechanism of uranium dioxide. I. The effect of temperature in hydrogen carbonate medium, *Geochim. Cosmochim. Acta* 63 (1999) 3097–3103.
- [60] J. de Pablo, I. Casas, J. Giménez, F. Clarens, L. Duro, J. Bruno, The oxidative dissolution mechanism of uranium dioxide. The effect of pH and oxygen, *MRS Proc.* 807 (2004) 83–88.
- [61] A. Martinez Esparza, M.A. Cunado, J.A. Gago, J. Quinones, E. Iglesias, J. Cobos, et al., Development of a Matrix Alteration Model (MAM) (ENRESA-Empresa Nacional de Residuos SA-01/05), Spain, 2005.

- [62] L. Wu, Y. Beauregard, Z. Qin, S. Rohani, D.W. Shoesmith, A model for the influence of steel corrosion products on nuclear fuel corrosion under permanent disposal conditions, *Corros. Sci.* 61 (2012) 83–91.
- [63] L. Wu, N. Liu, Z. Qin, D.W. Shoesmith, Modeling the radiolytic corrosion of fractured nuclear fuel under permanent disposal conditions, *J. Electrochem. Soc.* 161 (8) (2014) 3259–3266.
- [64] H. He, M. Broczkowski, K. O’Neil, J. Ofori, O. Semenikhin, D. Shoesmith, Corrosion of nuclear fuel (UO_2) inside a failed nuclear waste container. A review of research conducted under the Industrial Research Chair Agreement between NSERC, NWMO and Western University (January 2006 to December 2010), in: NWMO TR-2012-09, 2012.
- [65] J.L. Jerdon Jr., K. Frey, W. Ebert, A multiphase interfacial model for the dissolution of spent nuclear fuel, *J. Nucl. Mater.* 462 (2015) 135–146.
- [66] E. Ekeroth, Radiation Induced Oxidative Dissolution of UO_2 (Doctoral thesis), KTH Royal Institute of Technology, Stockholm, Sweden, Trita-KKE-Report, 0349-6465, 2006.
- [67] A. Barreiro Fidalgo, Experimental Studies of Radiation-Induced Dissolution of UO_2 : The Effect of Intrinsic Solid Phase Properties and External Factors (Doctoral thesis), KTH Royal Institute of Technology, Stockholm, Sweden, TRITA-CHE-Report, 2017, p. 23.
- [68] S. Nilsson, Radiation Induced Dissolution of Model Compounds for Spent Nuclear Fuel: Mechanistic Understanding of Oxidative Dissolution and Its Inhibition (Doctoral thesis), KTH Royal Institute of Technology, Stockholm, Sweden, Trita-CHE-Report, 2012, p. 30.
- [69] O. Roth, Redox Chemistry in Radiation Induced Dissolution of Spent NuclearFuel: From Elementary Reactions to Predictive Modeling (Doctoral thesis), KTH Royal Institute of Technology, Stockholm, Sweden, Trita-CHE-Report, 2008, p. 60.
- [70] M. Trummer, The Effect of Solid State Inclusions on the Reactivity of UO_2 : A Kinetic and Mechanistic Study (Doctoral thesis), KTH Royal Institute of Technology, Stockholm, Sweden Trita-CHE-Report, 2011, p. 32.
- [71] C. Poinssot, S. Gin, Long-term behavior science: the cornerstone approach for reliably assessing the long-term performance of nuclear waste, *J. Nucl. Mater.* 420 (2012) 182–192.
- [72] A. Sneijers, Understanding and physical and numerical modelling of the key processes in the near field and their coupling for different host rocks and repository strategies (NF-PRO), in: Final Report Contract FI6W-CT2003-002389. EUR23730, 2008. <https://cordis.europa.eu/docs/publications/1039/103938551-6_en.pdf>.
- [73] B. Grambow, J. Bruno, L. Duro, J. Merino, A. Tamayo, C. Martin, et al., Final Report of the Project MICADO: Model Uncertainty for the Mechanism of Dissolution of Spent Fuel in Nuclear Waste Repository, European Commission, Brussels, Belgium, 2005.
- [74] L. Johnson, C. Poinssot, C. Ferry, P. Lovera, Estimates of the instant release fraction for UO_2 and MOX fuel at $t = 0$, A Report of the Spent Fuel Stability (SFS) Project of the 5th Euratom Framework Program, NAGRA, Wettingen, Switzerland, 2004. NAGRA Technical Report 04-08.
- [75] L.Z. Evins, A. Valls, L. Duro, First Annual Meeting Proceedings Deliverable D1.10. DisCo Project, EC-Grant Agreement: 755443, 2018, <<https://disco-h2020.eu/>>.

Further reading

H. Kleykamp, The chemical state of fission products in oxide fuels at different stages of the nuclear fuel cycle, *Nucl. Technol.* 80 (1988) 412–422.

This page intentionally left blank

Advances in fuel chemistry during a severe accident

14

Update after Fukushima Daiichi Nuclear Power Station (FDNPS) accident

M. Kurata¹, M. Osaka¹, D. Jacquemain², M. Barrachin² and T. Haste²

¹Japan Atomic Energy Agency (JAEA), Tokai, Japan, ²Institute for Radiological Protection and Nuclear Safety (IRSN), PSN-RES/SAG, B.P. 3, St. Paul Lez Durance, France

14.1 Introduction

Comprehensive reviews on severe accident (SA) phenomenology have been published from time to time. The most recent and important one is “Bal Raj Sehgal, Nuclear Safety in Light Water Reactors: Severe Accident Phenomenology, SARNET, 2012 [1].” The current review attempts to focus on the chemistry under SA conditions, updated after the Fukushima Daiichi Nuclear Power Station (FDNPS) accident. Fuel/core degradation generally progresses during a rather short period in the entire SA sequence. The outlined features on the fuel/core degradation in the prototypic SA scenarios are mostly identified from the analysis of the fuel debris and from the various integral and separate-effect simulated-test results. However, the detailed reaction mechanisms are very complicated due to the overlap of many thermophysical and thermochemical processes. Hence, for prototypic SA scenarios, an understanding of the materials science involved was not given high priority. Consequently, various separate-effect models implemented in SA analysis codes are mainly developed by simplifications of prototypic conditions [typically using the Three Mile Island-2 (TMI-2) accident], because it is important to comprehensively model SA progression in a reasonable computation time frame.

On the other hand the importance of phenomenology of the fuel/core degradation based on the materials science knowledge was demonstrated by the FDNPS accident [2]. The inspections inside the primary containment vessel (PCV) for unit-2 and unit-3 of FDNPS showed large differences in the accident progression, in particular, regarding the lower head failure and the fuel debris accumulation in the pedestal region. In a real SA, operators will attempt to prevent or mitigate the accident progression by all means possible. These efforts might occasionally cause non-prototypic scenarios. In the accident sequence of unit-2 of FDNPS, for example, the operators tried to decrease the pressure of the reactor pressure vessel (RPV) by opening safety release valves (the objective was to facilitate water injection by fire engines). This caused a sudden decrease in the coolant level below the core plate

and in the fuel temperature because of the latent heat of coolant evaporation. Unfortunately, the flowing water injection by the fire engines did not fully succeed. This could have caused fuel/core degradation in a nonprototypic steam-starved condition and consequently influenced the accident progression of unit-2. To understand potential deviations from fuel/core degradation under temporary or extreme conditions compared to prototypic conditions, one should start from the materials science reaction chemistry. Minor chemical mechanisms that are neglected in the current simplified models might become important under nonprototypic scenarios.

Along with the light water reactor (LWR) accident progression accompanied by a temperature increase, fission products (FPs) in the fuel rods are released and transported with the coolant flow toward the outside of the reactor from the RPV via the reactor coolant system (RCS) to the reactor building (R/B) and then finally released to the environment. In order to accurately predict the source term of an LWR accident, knowledge of the release and transport behavior of FPs is required. FPs experience large temperature changes during transport from that the molten fuel (i.e., around 2000 K or higher down to the R/B region, i.e., below 400 K). This induces condensation of most FPs vapor species to form FP aerosols, except for several highly volatile vapor species of I and Ru.

Chemical reactions of FP vapor species in relatively high-temperature regions (e.g., RPV and RCS) with other FP vapor species and/or the various structural materials, such as steels and absorber materials, should be taken into account for the evaluation of the FP transport. In addition, the deposition of FPs onto concrete, metallic, and painted surfaces, together with aqueous chemistry effects, should be considered in the R/B in the lower temperature region (i.e., below 400 K). In regards to the transport of the two types of FPs formed: vapor species and aerosols, these can be calculated based on the thermal hydraulics of the reactor; however, the fractions of these vapor species, aerosols, and deposits can only be estimated. In this context, FP chemistry is of crucial importance (e.g., condensation conditions for aerosol formation, chemical reactions of the vapor species and aerosols with each other, and the reactions of these with various materials including fuel, structural materials, corium, and absorber materials). As the FP chemistry is fundamental to all aspects of their behavior, it has been intensively studied in the last few decades, and many results have been obtained so far.

FP chemistry became particularly important after the FDNPS accident. A range of chemical conditions needed to be considered for the three FNDPS units, which all experienced different SA progressions, such as possible steam starvation in unit-2. Moreover, other chemical issues emerged for the FDNPS investigations, such as chemical effects due to boron caused mainly by the boiling water reactor (BWR) configuration, FP release, and transport behavior in the aqueous phase that is formed by the debris cooling system, and so on.

In this chapter the recently updated knowledge on the reactor chemistry is discussed. In [Section 14.2](#), the chemistry of fuel/core degradation in-vessel and ex-vessel is discussed by M. Kurata [Japan Atomic Energy Agency (JAEA)], and M. Barrachin and T. Haste (IRSN). In [Section 14.3](#), the chemistry of FP behavior is discussed by M. Osaka (JAEA) and D. Jacquemain (IRSN).

14.2 Chemistry on fuel/core degradation

In general, fuel/core degradation is separately discussed in two regions: in-vessel and ex-vessel, according to the progression of SA and its influence on the environment. In-vessel progression is usually divided into the following three phases:

- early phase (fuel assembly degradation);
- transient phase (significant fuel relocation);
- late phase (corium pool formation and stratification, etc. before RPV failure).

The chemistry of both separate-effect interactions and integral phenomena need to be improved, corresponding to these phases.

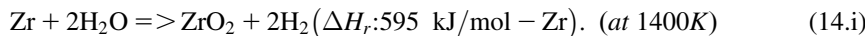
14.2.1 Chemistry in early phase fuel degradation

Fig. 14.1 indicates the major separate-effect interactions as a function of increasing temperature, which are related to the early phase fuel degradation under in-vessel conditions [3]. Although many separate interactions have to be taken into consideration, the focus will be on the chemistry of the following interactions:

- oxidation and hydrogen uptake of Zr-alloy (Zry) cladding;
- liquefaction between UO₂ fuel and Zry cladding;
- liquefaction of absorbers, control rod materials [pressurized water reactor (PWR)] and control blade materials (BWR), and subsequent interaction of liquefied absorber melts with Zry.

14.2.1.1 Oxidation and hydrogen uptake of Zry cladding

The reaction chemistry between Zry cladding and steam is of particular importance under accident conditions in LWRs, which not only includes SAs but also design basis accidents, such as loss of coolant accidents (LOCA).¹



The reaction is highly exothermic and the reaction rate gradually increases with increasing temperature. When the temperature reaches approximately 1473 K, significant interaction between the Zry and steam occurs, identified as a *reaction escalation* or *oxidation runaway* [4], and then it steeply accelerates the increase in temperature during SA conditions. The oxidation reaction of the Zry under steam atmospheres has been comprehensively studied and the reaction rate can be described by a parabolic expression, such as given in Fig. 14.2 [5]:

¹ Loss of Coolant Accident: a typical accident sequence for LWR. Loss of cooling water and depressurization of RPV are caused by a failure of cooling circuit, inadequate opening of valves or other reasons. The cooling capability of fuel decreases, and fuel is exposed under steam. This causes a steep oxidation of Zry and increase in fuel temperature. TMI-2 and Fukushima Daiichi accidents are typical cases of LOCA.

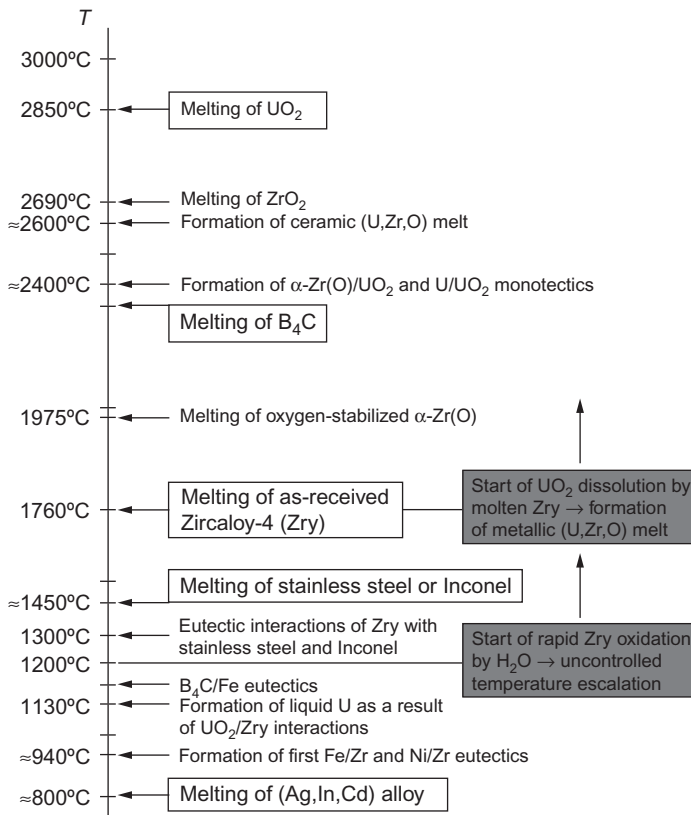


Figure 14.1 Important material reactions/interactions of core materials with increasing temperature.

Source: Quoted from B. Lewis, et al., J. Nucl. Mater. 380 (2008) 126–143.

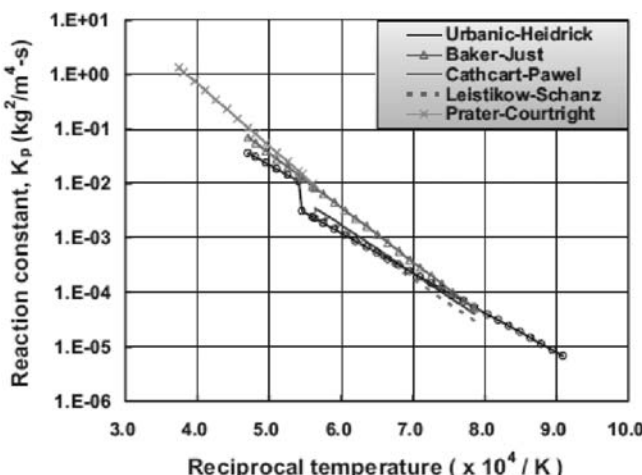


Figure 14.2 Oxidation reaction constant (K_p) of Zr-based alloy with temperature.

Source: Quoted from H.T. Kim, et al., J. Nucl. Sci. Technol. 44 (2007) 1385–1394.

$$\omega^2 = K_p t, \quad (14.1)$$

where ω is the mass of oxidized Zry per unit area (kg/m^2), K_p is the reaction rate constant ($\text{kg}^2/\text{m}^4/\text{s}$), and t is the reaction time (s).

The reaction rate constant can be expressed by an Arrhenius-type equation:

$$K_p = A \exp\left(-\frac{E}{RT}\right), \quad (14.2)$$

where A is the reaction constant ($\text{kg}^2/\text{m}^4/\text{s}$), E is the activation energy (J/mol), R is the gas constant (8.31 J/mol/K), and T is the temperature (K).

During normal operating conditions, a ZrO_2 layer of 20–30 μm thickness has already been formed on the Zry surface [3]. One can take this value into account for the initial oxidation condition. At the same time a small amount of hydrogen from the cladding oxidation has been accumulated in the bulk alloy (typically to a 100–200 ppm level in BWRs [6]). However, the stable, protective ZrO_2 surface layer has slowly grown under prototypic steady-state conditions, and it acts as a barrier against the hydrogen diffusion and uptake into the bulk alloy during a transient event, as long as the oxide layer remains intact. Accumulated hydrogen of 100–200 ppm is considered to be maintained in the bulk metal until the complete oxidation of the Zry [6].

On the other hand, a steam-starved atmosphere² is an important nonprototypic condition, which was potentially experienced in the accident progression of unit-2 of FDNPS. In the steam-starved atmosphere the mass increase of Zry cladding does not obey the parabolic law, which is shown in Fig. 14.2, due to the low content of steam in the atmosphere. This may limit oxidation and enhance hydrogen uptake by Zry cladding compared with more steam-rich atmospheres.

Under steam-starved conditions, oxygen diffuses from the surface ZrO_2 layer to the bulk alloy up the temperature gradient and then the bulk Zr metal transforms from bcc(β) to hcp(α) due to the stabilization of the α -phase by oxygen dissolution. There is a significant decrease in the hydrogen saturation concentration in the Zry as a function of oxygen content in the Zry. Fig. 14.3 shows the $\text{Zr}-\text{H}-\text{O}$ ternary phase diagram at 973 K [8,9], in which the influence of oxygen content on the hydrogen solubility is clearly observed. This phenomenon causes a local enrichment of hydrogen in pores and cracks near the metal–oxide interface in the steam-starved conditions, suggesting high values of hydrogen absorption by the remaining metal [10].

Then, the hydrogen uptake in the bulk alloy can occur in accordance with Sieverts' law. As indicated in Fig. 14.4, the hydrogen uptake in the Zry follows Sieverts' law and it means that this uptake is dominated by the partial pressure of

²Low flow rate of vaporized coolant into a core region potentially causes steam-starved atmosphere in the higher regions of the core, because almost all steam reacts with Zry in the lower regions and converted to hydrogen. In unit-2 of FDNPS a sudden decrease in the coolant level is considered to occur during the accident sequence, and its might cause a significant steam-starved condition [7].

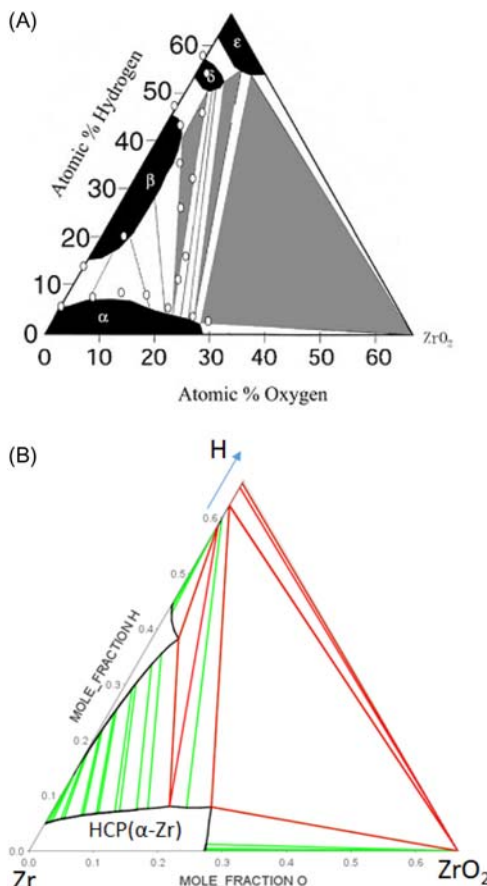


Figure 14.3 Zr–H–O ternary phase diagram at 973 K (A) experimental diagram and (B) calculated diagram using TAF-ID database.

Source: Quoted from (A) D. Setoyama, S. Yamanaka, J. Alloys Compd. 370 (2004) 144–148 and (B) TAF-ID database. <<http://www.oecd-nea.org/science/taf-id/>>.

hydrogen in the steam–hydrogen mixture atmosphere. Up to several thousand ppm of hydrogen can be accumulated in the Zry under steam-starved conditions [11]. This value is approximately an order of magnitude larger than the value accumulated in normal operation. It leads to a significant absorption of hydrogen in the bulk alloy in the steam-starved conditions and results in an exothermic reaction with a considerable increase in temperature of the bulk alloy.

It is well known that hydrogen solubility in Zr follows Sieverts' law [12]:

$$\left(\frac{H}{Zr}\right)_{at} = K_s \sqrt{pH_2}, \quad (14.3)$$

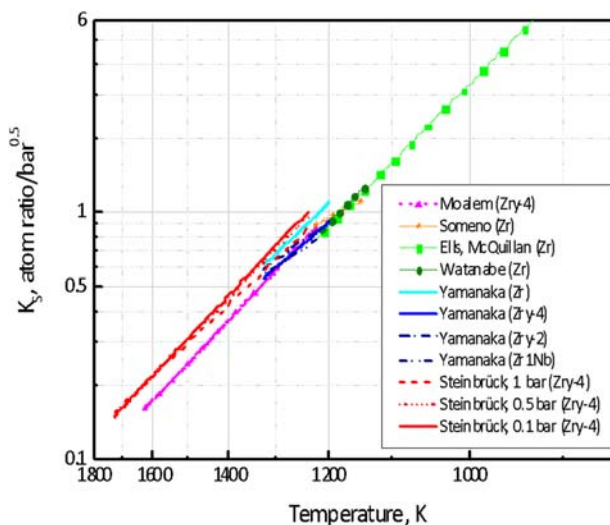


Figure 14.4 Sieverts' constant of hydrogen solubility in Zry.

Source: Quoted from M. Steinbrueck, Ann. Nucl. Energ. 64 (2014) 43–49.

where $(H/Zr)_{at}$ is the atom ratio of hydrogen to Zr, K_s is the Sieverts' constant ($\text{bar}^{-0.5}$), and pH_2 is the hydrogen partial pressure (bar).

The temperature dependence of Sieverts' constant is described by an Arrhenius-type equation:

$$K_s = \exp\left(\frac{\Delta_s S}{R} - \frac{\Delta_s H}{RT}\right), \quad (14.4)$$

where $\Delta_s S$ is the entropy of hydrogen solution (J/K/mol), and $\Delta_s H$ is the enthalpy of hydrogen solution (J/mol).

The Sieverts' law is verified by experimental studies up to at least an atomic ratio of $H/Zr = 0.7$, up to temperatures of 1730 K, and up to 100 kPa of hydrogen partial pressure [12].

A sim-test on the relation between the thickness of the surface ZrO_2 and the amount of hydrogen uptake was recently performed by the JAEA, using a sim-BWR fuel bundle sample (4 rod + 1 canister, 630 mm in height) [11]. Fig. 14.5 indicates the appearance and the cross section of the sample. The sample was quickly heated up to 1573 K and maintained for 10 minutes in a steam flow (less than 3.3 g/min with ~10% of Ar carrier gas) from the lower part. This test condition generated a typical steam-starved atmosphere in the canister (see Yamazaki et al. [11], for details). Fig. 14.6 shows the results. Currently, there is no data on the thickness of ZrO_2 in the lower position (less than 140 mm). However, formation of the thicker oxide layer was identified by visual observation. The amount of hydrogen uptake increases along with the steam flow, in which hydrogen partial pressure is gradually increasing. The value at the highest position is approximately comparable to the equilibrium value calculated by Sieverts' law.

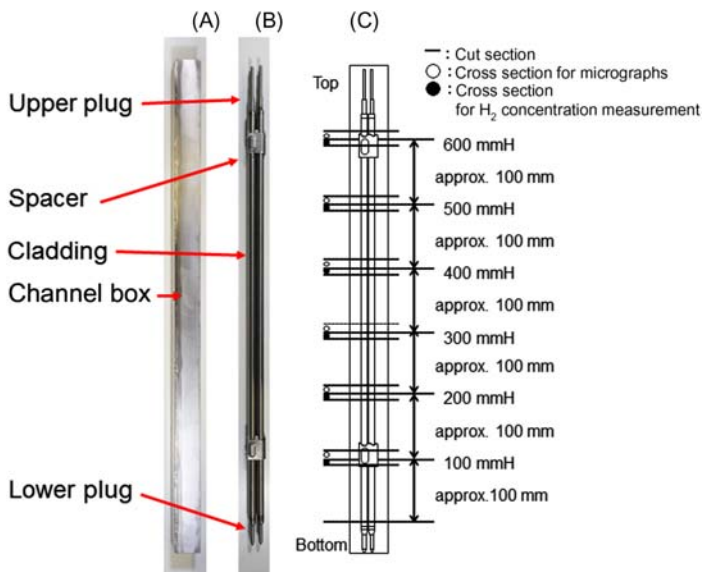


Figure 14.5 Appearance and cross section of the piece for sim-bundle oxidation test, (A) Zry canister, (B) Zry fuel bundle (containing Al₂O₃ sim pellets), and (C) schematic drawing of cutting section.

Source: Quoted from S. Yamazaki, et al., Proceedings of TOPFUEL2018, Prague, Czech, September 30–October 4, 2018.

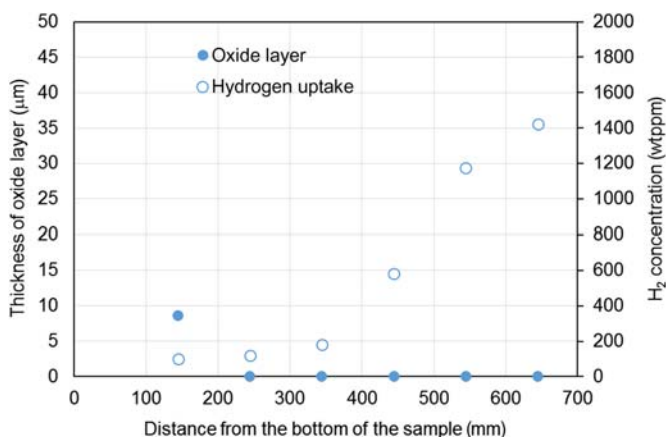


Figure 14.6 Vertical variation in oxide layer thickness and hydrogen uptake under steam-starved condition.

Source: Quoted from S. Yamazaki, et al., Proceedings of TOPFUEL2018, Prague, Czech, September 30–October 4, 2018.

These mechanisms for hydrogen absorption under steam-starved conditions will influence the tendency for hydrogen generation and its timing under accident conditions. The accumulated hydrogen can later be gradually released from the Zry at higher temperatures according to the temperature dependence of the Sieverts' constant resulting in reducing hydrogen solubility with increasing temperature. Typical LOCA conditions resulting in ballooning and burst of the Zry cladding can occur at approximately 1073 K in the hottest region of the fuel element [6,13]. Then, steam has access to the inside of the cladding and can cause oxidation of the inside surface. The hydrogen produced is easily absorbed by the near nonoxidized inner alloy surface leading to comparably high hydrogen concentrations above and below the burst position due to the local steam starvation. This effect is called secondary hydriding [14].

14.2.1.2 Liquefaction between UO_2 fuel and Zry cladding

The liquefaction phenomenon between UO_2 fuel and Zry alloy cladding is generally treated by SA experts using a pseudo-binary phase diagram between UO_2 and $\alpha\text{-Zr}$ [30 at.%O content, $\text{Zr}:O = 0.7:0.3$ as a molar ratio—hereafter, the latter phase is described as $\alpha\text{-Zr(O)}$], as shown in Fig. 14.7A [15]. This phase diagram was useful in a practical sense to develop a simplified fuel liquefaction model for SA analysis codes (the so-called eutectic interaction model). In the original *eutectic interaction model*, liquefaction and subsequent relocation are simply modeled to start at around 2173 K, which corresponds to the eutectic temperature in Fig. 14.7A. However, this particular liquefaction temperature was determined to be too low when validating the SA analysis codes using integral sim-test results where large degradation were observed [16]. Hence, an approximately 300 K higher value is currently being used as the liquefaction temperature implemented in the SA analysis codes (for the sake of convenience) to fit calculated results with the experimental observation of various integral tests. The underlining phenomena is unfortunately not well understood.

Kurata et al. [2] pointed out that Fig. 14.7A is not drawn using the proper ternary phase rule and then compared it to the thermodynamically correct phase diagram, as given in Fig. 14.7B. The phase boundaries in these two diagrams are significantly different, due to the reason that Fig. 14.7A is drawn using the phase rule for a binary system, although this system is essentially ternary among U, Zr, and O.³ In these diagrams, nevertheless, the fully liquid region (thick blue area) roughly exists

³In general, a phase diagram of oxide–oxide system can be “approximately” drawn based on binary phase rule, for example, $\text{UO}_2\text{--ZrO}_2$. However, the oxide–oxide system is essentially ternary and $\text{UO}_2\text{--ZrO}_2$ is a “pseudo-binary” cross section of the ternary system. Strictly put, one has to draw the “pseudo-binary” cross section based on ternary phase rule. A deviation from stoichiometry has to be taken into consideration. When one attempts to draw $\text{UO}_2\text{--ZrO}_2$ phase diagram using binary and ternary phase rules, respectively, an apparent difference will appear at around congruent melting point of $(\text{U},\text{Zr})\text{O}_2$ phase. In case strictly between $\text{UO}_{2.0}$ and $\text{ZrO}_{2.0}$, there is no congruent melting point in ternary phase rule's diagram (a small interval between solidus and liquidus will appear). These differences are generally negligible for oxide–oxide system, but one should not neglect in some metal–oxide systems, in which the metal has a certain solubility of oxygen. $\text{Zr(O)}\text{--UO}_2$ system is a typical case. As for the equilibrium state (shown as the phase diagram), one has to refer ternary phase rule, in which a small amount of liquid widely coexists with solid.

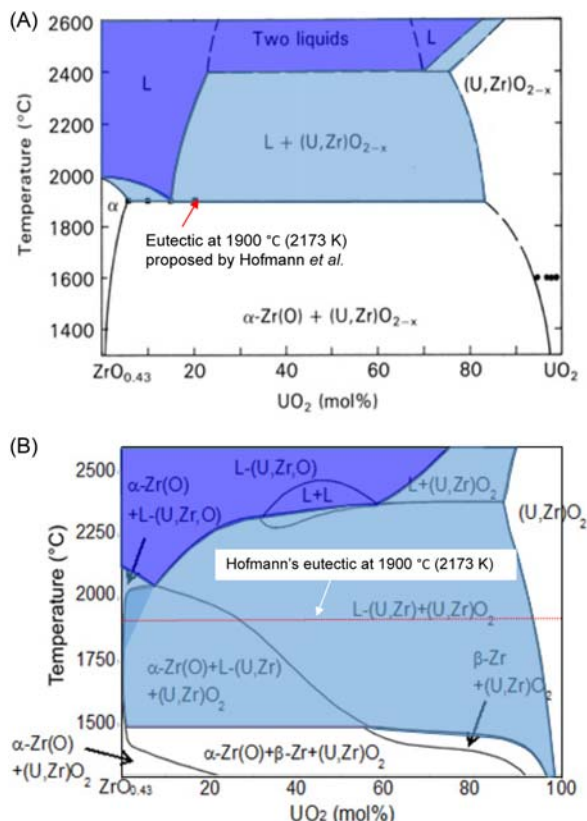


Figure 14.7 (A) Quasibinary phase diagram between $\alpha\text{-Zr(O)}$ and UO_2 proposed by Hofmann et al. Thick blue and light blue corresponds to fully liquid and solid–liquid mixture regions, respectively.⁴ (B) Quasibinary phase diagram between $\alpha\text{-Zr(O)}$ and UO_2 calculated using TAF-ID database. Thick blue and light blue corresponds to fully liquid and solid–liquid mixture regions, respectively. The red line corresponds to the hypothetical eutectic temperature.⁵

Source: Quoted from (A) P. Hofmann, D. Kerwin-Peck, J. Nucl. Mater. 124 (1984) 80–105 and (B) M. Kurata, et al., J. Nucl. Mater. 500 (2018) 119–140, color is added by a current author.

in the similar temperature and composition region and this might be the reason why Fig. 14.7A was practically useful for developing the simplified fuel liquefaction models.

⁴ Experimental data points are plotted as eutectic. However, in their separate-effect tests, they observed U-Zr metal liquid in lower temperatures. This suggests that these experimental data are not directly related to equilibrium interaction. 2173 K is considered to be a temperature above which liquefaction steeply progresses.

⁵ According to careful observation of this calculated phase diagram, approximately 2343 K is identified as a fully liquefaction temperature in Zr-rich region. Presumably, between 2173 K and 2343 K, liquefaction steeply progresses with increasing temperature.

On the other hand the following features are observed in Fig. 14.7B:

- the liquid–solid mixture region spreads widely to lower temperature regions;
- the “fully liquefied” temperature at around the hypothetical eutectic point is certainly higher than 2173 K.

The former observation is related to the detailed mechanism of liquefaction. Fig. 14.7A could hypothetically propose the following liquefaction mechanism. When the temperature reaches 2173 K, the Zry cladding is fully liquefied at this particular temperature by reacting with a certain amount of UO₂ and then a part of UO₂ remains as solid, according to the eutectic interaction between UO₂ and α -Zr(O). This eutectic interaction (if it happens in reality) is endothermic and a certain amount of latent heat is necessary for the completion of the eutectic reaction at 2173 K. Although this must influence the variation in temperature in accident progression, there are no experimental observations on the thermal arrest at 2173 K in various sim-tests.

On the other hand, Fig. 14.7B describes that liquefaction starts below 1573K, and a small amount of U-rich liquid is initially formed around the interface. The mechanism is identified to be a combination of reduction of UO₂ by Zr and following liquefaction of U–Zr alloy. The amount of liquid gradually increases with increasing temperature and simultaneously Zr and O gradually dissolve in the liquid (hence, the Zr and O compositions in the U–Zr–O liquid gradually increase). Although the total interaction is certainly endothermic, this mechanism does not need to show any clear thermal arrests due to the gradual liquefaction progression.

In fact, Hofmann et al. noted that the existence of the U–Zr metallic phase [which was estimated from its U-rich composition (85 wt.%U) to have a low melting point of \sim 1400 K] in the interaction layers between Zircaloy-4 cladding and UO₂ fuel, in a thin two-phase layer of α -Zr(O) with U–Zr metallic phase between the outer and inner α -Zr(O) layers adjacent to the UO₂ fuel [15,17,18]. However, in formulation of their pseudo-binary UO₂–Zr(O) phase diagram, these were not taken into account, probably because of their low volume.⁶

Many explanations can be invoked to explain the difference between Hofmann’s *hypothetical eutectic temperature* (2173 K) and *the value required in the integral SA codes* (\sim 2473 K). The detailed interaction mechanism between UO₂ and Zr is being studied at JAEA [19]. Fig. 14.8 indicates the cut surface of the sample, in which a cylindrical Zr rod was set in a UO₂ crucible and heated to 2173 K for 10 minutes in an Ar atmosphere. The Zry rod deforms to a round shape after heating. However, the energy-dispersed X-ray (EDX) analysis showed that the amount of liquid phase in the deformed Zr was very small (less than a few vol.%).

Fig. 14.9 summarizes the backscattered electron (BSE) image and the U and Zr maps on the cut surface after polishing. Two phases were clearly detected in the sample: U–Zr–O (liquid during heating) and α -Zr(O) (solid during heating). Even

⁶One has to take the accurate meaning of “eutectic” into consideration. According to materials science theory, eutectic temperature corresponds to solidus and hence no liquid can exist below eutectic temperature. Strictly put, Fig. 15.7A is not an “equilibrium” phase diagram but a so-called experimental phase diagram. It is suggested that previous experimental data regarding “eutectic” are not directly obtained from the eutectic interaction but the other steep phase transition.

around the original interface between UO_2 and Zr, the volume of the liquid is very small. These observations suggest that the previous sim-tests on the UO_2 and Zr interaction might detect a significant solid-phase deformation instead of liquefaction at around 2173 K. Also, a small amount of U was detected even in the top region of the deformed Zr. Provided that the phase relation in the sample locally attained the quasiequilibrium state due to sufficient U diffusion, the liquefaction mechanism can be properly outlined by a thermodynamic approach, based on U-Zr-O ternary phase diagrams. On the other hand, no apparent diffusion of Zr into the UO_2 crucible was observed. Fig. 14.10 indicates the recently updated U-Zr-O ternary phase diagram at 2393 K [9]. Even at 2393 K, which is 220 K higher than the hypothetical eutectic temperature, a certain amount of $\alpha\text{-Zr(O)}$ still remains in a part of the phase diagram. The liquefaction of the Zr region is thus evaluated to be complete at approximately 2400 K according to this thermodynamic approach. This value is certainly close to the *magic value*, but it is based on a more fundamental understanding of the material behavior. The relative stability among liquid, $\alpha\text{-Zr(O)}$, and UO_2 phases is important to evaluate the variation in liquefaction temperature as a function of composition. The details were discussed by Kurata et al. [2] using a Gibbs energy surface diagram.

The thermodynamic approach may suggest a more accurate approach to the liquefaction mechanism between UO_2 fuel and Zry cladding, instead of the *eutectic liquefaction model*. Fig. 14.11 illustrates a schematic image of the phase transition at around the interface between UO_2 and Zry. The following simplification might be proposed by assuming that liquid-contained layers are locally in a quasiequilibrium state. The interaction might be negligible even under LOCA conditions (typically at 1473 K) as well as under normal operation. Liquid formation is mostly negligible at relatively lower transient temperatures (typically 1773 K), due to

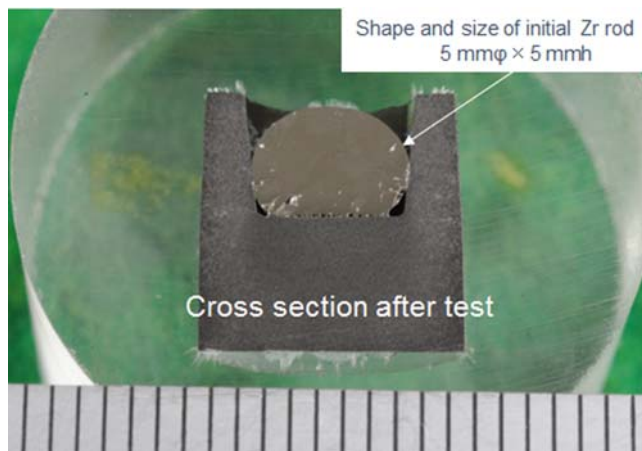


Figure 14.8 Cutting surface of the sample for $\text{UO}_2\text{-Zr}$ interaction test. (Heated at $2173 \text{ K} \pm 10 \text{ K}$ for 10 min in an Ar atmosphere.)

Source: Quoted from N. Shirasu, et al., Proceedings of FDR2019, International Topical Workshop on Fukushima Decommissioning Research, J-Village, Naraha, Fukushima, Japan, May 24–26, 2019, Paper No. 1067.

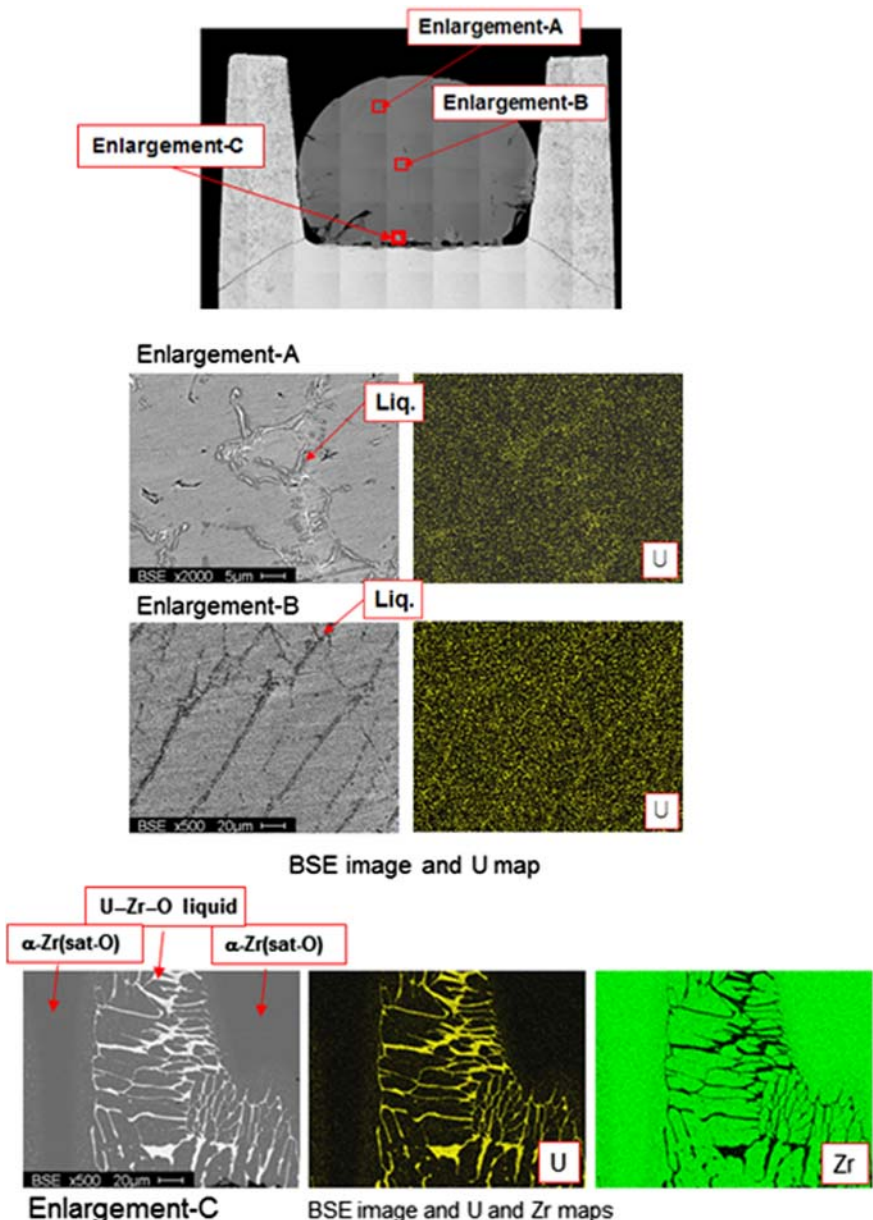


Figure 14.9 BSE image, U and Zr maps of cutting surface. (Heated at $2173\text{ K} \pm 10\text{ K}$ for 10 min in an Ar atmosphere.) BSE, Backscattered electron.

Source: Quoted from N. Shirasu, et al., Proceedings of FDR2019, International Topical Workshop on Fukushima Decommissioning Research, J-Village, Naraha, Fukushima, Japan, May 24–26, 2019, Paper No. 1067.

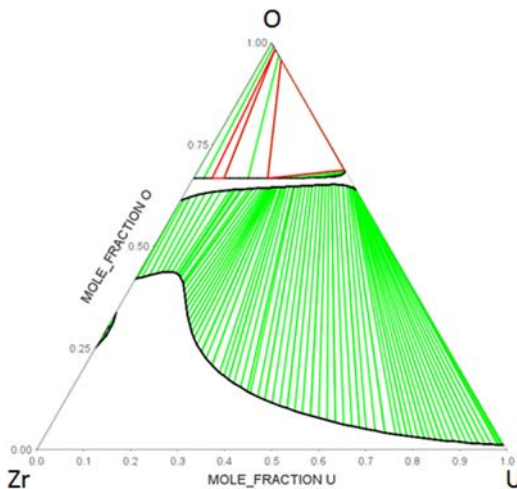


Figure 14.10 U–Zr–O ternary phase diagram at 2393 K (calculated using TAF-ID database [9]).

insufficient U diffusion to the Zr side, as shown in Fig. 14.11B. Here, the local equilibrium is only achieved in bulk UO_2 and in a very thin liquid-contained layer. Thus only the simplified model of the gradual one way oxygen diffusion in α - and β -Zr phases is necessary at lower temperatures (although of course experimental data on the O diffusion need to be obtained for validation).

When the temperature reaches the hypothetical eutectic temperature (i.e., 2173 K), U diffusion is accelerated and U diffuses into the entire region of Zry-bulk. This results in the formation of a small amount of liquid in the entire region of Zry-bulk. According to the recent JAEA data [2], a thin line shape liquid phase was observed in the Zry-bulk. The formation mechanism is still under discussion. Thus each layer is evaluated to locally attain its quasiequilibrium state. To validate the model, one needs to define a threshold temperature between Fig. 14.11B and C. Then, at around 2400 K, the Zry-bulk metal region is completely liquefied, as shown in Fig. 14.11D. On the other hand under steam-rich outer atmospheres, the outer surface of the Zry is oxidized with increasing temperature and the thickness is evaluated by using Fig. 14.2. This results in a situation like Fig. 14.11E, in which U–Zr–O liquid is sandwiched between the remaining UO_2 and the outer ZrO_2 . Here, one can simply evaluate the amount of remaining UO_2 , outer ZrO_2 , and U–Zr–O as well as the composition of U–Zr–O by a thermodynamic approach. Provided that the liquid-contained phase quickly achieves its quasiequilibrium state, the composition of U–Zr–O liquid might rapidly change up to the solubility limits of U and O in liquid Zr. Then, we can estimate the initial condition of the relocated U–Zr–O liquid by taking the temperature and oxygen potential hysteresis into consideration. The details of the reaction kinetics using this simplification are discussed by Kurata et al. [2].

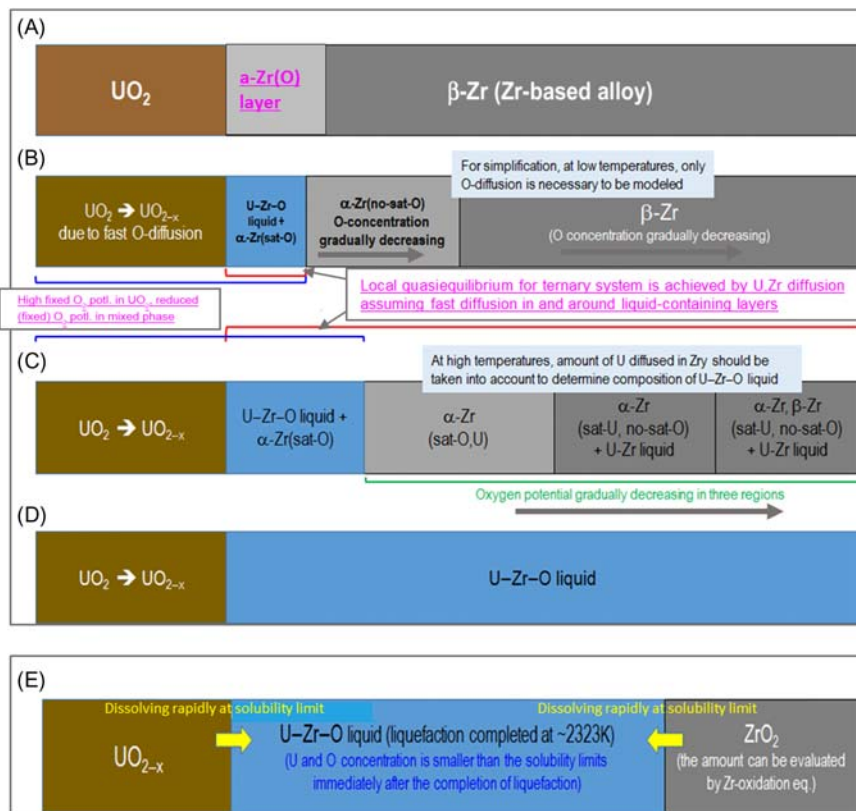


Figure 14.11 Schematic image of liquefaction progression at the interface between UO_2 fuel and Zry cladding: (A) in normal operation temperature (typically 623 K); (B) at lower temperature in transient (typically 1773 K); (C) at hypothetical eutectic temperature (2173 K); (D) complete liquefaction of Zr-bulk (2400 K); and (E) sandwich structure after complete liquefaction of Zr-bulk alloy.

14.2.1.3 Liquefaction of control rod/blade and following interaction with Zry

The main factor influencing the degradation of control rods or blades is the occurrence of eutectic interactions among their components. The basic phenomena are well established (see, e.g., [3,20–22]) and may be summarized in the following two categories: (1) for those with silver–indium–cadmium (AIC) and (2) those for boron carbide (B_4C) as absorber materials, respectively.

Silver–indium–cadmium control rod

The AIC absorber material melts at about 1073 K and initially remains within its stainless steel (SS) cladding tube without reaction with the steel because the system is thermodynamically stable.

Due to the eccentric location of the absorber rod within its Zircaloy-4 guide tube or due to ballooning of the SS cladding under internal gas pressure (particularly Cd vapor), firm contact can be established between the Zircaloy and the SS components and different eutectic melts can be formed between 1473 K and 1673 K, that is, below the melting point of the SS cladding. At this point the AIC melt can be released, relocating downward as the metallic melt pool largely involving Ag–In and steel components. In parallel, much of the Cd can be released to the coolant stream in vapor form [23], although a small amount can flow down with the melt. These behaviors were seen for example in CORA-13 [24] where the solidified melt at the bottom of the bundle contained about 40 wt.%Ag, about 7 wt.%In, and about 2 wt.%Cd.

The relocation takes place in the gap between the control rod cladding and the guide tube and downward along the outside of the guide tube and radially onto neighboring fuel rods. These melts can attack the cladding of neighboring fuel rods, promoting early and limited fuel dissolution. If there is no early contact between the SS and Zircaloy materials, rod failure will be delayed until the melting point of SS (up to 1723K) is reached. This may occur, for example, if ballooning of the control rod cladding is prevented by a high system pressure, or if there is an oxide film on the Zircaloy cladding caused by preoxidation that prevents direct metal-to-metal contact. These effects have been investigated systematically by a program of separate-effect tests at the Karlsruhe Institute of Technology (KIT) [25,26], which showed a very wide range of behavior, from slow failure with a gradual leakage of absorber materials on one extreme, through to explosion of the tested samples on the other.

Table 14.1 provides a summarized list of relevant experiments, including both integral and separate-effect tests. Control rod failure can occur over a wide range of temperatures, which strongly depends on the time when the cladding and guide tube come into contact.

Boron carbide control rod or blade

For boron carbide control rods, the SS of the cladding material is thermodynamically unstable with respect to the B_4C absorber material. Reaction can start above the eutectic temperature of about 1073 K; however, the solid–solid reaction is slow, and in practice the liquid phase only starts to appear from 1273 K [37]. Rapid liquefaction occurs above 1523 K as a result of interaction between the steel components (Fe, Cr, and Ni) with B_4C . The B_4C –SS melt under goes a eutectic reaction with the Zircaloy guide tube again to give Zircaloy liquefaction above 1523 K. As long as the guide tube is intact, the liquefied alloy composed of B_4C , SS, and Zircaloy is held in place or relocates internally in the gap between the cladding and guide tube.

Significant external relocation of B_4C -bearing melt occurs on failure of the oxide shell on the outside of the guide tube, which will depend on its thickness (hence on the oxidation history). A similar situation is experienced for BWR control blades, where the canister is made of Zircaloy (rather than the guide tube). The mass ratio of B_4C /SS is about 0.08 in BWRs and about 0.28 in PWRs using B_4C control rods.

Table 14.1 Silver–indium–cadmium control rod experiments.

Test	Rods	Failure temperature (K)	References
Bundle tests			
CORA average	18 rods	1578 ± 78	All tests, Haste and Plumecocq [27]
CORA-9	6.2	1693	High system pressure, 1 MPa, idem
CORA-29	4.6, 6.2	1695, 1677	Preoxidized, 4–10 m ZrO ₂ , idem
CORA average, without C-9 and C-29	15 rods	1556 ± 66	Haste and Plumecocq [27]
PBF SFD1.4	3 rods	~1700	High system pressure, 6.9 MPa, Petti et al. [28]
LOFT LP-FP-2	11 rods	1523–1623	Carboneau et al. [29] and Jensen et al. [30]
Phébus AIC	Center	1723	Repetto and Corregio [31]
Phébus FPT0	Center	1350–1450	Barrachin et al. [32]
Phébus FPT1	Center	1620	Payot et al. [33]
Phébus FPT2	Center	1620	Payot et al. [33]
QUENCH-13	Center	1415	First indication, by aerosol release, Sepold et al. [34]
	Center	1550–1650	Substantial relocation of melt, Dubourg et al. [35], and Steinbrück and Stegmaier [25]
Small-scale tests			
Winfirth separate- effect	27 samples	1689 ± 44	Range 1560 K–1760 K. Small samples, Bowsher et al. [36]
KIT separate- effect	11 rods	1542 ± 78	Range 1430 K–1720 K. Small samples, Steinbrück and Stegmaier [25]. Sample with no guide tube exploded at ~1720 K

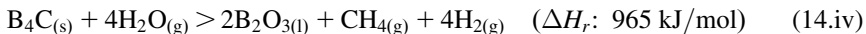
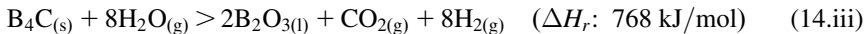
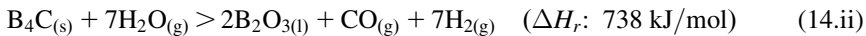
KIT, Karlsruhe Institute of Technology.

According to thermodynamic evaluation, the interaction between the SS and B₄C should produce more liquid with the decrease in the ratio of B₄C/SS, and then more flow down and less oxidation are expected. Exothermic oxidation of any freestanding B₄C by steam can occur, with associated production of hydrogen, carbon monoxide, carbon dioxide, methane, boric oxide, and boric acids, according to the temperature and steam availability, [22,38]. Recent experimental work was done at IRSN, France [BECARRE project as part of the International Source Term Program (ISTP)]. The work on oxidation of B₄C is reported by Dominguez et al. [39], and of

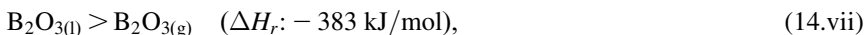
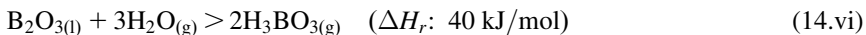
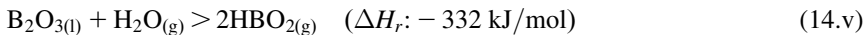
B_4C control rods by Dominguez and Drouan [40], while oxidation of $\text{B}_4\text{C}/\text{SS}$ mixtures is reported by Dominguez [41].

Much experimental work on B_4C degradation and interactions with steels and Zircaloy was also performed by KIT in support of their QUENCH program [42–45].

The oxidation reactions of B_4C are as follows:



One important issue regarding B_4C oxidation was the formation of methane, CH_4 , because of its potential to produce volatile organic iodine compounds. However, all experiments have revealed only very low production of CH_4 . This is in agreement with thermodynamic evaluation, which predict significant methane production only for temperatures below 873 K. The previous reactions are accompanied by evaporation and hydration reactions, which may be endothermic.



where (s), (l), and (g) indicate solid, liquid, and gas phases, respectively.

The eutectic melt may displace radially to neighboring fuel rods, where, being chemically aggressive, it can promote early fuel dissolution, as for the AIC case. In summary, Table 14.2 provides a list of relevant experiments, both integral sand separate-effect tests. The failure can occur over a wide range of temperatures, as noted for AIC rods in the previous subsection.

Reaction between B_4C –stainless steel melt and Zry channel box

After the Fukushima Daiichi accident, the importance of the interaction between B_4C –SS melt and a Zircaloy (Zry) channel box received increased attention among SA experts. The interaction is highly influenced by the preoxidizing conditions at the Zry surface. It might lead to different tendencies regarding the blockage of a control blade channel. Consequently, it might then lead to the different geometries regarding the fuel assembly degradation. In general, the assembly degradation in BWRs is considered to progress in a more heterogeneous manner than that in PWRs.

As previously mentioned, a stable oxide layer a few tens of microns thickness is formed on the surface of the Zry channel box wall under normal operating conditions. Under accident conditions the oxide thickness steeply increases following Zr/

Table 14.2 Boron carbide control rod experiments.

Test	Rods	Failure temperature (K)	Comments
Bundle tests			
ACRR-DF4	Blade	1250–1350 (relocation)	All tests, Haste and Plumecocq [27]
CORA-16		1200–1300	Hofmann et al. [21]; BWR-like control blade (temperature range quoted for failure of absorber element and relocation)
CORA-28	5 rods 1 rod 4 rods	1000–1200 (pressure loss) >1520 (pressure loss) 1370 (temperature deviations)	Hagen et al. [24]; BWR-like control blade. Time delay of 70 s between the beginning of B ₄ C-bearing melt formation and failure of fuel rod simulator cladding
CORA-W2	Center	1220 (pressure loss)	Hagen et al. [46]; VVER test with Zr–1%Nb cladding
QUENCH-07	Center	1300 (He detection) 1310 (CO detection)	Sepold et al. [34]; cylindrical control rod
QUENCH-09	Center	1280 (He detection) >1560 (CO detection)	Sepold et al. [34]; steam-starved phase to simulate Phébus FPT3, cylindrical control rod
Phébus FPT3	Center	1450 (guide tube temp.) >1510 (CO detection)	Payot et al. [33]; steam-starved phase, cylindrical control rod
Review	n/a	1450 (failure of guide tube oxide shell)	Steinbrück et al. [26]; from KIT QUENCH and associated separate-effect tests
Small-scale tests			
KIT box tests	–		Steinbrück et al. [47]; isothermal oxidation tests at 1073 K–1673 K in argon/steam mixture, transient oxidation tests at 1073 K–1773 K; four types of samples used, pellets and powder, French, German, and Russian origin
IRSN BECARRE tests	–	–	Dominguez et al. [39]; kinetics of B ₄ C oxidation in steam at various partial pressures and flow rates, 1473 K–2073 K Dominguez et al. [41]; eutectic interactions, oxidation of eutectic mixtures (up to 1800 K) Dominguez et al. [40]; control rod segments (up to 2273 K)

BWR, Boiling water reactor; KIT, Karlsruhe Institute of Technology.

steam interactions with increasing temperature. However, it might decrease or dissolve in the underlying metallic Zry under steam-starved conditions. Oxygen diffusion into the bulk Zr material simultaneously increases at high temperatures and becomes dominant over the surface oxidation. Since steam starvation possibly occurred during the early phase degradation of unit-2 at Fukushima Daiichi, a detailed understanding of the related phenomena is of particular importance for the core analysis of unit-2. These differences regarding preoxidation are considered to influence the degradation tendency of the control blade and channel box.

A general review of the integral and separate-effect tests on the related interactions was given by Kurata et al. [2]. When the B₄C–SS melt contacts the preoxidized Zry, the following reactions may occur:

- attack of the surface Zr oxide by the B₄C–SS melt;
- diffusion of oxygen from the inner interface of the surface oxide into the Zry-bulk;
- eutectic interactions between SS materials and Zr; and
- simultaneously with (3), compound formation between SS materials and Zr and B or C and Zr.

Reactions (1) and (2) make the surface oxide layer thinner. Hence, when the B₄C–SS melt contacts the Zry wall under steam-starved conditions, the surface oxide layer cannot prevent the eutectic reaction. This leads to reactions (3) and (4). In various integral tests [48,49], a highly exothermic reaction was observed in a relatively small region just after contact between the B₄C–SS melt and Zry, which originated from the reactions (3) and (4). Also, it was found that this particular exothermic reaction zone gradually relocated to the lower part of the sim-fuel assembly [49]. On the other hand, if a sufficient thickness of Zr-oxide layer was at first formed during the preoxidizing step in steam-rich conditions, it can almost prevent the eutectic reaction between the B₄C–SS melt and Zry and only the B₄C–SS melt relocates to the bottom region via control blade channels.

The reason why the highly exothermic reaction can be recognized by referring to the Fe–Zr binary phase diagram (see Fig. 14.12, from Massalski [50]). Here, Fe is representative of the SS materials. Two major eutectics are shown in the Zr- and Fe-rich regions, respectively. In the case of the reaction between the B₄C–SS melt and Zry, the eutectic in the Zr-rich region (Zr–FeZr₂/FeZr₃) becomes dominant, because the interaction progresses on the Zry surface. According to Fig. 14.12, the eutectic temperature in the Zr-rich region is approximately 1200 K, which is far lower than the temperature of the B₄C–SS melt (the latter melt is formed by the eutectic reaction between B₄C and the SS at ~1473 K). The same argument can be made for the Fe-rich end of the Fe–Zr system (Fe–Fe₂Zr eutectic). This suggests that the chemical state just after contact of the B₄C–SS melt with Zry deviates largely from the equilibrium state; hence, the entire system rapidly attempts to move toward the equilibrium state. Considering the local weight ratio between the SS and Zry on the horizontal cross section of fuel assembly (rich in Zry), the equilibrium state of the local system at approximately 1473 K might be a mixture of Zr-rich melt with a small amount of the SS materials (e.g., Fe–Fe₂Zr or Ni–Ni₅Zr) compounds.

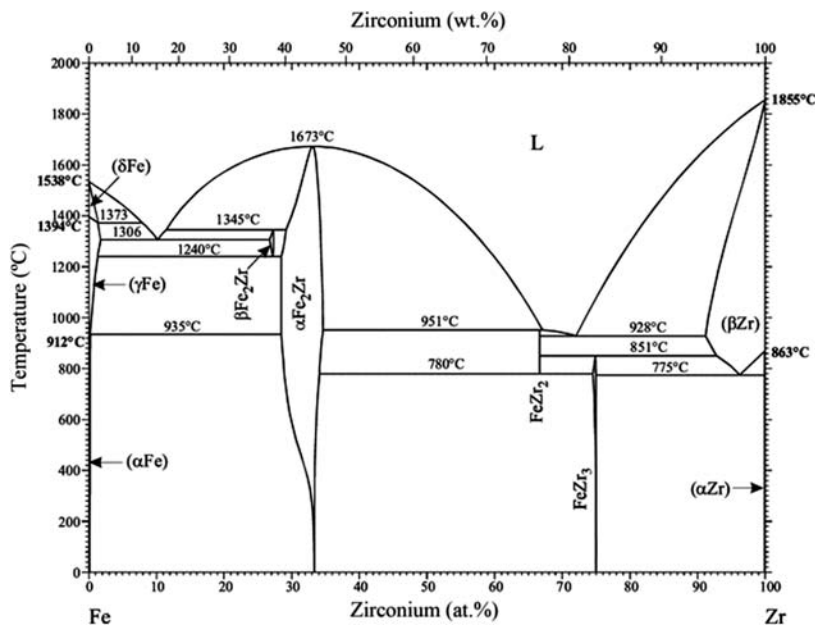


Figure 14.12 Fe–Zr binary phase diagram.

Source: Quoted from T.B. Massalski (Ed.), Binary Alloy Phase Diagrams, second ed., ASM International, Novelty, OH, 1990, ISBN 978-0-87170-403-0.

Two important issues are further addressed following the previous considerations, such as an axial phase;element separation between the Zr-rich melt and (Fe, Ni,Cr)₂Zr compounds and a formation of ZrB or Zr₂B. Provided that the eutectic reaction starts on the surface of Zry, the melt is considered to have a composition at around the eutectic point in the Zr-rich region of the Fe–Zr phase diagram. According to Fig. 14.12, the value is approximately 25 at.%Fe–75 at.%Zr and the liquefaction temperature is approximately 1200 K. This means that the Zr-rich melt selectively relocates to the lower regions of the fuel assembly. On the other hand, the melting temperature of (Fe,Ni,Cr)₂Zr compounds is approximately 1800 K; hence, these compounds selectively remain in the higher parts of the fuel assembly. This sequence causes an axial phase;element separation and consequently might cause a partial blockage in the control blade channel.

Under the condition in which the partial blockage happens, a small amount of steam might be continuously introduced into the degraded fuel assembly; hence, this might suppress the temperature of the fuel assembly below its fully molten temperature. This sequence might lead to a core degradation according to a BWR-drainage scenario [51]. Another issue is the formation of Zr boride; ZrB or Zr₂B, and its precipitation. These borides are far more stable than the Fe–boride. Hence, B is considered to be selectively trapped by Zr in the SS–B₄C–Zr melt, which is intermediately formed during the interaction process. The melting temperature of

these Zr borides is higher than approximately 3273 K [50] (although not accurately determined yet). Hence, the Zr boride tends to remain in the higher regions of the fuel assembly. The interaction between the Zr boride and steam might be important for the fuel debris characterization (currently, the related information is insufficient).

14.2.2 Chemistry in transition from early phase to late phase

This section is focused on the mechanisms responsible for the transition from the early to the late degradation phases in an SA sequence in a PWR or BWR. The *early phase* corresponds to the situation for which the core remains almost intact with possible formation of *local* molten pools resulting from interaction of the fuel and the cladding. During this phase, many events occur such as the degradation of the control rods (i.e., B₄C or Ag–In–Cd), cladding burst, oxidation of the Zircaloy cladding, SS oxidation, and interaction between the fuel and the cladding (in a solid state if the cladding is not yet melted or resulting in a dissolution process if the cladding is melted). The *late phase* is usually reached when *significant* fuel degradation occurs and consequently leads to solid and/or liquid material relocations toward the bottom of the vessel where they accumulate to eventually form a molten pool. In this latter situation the original core geometry is then partially or fully lost.

During a SA in a PWR/BWR, among many other degradation events, the interaction between Zry cladding and UO₂ (or MOX) fuel is usually considered the main event responsible for the destruction of the core geometry. In an accident sequence the reactor fuel may experience a variety of atmospheric conditions that determine the nature of the interaction between the Zircaloy cladding and the fuel and the temperature of fuel liquefaction. These conditions are dynamic and the fuel can be exposed to temperatures ranging between 900 K and 2800 K, pressure variations, and from highly oxidizing to reducing environments. According to an accident scenario, the fuel can be exposed to pressure ranging between 15 and 0.1 MPa; however, pressure variation is only important when the vessel or RCS fails. As a result, the liquid phases may form in a very complex way involving both spatial and temporal variations of compositions. The melt progression may start at different times at different places in the core and solidify on cool down at different temperatures, which may form blockages at different axial and radial locations. Another scenario that leads to the destruction of the core geometry may be the formation of rubble beds after embrittlement and cracking of fuel rod stacks. The collapse of the solid particles (e.g., ZrO₂ and UO₂) onto blockages (e.g., grids or solidified materials) can form debris beds and then, in the case of continuous heat up, results finally in a molten pool.

14.2.3 Chemistry in late phase degradation

While the behavior of the late phase core materials in defined geometries (e.g., debris bed or molten pool) is rather well understood, the transition between the intact bundle and the late phase geometries still remains an active subject of

research. As the late phase is of key importance for plant safety studies, such as hydrogen production when the core is reflooded, FP release and initial conditions for corium–vessel interaction, the material relocation processes have to be described in detail in safety analysis system codes. Despite many experimental investigations being performed in a fuel bundle geometry [3,21], these processes are still partially understood and therefore unsatisfactorily modeled as a result of this limited understanding. As an illustration, the recent benchmark exercise between SA codes within the OECD/NEA Benchmark Study of the Accident at the Fukushima Daiichi Nuclear Power Plant project [7] demonstrated this lack of knowledge and understanding of late phase degradation.

In the case of unit-1 of the FDNPS, which represents a BWR accident for which almost no action was effective to avoid core degradation, the comparison between the code predictions of hydrogen production (i.e., resulting from oxidation of the Zry cladding, the B₄C control rod, and the SS components) shows rather good agreement as long as the core is intact. In contrast, when the corium begins to relocate, the different simulation results of predicted hydrogen generation lead to very different estimates that varied by a factor of 3. At this stage, considering the lack of information on the detailed accident scenario and on the degradation state of the core at Fukushima, the analysis of code discrepancies would be too unreliable. Nevertheless, the relocation processes are usually triggered in most of the codes by user-defined criteria in order to model in as simple a fashion as possible the mechanisms of cladding failure. For example, the cladding fails in some codes when one of the two following criteria is fulfilled: either its temperature exceeds a certain threshold value and/or the zirconia thickness is lower than a limiting value. Such criteria quickly appeared to be inadequate to describe the experimental observations from the Phébus FP tests and more precisely the early slumping time of the irradiated fuels rods detected in these tests.

The Phébus FP programme [52] (Table 14.3) is one of the most ambitious projects devoted to core degradation in the event of a SA. Indeed, the Phébus FP test sequences led to core degradation far beyond any other integral experiment so far performed (~10% of the initial core mass). The facility provided prototypic reactor conditions, which allowed the study of basic phenomena governing core degradation through to the late phase (melt pool formation), hydrogen production, FP release and transport, circuit and containment phenomena, and iodine chemistry. The phenomena studied took place in the following conditions: (1) in the core region simulated by a 1 m long bundle of 20 irradiated fuel rods including a control rod, (2) in the primary system components for which a steam generator is simulated by a single inverted U tube, and (3) in the containment building simulated by a 10 m³ tank including a sump, a controlled atmosphere, and painted wet and dry (condensing and noncondensing) surfaces. All these three components were scaled down at roughly 1/5000 of the relative size of a typical French PWR 900-MWe power plant.

Even if significant results were obtained in past SA bundle meltdown tests, this program brought new findings in the field of the transition from the early to the late phase fuel degradations. Due to the in-pile characteristics of the Phébus FP tests,

Table 14.3 Phébus fission product (FP) test matrix.

Test	Type of fuel	Fuel degradation	Primary circuit	Containment	Date
FPT-0	Fresh fuel, 9 days preirradiation, 1 Ag–In–Cd rod	Melt progression and FP release in steam-rich environment	FP chemistry and deposits in noncondensing steam generator	Aerosol deposition, iodine radiochemistry at pH5	December 2, 1993
FPT-1	BR3 fuel \approx 23.4 GWd/tU, 1 Ag–In–Cd rod, reirradiation	As FPT-0 with irradiated fuel	As FPT-0	As FPT-0	July 26, 1996
FPT-2	As FPT-1, but with fuel burn up \approx 31.8 GWd/tU reirradiation	As FPT-1 under steam poor conditions	As FPT-1 with effect of boric acid in the steam	Evaporating sump at pH9	October 12, 2000
FPT-3	As FPT-1 with B ₄ C instead of Ag–In–Cd, fuel burn up 24.5 GWd/tU reirradiation	As FPT-2	As FPT-0	Evaporating sump at pH5 recombined coupons	November 18, 2004
FPT-4	EDF fuel average burn up 38 GWd/tU, no reirradiation, fuel + oxidized cladding pieces as a debris bed	Low-volatile FP and actinide release from the UO ₂ –ZrO ₂ debris bed up to melting	Integral filters in the test device, above the debris bed (no transport, no containment objectives)		July 22, 1999
			Detailed posttest analyses on filters		

the UO₂ fuel rod liquefaction and relocation mechanism are only *indirectly* identified on the basis of the thermal response of the bundle. It provides indications about the material movements that can be the results of partial or complete liquefaction of the fuel. The evidence of the loss of the fuel rod geometry *in these tests* was identified in the same range of temperature (i.e., 2500 K ± 200 K) [52], in spite of the different test conditions (e.g., strongly oxidizing ones in the two first tests FPT0 and FPT1, and weakly oxidizing ones in FPT2 and FPT3).

This low-temperature range for fuel liquefaction/relocation was rather unexpected, in particular for oxidizing conditions. In the first two tests, the steam-starved conditions were never attained, even in the upper part of the bundle. It means that the steam supply was sufficient in these tests for preventing any hydrogen-rich period in the upper part of the bundle. In these conditions a rather low fuel dissolution in this zone was expected. The post-test examinations revealed large areas of solidified ceramic phases of composition (U,Zr)O₂ between some surviving fuel rods. Veshchunov et al. [53] and Barrachin et al. [54] showed that the formation of these ceramic phases probably occurred after the completion of the oxidation process when the bundle started to cool down (the decrease of the temperatures was due to the fact that there was no more production of chemical energy due to the oxidation). These fully ceramic phases precipitated during the solidification of the U–O–Zr melts produced by the intensive fuel dissolution at the upper levels occurring during the oxidation phase. According to the U–O–Zr phase diagram [55], the solidification of these melts is expected to be also accompanied by the formation of metallic α -Zr(O) phase. This phase was absent from the observations performed at the upper part of the FPT0 and FPT1 test sections. It is explained by its further downward relocation from the upper levels to the intermediate ones where this phase interacted with the fully oxidized portion of fuel rods and then lowered their relocation/melting temperature.

The core degradation appears to be strongly linked to the failure of the cladding and its consequences on the relocation of significant metallic phase amounts from the upper levels to the lower ones. Different situations may happen. *If the cladding does not fail during the transient*, the rod-like geometry is kept and the cladding is completely oxidized and the fuel dissolution is then limited. As the results of thermal stresses, cladding and fuel relocate under solid fragments to form a debris bed. *If the cladding fails before its complete oxidation*, there is a possibility of the formation of local molten pools. The presence of these local molten pools (owing to their geometry in comparison with the rod-like one) tends to increase the amount of metallic zirconium able to dissolve the oxidized zirconium and fuel at that height. The relocation of such local molten pools formed (as an example in the FPT0 and FPT1) at the upper levels enhances the dissolution process at the lower levels.

As previously indicated, the loss of fuel rod geometry is dependent on the accident scenario. The application of the Phébus FP results to any other accidental scenario has to be considered with caution. As an illustration, in some of the small-scale VERCORS experiments [56] that used irradiated UO₂ (from 38 to 70 GWd/tU) and *fully oxidized cladding*, the fuel melting (or collapse) process was *directly* detected with a gamma detector at a temperature range of 2400 K–2600 K (similar

to Phébus FP) irrespective of the fuel burn up or the flow rates of hydrogen and steam, which varied from one test to another. The interaction between Zry cladding and UO₂ or MOX fuel cannot be invoked in the VERCORS tests where no metallic phase is present or in the Phébus FPT2 test where the amount of metallic phase produced at the upper levels of the test section was less significant than in the two first tests (FPT0 and FPT1), due to the lower temperatures reached in this test. Other mechanisms could potentially contribute to an earlier degradation of the core.

Several reports indicate the potential effect of UO₂–ZrO₂–FP interactions and then a UO₂ fuel melting temperature reduction with burn up [57–60]. Due to experimental difficulties of sample pollution, composition change during heating, and so on, these measurements have to be considered with caution. The FP effect on the UO₂ melting temperature is moderate (at least up to a burn up of 30 GWh/tU) [61]. As an illustration, the melting temperature of an irradiated fuel remnant containing 5–7 at.%Zr (which largely exceeds the Zr FP inventory) was shown to only decrease from 3120 K to 2950 K [62].

Manara et al. [63] reported accurate data indicating that hyperstoichiometric UO₂ has a significant reduction of the melting temperature, which is noncongruent. These results have been recently completed by new experimental data [64] on the melting transition of (U,Zr)O₂ in oxidizing conditions which shows that they may melt several hundreds of K below the melting point of the same material in an inert or reducing atmosphere. For example, a typical oxidized corium composition of U_{0.6}Zr_{0.4}O_{2.13} was observed to solidify at a temperature as low as 2493 K (such stoichiometric deviation is consistent with the estimates performed in FPT1 [32]). Then there is a possibility of fuel rod liquefaction at temperatures from 2500 K if fuel is hyperstoichiometric. Such an effect may have also played a role in the Phébus FP and the VERCORS tests.

The interaction between materials from control rods (AIC and boron carbide for absorber materials and SS from internal structures of the core) and refractory compounds (UO₂ and ZrO₂) was invoked to explain the apparent reduction of the liquefaction/relocation temperature of the fuel rods. It was the subject of considerable investigations to understand the core degradation after the accident at TMI-2. Olsen et al. underscored the fact that these structural materials in a *metallic* state do not attack the fuel [65]. In agreement with Olsen et al., the posttest observations of the Phébus FP tests did not show any significant impact of the metallic elements of the control rod even when a mixture relocated in the lower part of the Phébus FPT0 test section Zr (10–50 wt.%), In (10–40 wt.%), U (less than 15 wt.%), O (less than 10 wt.%), and SS (less than 5 wt%) were clearly indicative of the interaction between the control rod materials and the fuel rods, early in the transient. The current belief is that iron from the SS of control rod cladding and silver, *in the metallic state*, do not directly contribute to the dissolution of the fuel rods, but they are likely to lower the liquefaction temperature of the Zry cladding, and so lower the temperature of the initial interaction between the UO₂ fuel and the Zircaloy cladding (theoretically at 2023 K).

It should be noted, however, that iron (as well as chromium) in the oxidized state can significantly lower the liquefaction start temperature of UO₂ (i.e., eutectic

temperature in the $\text{UO}_2\text{--FeO}_{1+x}$ section at 1610 K according to Bechta et al. [66]) and ZrO_2 (eutectic temperature in the $\text{ZrO}_2\text{--FeO}_{1+x}$ section at 1605 K [67]). In TMI-2, Strain et al. [68] observed the presence of an eutectic oxide phase of $\text{Fe}\text{--Cr}\text{--O}/(\text{U},\text{Zr})\text{O}_2$ at the grain boundaries of the refractory matrix from the relocated material found at the lower vessel head: this confirmed findings of the significant ferrous phases in the $\text{UO}_2\text{--ZrO}_2$ solidified corium from the center of the reactor [18]. According to Strain et al., these $\text{Fe}\text{--Cr}\text{--O}$ eutectic phases in the grain boundaries of the $(\text{U},\text{Zr})\text{O}_{2 \pm x}$ refractory phase and in more extensive areas next to large voids were the origin of a possible “low-temperature” fuel relocation mechanism. The very large difference between the solidus temperatures of the uranium–zirconium oxide phases and the chromium and iron oxides would have allowed the $\text{UO}_2\text{--ZrO}_2$ refractory phase to continue to relocate like a wet sand at temperatures much lower than 2800 K, which is the minimum solidus temperature in the $\text{UO}_2\text{--ZrO}_2$ pseudo-binary system [69]. The mechanism of interaction between UO_2 and iron oxides [70] showed that at 1700 K the SS oxide liquid phase penetrates into the grain boundaries and partially dissolves the matrix, which could potentially lead to a loss of cohesion of the fuel.

If the observations performed after the Phébus FP release tests [54] confirmed Strain’s findings about the presence of SS oxides at the grain boundaries of the ceramic phases, it is not possible to come to a solid conclusion as was the case with TMI-2 about a key role of the SS oxides on the early slumping of the fuel rods in the Phébus FP tests. The onset temperature of UO_2 liquefaction by iron oxides depends on the partial pressure of oxygen [71]. Recently the eutectic points in the $\text{UO}_2\text{--ZrO}_2\text{--FeO}_x$ and $\text{UO}_2\text{--ZrO}_2\text{--Fe}_2\text{O}_3$ systems measured at 1600 K and 1610 K, respectively [72,73], allow quantification of this variation. Moreover, examination on melting point variation of $\text{UO}_2\text{--ZrO}_2\text{--FeO}$ mixes by laser flash method shows that the presence of more than 15 mol.% of FeO in these mixtures will result in the appearance of a solidus temperature of the order of 1650 K [18]. It shows that the melting range of the oxidic corium containing iron oxides can be very large and that relocation is possible for mixtures containing significant amount of FeO (at least 15 mol.%).

The effect of boron carbide, which is present in PWRs and BWRs on enhancing melt progression was detected in the Phébus FPT3 test. The steel of the sheath of the boron carbide control rod (or shroud in the case of a BWR control blade) reacts with boron carbide between 1533 K and 1623 K [74,75]. This interaction leads to a partial liquefaction of the control rod, liquefaction that generally induces the loss of its geometry. The interaction between the boron carbide and the Zircaloy of the guide tube leads to the liquefaction of the latter at a higher temperature of the order 1923 K (i.e., close to the eutectic temperature of the Zr-B phase diagram). The combined ruptures of the control rod and its guide tube allow the passage of water vapor and the oxidation of boron carbide to boron trioxide (B_2O_3) [39,42]. This oxide can vaporize above 1773 K but also in turn can react with the steam to form, depending on the conditions of temperature and partial pressure of water vapor, different boric acids [HBO_2 , H_3BO_3 , and $(\text{HBO}_2)_3$]. It can also interact with fuel rods (due to the dispersive mechanisms of B_4C control rod degradation induced by the CO presence) and contribute to their degradation.

The thermodynamics of the boron trioxide, uranium dioxide, and zirconium dioxide systems have not been studied extensively. Nevertheless, it has recently been shown experimentally [76] that boron trioxide can significantly reduce the liquefaction temperatures of the aforementioned refractory oxides and thus contribute to the degradation of fuel. Apart from the Phébus FP FPT3 test, the effect of boron carbide on the degradation has been observed elsewhere, for example, in the CORA-W2 experiment (with B₄C) [46] with its counterpart in CORA-W1 with no absorber material [24]. B₄C control rods then promote bundle degradation more than those of (Ag, In, and Cd) in terms of timing (earlier) and melt fluidity (increased due to the B₂O₃ presence, which decreases the ferrous or Zry-based melt viscosity). The effect of B₄C should then lead to faster flowing (less viscous) and more penetrative molten materials.

14.2.4 Chemistry on fuel degradation ex-vessel conditions

The most important fuel degradation for the ex-vessel conditions is molten core–concrete interaction (MCCI). In this section the comprehensive phenomenology on the MCCI progression and various separate effects are discussed:

- phenomenology;
- interface chemistry between molten core material and concrete;
- phase/element distribution during solidification;
- interaction with sea salt materials.

14.2.4.1 Phenomenology of molten core–concrete interaction

In case of rupture of the vessel, the corium resulting from the melting of the core and the internal structures fall down in the concrete reactor pit, which supports the R/B's internal structures and rests on the containment basemat; the cast-in-place reinforced concrete foundation serves to support the nuclear island structures.

At this stage, corium is usually a molten mixture of fuel materials, partially or totally oxidized Zircaloy claddings, nonvolatile FPs, and various structural materials (SS, in particular). After the TMI-2 PWR accident, a corium mixture with the following average composition 77 wt.%UO₂, 17%ZrO₂, 2%Ag, 1%Fe, 1%Cr, 1%Ni, 1%In was measured in the vessel lower head [77]. The metallic components represented only a few percent of the in-vessel corium mass. For a BWR (as at Fukushima Daiichi) where the amounts of metallic materials (SS and Zr) in the core initially present are much higher than for the corresponding (i.e., with the same power) PWR, the corium interacting with the concrete is expected to contain more metallic components.

Concrete is a heterogeneous material comprised cement, water, and aggregates. Cement in powder form acts as the binding agent when mixed with water and aggregates. Concrete that contains two different types of aggregates, the so-called gravels (coarse aggregates) and sand (fine aggregates of size lower than 5 mm), is often reinforced by steel bars (i.e., “rebar”).

The contact between corium and concrete leads to MCCI. This interaction results in a progressive ablation of the walls of the reactor pit and the basemat. It may lead

to a failure of the former and potentially result in leakage of radioactive products outside. The failure of the side walls of the reactor pit may lead to the corium coming in contact with nearby water, which can contribute to increasing the pressurization of the containment by vaporization. The production of gases generated by the ablation of the concrete also contributes to the pressurization of the containment with similar kinetic behavior corresponding to that of the ablation of the basemat, which may take place from one to several days. Note that the aerosol production that accompanies the corium–concrete interaction also impacts the evolution of the aerosol behavior in containment and therefore the source term,⁷ which is the amount of radioactive species released in the environment.

Research of the corium–concrete interaction aims to acquire the necessary knowledge to predict with an acceptable accuracy the kinetics of axial and radial ablation of the walls of the basemat and the reactor pit, and to predict the evolution of gases and aerosols produced during this interaction. The response of concrete to high thermal fluxes is complex and involves many phenomena and varies with temperature, ranging from ambient temperature to the melting point. The evolution of the concrete physico-chemistry with temperature is summarized next (much more details can be found in [78]):

- At low temperatures (about 373 K), there are different dehydration processes implying mainly the so-called tobermorite (a calcium silicate hydrate).
- In the temperature range from 673 K to 873 K, portlandlite $[(\text{Ca}(\text{OH})_2)]$ begins to decompose.
- Between 873 K and 1173 K the limestone aggregates (CaCO_3) begin to decompose with CO_2 release.
- Above 1473 K, some components of the cement begin to melt. Melting of the cement paste is highly influenced by its chemical composition. The temperature between 1473 K and 1773 K gives an order of magnitude of the melting range. Bazant and Kaplan [78] indicated that for a cement mixture consisting of between 63 and 71 wt.% lime, 18 and 30 wt.% silica, and 5 and 15 wt.% alumina with an iron oxide content of 7 wt.%, the melting point may be even lower than 1473 K.
- The melting temperature of the aggregates greatly varies from 1333 K for Basalt to 1973 K for Quartzite. When heated to 1973 K, silica melts to a glassy mass. This transition may be reduced to 1600 K in the presence of 1% alumina.

Given the high temperature of the molten materials from the vessel ($T > 2500$ K) due to the decay heat and the melting temperature of the concrete (around 1600 K for a siliceous concrete [79]), the corium–concrete interaction mainly consists of the melting of the concrete (in the SA codes, the effective melting temperature of the concrete usually corresponds to a temperature for which 30–50 vol.% is liquid).

The high-temperature corium in contact with the colder concrete can also lead to its (partial) precipitation, the debris being suspended in the liquid. After the initial transient, lasting from several minutes to a few hours (depending on many factors of

⁷ “Source term” refers to the amount of hazardous material, mainly fission products, released to the environment from a nuclear facility following an accident. It generally contains information on timing, location, and physical/chemical states in the containment.

the accident scenario), the main source of heat is the decay heat mainly generated in the oxidic phase. As the concrete is mainly composed of SiO_2 , CaCO_3 , and H_2O , its decomposition leads to the release of condensed phases (i.e., SiO_2 , and CaO) and gaseous (i.e., H_2O and CO_2) species in the melt. The melt therefore contains heavy oxides from the core (i.e., UO_2 and ZrO_2), light oxides from concrete (mainly SiO_2 and CaO), and metals (i.e., Fe, Cr, Ni, and Zr), all of which are subject to intense stirring induced by the decomposition gases released from the concrete.

The possible mixing of the metals with the condensed or gaseous oxide species can lead to potentially exothermic oxidation reactions and to the production of new gaseous species, such as H_2 , CO , and SiO . Oxidation of zirconium and chromium are highly exothermic processes that contribute to the initial interaction phase and potentially significant energy release in the melt. In addition to the reactions of metals with oxidizing gases from the concrete, the interaction between the metallic and the oxide phases at the condensed state has also to be considered. The interaction between metallic zirconium and siliceous concrete with low gas content may result in the zirconium oxidation by the reduction of silica.

The corium bath is therefore a multicomponent and multiphasic material (liquid, solid, and gas), composition and physical properties of which constantly evolve during MCCI due to the decomposition of concrete and chemical reactions. Solidus and liquidus temperatures were measured for different concretes (e.g., limestone, limestone sand, basalt, and siliceous and their mixtures with urania and zirconia [79]). Liquidus temperatures for corium–siliceous mixtures do not vary much with amounts of concrete in the range of 30%–80% and are around 2500 K, whereas for the same composition range, the solidus temperatures are about one thousand degrees lower. Experimental data related to the concrete–corium thermodynamics are relatively limited, even with the additional experimental measurements within the framework of the EC Enthalpy Program [80] and in the ISTC CORPHAD and PRECOS Programs at NITI [81,82]. This knowledge is usually incorporated in thermodynamic solution databases⁸ (e.g., [83–85]) which, when coupled with a Gibbs energy minimizer, are able to provide the phases in thermodynamic equilibrium for any composition and any temperature.

⁸In a conventional way and for a long time, knowledge of the thermodynamics of a material is captured by establishing a phase diagram, which is a graphical representation of the state of the material as a function, generally, of composition and temperature. The phase diagram is determined experimentally from measurements of different properties (phase change, temperatures, phase compositions after quenching, etc.). Reference books list these diagrams established by experiments, for simple materials, known as binary systems (that is to say composed of two chemical elements) and sometimes for the ternary systems (three elements). For corium–concrete mixtures the task is of a different magnitude given the large number of chemical elements to be considered and the large temperature range to cover. An experimental approach alone cannot meet this challenge, even if it remains indispensable. An alternative approach is to build the phase diagrams by calculation. For complex materials such as corium–concrete mixtures, the chosen approach is to determine, for each phase (solution and stoichiometric substance) likely to appear in the phase diagram, its macroscopic thermodynamic behavior. This behavior can be described for a constant pressure phase diagram calculation by the Gibbs energy, $\otimes G$. The solution database usually contains expressions for the Gibbs energy of all the possible phases.

The ablation rate of the vertical and horizontal concrete “walls” depends on the ratio between the flux received by the walls and the energy required for their ablation. The decomposition enthalpy to bring concrete from room temperature to total melting is between 1.8 and 2.5 MJ/kg depending on the nature of the concrete (siliceous or limestone-rich concrete) [86]. To determine the kinetics of ablation of these walls, the process is equivalent to calculating the distribution of the heat flow at the borders of the corium bath. It is generally considered that, because of the stirring induced by the gases, the liquid phase(s) constituting the corium–concrete bath is homogeneous, with strong temperature gradients and concentration gradients that may exist at the interfaces. With this approach, it can be seen that the heat flux at the boundaries of the bath can be expressed by means of a convective heat transfer coefficient and the temperature of interface between the corium bath and the medium separating the concrete from the corium. In the SA codes the ablation rate is schematically given by $\Phi/\Delta E$, where Φ is the heat flux to the interface between corium and concrete and ΔE , the concrete ablation enthalpy, calculated from the ambient temperature and ablation temperature (which is set to about 1600 K for a siliceous concrete). Neglecting heat generation in any crust, $\Phi = h_{\text{pool}} (T_{\text{bulk}} - T_i)$, where h_{pool} , is the heat transfer coefficient between the bulk of the melt and an interface temperature, T_i . This interface temperature is a function of the structure of the interface between the corium and the concrete. Depending on the flow rate of gas released by the concrete and the densities of the oxide and metal phases (which are only partially miscible), configurations with a single layer (oxide and metal mixed) or with several layers (oxide and metal separated according to their respective density) can occur. In the latter case the determination of the interface temperature and the heat exchange coefficient is therefore necessary not only at the interface between the layers and the concrete but also at the interface between the oxide liquid and the metal liquid.

14.2.4.2 *Interface interaction between molten core material and concrete*

Separate-effect tests on MCCI using sim-FDNPS concrete samples were mainly performed in Japan, which focused on several specific issues. A steep temperature gradient is likely to be generated between the molten core materials and concrete during MCCI. This certainly influences the characteristics of the fuel debris and the degraded concrete at, or around the interface regions, including the U-penetration depth and the dehydration depth in the degraded concrete. Sim-tests are being performed using a light-concentrating heating furnace [87].

Fig. 14.13A and B show a typical example and the appearance of a sim-debris pellet of $(\text{U}_{0.5}\text{Zr}_{0.5})\text{O}_2$ before and after heating, respectively. The sample was set on a basaltic concrete block and then heated from the top by means of concentrating light. Three layers were apparently observed in the cutting cross section of the sample, identified as a, b, and c in Fig. 14.13C. Secondary Electron Microprobe and Energy-Dispersed X-ray analysis (SEM–EDX) indicated that the top layer (a)

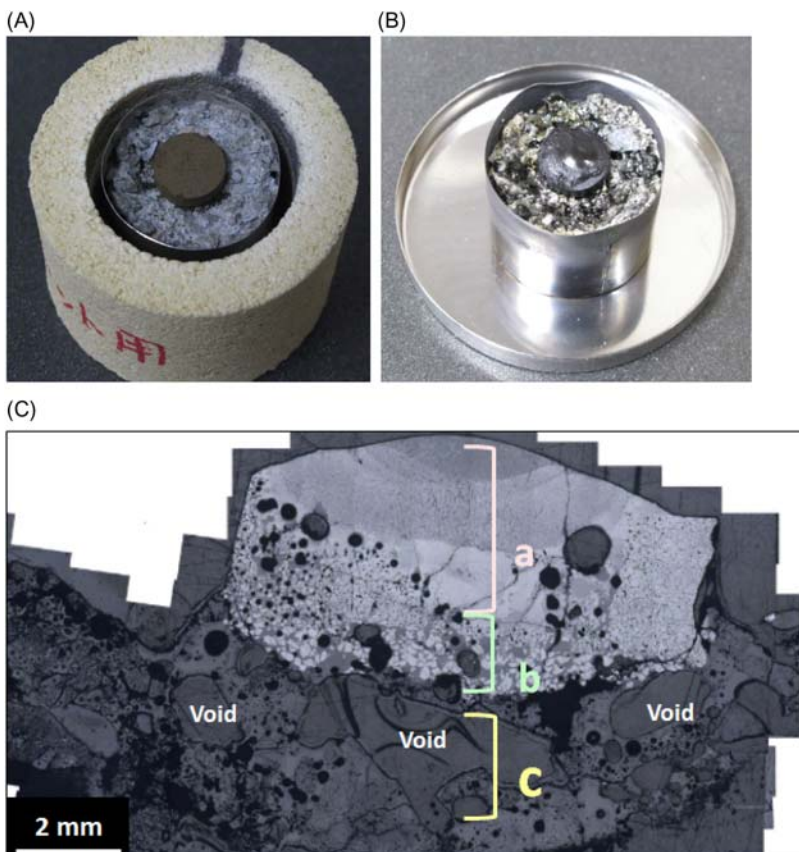


Figure 14.13 Appearance of test sample: (A) before heating and (B) after heating, and (C) polished cross section after heating.

Source: Quoted from A. Sudo, et al., Characterization of core melt/concrete interface region examined by light-concentrating heating technique, in: Presented at NuMat-2016, Montpellier, France, November 6–10, 2016.

consisted of two major phases: the as-melted $(\text{U},\text{Zr})\text{O}_2$ phase and silicate glass phase containing several percent of U and Zr. The quaternary phase diagram of $\text{UO}_2-\text{ZrO}_2-\text{SiO}_2$ (discussed in the following section) proposed that the temperature of this region during heating was approximately between 2273 K and 2773 K, and this region was completely melted during heating. The second layer (b) contained nonmelted $(\text{U},\text{Zr})\text{O}_2$ granules and a silicate glass matrix, suggesting that the silicate glass matrix phase was the only one that melted. In the third layer (c), segregated SiO_2 particles and gas voids were observed in the silicate glass matrix. Considering the

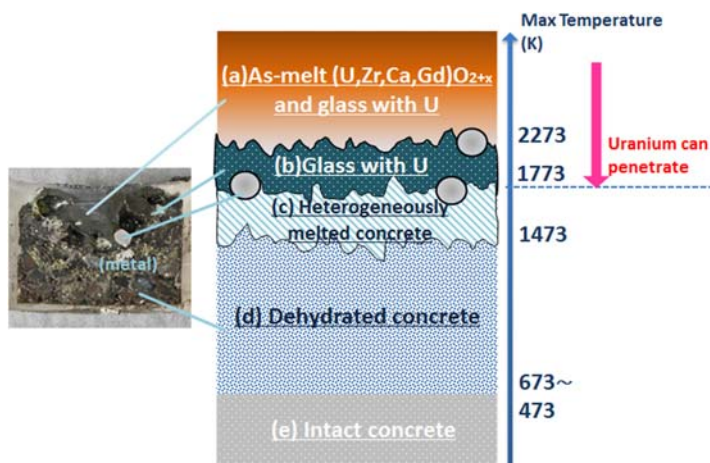


Figure 14.14 Illustration of degraded interface layers after MCCI: (A) as-melt (U,Zr,Ca,Gd) O_{2+x} and glass with U; (B) glass with U; (C) heterogeneously melted concrete; (D) dehydrated concrete; and (E) intact concrete. *MCCI*, Molten core–concrete interaction.

Source: Quoted from A. Sudo, et al., Characterization of core melt/concrete interface region examined by light-concentrating heating technique, in: Presented at NuMat-2016, Montpellier, France, November 6–10, 2016.

melting characteristics of the silicate glass phase, the temperature was approximately between 1473 K and 1773 K.

Fig. 14.14 illustrates the layered structure at and around the interface based on the foregoing observations. Two important issues on fuel debris characterization were addressed [87]:

- Uranium is able to penetrate into the degraded concrete in which the highest temperature is at around 1773 K;
- The basaltic concrete is severely degraded at temperatures higher than approximately 1473 K, and then the dehydration is expected at temperatures higher than approximately 673 K.

Various phases can be possibly generated in the MCCI-product. The phase relation and the hardness levels of these phases are essential information for fuel debris retrieval. Detailed analyses using sim-MCCI samples with a wide composition variation were performed mainly by JAEA [88]. General tendencies on the phase relation are summarized in Fig. 14.15. In reductive atmosphere conditions, a small amount of Al, Si, U, and Zr was contained in the metallic phase, in which Fe, Ni, and Cr were major components, and the formation of ZrB_2 was detected. With increasing oxygen potential in the system, Al, U, and Zr concentrations in the metallic phase were decreasing and $(Fe,Cr)B$ and $(Fe,Cr)_2B$ were detected instead of ZrB_2 . Mo and platinum group metals were always detected in the metallic phase. Major components of the oxidic phase were UO_2 , ZrO_2 , Al_2O_3 , and CaO in the

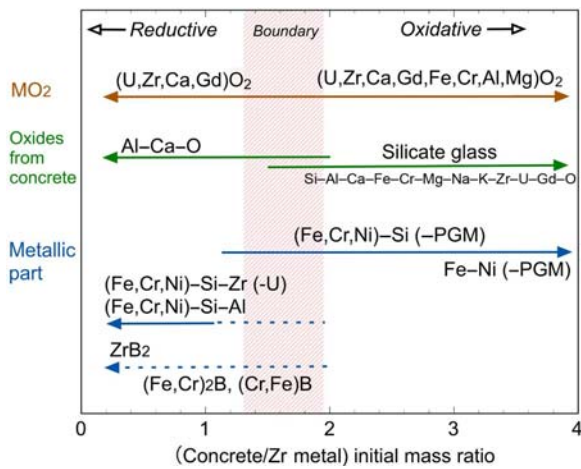


Figure 14.15 Oxidation/reduction trend in MCCI products as a function of concrete/Zr mass ratio. *MCCI*, Molten core–concrete interaction.

Source: Quoted from M. Takano, et al., Phases and morphology in the simulated MCCI products prepared by arc melting method, in: Presented at NuMat-2016, Montpellier, France, November 6–10, 2016.

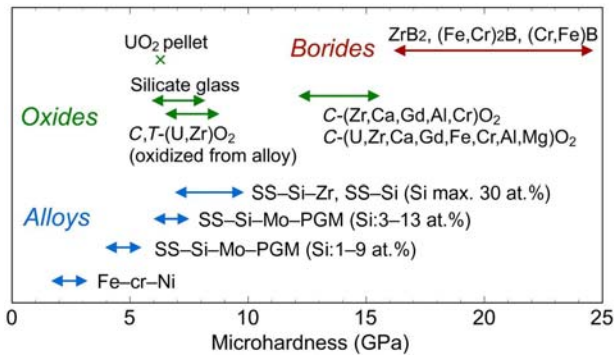


Figure 14.16 Microhardness of various phases detected in sim-MCCI products. *C* and *T* in the figure indicates cubic and tetragonal phases, respectively. *MCCI*, Molten core–concrete interaction.

Source: Quoted from M. Takano, et al., Phases and morphology in the simulated MCCI products prepared by arc melting method, in: Presented at NuMat-2016, Montpellier, France, November 6–10, 2016.

reducing atmosphere. Sea salt materials (Na, K, and Mg) and Gd were also dissolved in the oxidic phase. In an oxidizing atmosphere a small amount of Fe, Cr, and Si was able to be dissolved in the oxidic phase. Fig. 14.16 summarizes the

variation in the microhardness of various phases detected in the sim-MCCI products. An important concern for the fuel debris retrieval was identified in the figure, that is, the extreme hardness of borides, if they were formed in the accident conditions of FDNPS. Also, a certain increase in the hardness was observed for the cubic oxide phases, which were likely to have been generated by impurities included in the solidification of the MCCI-melt.

14.2.4.3 Phase/element distribution during solidification

Corium is considered to be generated in the core or the lower plenum regions of RPV along with the SA progression. In these melts, metallic and oxide layers are likely to be stratified. These melt layers are solidified in the convergence process. The cooling rate might certainly influence the phase/element distributions in these layers, in particular, in the oxide layers. The distribution of Gd and structural materials is of particular importance for the evaluation of recriticality of the solidified fuel debris.

Preliminary tests are ongoing at JAEA on the phase/element distributions examining the cooling rate [89,90]. Fig. 14.17 shows an example, which compares the morphology of solidified sim-corium with two different cooling rates (~ 800 and ~ 5 K/min). The former value was obtained by switching off the heater. The initial

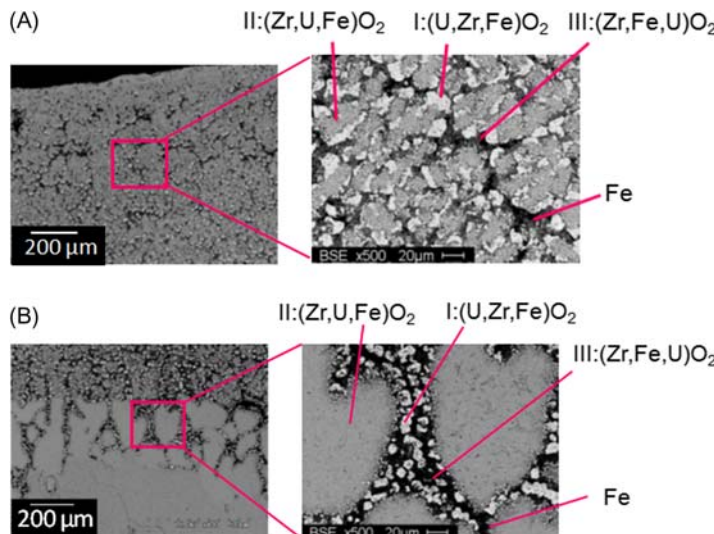


Figure 14.17 Morphology of solidified sim-debris [average composition: $36\text{UO}_2 - 46\text{ZrO}_2 - 18\text{FeO}$ (mol.%)]: (A) quick cooling (~ 800 K/min) and (B) slow cooling (~ 5 K/min).

Source: Quoted from A. Sudo, et al., Solidification behavior of the simulated oxide debris, in: Presented at AESJ Annual Meeting, Okayama, Japan, September 5–7, 2018 (in Japanese) (to be published in English).

composition is approximately $31\text{UO}_2\text{--}40\text{ZrO}_2\text{--}25\text{FeO}$ (mol.%) with a small amount of B_4C and sim-FP oxides in the sample. The sample weight was approximately between 100 and 150 g. The sample was heated to approximately 2873 K for 5 minutes to melt completely under an Ar atmosphere and then cooled to approximately 2573 K with these cooling rates, respectively. Then, the sample was quickly cooled without no holding time from approximately 2573 K to room temperature by switching off the furnace power. By comparing these two samples, one can observe the difference in the solidification process in solid/liquid mixture condition at high temperatures.

Three oxide and Fe-rich phases were detected in the polished cross section of the samples. For convenience, three oxide phases are named in this article as I:(U, Zr, Fe) O_2 , II:(Zr, U, Fe) O_2 , and III:(Zr, Fe, U) O_2 , respectively, by taking their average compositions into consideration. The Fe-rich phase was considered to form by chemical interaction between FeO and B_4C . Interesting phenomena are identified from the careful analysis of these oxide phases. Although the average compositions of three oxide phases are mostly overlapping in two samples, the condensation of the II:(Zr, U, Fe) O_2 phase was only observed in the low-cooling rate sample. Also, the FeO composition was almost determined to be approximately 12 ± 5 mol.% in all the oxide phases.

These compositions are plotted in the $\text{UO}_2\text{--}\text{ZrO}_2\text{--}\text{FeO}$ ternary diagram ([Fig. 14.18A](#)) with the reported ternary phase relations at 1583 K ([Fig. 14.18B](#), reported by Bechta et al. [[91](#)]). The average composition of I:(U, Zr, Fe) O_2 and III:(Zr, Fe, U) O_2 measured in the present samples are in reasonable accordance with the phase boundaries of the UO_2 - and ZrO_2 -rich solutions in the previous observation. The average composition of II:(Zr, U, O) O_2 is reasonably close to the initial composition of the present oxide melt before cooling, which was evaluated to be $36\text{UO}_2\text{--}46\text{ZrO}_2\text{--}18\text{FeO}$ (mol.%) by taking the interaction between FeO and B_4C into consideration. These phenomena might suggest the following processes take place during cooling:

- fine particles of I:(U, Zr, Fe) O_2 and III:(Zr, Fe, U) O_2 were precipitated in many places from the melt at temperatures higher than 2573 K (corresponding to the initial stage of the solidification);
- the remaining liquid regions then started to freeze separately before the sufficient condensation of these rapidly cooled solid particles;
- the remaining liquid regions started to form larger granules in the slow cooling process.

These tendencies might influence the macroscopic morphology and various physical/chemical properties of the fuel debris. These observations did not show any significant segregation of Gd and sim-FPs in these oxide phases and Gd oxide is likely to be homogeneously solidified with U and Zr oxides.

Other work on the $\text{FeO}\text{--}\text{UO}_2\text{--}\text{ZrO}_2$ system was carried out by NITI in the PRECOS project using differential thermal analysis and a Galakaov furnace to determine the phase relations at high temperature. They found two of the same phases [i.e., phases I:(Zr, U, Fe) O_2 and III:(Zr, Fe, U) O_2], but also an FeO-rich phase

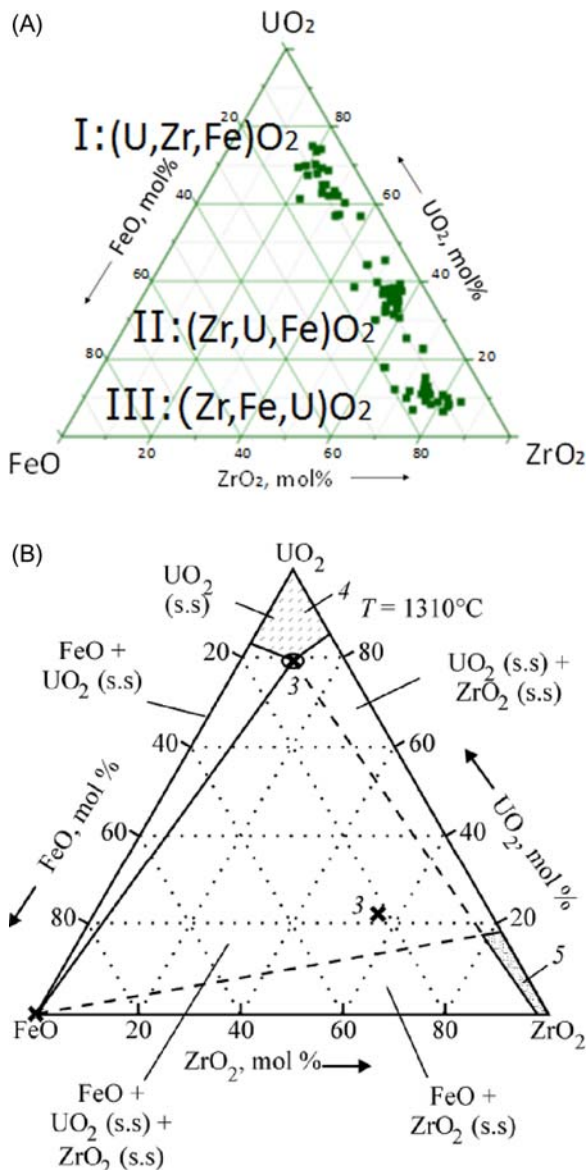


Figure 14.18 (A) Phase compositions detected in sim-fuel debris after cooling and (B) diagram of the phase equilibria detected in the FeO-UO₂-ZrO₂ system ($T = 1583\text{ K}$).
 Source: Quoted from (A) A. Sudo, et al., Solidification behavior of the simulated oxide debris, in: Presented at AESJ Annual Meeting, Okayama, Japan, September 5–7, 2018 (in Japanese) (to be published in English) and (B) S. Bechta, et al., Radiochemistry 50 (2011) 13–18, ISSN 1066-3622.

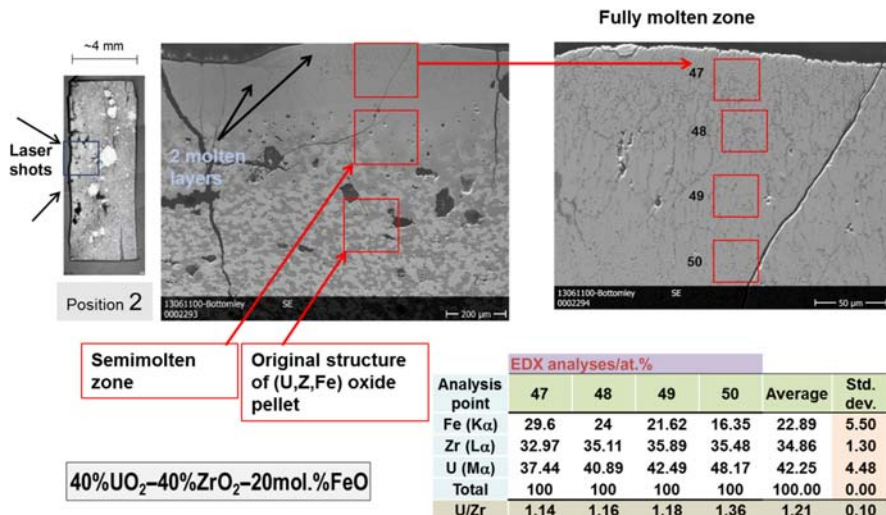


Figure 14.19 SEM investigation after laser flash heating of a 40%UO₂-40%ZrO₂-20 mol.%FeO sample.

Source: Quoted from Peehs, et al., Nucl. Technol. 46 (1979) 192–198.

with small amounts [91] (see Fig. 14.18B). On the other hand, they did not find II: (Zr,U,O)O₂. The reason why these differences occur is reasonably recognized from the difference in test conditions, such as sample size and oxygen potential. The experimental data obtained by NITI were mostly in its equilibrium state (because of a small sample) and the oxidation condition was deviated to hyperstoichiometry. Those by JAEA were away from the equilibrium state (because of the quick cooling of a sample, ~100 g in weight) and the oxidation condition was deviated to hyposstoichiometry (Fe-metal coexists). As for the characteristics of genuine fuel debris, these deviations from the equilibrium state has to be taken into consideration.

Further work was done by Bottomley et al. using the laser flash technique to heat presintered mixtures to melting temperature [92]. Influence of the heating history to phase distribution is discussed. Fig. 14.19 shows micrographs and EDX results of a 40%UO₂-40%ZrO₂-20 mol.%FeO sample with the once melted surface (and once semifused zone below). The analyses of the two-phase surface melt (primary grains with a secondary grain boundary) indicate a composition close to the overall composition. However, the deeper lying zones (e.g., zone 50) have higher UO₂ and reduced FeO content. Some segregation is observed where the sintered sample has been molten for a short period of time and has not been able to homogenize and has frozen in separate Fe- and U-Zr-rich phases. This influence has to be taken into consideration for fuel debris characteristics.

In addition, phase diagrams are essentially useful to identify phase stability and phase;element distribution in the MCCI products. The TAF-ID project is ongoing to improve the base multielement systems [9,85].

14.2.4.4 Interaction with sea salt materials

An important concern on the FDNPS fuel debris is the interaction with sea salt materials because fire engines injected seawater to cool degraded fuel materials. Some questions remain outstanding, including the quality of seawater that was injected, the stage of the accident at which seawater was injected, and the temperature the sea salt materials reacted with degraded core material in the three units. Nevertheless, preliminary studies on the interaction between the sea salt materials and the degraded fuels were performed mainly in JAEA to clarify the possible impacts of the sea-water injection on molten or solidified corium [93].

Two prototypic compositions of $(U,Zr)O_2$, such as $(U_{0.4}Zr_{0.6})O_2$ and $(U_{0.15}Zr_{0.85})O_2$, were chosen such as typical composition of the cubic phase and the Zr-rich tetragonal + monoclinic phase. The sintered pellets of two compositions were crushed, and the granules were mixed with powdered sea salt materials in an alumina crucible. The sea salt powder was synthesized by boiling out the seawater taken from the sea around Tokai-mura, Japan. After heat treatment at temperatures between 1088 K and 1668 K, Ca, Mo, Na, S, and Cl were detected in the sample. XRD analysis showed the existence of NaCl, MgO, CaSO₄, and Ca uranate (Ca–Na–U–O). Fig. 14.20 indicates, as an example, the SEM image and X-ray mapping of the interaction zone in the sample heated at 1250 K. Although MgO and NaCl were deposited on the oxide granules, a small amount of Ca and Na reacted selectively with UO₂ and formed a Ca-uranate layer on the oxide.

By accumulating these data, the general tendencies on the interaction as a functions of temperature and oxygen potential are summarized in Fig. 14.21. When only the sea salt is heated at temperatures higher than approximately 1300 K, many materials are volatilized with the exception of MgO. When the mixture of the $(U,Zr)O_2$ granules and sea salt materials is heated, a unique Ca-uranate phase containing a small amount of Na is likely to be formed. Under higher oxygen potential conditions, U₃O₈ is possibly formed with Ca uranate.

14.3 Fission product chemistry at severe accident of light water reactors

In this section, FP chemistry aspects are mentioned for each region of release and transport. Each section contains both a general description of the FP behavior in views of the chemistry and the highlighted issues after the FDNPS SA. As this occurred in three units having experienced different accident progressions, it means that various chemical processes had occurred and lead to many issues in the area of FP chemistry:

- FP-release from irradiated fuel during SA conditions;
- FP chemistry in the RCS;
- FP chemistry in the containment;
- FP chemistry in containment pools and in liquid scrubber containment venting systems.

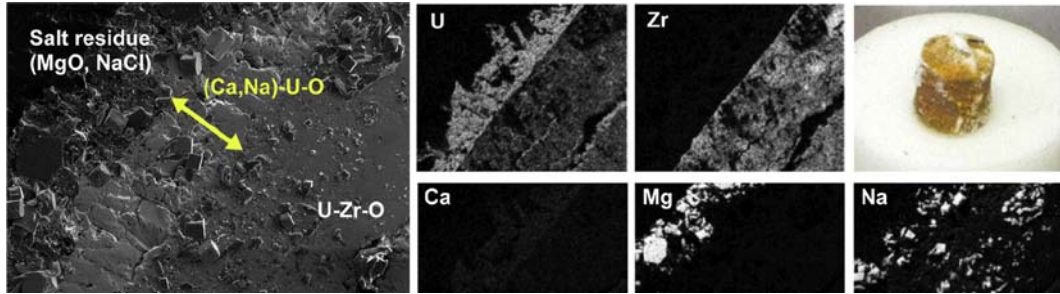


Figure 14.20 SEM image, X-ray mapping, and appearance of sim-debris pellet after reacting with sea salt materials.
Source: Quoted from M. Takano, T. Nishi, J. Nucl. Mater. 443 (2013) 32–39.

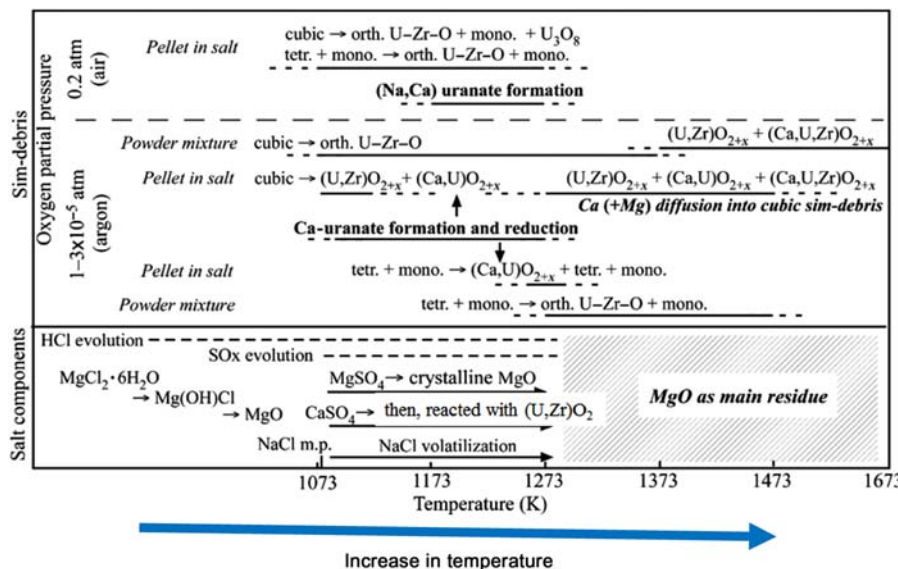


Figure 14.21 Schematic diagram for reactions and phase relationships in the sim-debris/salt system as a function of temperature and oxygen partial pressure, together with the salt components behavior.

Source: Quoted from M. Takano, T. Nishi, J. Nucl. Mater. 443 (2013) 32–39.

14.3.1 Chemistry of fission product release from irradiated fuel during severe accident

14.3.1.1 Main issues addressed before Fukushima Daiichi accidents

Basic process of fission product release from the fuel

Various kinds of FPs are generated in the fuel during reactor operation. Roughly speaking, the FP inventory is a function of fuel burn up and the fuel types [e.g., UO_2 or $(U,Pu)O_2$ (MOX) for LWR]. FPs are often categorized in terms of their half-lives, as shown in Table 14.4. Another important categorization is based on volatility of the FPs, which is also indicated in Table 14.4. The volatility is closely related to the chemistry of the FP element, and particularly to the degree of FP release to the environment. The latter categorization is important for considering the radiological impacts to the public and the environment.

Volatile FPs except for gases (Kr and Xe) are basically released from fuel pellets (or corium) by the following steps: intragranular diffusion to the grain boundary from the originally generated position inside the fuel grain, potentially precipitates into a separate phase, vaporization–condensation equilibrium there, migration to the open region through the open paths formed to the fuel surface. It is well known that most of platinum metal group (PGM; Ru, Rh, Pd), Tc, Mo, and alkaline earth (Sr, Ba) elements exist in the fuel according to their thermodynamic properties,

Table 14.4 Categorization of fission products (FPs) for the light water reactor accidents [1].

Active in the short term		Active in the medium term		Active in the long term	
FP	Half-life	FP	Half-life	FP	Half-life
Kr88	2.8 h	Zr95/Nb95	64/35 days	Kr85	10.7 years
Sr91/Y91m	9.5/0.8 h	Mo99	2.8 days	Sr90	28.6 years
Sr92/Y92	2.7/3.7 h	Ru103	39 days	Ru106	1.0 years
Y93	10.5 h	Sb127	3.8 days	Ag110m	0.7 years
Zr97/Nb97	17/1.2 h	I131	8.0 days	Sb125	2.8 years
Ru105/ Rh105	4.4/ 35.5 h	Te131m	1.2 days	Cs134	2.1 years
I133	20.8 h	Te132/I132	3.2 days/ 2.3 h	Cs137	30.1 years
I134	0.9 h	Xe133	5.2 days	Ce144	284 days
I135	6.6 h	Xe133m	2.2 days	Eu144	8.6 years
Xe135	9.1 h	Ba140/ La140	12.8/1.7 days		
Ce143	1.4 days	Ce141 Ce143 Nd147 Np239	32 days 1.4 days 11.1 days 2.43 days		
Key	XXX	Fission gas	XXX	Nonvolatile FP	
	XXX	Volatile FP	XXX	Actinide	

mainly as alloy precipitates (σ -phase or 5-metal precipitates) for PMG, Tc, and Mo, and complex oxides for the alkaline earth, respectively. Zr can be included in both phases according to the chemical conditions [e.g., $(\text{Ba}, \text{Sr})\text{ZrO}_3$ perovskite or gray phase observed in fuels]. Similarly, Cs can exist in other phases, such as Cs_2UO_4 , Cs_2MoO_4 , and CsI [94]. The important point is that the precipitates are in equilibrium according to the local chemical conditions surrounding the FPs, that is, temperature, atmosphere (local oxygen potential) and available elemental quantities, which vary during accidental conditions. This can cause different release behavior of some FPs in different fuel types (e.g., UO_2 or MOX) and burn up in the accident. The volatilities of some FPs are very sensitive to the oxidation-reduction conditions that vary during the accidental progression, such as a change in the $\text{H}_2\text{O}/\text{H}_2$ ratio and occurrence of air ingress. Such FPs having variable volatility are described later.

Attention should be paid to the chemical trapping phenomena of FPs by the neighboring cladding materials before being transported to the open space in the RPV. As an example, the volatile FPs; Te and Sb are known to be trapped by the Sn component in the Zry cladding.

Release behavior of fission products that are sensitive to the oxidation-reduction conditions

The release behavior of the PMG FPs (i.e., Ru, Rh, and Pd), Tc, and Mo and of the alkaline earth metals (i.e., Sr and Ba) is known to be sensitive to the oxidation-reduction conditions. As mentioned in the “Basic process of FP release from the fuel” section, these elements as well as Zr, form a precipitate made of Ru–Rh–Pd–Tc–Mo alloys and complex oxides [e.g., $(\text{Ba}, \text{Sr})\text{ZrO}_3$], respectively. The release of Sr and Ba are promoted under a reducing atmosphere causing the formation of volatile metallic species, while their oxides formed under steam atmosphere are low-volatile species. Results of the VERDON-1 FP release test from UO_2 fuel have shown no correlation between remaining Zr and Ba in the fuel, which would be caused by the selective release of Ba from the Zr–Ba-complex oxide precipitate [94,95]. The release of Mo is accelerated under oxidizing atmospheres resulting from the formation of highly volatile oxides such as MoO_3 . In the Phébus FPT2 test, Mo was not observed in the alloy precipitate in the upper part of the fuel in spite of the remaining Ru [96]. This indicated that different oxidative conditions in steam and air are required for two important FPs: Mo and Ru (details of the Ru behavior are mentioned later). The Mo speciation is uncertain, as Mo is multivalent and has a high chemical affinity for Cs. This causes the possible formation of cesium molybdates (i.e., Cs_2MoO_4). Moreover, the formation of a complex oxide species of Mo and I (i.e., I_2MoO_2) is also predicted [97]. Such complexity as seen for Mo-containing species makes evaluation of the release and transport behavior of Cs and I difficult. Thus the chemistry of Cs and I must be treated in the Cs–I–Mo–O–H system. Although it has been considered that released Cs vapor species take thermodynamically possible form of CsOH and CsI [98], a separate-effect test that vaporized a mixed powder of CsI and Mo under H_2O atmosphere implied the potential formation of Cs_2MoO_4 at the release stage [99]. As shown in the next section, it is considered that the chemical reaction between Cs and Mo mainly occurs during transport through RCS.

Among PMG FPs, Ru is important in view of its potentially high radiological impact under air ingress situations in a PWR SA. Ru is categorized as low-volatile element under the oxygen potential conditions of a steam atmosphere of an accident, when the chemical forms are Ru, RuO , and RuO_2 . However, once the higher oxygen potential conditions than those in steam appear following air ingress, then Ru can form the highly volatile vapor species RuO_4 . This feature leads to a complex behavior of Ru not only for the release stage from the fuel but also for the transport stage both through the RCS and in the PCV [96,100,101]. As for the Ru release from the fuel, vaporization as RuO_4 or remaining in the fuel as Ru/RuO_2 depend on the local oxidation-reduction conditions, namely, the oxygen-to-metal (O/M) ratio of the fuel and the kinetics of the O/M ratio change [102]. As an example of such O/M effects, less Ru release from MOX fuel than that from UO_2 fuel was observed in the VERDON-2 test under air ingress conditions. In the VERDON-2 test the MOX fuel was heated up for the investigation of FP release and transport behavior [103]. It was mentioned that the effects of low oxygen

potential of the MOX fuel are the main cause for the less Ru release. On the other hand, as an example of the effects of kinetics of the change in the O/M ratio, the cladding can play a role as an oxygen barrier against fuel oxidation. FP release test using fuel pellets surrounded by Zry cladding has shown a low Ru release rate compared with that without cladding [102]. This would be caused by the suppression of UO₂ oxidation, namely, increase of O/M ratio, by the fully oxidized Zry barrier, not by that of nonoxidized Zry, since the oxygen diffusion in the oxidized Zry was lower than that in Zry. Thus Ru release from the fuel is very complex phenomena and a further investigation is being conducted.

14.3.1.2 *Highlights from Fukushima Daiichi accidents (issues deserving further attention)*

There are several chemistry-related specific features for the SA of FDNPS. Among them, possible effects of the sea-water injection into the degraded core and B₄C control blade degradation are described here.

Alteration of release behavior of non/low-volatile fission products by sea-water injection

A thermodynamic assessment of the existence of sea-water component elements (Na, Cl) has been made for the investigation of alteration in FP speciation [104]. Results indicated a possibility of formation of volatile sodium/chlorine complex species (i.e., CsCl, Na₂MoO₄, and SrCl₂). It is worth noting that Sr might form highly volatile SrCl₂. Although it has been observed that Sr release and transport could be enhanced under a hydrogen reducing atmosphere [105], the formation of SrCl₂ might cause a similar situation. One possible phenomena induced by the release of SrCl₂ from the fuel is chemical trapping of Sr by the neighboring Zry cladding by the formation of the stable compound SrZrO₃ [106]. This might have an impact on the Sr distribution in the FDNPS debris, since Sr has been considered to accompany the fuel component, not the molten cladding component that can melt and relocate downward in the core prior to the fuel. The other possible phenomenon is the chemical reaction of SrCl₂ vapor with steel structural materials. Sr could react with the Si component in the steel to form Sr silicates considering their stability [107]. Another aspect regarding Sr for the FDNPS is the long-term source term via the aqueous phase. In the FDNPS the debris cooling system will be operating for the order of tens of years. The cooling water circulates from the degraded core to the R/B and turbine building via the PCV. Sr can be relatively easily transported to the outside of the RPV, since the leaching of Sr is considered the same level as that of Cs [108]. Therefore the long-term Sr source term monitoring will be mainly dependent on maintaining good cooling and ground-water decontamination to avoid aqueous phase transportation, which will be more important than vapor phase transport.

Boron release kinetics from degraded B₄C control blades

As described in [Section 14.2](#), the heterogeneous relocation of the fuel assembly and B₄C control blade should take place in BWR SAs. It has been considered that the

melting and relocation of the B_4C control blade occur prior to that of the UO_2 and Zry fuel assembly due to the lower eutectic temperature between B_4C and SS. The kinetics of this B_4C -SS interaction has also been established [109]. Although liquefaction of the fuel assembly by the attack of molten control blade materials has been investigated [49], vapor phase reaction between released B from the degraded control blade and released FPs should occur in the upper part of the RPV. The probable form of boron is considered to be BO_2 or H_3BO_3 [110]. Considerable work on the reaction of B_4C with SS and of these interacted (Fe, Ni) borides with steam, O_2 or Ar has been performed previously, and considerable boron oxides can be produced at an enhanced rate compared to steam- B_4C reactions [45].

In order to further evaluate the abovementioned reactions for the quantitative modeling, B release behavior from the molten control blade, in addition to that from intact B_4C , should be performed. However, boron release behavior could be reduced because of the low-temperature conditions in the lower part of the core, to where most of the molten control blade materials together with intact B_4C will have probably relocated [111]. Nevertheless, according to a first result of a study on the melting and relocation behavior of the fuel assembly and control blade conducted after the FDNPS SA, it was observed that solidified alloys of B_4C -SS were retained at a relatively high elevation, thus at relatively high temperatures, in the core [49]. As the release behavior of B vapor species from the solidified B_4C -SS alloys has hardly been investigated, this should be confirmed for accurate Cs chemistry determination in the presence of B during the transport stage.

14.3.2 Fission product chemistry in reactor coolant system, gas phase, and interactions with structure surface

14.3.2.1 Main issues addressed before Fukushima Daiichi accidents

The FP vapor species released from the fuel at high temperature are transported finally to the low-temperature PCV through the RCS. As the temperature decreases along with transport, condensation of the FP vapors to form aerosol or to deposit on the structural materials occurs, as schematically shown in the Fig. 14.22. Various FP chemistries among vapor, condensed liquid/solid aerosols, and structural materials during transportation should therefore be taken into consideration. In this section the main chemical aspects of the two systems, $Cs-I-Mo-O-H$ and $Ru-N-O-H$, are described in a representative temperature range of the RCS, from over 1000 K to 400 K. Note that the FP chemistry is affected by kinetics (especially at less than 1000 K) as well as by the thermal hydraulic conditions. This kinetic effect makes the FP chemistry quite complex. Thus it is difficult to fully understand the FP chemistry by preparing a full data set for all the chemical reactions taking place. Realistic approaches have been made by assuming likely FP chemical species obtained by analyses of the FP release and transport experimental results, such as those from the Phébus FP experiments.

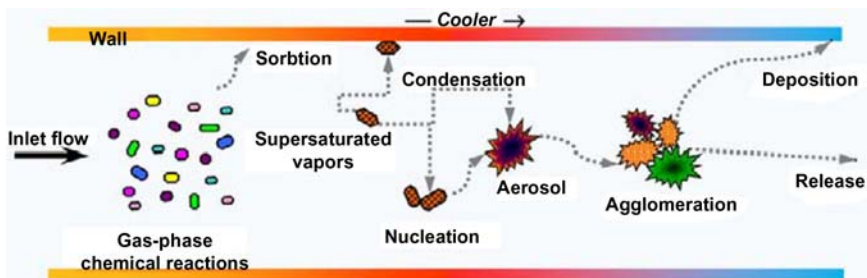


Figure 14.22 Schematic view of FP transport behavior during the transportation through the reactor cooling system [1]. *FP*, Fission product.

Cs—I—Mo—O—H chemistry during transport in the reactor coolant system

Regarding the chemistry of Cs—I—Mo—O—H system, an analysis has suggested the Cs_2MoO_4 as a possible vapor species released from the fuel [16]. Other analyses on Phébus FPT0 and FPT1 have shown deposits of low-volatile Cs_2MoO_4 in the hot leg region and its decomposition into CsOH and MoO_3 vapors to revaporize [112].

Recently basic research on the chemistry of Cs—I—Mo—O—H has been conducted by using separate-effect test setups. Chemical effects of Mo vapor on the gas I formation have been investigated in the framework of the CHIP program [101]. In this test, mixed compounds of CsI and MoO_3 with various Cs/I/Mo ratios were vaporized up to around 1800 K and then transported downward along the temperature gradient to around 400 K under a steam atmosphere.

Chemical analyses of deposits in the lower temperature region have shown the formation of Cs—Mo—O compounds having various chemical compositions. In addition, the formation of gaseous I_2 was observed in solutions of vapor trap device positioned after the outlet of the test setup. The experimental result and its analysis by SOPHAEROS code indicated chemical trap effects of Cs by Mo and following HI gas formation, respectively.

A similar test was also made by injecting I_2 gas, CsOH and MoO_3 vapors as precursors [113]. Results were compared with those using CsI and MoO_3 compound precursors to elucidate the feature of gaseous I_2 formation. It was concluded that the fraction of gaseous I_2 increased by Mo in oxidic form reacting with the CsI to form cesium molybdates (e.g., Cs_2MoO_4) and releasing gaseous I_2 under a steam atmosphere, while unreacted CsI aerosol was dominant under a reducing atmosphere. The SOPHAEROS analysis well reproduced this gaseous I_2 formation caused by the chemical reactions in Cs—Mo—O—H system, since the formation of Cs_2MoO_4 occurred at the high temperatures where the I—O—H reaction can rapidly reach the equilibrium state. However, discrepancy between the experiment and the analysis was seen in the valence state of Mo in the Cs—Mo—O-deposited compounds. This discrepancy suggested to be caused by insufficient thermodynamic data of cesium molybdates. Mo can possibly form various compositions due to the multivalence of Mo.

Ru—N—O—H chemistry during transport in the reactor coolant system

As described in [Section 14.3.1](#), Ru chemistry during transportation in the RCS region is very important mainly in terms of the RuO_4 deposition as RuO_2 and effects of other FPs on the RuO_4 transport [\[114\]](#). A recent review on RuO_4 transport indicated that some catalytic effects of the structural material surface and the effect of previously deposited FPs (e.g., RuO_2) on the decomposition of gaseous RuO_4 (or possibly RuO_3) to deposit RuO_2 or form RuO_2 aerosol [\[115\]](#).

The Phébus FP test results showed enhanced deposition at the region where the temperature gradient was steep. Separate-effect tests for Ru transportation using a RuO_2 compound precursor have been made under various atmospheres (air, N_2 , O_2 , and NO_2) with/without Ag/AgNO_3 particles as FP aerosol simulant [\[116\]](#). The fraction of gaseous RuO_4 increased under the N_2 and O_2 mixed atmosphere with a small fraction of NO_2 , which suggested this countered the oxidation of RuO_3 to form RuO_4 by a reduction of NO_2 . On the other hand the presence of steam and Ag aerosols decreased the fraction of RuO_4 drastically. This suggested promotion of Ru transportation in the lower temperature region in the form of RuO_2 aerosols or particles.

A similar study for the effect of aerosols on the Ru transport has also shown an interesting chemical effect, in addition to the promotion of gaseous Ru oxides to the lower temperature region [\[114\]](#). In this study, Ru transport tests were carried out by heating RuO_2 and CsI precursor compounds from 1300 K to 1700 K. Results showed that higher heating temperatures, namely, larger fractions of CsI aerosols generated by the higher CsI vaporization rate, promoted transportation of gaseous Ru oxides to the lower temperature region. In addition, the separation of I from CsI and oxidation to form iodine oxide compounds were suggested, and it would be linked to the reductions of RuO_4 to RuO_3 and RuO_3 to RuO_2 .

Remobilization of fission product deposits

As partly shown in the previous section, revaporation of deposits is an important issue for the evaluation of source terms in the late phase of SA, especially those of the volatile and gaseous FPs, such as CsOH , I_2 , HI , and RuO_4 . The revaporation can be induced by a hotter flow, by gas components different from those at the deposition such as by air ingress, and by increase in temperature of deposits by decay heat.

Regarding the revaporation of RuO_2 deposits, this is caused by air flow over the deposit surface leading to oxidation of RuO_2 to form RuO_4 [\[115\]](#). As released Ru from the fuel is reported to condense and deposit in relatively hotter regions in the RCS to form RuO_2 deposits, revaporation of the RuO_2 deposits should be accurately evaluated for the source term in the late phase.

As for the I revaporation, the VERDON-2 showed an interesting result in relation with the air ingress effect. FP release and transport from a MOX fuel were investigated under air ingress conditions in the VERDON-2 test. Almost complete revaporation of deposited I at around 600 K, transportation to the lower temperature regions, and deposition again at around 400 K were observed [\[103\]](#). On the other hand, it is worth noting that there is no transportation of revaporized Ru

toward the lower temperature regions. The main cause would be the lower release rate of Ru from the fuel due to the low oxygen potential MOX fuel, as described in previous sections.

A separate-effect test setup was constructed for detailed investigation of deposit revaporization behavior by using FP-deposited samples taken from the upper plenum part of Phébus FPT3 test [117,118]. Cs revaporation behavior was monitored by an online gamma-ray measurement system during the revaporation test. It was seen that Cs started to revaporize at around 813 K, and the air and reducing atmospheres caused a rapid revaporation. Te and Mo were also confirmed as FPs capable of revaporation. Further testing showed a similarly high Cs revaporation from irradiated Phébus FPT4 upper plenum deposits for both reducing, steam and oxidizing atmospheres. This together suggests that the original Cs species in the deposit reacts with other FP's or the atmosphere to produce the vaporizing species and that maybe different species are produced in different atmospheres [119].

14.3.2.2 Highlights from the Fukushima Daiichi accidents (issues deserving further attention)

Chemical impact of boron on the Cs—I—Mo—O—H system

Chemical effects of boron at the RCS region have been studied together with those of Mo, as in the Cs—I—Mo—B—O—H system. It has been found that similar effects were expected for B as those for Mo, as a whole. B is considered to be released as boric acid vapors, HBO_2 and H_3BO_3 , under the steam atmosphere mainly by the reaction of H_2O with B_2O_3 formed on the surface of B_4C or B_4C —SS mixture of the control rods. Several tests have shown boric acid deposition in the RCS region at relatively high temperature and demonstrate the extent of boric acid formation possible in SAs.

A blockage mainly made from the boric acid was observed in the Phébus FPT3 test [120]. While it was clearly restricting all transiting material physically, the blockage could also trap the Cs vapor and aerosols chemically, which can alter the FP transport behavior to the PCV. For example, it could consequently increase the fraction of gaseous I_2 transported to the PCV building. A separate-effect test has investigated mainly the chemical aspects of B effects by heating a mixture of CsI, B_2O_3 , and Mo precursors [121]. By the presence of B_2O_3 in the precursor, it was observed that most of iodine would transform into a gaseous form, as in the case of Mo addition (the Mo oxidized as MoO_3 appears to react with the Cs and release iodine). Besides, a glassy boron oxide-containing deposit was generated into which trapped Cs and a part of iodine but caused the release of the remaining iodine as gas. Thus B could have a certain impact in addition to Mo on the Cs and I chemistry during RCS transport. For example, the deposition of Cs as cesium molybdates could be affected in the presence of B by the comparable formation of cesium borate, which can affect the Cs distribution in the RCS region.

The B chemical effects have become more important after the FDNPS SA. The important point for the B effect evaluation is, as mentioned in Section 14.1, there is much more B species available in the SA and in a more localized form from the

BWR B₄C control blade. It could have led to different B species from those produced in an PWR accident (e.g., Phébus FPT3 with a more homogeneous geometry).

Basic phenomena of the revaporization from a CsI deposit were investigated in the presence of B vapor using a small test device having a temperature gradient tube along the FP transport path [122]. Revaporization of I was observed from the CsI deposited before the flow of B₂O₃ vapor or aerosol under Ar atmosphere. They found a reaction between B₂O₃ vapor/aerosol and CsI deposits caused the decomposition of CsI (observed by X-ray photoelectron spectroscopy) to form gaseous species, probably CsBO₂ and I₂ [123]. As such revaporization might be a considerable source term in the late phase of BWR SA sequence, further tests are being conducted using a similar experimental setup under steam atmosphere [124,125].

Cs chemisorption phenomena

In an effort toward the decommissioning of FDNPS, determining the distribution of Cs is of crucial importance in terms of considering the debris removal strategy. The localization of Cs in the upper part of RPV has been estimated by several site surveys [126]. Formation of stable Cs compounds by Cs chemisorption on the SS structures, such as the separator and dryer devices in the RPV, is possible. Cs chemisorption has been studied after the TMI-2 accident, and it was suggested from the elemental distribution result that Cs could be reacted with the Si component in the SS to form Cs silicates [127].

Although an Arrhenius-type Cs chemisorption model has been established incorporating a linear relationship for the Cs chemisorbed amount with the Cs vapor species concentration, it is insufficient for the FDNPS application. A renewed fundamental study for the investigation of Cs chemisorption has, therefore, been conducted. [128,129]. Cs chemisorption phenomena have been investigated under various conditions of temperature, atmosphere, CsOH vapor concentration, and contents of Si component in the SS at two Si contents, normal (about 1 wt.%) and high (about 5 wt.%). The normal levels showed Cs and Si association only at the subsurface level, but at high levels a near surface phase of SiO₂ was implied. In all cases, it was found that Cs reacted with Si to form various Cs silicates with and without Fe, for example, Cs₂Si₄O₉ and CsFeSiO₄, in the oxidized surface layer of SS, as shown in Fig. 14.23.

It is considered that precipitated SiO₂ appeared during the oxidizing process of the SS surface layer to react with Cs coming from the vapor phase [130]. Regarding the stability of Cs silicates formed, it is reported that the Cs silicates decompose at above 1300 K to release Cs under H₂-containing reducing atmospheres [131]. Besides, Cs could react with the Mo component, if contained in the SS, to form Cs molybdates [132]. On the other hand, other studies reported that the Cs molybdates vapor formed by the chemical reaction between Cs and Mo FP should induce Cs chemisorption on the SS at higher temperatures like as the case of CsOH vapor [121]. Although the high Si–content steel is not normal in the reactor, it nevertheless shows that if there are other sources of SiO₂ (e.g., concrete), then this can be a source of Cs absorption and influence the Cs and other FP-chemistry.

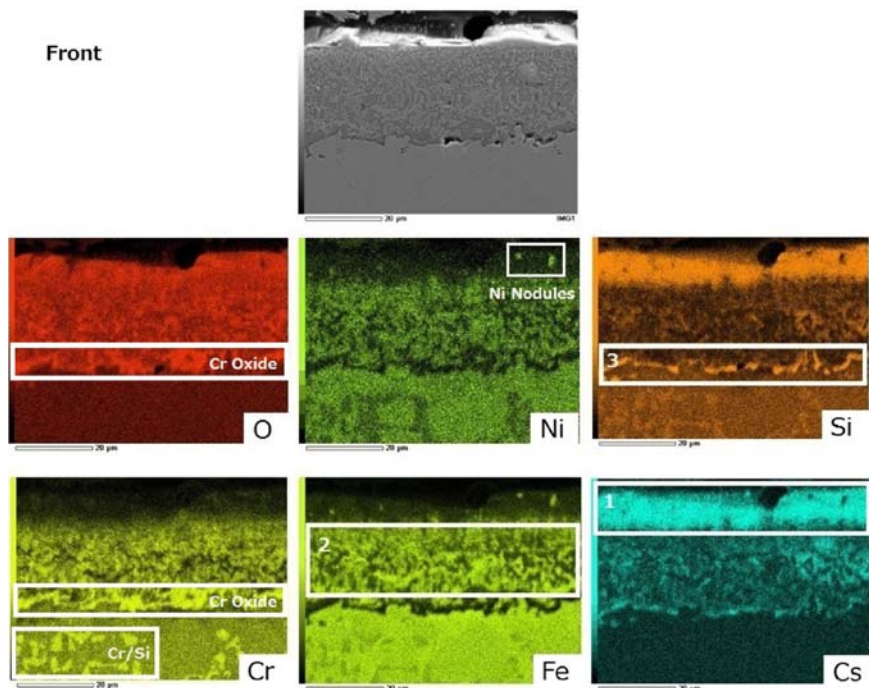


Figure 14.23 Elemental distribution on the surface of Cs chemisorbed stainless steel type 304 (5 wt.% Si) [128].

Other issues

Many studies for detailed analysis of Cs containing radioactive particles released from the FDNPS to the environment are being conducted. There reported to be mainly two types of particles having different diameters, either a few μm in size and hundreds of μm in size. It is difficult at the present to use this information for the FDNPS accident, such as formation mechanisms of the particles, chemical aspects inside the 1F reactor, and identification of 1F units derived. These challenges should become more effective when the analyzed information is combined with the evaluation of SA progression by using, for example, SA analysis codes.

Among the particle analyses work, it is interesting for the FP chemistry that the smaller particles with several μm diameter were revealed to be made of a silica matrix [133]. Although the Si source in the reactor has not been identified yet, it is of importance that Si should be added to the chemistry of Cs—I—Mo—B—O—H system, considering the abundance of Si in the reactor structural materials such as concrete, a minor component in the steel and so on. This feature would be further investigated along with the progress of the sample analyses for the FDNPS decommissioning work.

The other important issue, as mentioned in Section 14.3.1, is the long-term source term released in cooling waters by debris leaching. Especially Sr, Ba, and

long half-life nuclides such as actinides would be more released with time. A key parameter determining the slow release of FP and actinides from the corium matrix in water in the long term is the oxido-reducing conditions [134]. Indeed, the corium matrix dissolution is likely to be much higher under oxidizing conditions since the solubility of UO₂ in water is much higher under oxidizing conditions. This issue is important for waste management since categorization of the wastes in terms of their radioactive inventory should be made for effective waste management. Namely, ratios of activities of various radioactive nuclides to that of Cs-137 are different from waste to waste, that is, contaminated water, rubbles, and secondary wastes [108]. Evaluation of the FP chemical behavior in the aqueous phase would help such categorization.

14.3.3 Fission product chemistry in containment, gas phase, and interactions with containment surfaces

Seeing that temperatures in a Nuclear Power Plant (NPP) containment in an SA would hardly exceed 200 K, FPs would be expected to be present in the containment in condensed forms and as aerosols for most of them, with iodine and ruthenium being exceptions, as they may be present in significant amount as gaseous species in some accident scenarios,⁹ as discussed later in this section.

14.3.3.1 Chemistry aspects affecting the formation of fission product aerosols in the containment and related potential radioactive releases

Aerosols are addressed in some detail in the first place as their presence in the containment affects containment chemistry, in particular that of iodine, and eventual radioactive releases outside the containment (through containment leaks or during containment venting). Of particular interest is their nature, composition, and how they distribute between water pools and deposits on exposed nonsubmerged surfaces in containment. Chemistry in water pools is addressed in Section 14.3.4. Radioactive aerosols deposited on exposed surfaces are discussed below in particular as they may be a “delayed” source of radioactivity emission in the containment gas phase when remobilized after deposition or if unstable under thermal and radiation loads, such as, for instance, iodine aerosols releasing gaseous iodine.

Phébus FP tests have provided one of the most comprehensive sources of information on the nature of aerosols that can be expected in a containment during and following an in-vessel reactor core degradation phase [135], due to the representativeness of material inventories, highlighting their complex structure as they were shown to be 3–4 µm size agglomerates of multicomponent particles where the

⁹The word “significant” relates here to potential radiological consequences. One has to bear in mind that even if gaseous species fractions are low in the containment (say of the order of a percentage of their containment inventory), they may represent persistent sources of radioactive releases during the hours or days following the fuel degradation.

mass was dominated by Cs and Mo¹⁰ and by structural materials¹ (Sn, B in FPT3 performed with a B₄C control rod; Ag, Cd, In, and Sn in the FPT1 and FPT2 tests performed with a Ag–In–Cd control rod, Sn originating mostly from the cladding material). These aerosols also contained small fractions of other FPs such as a few percentage of Rb and Te and less than 1% of I, Ba, Ru, of fuel (U), and of cladding (Zr) materials. No major changes in nature and composition were observed by online gamma spectroscopy monitoring with progress in fuel degradation and melting during a test and with changes of carrier gas content (either steam-rich or H₂-rich) suggesting that an average type of aerosol reached the containment. When in containment, these aerosols deposited by gravitational settling on the exposed containment floor and the sump water pool surfaces, by diffusiophoresis on surfaces where steam was condensing (condensates eventually drained into the sump) and by deposition (physisorption) on dry surfaces. These deposition phenomena determined the aerosols and FP distribution in the containment after the in-vessel core degradation phase.

Even if Phébus tests only addressed specific accident scenarios, PWR-like compositions, and the in-vessel release phase, one can easily infer that in any accident, aerosols resulting from in-vessel degradation will mostly be composed of Cs and structural material present inside the vessel [other elements than in Phébus may however contribute significantly depending on reactor core material inventories, such as Si, and the nature of coolant (e.g., raw or seawater) used to cool down the damaged core]. These aerosols may also convey FPs other than Cs. The Mo contribution and the eventual presence of Cs₂MoO₄, as inferred from Phébus tests, will be significant only if conditions are oxidizing enough in-vessel for Mo release to be large [136] (Cs₂MoO₄ is then calculated in thermodynamic evaluations as the most probable species in RCS and containment [137]). When cesium molybdates compounds are not formed, cesium borates or silicates may form instead in the RCS and be conveyed to the containment. Cesium silicates compounds have been identified in TMI-2 [138].

It is also interesting to note that Te is expected to be present in significant amount if conditions prevailing in-vessel resulted in most of the Zr being oxidized, otherwise Te should be captured by Zr and remain mostly in-vessel [139]. As for Ru, only small amounts of it are expected to be conveyed with aerosols, as Ru is only released from the fuel when the fuel itself has been significantly oxidized, reaching oxygen over stoichiometry in the fuel matrix. Releases from the fuel can occur under steam, or air atmospheres, mainly as gaseous RuO₃ at high temperature [140].

VERCORS tests, and more recently VERDON tests, have shown that irradiated fuel can release high levels of Ru (e.g., up to 65% in VERDON tests [141]). The

¹⁰ Cs and Mo were present in similar proportions and represented about 40% of the aerosol mass in the containment in the FPT1 and FPT2 tests, performed with an Ag–In–Cd control rod, and up to 50% of the mass in the containment in the FPT3 test, performed with a B₄C control rod.

¹¹ Structural material represented about 50% of the aerosol mass [Ag (16%), Cd (15%), In (11%), and Sn (7%)] in the containment in the FPT1 and FPT2 tests and about 20% of the aerosol mass [Sn (12%) and B (10%)] in the containment in the FPT3 test.

highest release was under steam or air atmospheres and for high burn up UO₂ fuels. Significant deposition of the released Ru is expected to occur in the core structures and upper plenum or at the core exit, as integral and analytical experiments suggest, with formation and deposition of the most stable RuO₂ oxide. Significant fractions of Ru can also be transported further downstream in the primary circuit as RuO₂ aerosol and can deposit in the primary circuit surfaces. There is then the possible remobilization of Ru deposits as RuO₂ aerosols or revaporation as tetraoxide RuO₄ (RuO₄ being more stable at lower temperatures), which may reach the containment in significant amounts [140,142]. This is currently being experimentally studied in the OECD/NEA STEM2 program [142].

Aerosols deposition phenomena and the resulting overall aerosol distribution in the containment following an in-vessel degradation phase can be rather well predicted using classical aerosol deposition models [143] with realistic hypotheses on the aerosol distribution size and disregarding hydroscopic effects. Differences in the hydroscopic character of Cs compounds, for example, whether in highly hydroscopic form (e.g., CsOH) or forms with lower hydroscopic character (e.g., molybdates or silicates) may affect significantly the aerosol agglomeration or deposition in water pools. The aerosol chemistry will also play a role for deposit exposed to irradiation dose and thermal loads (including possible hydrogen combustion in an air-filled containment). A known example is the thermal or radiolytic instability of iodine-containing deposits which can decompose to release gaseous iodine and organic iodine forms and eventually contribute to “delayed” radioactive releases. These phenomena are currently being experimentally investigated in the OECD/NEA STEM2 [142] and THAI3 [144] programs. Contributions of these decomposition phenomena to potential iodine releases during an SA have still to be assessed but could be significant in the hours and days following fuel degradation.

Aerosol formation from a molten corium–concrete pool after RPV rupture during MCCI was investigated in the 1990s in the ACE phase C and BETA tests and in the OECD/MCCI and EC Framework Programs (LPP and MP projects) [143]. However, efforts regarding further model development and validation of aerosol formation and related chemical aspects have been limited, and there is currently little research activity in this area since it is generally admitted that most volatile FP releases should have occurred during the in-vessel degradation phase. However, depending on the extent of oxidation of corium material at the vessel rupture, significant release of some FP (e.g., Mo and Te) could still occur during the MCCI phase upon further material oxidation. Knowledge of aerosols amount, size, and composition as well as their formation during the MCCI phase is rather limited and warrants further investigation, in particular for situations where water is used to cool the corium ex-vessel.¹² Indeed, large steam masses produced by fuel–coolant interaction may then favor FP entrainment as aerosols and droplets in the containment atmosphere and result in containment pressurization with potential added radioactive release to the environment through containment leaks.

¹²This is currently a mitigation measure for many NPPs.

14.3.3.2 Iodine and ruthenium chemistry in containment gas phase and how it may affect radioactive release

Iodine and ruthenium may, depending on the accident scenario, form significant fractions of gaseous species in the containment: I_2 , HI, HOI, iodine oxides (I_xO_y), and organic iodides (Org-I) compounds for iodine and RuO_4 for ruthenium [142]. Knowledge of the amount and speciation of iodine and ruthenium gaseous species in the containment and of their evolution with time is of particular importance as iodine and ruthenium isotopes may contribute importantly to the radiological consequences, in the short term mainly, if continuously released through containment leaks and/or during containment venting. Related to venting, iodine oxides and RuO_4 stability in containment and the efficiency of retention with existing filters on venting lines are still under investigation in 2019 [142]. Org-I formation mechanisms and filtration have been the subject of large research efforts as Org-I retention under SA conditions is particularly challenging, much more for instance than I_2 retention.

Phébus tests have shown that significant fractions of gaseous iodine may reach the containment during the in-vessel degradation phase from few percentage in tests with a Ag–In–Cd control rod (FPT0, FPT1, and FPT2) up to 80% in the FPT3 test with a B_4C control rod [145,146]. The chemistry in the RCS played here a major role and was investigated in detail in the ISTP CHIP program [137,142] as presented in Section 14.3.2. Phébus tests also showed that in the containment, gaseous iodine fractions reached a low steady-state level after about a day (of the order, at most, of 0.1% of the initial inventory), depending on the test scenario and experimental phases, Org-I compounds represented between 20% and 80% of the gaseous iodine [145,146].

Again, Phébus tests addressed specific PWRs-like accident scenarios where gaseous iodine concentrations were efficiently reduced by different mechanisms: mostly capture by Ag–iodine reactions in FPT0 and FPT1 tests [145] (heterogeneous reactions of molecular iodine I_2 with Ag-containing particles in the containment sump and, possibly, in the atmosphere), with added hydrolysis reactions inhibiting iodine production at basic pH in FPT2 [145], capture of molecular iodine by exposed paints in FPT3 [146]. All these mechanisms reducing gaseous iodine concentrations in containment have been investigated in detail and are modeled in SA analysis codes [147,148]. pH effects (hydrolysis reactions) in sumps on iodine volatility have long been studied and are well modeled [149]. One more delicate part is to predict the pH evolution in sump and pools in an SA, addressing the complexity of material inventories added to water pools. Modeling of heterogeneous reactions of iodine with aerosol particles and paint is also more delicate if one wants to address specifically the complex structure of aerosols (i.e., their multicomponent nature) and of paint where it may be necessary to account for the efficiency of these mechanisms.

Phébus FP tests highlighted the importance of physicochemical phenomena in the containment atmosphere as sources of gaseous iodine [145,146] when it was earlier thought that the sump pool was the main source of gaseous iodine with a

strong effect of radiolytic and hydrolysis reactions depending on the sump pH, a basic pH strongly reducing gaseous iodine production by radiolysis in water [149] as will be further discussed in [Section 14.3.4](#). Following Phébus FP, research then focused on gas-phase phenomena

- interaction of gaseous I_2 with paints and gaseous organic compounds (e.g., methane) and organic iodides (Org-I) production [142,150];
- interaction of gaseous I_2 with reactive aerosols such as Ag particles [151];
- iodine-oxide (I_xO_y) particles formation/decomposition [142,152];
- gaseous iodine release by decomposition of iodine aerosols deposited on exposed surfaces by heat, humidity [153], and radiation-induced [142] phenomena.

when it essentially earlier focused on water pool chemistry.

The research was recently conducted in international initiatives such as the ISTP conducted by IRSN in the EPICUR facility [142], the OECD/NEA BIP-1 and BIP-2 [154] series conducted by Canadian Nuclear Laboratories, the OECD/NEA THAI-1 and THAI-2 [151] series conducted by Becker Technologies, and the OECD/NEA STEM [142] program conducted by IRSN. [Fig. 14.24](#) illustrates results obtained in the STEM experimental program that were used for the development of chemical models of Org-I formation from painted surfaces that adsorbed iodine and models of decomposition of deposited CsI aerosols under radiation, both further discussed later in this section.

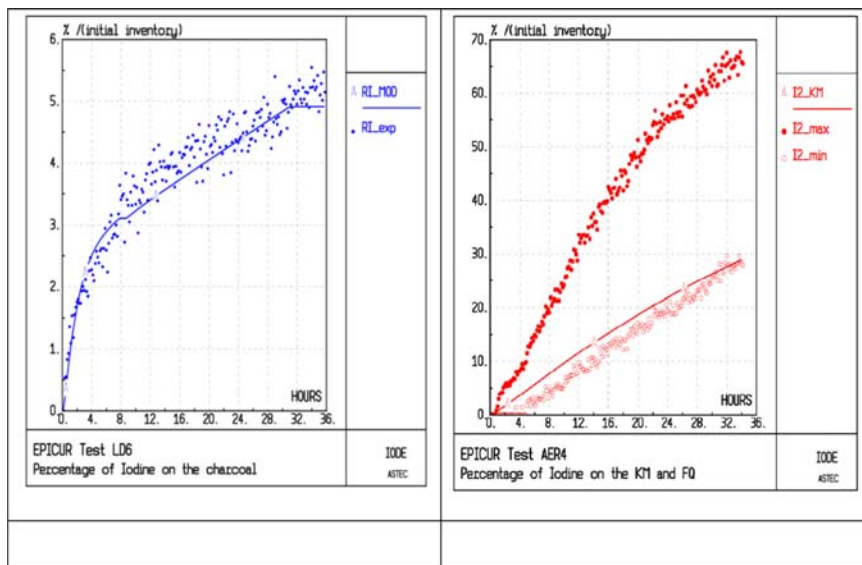


Figure 14.24 Example of IRSN EPICUR test results (STEM program) showing (left) kinetics of Org-I production under radiation from a painted coupon that adsorbed iodine and corresponding deduced modeling for the IRSN ASTEC code and (right) large gaseous I_2 release from surface-deposited CsI aerosols under irradiation.

Source: Reproduced from A.-C. Grégoire, et al., Ann. Nucl. Energy 101 (2017) 69–82.

Related to Ru behavior in containment, the amount of gaseous RuO_4 in containment will very much depend on the gas composition in the RCS and the containment—whether it favors RuO_4 revaporization from RCS surfaces and its stability under conditions prevailing in the containment [142,155]. Even if only of the order of 1% of the Ru inventory is conveyed as gas in containment, it could significantly contribute to the radiological consequences in the short term if leaking to the environment. Experimental and theoretical investigations are ongoing to develop models for RuO_4 revaporization, transport and reactivity in containment and its retention in filters when filtered containment venting is used as an SA management measure [142]. The objective is to complete the corresponding modeling by 2020 to assess more accurately the RuO_4 contribution to radiological consequences for SAs with significant fuel oxidation.

14.3.3.3 Focus on Org-I formation

OECD/NEA STEM program data were used to develop a detailed model of Org-I formation under radiation from painted surfaces in the containment [156]. When applied to Phébus FP test analyses, the model was shown to underestimate measured Org-I concentrations by about an order of magnitude [157]. It is suspected that a major route for Org-I formation in the containment, that is, the radiolytic formation of Org-I by the reaction between I_2 and organic radicals (formed from radiolysis of organic pollutants, such as methane, in the containment atmosphere), was overlooked. A simple model derived from Bartonicek data [158] was tested against Phébus FP data and yielded satisfactory results for calculated Org-I concentrations. Another potential effect that was not thoroughly studied is the ageing of paints (resulting both from long-term normal operation and the accident transient). Limited experimental investigations suggest that cumulative dose effects could significantly promote Org-I formation. Further experimental investigations and analytical studies are being performed since 2016 as part of OECD/NEA BIP-3 [154] and STEM-2 programs [142] to refine the modeling of Org-I formation. The objective is to complete the corresponding modeling by 2020 to assess more accurately the Org-I contribution to radiological consequences in SAs.

14.3.3.4 Focus on iodine aerosol stability

It was shown in the STEM program [142] that iodine aerosols (IOx , CsI , and CdI_2) deposited on surfaces were not stable under irradiation and produced significant amount of gaseous I_2 (see Fig. 14.24). Preliminary iodine aerosol decomposition models under radiation were deduced from the measured data. Reexamination of Phébus FP tests analyses shows that, when overlooking aerosols decomposition processes, the calculated I_2 concentrations are largely underestimated with the exception of the short-term iodine release phase to the containment. The addition of the iodine oxides decomposition processes improves the prediction, and the measured I_2 concentrations can be matched considering other iodine aerosol decomposition processes. However, models of iodine aerosol decomposition remain uncertain as

data for iodine oxides are too scarce—effects of reactive gases, particularly CO during MCCI phases, need to be investigated—and as complex multicomponent aerosols may be formed during an accident, as shown in Phébus FP tests [135]. Further experimental investigations and analytical studies are being performed since 2016 as part of STEM-2 program [142] to obtain data for more representative conditions and to refine the modeling of iodine aerosols decomposition. Heat- and humidity-induced decomposition may also be important as shown in [153] and should be considered. The objective is to complete the corresponding modeling by 2020 to assess more accurately the effect of aerosols decomposition on iodine source term evaluations.

14.3.3.5 Radioactive material transport and deposition in the containments in the three damaged units

Despite the large research programs undertaken internationally, knowledge of FP behavior and chemistry during the Fukushima Daiichi accident remains incomplete in 2019, for the most part due to limited available information, data, and the remaining uncertainties on the accident scenarios in the three damaged units [7]. Furthermore, the accident revealed specific or unexpected features that possibly challenge knowledge available before the accident took place. In this section, we highlight some of these features focusing on how they may affect behavior of radioactive aerosols and gas in the dry-well (the wet-well is addressed in the next section).

Radioactive material transport and deposition in containment in the three damaged units are addressed here as they should affect physicochemical phenomena. As long as the integrity of the RPV and the steam circuit (second barrier) were maintained, radioactive material was conveyed to the dry-well after scrubbing through the wet-well (pressure suppression pool). Scrubbing and chemistry in the wet-well are addressed in Section 14.3.4. After the failure of second barrier and depending on the extent and location of the breach, radioactive material had possibly been directly released to the dry-well. Considering current knowledge of the accident scenarios in the three damaged reactors, radioactive material has probably been initially mostly transferred to the dry-well in reactor 1 with early and extended failure of the second barrier and to the wet-well in reactor 2 where the second barrier was maintained for a longer time during core degradation. These differences in scenarios probably resulted, associated with the in-vessel FP release phases, in very different radioactive material inventories in the dry-well and different related physicochemical phenomena with significant radioactive aerosol transport to and deposition in the reactor 1 dry-well and mostly radioactive gas transport, and for gaseous iodine sorption onto surfaces, in reactor 2 dry-well where most radioactive aerosols should have been scrubbed in the wet-well. The scenario is much less clear for reactor 3 due to uncertainties of the timing and extent of the second barrier failure.

Concerning the composition of aerosols related to the in-vessel degradation phase, one could infer, founded on earlier reported background knowledge, the

probable existence of μm -sized particles containing Cs, Si, B, Sn, steel components (Fe, Zn, etc.), and probably Cl from seawater and with a lower probability Mo and Te since the conditions in-vessel were mostly reducing. However, in 2019, information on composition of aerosols produced during the in-vessel degradation phase remains scarce and is awaiting analyses of in-containment deposits.

For reactors where the RPV has been breached resulting in significant MCCI (reactors 1 and 3 for certain), existing background knowledge and information from the accident are too scarce at this time to assess the relative importance of radioactive aerosol formation during this phase and the possible aerosol composition.

Some radioactive particles containing Cs isotopes collected in the environment or in environmental sampling systems have been analyzed for their composition, Cs activity, distribution and speciation, and their formation tentatively assigned to specific phases of the accident in the reactor (in-vessel or ex-vessel) [159]. However, this assignment is not straightforward as (1) various types of particles in terms of size and composition have been identified in various collected samples, (2) accident progression was very different in each of the three damaged reactor, and (3) these particles mostly provide information on water insoluble Cs species or Cs species, which are encapsulated in water insoluble matrices (e.g., silicate glass matrix). Cs containing silicate glass particles have aroused specific interest in recent publications [159]. They were shown to be composed of O, Si, Cl, K, Fe, Zn, Rb, Sn, and Cs and attributed to aerosol formation during the MCCI phase. The inferred formation process starts from the formation of franklinite (Zn–Fe oxide) nanoparticles on which Cs and SiO_2 would condense resulting in glassy silicate particle containing FPs and steel components [159]. In some other particles the existence of pollucite ($\text{CsFeSi}_2\text{O}_6 \cdot n\text{H}_2\text{O}$) was established [159]. Pollucite could rather arise from Cs reaction with steel surfaces in-vessel or in hot parts of circuits. As long as analyses of deposits in various parts of the damaged units have not been performed, establishing for the in- and ex-vessel phases the relative importance of aerosols production, average aerosol compositions, and the chemistry involved in their formation, remains particularly challenging.

It should be further emphasized that in the longer term, water injected to cool down the damaged reactor core and the related steam evaporation–condensation in the dry-well has probably had the effect to wash down a significant part of deposited radioactive material (at least water-soluble material) with transfer of the contaminated liquids produced, first to the wet-well then to the environment where the containment has been breached (at different location in each of the damaged reactors).

Also, for reactors where the RPV has breached resulting in significant MCCI, cooling and leaching of ex-vessel fuel debris and molten fuel on the dry-well floor during MCCI should result, mostly during the early phase of fuel–coolant interaction, in FP remobilization by vaporization of highly contaminated liquid with (1) transfer, mostly as droplets, of radioactive aerosols in the dry-well atmosphere and (2) additional FP release from the fuel in the contaminated liquid phase through leaching. Degraded fuel leaching will then continue as long as cooling by a water flow is necessary.

14.3.3.6 Other aspects affecting physicochemical phenomena

Observations of degraded components after the accident indicate that unexpectedly high temperatures have probably been reached during the accident inside the containment dry-well (higher than 300 K). Such temperatures may result in degradation of dry-well components containing organic materials (e.g., paints) and others, which can affect FP chemistry, in particular that of iodine. One may also suspect that the combined effect of high temperature, high turbulent steam flows, and high radiation doses has affected, as shown by analytical testing [142], chemical stability of deposited radioactive aerosols and remobilized radioactivity during early phases of the accident. The available data and information are however too limited for an appropriate quantification of these phenomena at this time.

In addition, when addressing chemistry in the dry-well for the Fukushima Daiichi accident, one has also to bear in mind that the containment atmosphere is filled with nitrogen to avoid hydrogen combustion. This should in particular affect iodine chemistry, strongly limiting the formation of iodine oxides compounds in comparison for instance with PWR air-filled containments where iodine oxides play a significant role in iodine chemistry.

Finally, the initial temporary injection of seawater to cool the damaged reactors may have affected, in addition to the in-vessel degradation and FP release phase, leaching of damaged fuel and corrosion–erosion reactions in the long term and chemistry in the wet-well as discussed in [Section 14.3.4](#).

14.3.3.7 Remobilization and transfer of radioactivity for long-term accidents

Though Fukushima Daiichi accident conditions have been particularly challenging, current analyses of the accident show that some SA phenomena have not been sufficiently addressed to assess how they affect radioactive release in an SA. The physico-chemistry of in-vessel FP release and related transport and deposition in containment can be addressed with existing knowledge and modeling, with however some possible gaps related to Fukushima Daiichi accident specificities (e.g., seawater effects) and BWRs' specificities (related to in-vessel degradation progression as current knowledge has been mostly developed for PWRs). However, this is much less true for ex-vessel release phases with MCCI and remobilization phenomena from surface deposits in contaminated buildings (at Fukushima Daiichi, remobilization from both the containment dry-well and the R/B above the refueling floor¹³ may have contributed significantly to radioactive releases). Other phenomena requiring more attention are contamination of liquids during ex-vessel fuel–coolant interaction and for damaged fuel lixiviation on the long term. Some experiments are ongoing in 2019 in the OECD/NEA STEM-2 and THAI-3 projects to investigate iodine release by decomposition due to radiation doses or by remobilization by hydrogen combustion of surface-deposited cesium aerosols and adsorbed iodine.

¹³ Mostly for reactors 1 and 3, which have experienced hydrogen explosions.

Investigations related to leaching of damaged fuel, involving postaccident samples from Chernobyl-4, are also planned within the OECD/NEA TCOFF project, addressing in particular ageing of damaged fuel. Leaching processes are of particular importance for the management of contaminated liquids, including in the long term, Cs and Sr radioisotopes release. The management of contaminated liquids remains in 2019 a tremendous challenge at Fukushima Daiichi. By 2020 results of above-mentioned research programs should help quantify the importance of these phenomena for SA radioactive release and establish where further experiments and models developments are necessary.

14.3.3.8 Mitigation of radioactive releases for long-term accidents—further development and qualification of filtered containment venting systems

Important efforts were made in the past for the development and qualification of filtered containment venting systems (FCVS), but questions remain as to the efficiency and robustness of such systems in SA conditions as they may be envisaged after Fukushima Daiichi accidents [160,161]. For some countries where safety criteria associated with releases are becoming more stringent, a more efficient filtration could contribute to reduce further the radiological consequences. Such issues, along with the assessment of innovative filtration technologies, are being tackled in 2019 in research programs (e.g., in the French IRSN MiRE program [142], which complements investigations performed in the EU PASSAM program [160], or in the Japanese national program [162]).

In these programs the long-term trapping capabilities of different filtering medias for gaseous iodine species (I_2 and CH_3I) are investigated: liquid pool containing soda and thiosulfate¹⁴ (scrubbing), a sand layer (of interest for French PWRs equipped with sand-bed filters), charcoals- and aluminum-based metal-organic framework (MOF), and silver zeolites (innovative media).

Results for liquid scrubbers are addressed in [Section 14.3.4](#).

Sand-layer filters showed no retention for gaseous iodine species, either I_2 or CH_3I . This is not surprising as the tested sand has no reactivity with gaseous iodine species. Some tests performed with metallic aerosols deposited in the sand (Cs, Ag) indicated enhanced I_2 retention [157]. Further testing will be performed in France at IRSN to quantify I_2 retention on the metallic prefilter placed upstream of the sand-bed filter in the containments of French PWRs since metallic aerosols retained on this filter may trap a significant part of I_2 .

A systematic study involving experimentation and detailed modeling of the trapping mechanisms [163–166] was performed on three main kinds of porous materials—silver zeolites, charcoals- and aluminum-based MOF—searching for the most robust and efficient filtration media for I_2 and CH_3I in SA conditions. These porous materials were characterized before and after iodine trapping by different techniques in order to establish relationships between structural/chemical properties and

¹⁴ Both additives are added to promote gaseous iodine retention in alkaline solutions.

trapping capabilities. The objective was to gain sufficient knowledge for optimization of their structures to improve their trapping efficiencies and to assess their behavior in SA conditions.

For the time being, among all the investigated sorbents for CH_3I retention, silver-faujasite zeolites displayed the highest performances in terms of adsorption capacity and trapping stability for both I_2 and CH_3I , CH_3I being mostly trapped as AgI precipitates. It was shown that for irreversible iodine retention, (1) the preparation of the zeolite was very important, with Ag incorporation as Ag cation or Ag cluster producing more stable and efficient active trapping sites for gaseous iodine than Ag impregnation and (2) large-pore faujasite with a high number of dispersed active sites should be provided (which is obtained through incorporation of at least 10% weight of Ag with zeolite with Si/Al ratio of 2.5) to optimize exchanges with the fluid. It was also shown that the stability and efficiency of the tested silver-faujasite zeolites were not strongly challenged in the presence of steam, hydrogen, and carbon monoxide and when submitted to dose and temperatures, each parameter being taken separately. The potential effect of other gases (e.g., Cl and NO_x) and eventually of combined gases (H_2 , CO, Cl, NO_x , and H_2O) cumulated with dose and temperature remains to be studied. However, one should note that the study of such complex representative conditions has never been done for any filtering media. To conclude such optimization work provides promising robust and efficient filtering media for SA conditions that could be implemented in existing or new systems to enhance gaseous iodine filtration, particularly that of CH_3I .

14.3.4 Chemistry in containment pools and in liquid scrubber containment venting systems

14.3.4.1 Main issues addressed and knowledge gained before the Fukushima Daiichi accidents

Radioactive aerosols discussed in [Section 14.3.3](#) are transferred to sumps and pools in PWR containments either by gravitational settling or with condensing steam and to suppression pools in BWR containments by scrubbing. Extensive work has been performed in the past on aerosol scrubbing in pools [\[143\]](#) and on aqueous phase chemistry in sumps and pools, in particular that of iodine [\[149\]](#).

Related to pool scrubbing, either in suppression pools or in scrubbing FCVS, additional research has recently been performed in the European Commission PASSAM project [\[160\]](#) addressing mostly hydrodynamic aspects and aerosol retention. Work is currently continuing in the NUGENIA IPRESCA project where it has been recognized that modeling of hydrodynamic aspects has still to be significantly improved to provide reliable predictions in terms of radioactive aerosol and gas (mostly iodine species) decontamination factors.

Related to iodine scrubbing, chemical aspects have been the subject of investigations in relation to molecular iodine and organic iodides retention in FCVS [\[160,161\]](#). Molecular iodine retention may be efficiently managed by controlling the pH in the pool, maintaining it in alkaline conditions by adding alkaline

buffering species (e.g., sodium hydroxide or tetraborates). Then hydrolysis reactions convert molecular iodine to soluble ionic species (iodide and iodate). The pH has however to be maintained during the accident with sufficient amount of additives to counterbalance dilution with steam condensation in the pool and acidification when acidic compounds (e.g., nitric acid, which is a by-product of air radiolysis) dissolve in the pool.

Organic iodides retention is more challenging as it requires chemical additives, such as, for instance, thiosulfate (but others have been formulated as part of industrial developments [161]), which converts them into soluble ionic species. One of the challenges here is to maintain the efficiency of such additives during a SA despite significant changes with time in the pool chemical conditions (pH, oxygen potential, dilution with steam condensation, aerosol, and gas solubilization) and due to increasing radiation doses.

Recent results indicate that for liquid scrubbers, thiosulfate in large excess is rapidly decomposed under radiation to sulfuric acid. This results in tests in acidification of unbuffered solutions so that gaseous iodine is no longer retained efficiently in the liquid solution [142]. Despite thiosulfate decomposition, the alkaline pH can be maintained in solutions buffered with borate (alkaline pH). However, even if the pH was maintained alkaline, it was shown that significant fractions of iodine were removed by gas sparging from the solution [142]. Based on these results and knowledge of iodine chemistry under radiation, a model has been developed for the prediction of decontamination factors for gaseous iodine species as a function of thermal and chemical conditions of the solution as well as design of the scrubbers. The modeling suggests that HOI volatilization could explain the iodine content decrease in alkaline buffered solutions. Further work to test this hypothesis is still ongoing. Experiments and modeling done for CH_3I indicate that CH_3I retention in liquid scrubbers is limited (Decontamination Factor (DF) < 10) even in the presence of specific additives promoting CH_3I decomposition in the liquid phase [142]. All these results show that the control of chemical conditions in the scrubbing liquid phase in the long term during an SA is challenging (other acidification sources such as nitric acid formed by air radiolysis and CO_2 produced by MCCI in the containment should also be considered) and the evolution of the chemical conditions may reduce significantly gaseous iodine trapping efficiency in liquid scrubbers.

Related to FP chemistry in water pools in the containment, iodine chemistry has been the most extensively studied [149]. Major reactions affecting the iodine volatility [radiolysis (gaseous I_2 formation under radiation), hydrolysis (I_2 decomposition into iodides and iodates), gaseous Org-I formation, interaction with Ag particles (from Ag–In–Cd control rod)] with formation of nonsoluble AgI have been extensively investigated experimentally and they are appropriately modeled in major SA codes. It is well established that the iodine volatility can be greatly reduced by maintaining alkaline pH conditions in containment water pools during the accident or, for reactors equipped with Ag–In–Cd control rods, if the amount of reactive and accessible silver is sufficient to efficiently trap iodine.

For reactor calculations addressing gaseous iodine transfer to the containment atmosphere, uncertainties remain mostly on evolution during the accident of some

parameters affecting these reactions and the iodine volatility such as pH, oxygen potential, concentration of reactive impurities (e.g., chlorine and nitrate/nitrite), and extent of accessible reactive Ag (when Ag particles are present). Thus depending on the accident scenario, “realistic” hypotheses have to be used for the evolution of these parameters for such calculations.

14.3.4.2 *Highlights from the Fukushima Daiichi accidents—issues deserving further attention*

Pool scrubbing in suppression pools and scrubber filtered containment venting systems in relation to radioactive release mitigation

The Fukushima Daiichi accidents have highlighted that the effects of evolving hydrodynamic and chemical conditions on FP pool scrubbing efficiency in BWR suppression pools and in liquid FCVS deserve more attention. Most pool scrubbing investigations dated back to the 1980s and 1990s [143] with recently, additional experimental investigations performed by CIEMAT, RSE, and PSI in the European PASSAM project, which ended early in 2017 [160]. However, despite progress made in the understanding of scrubbing hydrodynamics (jet and churn-turbulent regimes) and aerosols retention in more representative conditions, modeling has still to be improved through a systematic analysis of parameters influencing scrubbing notably since it is unable to represent two-phase flow instabilities, which may strongly affect FP scrubbing efficiencies. More experiments tracking variables such as bubble sizes and shapes are needed. Also, more studies of chemistry effects on scrubbing of gas species (e.g., gaseous iodine species) are required. National initiatives in many countries are underway (France, Germany, Italy, Japan, Korea, Spain, and Switzerland) to progress in the modeling of pool scrubbing. A large international collaboration is currently being built within the NUGENIA association (IPRESCA project, led by Becker Technologies) to progress in scrubbing modeling based on directly dedicated experiments.

As to the chemistry in the liquid phase both in the dry-well and the wet-well, in particular that of iodine, it has probably been significantly influenced by the presence of “impurities” of different nature and origin, specifically: sea-water injection at the beginning of the accident with the presence, among others, of chlorine, bromine, and suspended organic matter, significant material degradation both in the wet-well and dry-well under high temperatures and doses (e.g., paints with organics formation, heat insulator and electrical cabling degradation, and radio-induced corrosion of metallic parts) as shown by observations of degraded material and the presence of large amount of sediments in dry-well waters in reactors 1 and 3. The effect of some impurities in sumps on iodine volatility was investigated in the past at PSI (chlorine and nitrate/nitrite) [167] and more recently at JAEA (sea-water compounds) following the accident [168]. Also, organic iodides formation in water pools from iodine reaction with organics has been extensively studied [149,150]. Though chemical reactions are known and models exist for some of these reactions, the challenge is to have appropriate data and information on the nature and

inventories of impurities in the damaged units and more generally for other reactor types and SA scenarios.

14.3.4.3 Chemistry in coolant liquid phase on the long term

After the Fukushima Daiichi accident, knowledge of water phase chemistry in the long term in relation to accident management involving long-term cooling of debris and corium in the containment was questioned (e.g., production of combustible gases by corrosion and radiolysis reactions, production of contaminated liquids involving degraded fuel leaching, possible clogging of cooling loops). The present modeling in SA system codes is not appropriate to model chemistry for long-term phases. Additional necessary research efforts to tackle these issues have been recently identified by an OECD/NEA work group on the long-term management of a SA in a NPP [169].

14.4 Conclusion

In this chapter, advances in chemistry related to nuclear fuel and structural materials degradation and FP release and transportation to the environment during a SA have been addressed. Importance to enhance the understanding and modeling of chemistry of complex systems has been discussed for better assessment of SA progression in- and ex-vessel and radiological consequences, particularly after the SA of FDNPS. This concerns in particular the following:

(In-vessel)

- Effect of structural materials interaction (i.e., B₄C, Zry, and SS) on the in-vessel degradation progression, expected to be more significant in BWRs than in PWRs due to the larger masses of these materials and the specific core geometry;
- Effect of B₄C and SS incorporation in the molten pool in the RPV lower plenum, which can promote the formation of a less dense metallic layer topping the molten pool with potential heat focusing effect on the RPV wall, of importance for analyses of in-vessel melt retention strategies;
- For BWRs, effect of larger Zr masses on the oxygen potential and FP release since they favor occurrence of steam-starved conditions, as was probably the case in the FDNPS accident sequences; and
- Progression of degradation for MOX fuel.

(Ex-vessel)

- Better prediction of end-state in-vessel composition (i.e., melt fraction, oxidation state, and Fe and FP content) and temperature, as initial conditions for transfer and spreading ex-vessel for better assessment of MCCI extent.

(FP behavior)

- Effect of chemistry on Cs transport and remobilization (i.e., formation, deposition and remobilization of the molybdates, borates, and silicates) to better assess radiological consequences related to Cs releases;
- Effect of the chemical forms of FP in fuel debris (precipitates or in the matrix) on release in water by leaching for long-term management.

The improvement of the knowledge of the fuel and FP chemistry has used fundamental and traditional research approaches, which often need a pretty long time, particularly to verify results with irradiated materials. However, new analysis methods, better use of simulated materials, improved modeling approaches, and more refined sampling techniques recently resulted in an acceleration in the accumulation of experimental/analytical data for better understanding of the SA phenomenology. The interaction between experts of nuclear materials and SA analysis is essential for improving nuclear safety. An OECD/NEA joint project on “Thermodynamic Characterization of Fuel debris and Fission Products, based on Scenario Analysis of Severe Accident Progression at the Fukushima Daiichi Nuclear Power Station (TCOFF)” is a successful example [170].

Readers, especially the next-generation scientists, should pay a particular attention to the process of establishment of consensus for the phenomena of fuel degradation and FP chemistry: “which phenomena are identified to be dominant and which ones are negligible, and under which conditions?” The chemistry of the SA is very complicated and extensive; it overlaps for SA analysis with many other domains of science, mathematics, and engineering. Thus if something new is found in an accident sequence, one often has to return to the original phenomenology, particularly chemistry, to reevaluate the importance of some phenomena that have been previously overlooked.

References

- [1] B.R. Sehgal, Nuclear Safety in Light Water Reactors: Severe Accident Phenomenology, SARNET, 2012.
- [2] M. Kurata, et al., *J. Nucl. Mater.* 500 (2018) 119–140.
- [3] B. Lewis, et al., *J. Nucl. Mater.* 380 (2008) 126–143.
- [4] M. Steinbrück, et al., FZKA-6829, Forschungszentrum Karlsruhe, 2004.
- [5] H.T. Kim, et al., *J. Nucl. Sci. Technol.* 44 (2007) 1385–1394.
- [6] OECD/NEA, State-of-the-art report, nuclear fuel behaviour in loss-of-coolant accident (LOCA) conditions, in: OECD/NEA No. 6846, 2009, ISBN 978-92-64-99091-3.
- [7] M. Pellegrini, et al., *Nucl. Technol.* 196 (2016) 198–210.
- [8] D. Setoyama, S. Yamanaka, *J. Alloys Compd.* 370 (2004) 144–148.
- [9] OECD/NEA joint project on Thermodynamics for Advanced Fuels -International Database (TAF-ID). TAF-ID database is available from: <<http://www.oecd-nea.org/science/taf-id/>>.
- [10] M. Grosse, et al., *J. Nucl. Mater.* 385 (2) (2009) 339–345.
- [11] S. Yamazaki, et al., Proceedings of TOPFUEL2018, Prague, Czech, September 30–October 4, 2018.
- [12] H.M. Chung, A.N. Garde, T.F. Kassner, Zirconium in the nuclear industry, in: ASTM STP 633, ASTM, Quebec, Canada, 1976, pp. 82–97.
- [13] M. Moalem, D.R. Olander, *J. Nucl. Mater.* 178 (1991) 61–72.
- [14] M. Grosse, et al., ASTM special technical publication, in: STP 1543, 2015, pp. 1054–1073.

- [15] P. Hofmann, D. Kerwin-Peck, *J. Nucl. Mater.* 124 (1984) 80–105.
- [16] R.O. Gauntt, Synthesis of VERCORS and Phebus data in severe accident codes and applications, in: SAND2010-1633, Sandia National Laboratory Report, 2010.
- [17] P. Hofmann, et al., *Nucl. Technol.* 87 (1987) 146–186.
- [18] D.W. Akers, et al., OECD Report NEA/CSNI/R(91)9, vol. 1 Appendix B, 1992.
- [19] N. Shirasu, et al., Proceedings of FDR2019, International Topical Workshop on Fukushima Decommissioning Research, J-Village, Naraha, Fukushima, Japan, May 24–26, 2019, Paper No. 1067.
- [20] T. Haste, et al., In-Vessel Core Degradation in LWR Severe Accidents: A State of-the-Art Report, EUR 16695 EN, 1995.
- [21] P. Hofmann, *J. Nucl. Mater.* 270 (1999) 194–211.
- [22] O. De Luze, et al., *Ann. Nucl. Energy* 61 (2013) 23–35.
- [23] A.C. Grégoire, T.J. Haste, *Ann. Nucl. Energy* 61 (2013) 63–74.
- [24] S. Hagen, et al., FZKA-5680, Forschungszentrum Karlsruhe, 1996.
- [25] M. Steinbrück, U. Stegmaier, Experiments on silver–indium–cadmium control rod failure during severe accident sequences, in: Jahrestagung Kerntechnik 2010, Berlin, May 4–6, 2010, Berlin; INFORUM GmbH, CD-ROM Paper 303.
- [26] M. Steinbrück, et al., *Nucl. Eng. Des.* 240 (2010) 1714–1727.
- [27] T. Haste, W. Plumecocq, Control rod and structural material release modelling in ELSA2, in: Presented at the International QUENCH Workshop, FZ Karlsruhe, October 13–15, 2003.
- [28] D. Petti, et al., *Nucl. Technol.* 84 (1989) 128–151.
- [29] M.L. Carboneau, et al., Experiment analysis and summary report for OECD LOFT experiment LP-FP-2, in: OECD LOFT-T-3806, OECD, 1989.
- [30] S.M. Jensen et al., PIE data and analyses for OECD LOFT LP-FP-2, in: OECD LOFT-T-3810, vol. 1, OECD, 1989.
- [31] G. Repetto, P. Corregio, Unpublished Work, IRSN, 1991.
- [32] M. Barrachin, et al., *J. Nucl. Mater.* 375 (2008) 397–409.
- [33] F. Payot et al., FPT3 final report, in: IRSN Report Phébus PF IP/11/589, DPAM/DIR-2011-206, Institut de Radioprotection et Sûreté Nucléaire, 2011.
- [34] L. Sepold, et al., *Ann. Nucl. Energy* 36 (2009) 1349–1359.
- [35] R. Dubourg, et al., *Progr. Nucl. Energy* 52 (2010) 97–108.
- [36] B. Bowsher, et al., Silver–Indium–Cadmium Control Rod Behaviour During a Severe Reactor Accident. Rep AEEW-R1991, United Kingdom Atomic Energy Authority, 1991.
- [37] P. Hofmann, et al., *Nucl. Technol.* 90 (1990) 226–244.
- [38] L. Barin, Thermochemical Data of Pre Substances, VCH Verlagsgesellschaft, Weinheim, Germany, 1989.
- [39] C. Dominguez, et al., *J. Nucl. Mater.* 374 (2008) 473–481.
- [40] C. Dominguez, D. Drouan, *J. Nucl. Mater.* 451 (2014) 111–119.
- [41] C. Dominguez, *J. Nucl. Mater.* 427 (2012) 140–151.
- [42] M. Steinbrück, *J. Nucl. Mater.* 336 (2005) 185–193.
- [43] M. Steinbrueck, *J. Nucl. Mater.* 400 (2010) 138–150.
- [44] M. Steinbrueck, et al., FZKA-Report 6979, Forschungszentrum Karlsruhe, 2004.
- [45] M. Steinbrueck, *Ann. Nucl. Energy* 64 (2014) 43–49.
- [46] S. Hagen et al., KfK-5363, Kernforschungszentrum Karlsruhe, 1994.
- [47] M. Steinbrück, *J. Nucl. Mater.* 334 (2004) 58–64.

- [48] R.O. Gauntt, L.L. Humphries, NUREG/CR-6527, SNL, 1997.
- [49] H. Shibata, et al., Proceedings of TOPFUEL2016, September 11–16, 2016, Boise Center, Boise, ID, 2016.
- [50] ISBN 978-0-87170-403-0 T.B. Massalski (Ed.), *Binary Alloy Phase Diagrams*, second ed., ASM International, Novelty, OH, 1990.
- [51] R. Wachowiak, Modular Accident Analysis Program (MAAP)-MELCOR crosswalk—Phase 1 study, in: EPRI-Report 3002004449, November 2014.
- [52] B. Clément, R. Zeyen, *Ann. Nucl. Energy* 61 (2013) 4–10.
- [53] M.S. Veshchunov, et al., *Nucl. Eng. Des.* 238 (2008) 2219–2229.
- [54] M. Barrachin, et al., *Ann. Nucl. Energy* 61 (2013) 36–53.
- [55] P.Y. Chevalier, et al., *Calphad* 28 (2004) 15–40.
- [56] Y. Pontillon, et al., *J. Nucl. Mater.* 344 (2005) 265–273.
- [57] J. Christensen, et al., *Trans. Am. Nucl. Soc.* 7 (1964) 390.
- [58] J. Christensen, Technical Report HW-69234, Hanford, WA, 1964.
- [59] J. Bates, *J. Nucl. Mater.* 36 (1970) 234–236.
- [60] S. Yamanouchi, et al., *J. Nucl. Sci. Technol.* 25 (1988) 528–533.
- [61] F.C. Iglesias, et al., *J. Nucl. Mater.* 270 (1999) 21–38.
- [62] C. Ronchi, M. Shiendlin, *Int. J. Therm.* 23 (2002) 293–305.
- [63] D. Manara, et al., *J. Nucl. Mater.* 342 (2005) 148–163.
- [64] S. Mastromarino, et al., *J. Nucl. Mater.* 494 (2017) 368–379.
- [65] C. Olsen, et al., *Nucl. Technol.* 87 (1989) 57–94.
- [66] S.V. Bechta, et al., *J. Nucl. Mater.* 362 (2007) 46–52.
- [67] S.V. Bechta, et al., *J. Nucl. Mater.* 348 (2006) 114–121.
- [68] R. Strain, et al., *Nucl. Technol.* 87 (1989) 187–190.
- [69] W.A. Lambertson, M.H. Mueller, *J. Am. Ceram. Soc.* 36 (1953) 365–368.
- [70] B. Adroguer, et al., Final Report, Corium Interactions and Thermochemistry (CIT) Project, Report INV-CIT(99)-P040, 1999.
- [71] W.D. Evans, et al., *Trans. Br. Ceram. Soc.* 63 (1964) 705–712.
- [72] V.I. Almjashev, et al., *J. Nucl. Mater.* 400 (2010) 119–126.
- [73] V.I. Almjashev, et al., *J. Nucl. Mater.* 389 (2009) 52–56.
- [74] L. Belovsky, et al., Proceedings of Fifth International Conference on Nuclear Engineering (ICON5), ICON5-2184 ASME, May 26–30, 1997.
- [75] P. Hofmann, et al., KfK-4598, Kernforschungszentrum Karlsruhe, 1989.
- [76] A. De Bremaecker, et al., European nuclear thermodynamic database for in- & ex-vessel applications (ENTHALPY), in: FISA-2003, Luxembourg, November 10–13, 2003.
- [77] D.W. Akers, R.K. McCardell, *Nucl. Technol.* 87 (1989) 214–223.
- [78] Z.P. Bazant, M.F. Kaplan, *Concrete at High Temperatures*, Pearson Education, 1991.
- [79] M.F. Roche, et al., Solidus and liquidus temperatures of core-concrete mixtures, in: NUREG/CR-6032, ANL-93/9, 1993.
- [80] S. Hellmann, ENTHALPY project—liquidus and solidus temperatures in the subsystem $\text{UO}_2\text{-ZrO}_2$ ($\text{SiO}_2\text{-FeO}_x\text{-CaO}\text{-Al}_2\text{O}_3\text{-Cr}_2\text{O}_3$), in: Report SAM-ENTHALPY(03)-D011, European Commission, Fifth EURATOM Framework Programme 1998–2002, 2003.
- [81] Y.N. Aniskevich, et al., Liquidus temperature measurements of a corium multicomponent mixture, Progress report, ISTC CORPHAD Project (2006).
- [82] E.V. Krushinov, et al., Investigation of ternary oxide systems: $\text{UO}_2\text{-FeO}\text{-SiO}_2$ system, Progress report, ISTC PRECOS Project (2012).

- [83] B. Cheynet, et al., Progress in nuclear thermodynamic databanking for MCCI applications, in: Proceedings of the OECD MCCI Seminar, Cadarache, France, October 10–11, 2007.
- [84] NUCLEA Thermodynamic Database, Institut de Radioprotection et Sûreté Nucléaire, CEN Cadarache, St Paul Lez Durance, 2018.
- [85] C. Guéneau, et al., FUELBASE, TAF-ID databases and OC software: advanced computational tools to perform thermodynamic calculations on nuclear fuel materials, in: The 7th European Review Meeting on Severe Accident Research (ERMSAR-2015), Marseille, France, 2015.
- [86] M. Peehs, et al., *Nucl. Technol.* **46** (1979) 192–198.
- [87] A. Sudo, et al., Characterization of core melt/concrete interface region examined by light-concentrating heating technique, in: Presented at NuMat-2016, Montpellier, France, November 6–10, 2016.
- [88] M. Takano, et al., Phases and morphology in the simulated MCCI products prepared by arc melting method, in: Presented at NuMat-2016, Montpellier, France, November 6–10, 2016.
- [89] A. Sudo, et al., Solidification behavior of the simulated oxide debris, in: Presented at AESJ Annual Meeting, Okayama, Japan, September 5–7, 2018 (in Japanese) (to be published in English).
- [90] I. Poznyak, et al., Study of the molten corium properties using cold crucible melting technology, in: Presented at Fifth NUGENIA-SARNET TA2.2 Review Meeting, Puerto de La Cruz, Spain, April 18–20, 2018.
- [91] S. Bechta, et al., *ISSN 1066-3622 Radiochemistry* **50** (2011) 13–18.
- [92] P.D.W. Bottomley, et al., *J. Nucl. Sci. Technol.* **52** (2015) 1217–1225.
- [93] M. Takano, T. Nishi, *J. Nucl. Mater.* **443** (2013) 32–39.
- [94] E. Geiger, et al., *J. Nucl. Mater.* **471** (2016) 25–33.
- [95] C. Le Gall, et al., *J. Nucl. Mater.* **495** (2017) 291–298.
- [96] M. Barrachin, et al., *J. Nucl. Mater.* **453** (2014) 340–354.
- [97] A. Bujan, et al., *Progr. Nucl. Energy* **53** (2011) 438–448.
- [98] L. Soffer, et al., Accident Source Terms for Light-Water Nuclear Power Plants, NUREG-1465, 1995.
- [99] M. Gouello, et al., *Nucl. Eng. Des.* **263** (2013) 462–472.
- [100] A. Gallais-During, et al., *Nucl. Eng. Des.* **277** (2014) 117–123.
- [101] P.M. Di Giuli, et al., *Ann. Nucl. Energy* **93** (2016) 65–82.
- [102] P. Giordano, et al., *Progr. Nucl. Energy* **52** (2010) 109–119.
- [103] A. Gallais-During, et al., *Ann. Nucl. Energy* **101** (2017) 109–117.
- [104] M. Kurata, et al., *Trans. At. Energy Soc. Jpn.* **12** (2013) 286–294.
- [105] S. Miwa, et al., *Nucl. Eng. Des.* **326** (2018) 143–149.
- [106] S. Yamanaka, et al., *J. Nucl. Mater.* **344** (2005) 61–66.
- [107] M. Catti, et al., *Acta Crystallogr. C* **39** (1983) 29–34.
- [108] Y. Koma, et al., *Nucl. Mater. Energy* **10** (2017) 35–41.
- [109] F. Nagase, et al., *J. Nucl. Mater.* **245** (1997) 52–59.
- [110] T. Haste, et al., *Ann. Nucl. Energy* **61** (2013) 102–121.
- [111] F.G. Di Lemma, et al., Boron release kinetics from mixed melts of boron carbide, stainless steel and Zircaloy—a literature review on the behavior of control rod materials under severe accidents, in: JAEA-Review 2016-007, Japan Atomic Energy Agency, 2016.

- [112] M.P. Kissane, et al., *Nucl. Eng. Des.* 236 (2006) 1210–1223.
- [113] A.-C. Grégoire, et al., *Ann. Nucl. Energy* 78 (2015) 117–129.
- [114] T. Kärkelä, et al., *Progr. Nucl. Energy* 99 (2017) 38–48.
- [115] T. Kärkelä, et al., *Ann. Nucl. Energy* 74 (2014) 173–183.
- [116] I. Kajan, et al., *Ann. Nucl. Energy* 100 (2017) 9–19.
- [117] K. Knebel, et al., *Progr. Nucl. Energy* 72 (2014) 77–82.
- [118] P.D.W. Bottomley, et al., *Ann. Nucl. Energy* 74 (2014) 208–223.
- [119] P.D.W. Bottomley, et al., *Nucl. Eng. Technol.* 38 (2006) 163–174.
- [120] T. Haste, et al., *Nucl. Eng. Des.* 246 (2012) 147–156.
- [121] J. Kalilainen, et al., *Nucl. Eng. Des.* 267 (2014) 140–147.
- [122] I. Sato, et al., *J. Nucl. Mater.* 461 (2015) 22–28.
- [123] T. Okane, et al., *Nucl. Eng. Des.* 297 (2016) 251–256.
- [124] M. Osaka et al., Results and progress of fundamental research on FP chemistry, in: Proceedings of ERMSAR2017, Warsaw, Poland, May 16–18, 2017.
- [125] N. Miyahara et al., Development of experimental and analytical technologies for fission product chemistry under LWR severe accident condition, in: Proceedings of WRFPM2017, Jeju, Korea, September 10–14, 2017.
- [126] Nuclear Damage Compensation and Decommissioning Facilitation Corporation (NDF), Technical Strategic Plan 2017 for Decommissioning of the Fukushima Daiichi Nuclear Power Station of Tokyo Electric Power Company Holdings, Inc., NDF Report4-64-65, 2017.
- [127] V.F. Baston, et al., A comparison of TMI-2 and laboratory results for cesium activity on reactor material surfaces, in: American Nuclear Society Winter Meeting, San Francisco, CA, November 10–14, 1985, *Trans. Am. Nuc. Soc.*, 1985, pp. 223–225.
- [128] F.G. Di Lemma, et al., *Nucl. Eng. Des.* 305 (2016) 411–420.
- [129] M. Kobata, et al., *J. Nucl. Mater.* 498 (2018) 387–394.
- [130] L. Zheng, et al., *J. Nucl. Mater.* 507 (2018) 327–338.
- [131] E. Suzuki, et al., *Progr. Nucl. Sci. Technol.* 5 (2018) 165–167.
- [132] F.G. Di Lemma, et al., *J. Nucl. Mater.* 484 (2017) 174–182.
- [133] Y. Satou, et al., *Anthropocene* 14 (2016) 71–76.
- [134] B. Grambow, C. Poinsot, *Elements* 8 (2012) 213–219.
- [135] M. Laurie, et al., *Ann. Nucl. Energy* 61 (2013) 122–134.
- [136] Y. Pontillon, et al., *J. Nucl. Mater.* 495 (2017) 363–384.
- [137] A.-C. Grégoire, et al., *Ann. Nucl. Energy* 101 (2017) 69–82.
- [138] V.F. Baston, K.J., Hofstetter, Three Mile Island accident: diagnosis and prognosis, in: Adherent Activity on Internal Surfaces, ACS Symposium Series, Developed from a Symposium at the 189th Meeting of the American Chemical Society, Miami Beach, FL, 1986, pp. 124–145.
- [139] J.L. Collins, et al., Behavior of fission product tellurium under severe accident conditions, in: International ANS/ENS Topical Meeting on Thermal Reactor Safety, San Diego, CA, February 2, 1986. Available from: <<https://www.osti.gov/biblio/6188157>>.
- [140] A. Auvinen, et al., *Nucl. Eng. Des.* 238 (2008) 3418–3428.
- [141] G. Ducros, et al., *Ann. Nucl. Energy* 61 (2013) 75–87.
- [142] L. Cantrel, et al., *J. Nucl. Eng. Rad. Sci.* 4 (2) (2018) 13. N° 020903.
- [143] State of the Art Report on Nuclear Aerosols, NEA/CSNI/R, (2009) 5.

- [144] OECD/NEA joint project on Thermal-hydraulics, Hydrogen, Aerosols and Iodine Project Phase 3 (THAI-3). The reports are available from: <<http://www.oecd-nea.org/jointproj/thai3.html>>.
- [145] B. Simondi-Teisseire, et al., *Ann. Nucl. Energy* 61 (2013) 157–169.
- [146] T. Haste, et al., *Nucl. Eng. Des.* 261 (2013) 333–346.
- [147] T. Haste, et al., *Nucl. Eng. Des.* 239 (2009) 3116–3131.
- [148] L. Bosland, et al., Proceedings of the International OECD/NEA/NUGENIA-SARNET Workshop on the Progress in Iodine Behavior for NPP Accident Analysis and Management, OECD/NEA/CSNI/R, (2016) 347–356.
- [149] State of the Art Report on Iodine Chemistry, NEA/CSNI/R, (2007) 1.
- [150] G.A. Glowa, et al., *Ann. Nucl. Energy* 74 (2014) 184–199.
- [151] S. Gupta et al., THAI experiments on volatility, distribution and transport behaviour of iodine and fission products in the containment, in: Proceedings of The International Iodine Workshop, NEA/CSNI/R(2016)5, Marseille, France, March 30–April 1, 2015, 2016, pp. 103–120.
- [152] S. Dickinson, et al., *Ann. Nucl. Energy* 74 (2014) 200–207.
- [153] T. Kärkelä, et al., Research at VTT on the transport and chemistry of iodine under primary circuit and containment conditions, in: Proceedings of The International Iodine Workshop, NEA/CSNI/R(2016)5, Marseille, France, March 30–April 1, 2015, 2016, pp. 79–87.
- [154] G.A. Glowa, et al., The main outcomes of the OECD Behaviour of Iodine (BIP) project, in: Proceedings of The International Iodine Workshop, NEA/CSNI/R(2016)5, Marseille, March 30–April 1, 2016, pp. 153–164.
- [155] C. Mun, et al., OECD-STEM Project and its follow-up STEM2, in: Proceedings of The International Iodine Workshop, NEA/CSNI/R(2016)5, Marseille, March 30–April 1, 2015, 2016, pp. 170–179.
- [156] L. Bosland, L. Cantrel, Iodine behaviour in the circuit and containment: modelling improvements in the last decade and remaining uncertainties, in: Proceedings of The International Iodine Workshop, NEA/CSNI/R(2016)5, Marseille, France, March 30–April 1, 2015, 2016, pp. 347–361.
- [157] L. Cantrel et al., IRSN R&D actions on FP behaviour for RCS, containment and FCVS in severe accident conditions, in: Proceedings of the 24th International Conference on Nuclear Engineering, vol. 4, Article number V004T13A023, Charlotte, NC, June 26–30, 2016, 2016.
- [158] B. Bartonicek, A. Habersbergerova, *Rad. Phys. Chem.* 28 (5/6) (1986) 591–600.
- [159] J. Imoto, et al., Isotopic signature and nanotexture of cesium-rich microparticles: release of uranium and fission products from the Fukushima Daiichi Nuclear Power Plant, *Sci. Rep.* 7 (2017) 5409. Available from: <https://doi.org/10.1038/s41598-017-05910-z>.
- [160] T. Albiol, et al., *Ann. Nucl. Energy* 116 (2018) 42–56.
- [161] D. Jacquemain, et al., Status Report on Filtered Containment Venting Systems, NEA/CSNI/R, (2014) 7.
- [162] T. Ishii, et al., Sorption of radioactive methyl iodide by silver doped zeolite for filtered venting system, in: International Conference on Nuclear Engineering, Proceedings of ICONE-4, V004T11A010, 2016.
- [163] S. Chibani, et al., *Phys. Chem. Chem. Phys.* 18 (36) (2016) 25574–25581.
- [164] S. Chibani, et al., *J. Chem. Phys.* 144 (24) (2016) 244705.

- [165] M. Chebbi, et al., *Microporous Mesoporous Mater.* 239 (2017) 111–122.
- [166] M. Chebbi, et al., *J. Phys. Chem., C* 120 (33) (2016) 18694–18706.
- [167] T. Lind, et al., A summary of the PSI investigations on iodine chemistry in the presence on impurities and additives, in: Proceedings of The International Iodine Workshop, Marseille, France, March 30–April 1, 2015, NEA/CSNI/R(2016)5, 2016, pp. 121–131.
- [168] K. Hata, et al., Effects of constituents of seawater on formation of volatile iodine by aqueous phase radiation chemistry, in: Proceedings of The International Iodine Workshop, Marseille, France, March 30–April 1, 2015, NEA/CSNI/R(2016)5, 2016, pp. 196–203.
- [169] D. Jacquemain, et al., Status Report on Long Term Management and Actions for a Severe Accident in a Nuclear Power Plant, NEA/CSNI/R, (2018) 13.
- [170] OECD-NEA joint project on Thermodynamic Characterisation of Fuel Debris and Fission Products Based on Scenario Analysis of Severe Accident Progression at Fukushima-Daiichi Nuclear Power Station (TCOFF). The information is available from <<https://www.oecd-nea.org/science/tcoff/>>.

This page intentionally left blank

Index

Note: Page numbers followed by “*f*,” “*t*,” and “*b*” refer to figures, tables, and boxes, respectively.

A

- 3A molecular sieve (3AMS), 499–500
- Absorption coefficient, 112
- ACAR method. *See* Annihilation radiation method (ACAR method)
- Accident tolerant fuels (ATFs), 379
- Actinoids (An), 119–120, 544
 - An-bearing nuclear fuels, 371
 - and fission products in UC, 224–225
 - oxides, 59–60
 - relative mole fraction, 225*f*
- Additive manufacturing (AM), 378
- Additives, 375, 379
 - to UO₂, 374–375
- ADU. *See* Ammonium diuranate (ADU)
- Advanced fabrication of UO₂, 375–379
 - AM, 378
 - field-assisted sintering of UO₂, 376–377
 - microwave sintering, 377–378
 - PIM UO₂, 378–379
 - sol–gel and hydrothermal routes for nanocrystalline UO₂ synthesis, 376
- Advanced Fuel Cycle Initiative program, 205
- Advanced high-temperature reactor (AHTR), 254
- Advanced reactor fuel fabrication
 - coated particle fuel fabrication, 403–405
 - high-density light-water reactor fuels, 399–403
 - molten-salt reactor fuel fabrication, 405–407
- Advanced reactor fuels, 371–372
- Advanced temperature and thermodynamic investigation by laser heating approach (ATTILHA), 104, 105*f*
- Aerodynamic enrichment process, 356–357

Aerosols, 556

- AES. *See* Auger electron spectroscopy (AES)
- AFM. *See* Atomic force microscopy (AFM)
- AFR. *See* Away from the reactor (AFR)
- AHTR. *See* Advanced high-temperature reactor (AHTR)
- AIC. *See* Silver–indium–cadmium (AIC)
- Aircraft reactor experiment (ARE), 252
- Alkaline leaching, 322, 323*f*
- Alloying, 387–392
 - additions to U–Si fuels, 402
 - casting, 371
- Alpha emitting isotopes, 319
- α -U (orthorhombic), 434
- Alternate TRISO fuels
 - to address CO formation, 236–237
 - fission product chemistry and transport, 237–241
- Alternative synthesis routes, 383
- Alumina (Al₂O₃), 205
- Aluminum, 497
 - alloy structural components, 274
 - hydroxides, 303–304
 - research reactor fuel cladding, corrosion of, 303–304
- AM. *See* Additive manufacturing (AM)
- American National Standard Institute, 333–334
- Americium (Am), 3
- Ammonium diuranate (ADU), 323, 336–337, 343, 372
- Ammonium nitrate (NH₄NO₃), 343
- Ammonium uranyl carbonate (AUC), 363–364, 372
- 3AMS. *See* 3A molecular sieve (3AMS)
- Analytical techniques, 89, 90*t*

- Annihilation radiation method (ACAR method), 127
- Anode, 75
- Aqueous sol–gel process, 403–405
- Aqueous uranyl nitrate, 342
- AR. *See* At reactor (AR)
- Arbeitsgemeinschaft Versuchsreaktor (AVR), 490
- Arc melting, 388–389
- ARE. *See* Aircraft reactor experiment (ARE)
- Arrhenius equation, 7
- Arrhenius-type equation, 559, 561
- As-cast uranium alloys, 397
- At reactor (AR), 475, 533
- ATFs. *See* Accident tolerant fuels (ATFs)
- Atomic force microscopy (AFM), 121
- ATTILHA. *See* Advanced temperature and thermodynamic investigation by laser heating approach (ATTILHA)
- AUC. *See* Ammonium uranyl carbonate (AUC)
- Auger Effect, 112–113
- Auger electron spectroscopy (AES), 121
- AVR. *See* Arbeitsgemeinschaft Versuchsreaktor (AVR)
- Away from the reactor (AFR), 533
- Azeotropic vaporization, 61b
- B**
- B_4C —stainless steel melt and Zry channel box, 572–576
- Back-scattered electrons (BSE), 123, 565–566
- image, U and Zr maps of cutting surface, 567f
- U–Zr–O ternary phase diagram, 568f
- Barium (Ba), 66
- BE. *See* Binding energy (BE)
- BECARRS project, 570–572
- Beryllium oxide (BeO), 252
- β -U (tetragonal), 434
- Binary and higher order oxide phase diagrams, 193–203
- ThO_2 – PuO_2 binary system, 197–203
- ThO_2 – UO_2 binary system, 195–196
- UO_2 – PuO_2 binary system, 195
- UO_2 – ThO_2 – PuO_2 diagrams, 203
- Binary phase diagram and relevant derivatives, 226–227
- melting /decomposition temperature, 228f
- nitrogen-uranium partial binary phase diagram, 226f
- Binary phase diagrams, 174, 174f
- Binding energy (BE), 111–112
- BN. *See* Boron nitride (BN)
- Boiling point (BP), 485–486
- in MSR, 257–258
- Boiling water reactor (BWR), 374–375, 473, 478, 556. *See also* Pressurized water reactor (PWR); Light water reactors (LWRs)
- average weight composition, 472f
- Boltzmann distribution law, 35–36
- Bolzmann’s equation, 40
- Boric acids, 581
- Boron, 534
- release kinetics from degraded B_4C control blades, 598–599
- Boron carbide (B_4C), 569
- control rod or blade, 570–572, 573t
- Boron nitride (BN), 114
- Bottom pouring, 390
- BP. *See* Boiling point (BP)
- Bragg’s law, 139–140
- Brillouin spectroscopy, 108, 110
- BSE. *See* Back-scattered electrons (BSE)
- “Burn-leach” analysis, 405
- BWR. *See* Boiling water reactor (BWR)
- C**
- Calcination, 337–338, 340–341
- Calculation of Phase Diagrams Method (CALPHAD), 15, 169–172, 170f
- Calendar year (CY), 471–472
- CALPHAD. *See* Calculation of Phase Diagrams Method (CALPHAD)
- Canada Deuterium Uranium (CANDU) reactor, 342–344, 473, 478, 493–494
- fuels, 527
- UO_3 to ceramic-grade UO_2 for, 342f
- Canonical ensembles, 36
- Canonical partition function, 37–39
- Carbide compounds (C_nCs), 239
- Carbide fuels, 222–225, 463
- actinoids and fission products in uranium monocarbide, 224–225
- binary phase diagram of U–C, 223

- clad carburization, 223–224
Carbon anode, 339
Carbon dioxide (CO_2), 322
Carbon monoxide (CO)
 corrosion of SiC, 235–236, 236/
 formation and effect on particle integrity,
 232–237
 alternate TRISO fuels to address CO
 formation, 236–237
 kernel migration, 233–235
 pressure vessel failure, 233
Carbon-14, 500
Carbonate, 69
 concentration in natural waters, 73b
Carbothermic reduction (CTR), 380
Carbothermic reduction and nitridation
 (CTR–N), 380–382
 process to produce UN pellets, 381f
Carbothermic reduction-nitridation,
 228–229
Casks/containers, storage in, 533–534, 534f
Casting, 387–392
Cathode, 75, 388
CEF. *See* Compound energy formalism
 (CEF)
Centre Industriel de Stockage GEOlogique
 (Cigeo), 538, 538f
Centrifugal force, 356
Ceramic fuel fabrication. *See also* Metallic
 fuel fabrication
 nitride fuel fabrication, 379–384
 oxide fuel fabrication, 372–379
 uranium borides, 385
Ceramic-grade UO_2 , 342
Cesium (Cs), 66, 239–240
 chemisorption phenomena, 603
 UCO TRISO fuel compacts, 240f
Cesium molybdates. *See* Cesium
 orthomolybdate (Cs_2MoO_4)
Cesium orthomolybdate (Cs_2MoO_4), 64,
 444, 597
 determination of sublimation and
 vaporization enthalpies of, 64b
Cesium uranate (Cs_2UO_4), 16
 enthalpy of formation, 17b
Cesium-Tellurium (Cs-Te), 229
Chemical exchange process, 357–361
Chemical kinetics, 3–8
 reaction rates, 4–7
temperature dependence of rate constants,
 7–8
Chemical potential, 25–29
 of ideal single-component gas,
 27–28
 of single-component condensed phase,
 28–29
Chemical reaction equilibria, 34–35
 equilibrium constant, 34
 Van't Hoff equation, 35
“Chemical shift” of photoemission peaks,
 118–119
Chemical solution, 29
Chemical state of fission products, 66–69
Chemical thermodynamics, 3, 9–15
 enthalpy, 12
 Gibbs energy, 13
 heat capacity, 13–15
 Helmholtz free energy, 12–13
 laws of thermodynamics, 10–11
 thermodynamic relations between state
 functions, 15
 thermodynamic system and state
 functions, 9–10
Chemisorbed water, 541
Chloride, 69, 514
Chloride volatility, 511–516
 interconversion of chlorides and fluorides,
 513–515
 in molten salts, 513
 overall assessment of, 515–516
 predominance diagram for U–Cl–O
 system, 514f, 515f
 processing of fuels, 512–513
 vapor pressure of MoF_6 , HF , and UF_6 ,
 511f, 512f
Chlorine chemical potentials, 67
Chromia (Cr_2O_3), 205–207, 374, 375f
Chromium additions, 374
Cigeo. *See* Centre Industriel de Stockage
 GEOlogique (Cigeo)
Clad carburization, 223–224
Clad temperature, 428
Clausing–Clapeyron equation, 63
Clausius inequality, 11
Closed nuclear cycles, 530–532
Co-D-Con. *See* Coextraction and
 decontamination (Co-D-Con)
Coated particle fuels, 231–242, 403

- Coated particle fuels (*Continued*)
 CO formation and effect on particle integrity, 232–237
 fabrication
 fluidize bed coater, 404f
 tristructural isotropic fabrication, 403–405
 oxygen potential and fission products, 241–242
 TRISO, 231–232, 231f
 COEX process, 503–504
 Coextraction and decontamination (Co-D-Con), 485, 504, 504f
 Coextrusion process, 394–396
 Cold rolling of as-cast product, 393–394
 Combustion calorimetry, 16
 Commercial oxide fuel production, 372–373, 373f
 Commercial powder metallurgy of UO₂, 373
 commercial powder metallurgy, 373
 solid-state synthesis, 373
 wet chemical processing, 372
 Complexation, 69–71
 Compound energy formalism (CEF), 164
 Conceptualization, 545
 Concrete, 582
 casks, 534
 Condensed phases, thermodynamics of, 15–35
 chemical potential, 25–29
 chemical reaction equilibria, 34–35
 mixing properties for gas, solid, and liquid solutions, 29–34
 chemical potential of gas, 29–30
 chemical potential of species, 30
 chemical solution, 29
 mixing and excess thermodynamic properties, 31–34
 Raoult's law and Henry's law, and standard states, 30–31
 molar thermodynamic properties, 15–25
 Configurational entropy, 32
 Congruent vaporization, 61b
 Containment pools, chemistry in, 615–618
 Coolant Accident, Loss of, 608
 Coolant liquid phase on long term, chemistry in, 618
 Copper-based alloys, 396
 Coreless heating, 389–390
 Corium, 582, 589
 Corrosion
 of aluminum research reactor fuel cladding, 303–304
 inhibition, 266–267
 Coulometry, 143–145
 Coupling of internal motion, 45–46
 Cs₂U₄O₁₂, 444
 Cs—I—Mo—O—H
 chemical impact of boron on, 602–603
 chemistry during transport in reactor coolant system, 600
 CTR. *See* Carbothermic reduction (CTR)
 CTR–N. *See* Carbothermic reduction and nitridation (CTR–N)
 Curium (Cm), 3
 CY. *See* Calendar year (CY)
- D**
- DBS. *See* Doppler broadening spectroscopy (DBS)
 De Broglie relation, 121–122
 Debye temperature, 21
 Deconversion, 361
 Deep geological disposal systems, 537
 Diatomic gas, 50b
 Differential scanning calorimetry (DSC), 90–94
 enthalpy of mixing, 93–94
 enthalpy of transition, 93
 heat capacity, 94
 melting point determination, 90–91
 phase equilibria in binary mixtures, 91–93
 Diffraction techniques, 139–142
 electron diffraction, 141–142
 XRD, 139–141
N'-Diocetyl-2-(2-hexyloxyethyl) malonamide (DMDOHEMA), 504–505
 Direct thermal method, 382–383
 Direct use of PWR fuel in CANDU (DUPIC), 493–494
 Dissociation energy, 48
 Dissolution of UO₃, 5b
 DMDOHEMA. *See* *N'*-Diocetyl-2-(2-hexyloxyethyl) malonamide (DMDOHEMA)
 DOE. *See* US Department of Energy (DOE)
 Dopants, 376–377, 546

- Doped fuels, 203–207, 206^t
corundum type oxide addition, 208^f
measured grain size *vs.* mole fraction,
206^f, 207^f
- Doppler broadening spectroscopy (DBS),
127
- Drop calorimetry, 24–25, 90, 95–97
- Drop measurement, 96, 96^f
- Dry conversion processes, 364–366
fluidized-bed, 365
kiln, 366
IDR route, 364–365
- Dry storage, 533–536
in casks/containers, 533–534, 534^f
in silos, 535, 535^f
in vaults, 535–536
- DSC. *See* Differential scanning calorimetry
(DSC)
- DUPIC. *See* Direct use of PWR fuel in
CANDU (DUPIC)
- E**
- EBR-II. *See* Experimental Breeder Reactor-2
(EBR-II)
- EBSID. *See* Electron back-scattered
diffraction (EBSID)
- EDS. *See* Energy dispersive X-ray
spectroscopy (EDS)
- EDX analysis. *See* Energy-dispersed X-ray
analysis (EDX analysis)
- EELS. *See* Electron energy loss
spectroscopy (EELS)
- Einstein temperature, 21
- Electrical work, 76
- Electrochemical techniques, 143–145
coulometry, 143–145
EMF, 143–145
- Electrolysis, 385
- Electromagnetic enrichment process,
353–354
- Electromagnetic isotope separation,
353–354, 354^f
- Electromagnetic work, 10
- Electromotive force (EMF), 75, 143–145
- Electron
diffraction, 141–142
microprobe, 442
- Electron back-scattered diffraction (EBSID),
142
- Electron energy loss spectroscopy (EELS),
125–126
- Electron microscopy and spectroscopy,
121–126
electron probe microanalysis, 126
SEM, 122–126
TEM, 122–126
- Electron probe micro-analyzer (EPMA), 126
- Electron spectroscopy for chemical analysis.
See Photoelectron spectroscopy
(PES)
- Electronic energy, 279
- Electronic partition function, 41–42
- Ellingham diagrams, 66–69, 67^f, 441^f, 442,
446
- EMF. *See* Electromotive force (EMF)
- Encapsulation in MSR, 263–265
- Energy, 10–11
dependence of absorption coefficient,
112–113
spectrum, 106
- Energy dispersive X-ray spectroscopy
(EDS), 123
- Energy-dispersed X-ray analysis (EDX
analysis), 565
- Enriched UF₆, 361
conversion of, 361–366
dry, 364–366
wet, 362–364
- Enriched UO₂, 361
conversion of, 361–366
- Enrichment process, 343–344, 344^f, 346^f
aerodynamic, 356–357
chemical exchange process, 357–361
electromagnetic, 353–354
gas centrifuge, 348–349
gaseous diffusion process, 350–351, 351^f
industrial-scale gaseous UF₆, 349^f
laser isotope, 352–353
thermal diffusion process, 354–355, 356^f,
357^f
uranium, 345–361
- Ensembles, 36–37
- Enthalpy, 12
of formation, 16–19
of Cs₂UO₄, 17^b
of mixing, 31–32
of DSC, 93–94
of transition of DSC, 93

- Entropy, 11
of mixing, 31–32
- EPMA. *See* Electron probe micro-analyzer (EPMA)
- ϵ -particles. *See* Metallic FPs
- Equilibrium constant, 34
- Error propagation law, 105–106
- ESRF. *See* European Synchrotron Radiation Facility (ESRF)
- 2-Ethylhexylphosphonic acid mono-2-ethylhexyl ester (HEH (EHP)), 506
- Euler–Maclaurin summation formula, 44
- EURO-Group Actinide Extraction (EURO-GANEX), 504–505, 505*f*
- European Synchrotron Radiation Facility (ESRF), 114–115
- Eutectic, 565
equilibrium, 53
interaction model, 563
liquefaction model, 566–568
melting, 92–93
- EXAFS. *See* Extended X-ray absorption fine-structure spectroscopy (EXAFS)
- Excess enthalpy and entropy of mixing, 32–34
- Excess molar Gibbs energy of mixing, 32
- Experimental Breeder Reactor-2 (EBR-II), 379
- Experimental methods, 89
diffraction techniques, 139–142
electrochemical techniques, 143–145
MS, 135–137
NMR, 131–135
SIMS, 137–139
spectroscopy techniques, 106–130
thermal analysis methods, 90–106
- Experimental phase diagram, 565
- Extended X-ray absorption fine-structure spectroscopy (EXAFS), 113, 115
- F**
- 5f electrons, 3
- Fabrication processes, 281–284
for metallic fuels
alloying and casting, 387–392
arc melting, 388–389
microwave melting, 392
VIM methods, 389–392
for novel fuel, 371
- Face-centered cubic (FCC), 434
- Factor Group Theory, 108–109
- Faraday constant, 76
- Fast breeder reactors (FBRs), 420–421, 421*t*, 427, 442, 445, 449, 457
- Fast neutron spectrum, 420
- Fast reactor core (FR core), 422, 428–429
axial temperature profiles in, 428*f*
- FBRs. *See* Fast breeder reactors (FBRs)
- FCC. *See* Face-centered cubic (FCC)
- FCCI. *See* Fuel–cladding chemical interaction (FCCI)
- FCVS. *See* Filtered containment venting systems (FCVS)
- FDNPS accident. *See* Fukushima Daiichi Nuclear Power Station accident (FDNPS accident)
- FeCrAl, 222
- Feeding distance, 391
- FHR. *See* Fluoride-cooled high-temperature reactor (FHR)
- FIB systems. *See* Focused ion beam systems (FIB systems)
- Fiber optics, 110–111
- Field-assisted sintering of UO₂, 376–377
- Field-assisted sintering technique. *See* Spark plasma sintering (SPS)
- Filtered containment venting systems (FCVS), 614
- First law of thermodynamics, 10–11
- First-order kinetic reaction, 5
- First-order transitions, 15, 55
- Fission gas, 238–239, 280–281, 528
- Fission product chemistry at severe accident of light water reactors, 593–618
chemistry of fission product release from irradiated fuel during severe accident, 595–599
highlights from Fukushima Daiichi accidents, 598–599
issues addressing before Fukushima Daiichi accidents, 595–598
- in containment pools and in liquid scrubber containment venting systems, 615–618
- fission product chemistry in containment, gas phase, and interactions with containment surfaces, 605–615

- aspects affecting physicochemical phenomena, 613
- chemistry aspects affecting formation of fission product aerosols, 605–607
- iodine aerosol stability, 610–611
- iodine and ruthenium chemistry, 608–610
- mitigation of radioactive releases for long-term accidents, 614–615
- Org-I formation, 610
- radioactive material transport and deposition, 611–612
- remobilization and transfer of radioactivity for long-term accidents, 613–614
- in reactor coolant system, gas phase, and interactions with structure surface, 599–605
- Cs—I—Mo—O—H chemistry during transport in reactor coolant system, 600
- highlights from Fukushima Daiichi accidents, 602–605
- issues addressing before Fukushima Daiichi accidents, 599–602
- remobilization of fission product deposits, 601–602
- Ru—N—O—H chemistry during transport in the reactor coolant system, 601
- Fission products (FPs), 419, 423–424, 438, 440, 444–445, 457, 527, 543, 556
- chemical state of, 66–69
- chemistry and transport, 237–241
- cesium and iodine, 239–240
- fission gas, 238–239
- fission product transport in reactor, 240–241
- palladium, 237
- silver, 237–238
- relative yield of isotopes, 425^f
- retention, 260
- SEM fractograph, 426^f
- speciation, 267–268
- transport in reactor, 240–241
- Fission-enhanced diffusion, 278–280
- Fissionable materials, 386
- Fissium (Fs), 389–390
- Flash laser facility (FLF). *See* Laser heating and spectrometric analysis (LHASA)
- Fluid(ized) bed conversion process, 365
- kiln, 366
- Fluoride, 69, 510, 513–514. *See also* Metallic fluorides
- salts, 255
- volatility, 508–511
- coseparation of Pu, Np, and U from bulk of UF₆, 509–510
- fluorinating agents, 508^t, 509
- separation methods, 509
- Fluoride-cooled high-temperature reactor (FHR), 249
- Fluorinating agents, 508^t, 509, 514–515
- Fluorination, 338–340
- direct fluorination of UF₄, 338–339
- fluorine production, 339
- UF₆ recovery, 339–340
- Fluorine (F₂), 262
- chemical potentials, 67
- gas, 339
- Focused ion beam systems (FIB systems), 124
- FPCs. *See* Fuel performance codes (FPCs)
- FPs. *See* Fission products (FPs)
- FR core. *See* Fast reactor core (FR core)
- Free water, 540
- French CHEMEX process, 358
- Fuel, 421
- axial swelling *vs.* burnup, 433^f
- cladding, 371
- element, 419
- soluble in fuel matrix, 66
- evolution with burnup of global fission gas, 432^f
- materials, 276–278, 278^t
- meat, 274
- phases, 284
- salt synthesis, 407
- swelling, 429–432
- systems, 230–231
- Fuel behavior under irradiation, 284–303
- aluminum-based, plate-type dispersion fuels, 282^f
- fabrication process for TRIGA fuels, 283^f
- U—Mo/Al system, 293–301
- uranium aluminides, 284–286

- Fuel behavior under irradiation (*Continued*)
 uranium oxides, 290–293
 uranium silicides, 286–290
 U–Zr–H fuel system, 301–303
- Fuel chemistry, 280
 advances in
 chemistry on fuel/core degradation, 557–593
 fission product chemistry at severe accident of light water reactors, 593–618
- Fuel fabrication, 371, 387
 advanced reactor fuel fabrication, 399–407
 ceramic fuel fabrication, 372–386
 metallic fuel fabrication, 386–399
- Fuel geometry, 274–275
 plate-type fuels, 274
 rod-and pin-type fuels, 275
 tubular fuels, 275
- Fuel performance codes (FPCs), 420
- Fuel/core degradation, 555–593
 chemistry in early phase fuel degradation, 557–576
 chemistry in late phase degradation, 576–582, 578*t*
 chemistry in transition from early phase to late phase, 576
 ex-vessel conditions, 582–593
 liquefaction of control rod/blade and interaction with Zry, 569–576
 material reactions/interactions of core materials, 558*f*
- Fuel–cladding chemical interaction (FCCI), 460–462
- Fukushima Daiichi accidents, issues addressing before, 595–602, 615–617
 basic process of fission product release from fuel, 595–596
 highlights from, 598–599, 602–605, 617–618
 alteration of release behavior of non-low-volatile fission products, 598
 boron release kinetics from degraded B₄C control blades, 598–599
 release behavior of fission products, 597–598
- Fukushima Daiichi Nuclear Power Station accident (FDNPS accident), 555
- Fully oxidized cladding, 579–580
- Fusion enthalpy, 56
- G**
 Galvanic cell, 73–77
 γ -U (bcc), 434
 Gang chopping, 480
 Gas bubble superlattice (GBS), 294–295
 Gas centrifuge, 348, 349*f*
 enrichment process, 348–349
 Gaseous diffusion process, 350–351, 351*f*
 GBS. *See* Gas bubble superlattice (GBS)
 Gd₂O₃, 207
 GEM. *See* Gibbs energy minimization (GEM)
 Gibbs energy, 13, 15, 25, 63, 162, 169
 of formation, 25
 of half-cell reactions, 77
 of mixing, 31–32
 of redox reaction and Nernst equation, 76–77
 surface diagram, 565–566
 Gibbs energy minimization (GEM), 160
 Gibbs phase rule, 50–51, 166
 Grand canonical ensemble, 36
 Gray phases, 450
- H**
 HABOG, 536, 536*f*
 Half-cell reactions, 75–76
 Half-life constant, 7*b*
 Halogens bromine, 443
 HANARO. *See* High-Flux Advanced Neutron Application Reactor (HANARO)
 Harmonic oscillator approximation, 42
 HBS. *See* High burnup structure (HBS)
 H–D–N synthesis method. *See* Hydring prior to nitridization synthesis method (H–D–N synthesis method)
- Headend processing
 for alternative or advanced fuels, 489–497
 configuration of pebble, 491*f*
 crush-burn-crush-burn-leach method, 492*f*

- mechanical headend for prismatic fuels, 493f
method to recover nuclear-grade graphite, 494f
TRISO fuels, 489–493
thorium-enhanced fuels, 494–497
decay chain for ^{232}U , 496f
pathways to produce ^{232}U , 495f
Zircaloy-clad fuels for hydrometallurgical separations, 478–489, 479f
- Heat capacity, 13–15, 258, 258f
of DSC, 94
at high temperatures, 24–25
at low temperatures, 20–24
- Heat, defined, 10–11
- Heat flux signal, 90–91
- Heat treatment, 397–399, 398f
- Heavy-water reactors, 473
direct reuse in, 473–474
reenrichment option, 474–475
REMIX, 475
- HEH (EHP). *See* 2-Ethylhexylphosphonic acid mono-2-ethylhexyl ester (HEH (EHP))
- Helikon vortex tube process, 356–357
- Helmholtz free energy, 12–13
- Henry's constant, 30
- Henry's law, 30–31
- Hess's law, 17–18
- HEU. *See* Highly enriched uranium (HEU)
- High burnup structure (HBS), 541
- High resolution liquid state NMR, 131
- High temperature gas-cooled reactors (HTGRs), 231–232
- High-density composite fuels for light-water reactors, 402–403
light-water reactor fuels, 399–403
alloying additions to U–Si fuels, 402
uranium silicide pellet fabrication, 400–402
- High-Flux Advanced Neutron Application Reactor (HANARO), 275
- High-level waste (HLW), 531
geological disposal, 536–539
storage
dry storage, 533–536
wet storage, 532–533
- High-resolution electron energy loss spectroscopy (HREELS), 121
- High-resolution solid-state NMR, 133–134
- High-temperature gas-cooled reactors (HTGRs), 489, 490f
- High-temperature heat capacity of NpO_2 , 26b
- Higher order system, 203
- Highly enriched uranium (HEU), 344
- Hindered rotation, 46–47
- HIP. *See* Hot isostatic pressing (HIP)
- HLW. *See* High-level waste (HLW)
- HOI. *See* Hydroiodic acid (HOI)
- Homogenization, 397
- Hot isostatic pressing (HIP), 380
- Hot rolling of as-cast metal fuels, 393
- HREELS. *See* High-resolution electron energy loss spectroscopy (HREELS)
- HTGRs. *See* High temperature gas-cooled reactors (HTGRs); High-temperature gas-cooled reactors (HTGRs)
- Hybrid aqueous processing, 506
- Hybrid processes, 478
- Hydride fuel, 231
- Hydriding prior to nitridization synthesis method (H–D–N synthesis method), 380, 382–383
- Hydrofluoric acid ($\text{HF}_{(\text{aq})}$), 362
- Hydrofluorination, 337–338
- Hydrogen peroxide, 326
uptake of Zry cladding, 557–563
- Hydrogen fluoride (HF), 262, 339
line installed at JRC Karlsruhe, 263f
- Hydroiodic acid (HOI), 498
- Hydrolysis, 69–71
- Hydrometallurgical separations, 502–506
- Hydroxide, 69
- Hyperstoichiometric carbide (MC_{1+x}), 463
- Hyperstoichiometric MOX, 458–459
- Hyperstoichiometric nitride (MN_{1+x}), 463
- Hypothetical eutectic temperature, 565

I

- IAEA. *See* International Atomic Energy Agency (IAEA)
- Ideal gas, 41–42
- Ideal single-component gas, chemical potential of, 27–28

- IDR. *See* Integrated dry route (IDR)
- IMSBR. *See* Indian MSBR (IMSBR)
- In-reactor behavior
- fuels chemistry, 462–464
 - fuel-cladding, 463–464
 - irradiated, 462
 - stable or long-lived fission products, 463f
- general description of fuel behavior, 420–432
- micrograph of a fast reactor MOX pellet, 429f
- microstructural evolution, 428–429
- radiation damage, 422–428
- standard phénix fuel pin, 422f
- thermal and fast reactor fuels, 420–421
- oxide fuel chemistry, 429–432
- In-reactor irradiation of nuclear fuel, 543
- In-situ leaching (ISL), 318, 320–324
- In-situ recovery. *See* In-situ leaching (ISL)
- Indian MSBR (IMSBR), 254
- Inductively coupled MS techniques, 136
- Industrial Centre for Geological Storage.
- See* Centre Industriel de Stockage Géologique (Cigeo)
- Inert gases, 66
- Inflections, 103–104
- Infrared (IR)
- detector, 104
 - spectroscopy, 108, 110
- Inhomogeneity, 397
- Inner pyrolytic carbon layer (IPyC layer), 231–232, 403
- Inorganic fluorides, 339–340
- Instant release fraction (IRF), 543–544
- Integral analyses, 175–177
- Integrated dry route (IDR), 364, 364f
- Interaction parameters, 164
- Interaction with sea salt materials, 593
- Interim-23 process, 496
- Intermetallic fuel compounds, 274, 389
- Internal energy, 41
- International Atomic Energy Agency (IAEA), 316, 533
- International Organization for Standardization (ISO), 333–334
- International Source Term Program (ISTP), 570–572
- Interstitial hole positions, 58
- Iodine, 239–240
- Iodine (I), 66, 443, 498–499
- aerosol stability, 610–611
 - chemistry, 608–610
- Ion exchange, 324–325
- Ion microprobes, 137–138
- Ionic liquid model, 164
- IPyC layer. *See* Inner pyrolytic carbon layer (IPyC layer)
- IRF. *See* Instant release fraction (IRF)
- Iron, 580–581
- Irradiated oxide fuel, 438–462
- chemical form of fission products, 440–453
 - computational thermodynamics to predict, 450–453
 - Cs uranate and molybdate phases, 444
 - fission products dissolved in matrix, 444–445
 - gaseous fission products, 442–443
 - gray phases, 450
 - Mendeleev periodic, 440f
 - metallic precipitates, 445–448, 450f
 - Pd rich phases, 449–450
 - phase diagram Pd–Te, 451f
 - phase diagrams, 446f, 447f, 452f
 - SEM image of peripheral part, 443f
 - fuel-cladding chemical interaction, 460–462, 462f
 - mass transport phenomena, 457–460
 - lenticular pores migrating, 459f
 - plutonium radial redistribution along, 460f
 - oxygen chemical potential, 453–457, 454f
- Irradiation effects, in-reactor behavior, 422–428
- ISL. *See* In-situ leaching (ISL)
- ISO. *See* International Organization for Standardization (ISO)
- Isobaric expansivity, 14–15
- Isoflash effect, 336
- Isothermal compressibility, 14–15
- Isotope enrichment
- aerodynamic, 359f
 - column for solvent extraction, 359f
 - ion exchange column for, 360f
- ISTP. *See* International Source Term Program (ISTP)

J

Japan Atomic Energy Agency (JAEA), 556
Joint oxyde-gaine (JOG), 461–462

K

Karlsruhe Institute of Technology (KIT), 569
KBS-3 concept for SNF disposal, 537, 537f, 545
KE. *See* Kinetic energy (KE)
KEMS. *See* Knudsen effusion MS (KEMS)
Kernel migration, 233–235
 in UO_2 particle irradiated, 234f
Kiln, 366
Kinetic energy (KE), 113
KIT. *See* Karlsruhe Institute of Technology (KIT)
Knudsen effusion method, 60
Knudsen effusion MS (KEMS), 136–137
Kohler schemes, 164, 165f
Krypton (Kr), 66, 500–501

L

Lab-scale process, 491
LAF technique. *See* LASer-Flash technique (LAF technique)
Lagrangian multipliers, 169
Lanthanoids, 3
Large geometry SIMS machines (LG SIMS machines), 139
Laser heating, 101–106
Laser heating and spectrometric analysis (LHASA), 101
Laser isotope enrichment process, 352–353
 separation processes, 353
LASer-Flash technique (LAF technique), 106, 107f
LEED. *See* Low-energy electron diffraction (LEED)
LEES. *See* Low-energy electron spectroscopy (LEES)
LEIS. *See* Low-energy ion scattering spectroscopy (LEIS)
LEU. *See* Low-Enriched Uranium (LEU)
Lever rule, 52–55
LG SIMS machines. *See* Large geometry SIMS machines (LG SIMS machines)

LHASA. *See* Laser heating and spectrometric analysis (LHASA)

LiF–PuF₃ pseudo-binary system, 91–92
LiF–ThF₄ liquid solution, mixing properties in, 33b
LiF–ThF₄–UF₄ system, 53–55
Light water reactors (LWRs), 52–53, 249, 315, 371, 422, 442–443, 445, 457, 461, 469, 471–472, 478, 481–483, 493–494, 501, 527, 556. *See also* Pressurized water reactor (PWR); Boiling water reactor (BWR)
additional component recycle, 478
hardware component recycle, 477
high-density composite fuels for, 402–403
plutonium distribution along UO_2 pellet radius, 458f
reuse of uranium from, 473–475
zirconium recycle and disposition options, 476–477

Liquefaction

of control rod/blade and interaction with Zry, 569–576
AIC control rod, 569–570, 571t
boron carbide control rod or blade, 570–572
Fe–Zr binary phase diagram, 575f
reaction between B₄C–stainless steel melt and Zry channel box, 572–576
between UO_2 fuel and Zry cladding, 563–568, 564f, 569f

Liquid metal–cooled fast reactor (LMFR), 253

Liquid scrubber containment venting systems, 615–618

Liquid state NMR, 131

Lixiviant materials, 320–321

LMFR. *See* Liquid metal–cooled fast reactor (LMFR)

LOCA. *See* Loss of coolant accidents (LOCA)

Long-term accidents mitigation of radioactive releases for, 614–615

remobilization and transfer of

radioactivity for, 613–614

Loss of coolant accidents (LOCA), 557

- Low-energy electron diffraction (LEED), 121
- Low-energy electron spectroscopy (LEES), 108
- Low-energy ion scattering spectroscopy (LEIS), 121
- Low-Enriched Uranium (LEU), 232, 342
- Low-temperature
- heat capacity of NaUO_3 , 22*b*
 - NMR, 131–133
 - solid-state NMR experiments, 131
- LWRs. *See* Light water reactors (LWRs)
- M**
- Macroscopic property of system, 36–37
- Magic angle spinning technique (MAS technique), 131
- Magic value, 565–566
- Magnesia, 326
- Magnesium fluoride, 510
- Magnox reactors, 343–344
- production of uranium metal for, 343
- MAS technique. *See* Magic angle spinning technique (MAS technique)
- Mass spectrometry (MS), 60, 89, 135–137
- KEMS, 136–137
- Materials Test Reactors (MTRs), 274
- Maxwell relations, 15
- MCCI. *See* Molten core–concrete interaction (MCCI)
- Mechanical processing, 371
- Mechanical work, 10
- Melt synthesis process, 400–401
- Melting
- enthalpy, 55–56
 - point, 255–257
 - determination of DSC, 90–91
 - liquidus projection of $\text{LiF}-\text{ThF}_4-\text{PuF}_3$ system, 256*f*
 - transition, 55–56
- Metal-organic framework (MOF), 614
- Metallic
- casks, 534
 - FPs, 528
 - fuels, 215–220, 386–387
 - precipitates, 66
 - tellurium, 267–268
- Metallic fluorides
- magnesium fluoride, 510
- selective trapping of impurities using, 510–511
- sodium fluoride, 510–511
- Metallic fuel fabrication, 371–372, 386–399. *See also* Ceramic fuel fabrication
- fabrication methods for metallic fuels, 387–399
- thermomechanical processing, 392–396
- Metallurgical additives, 373
- Metric ton of uranium (MTU), 471–472
- Microcanonical ensemble, 36
- Microshrinkage, 391
- Microwave
- melting, 392
 - sintering, 377–378
 - transparent material, 377–378
- Milling, 324–326
- ion exchange, 324–325
 - precipitation, 325–326
 - solvent extraction, 325
- Minimal data, 223–224
- Mining, 315–323
- methods of, 318–323, 319*t*
 - acid-leaching process, 321*f*
 - ISL, 320–323
 - open pit mining, 319–320
 - underground mining, 320
 - uranium bearing minerals, 316–318
 - uranium fuel cycle, 316*f*
 - uranium resources, 316
- Mixed oxides (MOXs), 188, 530–531
- fuel, 177–178, 437–438
 - oxygen potential for FBR, 455*f*
 - uranium–plutonium–oxygen phase, 438*f*
- MLIS. *See* Molecular laser isotope separation (MLIS)
- MOF. *See* Metal-organic framework (MOF)
- Molar enthalpy, 40
- Molar thermodynamic properties, 15–25
- enthalpy of formation, 16–19
 - Gibbs energy of formation, 25
 - heat capacity at high temperatures, 24–25
 - heat capacity at low temperatures, 20–24
 - reference and standard states, 15–16
 - standard entropy, 19–20
- Molar volume (V_m), 9

- Molecular laser isotope separation (MLIS), 352
- Molecular partitioning function, 36
- Molecular thermodynamic calculations, 41–42
- electronic partition function, 41–42
 - translational partition function, 41
- Molten core–concrete interaction (MCCI), 582
- appearance of test, 586*f*
 - degraded interface layers, 587*f*
 - interaction with sea salt materials, 593
 - interface interaction between molten core material and concrete, 585–589
 - morphology of solidified sim-debris, 589*f*
 - oxidation/reduction trend in, 588*f*
 - phase compositions detected, 591*f*
 - phase/element distribution during solidification, 589–592
 - phenomenology of, 582–585
 - SEM investigation, 592*f*
- Molten salt breeder reactor (MSBR), 250–251
- Molten salt fast reactor (MSFR), 254
- Molten salt reactor (MSR), 53–55, 249, 255*t*
- advantages, 249–251
 - challenges for MSR deployment, 251–252
 - effect
 - of oxygen impurities, 268
 - of soluble fission product impurities, 269
 - fuel concepts, 254
 - fuel fabrication, 405–407
 - pyrochemical fuel salt synthesis, 406–407
 - fuel production, 407*f*
 - fuel salt properties, 254–261
 - fission product retention, 260
 - heat capacity, 258
 - melting point, 255–257
 - pseudo-binary phase diagram, 259*f*
 - solubility of actinoids, 259
 - stability to radiation, 260–261
 - vapor pressure, 257–258
- history, 252–253
- measurements and experimental procedures, 261–265
- DSC crucible, 264*f*
- handling, 261
- high-temperature measurements, 263–265
- nickel crucible, 264*f*
- sample synthesis and purification, 261–263
- redox potential of fuel, 265–268
- renaissance, 253–254
- representation, 250*f*
- Molten salt recycle, 254
- Molten-salt reactor experiment (MSRE), 252, 253*f*, 405–406
- Molybdenum-based metallic fuels, 220
- uranium-molybdenum partial binary phase diagram, 221*f*
- Momentum conservation selection rule, 110
- Monatomic gas, 49*b*
- Morse potential, 43
- MOXs. *See* Mixed oxides (MOXs)
- MPC. *See* Multipurpose canister (MPC)
- MS. *See* Mass spectrometry (MS)
- MSBR. *See* Molten salt breeder reactor (MSBR)
- MSFR. *See* Molten salt fast reactor (MSFR)
- MSR. *See* Molten salt reactor (MSR)
- MSRE. *See* Molten-salt reactor experiment (MSRE)
- MTRs. *See* Materials Test Reactors (MTRs)
- MTU. *See* Metric ton of uranium (MTU)
- Muggianu schemes, 164, 166*f*
- Multikilogram-scale tests, 484
- Multiple interpolation, 164
- Multiple mitigation methods, 220
- Multipurpose canister (MPC), 534
- N**
- Nanocrystalline UO₂, 376
- National Reactor Universal (NRU), 275
- Natural uranium (NU), 473, 527
- NEA. *See* Nuclear Energy Agency (NEA)
- NEA-OECD. *See* Nuclear Energy Agency–Organization for Economic Cooperation and Development (NEA-OECD)
- Neptunium (Np), 3, 187
- Nernst equation, 265
- Neutron flux, 422

- Neutron (*Continued*)
 - neutron-absorbing material, 534
 - scattering, 108
- Neutronic codes, 440
- NEXAFS. *See* X-ray absorption near-edge spectroscopy (XANES)
- $(\text{NH}_4)_2\text{U}_2\text{O}_7$. *See* Ammonium diuranate (ADU)
- Niobia (Nb_2O_5), 205–207
- Niobium, 445
- Nitrate, 69, 503
- Nitric acid dissolution, 485–487
 - traditional process, 485–486
- Nitride consolidation methods, 383–384
- Nitride fuels, 226–229, 463. *See also*
 - Nuclear fuel
 - binary phase diagram and relevant derivatives, 226–227
 - fabrication
 - alternative synthesis routes, 383
 - CTR–N, 380–382
 - direct thermal method, 382–383
 - nitride consolidation methods, 383–384
 - UN synthesis and fabrication techniques, 380–384
 - forms, 379
 - incorporation of actinoids and fission products in UN, 229
 - relevance of carbon and oxygen impurities to in-pile performance, 228–229
- Nitrogen oxides (NO_x), 486
- NMR. *See* Nuclear magnetic resonance (NMR)
- Noble gases, 543
 - FPs, 442–443
- Noble metals, 229
- Non-oxide
 - compounds, 221
 - fuels, 222
 - non-oxide-based fuel types, 399–400
- Non/low-volatile fission products, alteration of release behavior of, 598
- Nonstoichiometry effect on thermodynamic properties, 56–60
- Nontraditional ceramic fuels, 220–231
 - carbide fuels, 222–225
 - forms, 229–231
 - fuel systems, 230–231
- uranium silicide compounds for light water reactor applications, 230
- nitride fuels, 226–229
- Normal spectral emissivity (NSE), 101–102
- Novel Uranium Extraction (NUEX) process, 503–504
- Nozzle process, 356
- $\text{Np}-\text{C}-\text{O}-\text{H}$ speciation diagram, 83*b*
- NpF_6 , 508–510
- $\text{Np}-\text{O}-\text{H}$ Pourbaix diagram, 81*b*
- NPP. *See* Nuclear power plant (NPP)
- NRU. *See* National Reactor Universal (NRU)
- NSE. *See* Normal spectral emissivity (NSE)
- NU. *See* Natural uranium (NU)
- Nuclear Energy Agency (NEA), 316, 502
- Nuclear Energy Agency-Organization for Economic Cooperation and Development (NEA-OECD), 69
- Nuclear fission, 471
- Nuclear fuel, 3, 229, 422, 478. *See also*
 - Nitride fuels; Thermochemistry of nuclear fuel
 - cycle, 315, 371
 - irradiation damages in, 423*t*
 - samples, 108–109
 - thermodynamics of nuclear fuel and fission products, 49–69
 - chemical state of fission products, 66–69
 - melting transition, 55–56
 - nonstoichiometry effect on thermodynamic properties, 56–60
 - phase diagrams, 49–55
 - sublimation and vaporization behavior, 60–66
- Nuclear magnetic resonance (NMR), 121, 131–135
 - examples of NMR spectra, 134–135
 - high-resolution solid-state, 133–134
 - liquid state, 131
 - low-temperature, 131–133
- Nuclear power plant (NPP), 527
- Nuclear reactions, 185–188, 188*t*
 - approximate mass proportions of plutonium isotopes, 187*t*
 - calcium fluorite structure, 186*f*
 - oxidation states and properties, 186*t*
- Nuclear technology, 469

O

O/M ratios. *See* Oxygen-to-metal ratios (O/M ratios)
Oak Ridge National Laboratory (ORNL), 251
OECD. *See* Organization for Economic Co-operation and Development (OECD)
Open nuclear cycles, 530–532
Open pit mining, 319–320
Organic iodides (Org-I), 608, 610
Organic solvent, 334
Organization for Economic Co-operation and Development (OECD), 316, 502
ORNL. *See* Oak Ridge National Laboratory (ORNL)
Oxalate, 69
Oxidation, 221–222, 481–482
 runaway, 557–559
 of Zr-based cladding, 7*b*
 of Zry cladding, 557–563
Oxide fuels, 203, 433–434
 fabrication
 additives to UO₂, 374–375
 advanced fabrication of UO₂, 375–379
 commercial oxide fuel production, 372–373, 373*f*
 irradiated oxide fuel, 438–462
UO₂ and (U, Pu)O₂ oxides, 433–437
 cavitation in uranium metallic fuel, 433*f*
 MOX fuel, 437–438
Oxide power reactor fuels
 binary and higher order oxide phase diagrams, 193–203
 crystal structures of various oxide nuclear fuels, 185
 doped fuels, 203–207
 nuclear reactions, 185–188
 phase diagrams involving UO₂, PuO₂, and ThO₂, 189–193
 plutonium–oxygen system and PuO₂, 191–192
 thorium–oxygen system and ThO₂, 192–193
 uranium–oxygen system and UO₂, 189–191
 thermal conductivity profiles for U–Pu–Th–O system, 188–189
Oxide precipitates, 66

Oxidizing nitric acid, 501

Oxido-reducing conditions, 604–605

Oxyfluorides, 508, 510

Oxygen

 chemical potential, 58

 effect of oxygen impurities, 268

 stoichiometry, 435, 437

 vacancies, 458–459

Oxygen bomb calorimetry, 17

Oxygen potential, 145, 453–454, 455*f*

 effects, 196

 and fission products, 241–242

 oxides from carbides, 241*f*

Oxygen-to-metal ratios (O/M ratios), 97–98, 597–598

P

Palladium (Pd), 237

 corrosion of SiC layer, 238*f*

PALS method. *See* Positron annihilation

 lifetime spectroscopy method (PALS method)

Partitioning function, 39

PCI. *See* Pellet–cladding interactions (PCI)

PCV. *See* Primary containment vessel (PCV)

Peak power node (PPN), 428

Pebble-bed nuclear fuel, 491–493

Pellet fabrication, 401–402, 402*f*

Pellet–cladding interactions (PCI), 374

Pertechnetic acid (HTeO₄), 501

PES. *See* Photoelectron spectroscopy (PES)

Ph ring. *See* Phenyl ring (Ph ring)

Phase diagrams, 49–55

 binary and higher order oxide, 193–203
 construction, 173–175

 binary phase diagrams, 174, 174*f*

 Pourbaix diagrams, 175

 ternary phase diagrams, 174

Cs–I, 443, 444*f*

Cs–Mo–O, 444, 445*f*

Cs–U–O, 444, 445*f*

Gibbs phase rule, 50–51

 involving UO₂, PuO₂, and ThO₂, 189–193

 plutonium–oxygen system and PuO₂, 191–192

 thorium–oxygen system and ThO₂, 192–193

- Phase diagrams (*Continued*)
 uranium-oxygen system and UO_2 , 189–191
 terminology and lever rule, 52–55
- Phase equilibria in binary mixtures of DSC, 91–93
- Phase stability, 386
- Phase/element distribution during solidification, 589–592
- Phébus FP programme/tests, 577, 581, 605–606, 608–609
 test matrix, 578*t*
- Phenyl ring (Ph ring), 134–135
- Phonon contribution, 22
- Phosphate, 69
- Photoelectron spectroscopy (PES), 116–121, 117*f*
- PHWR. *See* Pressurized heavy-water reactors (PHWR)
- Physically sorbed water, 540
- Physisorbed water. *See* Physically sorbed water
 “Picture frame”, 281–283
- PIE. *See* Postirradiation examination (PIE)
- PIM. *See* Powder injection molding (PIM)
- Planck radiance spectra, 103–104
- Plate-type fuels, 274
- Platinum-based thermocouples, 96
- Plutonium (Pu), 3, 387, 420
 radial evolution of bubbles in, 430*f*
- Plutonium dioxide, 59–60
- Plutonium–oxygen system and PuO_2 , 191–192
 Pu–O phase diagram as modelled, 192*f*
 Pu–O phase diagram emphasizing the PuO_{2-x} region, 193*f*
- Polarizability, 109
- Polyatomic gas, 51*b*
- Polycrystalline UO_2 fuel, 529
- Polymetallic iron-oxide, 316–318
- Polymorphs, 15
- Polythermal liquidus projection, 55
- Pool scrubbing in suppression pools, 617–618
- Positron annihilation lifetime spectroscopy method (PALS method), 126–127, 129*f*
- Positron annihilation spectroscopy, 126–130
- Positronium (Ps), 126
- Postirradiation examination (PIE), 425–426, 442
- Potassium hydroxide, 500
- Pourbaix diagrams, 77–81, 175, 176*f*
- Powder injection molding (PIM), 378
 UO_2 , 378–379
- Power reactor fuels
 coated particle fuels, 231–242
 metallic fuels, 216–220
 molybdenum-based metallic fuels, 220
 nontraditional ceramic fuels, 220–231
 zirconium-based metallic fuels, 216–220
- PPN. *See* Peak power node (PPN)
- Precipitation, 71–72, 325–326
- Pressure of nitrogen (P_{N_2}), 227
- Pressure vessel failure, 233
- Pressurized heavy-water reactors (PHWR), 332, 342
 ceramic-grade UO_2 production for, 342–343
- Pressurized water reactor (PWR), 420, 427, 429, 461, 557. *See also* Light water reactors (LWRs); Boiling water reactor (BWR)
 fuel, 470, 478, 493–494
 average weight composition, 472*f*
 in CANDU, 493–494
 Westinghouse, 471*f*
 metallograph on cross section, 430*f*
 neutron spectrum, 475
- Primary containment vessel (PCV), 555–556
- Primary ion beam, 137–138
- Probabilities, 36–37
- Protactinium (Pa), 187
- Prototypic SA, 555
- ^{239}Pu isotopes, 438, 527, 529–530
- PuF_6 , 508–510
- Pulsed electric current sintering. *See* Spark plasma sintering (SPS)
- PuO_2 , 187, 188*t*, 189–193
- PUREX process, 502–504
- PWR. *See* Pressurized water reactor (PWR)
- Pyrochemical fuel salt synthesis, 406–407
- Pyrochemical processes, 506–507
- Pyrometer calibration, 105–106
- Q**
- Quality control (QC), 405

- QUENCH program, 572
- R**
- R&D. *See* Research and development (R&D)
- R/B. *See* Reactor building (R/B)
- Radiation damage, 422–428
- radial temperature profiles in fuel rod in fast reactor, 427*f*
 - temperature distribution, 426–428
- Radiation-enhanced damage mechanisms, 542
- Radioactive material transport and deposition, 611–612
- Radioactive release mitigation for long-term accidents, 614–615
- Radioactive waste management, 533
- Radioisotope Na²², 127–128
- Raman effect, 109
- Raman spectroscopy, 108–110
- Raoult's law, 30–31
- Raoultian standard state, 31
- RAR. *See* Reasonably assured resources (RAR)
- Rare earth elements (RE elements), 445
- Rayleigh equation, 122
- RCS. *See* Reactor coolant system (RCS)
- RE elements. *See* Rare earth elements (RE elements)
- Reaction escalation, 557–559
- Reaction rates, 4–7
- Reactor building (R/B), 556
- Reactor coolant system (RCS), 556
- Reactor fuels, 273
- corrosion of aluminum research reactor fuel cladding, 303–304
 - evolution of research reactor fuel during operation, 278–281
 - fabrication processes, 281–284
 - fuel behavior under irradiation, 284–303
 - fuel geometry, 274–275
 - fuel materials, 276–278
- Reactor pressure vessel (RPV), 555–556
- Reasonably assured resources (RAR), 315
- Reconversion, 361
- Recycled uranium (RU), 473
- Redox equilibria basics, 72–83
- and Galvanic cell, 73–77
- Gibbs energy of redox reaction and Nernst equation, 76–77
- Pourbaix diagrams, 77–81
- speciation diagrams, 82–83
- Redox potential
- of fuel, 265–268
 - corrosion inhibition, 266–267
 - fission product speciation, 267–268
 - monitoring during reactor operation, 268
 - monitoring during reactor operation, 268
- Redox reaction, 73
- Reference states, 15–16
- Reflected light signal analysis (RLS analysis), 103
- Regenerated mixture (REMIX), 475
- uranium and plutonium content in, 475*t*
- Remobilization and transfer of radioactivity for long-term accidents, 613–614
- Remobilization of fission product deposits, 601–602
- REPA. *See* REprocessing-PArtitioning (REPA)
- Repository, 537–538
- Reprocessing and recycling
- alternative or advanced fuels, 489–497
 - characteristics of used nuclear fuel, 470–473
 - recoverable components in used nuclear fuel, 473*t*
 - off-gas treatment and emission controls, 497–501
 - carbon-14, 500
 - iodine, 498–499
 - krypton, 500–501
 - noble metals and other semivolatiles, 501
 - tritium, 499–500
- separations, 501–516
- fluoride volatility, 508–511
 - hybrid aqueous processing, 506
 - hydrometallurgical, 502–506
 - pyrochemical processes, 506–507
- Zircaloy-clad fuels for hydrometallurgical separations, 478–489, 479*f*
- REprocessing-PArtitioning (REPA), 503–504
- Research and development (R&D), 371–372
- scale arc melt furnace, 388*f*

- Research reactor fuel during operation, 278–281
- Rietveld refinement approach, 140–141
- Rigid rotor/harmonic oscillator model, limitations of, 47–48
- Rim effect, 529–530
- RLS analysis. *See* Reflected light signal analysis (RLS analysis)
- Rod-and pin-type fuels, 275
rod-type fuels, 277f
- Rolling process, 393–394
Stanat TA-215 Rolling Mill, 394f
- Rotational partition function, 43–45
- RPV. *See* Reactor pressure vessel (RPV)
- RU. *See* Recycled uranium (RU)
- Ru–N–O–H chemistry during transport in the reactor coolant system, 601
- Ruthenium chemistry, 608–610
- Ruthenium tetroxide (RuO_4), 501
- S**
- SA. *See* Severe accident (SA)
- Sackur–Tetrode equation, 41
- Scanning electron microscopy (SEM), 121–126, 285–286
- Scanning tunneling microscopy (STM), 121
- SCC. *See* Stress corrosion cracking (SCC)
- Schottky anomalies, 22–24
- Scrubber filtered containment venting systems, 617–618
- SE. *See* Secondary electrons (SE)
- Sea salt powder, 593
- Sea-water injection, 598
- Second law of thermodynamics, 11
- Second law method, 63
- Second-order kinetic reaction, 7
- Second-order transitions, 15
- Secondary Electron Microprobe and Energy-Dispersed X-ray analysis (SEM–EDX), 585–587
- Secondary electrons (SE), 123
- Secondary hydriding, 563
- Secondary ions mass spectrometry (SIMS), 121, 137–139
- Selection rules, 110
- Selenium (Se), 66
- SEM. *See* Scanning electron microscopy (SEM)
- Sensitivity of calorimeter, 96
- Separate-effect simulated-test, 555, 570, 574, 582
- Separation isotopes laser excitation (SILEX), 352–353, 353f
- Separative work units (SWU), 344–345
- SER state. *See* Standard element reference state (SER state)
- Setaram multi-detector high-temperature calorimeter, 95–96, 95f
- Severe accident (SA), 555
- SHE. *See* Standard hydrogen electrode (SHE)
- Sieverts' law, 559–561
- SILEX. *See* Separation isotopes laser excitation (SILEX)
- Silicate, 69
- Silos, storage in, 535, 535f
- Silver (Ag), 237–238
- Silver zeolite (AgZ), 499–500
- Silver–indium–cadmium (AIC), 569
control rod, 569–570
- Sim-FDNPS, 585
microhardness of various phases in, 588f
- Sim-test, 561
- SIMFUELS, 456
- SIMS. *See* Secondary ions mass spectrometry (SIMS)
- Single crystal XRD, 140
- Single-component condensed phase, chemical potential of, 28–29
- Sintering, 376–378
- SNF. *See* Spent nuclear fuel (SNF)
- Sodium carbonate (Na_4CO_3), 322
- Sodium chlorate oxidation, 321–322
- Sodium fluoride, 510–511
- Sodium hydroxide, 500
- Sol–gel and hydrothermal routes for nanocrystalline UO_2 synthesis, 376
- Solid sorbent systems, 498
- Solidification, 391
- Solubility, 71–72
of actinoids, 259
constants, 74b
curves, 52–53
- Soluble fission product impurities, effect of, 269
- Solution calorimetry, 16
- Solution thermodynamics

- applied to storage of spent fuel and geological disposal, 69–72
hydrolysis and complexation, 69–71
solubility and precipitation, 71–72
Solvent extraction, 325, 334, 502–506
Sommerfeld coefficient, 22
Spark plasma sintering (SPS), 371, 376–377, 383–384, 401–402
Speciation diagrams, 82–83
Spectroscopy, 50*b*, 106–130
 electron microscopy and spectroscopy, 121–126
 PES, 116–121
 positron annihilation spectroscopy, 126–130
 vibrational spectroscopy methods, 107–111
 XAS, 111–116
Spent nuclear fuel (SNF), 69, 405, 527
 dissolution and alteration of SNF under deep geological repository conditions, 543–546
 chemical processes, 544*f*
 international situation of temporary storage, 548*t*
generalities, 527–530
 microstructure of spent fuel, 529*f*
 relative radioactivity of typical LWR spent nuclear fuel, 528*f*
and high-level waste geological disposal, 536–539
management strategies, 530–532
 and high-level waste storage, 532–536
 status of total SNF discharged from NPPs, 531*f*
SPS. *See* Spark plasma sintering (SPS)
SS. *See* Stainless steel (SS)
Stability
 constants, 72*b*
 to radiation, 260–261
Stainless steel (SS), 569
Standard chemical potential, 27–28
Standard element reference state (SER state), 16
Standard entropy, 19–20
Standard hydrogen electrode (SHE), 75
Standard molar enthalpy of formation, 16
Standard states, 15–16, 30–31
Standard substance reference state, 16
Statistical thermodynamics to gases, 35–49
 Boltzmann distribution law, 35–36
 canonical partition function, 37–39
 ensembles and probabilities, 36–37
 molecular thermodynamic calculations, 41–42
partitioning function, 39
thermodynamic functions, 39–41
vibrational partition function, 42–49
Steam-starved atmosphere, 559
Stirling's approximation, 40
STM. *See* Scanning tunneling microscopy (STM)
Stoichiometry zone, 145
Stress corrosion cracking (SCC), 443
Strontium (Sr), 66
Sublimation, 60–66
Sulfate, 69
Sulfite, 69
Sulfuric acid, 320–321, 324
Surface processes, 119
SWU. *See* Separative work units (SWU)
Symmetric potential function, 47
Symmetry number, 43–44
Synchrotron radiation sources, 114
- T**
- T2EHDGA. *See* *N*'-Tetra (2-ethylhexyl) diglycolamide (T2EHDGA)
TAF-ID. *See* Thermodynamics of Advanced Fuels—International Database (TAF-ID)
Tailings, 326–328
TBP. *See* Tri-n-butyl phosphate (TBP)
TDB. *See* Thermochemical Database (TDB)
TDS. *See* Thermal desorption spectroscopy (TDS)
Tellurium (Te), 66
Tellurium-Tellurium (Ba-Te), 229
TEM. *See* Transmission electron microscopy (TEM)
TEM-BF. *See* Transmission electron microscopy-bright field (TEM-BF)
TEM-DF. *See* Transmission electron microscopy-dark field (TEM-DF)
Temperature, 35
 dependence of rate constants, 7–8
Ternary phase diagrams, 174, 175*f*
Ternary phase rule, 563–564

- N*⁺-Tetra (2-ethylhexyl) diglycolamide (T2EHDGA), 506
- N*⁺-Tetraoctyl diglycolamide (TODGA), 504–505
- TGA. *See* Thermo-gravimetric analysis (TGA)
- Thermal analysis methods, 90–106
- drop calorimetry, 95–97
 - DSC, 90–94
 - laser heating, 101–106
 - TGA, 97–100
- Thermal arrests, 103–104
- Thermal conductivity profiles for U–Pu–Th–O system, 188–189, 189f, 190f
- Thermal cycles, 106
- Thermal denitration, 336
- Thermal desorption spectroscopy (TDS), 121
- Thermal diffusion process, 354–355, 356f, 357f
- UF₆ diffusion columns, S-50 liquid, 358f
- Thermal diffusivity, 106
- Thermal excursions, 529–530
- Thermal functions, 42
- Thermal gradient, 235
- Thermal radiation pyrometers, 101–102
- Thermochemical Database (TDB), 69
- Thermochemical predictions, 159
- Thermochemistry of nuclear fuel. *See also*
- Nuclear fuel
 - CALPHAD method, 169–172
 - equilibrium in closed isothermal–isobaric system, 166–169
 - Gibbs Criteria, 168f
 - necessary conditions, 166–167
 - sufficient conditions, 168–169
 - GEM, 169
 - molar Gibbs energy, 172f
 - oxidation measurements, 171f
 - theoretical and modeling frameworks, 160f
 - thermodynamic laws, 161–162
 - thermodynamic properties, 162–165
- Thermodynamic databases, 169–170
- applications and limitations of
 - computational, 173–179 - modeled solidus and liquidus regions
 - HFA may form in MOX fuel, 178f
 - integral analyses, 175–177
- phase diagram construction, 173–175
- phase diagrams of Th–O system, 179f
- thermodynamic calculations, 177–179
- Thermodynamic(s)
- approach, 566–568
 - of condensed phases, 15–35
 - functions, 39–41
 - laws, 10–11, 161–162
 - first law, 10–11
 - second law, 11
 - third law, 11 - model of Th–U–Pu–O, 193
 - Th–O phase diagram, 193, 194f
 - of nuclear fuel and fission products, 49–69
 - relations between state functions, 15
 - system and state functions, 9–10
 - system composition, 9–10
- Thermodynamics of Advanced Fuels— International Database (TAF-ID), 175–176, 563–564
- Thermogram, 103
- Thermo-gravimetric analysis (TGA), 90, 97–100
- Thermomechanical processing, 392–396, 399
- coextrusion, 394–396
 - heat treatment, 397–399
 - rolling, 393–394
- Thionyl chloride (SOCl₂), 488–489, 489f
- Third law
- method, 63
 - of thermodynamics, 11
- ThO₂–PuO₂ binary system, 197–203, 201f, 202f
- phase diagram of, 200f
 - pseudo-binary phase diagram, 200f
 - UO₂–ThO₂–UO₃ pseudo-ternary phase, 202f
- ThO₂–UO₂ binary system, 195–196, 201f
- thermal arrests for six MOX, 199f
 - thermodynamic model of, 197f
 - UO₂–ThO₂ phase diagram reevaluated, 196f
 - UO₂–ThO₂–O pseudo-ternary, 204f
- Thorex, 497
- Thorium dioxide (ThO₂), 55–56, 187, 188t, 189–193
- Thorium MSR, 254

- Thorium oxide, 60
Thorium-enhanced fuels, 494–497
Thorium–oxygen system, 192–193
Three Mile Island-2 accident (TMI-2 accident), 555
Tie-line or conode, 53
“Tilt” pour. *See* Vacuum induction furnace
Titania (TiO_2), 205
TMI-2 accident. *See* Three Mile Island-2 accident (TMI-2 accident)
TODGA. *See* N° -Tetraoctyl diglycolamide (TODGA)
Traditional powder metallurgical methods, 371
Training, Isotope, General Atomics (TRIGA), 274
reactors, 301
Translational partition function, 41
Transmission electron microscopy (TEM), 121–126, 285–286
Transmission electron microscopy-bright field (TEM-BF), 124–125
Transmission electron microscopy-dark field (TEM-DF), 124–125
Transmission XAS measurements, 114
Transmutation process, 251
Transmuter concept, 254
Transuranium (TRU), 254, 471
Tri-n-butyl phosphate (TBP), 334, 484–485, 502
TRIGA. *See* Training, Isotope, General Atomics (TRIGA)
Tristructural isotropic coated particle (TRISO coated particle), 231–232, 231f, 403. *See also* Alternate TRISO fuels
Tristructural isotropic fabrication, 403–405
Tristructural isotropic particles (TRISO) particles, 371
Tritium, 499–500
released by cladding recycle, 500
released by voloxidation of fuel, 499–500
Tritium chloride, 488
Triuranium octaoxide (U_3O_8), 331–332
Triuranium octoxide, 486
TRU. *See* Transuranium (TRU)
TRU extraction–trivalent actinide lanthanide separation with phosphorus-reagent extraction from aqueous complexes (TRUEX–TALSPEAK), 506
Tubular fuels, 275
Two-dimensional defect structures, 281
- U**
 ^{234}U isotopes, 343–344, 475
 ^{235}U isotopes, 343–344, 352–354, 438, 527
 ^{236}U isotopes, 475
 ^{238}U isotopes, 343–344, 352–354, 529–530
U-Mo fuels, 220
U-Pu-Zr alloys, 218
U-Zr. *See* Uranium zirconium (U-Zr)
U–19Pu–10Zr fuel, 217
 U_3O_8 –Al system, 291
 U_3Si – U_3Si_2 system, 286
UC. *See* Uranium monocarbide (UC)
U–C binary phase diagram, 223, 224f
Ugine Séjournet process, 396
Ultraviolet PES (UPS), 116
U–Mo/Al system.
 See Uranium–molybdenum alloys system (U–Mo/Al system)
UN. *See* Uranium mononitride (UN)
Underground mining, 320
UNH. *See* Uranyl nitrate hexahydrate (UNH)
Unirradiated nuclear fuels, 104
 UO_2 – PuO_2 binary system, 195, 196f
 UO_2 – ThO_2 isopleths, 197
 UO_2 – ThO_2 – PuO_2 diagrams, 203, 205f
 UO_3 powders, 484–485
 UO_4nH_2O . *See* Uranyl peroxide (UO_4)
UOC. *See* Uranium ore concentration (UOC)
UPS. *See* Ultraviolet PES (UPS)
Uranium (U), 3, 316, 323, 407, 420, 434f, 473, 497, 527
alloys, 396
bearing minerals, 316–318, 318t
concentration, 285
conversion, 331–343
enrichment, 331, 343–361
isotope separation, 357
metal, 190, 386
mills, 324
purification, 334
refining/conversion, 334
resources, 316, 317f
Uranium aluminides, 284–286

- Uranium borides, 385
 micrograph of UN hot isostatically press, 385*f*
 micrographs of UN from SPS, 384*f*
- Uranium carbide. *See* Uranium monocarbide (UC)
- Uranium chlorides, 513
- Uranium dicarbide (UC₂), 223
- Uranium dioxide (UO₂), 56–57, 189–190, 232, 275, 291, 371, 420, 434–436, 470
 additives to, 374–375
 advanced fabrication, 375–379
 commercial powder metallurgy, 373
 fission product phases formed in, 456*t*
 fluorite crystalline structure, 435*f*
 fuels, 187, 188*t*, 189–193, 206
 liquefaction between Zry cladding and, 563–568, 564*f*, 569*f*
 gas release in irradiated, 431*f*
 partial pressure of O₂, 436*f*, 439*f*
 solid-state synthesis, 373
 UO₂-zirconium system, 230
- Uranium halides, 383
- Uranium hexafluoride (UF₆), 332–334, 333*t*, 338–340, 361, 474
 dry fluoride volatility process, 340–341, 341*f*
 in nuclear fuel cycle, 332–334, 332*f*
 quality and transportation of enriched, 361
 wet conversion processes for production of, 334–340
 concentration, 336
 denitration, 336–337
 dissolution, 334
 fluorination, 338–340
 hydrofluorination, 337–338
 reduction, 337
 solvent extraction, 334–336
- Uranium monocarbide (UC), 220–222, 379
 actinoids and fission products in, 224–225
- Uranium mononitride (UN), 220–221, 226, 379
 synthesis and fabrication techniques, 380–384
- Uranium ore concentration (UOC), 326, 331–332, 334, 335*f*
- Uranium oxide ceramics (UO₂ and U₃O₈), 274
- Uranium oxides, 290–293
 microstructure of U₃O₈, 292*f*
- Uranium oxy-carbide fuel (UCO), 232
- Uranium sesquicarbide (U₂C₃), 223
- Uranium silicides, 286–290
 breakaway swelling behavior, 289*f*
 compounds, 399–400
 microscopic swelling behavior, 287*f*
 nanoscale fission gas bubbles, 290*f*
 pellet fabrication, 400–402
 alloying additions to U–Si fuels, 402
 compound synthesis, 400–401
 pellet fabrication, 401–402, 402*f*
- Uranium tetrachloride (UCl₄), 337–338, 383
- Uranium tetraiodide (UI₄), 383
- Uranium trioxide (UO₃), 334, 342–343, 363–364
- Uranium zirconium (U-Zr), 216–217
- Uranium-molybdenum fuel, 220
- Uranium-nitrogen binary system, 226–227
- Uranium-oxygen system and UO₂, 189–191
 partial U–O diagram concentrating, 191*f*
- Uranium-plutonium dioxide ((U,Pu)O₂), 224
- Uranium-plutonium monocarbide fuel ((U, Pu)C fuel), 224
- Uranium–aluminum alloys, 284
- Uranium–boron binary system, 385
- Uranium–molybdenum alloys system (U–Mo/Al system), 293–301
 BSE images, 297*f*
 bubble formation, 300*f*
 EBSD of as-fabricated U–Mo fuel particle, 298*f*
 failures in U–Mo pin-type, 298*f*
 microstructure of interaction layer, 300*f*
 SEM micrograph, 301*f*, 302*f*
 TEM micrograph of fission gas, 296*f*
 time–temperature–transformation diagrams, 294*f*
 uranium-rich region, 294*f*
- X-ray diffraction data for a U–9Mo alloy, 295*f*
- Uranium–plutonium mononitride [(U,Pu)N], 379
- Uranium–zirconium (U-Zr), 218
 alloys, 216–217
 fuels, 217

- partial binary phase diagram, 218*f*
restructuring in, 218–219
zirconium content as calculated, 219*f*
- Uranium–zirconium hydride fuel system
(U–Zr–H fuel system), 274,
301–303
- Urano/uranoplutonate cesium compounds,
444
- Uranyl fluoride (UO_2F_2), 362–363
- Uranyl nitrate hexahydrate (UNH), 336
- Uranyl peroxide (UO_4), 323, 331–332
- UREX process, 482–483, 503–504
- US Department of Energy (DOE), 394–395
- US HTGR fuel, 236–237
- U–Zr–H fuel system.
See Uranium–zirconium hydride fuel system (U–Zr–H fuel system)
- V**
- Vacuum arc remelting (VAR), 389
- Vacuum drying method, 540
- Vacuum induction furnace, 390
- Vacuum induction melting methods (VIM
methods), 389–392
pilot scale tilt-pour VIM, 390*f*
- Van't Hoff equation, 35
- Vanadia (V_2O_5), 205
- Vapor pressure, 60, 257–258
- Vapor species, 556
- Vaporization behavior, 60–66
- VAR. *See* Vacuum arc remelting (VAR)
- Ventilation procedures, 535
- VERCORS tests, 579–580, 606–607
- VERDON-1 test, 175–176, 177*f*
- VERDON-2 test, 601–602
- Vibrational partition function, 42–49
coupling of internal motion, 45–46
hindered rotation, 46–47
limitations of rigid rotor/harmonic
oscillator model, 47–48
rotational partition function, 43–45
- Vibrational spectroscopy methods, 107–111
- VIM methods. *See* Vacuum induction
melting methods (VIM methods)
- Volatile
fluorides, 510
inorganic fluorides, 339–340
species, 66
zirconium tetrachloride, 488
- Voloxidation, 482–485, 484*f*, 499
coupled end-to-end demonstration at
multikilogram scale, 482–483
dissolution following advanced, 486–487
dissolution following oxygen-based,
486
- early development, 482
- of irradiated fuel, 483*f*
process using NO_2 , 484*f*
recent advanced methods, 483–485
- Voltage, 75
- W**
- Waste Isolation Pilot Plant (WIPP),
532
- Wavelength dispersive spectroscopy (WDS),
123
- Wet centralized storage, 532–533
- Wet chemical processing to produce UO_2 ,
372
- Wet conversion processes, 362–364
ADU route, 362–363, 362*f*
AUC route, 363–364, 363*f*
- Wet storage, 532–533
- White line (WL), 113–114
- WIPP. *See* Waste Isolation Pilot Plant
(WIPP)
- WL. *See* White line (WL)
- X**
- X-ray
absorption measurements, 114
fluorescence, 112–113
microanalysis, 442
photon, 111–112
- X-ray absorption near-edge spectroscopy
(XANES), 113
- X-ray absorption spectroscopy (XAS),
111–116
- X-ray diffraction (XRD), 98, 139–141,
262–263
- X-ray PES (XPS), 116
- XANES. *See* X-ray absorption near-edge
spectroscopy (XANES)
- XAS. *See* X-ray absorption spectroscopy
(XAS)
- Xenon (Xe), 66
- XPS. *See* X-ray PES (XPS)
- XRD. *See* X-ray diffraction (XRD)

Y

Y_2O_3 , 207
Yttrium (Y), 66, 445

Z

Zero-point energy, 42–43
Zircaloy (Zry), 7*b*, 52–53, 371, 395,
476–477
channel box, 572–576
cladding, 480–481, 563–568, 564*f*, 569*f*
Zircaloy-clad fuels, 478
clarification and accounting, 487
disassembly and decladding, 480–482
alternative mechanical-segmenting
methods, 480
chemical decladding methods, 480–481
hybrid decladding methods, 481–482
thionyl chloride–based chemical
decladding, 481, 481*f*
disposition of cladding, 487–489
current industrial practice, 487–488
zirconium recovery for alternative
dispositions, 488–489
nitric acid dissolution, 485–487
voloxidation, 482–485
Zirconium (Zr), 66, 387, 437, 445
metal, 476–477
metallic fuels, 216–220
fission product migration, 219–220
restructuring in U-Zr fuels, 218–219
solidus, 217*f*
recycle, 476–477, 500
interfaces, 476*f*
zirconium-based alloy, 371
Zirconium alloy. *See* Zircaloy (Zry)
Zirconium dioxide, 488
Zirconium oxide (ZrO_2), 481, 489
Zirconium tetrachloride ($\text{ZrCl}_4 \text{ SOCl}_2$),
488–489
Zr-based cladding, oxidation of, 7*b*
 ZrCl_4 , 488
gaseous, 480–481
Zr–H–O ternary phase diagram, 559, 560*f*
Zry. *See* Zircaloy (Zry)

WOODHEAD PUBLISHING SERIES IN ENERGY

A consolidated reference covering all stages of nuclear fuel chemistry, with particular focus on traditional and non-traditional fuel cycles, from mining and manufacturing, through to spent fuel management and disposal, including conventional fuels, accident tolerant fuels, molten salts, and other advanced fuels.

Advances in Nuclear Fuel Chemistry presents a high-level description of nuclear fuel chemistry based on the most recent research and advances. **Dr. Markus H.A. Piro** and his team of expert contributors from around the world cover all aspects of both the conventional uranium-based nuclear fuel cycle and non-conventional fuel cycles, including mining, refining, fabrication, and long-term storage, as well as discussing emerging nuclear technologies, such as accident tolerant fuels and molten salt materials.

Aimed at graduate students, researchers, and academics of Nuclear Energy and Engineering as well as practicing engineers and regulators, this book will provide the reader with one single reference to learn the fundamentals of classical thermodynamics and radiochemistry, before moving on to more advanced topics, such as fission product behaviour in irradiated fuel.

Key Features:

- Consolidates the latest research on nuclear fuel chemistry into one comprehensive reference, covering all aspects of traditional and non-traditional nuclear fuel cycles
- Includes contributions from world-renowned experts from many countries representing government, industry, and academia.
- Covers a variety of fuel designs – including conventional uranium dioxide, mixed oxides, research reactor fuels, and molten salt fuels – written by experts with hands-on experience of the development of such designs.

About the Editor

Dr. Markus H.A. Piro, Assistant Professor and Canada Research Chair (Tier II) in Nuclear Fuels and Materials at Ontario Tech University.

Technology and Engineering /
Power Resources

ISBN 978-0-08-102571-0



WP

WOODHEAD
PUBLISHING

An imprint of Elsevier
elsevier.com/books-and-journals



9 780081 025710